IEE Radar Series 15

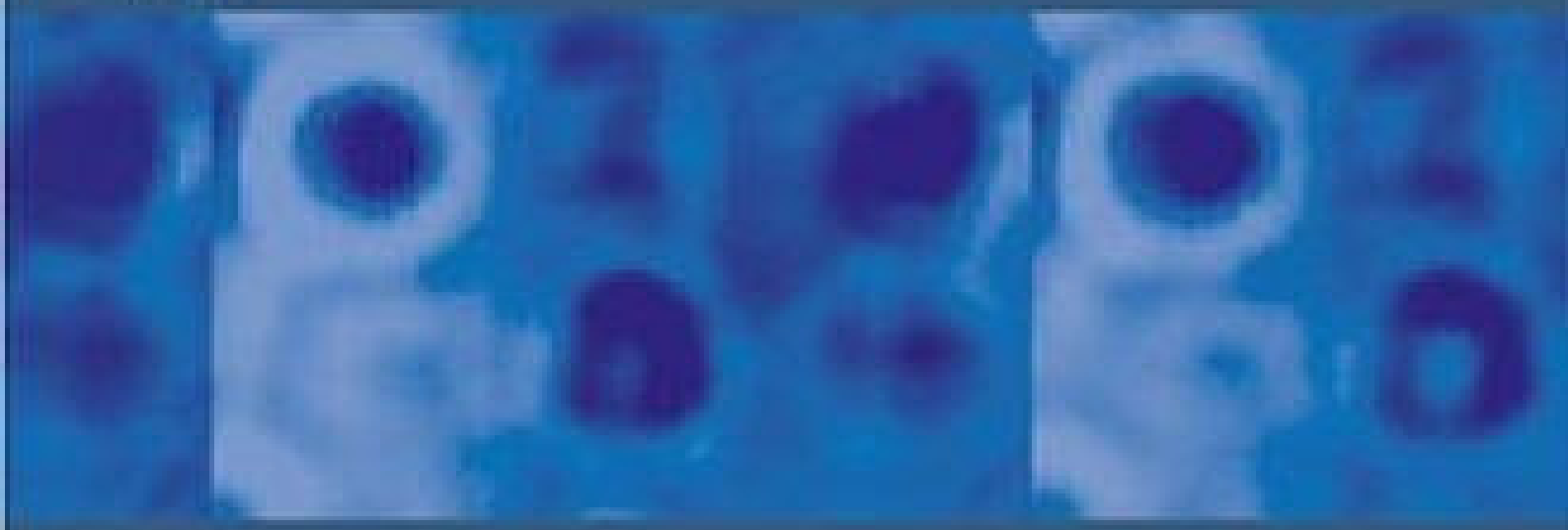

Ground Penetrating Radar 2nd Edition

Edited by David J. Daniels

Ground Penetrating Radar – 2nd Edition

Edited by
David J. Daniels

The Institution of Electrical Engineers

Published by: The Institution of Electrical Engineers, London,
United Kingdom

© 2004: The Institution of Electrical Engineers

This publication is copyright under the Berne Convention and the Universal Copyright Convention. All rights reserved. Apart from any fair dealing for the purposes of research or private study, or criticism or review, as permitted under the Copyright, Designs and Patents Act, 1988, this publication may be reproduced, stored or transmitted, in any forms or by any means, only with the prior permission in writing of the publishers, or in the case of reprographic reproduction in accordance with the terms of licences issued by the Copyright Licensing Agency. Inquiries concerning reproduction outside those terms should be sent to the publishers at the undermentioned address:

The Institution of Electrical Engineers,
Michael Faraday House,
Six Hills Way, Stevenage,
Herts., SG1 2AY, United Kingdom

While the authors and the publishers believe that the information and guidance given in this work are correct, all parties must rely upon their own skill and judgment when making use of them. Neither the authors nor the publishers assume any liability to anyone for any loss or damage caused by any error or omission in the work, whether such error or omission is the result of negligence or any other cause. Any and all such liability is disclaimed.

The moral right of the authors to be identified as authors of this work have been asserted by them in accordance with the Copyright, Designs and Patents Act 1988.

The CD in the back of this book includes an Evaluation Version of Mathcad® 11 Single User Edition, which is reproduced by permission. This software is a fully-functional trial of Mathcad which will expire 15 days from installation. For technical support, more information about purchasing Mathcad, or upgrading from previous editions, see http://www.mathcad.com.

Mathcad is a registered trademark of Mathsoft Engineering and Education, Inc., http://www.mathsoft.com. Mathsoft Engineering & Education, Inc. owns both the Mathcad software program and its documentation. Both the program and documentation are copyrighted with all rights reserved by Mathsoft. No part of the program or its documentation may be produced, transmitted, transcribed, stored in a retrieval system, or translated into any language in any form without the written permission of Mathsoft.

British Library Cataloguing in Publication Data

Daniels, David
Ground-penetrating radar. – 2nd ed. – (Radar, sonar, navigations & avionics)
1.Ground penetrating radar
I.Title II.Surface penetrating radar
621.3'848

ISBN 0 86341 360 9

Typeset in India by Newgen Imaging Systems (P) Ltd., Chennai, India
Printed in the UK by MPG Books Limited, Bodmin, Cornwall

Preface to the second edition

Since the first edition of 'Surface penetrating radar' was published in 1996 there has been an enormous increase in research work, in publications, in hardware developments, in equipment and in radar performance. The term ground penetrating radar (GPR) has now become the accepted terminology for the science and technology, so that it was considered more in line with current practice to title the book 'Ground penetrating radar' even though it is a direct descendant of the first edition of 'Surface penetrating radar'.

Ground penetrating radar has now reached a level of maturity, but there are still more performance gains to be made. One aim of this new edition is to provide a snapshot of the enormous range of applications for GPR. The problem with snapshots is that they are fleeting and often incomplete. I hope those working in the field that have not been involved with this edition will understand that it is impossible to be encyclopaedic and that there should be sufficient references and guides to sources of information to cover any omissions.

The first edition received a very encouraging response and I am particularly grateful for the interest of a number of contributors. The late Professor James Wait very kindly suggested changes to the original material in the early chapters, which improved the clarity of the presentation. I am also very grateful to Dr S. Evans from the University of Cambridge and to Dr Yi Huang from the University of Liverpool, who drew my attention to inconsistencies in the text.

The main aim of the second edition is to incorporate the advances in understanding and developments in techniques that have taken place since the first edition was written. The use of radar for the detection of buried objects is growing, and better understanding of the physics as well as improved technology has much enhanced the technology. GPR is now an established branch of radar technology. There is, however, much to be done in terms of improved signal processing and analysis and I hope that this flavour has permeated the second edition.

The second edition describes the key elements of the subject of surface-penetrating radar, and in general terms the inter-relationship between those topics in electromagnetism, soil science, geophysics and signal processing which form a critical part of the design of a surface-penetrating radar system. The objective in writing this book is to bring together in one volume all the core information on a technique which spans

a wide range of disciplines. While much of this is available in a range of different publications, it is dispersed and therefore less accessible by virtue of the disparate nature of many of the sources.

A further aim of the second edition is to provide an introduction for the newcomer to the field, as well as a useful source of further reading, information and references for the current practitioner and to bring the reader more current information.

By necessity, this book provides a snapshot of the field of ground penetrating radar and it is to be expected that further developments in hardware and signal processing techniques will incrementally improve the performance and extent of applications. If this book helps the newcomer to assess the potential of the technique correctly and apply it effectively, its purpose will be well served.

Several examples may illustrate the reason for the previous comment. A decade or more ago a suggestion was made that a particular ground-probing radar and its operator could detect targets the size of golf balls at a depth of 8 m. Clearly the wavelengths capable of propagating to 8 m would be so much larger than a golf ball sized target that the radar cross-sectional area of the latter would fade into insignificance, even noise. The persuasiveness of the claimant and the lack of understanding of basic physics on the part of the potential users enabled this kind of claim to be seriously proposed.

Unfortunately, such claims are still being made and there are still enough gullible people who are being dazzled by the prospects. Recently, claims were made in the US that a ground penetrating radar had been developed 'that can provide three-dimensional images of objects up to 45.7 m below the surface of land and sea. Such a device would allow verifiers to identify underground weapons facilities, like those of concern in Libya, Iraq and North Korea. The underwater detection capability could also be used to verify treaties dealing with submarines and nuclear weapons positioned on the seabed'. How well GPR would propagate through sea water is an interesting question given the known attenuation of sea water at radar frequencies. A careful analysis of some of the claims about the same radar was published by Tuley (2002). It is, however, concerning that such claims are still being made when it is clear that the basic physics has been well understood for decades.

Therefore a secondary objective in preparing this volume has been to provide a source of information which will allow potential users to assess the merits of claims, sound or otherwise. GPR is, like all other engineering techniques, firmly based on physical principles, which must be understood if the technique is to be properly applied. In reality a metre of wet clay or salt water is still largely opaque, even to the latest radar hardware, however well provisioned with arrays of microprocessors, artificial intelligence and neural networks.

It is hoped that the second edition may provide useful material for the expert or advanced practitioner in the discipline as many of the new contributions are by leaders in the field. The treatment of the subject is generally at that of first year undergraduate level, although some chapters may require a deeper knowledge of antenna and EM wave theory. The aim has been to provide a treatment which is readily accessible,

Because colour is expensive to produce, the second edition has line drawings and greyscale illustrations and is a hardback edition. However, additional material and colour images as well as audio visual (AV) files are contained on the

accompanying CD. The following software is needed to access the CD: Microsoft™ Word 2000, Microsoft™ Powerpoint 2000 and Media Player™ for the MPEG and video clips and Paint Shop Pro™. There is also an evaluation copy of MathCad™ to run the MathCad simulations, although both the signal and image processing toolboxes are needed for some worksheets.

After an introduction in Chapter 1 to set the scene, the general system considerations are discussed in Chapter 2. Chapter 3 considers some aspects of modelling, which is now a key means of evaluating both capability and data. Chapter 4 provides an introduction to the dielectric properties of earth materials and includes a consideration of the suitability of soils. The characteristics of antennas suitable for use in SPR systems are described in Chapter 5, and this is followed in Chapter 6 by a description of the various modulation techniques. Chapter 7 reviews the variety of signal processing options currently available. Indications are given of the range of options available and descriptions of how various workers have approached their design and implementation for a given application. The applications of the technology are reviewed in Chapter 8 (Archaeology), Chapter 9 (Civil engineering), Chapter 10 (Forensic applications), Chapter 11 (Geophysical applications), Chapter 12 (Mine detection), Chapter 13 (Utilities) and Chapter 14 (Remote sensing). Chapter 15 briefly considers the selection of equipment but, unlike the first edition, directs the reader to the websites of the companies concerned. Chapter 16 considers the licensing, radiological and EMC aspects of GPR and Chapter 17 details additional bibliographic material.

Reference

TULEY, M. T., RALSTON, J. M., ROTONDO, F. S., ANDREWS, A. M., and ROSEN, E. M.: 'Evaluation of EarthRadar unexploded ordnance testing at Fort A. P. Hill, Virginia', *IEEE Aerosp. Electron. Syst. Mag.*, 2002, **17**, (5), pp. 10–12

Acknowledgments

I am extremely grateful for the help that I received from many fellow workers in the field of ground penetrating radar. In particular, I would like to thank those who provided individual contributions to both the first and second editions.

I would also like to express my thanks and appreciation to the Directors of ERA Technology Ltd, UK, both for their support of research and development of the technology and for their assistance with the preparation of the first and second editions. I would like to thank my colleagues at ERA Technology, whose work on various programmes at various times provided the wherewithal to develop GPR techniques. In particular, I would like to thank Dr Jon Dittmer, Nigel Hunt, Paul Curtis, Dr Rajan Amin, Dr Duncan Brooks, Vince Brooker, Kevin Targett, Stefan Jennings, Giles Capps, Brian Kay, Oscar Mitchell, Ken Mann and Nick Frost and Dr Neil Williams, whose support for the technology has been invaluable. I am grateful to Pam Wheeler, who enthusiastically and patiently typed the manuscript, and to Shirley Vousden, who prepared all of the figures for the first edition.

When the first edition was published, I received many favourable comments on the concept. However, various errors somehow crept through the reviewing and proofreading process, and for these I must apologise. I believe that the second edition has removed these. I am particularly grateful to the late Professor James Wait of the University of Arizona, whose review and correspondence I really appreciated. I would also like to thank Dr Stan Evans of the University Engineering Department, Cambridge, and Dr Yi Huang of the University of Liverpool for their help and comments on the first edition which greatly enhanced the second edition.

Contributors

First edition

Dr S. Abrahamson
M. Bartha
H. F. Scott
Prof. J. Bungey
Dr R. de Vekey
Dr P. Hanninen
Dr R. A. van Overmeeren
Dr J. K. van Deen
Dr S. Tillard
Dr J. Fidler
Mr D. L. Wilkinson
Dr J. Cariou
Dr G. Schaber
Prof. T. Haglars
Ms F. Nicollin

The following companies and people provided information on equipment for the first edition: Greg Mills of GSSI (US), Sensors and Software (Canada), Redifon (UK), ERA Technology (UK), NTT (Japan) and MALA (Sweden).

Second edition

I am extremely grateful for the contributions to the second edition. Given the growth of GPR research, it is no longer possible for any individual to cover the complete field of GPR, and the input of the various contributors to the second edition provides some coverage of the extent of the growth of the subject. Contact details for the contributors to the second edition are included below.

Dr Steven A. Arcone
ERDC/USA CRREL
72 Lyme Road Hanover, NH 03755,
United States of America
T ++1 603 646 4368
F ++1 603 646 4644
steven.a.arcone@erdc.usace.army.mil

Dr Nigel J. Cassidy
Principal Research Fellow
Department of Applied and
Environmental Geophysics Group
School of Earth Sciences and
Geography
Keele University, Keele, Staffordshire,
ST5 5BG, United Kingdom
T ++1 782 583180
F ++1 782 583737
n.j.cassidy@esci.keele.ac.uk

Dr Chi-Chih Chen
Research Scientist
ElectroScience Laboratory, Ohio State
University Electrical Engineering
Department
1320 Kinnear Road, Columbus, Ohio,
43212, United States of America
T ++1 +614-292-7981
F ++1 +614-292-7297
Chen.118@osu.edu

Dr Richard J. Chignell
Technical Director, PipeHawk plc
Systems House, Mill Lane, Alton,
Hampshire, GU34 2QG,
United Kingdom
T ++44 1420 590990
F ++44 1420 590920
richard.chignell@pipehawk.com

David J. Daniels
Chief Consultant, Sensors, Electronic
Systems
ERA Technology Limited
Cleeve Road, Leatherhead, Surrey,
KT22 7SA, United Kingdom
T +44 1 372 367 084
F +44 1 372 367 081
david.daniels@era.co.uk

Les Davis
President, Terad Ltd
3509 Mississauga Road, Mississauga,
Ontario, LSL 2R9, Canada
T ++905 820 7643
F ++905 820 7643
terad@symatico.ca

Dr Xavier Dérobert
Researcher, Division for Soil Mechanics
and Site Surveying
Laboratoire Central des Ponts et
Chaussées, BP 4129-44341 Bouguenais,
France
T 00 +33 +2 40 84 59 11
F 00 +33 +2 40 84 59 97
xavier.derobert@lcpc.fr

Dr Jon K. Dittmer
Principal Engineer, Electronic Systems
ERA Technology Limited
Cleeve Road, Leatherhead, Surrey,
KT22 7SA, United Kingdom
T +44 (0)1372 367069
F +44 (0)1372 367081
jon.dittmer@era.co.uk

Dr James A. Doolittle
Research Soil Scientist, United States
Department of Agriculture-Natural
Resources Conservation Service
(USDA-NRCS)
11 Campus Boulevard Suite 200,

Newtown Square, PA 19073,
United States of America
T ++1 610-557-4233
F ++1 610-557-4136
jdoolittle@fs.fed.us

Dr Martin W. Fritzsche
Research Scientist, Machine Perception Lab
DaimlerChrysler Research & Technology, PO Box 2360,
D-89013 Ulm, Germany
T ++49-(0)731-505-2114
F ++49-(0)731-505-4105
martin.fritzsche@daimlerchrysler.com

Prof. Svein-Erik Hamran
Professor, Department of Geoscience
University of Oslo Postboks 1047
Blindern, N-0316 Oslo, Norway
T ++47 99 02 79 43
F ++47 22 85 42 15
s.e.hamran@geo.uio.no

Dr Yi Huang
Associate Professor, Department of Electrical Eng & Electronics
University of Liverpool, Liverpool
L69 3GJ, United Kingdom
T +44 151 794 4521
F +44 151 794 4540
Yi.Huang@liv.ac.uk

Dr Henrique Lorenzo
Associate Professor, Department of Natural Resources & Environmental Engineering
University of Vigo, EUET Forestal.
Campus A Xunqueira s/n. 36005 – Pontevedra, Spain
T +34 986 801 935
F +34 986 801 907
hlorenzo@uvigo.es

Dr Christiane Maierhofer
Head of Group, BAM Bundesanstalt für Materialforschung und – prüfung
Federal Institute for Materials Research and Testing Fachgruppe IV.4 – Zerstörungsfreie Schadensdiagnose und Umweltmessverfahren Division IV.4 – Non-Destructive Damage Assessment and Environmental Measurement Methods Unter den Eichen, 87 D-12205 Berlin
T ++49 +(0)30-8104 1441
F ++49 +(0)30-8104 1447
Christiane.Maierhofer@bam.de

Dr Cedric Martel
Senior Engineer, Electronic Systems
ERA Technology Limited, Cleeve Road, Leatherhead, Surrey, KT22 7SA,
United Kingdom
T +44 (0)1372 367000
F +44 (0)1372 367081
cedric.martel@era.co.uk

Dr Vega Pérez Gracia
Associate Professor
Departamento de Resistencia de Materiales y Estructuras en la Ingeniería
Universidad Politécnica de Cataluña
Mecánica aplicada. EUETIB.
Universidad Politécnica de Cataluña, C/Urgell 187, 08036 Barcelona, Spain
T ++34 93 413 73 33
F ++34 94 413 14 21
vega.perez@upc.es

Prof. Giovanni Picardi
Professor, Information and Communication Department – INFOCOM Dpt
University of Rome 'La Sapienza'

via Eudossiana 18-00184 Roma, Italy
T +39.06.44585455
F +39.06.4873300
picar@infocom.ing.uniroma1.it

Prof. Rocco Pierri
Professor, Department of Information Engineering
Seconda Universita' di Napoli
Via Roma 29 I81031, Aversa Italy
T +39 +081 5010242
F +39 +081 5037370
rocco.pierri@unina2.it

Prof. Michele Pipan
Associate Professor, Department of Geological, Environmental and Marine Sciences, University of Trieste
via Weiss, 1-34127 , Trieste, Italy
T +39 040 5582277
F +39 040 5582290
pipan@units.it

Prof. Carey Rappaport
Professor, Electrical and Computer Engineering
Northeastern University, Boston, MA, United States of America
T ++1(617) 373-2043 (v)
F ++1(617) 373-8627 (f)
rappaport@ECE.NEU.EDU

Dr Juergen Sachs
Associate Professor, Faculty of Electrical Engineering and Information Technology
Technical University of Ilmenau, POB 100565, D-98684 Ilmenau, Germany
T +49 3677 69 2623
F +49 3677 69 1113
juergen.sachs@tu-ilmenau.de

Prof. Hichem Sahli
Associate Professor, Department of Electronics and Information Processing
Vrije Universiteit Brussel, VUB-ETRO, Pleinlaan, 2-B-1050 Brussels, Belgium
T ++32 2 629 29 16
F ++32 2 629 28 83
hsahli@etro.vub.ac.be

Prof. Motoyuki Sato
Professor, Center for Northeast Asian Studies
Tohoku University, Kawauchi, Sendai 980-8576 Japan
T +81 +22 217 6075
F +81 +22 217 6075
sato@cneas.tohoku.ac.jp

Dr Timofei Savelyev
Department of Electronics and Information Processing
Vrije Universiteit, Brussel VUB-ETRO, Pleinlaan, 2-B-1050 Brussels, Belgium
T ++32 2 629 29 16
F ++32 2 629 28 83
tsavelyev@etro.vub.ac.be

Dr Bart Scheers
Lecturer, Department of Telecommunication
Royal Military Academy, Renaissancelaan 30, B-1000 Brussels, Belgium
T ++32-2-7376626
F ++32-2-7376622
bart.scheers@rma.ac.be

Luc Van Kempen
Department of Electronics and Information Processing
Vrije Universiteit, Faculty of Applied Sciences, ETRO Department, IRIS Research Group, Pleinlaan, 2-B-1050 Brussels, Belgium
T ++32 2 629 29 16
F ++32 2 629 28 83
lmkempen@etro.vub.ac.be

Dr Jan van der Kruk
Postdoctoral Research Associate
Institute of Geophysics, Swiss Federal Institute of Technology ETH
ETH-Hoenggerberg, CH-8093, Zurich, Switzerland
T (41-1) 6332659
F (41-1) 6331065
jvdkruk@aug.ig.erdw.ethz.ch

Dr Declan Vogt
CSIR Division of Mining Technology,
PO Box 91230, Auckland Park, 2006,
South Africa
T +27-11-358-0213
F +27-11-482-1214
dvogt@csir.co.za

Dr Bob Whiteley
Senior Principal Geophysicist
Coffey Geosciences Pty. Ltd,
142 Wicks Rd. North Ryde 2113 NSW
Australia
T ++61 2 9888 7444
F ++61 2 9888 9977
bob_whiteley@coffey.com.au

Prof. Dr Sci. Alexander G. Yarovoy
Professor, International Research Centre for Telecommunications and Radar
Delft University of Technology,
Mekelweg 4, 2628CD Delft,
The Netherlands
T ++31-15-2782496
F ++31-15-2784046
a.yarovoy@irctr.tudelft.nl

I would also like to thank the IEE and their publishing staff, particularly Sarah Kramer and Wendy Hiles whose help ensured that I kept on schedule. In addition I am grateful to Leslie Bondaryk of Mathsoft, whose advice on the Mathcad worksheets was especially useful.

Finally, I would like to thank my wife, Jenny, for her support, encouragement and patience during the time it has taken to write the second edition.

Contents

This page has been reformatted by Knovel to provide easier navigation.

This page has been reformatted by Knovel to provide easier navigation.

This page has been reformatted by Knovel to provide easier navigation.

This page has been reformatted by Knovel to provide easier navigation.

This page has been reformatted by Knovel to provide easier navigation.

This page has been reformatted by Knovel to provide easier navigation.

This page has been reformatted by Knovel to provide easier navigation.

This page has been reformatted by Knovel to provide easier navigation.

This page has been reformatted by Knovel to provide easier navigation.

This page has been reformatted by Knovel to provide easier navigation.

This page has been reformatted by Knovel to provide easier navigation.

This page has been reformatted by Knovel to provide easier navigation.

This page has been reformatted by Knovel to provide easier navigation.

This page has been reformatted by Knovel to provide easier navigation.

Chapter 1
Introduction

1.1 Introduction

The possibility of detecting buried objects remotely has fascinated mankind over centuries. A single technique which could render the ground and its contents clearly visible is potentially so attractive that considerable scientific and engineering effort has gone into devising suitable methods of exploration.

As yet, no single method has been found to provide a complete answer, but seismic, electrical resistivity, induced polarisation, gravity surveying, magnetic surveying, nucleonic, radiometric, thermographic and electromagnetic methods have all proved useful. Ground penetrating, -probing or surface-penetrating radar has been found to be a specially attractive option. The subject has a special appeal for practising engineers and scientists in that it embraces a range of specialisations such as electromagnetic wave propagation in lossy media, ultra wideband antenna technology and radar systems design, discriminant waveform signal processing and image processing. Most ground penetrating radars are a particular realisation of ultra-wideband impulse radar technology. Skolnik [1] considers that 'the technology of impulse radar creates an exciting challenge to the innovative engineer' and ground probing radar to have been a successful commercial venture although on a smaller scale than conventional radar applications.

The terms 'ground penetrating radar (GPR)', 'ground-probing radar', 'sub-surface radar' or 'surface-penetrating radar (SPR)' refer to a range of electromagnetic techniques designed primarily for the location of objects or interfaces buried beneath the earth's surface or located within a visually opaque structure. The term 'surface-penetrating' is preferred by the author as it describes most accurately the application of the method to the majority of situations including buildings, bridges, etc. as well as probing through the ground. However, the description 'ground penetrating radar' will be used to describe the technique as it has become almost universally accepted. The technology of GPR is largely applications-oriented and the overall design philosophy, as well as the hardware, is usually dependent on the target type and the material

of the target and its surroundings. The range of applications for GPR methods is wide and the sophistication of signal recovery techniques, hardware designs and operating practices is increasing as the technology matures.

More recent developments include airborne and satellite surveying as well as high-speed survey from vehicle mounted radars. There has been an enormous growth in research into GPR and it has not been possible to cover all the groups working in the field in this edition. Those working in the area will be able to use the publications of the IEE, IEEE, SPIE, the GPR conferences and workshops, *Geophysics* and other sources to ensure that they are fully up to date with the field. These are listed at the end of this chapter. This second edition represents a snapshot of technology, practice and future developments in the field at the time of publication but it is not exhaustive.

The first edition of the book was intended as an introduction to the subject. Most of the basic material has been retained and is aimed at the growing number of potential users who wish to gain an introductory understanding of the method at a level appropriate to the first year of undergraduate studies. It is assumed that, whatever the reader's background, be it in geophysics, civil engineering or archaeology, he or she has a basic understanding of physics and geophysics and understands that radar is an active measurement technique which allows the ranging and detection of targets. Although each chapter has been written in the form of a self-contained section relevant to its particular topic, the overall aim of the author has been to create a sufficiently wide-ranging treatment that will enable interested readers to investigate areas of particular interest in greater depth. To assist the reader, a list of suitable references is provided at the end of each chapter. The second edition develops some of the areas in more depth and hopefully will be found useful for those developing particular specialities.

Following early laboratory developments in the late 1960s and 1970s in both the US and UK commercial equipment has become more freely available and the GSSI Impulse Radar has become the most widely used commercial system. More recently, alternative equipment using various modulation techniques has become available and the market is expanding. However, the impulse radar has been the most successful design to date and probably accounts for 95% of the units in operation in the field.

The general structure of this volume is based on an earlier paper which was published in a special edition of the *IEE Proceedings Part F* [2] by Daniels *et al.* (1988), which served as an introduction to GPR techniques. This still serves well as a primer and the introduction is still relevant and is quoted below.

GPR in the hands of an expert provides a safe and noninvasive method of conducting speculative searches without the need for unnecessary disruption and excavation. GPR has significantly improved the efficiency of the exploratory work that is fundamental to the construction and civil engineering industries, the police and forensic sectors, security/intelligence forces and archaeological surveys.

1.2 History

The first use of electromagnetic signals to determine the presence of remote terrestrial metal objects is generally attributed to Hülsmeyer in 1904, but the first description

of their use for location of buried objects appeared six years later in a German patent by Leimbach and Löwy. Their technique consisted of burying dipole antennas in an array of vertical boreholes and comparing the magnitude of signals received when successive pairs were used to transmit and receive. In this way, a crude image could be formed of any region within the array which, through its higher conductivity than the surrounding medium, preferentially absorbed the radiation. These authors described an alternative technique, which used separate, surface-mounted antennas to detect the reflection from a sub-surface interface due to ground water or to an ore deposit. An extension of the technique led to an indication of the depth of a buried interface, through an examination of the interference between the reflected wave and that which leaked directly between the antennas over the ground surface. The main features of this work, namely CW operation, use of shielding or diffraction effects due to underground features, and the reliance on conductivity variations to produce scattering, were present in a number of other patent disclosures, including some intended for totally submerged applications in mines. The work of Hülsenbeck [3] in 1926 appears to be the first use of pulsed techniques to determine the structure of buried features. He noted that any dielectric variation, not necessarily involving conductivity, would also produce reflections and that the technique, through the easier realisation of directional sources, had advantages over seismic methods.

Pulsed techniques were developed from the 1930s onwards as a means of probing to considerable depths in ice [4, 5], fresh water, salt deposits [6], desert sand and rock formations [7, 8]. Probing of rock and coal was also investigated by Cook [9, 10], and Roe and Ellerbruch [11], although the higher attenuation in the latter material meant that depths greater than a few metres were impractical. A more extended account of the history of GPR and its growth up to the mid 1970s is given by Nilsson [12].

Renewed interest in the subject was generated in the early 1970s when lunar investigations and landings were in progress. For these applications, one of the advantages of ground penetrating radar over seismic techniques was exploited, namely the ability to use remote, noncontacting transducers of the radiated energy, rather than the ground contacting types needed for seismic investigations. Remote transducers are possible because the dielectric impedance ratio between free space and soil materials, typically from 2 to 4, is very much less than the corresponding ratio for acoustic impedances, by a factor which is typically of the order of 100.

From the 1970s until the present day, the range of applications has been expanding steadily, and now includes building and structural nondestructive testing, archaeology, road and tunnel quality assessment, location of voids and containers, tunnels and mineshafts, pipe and cable detection, as well as remote sensing by satellite. Purpose-built equipment for each of these applications is being developed and the user now has a better choice of equipment and techniques.

1.3 Applications

Recent progress has been one of continuing technical advance largely applications-driven, but as the requirements have become more demanding, so the equipment, techniques and data processing methods have been developed and refined.

GPR has been used in the following applications:

archaeological investigations
borehole inspection
bridge deck analysis
building condition assessment
contaminated land investigation
detection of buried mines (anti-personnel and anti-tank)
evaluation of reinforced concrete
forensic investigations
geophysical investigations
medical imaging
pipes and cable detection
planetary exploration
rail track and bed inspection
remote sensing from aircraft and satellites
road condition survey
security applications
snow, ice and glacier
timber condition
tunnel linings
wall condition

GPR has been very successfully used in forensic investigations. The most notorious cases occurred in the United Kingdom in 1994, when the grave sites, under concrete and in the house of Fred West, of the victims of the serial murderer were pinpointed. In Belgium, the grave sites of the victims of the paedophile, Dutroux, were detected in 1996. Both these investigations were carried out using GPR developed by ERA Technology and the ERA team.

Archaeological applications of GPR have been varied, ranging from attempts to detect the Ark to the exploration of Egyptian and North American Indian sites as well as castles and monasteries in Europe. The quality of the radar image can be exceptionally good, although correct understanding normally requires joint interpretation by the archaeologists and radar specialists.

Abandoned anti-personnel land mines and unexploded ordnance are a major hindrance to the recovery of many countries from war. Their effect on the civilian population is disastrous, and major efforts are being made by the international community to clear the problem. Most detection is done with metal detectors, which respond to the large amount of metallic debris in abandoned battlefield areas and hence have difficulty in detecting the minimum metal or plastic mine. GPR technology is being applied to this problem as a means of reducing the false alarm rate and providing improved detection of low metal content mines.

GPR has been used for surveying many different types of geological strata ranging from exploration of the Arctic and Antarctic icecaps and the permafrost regions of North America, to mapping of granite, limestone, marble and other hard rocks as well as geophysical strata.

The thickness of the various layers of a road can be measured using radar techniques. The great advantage is that this method is nondestructive and high speed (>40 km/h) and can be applied dynamically to achieve a continuous profile or rolling map. The accuracy of calibration tends to decrease as a function of depth because of the attenuation characteristics of the ground. The accuracy may be quite high (i.e. a few millimetres) for the surface wearing course but will degrade to centimetres at depths of one metre.

While most GPR systems are used in close proximity to the ground, airborne systems have been able to map ice formations, glaciers, and penetrate through forest canopy. Airborne GPR, processed using synthetic aperture techniques, has been used to detect buried metallic mines from a height of several hundred metres in SAR (synthetic aperture radar) mode. In addition the SIR-C satellite SAR radar has imaged buried artefacts in desert conditions, and the JPL website http://southport.jpl.nasa.gov/sir-c/ is an important source of radar imagery.

The main operational advantages of the technique can be described as follows. The antennas of a GPR do not need to be in contact with the surface of the earth, thereby allowing rapid surveying. Antennas may be designed to have adequate properties of bandwidth and beam shape, although optimum performance, especially where a small antenna-to-ground surface spacing is involved, will usually be obtained only by taking into account details of the geometry and the nature of the ground. Signal sources are available which can produce sub-nanosecond impulses or alternatively which can be programmed to produce a wide range of modulation types.

In general, any dielectric discontinuity is detected. Targets can be classified according to their geometry: planar interfaces; long, thin objects; localised spherical or cuboidal objects. The radar system can be designed to detect a given target type preferentially and is potentially capable of producing an image of the target in three dimensions, although little work has been done on this aspect of image presentation.

The signal attenuation at the desired operating frequency is the main factor to be considered when assessing the usefulness of radar probing in a given material. As a rule, material that has a high value of low-frequency conductivity will have a large signal attenuation. Thus gravel, sand, dry rock and fresh water are relatively easy to probe using radar methods, while salt water, clay soils and conductive ores or minerals are less so, but a reduction in the transmitted frequency means that even these materials can be adequately investigated, though at the expense of a reduced resolution between targets. GPR will work successfully in fresh water so that water content is not a complete guide to achievable penetration range.

GPR relies for its operational effectiveness on successfully meeting the following requirements:

(a) efficient coupling of electromagnetic radiation into the ground;
(b) adequate penetration of the radiation through the ground having regard to target depth;

(c) obtaining from buried objects or other dielectric discontinuities a sufficiently large scattered signal for detection at or above the ground surface;
(d) an adequate bandwidth in the detected signal having regard to the desired resolution and noise levels.

The essence of the technique is no different from that of conventional, free-space radar, but of the factors that affect the design and operation of any radar system the four requirements indicated earlier take on an additional significance in ground penetrating radar work. Specifically, propagation loss, clutter characteristics and target characteristics are distinctly different.

The radar technique is usually employed to detect backscattered radiation from a target. Forward scattering can also yield target information, although for sub-surface work at least one antenna would need to be buried, and an imaging transform would need to be applied to the measured data.

The designer of radar for ground-penetrating applications has two problems, not necessarily encountered by the designer of a conventional radar: designing to a limited budget and overcoming difficult signal recovery problems primarily associated with signal to clutter ratio. As the cost of processing falls, the designer can consider signal processing strategies previously thought uneconomic, and this will be likely to have a significant effect on system design and hence commercial viability.

For example, in early radars for ground-penetrating applications, it was considered necessary to employ wideband antennas with linear phase response, because of the resultant difficulties in deconvolving the antenna response. However, it is now possible to correct for nonlinear phase characteristics, if desired, at a reasonable cost by using appropriate signal processing techniques implemented in software.

GPR is vulnerable to extremely high levels of clutter at short ranges, and this rather than signal/noise recovery is its major technical handicap. The system to be specified should take this into account. Some basic guidelines can be suggested for the user of radar for ground probing applications.

It is important to define clearly the target parameters. There is a considerable difference between the target response from a buried pipe, a buried mine, a void or a planar interface. This has a major impact on antenna design, polarisation state and signal processing strategy and should be exploited.

The resolution and depth requirement needed should be clearly identified. This in turn sets the frequency and bandwidth of operation, which then influence the choice of modulation technique and hence the hardware design. The costs of over-specification can be considerable and the physics of propagation should be kept in mind.

The transmission loss characteristics will affect the selection of a system. It is unlikely that synthetic aperture or holographic schemes will work well in high-loss materials.

The display requirements can have a major impact on equipment costs. This has a fundamental bearing on the type of signal processing required. Image presentation obviously needs different signal processing from that required for target identification and classification. Signal processing must take account of the needs of the user and as

much as possible of the interpretation process should be done automatically, if GPR techniques are to gain widespread acceptance for routine use in, say, pipe and cable location. Recent developments have shown that it is possible to use a simple audio output for the man–machine interface, and this is discussed in Chapter 12.

The operational requirements are such that physical decoupling of the antenna from the surface should only be carried out where strictly necessary. This is not simply for reasons of power transfer but also for reduction of clutter and efficiency of transfer.

Some of the ancillary requirements of an operational ground penetrating radar system need more consideration. There is a need for an accurate, small-scale, low-cost position referencing system for use with radar for ground-penetrating survey techniques. For utilities it will be most important that data can be related to a true geographic reference, particularly when filed on digital mapping systems and used to define areas of safe working. It will be necessary to provide some means of scanning the antenna. Obviously a basic approach is the hand-held device but this places severe limitations on the signal processing strategies. Alternatives are robotic arms and miniature tracked vehicles; the former may limit the area of search but may be cheaper for surveying road and pavement areas, while the latter may be the most flexible, but will require accurate position referencing.

If the radar is to provide its operator with an image of targets under the ground surface, then online processing will be needed. With the projected developments in advanced microprocessors it is likely that significant amounts of online processing will soon become economically feasible.

1.4 Development

The key future development area will be signal processing and image recognition methods, and this requires development of core strategies generally based on deconvolution techniques. The future of GPR is considered to be based on short range geophysical exploration and nondestructive investigation. For short range geophysical exploration ground penetrating radar has already achieved some significant results. It is, however, in the area of nondestructive investigation of structures such as tunnels, roads, buildings and other examples of physical infrastructure of modern civilisation that GPR has an increasingly important role to play.

Potential customers could be energy and communications utilities, mineral resource exploration organisations, civil engineering organisations, nondestructive testing companies, military and security organisations, architects, archaeologists and scientific research establishments. Many of these organisations only wish to purchase surface-penetrating radars provided the price is within reasonable limits, and they may prefer to hire the services of a specialist surveying organisation or alternatively hire equipment. It is likely that the commercial definition of a reasonable price for either commercial equipment, hire or service, will be different from the military definition of a reasonable price for a radar.

In addition, the experience of many of those commercial organisations in relation to electronic equipment is of mainstream suppliers of conventional equipment. Suppliers of production quantities achieve economies of scale which are unlikely to apply in the case of a radar for ground-penetrating applications.

The designer of surface-penetrating radars must therefore take into account the type of markets which exist at present. However, the success of the current commercial radars is encouraging and suggests that evolutionary design processes could widen the market.

One possible design strategy for GPR could be seen as the development of a modular system. With this approach, frequency range, and hence antenna type, can be modified simply, and signal processing can be selected by choice of target and display format. This would allow economy in development and of production and result in a more commercially attractive product.

The potential cannot be overlooked of increasingly powerful microprocessors available at low cost, capable of carrying out sophisticated signal processing and then displaying the results so that interpretation by an expert is less important. This potential should provide the technology necessary for radar for ground-penetrating applications to gain wide acceptance as a valuable investigative tool capable of being used by the nonspecialist. However, the pattern recognition capability of the human brain is still unequalled and may remain so for many decades.

GPR is one of a very few methods available which allows the inspection of objects or geological features which lie beneath an optically opaque surface. Much funding to date has come from industries in the civil sector with a direct interest in the information that can be derived from ground penetrating radar exploration: the utilities (gas, electricity, water, telecommunications), oil and gas exploration companies, geophysical survey groups. The total expenditure is still small when compared with the investment, largely from military sources, in free space radar developments. However, it is generally considered that GPR has been a successful commercial venture even if its market sector value is not as large as some of the radar applications.

With improvements in the performance of ground penetrating radar systems will come wider commercial acceptance. The challenge for the designer is to speed up the rate of development. Ground penetrating radar technology will become more firmly established as its benefits are perceived and realised by users distinctly different from those of conventional free-space radar technology.

Spectrum usage is becoming ever more contested and hence licensing is becoming a key issue. The FCC and ETSI are in the process of regulating the use of the radio frequency spectrum in a way which will challenge the manufacturers and users of GPR. The reality is that GPR has caused no interference problems and much of the pressure by other users is based on unwarranted nervousness. However, new developments in noise radar and pseudo-random coded waveforms promise to further reduce the potential for interference to other spectrum users. This is discussed in Chapter 6.

Although GPR has achieved some spectacular successes, it would be unrealistic to leave the impression that GPR is the complete solution to the users' perceived

problem (whatever that may be). A GPR will detect, within the limits of the physics of propagation, all changes in electrical impedance in the material under investigation. Some of these changes will be associated with wanted targets, while others may not be. The radar has, in general, no way of discriminating, and much of the skill of the successful user currently comes from forming a conclusion from both the radar image and site intelligence. The more successful operators routinely exercise this discipline and procedure.

The potential user should therefore understand both the capabilities and limitations of the method. This book will have achieved that objective if the user employs radar in the right place at the right time in parallel with other geophysical exploration methods.

1.5 Further information sources

Further useful information can be gained from a variety of sources, and a list is given below of useful websites and institutions. A list of publications and sources is included in each Chapter.

1.5.1 Individual websites

Some of these websites are solely GPR, while others contain useful material related to GPR:

Dr David Noon's website at http://www.cssip.uq.edu.au/staff/noon/gprlist.html
Prof. Gary Olhoeft's website on http://www.g-p-r.com/
ARIS website at http://demining.jrc.it/aris/
DeTeC website at http://diwww.epfl.ch/lami/detec/detec.html
Eudem website at http://www.eudem.vub.ac.be/

1.5.2 GPR conferences

GPR 2000 – Gold Coast, Australia, 8th International Conference on Ground Penetrating Radar. David Noon, University of Queensland, email: noon@cssip.uq.edu.au
GPR '98 – Lawrence, Kansas, USA, 7th International Conference on Ground Penetrating Radar. Dr. Richard Plumb, University of Kansas, email: rplumb@binghamton.edu
GPR '96 – Sendai, Japan, 6th International Conference on Ground Penetrating Radar. Prof. Motoyuki Sato, Tohoku University, email: sato@cneas.tohoku.ac.jp
GPR '94 – Kitchener, Ontario, Canada, 5th International Conference on Ground Penetrating Radar. David Redman, Sensors & Software, email: dr@sensoft.ca
GPR '92 – Rovaniemi, Finland, 4th International Conference on Ground Penetrating Radar. Pauli Hanninen, Geological Survey of Finland
GPR '90 – Lakewood, Colorado, USA, 3rd International Conference on Ground Penetrating Radar. Prof. Gary Olhoeft, Colorado School of Mines, email: golhoeft@mines.edu

1988 – Gainesville, Florida, USA, 2nd International Symposium on Geotechnical Applications of Ground Penetrating Radar. Mary Collins, University of Florida, email: mec@gnv.ifas.ufl.edu
1986 – Tifton, Georgia, USA, 1st International Conference on Geotechnical Applications of Ground Penetrating Radar

1.5.3 International workshops on advanced GPR

IWAGPR Delft 01 – 1st International Workshop on Advanced Ground Penetrating Radar (International Workshop) published in 'Subsurface sensing technologies and applications' (Kluwer, June 2001)
IWAGPR Delft 03 – 2nd International Workshop on Advanced Ground Penetrating Radar (International Workshop). Web link: http://irctr.et.tudelft.nl/IWAGPR/

1.5.4 Institution of Electrical Engineers (UK)

See also Radar 2002
http://www.iee.org/Publish/Digests/conf2002.cfm
See *IEE Proceedings, Radar, Sonar and Navigation*
Web link http://ioj.iee.org.uk/journals/ip-rsn
See Edinburgh MD96 – Detection of abandoned landmines (Main Past Conference)
Web link: http://www.iee.org/Publish/Digests/conf1996.cfm
See Edinburgh MD98 – Second International Conference on the Detection of Abandoned Land Mines (Main Past Conference)
Web link: http://www.iee.org/Publish/ Digests/conf1998.cfm

1.5.5 Institute of Electrical and Electronics Engineers (USA)

Proceedings – particularly the Societies for:
Antennas and Propagation
http://www.ieeeaps.org/
Aerospace and Electronic Systems
http://ewh.ieee.org/soc/aes/
For Radar conferences see also
http://www.ewh.ieee.org/soc/aes/Conferences.html
Geoscience and Remote Sensing
http://www.ewh.ieee.org/soc/grss/
Microwave Theory and Transactions
http://www.mtt.org/

1.5.6 SPIE (International Society for Optical Engineering) conferences

SPIE Orlando: SPIE Detection and Remediation Technologies for Mines and Minelike Targets 1995 to 2003
http://spie.org/app/conferences/index.cfm?fuseaction=archive&year=2002

1.5.7 Geophysics

http://www.geo-online.org/

1.5.8 Sub-surface sensing technologies and applications

http://www.kluweronline.com/issn/1566-0184

1.6 References

[1] SKOLNIK, M. I.: 'An introduction to impulse radar'. Naval Research Laboratory Report 6755, November 1990

[2] DANIELS, D. J., GUNTON, D. J., SCOTT, H. F.: 'Introduction to subsurface radar', *IEE Proc.-F, Commun. Radar Signal Process.*, 1988, **135**, pp. 278–320

[3] HÜLSENBECK *et al.*: German Pat. No. 489434, 1926

[4] STEENSON, B. O.: 'Radar methods for the exploration of glaciers'. PhD Thesis, Calif. Inst. Tech., Pasadena, CA, USA, 1951

[5] EVANS, S.: 'Radio techniques for the measurement of ice thickness', *Polar Record*, 1963, **11**, pp. 406–410

[6] UNTERBERGER, R. R.: 'Radar and sonar probing of salt'. 5th Int. Symp. on Salt, Hamburg (Northern Ohio Geological Society), pp. 423–437

[7] KADABA, P. K.: 'Penetration of 0.1 GHz to 1.5 GHz electromagnetic waves into the earth surface for remote sensing applications'. Proc. IEEE S. E. Region 3 Conf., 1976, pp. 48–50

[8] MOREY, R. M.: 'Continuous sub-surface profiling by impulse radar'. Proc. Conf. Subsurface Exploration for Underground Excavation and Heavy Construction. Am. Soc. Civ. Eng., 1974, pp. 213–232

[9] COOK, J. C.: 'Status of ground-probing radar and some recent experience'. Proc. Conf. Subsurface Exploration for Underground Excavation and Heavy Construction. Am. Soc. Civ. Eng., 1974, pp. 175–194

[10] COOK, J. C.: 'Radar transparencies of mine and tunnel rocks', *Geophys.*, 1975, **40**, pp. 865–885

[11] ROE, K. C., ELLERBRUCH, D. A.: 'Development and testing of a microwave system to measure coal layer thickness up to 25 cm'. Nat. Bur. Stds., Report No.SR-723-8-79 (Boulder, CO), 1979

[12] NILSSON, B.: 'Two topics in electromagnetic radiation field prospecting'. Doctoral Thesis, University of Lulea, Sweden, 1978

Chapter 2

System design

2.1 Introduction

GPR has an enormously wide range of applications, ranging from planetary exploration to the detection of buried mines. The selection of a range of frequency operations, a particular modulation scheme, and the type of antenna and its polarisation depends on a number of factors, including the size and shape of the target, the transmission properties of the intervening medium, and the operational requirements defined by the economics of the survey operation, as well as the characteristics of the surface. The specification of a particular type of system can be prepared by examining the various factors which influence detectivity and resolution.

To operate successfully, ground penetrating radar must achieve:

(a) an adequate signal to clutter ratio
(b) an adequate signal to noise ratio
(c) an adequate spatial resolution of the target
(d) an adequate depth resolution of the target.

Most GPR systems detect the backscattered signal from the target, although forward transmission methods are used in borehole tomographic radar imaging.

This Chapter considers the principal factors affecting the design of a GPR in order to illustrate those factors which need to be considered. The aim is to illustrate the technical options available to the operator or designer. This is not a rigorous treatment of radar system analysis but does enable an order of magnitude estimate of the various loss components to be assessed. Many radar systems generate a fast rise time impulsive voltage, so the signal level is best considered from the point of view of voltages across particular nodes in the network. A consideration of this approach is given at the end of this section, and an expression suitable for evaluation using MathCAD™ is included, together with a series of modelled results for particular values.

A block diagram of a generic radar system is shown in Figure 2.1. The source of energy can be an amplitude, frequency or phase modulated waveform or noise signal, and the selection of the bandwidth, repetition rate and mean power will depend upon

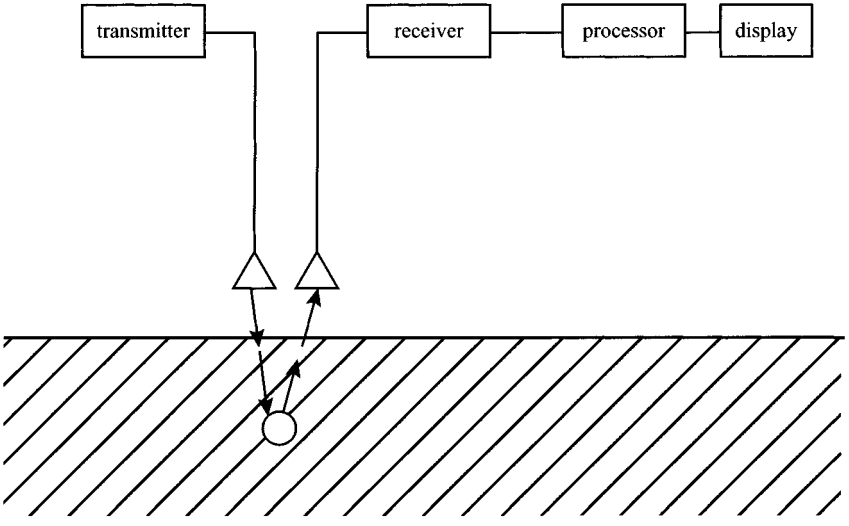

Figure 2.1 Block diagram of generic radar system

the path loss and target dimensions. The transmit and receive antennas will usually be identical and will be selected to meet the characteristics of the generated waveform. The receiver must be suitable for the type of modulation and down-conversion and possess an adequate dynamic range for the path losses that will be encountered. The various design options are shown in Figure 2.2, and will be discussed in Section 2.7 as well as in subsequent chapters.

An initial estimate of the range performance of the radar can be gained by considering the following factors: path loss, target reflectivity, clutter and system dynamic range. The spatial resolution of the radar can be determined by considering the depth and plan resolution separately.

The majority of GPR systems use an impulse time domain waveform and receive the reflected signal in a sampling receiver. However, more use has been made of FMCW and stepped frequency radar modulation schemes in recent years and, as the cost of the components decreases, it may be expected that more of these systems will be used, as their dynamic range can be designed to be greater than the time domain radar.

2.2 Range

2.2.1 Introduction

The range of a GPR is primarily governed by the total path loss, and the three main contributions to this are the material loss, the spreading loss and the target reflection loss or scattering loss.

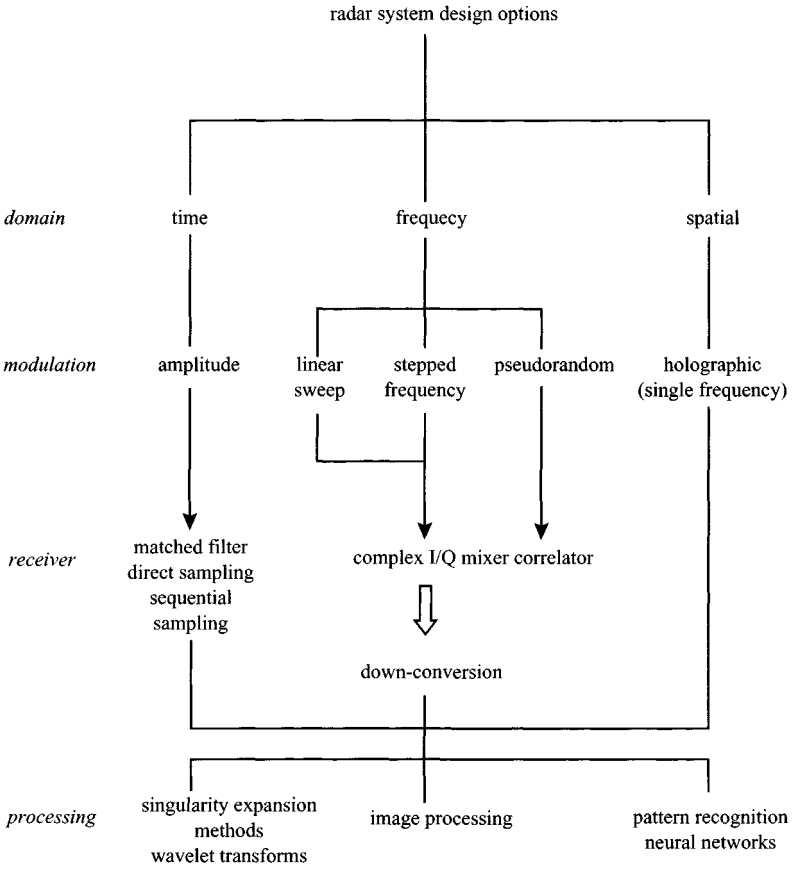

Figure 2.2 Ground penetrating radar system design options

An example of a simplified general method of estimation is given in this section. It should be noted that this contains many simplifying assumptions, which later chapters will discuss in more detail. The main assumption relates to the spreading loss. In conventional free-space radar the target is in the far field of the antenna and spreading loss is proportional to the inverse fourth power of distance provided that the target is a point source. In many situations relating to ground penetrating radar the target is in the near field and Fresnel zone and the relationship is no longer valid. However, for this example an R^{-4} spreading loss will be assumed, even though for a planar interface this is not valid and a correction is included.

The signal that is detected by the receiver undergoes various losses in its propagation path from the transmitter to the receiver (see Figure 2.3). The total path loss for a particular distance is given by

$$L_T = L_e + L_m + L_{t1} + L_{t2} + L_s + L_a + L_{sc} \tag{2.1}$$

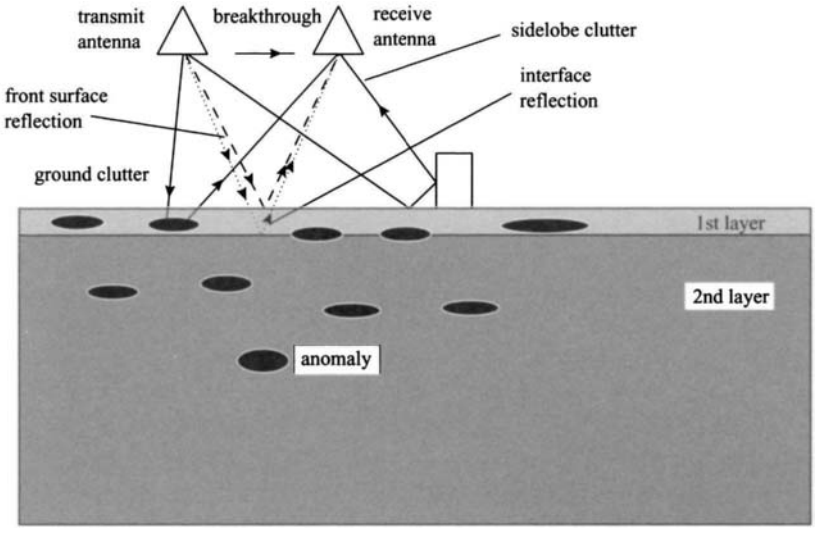

Figure 2.3 Physical layout of radar system

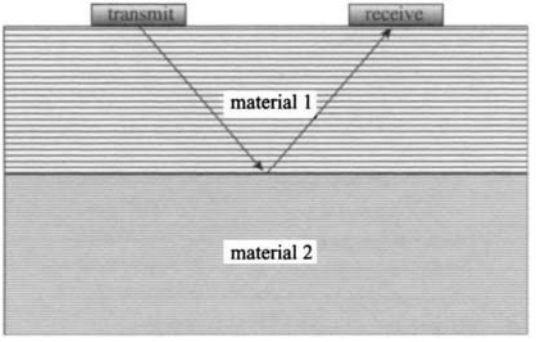

Figure 2.4 Outline arrangement of GPR system

where:

L_e = antenna efficiency loss in dB
L_m = antenna mismatch losses in dB
L_{t1} = transmission loss from air to material in dB
L_{t2} = retransmission loss from material to air in dB
L_s = antenna spreading losses in dB
L_a = attenuation loss of material in dB
L_{sc} = target scattering loss in dB

At a fixed frequency of, say, 100 MHz these losses may be estimated. In general, for accurate prediction, this calculation needs to be made over a wide band of frequencies, but for this example a single frequency is assumed. The radar to be considered is an impulse radar using planar loaded dipole antennas operated on the ground surface and the target is a planar interface at a depth of 1.0 m from the front surface of the material as shown in Figure 2.4. For this example, the lateral dimensions of the planar interface can be considered to be infinitely large. The example will assume that for the first layer of soil $e_r = 9$ and $\tan\delta = 0.1$ while for the second layer of soil $e_r = 16$ and $\tan\delta = 0.5$. This gives the modulus of impedance of the first layer as 125 Ω and the second as 89 Ω at a frequency of 100 MHz.

2.2.2 *Antenna loss*

The antenna efficiency is a measure of the power available for radiation as a proportion of the power applied to the antenna terminals. In the case of resistively loaded antennas the efficiency is not high and is the result of the need for wideband operation. It would be expected that over an octave bandwidth the efficiency of a loaded antenna would be 4 dB lower than that of an unloaded antenna, which might have a loss of 2 dB. For other types of antenna, i.e. the short axial horn, TEM horn, etc., the antenna efficiency is higher and lower losses can be expected.

In the example under consideration it is assumed that $L_e = -2$ dB per antenna, i.e. −4 dB for a pair of loaded dipole antennas.

2.2.3 *Antenna mismatch loss*

The antenna mismatch loss is a measure of how well the antenna is matched to the transmitter; usually little power is lost by reflection from antenna mismatch and is in the order of −1 dB.

2.2.4 *Transmission coupling loss*

In the case of antennas operated on the surface of the material the transmission loss from the antenna to the material is given by

$$L_{t1} = -20\log_{10}\left(\frac{4Z_mZ_a}{|Z_m + Z_a|^2}\right)\text{dB} \tag{2.2}$$

where:

Z_a = characteristic impedance of air, which equals 377 Ω
Z_m = characteristic impedance of the material,

$$Z_m = \left(\sqrt{\frac{\mu_0\mu_r}{\varepsilon_0\varepsilon_r}}\right)\frac{1}{(1+\tan^2\delta)^{\frac{1}{4}}}\left(\cos\frac{\delta}{2} + j\sin\frac{\delta}{2}\right) \tag{2.3}$$

Typically, for many earth materials $Z_m = 125$ Ω; hence $L_{t1} = -2.5$ dB.

2.2.5 *Retransmission coupling loss*

The retransmission loss from the material to the air on the return journey is given by

$$L_{t2} = -20 \log_{10} \left(\frac{4 Z_m Z_a}{|Z_m + Z_a|^2} \right) \text{dB} \tag{2.4}$$

Hence $L_{t2} = -2.5$ dB.

2.2.6 *Spreading loss*

The antenna spreading loss is conventionally related to the inverse fourth power of distance for a point reflector, and in this example the ratio of the received power to the transmitted power is given by

$$\frac{P_r}{P_t} = \frac{G_t A_r \sigma}{(4\pi R^2)^2} \tag{2.5}$$

where:

G_t = gain of transmitting antenna (loaded dipole) = 15
A_r = receiving aperture (loaded dipole) = 4×10^{-2} m^2
R = range to the target = 1.0 m
σ = radar cross-section ($\sigma = 1$ m^2).

Hence L_s can be defined as

$$\begin{aligned} L_s &= -10 \log_{10} \frac{G_t A_r \sigma}{(4\pi R^2)^2} \\ &= -21 \text{ dB} \end{aligned} \tag{2.6}$$

It should be noted that the radar range equation assumes a point source scatterer, which is not always the case. The range law may need adjusting for the different types of targets as shown in Table 2.1, and in this case a planar relationship is used.

The nature of the target influences the magnitude of the received signal. The following approximate relationships apply for targets, which extend across the zone illuminated by an antenna (i.e. its footprint).

Considerably more backscattered energy will be returned from a planar reflector at a given depth compared with other target types exhibiting similar dielectric contrasts. As the target assumed in this example is a planar interface, a correction to the R^{-4} law is necessary.

Table 2.1 Adjustment of range law for different types of target

Nature of target	Magnitude of received signal
Point scatterer (small void)	(target depth)$^{-4}$
Line reflector (pipeline)	(target depth)$^{-3}$
Planar reflector (smooth interface)	(target depth)$^{-2}$

2.2.7 Target scattering loss

In the case of an interface between the material and a plane, where both the lateral dimensions of the interface and the overburden are large, then

$$L_{sc} = 20\log\left(1 - \left|\frac{Z_1 - Z_2}{Z_1 + Z_2}\right|\right) + 20\log\sigma \tag{2.7}$$

Z_1 = characteristic impedance of first layer of material
Z_2 = characteristic impedance of second layer of material
σ = target radar cross-section

Note that the radar cross-section should be considered as a bistatic radar cross-section in relation to the antenna radiation patterns.

Typically, L_{sc} would be in the order of -1.6 dB for the interface between the first and second layers. In this example σ is considered to be unity, i.e. 0 dB, as the situation is equivalent to an infinite dielectric half-space.

Where the physical dimensions of the interface or anomaly are small, then the target scattering loss L_{sc} increases due to the geometry of the situation, and the returned signal becomes smaller. Under some conditions the physical dimensions of the anomaly are such as to create a resonant structure, which increases the level of the return signal and decreases the target scattering loss. It is possible to distinguish air filled voids and water filled voids by examination of their resonant characteristics and the relative phase of the reflected wavelet. Water has a relative dielectric constant of 81, which will serve to reduce the resonant frequency of any void by a factor of 9 ($\sqrt{\varepsilon_r}$), and this variation may be the means of identifying water filled voids.

Table 2.2 gives an indication of the radar cross-sectional area in free space. The dimensions should be corrected for the different wavelengths within the material. The following radar cross-sections are, of course, relevant only to extended scatterers, and this should be taken into account when calculating overall system losses.

Many of the targets being searched for by sub-surface radar methods are non-metallic, so their scattering cross-section is dependent upon the properties of the surrounding dielectric medium. Where the relative permittivity of the target is lower than that of the surrounding medium, such as an air-filled void below a concrete ground slab, the interface does not produce a phase reversal of the backscattered

Table 2.2 Radar cross-sections

Scatterer	Aspect	Radar CSA	Symbols
Sphere		$\sigma = \pi a^2$	a = radius
Flat plate arbitrary shape	Normal	$\sigma = \dfrac{4\pi A^2}{\lambda^2}$	A = plate area
Cylinder	Angle broadside	$\sigma = a\dfrac{\lambda \cos\theta \sin^2(kl \sin\theta)}{2\pi \sin^2\theta}$	a = radius l = length
Prolate spheroid	Axial	$\sigma = \dfrac{\pi b_0^2}{a_0^2}$	a_0 = major axis b_0 = minor axis
Triangular trihedral corner reflector	Symmetry axis	$\sigma = \dfrac{4\pi a^4}{3\lambda^2}$	L = side length

wave. Conversely, when the scattering is caused by a metallic boundary or where the relative permittivity of the target is larger than that of the surrounding medium, phase reversal occurs in the backscattered wave. This phenomenon may be used as a way of distinguishing between conducting and nonconducting targets.

The physical shape of the target will influence the frequency and polarisation of the backscattered wave and can be used as a means of preferential detection. The effect of the high permittivity of typical soil means that some targets, such as thin-walled plastic pipes, produce a stronger radar return when buried than when in free space. In such circumstances, the radar is responding primarily to the dielectric properties of the enclosed volume (i.e. the water or air-filled space within the pipe).

The type of target being sought (i.e. a sphere, a linear target such as a pipe or an interface) affects the choice of antenna type and configuration as well as the kind of signal processing techniques which may be employed. Generally, parallel arrangements of dipole antennas are suitable for most targets whereas crossed dipoles are more appropriate for either small or linear targets.

2.2.8 *Material attenuation loss*

The attenuation loss of the material is given by

$$L_a = 8.686 \times 2 \times R \times 2\pi f \sqrt{\left(\frac{\mu_0 \mu_r \varepsilon_0 \varepsilon_r}{2}\left(\sqrt{(1+\tan^2\delta)}\right) - 1\right)} \tag{2.8}$$

Table 2.3 Material loss at 100 MHz and 1 GHz

Material	Loss at 100 MHz	Loss at 1 GHz
Clay (moist)	5–300 dB m^{-1}	50–3000 dB m^{-1}
Loamy soil (moist)	1–60 dB m^{-1}	10–600 dB m^{-1}
Sand (dry)	0.01–2 dB m^{-1}	0.1–20 dB m^{-1}
Ice	0.1–5 dB m^{-1}	1–50 dB m^{-1}
Fresh water	0.1 dB m^{-1}	1 dB m^{-1}
Sea water	100 dB m^{-1}	1000 dB m^{-1}
Concrete (dry)	0.5–2.5 dB m^{-1}	5–25 dB m^{-1}
Brick	0.3–2.0 dB m^{-1}	3–20 dB m^{-1}

where:

f = frequency in Hz
$\tan\delta$ = loss tangent of material
ε_r = relative permittivity of material
ε_0 = absolute permittivity of free space
μ_r = relative magnetic susceptibility of material
μ_0 = absolute magnetic susceptibility of free space

A typical range of loss for various materials at 100 MHz and 1 GHz is shown in Table 2.3.

2.2.9 *Total losses*

From the previous sections the total losses that will occur at 100 MHz during transmission through 1 m of material of 2.7 dB/m attenuation and then reflection from a boundary interface, where $Z_1 = 125\,\Omega$ and $Z_2 = 89\,\Omega$ would be

$$\begin{aligned} L_T &= L_e + L_m + L_{t1} + L_{t2} + L_s + L_a + L_{sc} \\ &= -4\,\text{dB} - 1\,\text{dB} - 2.5\,\text{dB} - 2.5\,\text{dB} - 21\,\text{dB} - 5.5\,\text{dB} - 1.6\,\text{dB} \\ &= -38\,\text{dB} \end{aligned} \tag{2.9}$$

A basic model for this situation using Mathcad™ is given on the CD, and parameters can be changed to model different situations. On the CD click onto Gpr-signal-range.mcd to view the sheet. Change the parameter values for e_r and $\tan\delta$ to see the effect of material changes. A plot of the various components of the returned signal is given in Figure 2.5.

In the case of a time domain radar system it is more practical to consider peak voltages. The capability of a sub-surface radar system to detect a reflected signal of peak voltage V_r, if the peak transmitted voltage is V_t, can be termed the detectability

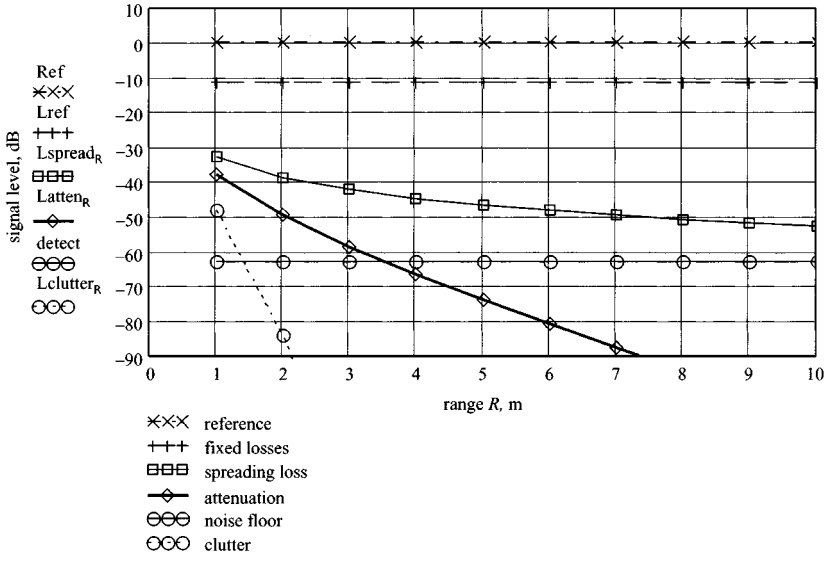

Figure 2.5 Signal amplitude against range

of the radar system,

$$D = 20\log(V_t/V_r)$$

The limiting factor of detectability is the noise performance of the receiver; hence the received voltage must be greater than the noise voltage generated by the latter.

In the case of the previously calculated loss, if the transmitter generates a pulse of peak magnitude 50 V, then the peak received signal would be 112 mV.

Most time domain radar receivers can detect a 1 mV signal even without averaging; hence a reflected wavelet of peak amplitude of 112 mV should be capable of being easily detected. This is only the case if the clutter signals are also low and the amplitude of the clutter signal should also be determined at the same range. Figure 2.5 shows a graph of the various signal levels plotted against range over the interval 1 to 10 m. Note that close to the antenna that is in the range 0 to 1 m, the above analysis is not applicable.

From the values of attenuation indicated above and the nature of the frequency dependence, it follows that for a given signal detection threshold the maximum depth of investigation decreases rapidly with increasing frequency. Most sub-surface radar systems operate at frequencies less than 2 GHz. Figure 2.6 shows for a range of materials measured by Cook [1] the maximum depth of penetration at which radar is likely to be able to give useful information and the approximate upper frequency of operation. Typical maximum depths of penetration rarely exceed 20 wavelengths, except in very low attenuation dielectric mediums. Often the depths of penetration will be much less, particularly in lossy dielectrics.

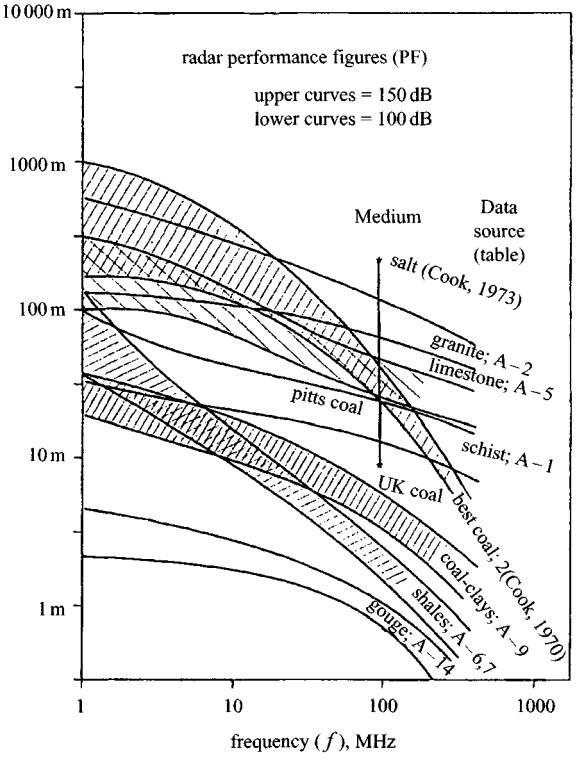

Figure 2.6 Radar probing range (after Cook [1])

It might be thought that a GPR needs to have as low a frequency of operation as possible to achieve adequate penetration in wet materials. However, the ability to resolve the details of a target or separately detect two targets is proportional to the size or spacing of the target in relation to the wavelength of the incident radiation. Consequently a high frequency is desirable for resolution. A compromise between penetration and resolution must be made and is an important consideration in either the selection of system bandwidth or the range of frequencies to be radiated.

Consideration needs also to be given to the fact that, not only does attenuation decrease with frequency, but so does target scattering cross-section. This leads to the situation where it is possible that, for certain targets, material properties and depths, the received signal decreases with frequency. This effect is shown in Figure 2.7 (from Daniels *et al.* [2]), where the ratio between the reflected power, at frequencies of 50 MHz and 500 MHz, at the ground surface has been calculated for small diameter metallic (broken line) or nonmetallic (solid line) cylinders.

In addition to the estimation of signal levels, it is possible to determine the probability of detection and the probability of false alarm for a particular target, and this is shown in Section 3.2.

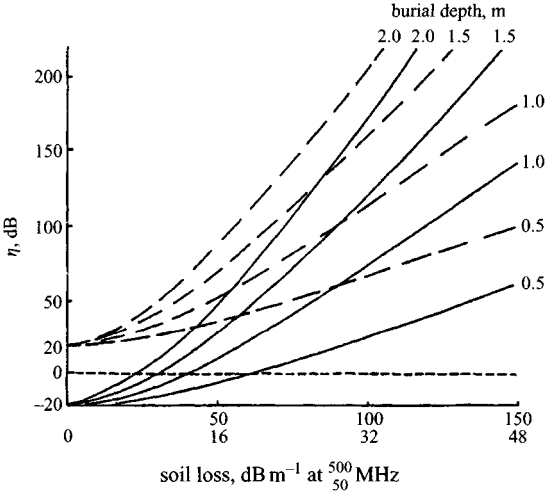

Figure 2.7 Received signal level of various targets (after Daniels et al. [2])

2.3 Velocity of propagation

It can easily be recognised that if the propagation velocity can be measured, or derived, an absolute measurement of depth or thickness can be made. For homogeneous and isotropic materials, the relative propagation velocity can be calculated from

$$v_r = \frac{c}{\sqrt{\varepsilon_r}} \text{ ms}^{-1} \tag{2.10}$$

and the depth derived from

$$d = v_r \frac{t}{2} \text{ m} \tag{2.11}$$

where ε_r is the relative permittivity and t is the transit time to and from the target.

In most practical trial situations the relative permittivity will be unknown. The velocity of propagation must be measured in situ, estimated by means of direct measurement of the depth to a physical interface or target (i.e. by trial holing), or by calculation by means of multiple measurements.

From Figure 2.8 it can be seen that if a hyperbolic spreading function can be measured then the propagation velocity can be derived from

$$v_r = 2\sqrt{\frac{x_{n-1}^2 - x_0^2}{t_{n-1}^2 - t_0^2}} \tag{2.12}$$

and the depth to the target

$$d_0 = \frac{v_r t_0}{2} \tag{2.13}$$

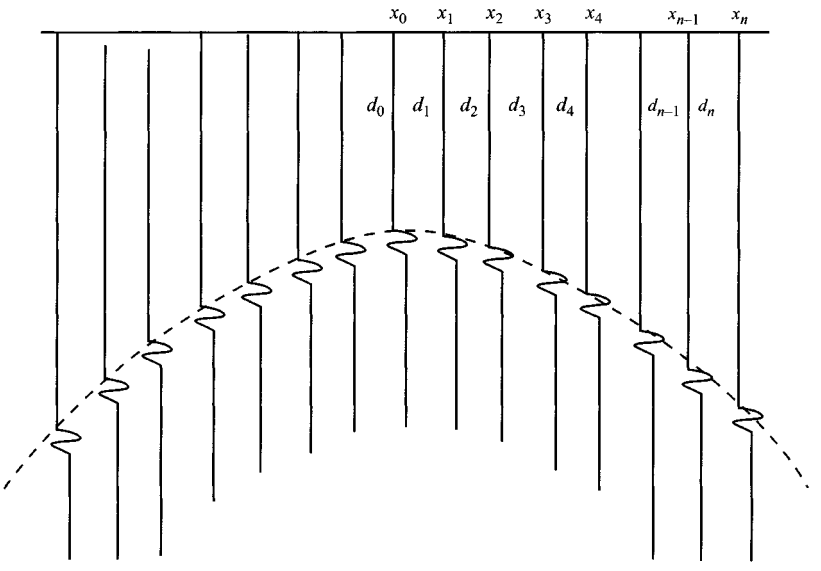

Figure 2.8 Hyperbolic spreading function

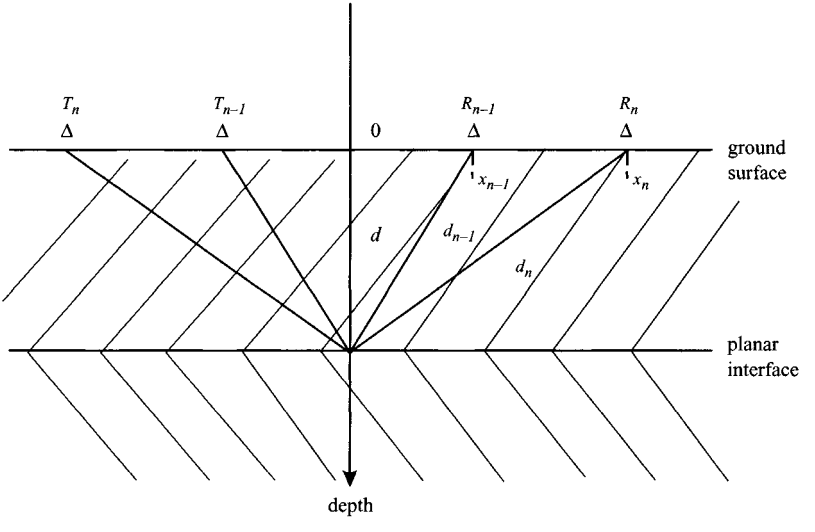

Figure 2.9 Common depth point estimation

An alternative method of calculating the depth of a single planar reflector is by means of the common depth point method. If both transmitting and receiving antennas are moved equal distances from the common centre point the same apparent reflection position will be maintained. The depth of the planar reflector can be

derived from

$$d_n = \sqrt{\frac{x_{n-1}^2 t_n^2 - x_n^2 t_{n-1}^2}{t_{n-1}^2 - t_n^2}} \tag{2.14}$$

where the two positions of the antenna are shown in Figure 2.9.

The variation of permittivity with frequency in wet dielectrics implies that there will be some variation in the velocity of propagation with frequency. The magnitude of this effect will generally be small for the range of frequencies typically employed for sub-surface radar work. A dielectric exhibiting this characteristic is said to be 'dispersive'. Where the material has different propagation characteristics in different

Table 2.4 Material propagation characteristics

Material	Relative permittivity	Propagation velocity, cm/ns	Wavelength	
			100 MHz cm	1 GHz cm
Air	1	30	300	30
Concrete	9	10	100	10
Freshwater	80	3.35	33	3

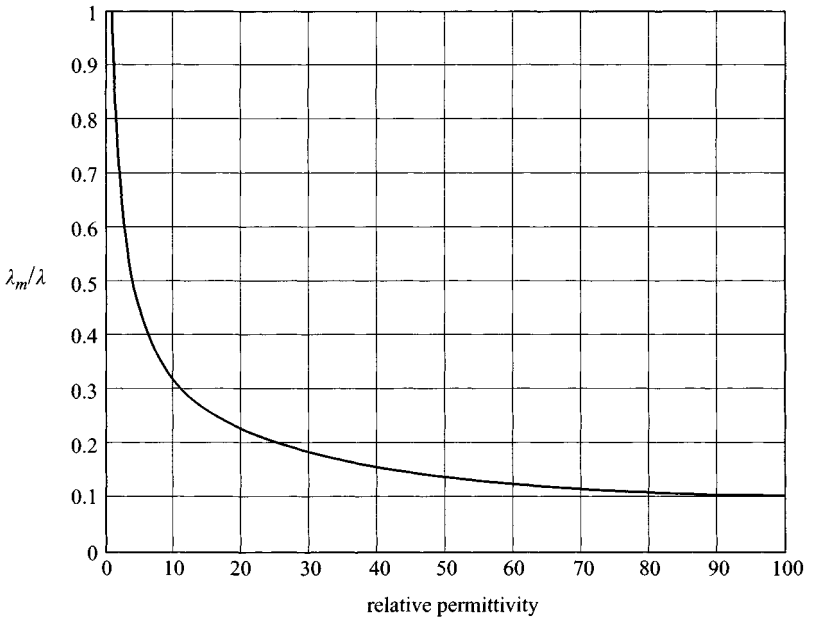

Figure 2.10 Normalised wavelength against relative permittivity

directions it is said to be anisotropic, and an example is coal in the seams prior to excavation, where the propagation characteristics normal to the bedding plane are different from those parallel to the plane.

In free space the propagation velocity, c, is 3×10^8 ms^{-1}. The velocity in air is very similar to that in free space and is normally taken as the same. In sub-surface radar work the elapsed time between the transmitted and received pulses is measured in nanoseconds (10^{-9} s) because of the short travel path lengths involved.

Propagation velocity decreases with increasing relative permittivity. The wavelength within the material also decreases as the velocity of propagation slows in accordance with the following relationship:

$$\text{wavelength } \lambda_m = \frac{v_r}{f} \tag{2.15}$$

The result of these effects is illustrated by Table 2.4; see also Figure 2.10.

2.4 Clutter

The clutter that affects a GPR can be defined as those signals that are unrelated to the target scattering characteristics but occur in the same sample time window and have similar spectral characteristics to the target wavelet. This is a somewhat different definition from conventional radar clutter and should be borne in mind when considering conventional methods of clutter filtering such as MTI, which would be inappropriate to apply to ground penetrating radar data.

Clutter can be caused by breakthrough between the transmit and receive antennas as well as multiple reflections between the antenna and the ground surface. Clutter will vary according to the type of antenna configuration, and the parallel planar dipole arrangement is one where the stability of the level of breakthrough is most constant. Typically a maximum level of -40 dB to -50 dB is encountered.

The planar crossed dipole antenna can be designed and manufactured to provide very low levels of breakthrough (>70 dB). However, it then becomes very susceptible to 'bridging' by dielectric anomalies on the near surface which can degrade the breakthrough in a random manner as the antenna is moved over the ground surface. The variability of the breakthrough is unfortunate as it is not usually amenable to signal processing. The same problem is encountered with planar spiral antennas. Local variations in the characteristic impedance of the ground can also cause clutter, as can inclusions of groups of small reflection sources within the material. In addition, reflections from targets in the side lobes of the antenna, often above the ground surface, can be particularly troublesome. This problem can be overcome by careful antenna design and incorporating radar absorbing material to attenuate the side and back lobe radiation from the antenna.

In general, clutter is more significant at short range times and decreases at longer times.

It is possible to quantify the rate of change of the peak clutter signal level as a function of time as in many cases this parameter sets a limit to the detection capability

of the radar system. The effect of clutter on system performance is shown in Figure 2.5, which illustrates the consequent limitation on near-range radar performance.

Various techniques have been investigated in the search for a method of reducing clutter. In the case of impulse radars using TEM horns or FMCW radars using ridged horns and reflectors, it has been found possible to angle the bore sight of the horn antennas to take advantage of the critical angle, thereby suppressing to some extent the ground surface reflection.

2.5 Depth resolution

There are some applications of sub-surface radar, such as road layer thickness measurement, where the feature of interest is a single interface. Under such circumstances it is possible to determine the depth sufficiently accurately by measuring the elapsed time between the leading edge of the received wavelet and a reference time such as the front surface reflection provided the propagation velocity is accurately known.

However, when a number of features may be present, such as in the detection of buried pipes and cables, then a signal having a larger bandwidth is required to be able to distinguish between the various targets and to show the detailed structure of a target. In this context it is the bandwidth of the received signal which is important, rather than that of the transmitted wavelet. The 'earth' acts as a lowpass filter, which modifies the transmitted spectrum in accordance with the electrical properties of the propagating medium. The results from a simplified model of this situation are shown in Figure 2.11, where the general pulse stretching can be seen for different rates of attenuation. A Ricker wavelet has been used as the source impulse as this is a typical impulse. Note that the output impulse has been auto-scaled for clarity and actually is severely attenuated as the lowpass filter slope is increased.

The required receiver bandwidth B' can be determined by considering the power spectrum of the received signal. The power spectrum results from the Fourier transform of the received signal wavelet. If the envelope of the wavelet function is considered, it is possible from the Rayleigh criterion for resolution to determine the receiver bandwidth. An alternative definition of the receiver bandwidth is given by Cook [1] and is derived from the autocorrelation function of the signal wavelet.

If $f(t)$ is the wavelet, then the autocorrelation function is given by

$$R_{11} = \int_{-\infty}^{\infty} f(t) f(t - \tau)\, \mathrm{d}\tau \tag{2.16}$$

The general shape of the autocorrelation function shown in Figure 2.12, which is related to the matched filtering resolution, can be used to define the bandwidth requirement. The autocorrelation function is, of course, related to the power spectrum of the received waveform and is therefore a useful measure. A receiver bandwidth in excess of 500 MHz and typically 1 GHz is required to provide a typical resolution of between 5 and 20 cm, depending on the relative permittivity of the material.

The required receiver bandwidth can be determined by considering the power spectrum of the received signal. The power spectrum results from the Fourier transform of the received signal wavelet and is shown in Figure 2.13.

If the envelope of the wavelet function is considered as shown in Figure 2.14, then it is possible from the Rayleigh criteria for resolution to determine a receiver bandwidth. An alternative definition of the receiver bandwidth is given in Reference [1] and is derived from the autocorrelation function of the signal wavelet.

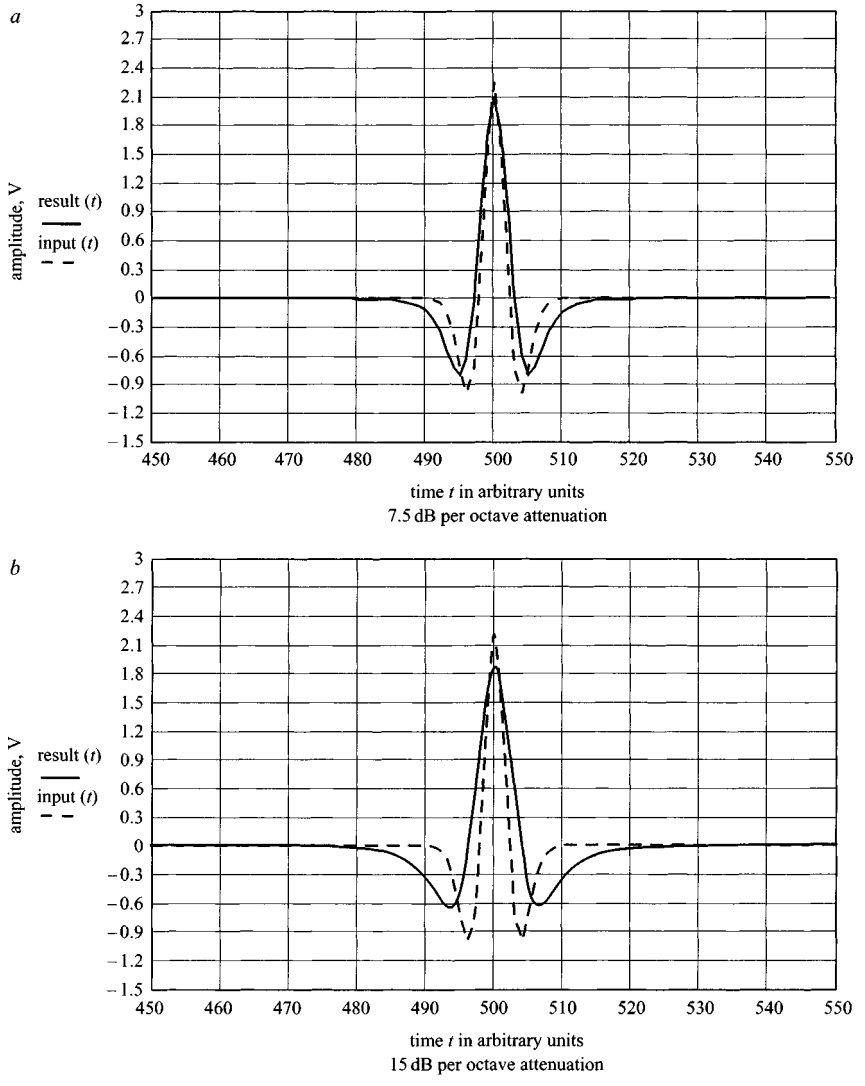

Figure 2.11 Effect of ground attenuation on pulse length

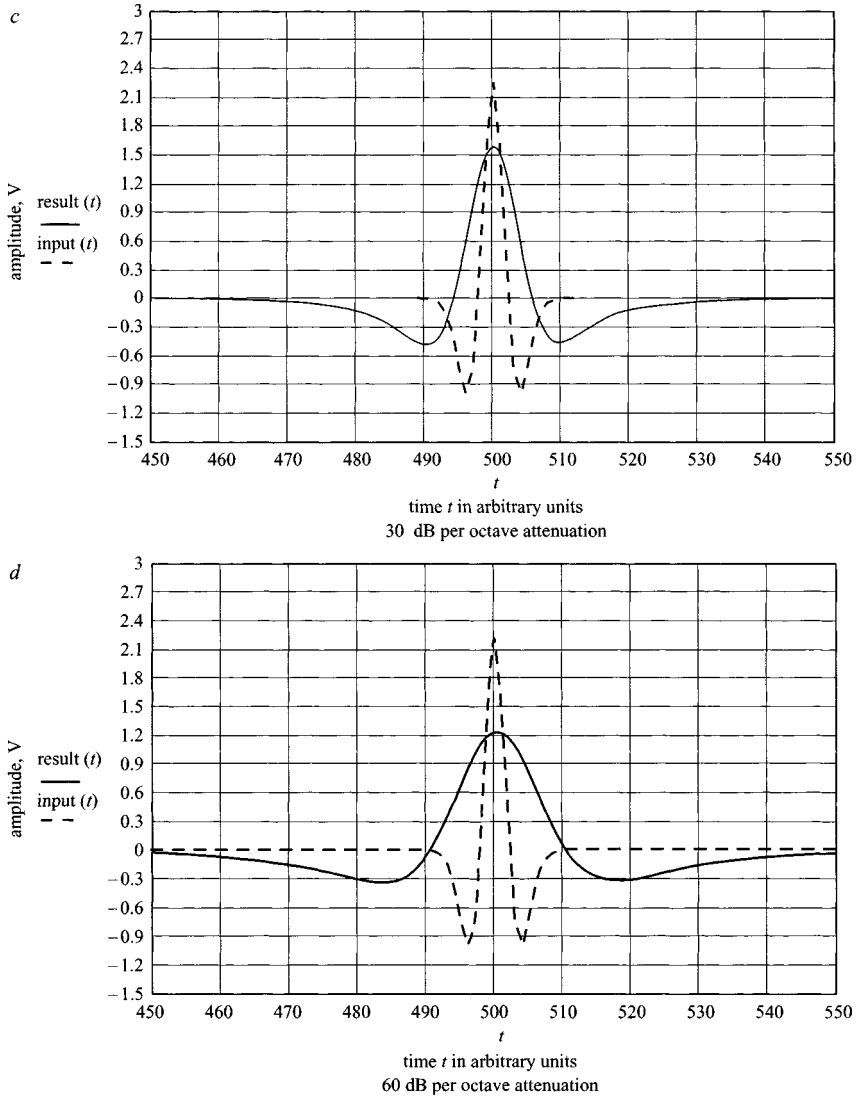

Figure 2.11 Continued

Although a greater depth resolution is achieved in wetter materials for a given transmitted bandwidth, earth materials with significant water content tend to have higher attenuation properties. This characteristic reduces the effective bandwidth, tending to balance out the change so that within certain bounds the resolution is approximately independent of loss within the propagating material.

Where interfaces are spaced more closely than one half wavelength the reflected signal from one interface will become combined with that from the other, as shown

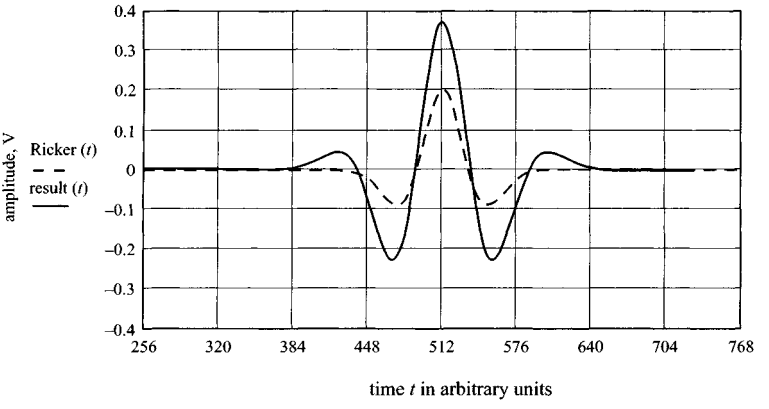

Figure 2.12 Autocorrelation of wavelet function

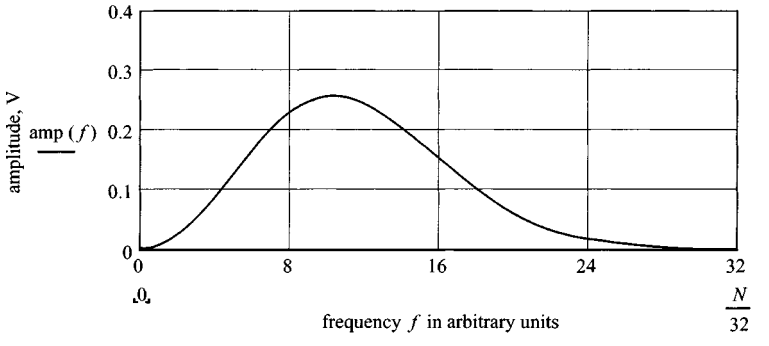

Figure 2.13 Spectrum of autocorrelation function of Ricker wavelet

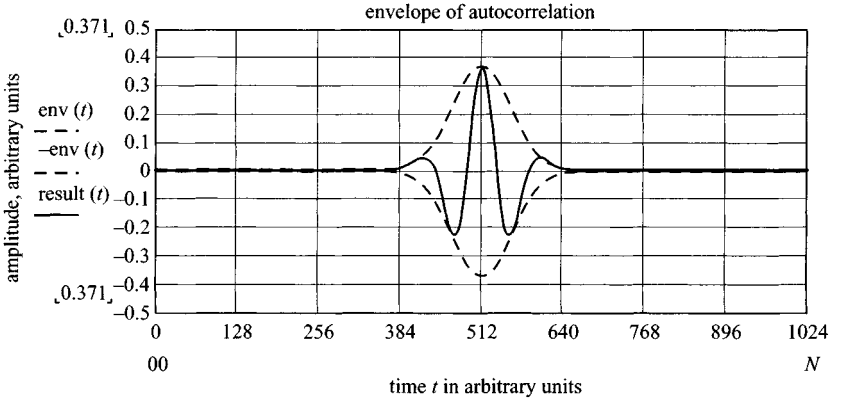

Figure 2.14 Envelope of autocorrelation function of Ricker wavelet

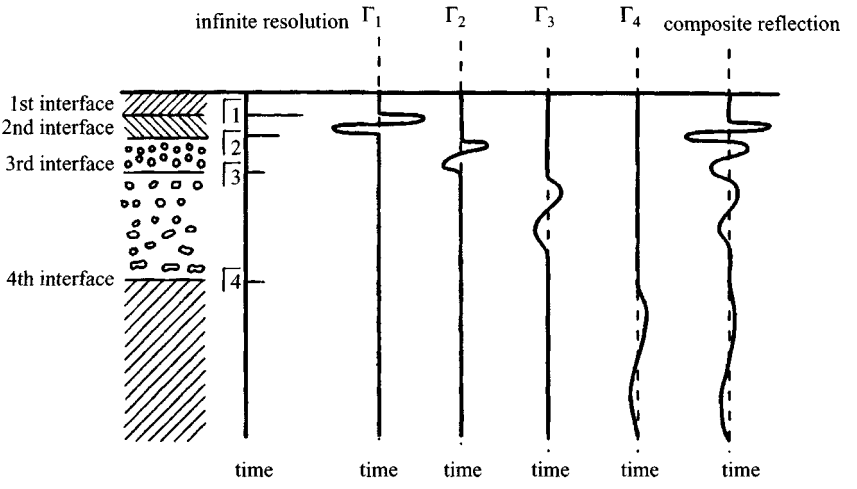

Figure 2.15 Convolution of multiple interface reflections

in Figure 2.15. In such circumstances some form of deconvolution processing would be required in order to recognise the responses from the individual interfaces and to enable them to be characterised and traced. However, such processing is not normally carried out during standard commercial radar surveys.

2.6 Plan resolution

The plan resolution of a subsurface radar system is important when localised targets are sought and when there is a need to distinguish between more than one at the same depth. Where the requirement is for location accuracy, which is primarily a topographic surveying function, the system requirement is less demanding.

The effect of the radiation footprint on the ground can be seen from Figure 2.16, where the distance between the radiating source and the ground surface has been increased from 0.1 m to 0.5 m (left to right). The ground area is 2 m by 2 m and it can be seen that the width of the 3 dB footprint increases considerably as the source is raised from the ground. The effect of this on the image resolution is also considerable as the convolution of the antenna pattern with the target causes a blurring of the target image as shown in Figure 2.17.

The plan resolution is defined by the characteristics of the antenna and the signal processing employed. In general, to achieve an acceptable plan resolution requires a high gain antenna. This necessitates an antenna with a significant aperture at the lowest frequency transmitted. To achieve small antenna dimensions and high gain therefore requires the use of a high carrier frequency, which may not penetrate the material to sufficient depth. When choosing equipment for a particular application it is necessary to compromise between plan resolution, size of antenna, the scope for signal processing and the ability to penetrate the material.

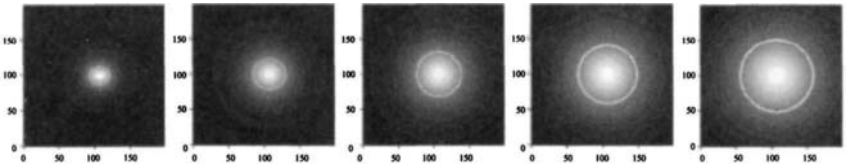

Figure 2.16 Radiation footprint on the ground from an isotropic source

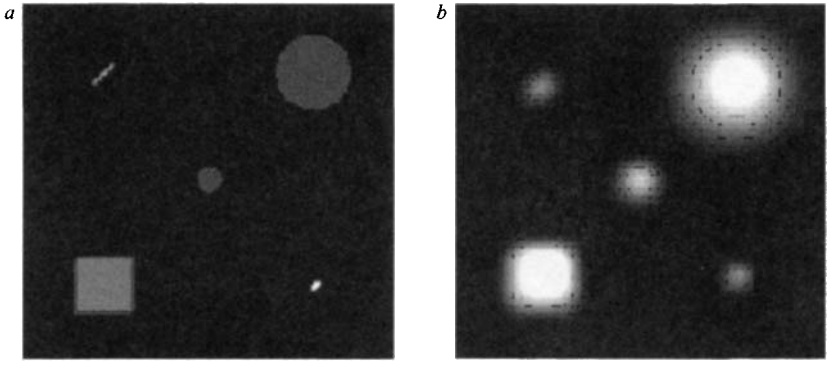

Figure 2.17 Effect of convolution of antenna footprint on radar image

Plan resolution improves as attenuation increases, assuming that there is sufficient signal to discriminate under the prevailing clutter conditions. In low attenuation media the resolution obtained by the horizontal scanning technique is degraded, but under these conditions the use of advanced signal processing techniques becomes feasible. These techniques typically require measurements made using transmitter and receiver pairs at a number of antenna positions to generate a synthetic aperture or focus the image. Unlike conventional radars, which generally use a single antenna, most GPR systems use separate transmit and receive antennas in what has been termed a bistatic mode. However, as the antenna configuration is normally mobile, the term bistatic is not really relevant.

The descriptions normally applied to the modes of geophysical survey appear more relevant and are therefore introduced. Geophysicists classify surveys in four main modes: common source, common receiver, common offset and common depth point, as shown in Figure 2.18.

Most GPR surveys use a common offset survey mode in which the separation between the transmitter and receiver is fixed. However, both common depth point and common source or receiver modes have also been used but require different signal processing approaches.

In the common offset mode the transmitter and receiver antennas are scanned above the ground surface over a buried target as shown in Figure 2.18. The received

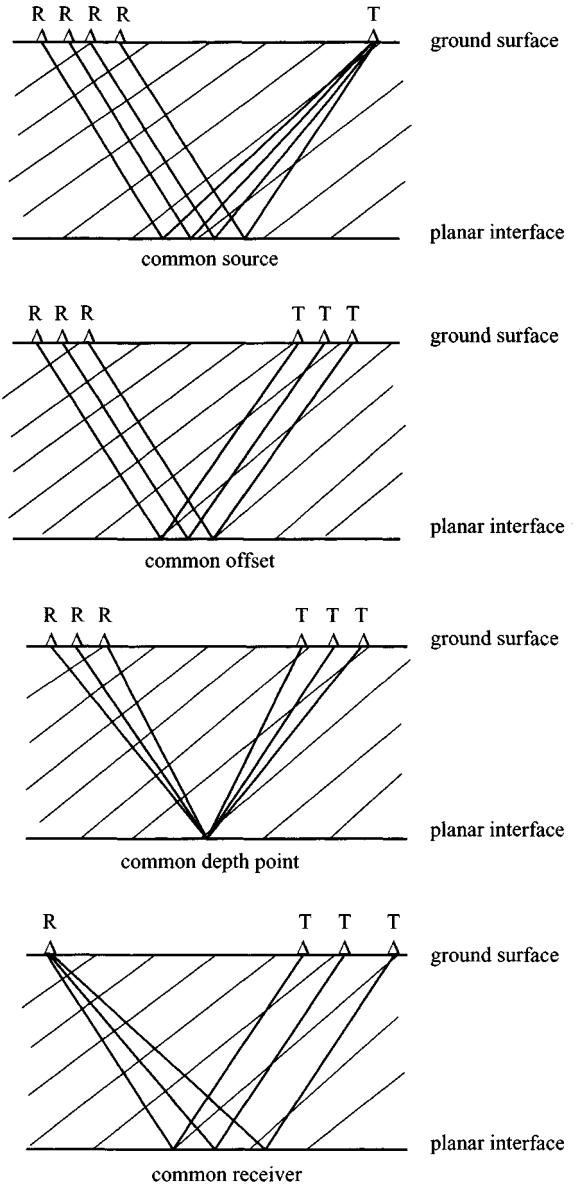

Figure 2.18 Geophysical survey modes

power for a point source scatterer in the far field can be shown to be proportional to

$$P_r = \frac{P_t \cos^4 \theta}{d^4} \exp(-2\alpha d \sec\theta) \tag{2.17}$$

where α is the attenuation coefficient and θ is the angle between the midpoint of the combined transmit–receive antenna and the vertical to the target.

Where the plan resolution is defined as the half power points of the spatial response of the scatterer at the plane of the surface, the resolution is approximated by

$$\Delta x = 4d\sqrt{\frac{\ln 2}{2 + \alpha d}} \tag{2.18}$$

This approximation takes no account of the antenna beam pattern in either x or y directions. However, it does indicate that as the attenuation increases the plan resolution improves, provided that adequate signal to noise and signal to clutter ratios are maintained. It should be noted that, in low attenuation materials, synthetic aperture processing can be applied and plan resolution is recovered.

Typically the improvement in resolution is most noticeable at depths greater than 1 m, and an improvement in resolution of 30% would be found in the plan resolution of targets buried at 2 m in materials of 9 dB m^{-1} and 30 dB m^{-1} attenuation.

2.7 System considerations

The majority of surface penetrating radars are based on the time domain impulse design. Alternative design options can be considered, and experimental versions of stepped frequency (SFCW) or synthesised impulse (SI), as well as frequency modulated (FMCW), noise or pseudo random coded (PRC), have been designed and built.

While the different modulation techniques are considered in detail in Chapter 6 it is useful to summarise the general attributes of each option (see Figure 2.19).

Time domain impulse radar systems are available commercially, and manufacturers usually offer a range of antennas and pulse lengths to suit the desired probing range. Depths of greater than 30 m require pulse lengths in the order of 40 ns (approximately a bandwidth of 50 MHz at a centre frequency of 25 MHz), and very short range precision probing may use pulse lengths of the order of or less than 1.0 ns – that is, an approximate bandwidth of 2 GHz at a centre frequency of 1 GHz.

Planar impulse radar antennas generally operate closely coupled to the ground and are usually designed so that the polarisation of the transmitted and received signals are parallel. The exception to this is the crossed dipole antenna, which has been used for detecting either linear features such as pipes, cables and cracks in the material or small targets such as buried plastic mines.

Most antennas have a relatively small footprint, which means that rapid and wide area surveying can only be achieved with multi-channel radar systems. For road survey such methods are cost effective and practical. An alternative to the planar antenna is the TEM horn, which can be used with a surface to antenna spacing of up to 1 m.

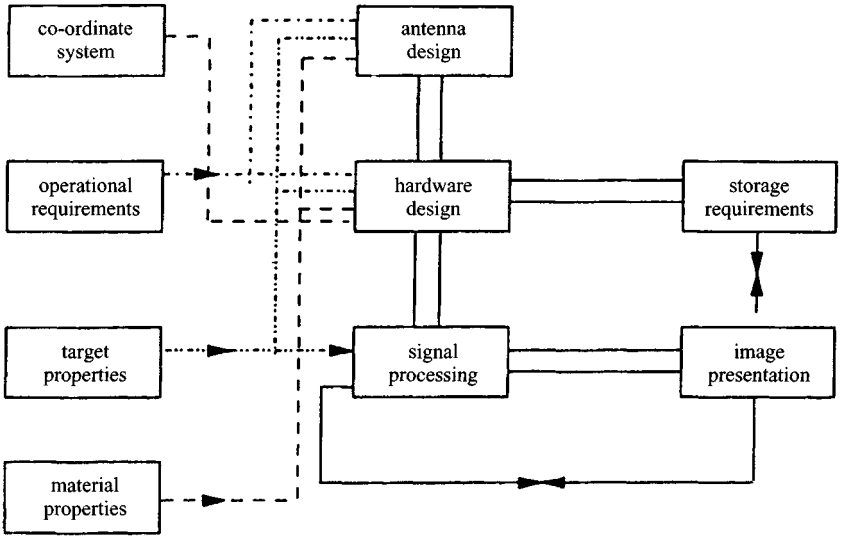

Figure 2.19 System design considerations

Although alternative modulation methods to the impulse radar have been used, there is very little commercially available FMCW, stepped frequency or synthesised pulse radar equipment, although this situation could change in the future.

Whatever system is considered it is important to consider the receiver dynamic range and sensitivity rather than the ratio of the peak transmitted signal to the minimum detectable signal.

A practical example will illustrate the reason for this. If a GPR is being used to survey the road and traverses a metal cover on the surface of the road the received signal will be maximum and may well saturate the receiver circuits. If the receiver cannot recover from this high level input within a few nanoseconds, all low level signals caused by targets deeper than and adjacent to the cover will go undetected. It is therefore the receiver performance and the method of signal down-conversion which must be considered as defining the overall performance. A receiver with a true dynamic range of 60 dB followed by an analogue to digital converter with a dynamic range of 96 dB (16 bits) is only capable of providing an effective dynamic range of 60 dB.

Great care should be taken when interpreting specifications to ascertain the true system performance.

2.8 References

[1] COOK, J.: 'Radar transparencies of mine and tunnel rocks', *Geophysics*, 1975, **40**, (5), pp. 865–885

[2] DANIELS, D. J., GUNTON, D. J., SCOTT, H. F.: 'Introduction to sub-surface radar', *IEE Proceedings F*, 1988, **135**, (4), pp. 278–321

Chapter 3

Modelling techniques

3.1 Introduction

Models of the GPR situation range from a simple single frequency evaluation of path losses to complete 3D time domain descriptions of the GPR and its environment. This Chapter introduces some of the approaches and provides a starting point for further exploration of the literature.

Modelling techniques include single frequency models, time domain models, ray tracing, integral techniques (MOM – method of moments) and discrete element methods. The finite-difference time-domain (FDTD) technique has become one of the popular techniques and can be developed to run on most desktop computers with relative efficiency.

The most basic model uses the radar range equation and enables an estimate of received signal level, dynamic range and probability of detection to be assessed. It has significant weaknesses in that most close range GPR systems are operating in the near field or even the reactive field of the antenna (which is also in a bistatic mode), whereas the model assumes a far field model. It is probably more relevant to the longer-range geophysical applications where the target is many tens of metres from the radar. This is described in Section 3.2. A transmission line model, which enables an A-scan representation to be generated, is described in Section 3.3 and is followed by a simulation using a finite-difference time domain (FDTD) method to model the field propagation of a typical GPR system. Sections 3.4 and 3.5 provide further and more detailed examples of modelling methods as applied to particular situations.

Other models are available from academic sources or as commercial products from vendors of GPR equipment and geophysical houses.

Work on the modelling of GPR antennas has been carried out by Huang *et al.* [1], Lee *et al.* [2] and Guangyou *et al.* [3] using an FDTD method, as well as by Martel *et al.* [4] and Meincke and Kim [5]. Particular attention has been paid to soil effects by Teixeira *et al.* [6, 7], Chew *et al.* [8], Oguz and Gurel [9], Liu and Fan [10],

Liu *et al.* [11], Rappaport and Weedon [12], and Gurel and Oguz [13]. Special consideration to rough surfaces has been made by Rappaport and El-Shenawee [14]. Three-dimensional modelling of GPR has been carried out by Zhan *et al.* [15], Gurel and Oguz [16], and Oguz and Gurel [17]. Further modelling techniques are explored by Desai *et al.* [18] and Wang *et al.* [19], who carried out a SAR simulation.

GprMax2D V1.5 (electromagnetic simulator for ground-probing radar) is freely available for teaching and research purposes and can be downloaded in either Windows™ or Linux (http://www.gprmax.org/) and was developed by Dr Antonis Giannopoulos of the University of Edinburgh. Modelling programmes are also available from Dr Gary Olhoeft from his website at http://www.g-p-r.com/, while commercial products are also available from http://www.ka.shuttle.de/software/Reflex/gpr.htm.

3.2 Received signal levels and probability of detection

The most basic model for assessment of signal level is derived from the radar range equation, which does, however, have severe limitations with respect to correct representation of the actual operation of a short range (<2 m) GPR system. However, it does enable a first order assessment of expected signal levels, and an example is given in this Section. The model is based on the equation for the voltage at the receiver as a function of range r and target radar cross-section σ given by

$$V(r,\eta) = \frac{V_0}{\tau}\frac{1}{c}\frac{A\sigma\kappa}{r'^2}\tau_g\rho_t 10^{-3}e^{(-k2r)} \tag{3.1}$$

where:

V_0 = peak radiated voltage in volts
T = pulse duration in seconds
C = speed of light in ms^{-1}
A = antenna effective aperture in m^2
σ = target cross-section in m^2
κ = number of averages
τ_g = transmission coefficient into ground
ρ_t = reflection coefficient from target
k = propagation coefficient
r = range in metres
r' = equivalent range corrected for refraction effect on antenna beam pattern.

In the example Mathcad™ model given in the Mathcad worksheets folder (on the CD) entitled GPR model, the antenna is set at a height of 15 cm above targets (dielectric cylinders of 1 cm thickness, ranging in size from 0.05 m to 0.5 m diameter (see Figure 3.1). The target has a value of ε_r of 2.2, the soil has an ε_r of 5 and $\tan\delta$ of 0.2, and the radar has a centre frequency of 1 GHz and an output pulse peak voltage

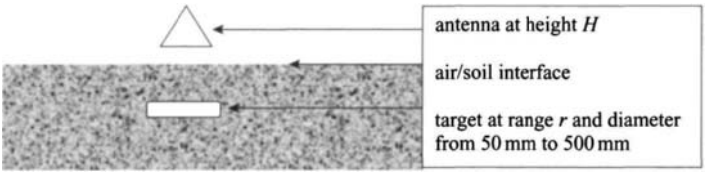

Figure 3.1 Physical layout of GPR system

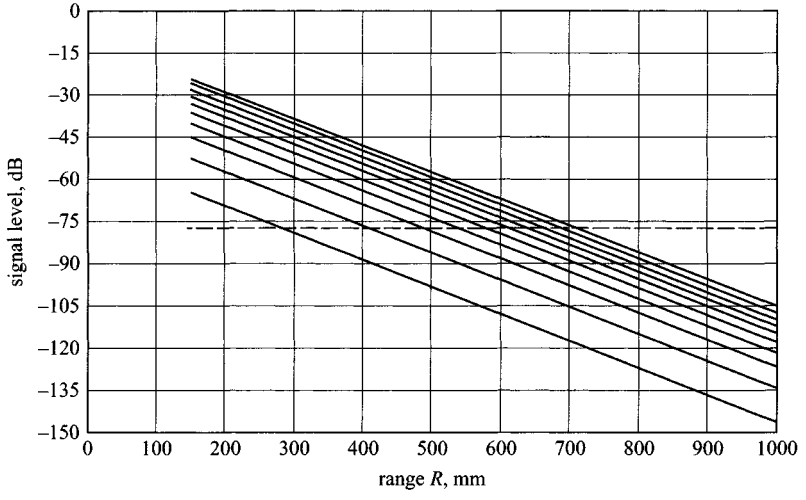

Figure 3.2 Graph of receiver voltage level in dBm as a function of target range in millimetres and target diameter (50 mm lowest to 500 mm highest)

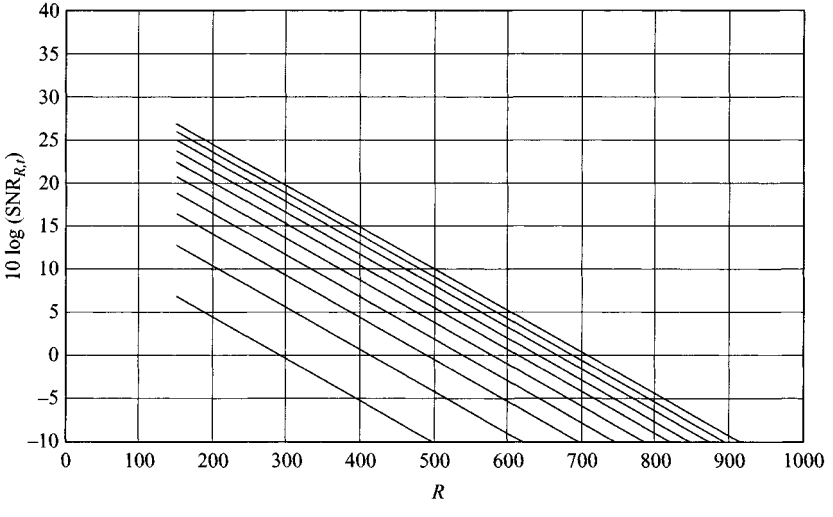

Figure 3.3 Graph of receiver signal to noise ratio in dB as a function of target range in millimetres and target diameter (50 mm lowest to 500 mm highest)

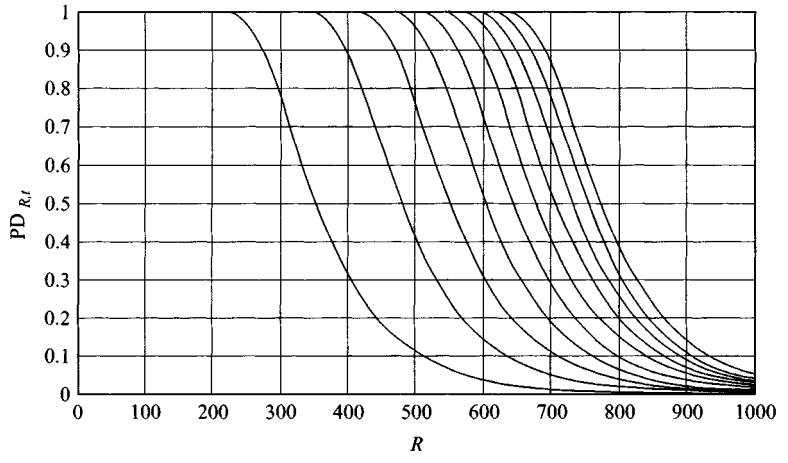

Figure 3.4 Graph of probability of detection as a function of target range in millimetres and target diameter (50 mm lowest to 500 mm highest)

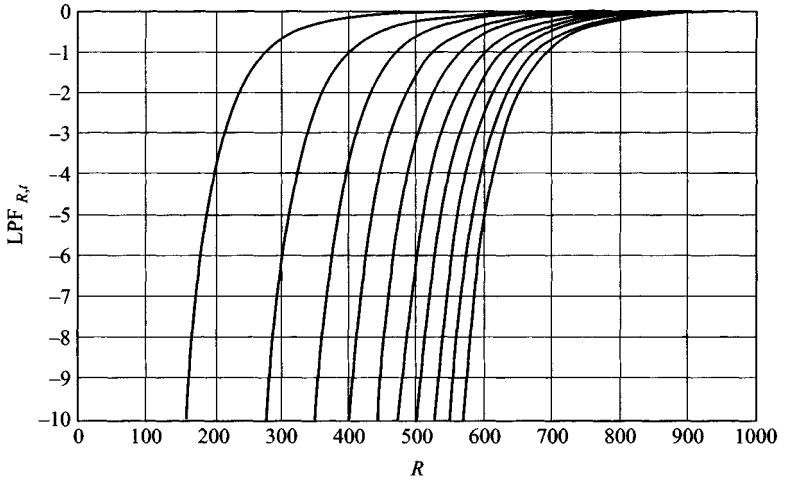

Figure 3.5 Graph of probability of false alarm (log scale) as a function of target range in millimetres and target diameter (50 mm lowest to 500 mm highest)

of 10 V. The radar receiver has an equivalent bandwidth of 3 GHz and an equivalent receiver noise voltage of 2.49×10^{-5} V.

The voltage at the receiver, the signal to noise ratio and the probability of detection and probability of false alarm were calculated and are shown in Figures 3.2 to 3.5.

The probability of detection (PD) is derived from the error function of the signal to noise ratio, and the probability of false alarm is derived from 1 minus the PD. Note that these values only relate to the receiver noise and do not include external sources of false alarms due to clutter.

3.3 Basic transmission line time domain model

The most basic model is that of the transmission line equivalent and is useful for assessing the time domain signature of a physical situation. A conceptually simple model can be used to gain an insight into the optimum centre frequency of operation, and an example is given in the Mathcad™ model, which can be found in the C3 layer model. The basic model is shown in Figure 3.6.

Each layer is modelled as an equivalent impedance and the transmission and reflection coefficients are calculated for each interface. The velocity of propagation and the material losses are included, although not the spreading losses. The reason for this is that the received A-scan would normally have time varying gain applied in the receiver and signal processing, and to introduce spreading loss and then compensate is an inefficient modelling exercise. In the Mathcad™ model only the first reflection is computed, although multiple internal reflections within each layer will be generated and a full representation should include these. Readers may wish to modify the programme to include multiple layer reflections as an exercise.

Each layer therefore has the following attributes:

Range to layer boundary $= r_n$
Loss tangent $= \tan \delta_n$
Relative dielectric constant $= \varepsilon_r$

The model calculates, for each layer, the propagation constants α_n and β_n and the impedance η_n, attenuation, equivalent time, and reflection and transmission coefficients. These are derived as follows, where the numbers denote the direction

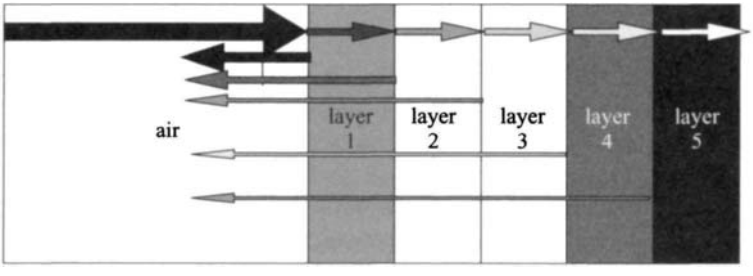

Figure 3.6 Layout of transmission line model

Table 3.1 Layer characteristics for transmission line model

Layer	Range, m	ε_r	Loss tangent	Material
0	0	1	0	air
1	0.3	6	0.31	lossy layer
2	0.6	1	0	air void
3	0.85	9	0.01	sub-base
4	1	16	0.1	wet base
5	infinite	25	0.1	wet bedrock

of propagation:

$$\begin{aligned}
\rho_{01} &:= \frac{\eta_1 - \eta_0}{\eta_1 + \eta_0} \quad \tau_{01} := \frac{2\eta_1}{\eta_1 + \eta_0} \quad \rho_{10} := \frac{\eta_0 - \eta_1}{\eta_0 + \eta_1} \quad \tau_{10} := \frac{2\eta_0}{\eta_0 + \eta_1} \\
\rho_{12} &:= \frac{\eta_2 - \eta_1}{\eta_2 + \eta_1} \quad \tau_{12} := \frac{2\eta_2}{\eta_2 + \eta_1} \quad \rho_{21} := \frac{\eta_1 - \eta_2}{\eta_1 + \eta_2} \quad \tau_{21} := \frac{2\eta_1}{\eta_1 + \eta_2} \\
\rho_{23} &:= \frac{\eta_3 - \eta_2}{\eta_3 + \eta_2} \quad \tau_{23} := \frac{2\eta_3}{\eta_3 + \eta_2} \quad \rho_{32} := \frac{\eta_2 - \eta_3}{\eta_2 + \eta_3} \quad \tau_{32} := \frac{2\eta_2}{\eta_2 + \eta_3} \\
\rho_{34} &:= \frac{\eta_4 - \eta_3}{\eta_4 + \eta_3} \quad \tau_{34} := \frac{2\eta_4}{\eta_4 + \eta_3} \quad \rho_{43} := \frac{\eta_3 - \eta_4}{\eta_3 + \eta_4} \quad \tau_{43} := \frac{2\eta_3}{\eta_3 + \eta_4} \\
\rho_{45} &:= \frac{\eta_5 - \eta_4}{\eta_5 + \eta_4} \quad \tau_{45} := \frac{2\eta_5}{\eta_5 + \eta_4} \quad \rho_{54} := \frac{\eta_4 - \eta_5}{\eta_4 + \eta_5} \quad \tau_{54} := \frac{2\eta_4}{\eta_4 + \eta_5}
\end{aligned} \tag{3.2}$$

The reflected signal from the fourth layer is derived as a delta function with an amplitude as a function of time given by

$$\text{fourthlayer}(t) := \begin{cases} (\tau_{01}\tau_{12}\tau_{23}\tau_{45}\rho_{43}\tau_{43}\tau_{32}\tau_{21}\tau_{10}a_{1r}a_{2r}a_{3r}a_{4r}) & \text{if } t = \text{offset} + f_{4t} \\ 0 & \text{otherwise} \end{cases} \tag{3.3}$$

The driving function is a Ricker wavelet and is convolved with each delta function, and the composite waveform is computed from the sum of all delta functions. The output from the model can be used to assess the A-scan waveform for the following example (Table 3.1).

The A-scan simulations given in Figures 3.7 to 3.10 show the effect of changing the centre frequency of operation on the resultant waveform.

The model can easily be modified in terms of centre frequency and layer parameters, and the reader is encouraged to experiment with the model and set up different physical situations and observe the effect on the A-scan. As would be expected, the A-scans given in Figures 3.7 to 3.10 show the improvement in resolution in going to higher frequencies and the consequent reduction in signal amplitude.

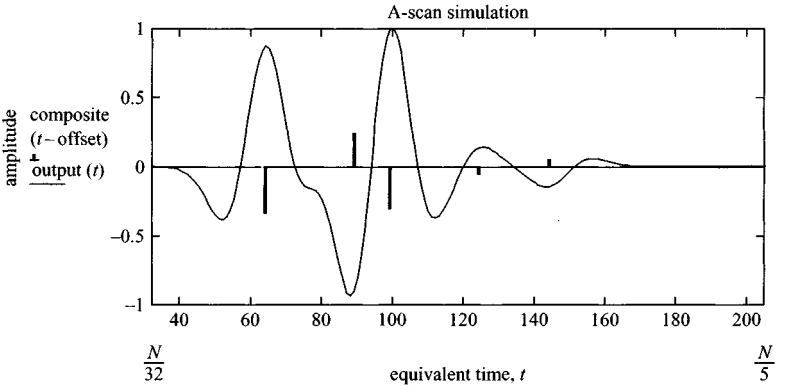

Figure 3.7 Simulation of A-scan using 100 MHz centre frequency

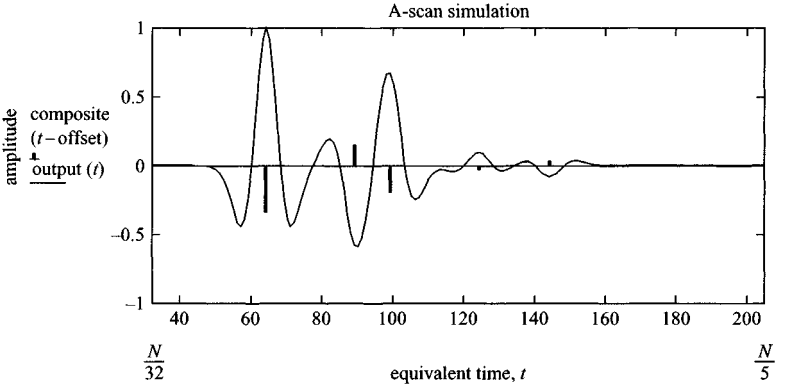

Figure 3.8 Simulation of A-scan using 300 MHz centre frequency

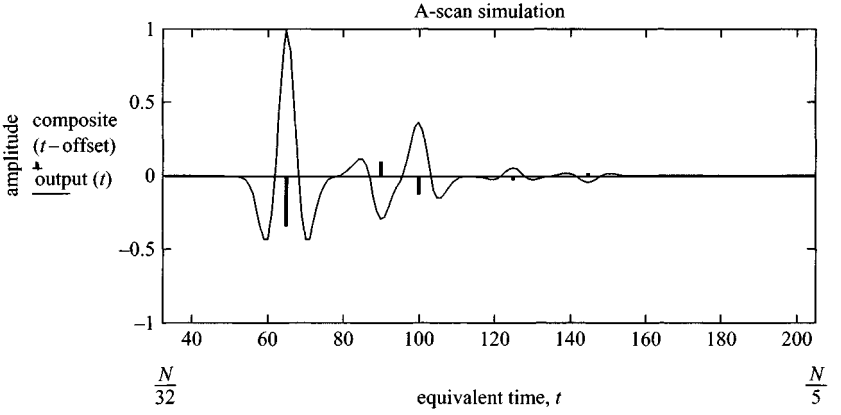

Figure 3.9 Simulation of A-scan using 500 MHz centre frequency

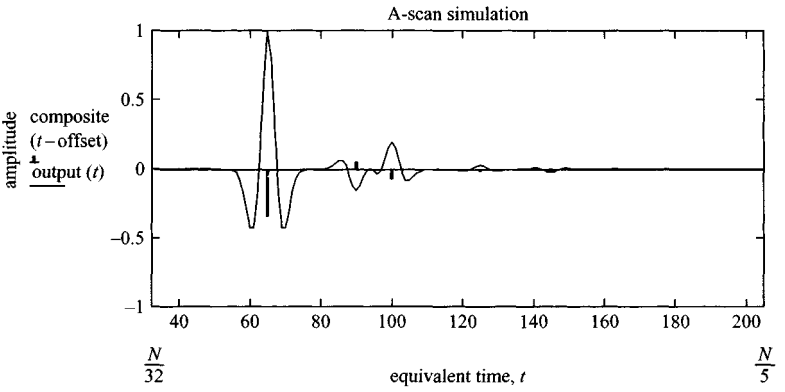

Figure 3.10 Simulation of A-scan using 750 MHz centre frequency

3.4 Model of antenna radiation and buried target interaction

In this Section, a finite-difference time domain (FDTD) method is used to model the field propagation of a typical GPR system. Some time domain field plots of a GPR antenna system operating above the ground and a buried object are presented. The objective is to acquire through the simulation an insight of EM propagation within the GPR scenario. The work was previously reported by Martel *et al.* [20]. This method offers the possibility to investigate the performance of a wide range of complex antennas operating in the presence of the ground at standoff distances. The advantage of the method is that it substantially reduces the computational resources needed and, additionally, it offers the possibility of selecting the best method for the analysis of the antenna and the ground sub-domains. The analysis of the ground sub-domain leads to a database for the response of the soil plus the target. Using these data, the performance of a complex antenna positioned at any desired distance or orientation relative to the ground can be modelled and optimised with minimal computational impact.

3.4.1 Model description

The antenna used for this purpose is a resistively loaded TEM horn [21]. It is 35 cm long with an aperture of 10 cm by 30 cm. The TEM horn has ultra-wideband capabilities from 200 MHz to 4 GHz, and a physical realisation is included in Section 5.3 . It is positioned above a metallic target buried in the ground. The distance between the horn aperture and the air–ground interface is 25 cm. The modelled target is a cylinder with a radius of 3.5 cm and a height of 5 cm. It is shallowly buried at about 2.5 cm below the air–ground interface. The ground is modelled as a uniform lossy material with a relative permittivity of 13 and a resistivity of 0.005 S/m. The air–ground interface is assumed to be perfectly flat.

3.4.2 Discretisation of the structures

The modelling of a stand-off GPR scenario where the antenna is at a significant distance from the ground as it is in this case is challenging because of the size of the

problem to analyse. In order to cope with the computation requirements, the FDTD model is truncated in two sub-geometries. One sub-geometry incorporates the antenna and another sub-geometry incorporates the air–ground interface. The antenna region is analysed with a high resolution to accurately model the radiator details (FDTD cubic cell size = 0.233 cm). On the other hand, the air–ground interface region is analysed with a lower resolution as fewer details are present and the field strength is significantly lower than in the radiating region. The FDTD cubic cell size for the ground region is 1.167 cm. An interpolation scheme of the field is used to ensure continuous propagation between the sub-geometries. The FDTD space is terminated by some absorbing boundary conditions of type Liao (second order).

3.4.3 Time domain field plots

A short duration time domain Gaussian pulse (1ns) is applied to the TEM horn and the electric field is computed at each time step. The simulation is run for a length of time of around 10 ns with a time step of 16 ps. Figure 3.11 shows the electric field

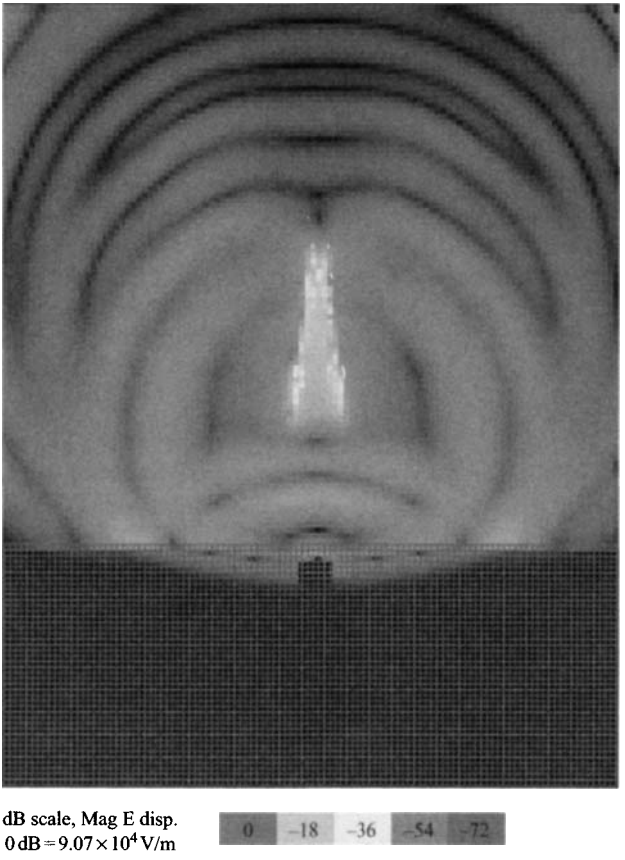

Figure 3.11 Electric field plot on a vertical cut plane after the main ground reflection

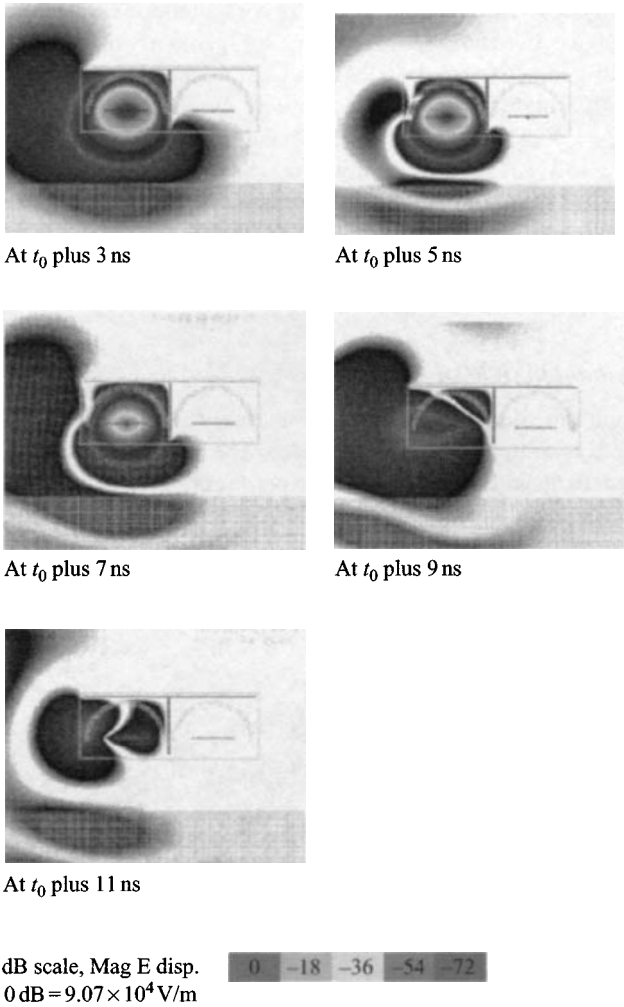

Figure 3.12 Modelled time sequence from the transmit antenna of a bistatic dipole pair

strength on the vertical plane cutting the antenna and ground geometry for a single frame. A complete time domain demo is presented in colour in the CD attached to this book. The various reflections and field propagation in the media surrounding the antenna can be seen from the demonstration. The full sequence of time frames can be seen on the PPT presentation.03-Modelling\demo1.ppt on the CD.

From the field plot, one can recognise the antenna structure and the strong field region on and inside the horn plate. The buried object is also visible. The main reflection caused by the air–ground interface can clearly be seen coming back towards

the antenna system. In addition, a weaker reflection coming from the buried object is starting to form and follows the air–ground interface reflection in time. This is a typical time domain characteristic of a stand-off GPR system. Moreover, other physical phenomena can be observed such as the free space loss and the wave speed reduction in the ground. It must be noted that the absorbing boundary conditions used are not sufficiently effective to predict accurately the input impedance of the antenna. It is, however, appropriate for the purpose of viewing the field propagation.

Similar techniques can be used to model other types of antenna, and comparisons of the radiated fields from a bistatic dipole antenna pair are shown in Figure 3.12.

3.5 Application of numerical modelling for the interpretation of near-surface ground penetrating radar

Dr Nigel Cassidy

In complex, heterogeneous environments, the evaluation, interpretation and analysis of GPR data is often complicated by the influence of near-field antenna coupling/induction effects, variations in antenna radiation pattern, the presence of inhomogeneous, anisotropic and lossy materials and the inevitable 'survey error' that arises due to the misuse of the GPR equipment. These complexities can make near-surface data interpretation a hit and miss affair, with the technique often being branded as unsuccessful, inappropriate or, at worst, a complete waste of time and money. In reality, these prejudices are often unfounded as the results of near-surface surveys can provide significant, yet sometimes subtle, information on the nature of the shallow sub-surface. Unfortunately, many of the advanced signal processing and analysis methods used in GPR data interpretation are poorly suited for use in complex, near-surface environments, primarily because of the limiting assumptions inherent in their mathematical descriptions (e.g. minimum-phase stationary wavelets, uniform half-space sub-surfaces, etc.). As a result, mathematical modelling has become an increasingly popular interpretation tool and is often used in conjunction with many of the more traditional signal or image processing techniques. There are many different modelling methods including ray tracing, integral techniques (MOM – method of moments) and discrete element methods. However, the finite-difference time-domain (FDTD) technique has become one of the most common in the past few years, particularly with the rapid increase in accessible and inexpensive computational resources.

For electromagnetic wave propagation problems the FDTD technique has certain advantages over other numerical modelling methods in that it:

- does not require the solution of Green's functions
- uses the direct implementation of Maxwell's electromagnetic field equations in three-dimensional space without the need for evaluating electric or magnetic potentials
- can be solved with explicit, closed form equations using matrix or incremental methods
- is robust, accurate and relatively straightforward to implement

- provides a total field solution (i.e. three-dimensional) and operates on both electric and magnetic field vectors
- can be applied to broadband, narrowband or harmonic time-domain problems
- is suitable for resonant or extended time problems
- allows different types of responses to be modelled, e.g. scattered and/or propagating fields, surface effects, currents, power density, etc.
- incorporates conductive, lossy dielectrics and dispersive magnetic materials
- can incorporate material property changes without the need to alter the mathematical description of the scheme
- can include arbitrary, three-dimensional sub-surface geometries, complex material features and sophisticated antenna designs by the use of different grid types and layouts
- is suited to either single processor or parallel operation
- is relatively straightforward to code in standard computational languages and is efficient on a variety of computer platforms
- allows comprehensive visualisation of the electromagnetic fields and waves in time and space.

3.5.1 Practical modelling schemes

There are a wide range of different electromagnetic FDTD formulations, each with individual advantages and disadvantages (see the excellent texts by Taflove [22, 23], and Kunz and Luebbers [24] for more detailed information), but each has a set of common elements that are key to the understanding of the technique.

In each case, the volume to be modelled is sub-divided into a three-dimensional grid (usually orthogonal) of individual 'field cells' of dimensions Δx, Δy, Δz. Within each cell, the electrical field (E) and the magnetic field (H) are described by component Cartesian $E(x, y, z)$ and $H(x, y, z)$ field vectors staggered in space in a manner that is referred to as 'Yee cell' geometry (Yee [25] – see Figure 3.13). With the use of a finite-difference approximation to the differential form of Maxwell's electromagnetic field equations, it is possible to calculate the electric field at any point in space (and time) from a knowledge of its neighbouring magnetic fields, and vice versa. If an incremental, time-varying electric 'source' is applied to one or more of the field vectors in the volume (as with the GPR antenna signal), then for a specific time increment, the total three-dimensional EM field is calculated by computationally stepping through each of the field calculations for every individual cell in sequence. This procedure is then repeated for the next time increment, etc., resulting in the time-dependent propagation of the EM wave through the volume.

In order to simulate the sub-surface physically, individual material properties are assigned to each cell (i.e. a permittivity, permeability and conductivity) and geometrically complex structures constructed by grouping together cells that share the same properties. With the use of appropriate source formulations, all modes of EM propagation, scattering and target interactions are modelled implicitly by the time

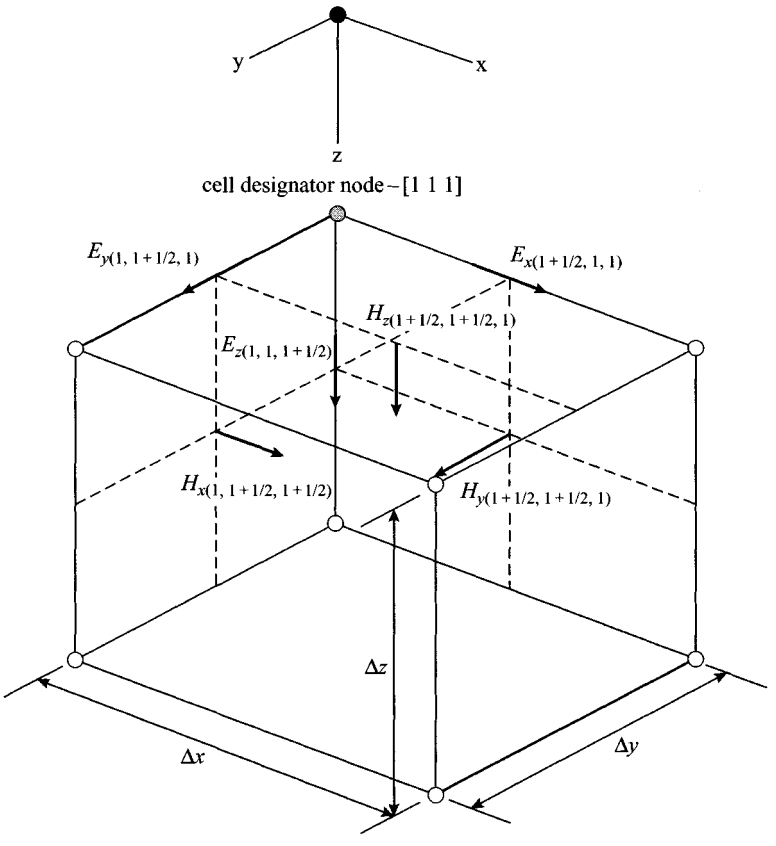

Figure 3.13 Individual 'Yee cell' geometry with component Cartesian electric (E) and magnetic (M) field vectors staggered in space

stepping scheme, resulting in the accurate simulation of signal reflection, scattering, attenuation and dispersion. To be of practical use, however, the modelling scheme must incorporate realistic antenna configurations, truthful sub-surface geometries and accurate material property descriptions. These additional components add computational complexity to the model and, at present, most FDTD modelling is conducted on high-powered single or parallel processing computers [26].

3.5.2 Modelling applications

The following examples illustrate the use of the FDTD modelling method for the improved understanding of GPR surveys in geological, geotechnical and archaeological near-surface environments. In each case, the propagating electromagnetic waves are modelled by a three-dimensional, staggered, orthogonal, fourth-order in space, centralised FDTD scheme developed by Cassidy and Murdie [27] from the original

formulation of Bergmann *et al.* [28]. It is total-field, explicit and robust, and provides accurate models of velocity and dispersion without the need for fine spatial sampling. The scheme includes:

- a wide range of materials having anisotropic and frequency-dependent permittivity, conductivity and, where necessary, magnetic permeability
- three-dimensional target features and complex sub-surface geometries
- realistic antenna designs including shields, efficient signal damping and accurate source signal descriptions
- 'memory variables' to determine the time, and therefore frequency, dependent effect of the materials on the propagating EM wave.

Equations for the one-, two- and three-dimensional cases can be found in Cassidy [29], Cassidy and Murdie [30] and Bergmann *et al.* [31], along with the appropriate stability conditions, error estimates and temporal/spatial sampling criteria.

3.5.3 Material property descriptions

Each sub-surface material is described by a complex permittivity, conductivity and magnetic permeability spectrum and, although the effect of the permeability is often negligible [32], it must be included when iron-oxide rich materials are present. The permittivity spectrum is described by a superposition of individual electric field and electric flux density relaxation times combined with a static permittivity. The complex conductivity is described by a static conductivity component and a conductivity relaxation time. These parameters can be obtained either by the dielectric testing of sub-surface materials or from theoretical/empirical models developed by Cole and Cole [33] and Debye [34].

3.5.4 Antenna design

The transmitting and receiving antennas are described both physically and numerically by identical half-wave, centrally fed, resistively loaded dipoles with a double PEC (perfect electric conductor) 'metal shield' being used to model the antenna enclosure. An end-terminated load resistor damps the antenna and is designed to match the input impedance at the central feed-point. The source wavelet, which is used to force the electric field vector at the feed-point, is an accurate representation of the true GPR pulse and is based on the recorded signal of a Sensors and Software PulseEKKO™ 1000 GPR in air. Developed from the standard Ricker pulse, the wavelet is smooth, continuous in both its first and second derivatives and can be optimised to suit the central frequency of any antenna [35].

3.5.5 Outer absorbing boundary conditions (ABC)

To restrict the size of the computational 'space' the modelled volume is truncated with an outer 'absorbing boundary condition' (or ABC) that either cancels out the outgoing waves, as in this case, or absorbs them numerically. A second order Higdon

ABC [36] has been used in this instance with parameters optimised for wave velocity and approach angle. This results in a maximum reflection error of <2% across all materials.

3.5.6 Example applications

3.5.6.1 Modelling near field antenna directivity and radiation patterns: In this example, the nature of near-field radiation is examined by modelling the E- and H-plane electromagnetic field patterns radiated from a shielded, 450 MHz half-wave dipole antenna located at the interface between air and oil of uniform permittivity $\varepsilon_r = 2.1$ (Figure 3.14). The antenna model is based on the shielded Sensors and Software Pulse Ekko 1000 system antenna and clearly illustrates the change in both radiation pattern and directivity with increasing near-field wave penetration. Instead of producing the commonly accepted far-field, unshielded radiation pattern, where the E-plane (or TM) field has a symmetrical, tri-lobate structure with a single, central lobe and two side lobes and the H-plane (or TE) pattern has a symmetrical 'twin-peaked' structure and no side lobes [37, 38], the fields are 'focused' by the shield to produce a narrow directivity pattern with the energy being primarily concentrated in a single, central lobe. This has important implications for the application of attribute analysis methods in the near-field (i.e. $<1.5\lambda$) as many of the current numerical processing and interpretation methods still incorporate far-field assumptions in their algorithms.

3.5.6.2 Modelling the response from buried foundation walls: The following two examples illustrate the use of the modelling scheme to assist in the understanding and interpretation of 200, 450 and 900 MHz near-surface GPR surveys at complex urban, industrial and archaeological sites. In the first example (Figure 3.15) both the observed and modelled GPR results are shown for a 450 MHz, co-planar, reflection survey collected across the centre of a 3 m wide, 3 m long, 0.8 m deep gravel/soil filled test pit containing a brick 'foundation wall' 0.3 m wide and 0.75 m deep [39]. With processing and interpretation of the real data alone, it is difficult to determine if the weak reflection event evident at approximately 16 ns in the GPR section has emanated from the base of the test pit or is, in fact, a result of multiple reflection in the top-soil layer. Even with the use of travel time/attribute analysis and various signal processing methods it was still not possible to prove which of the possible scenarios was correct. As the ground conditions in this area were particularly well known it was possible to build a very accurate model of the sub-surface and simulate the wave propagation to a high degree of precision. The modelled results revealed that the reflection from the basal interface was stronger than the multiple, had a different frequency spectrum and arrived slightly later than the multiple's signal. By comparing the modelled results to the observed data the correlation was strong enough to discard the multiple reflection hypothesis, resulting in an improved interpretation for the section. The modelled results also allowed the nature of the more subtle features (i.e. the wall diffractions and the bright spot associated with the top of the wall) to be determined correctly,

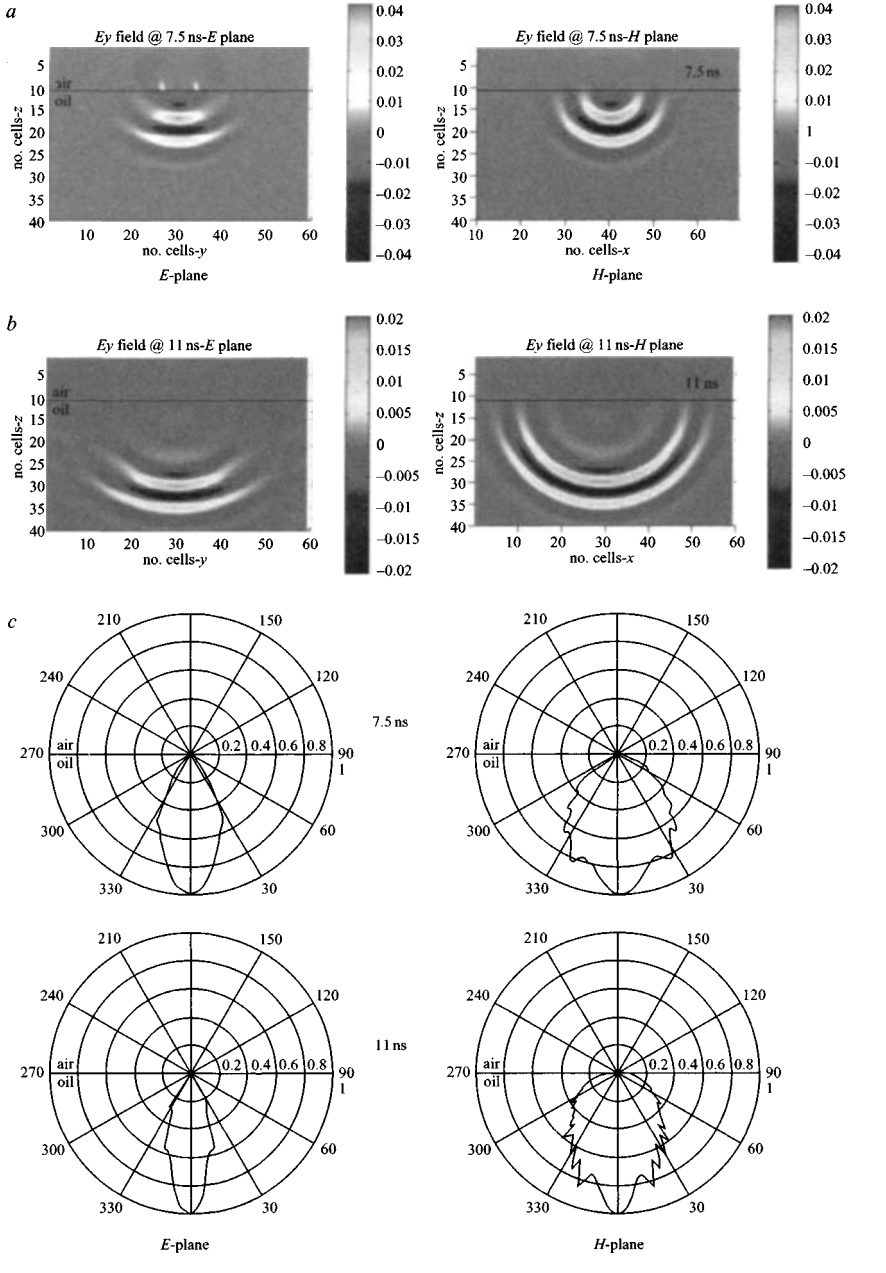

Figure 3.14 *Modelled electric field snapshots of a shielded 450 MHz dipole antenna located above the interface between air and oil*

a E_y component, E- and H-plane field snapshots at 7.5 ns travel time;

b E_y component, E- and H-plane field snapshots at 11 ns travel time;

c normalised antenna directivity at 0.86λ (for the 7.5 ns snapshot) and 1.5λ (for the 11 ns snapshot)

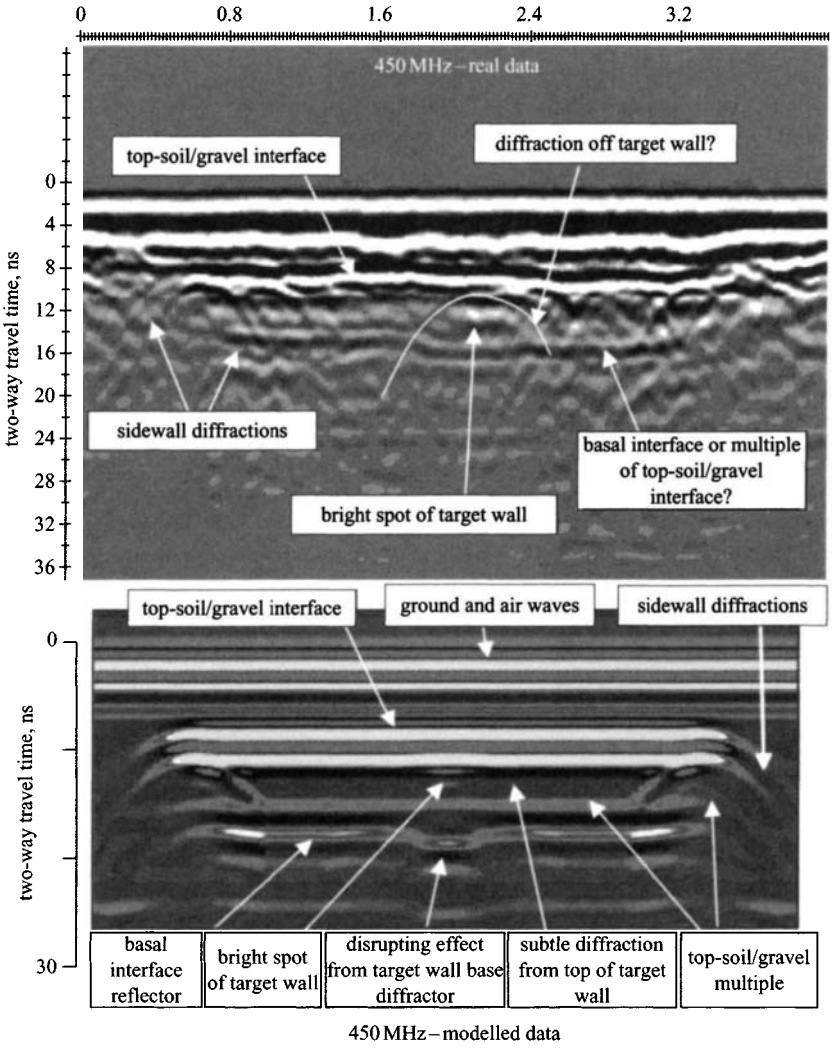

Figure 3.15 *450 MHz real and modelled GPR sections for the central survey of the 'foundation wall' test pit*
Raw data with de-wow and standard SEC gain correction applied; modelled data with constant gain applied

therefore assisting in the identification of features that were barely discernible in the real GPR section.

In the second example, the modelling scheme was used to interpret archaeological data from the Roman City of *Viroconium Cornoviorum* (Wroxeter), Shropshire, England to help understand the nature of the buried features and locate areas for

possible, future excavation. The site had been trial excavated some 30 years previously, resulting in important finds being discovered in a region containing a relatively well preserved, high-status villa. Unfortunately, the majority of the finds (and more importantly, the relevant archaeo-stratigraphic information) were confined to areas where the foundation walls of the villa had remained fully or partially intact. In areas that had been subjected to later destruction and/or 'robbing out', little information could be obtained from the excavation, primarily because the stratigraphic relationships had been lost. A combination of 200, 450 and 950 MHz GPR surveys, along with other geophysical methods, had been used to map the extent of the villa foundations and its neighbouring structures. Although the foundation walls were easily identified in the GPR sections, in most cases it was difficult to determine whether the features represented intact stonework or not. To aid the interpretation, a number of different sub-surface models were created with different states of preservation (e.g. intact blocks, rubble zones, robbed out and back-filled walls, etc.) with different target depths based on the excavated and geophysical evidence. The results shown in Figure 3.16 illustrate the use of the modelling to confirm the suspicion that a number of the reflection and diffractions events identified in this particular section were emanating from the disturbed remnants of two individual foundation walls.

The left-hand feature was believed to be the base of a partially robbed-out wall rather than a single, vertically extensive block, and a number of different modelling situations were used to test this hypothesis. The results of the models supported the 'robbed-out wall' interpretation, with the majority of the signal emanating from a coherent, intact block at a depth of approximately 0.5 m. This was consistent with other partially robbed out walls uncovered in the nearby excavations. Note how the 'masking' effect of the very shallow scatterer in the modelled section is reducing the amplitude of the plough layer reflector just below the block. This effect is also evident in an instantaneous amplitude analysis of the real data and suggests that this particular feature is a very shallow, single, isolated point source rather than the dominant component of a distributed rubble band or the upper extension of the deeper, wall base.

The form of the diffractions associated with the right-hand feature suggests that this wall is more incoherent in nature than the left-hand wall and is, therefore, likely to consist of rubble blocks (or zones of rubble) rather than a fully intact block. Once again, the final modelled section supports this hypothesis with the simulated response from a zone of rubble blocks, providing a reasonably accurate match to the observed data. The results of a recent, high-resolution magnetic gradiometry survey of the area supports these findings, where the signal definitions of the disturbed features are consistent with areas of known robbed out walls or rubble zones.

This example illustrates how the combined use of GPR modelling, excavated evidence and subsequent geophysical surveying has helped improve our understanding of the archaeological features at a complex and diverse site. As a result, this has assisted scheduling of a targeted, future excavation plan for the area, saving both time and money.

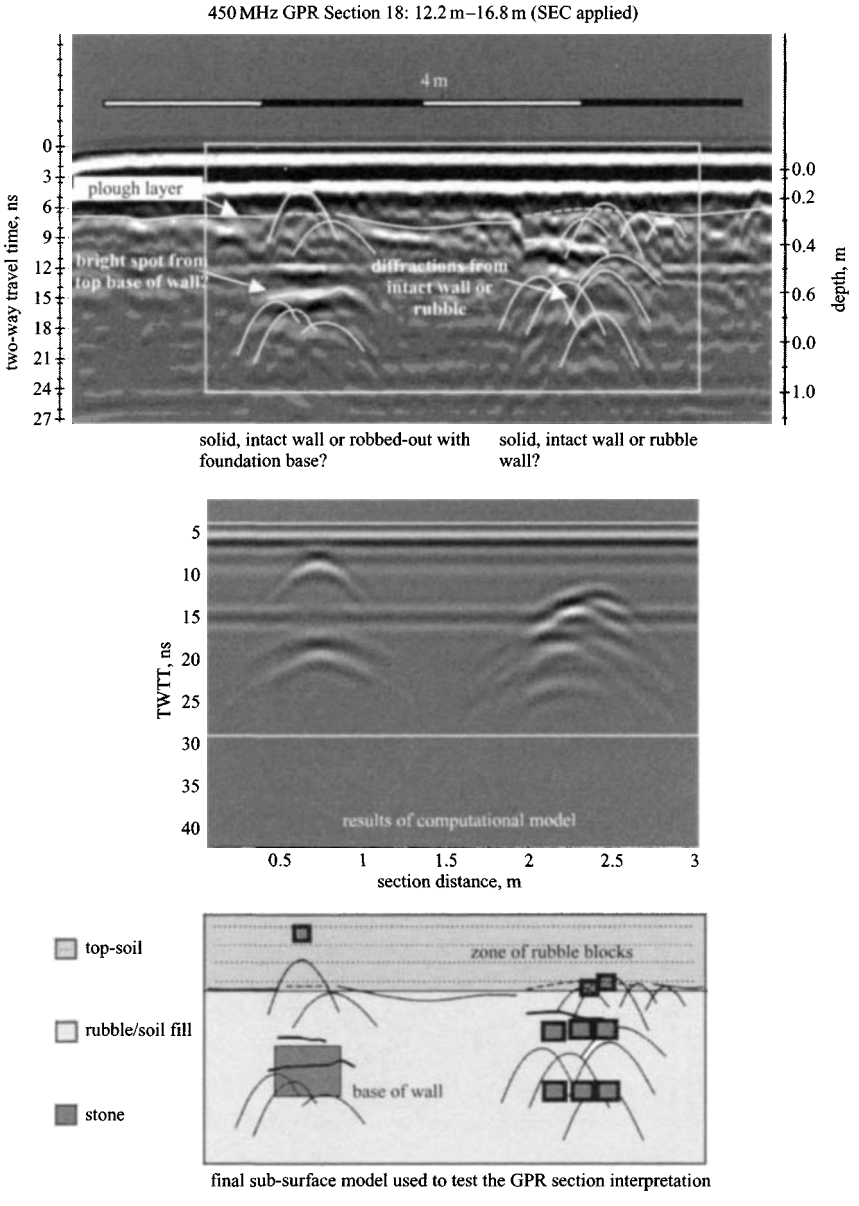

Figure 3.16 *450 MHz GPR section and corresponding FDTD model used to test the interpretation*

3.5.7 Modelling the response from defects in roadway construction

This final example illustrates the use of the modelling scheme in the assessment and verification of roadway construction. The model in Figure 3.17 was used to simulate the 900 MHz GPR response to defects typically associated with concrete roadway construction. A number of common problems were added to the subsurface model:

A and B, a 200 mm-thick concrete roadway overlying a sand/aggregate substrate; C, an air-filled void ~200 × 200 mm across and 20 mm deep located beneath the roadway slab; D, an identical void, but filled with muddy water instead of air; E, a 400 mm × 400 mm, 20 mm deep section of concrete that has de-laminated from the base of the roadway and fallen into an air filled void; F, a laterally extensive zone of

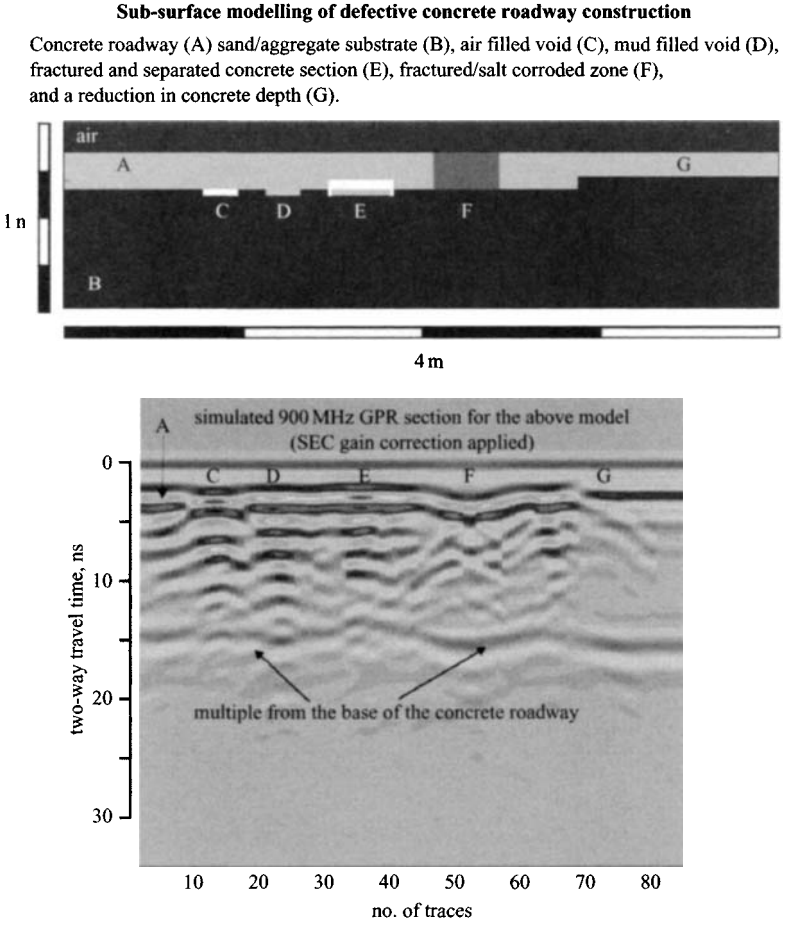

Figure 3.17 900 MHz GPR model of sub-surface defects in a 200 mm thick concrete roadway

fractured, salt corroded roadway; and G, a region where the thickness of the concrete roadway has been reduced to 160 mm instead of 200 mm (to simulate the effect of poor or negligent construction).

The GPR response to all the defects is clearly visible in the modelled section, although some of the anomalies are more prominent than others. A fairly strong reflection from the base of the concrete slab is evident at position (A), while its associated multiple is clearly visible in the latter part of the section. The identification of this multiple is particularly significant as, to the untrained eye, the feature could easily be mistaken for a second interface at depth. Likewise, the bright spot, diffractions and multiple from the air-filled void (B) are also visible in the modelled section. The anomaly from the muddy water filled void is evident, although the amplitude of the bright spot and the strength/size of the diffractions are notably reduced. It is interesting to note that the arrival time (and therefore phase) of this signal is slightly ahead of the corresponding air-filled void's response.

Despite the increased size of the delaminated concrete section, the response of this feature is very similar to the anomaly created by the muddy water filled void. This is also significant, as it shows that the presence of such a potentially hazardous defect would be difficult to determine under the conditions simulated in the model. In contrast, the fractured/salt corroded zone (F) can be easily identified and the region displays the classical velocity pull down effect associated with zones of lateral velocity reduction. The increased conductivity associated with this feature affects both antenna-ground coupling and signal attenuation, resulting in relatively lower signal amplitudes when compared to the rest of the roadway. This has an important implications for roadway evaluation as the effect of salt ingress and fracturing is one of the most significant factors in concrete deterioration. If, as the model suggests, subtle variations in signal attenuation can be attributed to saline intrusion then it raises the possibility of using GPR attribute analysis and wavelet techniques to highlight areas of potential concrete corrosion.

The reflection associated with the reduction in slab thickness (G) is particularly interesting as, on first inspection, it looks as if the slab has an *increased* thickness (i.e. the first arrival times appear later than the rest of the roadway slab). This is clearly not the case, and the 'delayed' signal is actually due to the destructive interference between the tail end of the near-field ground wave and the front end of the roadway basal reflection. Once again, to the untrained eye, this feature may have been interpreted incorrectly.

3.5.8 Summary

In each of the previous examples, the FDTD modelling scheme has been successful in improving the understanding and interpretation of near-surface GPR surveys. Even with recent advances in signal processing and image analysis, the data collected in complex, heterogeneous environments will always remain difficult to analyse – such is the nature of the problem. Recent successes have helped push numerical modelling methods into the wider GPR community and, as a result, more users are applying these methods to their own applications. With the development of more

efficient algorithms, improved techniques and given that the marketplace seems to have an insatiable desire for faster, more powerful computers, it is likely that numerical modelling methods will become a commonplace, interpretational tool for all GPR practitioners in the near future.

3.6 Modelling GPR surface roughness clutter effects for mine detection

Prof. Carey Rappaport

3.6.1 Introduction

The greatest impediment to detecting and classifying dielectric targets buried in natural soil backgrounds with GPR is the random clutter field generated by the rough ground surface. This is demonstrated by computational modelling of GPR wave propagation in air/soil and scattering from buried dielectric targets. Conclusions are drawn from the observed features that are somewhat unexpected. One important observation is that while target resolution increases with increasing frequency, the target features are harder to separate from the background clutter of the rough ground interface. The limitation on frequency is not the lack of penetration depth in lossy soil, but rather the greater phase effects of ground surface depressions and protrusions. Similarly, while a greater soil moisture level may increase the wave decay rate, it is the reduction in wavelength that makes the rough surface appear electrically larger, which increases clutter and makes the target harder to resolve.

Detecting nonmetallic manmade targets, such as plastic antipersonnel mines, buried in naturally varying soil with GPR is important and challenging. Although there are many means of noninvasively observing below the ground surfaces, GPR is commercially available and relatively inexpensive, environmentally robust, fast, and can be used at varying distances from the target. However, GPR has been disappointing in detecting shallow buried plastic objects in the field. Because the dielectric constant and electrical conductivity of the target is often similar to that of the surrounding soil and its size is comparable to the thickness of soil layer above it, detection and discrimination of the target are difficult. In addition, the soil dielectric constant may not be well characterised, and the ground surface will usually be rough, often with surface height variations of the order of the target burial depth. While there are many sources of clutter obscuring the mine target signal – including volumetric inhomogeneities (rocks, roots, metal fragments) and surface vegetation – the largest single source of undesirable signal is the ground surface itself. Since the ground presents a larger impedance mismatch with the air above it than with the low-contrast, nonmetallic target within it, its contribution to clutter is quite significant.

To quantify the frequency dependent effects of realistic soil backgrounds and surface geometries, we have computationally investigated the scattering of buried dielectric targets in accurately modelled soil with random rough surface boundaries. It is essential that the computational models used capture the relevant wave scattering

details of the random soil variation for any given frequency. Thus we chose the finite difference frequency domain (FDFD) method, which allows the arbitrary discretisation of the computational space into squares in two-dimensional calculations and cubes in three dimensions. The FDFD method is preferable to the FDTD time domain algorithm in the present analysis, because it computes the scattering response at a single frequency, giving the field distribution throughout the problem space. An additional advantage of FDFD is that there is no need to rely on special methods to handle frequency-dependent soil media in the time domain [1–3, 40–42].

The FDFD method can be made relatively fast. For a 300 × 200 point grid, terminated on each side by a perfectly matched layer (PML) [43] absorbing boundary condition [4], the entire evaluation on a 1.6 GHz Pentium Pro running the Matlab 5.3 sparse matrix solver is about ~1 min. Using a preconditioned GMRES iterative solution method, the CPU time for large grids of N unknown field values grows as $N \ln N$.

One important requirement for efficient FDFD code is the PML material absorber ABC. Since the PML is composed of just layers of propagation media with particular values of electric and magnetic conductivity, the sparse, symmetric structure of the simultaneous equation matrix is unaffected by the ABC.

The PML must be carefully formulated at the air/soil interface. With the usual PML boundary, it is assumed that this ABC terminates a region of free space. The electric and corresponding magnetic conductivities of the PML sub-layers build up from zero to the maximum value at its termination. For the PML termination to a uniform conductive scattering space, the conductivity of the first sub-layer must be slightly greater than that of the scattering space. Subsequent sub-layer permittivity and conductivity increase according to the anisotropic space mapping principle [5–7, 44–46], with corresponding magnetic conductivity increasing to keep the impedance of each PML sub-layer constant. Improvement in the effectiveness of the PML in the 2D Helmholtz equation based FDFD is attained by distributing the material dependence over three sub-layers according to the formula [8, 47]

$$\frac{E_{i+1,j}k'_{i-1/2} - E_{i,j}(k'_{i+1/2} + k'_{i-1/2}) + E_{i-1,j}k'_{i+1/2}}{k'_i k'_{i+1/2} k'_{i-1/2} \Delta^2} + \frac{E_{i,j+1} - 2E_{i,j} + E_{i,j-1}}{\Delta^2} + k_0^2(x,y)E_{i,j} = 0 \tag{3.4}$$

for a PML ABC at $x = 0$ or $x = x_{Max}$, where the relative wavenumber is $k'_i = 1 - j\sigma_i/\omega\varepsilon_0$ for the ith sub-layer with PML conductivity $\sigma_i = \sigma_0(1/N)^p$. A good choice of PML parameters is $n = 8$ and $\sigma_0 = 0.021/\Delta$, and $p = 3.7$ [46]. The background wavenumber $k_0(x,y) = \omega\sqrt{\mu\varepsilon}$ for background material permittivity ε and permeability μ.

To compute the scattered fields due to plane wave incidence on a target in a lossy half-space, the incident field in the nominal planar half-space is first determined analytically, using the standard transmission formulas. Then this field across the

support of both the target and the nonplanar interface perturbations is used as the excitation. That is, the source-free Helmholtz equation for total field,

$$[\nabla^2 + k^2(x, y)]E_z^{tot} = 0 \tag{3.5}$$

is rewritten in terms of material variations from the constant soil background, $k(x, y) = k_{back} + k_{scat}$, and in terms of incident (in both the air and soil backgrounds) and scattered electric field, $E_z^{tot} = E_z^{inc} + E_z^{scat}$. Here k_{back} is either k_{air} or k_{soil}, and k_{scat} is k_{targ} over the support of the target, or k_{air} or k_{soil} over the surface perturbations. Since E_z^{inc} solves the Helmholtz equation with background k_{back}, (1) becomes

$$\begin{aligned}[\nabla^2 + k_0^2(x, y)]E_z^{scat} &= -[\nabla^2 + k_0^2(x, y)]E_z^{inc} \\ &= -k_{soil}^2 O(x, y)E_z^{inc}\end{aligned} \tag{3.6}$$

where the object function is given for various cases as:

$$O(x, y) = \left\{ \begin{array}{l} (k_{\text{targ}}/k_{soil})^2 - 1 \\ (k_{air}/k_{soil})^2 - 1 \\ 1 - (k_{air}/k_{soil})^2 \end{array} \right\} \begin{array}{l} \text{over the target} \\ \text{over the surface depression} \\ \text{over the surface protrusion} \end{array} \tag{3.7}$$

for the cases when the scatterer is the buried target, a depression down into the nominal planar ground surface, or a protrusion up above the planar ground surface, respectively.

Note that this formulation is exact, unlike the Born approximation. Approximation is unnecessary, since FDFD calculates field values across the grid for all types of materials in any shape or form.

3.6.2 Target shape scattering characteristics

It is well known that sharp metallic corners are diffraction sources and that objects with corners scatter waves strongly. However, for low contrast nonmetallic objects, corners have a much smaller effect on scattered field. The degree of scattering by corners can be studied by examining the scattered fields throughout space. For the buried object problem, it has been suggested that by observing the corner scattered features, it would be possible to characterise the shape of the object. To test this conjecture, the fields can be modelled in and above the surface of a lossy dispersive soil model half-space.

The first row of Figure 3.18 shows the geometries of five representative buried two-dimensional scattering objects and their scattered fields for two test frequencies [9, 48]. In each case the target with material characteristics of TNT or plastic (dielectric constant $\varepsilon' = 2.9$, loss tangent $\tan\delta = 0.001$) is embedded in a half-space of material with electrical characteristics of dry sand ($\varepsilon' = 2.5$, loss tangent $\tan\delta = 0.01$) [10, 49]. The targets each have the same cross-sectional area of $\sim 100\,\text{cm}^2$, and are

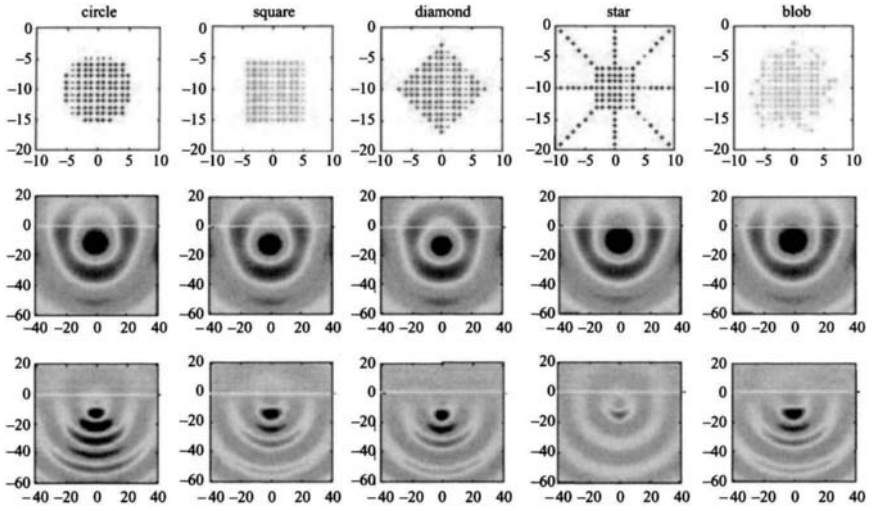

Figure 3.18 *Similarity of scattered fields*
First row: nominal geometry of five buried target shapes each with approximately the same area of 100 cm^2, 5 cm below ground surface. Soil assumed to be dry sand, targets modelled with electrical characteristics of TNT. Second row: real parts of fields scattered from the target shapes for 500 MHz excitation. Third row: real parts of fields scattered for 1 GHz excitation

buried at a nominal depth of 5 cm. In the first case the target is circular, obviously with no corners, while the second and third have square cross-sections with right angle corners. The fourth target models a mine with plastic fins. The last target is an irregularly shaped object typical of a naturally occurring clutter item, such as a rock.

The second row of Figure 3.18 shows the real part of the field scattered by each object in the sand half-space background due to a 500 MHz normally incident plane wave. Note that the field incident in the air above the ground surface (indicated by 0 on the vertical axes), the field specularly reflected from this interface, and the plane wave field transmitted through the interface, have all been suppressed to show the scattering field details. The real part of the scattered field is shown rather than its magnitude because it more clearly shows the wave behaviour. With intensity represented by shades of fill, it is clear that at 500 MHz there is almost no observable difference between targets with corners, smooth sides, flat reflective surfaces or concavities. Although the scattered field above the ground surface is fairly strong, providing detection information, it is practically impossible to distinguish the various targets from their scattered fields.

The third row of Figure 3.18 shows the scattered field for a 1 GHz normally incident plane wave. For this frequency, there are noticeable differences in the scattered

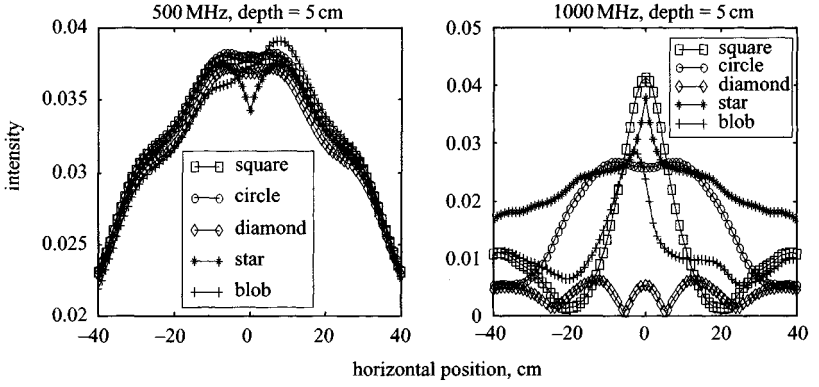

Figure 3.19 Magnitude of scattered field at the ground surface for the target shapes of Figure 3.18: 500 MHz excitation (left) and 1 GHz (right)

fields, but also the intensity of the waves above the ground surface is much lower than for the 500 MHz case. This is shown quantitatively in Figure 3.19, which gives the magnitude of the field exactly at the planar ground surface. The differences between the scattered fields are clear only at the higher frequency, but the overall scattered intensity is twice to six times smaller than for the 500 MHz excitation.

3.6.3 Rough surface modelling results

For the idealised geometry with a perfectly planar ground surface boundary, it would indeed be possible to identify objects with corners and to determine their orientations – as well as distinguish manmade from irregular objects – with increasingly higher frequency excitation. In the field, however, the ground is never flat. Surface roughness must be incorporated into the scattering analysis.

To study the clutter effects of rough ground surface on the target-scattered signal as a function of frequency, a series of 2D simulations were conducted. Figure 3.20 shows a depth cross-section of a typical geometry incorporating a rectangular mine-like target nominally buried 10 cm in sand, under a surface with an average height variation of 1 cm. The surface roughness curve has relatively small derivatives (never very steep) and is not correlated with the buried target position.

The field scattered from this rough surface scenario is compared to two other scattering geometries: first, the rectangular target buried below an ideal planar sand surface, and second just the rough surface alone, without the target. In each case the excitation is a normally incident plane from above with one of four possible frequencies: 480, 960, 1920 and 3840 MHz. Figure 3.21 shows the scattered wave pattern for 480 MHz excitation. The upper left plot in Figure 3.21 (and the three subsequent figures) is the planar boundary case, representing the scattered field with the analytically determined waves incident, reflected and transmitted from the planar ground surface suppressed.

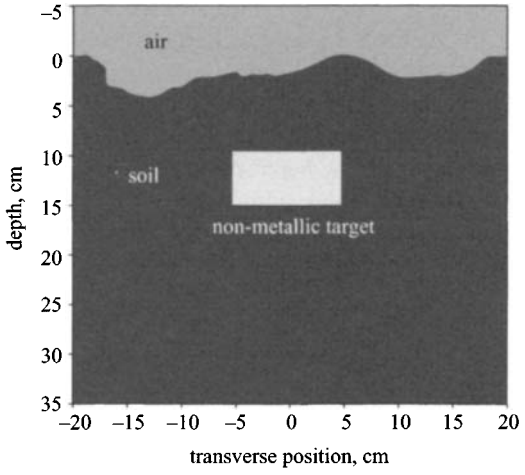

Figure 3.20 *Geometry of cross-section of sand with rough surface and buried TNT target used for 2D FDFD plane wave simulation*

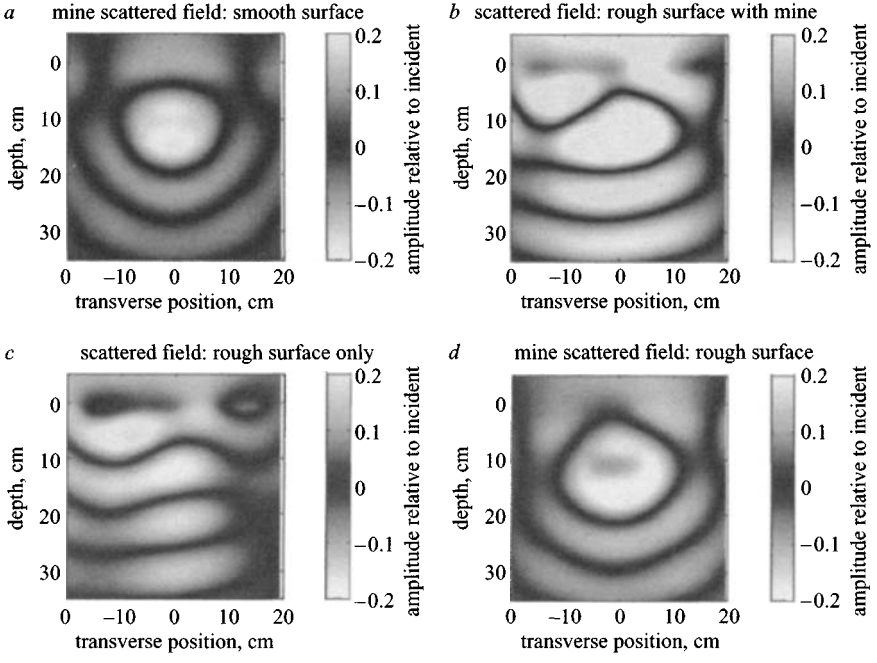

Figure 3.21 *Scattered 480 MHz field from the rectangular TNT target in a sand half-space*

a Planar boundary; *b* rough boundary; *c* the field scattered from just the rough surface perturbations without the mine target; *d* the numerical difference between the fields of *b* and *c*

The upper right image in Figure 3.21 indicates the scattered field for the rough surface with the target. Again the analytically determined incident, reflected and transmitted fields have been removed, showing the scattering due to the perturbations of the rough surface along with that of the target. It is these depressions and protrusions of the rough surface which give rise to the confusing clutter in realistic detection applications. Since the contrast ratio between the target and the sand background is about 0.85 while the ratio between sand and air is 2.5, the random surface scattering is predominant. This effect is clearly shown by observing the lower left image in Figure 3.21, which shows the scattering from just the rough surface alone.

The difference between the fields of Figure 3.21 *b* and *c* gives the field scattered by just the mine under the rough surface. Although this scattered field pattern is similar to the ideal planar interface case of Figure 3.21*a*, it is important to realise that it is generally unavailable, since the field scattered by the rough surface separately, without a target, cannot be measured.

Figure 3.22 shows the same set of scattered field calculations for 960 MHz excitation. In the upper left image, Figure 3.22*a*, the shape of the rectangular target is

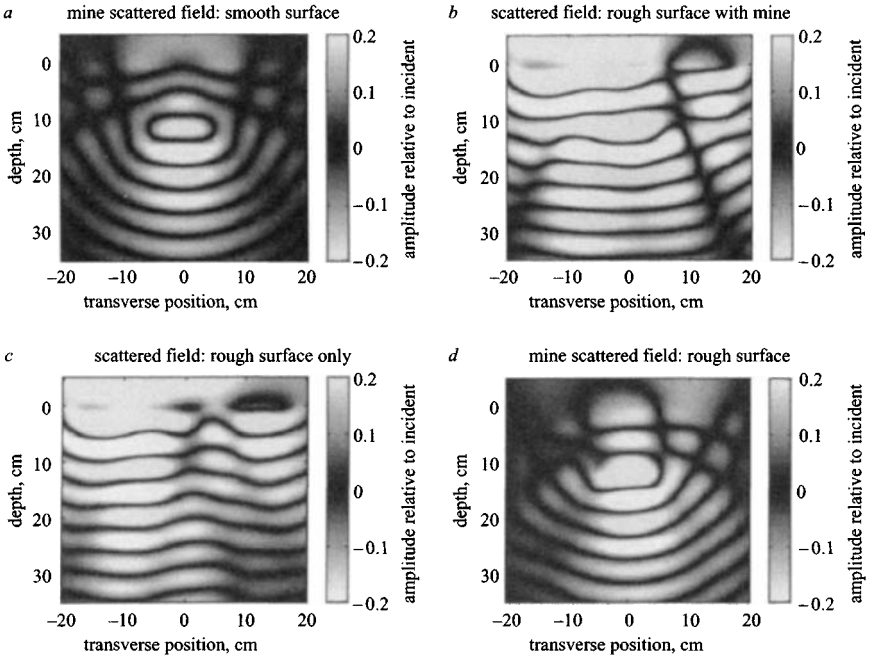

Figure 3.22 *Scattered 960 MHz field from the rectangular TNT target in a sand half-space*
a Planar boundary; *b* rough boundary; *c* the field scattered from just the rough surface perturbations; *d* the numerical difference between the fields of *b* and *c*

becoming more clearly discernible than at 480 MHz. However, the waves scattered by the same rough surface perturbations are becoming dominant. The difference field in Figure 3.22*d* still resembles the ideal field of Figure 3.22*a*, and would help to characterise the target as a rectangular anomaly, but this target scattered field is significantly less intense than the rough surface only scattered field of Figure 3.22*c*.

Doubling and redoubling the frequency to consider the possible target characterisation improvements results in the images of Figures 3.23 and 3.24. Here, both the ideal planar ground surface target scattered field and the numerical difference field images, Figure 3.23*a*, *d* and Figure 3.24*a*, *d* show quite recognisable scattering features. The forward scattered field clearly delineates the wide rectangular shape, and the backscattered field shows the interference effects from the finite top surface of the flat target. However, in both the 1920 and 3840 MHz cases, the field scattered from the rough surface perturbations overwhelms the target-scattered field. Even though the bulk of the reflected signal – that due to reflection from the nominal planar interface – has been removed, the roughness itself adds so much clutter that it is not possible to observe any target signal in its presence. The fields above the ground with and without the target, Figure 3.23*b*, *c* for 1920 MHz, and Figure 3.24*b*, *c* for 3840 MHz, are indistinguishable from each other.

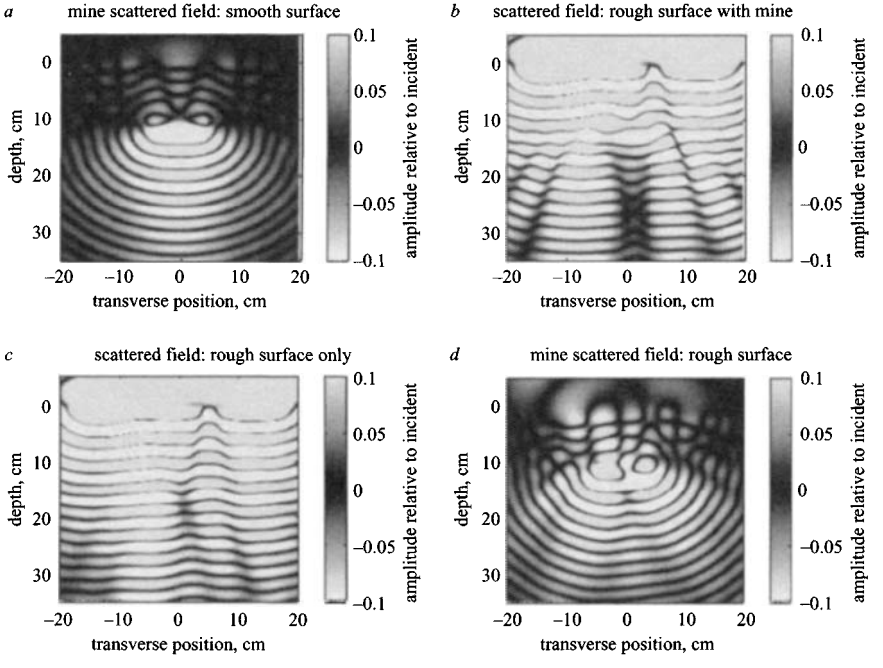

Figure 3.23 Scattered 1920 MHz field for the geometry of Figure 3.21

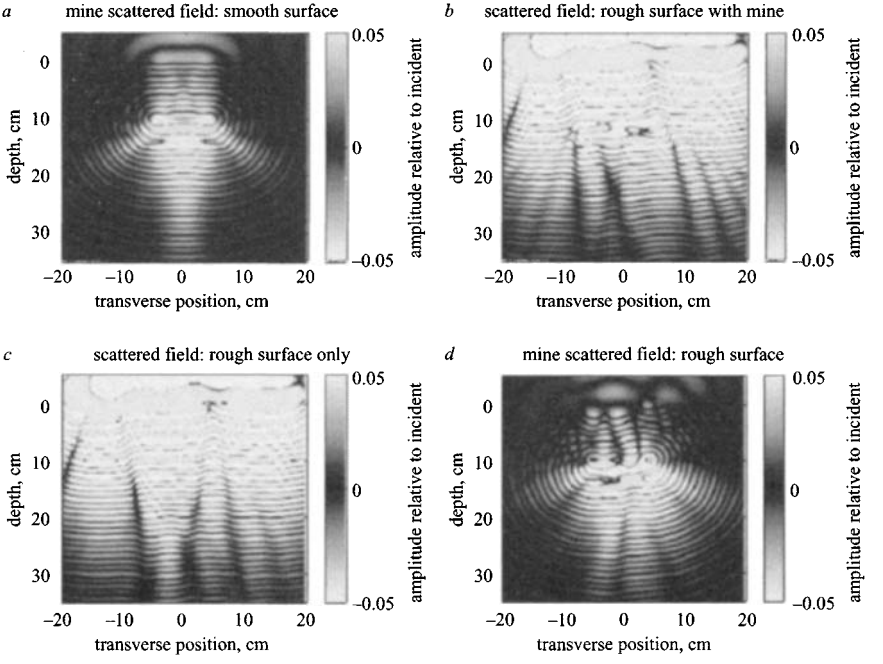

Figure 3.24 Scattered 3840 MHz field for the geometry of Figure 3.21

3.6.4 Summary

By increasing the illuminating frequency of ground penetrating radar, the resolving capability of an ideal underground sensing and imaging system improves. However, as the incident field wavelength shortens, the random rough ground surface perturbations become more significant.

The calculated scattered fields from various two-dimensional nonmetallic mine-like target shapes indicate that, although the target models are relatively simple, there is very little shape-distinguishing feature information available when the incident wave is at the typical GPR frequency of 500 MHz. At 1 GHz, shape features of 10 cm wide targets are quite evident, but a wide aperture (~50 cm) of multiple sensors across the ground surface is needed to measure the variations of scattered field. Clearly, for nonmetallic anti-personnel mine detection, frequencies above 500 MHz must be employed if there is to be any hope of distinguishing mines in terms of the shape of target anomalies in soil.

When the frequency of illumination becomes too high relative to the average size of the rough ground height variations, the fields scattered from these perturbations dominate the scattered field. Since the clutter field due to the random roughness cannot be measured or determined separately from the target, nor can its specific distribution be predicted, it will always overwhelm the target signal at higher frequencies.

3.6.5 Acknowledgments

The authors are grateful for the support of The Army Research Office MURI grant DAAG55-97-1-0013, and the Centre for Subsurface Sensing and Imaging Systems (CenSSIS) at Northeastern University, under the Engineering Research Centres Program of the National Science Foundation (award no. EEC-9986821).

3.7 Summary

The modelling of the GPR situation ranges from a simple consideration of the time domain signatures of multiple reflecting layers based on a transmission line approach to full three-dimensional SAR modelling. This Chapter has provided an initial insight into the range of the approaches that have been taken to predicting the reflected signals and fields from buried targets. Modelling of the GPR situation has significantly advanced over the past decade and some realistic field predictions are being generated. Section 3.5 notes that there are many different modelling methods including ray tracing, integral techniques (MOM – method of moments) and discrete element methods. However, the finite-difference time-domain (FDTD) technique has become one of the most common in the past few years, particularly with the rapid increase in accessible and inexpensive computational resources. The resources required to create effective models should be considered at the onset of a project as the simple methods described in Sections 3.3 and 3.4 can often yield useful insights into the basic capability of a particular GPR system performance. Section 3.6 provides a valuable insight into surface roughness effects, and this is of critical importance in assessing GPR performance as surface topography is often a limiting factor to performance. As the models become more sophisticated the effect of clutter will be included and this will allow more truly representative modelling of the GPR situation to take place. There is a need to devise equivalent clutter models to those that describe sea states for conventional naval radars. This will allow better prediction of the signal to clutter performance of GPR systems.

3.8 References

[1] HUANG, Z., DEMAREST, K., PLUMB, R.: 'Ground-penetrating radar antenna modeling'. Proc. Int. Geoscience and Remote Sensing Symposium, 1996. IGARSS '96. 'Remote sensing for a sustainable future', 27–31 May 1996, Vol. 1, pp. 778–780

[2] LEE, K., VENKATARAYALU, N. V., CHEN, C.-H., TEIXEIRA, F. L., and LEE, R.: 'Numerical modeling and characterization of fully polarimetric dielectric loaded horn-fed bow-tie (HFB) antenna for GPR applications using FDTD'. Proc. IEEE Antennas and Propagation Society Int. Symposium, 2002, Vol. 3, pp. 472–475

[3] GUANGYOU, F., ZHONGZHI, Z., and WINBING, W.: 'The calculation of a SP-GPR antenna near lossy media interface by FD-TD method'. Microwave

Conf. Proc., 1997. APMC '97, 1997 Asia-Pacific, 2–5 Dec. 1997, Vol. 3, pp. 1193–1196

[4] MARTEL, C., PHILIPPAKIS, M., DANIELS, D. J., and UNDERHILL, M.: 'Modelling the performance of realistic ultra-wide band ground penetrating radar (GPR) antennas'. Eleventh Int. Conf. on Antennas and propagation (IEE Conf. Publ. 480) Manchester, UK, 2001, pp. 655–659

[5] MEINCKE, P., and KIM, O.: 'Accurate antenna models in ground penetrating radar diffraction tomography'. Proc. IEEE Antennas and Propagation Society Int. Symposium, 2002, Vol. 4, pp. 306–309

[6] TEIXEIRA, F. L., CHEW, W. C., STRAKA, M., ORISTAGLIO, M. L., and WANG, T.: '3D PML-FDTD simulation of ground penetrating radar on dispersive Earth media'. Proc. IEEE Int. Geoscience and Remote Sensing Conf., 1997 (IGARSS '97) on Remote sensing – a scientific vision for sustainable development, 3–8 Aug. 1997, Vol. 2, pp. 945–947

[7] TEIXEIRA, F. L., CHEW, W. C., STRAKA, M., ORISTAGLIO, M. L., and WANG, T.: 'Finite-difference time-domain simulation of ground penetrating radar on dispersive, inhomogeneous, and conductive soils', *IEEE Trans. Geosci. Remote Sens.*, 1998, **36**, (6), pp. 1928–1937

[8] CHEW, W. C., TEIXEIRA, F. L., STRAKA, M., ORISTAGLIO, M. L., and WANG, T.: 'Parallel 3D PML-FDTD simulation of GPR on dispersive, inhomogeneous and conductive media'. Digest IEEE Antennas and Propagation Society Int. Symposium, 1997. 13–18 July 1997, Vol. 1, pp. 380–383

[9] OGUZ, U., and GUREL, L.: 'Simulation of TRT-configured ground penetrating radars over heterogeneous grounds'. Proc. IEEE Antennas and Propagation Society Int. Symposium, 2001, Vol. 3, pp. 757–760

[10] LIU, Q. H., and FAN, G.-X.: 'Simulations of GPR in dispersive media using a frequency-dependent PSTD algorithm', *IEEE Trans. Geosci. Remote Sens.*, 1999, **37**, (5), pp. 2317–2324

[11] LIU, C. R., LI, J., GAN, X., XING, H., and CHEN, X.: 'New model for estimating the thickness and permittivity of subsurface layers from GPR data', *IEE Proc. Radar Sonar Navig.*, 2002, **149**, (6), pp. 315–319

[12] RAPPAPORT, C. M., and WEEDON, W. H.: 'Efficient modeling of electromagnetic characteristics of soil for FDTD ground penetrating radar simulation'. Digest Antennas and Propagation Society Int. Symposium, 1996, 21–26 July 1996, Vol. 1, pp. 620–623

[13] GUREL, L., and OGUZ, U.: 'Simulations of ground-penetrating radars over lossy and heterogeneous grounds', *IEEE Trans. Geosci. Remote Sens.*, 2001, **39**, (6), pp. 1190–1197

[14] RAPPAPORT, C., and EL-SHENAWEE, M.: 'Modeling GPR signal degradation from random rough ground surface'. Proc. IEEE Int. Geoscience and Remote Sensing Symposium, 2000 (IGARSS 2000), Vol. 7, pp. 3108–3110

[15] ZHAN, Y., LIANG, C., and FANG, G.: 'Development of a 3-D GPR simulator using the FDTD method'. Proc. 5th Int. Symposium on Antennas, propagation and EM theory, 2000 (ISAPE 2000), pp. 459–467

[16] GUREL, L., and OGUZ, U.: 'Three-dimensional FDTD modeling of a ground-penetrating radar', *IEEE Trans. Geosci. Remote Sens.*, 2000, **38**, (4), pp. 1513–1521

[17] OGUZ, U., and GUREL, L.: 'Three-dimensional FDTD modeling of a GPR'. Proc. IEEE Antennas and Propagation Society Int. Symposium, 2000, Vol. 4, pp. 1990–1993

[18] DESAI, A. S., WILKINSON, A. J., and INGGS, M. R.: 'GPR SAR simulation and image reconstruction'. Proc. IEEE Int. Geoscience and Remote Sensing Symposium, 2001 (IGARSS '01), Vol. 5, pp. 2076–2078

[19] WANG, Y., LONGSTAFF, I. D., and LEAT, C. J.: 'SAR imaging of buried objects from MoM modelled scattered field', *IEE Proc. Radar Sonar Navig.*, 2001, **148**, (3), pp. 167–172

[20] MARTEL, C., PHILIPPAKIS, M., DANIELS, D. J., and UNDERHILL, M.: 'Modelling the performance of realistic ultra-wide band ground penetrating radar (GPR) antennas'. Eleventh Int. Conf. on Antennas and propagation (IEE Conf. Publ. 480, 2001), Manchester, UK, 2000, pp. 655–659

[21] MARTEL, C., PHILIPPAKIS, M., and DANIELS, D. J.: 'Time domain design of a TEM horn antenna for GPR'. EUREL's Millennium Conf. on Antennas and propagation, April 2000

[22] TAFLOVE, A. (ed.): 'Advances in computational electrodynamics – the finite-difference time-domain method' (Artech House, London, 1998)

[23] TAFLOVE, A.: 'Computational electrodynamics – the finite-difference time-domain method' (Artech House, London, 1995)

[24] KUNZ, K. S., and LUEBBERS, R. J.: 'The finite difference time domain method for electromagnetics' (CRC Press, London, 1993)

[25] YEE, K. S.: 'Numerical solution of initial boundary value problems involving Maxwell's equation in isotropic media', *IEEE Trans. Antennas Propag.*, 1966, **14**, (2), pp. 302–307

[26] CASSIDY, N. J., and TUCKWELL, G. W.: 'Mathematical modelling of ground-penetrating radar: parallel computing applications'. Proc. 9th Int. Conf. on Ground-penetrating radar (GPR2002), USA, 2000

[27] CASSIDY, N. J., and MURDIE, R. E.: 'The application of mathematical modelling in the interpretation of near-surface ground penetrating radar sections'. Proc. 8th Int. Conf. on Ground-penetrating radar (GPR2000), Australia, 2000, pp. 842–847

[28] BERGMANN, T., ROBERTSSON, J. O. A., and HOLLIGER, K.: 'Finite-difference modelling of electromagnetic wave propagation in dispersive and attenuating media', *Geophysics*, 1998, **63**, (3), pp. 856–857

[29] CASSIDY, N. J.: 'The application of mathematical modelling in the interpretation of ground-penetrating radar data'. Ph.D. Thesis, Keele University, 2001

[30] CASSIDY, N. J., and MURDIE, R. E.: 'The application of mathematical modelling in the interpretation of near-surface ground penetrating radar sections'. Proc. 8th Int. Conf. on Ground-penetrating radar (GPR2000), Australia, 2000, pp. 842–847

[31] BERGMANN, T., ROBERTSSON, J. O. A., and HOLLIGER, K.: 'Finite-difference modelling of electromagnetic wave propagation in dispersive and attenuating media', *Geophysics*, 1998, **63**, (3), pp. 856–857

[32] OLHOEFT, G. R., and CAPRON, D. E.: 'Laboratory measurements of the radio frequency electrical and magnetic properties of soils near Yuma, Arizona'. US Department of Interior USGS Open File Report 93-701, 1993

[33] COLE, K. S., and COLE, R. H.: 'Dispersion and absorption in dielectrics', *J. Chem. Phys.*, 1941, **9**, pp. 341–351

[34] DEBYE, P.: '*Polar molecules*', Chemical Catalog Co., New York, USA, 1929

[35] CASSIDY, N. J., and MURDIE, R. E.: 'The application of mathematical modelling in the interpretation of near-surface ground-penetrating radar sections'. Proc. 8th Int. Conf. on Ground-penetrating radar (GPR2000), Australia, 2000, pp. 842–847

[36] HIGDON, R. L.: 'Radiation boundary conditions for dispersive waves', *SIAM J. Numer. Anal.*, 1994, **31**, (1), pp. 64–100

[37] ANNAN, A. P.: 'Ground-penetrating radar: Workshop Notes' (Sensors and Software Inc., Ontario, Canada, June 1999)

[38] ARCONE, S. A.: 'Numerical studies of the radiation patterns of resistively loaded dipoles', *J. Appl. Geophys.*, 1995, **33**, pp. 63–76

[39] CASSIDY, N. J., and MURDIE, R. E.: 'The application of mathematical modelling in the interpretation of near-surface ground-penetrating radar sections'. Proc. 8th Int. Conf. on Ground-penetrating radar (GPR2000), Australia, 2000, pp. 842–847

[40] RAPPAPORT, C., and WEEDON, W.: 'A general method for FDTD modelling of wave propagation in arbitrary frequency-dispersive media', *IEEE Trans. Antennas Propag.*, 1997, **45**, (3) pp. 401–410

[41] RAPPAPORT, C., WU, S., and WINTON, S.: 'FDTD wave propagation modelling in dispersive soil using a single pole conductivity model, *IEEE Trans. Magnetics*, 1999, **35**, (3), pp. 1542–1545

[42] LUEBBERS, R., HUNSBERGER, F., KUNZ, K., STANDLER, R., and SCHNEIDER, M.: 'A frequency-dependent finite difference time domain formulation for dispersive materials', *IEEE Trans. Electromagn. Compat.*, 1990, **32**, (3), pp. 222–227

[43] BERENGER, J.: 'A perfectly matched layer for the absorption of electromagnetic waves', *J. Comput. Phys.*, **114**, Oct. 1994, pp. 185–200

[44] RAPPAPORT, C.: 'Interpreting and improving the PML absorbing boundary condition using anisotropic lossy mapping of space,' *IEEE Trans. Magn.*, 1996, **32**, (3), pp. 968–974

[45] RAPPAPORT, C., and WINTON, S.: 'Using the PML ABC for air/soil wave interaction modeling in the time and frequency domains,' *Int. J. Subsurf. Sens. Appl.*, 2000, **1**, (3), pp. 289–304

[46] MARENGO, E., RAPPAPORT, C., and MILLER, E.: 'Optimum PML ABC conductivity profile in FDFD,' *IEEE Trans. Magn.*, 1999, **35**, (3), pp. 1506–1509

[47] RAPPAPORT, C., KILMER, M., and MILLER, E.: 'Accuracy considerations in using the PML ABC with FDFD Helmholtz equation computation,' *Int. J. Numer. Model.*, 2000, **13**, (471), pp. 471–482

[48] RAPPAPORT, C., WU, S., KILMER, M., and MILLER, E.: 'Distinguishing shape details of buried non-metallic mine-like objects with GPR'. SPIE Aerosense Conf., Orlando, FL, Apr. 1999, pp. 1419–1428

[49] VON HIPPEL, A.: 'Dielectric materials and applications' (Wiley, New York, 1953)

Chapter 4

Properties of materials

4.1 Introduction

A significant number of researchers have extensively investigated the dielectric properties of earth materials. They have shown experimentally that for most materials which constitute the shallow sub-surface of the earth, which in this case is taken to be a zone of depths of 100 m or less, the attenuation of electromagnetic radiation rises with frequency and that at a given frequency wet materials exhibit a higher loss than dry ones. From this generalisation a number of predictions can be made relating to the performance of a surface-penetrating radar system. Before this can be done it is necessary to understand those characteristics of materials which affect both the velocity of propagation and attenuation.

An order of magnitude indication of the basic dielectric characteristics of various materials can be gauged from Table 4.1, which shows their conductivity and relative permittivity measured at a frequency of 100 MHz. The velocity of propagation is primarily governed by the relative permittivity of a material, which depends primarily upon its water content. At low microwave frequencies, including the range over which surface-penetrating radar systems operate, water has a relative permittivity of $\sim$80, while the solid constituents of most soils and man-made materials have, when dry, a relative dielectric constant ε_r in the range 2 to 9. The measured values of ε_r for soils and building materials lie mainly in the range 4 to 40. The absolute permittivity also varies with frequency, but is generally sensibly constant for most materials over the range of frequencies utilised for surface-penetrating radar work. The attenuation of a material is a more complex relationship and will be discussed in more detail in subsequent Sections of this Chapter.

The physical models which are used to predict the propagation of electromagnetic waves in dielectric materials have two main sources: electromagnetic wave theory and geometrical optics. The latter method is only relevant when the wavelength of the electromagnetic radiation employed is considerably shorter than the dimensions of the object or medium being illuminated and when the materials involved can be

Table 4.1 Typical range of dielectric characteristics of various materials measured at 100 MHz

Material	Conductivity, Sm^{-1}	Relative permeability
Air	0	1
Asphalt dry	$10^{-2} : 10^{-1}$	2–4
Asphalt wet	$10^{-3} : 10^{-1}$	6–12
Clay dry	$10^{-1} : 10^{0}$	2–6
Clay wet	$10^{-1} : 10^{0}$	5–40
Coal dry	$10^{-3} : 10^{-2}$	3.5
Coal wet	$10^{-3} : 10^{-1}$	8
Concrete dry	$10^{-3} : 10^{-2}$	4–10
Concrete wet	$10^{-2} : 10^{-1}$	10–20
Freshwater	$10^{-6} : 10^{-2}$	81
Freshwater ice	$10^{-4} : 10^{-3}$	4
Granite dry	$10^{-8} : 10^{-6}$	5
Granite wet	$10^{-3} : 10^{-2}$	7
Limestone dry	$10^{-8} : 10^{-6}$	7
Limestone wet	$10^{-2} : 10^{-1}$	8
Permafrost	$10^{-5} : 10^{-2}$	4–8
Rock salt dry	$10^{-4} : 10^{-2}$	4–7
Sand dry	$10^{-7} : 10^{-3}$	2–6
Sand wet	$10^{-3} : 10^{-2}$	10–30
Sandstone dry	$10^{-6} : 10^{-5}$	2–5
Sandstone wet	$10^{-4} : 10^{-2}$	5–10
Sea water	10^{2}	81
Sea-water ice	$10^{-2} : 10^{-1}$	4–8
Shale dry	$10^{-3} : 10^{-2}$	4–9
Shale saturated	$10^{-3} : 10^{-1}$	9–16
Snow firm	$10^{-6} : 10^{-5}$	6–12
Soil clay dry	$10^{-2} : 10^{-1}$	4–10
Soil clay wet	$10^{-3} : 10^{-0}$	10–30
Soil loamy dry	$10^{-4} : 10^{-3}$	4–10
Soil loamy wet	$10^{-2} : 10^{-1}$	10–30
Soil sandy dry	$10^{-4} : 10^{-2}$	4–10
Soil sandy wet	$10^{-2} : 10^{-1}$	10–30

considered to be electrical insulators. Optical theory is therefore most relevant to dry materials. Materials containing appreciable amounts of moisture will behave as conducting dielectrics, especially if the water contains ions. Most naturally occurring waters have some degree of ionic conduction and so act as aqueous electrolytes.

The variability of both material parameters and local geological conditions that is encountered in real life is such as to cause great difficulty in accurate prediction of propagation behaviour. This point should be noted when assessing the value of

predictive methods, as an accurate description by means of a theoretical approach may not adequately describe a situation with many degrees of freedom. Similarly it is often difficult to replicate the bulk material electromagnetic characteristics of a material in laboratory conditions using test cells. Even if the moisture content is correctly replicated, differences in density between in-situ and laboratory samples are difficult to minimise.

This Chapter considers, in sub-Sections 4.1 to 4.4, the basic physics of soils in terms of SPR/GPR propagation. Sub-Section 4.5, contributed by Dr Jim Doolittle of USDA and Professor Mary Collins of the University of Florida, considers the suitability of soils for SPR/GPR surveying in detail. Sub-Section 4.7 considers the properties of man-made materials, in particular concrete. Finally, Section 4.8 considers laboratory methods (contributed by Dr Yi Huang of the University of Liverpool) and field techniques of measuring soil properties.

Although all ultra-wideband radars transmit energy over at least an octave frequency band it is possible to make an order of magnitude estimation of their performance based on the centre frequency of operation. The objective of this Chapter is to provide an introduction into those parameters of materials that affect the performance of surface-penetrating radars. The relatively standard treatment given in this Chapter will, of course, only provide a guide to system performance and it is possible to consider a more complex treatment. However, the experimental practitioner will soon realise that accurate modelling is difficult to achieve within any reasonable budget due to the degrees of freedom needed. For this reason a simplified treatment is considered an adequate introduction.

4.2 Propagation of electromagnetic waves in dielectric materials

Maxwell's equations are the foundation for the consideration of the propagation of electromagnetic waves. In free space the magnetic susceptibility and electric permittivity are constants; that is, they are independent of frequency and the medium is not dispersive. In a perfect dielectric no propagation losses are encountered and hence there is no consideration of the attenuation, which occurs in real dielectric media.

Plane waves are good approximations to real waves in many practical situations, particularly in low loss and resistive media such as dry limestone and sands. More complicated electromagnetic wave fronts can be considered as a superimposition of plane waves, and this method may be used to gain an insight into more complex situations.

As a starting point, electromagnetic wave propagation can be represented by a one-dimensional wave equation of the following form. Propagation is taken along the z-axis, with perpendicular electric (E) and magnetic (H) fields as shown in Figure 4.1.

$$\frac{\partial^2 E}{\partial z^2} = \mu\varepsilon \frac{\partial^2 E}{\partial t^2} \tag{4.1}$$

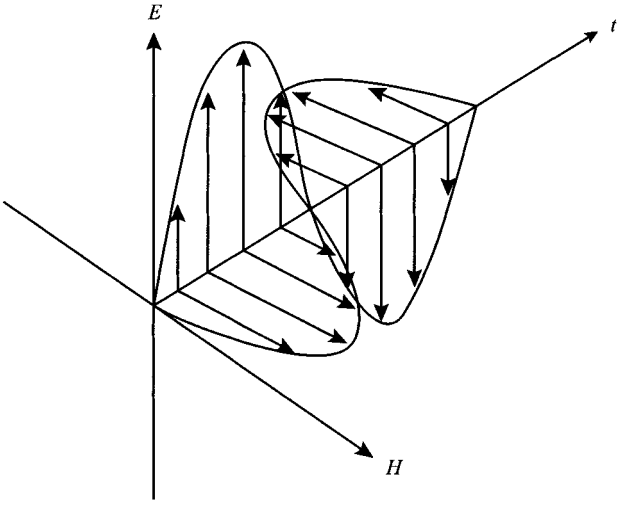

Figure 4.1 Propagation of electromagnetic waves in free space

where the velocity of propagation is

$$v = \frac{1}{\sqrt{\mu\varepsilon}} \tag{4.2}$$

the velocity of light in free space is

$$c = \frac{1}{\sqrt{\mu_0\varepsilon_0}} \tag{4.3}$$

where
absolute magnetic susceptibility of free space, $\mu_0 = 1.26 \times 10^{-6}\,\mathrm{Hm}^{-1}$
absolute electric permittivity of free space, $\varepsilon_0 = 8.86 \times 10^{-6}\,\mathrm{Fm}^{-1}$
absolute magnetic susceptibility of medium, $\mu = \mu_0\mu_r$
absolute electric permittivity of medium, $\varepsilon = \varepsilon_0\varepsilon_r$
and
ε_r is relative permittivity, having a value in the range 1 to 80 for most geological materials, and μ_r is relative magnetic susceptibility, being 1 for nonmagnetic geologic materials.

Hence,

$$v_r = \frac{c}{\sqrt{\varepsilon_r}} \tag{4.4}$$

The intrinsic impedance (the ratio of the electric to the magnetic field) of the medium is

$$\eta = \sqrt{\frac{\mu}{\varepsilon}} \tag{4.5}$$

A wave propagating in the positive z-direction in a perfect dielectric can be described by the following:

$$E(z) = E_0 e^{-jkz} \tag{4.6}$$

where the phase constant,

$$k = \frac{\omega}{v} = \omega\sqrt{\mu\varepsilon}\ \mathrm{m}^{-1} \tag{4.7}$$

This describes the change in phase per unit length for each wave component; it may be considered as a constant of the medium for a particular frequency and is then known as the wave number. It may also be referred to as the propagation factor for the medium.

The wavelength, λ, is defined as the distance the wave propagates in one period of oscillation. It is then the value of z which causes the phase factor to change by 2π:

$$k\lambda = 2\pi$$

Rearranging,

$$\lambda = \frac{2\pi}{\omega\sqrt{\mu\varepsilon}} = \frac{v}{f} \tag{4.8}$$

This is the common relationship between wavelength, phase velocity and frequency. In optics it is common to utilise a refractive index, η, given by

$$\eta = \frac{c}{v} = \sqrt{\mu_r \varepsilon_r} \tag{4.9}$$

taking $\mu_r = 1$ and $\eta = \sqrt{\varepsilon_r}$ for the frequency being considered.

Electromagnetic waves propagating through natural media experience losses, to both the electric (E) and magnetic (H) fields. This causes attenuation of the original electromagnetic wave. For most materials of interest in surface-penetrating radar the magnetic response is weak and need not be considered as a complex quantity, unlike the permittivity and conductivity. In the case of lossy dielectric materials, absorption of electromagnetic radiation is caused by both conduction and dielectric effects. It is not possible to distinguish, by measurement at a single frequency, the separate components of loss for such materials.

In general the complex permittivity, ε, and the complex conductivity, σ, may be expressed as:

$$\varepsilon = \varepsilon' - j\varepsilon'' \tag{4.10}$$

and

$$\sigma = \sigma' - j\sigma'' \tag{4.11}$$

where σ' and σ'' are real parts, ε' and ε'' are imaginary parts and $j = \sqrt{-1}$.

The nature of the parameter ε' relates to the electric permittivity, which may also be expressed in terms of relative permittivity. The parameter ε'' relates to losses associated with both conductivity and frequency. For practical purposes at frequencies

up to 1 GHz and conductivities below 0.1 Sm^{-1} the effect of the ε' term will be small and is commonly disregarded (i.e., ε taken as the real components ε', ε'') in such circumstances.

When measurements are made on a conducting dielectric, the parameters measured are the apparent permittivity and apparent conductivity:

$$\bar{\varepsilon} = \varepsilon'_e - j\varepsilon''_e \tag{4.12}$$

$$\bar{\sigma} = \sigma'_e - j\sigma''_e \tag{4.13}$$

The behaviour of a material may be specified either by its apparent permittivity or, equivalently, by its apparent conductivity, since

$$\bar{\sigma} = j\omega\bar{\varepsilon} \tag{4.14}$$

In terms of wave propagation equations, ε and σ always occur in the combination

$$\sigma + j\omega\varepsilon = \sigma'_e - j\omega\varepsilon'_e \tag{4.15}$$

where σ'_e is the real effective conductivity and ε'_e is the real effective permittivity:

$$\sigma'_e = \sigma' - \omega\varepsilon'' \tag{4.16}$$

$$\varepsilon'_e = \varepsilon' - \frac{\sigma''}{\omega} \tag{4.17}$$

From (4.5) the propagation of an electromagnetic field E_0 originating at $z = 0$, $t = 0$ in a conducting dielectric can be described by $E(z,t)$ at a distance, z, and time, t, by

$$E(z,t) = E_0 e^{-\alpha z} e^{j(\omega t - \beta z)} \tag{4.18}$$

The first exponential function is the attenuation term and the second the propagation term.

From the first exponential function it is seen that at a distance $z = 1/\alpha$ the attenuation is $1/e$. This distance is known as the skin depth, d, and provides an indication of the penetration depth of a surface-penetrating radar system. However, there are a number of other factors which influence the effective penetration depth, notably the strength of reflection from the target sought and the degree of clutter suppression of which the system is capable. These may reduce the calculated performance and must also be considered.

In general the parameters of interest for sub-surface radar applications are the attenuation and velocity of wave propagation.

In a conducting dielectric the phase constant is complex and is

$$k = \omega\sqrt{\mu(\varepsilon' - j\varepsilon'')} \tag{4.19}$$

The wave number may be separated into real and imaginary parts:

$$jk = \alpha + j\beta = j\omega\sqrt{\mu\varepsilon'\left(1 - j\frac{\varepsilon''}{\varepsilon'}\right)} \tag{4.20}$$

where α is the attenuation factor and β is the phase constant.

The parameters α and β can be related to σ and $j\omega\varepsilon$, giving expressions for α and β as shown below:

$$\alpha = \omega \sqrt{\left[\frac{\mu\varepsilon'}{2}\sqrt{1+\left(\frac{\varepsilon''}{\varepsilon'}\right)^2} - 1\right]} \quad \beta = \omega \sqrt{\left[\frac{\mu\varepsilon'}{2}\sqrt{1+\left(\frac{\varepsilon''}{\varepsilon'}\right)^2} + 1\right]} \tag{4.21}$$

The dimensionless factor $\varepsilon''/\varepsilon'$ is more commonly termed the material loss tangent.

The above expressions may be rearranged to provide the attenuation constant α in dB m^{-1} and the wave velocity, v, in ms^{-1}.

It can be seen from the above expressions that the attenuation constant of a material is, to a first order, linearly related (in dB m^{-1}) to frequency. It is not sufficient to consider only the low frequency conductivity σ_0 when attempting to determine the loss tangent over the frequency range 1.10^7 to 1.10^{10} Hz. In the case of a material that is dry and relatively lossless, it may be reasonable to consider that tan δ is constant over that frequency range. However, for materials that are wet and lossy such an approximation is invalid, as

$$\tan\delta = \frac{\sigma' + \omega\varepsilon''}{\omega\varepsilon' - \sigma''} \tag{4.22}$$

It is important to consider the magnitude of σ'' and ε'' in attempting to determine the value of tan δ. In general for lossy earth materials tan δ is large at low frequencies, exhibits a minimum at $\sim 1 \times 10^8$ Hz and increases to a maximum at several GHz, remaining constant thereafter. Accurate determination of attenuation must therefore consider all the coefficients, which comprise the expression for tan δ. It should be noted that the complex dielectric constant, and hence the loss factor, of a soil is affected by both temperature and water content. The general effect of increasing the temperature is to reduce the frequency of the dielectric relaxation, while increasing the water content also increases the value of the loss factor while shifting its peak frequency down. It is observed that the frequency of the maximum dielectric loss of the water relaxation in soils is reduced and occurs over a more limited frequency range when compared with conductive water. Tan δ can increase with frequency over the range 1×10^8 to 1×10^{10} Hz as the dipolar losses associated with the water content of the material become more significant and the conductivity losses reduce.

$$\tan\delta = \text{conductivity losses} + \text{dipolar losses}$$

$$\tan\delta = \frac{\sigma_{dc}}{\omega\varepsilon_0\varepsilon_r} + \frac{\varepsilon''}{\varepsilon'} \tag{4.23}$$

An approximation which enables an order of magnitude indication is that when σ is small

$$\tan\delta \approx \frac{\sigma'}{\omega\varepsilon'} \tag{4.24}$$

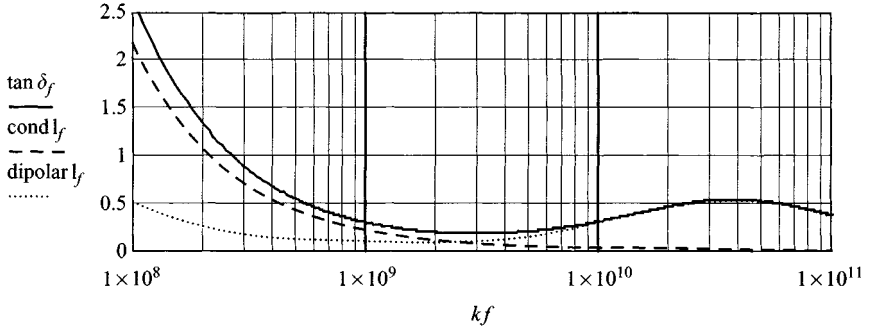

Figure 4.2 Dielectric losses as a function of frequency in Hz for a medium loss soil

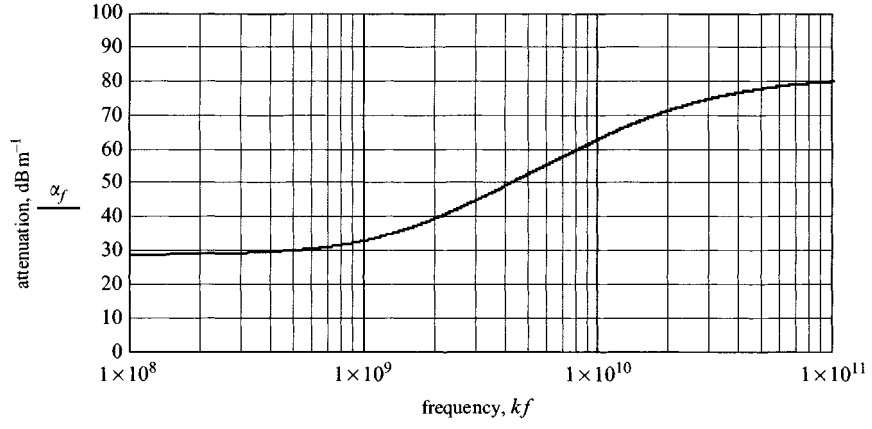

Figure 4.3 Material attenuation as a function of frequency for a medium loss soil

It is necessary to determine the dipolar losses from a consideration of the dielectric relaxation spectrum of the soil/water mixture under consideration. Typically for a mixture of sandy-clay soils (60% sand and 15% clay) with a water content of 25% the following losses could be expected. The dielectric mixture model as described by Peplinski *et al.* [1] is strictly applicable only over the range 0.3–1.3 GHz, although the original model developed by Hallikainen *et al.* [2] covered the range 1.4 to 18 GHz. A graph of dielectric losses for a medium loss soil is shown in Figure 4.2. Therefore its accuracy is limited to that frequency range. However, it gives a good insight into the wideband characteristics of soils.

A MathCAD™ worksheet to explore the dielectric loss characteristics of soils is provided in dielectric losses, and the reader is encouraged to vary the soil and water parameters as required.

A graph of attenuation versus frequency for such a material is shown in Figure 4.3 and the dielectric properties in Figure 4.4.

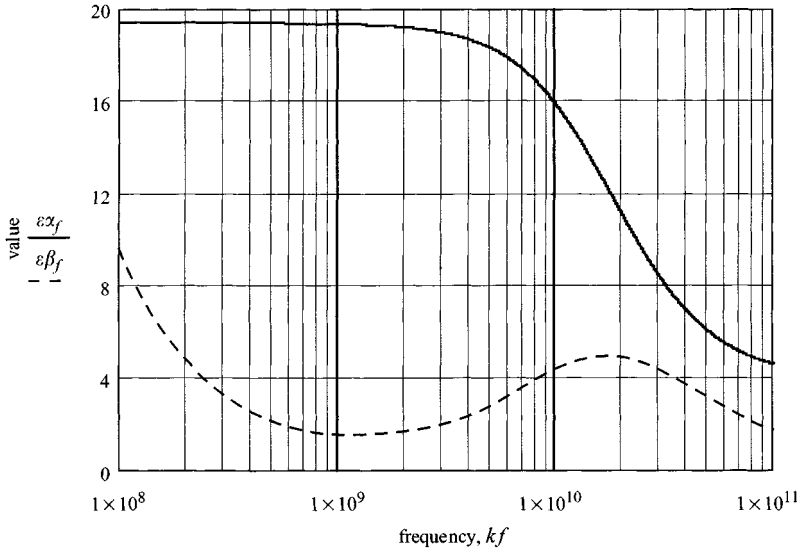

Figure 4.4 Dielectric properties ε' and ε'' of lossy soil as a function of frequency

The velocity of propagation is also slowed by an increase of loss tangent as well as relative dielectric constant,

$$v = c\left[\frac{\varepsilon'_e}{2\varepsilon_0}\left(\sqrt{(1+\tan^2\delta)}+1\right)\right]^{\frac{1}{2}} \tag{4.25}$$

However, $\tan\delta$ must be significantly greater than 1 for any slowing to occur, and it is reasonable to assume that for

$$\tan\delta < 1$$

$$v = \frac{c}{\sqrt{\varepsilon_r}} \tag{4.26}$$

In any estimation of received signal level it is necessary to consider the coefficients of reflection and transmission as the wave passes through the dielectric to the target as shown in Figure 4.5.

To do this we need to consider the intrinsic impedance of the various materials.

The intrinsic impedance of a medium is the relationship between the electric field, E, and the magnetic field, H:

$$\eta = \frac{E}{H} \tag{4.27}$$

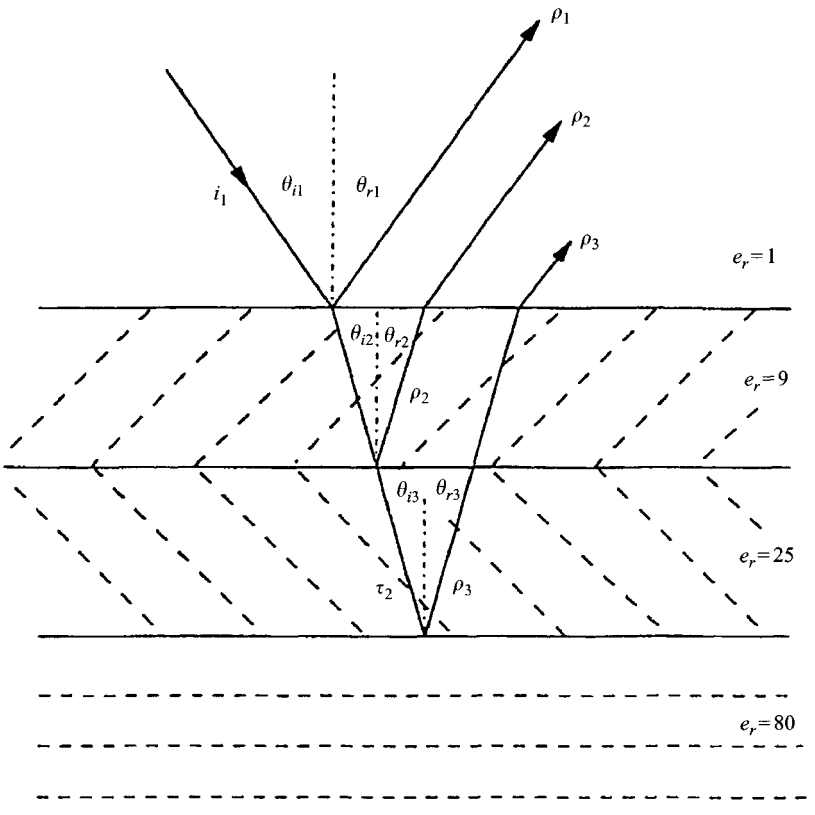

Figure 4.5 Multi-layer dielectric

η is a complex quantity that is calculated according to

$$\eta = \sqrt{\frac{-j\omega\mu}{\sigma - j\omega\varepsilon}} \tag{4.28}$$

The intrinsic impedance of the medium becomes

$$\eta = \sqrt{\frac{\mu}{\varepsilon}} = \sqrt{\mu}\left(\varepsilon'\left(1 - j\frac{\varepsilon'}{\varepsilon''}\right)\right)^{-\frac{1}{2}} \tag{4.29}$$

At the boundary between two media, some energy will be reflected and the remainder transmitted. The reflected field strength is described by the reflection coefficient, r:

$$r = \frac{\eta_2 - \eta_1}{\eta_2 + \eta_1} \tag{4.30}$$

where η_1 and η_2 are the impedances of medium 1 and 2, respectively.

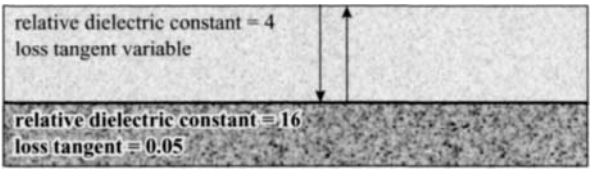

Figure 4.6 Layout of model for calculation

In a nonconducting medium, such as dry soil or dry concrete, and when considering only a single frequency of radiation, the above expression may be simplified and rewritten as

$$r = \frac{\sqrt{\varepsilon_{r2}} - \sqrt{\varepsilon_{r1}}}{\sqrt{\varepsilon_{r2}} + \sqrt{\varepsilon_{r1}}} \tag{4.31}$$

where ε_r is the relative permittivity of the medium.

The reflection coefficient has a positive value when $\varepsilon_{r2} > \varepsilon_{r1}$, such as where an air-filled void exists in a dielectric material. The effect on a pulse waveform is to change the phase of the reflected wavelet so that targets with different relative dielectric constants to the host material show different phase patterns of the reflected signal. However, the amplitude of the reflected signal is affected by the propagation dielectric of the host material, the geometric characteristics of the target and its dielectric parameters, as indicated in Figure 4.6.

Figures 4.7 and 4.8 show the predicted relative received signal at frequencies of 100 MHz and 1 GHz for a planar interface, where the first layer relative dielectric constant is 4. The second layer relative dielectric constant is 16 and has a loss tangent of 0.05.

The previous description is an elementary description of a situation, which is described with considerably more precision by Wait [3] and King *et al.* [4].

Wait initially considers the one-dimensional case of propagation of a transient field in a homogeneous infinite medium with conductivity σ, dielectric constant ε and permeability μ.

Wait's general method is to determine the form of the magnetic and electric fields at a distance from the source point. The transient fields are represented as Fourier integrals and, in the case where the driving function is a unit impulse, the time domain characteristics of the far field response are derived. Wait further develops the general approach for the case of a dipole on a dielectric half-space and concludes that the main feature of propagation in conducting media is that the waveform changes its shape as it propagates away from the source. As a consequence resolution is severely degraded. However, this loss of fidelity could also be used as an indicator of distance travelled.

King and Wu [4] treat the situation of the propagation of a radar pulse in sea water in similar general manner and draw a parallel to the treatment by Brillouin [5] and Sommerfeld [6] of the propagation of optical pulses in a linear, causally dispersive medium and in an updated form by Oughstrun [7]. King considers analytically the case of the near field generated by the rectangular pulse modulated current in an

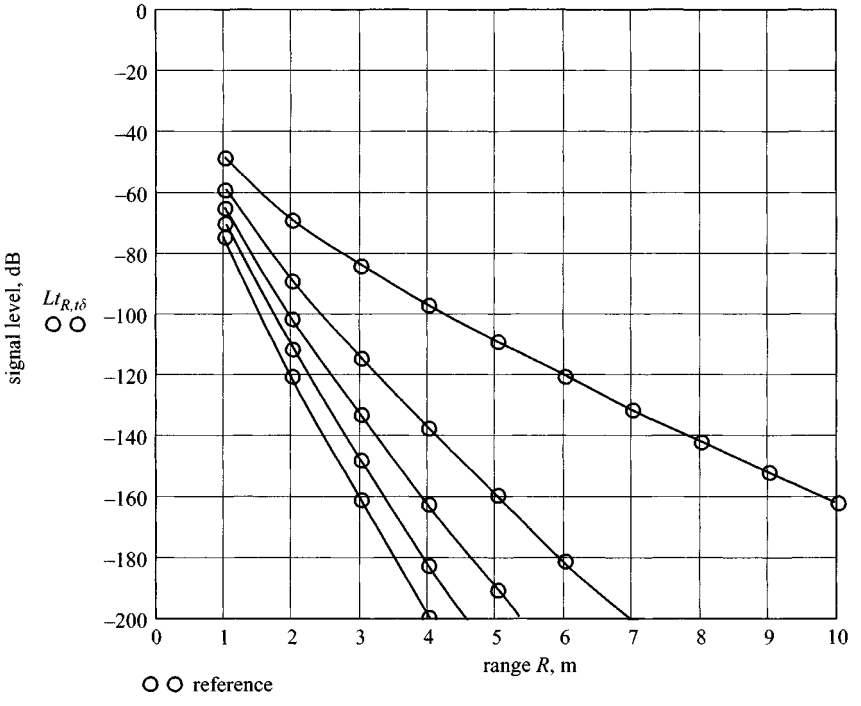

Figure 4.7 *Received signal level against range at 100 MHz*
Tan $\delta = 2.1 \times 10^{-3}$, 1.05×10^{-2}, 1.7×10^{-2}, 2.4×10^{-2} and 2.9×10^{-2}

electric dipole in sea water. This situation is a useful model for pulse propagation in a dissipative and dispersive medium from a dipole source. King concludes that the amplitude of the wave packet decays more rapidly than the amplitudes of the transient components. Finkelshteyn and Kraynyukov [8] also consider the effect of the medium on pulse propagation characteristics. Wait and Nabulsi [9] also consider the possibility of preforming the pulse shape to suit particular lossy media.

4.3 Properties of lossy dielectric materials

The electromagnetic behaviour of natural and man-made materials is generally complicated because all exhibit both dielectric and conducting properties. Their electromagnetic characteristics are controlled by the microscopic scale (atomic, molecular and granular) behaviour of the components making up the materials. The origins of various dielectric losses as a function of frequencies are shown schematically in Figure 4.9.

The effects occur at different frequencies, which creates a frequency dependency in the dielectric properties of these materials. Figure 4.10 illustrates the changes which take place in the relative permittivity, and the dielectric loss factor, over an extremely

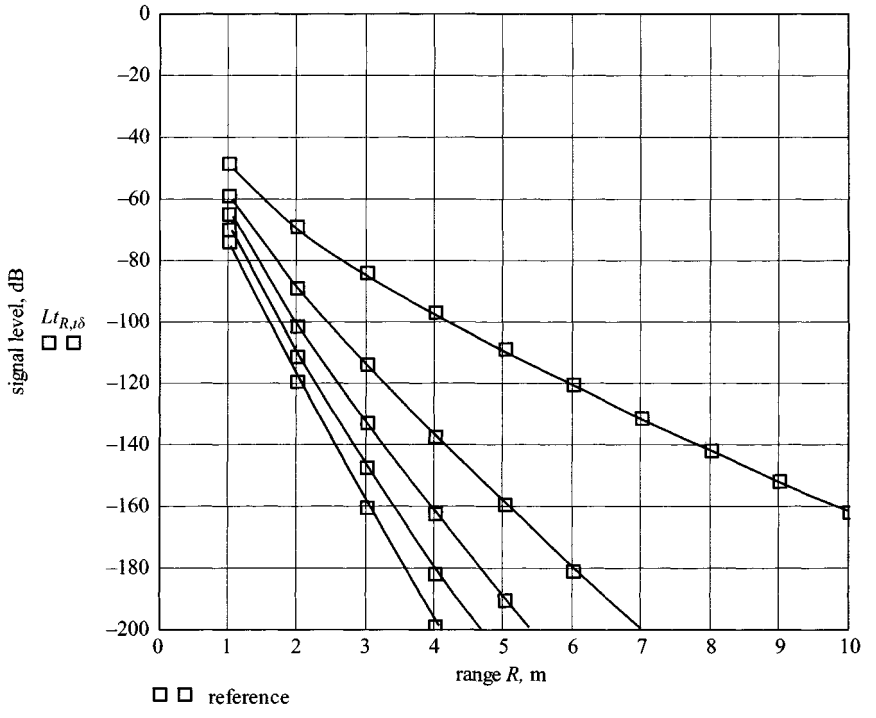

Figure 4.8 *Received signal level against range at 1 GHz*
Tan $\delta = 2.1 \times 10^{-6}$, 1.05×10^{-5}, 1.9×10^{-5}, 2.7×10^{-5} and 3.6×10^{-5}

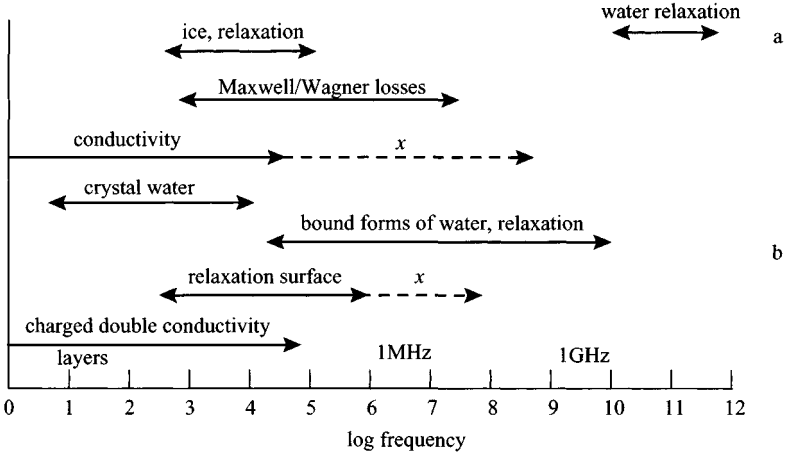

Figure 4.9 *Origin of dielectric losses in heterogeneous materials containing water (after De Loor [10])*

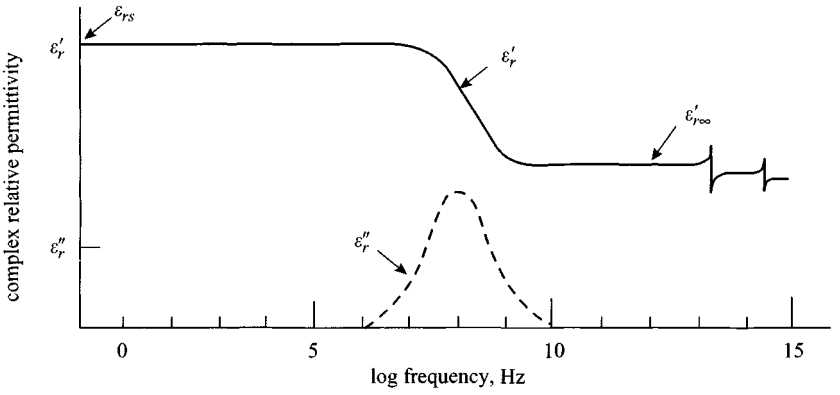

Figure 4.10 Schematic diagram of the complex relative permittivity relaxation region (atomic and electronic resonance regions) $\varepsilon_r = \varepsilon'_r - j\varepsilon''_r$

wide frequency range. In this idealised representation the relative permittivity effectively remains constant at high and low frequencies. However, there is a transition region over an intermediate frequency band where the dielectric properties change significantly with frequency. This region is of particular interest when it occurs in the microwave band. In the regions of electronic resonance ($\sim 10^{15}$ Hz) occur at frequencies far higher than those associated with surface-penetrating radar. Therefore they need not be considered any further in relation to the frequency range of interest.

The relaxation phenomenon portrayed relates to the disturbance of polar molecules by an impressed electric field, each molecule experiencing a force that acts to orientate the permanent dipole moment characteristic of the molecule parallel to the direction of the applied electric field. This force is opposed by thermodynamic forces. If an alternating electric field is applied, the individual molecules will be induced to rotate in an oscillatory manner about an axis through their centres, the inertia of the molecules preventing them from responding instantaneously. Similar translational effects can occur. The polarisation produced by an applied field (such as a propagating radar wave) is closely related to the thermal mobility of the molecules and is, therefore, strongly temperature dependent. In general, the relaxation time (which may be expressed as a relaxation frequency) depends on activation energy, the natural frequency of oscillation of the polarised particles, and on temperature. Relaxation frequencies vary widely between different materials. For example, maximum absorption occurs at very low frequencies in ice (10^3 Hz), whereas it takes place in the microwave region in water (10^6–10^{10} Hz). Thus the effects of this phenomenon could have a direct bearing upon the dielectric properties of materials at the frequencies employed by surface-penetrating radars, especially if moisture is present within a material. There are a number of other mechanisms, which cause a separation of positively and negatively charged ions resulting in electric polarisation. These mechanisms can be associated with ionic atmospheres surrounding colloidal particles (particularly clay minerals), absorbed water and pore effects, as well as interfacial phenomena between particles.

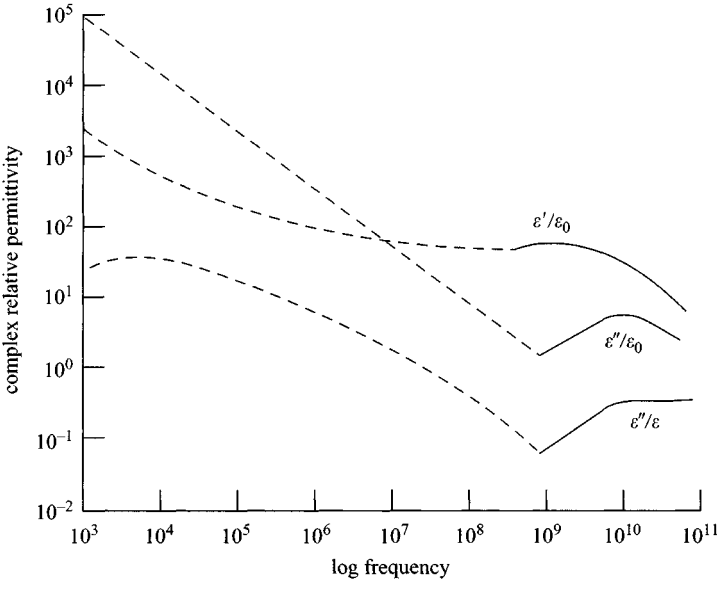

Figure 4.11 The complex relative permittivity and loss tangent of a silty clay soil at a water content of 15% wt (Hoekstra and Delaney [11])

This behaviour is illustrated in Figure 4.11, which shows the complex behaviour of a silty clay soil over the frequency range 10^3 to 10^{11} Hz.

Although the above is a basic description of a complex subject it does serve to explain the frequency dependent nature of the dielectric properties of the materials involved. This implies that there will be some variation in the velocity of propagation with frequency. Dielectrics exhibiting this phenomenon are termed dispersive. In this situation, the different frequency components within a broadband radar pulse would travel at slightly different speeds, causing the pulse shape to change with time. However, the propagation characteristics of octave band radar signals remain largely unaffected, and most commercial surface-penetrating radar systems fall into this category.

The determination of the dielectric properties of earth materials remains largely experimental. Rocks, soils and concrete are complex materials composed of many different minerals in widely varying proportions, and their dielectric parameters may differ greatly even within materials, which are nominally similar. Most earth materials contain moisture, usually with some measure of salinity. Since the relative permittivity of water is of the order of 80, even small amounts of moisture cause a significant increase of the relative permittivity of the material. An indication of the effect of moisture content on the relative permittivity of rock is shown in Figure 4.12.

A large number of workers have investigated the relationships between the physical, chemical and mechanical properties of materials and their electrical and in particular microwave properties. In general they have sought to develop suitable

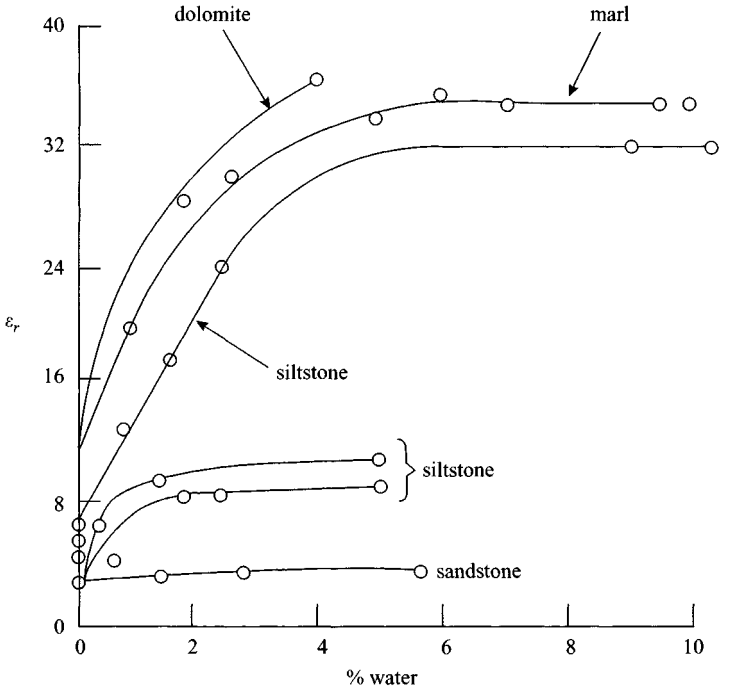

Figure 4.12 Effect of moisture content of rock on relative permittivity (after Hipp [12])

models to link the properties of the material to its electromagnetic parameters. Such models provide a basis for understanding the behaviour of electromagnetic waves within these media.

The influence of moisture content upon the dielectric properties of earth materials is significant and is well documented in the literature. Extensive measurements at 450 MHz and 35 GHz were made by Campbell and Ulrichs [13] on dry mineral and rock samples. The difference between the apparent permittivity at the two frequencies was small, supporting their conclusion that dry materials have no measurable dispersion at microwave frequencies. The relative permittivity varied from 2.5 for low-density rock types to 9.5 for high-density basaltic rocks, and the loss tangent ($\tan \delta$) was <0.1. Von Hippel [14] reports a series of measurements on soils at various water contents up to frequencies of 10 GHz. When the water content of his samples exceeded 10% by weight, a substantial decrease in relative permittivity and an increase in the loss tangent was observed at frequencies between 100 MHz and 10 GHz. This dispersion is considered to be due to the dielectric relaxation of water in soils.

There are a number of methods of classifying soils, and the Soil Survey of England and Wales classifies soil particles as shown in Table 4.2; see also Figure 4.13.

Table 4.2 Soil textual classification

Soil textual class	Diameter, mm
clay	<0.002
silt	0.002 to 0.06
fine sand	0.02 to 0.06
medium sand	0.06 to 0.2
coarse sand	0.06 to 2
stones	>2

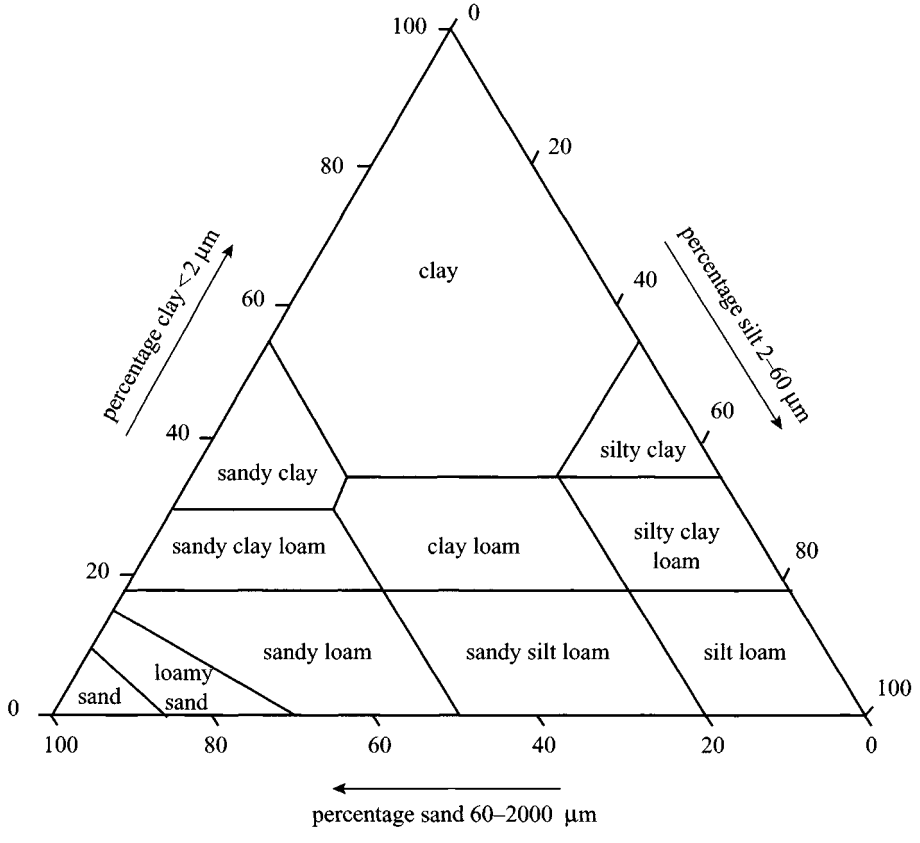

Figure 4.13 Triangular diagram of soil textural classes

Table 4.3 Attenuation and relative dielectric constant of various materials measured at 100 MHz

Material	Attenuation, dB m^{-1}	Relative permittivity range
Air	0	1
Asphalt dry	2–15	2–4
Asphalt wet	2–20	6–12
Clay dry	10–50	2–6
Clay wet	20–100	5–40
Coal dry	1–10	3.5
Coal wet	2–20	8
Concrete dry	2–12	4–10
Concrete wet	10–25	10–20
Freshwater	0.01	81
Freshwater ice	0.1–2	4
Granite dry	0.5–3	5
Granite wet	2–5	7
Limestone dry	0.5–10	7
Limestone wet	1–20	8
Permafrost	0.1–5	4–8
Rock salt dry	0.01–1	4–7
Sand dry	0.01–1	2–6
Sand wet	0.5–5	10–30
Sandstone dry	2–10	2–5
Sandstone wet	4–20	5–10
Sea water	100	81
Sea-water ice	1–30	4–8
Shale dry	1–10	4–9
Shale saturated	5–30	9–16
Snow firm	0.1–2	6–12
Soil clay dry	0.3–3	4–10
Soil clay wet	5–50	10–30
Soil loamy dry	0.5–3	4–10
Soil loamy wet	1–6	10–30
Soil sandy dry	0.1–2	4–10
Soil sandy wet	1–5	10–30

Table 4.3 provides an indication of the electromagnetic characteristics of a number of earth materials for typical operating frequencies utilised for surface-penetrating radar work.

In many instances the potential variation in the velocity of wave propagation over the frequency range of interest would be small and will be ignored. It would only be considered in special circumstances, perhaps where relative indications were required about major variations in the moisture content of a material. In general it is not possible to make a reliable estimate of propagation velocity or relative permittivity in a medium

from a single measurement without trial holing or other supplementary information. Even in the case where a measurement is carried out at one location, it is often found that significant variations in velocity will occur within comparatively short distances from the original location. This can lead to significant errors in the estimation of depths of reflectors or thickness of layers. One procedure which overcomes this limitation is known as common depth point surveying, which utilises two antennas in bistatic operation at a number of transmit and receive positions.

In the following Sections the characteristics of the various mediums that might be investigated by surface-penetrating radar are considered in more detail.

4.4 Water, ice and permafrost

The principal loss mechanism in rocks and soils, certainly at frequencies over 500 MHz, is the absorption of energy by water present in the pores. The dielectric relaxation properties of water are described well by a Debye relaxation with a single relaxation time [12]. Pure liquid water at 0°C exhibits a maximum absorption at 9.0 GHz; this increases as temperature rises, with the maximum absorption occurring at 14.6 GHz at 10°C. Figure 4.14 shows the dielectric relaxation spectrum for water at two temperatures [15].

A useful introductory summary of the properties of water, both liquid and solid, is provided by King and Smith [16], while Pottel [17] reviews the topic of aqueous electrolytes. All water encountered in earth materials has some degree of ionic conduction, and Pottel's treatment gives useful quantitative information to enable calculations to be made of the frequency dependence of dielectric properties. Cole and Cole [18] in a classic paper proposed a modified Debye relaxation equation for liquid water containing free ions. An indication of the variation in permittivity for a solution of NaCl and pure water is for values of ε_s between 63 and 73 and values of ε_∞ between 5 and 6. It has been found that the quoted range of values for ε_∞ is common to water and all aqueous solutions.

The dielectric properties of naturally occurring water (or ice) can be adequately described by the Debye theory or its modification when there is knowledge of its temperature and low frequency conductivity, with the other constants needed in the calculation being available in the literature. The velocity of wave propagation is slowed substantially with increasing ionic concentrations. This has the most pronounced influence at frequencies below 200 MHz, and above this frequency the wave velocity closely approaches that of pure water. At high conductivities the attenuation rises with frequency and there is no plateau in the loss curve before the rise due to resonance absorption takes place (De Loor [10] and Figure 4.10).

An understanding of the dielectric properties of water enables the propagation of electromagnetic waves to be assessed in a range of earth and construction materials. The principal loss mechanism in soils and rocks for frequencies above ~500 MHz is the absorption of energy by water in the pores. If the water content is large enough the permittivity of the material may be determined firstly by the dielectric properties of water and to a second order by those of the dry material.

For many applications the real effective permittivity and conductivity may be assumed to be

$$\varepsilon'_e = \varepsilon'$$
$$\sigma'_e = \sigma_{dc} + \omega\varepsilon'' \tag{4.32}$$

where σ_{dc} is the DC conductivity and ε' and ε'' are obtained from the Debye formula given by King and Smith [16]

$$\varepsilon(\omega) = \varepsilon' + j\varepsilon'' = \varepsilon_\infty + \frac{\varepsilon_s - \varepsilon_\infty}{1 + j\omega\tau} \tag{4.33}$$

where ε_∞ is high frequency (infinite) permittivity, ε_s is low frequency (static) permittivity and τ is relaxation time of water.

The variation of ε' and ε'' for water is presented as a function of frequency in Figure 4.14.

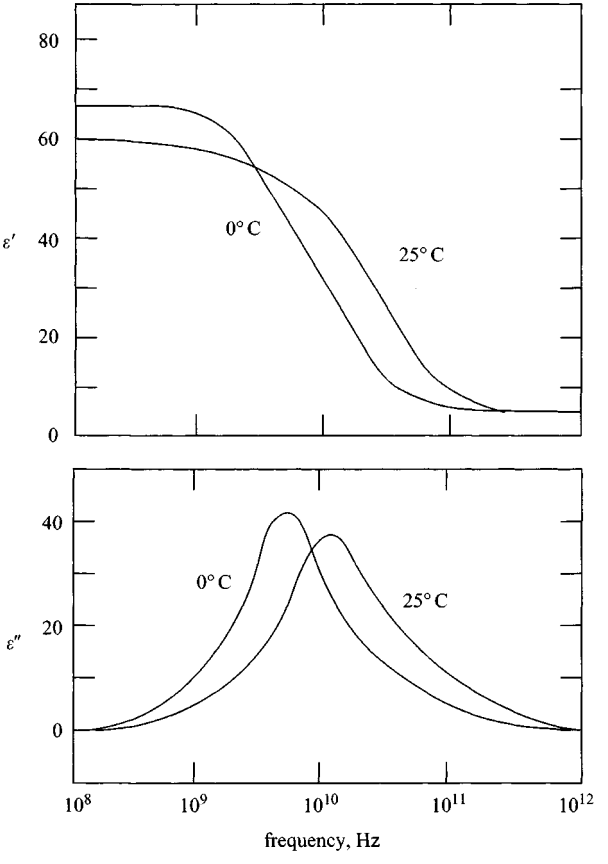

Figure 4.14 Dielectric relaxation spectrum of water at two temperatures (Hoekstra and Delaney [15])

The above assumes a very low pure water DC conductivity, with an associated low attenuation in the frequencies employed for surface-penetrating radar. In practice, impurities or the presence of free ions in water significantly increase conductivities in the resulting electrolyte. Cole and Cole [18] proposed a modified Debye relaxation equation for complex permittivity at angular frequency:

$$\varepsilon(\omega) = \varepsilon_\infty + \frac{\varepsilon_s - \varepsilon_\infty}{1 + j^{1-a}(\omega\tau)^{1-b}} \tag{4.34}$$

which reduces to the Debye relation when $a = b = 0$.

An approximately linear relationship was found between the concentration of the ionic solution and the deviation of the relaxation time τ from that of pure water, for up to 1 M concentration. It is also found that the DC conductivity, σ_{dc}, also varies linearly with concentration in weak solutions.

The complex permittivity of a liquid can be estimated for a given concentration, temperature and frequency on the basis of the equation for ε_ω and data obtained from the literature.

Ice is a material which has been extensively measured using surface-penetrating radar, both in the Antarctic and Arctic. Fresh-water ice displays very different properties from sea-water ice, and the latter is considered by Kovacs *et al.* [19] to be a complex, lossy, anisotropic dielectric consisting of pure ice, air, brine and possibly solid salts.

Generally, sea ice is classified by age into first, second and subsequent years and by structure. The latter is defined by the processes of growth, melt and deformation. Sea-water is an electrolyte comprising a multitude of salts of which sodium chloride is the dominant constituent (~80%). The formation of sea ice occurs in several separate phases which govern the geometric structure and hence the anisotropic electromagnetic characteristic of the ice. The initial growth phase of a few millimetres generates needles of ice, and these are termed fazil crystals. The second phase of growth occurs when the ice thickens and the initially random crystal orientation becomes more ordered and wider as the depth of ice increases. The ice crystals become vertically orientated as they grow downwards. As growth continues, the elongated crystals cause local freezing of the sea-water, effectively localising the water from the base and thus any remaining water in the spaces between the crystals increases its salt content. As the crystals grow they entrap local pockets of high salinity water. Underwater currents affect the orientation of the crystals and hence the anisotropy of the ice layers which form over many years.

Kovacs *et al.* [19] calculated that the apparent dielectric constant measured at 100 MHz decreased with increasing ice thickness and followed the trend established with field measurements. Kovacs' model of sea ice suggests that the relative dielectric constant at a frequency of 100 MHz increases in a nonlinear fashion from ~3.5 to 18 as the ice depth increases from 0.2 m to 0.7 m. Over the same depth range the attenuation at 100 MHz increases from ~10 dB m^{-1} to 50 dB m^{-1}.

Kovacs *et al.* [19] also showed that the coefficient of anisotropy, defined as the ratio of the major to minor axis of the polar plot of the reflection amplitude, could vary between 2.2 and 15. However, the situation he encountered in Alaska was

further complicated by the inclusion of different strata within the ice, which affected the orientation and growth pattern of the C-axis of the ice crystals. Radar survey work has also been carried out on the detection of ice in permafrost near the Alyeska pipeline in Alaska.

4.5 Dielectric properties of soils and rocks

The dielectric properties of soils and rocks are discussed in detail by De Loor [10], Hoekstra and Delaney [11], Hipp [20], Wang and Schmugge [21], Hallikainen *et al.* [2] and Wobschall [22], and extensive data are provided by Parkhomenko [23], Keller [24], Fuller and Ward [25], Campbell and Ulrichs [26], and Endres and Knight [27].

All of these authors consider in detail the theoretical effect of microscopic fluid distribution on the dielectric properties of partially saturated rocks. The electromagnetic characteristics of rocks include anisotropy, an enormous range (20 orders of magnitude) of DC conductivity, and an order of magnitude range in permittivity between about 2 or 3 for dry sandstone to 40 or so for wet porous rocks. The use of radar techniques to probe rock is usually intended to provide information about deep features where resolution is not usually critical. This permits the use of lower frequencies to aid penetration. Typical changes in relative permittivity with moisture content are shown in Figure 4.12 for several types of rock. These data were obtained at frequencies in the range of 0.1 to 1 MHz. The main exception to the requirement for long range is the probing of coal seams, where resolution is generally more important.

As values of permittivity and velocity of propagation are strongly influenced by the presence of moisture, there is clearly a relationship between these parameters and porosity of the medium. Work on rocks has shown the following relationships.

For layered material [28] with the electric field applied parallel to the bedding, for a particular frequency f,

$$\varepsilon_r = (1 - p)\,\varepsilon_m + p\varepsilon_w \tag{4.35}$$

where ε_r is permittivity of the layered material, ε_m is permittivity of the matrix, ε_w is permittivity of water and p is porosity ratio.

For layered material [28] with electric field applied perpendicular to the bedding, for a particular frequency f,

$$\varepsilon_r = \frac{\varepsilon_m \varepsilon_w}{(1 - p)\,\varepsilon_m + p\varepsilon_w} \tag{4.36}$$

from which velocity of propagation can be calculated. Alternatively, porosity can be calculated from

$$p = \frac{c}{v^2} = \frac{\varepsilon_m}{\varepsilon_m - \varepsilon_w} \tag{4.37}$$

Endres and Knight [27] have put forward a theoretical treatment of the effect of microscopic fluid distribution on the dielectric properties of partially saturated rocks.

Attempts have also been made by Hanai, amongst others, to model the dielectric behaviour of soils by extending the theory of dielectric mixtures produced by Wagner and others for emulsions of the oil-in-water type, establishing relationships of the following type:

$$\frac{\left(\varepsilon^* - \varepsilon_p^*\right)}{\left(\varepsilon_m^* - \varepsilon_D^*\right)} \left(\frac{\varepsilon_m^*}{\varepsilon^*}\right)^{0.33} = (1 - \phi) \tag{4.38}$$

where ϕ is volume fraction of the dispersed phase, ε_D^* is permittivity of the dispersed phase, ε_m^* is permittivity of the dispersing medium and ε^* is permittivity of the mixture.

The dielectric properties of soils have been studied for many years and there is now a large body of experimental data available as well as a range of theoretical models. Considerable difficulties are posed by the variability of the material, and none of the models developed is universally applicable. Simple models for dielectric loss tend to be deficient, with the major discrepancy between theory and experiment being the frequency dependence of the observable effects. The principal errors are understood to relate to the representation of the energy absorption by moisture, although there are numerous other factors which have a bearing on the matter.

Experimental studies (Hipp [12]) on soils have shown a rise in permittivity with water content and, at a given water content, a fall in permittivity with increasing frequency. Effective conductivity, and hence attenuation, rose both with frequency and water content. Figure 4.11 illustrates the dielectric behaviour of a silty clay soil at a moisture content of 15 wt.% over a wide range of frequencies after Hoekstra and Delaney [11].

Field measurements have produced a wide scatter of results primarily due to the inherent variability of the 'natural' environment caused by the presence of stones, boulders and localised regions of higher conductivity within the 'ground' mass. Such variations cause the dielectric parameters to change in a statistically unpredictable way as the radar antenna is scanned over the 'ground' surface introducing clutter into the received signal. There is no simple parameter, such as water content or low frequency conductivity, which can be used as a convenient measure of dielectric loss in the frequency range 100 MHz to 1 GHz.

Various workers have sought to employ a modified Debye model for describing the dielectric properties of moist soils. Bhagat and Kadaba [29] indicate that a relaxation mechanism alone is adequate at frequencies above ~1 GHz, but at lower frequencies the soil structure affects the results. De Loor [10] summarises the chief loss mechanisms occurring in soil and their frequency range of applicability. In comparing the relaxation of water in bulk and soil water, it is observed that the frequency at maximum dielectric loss is displaced to a much lower frequency in soils and that relaxation occurs over a narrower frequency band in soils than in bulk water.

Soil is not only a mixture of dielectrics, but even when the composition of a given sample is known in terms of its components and their individual properties, that alone is not sufficient to define its nature dielectrically. The particle sizes, the electrochemical nature of their boundaries and the way in which the water is

distributed, both physically and chemically, amongst the matrix also affects the behaviour. Wobschall [22] distinguishes, for example, between free water and pore water.

Systematic attempts have been made to produce models of the dielectric behaviour of soils which use parameters obtained independently of the dielectric measurements to be predicted. A number of models are believed to show reasonable agreement with experimental values over certain frequency ranges, but scope remains for further work on the subject of soil dielectric properties.

Wobschall [22] developed a theory of the complex dielectric permittivity of soils based on the semi-disperse model.

This is an extension of a three phase (particles, air, water) system developed from work carried out by Hanai [30]. Wobschall considers soil to consist of irregular particles containing micro/macroscopic air filled voids (pores) and crevices which become increasingly filled by water as the percentage water content increases.

Figure 4.15 shows the schematic composition of the soil suggested by Wobschall. The key element of the semi-disperse model is a phase of composition in which the

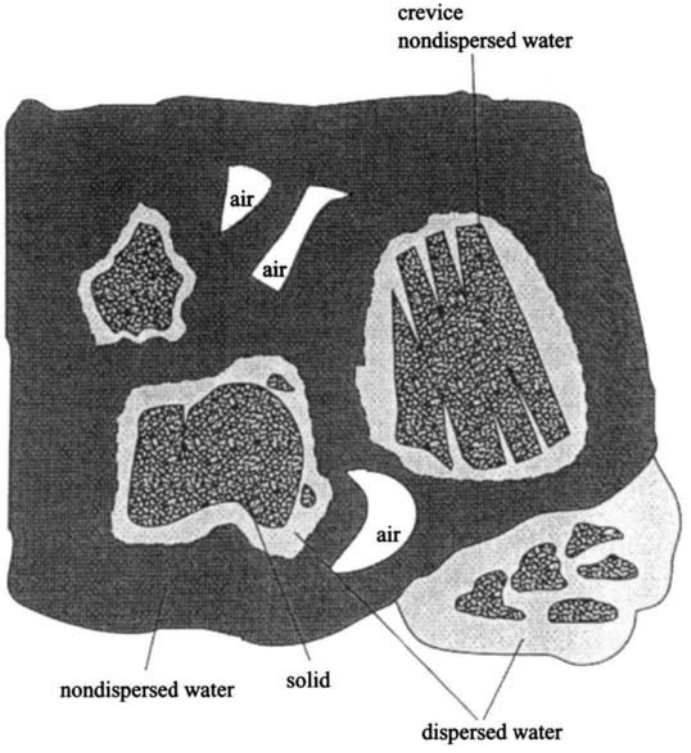

Figure 4.15 Particles and water dispersed in soil (after Wobschall [22])

solid particles contain dispersed water filled with micropores and around each particle is a coating of water. These particles and the entrapped air are dispersed throughout the remaining water. The procedure for calculation takes into account 10 parameters including the frequency, the volume fraction of water, the volume fraction of voids and conductivity of pore water and microcrevice water, the dispersed water fraction as well as the crevice water fraction.

There is, however, a sufficient body of information to enable an assessment to be made of the likely range of dielectric properties which might be encountered, assuming there is a detailed knowledge of the site in question.

4.6 Suitability of soils for GPR investigations

Dr James A. Doolittle (USDA-NRCS) and Dr Mary E. Collins (of Soil and Water Science Department, University of Florida)

4.6.1 Introduction

Soil is defined as 'a natural body comprised of solids (mineral and organic matter), liquid, and gases that occurs on the land surface, occupies space and is characterised by one or both of the following: horizons, or layers, that are distinguishable from the initial material as a result of additions, losses, transfers and transformations of energy and matter or the ability to support rooted plants in a natural environment' (Soil Survey Staff [36]). The definition continues to explain the three dimensions of soil. The upper limit is the interface between soil and air, plants, and shallow water. The lateral boundary is where soil grades to rock, ice and deep water. The lower boundary 'is most difficult to define' (Soil Survey Staff [31]). It is the boundary that separates soil from nonsoil. The lower depth of soil is commonly defined as where biological activity can no longer survive. Many soil scientists abruptly end the soil domain at a depth of 2 m, but many soil processes, features, horizons and layers continue below that depth. One of the problems soil scientists had was the lack of technology to easily look at deeper depths. Soil cores, pits and exposures have long provided soil scientists the only access to information concerning soils. Unfortunately, these methods provide incomplete information on soil continuums, as they are limited in depth, extent and number. Constrained by limited exposures and burdened by partial or detached information, inferences on the nature and properties of soils must be extended across the more expansive areas between cores or exposures.

In many areas, the characterisation of soils and soil properties can be improved with ground penetrating radar (GPR). As GPR can provide a continuous record of the sub-surface showing the presence, depth and lateral extent of certain soil horizons and features, it is useful in soil classification, characterisation and mapping. GPR provides high-resolution information that can aid interpretations and the extrapolation of information obtained with traditional surveying techniques [32].

solid particles contain dispersed water filled with micropores and around each particle is a coating of water. These particles and the entrapped air are dispersed throughout the remaining water. The procedure for calculation takes into account 10 parameters including the frequency, the volume fraction of water, the volume fraction of voids and conductivity of pore water and microcrevice water, the dispersed water fraction as well as the crevice water fraction.

There is, however, a sufficient body of information to enable an assessment to be made of the likely range of dielectric properties which might be encountered, assuming there is a detailed knowledge of the site in question.

4.6 Suitability of soils for GPR investigations

Dr James A. Doolittle (USDA-NRCS) and Dr Mary E. Collins (of Soil and Water Science Department, University of Florida)

4.6.1 Introduction

Soil is defined as 'a natural body comprised of solids (mineral and organic matter), liquid, and gases that occurs on the land surface, occupies space and is characterised by one or both of the following: horizons, or layers, that are distinguishable from the initial material as a result of additions, losses, transfers and transformations of energy and matter or the ability to support rooted plants in a natural environment' (Soil Survey Staff [36]). The definition continues to explain the three dimensions of soil. The upper limit is the interface between soil and air, plants, and shallow water. The lateral boundary is where soil grades to rock, ice and deep water. The lower boundary 'is most difficult to define' (Soil Survey Staff [31]). It is the boundary that separates soil from nonsoil. The lower depth of soil is commonly defined as where biological activity can no longer survive. Many soil scientists abruptly end the soil domain at a depth of 2 m, but many soil processes, features, horizons and layers continue below that depth. One of the problems soil scientists had was the lack of technology to easily look at deeper depths. Soil cores, pits and exposures have long provided soil scientists the only access to information concerning soils. Unfortunately, these methods provide incomplete information on soil continuums, as they are limited in depth, extent and number. Constrained by limited exposures and burdened by partial or detached information, inferences on the nature and properties of soils must be extended across the more expansive areas between cores or exposures.

In many areas, the characterisation of soils and soil properties can be improved with ground penetrating radar (GPR). As GPR can provide a continuous record of the sub-surface showing the presence, depth and lateral extent of certain soil horizons and features, it is useful in soil classification, characterisation and mapping. GPR provides high-resolution information that can aid interpretations and the extrapolation of information obtained with traditional surveying techniques [32].

4.6.2 GPR: a quality control tool for soil mapping and investigation

Since the late 1970s, GPR has been used as a quality control tool for soil mapping and investigations in the United States. In 1979, the use of GPR for soil surveys was successfully demonstrated in a study conducted in Florida [33, 34]. Because of the prevalence of sandy (> 70% sand) soils with favourable characteristics and contrasting subsoil, GPR has been used extensively in Florida to update soil surveys [35]. For over 20 years and throughout the United States, the Department of Agriculture-Natural Resources Conservation Service (USDA-NRCS) and several universities have used GPR to verify the taxonomic composition of soil map units and to document specific soil properties and variability. The use of GPR in soil surveys has provided information about the soil resource that could not be obtained without its use.

Traditionally, soil surveys are mapped on a county basis by a team of soil scientists. The soil scientists make soil observations at a limited number of point locations. This is a very slow and laborious task. To assist soil surveys, GPR is used to document the type, variability and depth of soils that occur within soil map unit delineations. Radar data are used to record the average taxonomic composition of the selected map units, the confidence interval and the confidence level of that data. Soils that are 'dissimilar' are also noted. This information is published in the soil survey.

Routinely for GPR soil studies, a traverse line or grid is established across a representative area. Typically, reference flags are inserted in the ground at uniform intervals along traverse or grid lines. More recently, GPS receivers, survey wheels or odometers have been used to record reference points and expedite field work. The interval between these reference points varies with the purpose of the survey and the anticipated variability of soils or soil features under investigation, but typically ranges from 0.5 to 15 m. Most commonly, a radar antenna is towed or dragged along a traverse or grid line with the operator impressing a mark on the radar record as each reference point is passed. After reviewing the radar record in the field, ground-truth soil descriptions are collected at a few selected reference points. These soil descriptions help to confirm radar interpretations and depth scales. Based on the soil descriptions, diagnostic sub-surface horizons, contrasting layers and or soil features are identified and traced laterally across the radar record. The taxonomic composition is determined by identifying the soil at each reference point and determining its frequency, or less typically, by measuring a soil's relative length on a radar record.

4.6.3 Suitability of soil properties for GPR investigations

Radar imagery must be of good interpretative quality as soil scientists are reluctant to use GPR in areas where the depth of penetration is too restricted or the interpretative quality poor. Where adverse soil conditions occur, the use of GPR is discontinued and soil scientists resort to traditional soil survey methods. Within the USA, because of this reluctance to use GPR in anything less than favourable soil conditions, much attention has focused on the distribution of soils and soil properties that are favourable to the use of GPR.

The performance of GPR is dependent upon the electrical conductivity of soils. Soils having high electrical conductivity rapidly attenuate the radar energy, restrict penetration depths, and severely limit the effectiveness of GPR. Factors influencing the electrical conductivity of soils include the amount and type of salts in solution and the clay content.

Electrical conductivity is a measure of the concentration of water-soluble salts in soils, and is directly related to the concentration of dissolved salts in solution, as well as the type of exchangeable cations and the degree of dissociation of these ions salts on soil particles (Soil Survey Staff [36]). In semi-arid and arid regions, soluble salts of potassium and sodium and less soluble carbonates of calcium and magnesium are more likely to accumulate in the upper part of the soils. These salts produce high attenuation losses that restrict the radar's penetration depths [37]. In some areas, high levels of calcium carbonate accumulate in soils and severely limit penetration depths [38]. Soils with calcareous layers are considered poorly suited to GPR. Because of their high electrical conductivity, *saline* and *sodic* soils are unsuited to GPR. In these soils, penetration is typically restricted to the surface layers (<0.25 m). However, Collins and Kurtz [39] reported the results comparing soil chemical properties and modelling the electrical characteristics from soils in three different locations of which two are arid: Arizona and Saudi Arabia. They found that, depending on the moisture content, buried objects in soils high in salts could be detected to depths as great as 1 m.

Because of their high adsorptive capacity for water and exchangeable cations, clays produce high attenuation losses. As a consequence, the penetration depth of GPR is inversely related to clay content. Doolittle and Collins [40] noted that, depending on antenna frequency and the chemistry of the soil materials, penetration depths could range from 5 to 30 m in sandy, 1 to 5 m in loamy (7 to 35% clay), to less than 0.5 m in clayey (>35% clay) soils. In addition, clay fractions dominated by smectite or vermiculite clay minerals have higher cation-exchange capacities and greater signal attenuation rates than fractions dominated by kaolinite, gibbsite and goethite.

4.6.4 Soil suitability maps for GPR investigations

Soil survey reports and databases prepared by the USDA provide information on soil properties that affect GPR. These reports are available for most areas of the United States. Hubbard *et al.* [41] developed a GPR suitability map of Georgia based on information contained in published soil survey reports. Collins [42] used a soil taxonomic classification system to create GPR suitability maps according to properties within the upper 2-m of soils. Collins and Kurtz [43], using the USDA-NRCS's State Soil Geographic (STATSGO) database, created several maps of the United States depicting the suitability of soils to GPR. They used soil taxonomics to predict the detection of buried objects. Doolittle *et al.* [44] also used the STATSGO database to prepare soil maps that show the distribution of several soil properties that affect GPR. Unfortunately, separate maps were prepared for each attribute, making GPR suitability assessments difficult. Doolittle *et al.* [45] used STATSGO attribute

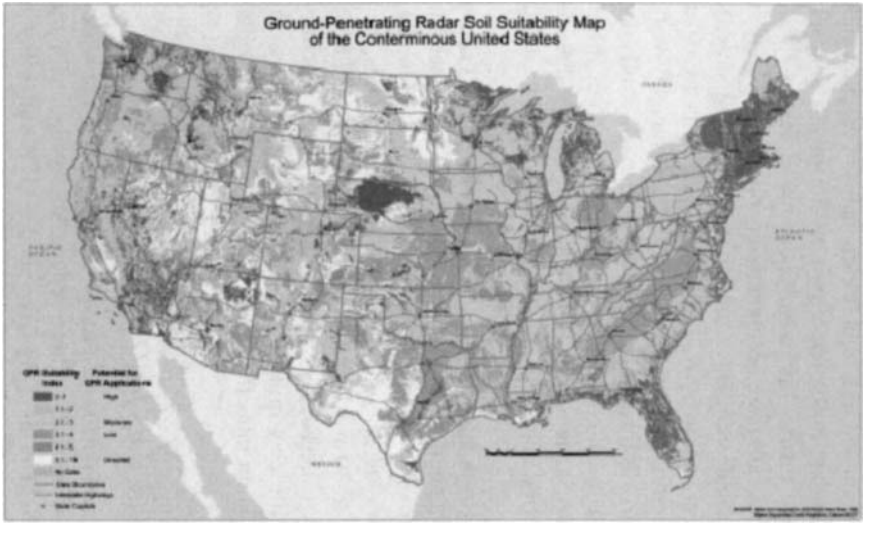

Figure 4.16 GPR soil suitability map of the conterminous United States (courtesy USDA-NRCS)

data on the clay and soluble salt contents of soils to develop a GPR soil suitability map of the conterminous United States. This map (Figure 4.16) conforms to major soil and physiographic units and can be used to assess the relative appropriateness of GPR for soil investigations within comparatively large areas.

4.6.5 Determining the depth to soil horizons

GPR has been used extensively to determine the depth to soil horizons. A soil horizon is a 'layer of soil or soil material approximately parallel to the land surface and differing from adjacent genetically related layers in physical, chemical, and biological properties or characteristics such as colour, structure, texture, consistency....' (Soil Science Society of America [46]). Knowing the existence and depth to horizons aids a soil scientist in properly classifying the soil.

Radar interpretations have provided data on the taxonomic composition of soil [35, 47–49]. The depths to some diagnostic sub-surface horizons used to classify soils have been charted with GPR. Where these horizons have abrupt upper boundaries that contrast with overlying horizons in physical (texture, bulk density, moisture) and chemical (organic carbon, calcium carbonate, sesquioxides) properties, they often produce strong reflections. GPR has been used to estimate the depth to argillic [48, 50–53], spodic [48, 51, 54], and placic [55] horizons. GPR has been used to chart the thickness of albic horizons and the depth to calcic, petrocalcic and petroferric horizons, and to duripans, fragipans [56–58] and traffic pans [59]. GPR has been used to infer soil colour and organic carbon content [51], assess the continuity of ortstein [60], the concentration of lamellae [61, 62], and the thickness of surface [48] and active [63] layers.

The effective use of GPR for soil survey investigations requires not only satisfactory penetration depths, but also soil horizons or features that produce distinct, readily identifiable and continuous reflection. Often, in areas where soil horizons or features are discontinuous or obscured by undesired clutter, a greater, more prohibitive number of ground-truth cores is required to properly identify radar reflections.

In some soils, while individual horizons cannot be identified, characteristic radar reflections can be used to identify soils. Mokma *et al.* [62] used the aggregate appearance of multiple reflectors and the depth of penetration to distinguish soils and estimate soil map unit composition in southwest Michigan. Here the thickness and frequency of lamellae (bands of finer-textured materials) are the primary criteria used to identify an argillic horizon and the classification of soils. Using a 120 MHz antenna, aggregate GPR reflections and penetration depths were associated with individual soils. Depth of penetration was inversely related to the number and frequency of finer-textured lamellae and total clay content. Unique and distinguishing radar signatures of five soils are shown in Figure 4.17*a*. In Figure 4.17*b*, a representative radar record from an area that had been mapped as dominantly Spinks (sandy, mixed, mesic Lamellic Hapludalf) and Coloma (mixed, mesic Lamellic Udipsamment) soils is shown.

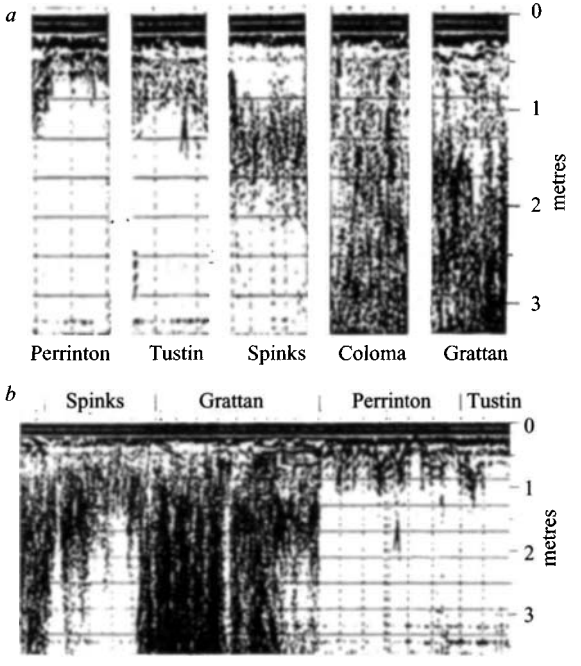

Figure 4.17 Differentiating soils on the basis of aggregate GPR reflections in southwest Michigan (courtesy USDA-NRCS)

4.6.6 Determining the depth to bedrock

In many regions, it is difficult to examine soils and determine the depths to bedrock with traditional soil survey tools. Rock fragments and irregular or weathered bedrock surfaces limit the effectiveness of coring methods [64]. GPR can be used to determine the depths to bedrock and reduce the number of required cores [32, 58, 65]. Where soils are suitable, GPR is more reliable and effective than traditional soil survey tools for determining the depth to bedrock and the composition of soil map units that are based on soil-depth criteria [64, 66].

In many upland soils, the soil/bedrock interface is abrupt and contrasting, and provides a well expressed and easily identifiable reflection on radar records. Often, this interface consists of smooth, continuous, high amplitude reflectors. Figure 4.18 is from an area of noncalcareous, sandy soils that formed in eolian sediments over Navajo sandstone in southern Utah. The radar record was collected with a 200 MHz antenna. The depth scale is in metres. The horizontal scale is ~25 m. A dark line has been used to show the interpreted depth to bedrock. In Figure 4.18, the overlying eolian sediments are isotropic and transparent to GPR. Tree roots cause the hyperbolas in the upper part of the radar record. In general, the underlying bedrock is contrasting and provides a strong and readily identifiable radar reflection. Bedding planes are evident in the Navajo sandstone. Some of these bedding planes cross the

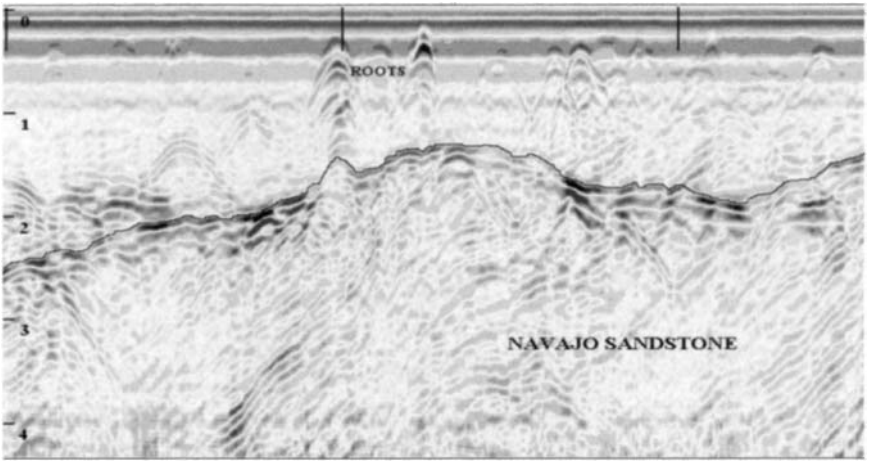

Figure 4.18 *Depth to sandstone bedrock in an area of Ustic Quartzipsamment in southern Utah (courtesy USDA-NRCS)*

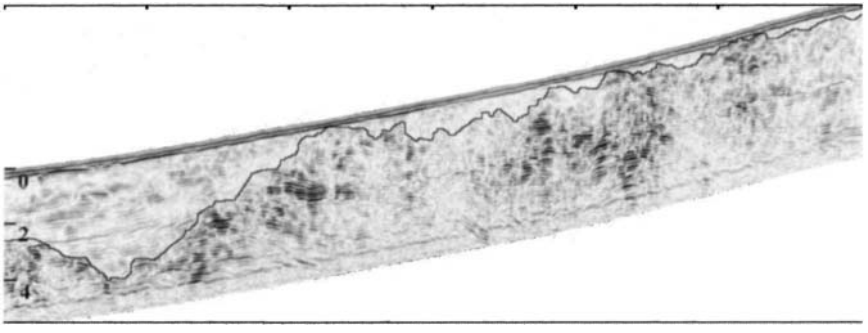

Figure 4.19 *Radar record showing the depth to bedrock in an area of Typic Kanhapludult, in western North Carolina (courtesy USDA-NRCS)*

soil/bedrock interface. Within the soil, these *bedding planes* are more weathered and were identified as lamellae.

The soil/bedrock interface is not always easily identifiable on radar records. In Figure 4.19, the soil/bedrock interface is indistinct and ambiguous. This radar record was collected with a 200 MHz antenna in an area of well drained, highly weathered soils within the Piedmont region of southeast USA. Soils are members of the fine, kaolinitic, thermic Typic Kanhapludult family and have formed in residuum weathered from sillimanite mica schist. In Figure 4.19, the depth scale is in metres. Multiple, inclined, planar reflectors implied lithologic rather than pedogenic features. The closest point at which these planar reflectors approach the soil surface was interpreted

as the depth to weathered bedrock. A dark line has been used to show the interpreted depth to bedrock. In this radar record, it is difficult to identify the soil/bedrock interface or differentiated soft and weathered bedrock from hard bedrock. Robillard *et al.* [67] associated variations in the amplitude of reflected signals to differences in rock hardness and mineralogy. In Figure 4.19, weakly expressed, planar reflectors can be observed overlying more strongly expressed planar reflectors. The shallower, more weakly expressed set is interpreted as saprolite or soft, highly weathered bedrock. The deeper lying, higher amplitude planar reflections are interpreted as hard bedrock. Higher amplitude reflections are associated with more contrasting, less weathered strata.

4.6.7 Determining the depth to soil water tables

The depth and movement of groundwater through landscapes affect the physical and chemical properties and the morphology of soils [68]. Traditionally, information on the depth and movement of groundwater has been obtained through measurements at monitoring wells. While wells provide detailed information about soil and hydrologic conditions at specific points, hydrologic conditions for the larger areas among and beyond the wells must be inferred.

Ground penetrating radar has been used effectively in areas of sandy soils to chart soil water table depths among wells and into nearby areas [69–72]. In addition, GPR has been used to provide data for hydrologic models [73, 74], define recharge and discharge areas [69, 72], predict ground-water flow patterns [70, 71, 75], and delineate near-surface hydrologic conditions [76]. GPR has also been used to detect perched water tables [77].

In Figure 4.20, the water table can be traced across a gently sloping area of Carver (uncoated, mesic Typic Quartzipsamment) soil in southeastern Massachusetts. The very deep, excessively drained Carver soil formed in stratified deposits of coarse and very coarse sands on outwash plains. In Figure 4.20 the depth scale is in metres. The survey line is 60 m long with reference points (dark vertical lines at the top of the Figure) spaced at 10 m intervals. The radar record was collected with a 120 MHz

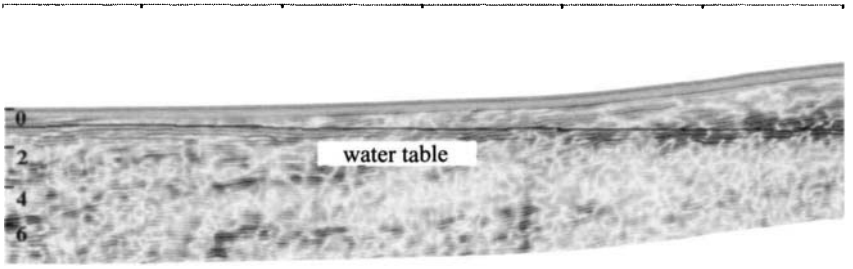

Figure 4.20 Water table in a Typic Quartzipsamment formed in glaciofluvial sediments (courtesy USDA-NRCS)

antenna. The radar record has been minimally processed using colour table and transformation options and distance and surface normalisation programs.

In sandy sediments, because of abrupt and strongly contrasting dielectric properties, the water table produces strong reflections and distinct images on most radar records [78]. In Figure 4.20, the water table produces high amplitude, continuous linear reflections that can be traced across the radar record. A dark line shows the approximate location of the water table. It varies in depth from about 1 m along the left-hand margin to about 3.5 m along the right hand margin of the radar record. In areas of sandy, nonstratified materials, the water table is usually distinct and interpretable. However, in some soils, soil horizons or geologic strata can obscure the water table. In Figure 4.20, the near horizontal reflections from the water table contrast with the more inclined reflections from strata within the glacial outwash. Had the water table and strata been parallel, the identification of the water table would have been more ambiguous.

4.6.8 Measuring soil moisture contents and the movement of water through sandy soils

Knowledge of the soil water content is needed for management decisions and irrigation scheduling. Davis *et al.* [79] observed that, over a range of different soils, a strong association exists between the water content and dielectric permittivity of soils. GPR and time domain reflectometry (TDR) have been used to measure dielectric permittivity and volumetric water content of soils [80, 81]. Compared with TDR, GPR is noninvasive and provides a more practical method for characterising and mapping spatial and temporal variations in soil water content over larger areas [82, 83].

GPR has been used to study the movement of water and pollutant through sandy soils. Vellidis *et al.* [84] used GPR to monitor the movement of a wetting front through sandy surface layers following an irrigation event. Water movement through sandy soil is not uniform and is strongly influenced by soil layering [85]. Coarser or finer textured layers redirect and concentrate water movement into preferential pathways. These pathways move water and solutes laterally over restrictive layers and downward through discontinuities in these strata. These flow paths or *fingers* occupy a small part of the soil but account for most of the water movement and chemical transport [86]. As preferential flow is concentrated, it is also faster, and water-borne chemicals are less subjected to degradation and absorption by the soil [86]. Several researchers [84–87] have used GPR to detect layers and preferential flow paths in sandy soils. Using 450 or 500 MHz antennas, these researchers determined the depth to restrictive soil layers and detected the locations of discontinuities or breaks in these layers. Water sampling devices, which were installed in these discontinuities, were found to provide a more representative sample of contaminants transported through the soil than randomly located instruments.

4.6.9 Determining the thickness of peat deposits

Pushing a metal rod through a column of peat and feeling for resistance or augering a small hole to observe the underlying materials are the traditional methods used

to inventory and map organic soil materials [88]. These methods are slow, labour intensive and costly. GPR can be used to provide information on the depth and volume of peat deposits at a level of detail that is comparable to information obtained with manual techniques [89, 90]. Compared with traditional methods, GPR is a more efficient tool for estimating peat thickness and characterising the sub-surface topography of the organic/mineral soil interface [91]. GPR has been used to estimate the thickness and volume of peat deposits [47, 91–99], distinguish layers having differences in degree of humification and volumetric water content [55, 91, 96, 99, 100], and to classify organic soils and assess rates of subsidence [52]. Lowe [101] used GPR to detect logs and stumps buried in peat deposits. GPR has also been used for such geotechnical applications in peat as road design and dike construction [88, 91, 102].

The electrical conductivity of peat is directly related to the concentration of total dissolved ions in the pore water and ultimately, the chemistry of the confining mineral sediments [103]. Typically, GPR surveys conducted in acidic, low nutrient, ombrotrophic bogs produce satisfactory results. However, results are generally poorer in alkaline, high nutrient, minerotrophic fens. Here, penetration depths are more restricted and, in deeper deposits, reflections from the organic/mineral soil interface are often either intermittent or indistinguishable. Ombrotrophic bogs are nutrient poor and have lower concentrations of the basic cations (calcium, magnesium and potassium) than the more nutrient enriched minerotrophic fens. In some fens, such as coastal marshes, high concentrations of dissolved salts completely absorb and attenuate the radar's energy within shallow (0 to 50 cm) depths. In peat, depths as great as 8.1 to 13 m have been reported [89, 92, 99].

Figure 4.21 is a representative radar record from a fen used for the production of cranberries in southeastern Massachusetts. The cranberry bed had been mapped as Freetown soil. The very deep, very poorly drained Freetown soil formed in more than 1.3 m of highly decomposed (sapric) organic materials. In Figure 4.21 the depth scale is in metres. The survey line is 90 m long with reference points (dark vertical lines at the top of the figure) spaced at 10 m intervals. The radar record was collected with a 120 MHz antenna. The radar record has been minimally processed using colour table and transformation options and a distance normalisation program.

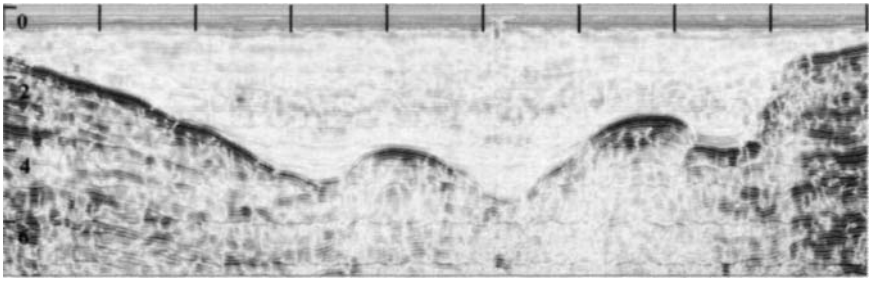

Figure 4.21 GPR record from an area of organic soils (Typic Haplosaprist) in Massachusetts (courtesy USDA-NRCS)

In Figure 4.21, abrupt and strongly contrasting changes in water content make the organic/mineral soil interface distinguishable on this radar record. This interface forms a conspicuous reflector that varies in depth from about 1.2 to 5.4 m. Weak planar reflectors are evident within the peat. While some reflections that occur at a constant depth are presumed to represent noise, the more irregular or wavy reflectors suggest layering within the peat. Often transitional layers composed of both organic and mineral soil materials form at the lower peat boundary. As these transitional layers have moisture contents that are intermediary between the organic materials above and the mineral materials below, they do not produce high amplitude reflections. In Figure 4.21, these more weakly expressed features appear in the lower part of each of the three conspicuous concavities.

4.6.10 Improving soil-landscape models

GPR has been used to improve soil-landscape models and soil map unit design and thus facilitate soil mapping on glacial-scoured uplands [104], wetland catena [55], coastal plain sediments underlain by limestone bedrock [49], or loess overlying sandy fluvial sediments [105]. GPR has been used to illustrate soil-bedrock relations on glacial-scoured uplands [64, 104] and on karst [49, 106, 107]. Recent advancements in processing technologies have facilitated the manipulation of large sets of radar data and the creation of three-dimensional radar images. These displays assist interpretations and provide unique, multiple viewpoints in which to analyse the sub-surface.

In Figure 4.22, a three-dimensional visualisation is used to view and analyse the depth and geometry of the water table and to understand flow patterns in a dunal

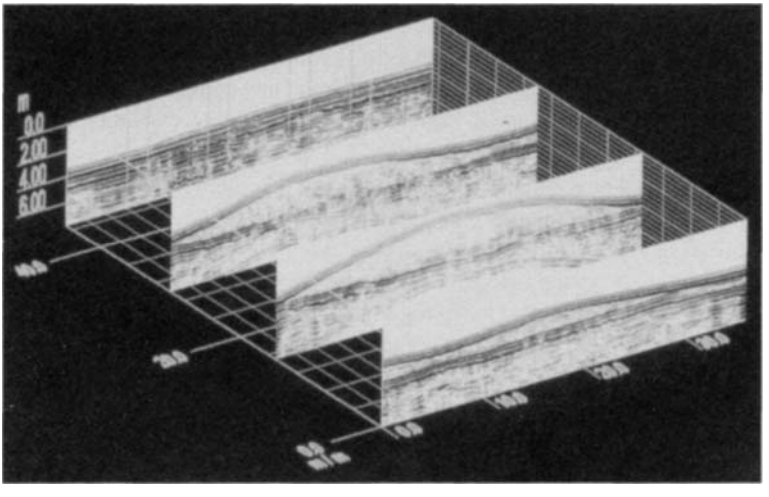

Figure 4.22 A fence diagram showing the depth and geometry of the water table to the topography of a low dune in North Dakota (courtesy USDA-NRCS)

landscape. To prepare this three-dimensional product, a 36 by 45 m grid was established across a small, low dune in southeast North Dakota. The grid interval was 3 m. Survey flags were inserted in the ground at each grid intersection and served as reference points. The elevation of each reference point was measured with a theodolite and stadia rod.

Radar data were collected along 16 equally spaced (3 m) east–west trending grid lines with a 200 MHz antenna. Each radar traverse was 36 m long. Lines were sequentially profiled with the radar in a back and forth, snake-like fashion. Data from these lines were processed into a three-dimensional image using processing software. Once processed, arbitrary cross-sections, insets and time slices can be quickly viewed from the three-dimensional data set. This imaging technique enables views of the sub-surface from nearly any perspective. The flexibility of three-dimensional visualisations facilitated the interpretation of spatial relationships and the analysis of the water table.

Figure 4.22 is a fence diagram showing four radar records across the low dune. Along the first three lines (lines $Y = 0$, 15 and 30 m) the water table appears to dip slightly beneath the dune. It is inferred from this diagram that the water is flowing from the margins of the dune into the dune's interior. The water table is difficult to identify on the northern-most line (line $Y = 45$ m). Most of this line lies within a wetland. Soils along this line were noticeably wetter and had thicker mats of vegetation. Strongly expressed, sub-surface planar reflectors are more numerous on this record. As these interfaces parallel the soil surface and the water table, the identification of the water table is more ambiguous.

4.7 Dielectric properties of man-made materials

As the evaluation of concrete structures is of particular importance more work is now being carried out on establishing the electrical properties of cements and concretes, especially at the higher frequencies associated with surface-penetrating radar applications. The earliest work which has been carried out has largely been related to DC or low frequency AC resistivity measurements and the development of models describing the mechanisms of conduction through Portland cement pastes. Such techniques have been used to study changes in the electrical characteristics of cement pastes and concretes during the stages of initial setting and the subsequent hardening process.

Concrete is a composite material formed by the addition of water to a mixture of cement, sand and coarse aggregate, together with a small quantity of air. A range of admixtures is available which may be added to the mix to modify the properties of concrete in either the fresh or hardened states, or both. A number of different types of cement are employed, although something in the order of 90% of all concrete is produced using ordinary Portland cements. A diverse range of rock types is used to provide the fine and coarse aggregates.

Hydration takes place between the cement and the water in the mix, producing a matrix of hydrates of various compounds, referred to collectively as cement paste, which binds the constituents together to form hardened concrete. The cement paste

contains a large number of interconnected voids, the capillary pores, which are the remnants of the water-filled spaces present in the fresh paste. Capillary pores are estimated to be in the order of 1 m and are mainly responsible for the permeability of the hardened cement paste. The permeability of concrete, and hence the volume of capillary pores, increases rapidly for water : cement ratios over 0.4. The permeability of a mature cement paste made with a water : cement ratio of 0.7 is in the order of 100 times that for one made with a water : cement ratio of 0.4.

After setting, a large amount of the free water within the mix is absorbed during the process of hydration, being used in the production of hydrates of various compounds. Water is also lost from the capillary pores as the concrete dries out. This occurs by evaporation at a rate which is dependent upon the water : cement ratio of the concrete, its age, the curing regime to which the member has been subjected and a number of other factors, including member size and environmental conditions.

Whittington *et al.* [108] discuss the conduction of electricity through the heterogeneous medium of concrete and report low frequency AC experimental determinations of changes in resistivity over a 3-month period from the time of casting. Their results show resistivity values increasing with time, achieving stable values after about 28 days, although it should be noted that their work was undertaken on moist specimens (i.e. specimens which were not permitted to dry out). It was found that the experimental curves for cement pastes and concretes follow the same trends, confirming the dominant role of the cement paste upon the electrical characteristics of concrete.

The electrical resistivity of typical aggregates particles used in concretes are several orders of magnitude higher than that of the concrete. Consequently the majority of current flow takes place through the paste (i.e. the path of least resistance). In a simplified electrical model concrete can generally be considered as a composite of nonconducting particles contained in a conductive cement paste matrix.

Nikkanen [109] has suggested that conduction through moist concrete is essentially electrolytic in nature, and tests by Hammond and Robson [110] and Monfore [111] support the view that conduction is by means of ions in the evaporable water in the capillary pores, the principal ions being calcium (Ca^{++}), sodium (Na^{+}), potassium (K^{+}), hydroxyl (OH^{-}) and sulphate (SO_4^{--}) since the amount of evaporable water in a typical cement paste varies from about 60% at the time of mixing to 20% after full hydration, and the electrical conductivity of the concrete should also be a function of time. Ionic conduction through the free evaporable water within the capillary pores will depend upon the species, concentration and temperature of the ions present in solution.

Another possible path for current flow is by means of electronic conduction through the cement compounds themselves, that is the gel, gel–water and unreacted cement particles, particularly compounds of iron, aluminium and calcium. Wyllie and Gregory [112] suggest that even physically immobile water will be involved in the conduction process.

Thus, the electrical conductivity of the paste depends upon the changes which both solid and solution phase (i.e. evaporable water) undergo. These changes are closely linked to each other. The composition and concentration of ions in the evaporable

water depend upon the soluble compounds within cement particles and the residual water. Conversely, the composition and structure of the solid phase depends upon the amount of water, both absorbed and chemically combined, within the cement compounds during the hydration process.

The above findings for DC and low frequency AC resistivity measurements indicate the changing nature of the general electrical characteristics of cement pastes and concretes during the first few weeks and months after casting. Further work needs to be carried out to establish the dielectric properties in this period at the higher frequencies associated with surface penetrating radar applications. It is clear that attenuation loss and velocity of wave propagation in concrete are dependent upon a number of factors including water content, mix constituents and the curing regime employed. 'Green' concrete may exhibit high values of both relative permittivity ($\varepsilon_r = 10$ to 20) and attenuation loss ($\alpha = 20$ to $50\,\mathrm{dB\,m^{-1}}$ at 1 GHz). When hydration and curing are effectively complete, at periods of possibly up to about six months, lower values may be measured such that $\varepsilon_r = 4$ to 10 and $\alpha = 5$ to $25\,\mathrm{dB\,m^{-1}}$ at 1 GHz. Thus, the performance of a surface-penetrating radar system may be affected considerably by the state of the concrete. Whittington [113] has investigated the use of the low frequency electrical characteristics of concrete as a measure of its mechanical properties. He reports a correlation between electrical resistivity and compressive strength over a limited range of resistivity variation. Such a correlation may be of relevance to surface-penetrating radar applications; however, considerable research work upon the high frequency characteristics of concrete would be required to establish its validity.

4.8 Laboratory measurements of dielectric materials

Dr Yi Huang

This Section provides a valuable introduction into the methods of measuring soil samples in the laboratory.

4.8.1 Introduction

The measurement of dielectric properties of materials at radio and microwave frequencies has been studied for many years. Numerous methods employing various sample sizes and shapes have been developed for basic research and industrial and medical applications [114–117]. At lower frequencies, a parallel plate capacitor [118] or an impedance bridge method can be used. In both methods, the models for the sample can be represented by a capacitor. At higher frequencies, resonant cavity, waveguide and transmission line methods are normally employed. In the resonant cavity technique, the resonant frequency shift determines the permittivity of the sample, whereas with waveguide and transmission line techniques, the reflection/transmission coefficients are measured for extracting the dielectric properties [116, 119]. A considerable amount of data has been accumulated over the years.

For GPR applications, the dielectric properties (permittivity and conductivity) are vital information for accurate estimation/prediction of the depth of the object

in question and the radar penetration depth. Although the general dielectric information of most materials is available, the dielectric properties of materials do vary quite considerably from one site to another even for the same type of material/soil; the in-situ properties of materials are therefore preferred. Unlike many other applications, the materials associated with GPR are normally composite, and the measurement of a small sample does not always provide meaningful and useful information for GPR data interpretation. In practice the effective permittivity and conductivity of bulk materials are required. Thus the laboratory measurement facilities for small samples are not suitable and some special ones are needed for GPR applications.

4.8.2 Measurement techniques

4.8.2.1 Time domain reflectrometry (TDR): TDR has become an established method for measuring the in-situ dielectric properties of material. It is widely used to determine the volumetric water content and conductivity of media [120] for the frequency range from a few MHz to about 1 GHz. As illustrated in Figure 4.23, the system consists of a signal generator, a transmission line sensor and a receiver. The signal generator transmits a pulse type signal to the open-ended sensor, which could be of various forms (such as coaxial line, 2-rod probe, 3-rod or even 4-rod probe) and is filled with or inserted into the material under test. The reflected signal is received and then processed by the receiver. This method measures the travel time t of the pulse signal along the transmission line probe with a known length D. The relative dielectric permittivity ε_r of the material can be estimated by

$$\varepsilon_r = \left(\frac{ct}{2D}\right)^2 \tag{4.39}$$

where $c = 3 \times 10^8$ m/s. In addition, the bulk material conductivity (a measure of soil salt content) may be obtained from the amplitude of the reflected TDR signal for the known probe configuration. In addition to the travel time and amplitude, the signal

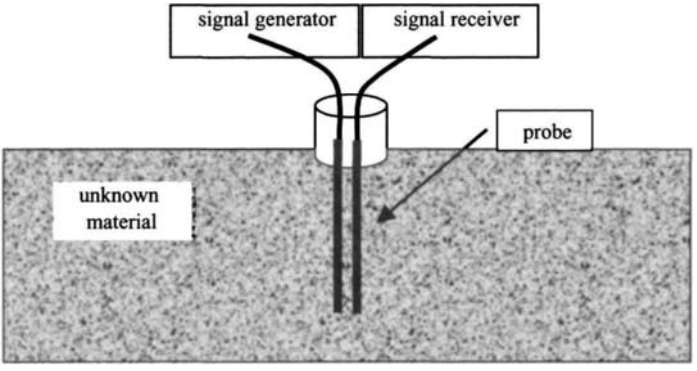

Figure 4.23 TDR for dielectric property measurements

waveforms also contain information on frequency-dependent dielectric properties that may be extracted by application of Fourier transform techniques [121] and can be used in the estimation of the Cole–Cole parameters. The operational frequency range is determined by the transmitted pulse signal and the probe configuration. This method is now well developed and many fine-made commercial products are available. The major common limitations for TDR are that:

(*a*) the measured values are the averaged permittivity and conductivity over the probe, not their distribution along the probe;
(*b*) the method is only applicable for the material immediately below the surface, not deep inside the medium.

4.8.2.2 Open-ended coaxial probe: As we have seen, TDR is a convenient method for measuring in-situ dielectric properties of a material, but it is intrusive in nature and could be a problem in some applications. In contrast, the open-end coaxial probe combined with a vector network analyser is a nonintrusive facility for measuring dielectric properties, as shown in Figure 4.24. Fundamental to the use of the coaxial probe is an accurate model relating the complex reflection coefficient at the probe aperture to the dielectric properties of the material contacting the probe. A few approaches to modelling the probe have been developed ranging from equivalent circuit models to variational methods. The simplicity of the lumped circuit models provides for the fastest computation over a limited range of frequency and permittivity. Variational methods give the best accuracy at the expense of computational speed. Detailed comparison of various probe models can be found from the literature [116]. The operational frequency range is determined by the configuration of the probe. It is assumed that, in the coaxial line only the TEM mode is excited, but higher order modes may be created at the interface between the probe and the material under test.

In addition to the modelling programme, a calibration process must be conducted in order to obtain the dielectric properties of the material. The common practice is to calibrate the system by measuring open circuit (air), short circuit (metallic shorting block) and deionised water ($\varepsilon_r = 80$). Good contact between the material and probe is very important as an airgap or fluid segregation will cause erroneous measurements.

The most well known commercial product of this type of measurement system is the Hewlett-Packard (now Agilent) HP-85070. The system comes with a software

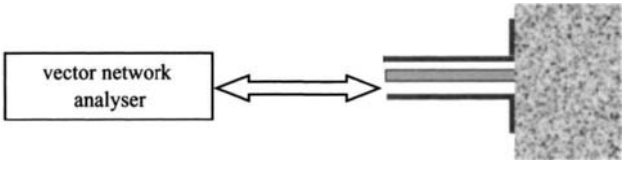

Figure 4.24 Open-ended coaxial probe for dielectric property measurements

Figure 4.25 A large open-end coaxial probe developed at Liverpool University

package and is suitable for the frequency range between 20 MHz and 20 GHz. However, this probe is very small, with an outer conductor radius $b < 5$ mm, which means that it is not suitable for bulk material and low permittivity material measurements. For GPR applications, a probe with larger dimensions is needed. A new probe with an outer conductor radius $b = 20.5$ mm, shown in Figure 4.25, was designed and built at the University of Liverpool, UK. The flange has a radius of 41.0 mm. The upper frequency limit is ~1.5 GHz, which is actually material dependent. A smooth transition was made from the 50 Ω transmission line to an N-type connector to minimise reflections. Time-domain measurements showed an impedance mismatch of <3% at the transition. It has been employed to characterise various materials, such as diesel, clay, hydrocarbon contaminated soils, wood and Teflon sheets. The results are in good agreement with those obtained by other methods.

The main problems with this method are:

(*a*) difficulty in calculating the permittivity and conductivity
(*b*) difficulty in eliminating the airgap between the probe and the material under test
(*c*) uncertainty in measurement of low permittivity, high loss and thin-sheet materials.

4.8.2.3 Coaxial transmission line system: For GPR applications, samples well below the surface may be easily obtained from such as a drilling sampler on a survey site; the above two systems cannot be used to characterise these samples. Other types of measurement systems are therefore required.

Transmission line systems are another widely accepted facility for dielectric material measurements, which can be divided into one-port and two-port systems. For a two-port system, all scattering parameters S11, S22, S12 and S21 must be

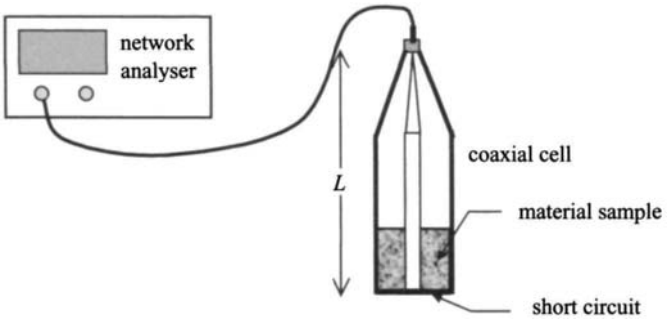

Figure 4.26 A one-port coaxial TEM cell measurement system

obtained to determine the complex permittivity of materials [116, 119]. This could be time-consuming when many samples need to be measured. In addition, the sample must be of the right size/amount to fit into the sample holder, which is difficult in some applications. It is not normally suitable for liquid or powder measurements. In contrast, a one-port transmission line system is more efficient and flexible, and only the reflection coefficient S11 is needed for data interpretation. A one-port coaxial system is shown in Figure 4.26, where one end of the coax is terminated by a short circuit (instead of an open circuit as in the previous case). Both liquid and solid samples can be placed easily into the sample holder. Unlike a two-port system, the amount of sample required for this system is relatively flexible, which is a very useful advantage when the system is employed to measure materials with various amounts. However, there are some problems with this system. For example, one of the major problems with this method is the data interpretation, especially when a transition section is introduced (the characteristic impedance is therefore not a constant). Very little work has been published on the data interpretation techniques of the large one-port system, which seems to be one of the major reasons that the short-circuited one-port system has never been as popular as the open-ended or two-port systems. Only a few small 50 Ω uniform coaxial cells appeared on the market.

One of our research projects was to measure the dielectric permittivity of ground materials (such as weak sandstone) at a range of moisture contents from dry to fully saturated over the frequency range 100–1000 MHz. The information obtained is intended for the GPR application, and thus the dielectric properties of a small sample are not representative enough for this kind of bulk material. The samples are obtained from the sub-surface using a window sampler (a common method in geophysics). The size of the samples has a large outer diameter of 103 mm, which is determined by the size of the drilling corer used on site. Ideally a coaxial cell with such a diameter should be employed, and thus the work of sample preparation can be reduced to a minimum. This is very important, since there are many samples to be measured and some samples are fragile and easily broken. Unfortunately, no cell of such a large size is commercially available. The only option we have is therefore to design the system ourselves. Since the system must be linked to a network analyser to obtain the reflection coefficient via a 50 Ω cable, a short transition section must be used to link a 50 Ω connector to the

large sample holder as indicated in Figure 4.26. Unfortunately, this transition section will result in the difficulty of impedance matching over a wide frequency band. If the system is not perfectly matched, the dielectric properties (such as the complex permittivity) cannot be interpreted directly from the measurement data. In order to minimise errors, the system is designed to have a 50 Ω intrinsic impedance, the same as the characteristic impedance of the standard coaxial line. It consists of three parts: the connection to an N-type connector, the transition section, and the uniform sample holder. The inside of the outer conductor of the cell is 105 mm, which is just big enough for the sandstone sample with a clearance to tolerate the geometrical variation of the sample. To meet the 50 Ω condition, the diameter of the inner conductor of the cell is 45 mm. This means that the upper frequency limit for the cell is 1317 MHz, which is the cutoff frequency of the first higher mode (TE10). In principle, there is no low frequency limit for this system. The transition section, which links the connector with the sample holder, is smoothly tapered to keep the impedance as 50 Ω along the line. The total length of the cell is 450 mm. Good conducting material (brass) is used so as to reduce the ohmic loss.

The cell was carefully machined in our mechanical workshop and the final product is shown in Figure 4.27, where the outer conductor of the transition section is removed, thus permitting the sample to be inserted and removed from the cell. Although the cell is designed as a 50 Ω matched system, this is not necessarily true in reality. To assess the performance of the cell, a time-domain measurement on the empty

Figure 4.27 A large coaxial cell made at Liverpool University

cell was conducted. The reflected signals at the discontinuities between sections are ~20 dB. This means that the cell is indeed finely made and only ~1% of the input power was reflected from these discontinuities. However, this does not mean that the system needs no calibration. In fact, such small discontinuities can still result in huge measurement errors. Thus, a calibration process is needed.

Normally, the calibration of a cell is performed by placing the three standard terminations (i.e. short, open and matched load) at the calibration plane and measuring the reflection and/or transmission, respectively. The calibration kit is standard and widely available on the market. However, for our coaxial cell, the size is not standard and hence the standard terminations cannot be used. It is possible to make open and short terminations at the reference plane, but it was not possible for us to make a matched load. Thus an alternative calibration method, three-point short-circuit approach, is proposed. The calibration plane is chosen near the boundary between the transition section and the uniform section of the sample holder. The effects of discontinuities between sections can therefore be removed by calibration. The calibration is successfully conducted by using a short termination placed at three different positions in the sample region. This short load is made of a flat brass ring that fits snugly into the uniform section of the coaxial cell.

Although it is relatively straightforward to measure the complex reflection coefficient using this one-port system, as mentioned earlier, the data interpretation is actually one of the major problems with this method. An improved data interpretation method was introduced [122]. To obtain the dielectric properties, a minimisation process has to be performed by defining an objective function as the difference between the measured and modelled reflection coefficients. A MATLAB programme has been written and the computation is very robust. There is no singularity involved in the calculation.

The system has been employed to measure such as contaminated soils [123] and sandstones [124]. A typical measurement result of sandstone is shown in Figure 4.28.

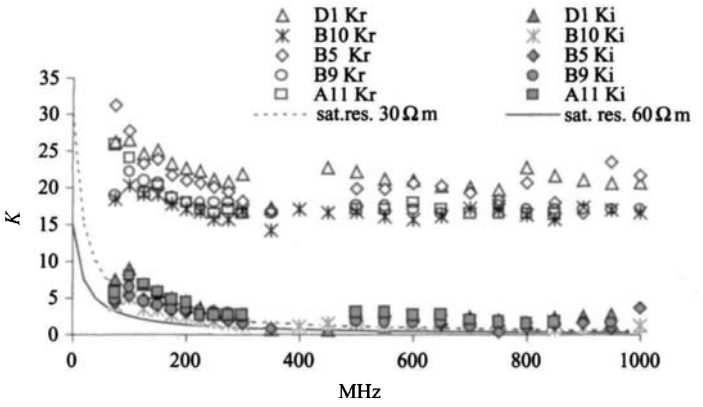

Figure 4.28 Dielectric response of saturated Sherwood sandstone (Ki response predicted from saturated DC resistivity assuming no relaxation losses)

Measurements using this new one-port dielectric measurement system have shown very good repeatability and accuracy. However, it has been realised that this simple dielectric measurement technique has the following drawbacks:

(*a*) In the data process, several local minima may be obtained for the objective function; thus a global minimisation method may be needed for automatic interpretation.
(*b*) The accuracy may be reduced if the thickness of the sample is not properly selected.
(*c*) The applicable frequency range is linked not just to the dielectric properties of the sample, but also to its thickness.

4.9 Field measurements of soil properties

There are a variety of methods of measuring soil parameters, and one technique, which is relatively straightforward to implement, is based on work by Al-Attar *et al.* [125].

This method is carried out using the following procedure and with reference to Figure 4.29.

The transmit probe can be excited by a time domain or frequency domain signal, and the receive probe is used to measure the amplitude and phase of the signal propagated through the soil at two positions which should be separated by at least $2\lambda_m$ at the lowest frequency of interest. The transmit probe and receive probe in position 1 should also be separated by a similar distance.

In the case of a time domain signal the received signals from positions 1 and 2 will be time domain wavelets, with the wavelet in position 2 being lower in amplitude and delayed in time compared with the wavelet measured in position 1.

If the two distances are known, then it can be shown [125] that by taking Fourier transforms of the windowed wavelets at positions 1 and 2 and then dividing the transform at 1 by that at 2, the amplitude and phase propagation characteristics of the soil can be determined noting that

$$\frac{F_{r1}(\omega)}{F_{r2}(\omega)} = \frac{H(\omega, r_1)}{H(\omega, r_1 + r_2)} \tag{4.40}$$

Hence the soil attenuation constant is given by (see Figure 4.30)

$$\alpha = -\frac{20}{r_2} \log_{10} \left[A(\omega) \frac{r_1 + r_2}{r_1} \right] \tag{4.41}$$

$$\varepsilon_r = \left(\frac{c}{r_2} \frac{\mathrm{d}\phi}{\mathrm{d}\omega} \right)^2 \tag{4.42}$$

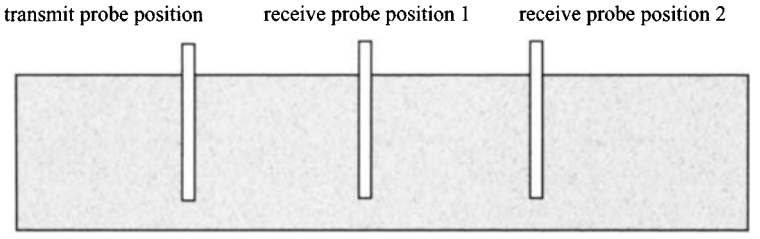

Figure 4.29 Field measurements of soil characteristics

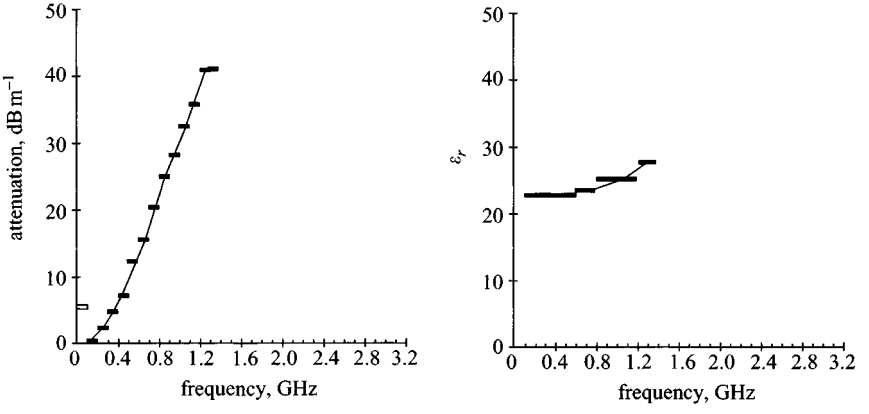

Figure 4.30 Attenuation and relative dielectric constant from a UK site with 17.5% water by weight and a DC resistivity of 9424 Ω [125]

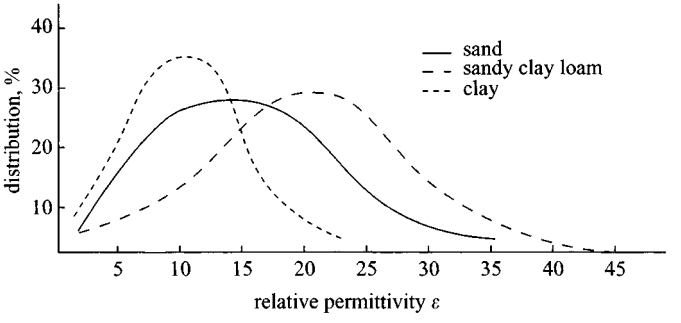

Figure 4.31 Variation of relative permittivity with soil type over a number of sites in the UK

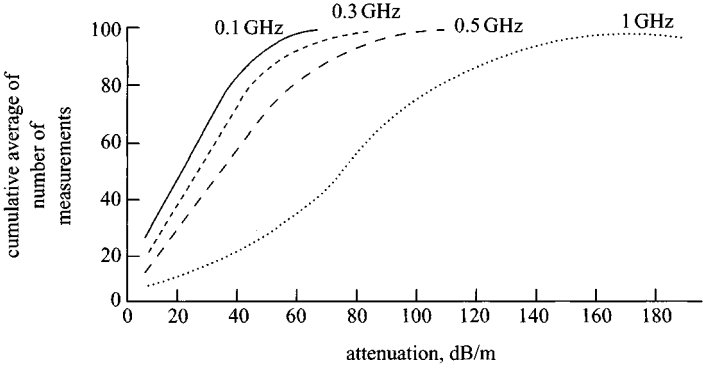

Figure 4.32 Cumulative variation of attenuation over a number of sites in the UK

From this method the statistical properties of UK soils as shown in Figures 4.31 and 4.32 were derived.

4.10 Summary

The most important microwave characteristics of soils are the relative dielectric constant and attenuation. There is an adequate body of literature available on these values as a function of microwave frequency. Further references can be assessed to obtain more information. The values can be used to predict the performance of surface-penetrating radars in typical soils with known moisture contents.

However, the actual performance of radars can vary quite considerably due to the wide variations often encountered in local material conditions. Not only is the range but also the resolution in depth affected by the attenuation of the material. An approximate empirical relationship is that the achievable depth resolution lies between 10% and 20% of the probing range.

An indication of the likely range of material properties can be seen from Figures 4.31 and 4.32, which refer to the distribution of measurements of dielectric constant and attenuation taken from a range of excavation sites in the UK. Note that for a nominal soil type the dielectric constant can vary considerably. Given a particular frequency, Figure 4.32 shows the percentage of sites with measured attenuations at selected frequencies.

Accurate measurement of depth can only be achieved by proper and frequent calibration of the velocity of propagation. This can be obtained using a multi-channel radar system or by secondary measurements. Generally, man-made materials prove to be a more heterogeneous medium for radar probing, and silty or heavy clay soils prove difficult to penetrate. Where the material is composed of mixtures containing, for example, rubble, the radar pulses are multiply reflected, thus creating a randomly orientated image.

4.11 References

[1] PEPLINSKI, N. R., ULABY, F. T., and DOBSON, M. C.: 'Dielectric properties of soils in the 0.3–1.3 GHz range', *IEEE Trans. Geosci. Remote Sens.*, 1995, **33**, (3), pp. 803–807

[2] HALLIKAINEN, M. T., ULABY, F. T., DOBSON, M. C., ELRAYES, M. A., and WU, L. K.: 'Microwave dielectric behaviour of wet soil', Parts I and II, *IEEE Trans.*, 1985, **GE-23**, (1), pp. 25–34

[3] WAIT, J. R.: 'Propagation of electromagnetic pulses in a homogeneous conducting earth', *Appl. Sci. Res., B: Electrophys. Acoust. Opt.*, 1960, **8**, pp. 213–253

[4] KING, R. W. P., and WU, T. T.: 'The propagation of a radar pulse in sea water', *J. Appl. Phys.*, 1993, **73**, (4), pp. 1581–1590

[5] BRILLOUIN, L.: *Ann. Phys. (Leipzig)*, 1914, **44**, p. 177

[6] SOMMERFELD, A.: *Ann. Phys. (Leipzig)*, 1914, **44**, p. 203

[7] OUGHSTRUN, K. E.: *Proc. IEEE*, 1991, **79**, p. 1379

[8] FINKELSHTEYN, M. I., and KRAYNYUKOV, A. V.: 'Estimation of the delay of super wideband radio pulses in a medium as applied to problems of subsurface radar'. English translation of paper originally published in *Radiotekhnika i Elektronika* (USSR), 1986, (11), pp. 2202–2208

[9] WAIT, J. R., and NABULSI, K. A.: 'Preforming an electromagnetic pulse in lossy medium', *Electron. Lett.*, 1992, **28**, (6), pp. 542–543

[10] DE LOOR, G. P.: 'The dielectric properties of wet materials', *IEEE Trans.*, 1983, **GE-21**, pp. 364–369

[11] HOEKSTRA, P., and DELANEY, A.: 'Dielectric properties of soils at UHF and microwave frequencies', *J. Geophys. Res.*, 1974, **79**, pp. 1699–1708

[12] HIPP, J. E.: 'Soil electromagnetic parameters as functions of frequency, soil density and soil moisture', *Proc. IEEE*, 1974, **62**, (1), pp. 98–103

[13] CAMPBELL, M. J., and ULRICHS, J.: 'Electrical properties of rocks and their significance for lunar radar observations', *J. Geophys. Res.*, 1969, **74**, pp. 5867–5881

[14] VON HIPPEL, A. R., (Ed.): 'Dielectric materials and applications' (MIT Press, Cambridge, MA, USA, 1954), p. 314

[15] HOEKSTRA, P., and DELANEY, A.: 'Dielectric properties of soils at UHF and microwave frequencies', *J. Geophys. Res.*, 1974, **79**, pp. 1699–1708

[16] KING, R. W. P., and SMITH, G. S.: 'Antennas in matter' (MIT Press, 1981)

[17] POTTEL, R.: 'Dielectric properties', in Franks, F. (Ed.): 'Water: a comprehensive treatise, Vol. 3: Aqueous properties of simple electrolytes' (Plenum Press, 1973), Chap.8

[18] COLE, K. S., and COLE, R. H.: 'Dispersion and absorption in dielectrics - I. Alternative current characteristics'. *J. Chem. Phys.*, 1941, **9**, pp. 341–351

[19] KOVACS, A., *et al.*: 'Electromagnetic property trends in sea ice'. CRREL Report 87–6, US Dept. of Energy

[20] HIPP, J. E.: 'Soil electromagnetic parameters as functions of frequency, soil density and soil moisture', *Proc. IEEE*, 1974, **62**, (1), pp. 98–103
[21] WANG, J. R., and SCHMUGGE, T. J.: 'An empirical model for the complex dielectric permittivity of soil as a function of water content', *IEEE Trans.*, 1980, **GE-18**, pp. 288–295
[22] WOBSCHALL, D.: 'A theory of the complex dielectric permittivity of soil containing water: The semidisperse model', *IEEE Trans.*, 1977, **GE-15**, pp. 49–58
[23] PARKHOMENKO, E. I.: 'Electrical properties of rocks' (Plenum Press, 1967)
[24] KELLER, G. V.: 'Electrical characteristics of the earth's crust', in Wait, J. R. (Ed.): 'Electromagnetic probing in geophysics' (Golem Press, 1971)
[25] FULLER, B. D., and WARD, S. K.: 'Linear system description of the electrical parameters of rocks', *IEEE Trans.*, 1970, **GE-8**, pp. 7–17
[26] CAMPBELL, M. J., and ULRICHS, J.: 'Electrical properties of rocks and their significance for lunar radar observations', *J. Geophys. Res.*, 1969, **74**, pp. 5867–5881
[27] ENDRES, A. L., and KNIGHT, R.: 'A theoretical treatment of the effect of microscopic fluid distribution on the dielectric properties of partially saturated rocks,' *Geophys. Prospect.*, 1992, **40**, pp. 307–324
[28] PARKHOMENKO, E. I.: 'Electrical properties of rocks' (Plenum Press, New York, 1967), p. 314
[29] BHAGAT, P. K., and KADABA, P. K.: 'Relaxation models for moist soils suitable at microwave frequencies', *Mater. Sci. Eng.*, 1977, **28**, pp. 47–51
[30] HANAI, T.: 'Dielectric theory on the interfacial polarisation for two phase mixtures', *Bull Inst. Chem. Res.*, Kyoto University, 1961, **39**, pp. 341–368
[31] Soil Survey Staff: 'Soil taxonomy, a basic system of soil classification for making and interpreting soil surveys'. Agriculture Handbook No. 436, 2nd edition. USDA-Natural Resources Conservation Service. US Government Printing Office, Washington, DC, 1999
[32] DAVIS, J. L., and ANNAN, A. P.: 'Ground-penetrating radar for high resolution mapping of soil and rock stratigraphy', *Geophys. Prospect.*, 1989, **37**, pp. 531–551
[33] BENSON, R., and GLACCUM, R.: 'Test Report: The application of ground-penetrating radar to soil surveying for National Aeronautical and Space Administration (NASA)'. Technos Inc. Miami, Florida, 1979
[34] JOHNSON, R. W., GLACCUM, R., and WOJTASINSKI, R.: 'Application of ground penetrating radar to soil survey', *Soil Crop Sci. Soc. Florida Proc.*, 1979, **39**, pp. 68–72
[35] SCHELLENTRAGER, G. W., DOOLITTLE, J. A., CALHOUN, T. E., and WETTSTEIN, C. A.: 'Using ground-penetrating radar to update soil survey information', *Soil Sci. Soc. Am. J.* 1988, **52**, pp. 746–752
[36] Soil Survey Staff: 'Soil survey manual'. US Department of Agriculture – Soil Conservation Service, Handbook No. 18, US Government Printing Office, Washington, DC, USA, 1993

[37] DOOLITTLE, J. A., and COLLINS, M. E.: 'Use of soil information to determine application of ground-penetrating radar,' *J. Appl. Geophys.*, 1995, **33**, pp. 101–108

[38] GRANT, J. A., and SCHULTZ, P. H.: 'Erosion of ejecta at Meteor Crater: Constraints from ground penetrating radar', in Proc. Fifth Int. Conf. on Ground-penetrating Radar, Kitchner, Ontario, Canada, 12–14 June 1994. Waterloo Centre for Groundwater Research and the Canadian Geotechnical Society, pp. 789–803

[39] COLLINS, M. E., and KURTZ, J. L.: 'Assessing GPR performance in three geographic regions', in Plumb, R. G. (Ed.): Proceedings of Seventh Int. Conf. on Ground-penetrating radar, 27–30 May 1998, Lawrence, Kansas. Radar Systems and Remote Sensing Laboratory, University of Kansas, pp. 171–176

[40] DOOLITTLE, J. A., and COLLINS, M. E.: 'A comparison of EM induction and GPR methods in areas of karst', *Geoderma*, 1998, **85**, pp. 83–102

[41] HUBBARD, R. K., ASMUSSEN, L. E., and PERKINS, H. F.: 'Use of ground-penetrating radar on upland coastal plain soils', *J. Soil Water Cons.*, 1990, **45**, (3), pp. 399–405

[42] COLLINS, M. E.: 'Soil taxonomy: a useful guide for the application of ground-penetrating radar', in Hanninen, P. and S. Autio (Eds.): Fourth Int. Conf. on Ground penetrating radar, 8–13 June 1992, Rovaniemi, Finland. Geological Survey of Finland, Special Paper 16, pp. 125–132

[43] COLLINS, M. E., and KURTZ, J. L.: 'A summary of soil characteristics and comparisons for ground penetrating radar assessments'. Report for the Army Research Laboratory, March 1997

[44] DOOLITTLE, J. A., COLLINS, M. E., and MOUNT, H. R.: 'Assessing the appropriateness of GPR with a soil geographic database', in Plumb, R. G. (Ed.): Proc. Seventh Int. Conf. on Ground-penetrating radar, 27–30 May 1998, Lawrence, Kansas. Radar Systems and Remote Sensing Laboratory, University of Kansas, pp. 393–400

[45] DOOLITTLE, J. A., MINZENMAYER, F. E., WALTMAN, S. W., and BENHAM, E. C.: 'Ground-penetrating radar soil suitability map of the conterminous United States', in Koppenjan, S. K., and Hua, L. (Eds.): Ninth Int. Conf. on Ground-penetrating radar. Proc. SPIE Vol. 4158, 30 April–2 May 2002, Santa Barbara, CA, pp. 7–12

[46] Soil Science Society of America: 'Glossary of soil science terms' (Madison, WI, 1997)

[47] COLLINS, M. E., SCHELLENTRAGER, G. W., DOOLITTLE, J. A., and SHIH, S. F.: 'Using ground-penetrating radar to study changes in soil map unit composition in selected Histosols', *Soil Sci. Soc. Am. J.*, 1986, **50**, pp. 408–412

[48] DOOLITTLE, J. A.: 'Using ground-penetrating radar to increase the quality and efficiency of soil surveys', in 'Soil survey techniques', *Soil Sci. Soc. Am. Special Pub. 20*, 1987, pp. 11–32

[49] PUCKETT, W. E., COLLINS, M. E., and SCHELLENTRAGER, G. W.: 'Design of soil map units on a karst area in West Central Florida', *Soil Sci. Soc. Am. J.*, 1990, **54**, pp. 1068–1073

[50] ASMUSSEN, L. E., PERKINS, H. F., and ALLISON, H. D.: 'Subsurface descriptions by ground-penetrating radar for watershed delineation'. Research Bulletin 340. The Georgia Agricultural Experiment Stations, University of Georgia, Athens, 1986

[51] COLLINS, M. E., and DOOLITTLE, J. A.: 'Using ground-penetrating radar to study soil microvariability', *Soil Sci. Soc. Am. J.*, 1987, **51**, pp. 491–493

[52] DOOLITTLE, J. A., and ASMUSSEN, L. E.: 'Ten years of applications of ground-penetrating radar by the United States Department of Agriculture', in Hanninen, P., and S. Autio (Eds.): Fourth Int. Conf. on Ground penetrating radar, 8–13 June 1992, Rovaniemi, Finland. Geological Survey of Finland, Special Paper 16, pp. 139–147

[53] TRUMAN, C. C., PERKINS, H. F., ASMUSSEN, L. E., and ALLISON, H. D.: 'Some applications of ground-penetrating radar in the southern coast plain region of Georgia'. The University of Georgia, Georgia Agricultural Experiment Stations Research Bulletin 362, 1988

[54] BURGOA, B., MANSELL, R. S., SAWKA, G. J., NKEDI-KIZZA, P., CAPECE, J., and CAMPBELL, K.: 'Spatial variability of depth to Bh horizon in Florida Haplaquods using ground-penetrating radar', *Soil and Crop Sci. Soc. Fla. Proc.*, 1991, **50**, pp. 125–130

[55] LAPEN, D. R., MOORMAN, B. J., and PRICE, J. S.: 'Using ground-penetrating radar to delineate subsurface features along a wetland catena', *Soil Sci. Soc. Am. J.*, 1996, **60**, pp. 923–931

[56] DOOLITTLE, J., HOFFMANN, G., McDANIEL, P., PETERSON, N., GARDNER, B., and ROWAN, E.: 'Ground-penetrating radar interpretations of a fragipan in Northern Idaho', *Soil Surv. Horiz.*, 2000, **41**, (3), pp. 73–82

[57] LYONS, J. C., MITCHELL, C. A., and ZOBECK, T. M.: 'Impulse radar for identification of features in soils', *J. Aerosp. Eng.*, 1988, **1**, pp. 18–27

[58] OLSON, C. G., and DOOLITTLE, J. A.: 'Geophysical techniques for reconnaissance investigations of soils and surficial deposits in mountainous terrain', *Soil Sci. Soc. Am. J.*, 1985, **49**, pp. 1490–1498

[59] RAPER, R. L., ASMUSSEN, L. E., POWELL, J. B.: 'Sensing hard pan depth with ground-penetrating radar', *Trans. ASAE*, 1990, **33**, pp. 41–46

[60] MOKMA, D. L., SCHAETZL, R. J., DOOLITTLE, J. A., and JOHNSON, E. P.: 'Ground-penetrating radar study of ortstein continuity in some Michigan Haplaquods', *Soil Sci. Soc. Am. J.*, 1990, **54**, pp. 936–938

[61] FARRISH, K. W., DOOLITTLE, J. A., and GAMBLE, E. E.: 'Loamy substrata and forest productivity of sandy glacial drift soils in Michigan', *Can. J. Soil Sci.*, 1990, **70**, pp. 181–187

[62] MOKMA, D. L., SCHAETZL, R. J., DOOLITTLE, J. A., and JOHNSON, E. P.: 'Assessing Bt horizon character in sandy soils using ground-penetrating radar: Implications for soil surveys', *Soil Surv. Horiz.*, 1990, **30**, (2), pp. 1–8

[63] DOOLITTLE, J. A., HARDISKY, M. A., and GROSS, M. F.: 'A ground-penetrating radar study of active layer thicknesses in areas of moist sedge and wet sedge tundra near Bethel, Alaska, U.S.A.', *Arctic Alpine Res.*, 1990, **22**, (2), pp. 175–182

[64] COLLINS, M. E., DOOLITTLE, J. A., and ROURKE, R. V.: 'Mapping depth to bedrock on a glaciated landscape with ground-penetrating radar', *Soil Sci. Soc. Am. J.*, 1989, **53**, pp. 1806–1812

[65] MOREY, R. M.: 'Continuous subsurface profiling by impulse radar', in Proc. ASCE Engineering Foundation Conf. on Subsurface exploration for underground excavations and heavy construction, Henniker, New Hampshire, 11–16 Aug. 1974, pp. 212–232

[66] SCHELLENTRAGER, G. W., and DOOLITTLE, J. A.: 'Systematic sampling using ground-penetrating radar to study regional variation of a soil map unit', in Mausbach, M. J., and L. P. Wilding (Eds.): 'Spatial variabilities of soils and landforms', *Soil Sci. Soc. Am. Special Publ. No. 28*, 1991, pp. 199–214

[67] ROBILLARD, C., NICOLAS, P., ARMIRAT, P., GARIEPY, M., and GOUPIL, F.: 'Shallow bedrock profiling using GPR'. GPR 94, Proc. Fifth Int. Conf. on Ground penetrating radar, 12–16 June 1994. Kitchener, Ontario, Canada. Waterloo Center for Groundwater Research, 1994, pp. 1167–1179

[68] RICHARDSON, J. L., WILDING, L. P., and DANIELS, R. B.: 'Recharge and discharge of groundwater in aquic conditions illustrated with flow analysis', *Geoderma*, **53**, pp. 65–78

[69] BOHLING, G. C., ANDERSON, M. P., BENTLEY, C. R.: 'Use of ground penetrating radar to define recharge areas in the Central Sand Plain'. Technical Completion Report G1458-03. Geology and Geophysics Department, University of Wisconsin-Madison, 1989

[70] DOOLITTLE, J. A., JENKINSON, B. J., FRANZMEIER, D. P., and LYNN, W.: 'Improved radar interpretations of water table depths and groundwater flow patterns using predictive equations', in Noon, D. (Ed.): Proc. Eight Int. Conf. on Ground-penetrating radar, 23–26 May 2000, The University of Queensland, Goldcoast, Queensland, Australia, pp. 488–495

[71] IIVARI, T. A., and DOOLITTLE, J. A.: 'Computer simulations of depths to water table using ground-penetrating radar in topographically diverse terrains', in 'Groundwater quality management', Proc. GQM 93, International Association of Hydrological Sciences, Tallinn, Estonia, September 1993, pp. 11–20

[72] JOHNSON, D. G. 'Use of ground-penetrating radar for determining depth to the water table on Cape Cod, Massachusetts', in Proc. First National Outdoor Action Conf. on Aquifer restoration, groundwater monitoring and geophysical methods, 18–21 May 1987, Las Vegas, Nevada. National Water Well Association, Dublin, Ohio, 1987, pp. 541–554

[73] TAYLOR, K. R., and BAKER, M. E.: 'Use of ground-penetrating radar in defining glacial outwash aquifers'. Proc. FOCUS Conf. on Eastern Regional Groundwater Issues, Stamford, Connecticut, 27–29 September 1988. National Water Well Association, Dublin, Ohio, 1988, pp. 70–98

[74] VIOLETTE, P.: 'Surface geophysical techniques for aquifers and wellhead protection area delineation'. Environmental Protection Agency, Office of Groundwater Protection, Washington, DC, 1987

[75] STEENHUIS, T. S., KUNG, K.-J. S., and CATHLES, L. M. III: 'Finding layers in the soil. Ground-penetrating radar as a tool in studies of groundwater contamination', *Eng. Cornell Q.*, 1990, **25**, (1), pp. 15–19

[76] BERES, M., and HAENI, F. P.: 'Application of ground-penetrating radar methods in hydrogeologic studies', *Groundwater*, 1991, **29**, (3), pp. 375–386

[77] FREELAND, R. S., REAGAN, J. C., BURNS, R. T., and AMMONS, J. T.: 'Sensing perched water using ground-penetrating radar – A critical methodology examination', *Appl. Eng. Agric., ASAE*, **14**, (6), pp. 675–681

[78] SHIH, S. F., DOOLITTLE, J. A., MYHRE, D. L., and SCHELLENTRAGER, G. W.: 'Using radar for groundwater investigation', *J. Irrig. Drain. Eng.*, 1986, **112**, (2), pp. 110–118

[79] DAVIS, J. L., TOPP, G. C., and ANNAN, A. P.: 'Electromagnetic detection of soil water content: Progress Report II', in 'Remote sensing and soil moisture and ground water', Workshop Proceedings, Canadian Aeronautics and Space Institute, Ottawa, Canada, November 1976, pp. 96–109

[80] HUISMAN, J. A., SNEPVANGERS, J. J. J. C., BOUTEN, W., and HEUVELINK, G. B. M.: 'Mapping spatial variations in surface water content: comparison of ground-penetrating radar and time domain reflectometry', *J. Hydrol.*, 2002, **269**, pp. 192–207

[81] WEILER, K. W., STEENHUIS, T. S., BOLL, J., KUNG, K.-J. S.: 'Comparison of ground-penetrating radar and time-domain reflectometry as soil water sensors', *Soil Sci. Soc. Am. J.*, 1998, **62**, pp. 1237–1239

[82] HUISMAN, J. A., SPERL, C., BOUTEN, W., VERSTRATEN, J. M.: 'Soil water content measurements at different scales: accuracy of time domain reflectometry and ground-penetrating radar', *J. Hydrol.* 2001, **245**, pp. 48–58

[83] VAN OVERMEEREN, R. A., SARIOWAN, S. V., and GEHRELS, J. C.: 'Ground penetrating radar for determining volumetric soil water content; results of comparative measurements at two test sites', *J Hydrol.*, 1997, **197**, pp. 316–338

[84] VELLIDIS, G., SMITH, M. C., THOMAS, D. L., and ASMUSSEN, L. E.: 'Detecting wetting front movement in a sandy soil with ground-penetrating radar', *Trans. ASAE*, 1990, **33**, (6), pp. 1867–1874

[85] TOMER, M. D., BOLL, J., KUNG, K-J. S., STEENHIUS, T., and ANDERSON, J. L.: 'Detecting illuvial lamellae in fine sand using ground-penetrating radar', *Soil Sci.*, **161**, pp. 121–129

[86] KUNG, K-J. S., and DONOHUE, S. V.: 'Improved solute-sampling in a sandy vadose zone using ground-penetrating radar', *Soil Sci. Soc. Am. J.*, 1991, **55**, pp. 1543–1545

[87] BOLL, J., VAN RIJN, R. P. G., WEILER, K. W., EWEN, J. A., DALIPARTHY, J., HERBERT, S. J., and STEENHUIS, T. S.: 'Using ground-penetrating radar to detect layers in a sandy field soil', *Geoderma*, 1996, **70**, pp. 117–132

[88] TURENNE, J.: 'Understanding cranberry soil maps'. *Cranberries*, April 1997, pp. 15–18

[89] ULRIKSEN, P.: 'Investigation of peat thickness with radar'. Proc. of 6th Int. Peat Congress, Duluth, Minnesota, August 1980, pp. 126–129

[90] Remotec Application Inc.: 'The use of impulse radar techniques for depth profiling of peat deposits'. National Research Council of Canada, Division of Energy Research and Development, Ottawa. Report NRCC 20982, DSS File No. 255R.31155-1-2630, 1982

[91] ULRIKSEN, C. P. F.: 'Application of impulse radar to civil engineering'. Doctoral Thesis, Department of Engineering Geology, Lund University of Technology, Lund, Sweden, 1982

[92] DOOLITTLE, J., FLETCHER, P., and TURENNE, J.: 'Estimating the thickness of organic materials in cranberry bogs'. *Soil Surv. Horiz.*, 1990, **31**, (3), pp. 73–78

[93] HANNINEN, P.: 'Application of ground penetrating radar techniques to peatland investigations', in Hanninen, P., and Autio, S. (Eds.): Fourth Int. Conf. on Ground-penetrating radar, 7–12 June 1992, Rovaniemi, Finland. Geological Survey of Finland, Special Paper 16, pp. 217–221

[94] PELLETIER, R. E., DAVIS, J. L., ROSSITER, J. R.: 1991. 'Peat analysis in the Hudson Bay Lowlands using ground penetrating radar', in Proc. Int. Geoscience and Remote Sensing Symposium, Helsinki, Finland, June 1991, pp. 2141–2144

[95] SHIH, S. F., and DOOLITTLE, J. A.: 'Using radar to investigate organic soil thickness in the Florida Everglades', *Soil Sci. Soc. Am. J.*, 1984, **48**, pp. 651–656

[96] TOLONEN, K., RUMMUKAINEN, A., TOIKKA, M., and MARTTILLA, I.: 'Comparison between conventional and peat geological and improved electronic methods in examining economically important peatland properties'. Proc. 7th Int. Peat Congress, Dublin, Ireland, 18–23 June 1984. The Irish National Peat Committee, 76 Lower Baggot St., Dublin, Ireland, pp. 1–10

[97] TURENNE, J. D.: 'Ground-penetrating radar surveys of cranberry beds in Plymouth County, Massachusetts', in Vendl, M., and Daniels, J.J. (Eds.): Proc. Second Government Users Workshop on Ground-penetrating radar. US Environmental Protection Agency and The Ohio State University, Columbus, Ohio, 1993, pp. 213–220

[98] WELSBY, J.: 'The utilization of geo-radar in monitoring cutover peatlands'. Proc. 8th Int. Peat Congress, Leningrad, USSR. International Peat Society, Jyska, Finland, 1988, pp. 99–107

[99] WORSFOLD, R. D., PARASHAR, S. K., and PERROTT, T.: 'Depth profiling of peat deposits with impulse radar', *Can. Geotech. J.*, 1986, **23**, (2), pp. 142–145

[100] CHERNETSOV, E. A., BELETSKY, N. A., and BAEV, M. YU.: 'Radar profiling of peat and gyttja deposits', in Proceedings 8th International Peat Congress, Leningrad, USSR, 1988. International Peat Society, Jyska, Finland, pp. 15–21

[101] LOWE, D. J.: 'Application of impulse radar to continuous profiling of tephra-bearing lake sediments and peats: an initial evaluation', *New Zealand J. Geol. Geophys.*, 1985, **28**, pp. 667–674

[102] SAARENKETO, T., HIETALA, K., and SALMI, T.: 'GPR applications in geotechnical investigations of peat for road survey purposes', in Hanninen, P., and Autio, S. (Eds.): Fourth Int. Conf. on Ground-penetrating radar, 7–12 June 1992, Rovaniemi, Finland. Geological Survey of Finland, Special Paper 16, 1992, pp. 293–305

[103] THEIMER, B. D., NOBES, D. C., and WARNER, B. G.: 'A study of the geoelectric properties of peatlands and their influence on ground-penetrating radar surveying', *Geophys. Prospect.*, 1994, **42**, pp. 179–209

[104] DOOLITTLE, J. A., REBERTUS, R. A., JORDAN, G. B., SWENSON, E. I., and TAYLOR, W. H.: 'Improving soil-landscape models by systematic sampling with ground-penetrating radar', *Soil Surv. Horiz.*, 1988, **29**, (2), pp. 46–54

[105] REBERTUS, R. A., DOOLITTLE, J. A., and HALL, R. L.: 'Landform and stratigraphic influences on variability of loess thickness in northern Delaware', *Soil Sci. Soc. Am. J.*, 1989, **53**, pp. 843–847

[106] COLLINS, M. E., PUCKETT, W. E., SCHELLENTRAGER, G. W., and YUST, N. A.: 'Using GPR for micro-analyses of soils and karst features on the Chiefland Limestone Plain in Florida', *Geoderma*, 1990, **47**, pp. 159–170

[107] COLLINS, M. E., CRUM, M., and HANNINEN, P.: 'Using ground-penetrating radar to investigate a subsurface karst landscape in north-central Florida', *Geoderma*, 1994, **61**, pp. 1–15

[108] WHITTINGTON, H. W., McCARTER, J., and FORDE, M.: 'The conduction of electricity through concrete', *Mag. Concrete Res.*, 1981, **33**, pp. 48–60

[109] NIKKANEN, P.: 'On the electrical properties of concrete and their application'. Valtion Teknillienen Tutkimuslaitos, Tiedotus, Sarja III Rakennus 60, 1962 (in Finnish)

[110] HAMMOND, R., and ROBSON, T. D.: 'Comparison of electrical properties of various cements and concretes', *The Engineer*, **199**, 21 Jan. 1975, pp. 79–80 and 28 Jan. 1975, pp. 114–115

[111] MONFORE, G. E.: 'The electrical resistivity of concrete', *J. PCA Res. Dev. Lab.*, 1968, **10**, (2), pp. 35–48

[112] WYLLIE, M. R., and GREGORY, G. H. F.: 'The generalised Kozeny-Carmen equation - Part 2: A novel approach to problems of fluid flow', *World Oil*, 1958, **146**, (5), pp. 210–228

[113] WHITTINGTON, H. W.: 'Low frequency electrical characteristics of fresh concrete', *IEE Proc. A*, 1986, **133**, (5), pp. 265–271

[114] VON HIPPEL, A.: 'Dielectric materials and applications' (Artech House, London, 1995)
[115] AFSAR, M. N., BIRCH, J. R., and CLARKE, R. N.: 'The measurement of the properties of materials', *Proc. IEEE*, 1986, **74**, (1), pp. 183–199
[116] STUCHLY, M. A., and STUCHLY, S. S.: 'Coaxial line reflection methods for measuring dielectric properties of biological substances at radio and microwave frequencies – a review', *IEEE Trans.*, 1980, **IM-29**, pp. 176–183
[117] DE LOOR, G. P.: 'The dielectric properties of wet materials', *IEEE Trans.*, 1983, **GE-21**, pp. 364–369
[118] SHEN, L. C., MAROUNI, H., ZHANG, Y. X., and SHI, X. D.: 'Analysis of parallel-disk sample holder for dielectric permittivity measurement', *IEEE Trans.*, 1987, **GRS-25**, pp. 534–540
[119] BAKER-JARVIS, J., VANZURA, E. J., and KISSICK, W. A.: 'Improved technique for determining complex permittivity with transmission/reflection method', *IEEE Trans.*, 1990, **MTT-38**, (8), pp. 1096–1103
[120] TOPP, G. C., DAVIS, J. L., and ANNAN, A. P.: 'Electromagnetic determination of soil water content: measurements in coaxial transmission line', *Water Resour. Res.*, 1980, **16**, pp. 574–582
[121] DALTON, F. N., HERKELRATH, W. N., RAWLINS, D. S., and RHOADES, J. D.: 'Time-domain reflectrometry: simultaneous measurement of soil water content and electrical conductivity with a single probe', *Science*, 1984, **224**, pp. 989–990
[122] HUANG, Y.: 'Design, calibration and data interpretation for a one-port large coaxial dielectric measurement cell', *Meas. Sci. Technol.*, 2001, **12**, pp. 111–116
[123] HUANG, Y., FANG, M. T. C., NGYEN, V. T., and ERIKSEN, A.: 'Dielectric properties of contaminated soils'. SPIE Int. Symposium on Subsurface sensors and applications, 1999, Vol. 3752, pp. 157–163
[124] WEST, L. J., HANDLEY, K., HUANG, Y., and POKAR, M.: 'Radar frequency dielectric dispersion in sandstone: implications for determination of moisture and clay content', *Water Resour. Res.*, 2003, **39**, (2), p. 1026
[125] AL-ATTAR, A., SCOTT, H. F., and DANIELS, D. J.: 'Wideband measurements of microwave characteristics of soils', *Electron. Lett.*, 1982, **18**, pp. 194–199

4.12 Bibliography

ANNAN, A. P., and DAVIS, J. L.: 'Methodology for radar transillumination experiments,' *Current Res. B. Geol. Surv. Canada*, 1978, **78-1B**, pp. 107–11
DE PASQUALE, G.: 'A ground penetrating radar for soil pattern recognition'. Proc. IEEE Int. Geoscience and Remote Sensing Symposium, (IGARSS '98), Vol. 2, 6–10 July 1998, pp. 853–855
EVJEN, H. M.: 'Theory and practice of low-frequency electromagnetic exploration', *Geophys.*, 1948, **13**, pp. 584–594

HANAI, T.: 'Electrical properties of emulsions', in Sherman P. (Ed.): 'Emulsion science' (Academic Press, 1969), Chap.5

HAYES, P. K.: 'An on-site method for measuring dielectric constant and conductivity of soils over a gigahertz bandwidth'. Technical Report 582X-1, Ohio State University Electroscience Laboratory, 1979

KELLER, G. V., and LICASTRO, P. H.: 'Dielectric constant and electrical resistivity of natural-state cores', *US Geol. Surv. Bull.*, 1959, **1052-H**, pp. 257–285

MAYHAN, R. J., and BAILEY, R. E.: 'An indirect measurement of the effective dielectric constant and loss tangent of typical concrete roadways', *IEEE Trans. Antennas Propag.*, 1975, **AP-23**, pp. 565–569

OGUZ, U., and GUREL, L.: 'Frequency responses of ground-penetrating radars operating over highly lossy grounds', *IEEE Trans. Geosci. Remote Sens.*, 2002, **40**, (6), pp. 1385–1394

OGUZ, U., and GUREL, L.: 'On the frequency-band selection for ground-penetrating radars operating over lossy and heterogeneous grounds'. IEEE Int. Antennas and Propagation Society Symposium, 2001, Vol. 3, pp. 761–764

OSWALD, B., ERNI, D., BENEDICKTER, H. R., BACHTOLD, W., and FLUHLER, H.: 'Dielectric properties of natural materials'. IEEE Int. Antennas and Propagation Society Symposium, 21–26 June 1998, Vol. 4, pp. 2002–2005

SCOTT, H. H., CARROLL, R. D., and CUNNINGHAM, D. R.: 'Dielectric constant and electrical conductivity measurements of moist rock: a new laboratory method', *J. Geophys. Res.*, 1967, **72**, pp. 5101–5115

TRAN, S. M., and McPHUN, M. K.: 'Obtaining unique solutions to Hanai's equation as used in Wobschall's semidisperse model of moist soil', *IEEE Trans.*, 1981, **GE-19**, pp. 69–70

WALKER, P. D., and BELL, M. R.: 'Subsurface permittivity estimation from ground-penetrating radar measurements'. Record of IEEE 2000 Int. Radar Conf., 2000, pp. 341–346

Chapter 5

Antennas

5.1 Introduction

Surface-penetrating radar presents the system designer with significant restrictions on the types of antennas that can be used. The propagation path consists in general of a lossy, inhomogeneous dielectric, which, in addition to being occasionally anisotropic, exhibits a frequency dependent attenuation and hence acts as a lowpass filter. The upper frequency of operation of the system, and hence the antenna, is therefore limited by the properties of the material. The need to obtain a high value of range resolution requires the antenna to exhibit ultra-wide bandwidth, and in the case of impulsive radar systems, linear phase response. The requirement for wide bandwidth and the limitations in upper frequency are mutually conflicting and hence a design compromise is adopted whereby antennas are designed to operate over some portion of the frequency range 10 MHz to 5 GHz depending on the resolution and range specified. The requirement for portability for the operator means that it is normal to use electrically small antennas, which consequently results generally in a low gain and associated broad polar radiation patterns. The classes of antennas that can be used are therefore limited, and the following factors have to be considered in the selection of a suitable design; large fractional bandwidth, low time sidelobes and in the case of separate transmit and receive antennas, low crosscoupling levels. The interaction of the reactive field of the antenna with the dielectric material and its effect on antenna radiation pattern characteristics must also be considered.

This Chapter should provide a useful guide to a complex subject but it is not intended to reduce the need for a designer to consult those references cited. Practically it is found that provided an antenna is properly matched it will couple well into a dielectric. The aspects of coupling, particularly as a function of distance from the interface, are described in detail by the authors cited, and for those interested the references should provide a useful source.

Recent interest in ultrawideband radar systems has coincided with the development of additional antenna designs, which can provide suitable performance, and

much work has been carried out on the development of antennas for ECM and ECCM applications as well as the propagation of high energy electromagnetic pulses. A useful reference to the general case of 'Antennas in matter' is given by King and Smith [1].

Further considerations in the selection of a suitable type of antenna are the type of target and the type of radar system. Where the target is, for example, a planar surface then linear polarisation is the obvious choice for the system designer. Where, however, the target is a buried pipe or cable then the backscattered field exhibits a polarisation characteristic, which is independent of the state of polarisation of the incident field. For linear targets it is possible to use orthogonally disposed transmit and receive antennas as a means of preferential detection. Essentially the received signal varies sinusoidally with angle between the antenna pair and the target. As it is inconvenient to physically rotate the antenna it is also possible to electronically switch (commutate) the transmit/receive signals to a set of multiple co-located antenna pairs. A further step along this overall strategy is to employ circular polarisation, which is essentially a means of automatically rotating the polarisation vector in space. However, circular polarisation inherently requires an extended time response of the radiated field, and in consequence either hardware or software deconvolution of the received signal is needed.

It has been found that very large diameter pipes exhibit depolarising effects, not from the crown of the pipe but from the edges. The choice of polarisation dependent schemes should thus be considered very carefully as it may not be possible to cover all possible sizes of targets with one antenna/polarisation scheme.

Where the radar system is a time domain system that applies an impulse to the antenna, the requirement for linear phase response means that only a limited number of types of antenna can be used unless the receiver uses a matched filter to deconvolve the effect of the frequency dependent radiation characteristics of the antenna. Where the radar system is frequency modulated or synthesised, the requirement for linear phase response from the antenna can be relaxed and log periodic horn or spiral antennas can be used as their complex frequency response can be corrected if necessary by system calibration.

Although a full analysis should consider the case of an impulse and consequently a full range of frequencies, it is instructive to examine the case of a single frequency as this provides an understanding as to the resultant radiation patterns of an antenna situated over a half-space.

The general situation of an antenna adjacent to a lossy half-space or indeed fully immersed into lossy materials has been considered by a number of workers. In this case of an electrically small linear antenna as shown in Figure 5.1 with a uniform current distribution, the electric and magnetic field components in free space are given by:

$$H_\phi = \frac{I_0 h}{4\pi} e^{-jkr} \left(\frac{jk}{r} + \frac{1}{r^2} \right) \sin\theta \tag{5.1}$$

$$E_r = \frac{I_0 h}{4\pi} e^{-jkr} \left(\frac{2\eta}{r^2} + \frac{2}{j\omega e r^2} \right) \cos\theta \tag{5.2}$$

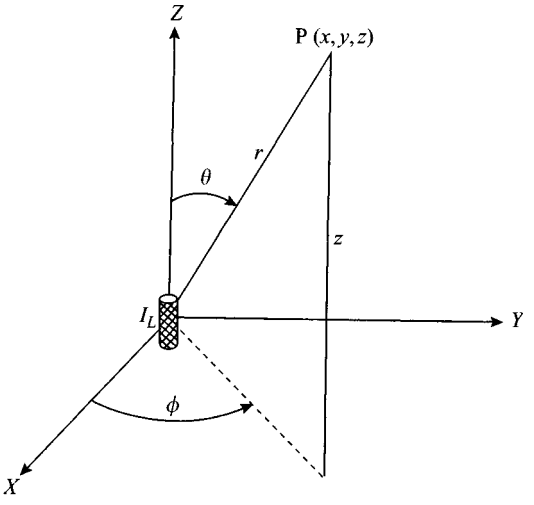

Figure 5.1 Electrically small antenna

$$E_\theta = \frac{I_0 h}{4\pi} e^{-jkr} \left(\frac{j\omega\mu}{r} + \frac{1}{j\omega e r^2} + \frac{\eta}{r} \right) \sin\theta \tag{5.3}$$

In the reactive field of the antenna when r is small the most important term is H_ϕ, which varies as $1/r^2$, and in E_r and E_ϕ those terms which vary as $1/r^3$. At large distances from the source the terms of E and H which are most significant are those varying as $1/r$. In the case of a half-wave dipole the far field intensity is

$$|E_\phi| = \frac{60 I_m}{r} \left(\frac{\cos\left(\frac{\pi}{2}\cos\theta\right)}{\sin\theta} \right) \tag{5.4}$$

The typical radiation pattern is shown in Figure 5.2.

In the case of an aperture antenna, as might be used in an FMCW or stepped frequency radar, the field at a point P(x, y, z) some distance from the aperture is given by the scalar field F(P) which is known as the Fresnel–Kirchhoff scalar diffraction field.

It is derived by integrating over the aperture area all elements $d\alpha$ and $d\beta$, comprising the radiating structure.

$$\mathrm{F(P)} = \frac{1}{4\pi} \int_{\text{area}} \mathrm{G}(\alpha,\beta) \frac{e^{-jkr}}{r} \left(\left(jk + \frac{1}{r} \right) \cos(n,r) + jk\cos(n,s) \right) d\alpha d\beta \tag{5.5}$$

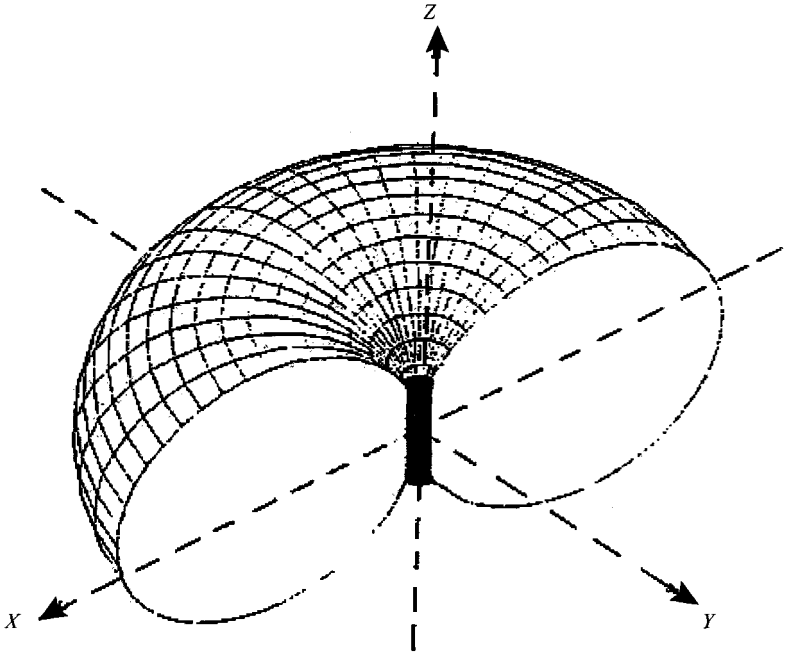

Figure 5.2 Radiation pattern of an electrically small antenna

where $G(\alpha, \beta)$ is the illumination of the field across the aperture, $k = 2\pi/\lambda$, n, r is the angle between the normal to the aperture and the r direction, and n, s is the angle between the normal to the aperture and the phase illumination across the aperture.

The expression for F(P) is traditionally separated into three regions depending on the assumptions made to solve the problem.

The first region is defined as the reactive near field and exists close to the aperture. It is generally considered that the above integral formulation is not rigorous as the boundary conditions are undefined.

The Fresnel region is considered to extend from the reactive near field and takes in a radiating near field region which extends to $2D^2/\lambda$, where D is the aperture's maximum dimension.

Skolnik [2] details a number of approximations which enable the scalar field in the Fresnel region to be defined as

$$F(P) = \frac{(1 + \cos\theta)}{2\lambda} \frac{e^{-jkz}}{R} \int_{\text{area}} G(\alpha, \beta) \exp\left(\frac{(x - \alpha)^2 + (y - \beta)^2}{2z} \right) d\alpha d\beta \tag{5.6}$$

However, these approximations restrict the Fresnel approximations to fields $\geq 8\lambda$ from the antenna aperture.

Table 5.1 Power density patterns in air and dielectric

Plane	Power	
	$S(\theta_\alpha)$ radiation pattern in air	$S(\theta_\alpha)$ radiation pattern in dielectric
H	$\alpha\left(\dfrac{\cos\theta_a}{\cos\theta_a + \eta\cos\theta_d}\right)^2$	$\alpha\eta\left(\dfrac{\eta\cos\theta_d}{\cos\theta_a + \eta\cos\theta_d}\right)^2$
E	$\alpha\left(\dfrac{\cos\theta_a\cos\theta_d}{\eta\cos\theta_a + \cos\theta_d}\right)^2$	$\alpha\eta\left(\dfrac{\eta\cos\theta_a\cos\theta_d}{\eta\cos\theta_a + \cos\theta_d}\right)^2$

Therefore any calculations relating to antenna radiation should consider the reactive near field and close-in Fresnel region as being the most likely zones of operation.

It is important to appreciate the effect of the material in close proximity to the antenna. In general this material, which in most cases will be soil or rocks, or indeed ice, can be regarded as a lossy dielectric and by its consequent loading effect can play a significant role in determining the low frequency performance of the antenna and hence surface-penetrating radar. The behaviour of the antenna is intimately linked with the material and, in the case of borehole radars, the antenna actually radiates within a lossy dielectric, whereas in the case of the surface-penetrating radar working above the surface the antenna will radiate from air into a very small section of air and then into a lossy half-space formed by the material. The behaviour of antennas both within lossy dielectrics and over lossy dielectrics has been investigated by Junkin and Anderson [3], Brewitt-Taylor *et al.* [4], Burke *et al.* [5] and Rutledge and Muha [6], and is well reported. The propagation of electromagnetic pulses in a homogeneous conducting earth has been modelled by Wait [7], and King and Nu [8], and the dispersion of rectangular source pulses suggests that the time domain characteristics of the received pulse could be used as an indication of distance.

The interaction between the antenna and the lossy dielectric half-space is also significant as this may cause modification of the antenna radiation characteristics both spatially and temporally and should also be taken into account in the system design. In the case of an antenna placed on an interface, the two most important factors are the current distribution and the radiation pattern. At the interface, currents on the antenna propagate at a velocity which is intermediate between that in free space and that in the dielectric. In general the velocity is retarded by $\sqrt{(\varepsilon_r + 1)/2}$.

The net result is that evanescent waves are excited in air whereas in the dielectric the energy is concentrated and preferentially induced by a factor of n^3:1.

The respective calculated far field power density patterns, in both air and dielectric, are given by Rutledge and Muha [6], and these are plotted for relative dielectric constants of 4, 6, 8 and 10 in Figures 5.3 and 5.4 (see also Table 5.1 and the Mathcad worksheet C5, antenna over dielectric).

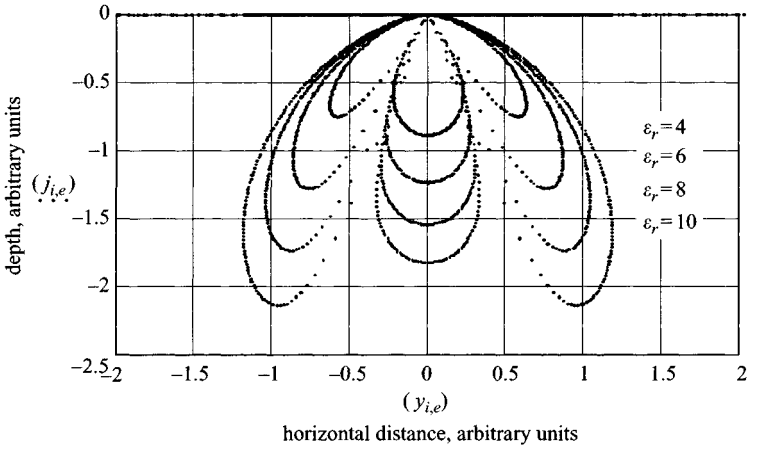

Figure 5.3 *E-plane plot of far-field power density of a current element radiating into a dielectric*

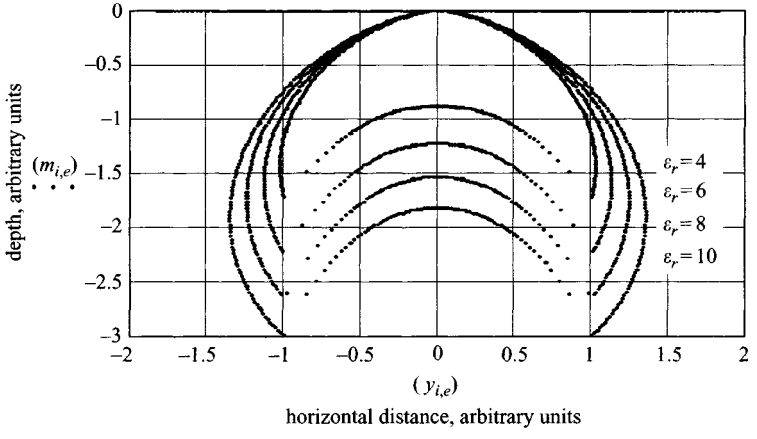

Figure 5.4 *H-plane plot of far-field power density of a current element radiating into a dielectric*

The above expressions assume that the current source contacts the dielectric whereas a more general condition is when the antenna is just above the dielectric. The sidelobes in the pattern are a direct result of reactive field coupling. A significant practical problem for many applications is the need to maintain sufficient spacing to avoid mechanical damage to the antenna. It can therefore be appreciated that the effect of changes in distance between the antenna and half-space cause significant variation in the resultant radiation patterns in the dielectric.

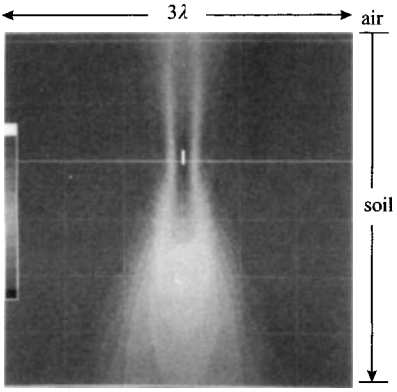

Figure 5.5 *Reconstruction of buried line scatterer for the model scanning at a height of 0.0625λ*

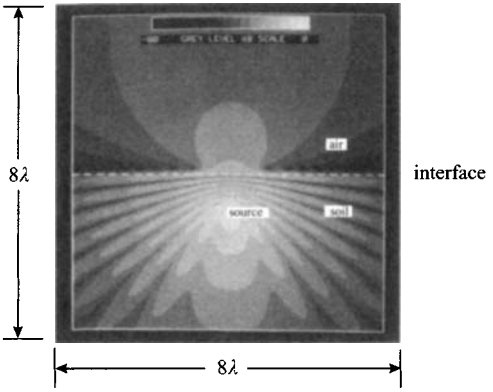

Figure 5.6 *Field pattern of a buried line source in a material* $\varepsilon_r = 16$, $\alpha = 0.5\,\mathrm{dB\,m^{-1}}$, $D = \lambda$

Where the source interface space is increased, the antenna field patterns are modified by a reduction in the effect of the reactive field.

This situation was considered by Junkin and Anderson [3], and the radiation characteristics of the antenna can be considered by examining two conditions; the first is where a line source is placed above and radiates into a half-space (Figure 5.5), and the other case where a line source is placed within and radiates out of a half-space [3]. In the case of a source above a half-space where the source–interface spacing is very small, the reactive fields are capable of inducing currents in the half-space dielectric, which subsequently become propagating waves. The situation of the waves reflected from a target can be considered from the point of view of a line source embedded in the dielectric half-space. This radiated field in free space is shown in Figure 5.6 [3] and it can be seen that surface waves play a significant role.

The overall configuration is further complicated by the use of separate transmit and receive antennas which causes a convolution of the separate radiation patterns to form a composite pattern.

The use of separate transmit and receive antennas is dictated by the difficulty associated with operation with a single antenna which would require an ultra-fast transmit–receive switch. As it is not yet possible to obtain commercially available ultra-fast transmit–receive switches to operate in the sub-nanosecond region with sufficiently low levels of isolation between either transmit and receive ports or break-through from the control signals, most surface-penetrating radar systems use separate antennas for transmission and reception in order to protect the receiver from the high level of transmitted signal. Therefore the crosscoupling level between the transmit and receive antenna is a critical parameter in the design of antennas for surface-penetrating radar and satisfactory levels are usually achieved by empirical design methods. Typically a parallel dipole arrangement achieves a mean isolation in the region of −50 dB, whereas a crossed dipole arrangement can reduce levels of crosscoupling to −60 dB to −70 dB. For the crossed dipole arrangement such levels are highly dependent on the standard of mechanical construction, and a high degree of orthogonality is necessary.

The crossed dipole is sensitive to variations in antenna to surface spacing and it is important to maintain the plane of the antenna parallel with the plane of material surface to avoid degrading the isolation.

In the following Sections we consider the various types of antenna that can be used with surface-penetrating radar. The two general types of antenna that are useful to the designer of surface-penetrating radar fall into two groups: dispersive and nondispersive antennas.

Examples of dispersive antennas that have been used in surface-penetrating radar are the exponential spiral, the Archimedean spiral, the logarithmic planar antenna, the Vivaldi antenna and the exponential horn. Examples of nondispersive antennas are the TEM horn, the bicone, the bow-tie, the resistive, lumped element loaded antenna or the resistive, continuously loaded antenna. A typical antenna used in an impulse radar system would be required to operate over a frequency range of a minimum of an octave and ideally at least a decade, for example, 100 MHz–1 GHz. The input voltage driving function to the terminals of the antenna in an impulse radar is typically a Gaussian pulse and this requires the impulse response of the antenna to be extremely short. The main reason for requiring the impulse response to be short is that it is important that the antenna does not distort the input function and generate time sidelobes. These time sidelobes would obscure targets that are close in range to the target of interest; in other words, the resolution of the radar can become degraded if the impulse response of the antenna is significantly extended. All of the antennas used to date have a limited low frequency performance unless compensated and hence act as highpass filters; thus the current input to the antenna terminals is radiated as a differentiated version of the input function.

In general it is reasonable to consider that the far field radiated electric field is proportional to the derivative of the antenna current.

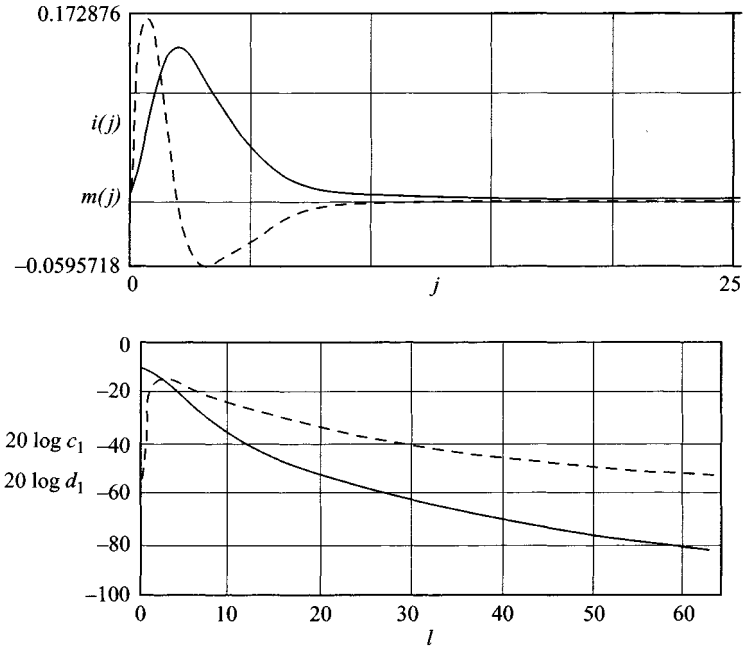

Figure 5.7 *Time domain and frequency domain response of an antenna when driven by an impulse*
Continuous line = input; dotted line = output; upper = time domain; lower = frequency domain

It has been shown that for a physically realisable causal pulse both the initial value of the antenna current and the initial value of the first derivative of the antenna current must be zero.

If we assume that

$$i(t) = I\left(\frac{t^2}{T}\right)e^{-2t/T} \tag{5.7}$$

then

$$e(t) = k\frac{\mathrm{d}i(t)}{\mathrm{d}t} \tag{5.8}$$

The current waveform and the radiated electric field are shown in Figure 5.7.

The following Sections of this Chapter will consider the various classes of antennas that can be successfully used. While these classes can be sub-divided into the classes of dispersive and nondispersive antennas, there are actually significant differences in design and in operation of different types within these broad categories. Therefore this Chapter considers element antennas, travelling wave antennas,

frequency independent antennas, aperture antennas and array antennas separately. It is useful, however, to consider the general requirements of the overall class of antennas, which can broadly be considered as being frequency independent. There are a number of requirements for frequency independent operation and these are as follows:

(i) excitation of the antenna from the region of the antenna from which high frequencies are radiated
(ii) a transmission region formed by the inactive part of the antenna between the feed point and the active region. This zone should produce negligible far field radiation
(iii) an active region from which the antenna radiates strongly because of an appropriate combination of current magnitude and phases
(iv) an inactive region created by means of reflection or absorption beyond the active region. It is essential that there is a rapid decay of currents beyond the active region. Efficient antennas achieve this by means of radiation in the active region, whereas the less efficient use resistive loading techniques to achieve this characteristic
(v) a geometry defined entirely by angles, i.e. the biconical dipole, conical spiral, planar spiral, are all defined by angle. These antennas maintain their performance over a frequency range defined by the limiting dimensions. Provided that in these cases, an extended impulse response is acceptable, these antennas provide a performance that can be useful.

5.2 Element antennas

Element antennas such as monopoles, dipoles, conical antennas and bow-tie antennas have been widely used for surface-penetrating radar applications.

Generally they are characterised by linear polarisation, low directivity and relatively limited bandwidth, unless either end loading or distributed loading techniques are employed, in which case bandwidth is increased at the expense of radiation efficiency. Various arrangements of the element antenna have been used such as the parallel dipole and the crossed dipole, which is an arrangement that provides high isolation and detection of the crosspolar signal from linear reflectors.

It is useful to consider those characteristics of a simple normally conductive dipole antenna which affect the radiation response to an impulse applied to the antenna feed terminals.

As shown in Figure 5.8, two current and charge impulses will travel along the antenna elements until they reach each end. At the end of the antenna the charge impulse increases while the current collapses. The charge at the end of the antenna gives rise to a reflected wave carried by a current travelling back to the antenna feed terminals. This process continues for a length of time defined by the ohmic losses within the antenna elements. As far as the radiation field is concerned the

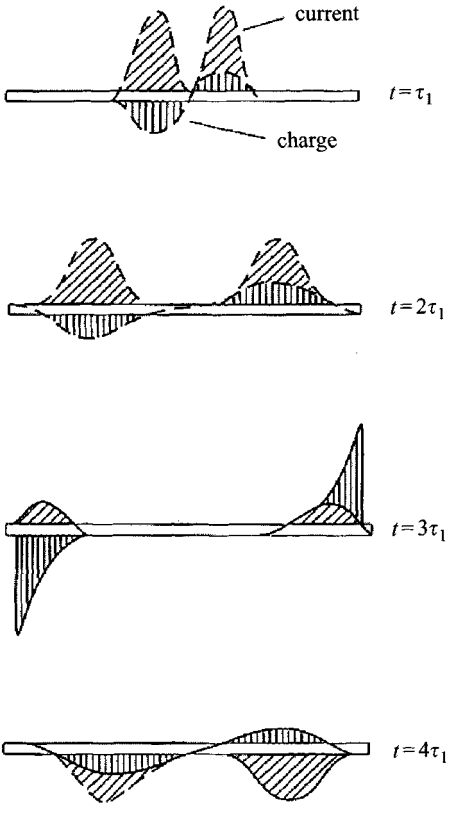

Figure 5.8 *Current and charge distribution on a conducting dipole antenna due to an applied impulse*

relevant parameters, electric field strength, displacement current and energy flow can be derived from consideration of Maxwell's equation.

The electric field component E_z is given by Kappen and Monich [9] as

$$E_z = -\frac{1}{4\pi\varepsilon_0}\int_{l_1}^{l_2}\left\{\frac{1}{c}\frac{\mathrm{d}l}{\mathrm{d}t}+\frac{\partial q}{\partial z'}\right\}\frac{1}{r}\,\mathrm{d}z' \tag{5.9}$$

and must equal zero at the surface of the antenna. This condition can only be satisfied at certain points along the element and implies that for a lossless antenna there is no radiation of energy from the impulse along the element. The radiated field is therefore caused by discontinuities, that is the feed point and end point are the prime sources of radiation. As would be expected, the time sequence of the radiated field can be visualised by the electric field lines as shown in Figure 5.9.

As it is required to radiate only a single impulse, it is important to eliminate either the reflection discontinuities from the far end of the antenna by end loading or reduce the amplitude of the charge and current reaching the far end. The latter can be

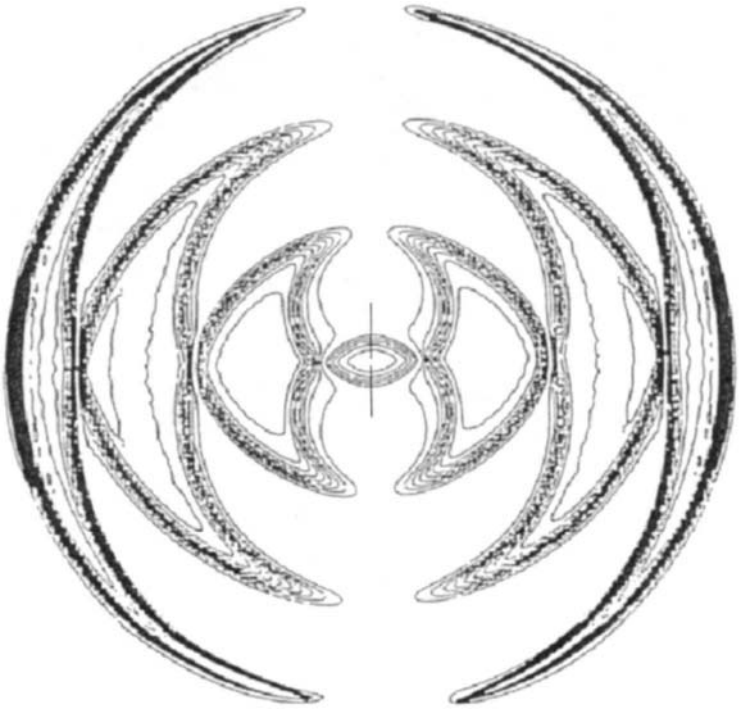

Figure 5.9 Radiated field pattern from a conducting dipole element due to an applied impulse

achieved either by resistively coating the antenna or by constructing the antenna from a material such as Nichrome, which has a defined loss per unit area. In this case the antenna radiates in a completely different way as the applied charge becomes spread over the entire element length and hence the centres of radiation are distributed along the length of the antenna.

In essence, the electric field E_z must now satisfy the condition

$$-\frac{1}{4\pi\varepsilon_0}\int_{l_1}^{l_2}\left\{\frac{1}{c}\frac{\mathrm{d}l}{\mathrm{d}t}+\frac{\partial q}{\partial z'}\right\}\frac{1}{r}\,\mathrm{d}z' = R'I \tag{5.10}$$

which implies that some dispersion takes place.

The electric field lines for the lossy element are now different from the lossless case and are shown in Figure 5.10. Further analysis of the radiation characteristics of a resistively coated dipole antenna is given by Randa *et al.* [10] and Esselle and Stuchly [11].

The parameters of the antenna such as input resistance, resistivity profile, etc. have all been extensively treated in a classic paper by Wu and King [12]. Lumped

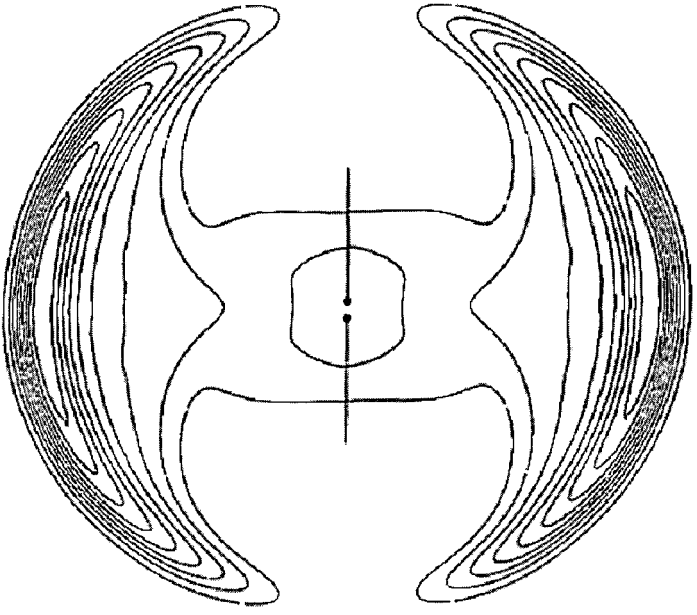

Figure 5.10 Radiated field pattern from a resistively loaded dipole element due to an applied impulse

element resistors can be placed at a distance $\lambda/4$ from the end of the antenna [13] and a travelling wave distribution of current can be produced by suitable values of resistance. The distribution of current varied almost exponentially with distance along the element. Instead of lumped element resistors a continuously distributed constant internal impedance per unit length can be used. The parameters of a centre fed cylindrical antenna can be characterised by a distribution of current equivalent to a travelling wave.

The cylindrical antenna with resistive loading has been shown by Wu and King [12] to have the following properties. The far field pattern of the antenna comprised both real and imaginary components, i.e.

$$F_m = \sqrt{F_r^2 + F_i^2} \tag{5.11}$$

where for a quarter-wave antenna:

$$F_r = \frac{1 + \cos^2\theta - 2\cos\theta\left(\frac{\pi}{2}\cos\theta\right)}{\left(\frac{\pi}{2}\right)\sin^3\theta} \tag{5.12}$$

$$F_i = \frac{-\frac{\pi}{2}\sin^2\theta + (1+\cos^2\theta)\cos\theta\left(\frac{\pi}{2}\cos\theta\right)}{\left(\frac{\pi}{2}\right)\sin^3\theta} \tag{5.13}$$

The efficiency of the antenna is given as

$$\eta = \frac{P_r}{P_r + P_a} \tag{5.14}$$

where P_r is radiated power and P_a is absorbed power.

For a resistively loaded antenna of the Wu–King type the efficiency is ~10% but rises to a maximum of 40% for antenna lengths of 40.

The resistivity taper profile for a cylindrical monopole has the form given by Rao [14],

$$R(z) = \frac{R_0}{1 - z/H} \tag{5.15}$$

where R_0 is the resistivity at the drive point of the element, H is the element length and z is the distance along the antenna.

A graph of resistivity versus length for a 200 mm element is shown in Figure 5.11. The overall efficiency of this type of antenna can be improved by reducing the value of R_0 and an increase of from 12% to 28% by reduction of R_0 to 0.3 R_0 was shown by Rao. Typical graphs of return loss and crosscoupling are shown in Figures 5.12 and 5.13. The typical time domain response of a continuously resistively loaded dipole is shown in Figure 5.14.

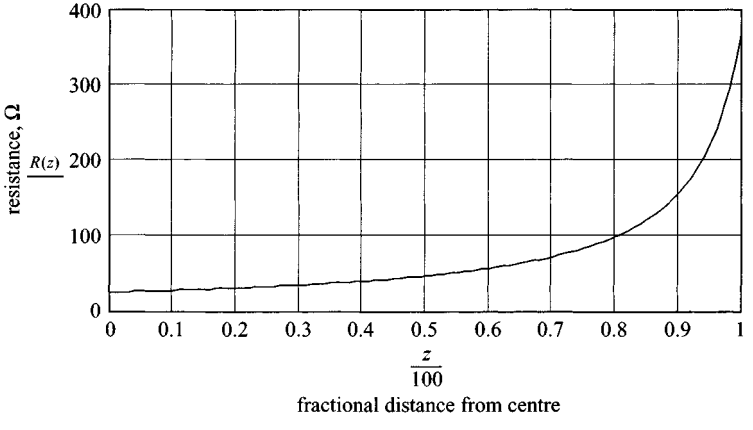

Figure 5.11 Resistivity profile of a 200 mm element

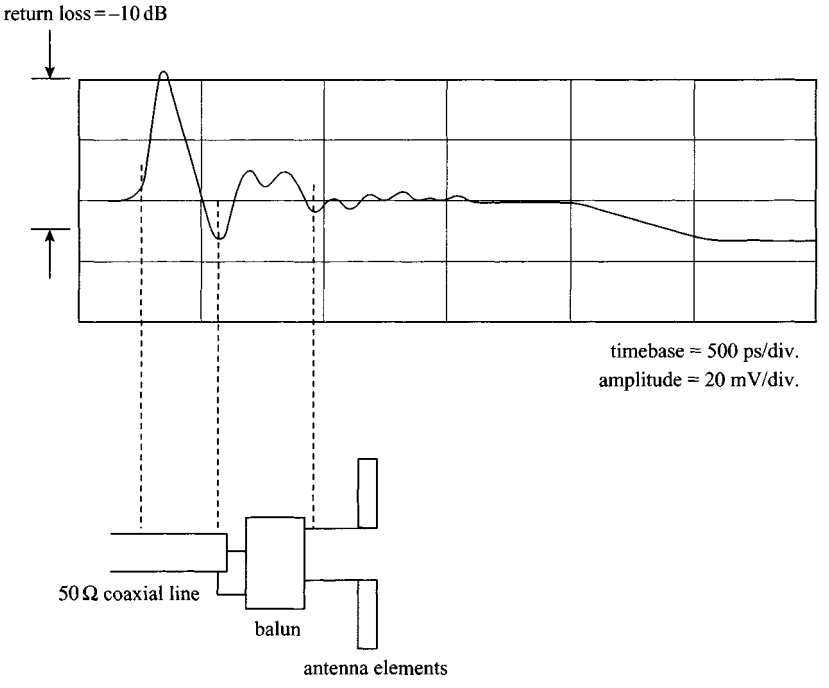

Figure 5.12 Time domain reflectometer return loss of a resistively loaded dipole

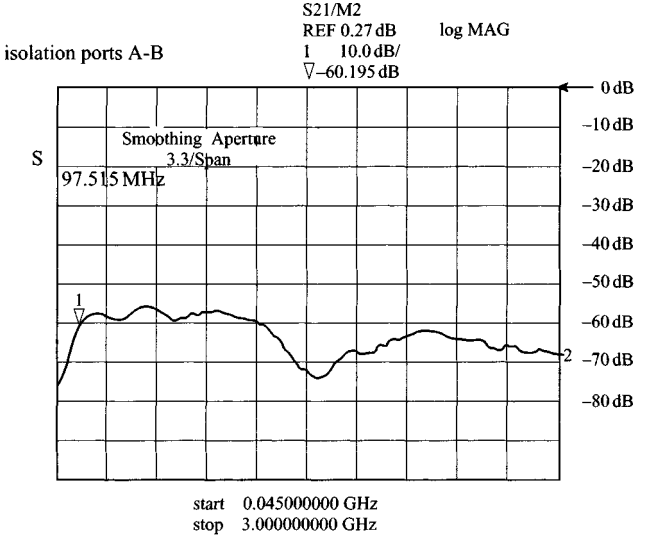

Figure 5.13 Crosscoupling of a pair of resistively loaded dipoles 45 MHz to 3 GHz

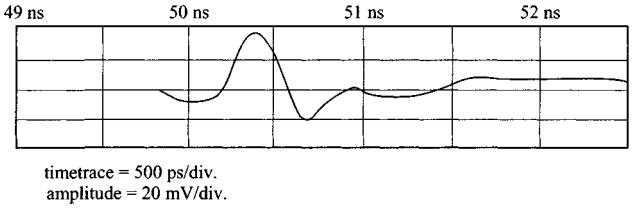

Figure 5.14 Free space impulse response of a nonresonant target using resistively loaded dipoles

Further improvement in bandwidth can be gained by matching the antenna with a compensation network, and a field probe has been developed, with a bandwidth of 20 MHz to 10 GHz, by Esselle and Stuchly [11]. Obviously the use of a compensation network further reduces efficiency, but with a high impedance receiver probe, a frequency range of 10 MHz to 5 GHz can be achieved.

Resistively loaded dipoles have been used as electric field probes for EMC measurement applications, and although the frequencies of operation are well in excess of that used for surface-penetrating radar applications, it is useful to consider the general approach adopted by Maloney and Smith [15].

Antennas have been developed by Kanda, initially using 8 mm dipoles, to measure frequencies up to 18 GHz, and subsequently 4 mm dipoles were used by Kanda (Randa *et al.* [10]) to measure over the frequency range 1 MHz to 40 GHz with an error of ±4 dB. The transfer function of this antenna is in the order of −50 dB, which illustrates the penalty which is paid for ultra-wideband width operation.

A design which offers improved efficiency over the continuously loaded resistive antenna is based on a pair of segmented blade antennas arranged in a butterfly configuration and fed in phase. Each blade consists of a series of concentric conducting rings connected together by chip resistors. Radial cuts are used to reduce transverse currents. The efficiency of this class of antenna is higher than the continuously loaded dipole without serious degradation of the time domain response.

The triangular bow-tie antenna has been widely used in commercial surface-penetrating radar systems. A triangular bow-tie dipole of 35 cm length with a 60° flare angle can provide useful performance over an octave bandwidth of 0.5 GHz to 1 GHz with a return loss of better than 10 dB, as shown by Brown and Woodward [16]. Evidently without some form of end loading such an antenna would not be immediately suitable for use with impulse radar systems and the triangular antenna normally uses end loading to reduce the ringing that would normally occur in an unloaded triangular plate antenna. The technique can also be used with a folded dipole and the use of terminating loads results in a transient response equivalent to one and a half cycles [17].

An alternative approach to antenna design is based on electric dipole radiation from a Hertzian magnetic dipole as developed by Harmuth [18], and Harmuth and Ding-Rong [19, 20], provided that the radiation components from current flowing in one direction can be isolated. The advantage of using the Hertzian magnetic dipole

lies in removing the need, as in the case of the electric dipole, to produce large currents and charges which do not contribute significantly to the far field radiation field.

In practice the generator must be shielded and absorbing ferrite is used to reduce currents flowing on the shield. The main advantage of the Hertzian magnetic dipole is the ability to produce very short pulses from electrically small antennas.

5.3 Travelling wave antennas

In this Section we shall consider the use of antennas capable of supporting a forward travelling TEM wave. In general, such antennas consist of a pair of conductors either flat, cylindrical or conical in cross-section, forming a V structure in which radiation propagates along the axis of the V structure as shown in Figure 5.15. Although resistive termination is used, this type of antenna has a directivity in the order of 10–15 dB, hence useful gain can still be obtained even with a terminating loss in the order of 3 dB to 5 dB. The travelling wave current on one of the cylindrical elements of a V antenna is given by Iizuka [21] and is also discussed by King [22],

$$I_t = I_a e^{-j\beta z} \tag{5.16}$$

Hence the azimuthal radiation field E is given by

$$E = \frac{j\omega\mu e^{-j\beta r}}{4\pi} \int_0^l I_0 e^{-j\beta z(1-\cos\theta)} \sin\theta \, dz \tag{5.17}$$

where R is the loading resistance, l is the length of the element, z is the distance from radiating source and θ is the angle in the H-plane.

This simplifies to

$$E_T(\theta) = \frac{1 - \exp(-j\beta(l_0 - l_1)(1 - \cos\theta))}{1 - \cos\theta} \sin\theta \tag{5.18}$$

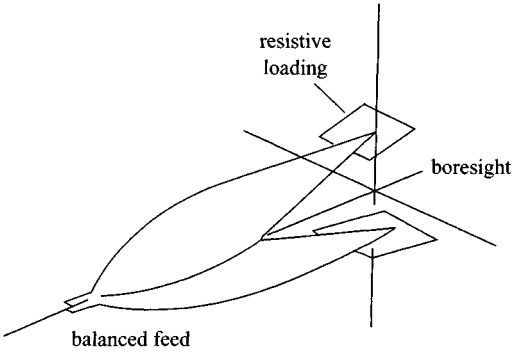

Figure 5.15 Travelling wave TEM antenna

However, a standing wave also exists caused by the resistive termination at the end of the antenna, and the contribution from this is given by

$$E_S(\theta) = j\frac{\exp(-j\beta(l_0 - l_1)(\cos\theta))}{\sin\theta}\left[\cos\left(\frac{\pi}{2}\cos\theta\right)\right.$$
$$\left.+j\left(\sin\left(\frac{\pi}{2}\cos\theta\right) - \cos\theta\right)\right] \tag{5.19}$$

The resultant field from one element can be derived from the sum of the contribution

$$E'(\theta) = E_T(\theta) + E_S(\theta) \tag{5.20}$$

and hence the field from both elements is

$$E = E'_U(\theta) + E_L(\theta) \tag{5.21}$$

where U denotes the upper element and L denotes the lower element.

The antenna will in fact radiate an impulse which is extended in time as a consequence of the geometry of the antenna. The pulse distortion on boresight is given by Theodorou *et al.* [23],

$$t = \frac{L}{v}(1 - \cos\alpha) \tag{5.22}$$

where α is the half-angle between the elements, L is the element length and v is the phase velocity of waves along the antenna.

Evidently a small flare angle and short element length help in reducing pulse extension.

The electric field on boresight is related to the time derivative of input current and is given by

$$E = \frac{-\mu_0 L \sin\alpha}{2\pi r}\frac{\partial I_1(t - r/u)}{\partial t} \tag{5.23}$$

The impedance of the antenna should vary in such a way that the derivative of impedance at the feed and end parts is a minimum and along the antenna is low.

Typically the characteristic impedance is given as a function of distance x as

$$Z_0(x) = Z_x \exp(-K_1 \cos K_2 x) \tag{5.24}$$

Hence

$$\frac{dZ_0(x)}{dx} \to 0 \quad \text{for } K_2 x = 0 \vee \pi \tag{5.25}$$

Usually the feed impedance is of the order of 50 Ω and the end impedance is desired to be equal to that of free space (377 Ω). However, there is usually a difference between the transmission line wave impedance characteristic and that of waves in free space, and a design to meet given criteria in terms of return loss must take this effect into account.

Graphs of both typical antenna impedance and rate of change of impedance as a function of length are shown in Figures 5.16 and 5.17.

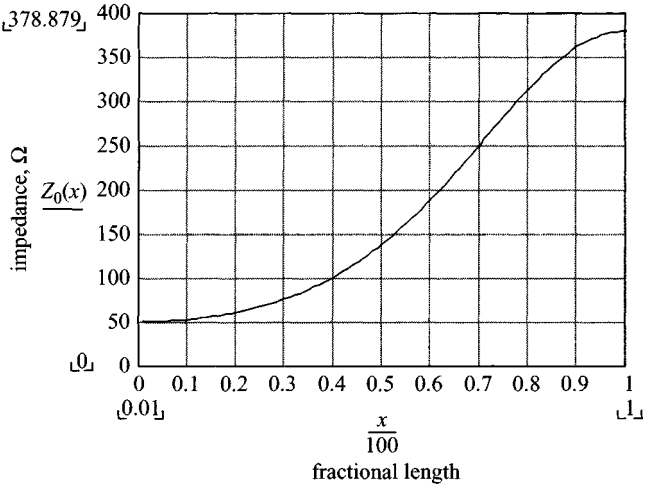

Figure 5.16 Characteristic impedance of a travelling wave antenna

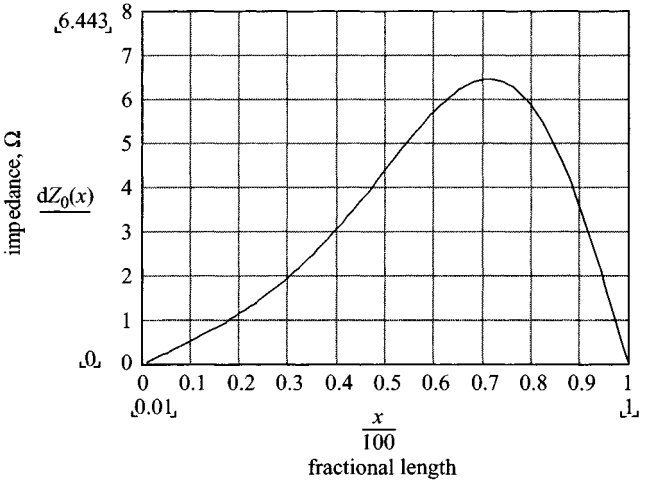

Figure 5.17 Rate of change of impedance of a travelling wave antenna

Using this characteristic a typical antenna-antenna time domain response is shown in Figure 5.18.

Improved directivity can be obtained using a V-conical antenna as shown by Shen *et al.* [24]. This is formed by a pair of triangular metal plates bent around a cone. The antenna is characterised by two angles, the flare half-angle and the azimuthal angle Ø. Further developments of the TEM horn design from the original design first described

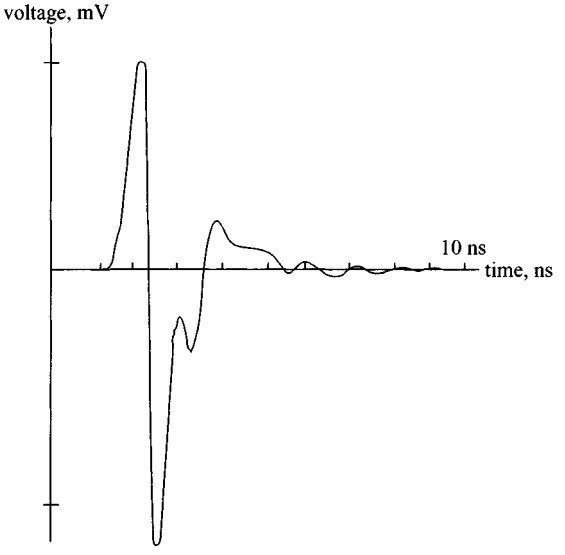

Figure 5.18 Time domain response of a pair of travelling wave antennas used in a face-to-face configuration

by Wohlers [25] are to be found in papers by Daniels [26], Evans and Kong [27], Reader *et al.* [28] and Foster and Tun [29].

A further development of the TEM horn is given by Martel *et al.* [30].

The antenna is composed of a set of spread 'fingers' forming the shape of a horn as shown in Figures 5.19 and 5.20. Each finger is a wire with a diameter of 1 mm and is resistively loaded at different locations along the length of the antenna. The feed component for the antenna is comprised of a 50 Ω coax, feeding a tapered parallel plate waveguide with a width of 30 mm and a height of 7 mm. A taper along the width of the top parallel plate is used as a transition to transform a 50 Ω unbalanced line into a 50 Ω balanced line.

Optimisation was undertaken on the geometry of the antenna, and the values and positions of the loaded resistances. The fixed parameters were the dimensions at the antenna feed point and the length of the antenna, which for practical purposes was set to 35 cm. The height and width of the horn aperture were the variable parameters of the geometry.

An investigation on the number of resistances was also undertaken. While the efficiency is not a critical issue, a compromise had to be found between the efficiency and the broadband response of the antenna. The usage of many resistances leads to a lower reflection coefficient but degrades the efficiency considerably. Reducing the number of resistances makes the antenna efficient but causes multiple reflections. After investigating the effect of the number of resistors on the performance of the antenna, the best compromise was to design the antenna with *five* resistors. The antenna has therefore been optimised with five resistors along the arms of the TEM

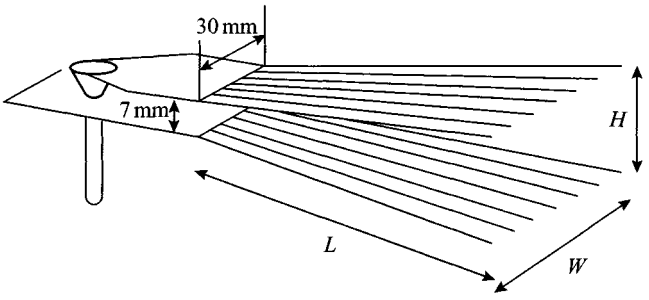

Figure 5.19 Antenna and feed geometry of loaded TEM horn

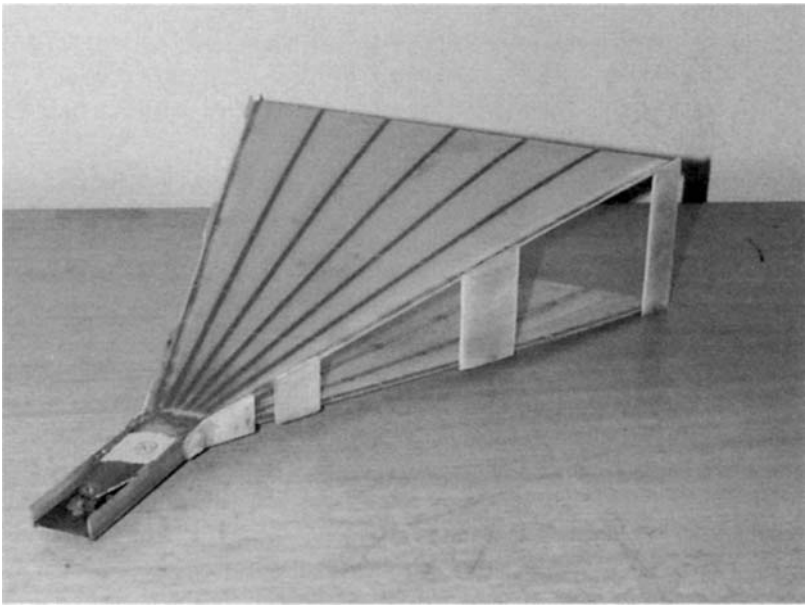

Figure 5.20 Photograph of loaded TEM horn

horn in order to achieve a satisfactory VSWR over the frequency range [100,1400] MHz. The method of moments (MoM) was used in the optimisation process. Within this framework the resistors were modelled as lumped loads.

An optimised geometry was determined with the following dimensions: $W = 30$ cm, $H = 10$ cm and $L = 35$ cm, where W is the aperture width of the horn, H is the aperture height of the horn and L is the length of the antenna.

Figure 5.21 shows the predicted VSWR in the frequency band [0,1400] MHz for the optimum design. The method using cascaded segments of strips agreed well

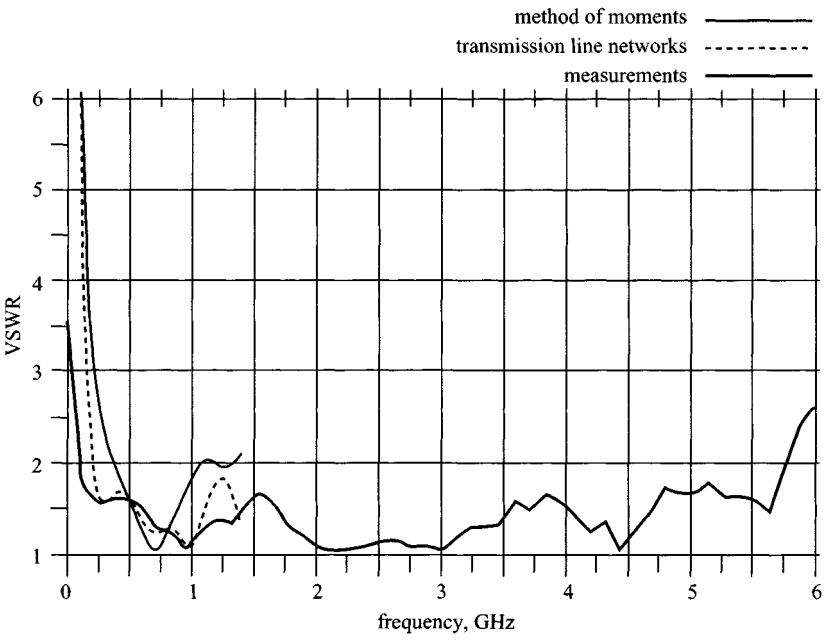

Figure 5.21 VSWR of loaded TEM horn antenna

with the MoM. The VSWR was better than 2 : 1 for frequencies between 400 and 1400 MHz. The best performance was achieved at 700 MHz.

The predicted time domain pulse of the optimum design is shown in Figure 5.22. The shape of the time domain antenna response is similar to a second derivative Gaussian signal. It can be seen that most of the internal reflections have been suppressed. The rate of decrease for the unwanted ringing is better than 9 dB/ns.

5.4 Impulse radiating antennas

Impulse radiating antennas (IRAs) are a class of focused aperture ultrawideband antennas designed to radiate extremely short electromagnetic pulses when fed by a fast rise time step waveform. Impulse radiating antennas (IRAs) have found applications such as foliage penetration, hostile target identification, buried object detection and broadband jamming. A typical IRA antenna is a reflector antenna fed by a pair of conical transmission lines connected in parallel at the focal point. A large (several metres) diameter reflector antenna is suitable for generating an impulsive radiated field amplitude of between 4 and 5 kVm^{-1} with a pulse duration of ~200 ps at a range of ~300 m. The spectrum of the radiated field extends from about 50 MHz to several GHz.

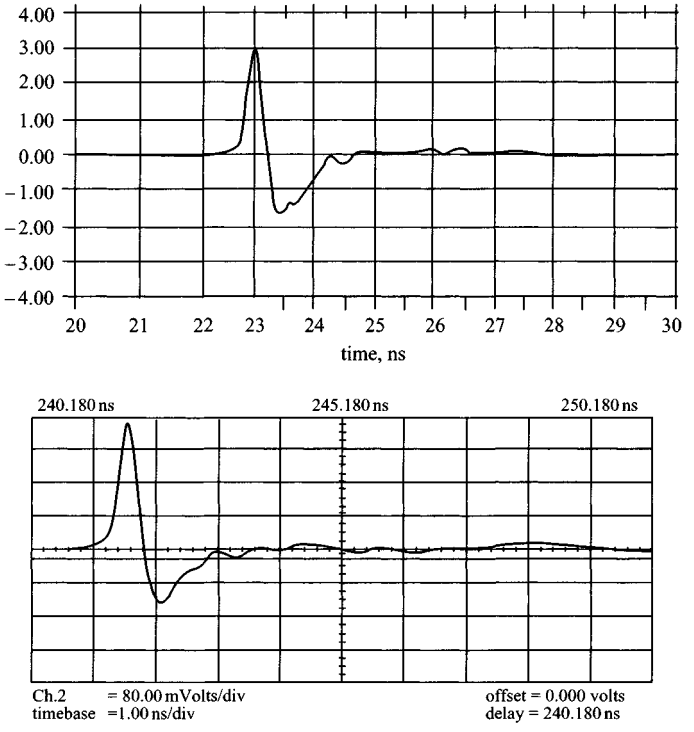

Figure 5.22 Predicted and actual pulse responses of TEM horn antenna

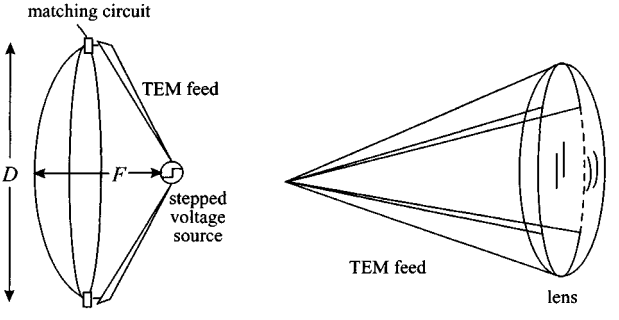

Figure 5.23 Generic constructions of impulse radiating antennas

IRAs are composed of a conical, nondispersive, TEM feed structure that is fed at the focal point of a reflector, although sometimes a lens may be used (see Figure 5.23). The radiated waveform is the time derivative of that applied to the feed because of diffraction effects. The reflector changes the TEM mode wave on the feed line into a plane wave and the gain of the antenna results in a very narrow beam of a degree or less.

Next Page

Much work has been carried out on the fundamental design of this type of antenna by Baum [31], Baum and Farr [32], Farr and co-workers [33–38], Buchenauer *et al.* [39] and Tyo *et al.* [40, 41]. For an IRA to radiate well collimated impulses, the feed point must be at the true focal point of either the reflector or the lens. Practical limitations result in defocusing, which has the adverse effect of distorting the radiated impulse and reducing the gain of the antenna. In addition to its use as a single element antenna, the IRA can be used in arrays. Tyo *et al.* [40] describe the development of a number of impulse radiating antennas (IRAs) for use in various ultra-wideband (UWB) and UWB high-power microwave (HPM) applications. Many of these antennas are designed to behave as differentiating antennas excited by a fast-rising step waveform, thereby resulting in a large-amplitude, narrow pulse in the far field. To mitigate some of the limitations of reflector IRAs and lens IRAs, a new class of IRAs – the array IRA – has been proposed and examined in a number of studies. The principal benefit that is realisable with an array IRA is the potential for electronic beam steering. Secondly, array IRAs will allow for far-field power combination from solid-state sources that are currently under development. In addition to these primary benefits, array IRAs provide a reduction in volume and the related mass of the antennas. It is important to note, however, that these benefits come at the cost of the added complexity associated with the precise timing of the array elements that is necessary for beam forming and far-field power combination. Further information on antenna design can be found at http://www.farr-research.com/, and an example of an IRA design is shown in Figure 5.24.

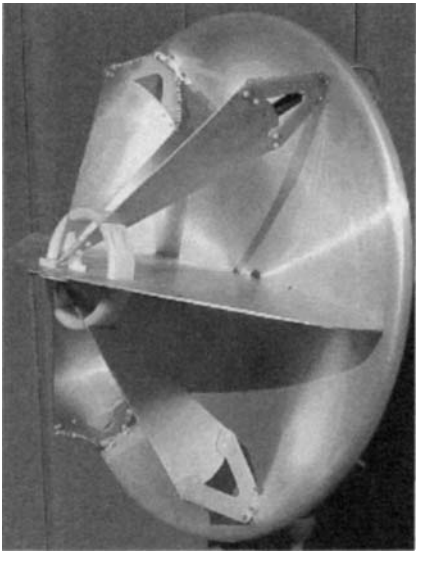

Figure 5.24 Impulse radiating antenna (Courtesy Farr Research Inc.)

5.5 Frequency independent antennas

This class of antennas has a geometry entirely defined by angles and exhibits a performance over a range of frequencies set by the overall dimensions of the structure. Typical examples are the biconical dipole, equiangular spiral and conical spiral. Log periodic structures can also provide broadband performance but are not completely defined in terms of angles [42].

Various developments of the spiral antenna or conical spiral antenna have been carried out by Miller and Landt [43], Pastol *et al.* [44], Dyson [45], Morgan [46], Kooy [47], Deschamps [48], Bawer and Wolfe [49] and Goldstone [50].

The impulse response of this class of antennas is extended and generally results in a 'chirp' waveform if the input is an impulse. The main reason for this is that the high frequencies are radiated in time before the low frequencies as a result of the time taken for the currents to travel through the antenna structure and reach a zone in which radiation can take place.

The geometry of the equiangular spiral is defined by

$$\rho = \kappa e^{a\phi} \tag{5.26}$$

as shown in Figure 5.25.

The two arm equiangular planar spiral can provide acceptable radiation patterns, which can be obtained with spirals of as little as 1.25 to 1.5 turns.

For a planar equiangular spiral the radiation pattern is bi-directional with equal lobes both front and back of the plane of the antenna. Uni-directional radiation can be achieved by backing the spiral with absorptive material on one side.

The near fields along the arms decay rapidly by as much as 20 dB per wavelength, and this reduction is a constant function of the ratio of the electrical length of the arm. Effectively the active arm length is a constant as frequency is increased; hence the effective aperture of the antenna increases with frequency. This characteristic of the equiangular spiral can also be viewed as a nonstationary phase centre,

Figure 5.25 Equiangular spiral antenna

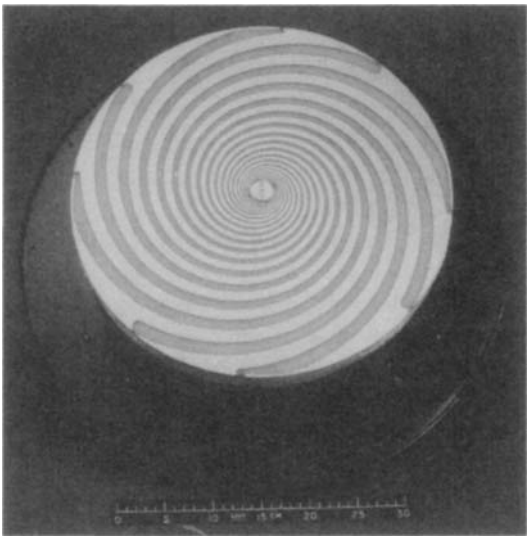

Figure 5.26 Photograph of multi-arm spiral antenna

which consequently causes dispersion of any impulsive signal applied to the feed terminals.

It is evident that at wavelengths which are of the same order as the length of the arms the polarisation of the radiated field is linear, and as the frequency is gradually increased becomes elliptical and then circular.

A photograph of a multi-arm equiangular spiral is shown in Figure 5.26. In this realisation eight separate arms are used to form a transmit pair arranged orthogonally to a receive pair and interleaved with screening arms to improve the isolation between the transmit and receive arms. Loading resistors were used to reduce late time currents. The radiation pattern of this antenna at 500 MHz is shown in Figure 5.27 and the on-axis axial ratio is shown in Figure 5.28.

In general the upper frequency of operation is defined by the accuracy of construction at the feed point or, in the case where the antenna is fed by a balun, the characteristics of the balun.

Where such antennas are excited by an impulsive input waveform the far field radiated waveform exhibits significant dispersion. The effect of dispersion can be corrected by deconvolution of the antenna response. A typical time domain characteristic of the equiangular spiral is shown in Figure 5.29.

The short pulse radiation characteristics of a conical spiral depend on the type of input waveform, which must be carefully selected to restrict the amount of very low frequency energy [50]. If, for example, a Gaussian impulse is applied then energy at very low frequencies becomes trapped in the antenna, which then functions as a resonant structure and radiates an extended far field waveform. Generally the antenna must be properly loaded to reduce radiation from such resonant currents.

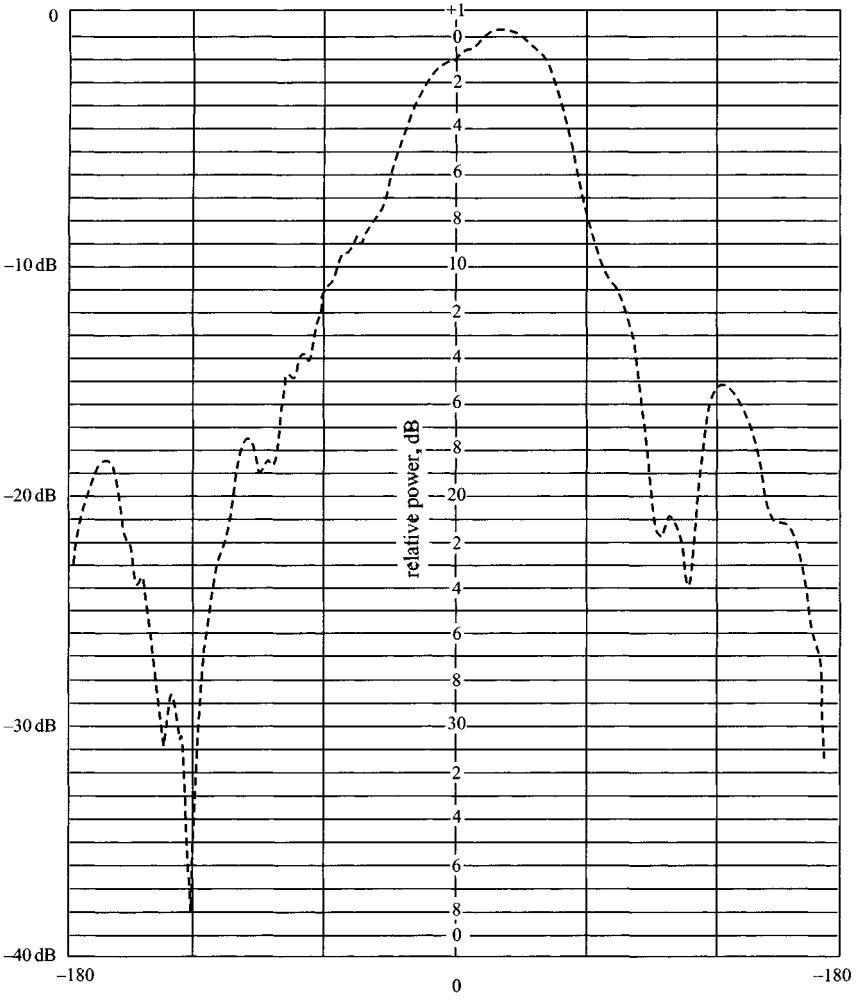

Figure 5.27 Radiation pattern of a single arm of a multi-arm spiral at 900 MHz

The main potential advantage of the planar equiangular spiral is the radiation of circular polarisation. Where the target, such as a pipe or cable, displays significant polarisation attributes, circular polarisation can be a means of preferential detection.

The Vivaldi antenna [51] also falls into the class of a periodic continuously scaled antenna structure and within the limiting size of the structure has unlimited instantaneous frequency bandwidth. It provides end fire radiation and linear polarisation and can be designed to provide a constant gain-frequency performance. The Vivaldi antenna consists of a diverging slot-form guiding conductor pair as shown in

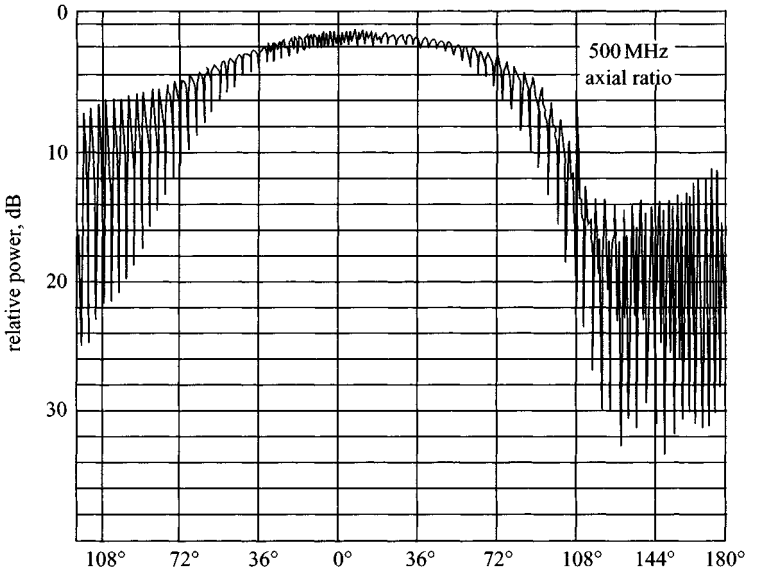

Figure 5.28 Axial ratio at 500 MHz of an equiangular spiral antenna

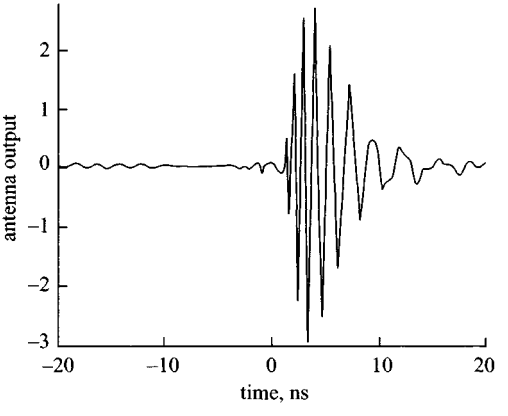

Figure 5.29 Time domain response of an equiangular spiral antenna

Figure 5.30. The curve of one of the guiding structures follows the equation

$$z = Ae^{kx} \tag{5.27}$$

Radiation is produced by a nonresonant travelling wave mechanism by waves travelling down a curved path along the antenna. Where the conductor separation is small, the travelling wave energy is closely coupled to the conductor but becomes less so as the conductor separation increases. The Vivaldi antenna provides gain when the

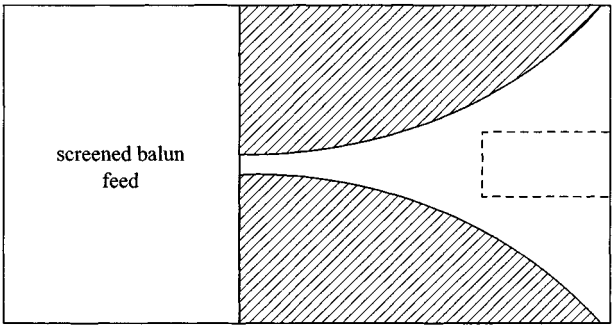

Figure 5.30 Vivaldi antenna

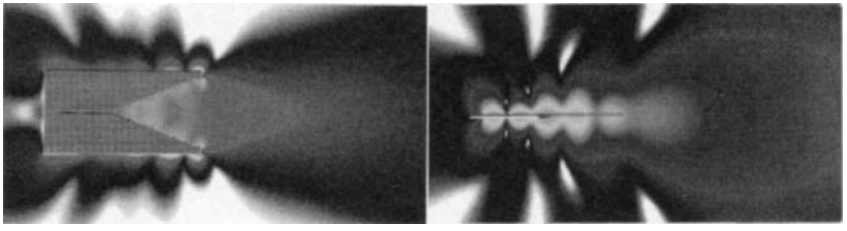

Figure 5.31 Calculated radiation patterns of elemental Vivaldi antenna (courtesy ERA Technology)

phase velocity of the travelling wave on the conductors is equal to or greater than that in the surrounding medium. Typical radiation patterns for an elemental Vivaldi are shown in Figure 5.31.

The lower cutoff frequency is defined by the dimensions of the conductor separation, being a half wavelength, and the gain is proportional to overall length. The impulse response of the antenna is extended due to the nonstationary phase centre but can, of course, be corrected by the use of a matched filter. Note that the sidelobe and backlobe radiation is significant unless suitable absorbers and screening are used.

5.6 Horn antennas

Horn antennas have found most use with FMCW surface-penetrating radars where the generally higher frequency of operation and relaxation of the requirement for linear phase response permit the consideration of this class of antenna. Exponentially flared TEM horns with dielectric loading have been developed to operate over decade bandwidths [52].The design of horn antennas is well covered in the literature, but of particular interest is the short axial length double-ridged horn as shown in Figure 5.32.

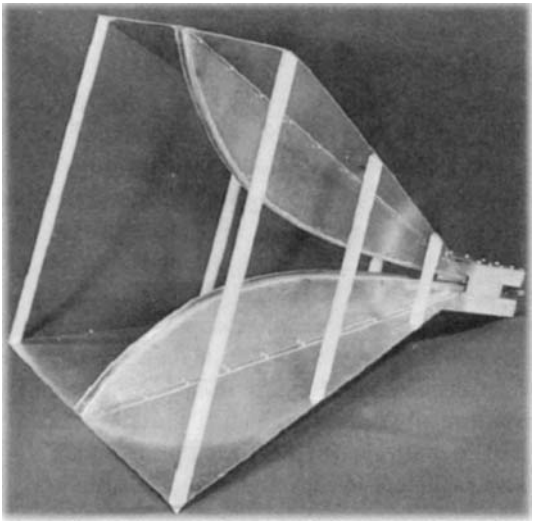

Figure 5.32 Short axial length double-ridged horn antenna (Daniels [53])

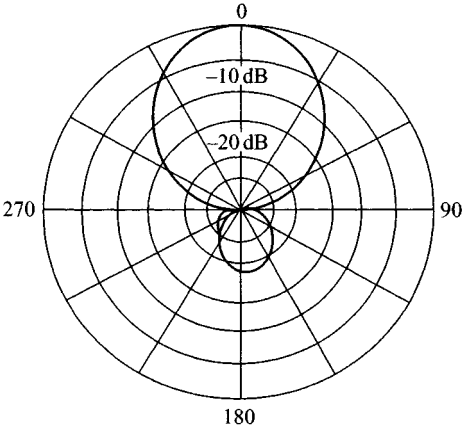

Figure 5.33 E-plane radiation pattern of a short axial length horn at 200 MHz (after Kerr [52])

This design can provide useful gain over a decade bandwidth using a logarithmic characteristic curve for the ridges. Typically the short axial length horn provides a VSWR of better than 2 : 1 and a gain of 10 dB over a frequency band of 0.2 GHz to 2 GHz for an axial length of 0.76 m. Typical radiation patterns are shown in Figures 5.33 and 5.34.

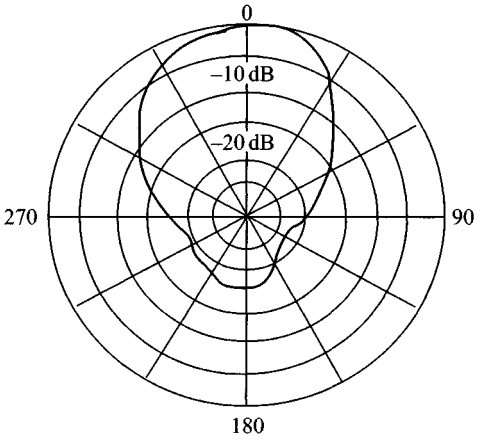

Figure 5.34 H-plane radiation pattern of a short axial length horn at 200 MHz (after Kerr [52])

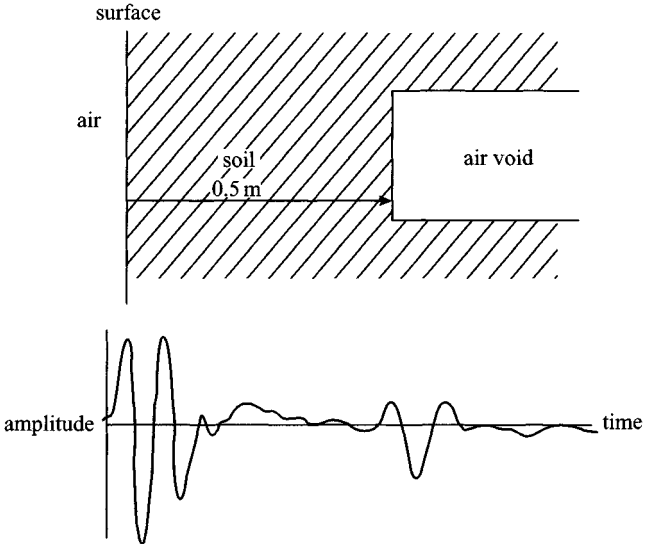

Figure 5.35 Time domain response of an exponential horn antenna (Daniels [53])

The concept of the ridged horn design can be adapted to form a quad-ridged horn operating from 0.3 to 1.9 GHz. A return loss of better than 10 dB and a crosscoupling level of better than 35 dB can be obtained. The quad-ridged horn can be used to extract information on the polarisation state of the reflected signal.

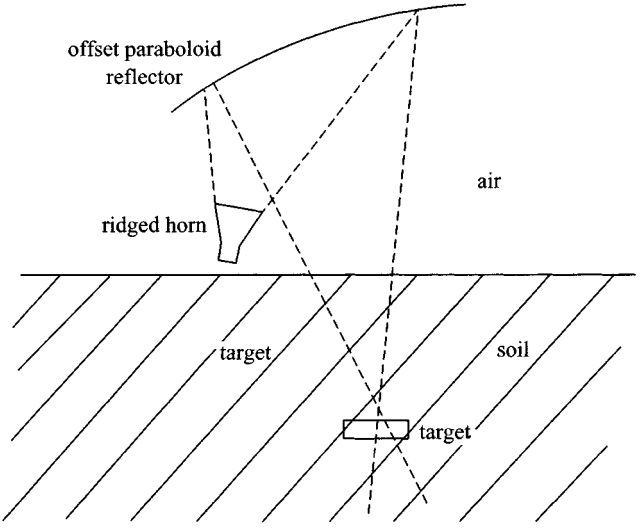

Figure 5.36 Arrangement of an offset-fed paraboloid reflector

An FMCW radar has been developed using an offset paraboloid fed by a ridged horn [54] (see Figure 5.35). The arrangement was designed to focus the radiation into the ground at a slant angle to reduce the level of the reflection from the ground. Care needs to be taken in such arrangements to minimise the effect of back and side lobes from the feed antenna, which can easily generate reflection from the ground surface.

Although horn antennas have been used mostly with FMCW systems, it is possible to radiate pulses, and the impulse response of a typical exponential horn antenna is shown in Figure 5.36.

Note that pulse shape is distorted by the limited low frequency performance due to the physical size of the antenna. In addition the exponential flare causes dispersion of the transmitted pulse.

The main advantage of the ridged horn is high aperture efficiency, although at high frequencies where the aperture is many wavelengths wide large phase errors will be present across the aperture unless the horn is long. The basic ridged horn design provides a characteristic impedance in the TE10 mode, which is given by

$$z = Z_0 e^{kx} \quad \text{for } 0 \leq x \leq \frac{l}{2} \tag{5.28}$$

where Z_0 is the characteristic impedance of the waveguide and k is the average of the start and end point impedances.

Experimentally, Walton and Sundberg [55] found that the width of the ridge should be increased in the flared section to avoid the excessive phase errors and the resulting loss of gain which occurs when the ridge is near the aperture.

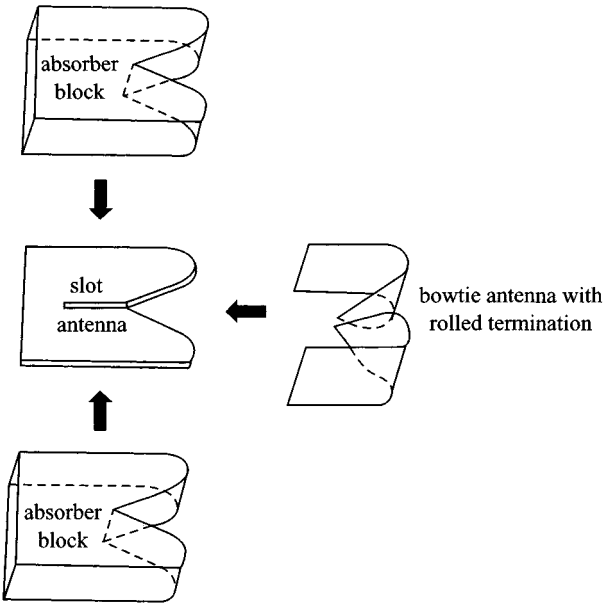

Figure 5.37 Composite horn antenna (after Lai)

It is normal to use a phase correcting lens, as typically the phase error is a quadratic function of the maximum aperture dimensions. Either a doubly plano-convex lens fed on the convex side can be used or a composite lens (one for each plane) can be employed.

Very often the horn antenna is used to feed an offset-fed parabolic reflector. In the case of time domain systems the reflector will introduce transient delays, and the transient time of a paraboloidal reflector, as shown in Figure 5.35, is given by Sun and Rusch [54]:

$$I_t = \frac{1}{c}\{D \sin\theta \cos(\phi_0 - \phi_m) + 2d \sin\theta_{\max} \cos(\phi_0 - \phi_m)\} \tag{5.29}$$

where the parameters are defined in Figure 5.36.

Lai obtained improvements in the performance of the ridged horn by the use of a combination of Vivaldi exponential slot line fed folded bow-tie and rolled termination (see Bibliography for Lai and Sinopoli, 1992) as shown in Figure 5.37.

The rolled termination (which is also loaded with absorber) is used to minimise edge diffraction, and well controlled radiation patterns can be produced over several octaves for a 70 cm 30° flare and plate angle antenna. Crosspolar levels are typically 20 dB below copolarised signal levels, and a VSWR of better than 2 : 1 over at least 3 octaves can be achieved.

5.7 Array antennas

Arrays of antennas are an obvious method of increasing the rate of survey of areas of the ground and have been designed and built for road survey and mine detection. Some examples of antenna configurations are given below. There are two approaches to array design. The first is simply to take a number of single channel radars, slave them with a master logger and arrange for the data to be appropriately logged. The other approach is to design the system as an integral array design and exploit the increased capability offered by combining multiple looks and SAR processing. Consideration as to whether the antenna/system should be downward look or forward look is important. A number of antenna array designs are discussed in the chapter on mines. With all array systems, it is important that the surface clutter is properly removed. Close coupling of the antenna to the ground surface is one method. An alternative relies on coherent subtraction but this often means that the ground topography must be relatively smooth. Where removal of the surface clutter is not easy then antennas operating off-normal incidence can be used. However, this in turn brings other problems and antenna near-field effects must be accounted for, and the effect of grazing angle can be a limitation as it limits the potential for full 3D imaging because of the refractive index of the ground compressing the beam within the soil.

All array systems are geared to generating an image of the buried targets, and for that accurate positioning of the array elements is crucial. This can be achieved with differential GPS (DGPS) systems coupled with inertial navigation systems (INS).

An example of the first approach to array design is that taken by the CART Imaging System ('CART' stands for 'computer assisted radar tomography') from Witten Technologies, Inc.; see www.wittentech.com/products_CART.html.

This uses a fixed array of nine transmitters and eight receivers. Each radar element in the array is a standard ultra-wideband GPR from Mala Geoscience that broadcasts an impulse with a frequency spectrum from about 50 to 400 MHz. The array is controlled by special electronics that fires the transmitter elements and controls the receivers in sequence to create 16 standard bi-static GPR channels covering a 2 m swath on the ground. In this standard 'bi-static' mode of operation, each transmitter fires twice in sequence, with each firing being recorded by an adjacent receiver. A multi-static mode, in which each transmitter fires once in sequence and is recorded by all the receivers, is also possible. The array can be towed by a vehicle or pushed in front of a modified commercial lawnmower at speeds up to about 1 km/h (30 cm/s).

Alternative approaches have been adopted by companies in the US (Planning Systems, GeoCenters, BASystems (ex GDE), Mirage, ARL, Jaycor, SRI, Coleman), UK (ERA Technology, Thales and PipeHawk), France (Thales, Satimo), Germany (Rheinmetall) and Israel (Elta), who have developed array systems as an integral design rather than combining existing single channel radars. Much of the interest in high speed array radar systems is for mine detection. Work is being carried out on various National (US, UK, Canada, Germany, France) as well as international CEU programmes, particularly for mine detection. Arrays are typically between 1 and 4 m in width and can operate at speeds up to $10\,\mathrm{km h^{-1}}$.

The key issues for the design of multi-element GPR systems lie in the channel-to-channel performance and tracking over the desired operational environmental range.

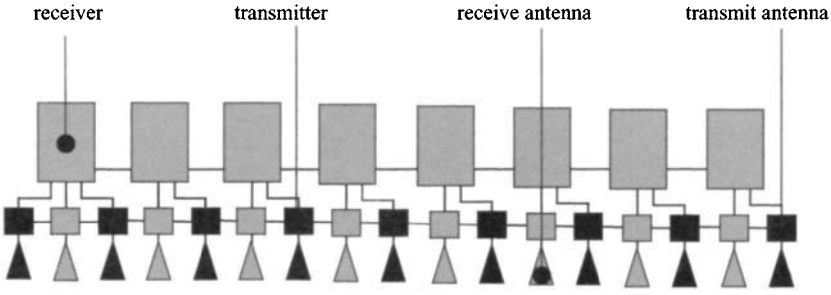

Figure 5.38 Block diagram of 16-channel radar system (courtesy ERA Technology)

A 32-channel GPR system, for example, must maintain calibration of both start time and time linearity for all channels to within demanding limits. In addition the relative gain and, if used, time varying gain profile, must also match to within close tolerances. Where the antenna array is spaced off the ground, there may also be the need to compensate for variations in surface topography. A further aspect to be considered is the antenna element spacing. This needs to be adequate to provide proper resolution of the wanted target, and it can be shown that the probability of detection with respect to small targets is closely related to the density of the elements of the antenna array. An example section showing 16 elements of a 4m wide swathe radar system with a total of 32 antenna elements is shown in Figure 5.38. This was developed as part of the UK Minder CAP programme on behalf of the UK MoD.

The architecture of the system is based around 16 receivers (8 only shown), each of which sequentially samples the signal incident on the receive antenna elements. The transmitters are synchronised by adjacent receivers and a central master clock. The system is designed to be modular in that it can be either increased in width or alternatively in density and up to 64 channels can be configured (see Figure 5.39). The transmitter–receiver modules can be used either singly or up to $N/2$, where N is the number of antenna elements. Radar images of buried mines are shown in Chapter 12.

A novel approach has been taken by Planning Systems in the United States. They have developed a forward look radar system based on an array of spiral antennas (see Figures 5.40 and 5.41).

However, the ability to carry out beam forming by means of inverse synthetic aperture processing could be potentially valuable in many applications.

Rutledge and Muha [6] consider the general situation of imaging antenna arrays, while Anderson *et al.* [56] consider the specific problem of wideband beam patterns from sparse arrays.

If an array of emitters is driven by a sequence of impulses without any differential time delay the radiated time sequence is as shown in Figure 5.42.

Note the gradual disappearance of the sidelobes as the radiated wave front propagates away from the array. If the sequences of impulses are controlled in time by means of a differential time delay between each element, the beam position can be steered as shown in Figure 5.43.

Figure 5.39 Photograph of downward look 32-channel array system used on MINDER system (courtesy ERA Technology)

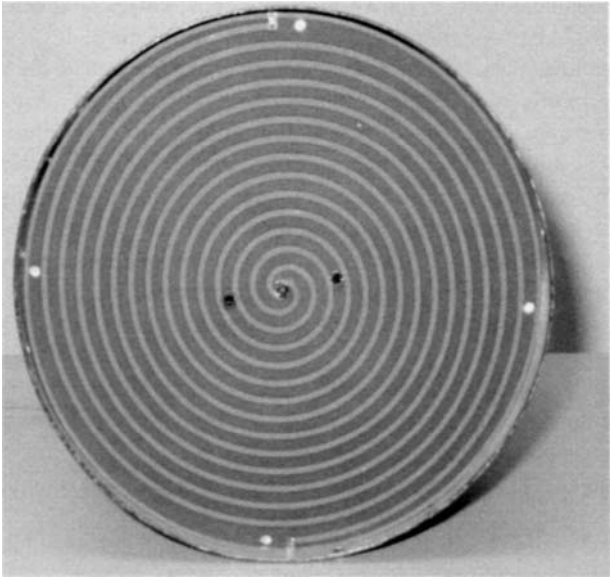

Figure 5.40 Archimedian spiral element (courtesy Planning Systems)

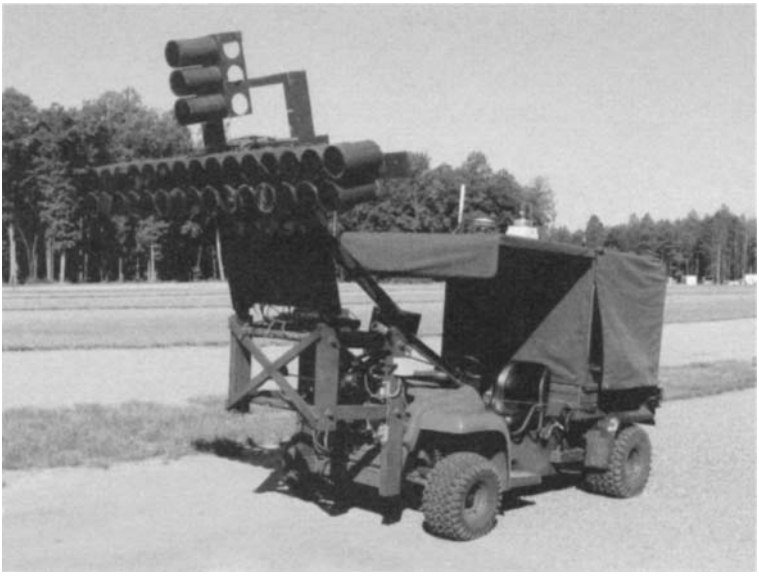

Figure 5.41 *Forward look array of Archimedian spiral antennas (courtesy Planning Systems)*

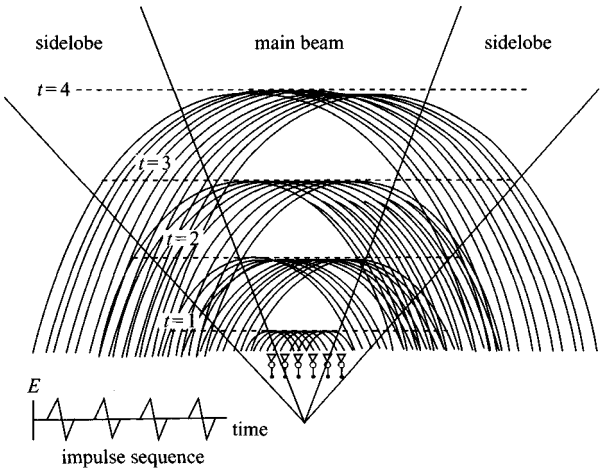

Figure 5.42 *Timed array antenna array*

The possibility of beam steering by means of time control exists, although the inter-element time delay is limited to a maximum equivalent to the distance between each element.

An alternative means of beam forming is by means of an array as shown in Figure 5.44. Here the objective was to create directivity in the azimuth plane

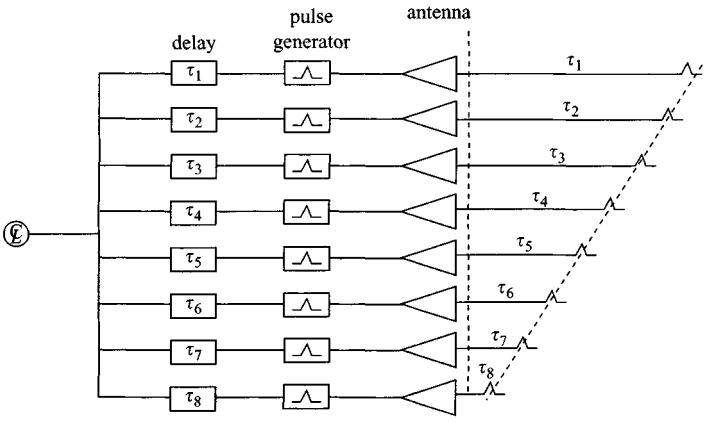

Figure 5.43 Beam steering by differential time delay

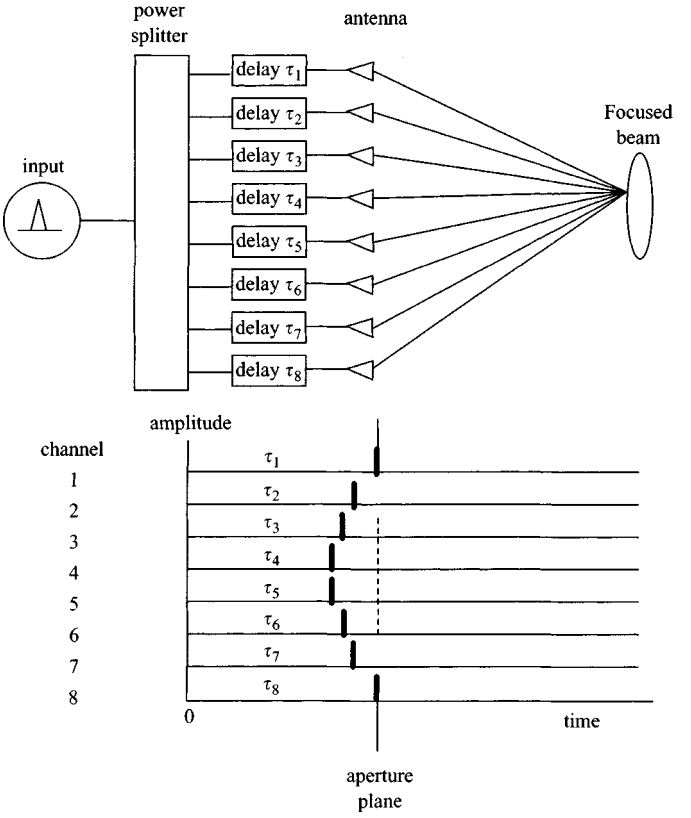

Figure 5.44 Beam forming by differential time delay

and was achieved by means of a beam forming network using wideband hybrid elements.

The use of timed transmitter arrays and inverse synthetic aperture processing of the signals from a receiver array offers the possibility of achieving considerably improved directivity over all the previous types of antennas discussed in this chapter. A 10 × 10 element array will have a peak sidelobe amplitude of −26 dB of the main lobe [56] and beam steering of up to 50° is feasible.

5.8 Polarisation

It is well known that linear targets such as small to medium diameter pipes act as depolarising features and a linearly polarised crossed dipole antenna rotated about an axis normal to the pipe produces a sinusoidal variation in received signal. However, the null points are a distinct disadvantage, because the operator is required to make two separate, axially rotated measurements at every point to be sure of detecting pipes at unknown orientations as shown in Figure 5.45.

An attractive technique is to radiate a circularly polarised wave which automatically rotates the polarised vector in space and hence removes the direction of signal nulls. Conventionally, circular polarisation refers to a steady-state condition during which a long duration pulse or CW waveforms are transmitted. For impulse radars, the pulse duration is very short (<5 ns) and hence a more complex transient situation is encountered.

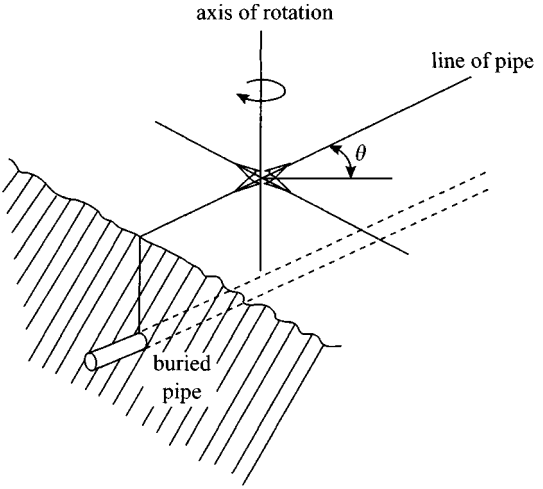

Figure 5.45 Crossed dipole measurement on a linear target

One method of radiating circular polarisation is to use an equi-angular spiral antenna. Unfortunately, the dispersive nature of this type of antenna causes an increase in the duration of the transmitted waveforms, and the radiated pulse takes the form of a 'chirp' in which high frequencies are radiated first, followed by the low frequencies. This effect, however, may be compensated by a 'spiking' filter, which may take the form of a conventional matched filter or a more sophisticated filter such as a Wiener filter. The use of such an antenna has been shown by British Gas [57] to be a useful method of implementing a pipe detection radar, and plastic pipes buried in wet clay have been detected up to a depth of 1.0 m.

A spiral antenna could be implemented as a multi-element planar structure as shown in Figure 5.26. However, this realisation may often fail to provide the expected performance because of several deficiencies. The limited physical dimensions of the spiral result in elliptical polarisation at low frequencies which can degrade to essentially linear polarisation. Reflections from the ends of the arms cause both clutter and degradation of the circularity of the polarisation. The proximity of the ground affects the reactive field of the antenna, resulting in nonsymmetrical loading and degradation of the far field pattern. An analysis of this type of antenna is given by Anders [58].

A plot of axial ratio measured in free space as a function of angle at a frequency of 500 MHz is shown in Figure 5.28 and shows an acceptable performance of 1 dB. However, at low frequencies the axial ratio degrades quite rapidly, reaching unacceptable values. Similarly, with commercially available baluns the high frequency axial ratio degrades. This situation has a significant effect on the envelope of the polarisation vectors of the transmitted pulse. The consequence of these deficiencies is that multiple angular measurements must be carried out, thus losing the original benefit of employing circular polarisation.

An alternative design possibility is to synthesise a circularly polarised signal. Any steady state wave of arbitrary polarisation can be synthesised from two waves orthogonally polarised to each other. In the design shown in Figure 5.46, a circularly polarised wave is produced by exciting vertically and horizontally polarised waves, each having the same amplitude and with a 90° phase difference between them.

The radiating elements are fed, via wideband (preferably decade) 180° and 90° hybrids, to radiate circular polarisation. If right hand circularly polarised signals are transmitted and received, the preferential detection of linear features (e.g. pipes) is achieved. If, however, right hand circularly polarised signals are transmitted and left hand circularly polarised signals are received, planar features are detected. Hence, if connections to the radiating elements are arranged and switched appropriately, the signals routed to the receiver contain different data according to the sense of polarisation. The data, therefore, can be processed separately and in a different manner in order to provide images of different targets in the material under investigation.

However, hardware deficiencies limit the performance; firstly, it is difficult to achieve wideband operation with 90° hybrids (at least over a decade) and, secondly, even the fastest, state of the art GaAs switches have unacceptably high, break-through levels. An alternative concept is that of the commutated multi-element crossed dipole array.

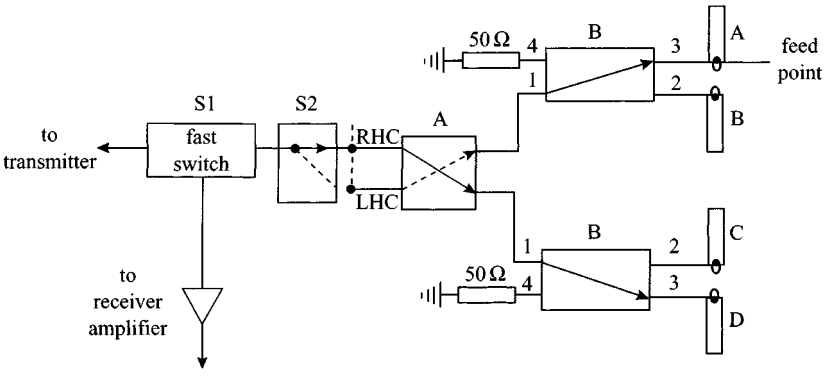

Figure 5.46 Synthesised polarisation arrangement

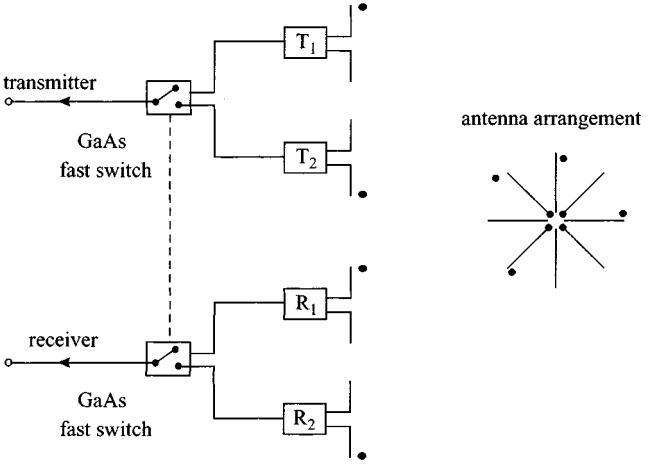

Figure 5.47 Eight element commutated antenna feed switching every alternate waveform

An example of an eight element antenna in which the crossed dipole pairs can be switched at intervals of up to 1 ms so that the two crossed dipole pairs are orientated between 0° and 45° is shown in Figure 5.47.

An extension of this design concept is where full commutation over 360° in 45° steps can be achieved, and this is shown in Figure 5.48. PIN diode switches are used to handle the transmitted power and operate at a switching interval of 1 s, thus achieving 360° rotation in ~10 s. The possibility of real time discrimination using filters based on recognition of the cos 2 amplitude variation of each range sample can be considered. Operationally such a system would have the advantage of being able to survey rapidly without the limitations imposed by mechanically rotated antennas.

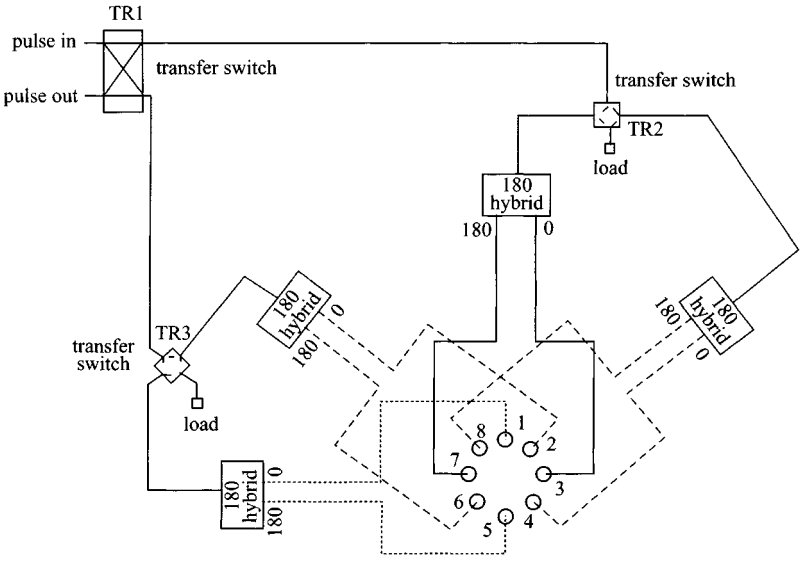

Figure 5.48 Fully commutated antenna arrangement

However, all of these schemes do not solve the problem of detecting deeply buried, large diameter pipes (>250 mm) for which the depolarisation of incident signals is low. In this case it may be necessary to detect the co-polar signal, and a parallel dipole antenna system may be needed.

Antenna design approaches based on commutated crossed dipoles, as described in this Section, could prove a successful means of detecting plastic pipes up to 250 mm diameter, provided the radar system has sufficient dynamic range and sensitivity.

5.9 Dielectric antennas

Dr Chi-Chih Chen

Artificial dielectric loading has been used with antennas for surface-penetrating radar. However, the finite size of the dielectric can cause problems in that energy becomes trapped in the dielectric and has the effect of causing a local resonance. Provided, therefore, that the antenna can be loaded in such a way that the dielectric appears semi-infinite, this problem is reduced.

An ultra-wide bandwidth (UWB) dielectric rod antenna has been developed by Chen *et al.* [59] from the Ohio State University ElectroScience Laboratory for application in detecting shallow targets, such as anti-personnel (AP) mines. This design was modified from the conventional narrow-bandwidth 'polyrod antenna' used for far-field applications. A unique feature of this antenna is that it can be calibrated on site and thus has very little antenna clutter. The illumination spot size can also be controlled by the antenna height. This results in lower surface clutter and better spatial resolution.

The lowest hybrid-mode mode is excited and guided along a circular dielectric waveguide. Such a mode has no cutoff frequency and thus is useful for broad applications. The electromagnetic energy is guided inside and outside the rod simultaneously. When the rod diameter is greater than one wavelength in the material, most energy is confined inside the rod. The external field becomes highly evanescent. The end of the rod is tapered to a point where the electromagnetic waves are radiated out with a broad beamwidth.

The above propagation and radiation properties were investigated by both direct field probing and numerical simulation using the three-dimensional finite-difference time domain (FDTD) technique. Calibration of the UWB rod antenna is done by pointing the rod to a short conducting cylinder whose theoretical response can be easily obtained. A prototype UWB rod antenna operated at 1 to 6 GHz frequency range was built and used in various field tests for the detection of buried anti-personnel mines. The measurement results indicated a very good data quality with good spatial resolution and little antenna clutter. This new antenna can also be applied to other GPR applications.

5.9.1 Introduction

A novel broadband dielectric rod antenna design was developed at the Ohio State University ElectroScience Laboratory for the detection of shallow objects such as landmines [59]. This design utilises a low-loss dielectric cylinder that is separated into launcher, waveguide and radiation sections as illustrated in Figure 5.49. The launcher section launches broadband electromagnetic energy into the rod using special broadband launcher arms. An example of the broadband launcher arm is given in Figure 5.50

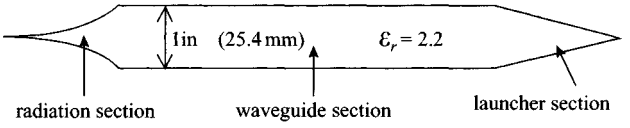

Figure 5.49 The launcher, waveguide and radiation sections of a typical broadband rod antenna design

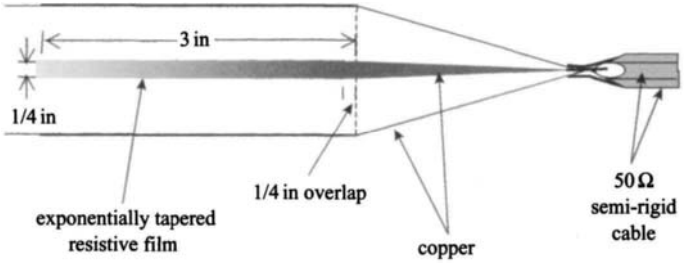

Figure 5.50 An example of the broadband launcher arm design using resistively terminated conical plates

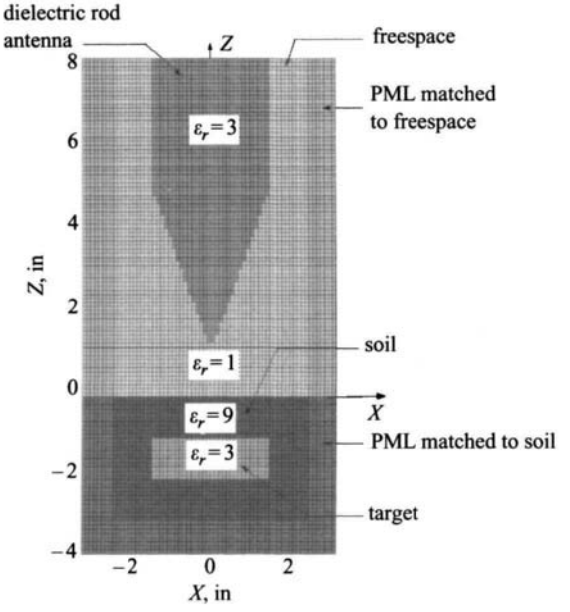

Figure 5.51 Modelling diagram for polyrod antenna

using resistively terminated conical plates. Both single- and dual-polarisation rod designs have been developed [60]. The waveguide section provides the needed isolation between the launcher and radiation sections. The radiation tip should be carefully designed to efficiently transfer the guided energy into radiation in the forward direction with a broad radiation pattern and spherical phase fronts. In order to minimise the interaction between the antenna and the target (or ground) to be tested, the radar cross-sectional (RCS) area of the tip should also be reduced via a proper tip geometry design (see Figures 5.51 and 5.52) [61]. The operation and characteristics of this new design have been verified and studied with the help of finite-difference time-domain models [62]. A simulation example is shown in Figure 5.53, where two snap-shots of the x-component of the guided and radiated electrical fields are plotted (see also Figure 5.54).

The rod antenna design has the following unique features that make it particularly suitable for detecting shallow and small anomalies such as buried antipersonnel mines or cracks (or voids) in pavement:

(i) Broad bandwidth gives good temporal resolution.
(ii) Low antenna-ground interaction reduces surface clutter and allows one to effectively calibrate out system (including antenna).
(iii) Small radiation aperture size provides superior spatial resolution during a close-range scanning.

The spatial resolution is usually determined by the height of the rod tip, ground refractive angle and target depth. As depth and height increase, the spatial resolution

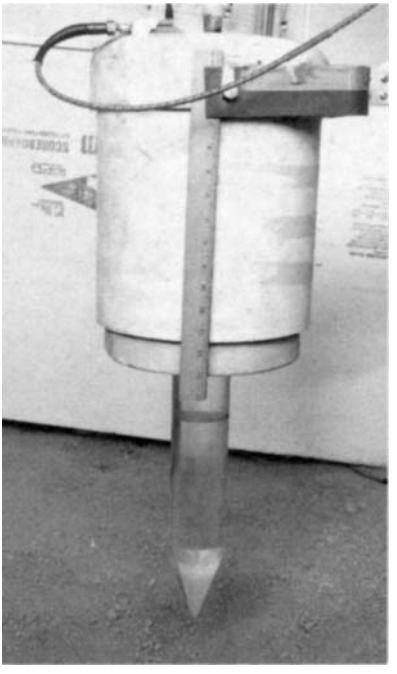

Figure 5.52 Photograph of polyrod antenna

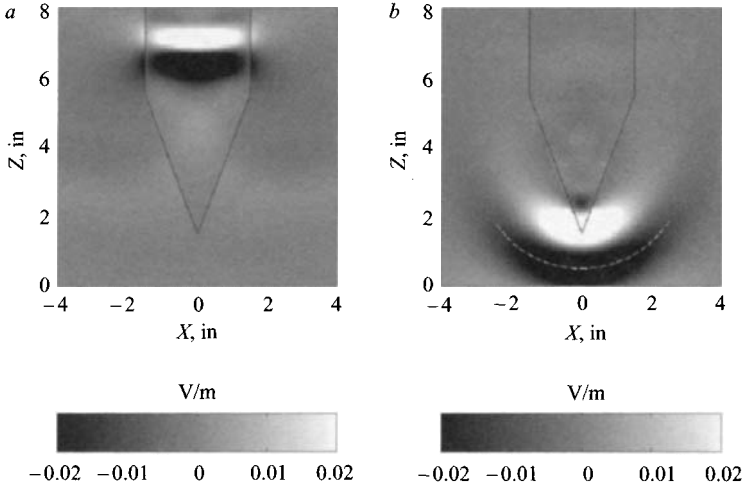

Figure 5.53 Numerical simulations of guided (a) and radiated (b) electromagnetic waves

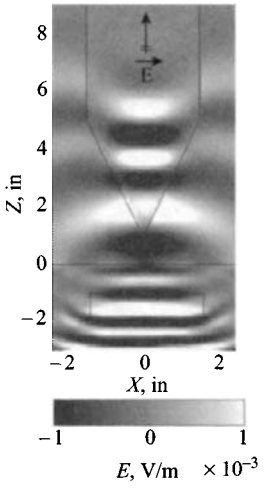

Figure 5.54 Radiated and scattered fields from polyrod antenna

reduces due to the beam spreading. A lower rod height reduces the illumination spot size on the ground. This not only improves the spatial resolution but also causes the surface scattering to spread less in time, thus improving the temporal (or depth) resolution. Figure 5.55 plots both measured and calculated magnitude distributions of radiated fields on a transverse plane located 2 in. away from the rod tip. It shows that the 3-dB spot size is <1.5 in. above 2 GHz. The horizontal scale indicates the field positions relative to the centre of the illumination spot. Note that the radiated pattern of the rod is approximately symmetric. Below 2 GHz, the rod size becomes relatively small in wavelength (in dielectric) and can no longer effectively confine the electromagnetic energy within the rod [63].

5.9.2 Summary

This Section has briefly discussed the new dielectric rod antenna design and its potential usefulness in detecting small, shallow sub-surface anomalies. Both numerical and experimental results were provided to demonstrate its good temporal and spatial resolution characteristics, which is important in locating and discriminating the anomaly to be detected. The low-scattering tip design also allows close-distance interrogation without significant antenna interaction that may distort the target's response and increase clutter level. The size of the rod can be reduced by using a high-dielectric material provided that proper launcher and radiation section designs are adopted. To operate at lower frequencies, the combination of a high-dielectric material and a larger diameter is needed to minimise antenna size while maintaining the one wavelength (in material) requirement. The application of the rod antenna in detecting and classifying buried landmines was presented. However, this antenna design should also be advantageous for other shallow GPR applications that

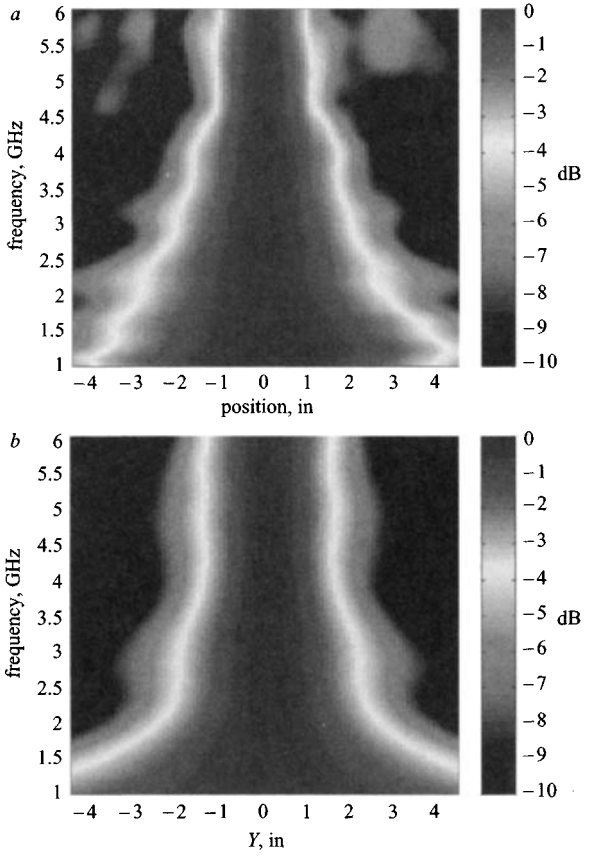

Figure 5.55 *The measured (a) and calculated (b) magnitude distribution of the fields illuminated on the ground surface 2 in away from the tip of the rod*

require nonintrusive interrogation, accurate target response, and high temporal and spatial resolutions.

5.10 Summary

The antennas used in surface-penetrating radar systems are, for reasons of portability, usually electrically small and consequently exhibit low gain. This has a profound effect on the performance of the overall system and is probably the only example of a radar system where antenna gain is, in general, so low. However, the bandwidth of the antennas is very much greater than that normally used in conventional radar systems, and surface-penetrating radars generally demonstrate very high range resolution.

The choice of antenna is generally straightforward. The resistively loaded dipole, bow-tie and TEM travelling wave antenna have been primarily used for the impulse

based radar. Where matched filtering can be incorporated in impulse radars then either horn or frequency independent antennas can also be considered.

All the classes of antenna discussed can be used in synthesised, FMCW or noise modulated radars.

Attention must also be given to the means by which the antenna is fed from the transmitter. Generally an antenna is a balanced structure but where cables are used to connect the antenna to the transmitter or receiver, some means is needed of transforming from the unbalanced configuration of the feed cable to the balanced structure of the antenna. On this frequency range, baluns are generally commercially available or, alternatively, purpose designed units can be constructed.

It may be found that multiple reflections between the transmitter and antenna can be troublesome and these can be avoided by making the feed cable long enough to place the reflection outside the time window of interest. This, however, may be undesirable as the cable will act as a lowpass filter unless compensated. An alternative is to mount the transmitter and receiver immediately adjacent to the antenna and this, if correctly designed, can remove the need for either a balun or feed cable.

The anticipated main developments in the field of antennas appear to be related to array antennas. The current interest in the development of free space ultra-wideband radar systems may result in the transfer of useful developments.

5.11 References

[1] KING, R. W. P., and SMITH, G. S.: 'Antennas in matter' (MIT Press, 1981)

[2] SKOLNIK, M. I.: 'Radar handbook' (McGraw Hill, 1970), pp. 6–11

[3] JUNKIN, G., and ANDERSON, A. P.: 'Limitations in microwave holographic imaging over a lossy half space'. *IEE Proc. F*, 1988, **135**, (4), pp. 321–329

[4] BREWITT-TAYLOR, C. R., GUNTON, D. J., and REES, H. D.: 'Planar antennas on a dielectric surface', *Electron. Lett.*, 1981, **17**, (20), pp. 729–731

[5] BURKE, G. J., JOHNSON, W. A., and MILLER, E. K.: 'Modelling of simple antennas near to and penetrating an interface', *Proc. IEEE*, 1983, **71**, (I), pp. 174–175

[6] RUTLEDGE, D. B., and MUHA, M. S.: 'Imaging antenna arrays', *IEEE Trans.*, 1982, **AP-130**, (Q), pp. 533–540

[7] WAIT, J. R.: 'Propagation of electromagnetic pulses in a homogeneous conducting earth', *Appl. Sci. Res. B*, 1960, **8**, pp. 213–253

[8] KING, A. W. P., and NU, T. T.: 'The propagation of a radar pulse in sea water'. *J. Appl. Phys.*, 1993, **73**, (4), pp. 1581–1589

[9] KAPPEN, F. W., and MONICH, C.: 'Single pulse radiation from a resistive coated dipole antenna'. Proc. Fifth Int. Conf. On Antennas and propagation, ICAP '87, York, UK, 1987. IEE Conf. Publ. 274, Vol. 1, pp. 90–93

[10] RANDA, J., KANDA, M., and ORR, K. D.: 'Resistively-tapered-dipole electric-held probes up to 40 GHz. Proc. IEEE Int. Symp. Electromagnetic compatibility, Cherry Hill, NI, USA, 1991, pp. 265–266

[11] ESSELLE, K. P., and STUCHLY, S. S.: 'A new broadband antenna for transient electromagnetic field measurements'. Proc. IEEE Symposium on Antennas and propagation – merging technologies for 90's, Dallas, TX, USA, 1990, pp. 1584–1587

[12] WU, T. T., and KING, R. W. P.: 'The cylindrical antenna with non-reflecting resistive loading', *IEEE Trans.*, 1965, **AP-13**, (5), pp. 369–373

[13] ALTSHULER, E. E.: 'The travelling-wave linear antenna', *IRE Trans. Antennas Propag.*, 1961, **9**, (4), pp. 324–329

[14] RAO, B. R: 'Optimised tapered resistivity profiles for wideband HF monopole – antenna'. Proc. IEEE Antennas & Propagation Society Symposium, 1991, Vol.2, pp. 711–713

[15] MALONEY, J. G., and SMITH, C. S.: 'The role of resistance in broadband, pulse-distortionless antennas'. Proc. IEEE Antennas & Propagation Society Symposium, 24–28 June 1991, Vol. 2, pp. 707–710

[16] BROWN, G. H., and WOODWARD, O. M.: 'Experimentally determined radiation characteristics of conical and triangular antennas', *RCA Rev.*, 1952, **13**, pp. 425–452

[17] YOUNG, M.,: 'Underground pipe detector'. US Patent 4 062 010, 1977

[18] HARMUTH, H. F.: 'Antennas for non-sinusoidal waves. Part III Arrays', *IEEE Trans.*, 1983, **EMC-25**, (3), pp. 346–357

[19] HARMUTH, H. F., and DING-RONG, S.: 'Antennas for non-sinusoidal waves. Part II Sensors', *IEEE Trans.*, 1983, **EMC-25**, (2), pp. 107–115

[20] HARMUTH, E.-I. F., and DING-RONG, S.: 'Large-current, short-length radiator for nonsinusoidal waves'. Proc. IEEE Int. Symposium on electromagnetic compatibility, Arlington, TX, USA, 1983, pp. 453–456

[21] IIZUKA, K.: 'The travelling-wave V-antenna and related antennas', *IEEE Trans.*, 1967, **AP-15**, (2), pp. 23–A43

[22] KING, R. W. D., and SMITH, G. S.: 'Antennas in Matter: Fundamentals, Theory and Applications' (MIT Press, USA, 1981)

[23] THEODOROU, E. A., GORMAN, M. R., RIG, R. R., and KONG, F. N.: 'Broadband pulse optimised antenna', *IEE Proc. H*, 1981, **128**, (3), pp. 124–130

[24] SHEN, H. M., KING, R. W. P., and WU, T.: 'V-conical antenna', *IEEE Trans.*, 1988, **AP-36**, (11), pp. 1519–1525

[25] WOHLERS, R. J.: 'The CWIA, an extremely wide bandwidth low dispersion antenna'. Abstracts of 20th Symposium, US Air Force R&D Programme, 1970

[26] DANIELS, D. J.: 'Short pulse radar for stratified lossy dielectric layer measurement', *IEE Proc. F*, 1980, **127**, (5), pp. 384–388

[27] EVANS, S., and KONG, F. N.: 'TEM horn antenna: input reflection characteristics in transmission', *IEE Proc. H*, 1983, **130**, (6), pp. 403–409

[28] READER, H. C., EVANS, S., and YOUNG, W. K.: 'Illumination of a rectangular slot radiator over a 3 octave bandwidth'. Proc. Fourth Int. Conf. on antennas and propagation, Cap '85, Coventry, UK, 1985. IEE Conf. Publ. 248, pp. 223–226

[29] FOSTER, P. R., and TUN, S. M.: 'Design and test of two TEM horns for ultrawideband use'. IEE Colloquium on Antennas and propagation problems of ultrawideband radar, IEE Colloquium Digest, London, 1993

[30] MARTEL, C., PHILIPPAKIS, M., and DANIELS, D. J.: 'Time domain design of a TEM horn antenna for ground penetrating radar', AP2000 Millennium Conf. on Antennas & Propagation, Davos, Switzerland/April 9–14 2000

[31] BAUM, C. E.: 'Aperture efficiencies for IRAs.' Digest IEEE Antennas and Propagation Society Int. Symposium, 1992. AP-S. Held in conjunction with: URSI Radio Science Meeting and Nuclear EMP Meeting, 18–25 July 1992, Vol.3, pp. 1228–1231

[32] BAUM, C. E., and FARR, E. G.: 'Impulse radiating antennas,' in H. L. Bertoni *et al.* (Eds.): 'Ultra wideband/short-pulse electromagnetics' (Plenum Press, New York, 1993), pp. 139–147

[33] FARR, E. G.: 'Analysis of the impulse radiating antenna'. Digest IEEE Antennas and Propagation Society Int. Symposium, 1992. AP-S. Held in conjunction with: URSI Radio Science Meeting and Nuclear EMP Meeting, 18–25 July 1992, Vol.3, pp. 1232–1235

[34] FARR, E. G., and BAUM, C. E.: 'The radiation pattern of reflector impulse radiating antennas: early-time response', Sensor and Simulation Note 358, June 1993

[35] FARR, E. G., BAUM, C. E., and BUCHENAUER, C. J.: 'Impulse radiating antennas, Part II', in Carin, L. *et al.* (Eds.): 'Ultra wideband/short-pulse electromagnetics 2', (Plenum Press, New York, 1995), pp. 159–178

[36] FARR, E. G., and FROST, C. A.: 'Development of a reflector IRA and a solid dielectric lens IRA, Part I: Design, predictions and construction'. Sensor and Simulation Note 396, April 1996

[37] FARR, E. G., BAUM, C. E., PRATHER, W. D., and BOWEN, L. H.: 'Multifunction impulse radiating antennas: theory and experiment'. Ultra-wideband short-pulse electromagnetics 4, 14–19 June 1998, pp. 131–144

[38] FARR, E. G., and BOWEN, L. H.: 'Recent progress in impulse radiating antennas'. Digest IEEE Conf. on Ultra wideband systems and technologies, 21–23 May 2002, pp. 337–340

[39] BUCHENAUER, C. J., TYO, J. S., and SCHOENBERG, J. S. H: 'Aperture efficiencies of impulse radiating antennas'. Ultra-wideband short-pulse electromagnetics 4, 14–19 June 1998, pp. 91–108

[40] TYO, J. S., BUCHENAUER, C. J., and SCHOENBERG, J. S. H.: 'Beamforming in time-domain arrays'. Proc. IEEE Antennas and Propagation Society International Symposium, 1999, 11–16 July 1999, Vol. 3, pp. 2014–2017

[41] TYO, J. S.: 'Optimisation of the TEM feed structure for four-arm reflector impulse radiating antennas'. *IEEE Trans. Antennas Propag.*, 2001, **49**, (4), pp. 607–614

[42] RUMSEY, V. H.: 'Frequency independent antennas'. Electrical Science Series (Academic Press, 1966)

[43] MILLER, E. K., and LANDT, J. A.: 'Short-pulse characteristics of the conical spiral antenna', *IEEE Trans.*, 1977, **AP-25**, (3), pp. 621–626
[44] PASTOL, Y., ARSAVALINGAM, G., and HALBOUT, J.-M.: 'Transient radiation properties of an integrated equiangular spiral antenna'. Proc. IEEE Symposium on Antennas and propagation – merging technologies for 90s, Dallas, TX, USA, 1990, pp. 1934–1937
[45] DYSON, J. D.: 'The equiangular spiral antenna', *IRE Trans.*, 1959, **AP-7**, pp. 181–187
[46] MORGAN, T. E.: 'Spiral antennas for ESM'. *IEE Proc. F*, 1985, **132**, (4), pp. 245–251
[47] KOOY, C.: 'Impulse response of a planar sheath equi-angular spiral antenna', *Arch. Elektron. Uebertrag.tech*, 1984, **38**, (2), pp. 89–92
[48] DESCHAMPS, G.: 'Impedance properties of complementary multiterminal planar structures', *IRE Trans.*, 1959, **AP-7**, pp. 5371–5378
[49] BAWER, R., and WOLFE, J. J.: 'The spiral antenna'. IRE National Convention Record, Part J, 1960, pp. 84–95
[50] GOLDSTONE, L. L.: 'Termination of a spiral antenna', *IBM Tech. Discl. Bull.*, 1983, **25**, (11a), pp. 5714–5715
[51] GIBSON, P. J.: 'The Vivaldi aerial'. Proc. Seventh European microwave conf., Microwave Exhibitions & Publishers Ltd., 1979, pp. 101–105
[52] KERR, J. L.: 'Short axial length broad-band horns', *IEEE Trans.*, 1973, **AP-21**, pp. 710–714
[53] DANIELS, D. J.: 'The use of radar in geophysical prospecting'. IEE Int. Conf. 'Radar 77', 1977
[54] SUN, E.-Y., and RUSCH, W. V. T.: 'Transient analysis of large reflector antennas under pulse-type excitation'. Proc. IEEE Antennas & Propagation Society Symposium, 1991, pp. 674–677
[55] WALTON, K. L., and SUNDBERG, V. C.: 'Broadband ridged horn design', *Microw. J.*, 1964, **4**, pp. 96–101
[56] ANDERSON, F., FULLERTON, L., CHRISTENSEN, W., and KORTEGAARD, B.: 'Wideband beam patterns from sparse arrays'. Proc. First Los Alamos Symposium on Ultra-wideband radar (CRC Press, 1990)
[57] SCOTT, H. E., and GUNTON, D. J.: 'Radar detection of buried pipes and cables'. Institution of Gas Engineers, 53rd Annual Meeting, London, UK, 1987, Communication 1345
[58] ANDERS, R.: 'On the complete calculation of the equiangular spiral antenna'. Proc. 20th Int. Symposium on Antennas and propagation, Japan, 1971, pp. 19–20
[59] CHEN, C.-C., RAMA RAO, K., and LEE, R.: 'A tapered-permittivity rod antenna for ground-penetrating radar applications', *J. Appl. Geophys.*, 2001, **47**, (3–4), pp. 309–316
[60] CHEN, C.-C.: 'Broadband dielectric probe prototype development for near-field measurements'. ElectroScience Laboratory Technical Report 743119, The Ohio State University, January 2003

[61] DIEZ, P. A., CHEN, C.-C., and BURNSIDE, W. D.: 'Broadband, near-field dielectric probe'. Proc. 2001 Antenna Measurement Techniques Association (AMTA) Symposium, Boulder, Colorado, 2001

[62] CHEN, C.-C., RAMA RAO, K., and LEE, R.: 'A new ultra-wide bandwidth dielectric rod antenna for ground-penetrating radar applications', *IEEE Trans. Antennas Propag.*, 2003, **51**, (3)

[63] MUELLER, G. E., and TYRRELL, W. A.: 'Polyrod antennas', *Bell Syst. Tech. J.*, 1947, **XXVI**, pp. 837–851.

5.12 Bibliography

BAUM, C. E.: 'Intermediate field of an impulse-radiating antenna'. Ultra-wideband short-pulse electromagnetics 4, 14–19 June 1998, pp. 77–89

CHEN, C.-C., HIGGINS, M. B., O'NEILL, K., and DETSCH, R.: 'UWB full-polarimetric horn-fed bow-tie GPR antenna for buried unexploded ordnance (UXO) discrimination'. Proc. IGARSS 2000, IEEE Int. Geoscience and Remote Sensing Symposium, 2000, Vol. 4, pp. 1430–1432

DANIELS, D. J.: 'Radar for non-destructive testing of materials'. IEE Colloquium 'Measurements, modelling and imaging for non-destructive testing', London, 27 Mar 1991

HOFFMANN, R. K.: 'Handbook of microwave integrated circuits' (Artech House, 1987), pp. 152–154

LAI, A. K. Y., and SINOPOLI, L.: 'A novel antenna for ultra-wide-band applications', *IEEE Trans.*, 1992, **AP-40**, (7), pp. 755–760

LESTARI, A. A., YAROVOY, A. G., and LIGTHART, L. P.: 'Improvement of bow-tie antennas for pulse radiation'. Proc. IEE Antennas and Propagation Society Int. Symposium, 2002, Vol. 4 , pp. 566–569

MALONEY, J. G., and SMITH, G. S.: 'Optimisation of a conical antenna for pulse radiation: an efficient design using resistive loading,' *IEEE Trans. Antennas Propag.*, 1993, **41**, pp. 940–947

MARCUVITZ, N.: 'Waveguide handbook.' IEE Electronic-Wave Series, 1951, pp. 180–183

MARTEL, C., PHILIPPAKIS, M., DANIELS, D. J., and UNDERHILL, M.: 'Modelling the performance of realistic ultra-wide band ground penetrating radar (GPR) antennas'. Eleventh International Conference on Antennas and Propagation, IEE Conf. Publ. No. 480, **2**, 17–20 April 2001, pp. 655–659

MONTOYA, T. P., and SMITH, G. S.: 'Resistively-loaded Vee antennas for short-pulse ground-penetrating radar'. Digest IEEE Antennas and Propagation Society Int. Symposium, 21–26 July 1996, Vol. 3, pp. 2068–2071

MORROW, I. L., PERSIJN, J., and VAN GENDEREN, P.: 'Rolled edge ultra-wideband dipole antenna for GPR application'. Proc. IEEE Antennas and Propagation Society Int. Symposium, 2002, Vol. 3 , pp. 484–487

NISHIOKA, Y., MAESHIMA, O., UNO, T., and ADACHI, S.: 'FDTD analysis of resistor-loaded bow-tie antennas covered with ferrite-coated conducting cavity for subsurface radar', *IEEE Trans. Antennas Propag.*, 1999, **47**, (6), pp. 970–977

PHELAN, M., SU, H., and LOVETRI, J.: 'Near field analysis of a wideband log-spiral antenna for 1–2 GHz GPR'. IEEE Canadian Conf. on Electrical and computer engineering, 2002, (CCECE 2002), Vol. 1, pp. 336–341

VALLE, S., ZANZI, L., SGHEIZ, M., LENZI, G., and FRIBORG, J.: 'Ground-penetrating radar antennas: theoretical and experimental directivity functions', *IEEE Trans. Geosci. Remote Sens.*, 2001, **39**, (4), pp. 749–759

VENKATARAYALU, N. V., CHEN, C.-C., TEIXEIRA, F. L., and LEE, R.: 'Impedance characterization of dielectric horn antennas using FDTD'. Proc. IEEE Antennas and Propagation Society Int. Symposium, 2002, Vol. 4, pp. 482–485

YAROVOY, A. G., SCHUKIN, A. D., KAPLOUN, I. V., and LIGTHART, L. P.: 'The dielectric wedge antenna', *IEEE Trans. Antennas Propag.*, **50**, (10), pp. 1460–1472

Chapter 6

Modulation techniques

6.1 Introduction

Each of the various modulation techniques used for ground penetrating radar systems has its relative merits, and in this Chapter we consider the general system architecture and system specifications associated with each.

The most frequently used system design is that of the impulse radar, and the majority of commercially available radar systems use short pulses or impulses which generally come in the category of amplitude modulation (AM). The next most frequently used modulation technique is frequency modulation (FM) followed by synthesised pulse (SPM), holographic (HM) and finally coded and noise modulation (NM). In this Chapter we consider the most commonly used techniques in turn and discuss the key parameters, which need to be considered in the design process.

It is useful to state the relationship between a time domain function $f(t)$ and its representation in the frequency domain $f(\omega)$. Fourier transform methods can be used to show

$$F(f(t)) = f(\omega) \tag{6.1}$$

that is

$$f(\omega) = \frac{1}{2\pi}\int_{-\infty}^{\infty} f(t)e^{j\omega t}\,\mathrm{d}t \tag{6.2}$$

The fast Fourier transform (FFT) is often used to compute the transform, but certain well established restrictions must be borne in mind due to its finite limitations. Here we shall consider only the results of applying the Fourier transform over infinite limits.

A real function such as a monocycle is given by the expression

$$\begin{aligned} &f(t) = A\sin(\omega' t) \quad \text{over the range } -\frac{\tau}{2} \le t \le \frac{\tau}{2} \\ &f(t) = 0 \quad \text{elsewhere} \end{aligned} \tag{6.3}$$

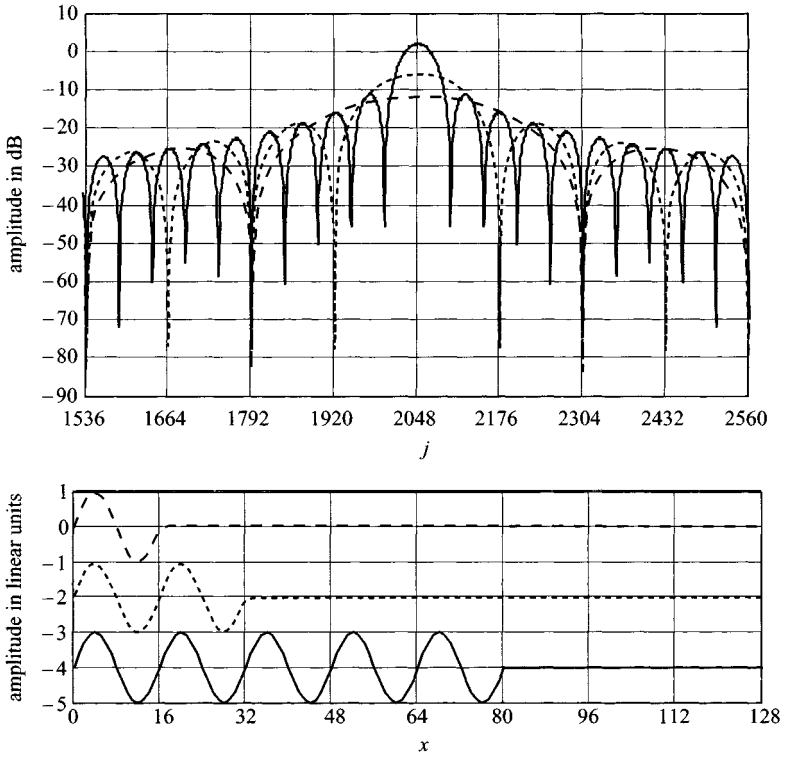

Figure 6.1 Frequency domain and time domain representations of a pulse with 1, 2 and 10 cycles

The Fourier transform of $f(t)$ is given by

$$F(\omega) = \frac{1}{2\pi} \int_{-\tau/2}^{\tau/2} A \sin(\omega t) e^{-j\omega t} \, dt \tag{6.4}$$

that is,

$$f(\omega) = \frac{1}{2\pi} [\sin c(\omega' + \omega)\tau - \sin c(\omega' - \omega)\tau] \tag{6.5}$$

and takes the form shown in Figure 6.1. From this it can be seen that the required bandwidth is significant. However, in most cases the material acts as a lowpass filter and attenuates the higher frequencies. Thus, the system designer must therefore consider the effect of the material on system performance, as the general effect is to distort the received time domain waveform by extending its duration and reducing the bandwidth of received information.

Faithful transmission of the particular modulated wave imposes certain requirements on the hardware used in each type of system, and we shall consider each of these in turn in the following Sections. Considerable bandwidth is required to achieve adequate levels of resolution for ground penetrating radar, and the resolution equivalent to a monocycle dictates a bandwidth in the order of three to five octaves. This is a significant requirement and increases the cost and complexity of the transmitter–receiver system. Evidently, as the bandwidth of the system decreases, the effect is to increase the duration of the radiated/received signal, and hence a compromise is reached between the desired resolution/system bandwidth and the characteristics of the material being probed.

The following Sections examine the different classes of modulation and the general system architecture and hardware used to construct a suitable radar system. In general, the output from most systems results in an equivalent time domain representation of the waveform, and hence subsequent signal processing methods will only be referred to where system architecture is different, as for example in the case of holographic imaging radar. It is useful to compare and contrast the fundamental range resolution of various signals, particularly for small targets close in range to large targets, and one approach is given below from an original paper by Daniels [1].

6.2 Resolution of ultra-wideband signals

6.2.1 Introduction

Ultra-wideband signals are used to enable the high-resolution measurement of target features very much less than the target size or, alternatively, of responses from local scattering centres. Radar, sonar, ultrasonic or other active measurement systems can transmit such signals.

A typical measurement system, such as a ground-probing radar system, transmits an ultra-wideband signal through the ground and detects the weak back-scattered signal from the target or targets, which could be dielectric cylinders (mines). A diagram of such a measurement system is shown in Figure 6.2.

The ability of the measurement system to detect both targets is related to the type of waveform and the detection process of the receiver. The relative levels of the two received signals depend on the attenuation of the lossy media, as well as the radar cross-sections of the targets. The level of the signal reflected from the smaller target

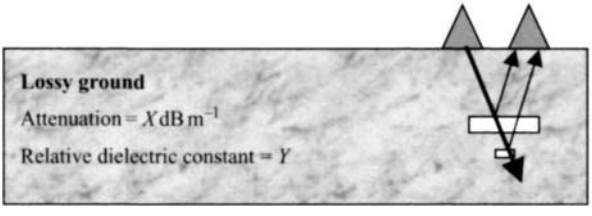

Figure 6.2 Outline diagram of measurement process

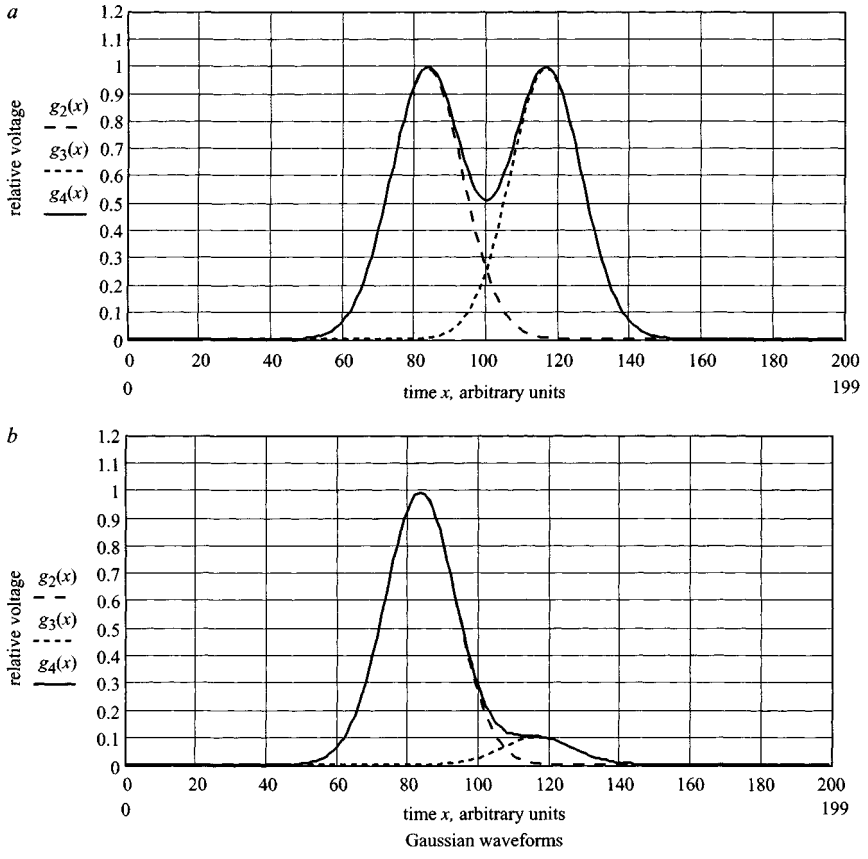

Figure 6.3 Resolution criteria for Gaussian waveforms

may be much lower than from the larger target. The normal Rayleigh criteria for the resolution of equal amplitude targets shown in Figure 6.3*a* are clearly unsuitable for the case where the reflected signal from one target is −20 dB of the other (Figure 6.3*b*).

Note that, in all the graphs shown in this Chapter, both time and frequency are plotted in arbitrary dimensionless units.

It is useful to consider what criteria should be adopted for range resolution in a lossy medium. This can be done by considering the relative signal levels in dB as a function of distance for a range of material attenuation, as shown in Figure 6.4.

It can be seen that, for the case of an attenuation of $100\,\mathrm{dBm}^{-1}$, the slope of the graph at a range of 30 cm is $\sim 10\,\mathrm{dB\,ns}^{-1}$. This suggests that, for two targets with equal reflecting cross-sections and 10 cm apart in range (equivalent to 2 ns), the envelope of the first reflection should be < -20 dB of its peak value, at a distance of 10 cm, if the second target is to be detected. If the second target has a lower reflecting cross-section than the first, the requirement in terms of decay is even more severe.

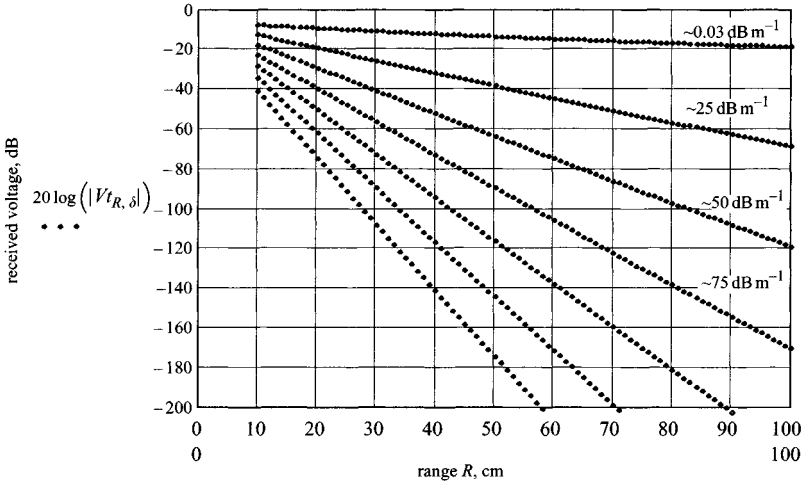

Figure 6.4 *Received signal in dB versus range in centimetres in a lossy medium for a range of material attenuation (increasing by 25 dB m^{-1}) and a relative dielectric constant of 9*

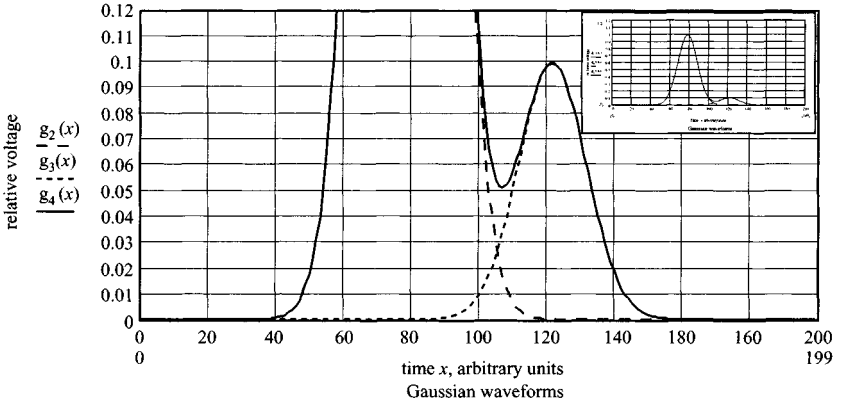

Figure 6.5 *Detection of a weak target adjacent to a strong target, for Gaussian envelopes*
Full graph shown inset

An example for a Gaussian envelope is shown in Figure 6.5, where the separation must be equal to the width of the greater signal at a level of 10% of the peak of the larger signal.

The ability of the measurement system to resolve the reflections from the two targets depends on an adequate signal to noise ratio. In this Chapter it is assumed that this is the case and the peak value of the envelope of the signal is significantly

greater than the rms value of the noise or alternatively the noise tends to zero. In the case of a ground-probing radar system, the noise within the radar receiver is largely determined by the bandwidth and noise figure of the receiver. This Chapter does not address the optimisation of signal characteristics taking into account the dispersive and lossy propagation medium. Pre-compensation for the propagation characteristics is one approach to waveform optimisation. Practically, the choice of radar system and signal is limited to time domain, frequency domain or noise modulation, and this Chapter considers signals with near equal received bandwidths.

6.2.2 *Consideration of waveform characteristics*

Various processing techniques can be selected to provide optimisation of features of a received signal, and the Wiener filter is such an example. This Chapter compares the relative performance of a generic system using a direct detection receiver and a matched filter receiver. A time domain radar system, using a direct receiver, transmits an impulse wavelet and recovers the reflected signal using a sequential sampling receiver. A frequency domain radar system transmits a frequency-modulated waveform and recovers the reflected signal using a matched filter receiver, as does a noise-modulated radar.

The matched filter receiver provides an optimum signal to noise ratio, output of radar signals [2] in the presence of noise. The radar signal is processed by a receiver that crosscorrelates the received waveform with a suitably time delayed version of the transmitted waveform. The output results in a compressed pulse in which the amplitude of the latter and its position in delay time is related to the target radar characteristic. This type of receiver is widely used to process chirp, step frequency, and coded and noise waveforms, and the design of such waveforms is described extensively in the literature. The following references provide suitable treatments: [3–6]. The case of the ultra-wideband, short duration, impulse has been less extensively described, although Astanin and Kostylev [7] analyse the case of radar receivers that directly measure the reflected waveform. Most linear frequency modulated pulse compression radar waveforms are real functions of the type

$$f(t) = a(t)\cos(\omega_0 t + \phi(t)^{\beta}) \tag{6.6}$$

where $\beta > 1$ and the envelope $a(t)$ and the phase modulation are relatively slowly varying time functions compared with $\cos(\omega_0 t)$. This is not the case for some of the time domain waveforms that will be considered, where additionally the phase term is not relevant. It is the objective of this Chapter to consider their equivalent post-detection performance, as far as range resolution is concerned. For that reason, the comparison of the detected waveforms is between output of a correlation detector (envelope of the autocorrelated frequency modulated waveforms) and a direct detector (envelope of the original wavelet).

6.2.3 *Definition of the waveforms*

It is necessary that the spectral density functions of the signals considered have zero content at DC, because the measurement systems that are being considered use transducers or antennas than do not radiate or receive DC signals. For that reason, the condition of a zero frequency carrier is excluded from this consideration and it is assumed that the centre or nominal carrier frequency of the signal is appreciably greater than DC and the bandwidth of the signal is large. In the case of short duration, impulsive, time domain signals, the value of the parameter of a centre frequency becomes less important.

The condition of zero DC content is satisfied by any practical radar signal that is transmitted and received and must also be true of any modelled signal. In all of the modelled signals described in this Chapter, all have been passed through a highpass filter to ensure that the DC component of the signal is zero.

From Galati [6],

$$F(0) = \int_{-\infty}^{\infty} f(t)e^{-j\omega t}\,\mathrm{d}t\big|_{\omega=0} = 0 \tag{6.7}$$

The energy of a signal $f(t)$ with finite energy is given by

$$E = \int_{-\infty}^{\infty} |f(t)|^2\,\mathrm{d}t \tag{6.8}$$

and the energy based on the complex envelope of this signal is given by

$$E = \int_{-\infty}^{\infty} |\tilde{f}(t)|^2\,\mathrm{d}t \tag{6.9}$$

where $\tilde{f}(t) = a(t)\cos(\omega_0 t + \phi(t))$ and is defined as a bandlimited signal.

The envelope of such a signal is defined as

$$\mathrm{env}(t) = [\tilde{f}(t)^2 + h_h(\tilde{f}(t))^2]^{0.5} \tag{6.10}$$

where $h_h(\tilde{f}(t))$ is the Hilbert Transform $\tilde{f}(t)$.

The matched filter output of a signal $f(t)$ is given by the autocorrelation of the transmitted signal

$$s_0(t) = k\int_{-\infty}^{\infty} f^*(\tau)f(t+\tau)\,\mathrm{d}(\tau) \tag{6.11}$$

The selection of a suitable waveform for transmission, at least in terms of resolution, can be considered a function of the duration of the complex envelope of the measured signal. The objective of this Chapter is to show that, for some particular classes of

signals, the duration of

$$k\text{env}(f_0(t)) < k\text{env}(s_0(t)) \quad \text{where } k < 1$$

The next Section considers three classes of waveform, all with equal energy and with nearly equivalent 3 dB spectral characteristics. Although they have similar autocorrelation functions, the duration of the envelope function for the directly detected signals is less than that of the matched filter signals.

6.2.4 Time domain wavelet signals

The three waveforms that are considered are a Ricker wavelet, a sine wavelet and a sine wavelet with after-ring. The latter waveform is typical of the waveform radiated by an ultra-wideband antenna or a well damped, ultrasonic transducer.

A Ricker wavelet is defined as the second differential of a Gaussian function and is the general form of a waveform that results from the application of a Gaussian impulse to an impulse radiating antenna or transducer system. The Gaussian function and hence the envelope of the Ricker wavelet is characterised by a slow build-up and decay of energy at the extremes of the function. The sine wavelet is a similar type of waveform but is characterised by a localised concentration of energy. Both avoid sudden transitions at the extremes of the envelope of the wavelet.

A Ricker wavelet is given by

$$f_0(t) = \frac{\mathrm{d}^2(e^{-at^2})}{\mathrm{d}t^2} \tag{6.12}$$

A sine wavelet is given by

$$\begin{aligned} f_1(t) &= A\sin(2\pi ft)\sin\left(\frac{2}{3}\pi ft\right), \quad \tau_1 \le t \le \tau_2 \\ f(t) &= 0, \quad t \le \tau_1, t \ge \tau_2 \end{aligned} \tag{6.13}$$

where $\tau_1 = N/8, \tau_2 = N/4$.

A sine wavelet with after-ring is given by

$$f_1(t) = A\sin(2\pi ft)e^{-\alpha t}, \quad t \ge \tau_2 \tag{6.14}$$

where $\tau_1 = N/8$, $\tau_2 = N/4$, $\alpha = 0.01$.

Frequency/amplitude modulated signals: The general form for a linear frequency modulated pulse compression signal was given in (6.6). A Hamming weighted, chirp waveform is of the form

$$f(t) = A\sin\left(2\pi(f_0t) + (f_0t)^k\right)\left(0.08 + (1 - 0.08)\sin\left(\pi\frac{t}{N}\right)^2\right) \tag{6.15}$$

where $k = 2.05$, $A = 1$ and t and N are related to the duration of the waveform.

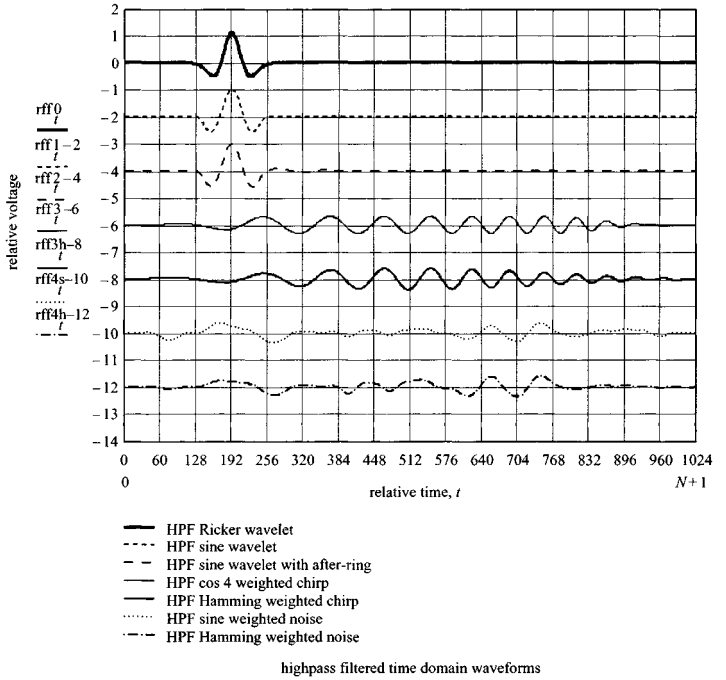

Figure 6.6 Time domain characteristics of signals

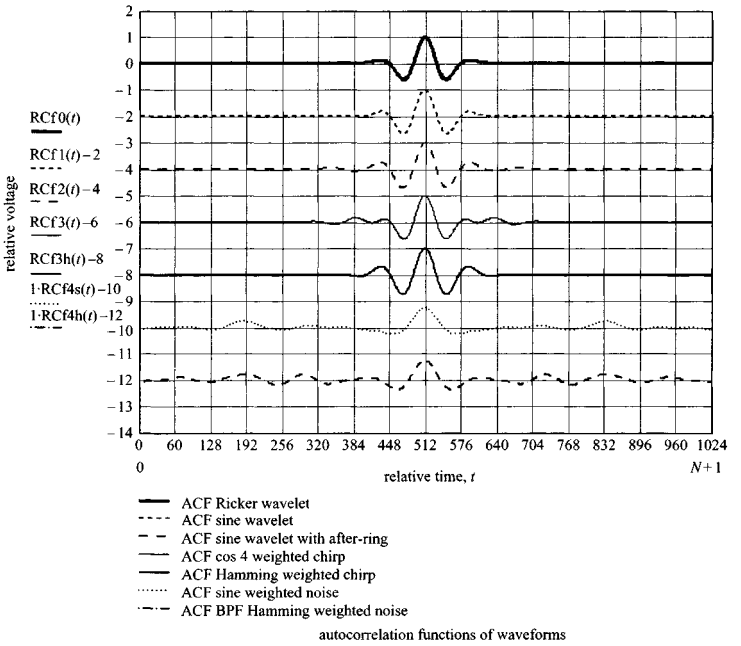

Figure 6.7 Autocorrelation functions of signals (shown centralised)

A cosine weighted, chirp waveform is of the form

$$f(t) = A\sin(2\pi(f_0 t) + (f_0 t)^k)(W(t)) \tag{6.16}$$

where

$$W(t) = \sin\left(\frac{2\pi t}{\beta}\right)^4 \quad \text{for } 0 \leq t \leq \beta,\ N - \beta \leq t \leq N$$

$$W(t) = 1 \quad \text{for } \beta \leq t \leq N - \beta$$

6.2.5 *Noise signals*

The noise waveform is white noise, with a normal distribution, a mean value of 0 and a standard deviation of 1.1. The noise waveform was modulated by an envelope taper to avoid transients at the start and end of the sequence. These are respectively a sine taper and a Hamming taper.

6.2.6 *Comparison of signals*

Figure 6.6 shows the signals under consideration and Figure 6.7 their autocorrelation functions. It can be seen that, apart from the noise waveforms, which possess significant sidelobes, the autocorrelation functions are very similar.

6.2.7 *Comparison of spectra*

If the power spectral density of the Ricker wavelet, a sine wavelet and a sine wavelet with after-ring are compared, it can be seen that the main lobe energy is nearly equivalent at the −3 dB level, although the −20 dB bandwidths are not identical (Figure 6.8). These spectra satisfy the condition given in (6.6).

The same comparison can be made between the spectra of the Ricker wavelet and the two frequency modulated signals (Figure 6.9).

While the envelopes of the sidelobes of the spectra are different, the −3 dB width of the main lobe is nearly identical in all cases. As will be discussed in Section 6.2.9, the sidelobe level of different signals also has a bearing on the resolution that can be achieved in the case of weak targets adjacent to strong targets. The spectra of the noise signals also follow the same trend.

6.2.8 *Comparison of signal envelopes*

When comparing the envelopes of the signals it is important to compare the detected outputs. In the case of the Ricker and sine wavelets, the receiver can directly detect the wavelet by means of a sequential sampling receiver; hence, it is sufficient to determine the envelope of the wavelet (Figure 6.10). However, in the case of the frequency modulated or noise waveform, the receiver performs a matched filter or

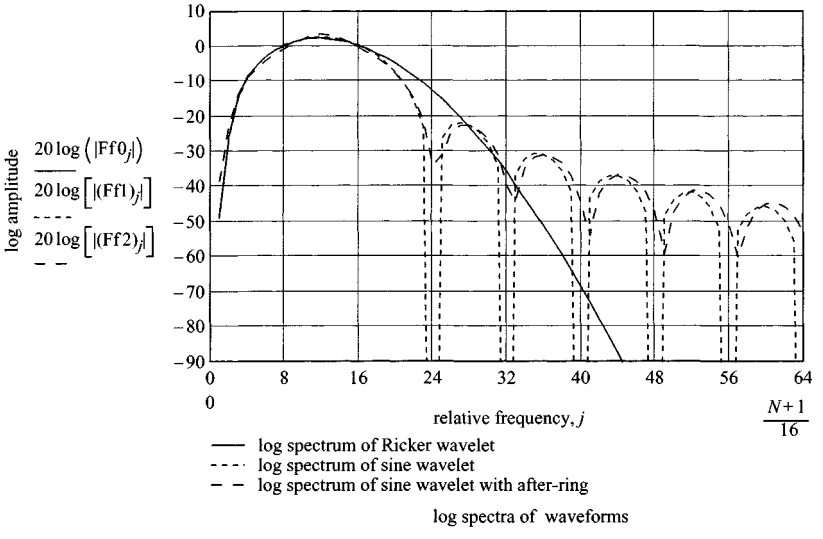

Figure 6.8 *Comparison of power spectra of a Ricker wavelet, a sine wavelet and a sine wavelet with after-ring versus relative frequency*

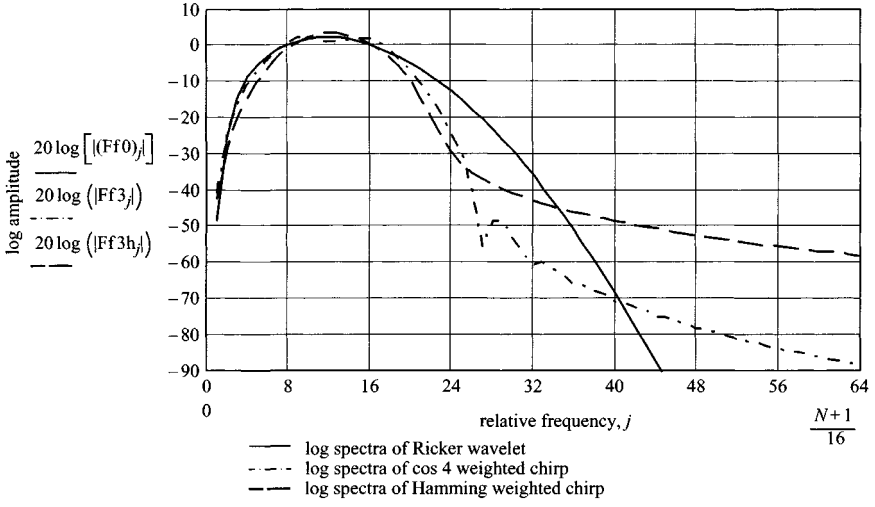

Figure 6.9 *Comparison of power spectra of a Ricker wavelet, a cosine weighted and Hamming weighted chirp waveform versus relative frequency*

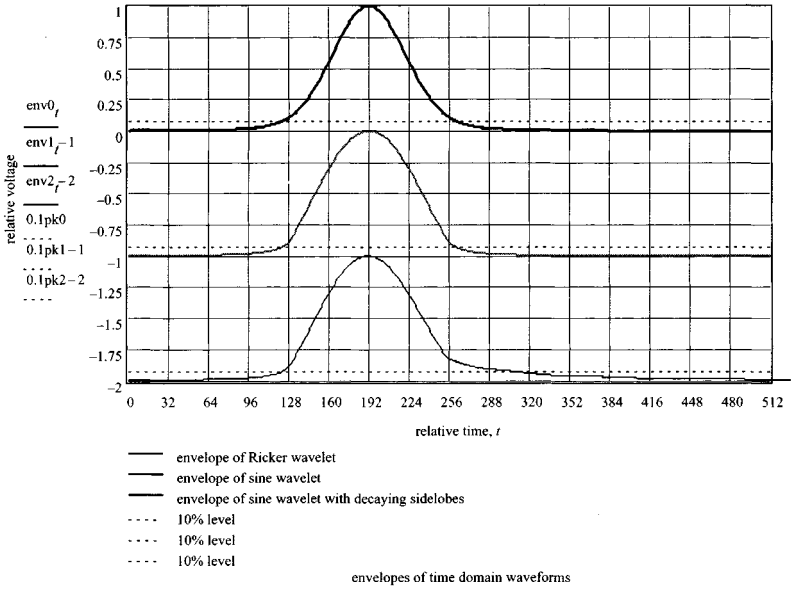

Figure 6.10 Comparison of envelopes of a Ricker wavelet, sine wavelet and sine wavelet with after-ring together with the 10% of peak level shown

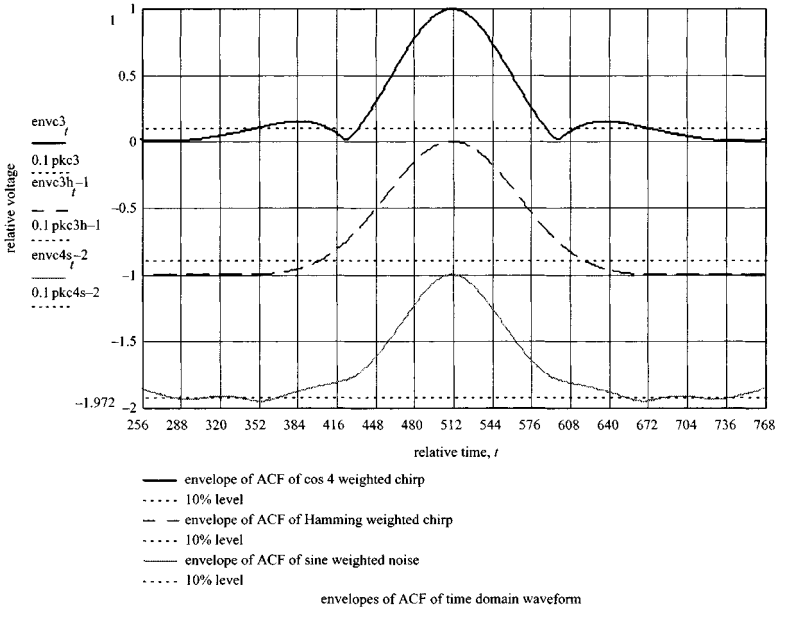

Figure 6.11 Comparison of envelopes of ACF of a cosine and Hamming weighted chirp signal and a Hamming weighted noise waveform together with the 10% of peak level shown

correlation operation and hence it is the envelope of the correlation function that must be compared (Figure 6.11).

6.2.9 Comparison of envelope sidelobe performance

For a measurement system operating in a lossy medium, the sidelobe performance in the time domain is critical to the resolution of a weak target adjacent to a strong target. Therefore, it is useful to view the envelopes shown in Figures 6.12 and 6.13 plotted on a log scale. In most time domain measurements systems the output is processed in a linear scale, but frequency domain systems often show the processed output on a dB scale.

It can be seen that, from the set of signals considered, the width of the envelopes of the directly detected signals is less than the envelopes of the output from a matched filter process; this includes the sidelobes (see Table 6.1).

The exact shape of the radiated spectral energy is very important in achieving very low sidelobe levels in the time domain and is considered by Daniels [8], and Noon and Stickley [9]. These authors point out that truncations of the radiated spectra have an effect analogous to the Gibbs phenomenon. This is to induce time domain sidelobes because of sharp transitions at the extremes of the band edges of the frequency of the radiated waveform. These transitions can be caused by the bandpass characteristics of antennas or by limitations in the transmitted range of frequencies.

6.2.10 Summary

Designers of measurement systems that work in lossy media may consider the inherent resolution characteristics of the received signal to be of equal or greater importance to the signal to noise ratio. This Chapter compares the resolution performance of some of the basic types of signal that can be used. The comparison was based on equal energy of the signals in the time domain and equal 3 dB bandwidths of the main lobe of their respective spectra. A high signal to noise ratio of all the waveforms was assumed.

From the signals considered, the short duration impulse wavelets, detected using a direct receiver process, offer the highest resolution. The chirp signals using a receiver that employs a matched filter correlation process for detection offered less resolution and the noise signals the worst. This may be critical, as in the case of a ground probing radar designed to detect small plastic anti-personnel mines in lossy soils. The frequency domain signals considered were rapidly changing functions of time with respect to centre frequency and relatively short sequences. It is conjectured that both the frequency modulated and noise signals would have performed better with a longer, lower amplitude sequence, but this remains to be shown. A future consideration could be to extend the comparison to signals with a constant time–bandwidth product, slowly varying functions of time with respect to centre frequency and the lower signal to noise ratios.

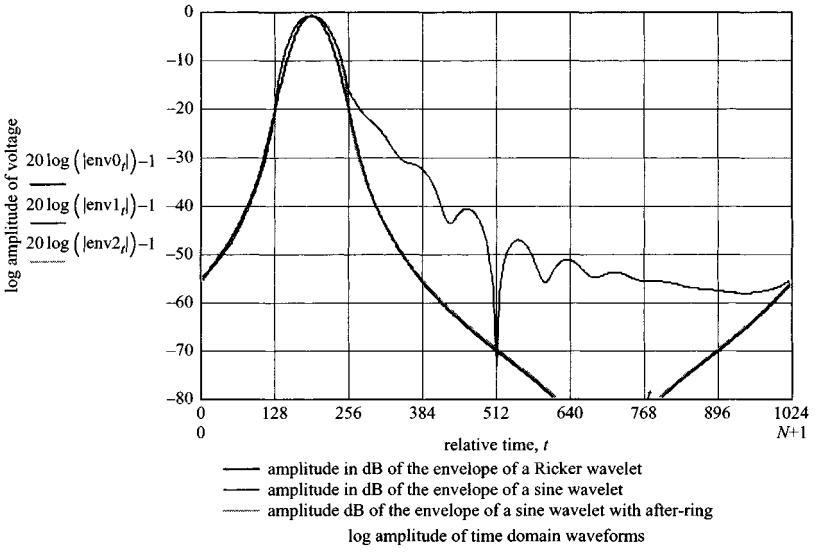

Figure 6.12 Comparison of time sidelobes in dB of envelopes of a Ricker wavelet, sine wavelet and sine wavelet with after-ring

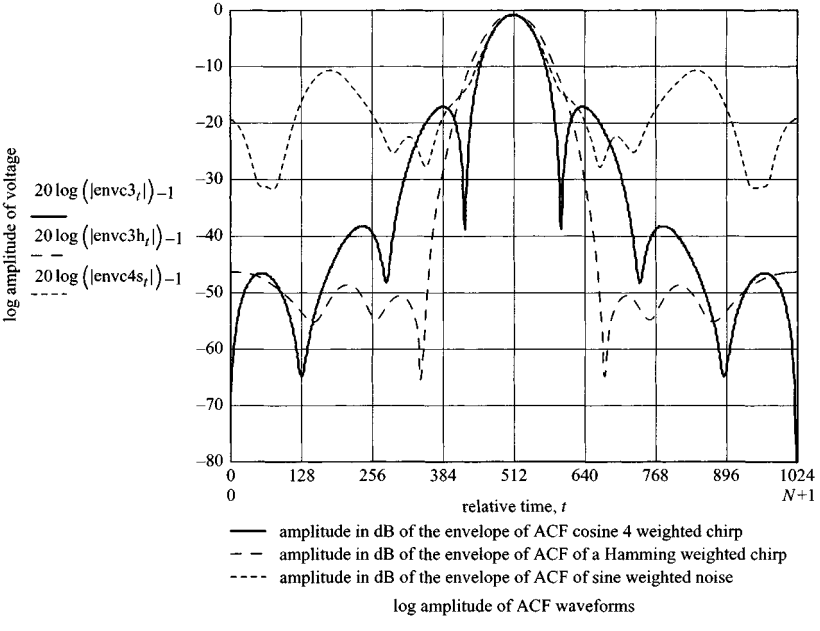

Figure 6.13 Comparison of time sidelobes in dB of envelopes of a cosine weighted and Hamming weighted chirp and a sine weighted noise signal

Table 6.1 Comparison of main parameters of the signals

Waveform (envelope)	Main lobe width at −20 dB	Envelope width at −40 dB	First sidelobe level, dB	Rate of decay of sidelobes	Symmetry
Ricker	1.00	1.78	NA	NA	NA
Sine wavelet	1.00	1.78	NA	NA	NA
Sine wavelet+ after-ring	1.125	2.6	NA	10 dB per main lobe	asymmetric
ACF cosine weighted chirp	1.1	2.47	−17	16 dB per main lobe	symmetric
ACF Hamming weighted chirp	1.68	3.36	>−48.5	level at −50 dB	symmetric
ACF sine weighted noise	2.07	>5	−12	level at −20 dB	symmetric

6.3 Amplitude modulation

The majority of ground penetrating radar systems have used impulses of radio frequency energy variously described as baseband, video, carrierless, impulse, monocycle or polycycle. The simplified general block diagram of an amplitude-modulated system is shown in Figure 6.14, together with a timing diagram as shown in Figure 6.15.

A sequence of pulses, typically of amplitude within the range between 20 V and 200 V and pulse width within the range 200 ps to 50 ns at a pulse repetition interval of between several hundred microseconds and 1 μs, depending on the system design, is applied to the transmit antenna. It is quite feasible to generate pulses of several hundred kV, albeit at long repetition intervals. The output from the receive antenna is applied to a flash A/D converter or a sequential sampling receiver. This normally consists of an ultra-high-speed sample-and-hold circuit. The control signal to the sample-and-hold circuit which determines the instant of sample time is sequentially incremented each pulse repetition interval. For example, a sampling increment of $t = 100$ ps is added to the previous pulse repetition sampling interval to enable sampling of the received signal at regular intervals, as indicated below:

$$T_s = T + nt' \quad \text{for } n = 1 \text{ to } N \tag{6.17}$$

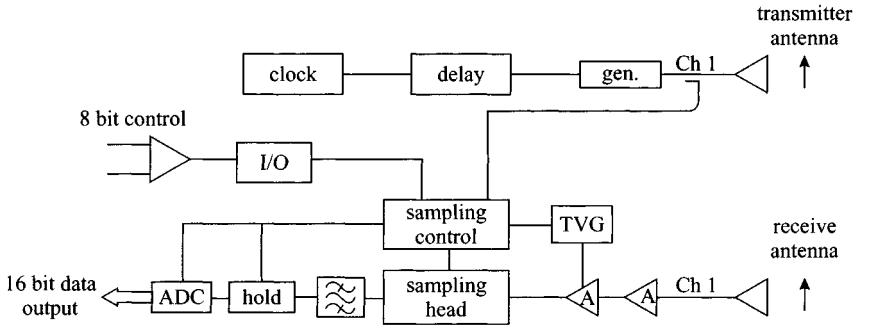

Figure 6.14 Transmitter–receiver architecture

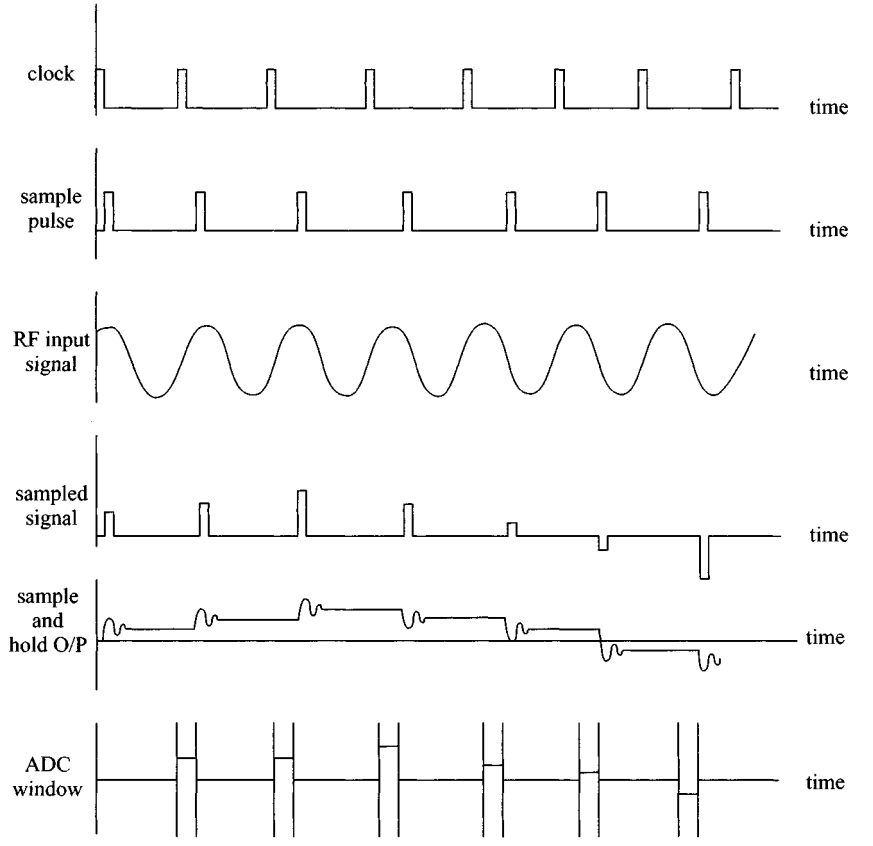

Figure 6.15 Sequential sampling receiver timing

where T is the pulse repetition time, t' is the sampling interval and N is the total number of samples.

Certain important limitations in terms of sampling interval should be noted. From the sampling theorem, the sampling interval must be such as to comply with the Nyquist relationship

$$t' \leq \frac{1}{2B} \tag{6.18}$$

where B is the bandwidth of interest. In practice, a greater number of samples is normally required for accurate reconstruction and the sampling interval is generally taken as

$$t' \leq \frac{1}{5B} \tag{6.19}$$

The principle of the sampling receiver is therefore a down-conversion of the radio frequency signal in the nanosecond time region to an equivalent version in the micro- or millisecond time region. The incrementation of the sampling interval is terminated at a stage when, for example, 256, 512 or 1024 sequential samples have been gathered. The process is then repeated. There are several methods of averaging or 'stacking' the data; either a complete set of samples can be gathered and stored and further sets added to the stored data set or alternatively the sampling interval is held constant for a pre-determined time to accumulate and average a given number of individual samples. The first method needs a digital store but has the advantage that each waveform set suffers little distortion if the radar is moving over the ground.

The second method does not need a digital store and a simple lowpass analogue filter can be used. However, depending on the number of samples that have been averaged, the overall waveform set can result in being 'smeared' spatially if the radar is moving at any speed.

The stability of the timing increment is very important and generally this should be 10% of the sampling increment; however, practically stability in the order of 10 ps to 50 ps is achieved. The effect of timing instability is to cause a distortion, which is related to the rate of change of the RF waveform. Evidently, where the RF waveform is changing rapidly, jitter in the sampling circuits results in a very noisy reconstructed waveform. Where the rate of change of signal is slow, jitter is less noticeable. Normally, control of the sampling converter is derived from a sample of the output from the pulse generator to ensure that variations in the timing of the latter are compensated automatically.

The key elements of this type of radar system are the impulse generator, the timing control circuits, the sampling detector and the peak hold and analogue to digital converter.

The impulse generator is generally based on the technique of rapid discharge of the stored energy in a short transmission line. The most common method of achieving this is by means of a transistor operated in avalanche breakdown mode used as the fast switch and a very short length of transmission line. A typical circuit arrangement

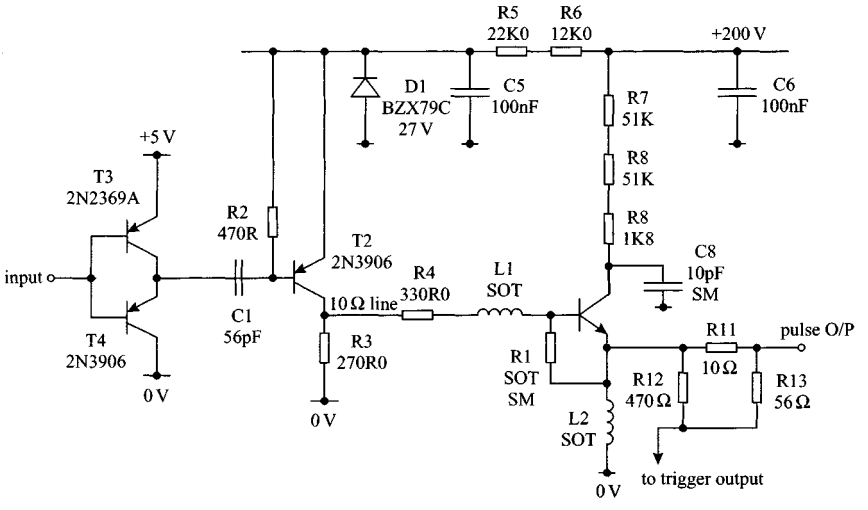

Figure 6.16 Avalanche transistor impulse generator

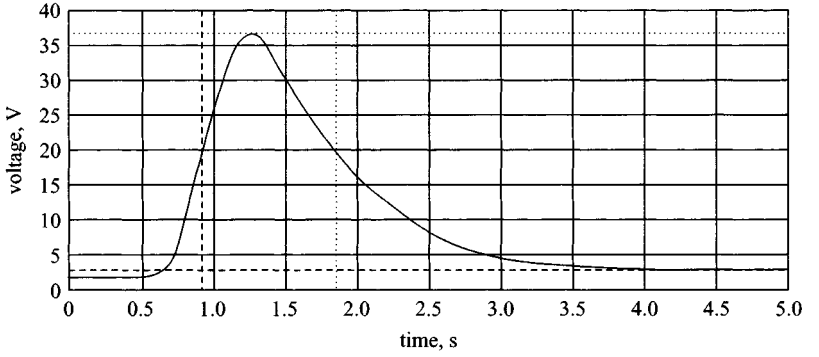

Figure 6.17 Typical voltage waveform generated by the circuit of Figure 6.16

is shown in Figure 6.16 and this provides an output of 100 V with duration of 1 ns as shown in Figure 6.17. The frequency domain characteristics of such an impulse are shown in Figure 6.18. If shorter duration impulses are required it is possible to use a step recovery diode to generate impulses of durations in the order of 200 ps, and a typical output voltage is in the region of 30 V.

Evidently, the repetitive nature of the pulse causes line spectra in the frequency domain. The typical repetition time interval for an avalanche transistor impulse generator is in the order of 0.1 s to 10 s, while the step recovery diode must be chosen specifically to match the repetition interval to ensure that charge carrier recombination can take place.

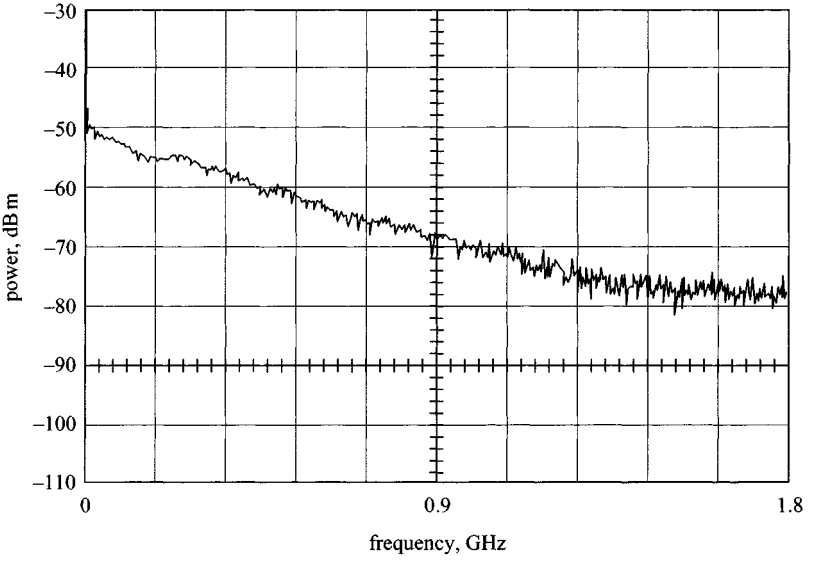

Figure 6.18 Typical spectrum of the waveform generated by the circuit of Figure 6.16

Other methods of generating impulses use power FETs, and voltage impulses up to 10 kV have been generated [10]. An alternative means of generating high power impulses is based on the use of a photoconductive semiconductor switch (PCSS) to discharge a capacitor into a shorted transmission line. A picosecond laser pulse is used to rapidly switch the conducting–nonconducting state of a semiconductive material such as GaAs. Typical output voltages of 14 kV in 50 Ω impedance for a duration of nanoseconds or less have been produced [11].

A further variation on this technique is the frozen wave generator shown in Figure 6.19. This consists of several segments of transmission lines connected in series by means of picosecond photoconductive switches. The output from the ensemble is a sequential waveform of arbitrary characteristic, i.e. a 'frozen wave'. Output voltage in the kilovolt range has been generated [12].

Several factors need to be considered in the design of impulse sources, and these are reliability, jitter and repetition rate. In the case of avalanche devices the avalanche process is statistical by nature and is accompanied by jitter. In the case of optical devices the physics of the device must be considered, as the lifetime of the carriers determines the recombination time of the material, and in the case of silicon it may restrict the repetition frequency of the switch. GaAs, on the other hand, exhibits a recombination time of 1 ns. Optical switches may exhibit a reliability of up to 108 operations, which means that their lifetime can be significantly reduced by operation of the radar at high pulse repetition rates.

The high speed sampling approach conventionally used to display fast waveforms produces a low S/N ratio because the spectrum of the sampling pulse is a poor match

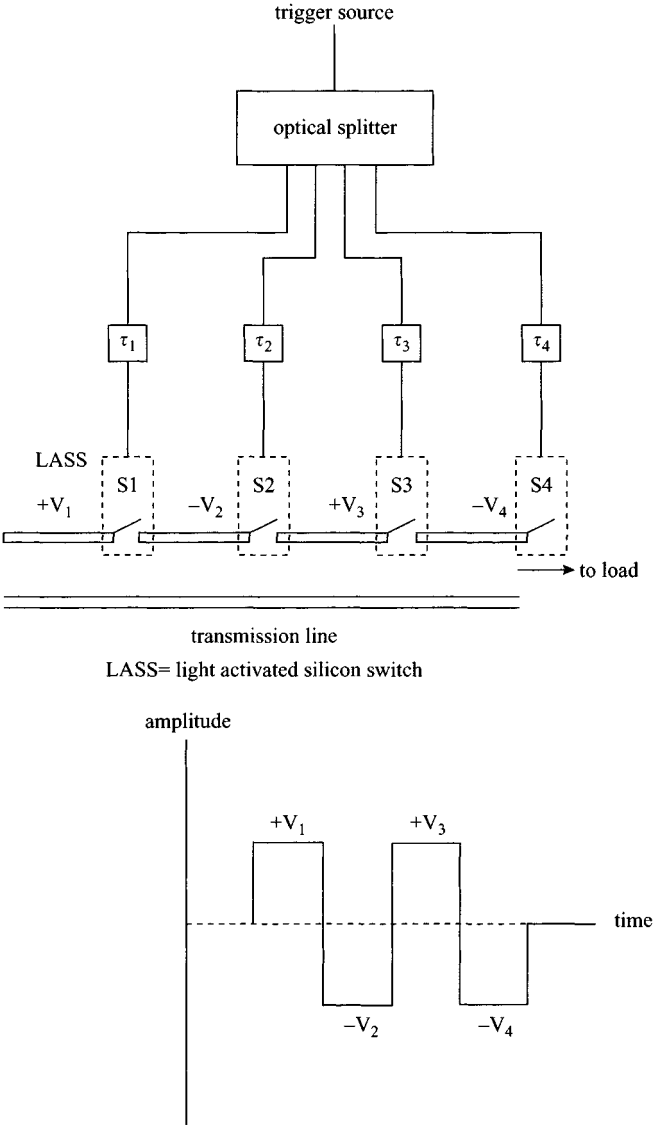

Figure 6.19 *Frozen wave pulse generator*
LASS = light activated switch

for that of the received pulse. Being an essentially nonselective filter, it allows large amounts of noise energy to enter the receiver. Also, the sampling circuit tends to add milliamp level unbalanced currents as well as sampling pulse noise to its output. Although a quite acceptable tradeoff for usual laboratory purposes, this may be unacceptable for receivers with sensitivity in the microvolt range.

Alternative methods of data acquisition are based on high-speed analogue to digital converters or the crosscorrelator receiver. There are several methods of acquiring the high bandwidth RF signals output from the receiver: direct analogue to digital conversion using high speed (flash) A-D converters, frequency selection followed by high speed A-D conversion, or sequential sampling. Typical flash A-D converters feature large signal bandwidths of many hundreds of MHz, sampling jitter less than 5 ps and 8-bit resolution. At bandwidths over 500 MHz typical sampling resolutions are 4 bit and a more complex system architecture is found. In general most current generation impulse radars use high-speed A-D conversion receivers for bandwidths below 200 MHz, where greater resolution can be achieved. An alternative receiver architecture is based on subdividing the RF frequency band and mixing the individual band to separate intermediate frequency bandwidths of 200 MHz that can then be separately A-D sampled.

The wideband crosscorrelator receiver can use coherent processing and, if required, time dithered decoding. The crosscorrelator is equivalent to a matched filter but has more flexibility. The reference waveform can be matched to the transmitted waveform, or in the case of radar, to the complex signature of a particular target, and can be changed in real time if needed. The components required to construct the crosscorrelator are small, inexpensive, low power and compatible with VLSI techniques. It is thus possible to have a large number of correlators operating independently in parallel to achieve the throughput necessary to provide high resolution, real-time, time-coded operation. Sampling as referred to earlier is a time extending process with which a high frequency repetitive signal is duplicated at a lower repetition rate. This type of sampling, where each sample is taken at a fixed frequency with the period of time between samples remaining constant, is known as coherent sampling.

The most basic sampling gate is a simple single diode as shown in Figure 6.20. The diode is essentially a switch, normally 'open' (diode reverse-biased). A short

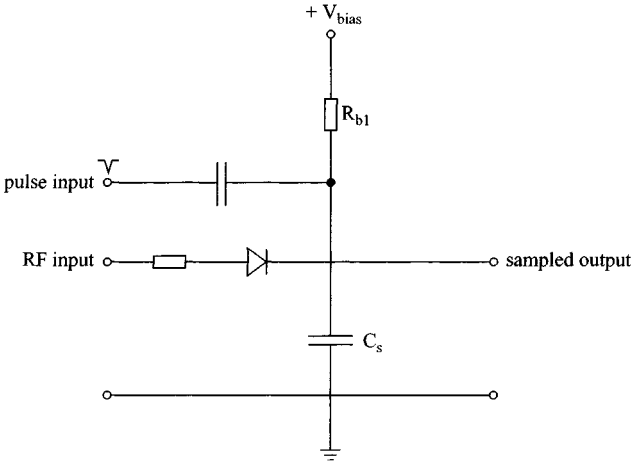

Figure 6.20 Single diode sampling gate

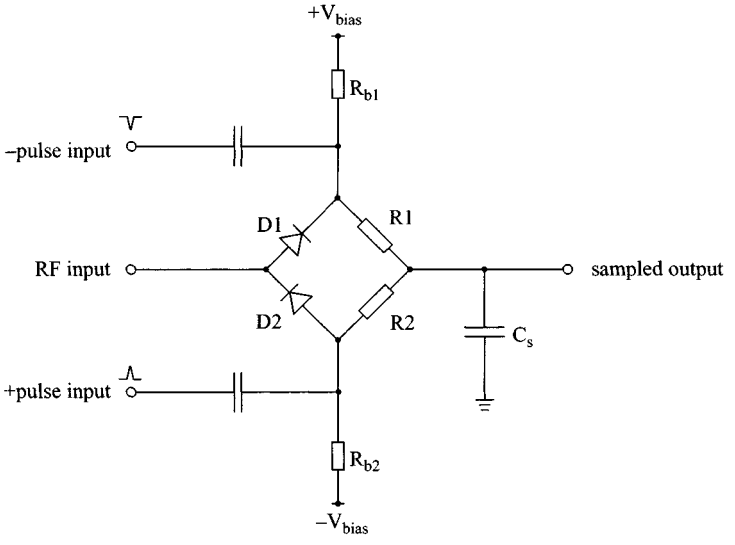

Figure 6.21 Dual gate sampling diode

pulse momentarily closes the switch (diode forward-biased), allowing charge to flow from the source to be stored in the capacitor C_s, which results in a voltage across C_s proportional to the input signal. The pulse width must be narrow compared to the period of the input signal so that the sample corresponds to a specific portion of the input waveform. The capacitor charging time must be fast enough to accept the charge during this pulse time.

The problems of isolation between the signal circuit and the sampling pulse and bias circuits can be serious with the single diode sampler. A two-diode sampler, shown in Figure 6.21, has a low sampling efficiency. The efficiency can be improved by substituting two more diodes for the two resistors in the bridge.

The four-diode sampling gate shown in Figure 6.22 is the most commonly used. In a sampling system it would be situated between the input source and the input capacitor of an amplifier. The diodes are normally reverse biased so that the input signal does not cause them to conduct. Sampling is initiated with very narrow pulses, which overcome the reverse bias and switch the diodes into conduction. The low impedance paths allow the amplifier input capacitor to be charged to a voltage proportional to the input voltage. Owing to the short charging time the capacitor may not be charged to the full input voltage. (Some systems include feedback control circuits to continue charging the capacitor in between pulses until the capacitor voltage equals the input voltage.) The capacitor remains charged until the next pulse.

The reverse bias applied to the sampling gate diodes is a critical factor in the operation of a sampler. It must be large enough to prevent input signals driving the diodes into conduction and small enough to allow the gating pulses to forward bias the diodes during the sampling periods to achieve maximum sampling efficiency.

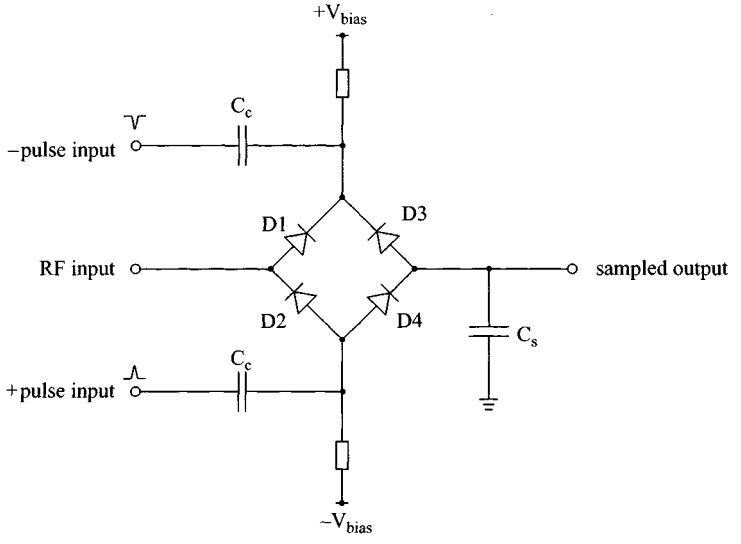

Figure 6.22 Quad diode sampling gate

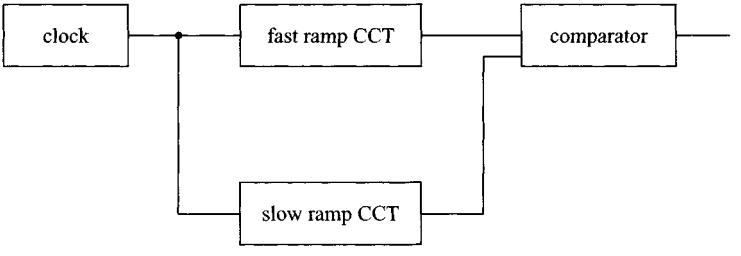

Figure 6.23 Dual ramp timing circuit

Both dc and ac balance of the sampling gate bridge are essential in achieving the symmetry required for optimum performance of the sampler. The conditions of balance require that the four sampling diodes be matched, the two reverse bias voltages are equal and opposite, and the sampling gate control voltage is identical in wave shape except for polarity. One method of providing identical control gate signals is to derive them from the identical and bifilar-wound windings of a transformer. A narrow pulse can be produced as a result of differentiation of a rectangular pulse with a small coupling capacitor. If required, using step recovery diodes before coupling through the capacitor can reduce pulse rise times.

The timing control circuits are a key element of the receiver, and the standard method of generating a sequence of incremented pulses is by means of a dual ramp circuit as shown in Figure 6.23. The fast ramp is at the same rate as the pulse repetition

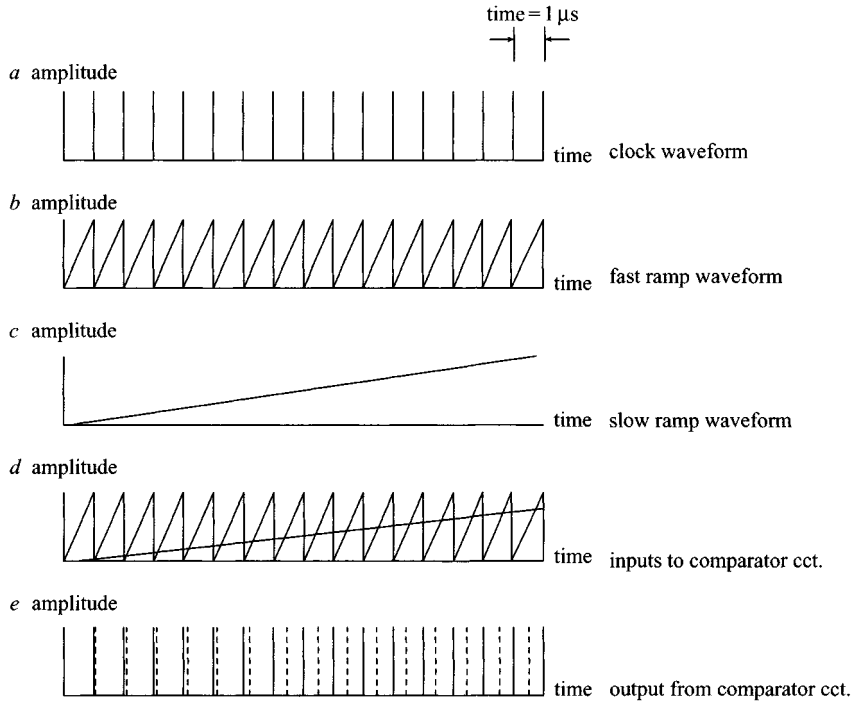

Figure 6.24 Dual ramp timing waveforms

time, while the slow ramp is set to provide the desired number of samples, i.e. 256, 512 or 1024. The timing sequence for this is shown in Figure 6.24.

The ramp circuits can be designed using analogue or digital circuits. In the case of analogue circuits the main building block is an integrator circuit, whereas in the case of a digital design suitable integrated circuits are available in the form of Analog Devices' AD9500 digital delay IC.

Evidently, time stability of these circuits is vitally important and, for example, a 512 ns time window with 256 samples requires one sample every 200 ps increment. However, this increment occurs every 1 s, and hence timing stability must be 1 s + 200 ps ± 20 ps, i.e. 1000.2 ns ± 20 ps, i.e. ±0.002%. Great care is therefore needed in circuit design to achieve adequate stability.

The dynamic performance of an impulse (amplitude modulated) radar can be estimated from the following example (see Table 6.2).

A graph of received signal strength versus time is shown in Figure 6.25. From this it can be seen that the operating range of the radar system lies between the boundaries defined by the functions defined by the clutter profile, target reflection loss and the limit of sensitivity due to the noise figure of the receiver.

It can be readily appreciated that the limited dynamic range of the sampling receiver limits the performance of the radar.

Table 6.2 Typical operating characteristics for a time domain radar

Transmitter		
Peak power	50 W	(46.9 dB m)
Mean power	50 mW	(16.98 dB m)
Antenna and cable losses	−16.9 dB	
Peak radiated power	1 W	(30 dB m)
Mean radiated power	1 mW	(0 dB m)
Impulse duration	1 ns	
Impulse repetition time	1 μs	
System clutter profile (rate of decay of time sidelobes and crosscoupling)	30 dB/ns	
Receiver		
RF bandwidth	1 GHz	
Equivalent thermal noise (300 k)	4.14×10^{-12} W(−84 dB m)	
Noise figure of sampling head	40 dB	
Noise floor	−44 dB m	
Maximum input signal level	7 dB m	
RF dynamic range	53 dB	
Time varying gain	40 dB	
Equivalent RF dynamic range	93 dB	
Averaging signal to noise improvement	25 dB	
Receiver equivalent dynamic range	118 dB	

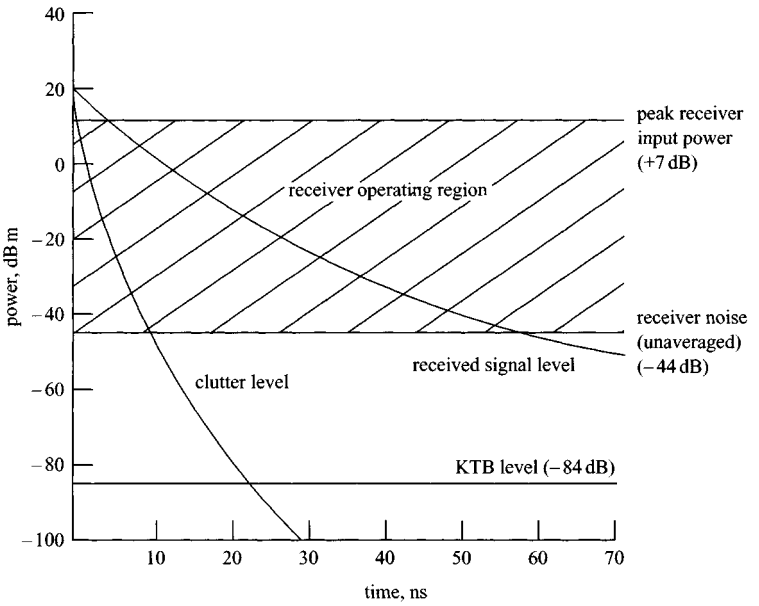

Figure 6.25 Received signal against time for a sequential sampling receiver

The poor noise figure of the sampling gate can be improved by using a wideband low noise RF amplifier prior to the gate. The typical noise figure of a 1 GHz amplifier is 2.4 dB, and hence an immediate improvement in system noise figure is achieved. However, the sampling gate may now be vulnerable to saturation by high level signals caused by targets at very short ranges.

The solution to this problem is to incorporate an additional RF amplifier whose gain can be varied as a function of time. In practice, this is most easily achieved in synchronism with the pulse repetition rate. This avoids undesirable intermodulation effects, which can occur if the gain is changed in real time. This technique enables the receiver to be operated at maximum sensitivity without encountering overload problems. Ideally, the gain/time characteristic should be related to the attenuation and reflection characteristics of the material under investigation. Hence, an adaptive calibration method is advisable.

Generally, a compression range of up to 40 dB can be expected, and this is adequate to compress most of the high-level close range signals. The optimum technique is to use an adaptive signal level compression whereby the peak received signal as a function of time is adaptively set to a predetermined value by means of LNA gain adjustment.

It is also possible to improve the dynamic range by averaging the received signal, and this improvement is given in dB by

$$A = 20 \log \sqrt{N} \tag{6.20}$$

where N is the number of averages.

However, the rate of improvement quickly decreases as N is increased and, practically, 16 averages provide a reasonable improvement without excessive time penalties.

The frequency range of the output signal usually occupies a bandwidth up to 20 kHz. In the case of a radar operating at a repetition rate of 1 μs with 256 samples, each averaged 16 times, the ensemble down-converted signal is repeated at the time given by

$$\tau' = \tau_r N_a N_s \tag{6.21}$$

which, for the values given above, is equal to

$$\tau' = 1 \times 10^{-6} \times 16 \times 256 = 4\,\text{ms}$$

Hence the bandwidth of the down-converted signal is given by

$$B = 1/5\tau' \tag{6.22}$$

where τ' is the equivalent down-converted time per sample, and $B = 1/5\tau_r N_a = 12\,500$ Hz.

Note that the true noise bandwidth of the receiver is defined by the RF bandwidth, and the noise energy is converted together with the signal.

The dynamic range of the analogue to digital converter, which follows the sampling head, should be matched to the dynamic range of the latter and typically, a 12-bit or 16-bit converter is used.

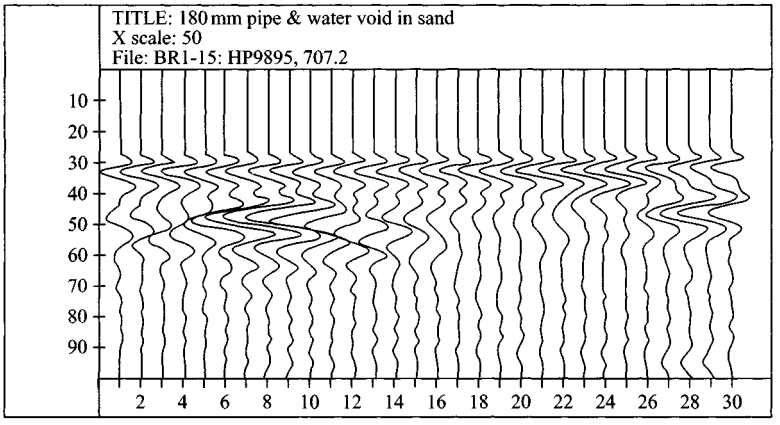

Figure 6.26 *Example of time-domain signal from two buried targets (courtesy ERA Technology)*
Vertical scale 3 ns = 10 units; horizontal scale 20 mm = 1 increment

When constructing impulse radar systems it is necessary to ensure that adequate decoupling of the internal power supplies is achieved as the effect of impulsive noise from switched mode power supplies on the sampling circuits can result in serious degradation of the overall system performance. Hence, good engineering practice must be maintained in the design and layout of the RF circuits.

It is also important to consider the physical layout of the sampling receiver, pulse generator and antennas. Two options are available. The antenna can be directly connected to the transmitter and receiver circuits or it can be interconnected via a length of high quality RF cable. In the latter case the physical length serves to electrically separate the reflected signals caused by the antenna and the transmitter/receiver circuits. However, the cable acts as a lowpass filter, which degrades the system resolution. Where the antennas are directly connected, multiple echoes can prove difficult to reduce to low levels and some design skill is needed to achieve acceptable results. Additionally the physical proximity of electronic components to the antennas may disturb their radiation characteristics.

Typical examples of time domain signals received from buried targets are shown in Figures 6.26 and 6.27.

6.4 Frequency modulated continuous wave (FMCW)

Frequency modulated continuous wave (FMCW) radar systems have been used in preference to AM systems where the targets of interest are shallow and frequencies above 1 GHz can be used. As the centre frequency of operation increases it is easier to design and build FMCW radars with wide bandwidths, whereas it becomes progressively more difficult to design AM systems. The block diagram of a typical FMCW radar is shown in Figure 6.28.

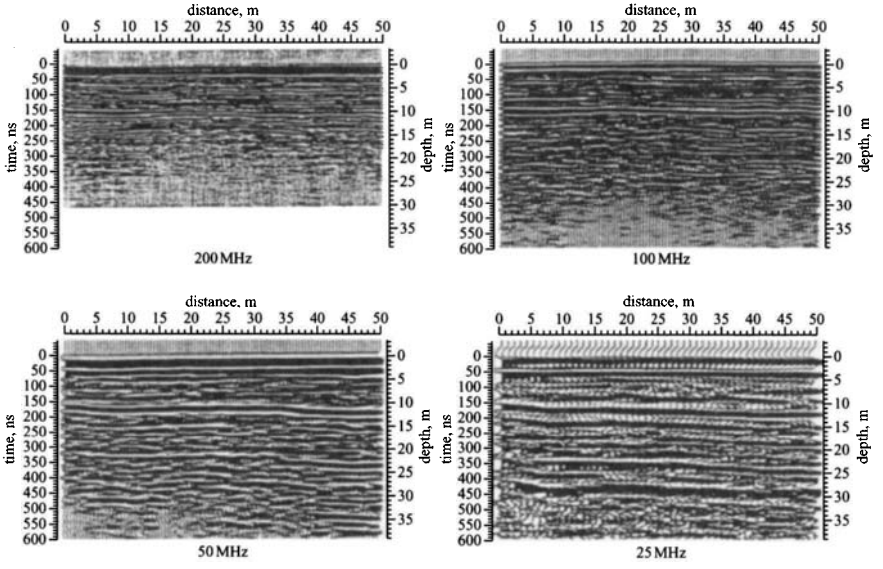

Figure 6.27 Examples of time domain signals as a function of centre frequency (TNO)

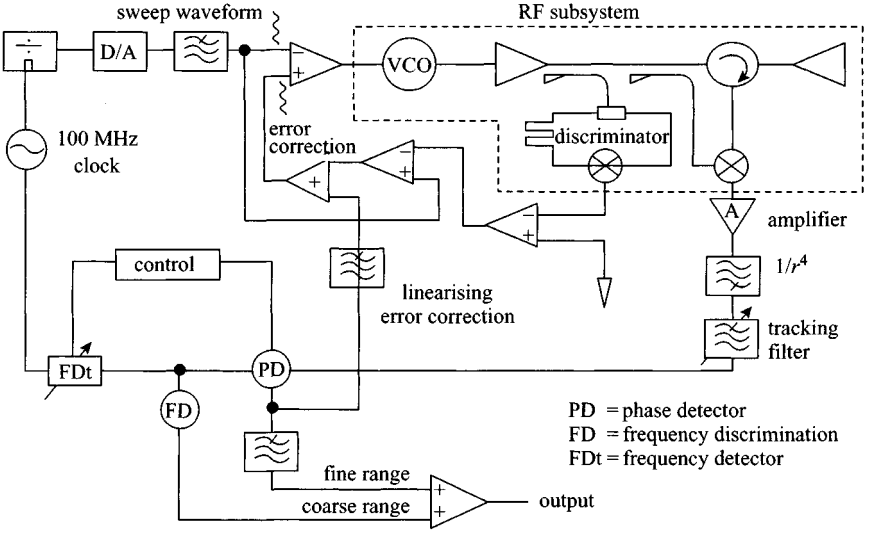

Figure 6.28 Block diagram of an FMCW radar system

The main advantages of the FMCW are the wider dynamic range, lower noise figure and higher mean powers that can be radiated. In addition, a much wider class of antennas, i.e. horns, logarithmic etc., is available for use by the designer. In this Section we will consider continuously changing frequency modulation.

An FMCW radar system transmits a continuously changing carrier frequency by means of a voltage-controlled oscillator (VCO) over a chosen frequency range on a repetitive basis. The received signal is mixed with a sample of the transmitted waveform and results in a difference frequency which is related to the phase of the received signal – hence its time delay and hence the range of the target. The difference frequency or intermediate frequency (IF) must be derived from an I/Q mixer pair if the information equivalent to a time domain representation is required, as a single ended mixer only provides the modulus of the time domain waveform.

In an FMCW radar the transmitter frequency is changed as a function of time in a known manner. If the change is linear then a target return will exist at a time T_d given by

$$T_d = 2R/c \tag{6.23}$$

where R is the range in metres and c is the velocity of light in metres per second.

If this target return signal is mixed with the transmitted signal, a beat frequency, termed the IF (intermediate frequency), will be produced.

This will be a measure of the target range, as shown in Figure 6.29. If the transmitted signal is modulated with a triangular modulating function at a rate over a range,

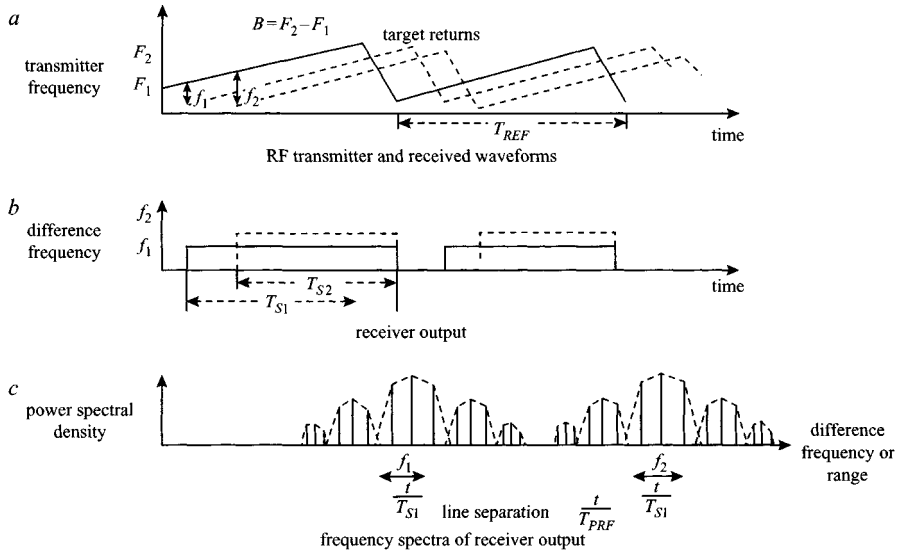

Figure 6.29 FMCW timing diagram and IF waveforms

then the intermediate frequency is given by

$$f = \frac{4Rf_m\Delta f}{c} \tag{6.24}$$

where f_m is the modulation frequency in Hz and Δf is the frequency deviation in Hz.

The choice of modulating waveform defines the resultant IF spectrum, and it is desirable to minimise the bandwidth of the IF spectrum due to a single target in order to optimise the target resolution. If the IF were generated by a continuous linear frequency deviation, then the IF spectrum would consist of a sum and difference frequency, a dc component and various other frequencies resulting from the mixer's nonlinear properties, assuming that the mixer had a perfect square law characteristic. For practical purposes, only the difference frequency will be considered.

However, the repetitive nature of the modulating waveform causes points in the IF time waveform where the amplitude drops to zero. This can be regarded as an amplitude modulation of the IF signal.

If the case of a single target is considered, then the IF waveform as a function of time would be given by

$$f_{IF}(t) = A\sin\omega_{if}t \tag{6.25}$$

The repetitive nature of the RF sweep effectively convolves the basic IF waveform with line spectra

$$f'_m(t) = F(A\sin\omega_{if}t) * F(f_m(t)) \tag{6.26}$$

The Fourier transform of $f_{IF}(t)$ is

$$F(A\sin(\omega_{if}t)) = F\left[A\left(\frac{e^{j\omega_{if}t} - e^{-j\omega_{if}t}}{-j2}\right)\right] \tag{6.27}$$

$$= -A(j\pi\delta(\omega - \omega_{if}) + j\pi\delta(\omega + \omega_{if})) \tag{6.28}$$

The Fourier transform of $f'_m(t)$ can be derived after rearranging the integration period:

$$f'_m(t) = 1 \quad \text{for } 0 < t < (T - \tau)$$
$$= 0 \quad \text{for } (T - \tau) < t < (T)$$

Rearranging the time axes:

$$f'_m(t) = 1 \quad \text{for } (-T/2 + \tau/2) < t < (T/2 - \tau/2)$$
$$= 0 \quad \text{for } (-T/2) < t < (T/2 + \tau/2), (-T/2 - \tau/2) < t < (T/2)$$

$$F\{f'_m(t)\} = \frac{A}{T}\int_{-\frac{T}{2}+\frac{\tau}{2}}^{\frac{T}{2}-\frac{\tau}{2}} \exp(jn\omega_m t)\,\mathrm{d}t = \frac{A}{T}\int_{-\frac{T'}{2}}^{\frac{T'}{2}} \exp(jn\omega_m t)\,\mathrm{d}t \tag{6.29}$$

where n is the harmonic number,

$$F\{f'_m(t)\} = \frac{AT'}{T}\frac{\sin\{(n\omega_m T'/2)\}}{(n\omega_m T'/2)} \tag{6.30}$$

where $T' = (T - \tau)$, and

$$F\{f'_m(t)\} = \frac{A(T-\tau)}{T} \frac{\sin\{(n\omega_m(T-\tau)/2)\}}{(n\omega_m(T-\tau)/2)} \tag{6.31}$$

Hence the IF spectrum is given by

$$f_{if} = A\Bigg((-j\pi\delta(\omega - \omega_{if}) + j\pi\delta(\omega + \omega_{if})) \otimes \left(\frac{(T-\tau)}{T} \frac{\sin\{(n\omega_m(T-\tau)/2)\}}{(n\omega_m(T-\tau)/2)} \right) \Bigg) \tag{6.32}$$

It can be seen that the periodic IF signal consists of an envelope function, $(\sin x)/x$, enclosing a line function. In essence, the FMCW radar measures the phase of the IF signal, which is directly related to the target range. The frequency of the IF signal can be regarded as a measure of range. An inverse frequency–time transform can reproduce a time domain equivalent to the impulse radar.

The FMCW radar system is particularly sensitive to certain parameters. In particular, it requires a high degree of linearity of frequency sweep with time to avoid spectral widening of the IF and hence degradation of system resolution.

This effect can be illustrated by considering the case of FMCW radar with varying degrees of nonlinearity as shown in Figures 6.30 and 6.31. The IF spectrum is shown

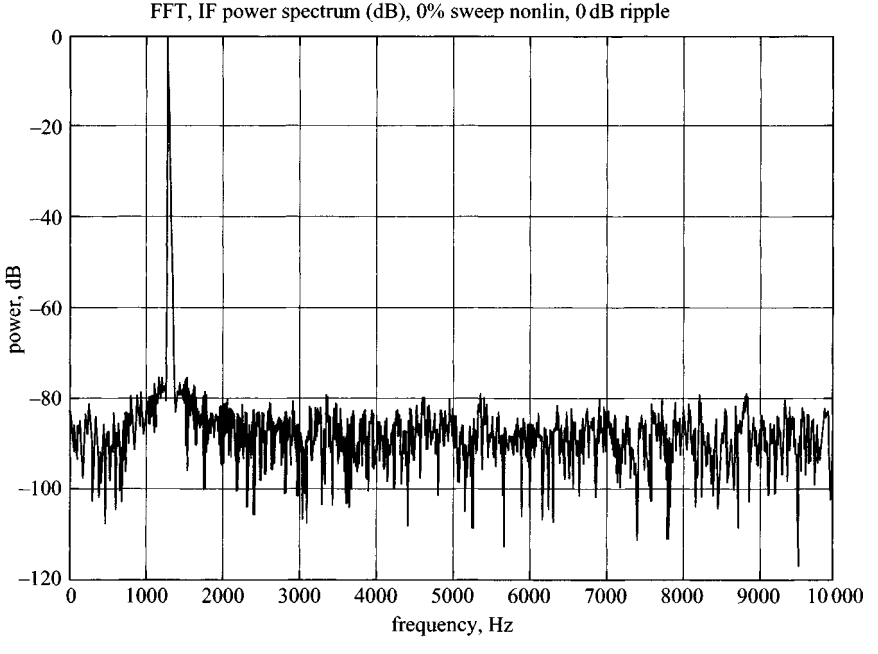

Figure 6.30 IF power spectrum for zero sweep nonlinearity (courtesy ERA Technology)

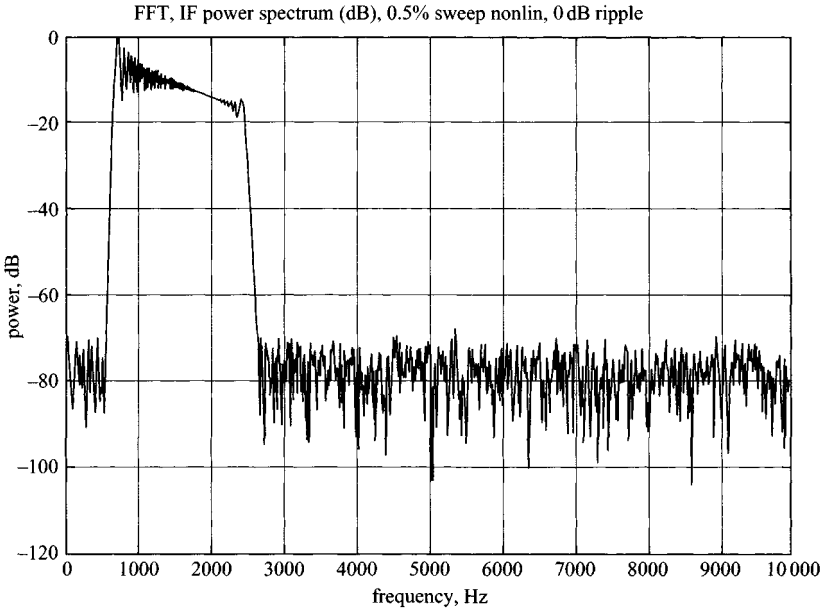

Figure 6.31 IF power spectrum for 0.5% sweep nonlinearity (courtesy ERA Technology)

for two cases: (*a*) perfect (zero nonlinearity) and (*b*) 0.5% nonlinearity. The main effect is to broaden the width of the IF spectrum as the extent of nonlinearity increases and increase the sidelobe level. Practically a useful system should aim to keep all nonlinearities <0.1%. A further parameter, which must be carefully controlled, is the purity of the spectral output. Both the phase noise spectrum and inband harmonics should be reduced to low levels. In the case of inband harmonics, the effect is to generate clutter, while in the case of phase noise the effect is to reduce the sensitivity of the radar for adjacent targets.

The dynamic performance of FMCW radar for a triangular sweep waveform can be estimated from the following example. A system with the characteristics given in Table 6.3 is considered.

A graph of received signal versus range is shown in Figure 6.32. From this it can be seen that the operating range of the radar system lies between the boundaries defined by the system dynamic range clutter profile and target reflection loss. The greater dynamic range of the FMCW radar is a significant advantage provided that the sweep linearity can be maintained and the spectral broadening and sidelobes of the IF envelope minimised. A graph of the ratio of peak/sidelobe level as a function of linearity for several ranges [13] is shown in Figure 6.33.

It is also important that the frequency of the output is stable over time as instability reduces the calibration accuracy, and hence comparison of measurements taken at different times cannot be carried out.

Table 6.3 Characteristics of an FMCW radar

Transmitter		
Peak power	500 mW	(26.9 dB m)
Antenna and cable losses	−9 dB	
Mean radiated power	61 mW	(17.9 dB m)
Repetition time	1 ms	
System clutter profile (rate of decay of antenna time sidelobes/crosscoupling, intermodulation products and LO phase noise)	10 dB/ns	
Receiver		
RF bandwidth	1 GHz	
IF bandwidth	13.3 kHz per metre (free space)	
Equivalent thermal noise (300 k)	5.52×10^{-17} W (−132 dB m)	
Mixer noise figure	8 dB	
Minimum signal level	−124 dB m	
Maximum signal level	10 dB m	
Dynamic range	134 dB m	
Mixer intermodulation products	−30 dBc	
LO phase noise	See manufacturer spec.	

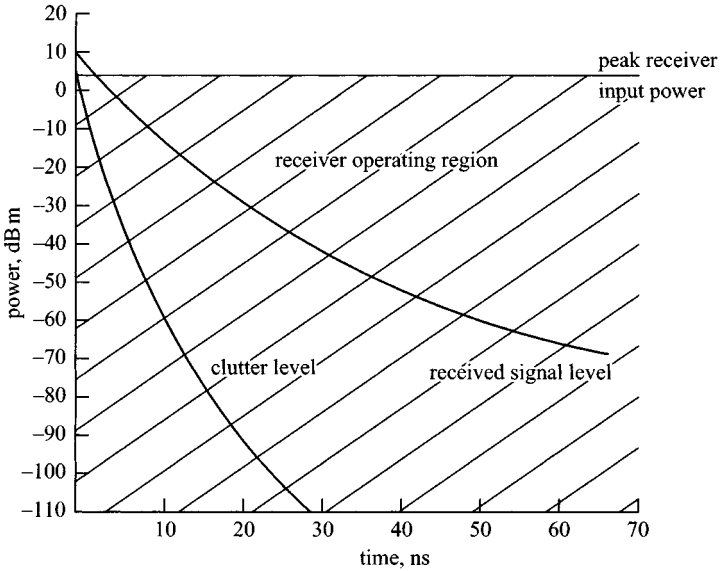

Figure 6.32 Received signal level against time for an FMCW radar

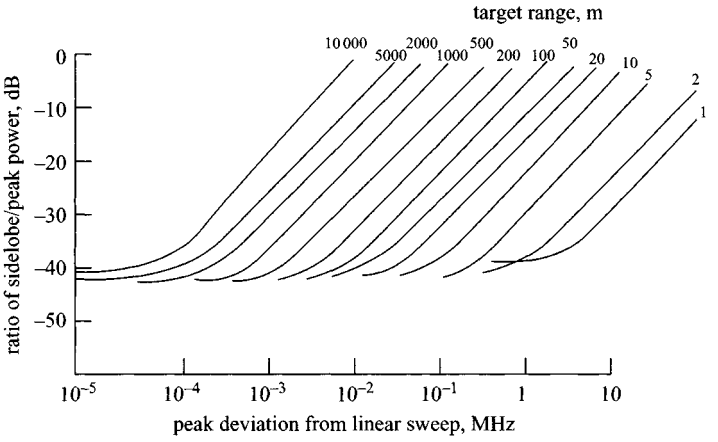

Figure 6.33 Peak to sidelobe ratio as a function of sweep nonlinearity (after Dennis and Gibbs)

There are other particular features of an FMCW radar system, which must be considered. With reference to Figure 6.28, the system block diagram, it will be seen that a buffer amplifier is incorporated. The purpose of this is to reduce the effect of changes in VSWR over the range of swept frequencies causing 'frequency pulling' of the VCO. Changes in VSWR can be caused by variations in antenna to surface spacing or by changes in the characteristics of components such as the circulator or mixer. The isolation (S_{12}) of the buffer amplifier should be sufficient to reduce frequency pulling to insignificant levels.

The amplitude–frequency transfer characteristics of all of the components in an FMCW radar system should be substantially flat. Ideally, amplitude ripple levels should be $< \pm 0.25$ dB, otherwise the radiated waveform will exhibit an amplitude modulation which will cause spectral spreading of the IF waveform, with a resultant loss of solution and system performance.

The FMCW radar shown in Figure 6.28 contains a number of features to enable the linearity of the radar system to be optimised. The first element is a microwave discriminator, which provides an output voltage whose frequency should be a constant. Variation from a fixed value provides an error voltage, which is used to compensate the drive voltage for the microwave voltage controlled oscillator. Provided the delay time in the discriminator is short, the loop bandwidth of the control loop is adequate and the rate of sweep is appropriately selected, the sweep waveform can be compensated in real time for the inevitable nonlinearities which are found with a varactor diode tuning element. Such devices do not exhibit a linear capacitance/tuning voltage low, and require either static or dynamic linearisation.

In the block diagram shown, a tracking filter is included to acquire information from the air–material interface reflection and use this to calibrate the radar.

The output from the IF will, in the case of the antenna transmitting into an infinite lossy dielectric half-space, contain signals due to imperfections in the radar system

itself. These will be chiefly caused by, in order of significance, reflected energy from the antenna mismatch, leakage from port 1 to port 3 of the circulator, and leakage via the directivity of the coupler.

As most of these signals will be at very low frequencies, a highpass filter in the IF signal path can be used to reduce their effect. The same filter can be used to compensate for the spreading loss in free space encountered by the radiated and reflected signal. In voltage terms, an R^{-2} variation translates to a highpass filter with a 12 dB per octave attenuation characteristic.

In the case of a complex mixer with *I/Q* outputs, similarity of the mixer characteristics is important and a well matched pair should be selected.

The complex output from the mixer consists of a set of frequencies representing reflections from individual targets. If an inverse Fourier transform is carried out, then a time domain representation of the target reflections can be generated. However, it is well known that the resolution of the fast Fourier transform is sub-optimum for most spectral analysis and a range of alternative transforms can be used to obtain improved resolution. In a classic paper, Kay and Marple [14] discussed alternative transform techniques and showed that the following methods could provide improved performance compared with the FFT. This aspect is discussed in greater detail in Chapter 7 on signal processing.

Typical examples of frequency-modulated signals received from buried targets are shown in Figures 6.34 and 6.35. Further references to FMCW radars are found in papers by Adler and Jacobs [15], Al-Attar *et al.* [16], Botros *et al.* [17], Carr *et al.* [18], Farmer *et al.* [19], Garvin and Inggs [20], Hua *et al.* [21], Ji-Chang [22], Olver *et al.* [23], Olver and Cuthbert [24], Peebles and Stevens [25], Stove [26], Transbarger [27] and Yamaguchi *et al.* [28–30].

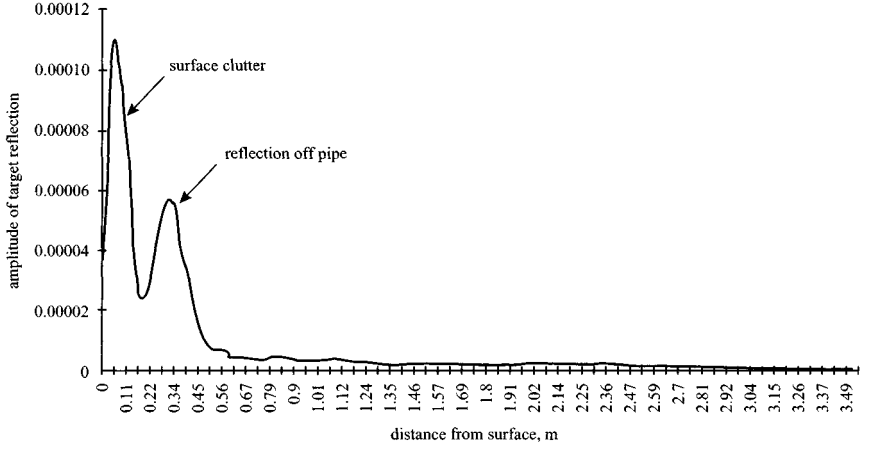

Figure 6.34 Typical FMCW radar received signal versus range in metres (courtesy ERA Technology)

Next Page

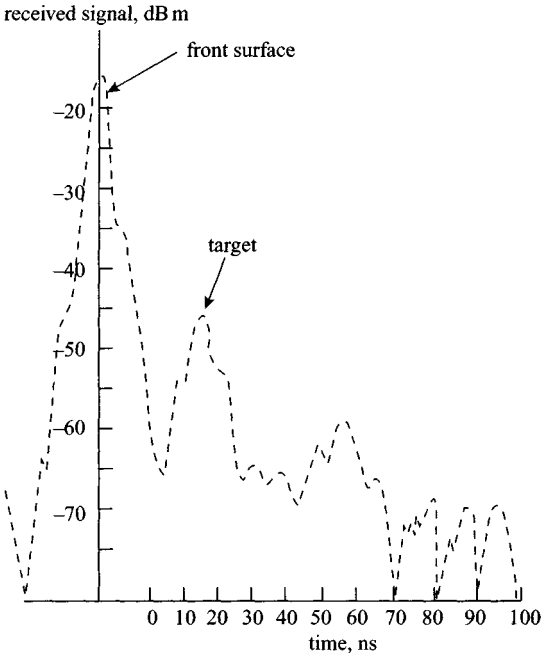

Figure 6.35 Typical FMCW radar received signal versus time (log amplitude scale)

6.5 Synthesised or stepped frequency radar

A synthesised system is essentially stepped frequency continuous wave radar [31, 32]. Any repetitive pulsed signal can be transformed to a frequency domain representation, which will consist of line spectra whose frequency spacing is related to the pulse repetition rate and envelope is related to the pulse shape. Hence, a repetitive impulsive waveform can be synthesised by transmitting a sequential series of individual frequencies whose amplitude and phase are accurately known. An analysis of the design of hardware and signal processing for an SFCW GPR system is given by Langman [33].

Two forms of the synthesised radar can be considered. The first and simplest system is a stepped frequency continuous wave as shown in Figure 6.36. The second form is more complex in that each individual frequency is appropriately weighted in amplitude and phase prior to transmission.

In both cases the difference frequency is of course composed of contributions from all targets up to and beyond the ambiguous range given by

$$R_{amb} = \Delta R N \tag{6.33}$$

where ΔR is the range resolution and N is the number of frequency steps.

The radar radiates a sequence of N frequencies and the amplitude and phase of the received and down-converted signal is stored. A complex inverse fast Fourier

Previous Page

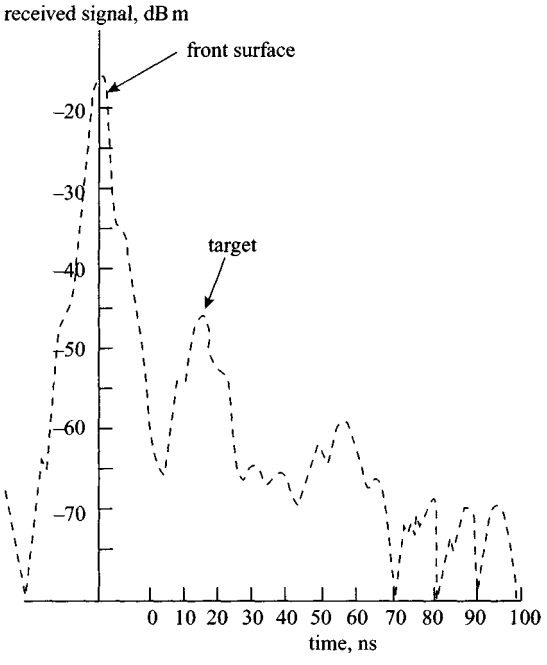

Figure 6.35 Typical FMCW radar received signal versus time (log amplitude scale)

6.5 Synthesised or stepped frequency radar

A synthesised system is essentially stepped frequency continuous wave radar [31, 32]. Any repetitive pulsed signal can be transformed to a frequency domain representation, which will consist of line spectra whose frequency spacing is related to the pulse repetition rate and envelope is related to the pulse shape. Hence, a repetitive impulsive waveform can be synthesised by transmitting a sequential series of individual frequencies whose amplitude and phase are accurately known. An analysis of the design of hardware and signal processing for an SFCW GPR system is given by Langman [33].

Two forms of the synthesised radar can be considered. The first and simplest system is a stepped frequency continuous wave as shown in Figure 6.36. The second form is more complex in that each individual frequency is appropriately weighted in amplitude and phase prior to transmission.

In both cases the difference frequency is of course composed of contributions from all targets up to and beyond the ambiguous range given by

$$R_{amb} = \Delta R N \tag{6.33}$$

where ΔR is the range resolution and N is the number of frequency steps.

The radar radiates a sequence of N frequencies and the amplitude and phase of the received and down-converted signal is stored. A complex inverse fast Fourier

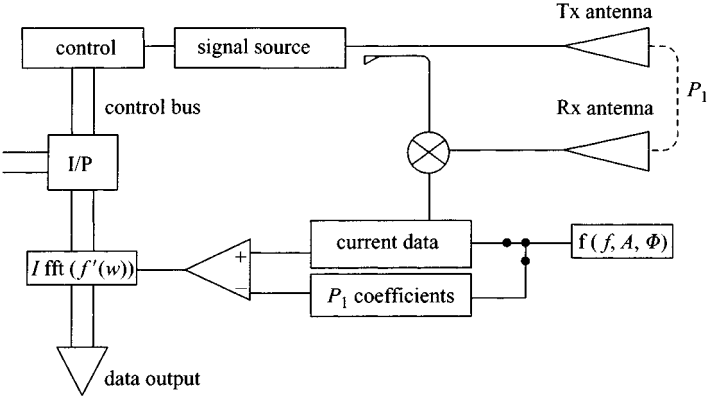

Figure 6.36 Block diagram of a stepped frequency radar system

transform or equivalent algorithm is then used to produce a time domain version of the reflected signal.

The range resolution is given by

$$\Delta R = \frac{c}{2N\Delta f} \tag{6.34}$$

For example, radar using 256 steps with a frequency increment of 5 MHz would achieve a range resolution in air of

$$\Delta R = 3 \times 10^8/2 \times 256 \times 5 \times 10^6$$

and an ambiguous range

$$R_{amb} = 29.95\,\text{m}$$

If the signal transmitted by the radar is given by

$$E'_T = E_T \exp(-j\omega t)$$

in the case of a lossy medium and a single target the received signal can be considered as

$$E_R = \frac{E_T}{R^2}\sigma \exp\{j(2kR - \omega t)\} \tag{6.35}$$

where R is the range to the target, σ is the target scattering cross-section and k is the propagation constant.

The received signal can be represented by a phasor as shown in Figure 6.37. As the operating frequency is changed such that k changes by Δk, the phasor rotates by an angle equal to $2\Delta kR$.

Evidently the amount of rotation is related to the target range. If the transmitted signal is incrementally increased, the frequency of the received signal will be related to the range, taking into account the propagation constant.

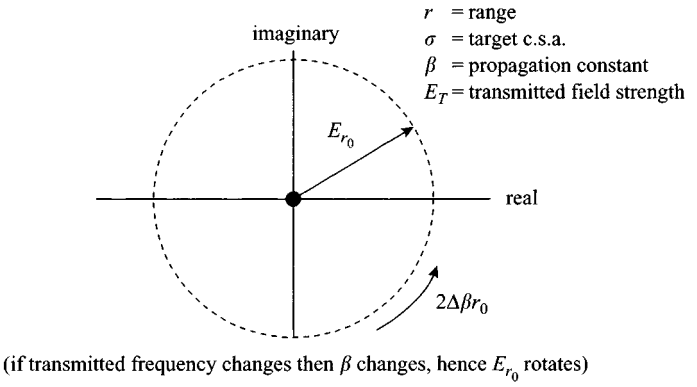

Figure 6.37 Phasor representation of measured signal from a single target

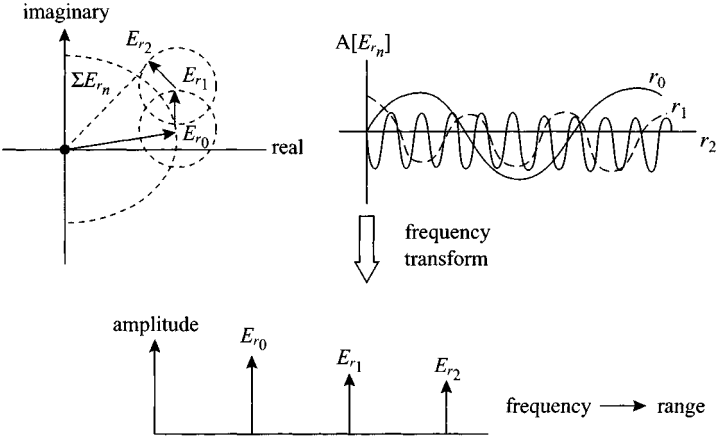

Figure 6.38 Phasor representation of received signal from multiple targets

For multiple targets the received signal becomes the phasor sum of all contributions as shown in Figure 6.38,

$$E'_R = \sum_{n=0}^{N-1} E_{rn} \tag{6.36}$$

The range to each target can be determined by performing a suitable transform with respect to the steps of frequency. The received signal can be expressed as

$$E_n = \sum_{k=0}^{N-1} \frac{\sigma_k E_T}{r_k^2} \exp\{j4\pi\{(f_0 + n\Delta f)r_k\}/c\} \tag{6.37}$$

where r_k is the distance to the kth target, σ_k is the target scattering coefficient, f_0 is the start frequency, Δf is the frequency increment and n is the number of frequency steps.

This equation can be seen to take the form of a discrete Fourier transform and therefore the scattering magnitude of σ_k can be obtained using a fast Fourier transform to indicate depth, in quantised steps, of a target.

A synthesised system may be operated such that the received signal may be integrated as long as convenient in relation to the radar survey speed. Typically each frequency might be transmitted for a time of 100 s and the resulting intermediate frequency integrated for this interval, thus providing a receiver bandwidth of

$$B = 1/\tau$$

which for this time would equal 10 kHz.

Evidently the receiver thermal noise over this bandwidth is very much lower than that of the receiver of the time domain radar, and an improvement of typically 50 dB in noise performance compared with the latter can be achieved.

In the case of synthesised radar simple anti-aliasing filters cannot remove contributions to the received signal outside the ambiguous range. It is therefore important to choose operating parameters that minimise the aliasing effect. One method is to determine the range gate of the target iteratively. The initial measurement is taken with low resolution and large ambiguous range. The range to the target is determined and the resolution is then increased.

Normally the radar is calibrated both to establish a reference plane for measurement as well as to reduce the effect of variation of the frequency characteristics in components and antennas.

The radar system will introduce additional phase shifts on the transmitted and received system. These will be caused by the electrical lengths of the signal paths to the antennas and the effective radiation phase centre of the antennas. This means that the phases of the transmitted and received signals will be different at each integer frequency and will require compensation.

One method of calibrating the radar [32] is to place a known reflector at a defined distance from the antennas. A metallic plane is suitable. The compensation factors can be adjusted such that the indicated range then equates to the actual range. Essentially,

$$E_n = \frac{E_T \sigma}{r_{ref}^2} \exp\{j(2k_{ref} - \omega t) + j\phi_{ref}\} \tag{6.38}$$

Evidently it is important that the recorded values of amplitude and phase at each frequency are accurately related. Any temporal variation in the system characteristics, which degrades the system calibration, will of course reduce the resolution and accuracy of measurement.

In addition, the repeatability of the frequency is important and must be such that the calibration remains valid.

The main advantages of a stepped frequency continuous wave radar are its ability to adjust the range of frequencies of operation to suit the material and targets under

investigation, a higher mean radiated power level per spectral line, and the ability to integrate the received signal level, hence improving the system sensitivity.

The calibration of the radar does, of course, depend on stable system characteristics and antenna parameters that are invariant with front surface-antenna spacing.

The synthesised pulse radar is a variant of the stepped frequency continuous wave radar in that the relative amplitudes and phases of the transmitted frequencies are adjusted on transmission in order to synthesise the desired pulse waveform.

A significant advantage for this approach is that it is possible, within limits, to take account of the frequency characteristics of the antennas. For example, weighting the amplitude of the low frequency spectral lines can compensate the low frequency cutoff point of an antenna.

However, the requirement to maintain an accurate phase relation between each of the spectral lines is difficult to achieve in real time. It is generally easier to carry out computation on down-converted and recorded data; hence the stepped frequency continuous wave radar is a more economical design option.

6.6 Noise modulated radar

6.6.1 Introduction

Noise modulated radar offers some very attractive possibilities to the designer of GPR systems. The radiated power is evenly spread throughout the spectrum and the receiver is less susceptible to interference. However, until recently such systems were relatively rare. Developments over the last few years are changing that situation, and more efforts are being put into the development of noise radar systems. Guosui *et al.* [34] describe the development of random signal radar (RSR) over the past 30 years. They review conventional methods of implementing such as correlation, spectrum analysis and autocorrelation, and consider the advantages and disadvantages of noise frequency modulation CW radar and random binary phase-coded CW radar.

Some of the key design issues in terms of noise radar are the ambiguity function and the range sidelobe suppression. Dawood and Narayanan [35] consider the underlying issues in terms of optimising the ambiguity function. They developed an ultrawideband (UWB) random noise radar system which transmits an ultrawideband random noise (Gaussian) waveform with uniform power spectral density (PSD) in the 1–2 GHz frequency range. They showed that for a random noise radar a correlator matched to the transmit process is required and that, for a UWB transmit random process, the compression or stretch due to the range rate on the envelope of the return process cannot be ignored.

When applied in airborne imaging surveillance, ultra-wideband (UWB) random noise radars have their special merits. Xu and Narayanan [36] showed that because of the randomness and the ultra-wide bandwidth of the transmit and receive signals, such radars can be used for covert detection and identification, and are immune from hostile detection and jamming while preserving very high range resolution. However, the images are plagued with artefacts caused by high range sidelobes. They proposed

a new technique for the range sidelobe suppression of UWB random noise radar, which combines median and apodisation filtering.

A key development has been by Dr Juergen Sachs of the Technical University of Ilmenau, Germany, and the MEODAT company, who have jointly developed an integrated circuit SiGe-technology radar 'chip'. This offers considerable potential and is described in the following Section.

6.6.2 *M-sequence radar*

Dr Juergen Sachs

A maximum length binary sequence, in short an M-sequence, is a special kind of pseudo-random binary sequence (PRBS). PRBS signals $x(t)$ are periodic and as such they are not really random. They have, however, properties which are very close to those of real random signals – for example, a short, pulse-like autocorrelation function $R_{xx}(\tau)$:

$$R_{xx}(\tau) = \frac{1}{T}\int_T x(t)\,x(t+\tau)\,\mathrm{d}\tau \longrightarrow \text{pulse-like} \tag{6.39}$$

The power spectrum of the signal $x(t)$ is given by the Fourier transform of its autocorrelation function:

$$S_{xx}(f) = \int_{-\infty}^{\infty} R_{xx}(\tau)\,e^{-j2\pi f\tau}\,\mathrm{d}\tau \tag{6.40}$$

The PRBS signals consist of elementary impulses (chips), which are seemingly randomly distributed within a signal period.

A signal having a short autocorrelation function has a large bandwidth and thus it can, in principle, be used as a stimulus in high-resolution, ultra-wideband (UWB) radar. It is, however, not beneficial to consider the received signals $y(t)$ (caused, for example, from the backscattering of a PRBS at a target) immediately as they cannot be interpreted due to their random nature. The situation changes by examining the crosscorrelation function $R_{yx}(\tau)$ between stimulus and receive signal as in (6.41):

$$R_{yx}(\tau) = \frac{1}{T}\int_T y(t)\,x(t+\tau)\,\mathrm{d}\tau \tag{6.41}$$

The information of interest is the shape of the impulse response function (IRF) $h(t)$ between the feed points of the transmit and receive antennas. It contains the scattering behaviour of the targets (embedded by the radiation behaviour of the antennas). The IRF, as well as autocorrelation and crosscorrelation functions, are related by a convolution in (6.42).

$$R_{yx}(\tau) = h(\tau) \otimes R_{xx}(\tau) \tag{6.42}$$

For comparison the direct relation between the stimulus $x(t)$ and the system response $y(t)$, is given in $y(t) = h(t) \otimes x(t)$.
(6.42) simplifies to:

$$R_{yx}(\tau) \sim h(\tau) \quad \text{for } R_{xx}(\tau) = \delta(\tau) \tag{6.43}$$

if the autocorrelation function is a Dirac pulse $\delta(t)$.

Practically, (6.43) means that the crosscorrelation function between the receive and stimulus is proportional to the impulse response function as long as the autocorrelation function of the stimulus is narrow compared to the impulse response of the device under test. Translated to the spectral domain, (6.43) requires a bandwidth of the stimulus exceeding that of the device under test. Finally, (6.43) comprises a corresponding approach as used for the classical impulse excitation. There is accordingly no large difference in data interpretation between impulse technique and correlation technique if one exchanges the stimulation pulse $x(t)$ by the autocorrelation function $R_{xx}(\tau)$ and received signal $y(t)$ by the crosscorrelation function $R_{yx}(\tau)$.

On first examination, the correlation technique complicates the determination of the impulse response function $h(t)$, since the function $R_{yx}(t)$ must be determined, whereas the impulse technique is satisfied even with the captured signal $y(t)$. However, the correlation technique opens up many different practical solutions, since the designer is not limited to a particular signal shape as with the impulse technique. Equation (6.43) in connection with (6.40) only requires a stimulus signal with a large bandwidth, irrespective of their time domain characteristics.

Probably the most important result is the ability to replace impulsive waveforms by signals, which spread their energy equally over a long time, hence reducing the peak power. For this reason, the electronics only has to handle low voltage signals, which allows for monolithic circuit integration and fewer problems with limiting effects. Furthermore, the charge and discharge of parasitic circuit elements profits from low voltage variations, which results in an increased bandwidth of the signals.

The backscattered waveform must, however, be compressed in the receiver to recover the range resolution. In that sense, the impulse compression is nothing more than the correlation according to (6.41). The impulse compression is implemented by a matched filter in many cases. That means, one expresses the correlation (6.41) by a convolution provided by a filter having an impulse response function $h_m(t) = x(-t)$, which is equal to the time inverse of the transmit signal $x(t)$. It is, however, not possible to build an analogue matched filter for ultra-wideband signals. A so-called sliding correlator could be an alternative to convert (6.41) by electronic means. This requires an auxiliary PRBS-generator in the receiver, a wideband multiplier (mixer) and a lowpass filter (integrator). The auxiliary PRBS-source has to provide the same signal as the main PRBS-source in the transmitter. By shifting stepwise, the initial state of that auxiliary PRBS-source, the delay τ can be changed. Thus, one is able in this way to gain the crosscorrelation function $R_{yx}(\tau)$ successively. This method is, however, awkward and less flexible.

Furthermore, the output signal of the sliding correlator as well as the matched filter is again a short, pulse-like signal, which tends to overload the follow-up electronics. From that viewpoint, a digital impulse compression is to be preferred since

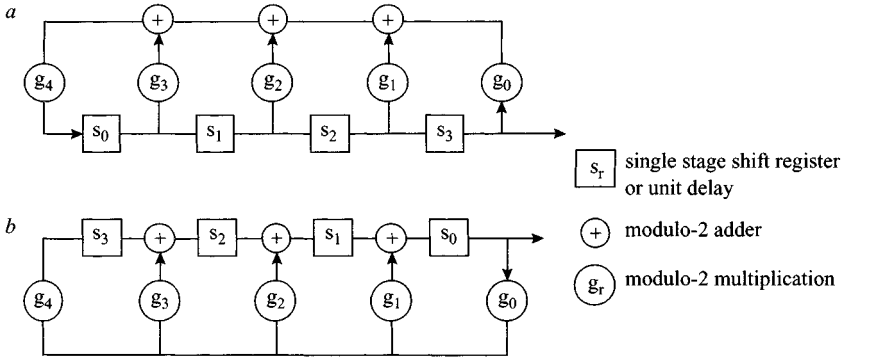

Figure 6.39 *State-machine model of a general 4th-order shift-register generator*
a Fibonacci feedback generator; *b* Galois feedback generator

high dynamic signals as pulses can always be handled by an appropriate number format. The stepped-frequency radar uses this approach since it provides an 'impulse compression' of sine waves via the inverse Fourier transform. Finally, the stepped-frequency radar is nothing more than a specific conversion of (6.41) via a more or less effective way into the frequency domain.

A direct and neat way to solve (6.41) for UWB applications up to the GHz range is the use of M-sequences. Some illustrations on the mathematical and number theoretical bases of M-sequences are to be found in Peterson *et al.* [37]. A simple way to generate M-sequences is given by the use of digital linear feedback shift registers. Figure 6.39 shows the general structure of such a shift-register generator. Shift-register sequences having the maximum possible period for a given number of register stages are called maximum length binary sequence or simply M-sequence. However, for every shift-register length there exists only one or a few feedback combinations, which actually leads to an M-sequence. A table summarising all allowed combinations up to an order of 40 of the shift-register is also given in Xiang [38]. One period of the M-sequence covers all possible states of the shift register except the state 000...0. Consequently, one period of the output signal contains $N = 2^n - 1$ chips if n is the order of the shift register.

The single stage shift register is simply a D flip-flop which is pushed by a clock generator of frequency f_c. It provides a unit delay of $t_c = 1/f_c$. The state of the flip-flop r is represented by $s_r \in \{0, 1\}$. The modulo-2 adder is an XOR-gate and the modulo-2 multiplication is nothing but a connection if $g_r = 1$ or a no-connection for $g_r = 0$.

Some properties of an M-sequence shall be demonstrated with the example of a 4th-order shift-register generator. In this case, there is only one possibility to arrange the feedback: it is $g_4 = g_1 = g_0 = 1$ and $g_3 = g_2 = 0$. The states of one period of the output signal results in $x_n = m_n = \{111100010011010\}$. For measurement purposes this sequence is used to stimulate the systems under test. However, both states 0 and 1 usually represent the same (absolute) value V_{MS} of signal voltage but

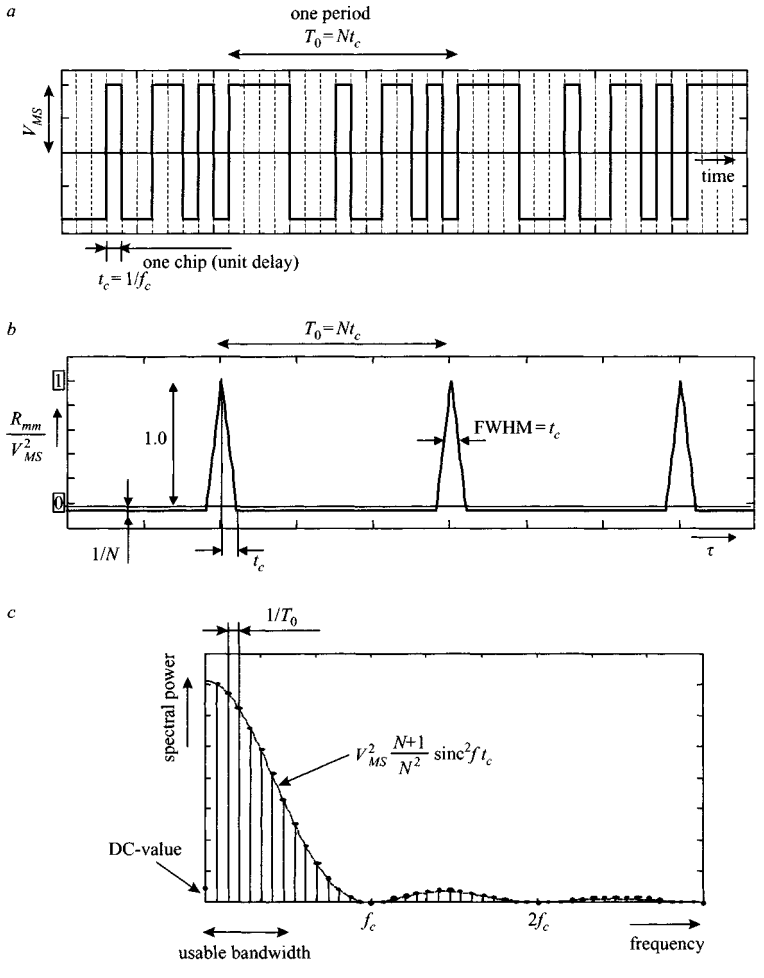

Figure 6.40 Time shape (a), autocorrelation function (b) and power spectrum (c) of an idealised 4th-order M-sequence

they are of opposite sign. Thus, the rms-value of such a bipolar stimulus is identical to V_{MS}. The typical (idealised) time shape of a bipolar M-sequence is represented in the upper part of Figure 6.40. For comparison, the time shape of a real M-sequence is shown in Figure 6.41. Note that only a portion of the complete curves is represented in order to be able to see details. Only 20% of one period is shown and the spectrum is restricted to the range from DC to 1 GHz. The period of the transmit signal determines the ambiguity range R_0 of a radar, i.e.

$$R_0 = \frac{c\,T_0}{2} = \frac{cN}{2f_c} \tag{6.44}$$

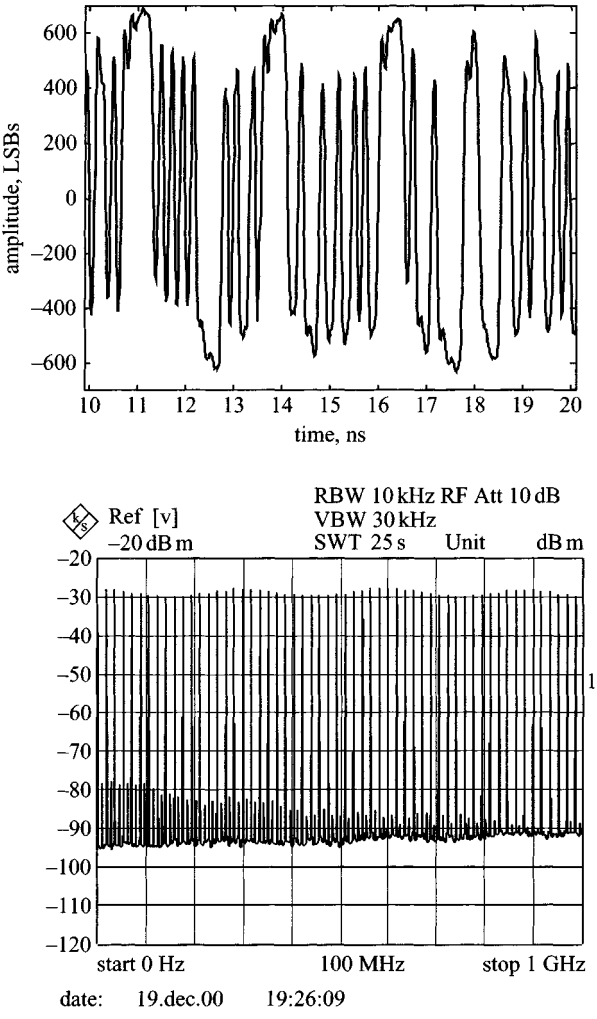

Figure 6.41 *Time shape and power spectrum of a real 9th-order M-sequence pushed by a 9 GHz clock*

where c is the speed of light and f_c represents the rate of the clock generator, which drives the shift register.

The autocorrelation function (see Figure 6.40) of an M-sequence is a periodic function of short triangles. Its FWHM-value corresponds to the unit delay t_c of the shift register. Therefore, the theoretical range resolution of an M-sequence radar is

$$\delta_{r,idealised} = \frac{c\Delta t_{-3\text{dB}}}{2} \approx 0.6ct_c = 0.6\frac{c}{f_c} \tag{6.45}$$

The value Δt_{-3dB} herein refers to the minimum time distance which allows us to separate two identical triangular pulses by a −3 dB depression of the sum signal.

It can be seen from Figure 6.40 that by increasing the clock rate f_c the autocorrelation approaches a (periodic) Delta-function as was required by (6.42) for the determination of the impulse response function $h(t)$ for a DUT.

The power spectrum of the M-sequence results from Fourier transforming its autocorrelation function, i.e. which results in a line spectrum having an envelope determined by a sinc^2-function (see Figures 6.40 and 6.41). Nearly 80% of the energy of an M-sequence is concentrated within the frequency interval DC to $f_c/2$. Thus it is wise to limit the usable bandwidth to $B = f_c/2$. Otherwise, the receiver noise increases proportionally compared to the signal power, which will degrade the range resolution performance. Thus, a more realistic value for the range resolution results in

$$\delta_r \approx \frac{c}{2B} = \frac{c}{f_c} \tag{6.46}$$

which is close to the ideal value given by (6.45).

As shown, the minor restriction to a bandwidth of $B = f_c/2$ has practically no influence on the radar resolution, but it has a decisive impact on the whole design of the M-sequence radar system. As shown below, this concerns mainly two aspects – the implementation of the crosscorrelation (see equation 6.41) and the control of the signal gathering.

As noted above, the goal is to determine the impulse response function $h(t)$ of the transmission channel – transmit antenna – scatterer – receive antenna. This is achieved by stimulating the DUT by an M-sequence $x(t) = m(t)$ and capturing the response $y(t)$ of the DUT. The impulse response function $h(t)$ corresponds approximately to the crosscorrelation function $R_{ym}(\tau)$ between $m(t)$ and $y(t)$, if the bandwidth B_{DUT} of the DUT is below $B_{DUT} < B = f_c/2$ (see also equation 6.43).

To respect the Nyquist theorem, a maximum bandwidth of $B = f_c/2$ implies a minimum sampling (digitising) rate of f_c, i.e. one sample per chip of the M-sequence. Thus, a complete set of measurement data covers a sequence of N data samples of the M-sequence $m(n) = \{m_1 \quad m_2 \quad m_3 \quad \cdots \quad m_N\}$ and of N data samples of the DUT response $y(n) = \{y_1 \quad y_2 \quad y_3 \quad \cdots \quad y_N\}$. Since all signals are periodic, the determination of the crosscorrelation function $R_{ym}(n)$ (see equation 6.41) represents a cyclic procedure which can be expressed by the matrix relation (6.47),

$$\begin{bmatrix} R_{ym,1} \\ R_{ym,2} \\ R_{ym,3} \\ \vdots \\ R_{ym,N} \end{bmatrix} = \begin{bmatrix} m_1 & m_2 & m_3 & \cdots & m_N \\ m_N & m_1 & m_2 & \cdots & m_{N-1} \\ m_{N-1} & m_N & m_1 & \cdots & m_{N-2} \\ \vdots & \vdots & \vdots & \ddots & \vdots \\ m_2 & m_3 & m_4 & \cdots & m_1 \end{bmatrix} \cdot \begin{bmatrix} y_1 \\ y_2 \\ y_3 \\ \vdots \\ y_N \end{bmatrix} \tag{6.47}$$

respectively

$$\mathbf{R}_{ym} = \mathbf{M} \cdot \mathbf{Y}$$

It should be noted that (6.47) describes a general way to provide the correlation function of periodic signals. It is not exclusively restricted to the use of M-sequences. Thus (6.47) can be used to provide the crosscorrelation function referring to the sampled idealised M-sequence (see Figure 6.40) as well as referring to the real M-sequence (see Figure 6.41) if it is gathered by a reference channel.

In many applications where one is usually satisfied with the idealised M-sequence as reference, the elements of the matrix **M** are exclusively $+1$ or -1 (respectively, $+V_{MS}$ or $-V_{MS}$). By permutation and adding a 'dummy' row and column, **M** can be expressed by a Hadamard matrix **H** (see [38] for details),

$$\mathbf{M} = \mathbf{P} \cdot \mathbf{H} \cdot \mathbf{Q} \tag{6.48}$$

The **M**-matrix is of order N by N, i.e. $2^n - 1$ by $2^n - 1$, and the **H**-matrix is of order 2^n by $2^n \cdot$ **P** and **Q** represent permutation matrices. They are of order $2^n - 1$ by 2^n and 2^n by $2^n - 1$, respectively. Every column and row of these matrices contains only one element at maximum with the value 1. The remaining elements are zero. Thus, (6.48) is not connected to an extensive matrix multiplication. It rather corresponds to a simple rearrangement of rows and columns.

Hadamard matrices having an order of a power of two can be built from a simple rule:

$$\mathbf{H}_1 = 1$$

$$\mathbf{H}_{2r} = \begin{bmatrix} \mathbf{H}_r & \mathbf{H}_r \\ \mathbf{H}_r & -\mathbf{H}_r \end{bmatrix} \tag{6.49}$$

Joining (6.47) and (6.48), the calculation of the crosscorrelation $\mathbf{R}_{ym}$ is finally attributed to a re-ordering of data samples and a multiplication with a Hadamard matrix. By the fast Hadamard transform (FHT), this multiplication can be undertaken in a very effective way. The FHT is organised by butterfly operations similar to that of the FFT. The FHT butterfly, however, only contains addition and subtraction operations, as demonstrated in Figure 6.42 for the two simplest examples.

The practical result of the above described procedure is represented in Figure 6.43. It was gained by connecting the output of a 9-stage shift register via an attenuator to the signal gathering unit. The shift register was driven by a 9 GHz clock (compare also Figure 6.44).

The spurious signals onto the impulse base are caused by the imperfection of the real M-sequence; these may be eliminated from the data by calibration and deconvolution, respectively, by referring the crosscorrelation to the real transmitted M-sequence.

The data gathering must respect the Nyquist criteria, which poses a challenging task for every digitised RF-receiver. Fortunately, the Nyquist criteria can be met more easily by an undersampling method if periodic signals are used. (Undersampling means that only one or a few data points are gathered within each signal period.) The points must, however, be different at every period. By rearranging the captured samples, one finally obtains an impression of the waveform. The virtual time distance Δt_v between these data samples can be quite narrow even if the real sampling rate is

$$\mathbf{H}_2 \cdot \mathbf{A} = \begin{bmatrix} 1 & 1 \\ 1 & -1 \end{bmatrix} \cdot \begin{bmatrix} a \\ b \end{bmatrix} \qquad \mathbf{H}_4 \cdot \mathbf{A} = \begin{bmatrix} 1 & 1 & 1 & 1 \\ 1 & -1 & 1 & -1 \\ 1 & 1 & -1 & -1 \\ 1 & -1 & -1 & 1 \end{bmatrix} \cdot \begin{bmatrix} a \\ b \\ c \\ d \end{bmatrix}$$

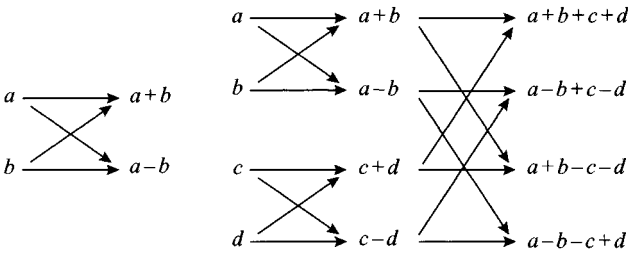

Figure 6.42 *Multiplication of a vector with a Hadamard-matrix by butterfly operations*
The examples show the elementary butterfly for an $\mathbf{H}_2$-matrix and the operations for the next higher order $\mathbf{H}_4$

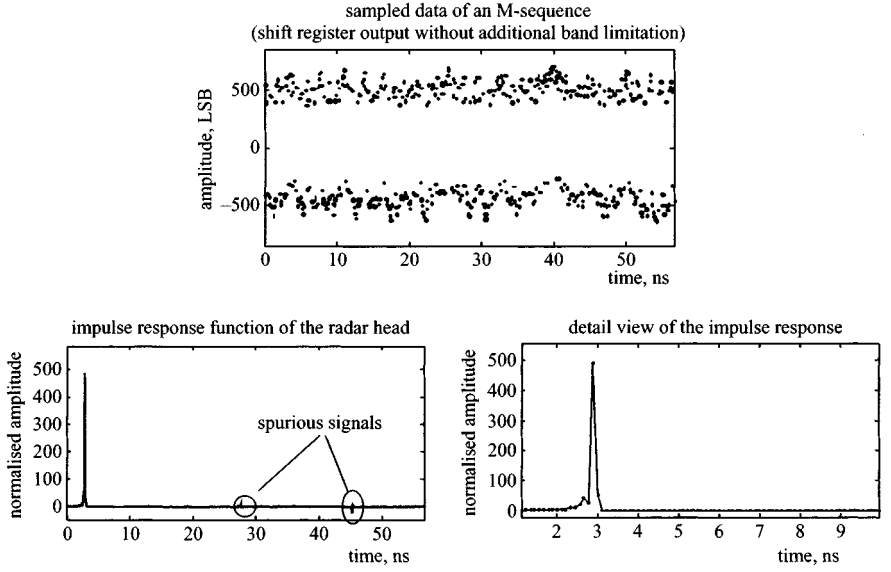

Figure 6.43 *Sampled data and impulse response function of a 9 GHz 9-stage M-sequence radar gained from the crosscorrelation function between gathered data and idealised M-sequence*

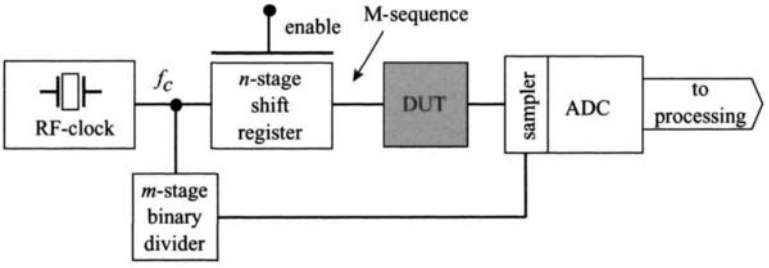

Figure 6.44 *Basic structure of an M-sequence radar*
The DUT consists of the transmit antenna, the scattering scenario and the receive antenna

very low. The inverse of Δt_v corresponds to the so-called equivalent sampling rate $f_{s,eq}$. Thus, by such an approach, the equivalent sampling rate has to meet the Nyquist criteria and not the real sampling rate. This simplifies the electronics and reduces the system costs. It is widely used in many wideband data gathering systems.

Even if undersampling greatly simplifies the data gathering, the correct and stable control of its timing is still a challenge because the precision of this timing strongly determines the overall performance of the radar system. One of the most important features of the M-sequence approach is that this timing can be performed in a very stable and exact way. Remember, one data sample is needed per chip of the M-sequence and the sequence length covers $2^n - 1$ chips. Every beat of a generator pushing the shift register releases one chip. This means that if the sampling rate equals the clock rate, only one period is needed to gather all data but the measurement rate is extremely high (real time sampling). If the sampling rate equals half the clock rate, the odd numbered data samples are captured during the first period of the M-sequence and the even numbered samples are gained within the second period. Thus, by halving the sampling rate, two periods are required to complete the data set. Quartering the sampling rate involves four periods in the measurement process. The data samples having the numbers $1, 5, 9 \ldots N - 2$ are gathered within the first period. The second one provides the samples of number $2, 6, 10, \ldots N - 1$, the third provides the samples $3, 7, 11, \ldots N$ and the remaining samples $4, 8, 12, \ldots N - 3$ are captured within the fourth period. The example implies that any sampling rate which corresponds to a power of two fraction of the clock rate f_C is able to control the data gathering. In other words, the sampling process in an M-sequence radar is controlled by a binary divider. The more stages it has the lower the sampling rate is (the simpler the electronics may be) but the slower the measurement proceeds.

Summarising the above leads finally to the basic block schematic diagram, Figure 6.44, of the M-sequence radar. The whole system is controlled by a single-tone RF-generator with good phase noise and drift characteristics. The shift register provides the stimulus signal and the binary divider controls the data gathering. As usual for digital circuit elements, the shift register can be additionally controlled by an enabling-gate. This provides the opportunity to construct and to operate multi-channel

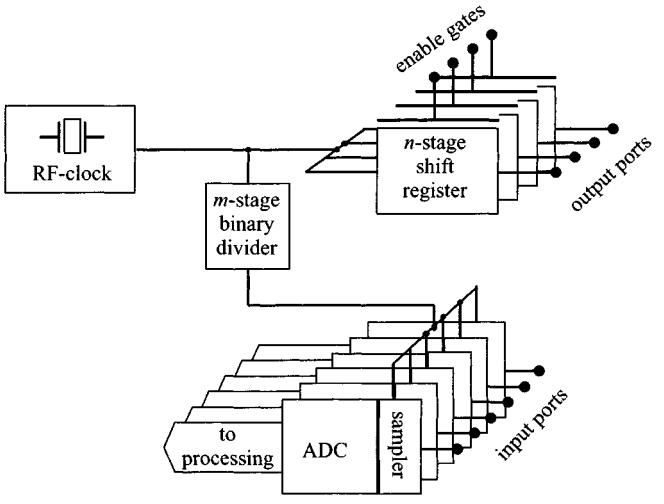

Figure 6.45 Multichannel arrangement

arrangements as UWB-antenna arrays in a simple fashion; Figure 6.45 shows the schematics. The whole measurement procedure covers a minimum of K steps if K stimulation channels are involved. Within one step only one shift register is switched active, and the remaining registers are disabled. The receiver channels are gathering the data in parallel.

The measurement data are captured before digitising by a sampling gate (Figure 6.44), which is either working in a track-and-hold or a sample-and-hold mode. In contrast to the classical approach, the sampling gate is controlled by a binary divider and not by ramp voltage, which is crossing a moving threshold (see dual ramp timing circuit, Figure 6.23). This results in an absolute linear time scale of the measurement data since the divider has to run through all its states before it releases the next sample. Thus, small differences between the individual stages have no effect.

Furthermore, the divider guarantees an excellent jitter and drift performance, as shown in Figure 6.46. The fundamental principle of a timing system works by detecting the crossing of a threshold by a voltage ramp; however, neither the threshold nor the ramp are ideal. They are subjected to slow offset variations and random errors, which causes time drift and jitter. Considering the simple model in Figure 6.46, the rms-jitter is approximately given by

$$t_j \approx t_r \frac{n_{rms}}{V_0} \tag{6.50}$$

That is, the jitter is proportional to the rise of the reference waveform. The shorter the rise time is the better the jitter rejection will be. Time drift can be considered in the same way, resulting in a corresponding behaviour if the threshold, for example, underlies slow offset variations. The timing control of the M-sequence radar is based

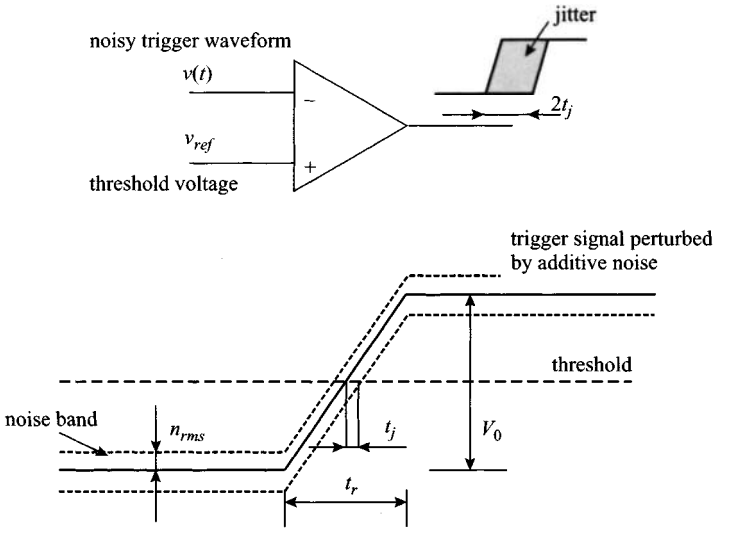

Figure 6.46 Origin of jitter by flank triggering

completely on sharp pulses. This concerns both the shift-register generator and the binary divider. Thus, good jitter and drift rejection is provided by principle.

Finally, the overall stability of the system is determined to a great extent by the RF-clock generator. The stability of the M-sequence radar approaches the performance of a network analyser. Consequently, usual network analyser techniques to increase the system performance by calibration routines can be adopted. Thus, inevitable imperfections of the UWB hardware can be partially compensated by calibration and software if necessary. It is emphasised here once again that the first priority in order to succeed in calibration is determined by the system's long-term stability. Circuit ageing and temperature influence will also act upon the frequency and quality of such a calibration. Since the shift-register generator and sampling gate, which are the most critical parts in this sense, are quite different circuits they will behave differently with ageing and temperature variations. To suppress this effect, it is recommended to capture both the transmit as well as the receive signal by identical circuits as it can be expected that identical circuits behave similarly with ageing and temperature.

The maximum operational bandwidth of the radar system is mainly determined by the maximum value of the clock rate of the shift-register generator. This is once again limited by the gate delay within the flip-flop, respectively the XOR-gate. To minimise this, one is forced to reduce the circuit size by a monolithic integration. Several semiconductor technologies are available for this purpose, depending on the required bandwidth and manufacturing costs. A good performance with regard to costs and bandwidth is provided by the SiGe-technology, which permits clock rates well beyond 10 GHz. Figure 6.47 represents an example of a practical implementation. Two customer chips are mounted on a multi-layer LTCC (low temperature co-fired ceramic) for wiring. These are the sampling gate (operating in the T&H-mode) and the

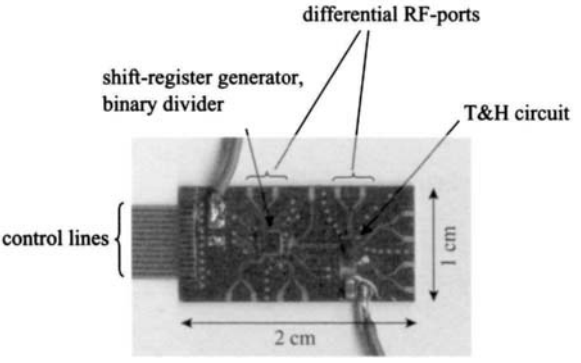

Figure 6.47 Heart of RF-part of M-sequence radar (courtesy MEODAT GmbH)

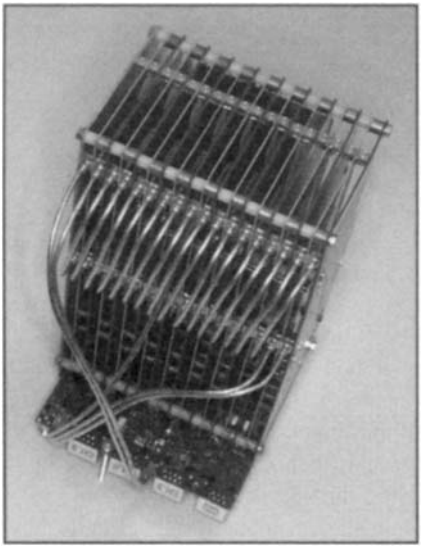

Figure 6.48 Complete RF-part of all 9 channels of a 3 × 3 UWB-radar array for landmine detection (courtesy MEODAT GmbH and QinetiQ)
Each of the channels is able to transmit and to receive

shift-register generator joint with the binary divider. The circuit layout is completely differential in order to reduce crosstalk effects. This is important to consider because even if the used circuit principles come from digital circuitry, their analogue behaviour is employed. A further example is shown in Figure 6.48, representing a multichannel system. Owing to the concept of a centralised main clock for all sub-systems, good synchronism between channels is achieved.

Analogue to digital conversion, signal processing and operational control could be theoretically undertaken by a normal DSP-board or a PC. However, this would cause losses in the system performance concerning dynamic range and real-time capabilities.

It is for this reason that it is appropriate to apply special hardware to enable averaging for noise reduction, even if only a short measurement time is available, or to gather high speed data for highly time variable targets.

6.7 Single frequency methods

Single frequency methods of imaging are based on the technique of viewing the target from a number of physically different positions in an aperture over the target recording the amplitude and phase of the received signal and then mathematically reconstructing an image of the radiating source. Essentially a synthetic aperture is constructed over a defined aperture at the measurement plane.

In general, most antennas used in ground penetrating radar have relatively low gain and hence a wide beamwidth which results in poor resolution in either x or y dimensions. Synthetic aperture methods aim to increase x or y resolution by synthetically generating an antenna with a large aperture and consequent reduced beamwidth.

The synthetic aperture array must consist of a minimum number of samples to avoid aliasing. The minimum number is given by [39]

$$N = \frac{2R\beta^2}{\lambda} \tag{6.51}$$

where β is the antenna beamwidth in radians, R is the range to the target and λ is the radiated wavelength.

There are several variations on the synthetic aperture method which can be considered. Where a single frequency is used, holographic methods can be employed to generate an image. The holographic method records the amplitude and phase of the received signal in a plane over the target. This function is then correlated with a test function which is set to provide a maximum value of the crosscorrelation where reflection occurs and to be zero elsewhere.

The holographic image reconstruction method is defined in the two-dimensional case by the correlation between the test function $h(x,t)$ and the received signal $v_r(x_r,t)$, where x is the co-ordinate vector of the imaging point and x_r is the co-ordinate vector of the receiving point, as shown in Figure 6.49, and $v_r(x_r,t)$ is the signal received at the receiving point.

The linear operation to reconstruct the image is defined by [39]

$$b(x) = \iiint_{-\infty}^{\infty} v_r(x_r,t)h(x - x_r t)\,\mathrm{d}t\mathrm{d}x_r\mathrm{d}y_r \tag{6.52}$$

As the received signal can be considered to be:

$$v_l(x_r,t) = \frac{1}{2\pi}\int_{-\infty}^{\infty} V(x_r,\omega)\exp j(\omega t)\,\mathrm{d}\omega \tag{6.53}$$

$$v_r(x_r,t) = \frac{1}{2\pi c}\iint \frac{\cos\theta}{r^2}\sigma(x)\frac{\mathrm{d}}{\mathrm{d}t}\frac{(t-2r)}{c}\,\mathrm{d}x\mathrm{d}y \tag{6.54}$$

where $\sigma(x)$ is the reflectivity of the target.

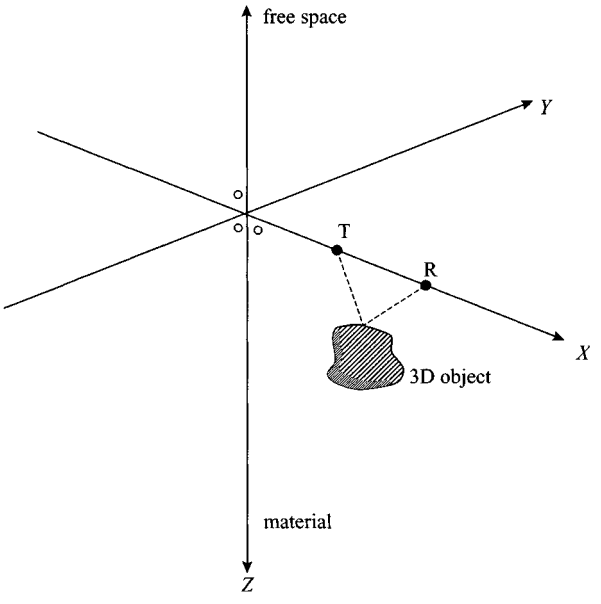

Figure 6.49 Co-ordinates of holographic imaging system

Hence the image function of the object T is

$$b(x) = \frac{1}{2\pi c}\iint_s \sigma(x_r) b_0(x - x_r)\,\mathrm{d}x\mathrm{d}y \tag{6.55}$$

where

$$b_0(x) = \iiint \frac{\cos\theta}{|x - x_r|^2}\frac{\mathrm{d}}{\mathrm{d}t}\frac{(t - 2|x - x_r|)}{c} h(x_r, t)\,\mathrm{d}x\mathrm{d}y \tag{6.56}$$

The effect of material attenuation is significant as the general effect is to apply a windowing function across the recording aperture, thus limiting its useful size in relation to sharply focused images as shown in Figure 6.50.

In addition, the effect of both material attenuation and relative permittivity on the antenna beamwidth should be considered. As the values of loss and relative permittivity increase, the beamwidth of the antenna decreases, and this degrades the gain of the synthetic aperture. In general, synthetic aperture methods are most useful in lower loss materials. Typical images are shown in Figure 6.51.

Single frequency methods require accurate recording over a line and over the complete aperture. This accurate registration of the data is important and is somewhat difficult to achieve under field conditions. Most previous work [39, 40] used accurate mechanical scanning *X-Y* frames, and the practical difficulties of using these in real life conditions have limited the use of single frequency holographic methods. However, advances in low cost robotic technology may overcome some of the past hurdles.

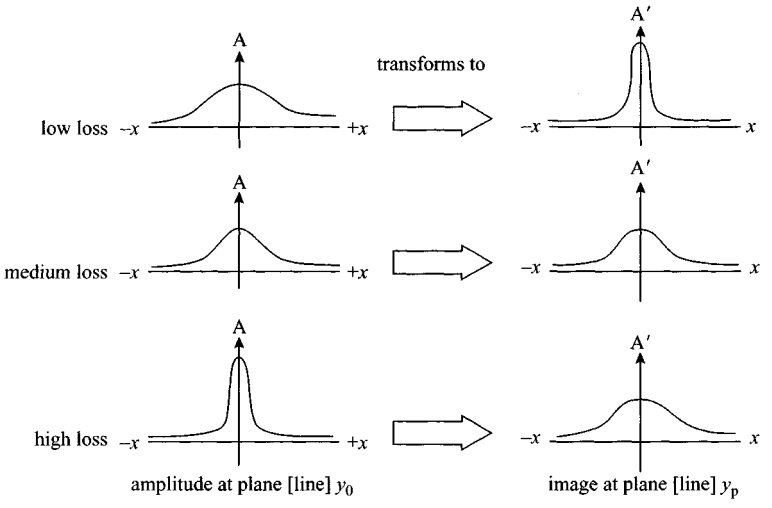

Figure 6.50 Effect of material attenuation on radar synthetic aperture image

Alternative methods of multi-frequency image reconstruction are based on diffraction stack migration, Kirchhoff's methods and Green's function methods, which will be referred to in Chapter 7 on signal processing.

6.8 Polarisation modulation

Any target which possesses a linear scattering geometry can be identified by means of its polarisation scattering matrix.

In the case of a linear target,

$$\mathbf{E}_s = \mathbf{S}\mathbf{E}_i \tag{6.57}$$

where

$$\mathbf{E}_s = \begin{bmatrix} E_x^s \\ E_y^s \end{bmatrix} = \begin{bmatrix} S_{xx} & S_{xy} \\ S_{yx} & S_{yy} \end{bmatrix} \begin{bmatrix} E_x^i \\ E_y^i \end{bmatrix} \tag{6.58}$$

and the predominantly linear feature lies in the x-axis and is lower in impedance than the surrounding material, then the parameter S_{xx} predominates. This is usually the case for buried metal targets, whereas in the case of plastic, where the dielectric surround has a higher impedance than the target, $S_{yy} > S_{xx}$. As S_{xy} and S_{yx} tend to zero, then the backscattered **E** field is largely parallel to the target axis in the case of a parallel incident **E** field applied to a linear metallic target.

When a plastic pipe is illuminated with an orthogonal incident **E** field the backscattered **E** field is the largest component of the reflected signal.

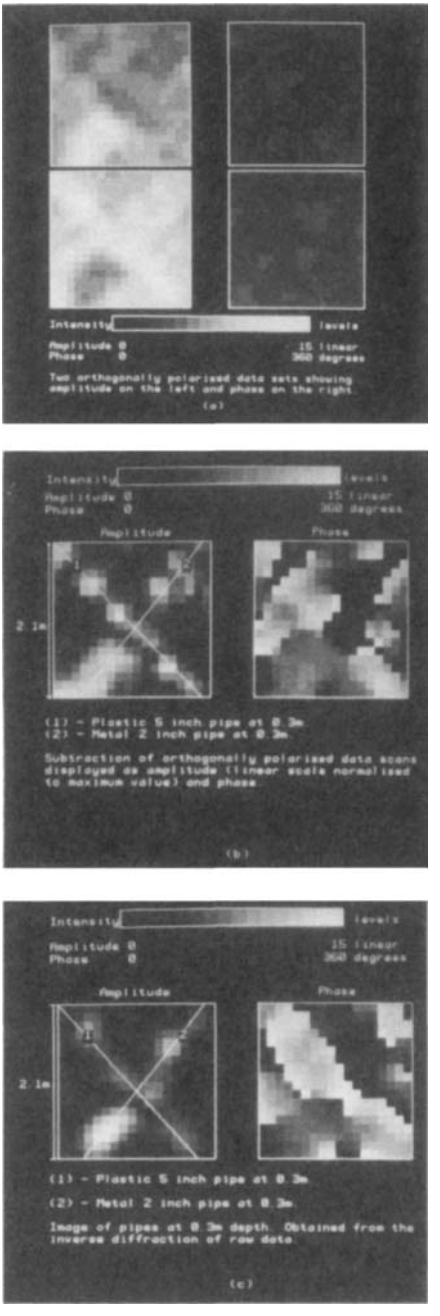

Figure 6.51 Holographic data from two orthogonal scans: (a) data; (b) subtracted; (c) focused in the object plane (after Junkin)

Many systems have exploited this polarisation sensitivity by using orthogonal transmit and receive antennas. The crossed dipole exhibits a much lower crosscoupling than a copolarised pair and this improves the system detectivity.

It is well known that targets such as pipes, as well as shells of various calibres and cracks, act as depolarising features. A linearly polarised crossed dipole antenna rotated about an axis normal to the target produces a sinusoidal variation in received signal. However, the null points are a distinct disadvantage because the operator is required to make two separate, axially rotated measurements at every point to be sure of detecting pipes at unknown orientations.

If such a crossed dipole is rotated around its own axis, the amplitude of the received signal will vary sinusoidally with the angular rotation of the antenna. Following Daniels *et al.* [41],

$$E_s = E_t\,(-\sin\theta\cos\theta)\begin{bmatrix} S_{xx} & S_{xy} \\ S_{yx} & S_{yy} \end{bmatrix}\begin{bmatrix} \cos\theta \\ \sin\theta \end{bmatrix} \tag{6.59}$$

Hence if S_{xy} and S_{yx} are neglected, then

$$E_s = E_t\left\{\frac{1}{2}(S_{xx} - S_{yy})\sin 2\theta\right\} \tag{6.60}$$

In real life, additional received signals caused by a variety of factors such as changes in crosscoupling between the crossed dipoles due to objects or variations in local impedance on the ground surface will contribute to E_r, which can be rewritten as

$$E_r = K_1\cos\theta + K_2 E_t\{(S_{xx} - S_{yy})\sin 2\theta\} \tag{6.61}$$

The need for rotation of the antenna is physically restrictive, and electronic means of rotation have been considered.

One design possibility is to synthesise a circularly polarised signal. Any wave of arbitrary polarisation can be synthesised from two waves orthogonally polarised to each other. As shown in Chapter 5, Section 5.8, a circularly polarised wave is produced by exciting vertically and horizontally polarised waves, each having the same amplitude and with a 90° phase difference between them.

The radiating elements are fed, via wideband (preferably decade) 180° and 90° hybrids, to radiate circular polarisation. If right-hand circularly polarised signals are transmitted and received, the preferential detection of linear features is achieved. If, however, right-hand circularly polarised signals are transmitted and left-hand circularly polarised signals are received, planar features are detected. Hence, if connections to the radiating elements are arranged and switched appropriately, the signals routed to the receiver contain different data according to the sense of polarisation. The data, therefore, can be processed separately and in a different manner to provide images of different targets in the material under investigation.

Unfortunately hardware deficiencies limit the performance; firstly, it is difficult to achieve wideband operation with 90° hybrids (at least over a decade) and, second, even the fastest state-of-the-art GaAs switches have unacceptably high break-through levels.

In view of these difficulties the feasibility of using a commutated multi-element crossed dipole array can be considered, and this technique is rotating linear rather than circular polarisation.

A simple option is an eight-element antenna in which the crossed dipole pairs can be switched at intervals of up to 1 ms so that the two crossed dipole pairs are orientated between 0° and 45° as shown in Figure 5.47. This antenna proved to be successful proof of the concept demonstrator.

Full commutation over 360° in 45° steps could be achieved as shown in Chapter 5, Section 5.8 by using PIN diode switches (to handle the transmitted power) operating at a switching interval of 1 s, thus achieving 360° rotation in ~10 s. The possibility of real time discrimination using filters based on recognition of the $\cos 2\theta$ amplitude variation of each range sample is also possible. Operationally, such a system would have the advantage of being able to survey rapidly without the limitations imposed by mechanically rotated antennas.

Conventionally, circular polarisation refers to a steady-state condition during which a long duration pulse or CW waveforms are transmitted. For impulse radars, the pulse duration is very short (<5 ns) and hence a more complex transient situation is encountered. In general, several cycles of transmitted wave are needed to establish the state of circular polarisation.

One method of radiating circular polarisation with an impulse waveform is to use an equi-angular spiral antenna. Unfortunately, the dispersive nature of this type of antenna causes an increase in the duration of the transmitted waveforms, and the radiated pulse takes the form of a 'chirp' in which high frequencies are radiated first, followed by the low frequencies. This effect, however, may be compensated by a 'spiking' filter, which may take the form of a conventional matched filter or a more sophisticated filter such as a Wiener filter. The use of such an antenna has been shown [42] to be a useful method of implementing pipe detection radar, and plastic pipes buried in wet clay have been detected up to a depth of 1.0 m. Further references are found in Ueno and Osumi [43], Junkin and Anderson [44], Anderson and Richards [45], Osumi and Ueno [46, 47] and Tanaka *et al.* [48].

6.9 Summary

The vast majority of ground penetrating radar systems that have been built are based on the time domain amplitude modulated system approach. The general simplicity of concept and relatively lower cost of production when compared with frequency modulated or step frequency radar systems have been powerful reasons up till now for the choice of impulse radar methods. However, the technical performance of impulse radar systems is generally severely limited by the receiver, which is a sampling down-converter exhibiting a poor noise figure and conversion efficiency.

For this reason attention has been paid to alternative designs. The continuous wave frequency modulated system design requires a high performance in terms of linearity of frequency sweep with time, and this is often difficult to achieve within tight budget constraints. The step frequency continuous wave radar offers considerable promise for

the future now that the performance of synthesised frequency sources has improved and their cost has decreased. The major advantage of the frequency modulated systems is their improved receiver performance in terms of dynamic range compared with the impulse radar system. Noise modulation techniques offer considerable potential advantages, and developments are gathering pace.

Single frequency systems using holographic image reconstruction techniques have been shown to be viable but the physical difficulty of accurately recording over an aperture has tended to limit their use.

6.10 References

[1] DANIELS, D. J.: 'Resolution of UWB signals', *IEE Proc. Radar Sonar Navig.*, 1999, **146**, pp. 189–194

[2] COOK and BERNFELD: 'Radar signals, an introduction to theory and application'. ISBN 0-89006-733-3 (Artech House), p. 9

[3] SKOLNIK, M.: 'Radar handbook, 2nd edition'. ISBN 0-07057913-X, (McGraw-Hill), Chap. 10

[4] NATHANSON: 'Radar design principles'. ISBN 07-046047-7, Chap 8

[5] WEHNER: 'High resolution radar'. ISBN 0-089006-194-7, Chap. 4

[6] GALATI: 'Advanced radar techniques and systems'. IEE Radar, Sonar, Navigation and Avionics Series, Vol. 4, p.104

[7] ASTANIN and KOSTYLEV: 'Ultra-wideband radar measurements systems'. IEE Radar, Sonar, Navigation and Avionics Series, Vol. 7, ISBN 0 85296 894 9, Chap. 1

[8] DANIELS, D. J.: 'Ultra-wideband detection of buried objects'. Proc. IEEE IGARSS 3–8 August 1997, Singapore, pp. 1278–1281

[9] NOON, D., and STICKLEY, G. F.: 'Antenna ring-down, range sidelobes and quality factor of time and frequency domain GPR systems'. Proc. Seventh Int. Conf. on Ground penetrating radar, 27–30 May 1998, Kansas

[10] HARES, J. D.: 'Applications for solid-state high-voltage pulsers', *Eng. Sci. Educ. J.*, 1992, **1**, (3), pp. 113–120

[11] POCHA, M. D., DRUCE, R. L., WILSON, M. J., and HOFER, W. W.: 'Avalanche photoconductive switching'. 7th IEEE Pulsed power Conf., Monterey, CA, USA, June 1989. IEEE Cat. No.89, CH2687-2, pp. 866–868

[12] LEE, C. H.: 'Generation of high power ultrawideband electrical impulse by opto-electronic technique'. Proc. IEEE MTT-S Int. Microwave Symposium, Boston, MA, USA, 10–14 June 1991, IEEE Cat.No.91 CH28704, Vol. 1, pp. 375–378

[13] DENNIS, P., and GIBBS, S. E.: 'Solid-state linear FM/CW radar systems – their promise and their problems'. IEEE Proc Int. Microwave Symposium, Atlanta, GA, USA, June 1974, pp. 340–342

[14] KAY, S., and MARPLE, S. L.: 'Spectrum analysis. A modern perspective', *Proc. IEEE*, 1981, **69**, (11), pp. 1380–1419

[15] ADLER, D., and JACOBS, M.: 'Application of a narrowband FW-CW system in the measurement of ice thickness'. Proc. IEEE MTT-S Int. Microwave

Symposium, Atlanta, GA, USA, 14–18 June 1993, Vol. 2, pp. 809–812, IEEE Cat. No. 93CH3277-1

[16] AL-ATTAR A., DANIELS, D. J., and SCOTT, H. F.: 'A novel method of suppressing clutter in very short-range radars'. RADAR-82, Proc. IEE Int. Radar Conf., London, UK, 18–20 October 1982, pp. 419–423

[17] BOTROS, A. Z., OLVER, A. D., CUTHBERT, L. G., and FARMER, G.: 'Microwave detection of hidden objects in walls', *Electron. Lett.*, 1984, **20**, pp. 379–380

[18] CARR, A. G., CUTHBERT, L. G., and LIAU, T. F.: 'Signal processing techniques for short-range radars applied to the detection of hidden objects'. 7th IEEE European Conf. on Electrotechnics, EUROCON 88, Paris, France, April 1986, pp. 641–646

[19] FARMER, G. A., CUTHBERT, L. G., OLVER, A. D., and BOTROS, A. Z.: 'Distinguishing between types of hidden objects using an FMCW radar', *Electron. Lett.*, 1984, **20**, pp. 824–825

[20] GARVIN, A. D. M., and INGGS, M. R.: 'Use of synthetic aperture and stepped frequency continuous wave processing to obtain radar images'. South African Symposium on Communications and signal processing, COMSIE 91, Pretoria, South Africa, 1991, pp. 32–35

[21] HUA, L., COOPER, D. C., and SHEARMAN, E. D. R.: 'A prototype FMCW radar using an analogue linear frequency sweep'. Proc. IEE Colloquium on High time-bandwidth product waveforms in radar and sonar, London, 1 May 1991, IEE Digest No.093, pp. 11/1–3

[22] JI-CHANG, F.: 'A new method of signal processing with high range resolution and reduced wide-bandwidth for linear-FMCW radar', *AMSE Rev.*, 1990, **14**, (1), pp. 59–63

[23] OLVER, A. D., CUTHBERT, L. G., NICOLAIDES, M., and CARR, A. G.: 'Portable FMCW radar for locating buried pipes'. Radar 82 Conf., London, 1982, IEE Conf. Publ. 216, pp. 413–418

[24] OLVER A. D., and CUTHBERT L. G.: 'FMCW radar for hidden object detection', *IEE Proc. F. Commun., Radar Signal Process.*, 1988, **135**, pp. 354–361

[25] PEEBLES, P. Z., and STEVENS, G. H.: 'A technique for the generation of highly linear FM pulse radar signals', *IEEE Trans. Mil. Electron.*, 1965, **9**, pp. 32–38

[26] STOVE, A. G.: 'Linear FMCW radar techniques', *IEE Proc. F*, 1992, **139**, (5), pp. 343–351

[27] TRANSBARGER, O.: 'FM radar for inspecting brick and concrete tunnels materials evaluation', 1985, **43**, (10), pp. 1254–1261

[28] YAMUGUCHI, Y., SENGOKU, N., and ABE, T.: 'FM-CW radar applied to the detection of buried objects in snowpack'. Proc. IEEE Int. Symposium on Merging technologies for the 90s, Dallas, TX, USA 7011, May 1990, IEEE Cat No. 90CH2776-3, Vol. 2, pp. 738–741

[29] YAMAGUCHI, Y., MARUYANA, Y., KAWAKAMI, A., SENGOKO, M., and ABE, T.: 'Detection of objects buried in wet snowpack by FM-CW radar', *IEEE Trans. Geosci. Remote Sens.*, 1991, **29**, (2), pp. 201–208

[30] YAMAGUCHI, Y., MITSUMOTO, M., SENGOKU, M., and ABE, T.: 'Synthetic aperture FM-CW radar applied to the detection of objects buried in snowpack'. Int. IEEE Symp. Digest Antennas and Propagation, May 1992, pp. 1122–1125

[31] INGGS, M., and GARRISS, A.: 'A stepped frequency CW ground probing radar'. MRSI Microwave signature 92, pp. 1–4

[32] IIZUKA, Z., and FREUNDORFER, A.: 'Step frequency radar', *J. Appl. Phys.*, 1984, **56**, pp. 2572–2583

[33] LANGMAN, A.: 'The design of hardware and signal processing for a SFCW GPR'. PhD Thesis, University of Capetown, March 2002

[34] GUOSUI, L., HONG, G., and WEIMIN, S.: 'Development of random signal radars', *IEEE Trans. Aerosp. Electron. Syst.*, 1999, **35**, (3), pp. 770–777

[35] DAWOOD, M., and NARAYANAN, R. M.: 'Ambiguity function of an ultra-wideband random noise radar'. IEEE Antennas and Propagation Society Int. Symposium, 2000, Salt Lake City, UT, USA, Vol. 4, pp. 2142–2145

[36] XU, X., and NARAYANAN, R. M.: 'Range sidelobe suppression technique for coherent ultra wide-band random noise radar imaging', *IEEE Trans. Antennas Propag.*, 2001, **49**, (12), pp. 1836–1842

[37] PETERSON, R. L., ZIEMER, R. E., and BORTH, D. E.: 'Introduction to spread spectrum communications' (Prentice Hall, Englewood Cliffs, NJ, 1995)

[38] XIANG, N.: 'A mobile universal measuring system for the binaural room-acoustic modelling technique'. Dissertation, Ruhr-Universität Bochum, Germany, 1991

[39] OSUMI, N., and UENO, K.: 'Microwave holographic imaging method with improved resolution', *IEEE Trans.*, 1984, **AP-32**, pp. 1018–1026

[40] ANDERSON, A. P.: 'Microwave holography', *Proc. IEE*, 1977, **124**, (11R), pp. 946–962

[41] DANIELS, D. J., GUNTON, D. J., and SCOTT, H. F.: 'Introduction to subsurface radar', *IEE Proc. F*, 1988, **135**, (4), pp. 278–321

[42] SHAW, M. R., MILLARD, S. G., HOULDEN, M. A., AUSTIN, B. A., and BUNGEY, J. H.: 'A large diameter transmission line for the measurement of the relative permittivity of construction materials', *Br. J. Non-Destr. Test.*, 1993, **35**, (12), pp. 696–704

[43] UENO, K., and OSUMI, N.: 'Underground pipe detection based on microwave polarisation effect'. Proc. Int. Symp. Noise and clutter rej., Tokyo, 1984, pp. 673–678

[44] JUNKIN, G., and ANDERSON, A. P.: 'Limitations in microwave holographic synthetic aperture imaging over a lossy half-space', *IEE Proc. F, Commun. Radar Signal Process.*, 1988, **135**, pp. 321–329

[45] ANDERSON, A. P., and RICHARDS, P. J.: 'Microwave imaging of sub-surface cylindrical scatterers from cross-polar backscatter', *Electron. Lett.*, 1977, **13**, pp. 617–619

[46] OSUMI, N., and UENO, K.: 'Microwave holographic imaging of underground objects', *IEEE Trans. Antennas Propag.*, 1985, **AP-33**, pp. 152–159

[47] OSUMI, N., and UENO, K.: 'Detection of buried plant', *IEE Proc. F., Commun. Radar Signal Process.*, 1988, **135**, pp. 330–342
[48] TANAKA, H., KAWONO, A., KOYANAGI, M., and MATSUURA, M.: 'Development of radar-based pipe locator'. Proc. 16th World Gas Conference, Munich Pub. Int. Gas Union, 1985

6.11 Bibliography

CHEN, C.-C.: 'Fully-polarimetric ground penetrating radar application'. IEEE Int. Antennas and Propagation Society Symposium, 2001, Vol. 4, pp. 604–607
JUNKIN, G., and ANDERSON, A. P.: 'A new system for microwave holographic imaging of buried services'. Proc. 16th Eur. Microwave Conf., 1986, pp. 720–725
LANGMAN, A., and INGGS, M. R.: 'Pulse versus stepped frequency continuous wave modulation for ground penetrating radar'. Proc. IEEE Int. Geoscience and remote sensing Symposium, 2001 (IGARSS '01), Vol. 3, pp. 1533–1535
LANGMAN, A., DIMAIO, S. P., BURNS, B. E., and INGGS, M. R.: 'Development of a low cost SFCW ground penetrating radar'. Proc. Int. Geoscience and remote sensing Symposium, 1996 (IGARSS '96) 'Remote sensing for a sustainable future', 27–31 May 1996, Vol. 4, pp. 2020–2022
LOUBRIEL, G. M., AURAND, J. F., DENISON, G. J., RINEHART, L. F., BROWN, D. J., ZUTAVERN, F. J., MAR, A., O'MALLEY, M. W., HELGESON, W. D., and CARIN, L.: 'Optically-activated GaAs switches for ground penetrating radar and firing set applications'. 12th IEEE Int. Pulsed Power Conf., 1999. Digest of Technical Papers. Vol. 2, pp. 673–676
ORME, R. D., and ANDERSON, A. P.: 'High-resolution microwave holographic technique: application to the imaging of objects obscured by dielectric media', *Proc. IEE*, 1973, **120**, pp. 401–406
RICHARDS, P. J., and ANDERSON, A. P.: 'Microwave images of sub-surface utilities in an urban environment'. Proc. 8th Eur. Microwave Conf., 1978, pp. 33–37
STICKLEY, G. F., NOON, D. A., CHERNLAKOV, M., and LONGSTAFF, I. D.: 'Preliminary field results of an ultra-wideband (10-620 MHz) stepped-frequency ground penetrating radar'. Proc. IEEE Int. Conf. Geoscience and Remote Sensing, 1997 (IGARSS '97), 'Remote sensing – a scientific vision for sustainable development', 3–8 Aug 1997, Vol. 3, pp. 1282–1284
VAN GENDEREN, P.: 'The effect of phase noise in a stepped frequency continuous wave ground penetrating radar'. Proc. CIE Int. Conf. on Radar, 2001, pp. 581–584

Chapter 7

Signal processing

7.1 Introduction

The objective of this Chapter is to provide an introduction to those methods that have been used to process data. The area of signal processing is so extensive that only a basic introduction to the topic is possible. The recommended references will provide further material for those wishing to investigate the topic in greater detail.

Inevitably, some users may consider that their favourite method has not been given sufficient prominence or that some combinations of methods may provide improved performance. Unfortunately, it is impossible to satisfy all interests.

The author's view is that signal processing is primarily a means of reducing clutter. Fundamentally, the signal to clutter ratio of the radar data is the key to target detection. Most system noise in GPR systems can be reduced by averaging. GPR is heavily contaminated by clutter, and reduction of this is a key objective. The cost–benefit of implementation should be clearly demonstrated before superficially attractive but practically unsound methods are incorporated. Clearly, the wide range of targets, applications and situations encountered is likely to task even the most robust algorithm, and the user should assess the latest algorithm with some care.

The general objective of signal processing as applied to surface-penetrating radar is either to present an image that can readily be interpreted by the operator or to classify the target return with respect to a known test procedure or template.

The image of a buried target generated by a GPR radar will not, of course, correspond to its geometrical representation. The fundamental reasons for this are related to the ratio of the wavelength of the radiation and the physical dimensions of the target. In most cases for surface-penetrating radar the ratio is close to unity. This compares very differently with an optical image, which is obtained with wavelengths such that the ratio is considerably greater than unity.

In surface-penetrating radar applications, the effect of combinations of scattering planes, for example, the corner reflector, can cause 'bright spots' in the image, and variations in the velocity of propagation can cause dilation of the aspect ratio of the

image. While many images can be focused to reduce the effect of antenna beam spreading, regeneration of a geometric model is a much more complex procedure and is not usually attempted.

An alternative approach, which seeks to reduce the workload on the operator, is to correlate the image with a known template and derive a spatial correlation coefficient. Promising results have been obtained using pole-zero methods as well as neural network approaches.

A major source of error in GPR data is the reflection from the surface of the ground. Abrahamsson *et al.* [1], O'Neill *et al.* [2] as well as Wu *et al.* [3] report on methods to reduce the effect of ground surface.

The general procedure when processing data is to store the data in the appropriate dimensional format and then apply appropriate algorithms.

With reference to Figure 7.1 the data can be considered to be of the form

$$f(x, y, z) = A(x_i, y_j, z_k) \tag{7.1}$$

over the ranges $k = 1$ to N, $j = 1$ to M, and $i = 1$ to P.

Note that time and depth of the Z-axis can be considered to be interrelated by the velocity of propagation.

A single waveform or A-scan is defined as

$$f(z) = A(x_i, y_j, z_k) \tag{7.2}$$

over the range $k = 1$ to N, $i =$ constant, $j =$ constant.

An ensemble waveform set or B-scan is defined as

$$f(x, z) = A(x_i, y_j, z_k) \tag{7.3}$$

over the range $k = 1$ to $N, i = 1$ to $P, j =$ constant
or

$$f(y, z) = A(x_i, y_j, z_k) \tag{7.4}$$

over the range $k = 1$ to $N, j = 1$ to $L, i =$ constant.

An ensemble waveform set of a C-scan is defined as

$$f(x, y, z) = A(x_i, y_j, z_k) \tag{7.5}$$

over the range $j = 1$ to $M, i = 1$ to P, for a selected value of Z or range of values of Z.

In general, most published surface-penetrating radar data have been processed and presented in either A-, B- or C-scan form. The processes applied to each data format can be broadly classified as follows:

(*a*) A-scan processing
(*b*) B-scan processing. Note that the dimensions can be considered interchangeable, that is, the same processes may be useful for x-z, x-y or y-z planes.

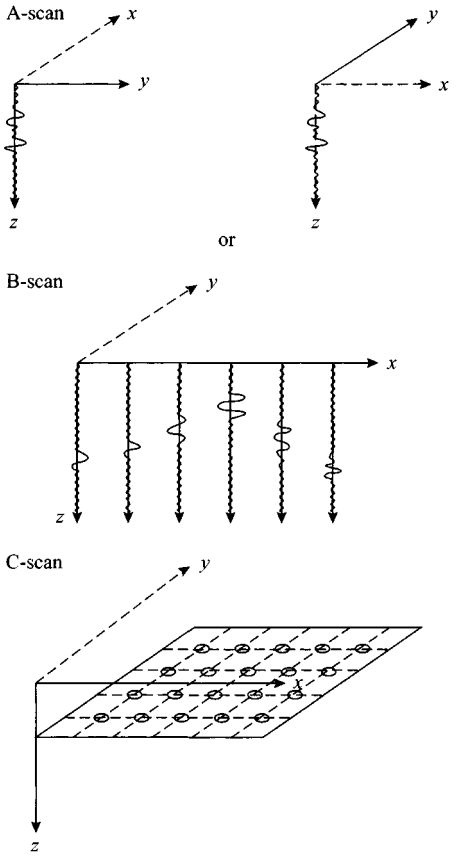

Figure 7.1 Co-ordinate system for scan description

(*c*) C-scan processing. Note that the spatial three-dimensional data can be used to reconstruct representations of three-dimensional images.

Most of the description in the following Chapter is relevant to a time series data set. Most amplitude modulated radar systems generate time domain data but frequency domain radar systems such as FMCW initially generate a frequency domain data set, which requires transformation to the time domain equivalent. Other modulation schemes such as pseudo-random coding or noise modulation require a crosscorrelation of the received signal with a template.

There is no fundamental difference in the information content of the data output from any modulation scheme provided, of course, that the amplitude and phase information is retained in the receiver conversion process.

In general it is the range to the target which is of most interest, and as this is fundamentally equivalent to time, the time series data set is most relevant. However, there will be occasions when it is more appropriate to use alternative descriptions.

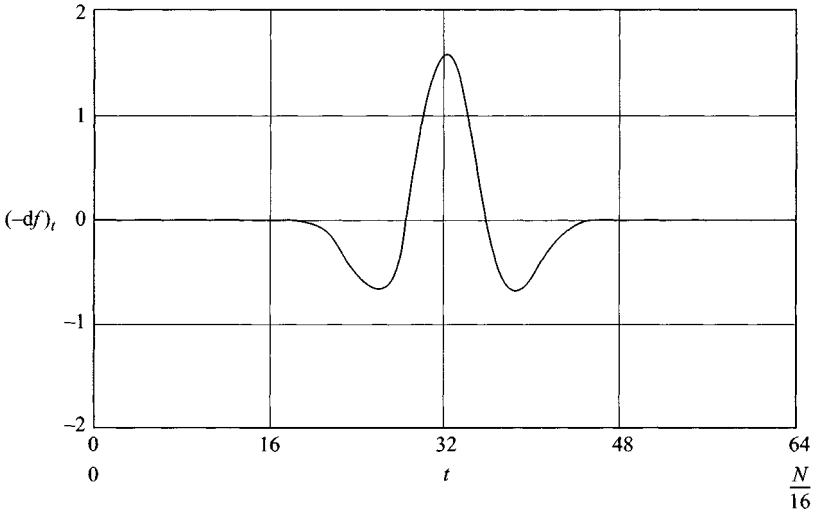

Figure 7.2 Time domain wavelet

Many of the processing techniques that have been applied to surface-penetrating radar data have been developed for other applications, and in addition to radar, acoustic, ultrasonic and seismic processing methods have been freely employed.

In reality the time series under consideration represents only the sampled values of a continuous time function and hence is a restricted version of the latter. In addition it has a limited time duration compared with an analytic function, which can be considered to have infinite time duration. The finite number of samples stored and processed represents a truncated portion of a time series and can be termed a sample time series.

A wavelet can be considered as a transient event with a definite time of arrival and a finite energy content as shown in Figure 7.2.

The general processing problem encountered in dealing with surface-penetrating radar data is in the widest sense the extraction of a localised wavelet function from a time series which displays very similar time domain characteristics to the wavelet. This time series is generated by signals from the ground and other reflecting surfaces, as well as internally from the radar system.

Unlike conventional radar systems in which the target can generally be regarded as being in motion compared with the clutter, in the surface-penetrating radar case, the target and the clutter are spatially fixed and the radar antenna is moved with respect to the environment.

In all the following discussions it is assumed that data are recorded to an adequate resolution and bandwidth. This means digitisation to at least 12 or 16 bits (72 dB or 96 dB system dynamic range) for an A-scan record length of typically 256 or 512 samples, which entails a data storage capacity of at maximum 1 kbyte per A-scan unless data compression techniques are used.

The capacity required to store a B-scan depends upon the overall length of line survey and spatial sampling interval. To achieve an adequate spatial resolution depends on the size of the object, and typically a convenient length is 512 A-scans, and hence a B-scan may require 0.512 Mbytes of data storage. With the data storage capabilities of hard disk drives (100 Gbyte) and tape back-up stores no serious difficulties should be encountered in storing site survey data. Alternatively, data compression techniques can be used to provide up to a 20:1 level of data compression.

Before discussing the various signal processing methods it is useful to state some basic definitions.

The statistical properties of a time series can be determined by considering either a large number of similar signals at any one instant in time, which is termed an ensemble value, or alternatively one signal at a number of intervals of time, termed a time value.

If the two properties are equal then the function or set of functions is said to be ergodic. To be ergodic a function must be a stationary signal, although the converse is not necessarily true.

A continuous function with the same long term properties is defined as a statistically stationary function, and suitable examples are sinusoidal functions or white noise. In contrast, impulsive signals are considered to be statistically nonstationary.

A random signal which has a definite probability as to its content is termed a stochastic signal and, for example, white noise plus a sine wave is termed a stochastic signal.

A minimum phase system or function is defined as having no poles or zeros in the RH half of the S-plane. Note that RH zeros make a non-minimum-phase system but RH poles make an unstable system. Conjugate pairs on the axis indicate a marginally stable system.

7.2 A-scan processing

The received time waveform can be described as the convolution of a number of time functions each representing the impulse response of some component of the radar system in addition to noise contributions from various sources – hence the received time waveform (Daniels *et al.* [4])

$$f_r(t) = f_s(t) \otimes f_{a1}(t) \otimes f_c(t) \otimes f_{gf}(t) \otimes f_t(t) \otimes f_{gr}(t) \oplus f_{a2}(t) + n(t) \tag{7.6}$$

where

$f_s(t)$ = signal applied to the antenna
$f_{an}(t)$ = antenna impulse response
$f_c(t)$ = antenna crosscoupling response
$f_{gd}(t)$ = ground impulse response (d denotes direction)
$f_t(t)$ = impulse response of target
$n(t)$ = noise.

Each contribution has its own particular characteristics which need to be considered carefully before application of a particular processing scheme.

Ideally the signal applied to the antenna should be a Dirac function but practically is more like a skewed Gaussian impulse of defined time duration.

Most antennas used in surface-penetrating applications have a limited low frequency response and tend to act as highpass filters effectively differentiating the applied impulse, hence creating a wavelet. In most cases near identical antennas are used and if these are spaced sufficiently far from the ground surface then $f_{a1}(t) = f_{a2}(t)$. In the case of antennas operated in close proximity to the ground, then both $f_{a1}(t)$ and $f_{a2}(t)$ are variant with changes in the ground surface electrical parameters.

Any processing scheme which relies on invariant antenna parameters should take into account the mode of operation of the antennas and the degree of stability that is practically realisable.

The antenna crosscoupling response $f_c(t)$ is composed of a fixed contribution $f_c'(t)$ due to antenna crosscoupling or reflection and a variable contribution $f_c''(t)$ due to the effect of the ground or nearby objects. Hence $f_c(t) = f_c'(t) + f_c''(t)$. It has been found possible to reduce the amplitude of $f_c(t)$ to very low levels; in the case of crossed dipole antennas to below -70 dB and in the case of parallel dipole antennas to below -60 dB. However, $f_c''(t)$ can be significantly larger and degrades the overall value of $f_c(t)$ to -40 dB. The value of $f_a(t)$ is determined by any local inhomogeneities in the soil or by any covering material, whether of mineral or vegetable origin. There is unfortunately little that can be done to predict variations in $f_c''(t)$ and it is not amenable to treatment by many processing algorithms. The variation in $f_c''(t)$ is much greater with the crossed dipole antenna than the parallel dipole.The ground impulse response $f_g(t)$ can be determined from its attenuation and dielectric constant across the frequency range of interest.

The target impulse response can be composed of the convolution of the wanted target response, together with many other reflectors, which may not be wanted by the user but which are valid reflecting targets as far as electromagnetic waves are concerned. The time separation of the targets is related to their physical spacing as well as the velocity of propagation, which can vary depending on the material properties.

Where the targets are well separated in range, it is relatively straightforward to separate the radar reflections, but this becomes progressively more difficult as targets become closer together, as instead of individual delta functions a series of overlapping (in time) wavelet functions of different characteristics exists.

Before considering the more sophisticated methods of recovering and processing the wavelets there is a range of simple processing methods, which can be applied to each individual A-scan.

7.2.1 Zero offset removal

An important process operation is to ensure that the mean value of the A-scan is near to zero. This assumes that the amplitude probability distribution of the A-scan

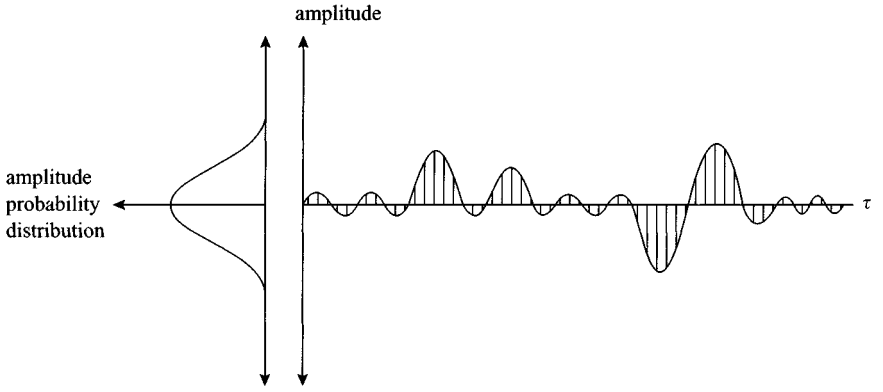

Figure 7.3 A-scan sample time series

is symmetric about the mean value and not skewed and that the short time mean value is constant over the time duration of the A-scan, as shown in Figure 7.3. It is generally less likely that the amplitude probability distribution is skewed, but where RF time varying gain is incorporated and the sampling gate exhibits a DC offset, the short time mean value may vary over the time duration of the A-scan.

Any signal processing algorithm should cater for these situations. For example, a simple algorithm such as

$$A'_n(t) = A_n(t) - \frac{1}{N}\sum_{n-0}^{N} A_n(t) \tag{7.7}$$

where $A_n(t)$ = unprocessed data sample, $A'_n(t)$ = processed data sample and n = sample number, will only work where the short term mean value is constant and the amplitude probability distribution is symmetric.

7.2.2 *Noise reduction*

An important processing technique is noise reduction and can be achieved by either averaging each individual sample of the A-scan or storing and averaging repeated A-scans. The general effect is to reduce the variance of the noise and gives an improvement in signal to noise ratio equal to $10\log_{10}N$.

The general form of the filtering operation is given by

$$A'_n(t) = A'_{n-1}(t) + \frac{\left[A_n(t) - A'_{n-1}(t)\right]}{K} \tag{7.8}$$

where $A'_n(t)$ = averaged value and $A_n(t)$ = current value. The factor K may be chosen to be related to n, N or a fixed value, which will weight the averaged value appropriately.

The time spent averaging must take into account the speed at which the radar is moved, as unless the physical location is sensibly constant during averaging, data

will become contaminated by adjacent samples. Averaging has no effect on clutter but reduces random noise. It is likely that the main contribution to the overall noise level is caused by the radar receiver, and this can be very high for the time domain, sampling receiver. In this case much of the noise is caused by timing jitter and can be considered to be worse on the rise and fall times of signals. The noise is therefore spectrally biased towards the high frequency region of the band of frequency operation.

7.2.3 Clutter reduction

Clutter reduction can be achieved by subtracting from each A-scan an averaged value of an ensemble of A-scans or B-scans taken over the area of interest, i.e.

$$A'_{n,a}(t) = A_{n,a}(t) - \frac{1}{Na}\sum_{a=1}^{Na} A_{n,a}(t) \tag{7.9}$$

where $n = 1$ to N (N = number of samples), $a = 1$ to N_a (N_a = number of A-scan waveforms), $A_{n,a}(t)$ = unprocessed A-scan and $A'_{n,a}(t)$ = processed A-scan.

This method works well for situations where the number of targets is limited and they are physically well separated. Evidently, the summation of the average value will include contributions from all targets, and the greater the number the less will be the difference that results.

In situations where there is a planar interface within the area of interest, then this process has the unfortunate effect of removing most of the wavelet caused by the interface. Hence, it is important to choose both N and N_a with care to optimise the process for a particular situation.

Fundamentally it is assumed that the material properties vary in a random manner over the volume of interest and the averaged value $f_r(t)$ represents the convolution of

$$f_r(t) = f_s(t) \otimes f_{a1}(t) \otimes f_c(t) \otimes f_{gf}(t) \otimes f_t(t) \otimes f_{gr}(t) \otimes f_{a2}(t) \tag{7.10}$$

The main uncertainty lies in the lack of random variability of the ground properties and the effect this has on $f_r(t)$.

Analysis of the statistical nature of the variability has been carried out by Caldecott *et al.* [5]. This method derives a standard deviation time function from an ensemble of zero mean A-scans. Each unprocessed A-scan is compared with the standard deviation time function, and samples which are greater than the standard deviation time function by a predetermined amount, i.e. one, two or three σ, are defined as significant. An alternative version of this process is

$$A'_{n,a}(t) = A_{n,a}(t) - \frac{K}{Na}\sum_{a=1}^{Na} A_{n,a}(t) \tag{7.11}$$

where K is a variable related to the required magnitude of the standard deviation.

This process can also be applied to a selected section of the A-scan in order to remove clutter associated with a particular region of time. For example, the antenna response can be removed following acquisition of an A-scan from a calibrated target.

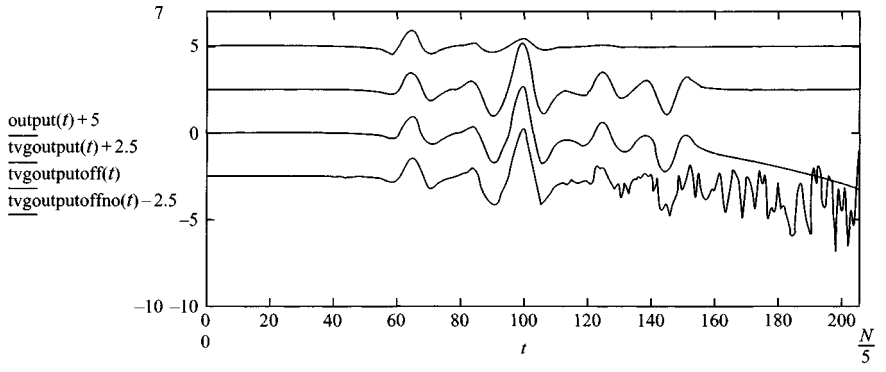

Figure 7.4 Effects of time varying gain on A-scan

7.2.4 *Time varying gain*

The received signal is reduced in amplitude compared with the transmitted signal as a result of both attenuation by the medium of propagation and by the path or spreading loss encountered in travelling to and from the target:

$$A'_n(t) = A'_n(t)\,kn \tag{7.12}$$

where k is the weighting function of the sample number.

To apply time varying gain to compensate for these losses, several conditions must be met. There should be a zero mean value of the A-scan, otherwise significant DC offsets will be created at late times. The noise levels at late times should be low, else the general late time noise will be increased. Great care is needed to apply time varying gain in a smoothly and continuously varying way, which corresponds to correction of physical loss mechanisms. These effects are shown in Figure 7.4, which shows the modelled A-scan (upper graph), from top to bottom a correctly applied time varying gain, then the effect of a small negative DC offset, and finally in the lower graph the effect of both a small negative DC offset and noise on the signal.

Stepped or rapid gain variation along the time axis can modulate the unprocessed signal and generate artificial wavelets. In general, such variations are to be avoided unless there has been careful assessment of the propagation path losses as a function of time.

It is more prudent to record data that has a known time varying gain or better still none at all. This reduces the possibility of data becoming subjectively 'improved' by the field operator of the radar.

7.2.5 *Frequency filtering*

Highpass filtering of the A-scan data is a useful means of improving the signal to clutter ratio in situations where clutter is caused by additional low frequency energy generated by antenna ground interactions. In addition, excessive high frequency noise can usefully be reduced by lowpass filtering. Many commercially available radar

systems offer a range of filter options, and the choice of settings of bandwidths, slope etc. is left to the operator. Such a filter should in general exhibit a minimum phase response to reduce phase distortion of the filtered wavelets.

7.2.6 *Wavelet optimisation or deconvolution techniques*

The general principle of wavelet optimisation is to filter the sample time series in such a way that the desired output from the filtering process is an impulse function representing the deconvolution of the wanted signal. Such an impulse is variously known as a Dirac or Delta function, a unit impulse or spike. However, this ideal outcome is not usually achievable and the optimum filter is one where the energy of the difference between the desired and actual filters is minimised. This is termed an optimum or least squares filter:

$$E^2 = t \xrightarrow{\lim} \infty \frac{1}{2t} \int_{-t}^{t} \{y(t) - d(t)\}^2 \mathrm{d}t \tag{7.13}$$

where $y(t)$ = actual output and $d(t)$ = desired output.

This is known as the Wiener least mean-square-error criteria and the general filtering process is termed a Wiener filter. Considerable work on wavelet optimisation has been carried out for seismic or geophysical signal analysis, for which the data show many similarities to surface-penetrating radar data.

The Wiener filter can be adjusted for several situations and, in the case where the signal is modified by additive white Gaussian noise, the optimum filter is a matched filter which is a standard approach to conventional radar signal processing. A matched filter is mathematically identical to a correlation receiver and provides an output

$$H(t) = \int_{-\infty}^{\infty} e(\tau)\, s(\tau_0 - (t - \tau))\mathrm{d}\tau \tag{7.14}$$

where $e(\tau)$ = input signal, $s(\tau_0 - (t - \tau))$ = time reverse of the input signal and τ_0 = delay required to meet causality requirements.

For this filter the output is maximum at $\tau_0 = t$.

An alternative realisation of the Wiener filter is the inverse filter. In this case the spectral response of the filter is the reciprocal of the signal spectrum, although in fact the extremes of the frequency range are limited to avoid excessive out of band energy degrading the output from the filter.

The frequency characteristic of an inverse filter is given by

$$H(f) = \frac{S(f)}{N' + K|S(f)|^2} \tag{7.15}$$

where $S * f$ = the Fourier transform of the time reverse of the signal, N' = the noise power (halved), $S(f)$ = signal spectrum and $K|S(f)|^2$ = clutter power.

The inverse filter results from the case where the clutter is largest and the matched filter results from the case where the noise predominates.

A comparison of the performance of several different configurations of filter is given in an excellent treatment by Robinson and Treitel [6]. The least squares filter,

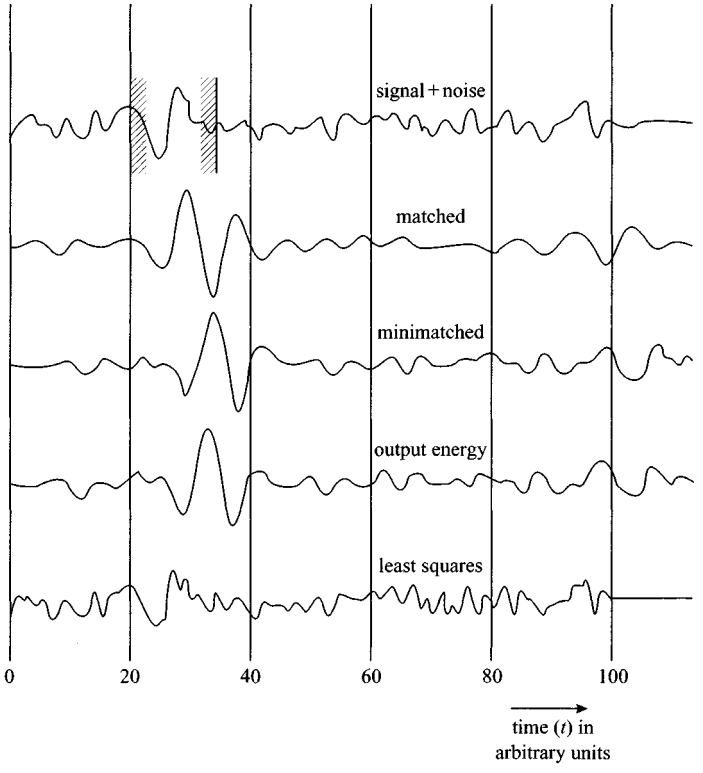

Figure 7.5 Methods of detection of a signal immersed in white noise (after Robinson and Treitel [6])

optimised to provide a near delta function output, was compared with a matched filter, a mini-matched filter and an output energy filter as shown in Figure 7.5.

It can be seen that the least squares filter does not produce a high amplitude output in the presence of noise, whereas the matched filter does. Note, however, that the output of the matched filter shows the effect of the different phase lag characteristics of the latter compared with the mini-matched and output energy filters. The least squares filter does provide the optimum output in the case where the noise is significantly lower than the signal.

The selection of a suitable filter is therefore dependent upon the characteristics of the signal. As the sample data set is composed of signal, noise and clutter, the question of the stability of the filter must be considered. It is not possible to achieve infinite resolution of the filter output and, unless certain restrictions are placed, both on the filter coefficients and the characteristics of the sample data set, the filter will behave in an unstable manner.

As most of the processing of surface-penetrating radar data is carried out using digital filtering, and mainly in the form of software algorithms, it is instructive to

consider an example of those aspects of the design of a digital inverse filter which affect performance and stability.

If we assume that a sampled data set described by $d_0, d_1, d_2, d_3, \ldots, d_n$ is the input to a filter which then transforms the input to an output of unit magnitude at $t = 0$, then

$$h_t = \sum_{n=0}^{t} d_n f_{t-s} \tag{7.16}$$

for all positive values of t, where $h_t = 1$ for $n = 0$ and $h_t = 0$ for $n = 1$ to t.

The required filter will be the time inverse of the input data series and will possess an infinite length of weighting coefficients or memory function.

Provided

$$\sum |f_{t-n}|^2 > 0 \tag{7.17}$$

the filter will be stable.

If the coefficients are derived using the z-transform in order to represent the example in terms of unit delay, then the input to the filter is given by

$$D(z) = d_0 + d_1 z + d_2 z^2 + d_3 z^3 \cdots \tag{7.18}$$

and the output

$$H(z) = 1$$

then

$$H(z) = D(z)F(z) \tag{7.19}$$

where

$$F(z) = \frac{H(z)}{D(z)} = \frac{1}{D(z)} \tag{7.20}$$

Hence

$$f_0 + f_1 z + f_2 z^2 \cdots = \frac{1}{d_0 + d_1 z + d_2 z^2 \cdots} \tag{7.21}$$

If we consider an input with two terms, the right-hand side is expanded by the binomial theorem,

$$f_0 + f_1 z + f_2 z^2 \cdots = 1 - kz + k^2 z^2 - k^3 z^3 \cdots \tag{7.22}$$

Then, equating coefficients,

$$(f_0, f_1, f_2, f_3, \ldots) = \left(1, -k, k^2, -k^3, \ldots\right) \tag{7.23}$$

If $k < 1$, that is the input function is a minimum delay wavelet, it can be seen that the values of the filter coefficient will converge to zero, whereas if $k > 1$, the series will diverge and the filter will be unstable. Thus, the causal or one-sided filter is limited to processing minimum delay wavelet functions.

This limitation can be overcome by generating a noncausal filter function. This can only be synthesised as having recorded the signal there is no restriction on operating in real time. Hence the noncausal filter can operate in nonreal time with a set of coefficients that cater for minimum delay and maximum delay wavelet functions. A noncausal filter will have coefficients that extend equally either side of a nominal zero time. Alternatively, we can consider such a filter as possessing an inherent time delay. The time delay or lag of the filter can be optimised to provide the minimum error energy which, when normalised, equates to the average squared error e divided by the autocorrelation function of the desired output at the zero lag time.

When $e = 0$ the required and actual filter outputs are equal for all values of time, and vice versa. The filter performance can be defined in terms of efficiency as

$$\eta = 1 - e \tag{7.24}$$

For any filter the filter length and filter lag can be separately chosen to optimise η. However, if the filter length is larger than the separation between wavelets, then the filter output will contain 'leaked' energy from any adjacent wavelet and will be sub-optimum. The objective of optimum filtering is to generate an output shape – Gaussian, Delta function etc. – from an input wavelet which exists in a general noise background using the minimum duration filter with a high value of η.

A relevant application of this approach is given by Ueno and Osumi [7], who used the general method to produce a mixed delay filter to provide optimum matched filtering. Coatanhay [8] considered optimisation methods of deconvolution.

More recent developments in wavelet theory have introduced the concept of the wavelet transform (WT), which is relevant to the analysis of nonstationary signals such as the output from ultra-wideband radar systems. Wavelet transforms are a class of transforms which decompose signals into a set of base functions or wavelets. These are obtained from a single elementary wavelet by expansion, contraction or shifting. The short time Fourier transform (STFT) is the precursor of the WT and maps a signal onto a time–frequency plane as a time–frequency representation of the signal.

The Fourier transform is concerned with transformations applied to stationary signals, i.e. those signals whose properties do not evolve with time – sine waves, for example.

The Fourier transform of $x(t)$ is given by

$$F(\omega) = \frac{1}{2\pi}\int_{-\infty}^{\infty} x(t)\, e^{-j2\pi ft}\, \mathrm{d}t \tag{7.25}$$

and the global domain is that of frequency. The Fourier transform is not well suited to sudden changes in time in a nonstationary signal as the transform $F(x(t))$ becomes spread out over the frequency domain. The STFT considers a signal over a limited time window $g(t)$ centred at time τ. Hence the STFT

$$F(\tau, \omega) = \frac{1}{2\pi}\int x(t)\, g*(t-\tau)\, e^{-j2\pi ft}\, \mathrm{d}t \tag{7.26}$$

Essentially the STFT introduces a frequency dependence with time by filtering the signal 'at all times' with a bandpass filter centred on each individual frequency and

whose impulse response is that of the window function. The descriptive principle is similar to that of a score of a piece of music in which frequencies are 'played' in time.

The main limitation of the STFT is its inability to resolve more closely than the equivalent width of the bandpass filter, i.e.

$$\text{time–bandwidth product} = \Delta t \Delta f > \frac{1}{4\pi} \tag{7.27}$$

which is fundamentally related to the Uncertainty Principle.

The way of improving this limitation is to vary Δt and Δf in the time–frequency plane in order to obtain variable resolution. The STFT employs a constant value of $g(t)$ and exhibits a constant bandwidth. It is varied so as to provide constant proportional bandwidth, i.e.

$$\frac{\Delta f}{f} > k \tag{7.28}$$

It is possible to achieve good time resolution at high frequencies and good frequency resolution at low frequencies. This is the basis of the continuous wavelet transform (WT), in which a prototype wavelet $h(t)$ serves as the basic wavelet and is scaled as appropriate; hence

$$h_a(t) = \frac{1}{\sqrt{|a|}} h\left(\frac{t}{a}\right) \tag{7.29}$$

and the transformed wavelet is given by

$$F_\omega(\tau, a) = \frac{1}{\sqrt{|a|}} \int_{-\infty}^{\infty} x(t) h \otimes \left(\frac{t-\tau}{a}\right) \mathrm{d}t \tag{7.30}$$

It is usually more convenient to display the power spectral density of a function rather than the real and imaginary components of its two sided spectrum. The power spectral density function of a normal Fourier spectrum has equivalence in what is termed a spectrogram for the STFT or a scalogram for the WT.

The spectrogram of an STFT is defined as

$$SPEC_x(t, f) = |STFT(t, f)|^2 \tag{7.31}$$

and the scalogram of a WT is defined as

$$SCAL_x(t, f) = |WT(t, f)|^2 \tag{7.32}$$

and both are convenient ways of viewing the signal in an analogous manner to the power spectral density.

Care should be exercised in the use of particular WTs as there is an implicit assumption of linearity.

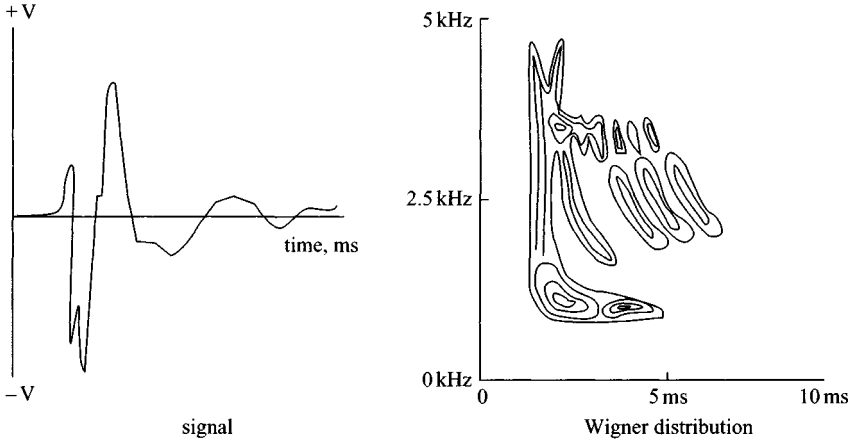

Figure 7.6 Wigner distribution

The spectrogram of the signals $C_1x_1(t) + C_2x_2(t)$ is not given by $SPEC_{x1}(t, f) + SPEC_{x2}(t, f)$ because the operation of squaring implies a quadratic superposition that is

$$SPEC_x(t, f) = |C_1|^2 SPEC_{x1} + |C_2|^2 SPEC_{x2} + C_1C_2SPEC_{x1x2} + C_2C_1SPEC_{x2x1} \tag{7.33}$$

The latter terms are known as interference terms and increase quadratically with the number of pairs of terms.

A range of WTs is available for analytical purposes, and further details can be found in Hlawatsch and Boudreaux-Bartels [9]. Wavelet techniques applied to stratigraphic analysis are reported by Rehmeyer and Aravena [10] and Carevic [11].

The key feature of the various time–frequency representations such as the STFT, spectrogram, WT, scalogram, Gabor transform and Wigner distribution is that they allow successful analysis of nonstationary signals either in the form of wavelets or chirp (linear FM) signals and enable much clearer target identification than conventional spectral analysis techniques. An example of a Wigner distribution (Rioul and Vetterli [12]) is given in Figure 7.6.

There is the distinct possibility of multiple echoes or reverberations in surface-penetrating radar. These can occur as a result of reflections between the antenna and the ground surface or within cables connecting the antennas to either the receiver or transmitter. The effect of these echoes can be considerably increased as a result of the application of time varying gain. This can easily be appreciated by considering the case of an antenna spaced at 0.5 m from the ground surface. Multiple reflections will occur every 1 m (twice the separation) and will decrease at a rate equal to the product of the ground surface reflection coefficient and the antenna reflection coefficient.

This product is likely to be −15 dB, and hence a series of echoes will occur every 3.3 ns, decreasing by 15 dB each time.

This problem may be partially overcome by suitable signal processing algorithms, which can be applied to the sampled time series output from either time domain or frequency domain radars. The general expectation is that all the individual reflections will be minimum delay. This expectation is generally reliable because most reflection coefficients are less than unity; hence the more the impulse is reflected and re-reflected the more it is attenuated and delayed. As a result, the energy is concentrated at the beginning of the train of wavelets.

The simplest method of removing multiple reflections is by means of a filter of the form

$$F(z) = \frac{1}{1 + cz^n} \tag{7.34}$$

In essence, this filter subtracts a delayed (by n) and attenuated (by c) value of the primary wavelet from the multiple wavelet train at a time corresponding to the arrival of the first reflection.

An alternative method relies on the use of filtering techniques applied to signals that have been combined by multiplication and by convolution. Such methods are termed homomorphic deconvolution filtering and rely on the fact that multiple reflections cause periodicity in the spectra of sampled data as shown in Figure 7.7 (Randall and Lee [13]).

The frequency spacing can be determined by taking the logarithm of the spectrum and then carrying out a spectral analysis of the new frequency series. This domain is known as the cepstrum and is given by

$$C_c(t) = F'[c \log\{F(F(t))\}] \tag{7.35}$$

The essence of operation in the cepstrum is that convolutions in the time domain are transposed to additions in the cepstrum. As phase information is retained it is possible to eliminate multiple echoes, i.e. wavelets, in the time domain by subtracting these in the cepstrum and then inverse transforming to recover the original time series. The most significant difficulty of carrying out a complex logarithm is that the phase of the complex log must be a continuous function, hence discontinuities at intervals of 2 must be removed. An example of a cepstrum filtering operation is shown in Figure 7.8, and it can be seen to be highly effective at multiple echo removal.

An alternative method of resolving overlapping echoes is based on the use of the multiple signal characterisation or MUSIC algorithm. The latter is a high resolution spectral estimation method and is used to estimate the received signals' covariance and then perform a spectral decomposition. Although computationally intensive, evaluation of the technique by Schmidt [14] gave promising results.

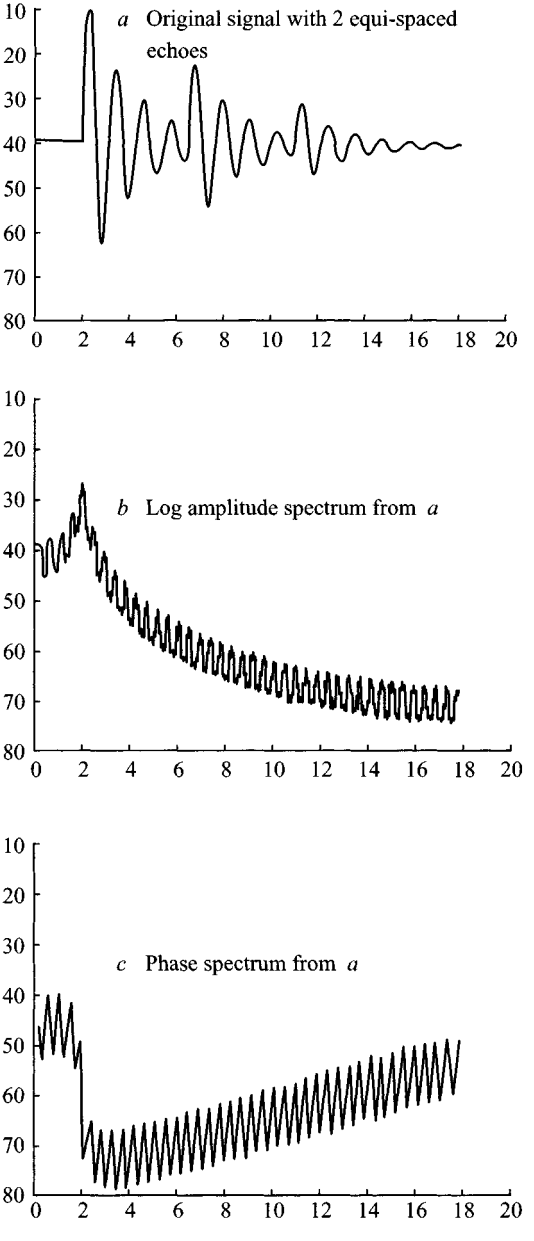

Figure 7.7 Multiple echoes and their amplitude and phase spectrum (Randall and Lee [13])

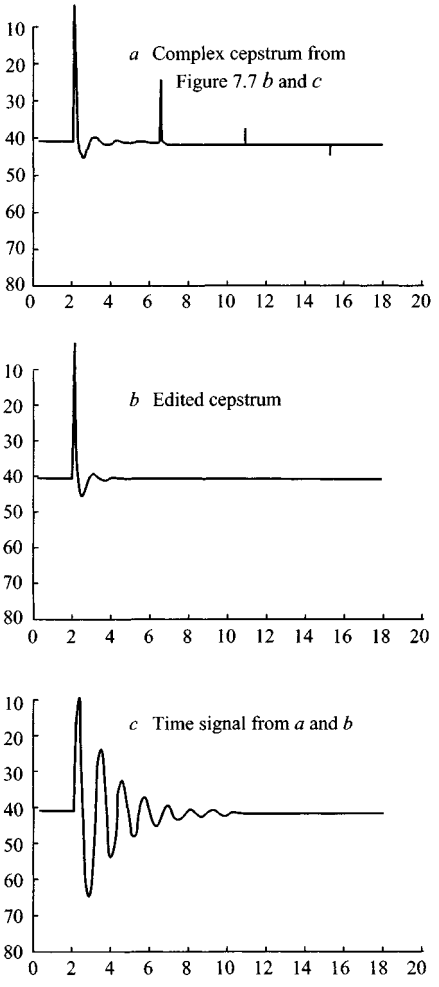

Figure 7.8 Cepstrum of Figure 7.7 and echo removal process

7.2.7 Target resonances

The application of analytical methods of target discrimination started with the application of Prony's method (1795)* to target recognition. The basis of the technique is that every object will possess a unique resonant characteristic. Hence every target can be identified in terms of its resonant characteristic.

Van Blaricum and Mittra [15] modelled a waveform by a series of exponentials in which the amplitude and delay constant are variable, i.e.

$$P(t) = \sum_i a_i e^{\alpha_1 t} \tag{7.36}$$

* PRONY, G. R. B.: 'Essai experimental et analytique', *J. L'Ecole Polytechnique Paris*, **1**, (2), p. 96.

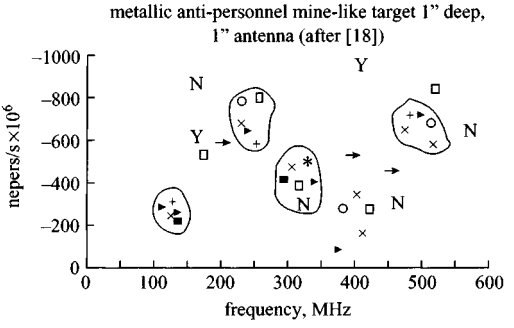

Figure 7.9 S-plane analysis of data

A discretised version of the above gives

$$\alpha_n = \sum_{n=1}^{N/2} A_n \exp j\phi_n \exp(\alpha_n + j\omega_n) n\Delta t \tag{7.37}$$

where A_n = amplitude, ϕ_n = phase, α = damping factor and ω = frequency.

In its basic form Prony's method is inherently an ill conditioned algorithm and is highly sensitive to noise and estimates of the number of poles at present in the data.

It can, therefore, be understood that for targets buried in a lossy medium the high frequency signal information is low and hence the signal to noise ratio is such as to make Prony processing very vulnerable. Indeed, Dudley [16] points out that 'since all real data are truncated only approximations to the resonances are ever available even in the limit of vanishing noise'.

Recent developments have improved the robustness of the method as a means of detecting shallowly buried anti-tank or anti-personnel mines.

Work by Chan *et al.* [17] demonstrated the feasibility of the technique as a means of mine detection.

In general the received signal is represented as

$$C_r(t) = \sum_{n=1}^{N} a_i e^{s_1 t} \tag{7.38}$$

where s_1 are the complex resonant frequencies in the complex frequency plane (S-plane), i.e. $s = \alpha + j\omega$.

A typical S-plane representation from various buried targets is shown in Figure 7.9.

There are two realisations of the Prony method – the classical or the eigenvalue method – and details of these are discussed in Chan *et al.* [19]. The eigenvalue method was found to give better results, and with reference to (7.37) it is found that analysis of the wavelet resulting from the resonance is highly sensitive to the choice of the parameters. In addition, a wide dynamic range is needed to cater for both the early and late time portions of the wavelet.

Many of the signal processing techniques applied to the data generated by surface-penetrating radar come from other disciplines such as geophysics and acoustics. There

have been significant developments in ultra-wideband free space radar technology, and one goal of much research currently being carried out is the unique identification of a target from its ultra-wideband impulse response.

An appreciation of these techniques is valuable when considering their application to surface-penetrating radar data, and the following Section reviews the main features of the approach.

Free space scattering from resonant bodies has received considerable attention, and the singularity expansion method (SEM) is established as a means of target recognition. Much work in this area has been carried out by Webb [20], Baum *et al.* [21], Chen *et al.* [22], Kennaugh [23], Kennaugh and Moffatt [24], Fok and Moffatt [25], and Rothwell *et al.* [26]. The SEM suggests that the late time scattered field of a target can be represented as the sum of excitation independent natural resonance modes, which depend on the detailed size and shape of the target.

An extension to the concept of nonspecific impulse illumination is that of discriminant functions designed to annihilate certain selected natural frequency constituents of the target response. The K-pulse originated by Kennaugh [24] is defined as that wavelet of minimum length which, when convolved with the target response, minimises or 'kills' all the natural modes in the resulting target response. Further developments in this area have resulted in the E-pulse (E = extinction) and the S-pulse (S = single mode).

The E-pulse is synthesised to minimise, when convolved with a band-limited late time target pulse response, all natural modes existing in that response. As the scattered free-space far field response of a conducting target can be expressed as

$$e(t) = \sum_{n=1}^{N} a_i e^{\sigma_1 t} \cos(\omega_n t + \phi_n) t > \tau_L \tag{7.39}$$

where τ_L is the start point of the late time response, $e(t)$ is convolved with an extinction pulse wavelet $E(t)$ such that

$$c(t) = e(t) \otimes E(t) = 0 \tag{7.40}$$

The reader is referred to Baum [22] for details of the procedure for determining $e(t)$. Further work on classification of GPR signatures by complex natural resonances is reported by Chen *et al.* [27], Guangyou and Zhongzhi [28], and Nag and Peters [29].

7.2.8 Spectral-analysis methods

For those surface-penetrating radar systems using FMCW, stepped frequency or synthesised sources, the receiver produces a frequency domain signal which is then transformed to the time domain. Usually this is carried out using a fast Fourier transform (FFT). There are, however, several limitations of the FFT algorithm. While these are well documented, it is useful to review the capabilities of the FFT and alternative spectral estimation methods. The reader is referred to the classic paper by Kay and

Marple [30], who detailed the following methods:

(i) conventional methods, Blackman Tukey, periodogram
(ii) modelling and parameter identification approaches
(iii) rational transfer function modelling methods
(iv) autoregressive (AR) power spectral density estimation
(v) moving average (MA) power spectral density estimation
(vi) autoregressive moving average (ARMA) power spectral density estimation
(vii) Pisarenko harmonic decomposition
(viii) Prony energy spectral density estimation
(ix) Prony spectral line estimation
(x) maximum likelihood method (MLM)
(xi) maximum entropy methods (MEM).

More recent developments include

(xii) multiple signal classification (MUSIC).

The objective of this Section is not to describe all these methods in detail as there is adequate cover in the literature. However, highlighting of the underlying principles and capabilities of various spectral estimation methods should provide the reader with an introduction to the options which can be considered.

The FFT approach, while computationally efficient (via the Cooley–Tukey or Blackman Tukey algorithm), suffers from several limitations. Firstly it has a frequency resolution in Hz which is approximately equal to the reciprocal of the sample window duration in seconds. Secondly, the action of sampling the data for a defined time or 'window' causes leakage of energy from the main lobe of a spectral response into the sidelobes. As most data from surface-penetrating radar occurs in short data sequences, the windowing effect can be particularly difficult to counter while at the same time maintaining resolution. It should be noted that when the signal to noise ratio is low the results of the conventional FFT approach are comparable with the more modern spectral estimation techniques.

In general the modelling approach to spectrum analysis is carried out in three stages: firstly the selection of an appropriate time series model; secondly an estimation of the parameters of the assumed model using either the sampled data or the auto-correlation lags; and finally substitution of the estimated model parameters into the theoretical power spectral density function. The selection of the time series model is governed by estimation and identification methods of linear systems theory. The modelling approach enables assumptions to be made concerning the time series outside the measurement window and hence eliminates the problems associated with windowing functions.

Three approaches to non-Fourier spectral estimation methods are: autoregressive (AR), moving average (MA) and autoregressive moving average (ARMA).

The autoregressive or feedback model is described by

$$y_n = a_0 x_n - a_1 x_{n-1} - a_2 x_{n-2} \ldots a_n x_{n-N} \tag{7.41}$$

where n is the sample variable, x is the input and y the output variable. In terms of the z-transform,

$$y_n = \frac{1}{a_0 - a_1 z - a_2 z^2 \ldots a_n z^n} x_n \tag{7.42}$$

As in general the denominator can be considered to be a polynomial denoted by $A_n(z)$, then

$$Y(z) = \frac{1}{A_n(z)} X(z) \tag{7.43}$$

In the case of the AR model it is necessary to determine algorithms to solve the power spectral representation of (7.42). As $z = e^{j\omega}$ it can be appreciated that as

$$F(\omega) = |Y(\omega)| \tag{7.44}$$

then

$$F(\omega) = \frac{1}{|A(\omega)|^2} |Y(\omega)|^2 \tag{7.45}$$

There are two methods of solving the AR model, either by the Yule–Walker or Burg method. The Yule–Walker method tends to emphasise the spectral aspects at the expense of peak definition. The method originated by Burg is based on a technique known as maximum entropy. The entropy or unpredictability of a time series is proportional to the integral of the log of its power spectrum. An estimate of the power spectrum produced by the MEM method corresponds to the least predictable time series consistent with the autocorrelation function lags. The AR method tends to define the peak spectral response at the expense of spectrum shape.

The moving average (MA) or feed forward model is described by

$$y_n = b_0 x_n + b_1 x_{n-1} + b_2 x_{n-2} \cdots b_n x_{n-N} \tag{7.46}$$

where y_n represents the output of the linear convolutional filter for the input. The output of the MA model is a linear combination of present and past values of the system input sequence. When the input is white noise the output is called a moving average process of order n, i.e. MA (n).

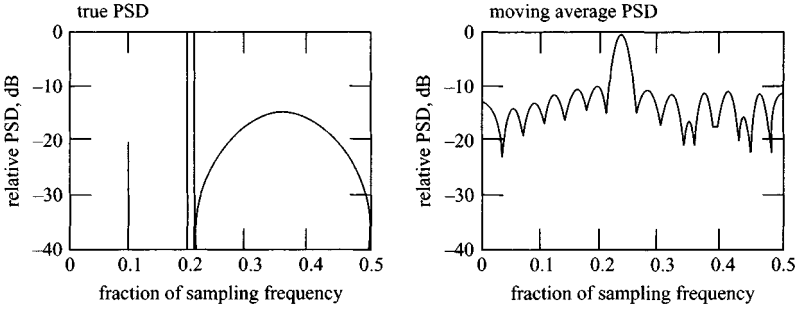

Figure 7.10 *Illustration of various spectra for the same 64-point sample sequence (Kay and Marple [30])*
1 = true power spectral density (PSD); 7 = moving average PSD

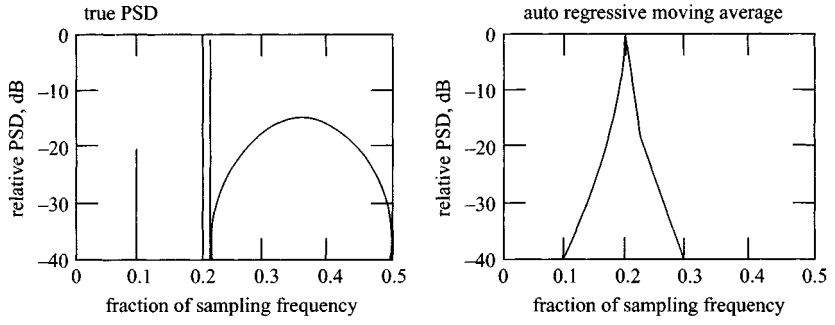

Figure 7.11 *Illustration of various spectra for the same 64-point sample sequence (Kay and Marple [30])*

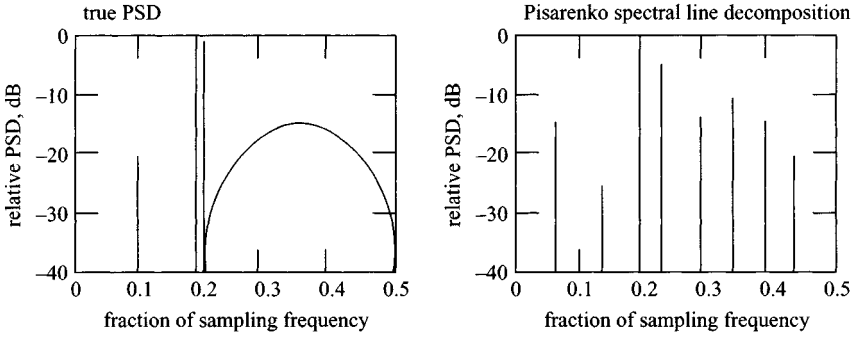

Figure 7.12 *Illustration of various spectra for the same 64-point sample sequence (Kay and Marple [30])*

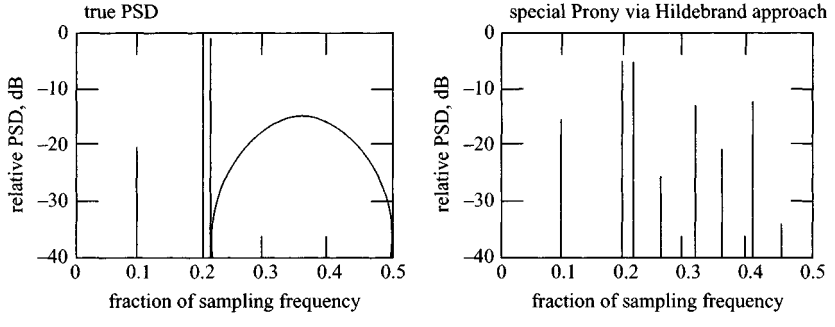

Figure 7.13 *Illustration of various spectra for the same 64-point sample sequence (Kay and Marple [30])*

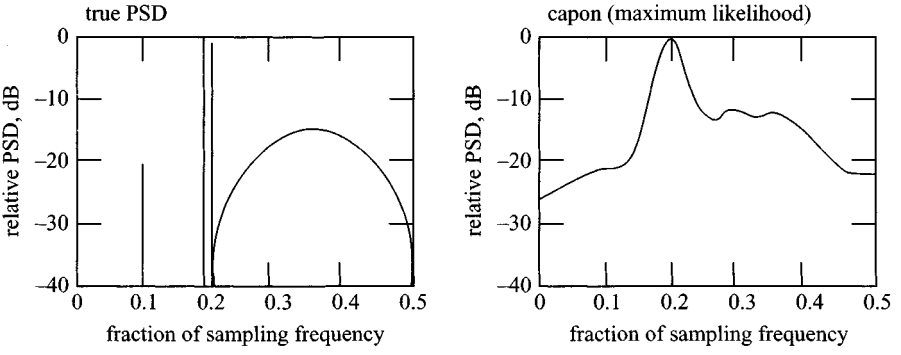

Figure 7.14 Illustration of various spectra for the same 64-point sample sequence (Kay and Marple [30])

In terms of the z-transform,

$$y_n = (b_0 + b_1 z + b_2 z^2 \cdots b_n z^n) x_n \tag{7.47}$$

The polynomial on the right-hand side of (7.46) can be expressed as $B_n(z)$; hence

$$Y(z) = B_n(z) x(z) \tag{7.48}$$

In a similar manner to the AR model, the spectral representation is given by

$$F(\omega) = |B_n(\omega)|^2 |X(\omega)|^2 \tag{7.49}$$

The MA approach yields a reasonable approximation to the spectrum but tends to offer similar performance to the Blackman–Tukey PSD.

The ARMA model evidently contains both AR and MA elements, and it can be shown that

$$F(\omega) = \frac{|B_n(\omega)|^2}{|A_n(\omega)|^2} |X(\omega)|^2 \tag{7.50}$$

Kay and Marple [30] compared results of spectral estimation methods for various approaches, and these are shown in Figures 7.10 to 7.14.

An alternative approach is that given by the MUSIC algorithm, which produces a spectral estimation from the autocovariance matrix via eigenvector-value decomposition. An example of the resolution of a pair sinusoidal waveform is shown in Figure 7.15, which compares various results from different methods.

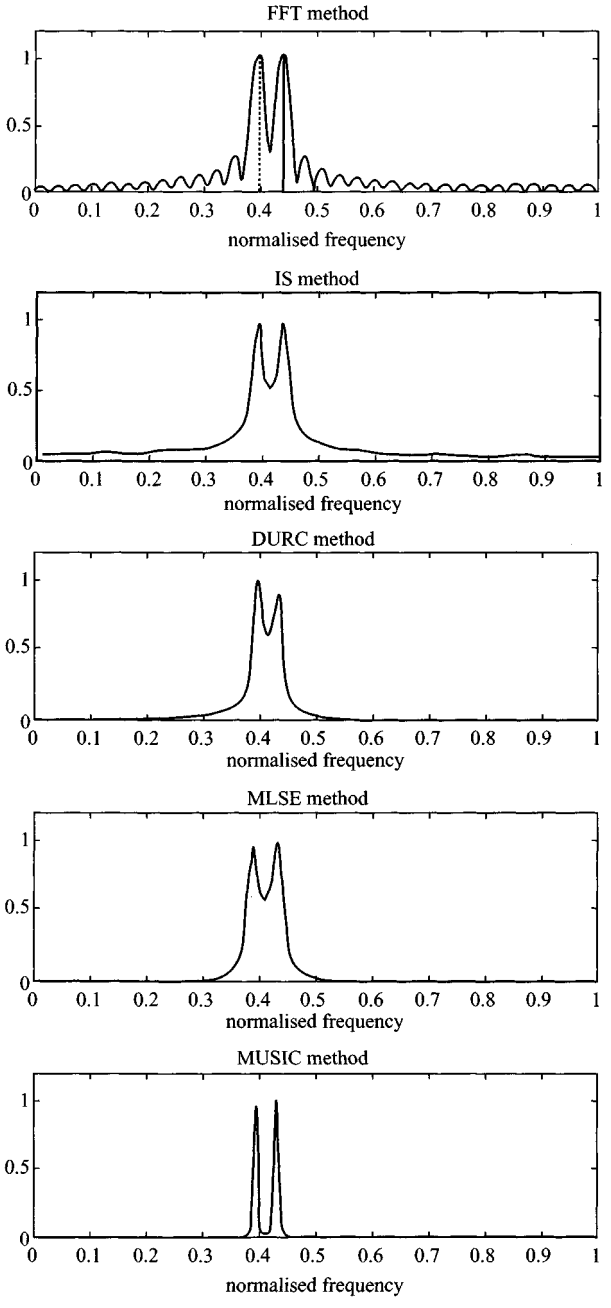

Figure 7.15 *Comparison of MUSIC method of spectral analysis with a range of alternatives*

7.2.9 Examples of processing techniques

A set of examples of various methods of A-scan processing are shown in Figures 7.16 to 7.23. They are shown as greyscale B-scans to illustrate the effect of applying various algorithms on a radar image of three plastic pipes buried in wet sand at depths up to 1.3 m:

Figure 7.16 shows the effect of applying the flat gain profile of 0 dB m^{-1}
Figure 7.17, a correct gain profile of 5 dB m^{-1}
Figure 7.18, an excessive gain profile of 15 dB m^{-1}
Figure 7.19, a lowpass filter to data corrupted by mobile phone interference

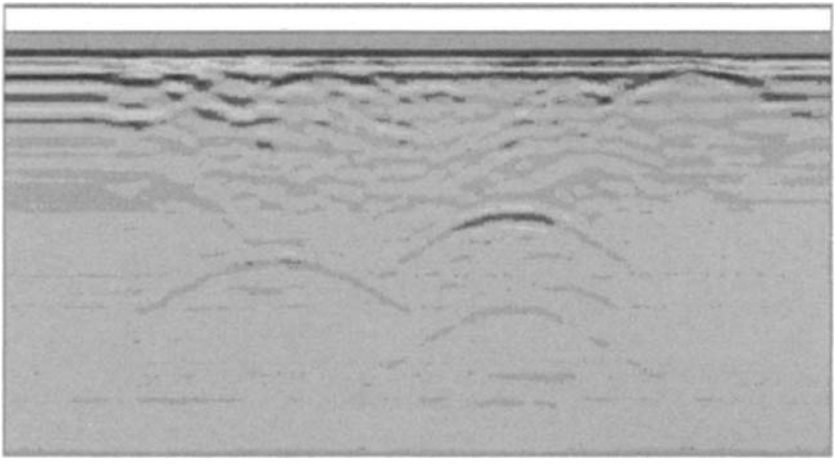

Figure 7.16 Gain profile flat (courtesy ERA Technology)

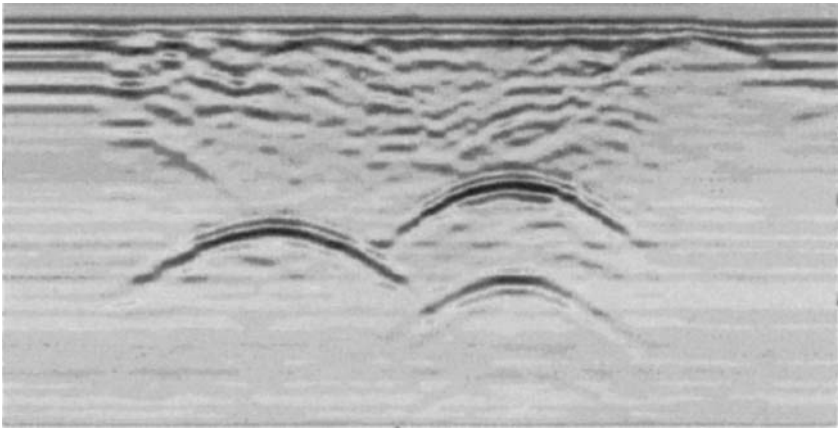

Figure 7.17 Gain profile at 5 dB m^{-1} (correct) (courtesy ERA Technology)

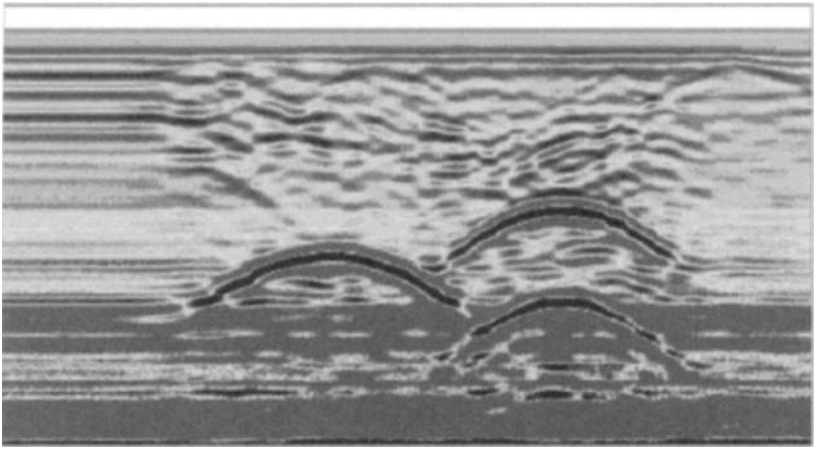

Figure 7.18 Gain profile at 15 dB m^{-1} (excessive) (courtesy ERA Technology)

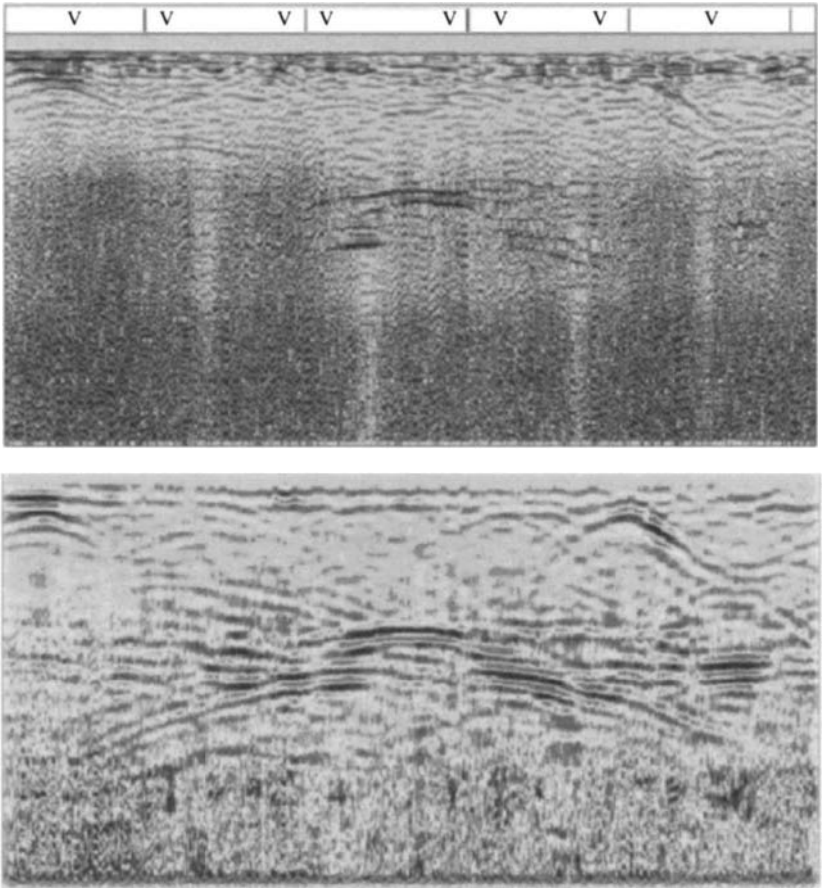

Figure 7.19 Lowpass filtered data (courtesy ERA Technology)

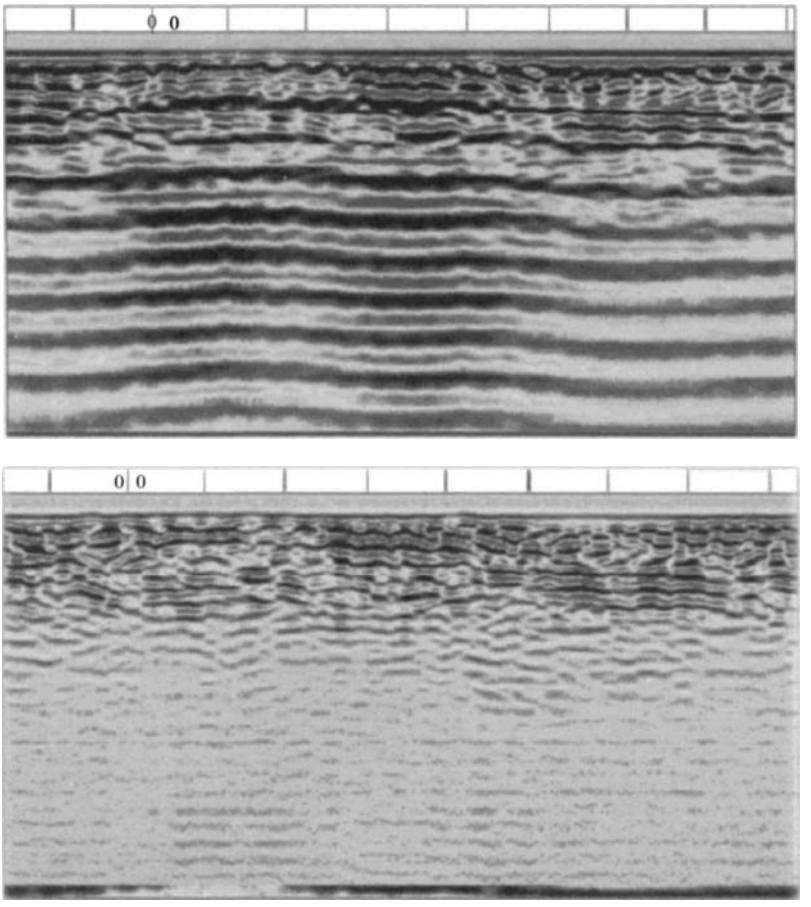

Figure 7.20 Highpass filtered data (courtesy ERA Technology)

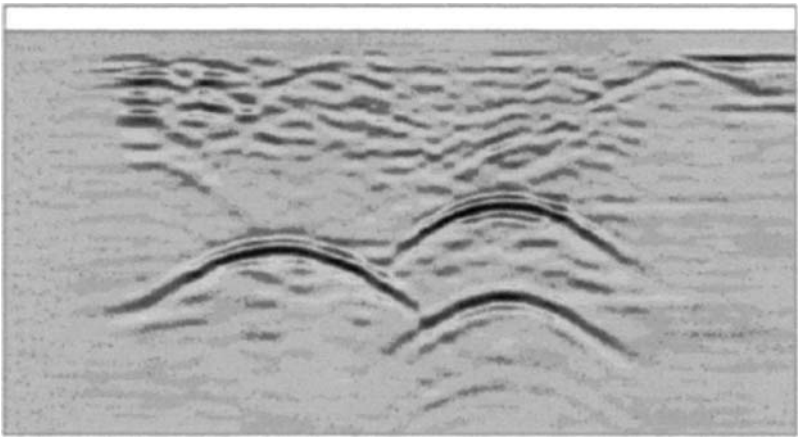

Figure 7.21 Average removed data (courtesy ERA Technology)

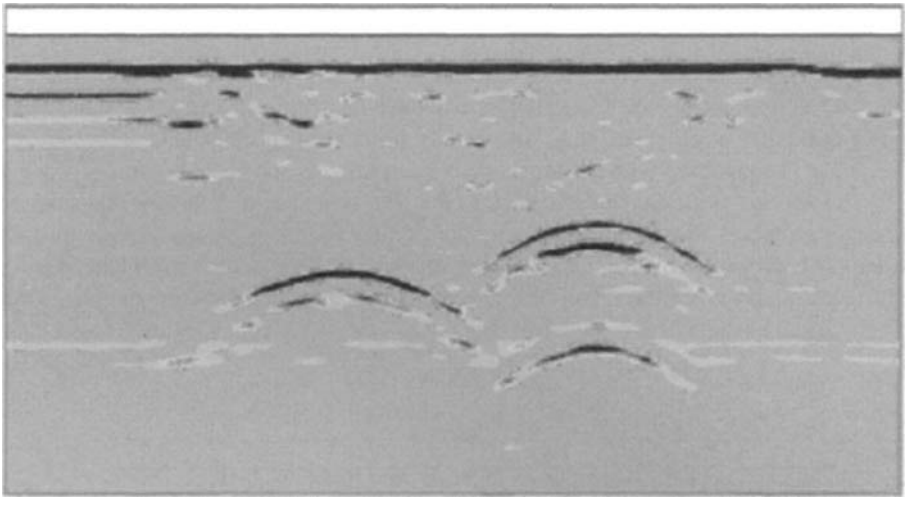

Figure 7.22 Absolute threshold positive going data (courtesy ERA Technology)

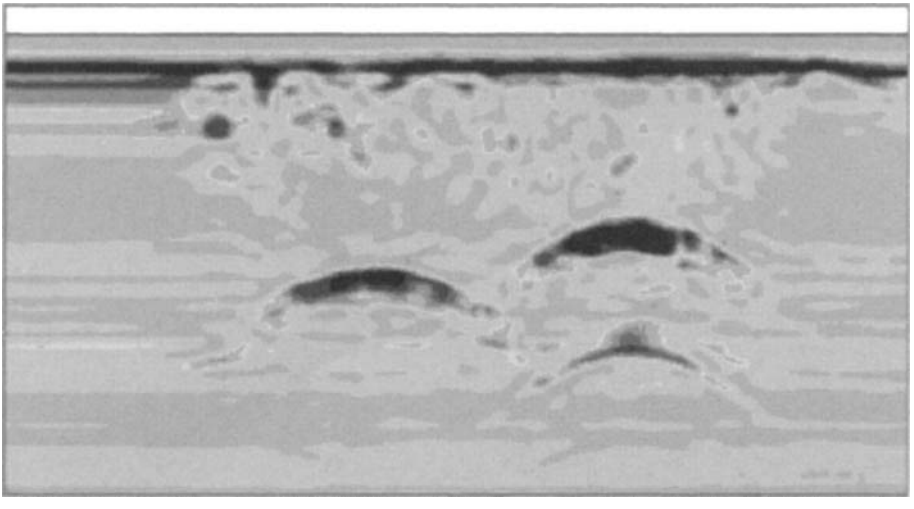

Figure 7.23 Peak envelope applied to data (courtesy ERA Technology)

Figure 7.20, a highpass filter to data corrupted by close in target resonances
Figure 7.21, an average removal filter to the data from Figure 7.17, which removes consistent signals
Figure 7.22, an absolute threshold positive going data
Figure 7.23, a peak envelope to the data from Figure 7.17.

7.3 B-scan processing

If we consider an ensemble set of time samples comprising a B-scan, there are a number of approaches to signal processing which can be considered. The data, even after optimal A-scan processing, are usually unfocused in that the spatial antenna response is convolved with the target spatial response as shown in Figure 7.24.

In the case of planar features such as the interfaces between layers in a road or the water table in a geophysical survey, it may be considered uneconomic to focus the data (see Figure 7.25). However, for small or complex objects it may be valuable to reduce the effect of the spatial smearing caused by the antenna. This

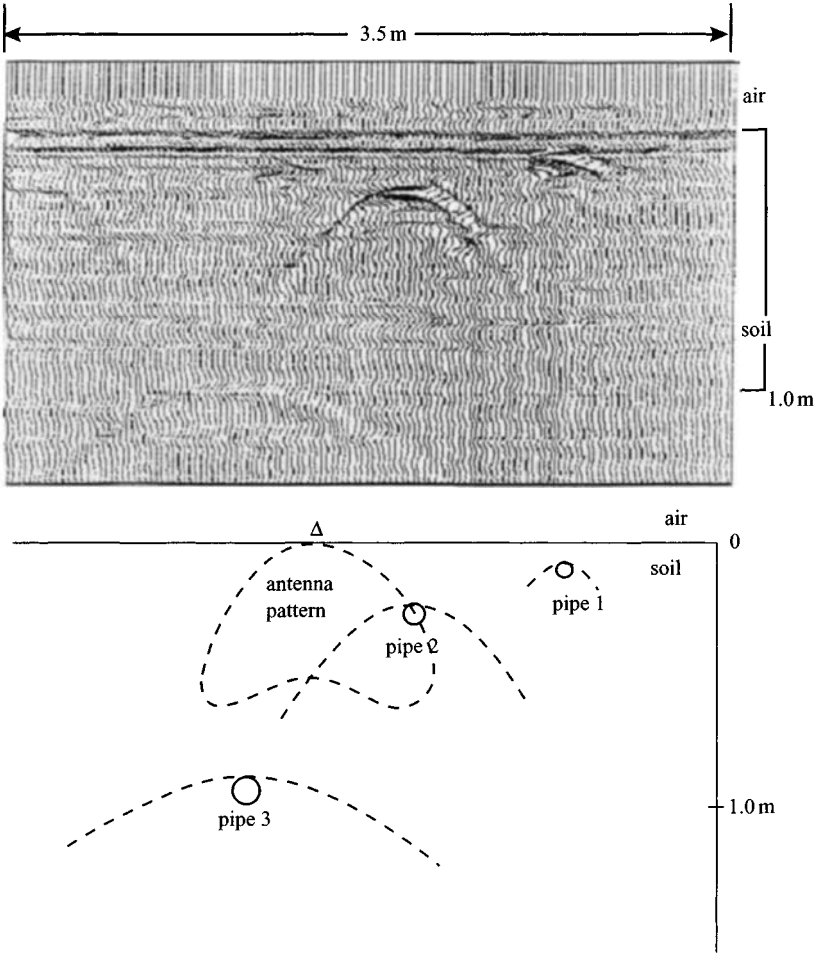

Figure 7.24 Convolution of antenna pattern with targets (ERA Technology)

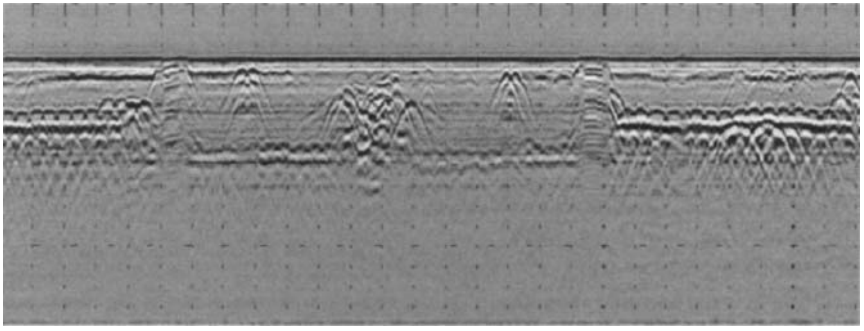

Figure 7.25 *B-scan of reinforced concrete floor (courtesy ERA Technology)* Vertical scale 26 ns, horizontal scale 3 m

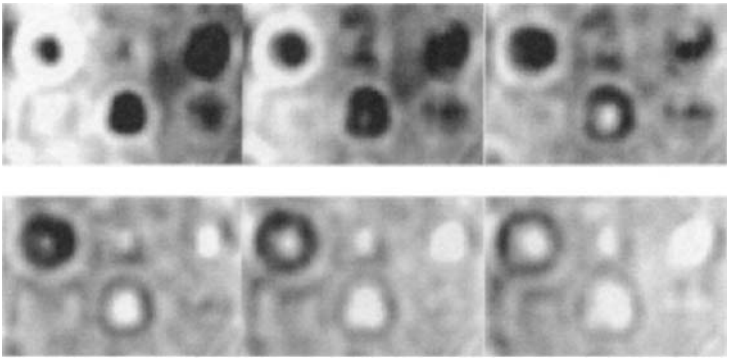

Figure 7.26 *Sequence of unfocused C-scans of a set of six buried AT mine targets at increments of 10 mm (courtesy ERA Technology)*

Chapter considers several approaches to B-scan processing, the chief of which is based on migration of the data.

7.4 C-scan processing

Although a C-scan is essentially an x, y plane at a selected value of Z or range of values of Z, many of the processes described in the previous Sections can be applied. It is, however, important to focus the data, otherwise spurious features will appear at depths below the target. It is also important to ensure that adequate allowance is made for the sampling range, otherwise the familiar problems associated with windowing a data set will occur. Typical examples of C-scan processing are shown in Figure 7.26, which shows data from buried AT landmines.

Previous Page

7.5 Migration

The migration process essentially constructs the target reflector surface from the record surface. The migration technique has been much developed in acoustic, seismic and geophysical engineering and was originally developed in two-dimensional form by Hagedoorn [31]. More recent developments employ wave equation methods such as Kirchhoff migration, finite difference migration and frequency wave-number migration. An excellent tutorial paper is given by Berkhout [32] as well as by Schneider [33] and by Robinson and Treitel [6]. In essence, the problem of data focusing can be considered from the point of view of a source of radiation, i.e. a point reflector and the measured wavefront as shown in the simulated data of Figure 7.27.

A relatively straightforward geometric approach can be used in the two-dimensional case of a material with known constant velocity. If the measured time to the point reflector is t, then the distance to the point reflector is given by $z = vt/2$. At any position along the x-axis the distance z is also given by

$$z_i = \sqrt{(x_i - x_0)^2 + z_0^2} \tag{7.51}$$

This equation shows that the measured wavefront appears as a hyperbolic image or a curve of maximum convexity. The geometric migration technique simply moves or migrates a segment of an A-scan time sample to the apex of a curve of maximum

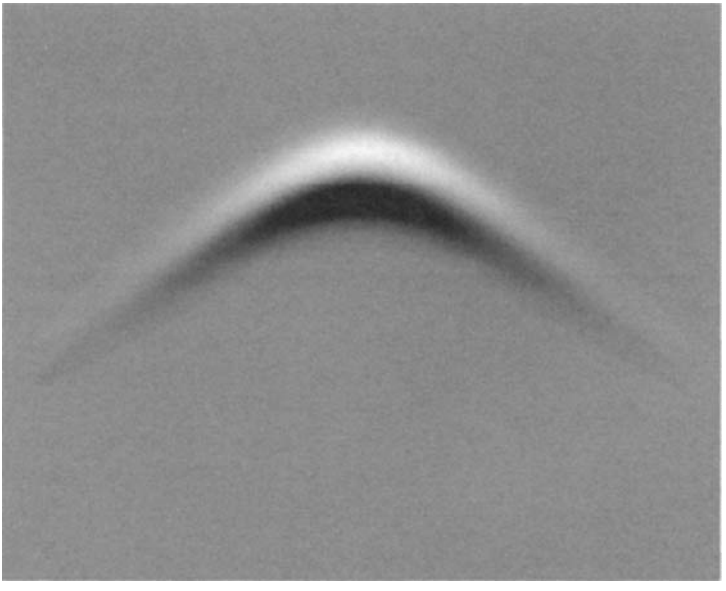

M

Figure 7.27 Migration of a waveform from a point source

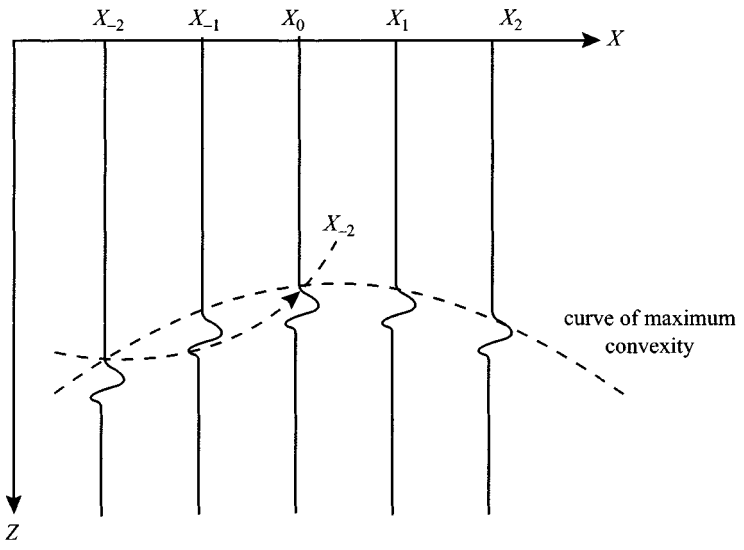

Figure 7.28 Maximum convexity migration

convexity. The hyperbolic curve needs to be well separated from other features and a good signal to noise ratio is needed.

An alternative method is known as the maximum convexity migration and is computationally intensive but straightforward in concept. The method assumes a semi-hyperbolic maximum convexity function and sums the value of each separate A-scan at the point at which it intersects the semi-hyperbolic focus over the ensemble data set. All in-phase energy adds in phase, whereas noncoherent energy is usually out of phase and tends to zero. The method assumes a constant velocity and must, of course, be adjusted as a function of depth. It also requires that each and every possible point is examined. Care must also be taken over the window after which the summation is carried out. The process is shown diagrammatically in Figure 7.28.

The alternative process to maximum convexity migration is wavefront migration. In this process every section of the individual A-scans comprising a B-scan is mapped to a migrated B-scan. The mapping function is, in the constant velocity case, a semicircle of radius equal to the depth of the section. This process is repeated for each section of the individual A-scan and for all A-scans, and the resultant output is the superposition of all the migrated sections. The process is shown in Figure 7.29 and it can be seen that wavelets from neighbouring A-scans add constructively to produce a focused reflection point.

The methods described in the previous paragraphs illustrate the general principle of migration but are relatively unsophisticated methods, which are limited to the constant velocity situation and assume a point source reflector.

Alternative and more comprehensive techniques use wave equation methods. Berkhout [32] showed that wave field extrapolation techniques are based on three

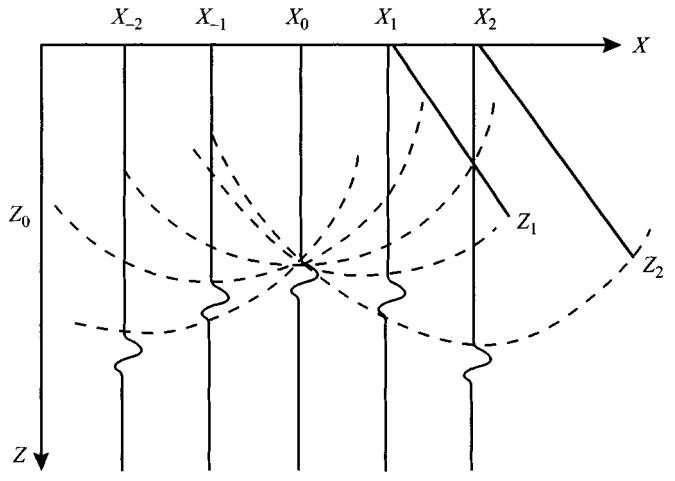

Figure 7.29 Wavefront migration

methods: the Kirchhoff summation approach, the plane wave method (F-K method) and the finite difference method.

Although the methods described by Berkhout are founded in acoustic propagation theory, which is based on a scalar wave equation, they are still relevant to surface-penetrating radar data even though the latter are derived from electromagnetic soundings. The general process of imaging of such data consists of two operations. The first consists of a wave field extrapolation whereby, using a scalar wave equation, the recorded data are transformed into a new data series which represents simulated recordings at new positions of the measurement plane. The second operation of imaging generates the data around the zero time travel position of the simulated recording related to planes within the B-scan or C-scan.

The wave field at the ground or material surface is given by $(x, 0, t)$, and the A-scan observed at the surface is given by (x, z, t). Note that time is considered as positive and the value $(x, 0, t)$ represents all time information along the line x.

The wave field at the reflector is given by $(x, z, 0)$, as shown in Figure 7.30.

The procedure for evaluating the reflector surface is given by Robinson and Treitel [6] using the Fourier transform approach as frequency-wave-number domain migration. The method is carried out in three stages, the first being given by

$$F(k_x, \omega) = \int_{-\infty}^{\infty} \int_{-\infty}^{\infty} v(x, 0, t) \exp(-t(\omega t + k_x x)) \, dx dt \tag{7.52}$$

where k_x = horizontal wavenumber, k_z = vertical wavenumber, ω = angular frequency and c = propagation velocity of the medium.

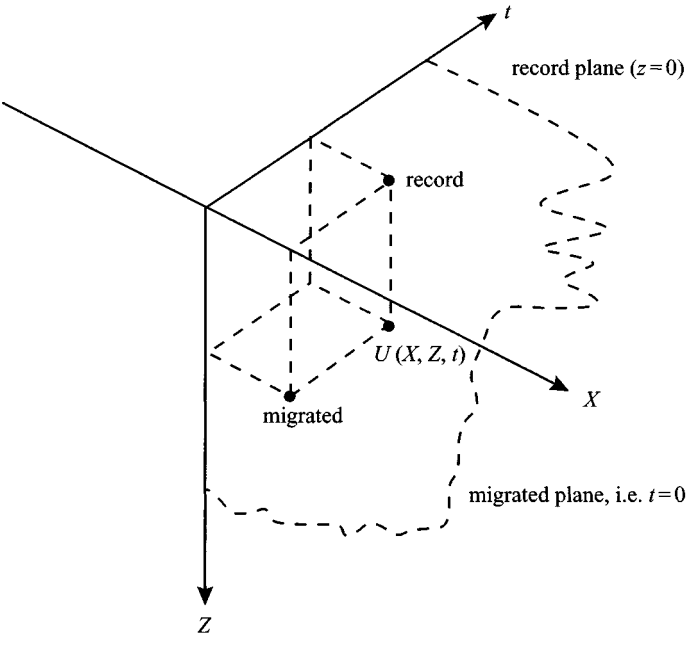

Figure 7.30 Fields at reflector

From this a two-dimensional Fourier transform is determined by

$$A(k_x, k_z) = F\left[k_x c k_z \left\{1 + (k_x/k_z)^2\right\}\right] \frac{c}{\sqrt{\left(1 + (k_x/k_z)^2\right)}} \tag{7.53}$$

The reflector can then be derived as the inverse transform of $A(k_x, k_z)$, where

$$v(x, z, 0) = \frac{1}{4\pi^2} \int_{-\infty}^{\infty} \int_{-\infty}^{\infty} A(k_x, k_z) \exp(j(k_x x + k_y z)) \mathrm{d}k_x \mathrm{d}k_z \tag{7.54}$$

The frequency wave number approach described above was first developed by Stolt and then used by Hogan [34] to migrate ground penetration radar data. However, Fisher and McMechan [35] comment that the method is difficult to implement efficiently when the propagation velocity varies. Fisher compared the Kirchhoff diffraction method with the reverse-time migration approach, which has the advantage of taking into account arbitrary velocity variations.

This is particularly important as, when migration velocities are chosen that are lower than the correct velocity, diffraction 'tails' will extend downwards from the reflector location. When the migration velocity is too high the tails will extend upwards from the reflector location.

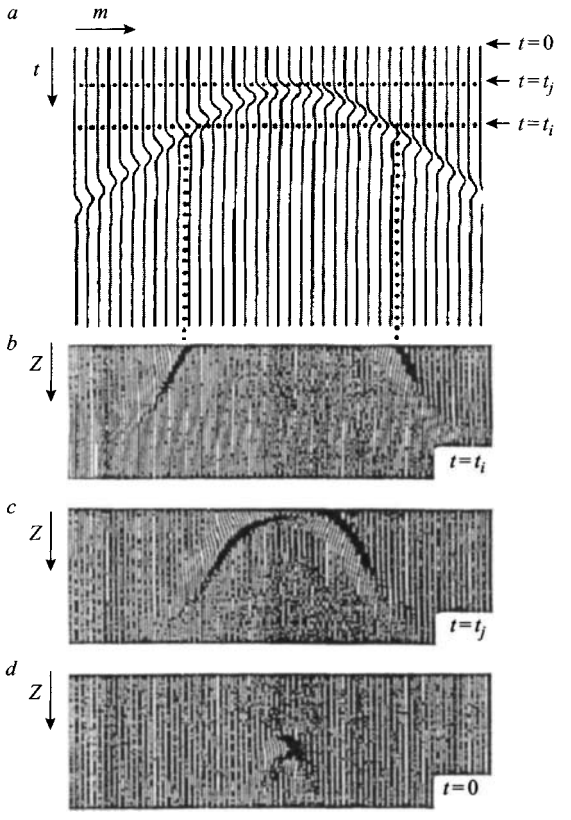

Figure 7.31 Reverse time migration

The scalar wave equation is given by Mitchell [36]:

$$\frac{\partial^2 U}{\partial x^2} + \frac{\partial^2 U}{\partial z^2} = \frac{1}{v(x,z)} \frac{\partial^2 U}{\partial t^2} \tag{7.55}$$

where U is the scalar wave field and $v(x, z)$ is the local propagation velocity.

The wave equation can be solved via an explicit second order central finite difference method.

These methods have been developed by Claerbout [37] and McMechan [38], and an example of reverse time migration is shown in Figure 7.31.

Computer programs to carry out migration are reported in the literature, and Siggins [39] includes an example of a convolution method written in 'C'. Further examples of migration techniques applied to GPR data are given by Anxue *et al.* [40], Plumb and Leuschen [41], Leuschen and Plumb [42], and Xu *et al.* [43].

7.5.1 *Migration technique based on deconvolution*

Dr Bart Scheers, Marc Acheroy (ELTE Department, Royal Military Academy) and André Vander Vorst (Hyperfréquences UCL, Belgium)

7.5.1.1 Introduction: Reflections on a point scatterer located below the surface appear, due to the beamwidth of the transmitting and the receiving antenna, as hyperbolic structures in an image. This can be easily verified, using the geometry shown in Figure 7.32*a*. Suppose a homogeneous half-space with a propagation velocity of v and the transmitting and receiving antennas close to each other, so that they can be considered as one antenna (monostatic case). The co-ordinate system is represented on Figure 7.32*a*. A point scatterer at a position $(0, z_0)$ in the half-space will be located by the antenna pair, situated in $(x, 0)$ at a distance $\sqrt{x^2 + z_0^2}$. So, in the recorded data $b(x, t)$, represented in Figure 7.32*b*, the reflection on the point scatterer appears in each position after a time

$$t = 2\sqrt{x^2 + z_0^2}/v \tag{7.56}$$

Equation (7.54) represents a hyperbola with a vertical axis and an apex in $(0, 2z_0/v)$. The shape of the hyperbola is a function of the antenna configuration (monostatic, bi-static), the depth of the point scatterer z_0 and the propagation velocity profile in the ground. The hyperbolic defocusing of an object can be corrected for in the data processing, which is called migration or SAR processing.

The aim of migration techniques is to focus target reflections in the recorded data back into their true position and physical shape. In this respect, migration can be seen as a form of spatial deconvolution that increases spatial resolution. The first migration methods were geometric approaches. After the introduction of the computer, more complex techniques, based on the scalar wave equation, were

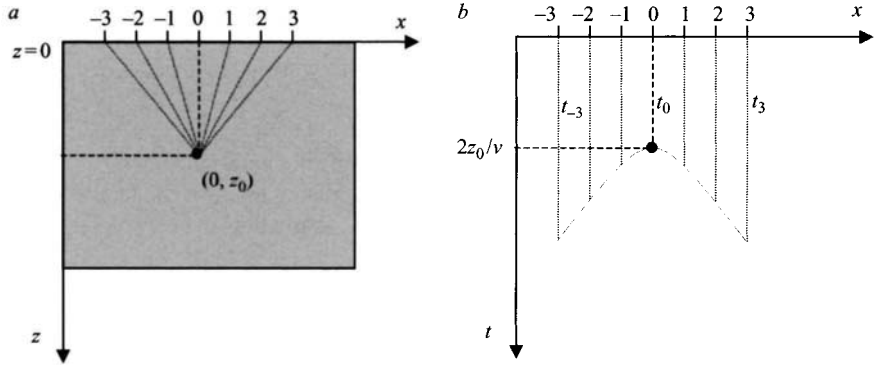

Figure 7.32 (a) Point scatterer at position $(0, z_0)$*; (b) recorded data* $b(x, t)$

introduced. These methods involve back-propagation or inverse extrapolation to remove the effects of wave field propagation. A good overview of migration techniques is given in references [32, 44]. Most of the migration methods found their origin in the field of seismic, and were later on also applied on radar images. Almost none of these methods, however, include system aspects of the radar like the waveform of the excitation source, the impulse response of the antennas, the antenna pattern, etc. Furthermore, most of the migration methods consider the ground as being loss-less and without dispersion. It can be expected that a migration technique that takes into account the characteristics of the radar system and possibly the characteristics of the ground would perform better. In this Chapter a novel migration method is presented that takes into account the system and ground characteristics.

7.5.1.2 Time-domain model of the GPR: A key element in the migration method is the point-spread function of the GPR, i.e. a synthetic C-scan of a small isotropic point scatterer buried in the ground at a certain depth. This point spread function can be obtained by forward modelling. In this Chapter a time-domain model of the GPR system is used for the forward modelling. The time-domain model is obtained by considering the total system 'GPR-ground-target' as a cascade of linear responses, resulting in a *time-domain GPR range equation*. The time-domain GPR range equation allows us to calculate the received voltage $V_{rec}(t)$ at the output of the receiving antenna in terms of excitation voltage $V_S(t)$, radar characteristics and target. Figure 7.33 shows a schematic representation of the different parts in this cascade, e.g. the pulse generator, the antennas modelled by their normalised impulse response [45, 46], the $1/R$ spreading losses, the transmission coefficients on the air–ground interface, the propagation through the ground and the scattering on the target in the ground.

Mathematically the time domain GPR range equation is expressed as [47]

$$V_{rec}(t) = \frac{T_{a-g}T_{g-a}}{8\pi^2 R_t R_r c} g_d(t) \otimes h_{N,Tx}(\vec{a}_i, t) \otimes \Lambda_{1,1}(\vec{a}_i, \vec{a}_s, t) \otimes h_{N,Rx}(-\vec{a}_s, t) \otimes \frac{\mathrm{d}V_s(t)}{\mathrm{d}t} \tag{7.57}$$

where:

$V_S(t)$ is the excitation voltage applied at the transmitting antenna
$\vec{a}_i$ is the direction of radiation of the transmitting antenna towards the target
$\vec{a}_s$ is the direction of the scattered field from the target towards the receiving antenna
$h_{N,Tx}(\vec{a}_i, t)$ is the normalised IR of the transmitting antenna in the direction $\vec{a}_i$
$h_{N,Rx}(-\vec{a}_s, t)$ is the normalised IR of the transmitting antenna in the direction $-\vec{a}_s$
$g_d(t)$ is the impulse response representing the two-way path length loss and the dispersion in the ground
$\Lambda_{1,1}(\vec{a}_i, \vec{a}_s, t)$ is the IR of the target (the time equivalent of the square root of the target radar cross-section)

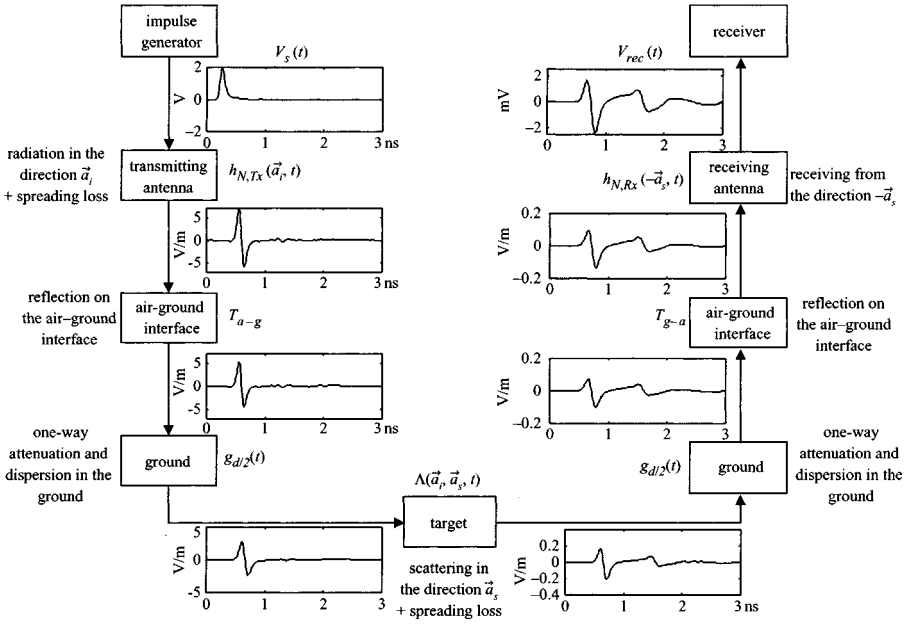

Figure 7.33 Schematic representation of the different parts in the time-domain GPR range equation

R_t is the total path length from the transmitting antenna to the target
R_r is the total path length from the receiving antenna to the target
T_{a-g} is the transmission coefficient at the air–ground interface (air to ground)
T_{g-a} is the transmission coefficient at the air–ground interface (ground to air).

In the next two sub-Sections the impulse responses of the antennas and the ground will be explained in more detail.

7.5.1.3 Normalised impulse response of the antennas: A common way of describing antennas in the time domain is by means of their impulse response. Different types of impulse response (IR) can be defined. We opted for the normalised impulse response (normalised IR), i.e. an impulse response integrating all frequency dependent antenna characteristics [45, 46]. In this way, the time domain antenna equations, expressed in terms of the normalised IR, become very simple and accurate to use. No assumptions about frequency dependent terms have to be made. For two identical antennas, $h_{N,Tx} = h_{N,Rx}$. The normalised IR on boresight is easy to measure, using two identical antennas and a vector network analyser [45]. Figure 7.34 shows the normalised IR on boresight of a TEM horn antenna, designed for a laboratory UWB GPR [47].

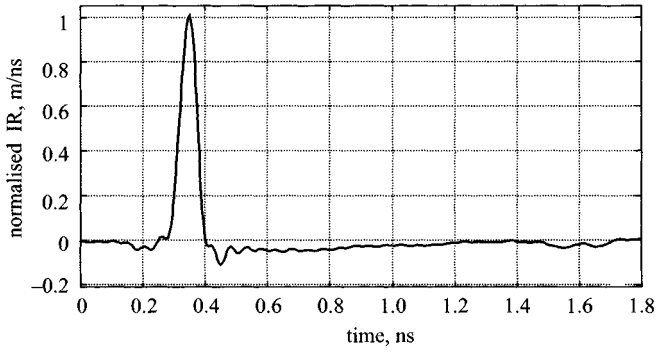

Figure 7.34 Normalised IR of TEM horn antenna

7.5.1.4 Impulse response of the ground: The best way to introduce the propagation losses in the ground is to represent the ground as a lowpass filter. The transfer function of this filter, representing a propagation of d metres in the ground, is given by $H_d(\omega) = e^{-(\alpha+j\beta)d}$, where α is the attenuation constant [Np/m] of the medium and β the phase constant [rad/m]. Both constants are a function of frequency, the real part of the permittivity ε' and the loss tangent $\tan\delta$. For a given soil, i.e. texture, density and moisture content, and for a given two-way path length d in the ground, the impulse response $g_d(t)$ of the soil, representing the propagation losses, is then calculated as [47]

$$g_d(t) = \frac{d\sqrt{\mu\varepsilon'}(\tan\delta)/2}{\pi\left[\left(t - d\sqrt{\mu\varepsilon'}\right)^2 + \left(d\sqrt{\mu\varepsilon'}\tan\delta/2\right)^2\right]} \tag{7.58}$$

7.5.1.5 Development of the migration method: The migration method is based on the deconvolution of the recorded data with the point-spread function of the GPR system, calculated using the time-domain model as presented in the previous Section. This deconvolution only makes sense if the acquisition process by the GPR is a convolution between the structures present in the sub-surface and the point-spread function of the system. The latter is true under certain assumptions. Suppose a co-ordinate system as represented in Figure 7.35. The antenna configuration is a bistatic configuration and there are only variations in propagation velocity in the downward direction. The 3D data $b(x, y, z = 0, t)$ are recorded on a regular grid by moving the antennas in the xy-plane at $z = 0$.

Assume, initially, that there is only one small isotropic point scatterer present in the sub-surface, located at $\vec{r}_o = (x_o, y_o, z_o)$ and characterised by an impulse response $\Lambda_o(t_o)$, independent of the incident direction. Note that, in the most general case, the IR of the localised isotropic point scatterer does not necessarily have to be a Dirac impulse as a function of time. For the antennas at any position $\vec{r}_a = (x_a, y_a, z = 0)$,

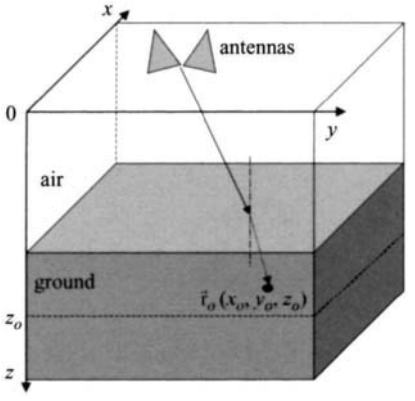

Figure 7.35 Configuration and representation of the co-ordinate system

the received voltage, representing an A-scan, can be written according to (7.57) as

$$b(\vec{r}_a,t) = \frac{T_{a-g}T_{g-a}}{8\,\pi^2 R_t R_r\, c} g_d(t) \otimes h_{N,Tx}(\vec{a}_i,t) \otimes \Lambda_o(t) \otimes h_{N,Rx}(-\vec{a}_s,t) \otimes \frac{\mathrm{d}V_s(t-t_d)}{\mathrm{d}t} \tag{7.59}$$

where t_d represents the exact two-way travelling time between the antennas and the point target, taking into account the different propagation velocities in the media.

By grouping all the factors, except for the IR of the point target, in one factor $w(\vec{r}_a,\vec{r}_o,t)$, (7.59) becomes

$$b(\vec{r}_a,t) = w(\vec{r}_a,\vec{r}_o,t) \otimes_t \Lambda_o(t) \tag{7.60}$$

The symbol $\otimes_t$ is introduced to clearly indicate that the convolution in (7.60) is a convolution in time. For a given configuration, all the factors in (7.59) are known, and hence $w(\vec{r}_a,\vec{r}_o,t)$ can be easily calculated. Furthermore, for the antennas at $z = 0$ and the point scatterer at a fixed depth $z = z_o$, the response $w(\vec{r}_a,\vec{r}_o,t)$ is a function of $\vec{r}_o$ and $\vec{r}_a$ only by their difference, and (7.60) can be written as

$$b(\vec{r}_a,t) = w(\vec{r}_a - \vec{r}_o,t) \otimes_t \Lambda(\vec{r}_o,t) \tag{7.61}$$

If an object can be modelled by a set of independent small isotropic point scatterers, all at approximately the same depth $z = z_o$, the output voltage $b(\vec{r}_a,t)$ will be a combination of the contribution of each individual point scatterer, which is clearly a convolution in space if we assume that the operation is linear:

$$b(x_a,y_a,t) = \iint_{x,y} \int_{\tau} w(x_a - x, y_a - y, z_o, t-\tau)\Lambda_{zo}(x,y,\tau)\,\mathrm{d}\tau\mathrm{d}x\mathrm{d}y \tag{7.62}$$

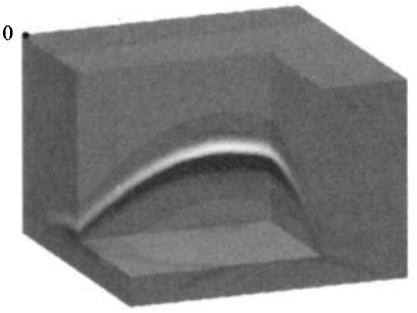

Figure 7.36 Synthetic C-scan of a fictive point scatterer at a depth of 6 cm below the air–ground interface, calculated by forward modelling

Equation (7.62) represents a space–time convolution along the co-ordinates x, y and t, and can be written as

$$b(x, y, t) = w(x, y, z_o, t) \otimes_{x,y,t} \Lambda_{zo}(x, y, t) \tag{7.63}$$

where $\Lambda_{zo}(x, y, t)$ is a 3D matrix, called the scattering matrix [32], and contains the responses associated with the distributed point scatterers at approximately a depth z_o. The symbol $\otimes_{x,y,t}$ denotes a space–time convolution along the co-ordinates x, y and t. The 3D matrix $w(x, y, z_o, t)$ represents the point spread function of the GPR system for a depth z_o. In practice the point spread function $w(x, y, z_o, t)$ is calculated by using (7.59) for different antenna positions $\vec{r}_a$ on a regular grid in the xy-plane at $z = 0$ and a small fictive point scatterer with IR $\delta(t)$, at a depth z_o. In other words it can be seen as a synthetic C-scan of a small fictive isotropic point scatterer. Figure 7.36 shows the 3D point spread function of the system at a depth of 6 cm below the air–ground interface (with the antennas 25 cm above the ground). In the point spread function, as it is obtained by forward modelling, all the information on the system, like the waveform of the excitation source, the IR of the antennas, the antenna pattern, the attenuation and dispersion in the ground etc. is included.

Although the point spread function $w(x, y, z_o, t)$ is space variant (function of z_o), its shape will not change very much with depth. In practice, the point spread function for a given depth can be used for a broad depth range. As a consequence, the space–time convolution can be considered as space (depth) invariant and the migrated 3D image, denoted $\hat{\Lambda}(x, y, t)$ can be calculated in one step by

$$\hat{\Lambda}(x, y, t) = b(x, y, t) \otimes_{x,y,t} w(x, y, z_o, t)^{-1} \tag{7.64}$$

where $\hat{\Lambda}(x, y, t)$ denotes the spatial image of $\Lambda_{zo}(x, y, t)$, i.e. the migrated image, $b(x, y, t)$ is the recorded C-scan that is to be migrated, and $w(x, y, z_o, t)$ is the point spread function for a fixed depth $z = z_o$.

7.5.1.6 Implementation of the migration method: From the mathematical point of view, solving (7.64) can cause some problems. Because of the bandlimited nature of the system and the effects of noise, (7.64) is a classical ill-posed problem. A fast

and computationally nonintensive mathematical solution for the deconvolution is to perform it in the frequency–wavenumber domain, by means of a Wiener filter [48]. A Wiener filter is an optimal filter that minimises the variance of the error between the restored image and the original image before degradation, under the assumption of a signal-independent noise, a linear degradation and stationarity of the images.

Let $B(k_x, k_y, \omega)$ be the 3D Fourier transform of the recorded data $b(x, y, t)$ with respect to the x, y and the t co-ordinates:

$$B(k_x, k_y, \omega) = \iiint b(x, y, t) e^{ik_x x + ik_y y - i\omega t} \, \mathrm{d}x \mathrm{d}y \mathrm{d}\omega \tag{7.65}$$

Taking the Wiener filter approach, the restored image in the frequency–wavenumber domain is given by

$$\hat{\Lambda}(k_x, k_y, \omega) = \frac{B(k_x, k_y, \omega) W^*(k_x, k_y, \omega)}{W(k_x, k_y, \omega) W^*(k_x, k_y, \omega) + \frac{P_n(k_x, k_y, \omega)}{P_\Lambda(k_x, k_y, \omega)}} \tag{7.66}$$

where $W(k_x, k_y, \omega)$ is the 3D Fourier transformation of the calculated point spread function, $W^*(k_x, k_y, \omega)$ its complex conjugate, $P_n(k_x, k_y, \omega)$ the spectral density of the noise in the image, and $P_\Lambda(k_x, k_y, \omega)$ the spectral density of the original image.

The main problem with the Wiener filter is that it can be difficult to get a good estimation of the spectral density of the noise and the spectral density of the image before degradation, which is a priori not known. A classical solution is to replace the ratio of the two power spectral densities by a constant parameter μ, also called the water level parameter. It will prevent (7.66) becoming too large for very small values of $W(k_x, k_y, \omega)$.

Finally, the migrated image is given by the inverse 3D Fourier transform of $\hat{\Lambda}_{zo}(k_x, k_y, \omega)$:

$$\hat{\Lambda}(x, y, t) = \frac{1}{2\pi} \iiint \hat{\Lambda}(k_x, k_y, \omega) e^{-i(k_x x + k_y y - \omega t)} \, \mathrm{d}k_x \mathrm{d}k_y \mathrm{d}\omega \tag{7.67}$$

The migration scheme is resumed in the following steps. The point spread function is calculated for a given soil type and burial depth. The burial depth is chosen to be the most likely depth for an object. The calculation of the point spread function only has to be done once. The 3D Fourier transform of the recorded data is calculated by (7.65). The data are filtered by the Wiener filter as in (7.66). The inverse 3D Fourier transform of the filtered data is calculated, represented in (7.67), resulting in the migrated image.

As already mentioned, this migration scheme is very simple and not computationally intensive. Suppose a 3D raw image of $32 \times 32 \times 256$ points representing an area of 64 cm by 64 cm with a step of 2 cm in both lateral directions. The 3D Fourier transformation, the filtering and the inverse transformation of this dataset only takes 76 MFLOPS, which means that it can easily be implemented in real time.

7.5.1.7 Results of the migration method: The migration by deconvolution is applied on data taken by a laboratory UWB GPR [47], with the antennas mounted on the

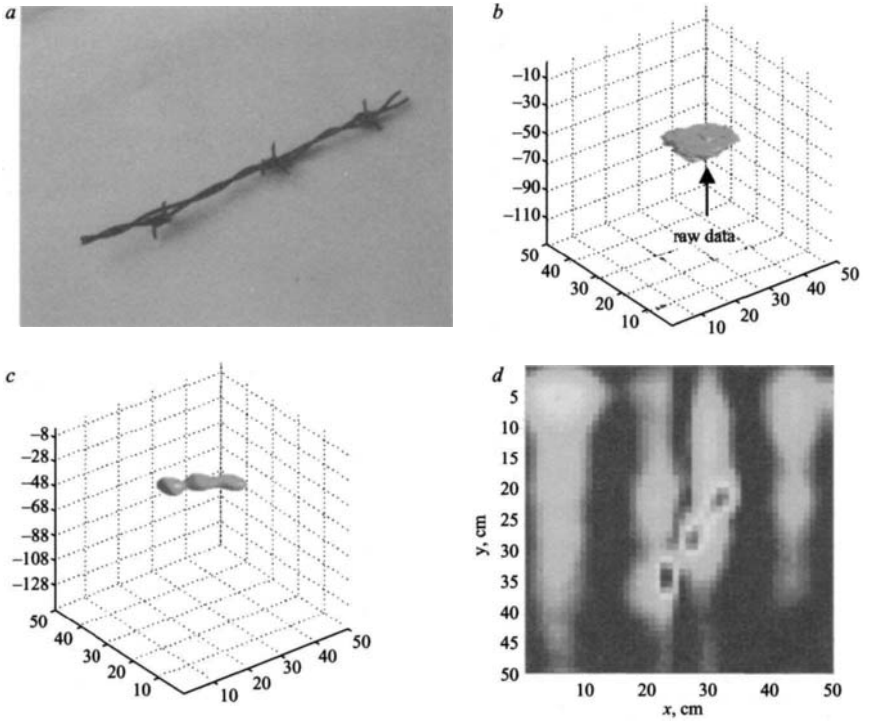

Figure 7.37 *Migration by deconvolution applied on barbed wire (length of 20 cm) buried at 5 cm*
a Photograph of the barbed wire; *b* 3D C-scan representation of raw data; *c* 3D C-scan representation of migrated data; *d* projection of migrated C-scan in a horizontal plane

indoor xy-scanning table. The data are acquired over an area of 50 cm by 50 cm with a step of 1 cm in both x- and y-directions. Figure 7.37 shows the results of the migration method on a piece of 20 cm barbed wire, buried at 5 cm of depth in sand. Figure 7.37*d* represents a two-dimensional C-scan of the migrated image. The shape of the barbed wire in (*d*) can easily be distinguished and even contains the three sets of pins present on the real wire. Note that the dimensions of the object in the migrated images approach the dimensions of the real objects.

The aim of migration is to focus reflections on objects back into the true physical shape of the object but also into its true position. To illustrate the latter, we show in Figure 7.38*a* the raw B-scan on an oblique mine. The mine was buried under an angle of about 30° in dry sand, with the highest point of the mine at a depth of 5 cm. In the raw B-scan at the left, the strongest reflections on the mine are found in the lower right corner of the image, whereas in reality the mine is situated in the middle of the image, indicated by the rectangular box in the image. The explanation for this shift is simple. When the antennas are right above the oblique mine, the mine

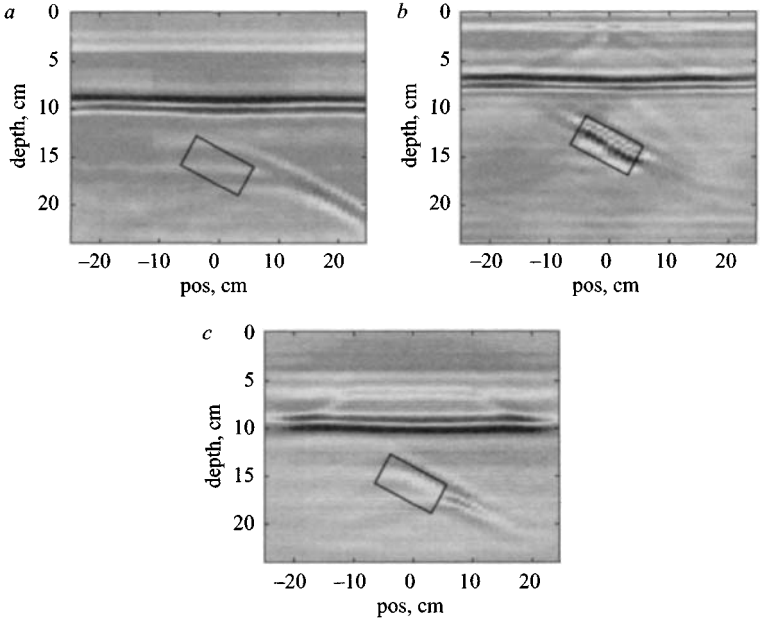

Figure 7.38 *Oblique antipersonnel mine under an angle of 30°*
a B-scan of raw data; *b* after migration by deconvolution; *c* after Kirchhoff migration

will have a strong reflection in a direction away from the receiving antenna. For the antennas in the direction perpendicular to the flat top of the mine, the reflections on the mine towards the receiving antenna will be stronger than when the antennas are right above the oblique mine, leading to a displacement of the target in the raw data. After migration by deconvolution, however, the target is found in its true position, as shown in Figure 7.38*b*. The migrated image not only shows the object in its true position, but also clearly shows that the object is oblique. Other migration methods, like Kirchhoff migration [32] and F-K migration [32] were also applied on the same data, but with poorer results than with the migration by deconvolution method. Figure 7.38*c* shows the result after Kirchhoff migration. The migrated image is better than the raw one, but the Kirchhoff migration is not able to bring the target completely back in to its actual position.

The previous results are obtained on data that are acquired in the laboratory, where all conditions are well controlled and where the air–ground interface is flat. In reality this is not the case. Ground characteristics like permittivity and attenuation are often not known and have to be estimated. The air–ground interface can be very rough and can introduce additional clutter, which eventually might interfere with the reflections on the target. Furthermore, the ground is not always homogeneous and it can be expected that the UWB GPR, which yields a high resolution, is sensible to these inhomogeneities. The data represented in Figure 7.39 are acquired over an area of

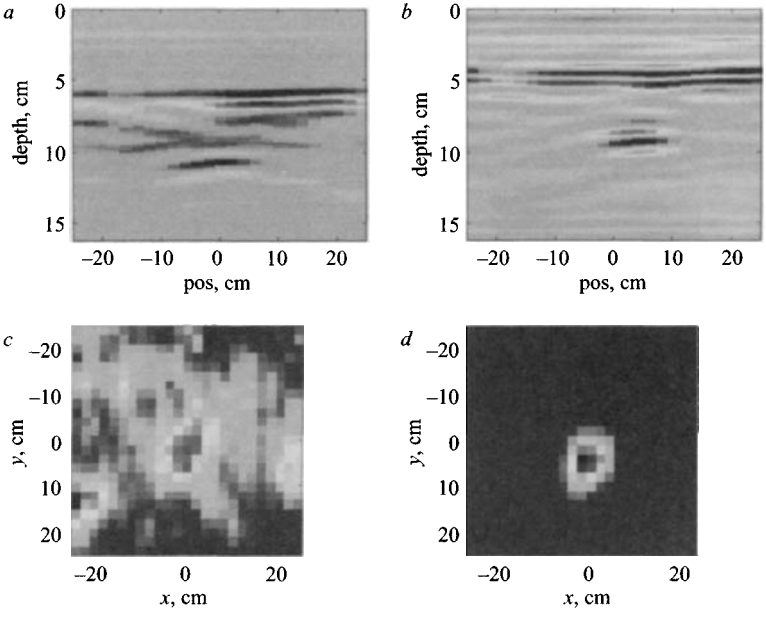

Figure 7.39 *Antipersonnel mine in gravel at 5 cm of depth*
a B-scan of raw data; *b* B-scan of migrated data; *c* projection of raw data C-scan in a horizontal plane; *d* projection of migrated C-scan in a horizontal plane

50 cm by 50 cm in steps of 2 cm (which is still small enough to avoid aliasing in the x- and y-directions). Figure 7.39 shows a 2D representation of a B-scan and a C-scan of a PMN mine, buried in gravel at a depth of 5 cm, before and after migration. In the images of the raw data, there is a lot of clutter present and the shape of the mine is not clear. After migration, most of the clutter has disappeared and the circular shape and dimensions of the mine become correct.

7.5.1.8 Summary: The raw 3D images recorded by a GPR are often difficult to interpret for an operator. Owing to the beamwidth of the antennas, a target in the ground is already seen by the GPR system even when it is not exactly under the antennas. As a consequence, the recorded data will be unfocused. Focusing techniques to reduce the influence of the beamwidth of the antennas are called migration techniques. Most of the existing migration techniques, however, do not take into account the characteristics of the acquisition system and the ground characteristics. We therefore proposed a migration technique, called migration by deconvolution. The novelty of the algorithm is that it uses the time domain model of the GPR and hence does take into account the system and ground characteristics. The migration method is simple and fast. We calculate by forward modelling a synthetic point spread function of the UWB GPR. This point spread function is then used to be deconvolved from

the recorded data. The method is evaluated on data coming from a UWB GPR. The results of the migration method are found to be very good and in any case better than conventional migration methods like Kirchhoff or F-K migration. After migration of the data, the UWB GPR gives enough resolution in the lateral directions to give an idea of the shape and, in favourable circumstances, of the dimensions of the buried object. The migration method is also able to focus reflection on oblique objects back into their true position and considerably reduces the clutter in a GPR image.

7.5.2 Synthetic aperture processing

Much work has been reported on SAR techniques and Stickley *et al.* [49], Kagalenko and Weedon [50], Milisavljevic and Yarovoy [51], and Brandstadt *et al.* [52] have applied SAR techniques to GPR processing. As the antenna of a surface-penetrating radar moves, the process can be considered analogous to the antenna of a synthetic aperture radar (SAR). However, the attenuation of the earth material limits the improvement that can be obtained by effectively windowing the synthetic aperture. Synthetic aperture processing requires measurements to be made at a number of antenna positions (i.e. a B-scan) and then combined to simulate a narrow beam. The improvement that can be gained is related to the length of the synthetic aperture.

In general the resolution in either the x- or y-direction of an antenna used in an SAR is given by

$$\delta_x = 2Z\theta_x \quad \text{or} \quad \delta_y = 2Z\theta_y \tag{7.68}$$

where Z is the depth of the target and θ is the beamwidth.

As most surface-penetrating radar antennas are dielectrically loaded dipoles, the beamwidth is in the order of $\pi/2$, and hence the resolution is poor. If the equivalent antenna phase front is considered to be a plane wave and is uncorrected, the SAR is termed unfocused and the effective aperture is given by Skolnik [53] as $R\theta$, and hence the resolution is given by

$$\delta_y = \sqrt{z\lambda}/2 \tag{7.69}$$

As most surface-penetrating radar antennas are not used in plane wave conditions and are most likely to be operated in the near field and Fresnel regions, it is necessary to provide an amplitude and time delay correction for each range.

In the Fresnel region the resolution in free space would be given by

$$\delta_x = \frac{z}{2} \tag{7.70}$$

However, the effect of attenuation is to reduce the resolution and, assuming an inverse fourth power relationship of received power with depth, Daniels *et al.* [4] give

$$\delta_x = 4z\sqrt{\frac{\ln 2}{2 + \alpha z}} \tag{7.71}$$

where α is the attenuation constant in dB/m.

It can be concluded therefore that horizontal resolution improves as the material attenuation increases, whereas the resolution of a synthetic aperture would degrade under conditions of increasing attenuation.

In most situations the target is close, at least in terms of average wavelength, to the measurement plane and thus some of the methods described in the previous Section become more relevant. Holographic synthetic aperture imaging methods have been developed for the single frequency case by Junkin and Anderson [54] and for the multi-frequency case by Osumi and Ueno [55].

The field strength at any point on the record surface can be derived from Fresnel–Kirchhoff diffraction theory for a spherical wave in lossy dielectric, and is given by [55]

$$v(x_0,t) = \frac{1}{2\pi v}\iint p(x)\frac{z(l_t+l_r)}{l_t l_r}\exp(-\alpha(l_t+l_r))U'\left(t-\frac{l_t+l_r}{v}\right)\mathrm{d}x\mathrm{d}y \tag{7.72}$$

where v is the propagation velocity, α is the attenuation constant, l_t is the transmit path distance, l_r is the receive path distance and U' is the time derivative of the input pulse waveform $u(t)$.

The image reconstruction implies the estimation of reflectance $p(x)$ from the transmitted signal and a set of recorded returns. The holographic process correlates the set of recorded returns and test functions and gives an image function

$$b(x) = \iiint_{-\infty}^{\infty} U(x_0,t)h(x-x_0,t)\,\mathrm{d}t\mathrm{d}x_0\mathrm{d}y_0 \tag{7.73}$$

The key to the imaging process is the optimisation of the test function, and the various references deal with this process in greater detail.

SAR methods have been applied to single frequency, impulse and FMCW radars, and Yamaguchi *et al.* [56] describe the process of determination of the object reflection distribution function. In the case of an FMCW radar a B-scan data set is recorded.

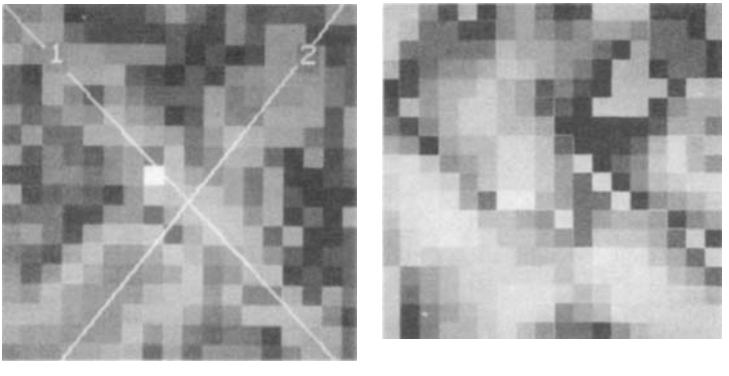

Figure 7.40 Holographic image focused to the object plane (Junkin)

The process of producing the target distribution comprises Fourier transforming each A-scan and multiplying this by the Fourier transform of the inverse propagation function. The product is then inverse transformed. A typical holographic SAR image is shown in Figure 7.40.

7.6 Image processing

An alternative method of B-scan processing is based on image processing techniques. Here it is assumed that the basic level processing has been carried out and the C-scan is presented either as a greyscale or colour coded image as shown in Figure 7.41. As radar data are bipolar in contrast to data derived from optical sensors, it is normal to encode the amplitude of the radar data in a defined manner. Hence, the amplitude scaling for greyscale would assign most negative values to black and most positive to white. Colour coding is more complex and it is found preferable to limit the range of the colour palette as the eye is more sensitive to intensity within a particular colour range rather than a wide range of colours, which can be found confusing.

The general method of image processing is well established. Normally a two-dimensional mask filter, whose coefficients are set to those of the image of the target (for which analysis is required) is convolved with the data. Alternatively, a three-dimensional data set is recorded for subsequent processing and two-dimensional data images in any orthogonal plane produced. Image processing techniques involve filtering operations which require fast execution of two-dimensional convolution algorithms. These can be divided into four categories:

1 lowpass
2 highpass
3 edge detection
4 template matching.

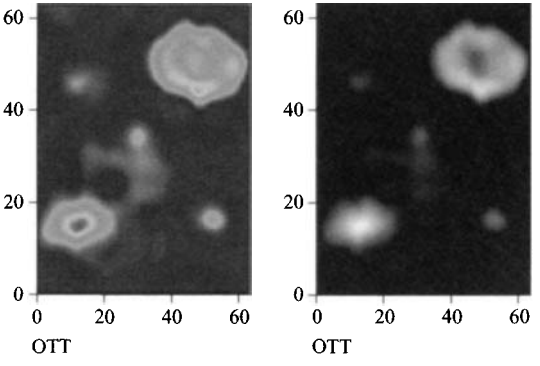

Figure 7.41 Example C-scans using buried AT and AP mines

All four types are commonly implemented by convolving the input data with a two-dimensional array of filter coefficients called the kernel. Each type performs a different function in the image enhancement-restoration process and multiple types can be used to improve the image visibility. The most common convolution kernels are 3×3 and 5×5, and sets of commonly used kernels are listed below.

(*a*) 3 by 3 Highpass
Highpass filter (divisor = 1)

$$\begin{matrix} -1 & -1 & -1 \\ -1 & 9 & -1 \\ -1 & -1 & -1 \end{matrix}$$

(*b*) 3 by 3 Lowpass
Lowpass filter (divisor = 9)

$$\begin{matrix} 1 & 1 & 1 \\ 1 & 1 & 1 \\ 1 & 1 & 1 \end{matrix}$$

(*c*) 3 by 3 Laplacian
Laplacian filter (divisor = 1)

$$\begin{matrix} -1 & -1 & -1 \\ -1 & 8 & -1 \\ -1 & -1 & -1 \end{matrix}$$

(*d*) 3 by 3 Horizontal line enhancement
Horizontal line enhancement (divisor = 1)

$$\begin{matrix} -1 & -1 & -1 \\ 2 & 2 & 2 \\ -1 & -1 & -1 \end{matrix}$$

Lowpass filtering smoothes an image so that large objects are transformed into homogeneous zones and small objects are reduced in intensity and/or merged into the larger regions. In the process, edges are reduced in intensity so that the details of an object are lost and objects in close proximity to each other are combined.

Highpass filtering performs the opposite function. Here, fine details that might be missed in the original image are increased in intensity. Note that the same mathematical operation as that for the lowpass filter is performed here; only the coefficients in the kernel have been changed.

Edge detection (or extraction) amplifies abrupt changes in intensity of an image and removes all other information. The three basic kinds of edge detection are the Laplacian, the Prewitt and the Sobel operators. The Sobel and Prewitt operators have the advantage of providing edge direction information. However, they require two or more passes, one for each edge direction. On the other hand, the Laplacian operator is isotropic, that is, it extracts the image edges from all directions. Edge detectors provide the same type of information as highpass filters (that is, they amplify details in an image) but are more amenable to post filtering; small changes in intensity can

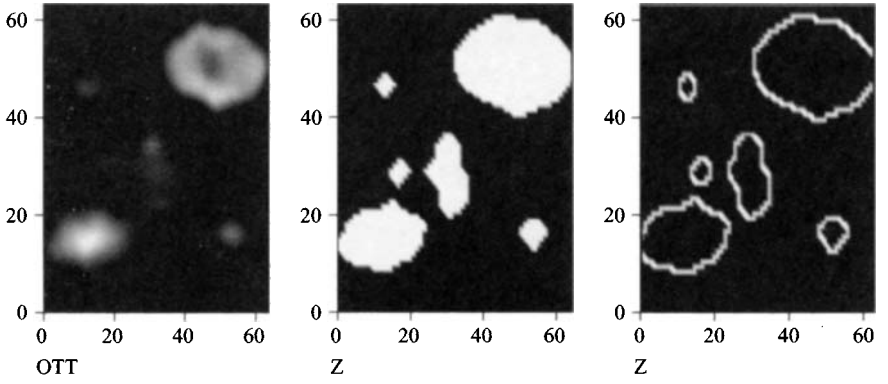

Figure 7.42 Image processing of radar C-scan data from Figure 7.41

be eliminated from further processing by comparing the output of the edge detector to a threshold value and discarding pixel values below the threshold.

Template matching, or matched filtering, convolves the image with a kernel that contains a pattern to be detected in the data. Template matching is also often used in texture and pattern recognition to determine which parts of an image are most likely to contain targets. In processing radar data, several important factors must be considered. Firstly, unlike image data, radar data are bipolar, and hence an initial operation to convert radar data to unipolar data is necessary. This can be achieved by either converting radar data to absolute data or thresholding at zero to give positive going or negative going data only. Second, the radar image does not correspond to geometric patterns and it will be necessary to identify suitable kernel coefficients which are appropriate to the radar image pattern rather than a geometrical model.

Examples of processing of the images in Figure 7.41 are shown in Figure 7.42.

The processing in Figure 7.42 is based on a Melem transform (b) of the basic data (a) followed by a Canny edge detector (c). It successfully identifies the five mines, two AT mines (upper right and lower left) and three AP mines (upper left, central and lower right). Image processing techniques have been applied to GPR data by Wu and Liu [57], Polat and Meincke [58], Dourthe and Pichot [59], Williams *et al.* [60], Xu and Miller [61], Kleinmann *et al.* [62], Homer *et al.* [63], Walker and Bell [64], van den Berg *et al.* [65], and Morrow and van Genderen [66].

Further development of radar image processing by means of the Hough transform is reported by Kaneko [67].

Essentially the Hough transform transforms a line in image space to a point in polar co-ordinate space. A straight line may be described by the equation

$$\rho = x \cos\theta + y \sin\theta \tag{7.74}$$

and the Hough transform becomes a point in (θ, ρ) space.

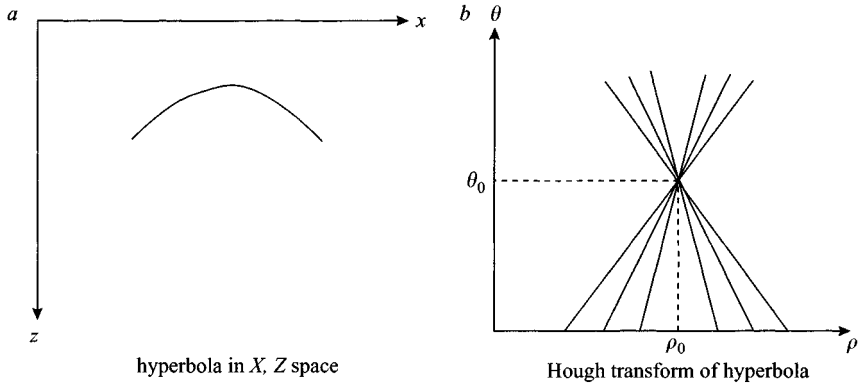

Figure 7.43 Hough transform of hyperbola

A hyperbolic reflection transforms to a set of lines as shown in Figure 7.43.

The method proposed by Kaneko [67] extracts lines and curves, such as the hyperbolic reflection generated by a pipe, or pipes, from the radar image by means of a two-stage process. The first Hough transform uses the first derivative of edge contours to provide an initial fast estimate of the wanted target. The second part of the process uses a second derivative of the edge contours to improve the accuracy of the Hough transform.

7.7 Deconvolution techniques

Dr Timofei Savelyev, Luc Van Kempen and Professor Hichem Sahli

7.7.1 Linear and circular deconvolution

There are two types of convolution, namely linear and circular convolution. Linear convolution is introduced for the nonperiodic signals; circular convolution is used in the case of periodicity [68]. Assume an original signal vector $\mathbf{x}$ with N elements and a finite impulse response (FIR) filter of order $M-1$ which has an impulse response $\mathbf{h}$ of length M. As for an infinite-impulse response filter, its impulse response is always appropriately truncated in digital signal processing. Then the output of the filter equals convolution of $\mathbf{x}$ and $\mathbf{h}$, resulting in a vector $\mathbf{y}$ of length $N+M-1$:

$$\mathbf{y} = \mathbf{h} \otimes \mathbf{x} \tag{7.75}$$

$$y(t) = \int_{-\infty}^{+\infty} x(\tau)h(t-\tau)\,\mathrm{d}\tau = \int_{0}^{t} x(\tau)h(t-\tau)\,\mathrm{d}\tau \tag{7.76}$$

$$y[m] = \sum_{n=0}^{m} x[n]h[m-n] \tag{7.77}$$

This is a typical case of linear convolution. It can be rewritten in a matrix form as

$$\mathbf{y} = \begin{Vmatrix} h(1) & h(1-1) & h(1-2) & \dots & h(1-(N-1)) \\ h(2) & h(2-1) & h(2-2) & \dots & h(2-(N-1)) \\ h(3) & h(3-1) & h(3-2) & \dots & h(3-(N-1)) \\ \dots & \dots & \dots & \dots & \dots \\ h(M) & h(M-1) & h(M-2) & \dots & h(M-(N-1)) \\ \dots & \dots & \dots & \dots & \dots \\ h(M+N-1) & h(M+N-2) & h(M+N-3) & \dots & h(M+N-1-(N-1)) \end{Vmatrix} \cdot \begin{Vmatrix} x(1) \\ x(2) \\ x(3) \\ \dots \\ x(N) \end{Vmatrix} \tag{7.78}$$

Due to the principle of causality and to the finiteness of the impulse response,

$$h(k) = 0 \quad \text{for } k < 1 \quad \text{and } k > M + N - 1 \tag{7.79}$$

$$\mathbf{y} = \begin{Vmatrix} h(1) & 0 & 0 & \dots & 0 \\ h(2) & h(1) & 0 & \dots & 0 \\ h(3) & h(2) & h(1) & \dots & 0 \\ \dots & \dots & \dots & \dots & \dots \\ h(M) & h(M-1) & h(M-2) & \dots & 0 \\ \dots & \dots & \dots & \dots & \dots \\ 0 & 0 & 0 & h(M) & h(M-1) \\ 0 & 0 & 0 & 0 & h(M) \end{Vmatrix} \cdot \begin{Vmatrix} x(1) \\ x(2) \\ x(3) \\ \dots \\ x(N) \end{Vmatrix} = \mathbf{Hx} \tag{7.80}$$

where $\mathbf{H}$ is a band Toeplitz matrix with dimensions $N + M - 1 \times N$.

In the case of periodicity of an input signal and impulse response with period L, their convolution is said to be circular and can be expressed by the formulas (7.81) and (7.82) [68]:

$$y_p[m] = \sum_{n=0}^{L-1} x_p[n] h_p[m-n] \tag{7.81}$$

$$Y_p[k] = X_p[k] \cdot H_p[k] \tag{7.82}$$

in time and frequency domains correspondingly.

To apply the fast Fourier transform (FFT) and (7.82) the linear convolution can be extended to the circular one by the padding with zeros of vectors $\mathbf{x}$ and $\mathbf{h}$ up to the length of $L = N + M - 1$. Then vectors $\mathbf{x}$, $\mathbf{h}$ and $\mathbf{y}$ represent one period. In the time domain this convolution is given by

$$\mathbf{y} = \begin{Vmatrix} h(1) & 0 & 0 & \dots & 0 \\ h(2) & h(1) & 0 & \dots & 0 \\ h(3) & h(2) & h(1) & \dots & 0 \\ \dots & \dots & \dots & \dots & \dots \\ h(L) & h(L-1) & h(L-2) & \dots & h(1) \end{Vmatrix} \cdot \begin{Vmatrix} x(1) \\ x(2) \\ x(3) \\ \dots \\ x(L) \end{Vmatrix} = \mathbf{Hx} \tag{7.83}$$

The convolution matrix $\mathbf{H}$ is a lower-triangular $L \times L$ Toeplitz matrix here.

Linear and circular deconvolution can be introduced with respect to linear and circular convolution correspondingly. Then circular deconvolution could be given by

$$\mathbf{x} = \mathbf{H}^{-1}\mathbf{y} \tag{7.84}$$

This solution is acceptable for the exact data. If we have a noisy realisation $\mathbf{y}^{\delta}$ (δ stands here for the indication of noise presence), the deconvolution should be computed as a solution of the *normal equation*

$$\mathbf{H}^{\mathrm{T}}\mathbf{H}\mathbf{x} = \mathbf{H}^{\mathrm{T}}\mathbf{y}^{\delta} \tag{7.85}$$

$$\hat{\mathbf{x}} = (\mathbf{H}^{\mathrm{T}}\mathbf{H})^{-1}\mathbf{H}^{\mathrm{T}}\mathbf{y}^{\delta} \tag{7.86}$$

This solution minimises $\|\mathbf{y}^{\delta} - \mathbf{H}\hat{\mathbf{x}}\|^2$ (here and further we use the 2-norm) and is well known as the *least-squares solution* or the *normal solution*. In this case it is a best-approximate solution.

If we have the exact data but the convolution matrix is singular, a best-approximate solution is the *normal pseudosolution*

$$\hat{\mathbf{x}} = \mathbf{H}^{\#}\mathbf{y} \tag{7.87}$$

where $^{\#}$ stands for the Moore–Penrose generalised inverse or the pseudo-inverse.

The normal pseudo-solution holds for a rectangular convolution matrix, i.e. for linear deconvolution. In practice, circular deconvolution is more attractive for the following reasons. The length of the signal vector does not change after deconvolution, and this is important because the exact duration of a signal is not known a priori in many cases.

The convolution matrix is a lower-triangular Toeplitz matrix, which introduces better possibilities for its inversion. Deconvolution can be done in the frequency domain via an FFT, and the GPR signals have a periodic structure.

7.7.2 *Deconvolution in UWB GPR processing as an ill-posed inverse problem*

The GPR impulse response includes the impulse responses of transmitter, receiver, transmitting and receiving antennas. It represents an impulse with a few lobes (Figure 7.44). The first element of the system impulse response is either equal or close to zero. It means that the lower-triangular matrix **H** has zeros or almost zeros on its main diagonal and, therefore, **H** is either singular or close to singularity. It is a badly conditioned matrix.

A problem is said to be ill posed if at least one of the following properties does not hold, according to Hadamard's definition of well posedness [69]:

1. For all admissible data, a solution exists.
2. For all admissible data, the solution is unique.
3. The solution depends continuously on the data (can be computed in a stable way).

In this case none of those properties are met. Singularity of the convolution matrix results in absence of an exact solution (7.84). In practice the measurements

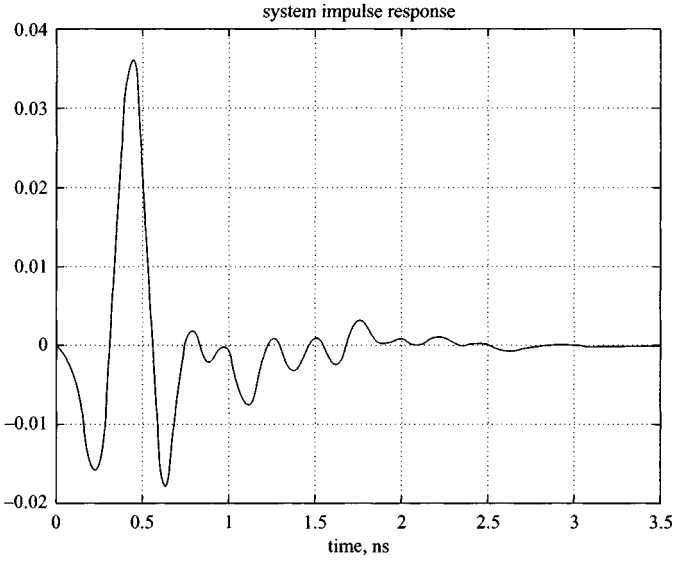

Figure 7.44 UWB GPR impulse response

of **y** and **h** are noisy while the inversion of the badly conditioned convolution matrix is an *unstable* operation dependent on any perturbation of the data. Therefore the solutions of (7.86) and (7.87) cannot be unique and do not depend continuously on the noisy data. Hence the deconvolution problem in UWB processing is an ill posed inverse problem.

7.7.3 Regularisation methods and deconvolution algorithms

To solve an ill posed problem the regularisation methods were developed. The main idea of regularisation is to find out a solution minimising the *smoothing functional*

$$\Phi_\alpha(\hat{\mathbf{x}}, \mathbf{y}^\delta) = \|\mathbf{y}^\delta - \mathbf{H}\hat{\mathbf{x}}\|^2 + \alpha F(\hat{\mathbf{x}}) \tag{7.88}$$

where $\hat{\mathbf{x}}$ is the estimate of the solution, $\mathbf{y}^\delta$ is the received signal with system noise, α is the regularisation parameter and $F(\hat{\mathbf{x}})$ is the stabilising functional or stabiliser.

Different regularisation methods use different stabilisers. A classical method is Tikhonov regularisation, with the smoothing functional

$$\Phi_\alpha(\hat{\mathbf{x}}, \mathbf{y}^\delta) = \|\mathbf{y}^\delta - \mathbf{H}\hat{\mathbf{x}}\|^2 + \alpha\|\hat{\mathbf{x}}\|^2 \tag{7.89}$$

Its minimiser or a regularised solution is

$$\mathbf{x}_\alpha^\delta = (\mathbf{H}^T\mathbf{H} + \alpha\mathbf{I})^{-1}\mathbf{H}^T\mathbf{y}^\delta \tag{7.90}$$

where **I** is an identity matrix.

The task is to define the regularisation parameter α, which must provide the following:

$$\lim_{\delta \to 0} \mathbf{x}_\alpha^\delta = \mathbf{x}^\# \tag{7.91}$$

where $\mathbf{x}^\#$ is the normal pseudosolution.

There are three approaches to the estimation of α: heuristic methods; a priori rule; a posteriori rule.

The heuristic methods are used when it is impossible to estimate the noise level of data and, therefore, other methods are inapplicable. The main advantage of the heuristic approach is that the solution represents a good compromise between data fitting and penalising the norm after reconstruction (convolution). The main drawback is the necessity of computations for a large range of α. One of those methods is the L-curve method [69], where a plot of the approximation norm $\|\mathbf{x}_\alpha^\delta\|$ versus the residual norm $\|\mathbf{y}^\delta - \mathbf{H}\mathbf{x}_\alpha^\delta\|$ in a log-log scale resembles the letter 'L', and its 'corner' point is considered to be a best-approximate solution.

An a priori rule is based on the knowledge of $\alpha = \alpha(\delta)$ – dependence on the noise level of data. In practice this dependence is almost never known.

An a posteriori rule involves the knowledge of $\alpha = \alpha(\delta, \mathbf{y}_\alpha^\delta)$ – dependence on the noise level and on the reconstructed data $\mathbf{y}_\alpha^\delta = \mathbf{H}\mathbf{x}_\alpha^\delta$. The Morozov criterion or the *discrepancy principle* is used:

$$\|\mathbf{y}^\delta - \mathbf{H}\mathbf{x}_\alpha^\delta\| \leq \tau\delta \tag{7.92}$$

where $\tau > 1$. The regularisation parameter can be chosen via comparison between the discrepancy and the assumed bound for the noise level.

The direct application of the Morozov criterion to Tikhonov regularisation requires the computation of a solution to (7.90), the subsequent reconstruction and the check whether the condition (7.92) is satisfied. If not, it is necessary to change α and to repeat the procedure until (7.92) holds.

One can use another implementation of the discrepancy principle

$$\|\mathbf{y}^\delta - \mathbf{H}\mathbf{x}_\alpha^\delta\| \leq \tau\delta \leq \|\mathbf{y}^\delta - \mathbf{H}\mathbf{x}_\beta^\delta\| \tag{7.93}$$

for some β satisfying $\alpha \leq \beta \leq 2\alpha$.

The steps to process the explicit algorithms of the deconvolution can be written as follows.

7.7.3.1 Algorithm 1. Direct Tikhonov regularisation with the discrepancy principle:

1. $\alpha_0 = \delta^{\frac{2}{3}}, \tau = 1.1$.
2. For $k = 1, 2, \ldots, N$ (loop with the increasing α), evaluate $\mathbf{x}_k(\alpha_{k-1})$ and $\mathbf{x}_k(2\alpha_{k-1})$ according to (7.90).
   If (7.93) is satisfied then halt processing and the final solution $\mathbf{x}_\alpha^\delta = \mathbf{x}_k(\alpha_{k-1})$.
   If (7.93) is not satisfied then $\alpha_k = 2\alpha_{k-1}$ and continue the loop.

3. If the solution has not been determined, then evaluate the same loop for decreasing α with $\alpha_k = \alpha_{k-1}/2$.
4. The number of steps N must be limited by appropriate maximal time for solving the task.

This algorithm is a straightforward implementation of Tikhonov regularisation and is not efficient from a computational point of view.

Another a posteriori approach to find out α deals with a nonlinear matrix equation [69, p.123]

$$\alpha^3 \left\| \left(\mathbf{H}\mathbf{H}^{\mathrm{T}} + \alpha \mathbf{I} \right)^{-\frac{3}{2}} \mathbf{y}^{\delta} \right\|^2 = \tau \delta^2 \tag{7.94}$$

Having solved that equation, we can obtain a best-approximate solution with only one computation of (7.90). The main computational burden here is referred to solving (7.94), which is a difficult task and requires the implementation of a separate iterative algorithm.

7.7.3.2 Algorithm 2. Direct Tikhonov regularisation with the nonlinear equation:

1. $\alpha_0 = \delta^{\frac{2}{3}}, \tau = 1.1$.
2. Evaluate (7.94) to find out an optimal α.
3. Evaluate (7.90) to find out a regularised solution $\mathbf{x}_{\alpha}^{\delta}$.

The described direct methods and algorithms always have a solution even in the case of underestimated noise level.

Iterative regularisation methods. Unlike the direct methods of regularisation, the iterative methods do not include sophisticated computations and therefore they are considerably faster for big vectors and matrices. Also those methods do not require large computer resources. In the meantime, the iterative methods provide good accuracy. Their drawback is sensitivity to the noise level. If this is underestimated, then the methods do not converge and so do not have a solution at all.

Most iterative methods are based on a transformation of the normal equation into equivalent equations like

$$\mathbf{x} = \mathbf{x} + \mathbf{H}^{\mathrm{T}}(\mathbf{y} - \mathbf{H}\mathbf{x}) \tag{7.95}$$

A classical iterative method illustrating this transformation is the Landweber iteration

$$\mathbf{x}_k^{\delta} = \mathbf{x}_{k-1}^{\delta} + \mathbf{H}^{\mathrm{T}}(\mathbf{y}^{\delta} - \mathbf{H}\mathbf{x}_{k-1}^{\delta}) \tag{7.96}$$

The iteration index k plays the role of the regularisation parameter α and the stopping rule plays the role of parameter choice method. For the Landweber iteration the Morozov criterion is usually applied as a stopping rule.

One of the accelerated iterative methods is a ν-method of regularisation [69, p. 167],

$$\mathbf{x}_k^\delta = \mathbf{x}_{k-1}^\delta + \mu_k(\mathbf{x}_{k-1}^\delta - \mathbf{x}_{k-2}^\delta) + \omega_k \mathbf{H}^{\mathrm{T}}(\mathbf{y}^\delta - \mathbf{H}\mathbf{x}_{k-1}^\delta) \tag{7.97}$$

The use of difference between results of two preceding iterations improves the speed of convergence.

The parameter ν represents the order with which the approximation error decreases:

$$\left\| \mathbf{x}^{\#} - \mathbf{x}_k^\delta \right\| = \mathrm{O}(k^{-2\nu}), \quad k \to \infty \tag{7.98}$$

Also ν controls an asymptotic growth of coefficients μ_k and ω_k, and consequently the speed of convergence. The parameter ν can be chosen equal to 1.

Numerically it is more efficient to base the computation of $\mathbf{x}_k^\delta$ on intermediate quantities $\mathbf{z}_k^\delta$ via $\mathbf{x}_k^\delta = \mathbf{H}^{\mathrm{T}}\mathbf{z}_k^\delta$. With respect to that, the following algorithm of deconvolution has been developed.

7.7.3.3 Algorithm 3. Iterative regularisation with ν-method

1. $\nu = 1, \mu_0 = \left\|\mathbf{y}^\delta\right\|^2, \alpha_0 = 1, \tau = 1.1, \mathbf{z}_0^\delta = 0, \mathbf{x}_0^\delta = 0, \sigma_1 = \|\mathbf{H}\|_2, \widetilde{\mathbf{H}} = \dfrac{1}{\sigma_1}\mathbf{H}$
2. $\mu_1 = 0, \omega_1 = \dfrac{4\nu+2}{4\nu+1}, \mathbf{z}_1^\delta = \dfrac{4\nu+2}{4\nu+1}\mathbf{y}^\delta, \mathbf{x}_1^\delta = \widetilde{\mathbf{H}}^{\mathrm{T}}\mathbf{z}_1^\delta$
3. For $k = 2, 3, \ldots$

$$\mu_k = \frac{(k-1)(2k-3)(2k+2\nu-1)}{(k+2\nu-1)(2k+4\nu-1)(2k+2\nu-3)}$$

$$\omega_k = 4\frac{(2k+2\nu-1)(k+\nu-1)}{(k+2\nu-1)(2k+4\nu-1)}$$

$$\mathbf{z}_k^\delta = \mathbf{z}_{k-1}^\delta + \mu_k(\mathbf{z}_{k-1}^\delta - \mathbf{z}_{k-2}^\delta) + \omega_k(\mathbf{y}^\delta - \widetilde{\mathbf{H}}\mathbf{x}_{k-1}^\delta)$$

$$\mathbf{x}_k^\delta = \widetilde{\mathbf{H}}^{\mathrm{T}}\mathbf{z}_k^\delta$$

$$\alpha_k^{-1} = 1 + \frac{k(2k-1)(2k+2\nu-1)}{(k+2\nu)(2k+4\nu+1)(2k+2\nu+1)}\alpha_{k-1}^{-1}$$

$$\beta_k = \frac{(2\nu+0.5)^2}{(2k+2\nu+1)^2}\alpha_k$$

$$\eta_k = (1-\alpha_k)\eta_{k-1} + \beta_k \left\|\mathbf{z}_k^\delta - \mathbf{z}_{k-1}^\delta\right\|^2$$

If $\eta_k \le \tau\delta^2$, then stop.

4. The final solution $\mathbf{x}^\delta = \sigma_1 \widetilde{\mathbf{H}}^{\mathrm{T}}\mathbf{z}_{k-1}^\delta$. (7.99)

Note that the convolution matrix should be normalised before its first use in the algorithm and at the final step the matrix should be restored after satisfying the stopping rule at the kth iteration; $\mathbf{z}_{k-1}^{\delta}$ is required for the final solution.

7.7.3.4 Data noise level estimation: accuracy and stability of deconvolution: The art of applying the regularisation methods to deconvolution is to find out the right compromise between accuracy and stability of the approximated solution. Accuracy is characterised by the norm of the difference between the given and reconstructed data $\|\mathbf{y}^{\delta} - \mathbf{H}\mathbf{x}_{\alpha}^{\delta}\|$, stability by norm of the approximation $\|\mathbf{x}_{\alpha}^{\delta}\|$. Deconvolution stability or, more accurately, its instability, appears as *ringing* in the deconvolved vector $\mathbf{x}_{\alpha}^{\delta}$. The plot of $\log \|\mathbf{x}_{\alpha}^{\delta}\|$ versus $\log \|\mathbf{y}^{\delta} - \mathbf{H}\mathbf{x}_{\alpha}^{\delta}\|$ gives an L-curve, which is used in heuristic methods. If the residual norm is small (case of high accuracy), then $\|\mathbf{x}_{\alpha}^{\delta}\|$ changes drastically in dependence on α and represents the vertical part of the L-curve. If $\|\mathbf{y}^{\delta} - \mathbf{H}\mathbf{x}_{\alpha}^{\delta}\|$ is big enough, then $\|\mathbf{x}_{\alpha}^{\delta}\|$ becomes stable and represents the horizontal part of the L-curve. In a posteriori regularisation methods both accuracy and stability depend on the noise level of the data. The task is to find out that level.

Consider the energy of a noisy vector: for an additive white noise the total vector energy equals the sum of the signal and noise energies:

$$\|\mathbf{y}^{\delta}\|^2 = \|\mathbf{y} + \mathbf{n}\|^2 = \|\mathbf{y}\|^2 + \|\mathbf{n}\|^2 \tag{7.100}$$

So the noise level can be defined as the norm of the noise vector:

$$\delta = \|\mathbf{n}\| \tag{7.101}$$

Also we can confirm this definition with the discrepancy principle. In the ideal case, when the reconstructed data coincide with the exact data, (7.92) can be rewritten as

$$\mathbf{y}^{\delta} - \mathbf{H}\mathbf{x}_{\alpha}^{\delta} = \mathbf{y}^{\delta} - \mathbf{y} = \mathbf{n} \tag{7.102}$$

$$\|\mathbf{n}\| \leq \tau\delta$$

Obviously, the noise level can be found with the statistical approach

$$\delta_{\max} = \mathrm{E}\{\|\mathbf{n}\|\} = \sigma\sqrt{N} \tag{7.103}$$

where the operator $\mathrm{E}\{o\}$ stands for averaging, σ is noise standard deviation and N is the length of the vector.

Equation (7.103) determines the maximal noise level, which provides excellent stability of the deconvolution results. However, numerical experiments with the real GPR data showed that accuracy of the regularised deconvolution can be significantly improved without loss of stability for a noise level lower than (7.103). It can be explained that accuracy depends on the signal to noise ratio (SNR) rather than on the noise content in a received signal.

We propose another approach to estimate the noise level. Consider the energy of noisy data,

$$\|\mathbf{y}^{\delta}\|^2 = \|\mathbf{s}\|^2 + \|\mathbf{n}\|^2 = \|\mathbf{s}\|^2 + \delta^2$$

which we rewrite as

$$\frac{\|\mathbf{y}^\delta\|^2}{\delta^2} = 1 + \frac{\|\mathbf{s}\|^2}{\delta^2} = 1 + SNR$$

$$\delta^2 = \frac{\|\mathbf{y}^\delta\|^2}{1 + SNR}$$

The maximal or peak SNR

$$SNR_{\max} = \frac{s^2_{\max}}{\sigma^2} \approx \frac{y^2_{\max} - \sigma^2}{\sigma^2}$$

Now we can obtain an estimate of noise level as

$$\delta^2_{\min} = \frac{\|\mathbf{y}^\delta\|^2}{1 + SNR_{\max}} = \frac{\|\mathbf{y}^\delta\|^2}{1 + \frac{y^2_{\max} - \sigma^2}{\sigma^2}} = \frac{\|\mathbf{y}^\delta\|^2}{y^2_{\max}}\sigma^2$$

$$\delta_{\min} = \frac{\|\mathbf{y}^\delta\|}{|y^\delta_{\max}|}\sigma \tag{7.104}$$

So we receive the lower estimate of noise level, which maintains stability and results in better accuracy than (7.103).

Equation (7.104) is an *adaptive* algorithm with respect to the received signal. Unlike (7.103) it estimates for a certain signal its own noise level relatively to the maximal signal's peak. The noise deviation of the measuring system noise can usually be estimated before experiments and used as a parameter for deconvolution algorithms.

The estimation of noise level based on peak SNR fits well in the processing of nonstationary rapidly decaying signals as UWB signals are.

For the accuracy estimation, we propose to use the normalised RMS error

$$e = \frac{\|\mathbf{y}^\delta - \mathbf{H}\mathbf{x}^\delta_\alpha\|}{\|\mathbf{y}^\delta\| + \|\mathbf{H}\mathbf{x}^\delta_\alpha\|}100\% \tag{7.105}$$

This can be interpreted as the relative distance between two vectors to be compared. It is Ø when the vectors coincide and 100 per cent when the vectors have the same origin, length and opposite directions.

7.7.3.5 Numerical results: The first trial to check how regularised deconvolution works, is deconvolving data out of the same data. Theoretically, it must result in a *delta-function*. We make this *auto-deconvolution* using the ν-method and Algorithm 3 for the impulse response depicted in Figure 7.44. The estimate of noise standard deviation is $\sigma = 1.7613 \times 10^{-4}$. The noise level is defined according to (7.104). The result of the deconvolution shown in Figure 7.45 is not a delta-function. Obviously, the more accurate the deconvolution the closer its result to a delta-function. The relative distance between the original and reconstructed impulse response is 0.21%. For noise level defined from (7.103) this distance is 0.89%. Now we divide σ by 1000

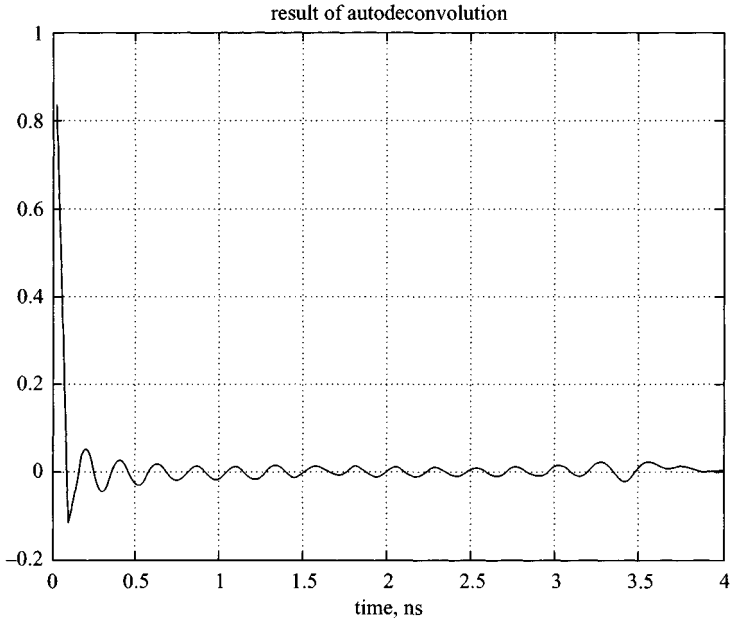

Figure 7.45 *Autodeconvolution with noise standard deviation estimate* $\sigma = 1.7613 \times 10^{-4}$

and substitute it into (7.104). Its result represented in Figure 7.46 is a delta-function. The corresponding relative distance equals 0.0002%.

Auto-deconvolution remains stable independently of the estimate of noise level because the convolution matrix is formed from the input data. Auto-deconvolution illustrates the possibility to decrease intentionally a parameter standing for noise level in order to obtain better accuracy.

Now consider deconvolution for a signal from an anti-personnel mine PMN-2. The signal was received by a GPR with impulse response and noise deviation mentioned above. Deconvolution has been carried out using Algorithm 3. The fixed noise level estimate (7.103) resulted in error of deconvolution of 13.78% (Figure 7.47*b*), while the estimate (7.108) resulted in an error of 1.60% (Figure 7.47*c*). The use of noise standard deviation $\sigma/10$ in (7.108) resulted in an error of 0.21% but with considerable ringing (Figure 7.48*d*). These results show that the use of the adaptive noise level estimate (7.108) provides excellent accuracy of deconvolution with minimal ringing.

As shown in Figure 7.48, deconvolution shifts the signal back in time by effective duration of the GPR impulse response, depicted in Figure 7.44. In that particular example, the shift is about 1 ns, corresponding to the duration of the most energetic part of the impulse response. This is the fundamental effect of deconvolution which should be accounted for GPR signal processing. Since the GPR impulse response remains the same, the time shift is constant.

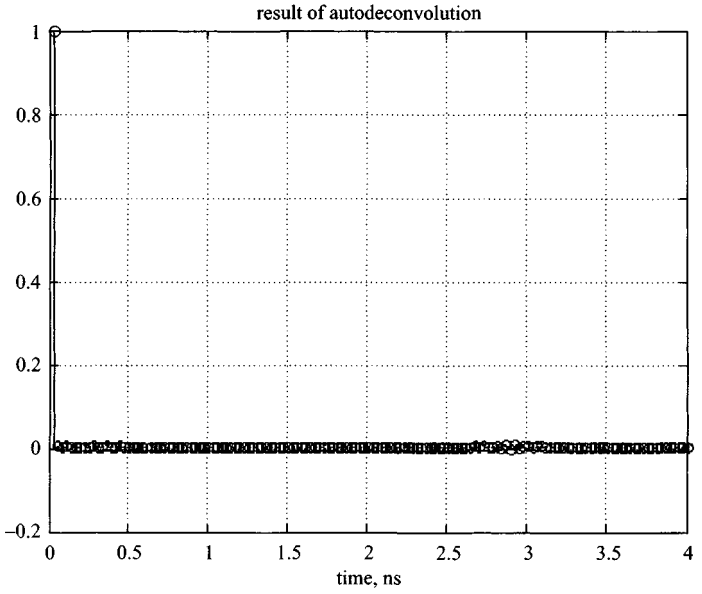

Figure 7.46 Autodeconvolution with intentionally decreased noise standard deviation estimate $\sigma/1000 = 1.7613 \times 10^{-7}$

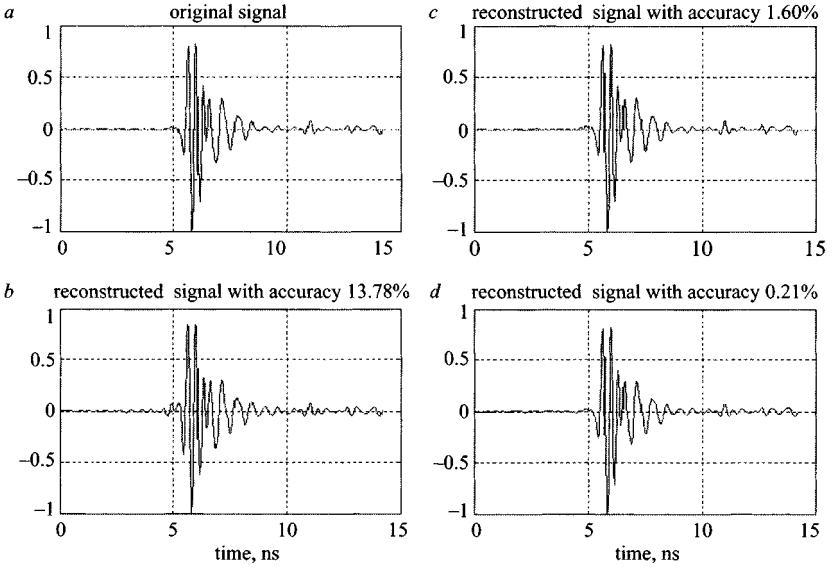

Figure 7.47 Original (a) and reconstructed signals: (b) fixed noise level estimate; (c) adaptive noise level estimate; (d) adaptive noise level estimate with $\sigma/10$

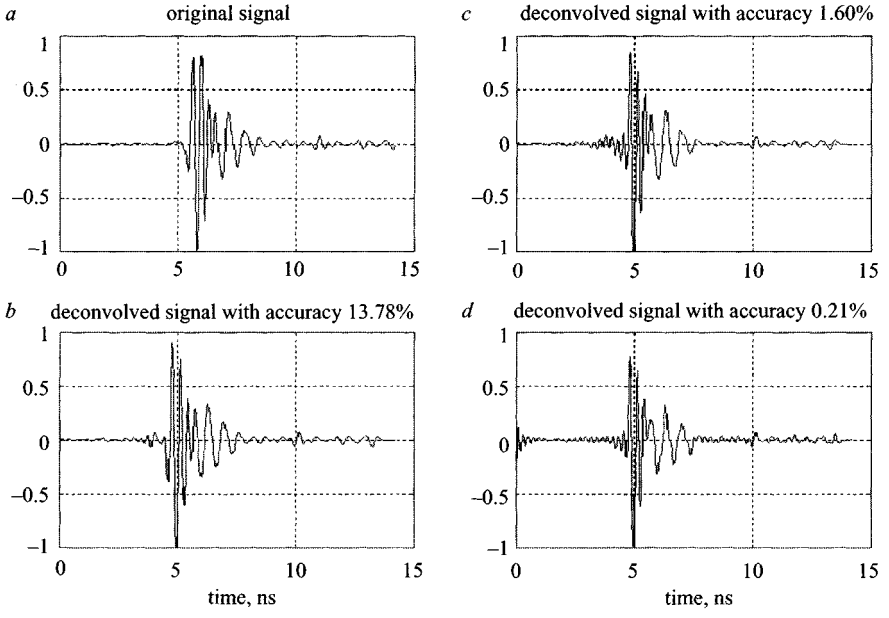

Figure 7.48 *Original (a) and deconvolved signals: (b) fixed noise level estimate; (c) adaptive noise level estimate; (d) adaptive noise level estimate with $\sigma/10$*

7.7.3.6 Comparative performance of the deconvolution algorithms: For comparison of performances, the deconvolution algorithms 1–3 have been implemented for the signal depicted in Figure 7.47. The length of corresponding vectors was 512 elements, and the size of the convolution matrix was 512 by 512. The adaptive noise level estimate was used.

The comparison was based on three factors: accuracy (the relative distance); computational speed (time of computation and number of iterations); computational burden measured by a number of floating point operations (FLOPS).

The time of computation and the number of FLOPS which are required for executing a program can be obtained with built-in MATLAB routines. Performance of the deconvolution algorithms is represented in Table 7.1. The first two algorithms are direct with respect to a solution, but iterative with respect to the regularisation parameter, which is why their computational speed is measured in iterations. The time of computation depends on computer performance and can be considered only as a comparative index, while other figures remain the same on different computers.

The iterative algorithm with the ν-method showed the best performance. It is the fastest, most accurate and most economical algorithm in comparison with other algorithms.

Next Page

Table 7.1 Relative performance of deconvolution algorithms

Algorithm	Error, %	Computational speed	Computational burden
1. Tikhonov with the discrepancy principle	1.84	159.23 s 6 iterations	10506 MFLOPS
2. Tikhonov with the nonlinear equation	5.07	1118 s 29 iterations	98411 MFLOPS
3. ν-method	1.60	7.42 s 10 iterations	373 MFLOPS

7.7.3.7 Summary: Deconvolution in UWB signal processing is an ill posed inverse problem. Tikhonov regularisation and the ν-method were considered for its solution. The data noise level should be defined as a compromise between accuracy and stability of deconvolution, and an adaptive noise level estimate has been proposed. The relative distance between an original signal and its reconstruction has been proposed as a numerical measure of deconvolution accuracy.

Two direct and one iterative deconvolution algorithm with regularisation were developed and tested, and the iterative algorithm with ν-method showed the best performance.

7.8 Multi-fold, multi-component and multi-azimuth GPR for sub-surface imaging and material characterisation

Prof. Michele Pipan, Emanuele Forte, Giancarlo Dal Moro, Monica Sugan and Icilio Finetti

7.8.1 Introduction

GPR can provide shallow sub-surface images sharper than any other geophysical technique in the 0–5 m depth range and quantitative information about EM properties of materials. It is therefore best suited for the noninvasive high-resolution study of the near surface. Advances in UWB equipment and dedicated data processing methods have recently improved performances of GPR and fostered the successful application of the method at depths ranging from a few centimetres (UXO detection) to different kilometres (glaciology), as illustrated by several examples in this book.

The two crucial tasks of the noninvasive method, namely sub-surface imaging and characterisation of materials, are best accomplished by GPR methods that exploit redundant information. In this Section we show examples of successful application of such techniques, in particular linear multi-fold, azimuthal multi-fold and multi-polarisation (multi-component) methods.

Focusing of the radar wave field and clutter reduction are the key issues in image enhancement. Focusing is based on migration techniques that require knowledge of the velocity of radar waves in the sub-surface. Clutter reduction benefits from multiple

Table 7.1 Relative performance of deconvolution algorithms

Algorithm	Error, %	Computational speed	Computational burden
1. Tikhonov with the discrepancy principle	1.84	159.23 s 6 iterations	10506 MFLOPS
2. Tikhonov with the nonlinear equation	5.07	1118 s 29 iterations	98411 MFLOPS
3. ν-method	1.60	7.42 s 10 iterations	373 MFLOPS

7.7.3.7 Summary: Deconvolution in UWB signal processing is an ill posed inverse problem. Tikhonov regularisation and the ν-method were considered for its solution. The data noise level should be defined as a compromise between accuracy and stability of deconvolution, and an adaptive noise level estimate has been proposed. The relative distance between an original signal and its reconstruction has been proposed as a numerical measure of deconvolution accuracy.

Two direct and one iterative deconvolution algorithm with regularisation were developed and tested, and the iterative algorithm with ν-method showed the best performance.

7.8 Multi-fold, multi-component and multi-azimuth GPR for sub-surface imaging and material characterisation

Prof. Michele Pipan, Emanuele Forte, Giancarlo Dal Moro, Monica Sugan and Icilio Finetti

7.8.1 Introduction

GPR can provide shallow sub-surface images sharper than any other geophysical technique in the 0–5 m depth range and quantitative information about EM properties of materials. It is therefore best suited for the noninvasive high-resolution study of the near surface. Advances in UWB equipment and dedicated data processing methods have recently improved performances of GPR and fostered the successful application of the method at depths ranging from a few centimetres (UXO detection) to different kilometres (glaciology), as illustrated by several examples in this book.

The two crucial tasks of the noninvasive method, namely sub-surface imaging and characterisation of materials, are best accomplished by GPR methods that exploit redundant information. In this Section we show examples of successful application of such techniques, in particular linear multi-fold, azimuthal multi-fold and multi-polarisation (multi-component) methods.

Focusing of the radar wave field and clutter reduction are the key issues in image enhancement. Focusing is based on migration techniques that require knowledge of the velocity of radar waves in the sub-surface. Clutter reduction benefits from multiple

data from the same sub-surface location. Multi-fold methods can provide an adequate solution for both problems.

Target characterisation implies reconstruction of images where properties of sub-surface scatterers are correctly represented. Multi-component imaging algorithms can accomplish such tasks [70], which exploit knowledge of transmitter and receiver antenna radiation characteristics and incorporate wave speed, polarisation and amplitude of the scattered electric field. However, the data acquisition and computational costs of such methods do not presently allow their extensive application but for academic purposes. An alternative strategy is based on the analysis of amplitude variations versus azimuth and offset at different polarisations. The cost of such approaches is limited and the technique allows us to optimise data acquisition parameters in single-fold and multi-fold surveys depending on target characteristics.

7.8.2 Data acquisition

We used a Malå Geoscience RAMAC system, equipped with 250, 500 and 800 MHz shielded antennas, to obtain all the radar datasets shown in this Section. Multiple common offset data acquisition schemes, i.e. iterated data acquisition along the same profile using different transmitter-receiver antenna separation, are a convenient solution to obtain multi-fold datasets in case a multi-channel system is not available. In the latter case, however, the difficulty of sliding multiple antennas at constant offset on rough surfaces may seriously hamper multi-fold data acquisition. Frames and numerically controlled systems are used for accurate and cost effective multi-offset/multi-component data acquisition in the case of laboratory experiments or measurements performed over small areas. Such solutions are further implemented in commercial systems, mainly for underground utilities detection. In the present study, we have used shielded antennas kept at fixed distance and orientation by Kevlar strings.

7.8.3 Data processing

The basic processing sequence for single-fold and multi-fold data (when treated as separate common-offset) is reported in Table 7.2.

Sequence 1 produces the filtered section where the position of the imaged targets is not correct and diffraction hyperbolas are not collapsed. Such a section can be exploited to reconstruct sub-surface models in the case of azimuthal isotropy, i.e. for horizontally layered media and vertical velocity variations only. Identification of point and linear scatterers such as, for example, underground utilities perpendicular to the GPR profile, can be further successfully performed, provided that diffraction hyperbolas do not smear the response and decrease resolution below the threshold requested for the interpretation of the targets. Sequence 2 produces the migrated and filtered section, which should provide a better sub-surface reconstruction. It should be stressed that the order of migration and filtering cannot be interchanged, unless the transfer function of the filter is kept constant in time, which means that the filter is not time-variant. This can be done in particular when shallow conductive layers (such

Table 7.2 Basic processing sequence for single-fold and multi-fold data (as separate common offset)

Dewow	
Background removal	
Amplitude correction	
Deconvolution	
1	2
Time-variant filtering (TVF)	Migration
	Time-variant filtering (TVF)

Table 7.3 Processing sequences for multi-fold data, vertically varying velocity field

a	Dewow	
b	Background removal	
c	Preliminary amplitude correction	
d	Pre-stack gather editing	
e	Deconvolution	
f	Velocity analysis	
g	Velocity based amplitude correction	
h	Pre-stack coherent noise removal	
Stack		
3		4
Post-stack time migration (TM)		Post-stack depth migration (DM)
TVF		Depth-variant filtering (DVF)
Time to depth conversion		

as clayey soils) or large numbers of scatterers reduce the penetration. The number of samples available in the useful part of the GPR section is then too small to allow the application of a time-varying operator.

We apply different processing sequences to multi-fold data depending on the velocity field characteristics. The basic sequences are reported in Tables 7.3 and 7.4.

This choice is not only related to structural characteristics of the sub-surface volume, as in the case of horizontally layered soils that exhibit horizontal velocity gradients due to variations in water content. In such cases, time migration techniques are inadequate. Mild and severe horizontal velocity variations require application of sequences 5 and 6, respectively. Crucial steps in the imaging process are pre-stack coherent noise removal (see, for example, References [71, 72]) and those involving the analysis and reconstruction of the velocity field, namely step i in sequence 5 and j, k, l in sequence 6. DMO processing (i) implies a two-step velocity analysis, before and after application of the DMO correction (see, for example, Reference [73]).

Table 7.4 Processing sequences for multi-fold data, vertically and laterally varying velocity field

Steps a to h from Table 7.3	
5	6
i Dip MoveOut (DMO) processing	j Initial velocity–depth model building
Stack	k Kirchhoff pre-stack depth migration (PSDM)
Post-stack time migration	l Velocity–depth model upgrading
TVF	Final Kirchhoff PSDM
	DVF

In the case of severe lateral radar velocity variations, our strategy encompasses an initial velocity-depth (V-z) model building (j) in two steps: we first convert root mean square velocities (V_{RMS}) obtained from CMP analysis into interval velocities (V_{INT}) as a function of time by applying a horizontal smoothing. We then convert $V_{INT}(t)$ to $V_{INT}(z)$ by applying a vertical smoothing. The two-step smoothing proves effective in processing data from shallow sediments, where variable water content and prograding or accretionary structures introduce rapid velocity variations. V-z models are updated after PSDM by means of residual moveout analysis performed on common reflection point (CRP) gathers. Two main benefits can be expected from accurate V-z model reconstructions, namely improved sub-surface images and information about variations in the dielectric constant, which for low-loss (i.e. $\tan \delta < 1$) materials is directly related to the radar wave velocity. Such information cannot be attained by single-fold methods.

7.8.4 Results

Figure 7.49 shows an example of common mid point (CMP) gather obtained in sediments of an alluvial plain in northern Italy. The low attenuation and homogeneous characteristics of each sedimentary layer (from sands to gravelly sands) are responsible for the wide offset range (0.5–4.2 m) and excellent response in the far offset range (Figure 7.49*a*). The ground wave (G) allows a straightforward determination of near surface velocity, while reflections (R) are clearly interpretable in the full two-way-time range (up to 180 ns). The normalised crosscorrelation velocity spectrum (Figure 7.49*b*) exhibits well focused coherency values due to the high signal-to-noise ratio (SNR > 30 dB), even if departures from hyperbolic moveout arise from minor lateral velocity variations and prevent a perfect moveout correction (Figure 7.49*c*). A comparison between different imaging strategies is shown in Figure 7.50.

The GPR profile crosses a prograding structure related to the progressive accumulation of sediments deposited by a stream over a series of flat layers. Figure 7.50*b* shows the image enhancement provided by a 1200% stack in comparison with the single-fold section of Figure 7.50*a*. The complete series of foresets is clearly interpretable in the stack section as well as the flat underlying sedimentary sequence. A strong basal reflector shows up at ~100 ns in the single-fold and stack record,

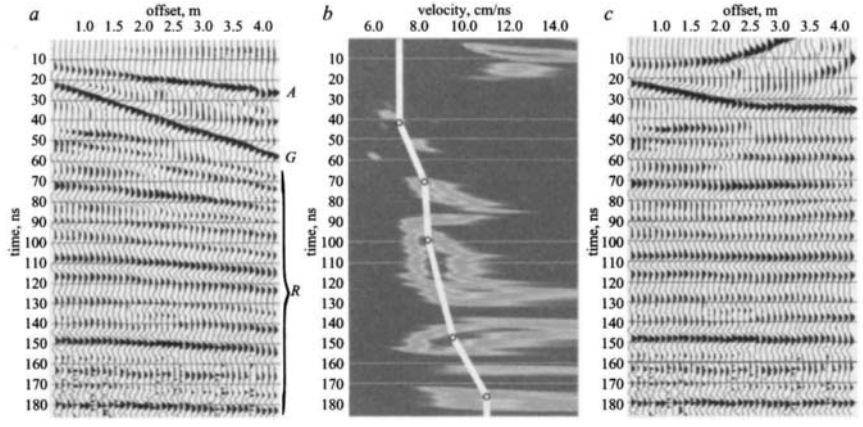

Figure 7.49 *(a) Example of 250 MHz large offset-range CMP (0.5–4.2 m) from an alluvial plain in northern Italy after processing: (A) Air wave, (G) ground wave, (R) reflections; (b) normalised crosscorrelation velocity analysis with superimposed velocity function; (c) CMP after NMO correction*

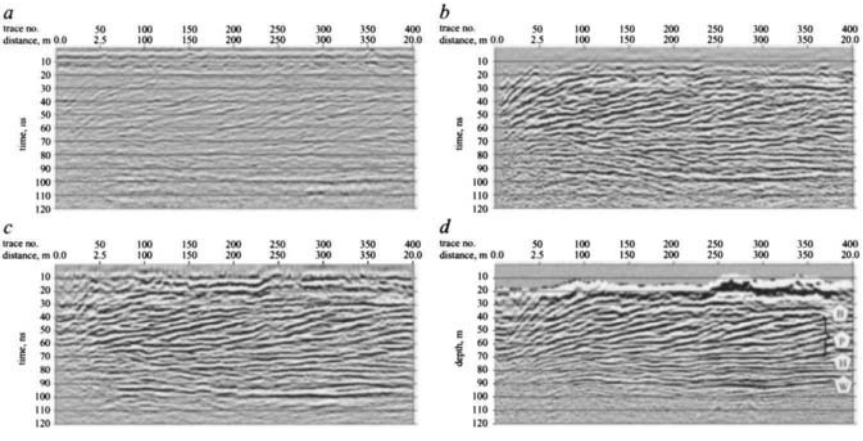

Figure 7.50 *(a) 250 MHz single-fold section (offset 1.2 m) from the Isonzo river bank (Italy) after standard processing; (b) stack section (1200% fold); (c) post-stack Kirchhoff time-migrated section; (d) pre-stack Kirchhoff depth-migrated section:* (B) *base of agricultural layer,* (P) *prograding alluvial sequence,* (H) *top of flat layer,* (W) *water table*

which is related to the water table. The correct structure of the prograding sequence and the erosional channel located between 0.0 and 2.5 m are properly imaged in the migrated sections of Figure 7.50*c*, *d*. PSDM is not always necessary to produce a correct image from multi-fold data, as demonstrated by the example of Figure 7.51.

Stack 500 MHz data (Figure 7.51*b*) from a sandy beach in north Italy allow the identification of gently dipping layers that cannot be interpreted in the single-fold section of Figure 7.51*a*. Post-stack F-K migration (Figure 7.51*c*) reconstructs the correct dip of layer boundaries (L) and location of the discontinuity (D) by focusing the diffraction hyperbolas where the layer boundaries show an interruption, possibly due to differential compaction or human activity (excavation). The benefits of 2D multi-fold imaging can be extended to the reconstruction of 3D sub-surface models by combining multiple sections (Figure 7.52).

This is of particular interest to avoid mis-ties, to correlate fractures and faults and to reconstruct complex sub-surface structures, as in the case of archaeological targets. The example in Figure 7.52 successfully images a soil-limestone contact and allows a detailed reconstruction of bedrock topography and related structures. An alternative strategy is to cut the data volume along planes or irregular surfaces. Horizontal cuts are known as time-slices and are extensively used in archaeological and engineering applications.

The example in Figure 7.53 shows the reconstruction of a buried rain-water tank in vertical (A) and horizontal (B) cross-section. Steel rebars spaced 4 m apart are successfully imaged both by the vertical and horizontal cross-sections. In the case of deeper targets and less favourable SNR, the identification of weak reflectors in noisy background may require the application of further data processing procedures, such as computation of instantaneous attributes and dedicated coherent noise removal techniques. The pre-stack domain allows the application to a variety of records, such as common offset sections, common shot or common mid point gathers. Separate processing of such records results in enhanced stack and migrated data.

The example in Figure 7.54 shows that the stack of instantaneous phase common offset sections computed by means of wavelet transform [74] allows enhanced interpretation of echoes from a series of dipping reflectors (D) beneath waste (C). Controlled conditions allow an analysis of the performances of multi-fold/multi-azimuth techniques.

In Figure 7.55, we show the comparison of synthetic and real 800 MHz data obtained from a sandbox facility with buried pipes of different characteristics (metal/PVC; PVC filled by different fluids; 10 cm diameter, 40 cm depth). The correspondence between numerical simulation and field data is apparent. If we extend the analysis to different offsets and azimuth we obtain a double result. We can identify the content of the pipe based on the different response as a function of azimuth and offset (Figure 7.56, rows A and B).

In this case, a reflector beneath the pipe allows a more reliable discrimination that is less affected by the quantity of fluid within the pipe (Figure 7.56, row A). We can further exploit the amplitude versus offset/azimuth (AVOA) analysis to identify the optimum offset/azimuth combination, which provides the highest amplitude response in the perspective of extensive surveys for buried utilities detection. A preliminary

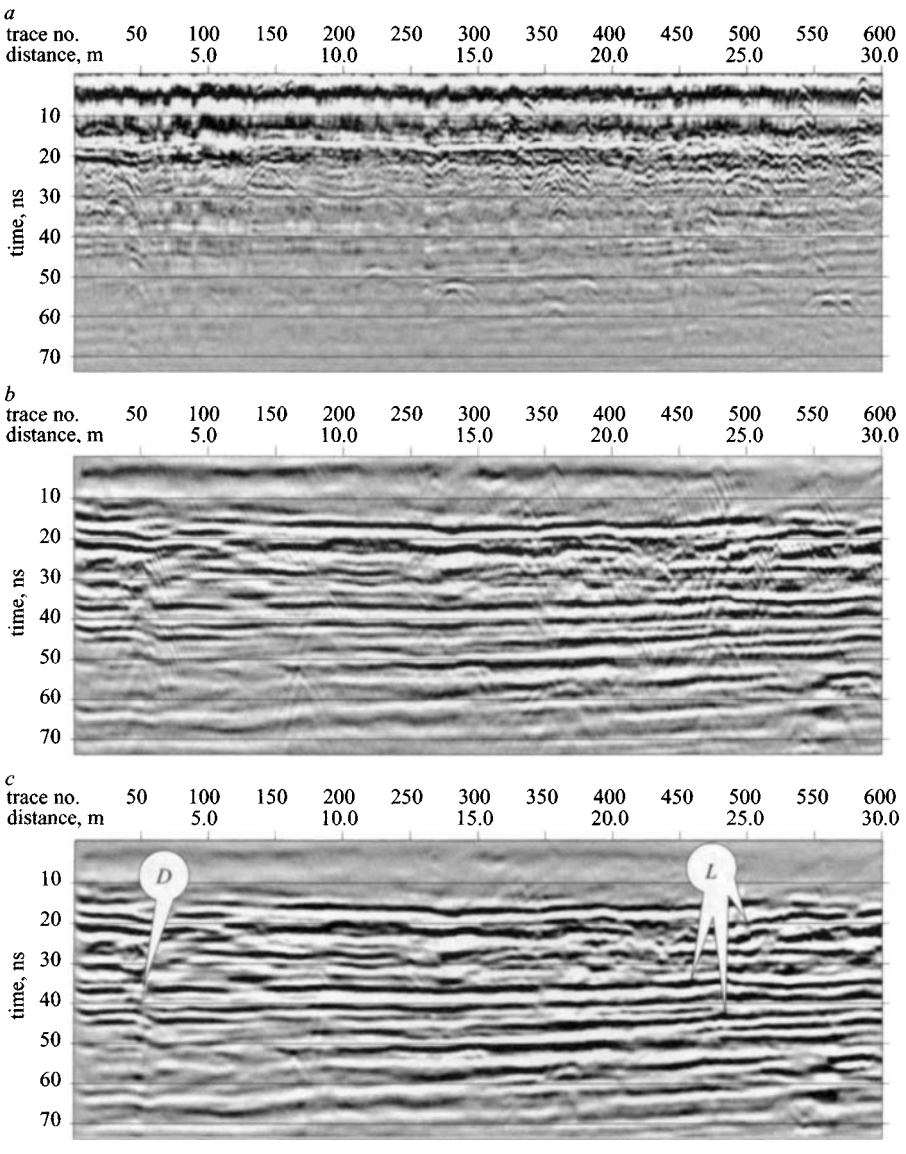

Figure 7.51 *(a) 500 MHz single-fold section (offset 0.6 m) from a sand beach (Italy) after standard processing; (b) stack section (1000% fold); (c) post-stack F-K migrated section: (L) moderately dipping layers with different slopes, (D) example of lateral discontinuity*

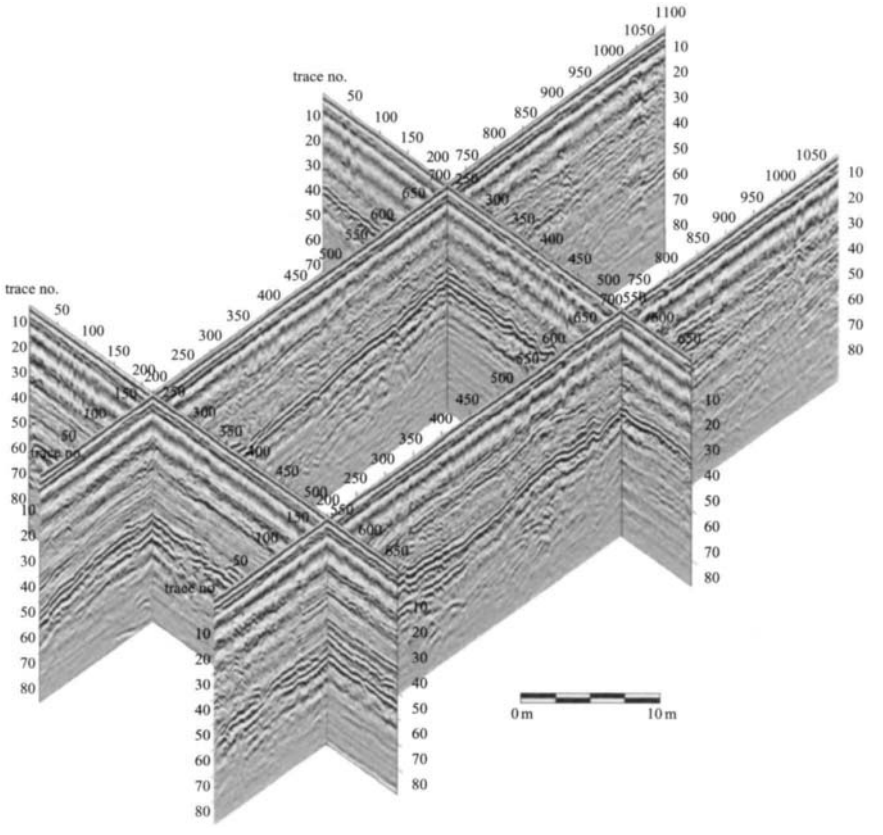

Figure 7.52 *Example of 3D visualisation of a 500 MHz GPR stack dataset (1200% fold)*

AVOA test performed in the area of interest allows an optimised selection of data acquisition parameters. Target characterisation and selection of optimum data acquisition parameters can be extended to the case of multiple polarisations, as illustrated by Figure 7.57 (800 MHz data).

Columns 1 and 2 refer to co-pole and crosspole configuration, respectively, while rows A and B report the results from PVC pipe (10 cm diameter, 40 cm depth) filled by air and freshwater, and row C is the response of a metal pipe. In the case of cylindrical targets, such as pipes, the response is in good agreement with well established theoretical models. In the case of more complex targets, such as buried cultural heritage, vertical or lateral coherence (i.e. target geometry) is not always adequate to discriminate potential targets, and the AVOA response for different antenna configurations (co-pole, crosspole) can be exploited to classify the echoes and perform a target-oriented interpretation.

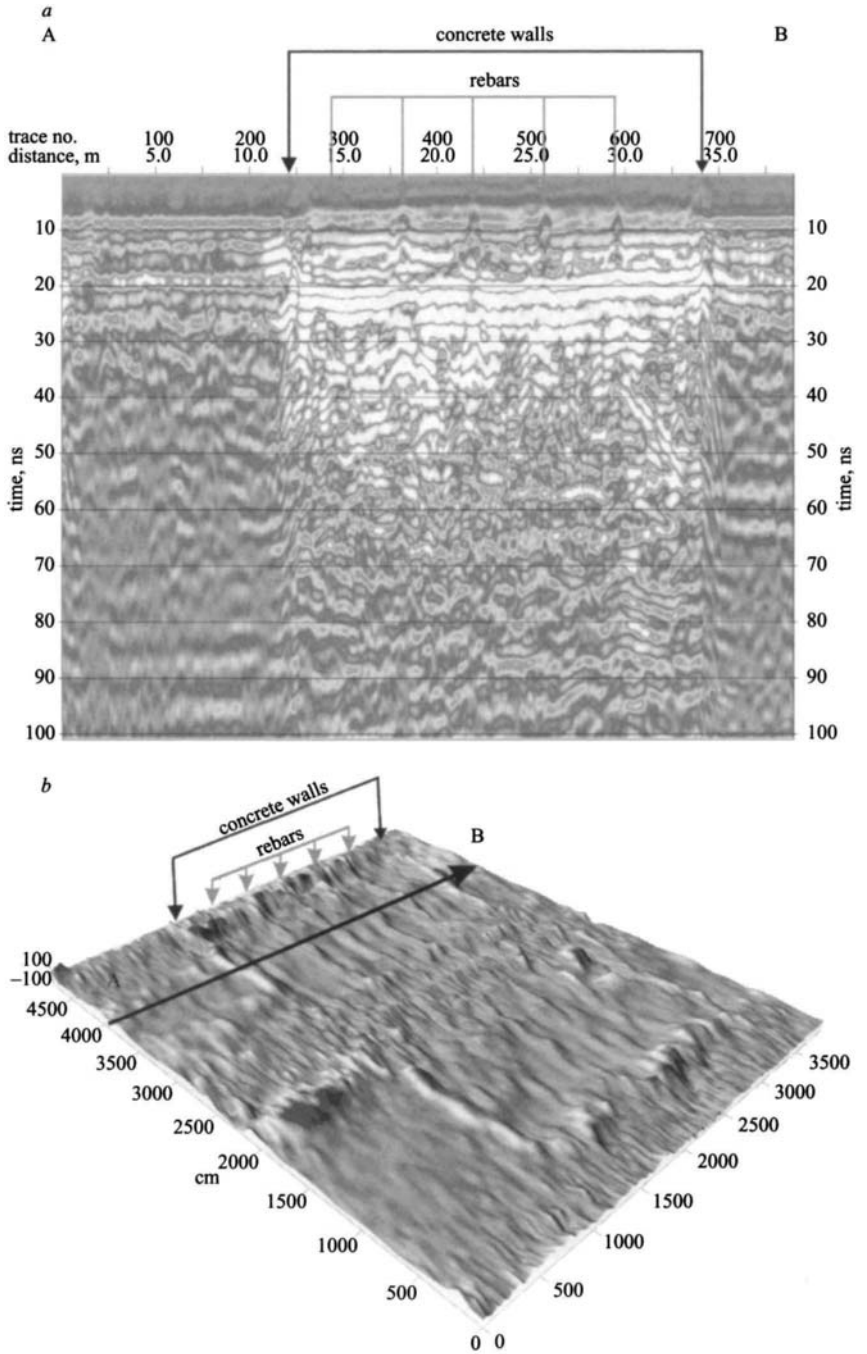

Figure 7.53 *(a) 400 MHz stack section of a concrete platform with rebars; (b) 11 ns timeslice (about 40 cm) across the stack GPR data volume*

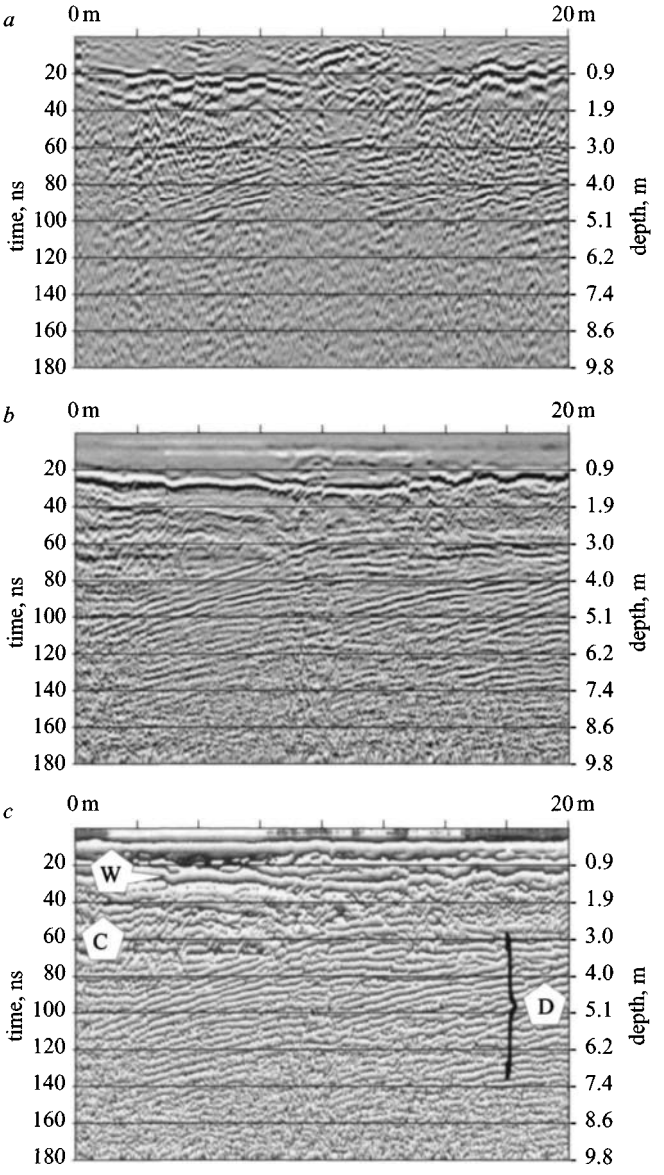

Figure 7.54 *(a) 250 MHz single-fold section (offset 1.0 m) from a brownfield; (b) stack section (1200% fold); (c) instantaneous phase of stack section:* (W) *base of waste disposal,* (C) *chaotic zone,* (D) *dipping horizons*

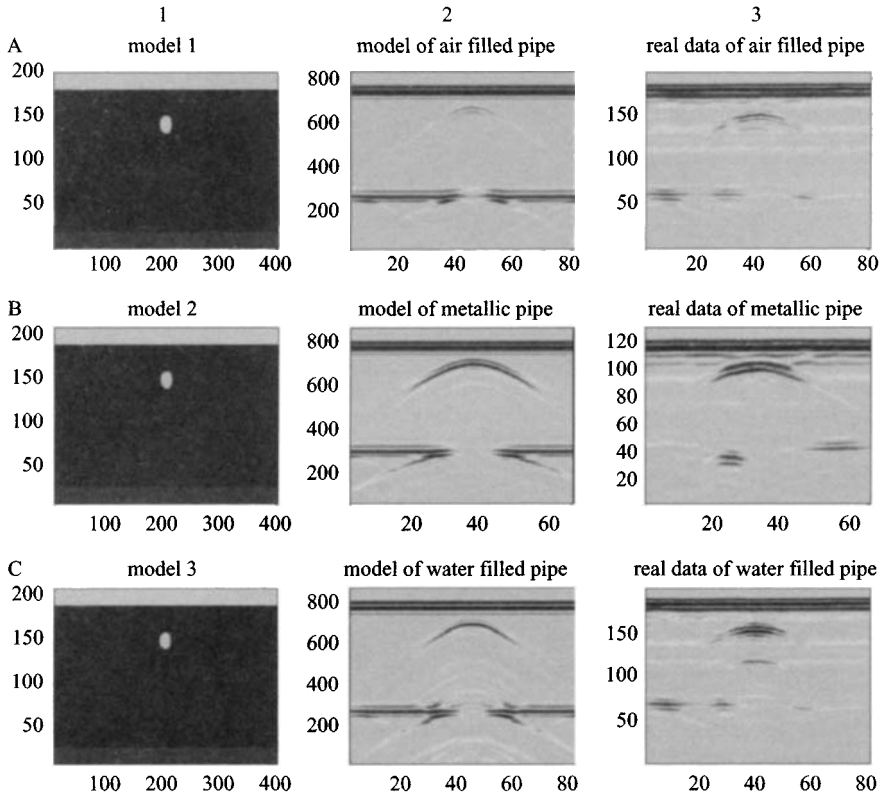

Figure 7.55 *Columns* 1 *to* 3*:* (1) *sub-surface model used for numerical simulation,* (2) *synthetic GPR data (FDTD numerical simulation) and* (3) *real GPR data. Rows A to C:* (A) *air filled PVC pipe,* (B) *metallic and* (C) *fresh water filled PVC pipe*
The pipe was placed into a sandbox with metallic bottom

7.8.5 Discussion

Multi-fold methods offer data redundancy that can be successfully exploited to obtain enhanced sub-surface images, discriminate coherent noise from signal, and evaluate EM properties of soils, rocks and buried targets. Pre-stack depth migration techniques allow imaging in complex sub-surface conditions and reconstruction of accurate V-z models, which are of interest for the analysis of vertical and lateral variations of the dielectric constant. Data derived spatial stacking operators (see, for example, Reference [75]) are an alternative imaging solution that does not depend on the V-z model but are based on data-derived kinematic attributes. Such attributes can be determined by means of optimisation procedures and successively exploited to

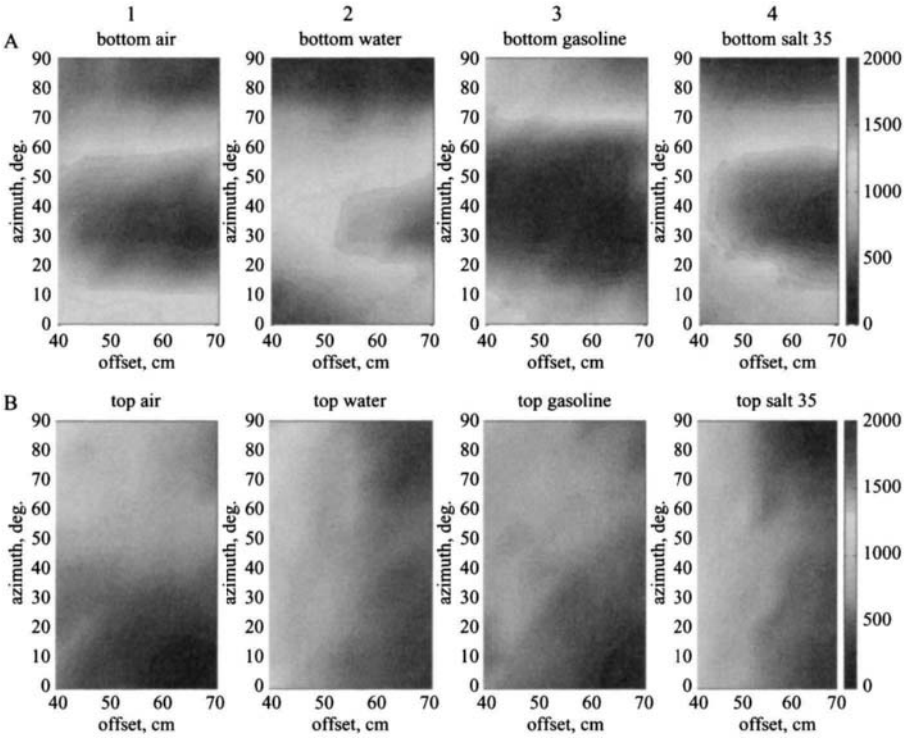

Figure 7.56 *GPR AVO (amplitude versus offset) and AVA (amplitude versus azimuth) analysis performed on a PVC pipe filled with different fluids* Columns 1 to 4: (1) air, (2) fresh water, (3) gasoline and (4) salt water (salinity about 35%). Rows A and B: (A) amplitude of reflection from metal base and (B) amplitude of reflection from top of the pipe

obtain the V-z model. This is certainly a promising strategy, particularly in complex sub-surface conditions where the interpretation of pre-stack and common-offset data is difficult and an interpretive approach to V-z model reconstruction is not feasible. AVOA analysis offers a solution to characterise and classify sub-surface targets, which may be effectively implemented by exploiting multi-channel systems. The data redundancy provided by the multi-fold method not only enhances processing and imaging results but also improves the interpretation of complex targets, as in the case of archaeological applications. The combined interpretation of pre-stack data (CMP and CRP gathers, common-offset sections at different offsets) and stack or migrated data allows discrimination of coherent noise from signal, the identification of weak signals in noisy background and the tracking of complex and irregular reflectors buried in chaotic soils. Such tasks exploit primary signal coherency in the

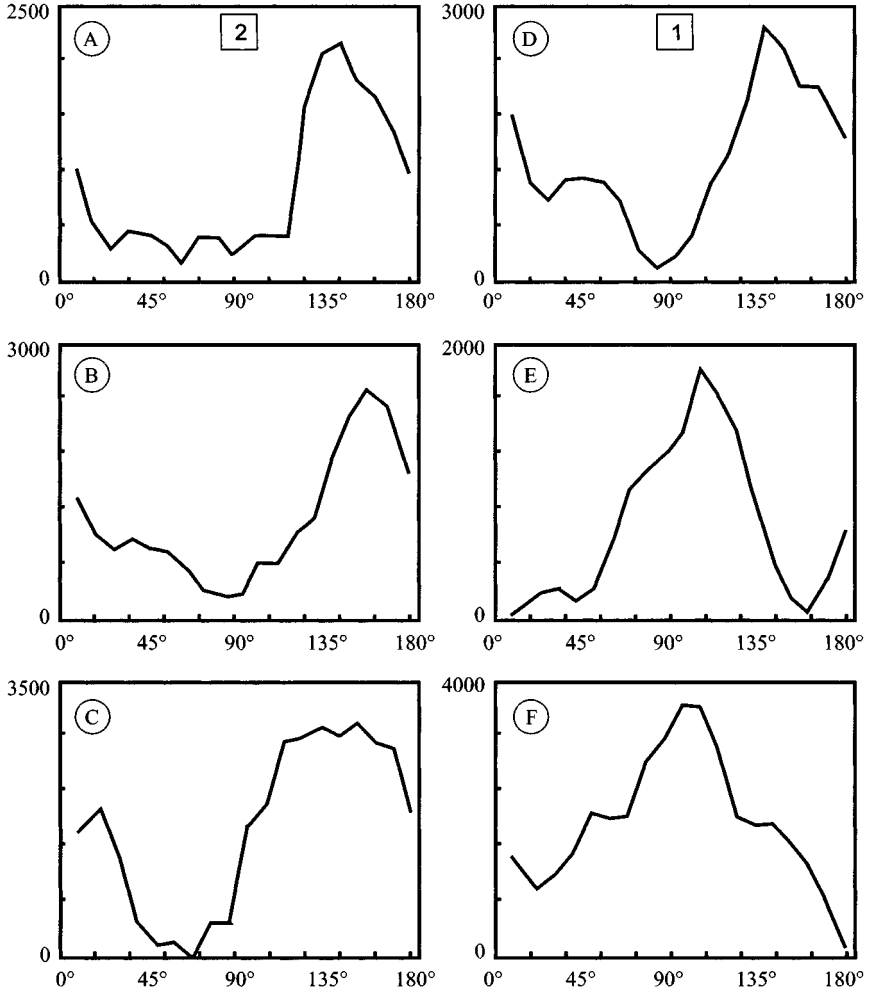

Figure 7.57 *Multi-azimuth analysis of the GPR response from pipes (800 MHz GPR data from sandbox). Columns* 1 *and* 2*:* (1) *Co-pole and* (2) *crosspole configuration.* (A)–(D) *air filled PVC pipe,* (B)–(E) *fresh water filled PVC pipe and* (C)–(F) *metallic pipe*

pre-stack domain and analysis and comparison of target response in the near and far offset range. The elusive nature of archaeological targets, whose dimensions, shape, orientation and physical properties are most often unknown and which are in many cases characterised by low contrast (such as mud-bricks in loams), requires a multi-fold approach to obtain the necessary constraints for a reliable sub-surface model.

7.9 Microwave tomography

Prof. Rocco Pierri, Angelo Liseno (Seconda Universitá di Napoli) and Raffaele Solimene (Universitá Mediterranea di Reggio Calabria)

7.9.1 Introduction

Ground penetrating radar generally produces an image which requires considerable skill, ability and experience in interpretation of data to detect and localise multiple targets, and this unavoidably introduces an element of subjectivity to the process.

The scientific community has endeavoured, during recent years, to develop techniques in order to make the analysis more 'objective'. The technique under consideration is the *tomographic approach* [76], which consists in determining an image of the spatial features of the object. This allows detection and localisation of the object as well as the ability to retrieve information about its shape, dielectric permittivity and conductivity. Tomographic techniques are fraught with the difficulty of processing the data to find a solution of the mathematical relationship between the quantities to plot (i.e. the dielectric permittivity and conductivity profiles) and the measurements of the scattered field [77].

This Section considers the problem that we will henceforth illustrate – that of reconstructing the electromagnetic properties of an object (permittivity and conductivity) from measurements of certain 'observable' quantities (the electromagnetic scattered field), which is also known as an *electromagnetic scattering inverse problem* [78]. Conceptually, this is not much different from other possible inverse problems arising, for instance, from the use of acoustic waves [78]. The only difference lies in the involved equations and in that, while our purpose is to 'see' the interior of an object through microwaves, in acoustics one aims at 'hearing' the characteristics of the scatterer under test [79].

Before proceeding further, it is necessary to note that the possibility of 'looking' at the interior of an object is based on the fact that the incident wave penetrates inside the object itself, collects information about its interior and finally is scattered, delivering such information to the sensors. Although the capability of penetrating objects is part of the features of microwaves, there exists, however, a class of 'impenetrable' objects. Rigorously speaking, 'impenetrable' are objects made up of perfect conductors, whereas objects made up of 'strong conductors' are 'almost impenetrable', in the sense that the impinging wave penetrates inside the object only to a shallow depth [80]. For such a class of objects, it is thus possible to reconstruct only the objects' shape [81, 82] but not to 'look' inside them. This is what happens at optical frequencies, when the impinging electromagnetic radiation does not significantly penetrate inside objects of which our eyes are capable of seeing only the shape but not the interior.

Nevertheless, in the following we refer to penetrable objects only and, therefore, to the reconstruction of their internal features, but we explicitly point out that it is possible to perform an analogous discussion also for impenetrable scatterers.

7.9.2 Formulation of the tomographic approach

To understandably illustrate the mathematical equations linking the field measurements to the quantities to be determined (that is, the spatial behaviour of permittivity

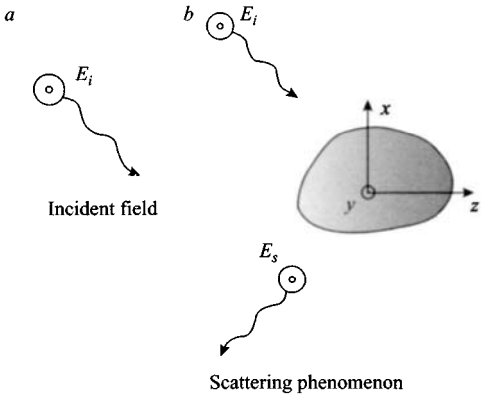

Figure 7.58 Representation of incident and scattered fields

and conductivity) and the difficulties affecting the research of their solution, we will refer to the (mathematically) simpler case when the object is not buried but stands alone in free space.

To this end, let us thus consider an electromagnetic field, which we call *incident*, propagating in free space (Figure 7.58*a*) when the object to test is initially absent. In such a situation, the incident field is the only solution of Maxwell's equations and propagates while nothing of physical interest happens [80]. If, on the contrary, the object is present, the result of the interaction between the incident field and the object itself is a *scattered field* (see Figure 7.58*b*), so that we can express the total field (that is, the field satisfying the Maxwell equations now in presence of the object) as the sum of the incident field plus the scattered one. Basically, the incident wave 'interrogates' the object, which in turn 'answers' through the scattered wave, which depends on the object's nature.

For the sake of simplicity, we will consider a 'two-dimensional' geometry, that is we will suppose the object to test to be infinite along the y-direction and with a permittivity dependent only on the x and z co-ordinates ($\varepsilon_{\text{eq}} = \varepsilon_{\text{eq}}(x, z)$). We will also assume the incident field radiated by time-harmonic infinitely long and isotropic current filaments parallel to the y-axis and having fixed frequency [81]. In these hypotheses, the equations governing the scattering phenomenon simplify from vectorial to scalar [83].

By considering the situation depicted in Figure 7.58*b*, the equations one arrives at are the following [83]:

$$E(x,z) = E_i(x,z) + k_b^2 \iint_{\Omega} H_0^{(2)}\left(k_S\sqrt{(x-x')^2+(z-z')^2}\right)\frac{(\varepsilon_{eq}(x',z')-\varepsilon_b)}{\varepsilon_b} \times E(x',z')\,dx'dz' \quad (x,z) \in \Omega \tag{7.106}$$

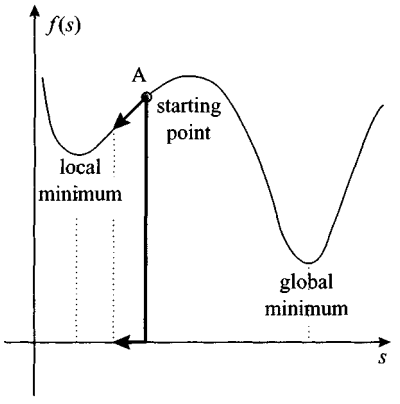

Figure 7.59 *A minimisation procedure starting from point A and moving according to the decrease of function f(s) converges in a local minimum*

$$E_s(x,z) = k_b^2 \iint_{\Omega} H_0^{(2)}\left(k_S\sqrt{(x-x')^2+(z-z')^2}\right)\frac{\left(\varepsilon_{\text{eq}}(x',z')-\varepsilon_b\right)}{\varepsilon_b} \times E(x',z')\,dx'dz' \quad (x,z)\in\Sigma \tag{7.107}$$

where $H_0^{(2)}(\cdot)$ is the Hankel function of zero order and the second kind, $E_s = E_s(x,z)$ is the measured scattered field, ε_b and μ are the dielectric permittivity and magnetic permeability of the homogeneous host medium, respectively, $k_b = \omega\sqrt{\varepsilon_b\mu}$, $\varepsilon_{\text{eq}} = \varepsilon_{\text{eq}}(x,z) = \varepsilon(x,z) - j(\sigma(x,z)/\omega)$ is the *equivalent permittivity* we are searching for, ε and σ are the object's dielectric permittivity and conductivity, respectively, $\omega = 2\pi f$, f being the working frequency, $E = E(x,z)$ is the total field inside the object and $E_i = E_i(x,z)$ is the incident field. The first equation holds on the measurement points on Σ and the second inside the object enclosed in the domain Ω. The unknown of these equations is the function $\varepsilon_{\text{eq}}(x,z)$, whereas the data are represented by E_s.

Imaging, or tomographic reconstruction of the object, amounts to solving the above equations for $\varepsilon_{\text{eq}}(x,z)$ when E_s is known [84].

One of the main difficulties in the resolution of (7.106) and (7.107) may be ascribed to the nonlinearity of the relationship between E_s and $\varepsilon_{\text{eq}}(x,z)$. This entails that, when the solution is searched for as the equivalent permittivity minimising a cost function accounting for the 'difference' between the measured scattered field and the theoretically predicted one, owing to the nonlinearity of the unknown-data link, such a cost function could exhibit local minima besides the global one. A local minimum could be mistaken, by a minimisation algorithm, for the global one and thus could lead to a 'false solution' [85] (see Figure 7.59).

A way to overcome the drawback introduced by nonlinearity is that of employing approximations linearising the relationship between the measurements and the unknown permittivity function (of course, if possible). In particular, if we know a priori that the permittivity of the object under test is sufficiently close to that of

free space, the object is 'small' [86] (where 'small' in electromagnetic applications means with respect to the working wavelength λ) and the permittivity has smooth rates of variation [87], then we can deal with it as a 'weak scatterer', in the sense that, from the field's point of view, the presence of the object makes just a little difference with respect to the case in which the object is absent. A *visible* example of a weak scatterer is a window-pane: indeed, because of its permittivity close to that of air, it introduces just a little perturbation on the propagation of sunbeams which, thus, can enter almost undisturbed inside our houses. For a weak scatterer it is possible to approximate the total field E inside the object as the incident one, thus neglecting the scattered field inside the object itself. Such approximation is known as the 'Born approximation' (Born and Wolf [86], Brancaccio *et al.* [87] and Slaney *et al.* [88]). Incidentally, a different linearising approximation of interest in sub-surface applications is the 'distorted Born' approximation [83–89]. It holds when the object, buried beneath the earth's surface, has a permittivity close to that of the host medium. In this case, the field inside the object can be approximated with the field in the host medium in the absence of the object, and thus depends on the medium's permittivity itself.

If we suppose to measure the scattered field *far enough* from the object, i.e. some wavelengths off the object, then the Born approximation allows us to extract from the scattered field information on the Fourier transform of the unknown equivalent permittivity. Accordingly, the objects that can be 'correctly reconstructed' are those which are not filtered out by the limited performances of the employed tomographic reconstruction procedure, as will be more clear in the sequel. Furthermore, a parameter worth analysing when evaluating the performances of a reconstruction algorithm is *resolution* [90, 91], i.e. the capability to distinguish nearby objects.

Investigating the filtering undergone by the unknown equivalent permittivity and/or the resolution limits is of fundamental importance to appropriately interpret the outcome of reconstructions. What would happen indeed if, having, for instance, no idea of resolution, two landmines were mistaken as one? Knowing resolution would have put us on our guard against the presence of two landmines!

In the following Sections, we present some case studies and also describe how the parameters of the measurement configuration help in determining spatial filtering and resolution limits.

7.9.3 Key point of imaging: spatial filtering

Let us begin by considering the case in which the object is embedded in free space and suppose that the current filament can assume positions on a circle Σ surrounding the object as in Figure 7.60*a*. We measure the scattered field on Σ for each position assumed by the illuminating current filament on Σ itself. We will assume the circle's radius to be great enough such that the transient phenomena are reduced. In this case, it can be shown that the scattered field measurements are related to those Fourier harmonics of the function $(\varepsilon_{eq}(x, z) - \varepsilon_0)/\varepsilon_0$ contained inside a disk D_1 of radius $2k_0$, where $k_0 = 2\pi/\lambda$ is the free space wavenumber and ε_0 is the free space dielectric permittivity (see Figure 7.60*b*). At this point, one could observe that, since

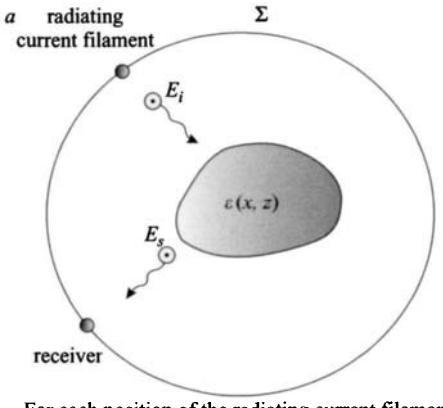

For each position of the radiating current filament, the scattered field is measured over all Σ

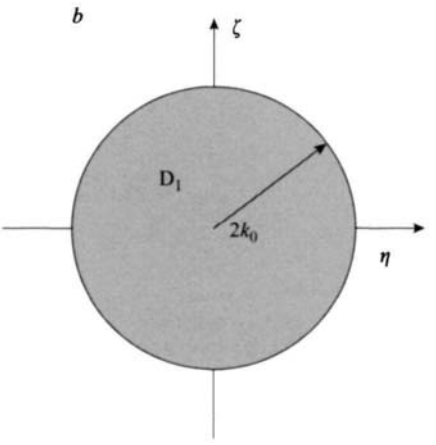

Spectral coverage for the measurement configuration in Figure 7.60*a*. η and ζ are the conjugate variables of x and z, respectively

Figure 7.60 Spatial imaging configuration

the scattered field is actually the Fourier transform of $(\varepsilon_{eq}(x, z) - \varepsilon_0)/\varepsilon_0$ having a compact support (indeed, $(\varepsilon_{eq}(x, z) - \varepsilon_0)/\varepsilon_0$ is nonzero only for points inside the object, but vanishes outside of it), such a transform is analytical [78], and thus can be extrapolated outside the disk D_1. It seems, thus, to be possible to know the entire Fourier spectrum of the unknown permittivity function. Indeed, one could proceed by calculating successive derivatives of the Fourier transform for some point inside D_1 and afterwards form a Taylor series. Unfortunately, the analytical extrapolation is an *unstable* procedure. That is, 'small' errors on the spectrum inside D_1, due to the unavoidable presence of noise, could lead to 'large' errors on the prolonged Fourier transform, this last becoming totally unreliable. The result is that the only information about the unknown permittivity function one can extract from these measurements regards approximately just the Fourier harmonics of the permittivity contained inside the above mentioned disk, whereas information referring to the Fourier harmonics contained outside such a disk cannot be restored [92, 93].

In other words, because of the presence of noise on data, approximately no information about the Fourier harmonics outside D_1 can be extrapolated from the knowledge of the spectrum inside the circle D_1 itself. Accordingly, if the object's permittivity function has a significant harmonic content inside that circle, the permittivity function will be 'well reconstructed'. If, on the contrary, the unknown permittivity has a significant harmonic content also outside the circle, then only a lowpass version of it will be restored. Moreover, as long as the frequency increases, the extension of the disk containing the retrievable Fourier harmonics of the permittivity function enlarges since its radius $2k_0$ grows with the working frequency. Therefore, the use of higher frequencies would be favourable from this point of view. Unfortunately,

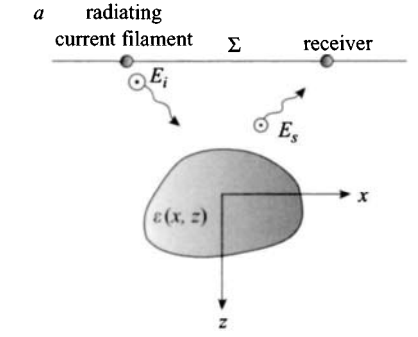

Reflection measurement configuration

Spectral coverage for the measurement configuration in Figure 7.61*a*. η and ζ are the conjugate variables of x and z, respectively

Figure 7.61 Reflection measurement configuration

when employing higher frequencies one should take account of the fact that this is in conflict with the validity of the Born approximation which, as mentioned above, requires the object to be 'small' with respect to the working wavelength.

In the above examined measurement configuration, the object was illuminated all around and the scattered field measurements performed, likewise, all around for each position of the radiating current filament. We now approach a reflection measurement configuration, of major interest in sub-surface applications – that is, suppose we illuminate the object only from one side and measure the scattered field by the same side (see Figure 7.61*a*). The measurement configuration we are going to refer to is depicted in Figure 7.61*a*, where transmitters and receivers move across a straight infinitely long line. It is noteworthy that such a measurement configuration is equivalent to that in which the measurement domain is a semicircle. Nevertheless, a straight line has been chosen since it better matches the geometry of a planar air–soil interface, as we will see in the following. We expect further limitations on the recoverable spectrum as compared to those arising in the previous case since a part of the information collected in the former measurement configuration is now no longer exploited. Indeed, in this case the recoverable Fourier spectrum of the permittivity function reduces to the domain D_2 as depicted in Figure 7.61*b*, where some 'holes' in the spectral coverage, as compared with D_1, now appear. In particular, if we define as 'depth' the direction orthogonal to the measurement line, the permittivity function now approximately undergoes a bandpass spatial filtering in depth and a lowpass spatial filtering along the 'transversal' direction, i.e. along the direction parallel to that of the measurement line. Note how, due to the presence of 'spectral holes' depicted in Figure 7.61*b* [89], the use of lower frequencies would enable 'filling up' of the holes. When many sets of measurements at different frequencies are used, the extent of the holes depends on the adopted lower frequency. Finally, as in the previous case, the use of a higher frequency improves the extent of the domain D_2 still further.

So far, we have assumed the object to be embedded in free space. However, situations of interest in sub-surface prospecting require the unknown object to be buried in the ground. To model such a situation, we will suppose the (two-dimensional) space

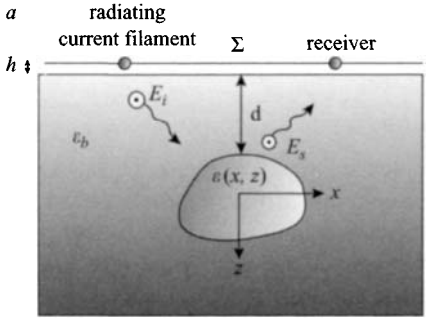

Sub-surface sensing 'reflection measurement configuration'

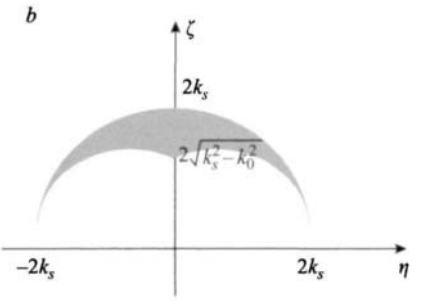

Spectral coverage for the measurement configuration in Figure 7.62*a*. η and ζ are the conjugate variables of x and z, respectively

Figure 7.62 Sub-surface reflection measurement configuration

to be divided into two half-spaces separated by a plane interface (Figure 7.62*a*). The upper half-space, representing the region in which the sensors lie, is free space, whereas the lower half-space, that is the region of space in which the object is embedded, is assumed to consist of a homogeneous and lossless medium having relative dielectric permittivity ε_b. From a geometrical point of view, the measurement configuration depicted in Figure 7.62*a* is analogous to that above described, with the difference that now the sensors and the object are separated by the air–soil interface [94]. In contrast with the previous cases, we will now employ the distorted Born approximation to linearise the unknown-data relationship. When the measurement line lies over the air–soil interface ($h = 0$, see Figure 7.62*a*), i.e. the sensors are placed over the ground, and the object is buried as deep as at least the wavelength λ_b in the lower half-space (that is, $d > \lambda_b$; see Figure 7.62*a*), then the spectral coverage is the same as that in Figure 7.61*b*, provided we replace k_0 with $k_b = \omega\sqrt{\varepsilon_b \mu_0}$ [89], and the same considerations on the spatial filtering undergone by the permittivity function and on the possibility of extending the covered domain by means of other frequencies still hold. Note that this result is the one we would obtain by also assuming the upper half-space filled by a homogeneous medium having dielectric permittivity equal to ε_b. On the contrary, when the quota of the measurement line is greater than some free-space wavelengths ($h > \lambda$), then, as may be appreciated by Figure 7.62*b*, the spectrum undergoes a shrink [87]. In particular, the entity of the shrink is enforced as the permittivity ε_b of the lower half-space increases. Indeed, the term $2\sqrt{k_b^2 - k_0^2}$ tends to $2k_b$ as ε_b tends to infinity. This is due to the fact that, owing to the *total reflection phenomenon*, some of the plane waves propagating from the object towards the air–soil interface become evanescent in the upper half-space. These evanescent waves, by decaying exponentially fast while going off from the air–soil interface, reach the measurement line at a negligible level so that the information carried by the corresponding plane wave propagating in the lower half-space is unavoidably lost. Moreover, as the permittivity ε_b increases, the total reflection

phenomenon involves an even wider set of directions of propagation, thus justifying the increase of the shrink effect.

7.9.4 Key point of imaging: resolution limits

In the previous Section, the influence the measurement configuration has on the performances of the reconstruction algorithm in terms of filtering undergone by the permittivity function has been described and a brief outline on the use of multiple frequencies has been given. Also, we acknowledge that actual measurement configurations require the measurement line to be finite.

The performances of the reconstruction procedure can be given in terms of the *achievable resolution limits* [90], that is in terms of the smallest detail of the unknown permittivity function the reconstruction algorithm is able to distinguish.

The aim of this Section is to analyse how the parameters of the measurement configuration, that is the finiteness of the extent of the measurement line and the range of the employed frequencies, affect the performances of the reconstruction algorithm. Our point of view will be focused on the achievable spatial resolution while reconstructing the permittivity function rather than on the spatial filtering it undergoes as done here above. Moreover, we will pursue this goal by referring to simplified situations. In particular, we will assume a finite measurement line and suppose the object to be a dielectric strip embedded in free space and parallel or orthogonal to the measurement line itself (see Figure 7.63*a*, *b*).

This will allow us to study *transversal resolution* and *depth resolution* separately. The measurement line will be assumed to be located in the *Fresnel-paraxial zone* [86]

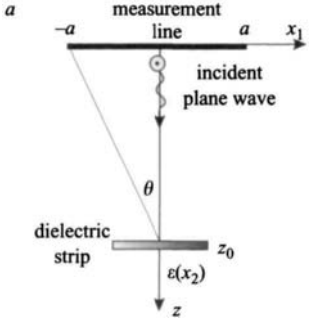

Study of *transversal resolution*: the case of a dielectric strip parallel to the measurement line

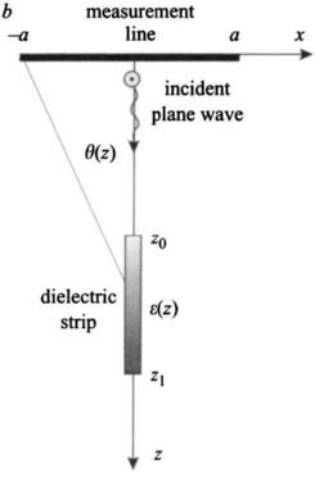

Study of *depth resolution*: the case of dielectric strip orthogonal to the measurement line

Figure 7.63 Transversal and depth resolution

with respect to the scattering object, and the Born approximation will once more be assumed. At variance with the cases examined in the previous Section, we assume the impinging field to be a plane wave with fixed angle of incidence.

Let us consider first the case depicted in Figure 7.63*a* in which the dielectric strip is parallel to the measurement line. It can be shown [95] that, if the incident field is at a fixed frequency, the transversal resolution limits Δx while reconstructing the permittivity function $\varepsilon(x)$ are given by

$$\Delta x = \frac{z_0 \lambda}{2a} \tag{7.108}$$

In other words, if the dielectric strip were composed of only two point scatterers located at x_1 and x_2, as depicted in Figure 7.63*a*, then, following the reconstruction procedure, it would be possible to distinguish them if they were far more than the transversal resolution limits Δx.

In the hypothesis of small *divergence angle* θ, which is reasonable in the Fresnel-paraxial zone, the ratio a/z_0 can be approximated by θ, and (7.108) recast as

$$\Delta x \cong \frac{\lambda}{2\theta} \tag{7.109}$$

As can be seen, resolution improves, that is Δx decreases, as the divergence angle θ enlarges. This is consistent with the fact that, as θ enlarges, the extent of the measurement line increases, thus allowing collection of even 'greater amounts of information' about the unknown permittivity function. Note also that the minimum separation by which two scattering points must have to be distinguished does not depend on the position of the scattering points themselves. This can be explained by observing that, in the hypothesis of small divergence angle, the points of the dielectric strip are 'observed' by the sensors on the measurement line under almost the same 'observation angles', as is clarified by Figure 7.63*a*.

Let us now turn to consider the case depicted in Figure 7.63*b*, where the dielectric strip is orthogonal to the measurement line. It can be shown [96] that, if the incident field is again at a fixed frequency, depth resolution limits Δz while reconstructing the permittivity function $\varepsilon(z)$ are given by

$$\Delta z = \frac{2\lambda z^2}{a^2 - 2\lambda z} \tag{7.110}$$

As may be seen, contrary to the case when the dielectric strip is parallel to the measurement line, depth resolution is now no more uniform along the strip since Δz depends on z. In particular, resolution degrades, i.e. Δz increases, as z increases. In other words, the spacing by which two point scatterers (see Figure 7.63*b*) must have to be distinguished by the reconstruction procedure depends on the positions assumed by the point scatterers themselves. In particular, the deeper the location of the point scatterers, the greater the spacing. If we rearrange (7.110) in terms of divergence

angle as follows (see Figure 7.63*b*),

$$\Delta z = \frac{2\lambda/\theta(z)^2}{a^2 - 2(\lambda/a)/\theta(z)} \tag{7.111}$$

then we can explain the worsening in depth of resolution by observing that, as long as a point scatterer is deeper located, it is 'observed' by the sensors under narrower sets of angles (see Figure 7.63*b*). Accordingly, as long as a point scatterer is more deeply located, the sensors on the measurement line collect even 'lower amounts of information' about it. Roughly speaking, this is what happens to our own eyes: while objects are far away from us we cannot see even larger details.

We conclude this 'running shot' on resolution limits by putting a question: what if we employ a set of plane waves having frequencies inside $[f_{\min}, f_{\max}]$ [97], that is we adopt a 'multi-frequency' illumination? It can be seen [98] that the dependence on depth of resolution can be mitigated by a multi-frequency strategy and depth resolution improved at the same time. In particular, it can be shown that in such a case depth resolution becomes almost independent of z and is given approximately by

$$\Delta z = \frac{\lambda_{\min}\lambda_{\max}}{2(\lambda_{\max} - \lambda_{\min})} \tag{7.112}$$

where $\lambda_{\max}$ and $\lambda_{\min}$ are the minimum and maximum wavelengths, respectively, corresponding to the maximum and minimum exploited frequencies $f_{\min}$ and $f_{\max}$, respectively. Incidentally, note that, through a multi-frequency illumination, depth resolution (7.112) improves as $\lambda_{\min}$ diminishes, whereas, for a fixed $\lambda_{\min}$, it approaches $\lambda_{\min}/2$ as $\lambda_{\max}$ tends to infinity. Equation (7.112) can also be rewritten as

$$\Delta z = \frac{\lambda_c}{2B_r} \tag{7.113}$$

where B_r is the fractional bandwidth [99], defined as $(f_{\max} - f_{\min})/2$, f_c is the *mean frequency* given by $(f_{\max} + f_{\min})/2$, and λ_c is the wavelength corresponding to the mean frequency.

Finally, when an object having permittivity varying both with x and with z is considered, within the above assumption (Fresnel-paraxial approximation and multi-frequency illumination) the above estimates for transverse and depth resolution still hold [100].

We end this Chapter by showing some tomographic reconstruction as reported in Figure 7.64.

In particular, Figure 7.64 refers to the measurement configuration having $\lambda_{\max} = 1.5\lambda_{\min}$ and $a = 35\lambda_{\min}$. Furthermore, we assume the scattering objects belonging to the rectangular investigation domain $\Omega = [-5\lambda_{\min}, 5\lambda_{\min}] \times [70\lambda_{\min}, 85\lambda_{\min}]$. Figure 7.64 shows the tomographic reconstructions of two pulse objects located at different depths and with different separation distances. First note that a pulse object is reconstructed as a spot whose size is a measure of the achievable resolution limits. Moreover, the two objects appear well distinct down to a depth separation of $1.5\lambda_{\min}$, which is the depth resolution estimate returned by (7.113).

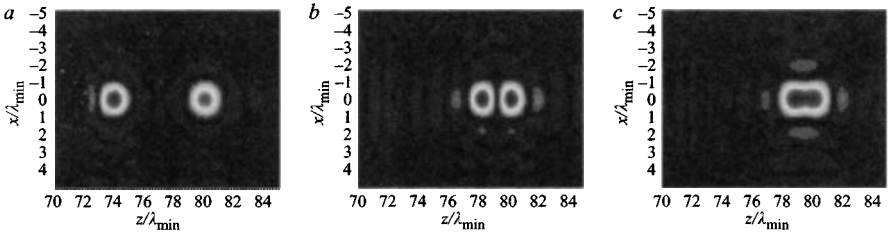

Figure 7.64 *Reconstruction of two pulse objects at different separation distance: (a) first object located in $(0, 74\lambda_{min})$ and second object located in $(0, 80\lambda_{min})$; (b) first object located in $(0, 78.5\lambda_{min})$ and second object located in $(0, 80\lambda_{min})$; (c) first object located in $(0, 79\lambda_{min})$ and second object located in $(0, 80\lambda_{min})$*

7.10 Minimising clutter

7.10.1 *Reduction of unwanted diffractions and reflections from above-surface objects*

Dr Jan van der Kruk

During a GPR survey, special attention must be paid to objects that are present above the earth's surface. Due to the low losses in air and the high wave speed, reflections from above the surface can obscure the sub-surface data and make the interpretation of GPR data a difficult task. The amplitude of these unwanted reflections strongly depends on the radiation characteristics (amplitude and polarisation) of the emitted GPR signals. In Figure 7.65, the amplitude and polarisation of the far-field radiation patterns generated by a dipole antenna [101] are compared with the results for the total field, which are obtained by evaluating the integral expressions. Although the far-field radiation pattern is a reasonable approximation to that of the total field, there is a significant error near the critical angle θ_c and near the interface.

The vertically polarised total-field has a relatively large amplitude near the interface in the upper half-space in the E-plane, whereas the horizontally polarised total-field has a small amplitude near the interface in the H-plane (Figure 7.65). A consequence of these radiation characteristics is that strong reflections arise from vertical-standing objects in the E-plane of the antennas. A typical example of above-surface reflections is shown in Figure 7.66. The measurements were carried out with the trees present in the E-plane of both antennas. The large hyperbolas with gently dipping tails are diffractions from the trees, whereas the small hyperbolas with steeply dipping tails are diffractions from pipes present in the sub-surface. The CMP results depicted in Figure 7.66*c* show that events 3 and 4 have small moveouts, indicating that they have travelled with the speed of light.

It is expected that the amplitudes of diffractions from the same trees would be markedly smaller when they are present in the H-plane of the antennas, because the polarisation of the electric field is then perpendicular to them and amplitudes near the interface in the H-plane are smaller than those in the E-plane. The results

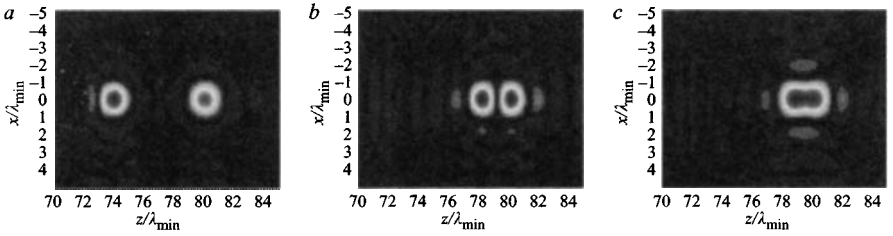

Figure 7.64 *Reconstruction of two pulse objects at different separation distance: (a) first object located in $(0, 74\lambda_{min})$ and second object located in $(0, 80\lambda_{min})$; (b) first object located in $(0, 78.5\lambda_{min})$ and second object located in $(0, 80\lambda_{min})$; (c) first object located in $(0, 79\lambda_{min})$ and second object located in $(0, 80\lambda_{min})$*

7.10 Minimising clutter

7.10.1 *Reduction of unwanted diffractions and reflections from above-surface objects*

Dr Jan van der Kruk

During a GPR survey, special attention must be paid to objects that are present above the earth's surface. Due to the low losses in air and the high wave speed, reflections from above the surface can obscure the sub-surface data and make the interpretation of GPR data a difficult task. The amplitude of these unwanted reflections strongly depends on the radiation characteristics (amplitude and polarisation) of the emitted GPR signals. In Figure 7.65, the amplitude and polarisation of the far-field radiation patterns generated by a dipole antenna [101] are compared with the results for the total field, which are obtained by evaluating the integral expressions. Although the far-field radiation pattern is a reasonable approximation to that of the total field, there is a significant error near the critical angle θ_c and near the interface.

The vertically polarised total-field has a relatively large amplitude near the interface in the upper half-space in the E-plane, whereas the horizontally polarised total-field has a small amplitude near the interface in the H-plane (Figure 7.65). A consequence of these radiation characteristics is that strong reflections arise from vertical-standing objects in the E-plane of the antennas. A typical example of above-surface reflections is shown in Figure 7.66. The measurements were carried out with the trees present in the E-plane of both antennas. The large hyperbolas with gently dipping tails are diffractions from the trees, whereas the small hyperbolas with steeply dipping tails are diffractions from pipes present in the sub-surface. The CMP results depicted in Figure 7.66*c* show that events 3 and 4 have small moveouts, indicating that they have travelled with the speed of light.

It is expected that the amplitudes of diffractions from the same trees would be markedly smaller when they are present in the H-plane of the antennas, because the polarisation of the electric field is then perpendicular to them and amplitudes near the interface in the H-plane are smaller than those in the E-plane. The results

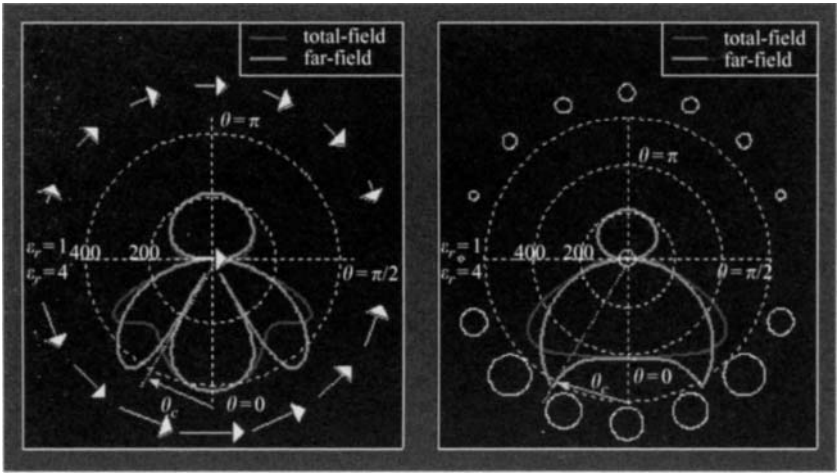

Figure 7.65 *Comparison of total-field and far-field amplitudes of the spherical electric field components E_θ in the E-plane (left) and E_ϕ in the H-plane (right) at a distance of 1 m from a 500 MHz electric dipole*
Polarisation directions are indicated by arrows (left) and circles (right)

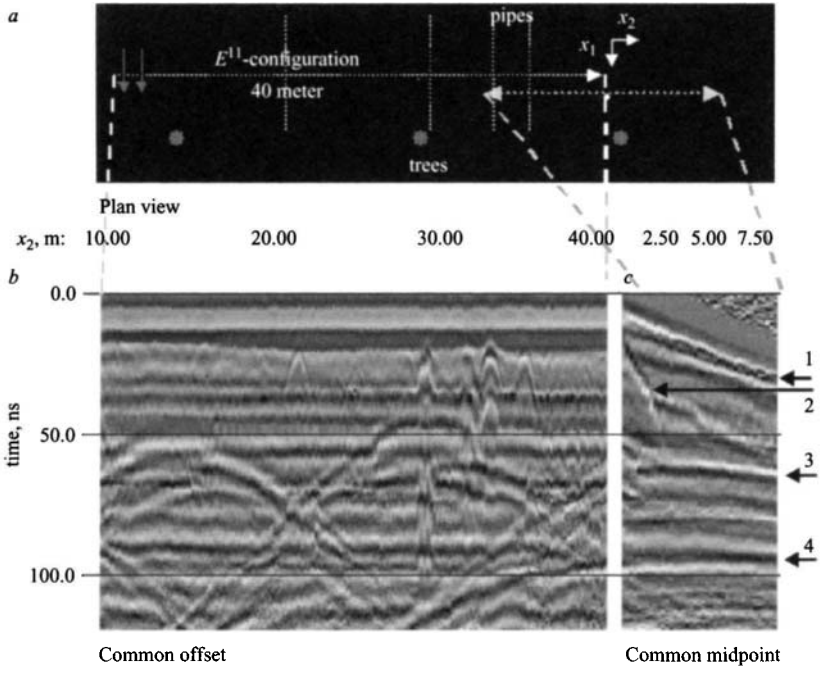

Figure 7.66 *(a) Plan view of survey in Delft with corresponding (b) common-offset results and (c) common-midpoint results*

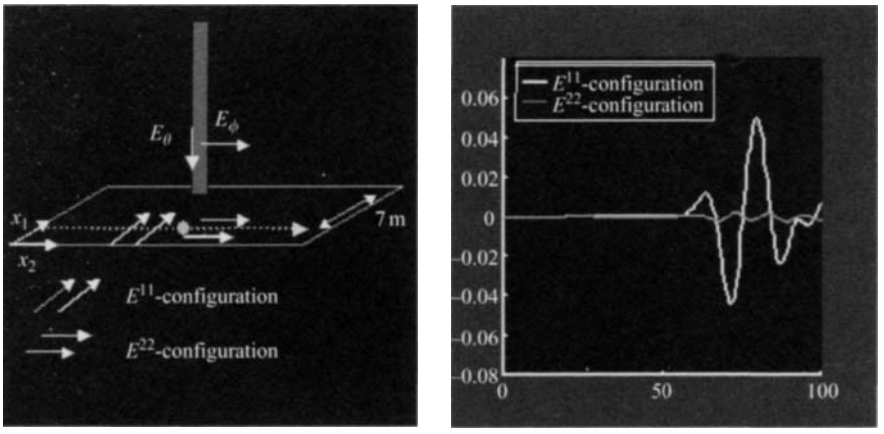

Figure 7.67 *Vertically oriented object present above the surface with corresponding calculated reflections for the E^{11}- and E^{22}-configuration*
Dot in left figure identifies observation point of synthetic data shown on the right side

of numerical modelling using a three-dimensional modelling package [102] confirm these expectations. In Figure 7.67, the diffractions from a 'tree' are depicted for the perpendicular-broadside (E^{11}) and parallel-broadside (E^{22}) configurations, calculated for a location 7 m from the tree. The tree was present in the E-plane of the E^{11}-configuration. It returned a diffraction with an amplitude that was 21 times larger than that for the E^{22}-configuration. Similar analyses have been carried out for a range of objects [103].

In conclusion, to reduce unwanted above-surface diffractions and reflections, the antenna configuration should be chosen such that the emitted electric field is perpendicularly polarised with respect to the objects that are present along the survey line: vertical objects should be present in the H-plane and horizontal objects should be present in the E-plane whenever possible.

7.10.2 *Clutter in radar data caused by reflections from external anomalies*

Dr Vega Pérez Gracia

This study was partially supported by the 'Ministerio de Ciencia y Tecnología' and by FEDER (research projects number REN 2000-1740-C05-01 RIES and REN 2001-2418-C04-01). Additional support was give by the Civil Engineering School (ETSECCPB).

Clutter in GPR data produces confused radar records. Clutter is caused by numerous effects, multiple reflections, reverberation, coupling signals, external reflections, etc. The clutter caused by external reflections appears when reflected signals coming from the outside of the target zone arrive at the antenna. Clutter mainly affects the

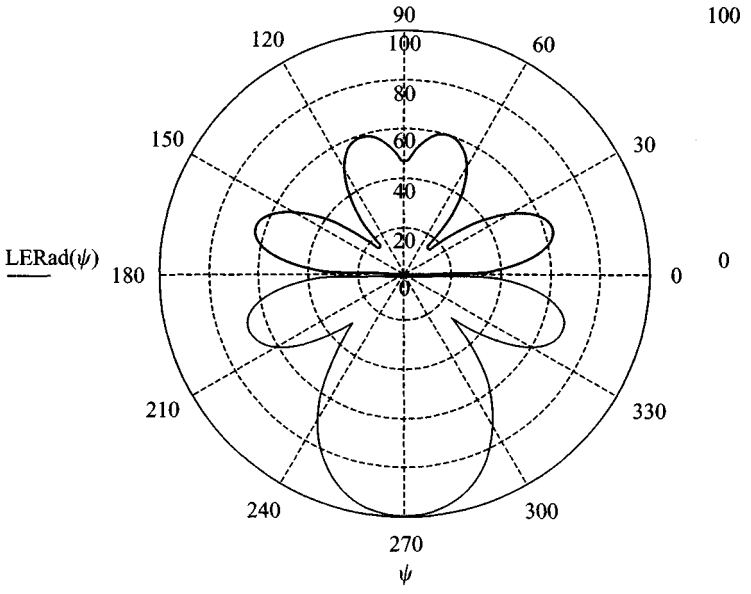

Figure 7.68 Generic antenna radiation pattern showing main lobe, sidelobes and back lobes

GPR data when the antenna used is nonshielded, and when data acquisition conditions encompass high reflective surfaces outside the target area. Those surfaces could be walls, roofs, etc. The main cause of clutter is a lack of directivity of the antenna. Generic antennas have a main lobe, sidelobes and back lobes as shown in Figure 7.68.

The signals arising from the different reflections are superposed on one another, and the GPR record becomes confused. Where the reflections are caused by the roof of a building in the back lobe of an antenna, it can be readily understood that the propagation velocity is greater than in the material under investigation, the signal levels may be low but can often be similar to that of the target by virtue of the lower attenuation in the air and the range to the clutter reflections can be much greater than that to the target. It is important to identify the anomalies caused by this kind of clutter in order to interpret the radar data correctly.

We performed several experiments in order to analyse clutter and to identify it in the radar data. The first one was carried out with a 100 MHz centre frequency antenna, during the study of the Cathedral of Valencia (see Figure 7.69). The range used during that experiment was 300 ns. The top parts of the cathedral domes are constructed of iron and are about 15 and 20 m from the floor. The two-way travel time of the reflections from those vaults is about 100 and 135 ns when the antenna is placed on the floor. Figure 7.69 is a photograph of the main nave. The downward looking radar profile crosses this nave, from one lateral chapel to the chapel placed in front. Figure 7.70 shows the radar data obtained and the interpretation of that data.

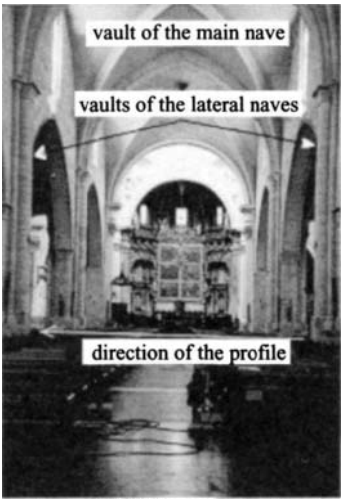

Figure 7.69 *Vault of main nave, where reflection that causes image on GPR record was produced*

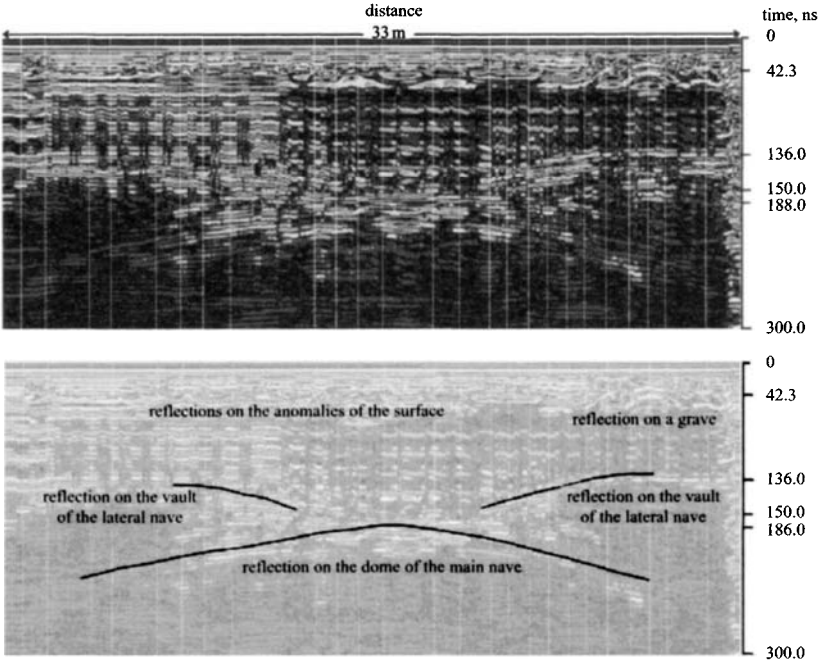

Figure 7.70 *Radar data obtained by using a 300 ns range, and interpretation of the events recorded*
External reflections cause the most visible images

The GPR data of Figure 7.70 shows clearly the reflections on the central vault and lateral vaults (which are lower than the central one).

To ensure that the external clutter is acquired, the range of the data acquisition is set to 300 ns, because the expected signals will arrive at about 150 ns (two-way travel time).

The central part of the vault of the Cathedral is metal. The high reflection coefficient of this material produces the images of Figure 7.70, where strong hyperbolic reflections are recorded. The two-way travel time of the central event in Figure 7.70 is about 150 ns. Using the wave velocity in the air (about 30 cm/ns), this time corresponds to a distance of 18 m, which is the range to this clutter source.

Those reflections could be identified as reflections produced by features within the medium, and this causes difficulty in interpreting the GPR data. A superficial interpretation of Figure 7.70 using an average velocity about 7.5 cm/ns would place an anomaly at 5.6 m depth. The mix of reflections coming from different media, in the same GPR data, is the cause of confusion.

To avoid these problems, an accurate planning of the radar data acquisition must be carried out taking into account the characteristics of the antennas before the field work. In addition, during the radar data acquisition, it is necessary to annotate the distances to the external anomalies, which could cause this kind of reflection. It is important to take note of the height of the roofs when works are carried out in buildings. Alternatively, it is possible to cover the top surface of the antenna with absorbing material to eliminate the unwanted clutter. Such material, known as radar absorbing material (RAM), is built into screened antennas.

The clutter reflection under consideration in the GPR data in Figure 7.69, corresponds to the anomaly. The spatial distribution of the reflection (hyperbolic) is due to the survey path of the antenna (see Figure 7.71). The metal on the top of the vault produces the strongest reflection. The two-way travel time depends on the distance to the anomaly, which varies during the antenna survey path.

The main reflections in the GPR record could be represented on a graph in order to analyse this clutter. As an example, the reflection of Figure 7.71 could be represented using a 150 ns two-way travel time and a medium velocity of 30 cm/ns. This curve and the curve obtained using a 150 ns two-way travel time and 7.5 cm/ns velocity are both compared (Figure 7.72). The curve obtained in the first case is similar to the recorded reflection, while the second curve is quite different. Then, the radar reflection on Figure 7.70 is associated with an external reflection.

This example was about the clutter caused in elements in the back lobe of the antenna. It is also necessary to consider the lateral elements that could introduce similar clutter in the GPR data.

In the example shown in Figure 7.73, the signal at the left of the image is caused by the reflection of the energy on a metallic ventilator. The metallic ventilator was in a tunnel. This radar data was obtained during the study of a tunnel (see Figure 7.73). The aim of that study was to locate structural problems, water filtrations and voids in the rock massif. The antenna used to perform this study had a 500 MHz centre frequency. The range of the data acquisition was 100 ns. Figure 7.74 shows the radar

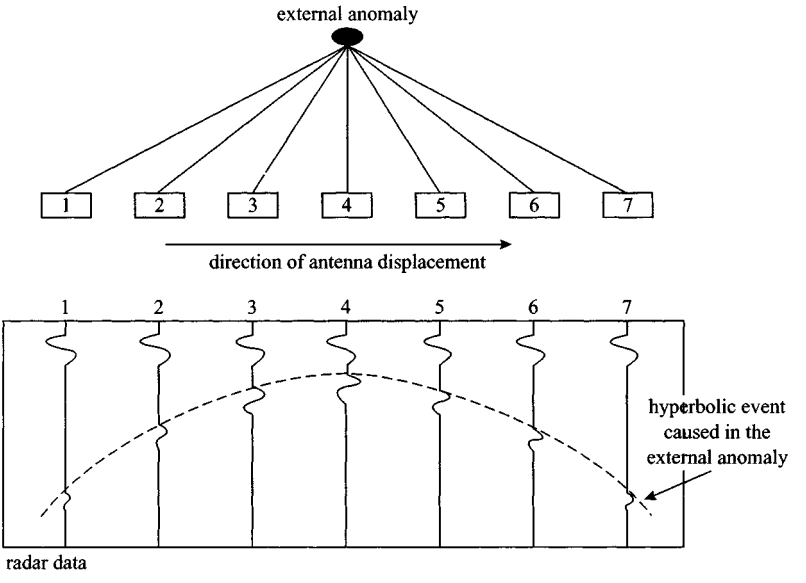

Figure 7.71 *Hyperbolic anomaly caused by reflection on an external anomaly*
This record is superimposed on the data coming to the medium

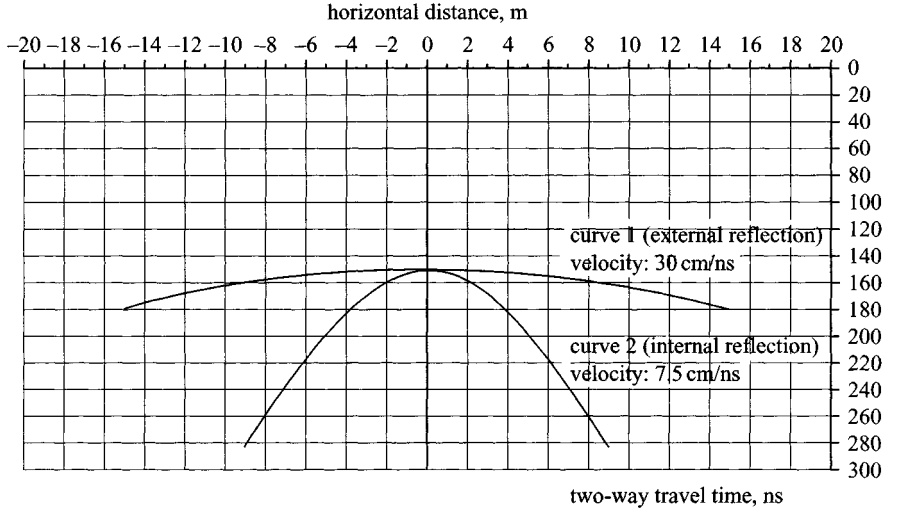

Figure 7.72 *Curves obtained for 30 cm/ns (air velocity) and 7.5 cm/ns (medium velocity)*
The first curve is similar to the central reflection in Figure 7.70

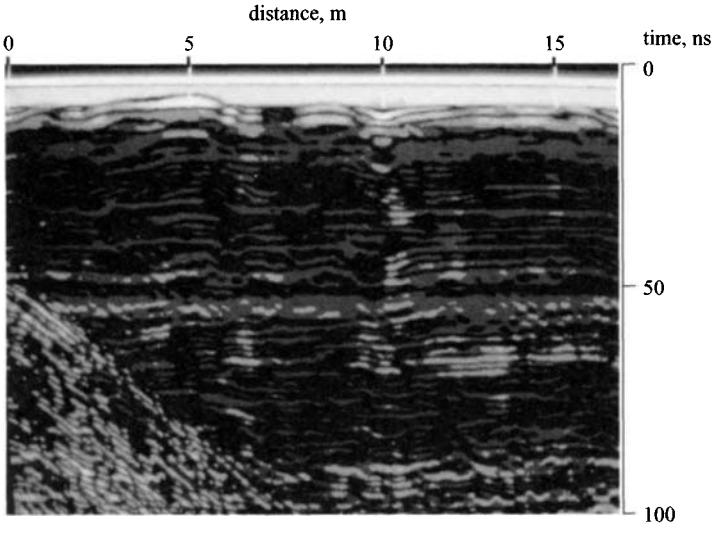

Figure 7.73 *Radar data obtained during the study of a tunnel*
The record contains the clutter produced in anomalous elements outside the studied medium

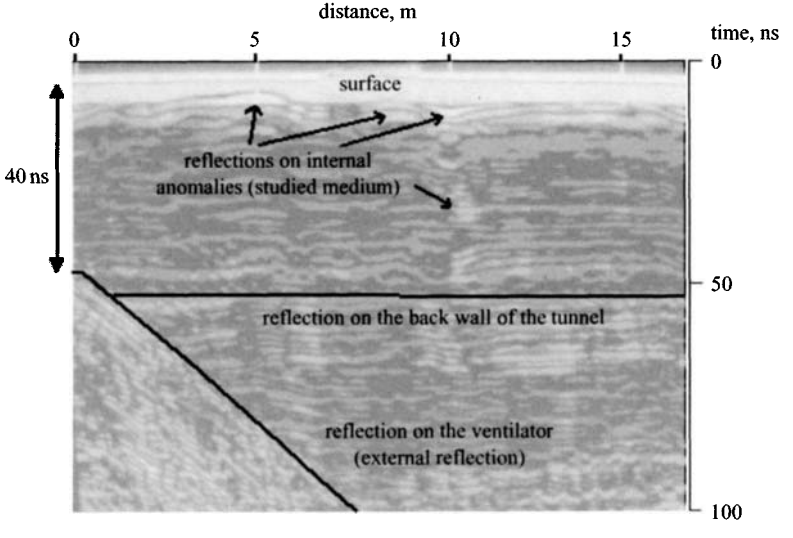

Figure 7.74 *Interpretation of the radar data shown in Figure 7.73*

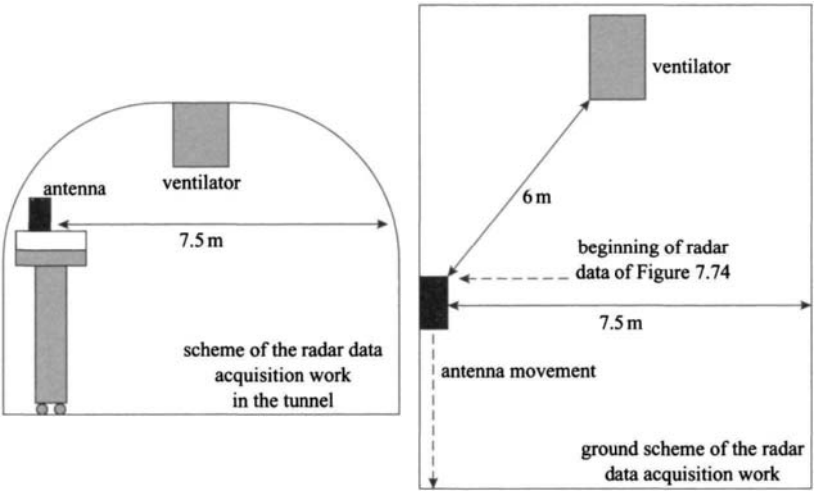

Figure 7.75 *Scheme of the GPR data acquisition work*
The scheme shows the position of the external elements and the position of the antenna

data interpretation of Figure 7.73. Figure 7.75 shows the scheme of the radar data acquisition.

The antenna radiates the energy mainly into the medium, but it also radiates a small part of this energy laterally in the sidelobes. This lateral radiated energy is the cause of the recorded clutter. The high reflection coefficient of the metallic ventilator, and the low loss energy during the wave propagation in air, causes this clutter.

The minimum distance between the antenna and the ventilator was 6 m, which corresponds to 40 ns (two-way travel time). In Figure 7.74 that clutter appears at this expected time. The reflection from the ventilator appears linear due to the relative survey path of the antenna.

In addition, the reflection on the back surface of the tunnel (Figure 7.74) is recorded. It is a reflection constant during all the record, because the distance between both walls of the tunnel ($\sim$7.5 m) is constant.

To interpret the radar data, first we design the clutter reflections in a graph in order to identify them. Figure 7.76 shows those graphs. The obtained curves correspond to the GPR clutter data.

It is important to identify the sources of clutter in order to perform an accurate radar data interpretation. When the external anomalies are known, it is possible to graph and to analyse the expected clutter, and to compare the graph results, which are estimated using the wave propagation velocity in the air, with the reflections obtained in the GPR data. To graph those expected reflections, it is important to carry out an accurate radar data acquisition, taking note of the external anomalies that could cause clutter, and know the distance between those anomalies and the antenna.

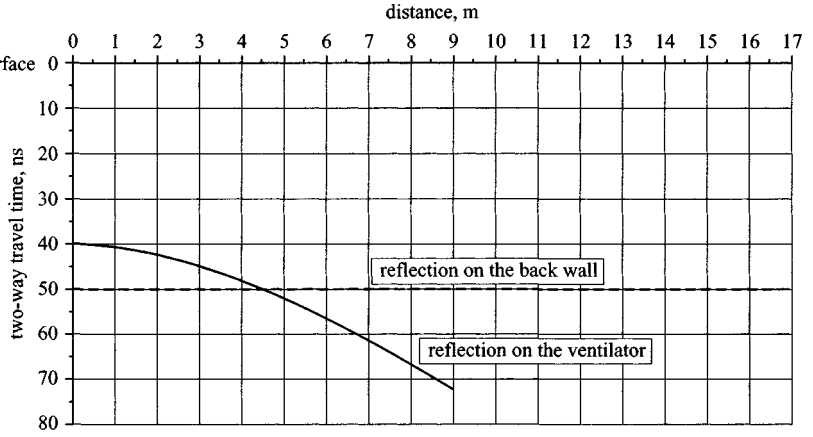

Figure 7.76 Expected clutter caused by the reflections on the lateral and back anomalies

7.11 Summary

This Chapter has introduced basic signal processing techniques and has, by means of contributions, provided examples of some of the methods and principles of GPR processing being currently developed.

The selection of suitable signal processing methods must start from a clear appreciation of the modulation technique and the likely form of the received wavelet. The main initial objective is to select suitable processing to optimise the wavelet output in terms of each individual A-scan sample time series, and deconvolution techniques have been described. If the subsequent objective is to generate an image it is reasonable to consider some type of 3D 'spiking' filter or migration of the data. If, however, the objective is to classify the wavelet, i.e. by Prony processing, then 'spiking' filters are not appropriate. Consideration can also be given to the removal of multiple reflections. Once the A-scan data are optimised, processing methods based on B-scan data sets can be considered. Again, if the objective is image 'spiking' or focusing, a number of migration or synthetic aperture methods are available, each of which is more or less tolerant to variations in propagation conditions. Examples of the application of migration techniques have been given. Where this method is not preferred, image pattern recognition techniques based on standard image processing methods of template matching can be used. Transforms such as Hough or neural network techniques can also be considered.

The Chapter has also considered some of the issues that can give rise to false targets and shown the importance of proper recording of site characteristics. This can mitigate against the possibility of incorrect analysis where ground truth is unavailable.

An extensive list of references relating to signal and image processing has been included as an aid to the reader in exploring the substantial effort that has been made to

optimise GPR data. It is to be expected that this will continue to improve the recovery of signal information in GPR data.

7.12 References

[1] ABRAHAMSSON, R., LARSSON, E. G., LI, J., HABERSAT, J., MAKSYMONKO, G., and BRADLEY, M.: 'Elimination of leakage and ground-bounce effects in ground-penetrating radar data'. Proc. 11th IEEE Signal Processing Workshop on Statistical signal processing, 2001, pp. 150–153

[2] O'NEILL, K., HAIDER, S. A., GEIMER, S. D., and PAULSEN, K. D.: 'Effects of the ground surface on polarimetric features of broadband radar scattering from subsurface metallic objects', *IEEE Trans. Geosci. Remote Sens.*, 2001, **39**, (7), pp. 1556–1565

[3] WU, R., CLEMENT, A., LI, J., LARSSON, E. G., BRADLEY, M., HABERSAT, J., and MAKSYMONKO, G.: 'Adaptive ground bounce removal', *Electron. Lett.*, 2001, **37**, (20), pp. 1250–1252

[4] DANIELS, D. J., SCOTT, H. F., and GUNTON, D. J.: 'Introduction to subsurface radar', *IEE Proc. F*, 1988, **135**, (4), pp. 278–321

[5] CALDECOTT, R., YOUNG, J. D., HALL, J. P., and TERZUOLI, A. J.: 'An underground obstacle detection and mapping system'. Electro Science Laboratory, Ohio State University, report EL-3984, 1985

[6] ROBINSON, E. A., and TREITEL, S.: 'Geophysical signal analysis' (Prentice-Hall, 1980)

[7] UENO, K., and OSUMI, N.: 'Underground pipe detection based on microwave polarisation effect'. Proceedings of International Symposium on Noise and clutter rejection, Tokyo, Japan, 1984, pp. 693–781

[8] COATANHAY, A.: 'Optimized GPR signal deconvolution using an adaptative conjugate gradient method'. Proc. IEEE Int. Geoscience and Remote Sensing Symposium, 2002 (IGARSS '02), Vol. 1, pp. 340–341

[9] HLAWATSCH, F., and BOUDREAUX-BARTELS, C. F.: 'Linear and quadratic time-frequency signal representations', *IEEE Signal Process. Mag.*, 1992, **9**, pp. 21–69

[10] REHMEYER, D. L., and ARAVENA, J. L.: 'Wavelets and neural nets for stratigraphic analysis' Int. Geoscience and Remote Sensing Symposium, 1994 (IGARSS '94). 'Surface and atmospheric remote sensing: technologies, data analysis and interpretation', 8–12 August 1994, Vol. 4, pp. 2117–2119

[11] CAREVIC, D.: 'Wavelet-based method for detection of shallowly buried objects from GPR data'. Proc. IDC 99, Information, decision and control, 1999, pp. 201–206

[12] RIOUL, O., and VETTERLI, M.: 'Wavelets and signal processing'. *IEEE Signal Process. Mag.*, 1991, **8**, pp. 14–38

[13] RANDALL, R. B., and LEE, J.: 'Cepstrum analysis', Bruel and Kjaer Technical Review, 1981

[14] SCHMIDT, R. O.: 'Multiple emitter location and signal parameter estimation', *IEEE Trans.*, 1986, **AP-34**, (3), pp. 276–280

[15] VAN BLARICUM, M., and MITTRA, K.: 'Problems and solutions associated with Prony's method for processing transient data', *IEEE Trans.*, 1978, **AP-26**, (1), pp. 174–182

[16] DUDLEY, D. G.: 'Progress in identification of electromagnetic systems', *IEEE Antennas Propag. Newslett.*, August 1988, pp. 5–11

[17] CHAN, L. C., MOFFATT, D. L., and PETERS, L.: 'Subsurface radar target imaging estimates'. *IEEE Trans.*, 1981, **AP-29**, pp. 413–417

[18] OREGON STATE UNIVERSITY: OSU Contract DAAK 70-77-C-0114 Report-Figure 21

[19] CHAN, L. C., PETERS, L., and MOFFATT, D. L.: 'Improved performance of a subsurface radar target identification system through antenna design'. *IEEE Trans.*, 1981, **AP-29**, pp. 307–311

[20] WEBB, L.: 'Radar target discrimination using K-pulse from a "fast" Prony's method'. PhD dissertation, Department of Electrical Engineering & Systems Science, Michigan State University, 1984

[21] BAUM, C. E., ROTHWELL, E. J., CHEN, K. M., and NYQUIST, D. P.: 'Singularity expansion method'. *Proc. IEEE*, 1991, **79**, (10), pp. 1481–1492

[22] CHEN, K. M., NYQUIST, D. P., KOTHWELL, E. J., WEBB, L. L., and DRACHMAN, B.: 'Radar target discrimination by convolution of radar returns with extinction pulses and single-mode extraction signals'. *IEEE Trans.*, 1986, **AP-34**, pp. 896–904

[23] KENNAUGH, E. M.: 'The K-pulse concept', *IEEE Trans.*, 1981, **AP-29**, (2), pp. 327–331

[24] KENNAUGH, E. M., and MOFFATT, D. L.: 'Transient and impulse response approximations', *Proc. IEEE*, 1965, **55**, (8), pp. 893–901

[25] FOK, F. Y. S., and MOFFATT, D. L.: 'The K-pulse and E-pulse', *IEEE Trans.*, 1987, **AP-35**, (ii), pp. 1325–1326

[26] ROTHWELL, E. J., CHEM, K. M., and NYQUIST, O. P.: 'Extraction of the natural frequencies of a measured response using E-pulse techniques'. *IEEE Trans.*, 1987, **AP-35**, pp. 713–728

[27] CHEN, C. C., PETERS, L., Jr., and BURNSIDE, W. D.: 'Ground penetration radar target classification via complex natural resonances'. Antennas and Propagation Society International Symposium, 18–23 June 1995. AP-S Digest, Vol. 3, pp. 1586–1589

[28] GUANGYOU, F., and ZHONGZHI, Z.: 'Measurement and numerical calculation about the resonance properties of objects buried in a lossy half-space'. Microwave Conf. Proc., 1997 (APMC '97), 1997 Asia-Pacific, 2–5 December 1997, Vol. 3, pp. 1021–1024

[29] SOUMYA NAG, and PETERS, L., Jr.: 'Ramp response signatures of dielectric targets, especially land mines'. Proc. IEEE Int. Geoscience and Remote Sensing Symposium, 6–10 July 1998 (IGARSS '98), Vol. 1, pp. 213–215

[30] KAY, S. M., and MARPLE, S. L.: 'Spectrum analysis – a modem perspective', *Proc. IEEE*, 1981, **69**, pp. 1380–1419
[31] HAGEDOORN, J. G.: 'A process of seismic reflection interpretation', *Geophys. Prospect.*, 1954, **2**, pp. 85–127
[32] BERKHOUT, A. J.: 'Wave field extrapolation techniques in seismic migration, a tutorial', *Geophysics*, 1981, **46**, pp. 1638–1656
[33] SCHNEIDER, W. A.: 'Integral formulation for migration in two and three dimensions', *Geophysics*, 1978, **43**, pp. 49–76
[34] HOGAN, G.: 'Migration of ground penetrating radar data. Abstracts of 59th annual international meeting on Social exploitation of geophysics, 1988, pp. 345–317
[35] FISHER, E., and McMECHAN, G. A.: 'Examples for reverse-time migration of single-channel, ground-penetrating radar profiles', *Geophysics*, 1992, **57**, (4), pp. 577–586
[36] MITCHELL, A. R.: 'Computational methods in partial differential equations' (John Wiley, 1969)
[37] CLAERBOUT, J. F.: 'Imaging the earth's interior' (Blackwell Scientific Publications, Palo Alto, 1985)
[38] McMECHAN, G. A.: 'Migration by extrapolation of time dependent boundary values', *Geophys. Prospect.*, 1983, **31**, pp. 413–428
[39] SIGGINS, A. F.: 'Ground penetrating radar in geotechnical applications', *Explor. Geophys.*, 1990, **21**, (3–4), pp. 175–186
[40] ANXUE, Z., JIANG, Y., WANG, W., and WANG, C.: 'Experimental studies on GPR velocity estimation and imaging methods using migration in the frequency—wavenumber domain', Proceedings of ISAPE 2000 (5th International Symposium) on *Antennas, Propagation and EM Theory*, Beijing, China, 2000, pp. 468–473
[41] PLUMB, R. G., and LEUSCHEN, C.: 'A class of migration algorithms for ground-penetrating radar data'. Proc. IEEE Int. Geoscience and Remote Sensing Symposium, 1999 (IGARSS '99), Vol. 5, pp. 2519–2521
[42] LEUSCHEN, C. J., and PLUMB, R. G.: 'A matched-filter-based reverse-time migration algorithm for ground-penetrating radar data' *IEEE Trans. Geosci. Remote Sens.*, 2001, **39** (5), pp. 929–936
[43] XU, X., MILLER, E. L., RAPPAPORT, C. M., and SOWER, G. D.: 'Statistical method to detect subsurface objects using array ground-penetrating radar data', *IEEE Trans. Geosci. Remote Sens.*, 2002, **40**, (4), pp. 963–976
[44] YILMAZ, O.: 'Seismic data processing'. Society of Exploration Geophysicists, Tusla, OK, 1987
[45] SCHEERS, B., ACHEROY, M., and VANDER VORST, A.: 'Time domain simulation and characterisation of TEM horns using normalised impulse response', *IEE Proc., Microw. Antennas Propag.*, 2000, **147**, (6), pp. 463–468
[46] FARR, E. G., and BAUM, C. E.: 'Time domain characterization of antennas with TEM feeds'. Sensor and Simulation Notes, Note 426, Air Force Research Laboratory, USA, 1998

[47] SCHEERS B.: 'Ultra-wideband ground penetrating radar, with applications to the detection of anti-personnel landmines'. Doctoral thesis, Université Catholique de Louvain and Royal Military Academy, Belgium, March 2001

[48] ANDREWS, H. C., and HUNT, B. R.: 'Digital image restoration' (Prentice Hall, New Jersey, 1977)

[49] STICKLEY, G. F., LONGSTAFF, I. D., and RADCLIFFE, M. J.: 'Synthetic aperture radar for the detection of shallow buried objects'. In 'The detection of abandoned land mines: a humanitarian imperative seeking a technical solution', EUREL Int. Conf. (Conf. Publ. No. 431), 7–9 Oct 1996, pp. 160–163

[50] KAGALENKO, M. B., and WEEDON, W. H.: 'Comparison of backpropagation and synthetic aperture imaging algorithms for processing GPR data'. Antennas and Propagation Society Int. Symposium, 21–26 July 1996. AP-S Digest, Vol. 3, pp. 2179–2182

[51] MILISAVLJEVIC, N., and YAROVOY, A. G.: 'An effective algorithm for subsurface SAR imaging'. Proc. IEEE Antennas and Propagation Society International Symposium, 2002, Vol.4, pp. 314–317

[52] BRANDSTADT, J. A., GEORGE, A. D., KRUMME, M. A., MOORE, J., LYNCH, E. D., and BROWN, R. D.: 'Real-time processing for ultra-wide SAR sub-surface sensing'. Record of 1999 IEEE Radar Conf., pp. 213–217

[53] SKOLNIK, M. I.: 'Introduction to radar systems' (McGraw Hill, 1970, 2nd edn)

[54] JUNKIN, G., and ANDERSON, A. P.: 'A new system for microwave holographic imaging of buried services'. Proceedings of 16th European Microwave Conference, 1986, pp. 720–725

[55] OSUMI, N., and UENO, K.: 'Detection of buried plant', *IEE Proc. F*, 1988, **135**, (4), pp. 330–342

[56] YAMAGUCHI, Y., SENGOKU, N., and ABE, T.: 'FM-CW radar applied to the detection of buried objects in snowpack'. Proc. Int. Symposium on Antennas and propagation – merging technologies for 90s, Dallas, TX, USA, 1990, pp. 738–741

[57] WU, Z., and LIU, C.: 'An image reconstruction method using GPR data', *IEEE Trans. Geosci. Remote Sens.*, 1999, **37**, (1), pp. 327–334

[58] POLAT, B., and MEINCKE, P.: 'Ground penetrating radar imaging of buried metallic objects'. IEEE Int. Antennas and Propagation Society Symposium, 2001, Vol. 4, pp. 264–267

[59] DOURTHE, C., and PICHOT, Ch.: 'Microwave imaging algorithms for arbitrary space and time incident waveforms using ultrawide bandwidth GPR technique'. In 'The detection of abandoned land mines: a humanitarian imperative seeking a technical solution', EUREL Int. Conf. (Conf. Publ. No. 431), 7–9 Oct 1996, pp. 124–127

[60] WILLIAMS, G. D., OWEN, C., and FENNING, P. J.: 'Fracture imaging in sandstones using high resolution ground penetrating radar'. IEE Colloquium on Radar and microwave techniques for non-destructive evaluation, 20 Nov 1995, pp. 6/1–6/2

[61] XU, X., and MILLER, E. L.: 'Adaptive difference of Gaussians to improve subsurface object detection using GPR imagery'. Proc. Int. Conf. on Image processing, 2002, Vol. 2, pp. II-457–II-460

[62] KLEINMANN, L., LAUGKS, J., and NICK, K.-P.: 'Image processing and pattern recognition in ground penetrating radar data'. Int. Geoscience and Remote Sensing Symposium, 1993. IGARSS '93. 'Better understanding of Earth environment'. 18–21 Aug. 1993, Vol. 4, pp. 1903–1906

[63] HOMER, J., TANG, H. T., and LONGSTAFF, I. D.: 'Radar imaging of shallow buried objects' Proc. IEEE Int. Geoscience and Remote Sensing Symposium (IGARSS '99), 1999, Vol. 5, pp. 2477–2479

[64] WALKER, P. D., and BELL, M. R.: 'Non-iterative GPR imaging through a non-planar air-ground interface'. Proc. IEEE Int. Geoscience and Remote Sensing Symposium, 2001 (IGARSS '01), Vol.3, pp. 1527–1529

[65] VAN DEN BERG, P. M., ABUBAKAR, A., BUDKO, N. V., and REMIS, R. F.: 'Imaging and inversion of buried objects using GPR'. Proc. IEEE Int. Geoscience and Remote Sensing Symposium, 2001 (IGARSS '01), Vol.3, pp. 1377–1380

[66] MORROW, I. L., and VAN GENDEREN, P.: 'Effective imaging of buried dielectric objects', *IEEE Trans. Geosci. Remote Sens.*, 2002 **40**, (4), pp. 943–949

[67] KANEKO, T.: 'Radar image processing for locating underground linear objects', *IECIE Trans.*, 1991, **74**, (10), pp. 3451–3459

[68] RABINER, L. R., and GOLD, B.: 'Theory and application of digital signal processing' (Prentice-Hall, Inc. Englewood Cliffs, New Jersey, 1975)

[69] ENGL, H. W., HANKE, M., and NEUBAUER, A.: 'Regularization of inverse problems' (Kluwer Academic Publishers, 1996)

[70] VAN DER KRUK, J.: 'Three-dimensional imaging of multi-component ground penetrating radar data'. PhD Thesis, Delft University of Technology, 2001. ISBN 90-9014706

[71] YILMAZ, Ö.: 'Seismic data analysis'. Society of Exploration Geophysicists, 2001. ISBN 1-56080-098-4

[72] PIPAN, M., FORTE, E., GUANGYOU, F., and FINETTI, I.: 'High resolution GPR imaging and joint characterization in limestone', *Near Surf. Geophys.*, 2003, **1**, pp. 39–55

[73] HALE, D.: 'Dip moveout processing', Society of Exploration Geophysicists, 1991. ISBN 1-56080-053-4

[74] GUANGYOU, F., and PIPAN, M.: 'Synthetic and field examples of GPR profile improvement using two phase detection techniques', *Geophysics*, 2003, **68**, pp. 554–558

[75] JÄGER, R., MANN, J., HÖCHT, G., and HUBRAL, P.: 'Common-reflection-surface stack: Image and attributes', *Geophysics*, 2001, **66**, pp. 97–109

[76] BOLOMEY, J. C., and PICHOT, C.: 'Microwave tomography: from theory to practical imaging systems', *Int. J. Imaging Syst. Technol.*, 1990, **2**, pp. 144–156

[77] LESSELIER, D., and DUCHÊNE, B.: 'Wave-field inversion of objects in stratified environments: from back-propagation schemes to full solutions', in Stone, R. (Ed.): 'Review of radio science 1993–1996' (Oxford University Press, Oxford, 1996), pp. 235–268

[78] BERTERO, M., and BOCCACCI, P.: 'Introduction to inverse problems in imaging'. (Institute of Physics, Bristol, UK, 1998)

[79] KAC, M.: 'Can one hear the shape of a drum?', *Am. Math. Monthly*, 1966, **73**, (4), Part II, p. 1

[80] JACKSON, J. D.: 'Classical electrodynamics' (J. Wiley & Sons., New York, 1999)

[81] PIERRI, R., LISENO, A., and SOLDOVIERI, F.: 'Shape reconstruction from PO multifrequency scattered fields via the singular value decomposition approach', *IEEE Trans. Antennas Propag.*, 2001, **49**, (9), pp. 1333–1343

[82] PIERRI, R., and LISENO, A.: 'Imaging perfectly conducting objects as support of induced currents: Kirchhoff approximation and frequency diversity', *J. Opt. Soc. Am. A*, **19**, (7), 2002, pp. 1308–1319

[83] CHEW, W. C.: 'Waves and fields in homogeneous media' (IEEE Press, New York, USA, 1995)

[84] DEMOMENT, G.: 'Image reconstruction and restoration: overview of common estimation structures and problems', *IEEE Trans. Acoust. Speech Signal Process.*, 1989, **37**, (12), pp. 2024–2036

[85] ISERNIA, T., PASCAZIO, V., and PIERRI, R.: 'On the local minima in a tomographic imaging technique', *IEEE Trans. Geosci. Remote Sens.*, 2001, **39**, (7), pp. 1596–1607

[86] BORN, M., and WOLF, E.: 'Principles of optics' (Cambridge University Press, Oxford, 1999)

[87] BRANCACCIO, A., LEONE, G., and PIERRI, R.: 'Information content of Born scattered fields: results in the circular cylindrical case', *J. Opt. Soc. Am. A*, 1998, **15**, (7), pp. 1909–1917

[88] SLANEY, M., KAK, A. C., and LARSEN, L. E.: 'Limitation of imaging with first order diffraction tomography', *IEEE Trans. Microw. Theory Tech.*, 1984, **MTT-32**, pp. 860–874

[89] PIERRI, R., LEONE, G., SOLDOVIERI, F., and PERSICO, R.: 'Electromagnetic inversion for subsurface applications under the distorted Born approximation', *Il Nuovo Cimento*, 2001, **24C**, (2), pp. 245–261

[90] DEN DEKKER, A. J., and VAN DEN BOS, A.: 'Resolution: a survey', *J. Opt. Soc. Am. A*, 1997, **14**, (3), pp. 547–557

[91] STACEY, D. N.: 'Rayleigh's legacy to modern physics: high resolution spectroscopy', *Eur. J. Phys.*, 1994, **15**, pp. 236–242

[92] BENDINELLI, M., CONSORTINI, A., RONCHI, L., and FRIEDEN, B. R.: 'Degrees of freedom, and eigenfunctions, for the noisy image', *J. Opt. Soc. Am.*, 1974, **64**, (11), pp. 1498–1502

[93] TORALDO DI FRANCIA, G.: 'Degrees of freedom of an image', *J. Opt. Soc. Am. A*, 1969, **59**, pp. 799–804

[94] HANSEN, T. B., and JOHANSEN, P. M.: 'Inversion scheme for ground penetrating radar that takes into account the planar air-soil interface', *IEEE Trans. Geosci. Remote Sens.*, 2000, **38**, (1), pp. 496–506

[95] PIERRI, R., LISENO, A., SOLIMENE, R., TARTAGLIONE, F., and SOLDOVIERI, F.: 'Resolution limits in the Fresnel zone: roles of aperture and frequency', *Subs. Sens. Tech. Appl.*, 2002, **3**, (1), pp. 1–18

[96] PIERRI, R., LISENO, A., SOLDOVIERI, F., and SOLIMENE, R.: 'In-depth resolution for a strip source in the Fresnel zone', *J. Opt. Soc. Am. A*, 2001, **18**, (2), pp. 352–359

[97] CHERNIAKOV, M., and DONSKOI, L.: 'Frequency band selection of radar for buried object detection', *IEEE Trans. Geosci. Remote Sens.*, 1999, **37**, (2), pp. 838–845

[98] PIERRI, R., LISENO, A., SOLIMENE, R., and TARTAGLIONE, F.: 'In-depth resolution from multi-frequency Born fields scattered by a dielectric strip in the Fresnel zone', *J. Opt. Soc. Am. A*, 2002, **19**, (6), pp. 1234–1238

[99] CARSON, A. B.: 'Communication systems' (McGraw-Hill, Singapore, 1986)

[100] PIERRI, R., LISENO, A., and SOLDOVIERI, R.: 'Improving a shape reconstruction algorithm with thresholds and multi-view data', *Int. J. Electron. Commun.* (AEÜ), **58**, (2), 2004, pp. 118–124

[101] ENGHETA, N., PAPAS, C. H., and ELACHI, C.: 'Radiation patterns of interfacial dipole antennas', *Radio Sci.*, 1982, **17**, (6), pp. 1557–1566

[102] REMIS, R. F.: 'Reduced-order modelling of transient electromagnetic fields'. PhD thesis, Delft University of Technology, 1998

[103] VAN DER KRUK, J., and SLOB, E. C.: 'The influence of the soil on reflections from above surface objects in GPR data'. Proc. Eighth Int. Conf. on Ground-penetrating radar, Gold Coast, Australia, 2000, pp. 448–452

7.13 Bibliography

ASTANIN, L. Y., and KOSTYLEV, A. A.: 'Ultra-wideband radar measurements: analysis and processing' (IEE, London, 1997)

BUDKO, N. V., VAN DEN BERG, P. M.: 'Linearized multi-frequency inversion of ground penetrating radar data'. IEEE Int. Antennas and Propagation Society Symposium, 2001, Vol.4, pp. 256–259

CHEN, C. C., NAG, S., BURNSIDE, W. D., HALMAN, J. I., SCHUBERT, K. A., and PETERS, L.: 'A standoff, focused beam land mine radar', *IEEE Trans. Geosci. Remote Sens.*, 2000, **38**, (1), pp. 507–514

DANIELS, D. J.: 'Surface penetrating radar'. IEE Press: Radar, Sonar, Navigation and Avionics Series 6, London, UK, 1996

DOGARU, T., and CARIN, L.: 'Time-domain sensing of targets buried under a Gaussian, exponential, or fractal rough interface', *IEEE Trans. Geosci. Remote Sens.*, 2001, **39**, (8), pp. 1807–1819

FAN, G. X., LIU, Q. H., and HESTHAVEN, J. S.: 'Multi-domain pseudospectral time-domain method for lossy media'. IEEE Int. Antennas and Propagation Society Symposium, 2001, Vol.4, pp. 842–845

FISCHER, C., YOUNIS, M., and WIESBECK, W.: 'Multistatic GPR data acquisition and imaging'. Proc. IEEE Int. Geoscience and Remote Sensing Symposium, 2002 (IGARSS '02), Vol.1, pp. 328–330

FRANCHOIS, A., JOISEL, A., PICHOT, C., and BOLOMEY, J. C.: 'Quantitative microwave imaging with a 2.45-GHz planar microwave camera', *IEEE Trans. Med. Imaging*, 1998, **17**, (4), pp. 550–561

GENTILI, G. G., and SPAGNOLINI, U.: 'Electromagnetic inversion in monostatic ground penetrating radar: TEM horn calibration and application', *IEEE Trans. Geosci. Remote Sens.*, 2000, **38**, (4), pp. 1936–1946

GOODMAN, D.: 'Ground-penetrating radar simulation in engineering and archaeology', *Geophysics*, 1994, **59**, (2), pp. 224–232

GRASMUECK, M.: '3-D ground penetrating radar applied to fracture imaging in gneiss', *Geophysics*, 1996, **61**, (4), pp. 1050–1064

HAIZHONG, Y., and XIAOJIAN, Y.: 'Derivative seismic processing method for GPR data'. IEEE Int. Geoscience and Remote Sensing, 1997 (IGARSS '97). 'Remote sensing – a scientific vision for sustainable development'. 3–8 Aug. 1997, Vol. 1, pp. 145–147

HALE, D.: 'Dip moveout processing'. Society of Exploration Geophysicists, 1991, ISBN 1-56080-053-4

HANSEN, T. B., and JOHANSEN, P. M.: 'Inversion scheme for ground penetrating radar that takes into account the planar air-soil interface', *IEEE Trans. Geosci. Remote Sens.*, 2000, **38**, (1), pp. 496–506

HO, K. C., and GADER, P. D.: 'A linear prediction land mine detection algorithm for hand held ground penetrating radar', *IEEE Trans. Geosci. Remote Sens.*, 2002, **40**, (6), pp. 1374–1384

JOHANSEN, P. M.: 'A 2.5-D diffraction tomography inversion scheme for ground penetrating radar' IEEE Int. Antennas and Propagation Society Symposium, Aug. 1999, Vol. 3, pp. 2132–2135

KOVALENKO, V., and MASALOV, S. A.: '2D matrix filtering of ground penetrating radar data'. Proc. Int. Conf. on Mathematical methods in electromagnetic theory, MMET 2000, Vol.1, pp. 236–238

KOVINTAVEWAT, P., OZGUNES, I., KURTAS, E., BARRY, J. R., and McLAUGHLIN, S. W.: 'Generalized partial-response targets for perpendicular recording with jitter noise', *IEEE Trans. Magn.*, 2002, **38**, (5), pp. 2340–2342

LASRI, T., GLAY, D., MAMOUNI, A., and LEROY, Y.: 'Non-destructive testing of materials by microwave systems', *Electron. Lett.*, 1998, **34**, pp. 470–471

LI, X., and HAGNESS, S. C.: 'A confocal microwave imaging algorithm for breast cancer detection', *IEEE Microw. Wirel. Compon. Lett.*, 2001, **11**, (3), pp. 130–132

LO, Y. T., and LEE, S. W.: 'Antenna handbook: theory, applications and design' (Van Nostrand, New York, 1988)

MATHIESON, I., BETTLES, E., DITTMER, J., and READER, C.: 'The national museums of Scotland. Saqqara survey project, Earth sciences 1900–1998', *J. Egypt. Archeol.*, 1999, **85**, pp.21–43

MEINCKE, P.: '2.5D far-field diffraction tomography inversion scheme for GPR that takes into account the planar air-soil interface'. IEEE Int. Antennas and Propagation Society Symposium, 2001, Vol.2, pp. 662–665

MEINCKE, P.: 'Linear GPR inversion for lossy soil and a planar air-soil interface', *IEEE Trans. Geosci. Remote Sens.*, 2001, **39** (12), pp. 2713–2721

MOLYNEUX, J. E.: 'Ground penetrating radar tomography'. Int. Conf. on Acoustics, speech, and signal processing, 1995 (ICASSP-95), 9–12 May 1995, Vol. 5, pp. 2813–2816

NYFORS, E.: 'Industrial microwave sensors – A review', *Subs. Sens. Tech. Appl.*, 2000, **1**, (1), pp. 23–43

O'NEILL, K.: 'Broadband bistatic coherent and incoherent detection of buried objects beneath randomly rough surfaces', *IEEE. Trans. Geosci. Remote Sens.*, 2000, **38**, (2) pp. 891–898

PÉREZ-GRACIA, V.: 'Radar de Subsuelo. Evaluación para aplicaciones en arqueología y en patrimonio histórico-artístico'. Tesis doctoral, Universidad Politécnica de Cataluña, 2001, pp. 601–689. ISBN: 84-699-6884-X. Dep. legal: B-52288-2001

RAMPA, V., and SPAGNOLINI, U.: 'Multi-layer detection/tracking for monostatic ground penetrating radar'. Proc. Int. Geoscience and Remote Sensing Symposium, 1996 (IGARSS '96). 'Remote sensing for a sustainable future.' 27–31 May 1996, Vol. 4, pp. 2038–2040

RANDALL, R. B., and LEE, J.: 'Cepstrum analysis', *Bruel & Kjaer Tech. Rev.*, 1981, (3)

SAI, B., and LIGTHART, L. P.: 'Characterization of local 3D rough surfaces using uwb near-range phase-based GPR signatures from wide-beamwidth antennas'. Proc. IEEE Int. Geoscience and Remote Sensing Symposium, 2002 (IGARSS '02), Vol. 6, pp. 3582–3584

SAI, B., and LIGTHART, L. P.: 'Wideband short-range GPR interferometric phase processing for 3D rough surfaces with correction of antenna phase distortions'. Proc. IEEE Antennas and Propagation Society International Symposium, 2002, Vol.3, pp. 688–691

SHRESTHA, S. M., ARAI, I., MIWA, T., and TOMIZAWA, Y.: 'Signal processing of ground penetrating radar using super resolution technique'. Proc. IEEE Radar Conf., 2001, pp. 300–305

SPAGNOLINI, U., and RAMPA, V.: 'Multitarget detection/tracking for monostatic ground penetrating radar: application to pavement profiling', *IEEE Trans. Geosci. Remote Sens.*, 1999, **37**, (1), pp. 383–394

VAN DER MERWE, A., and GUPTA, I. J.: 'A novel signal processing technique for clutter reduction in GPR measurements of small, shallow land mines', *IEEE Trans. Geosci. Remote Sens.*, 2000, **38**, (6), pp. 2627–2637

WALKER, P. D., and BELL, M. R.: 'Noniterative techniques for GPR imaging through a nonplanar air-ground interface', *IEEE Trans. Geosci. Remote Sens.*, 2002, **40**, (10), pp. 2213–2223

XU, X., and MILLER, E. L.: 'Optimization of migration method to locate buried object in lossy medium'. Proc. IEEE Int. Geoscience and Remote Sensing Symposium, 2002 (IGARSS '02), Vol.1, pp. 337–339

YAROVOY, A. G., DE JONGH, R. V., and LIGTHART, L. P.: 'Transmission of electromagnetic fields through an air-ground interface in the presence of statistical roughness'. Proc. IEEE Int. Geoscience and Remote Sensing Symposium, 6–10 July 1998 (IGARSS '98), Vol. 3, pp. 1463–1465

ZHANG, G., TSANG, L., and KUGA, Y.: 'Studies of the angular correlation function of scattering by random rough surfaces with and without a buried object', *IEEE Trans. Geosci. Remote Sens.*, 1997, **35**, (2), pp. 444–453

ZHOU, H., and SATO, M.: 'Application of vertical radar profiling technique to Sendai Castle', *Geophysics*, 2000, 65, (2), pp. 533–539

Chapter 8
Archaeology

8.1 Introduction

John Fidler
English Heritage, UK

Surface-penetrating radar has been used to locate voids, inconsistencies and buried metalwork in a wide variety of structures: mediaeval cathedrals, castles, Egyptian pyramids and even the Ark. However, certain requirements need to be considered.

Geophysicists and electrical/radar engineers are not architects, structural engineers or building surveyors and their knowledge and understanding of construction systems and faults is understandably limited, which affects their interpretation of the radar images. The building professionals' hopes and expectancies for remote sensing outstrip their perception of the actual capabilities of radar techniques. Only by having both sets of professionals working as a team on site and subsequently in the office can misinterpretation be eliminated. It is not acceptable for one group to survey and interpret the building and for the other to receive and accept the results.

Radar is best employed alongside magnetometers, resistance and radio-detection devices etc., with a thorough-going visual assessment of the building or ground of interest. The best surveys establish a hypothesis of construction and deformation/decay. They model this hypothesis off the building, by creating freestanding facsimiles in cross-section which can be compared with the radar signals, and vary configurations identified to unique signatures so that data from the actual building can be properly interpreted.

Like all geophysical techniques, GPR must be intelligently applied to the task in hand. For example, the search for the postulated remains of Noah's Ark on Mt Ararat is described in detail on the following website, http://www.noahsarksearch.com/bj98summary.htm.

This source discloses that in 1988, Dr. Charles Willis of Fresno, California used ground penetrating radar (GPR) successfully to survey and profile the ice under the eastern summit plateau and over the high ridge into the saddle between the two summit

peaks. No evidence of Noah's Ark was found, but good science prevailed, and another area was eliminated.

In 1989, Chuck Aaron, Bob Garbe and B.J. Corbin attempted to use GPR on the western summit plateau, but were limited by ice conditions and a GPR unit that could not continuously profile under the ice. The team was successful in determining the depth of the ice to be over 250 feet thick in some areas, thus giving credence to those that believe the western plateau is a caldera or sunken volcanic cone. Mt Ararat is being successively surveyed and areas eliminated by the use of GPR.

Examples of selected archaeological applications for GPR are described in the following Sections and further reading and references are provided at the end of the Chapter.

8.2 Fountains Abbey, UK

David J. Daniels

Fountains Abbey, in North Yorkshire, founded in 1134 by the Cistercians, is an outstanding example of a mediaeval monastery. It stands in the valley of the River Skell and the existing ruins give a clear impression of life in one of England's greatest and best preserved abbeys. Although the first construction was of timber, the Abbey grew to encompass a stone built church 360 ft long with a 168 ft tower. The Cellarium with its double row of arches is an inspiring reminder of monastic life. Photographs of the Abbey are shown in Figure 8.1, and a plan is shown in Figure 8.2. In collaboration with the University of York's Department of Electronics, ERA Technology carried out a survey of parts of the grounds of the Abbey.

Of considerable interest is the site of a Guest Hall, no longer in existence, and examples of a radar survey are shown in Figure 8.3. In this Figure the radar image shows two main features. The strongest feature is on the right-hand side, and also shown in Figure 8.3 is the remains of a pillar which is conjectured to be a support for part of the Guest Hall. Also to be seen are horizontal lines, which are believed to denote the position of the original floor of the Guest Hall (see Figure 8.4). The key features are the remains of pillars and the contours of earlier floor levels.

Other features, which were detected under the Cellarium (see Figure 8.5) and the Infirmary Hall, were the culverts directing the River Skell, which in previous times functioned as the water system. The radar image of the culverts under the Cellarium is shown in Figure 8.6 and an interpretation is shown in Figure 8.7, which is a typical example of how much detail a radar image can provide of underground features. The radar image in this particular case is unfocused and therefore most of the reflections give rise to hyperbolic traces. This is particularly noticeable when caused by the corner reflectors formed by the river water and the masonry side wall of the culvert. Other hyperbolic reflectors can also be seen and these are caused by the masonry side supports of the culvert. (ERA Technology gratefully acknowledges the assistance of English Heritage in permitting access to the archaeological site at Fountains Abbey, which is owned by The National Trust and in the care of English Heritage.)

Figure 8.1 Fountains Abbey, UK

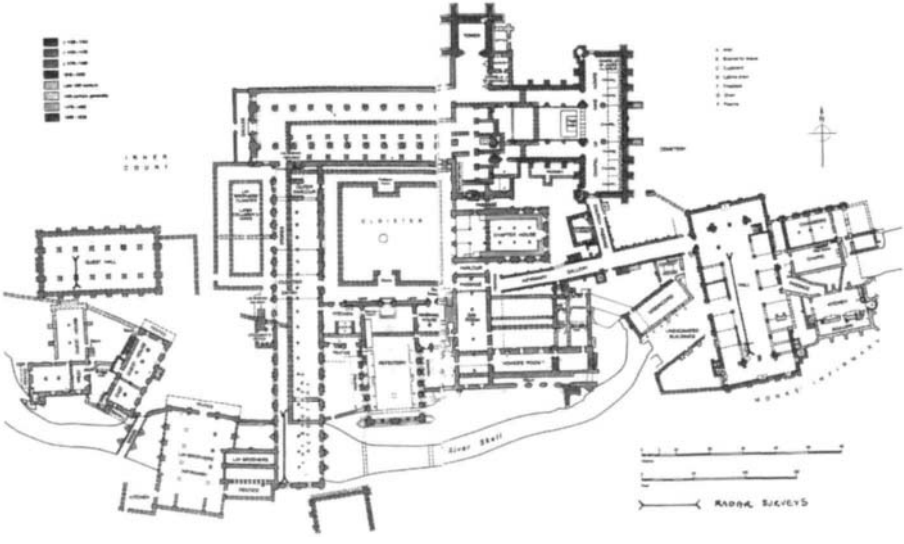

Figure 8.2 Plan of Fountains Abbey

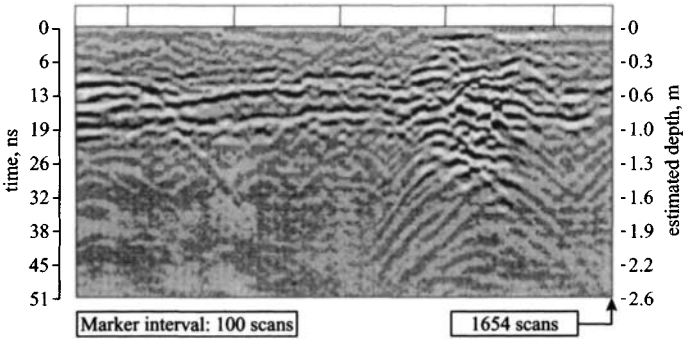

Figure 8.3 Radar image of foundation remains of the Guest Hall

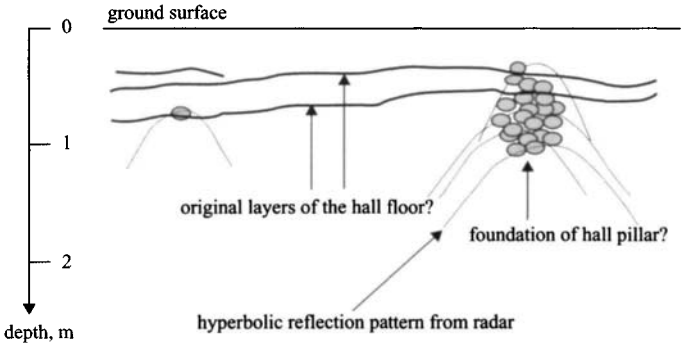

Figure 8.4 Interpretation of radar image of Guest Hall

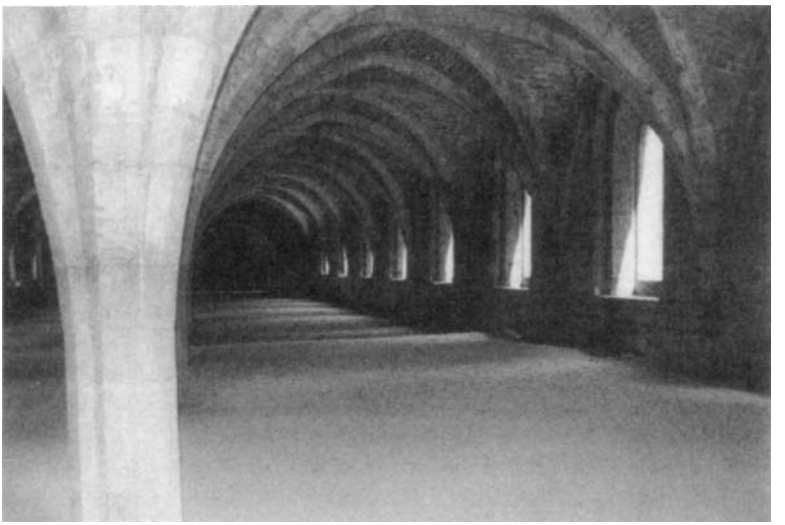

Figure 8.5 Photograph of Cellarium (courtesy of English Heritage and The National Trust)

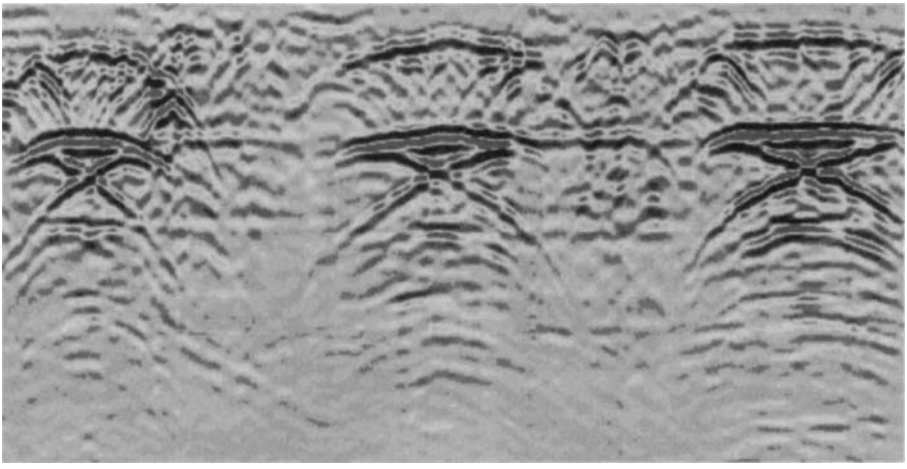

Figure 8.6 Radar image of culverts under the Cellarium

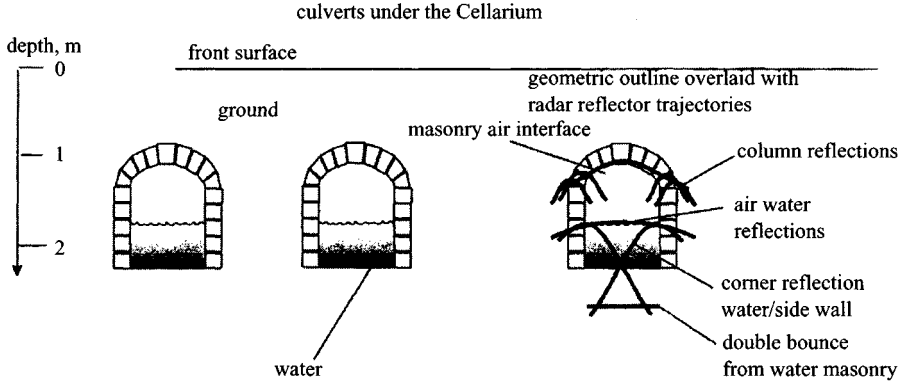

Figure 8.7 Interpretation of culverts under the Cellarium

8.3 Saqqara, Egypt

Dr Jon Dittmer

Since 1990, the Saqqara Geophysical Survey Project, under the auspices of the National Museum of Scotland and the Glasgow Museums, has been carrying out geophysical and archaeological surveys at Saqqara. Saqqara forms part of the necropolis of the ancient Egyptian capital city of Memphis. Saqqara is a modern and, in terms of the necropolis, an entirely false division. The burial grounds extend from Abu Roash, just to the north of Cairo, southwards through Giza, AbuSir, Saqqara and Dahshur to

Figure 8.8 Radar survey near the Step Pyramid at Saqqara

Meidum, ~20 km to the south. The site of Saqqara is dominated by the famous Step Pyramid of the 3rd Dynasty ruler, King Zoser.

The geophysical survey has mainly concentrated on magnetometry, due to the abundance of mudbrick structures, which produce excellent anomalies, and resistivity. However, one season was devoted to using GPR. Radar surveys were carried out on a number of sites in the concession (see Figure 8.8).

The main monument is known as the Gisr el-Mudir, which consists af a 400 m east to west by 600 m north to south stone enclosure. The walls are of extremely crude construction, but massive. This monument may constitute one of the oldest stone buildings in Egypt, and hence the world. One of the main goals of the project has been to determine what, if anything, lies within the enclosure. Despite many years of surveying, nothing has been found apart from a small area of mudbrick pavement. However, the exact location of the south wall was not known, and it was thought that in fact no wall existed, and the southern extent of the Gisr el-Mudir was defined by a man-made gravel ridge. To verify this, the GPR was scanned from the crest of this ridge to some 50 m to the south. Measurements were carried out every 20 m along the length of the wall. Figure 8.9 shows one such profile and Figure 8.10 shows an interpretation of the section. The large sand filled ditch proved to be a fairly consistent feature along the length of the entire wall. Subsequent excavation has shown that the southern wall was acually built within this trench. Most of the stone has since been

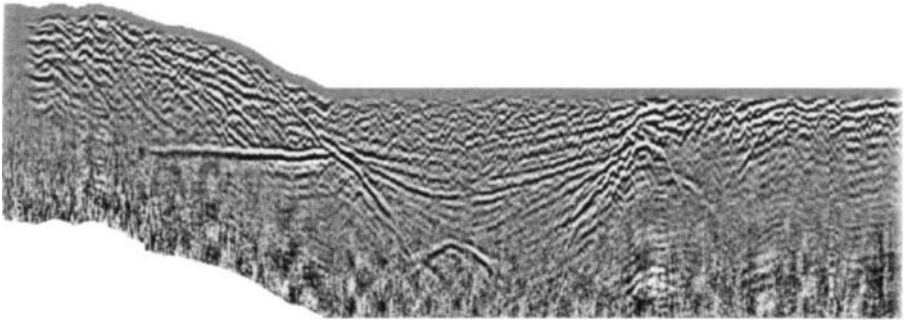

Figure 8.9 Radar image of the south wall (est. 2000 BC) buried under desert sand

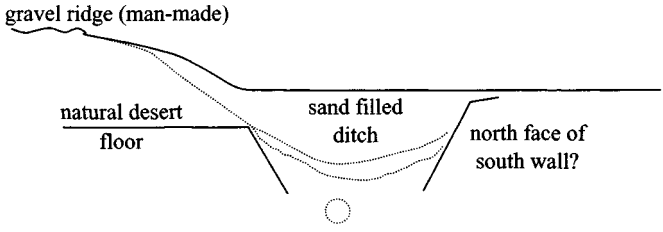

Figure 8.10 Interpretation of the radar image of the south wall (est. 2000 BC) buried under desert sand

robbed. It is interesting to note the radar's ability to detect the depositional layers within the sand filling of the trench.

Figures 8.11 to 8.14 show topographically corrected radar sections crossing the west wall of the Gisr el-Mudir. Again, layering within the sand is visible, particularly in the sand which has built up against the wall.

Aerial photographs indicate that just to the east of the Gisr el-Mudir enclosure, there may exist another similar, albeit smaller, enclosure. The project team carried out a magnetometry survey of the area, in an attempt to map any internal buildings. The survey revealed that there was in fact a row of small temple like structures. Figure 8.15 shows the entrance steps to one of these temples.

A number of radar sections had been measured over this area previously, and in view of the magnetometry results, the radar profiles were re-examined. The sections had been measured on 25 m centres, so it was purely by chance that one radar line went straight down the flight of steps and this profile can be seen in Figure 8.16.

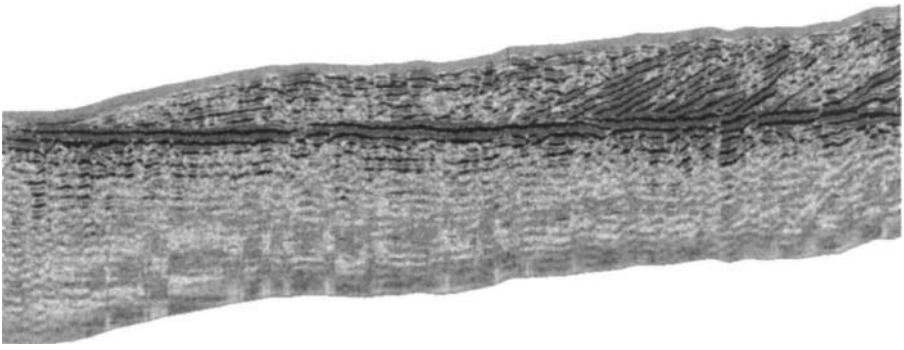

Figure 8.11 *Radar image of section 1 of wall (est. 2000 BC) buried under desert sand*

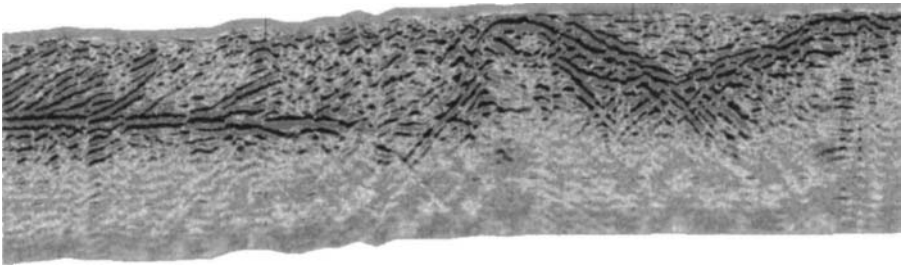

Figure 8.12 *Radar image of section 2 of wall (est. 2000 BC) buried under desert sand*

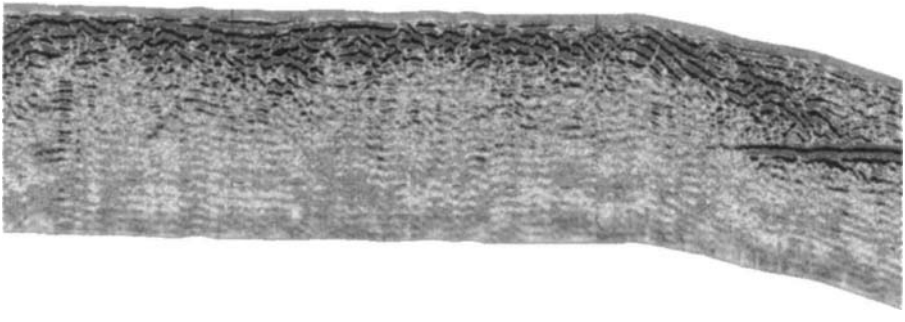

Figure 8.13 *Radar image of section 3 of wall (est. 2000 BC) buried under desert sand*

Figure 8.14 *Radar image of section 4 of wall (est. 2000 BC) buried under desert sand*

Figure 8.15 *Temple steps*

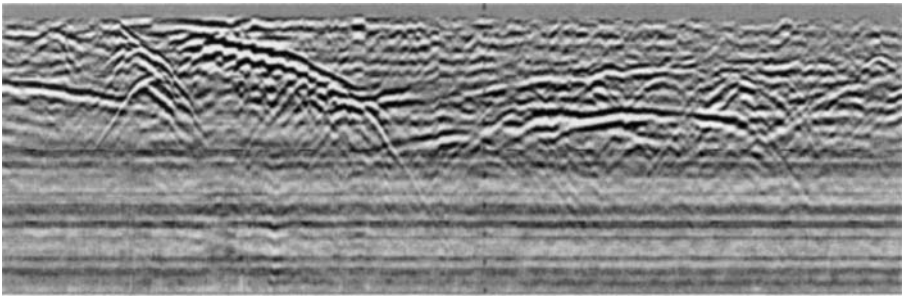

Figure 8.16 Radar section along the flight of steps

8.4 The Crypt of the Cathedral of Valencia

Dr Vega Pérez Gracia, Dr Lluis G. Pujades and Dr José A. Canas
Universidad Politécnica de Cataluña, Spain

A GPR survey of Valencian Cathedral was performed in order to determine the position of archaeological remains, which are documented in the archives of the Cathedral. The objective of this survey was to confirm ancient cartography and documentation. A historical investigation and a geophysical survey using GPR were carried out. The latter enabled the location of structures whose position was not exactly documented in the original archive papers.

Valencia is a historic city which was founded by the Romans in the year 138 BC. It was invaded later by the Visigoths, and then by the Moors, who made the city into an economic and cultural centre. Valencia was conquered from the Moors by 'El Cid'. However, it was not fully freed until 1238, by James the First of Aragon, who incorporated it into the Kingdom of Aragon. Valencia became the capital of the confederation and during the 14th and 15th centuries became one of the leading economic centres of the Mediterranean.

Excavations carried out near the Cathedral showed the Roman layer depth at <2 m. In fact, the Cathedral is a conglomeration of different architectonic styles, which indicates the different constructive epochs. The emplacement of the actual church is probably the same emplacement as that of the disappeared Arabian mosque of the city, which was built over the remains of a Roman circus. Several photographs taken during the radar data acquisition work show the amalgam of constructive styles (Figure 8.17).

The radar survey was carried out using two different antennas: a 500 MHz and a 100 MHz centre frequency antenna. The first one allows us to obtain radar images from a depth of ~ 2 m. The second one is not a shielded antenna. Therefore, the external reflections produce a strong noise, which forces an accurate radar data analysis to separate the signal of the noise and identify the investigated anomalies.

The performed GPR profiles are indicated over a plan of the Cathedral (see P1, P2, ..., in Figure 8.18). The numbers over the Figure are related to the following sections of the Cathedral: (1) the main nave, (2) the lateral naves, (3) the ambulatory, (4) the transept and (5) the altar. Capital letters A, C, D, E, F, I, J, K and

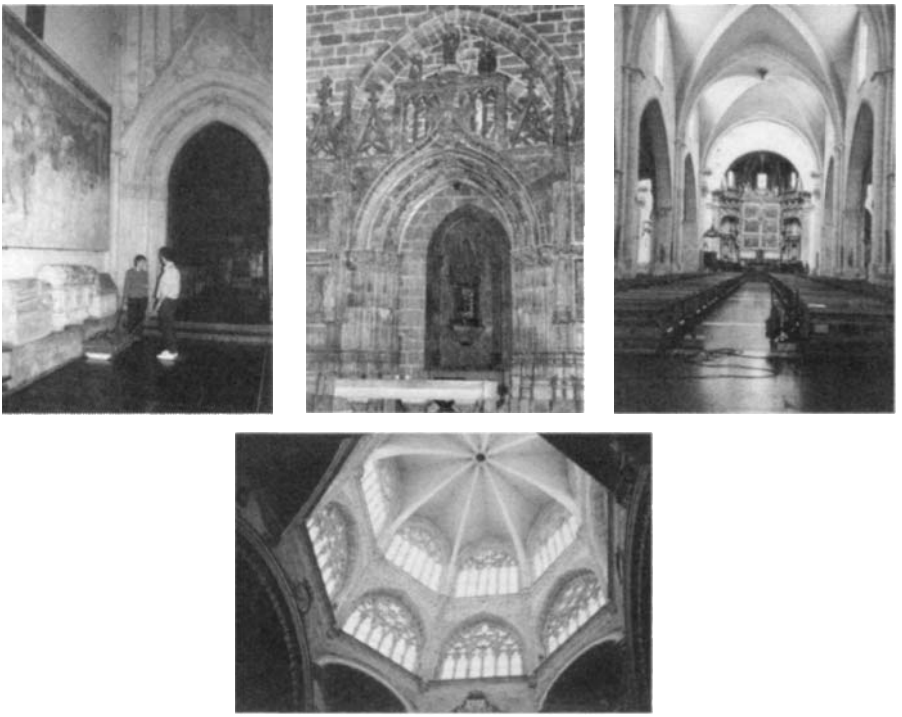

Figure 8.17 Details of Valencian Cathedral

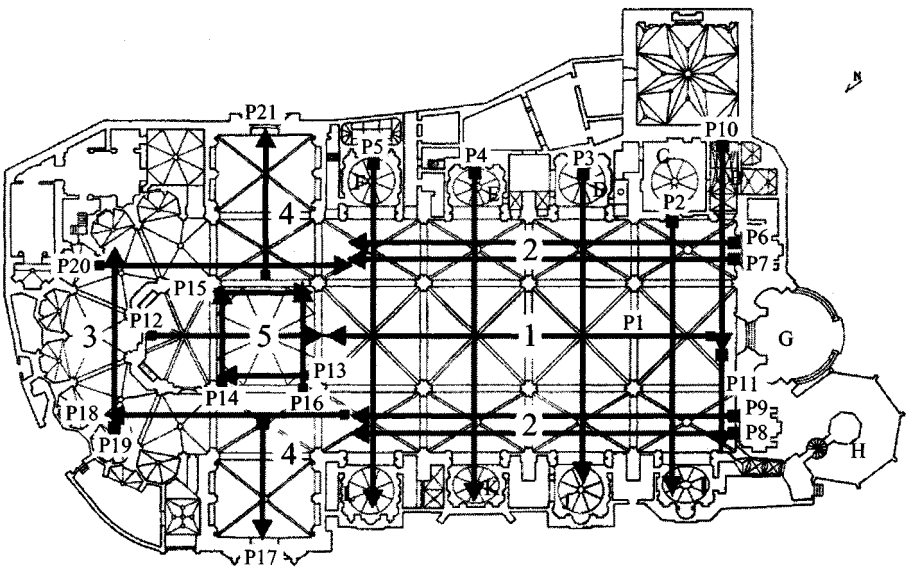

Figure 8.18 Plan of the Cathedral

L correspond to the chapels, B to the access to the 'Santo Cáliz' chapel, G to the main entrance and H to the tower called Miquelet.

The different areas and the radar profiles are indicated.

The radar data enabled anomalies to be detected and located. These may have been associated with walls and foundations of houses associated with the Cathedral prior to its enlargement. In addition, several anomalies corresponding to graves, temporary vaults and crypts were detected and located.

Some examples of the radar data obtained in two crossed profiles are shown in Figures 8.19 and 8.20. The first image (Figure 8.19) is the radar image from the last half part of the P1 profile. This profile is 50 m long, but the image of Figure 8.20 shows the radar section of the last 15 m of that profile, which covers from the middle of the main nave to the altar. A 100 MHz centre frequency antenna was used to obtain

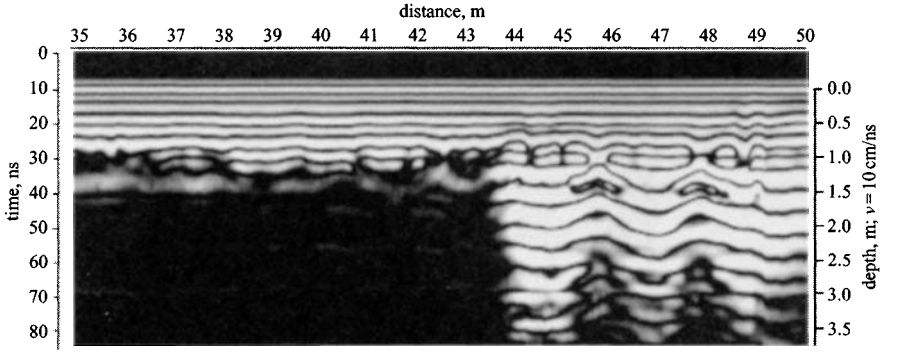

Figure 8.19 Last 15 m of the P1 profile obtained with a 100 MHz centre frequency antenna

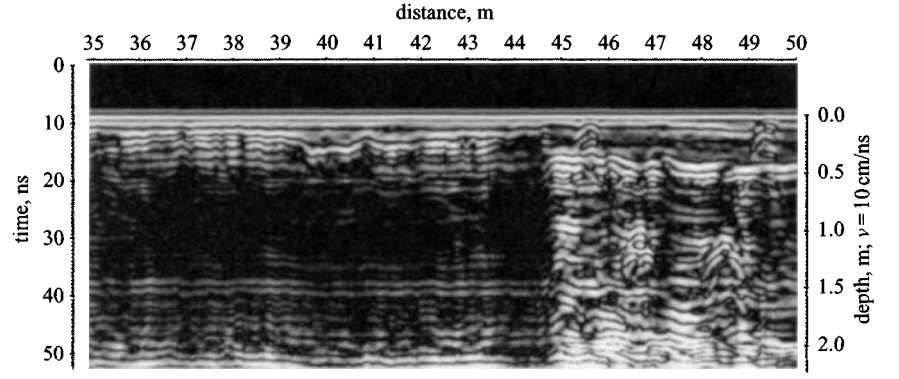

Figure 8.20 The last 15 m of the P1 profile obtained with a 500 MHz centre frequency antenna

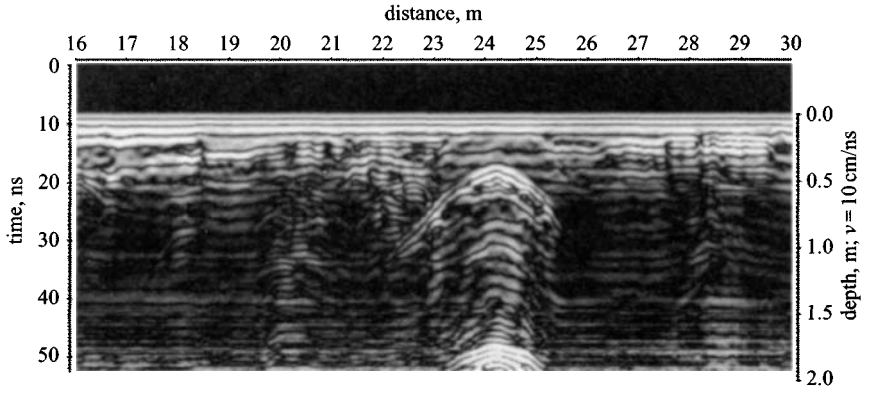

Figure 8.21 Radar data obtained with a 500 MHz centre frequency antenna

those data. Figure 8.21 presents the same part of that profile, but obtained by using a 500 MHz centre frequency antenna.

Both profiles show strong reflections between 44 and 45 m. Similar reflections can be seen at the end of the radar data. These images on the radar data are produced by the reflections in the contact between the soil and the main crypt of the Cathedral. The vertical resolution of the 500 MHz antenna enables the two-way travel time of the reflected signal to be determined. Hence it allows the depth of the anomaly to be estimated (Figure 8.20). Inspection of shallow depths using the 100 MHz antenna data give inaccurate results (Figure 8.19) because the reflection in the crypt is coupled to the reflection in the surface of the medium and to the internal first signal of the antenna. The two-way travel times were converted into depths using the wave average velocity, which was obtained to characterise this area of the Cathedral. The average velocity was obtained from the analysis of the hyperbolic events produced in buried objects – graves and ossuaries – and also the reflections in the same crypt. The relative permittivity obtained was about 9, and therefore the average velocity in this area was assumed to be 10 cm/ns.

Figure 8.21 shows the radar data obtained in the profile P5, which crosses profile P1. The middle part of that profile is represented in the Figure. The crypt is well detected between 23 and 25 m. At this point, profiles P1 and P5 cross at 45 and 24 m distances, respectively. The radar data shown in Figure 8.21 were obtained with the 500 MHz antenna.

Finally, Figure 8.22 shows the superposition of the radar records corresponding to the P1 and P5 profiles. The composition of both images displays the correlations between the reflections recorded, corresponding to the studied anomaly.

The radar survey enabled the location of the anomalies to be determined, and from this confirmation of the archival data was achieved. A comparison between the centre frequencies was made. The depth of investigation was <2 m, because the oldest remains (Roman layer) are located at that depth. Both antennas allow us to arrive to this maximum depth, but the 100 MHz, which has a longer time pulse, has

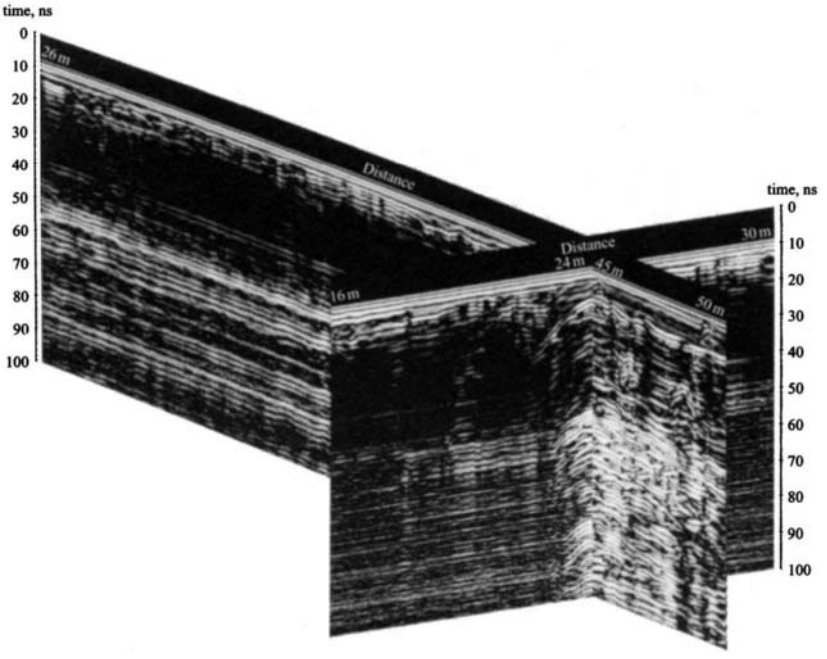

Figure 8.22 Composition of profiles P1 and P5

not enough resolution to determine the exact arrival of the shallower reflected signals. Although the signals are clearly seen in the 100 MHz antenna images, the coupling effects between those signals and the reflections on the surface (pavement of the church) produce confusing results. To obtain correct results estimating the depths by converting the two-way travel time it is necessary to determine accurately the time arrival of the reflections which is possible when the antenna used to perform the survey has better vertical resolution.

Acknowledgments

This study was supported in part by the 'Ministerio de Ciencia y Tecnología' and by FEDER (research projects number REN 2000-1740-C05-01 RIES and REN 2001-2418-C04-01). Additional support was give by the Civil Engineering School (ETSECCPB).

8.5 Historic masonry structures

Dr Christiane Maierhofer

In most cases historical masonry is very inhomogeneous, even if it appears simple and uniform from the surface. Therefore, testing methods are required which enable the investigation of the whole volume of the structure along large areas. This is only

possible by using nondestructive or minor-destructive testing (NDT/MDT) methods, not only to preserve the building, but also to avoid disturbing the state of stress and strain of the structure. During the last ten years, it has been shown that ground penetrating radar (GPR) is a very useful nondestructive testing method for the investigation of the following problems of masonry.

8.5.1 Church of S. Maria Rossa, Milan, Italy

The Church of S. Maria Rossa was built in different phases from the 9th/10th to the 13th centuries over older buildings [1]. Some modifications and repairs were made in 1783 and 1966. The present building shows parts of various ages. Excavations under the floor allowed us to find portions of floors, mosaics and fragments of walls of the previous Roman (ageing 2nd century) and paleo-Christian buildings (5th century). The walls were made of solid bricks and lime mortars. The Church was originally all frescoed, but at present it is possible to see only some traces of the ancient decoration. The water table is high, nearly superficial, in the area where the Church is situated. The Church is at present under the street level (see Figure 8.23), close to an artificial channel (Naviglio). Furthermore, the soil leans against the Church walls in the north side on the Naviglio channel. The area of the Church is characterised by the presence of several small channels built for agricultural necessities. All these factors produce a great presence of moisture which rises by capillary through the walls. Two photographs from the Church are shown in Figure 8.24.

For structural as well as for moisture investigations, radar measurements were performed at three areas which are marked in the plan view in Figure 8.23. For the determination of depth resolved moisture distribution, microwave transmission measurements in thin boreholes using two small dipole antennas were accomplished [2–4]. These investigations were performed in close co-operation with Luigia Binda and co-workers from Politecnico di Milano, Italy.

At area 1, the brick wall is almost the original one with a texture of solid brick and hydrated lime mortars. The thickness of the walls is ~72 cm. This area is localised under the street level, in direct contact with the soil. Thus, a very high moisture content was expected. In the radar images recorded with the 500 MHz antenna as shown in Figure 8.25*a*, reflections from the backside are hardly visible due to the very high moisture content and due to the presence of soil directly at the back-side, which has a similar dielectric constant to that of the wet brick material. From some of these very weak reflections, a mean integrated real part of the complex permittivity of about 12.8 could be calculated with an absolute error of 1.0. Extrapolating the calibration curves of Maierhofer *et al.* [5], this corresponds to an absolute moisture content of ~25 vol%.

In Figure 8.25*b*, the depth resolved real part of the complex permittivity determined with the microwave borehole system is presented. Here, the real part of the complex dielectric constant increases up to 17 in the middle of the wall while it decreases to 11 and below at the front and back sides. The mean real part is equal to 12.4, which is close to the value obtained by radar. Both values are included in Figure 8.25*b* as parallel lines.

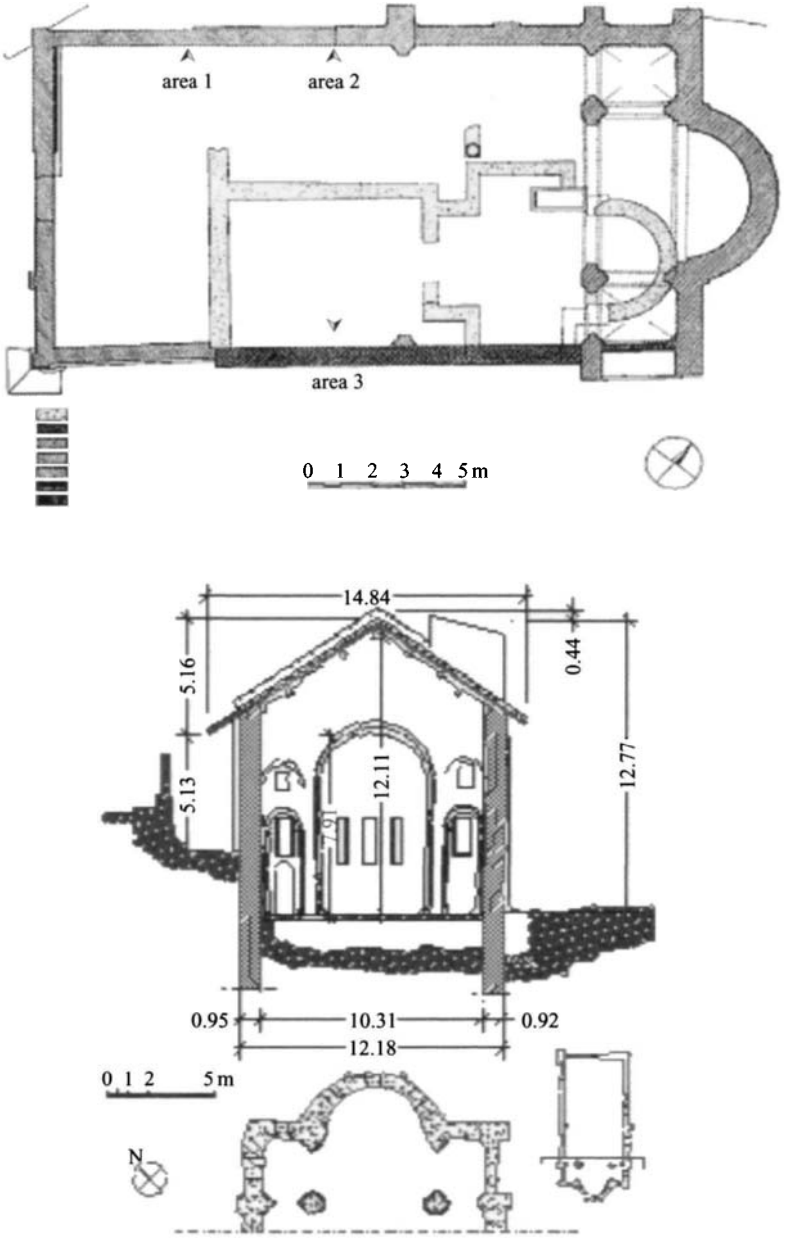

Figure 8.23 *Plan view and section of the Church of S. Maria Rossa*
The locations of the three areas investigated are indicated by arrows

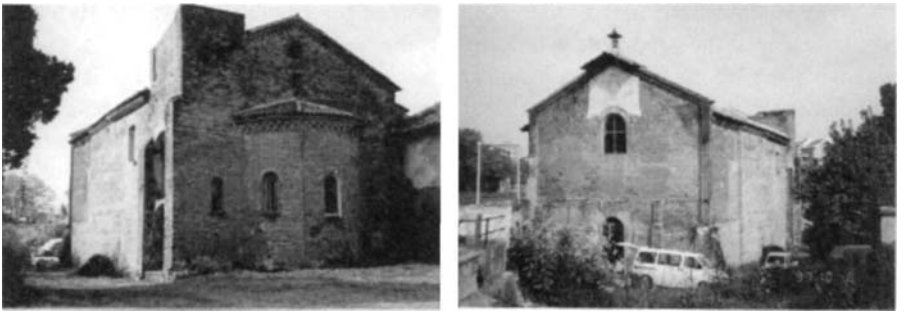

Figure 8.24 *The Church of S. Maria Rossa*

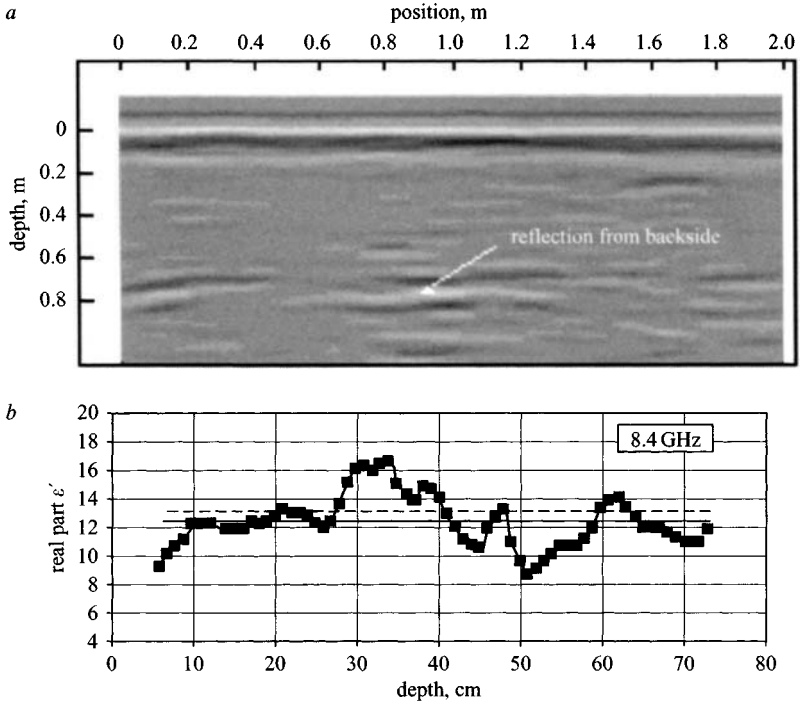

Figure 8.25 *(a) Radar data recorded with the 500 MHz antenna and (b) depth resolved distribution of the dielectric constant and thus the moisture content as determined with the microwave borehole system at area 1*
Dashed line: mean relative dielectric constant determined with radar; full line: mean relative dielectric constant determined with the microwave borehole system

Area 3 is localised in the most ancient part of the Church (dating 9th/10th century), located at the south side. Close to this area there is an in-filled door. This work was done during the repairs of 1966. The brickwork is characterised by new brick and cement mortars. Figure 8.26*a* shows the radar images of a horizontal scan in the middle of area 3, recorded with the 900 MHz antenna. On the right side of the radar images, the reflection from the back-side is very clear. Thus, the depth scale of the radar images was calibrated from the known thickness of the wall of 60 cm (length of the boreholes). From the back-side reflection, a real part of permittivity of about 4 was calculated. On the left side of the radar images, no back-side reflection is visible but a very strong reflection occurs at a depth of ~20 cm. This reflection might be due to a detachment at the interface of the new brick material to the old material. After the radar measurements, a brick was removed from this area and a void was found with a thickness of ~25 cm. Thus it can be concluded that this region consists of two leaves: the internal leaf is made of new brickwork having a thickness of ~22 cm while the external leaf has a greater depth and is made of old brick material. The depth resolved real part, which was determined at 10.4 GHz with the microwave borehole method, is demonstrated in Figure 8.26*b*. This shows a maximum value of the real part of 5.8 at a depth of 11 cm and a mean value of 5.1 being relatively dry.

8.5.2 Altes Museum, Berlin, Germany

The Altes Museum in Berlin, Germany, was built from 1822 to 1830 by Karl Friederich Schinkel (Figure 8.27). For the planning and preparation of restoration, the internal structure of the brickwork of the rotunda in the centre of the building had to be investigated nondestructively by radar. The main aim was the location of voids and larger hollow spaces which might be used as installation wells.

All radar measurements were performed with the 500 MHz antenna in reflection configuration along both sides (surfaces) of the exterior walls of the rotunda in horizontal traces. These horizontal traces are all included in the plan view of the rotunda in Figure 8.28 as arrows and are marked by numbers. The height of the traces related to the ground floor of the rotunda was 1 m.

In the following, two selected radar images are presented. Figure 8.29 shows the radar images of trace no. 4, which was recorded from the inside of the rotunda along a distance of 16.6 m. In these radar images many reflections are visible. Five of them, marked with letters, can be easily related to hollow spaces:

a: Reflection directly below the surface along a distance from 0.96 to 2.6 m. This reflection can be related to a niche which was used for the room heater (radiator).
b: Reflection at a depth of 1.5 m at a distance of 6.4 m. This reflection occurs at the inner side of the staircase.
c, d: Reflections at depths of 1.9 and 1.13 m at distances of 9 and 12.5 m. These reflections can be related to small chambers inside the brickwork.
e: Reflection at a depth of 1.55 m, at a distance of 13.7 to 14.6 m, which is the reflection at the back-side of the wall.

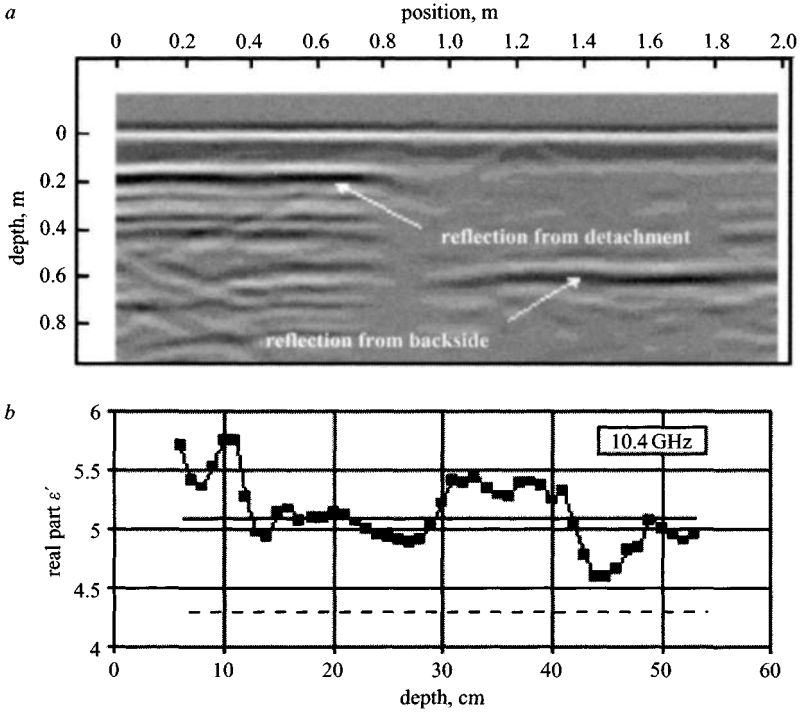

Figure 8.26 *(a) Radar data recorded with the 900 MHz antenna and (b) depth resolved distribution of the relative dielectric constant*
The moisture content as determined with the microwave borehole system at area 3; dashed line: mean relative dielectric constant determined with radar; full line: mean relative dielectric constant determined with the microwave borehole system

Figure 8.27 *(a) Portico facade of the Altes Museum as shown from the Lustgarten; (b) perspective from inside of rotunda*

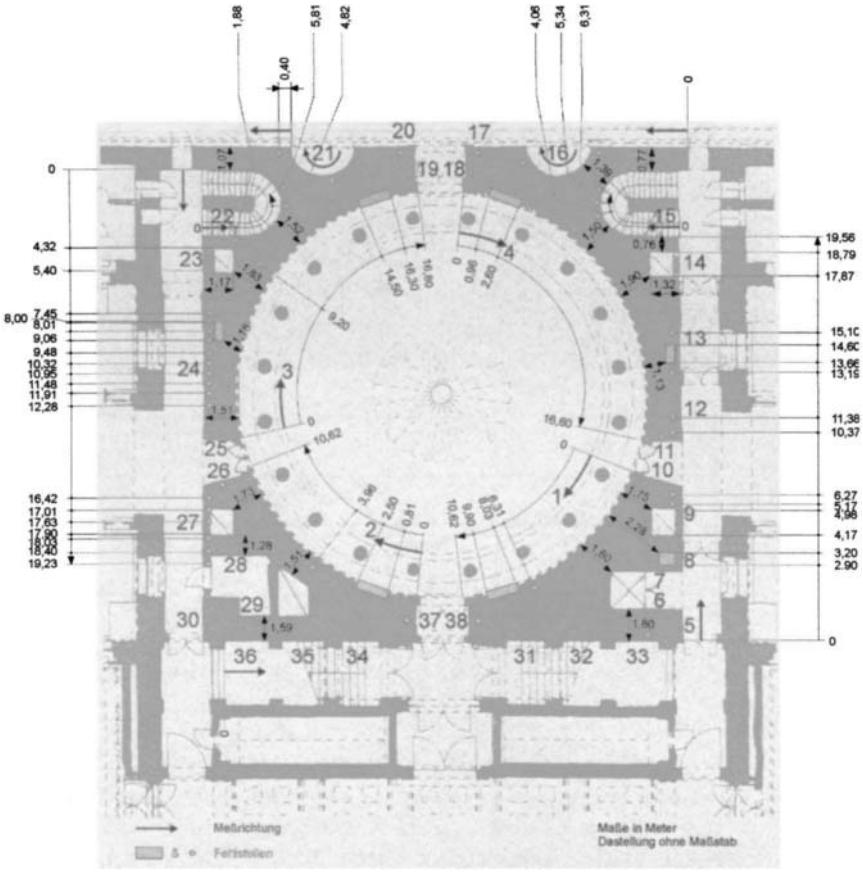

Figure 8.28 *Plan view of the rotunda inside Altes Museum showing the radar traces and the localised voids and larger hollow spaces*

Figure 8.30 shows radar images containing the traces 12, 13 and 14 which were recorded at the back-side of the same wall as trace no. 4. Here, seven reflections can be related to the following structures:

a: Reflection from a depth of 1.57 cm, which can be related to the back-side of the wall (comparable to reflection e in Figure 8.29).

b, c, d, e: Reflections from depths between 0.1 and 0.3 m and in distances of 10.37, 11.38, 13.19 and 15.1 m related to the beginning of the trace. From the shape of the hyperbolas it can be concluded that these reflections belong to regular voids or to vertical pipelines (electricity, water etc.).

f, g: Reflections from a depth of 0.3 m at distances between 13.7–14.6 m and 17.9–18.8 m. These reflections belong to two small chambers (comparable to reflections c and d in Figure 8.29).

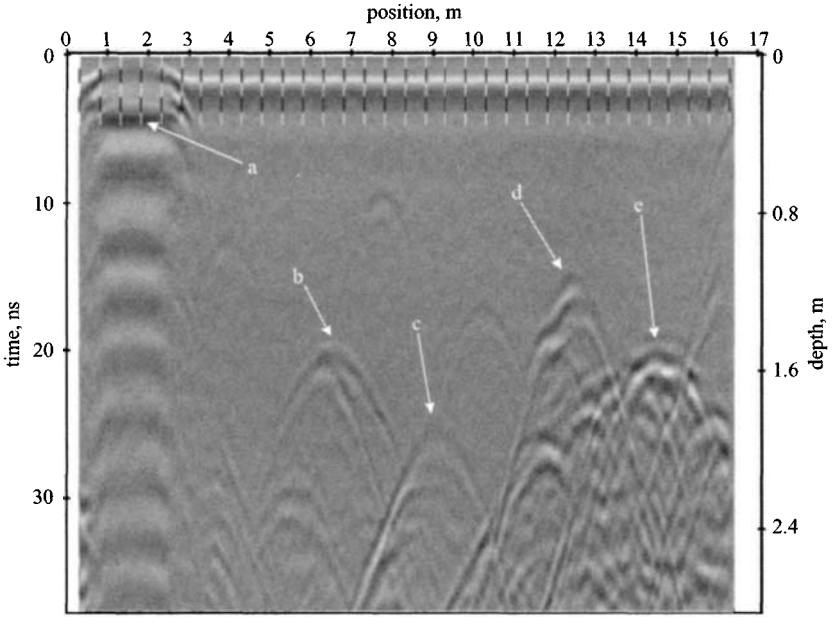

Figure 8.29 *Radar images of trace no. 4 recorded with the 500 MHz antenna from the inside of the rotunda*

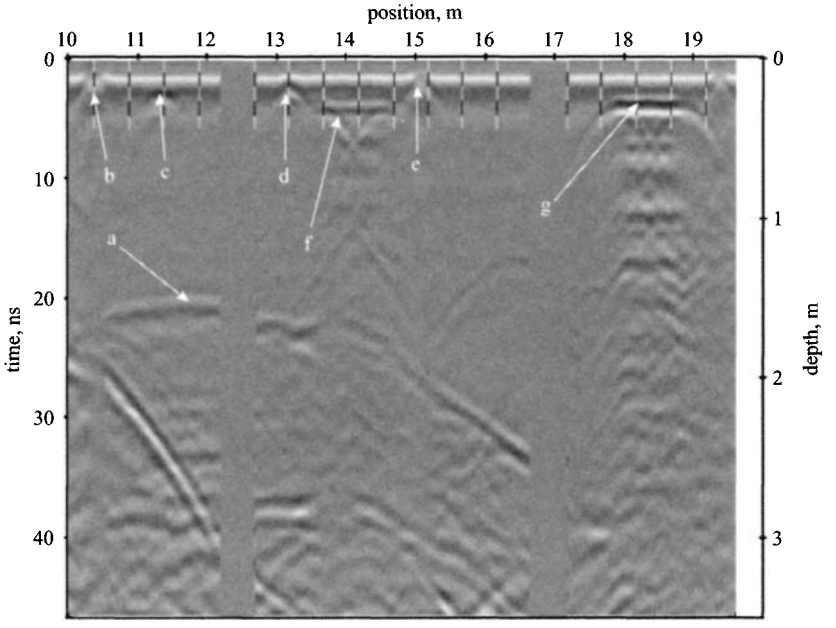

Figure 8.30 *Radar images of the connected traces no. 12, 13 and 14 recorded with the 500 MHz antenna from the outside of the rotunda*

All pipelines and hollow spaces inside the brick wall of the rotunda which were detected by radar are visualised in Figure 8.28. In addition to the known chambers and structures, three additional chambers and several voids and/or pipelines could be localised. In some areas, the actual thickness of the wall could be determined. In all radar images, the reflections were very clear, which is a hint for homogeneous and dry brickwork. In some radar images additional weak reflections could be observed deep inside the brickwork which were not related to any structures and which might not be relevant for the restorations.

8.5.3 *Location of metallic anchors and clamps fixing the facade of a Gothic cathedral*

For restoration of a gothic cathedral, the position of metallic anchors, clamps and dowels fixing the sandstone facade (Figure 8.31*a*) has to be determined. This was required for removing the facade elements as well as for testing the condition of the fixing elements.

Clamps always connect neighbouring sandstone blocks, have a horizontal orientation and are located in horizontal joints. Dowels connect sand lime blocks positioned one upon the other, have a vertical orientation and are located in the middle of a horizontal joint. To fix the sandstone facade to the masonry wall behind, dowels are used positioned in the horizontal joints.

The measurements have been performed with a 1.5 GHz antenna (GSSI, SIR 10 A). To trigger the impulses a survey wheel was used. The position of crossed joints was blazed in the radar images using the manual marker. For all measurements, the whole

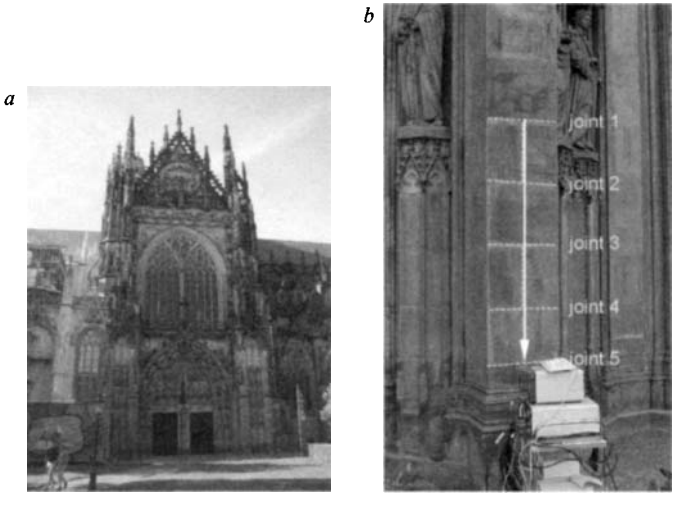

Figure 8.31 *(a) Western pediment of the gothic cathedral; (b) vertical radar trace (white arrow) in the middle of a pillar*
The joints are marked by dashed lines

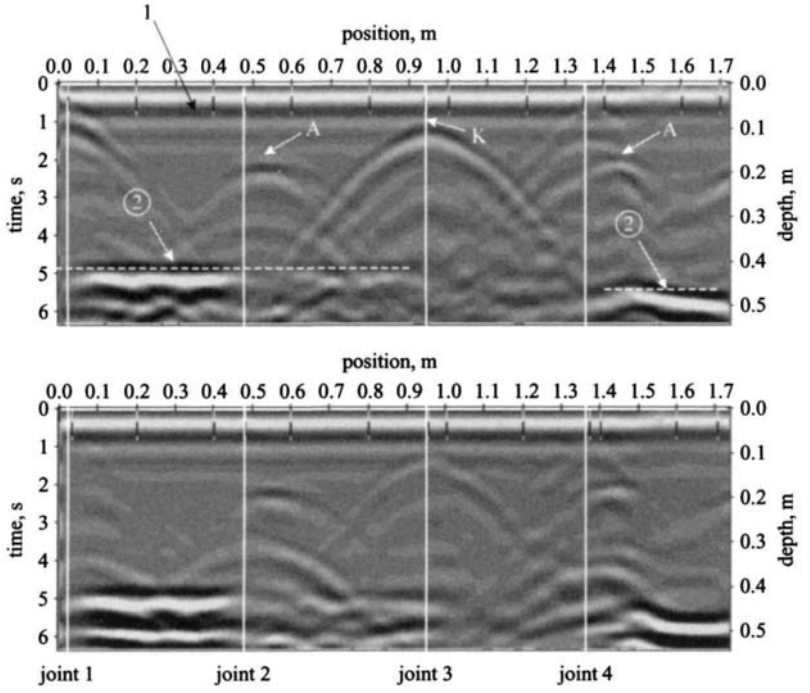

Figure 8.32 *Radar images of the vertical trace in the middle of the pillar from top (left) to bottom (right)*
Top: Radar images with horizontal polarisation. Bottom: Radar images with vertical polarisation. The positions of the trace as well as of the joints are shown in Figure 8.31. 1: Reflection from the surface; 2: reflection from the back-side of the sandstone blocks; A: anchor; K: clamp

surface of the antenna had contact to the surface of the facade. Each trace had been recorded in both polarisation configurations of the antenna. The propagation velocity of the electromagnetic impulses was determined at an area with known thickness and was $v = 0.17 \times 10^9$ m/s.

In the following, the results related to the investigation of the pillar in Figure 8.31*b* are presented. Among other things one vertical trace was recorded with the 1.5 GHz antenna in the middle of the pillar above the vertical joints. Measurements in horizontal and vertical polarisation of the antenna related to the trace were performed. These two radar images are visualised in Figure 8.32.

In both radar images, the reflection from the surface is seen at a depth of 0 cm (1). At a depth of 41 cm (between joint 1 and 3) and of 47 cm (between joint 4 and 5) the reflection from the back-side of the sandstone blocks appears (2). The back-side reflection between joints 3 and 4 is outside the presented depth scale; this sandstone block has a thickness of 80 cm.

At the height of joint 3, a reflection hyperbola is visible at a depth of (10 ± 2) cm (K). The intensity of this reflection is much higher for the horizontal polarisation (top radar images). Therefore, this reflection can be correlated to a clamp which is horizontally orientated.

5 cm below joint 2 and also below joint 4, at each position a hyperbola at a depth of (18 ± 2) cm can be detected (A). The intensity of these reflections is similar for both polarisation configurations. Therefore, each reflection can be related to an anchor which is positioned in the horizontal joints and which penetrates into the sandstone block below. Some additional reflections at joint 4 cannot be clearly related to construction elements.

For further references to the determination of moisture content and distribution see References [2–16]. The investigation of the inner structure of masonry (double leaves, thickness of single leave, location of large voids and cavities) is covered in References [17–26].

References to the location of metallic and wooden mounting parts (i.e. anchors, bars and joint belts are found in Reference [27], and the location of buried structures (foundations, barrel faults, ducts) in Reference [28].

8.6 Summary

The application of GPR in archaeology has developed over the past decade. This Chapter has provided a snapshot of applications ranging from the Egyptian civilisation to European medieval structures. Many more papers and conferences specific to the use of GPR are now available. An International Conference on GPR in Archaeology was held in Nara, Japan, 16–17 February 2001, and references to the papers from that conference are provided. Work by Pirri [29] and Boryssenko [30] provides further insight into the uses of GPR in archaeology.

Websites on the specific use of GPR in archaeology are located at:

http://e-tiquity.saa.org/~etiquity/1/petra07.html
http://www.du.edu/~lconyer/
http://www.bradford.ac.uk/acad/archsci/subject/archp_nf.htm
http://www.joeinfo.com/gpr/

However, the original introduction by John Fidler is still relevant to the use of GPR as being one among a number of geophysical tools for archaeological investigation. GPR can be used to great effect but needs to be employed as part of a team effort with trained archaeologists to obtain the greatest benefit.

8.7 References

[1] LUCARELLI, C., and NASTASE, M.: Aspetti preliminaru al progetto di recupero di, Cascina Chiesa Rossa, L'evoluzione del complesso e l'approccio sperimentale alla fase di rilevamento, M.Sc. Thesis work supervised by BINDA, L., GUZZETTI, F., Faculty of Architecture, Politecnico of Milan, Milan

[2] MAIERHOFER, C., LEIPOLD, S., SCHAURICH, D., BINDA, L., and SAISI, A.: 'Determination of the moisture distribution in the outside walls of the S. Maria Rossa using radar'. Proc. 7th Int. Conf. on Ground penetrating radar (GPR), Kansas, USA, 1998, Radar Systems and Remote Sensing Laboratory, Vol. 2, pp. 509–514

[3] RUDOLPH, M., SCHAURICH, D., and WIGGENHAUSER, H.: 'Feuchteprofilmessungen mit Mikrowellen in Mauerwerk', in Wiggenhauser, H., Müller, H. S., and Girlich (Eds.): 'Tagungsbericht Feuchtetag' (DGZfP, Berlin, 1993), pp. 44–56

[4] KÄÄRIÄINEN, H., RUDOLPH, M., and WIGGENHAUSER, H.: 'Moisture measurement in building materials with microwaves'. *VTT Publ.*, 1998, **357**, Technical Research Centre of Finland, Espoo, 73 pp.

[5] MAIERHOFER, C., LEIPOLD, S., and WIGGENHAUSER, H.: 'Investigation of the influence of moisture and salt content on the dielectric properties of brick materials using radar'. Proc. 7th Int. Conf. on Ground penetrating radar, Lawrence, USA. Radar Systems and Remote Sensing Laboratory, 1998, Vol. 2, pp. 477–484

[6] ARNDT, D., BORCHARDT, K., CROY, P., GEYER, E., HENSCHEN, J., MAIERHOFER, C., NIEDACK-NAD, M., RUDOLPH, M., SCHAURICH, D., WEISE, F., and WIGGENHAUSER, H.: Anwendung und Kombination zerstörungsfreier Prüfverfahren zur Bestimmung der Mauerwerksfeuchte im Deutschen Dom. Forschungsbericht 200 der BAM, Berlin (Wirtschaftsverlag NW Verlag für neue Wissenschaft, Berlin, 1994), 75 pp.

[7] KAHLE, M.: 'Feuchtemessungen an historischem Mauerwerk mit dem Radarverfahren', in Wiggenhauser, H., MÜLLER, H. S., and GIRLICH, N. (Eds.): 'Tagungsbericht Feuchtetag' (DGZfP, Berlin, 1993), pp. 57–67.

[8] KAHLE, M.: 'Das Radarverfahren zur Feuchtedetektion in historischem Mauerwerk', in Kupfer, K. (Ed.): 'Materialfeuchtemessung, Grundlagen – Verfahren – Geräte – Applikationen' (Expert-Verlag, Renningen, 1997), pp. 335–346

[9] WEISE, F., HENSCHEN, J., HOFFMANN, D., NIEDACK-NAD, M., RUDOLPH, M., and SCHAURICH, D.: 'Complex investigations of the moisture balance in structural members made of natural stone – a case study of the Berlin Zeughaus, in RIEDERER, J. (Ed.): Proc. 8th Int. Congress on Deterioration and conservation of natural stone, Berlin: möller druck und verlag gmbh, 1996, Vol. 1, pp. 441–451

[10] COLLA, C., and MAIERHOFER, C.: 'Investigations of historic masonry via radar reflection and tomography', in Noon, D. (Ed.): 8th Int. Conf. on GPR 2000, Gold Coast, Australia, Brisbane, 2000. SPIE Vol. 4084, pp. 893–898

[11] MAIERHOFER, C., and COLLA, C.: 'Influence of moisture content on the detection of structural features in building construction using impulse radar', in Alampalli, S. (Ed.): 'Structural materials technology IV, an NDT Conference', Atlantic City, NJ (Technomic Publishing Co., Inc., Lancaster, Basel, 2000), pp. 343–349

[12] WOLTER, B., DOBMANN, G., MAIERHOFER, C., and WIGGENHAUSER, H.: 'Non-destructive methods for moisture measuring',

in Forde, M. C. (Ed.): Proc. (CDROM) 8th Int. Conf. on Structural faults and repair, London, UK Edinburgh: (Engineering Technics Press, Edinburgh, 1999)

[13] MAIERHOFER, C., and WÖSTMANN, J.: 'Investigation of dielectric properties of brick materials as a function of moisture and salt content using a microwave impulse technique at very high frequencies'. *NDT&E Int.*, 1998 **31**, (4), pp. 259–263

[14] KÄÄRIÄINEN, H., RUDOLPH, M., SCHAURICH, D., TULLA, K., and WIGGENHAUSER, H.: 'Moisture measurements in building materials with microwaves', in UOMOTO, T. (Ed.): Proc. Seiken Symposium No. 26, Non-Destructive Testing in Civil Engineering 2000, Tokyo, Japan, (Elsevier, 2000), pp. 199–207

[15] MAIERHOFER, C., and WOLTER, B.: 'Non-destructive testing methods for moisture determination' Proc. NDT in Progress, Trest, CZ, Czech Society for NDT, Prag: (Eigenverlag, Prague, 2001), pp. 41–54

[16] MAIERHOFER, C., SCHAURICH, D., and WIGGENHAUSER, H.: Feuchte- und Salzmessungen von Ziegeln mit einer TDR-Sonde, in WIGGENHAUSER, H., and MÜLLER, H. S. (Eds.): 'Tagungsbericht Feuchtetag' (BAM, Berlin, 1995), pp. 328–330

[17] COLLA, C., FORDE, M. C., and DAS, P. C.: 'Radar imaging in composite masonry structures', in FORDE, M. C. (Ed.): Proc. 7th Int. Conf. on Structural faults and repair (Engineering Technics Press, Edinburgh, 1997, Vol. 3), pp. 493–504

[18] MAIERHOFER, C., BORCHARDT, K., and HENSCHEN, J.: 'Application and optimisation of impulse-radar for non-destructive testing in civil engineering', in SCHICKERT, G., and WIGGENHAUSER, H. (Eds.): Proc. Int. Symposium NDT-CE, 1995, (DGZfP, Berlin, 1995), pp. 663–672

[19] BINDA, L., LENZI, G., and SAISI, A.: 'NDE of masonry structures: use of radar test for the characterisation of stone masonries', in FORDE, M. C. (Ed.): Proc. 7th Int. Conf. on Structural faults and repair (Engineering Technics Press, Edinburgh, 1997, Vol. 3), pp. 505–514

[20] MAIERHOFER, C., KRAUSE, M., and WIGGENHAUSER, H.: 'Non-destructive investigation of sluices using radar and ultrasonic impulse echo', *NDT& E Int.*, 1998, **31**, (6), pp. 421–427

[21] MAIERHOFER, C., WÖSTMANN, J., SCHAURICH, D., and KRAUSE, M.: 'Radar investigation of historical structures', in UOMOTO, T. (Ed.): Proc. Seiken Symposium No. 26, non-destructive testing in civil engineering 2000, (Elsevier, 2000), pp. 529–537

[22] MAIERHOFER, C.: 'Radar investigation of masonry structures', *NDT& E Int.*, 2001, **34**, (9), pp. 139–147

[23] KAHLE, M., and ILLICH, B.: Einsatz des Radarverfahrens zur Erkundung von Struktur und Zustand historischen Mauerwerks. *Bautechnik*, 1992, **69**, (7), pp. 342–353

[24] KAHLE, M., ILLICH, B., and WENZEL, F.: Untersuchungen an den Pfeilern der St. Wolfgangskirche in Schneeberg. *Bautechnik*, 1993, **70**, (7), pp. 416–424

[25] McCANN, D. M., and FORDE, M. C.: 'Review of NDT methods in the assessment of concrete and masonry structures', *NDT& E Int.*, 2001, **34**, pp. 71–84
[26] BINDA, L., LENZI, G., and SAISI, A.: 'NDE of masonry structures: use of radar test for characterisation of stone masonries', in FORDE, M. (Ed.): Proc. 7th Int. Conf. on Structural faults and repair (Engineering Technics Press, Edinburgh, 1997, Vol. 3), pp. 505–514
[27] LUALDI, M., and ZANZI, L.: 'GPR investigation to reconstruct the geometry of the wooden structures in historical buildings', in NOON, D. (Ed.): 8th Int. Conf. GPR 2000, Gold Coast, Australia, Brisbane: SPIE Vol. 4084, 2000
[28] KAHLE, M., ILLICH, B., and BSEREXHE, B.: Erkundung des Untergrundes der Kathedrale von Autun mit dem Radarverfahren. Universität Karlsruhe, Jahrbuch, 1990
[29] PIRRI, M., LOMBARDO, P., BUCCIARELLI, T.: 'Performance assessment of wide-band pulsed GPR for archaeological applications'. Proc. IEEE Int. Geoscience and remote sensing Symposium, 2000 (IGARSS 2000), Vol.5, pp. 2385–2387
[30] BORYSSENKO, A.: 'Subsurface radar imaging of underground archeological objects in Kyiv Petcherskaja Lavra, Kyiv, Ukraine'. Proc. IEEE Canadian Conf. on Electrical and computer engineering, 1999, Vol.2, pp. 855–860

8.8 Bibliography

DABAS, M., and TITUS, H.: 'GPR and ES surveying for assessment of the remains under the Cathedral of Saint-Etienne d'Auxerre (France)'. Int. Conf. on GPR in archaeology, Nara, 16–17 February 2001

EDER-HINTERLEITNER, A., SEREN, S. S., MELICHAR P., and NEUBAUER, W.: 'Combination of high resolution geomagnetik and GPR prospections of roman sites in Austria'. Int. Conf. on GPR in archaeology, Nara, 16–17 February 2001

GOODMAN, D., YASUSHI, N., PIRO, S., GAFFNEY, V., and PATTERSON, H.: 'Analysis of GPR 3-D renders from the Forum Novum, Italy'. Int. Conf. on GPR in archaeology, Nara, 16–17 February 2001

GRACIA, V. P., CANAS, J. A., PUJADES, L. G., CLAPÉS, J., CASELLES, O., GARCÍA, F., and OSORIO, R.: 'GPR survey to confirm the location of ancient structures under the Valencian Catedral (Spain)', *J. Appl. Geophys.*, 2000, **37**, pp. 167–174

GRACIA, V. P.: 'Radar de Subsuelo. Evaluación para aplicaciones en arqueología y en patrimonio histórico-artístico'. Tesis doctoral, Universidad Politécnica de Cataluña, 2001, pp. 601–689. ISBN: 84-699-6884-X. Dep. legal: B-52288-2001

NAKANO, T., and SAKAI, H.: 'GPR survey with the study of dielectric property on the moat structure at the archaeological remains'. Int. Conf. on GPR in Archaeology, Nara, 16–17 February 2001

NEUBAUER, W.: 'Large scale GPR surveys on roman buildings'. Int. Conf. on GPR in archaeology, Nara, 16–17 February 2001

OH, H.: 'Archaeological GPR survey at burial unmounded area in Pubchonni Wonjoo, Korea'. Int. Conf. on GPR in archaeology, Nara, 16–17 February 2001

PIRO, S.: 'The analysis of the Roman Theatre of Aosta (Northern Italy) using non-destructive GPR method'. Int. Conf. on GPR in archaeology, Nara, 16–17 February 2001

PIRO, S., GOODMAN, D., and NISHIMURA, Y.: 'High-resolution GPR surveys for the study and characterisation of Forum Novum site (Vescovio, Rieti – central Italy)'. Int. Conf. on GPR in archaeology, Nara, 16–17 February 2001

PIRO, S., GOODMAN, D., and NISHIMURA, Y.: 'The study and characterisation of Traiano's Villa (Altopiani di Arcinazzo – Roma) using high-resolution integrated geophysical surveys'. Int. Conf. on GPR in archaeology, Nara, 16–17 February 2001

SEREN, S. S., EDER-HINTERLEITNER, A., MELICHAR, P., and NEUBAUER, W.: 'GPR prospection in the "Oberstadt" of Ephesos (Turkey).' Int. Conf. on GPR in archaeology, Nara, 16–17 February 2001

SEREN, S. S., EDER-HINTERLEITNER, A., MELICHAR, P., and NEUBAUER, W.: 'A geophysical survey to locate the Roman Station Clunia, Austria. An example for a combination of geomagnetic-, resistivity- and GPR-prospection'. Int. Conf. on GPR in archaeology, Nara, 16–17 February 2001

TRINKS, I., WACHSMUTH, D., and STÜMPEL, H.: 'Processing and visualisation of 4D-GPR data'. Int. Conf. on GPR in archaeology, Nara, 16–17 February 2001

Chapter 9

Civil engineering

9.1 Introduction

This Chapter describes some of the civil engineering applications of GPR and considers roads and pavements, concrete structures, bridges and tunnels. GPR has become an established and routine method of inspection of civil engineering structures. Further information can be found by contacting the appropriate national authorities, some of whose websites are referenced.

9.2 Roads and pavements

Roads and highways carrying vehicular traffic are described as having pavements. In the UK, the word pavement is often loosely used to describe that part of the infrastructure used by pedestrians. In North America, this would be known as the sidewalk. In the following Section, the word pavement should be understood to describe the structure of roads or highways.

GPR systems can be used either hand propelled (Figure 9.1) or alternatively mounted on a vehicle (Figure 9.2). The radar may take the form of a single line survey or may be an array covering one carriageway of the pavement.

Vehicle based systems can survey pavements speedily, economically, safely and with minimum disruption to existing traffic. GPR technology is widely used in Europe and North America. In the UK the Highways Agency routinely contracts radar surveys of the road network, and the TRL, in conjunction with the County Surveyors' Working Party, monitor developments in the technique. In the United States the Strategic Highway Research Program (SHRP), the Federal Highway Administration (FHWA), and several States and other agencies have all evaluated the benefits of high speed GPR surveys. In China, Xiaojan [1] reports on the application of GPR techniques to civil engineering structures.

Compared with traditional coring methods, GPR can provide far more extensive measurement coverage at orders of magnitude less cost. Typical vehicle mounted

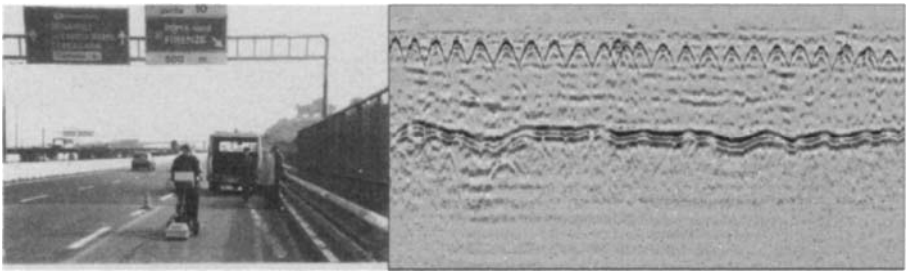

Figure 9.1 *GPR survey of road pavement showing reinforcing and sub-base layer (courtesy ERA Technology)*
Horizontal scale 3 m; vertical scale 0.7 m

Figure 9.2 *8-Channel, 1 m-wide experimental vehicle mounted radar system (courtesy ERA Technology)*

radar can cover up to 300 km per day at normal traffic speeds. Wu [2] reports on recent developments in road surveying.

The accuracy of GPR is reported as being 3–5% for new asphalt, 5–10% for existing asphalt, 5–10% for concrete and 8–15% for the granular sub-base. It must be borne in mind that this requires a regular calibration of the velocity of propagation in order that localised variations in water content do not invalidate the calibration. Further, it should be noted that there will be some situations where the contrast level between the layers results in inadequate data. An example of single channel radar survey data is shown in Figure 9.3.

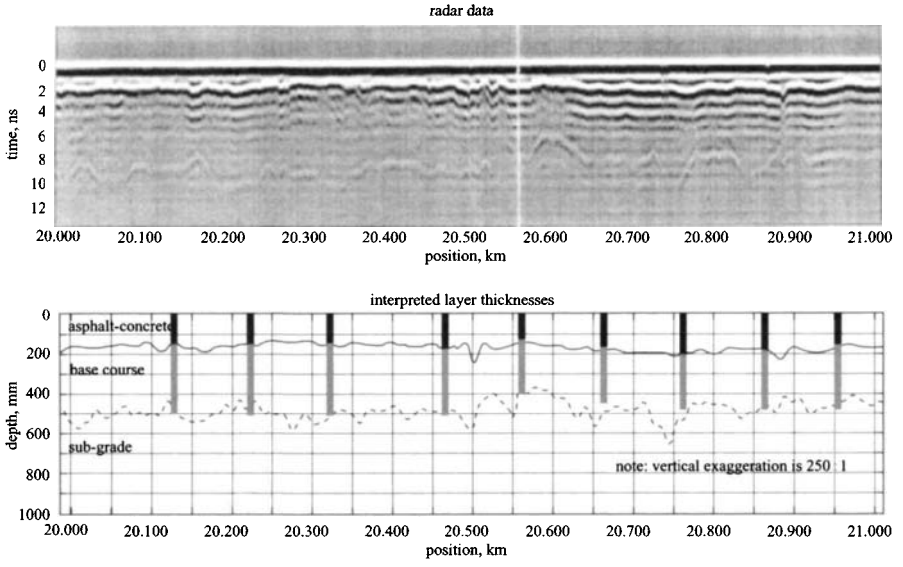

Figure 9.3 Radar analysis of asphalt and base course thickness (courtesy Road Data Ltd)

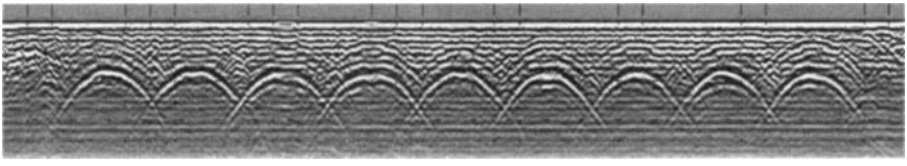

Figure 9.4 Radar survey of nine-arch bridge (courtesy ERA Technology)

Further information can be found in References [3–8]. A good example of the radar surveying of bridges is given in Figure 9.4, which shows a nine-arch bridge. The horizontal scale is 1 m per linear increment and the vertical scale is 51.2 ns. The distance between the deck of the bridge and the top of the arches is 1 m.

9.2.1 Roads in the UK

D. L. Wilkinson
Durham County Council, UK

Roads or pavements can be constructed in a number of ways and can be classified into flexible or rigid types. Flexible construction uses bituminous materials and rigid construction includes a concrete layer, which may be unreinforced or reinforced. Virtually all road constructions are built up with layers of different materials. One of the major indicators of condition is the strength of the road pavement, and this is measured by the deflectograph. This is a heavy vehicle, which measures the deflection

of the pavement under the transient loading of its rear mellining (courtesy of British Rail) wheels. These deflections are then analysed, together with other data such as traffic flow and pavement thickness and condition, to provide an estimate of the residual life of the pavement. The deflections can also be used to calculate an overlay thickness to provide a pavement with a given future life.

Radar techniques may be used to determine the thickness of bituminous layers and concrete slabs, the spacing and location of slab reinforcement, their depth of cover, dowel bars, joining slabs and cracking and, for unreinforced or widely spaced reinforcing, the position of cracks beneath slabs.

Pavement thickness has traditionally been determined by drilling and extracting cores, and pavement condition by excavating trial holes. Disadvantages of these methods are damage to the road structure and provision of information only at widely spaced points. In the early 1980s it was realised that ground penetrating radar might be able to provide this information, and a few pavement engineers tried the technique with some success. In addition to establishing pavement-layer thickness, they were finding that the technique was useful in establishing ground conditions below the pavement layers – a task that can be performed by trial pitting but is expensive.

By 1990, a number of radar surveys had been carried out in the UK and the technique promised to be a success. However, the experience was fragmented and the requirements of radar surveys varied from scheme to scheme and between pavement engineers. Radar providers needed a better perception of the rock pavement engineer's requirements for the technique so that developments in equipment could be concentrated on what was needed. After consultation, the County Surveyors' Society, through its Data Collection Working Party, produced 'Guidelines for the development of ground radar' in 1991. The tunnel lining (courtesy of British Rail) guidelines included requirements for accuracy, calibration, robustness, the ability to locate results to specific positions on the road, and computerisation of results. Secondary requirements were seen as ability to differentiate between sound and broken materials in the bituminous layers, and the presence of defects such as voids, delamination between layers, cracking of the surface layer and moisture content variation in the granular layers. Since the guidelines were published the technique has moved on. Accuracy has increased to the point where it matches coring. Repeatability and reproducibility are acceptable. Operators are offering high-speed surveys with results referenced to the road network and low-speed surveys where more detail is required.

Demonstrations of equipment have been given to the Data Collection Working Party and the Transport Research Laboratory. The DCWP demonstration has shown that accuracy and agreement on interface depths between different operators is good on roads with a predictable construction. However, apart from motorways, trunk roads and major 'A' class roads, most roads have been built up over the years in a piecemeal fashion. It was found that on this type of road operators agreed on the major interface depths, but were sometimes unable to agree on material types and picked up varying minor interfaces (e.g. thin layers of regulating material, internal layers within, for example, a sub-base). On this type of road it would, therefore, be essential to correlate radar surveys with road coring and, possibly, trial pitting. It has

to be said that roads with a predictable construction, although comprising only about 20% of the total road network, receive a large proportion of maintenance funding – perhaps 80%.

The DCWP demonstration was mainly of low-speed equipment but one operator demonstrated his equipment at high speed. He obtained results of comparable accuracy with the best of the low-speed-equipment operators. This demonstration, and trials carried out elsewhere, have shown that high-speed surveys offer an opportunity to survey long stretches of the major road network without the need for traffic control. This is an important consideration because traffic control is expensive and causes delay and danger to motorists.

Test results are shown in Figure 9.5. The improvement in accuracy of ground penetrating radar over the past few years has been encouraging, and increased use of the technique should lead to further improvements. A survey in 1994 found that 32 County Councils had used ground penetrating radar to solve a variety of pavement and structural problems. Further use of ground radar by local authorities is being held up by the lack of a specification for the work and by the difficulty authorities unfamiliar with the technique have in selecting operators for a tender list. In 1994, the Department of Transport issued an Advice Note (HA 72-94) entitled 'Use and limitation of ground penetrating radar for pavement assessment'. This document is of assistance when preparing a ground penetration radar survey contract. Since then

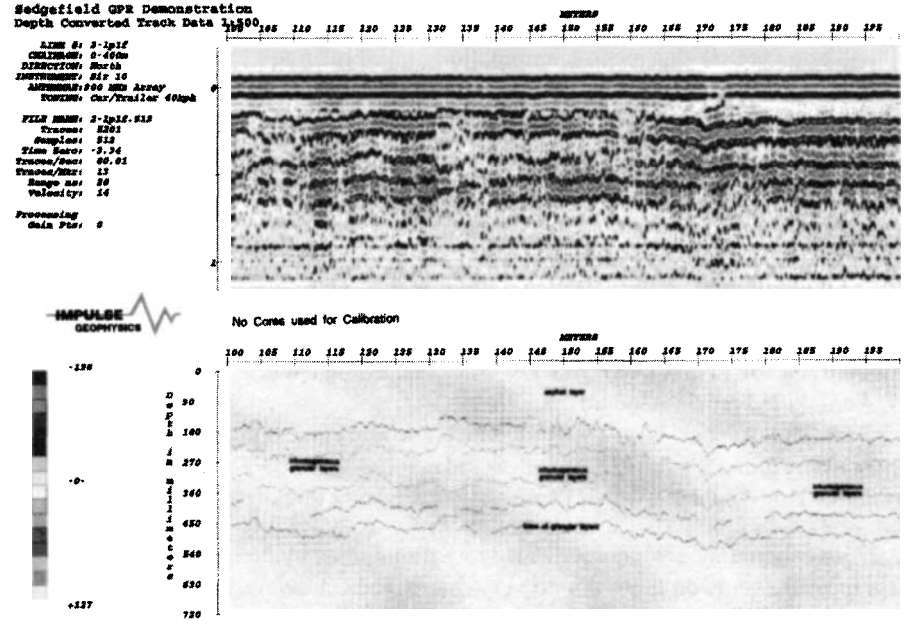

Figure 9.5 *Test results from UK trials for road surface analysis (courtesy Impulse Geophysics)*

GPR has become an established method of road survey and has moved from the research stage to maturity.

9.2.2 Step-frequency radar technique applied on very-thin layer pavements
Dr Xavier Dérobert

9.2.2.1 Introduction: Identifying the thickness of a roadway pavement layer is one of the major topics of interest in the field of civil engineering. Obtaining appropriate information on a roadway's various layers proves critical to the evaluation and prediction of pavement mechanical behaviour, the optimisation of a road maintenance strategy and on-site quality control. Traditionally, information on pavement layer thickness is obtained from pavement coring and/or road databases. Nevertheless, such information is seldom well documented and coring is highly local and, by nature, destructive.

Over the past few years, radar systems have led to a powerful nondestructive testing technique that features several major advantages, such as a high acquisition rate, global monitoring through quasi-continuous measurements, and production of a mapping of the various layers thanks to the penetration of electromagnetic (EM) waves in the observed medium. Among the existing technologies, GPR systems dedicated to road inspection have given rise to faster systems operating at higher frequencies, as a result of the development of semiautomatic processing software [9, 10], allowing for thickness determination on layers up to 5 cm thick.

Concurrently, the performance of innovative pavement structures has been improving, thereby allowing road construction companies, especially in France, to offer a line of high-performance mechanical products for very thin surfaces [11]; this trend has developed for both economic and ecological reasons. High-value-added products are attractive to municipal authorities, by virtue of reducing the need for periodic roadway milling, as well as to highway construction companies who are simply looking to apply a wearing course onto a structurally sound pavement. As a result, the following products have been derived:

- Thin Asphalt layer (TAS), which specifies an average layer thickness of less than 4 cm ([12] French Standard)
- Very Thin Asphalt layer (VTAS), which specifies an average layer thickness of between 2 and 3 cm ([13], French Standard)
- Ultra Thin Asphalt layer (UTAS), an average layer thickness of less than 2 cm.

Conventional radar techniques encounter limitations in the effort to obtain thickness measurements on these thin to very thin pavement layers. Such obstacles have not yet been overcome by commercial devices due to their incapacity of operating over ranges of several gigahertz (central frequency limited to 2 GHz).

Within this context, the LCPC (French national civil engineering research laboratory) has been involved for over 15 years in GPR techniques applied to road layer

thickness measurements [14, 15]. Research has focused on the design of a step-frequency radar technique capable of operating with very high central-frequency synthetic pulses over ranges of several gigahertz.

Independently of GPR impulse research, the step-frequency technique has been studied for years in the field of geophysics, primarily in order to reach a higher dynamic range with low internal noise, thus enabling investigation at greater depths [16, 17]. Since a network analyser features a broad operating frequency range, both deep and shallow testing can be conducted, depending on the chosen frequency band of the antennas and the type of application. This state-of-the-art technique has already been used in reinforced concrete inspections of decks and bridges, which were performed as part of a study on ultra-wide bandwidth antennas centred in the 3–5 GHz range [18], within the framework of a European project.

9.2.2.2 Step-frequency radar technique: A laboratory measurement device (a commercial network analyser) is used as both a radar generator and receiver. A synthetic pulse is reconstructed in the time domain, from a multi-frequency signal, using the network analyser and then transmitted to the radiating antenna. This then radiates a monochromatic wave series into the road pavement medium. Each EM wave is reflected and transmitted by the successive EM interfaces (i.e. in our case, successive interfaces of different road layers). The receiver converts the reflected EM waves into a recorded electric signal in which both the real and imaginary parts of the signal are retained. The recorded signal is mathematically transformed using an inverse Fourier transform in a time signal, similar to GPR impulse signals, containing echoes from reflections at the medium interfaces.

The major benefit of the system (step-frequency technique + Vivaldi antennas) stems from the potential for controlling an ultra-wideband around the central frequency for a given application, thereby allowing the construction of very short pulses at high central frequencies of over 2 GHz.

An HP8753C network analyser has been used for the various tests carried out. Owing to the low EM loss characteristic of the materials considered in our application, a high acquisition rate is attained without altering the shape of an ideal transmitted pulse. The parameters are thus chosen as follows: an output power of 10 dBm, a low frequency number (101 or 201), and a large filter bandwidth of 3000 Hz for a frequency band of 500 MHz–6 GHz.

9.2.2.3 The antennas: An ultra-wideband antenna has been developed at the Electronics, Antennas and Telecommunications Laboratory (LEAT), working in conjunction with LCPC [19]. The main activity of LEAT (affiliated with the University of Nice-Sophia Antipolis, France) involves the study of microstrip antennas from theoretical, numerical and experimental perspectives and EM research in general. The ultra-wideband antenna developed for road applications and shown in Figure 9.6 below belongs to the family of Vivaldi antennas [14, 20]. It has been created using the 'stripline' technology, displays a small lateral dimension and yields a bandwidth of greater than one decade (458 MHz–10 GHz).

Figure 9.6 *Step-frequency device in acquisition mode*
The network analyser and PC are on a truck; on the left are the Vivaldi-like antennas

All of the following experimental work was conducted in an air-coupled configuration, which implies the use of two antennas positioned at a constant height over the pavement.

9.2.2.4 Test site measurements: For GPR dynamic measurements, a customised software program, run from a laptop PC, enables recording data from the network analyser. Antennas are installed with a constant offset (distance between antennas) and then pulled over the road test sites (see Figure 9.6). Thanks to the LCPC large-scale testing facilities for roads (that include a dedicated site for performing GPR testing and a circular pavement fatigue test track), which are composed of distinct sections of various known roadway structures, several radar profile measurements could be derived.

Results were then compared with classical GPR profiles (using a GSSI device with the 1.5-GHz antenna – hence two antennas in one box). To facilitate comprehension of the test set-up, Table 9.1 summarises some of the technical abbreviations used and lists their respective acronyms.

The LCPC circular pavement fatigue test track is 6 m wide and 120 m long; it is usually constructed in four 30-m-long sections for the full-scale accelerated testing of pavements. A loading machine can apply between 50 and 70 kN at 70 km/h on four single half-axles (see Figure 9.7).

The system can operate under automatic surveillance practically 24 h a day. A large number of load applications per day reduces the time required to conduct

Table 9.1 Glossary of terms

Bituminous concrete	BC
Bitumen-bound granular material	BBGM
Cement-bound granular material	CBGM
Sand cement	SC
Unbound granular material	UGM
Thin asphalt surfacing	TAS
Very thin asphalt surfacing	VTAS

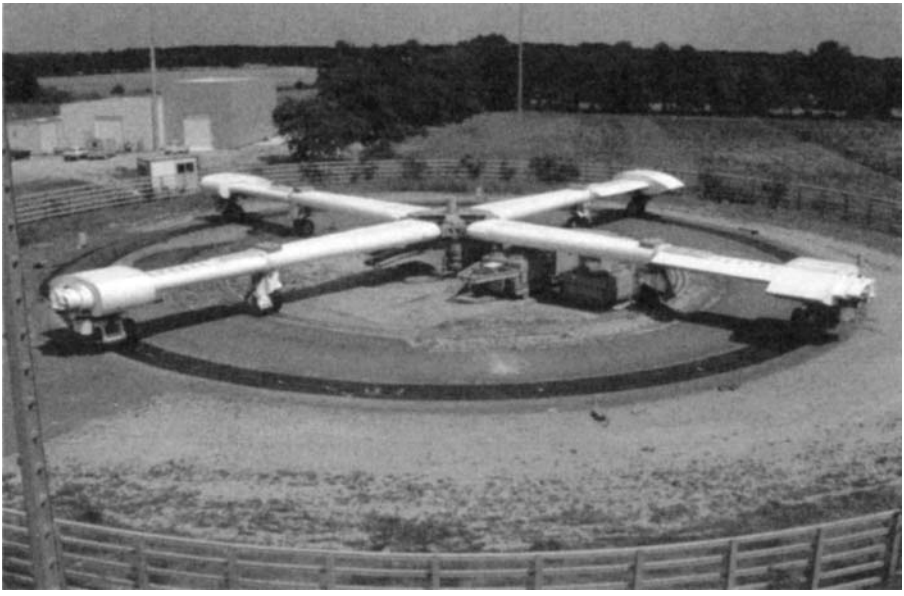

Figure 9.7 LCPC circular pavement fatigue test track set-up

an experiment. A typical experiment on a pavement structure, which requires 2 million load applications (corresponding to an equivalent of 12 years of road life), can be performed within a 3-month period. Both the production and application of pavement materials are carried out with conventional construction equipment under very carefully controlled conditions. For this reason, the test site is very attractive and effective as regards GPR experiments.

The objective of the study has been to evaluate the performance and limitations of the step-frequency technique (for a 3-GHz central frequency) on thin pavements. To do so, we have tested several sections with various thicknesses of asphalt surfaces: BC, TAS and VTAS.

9.2.2.5 Bituminous concrete and thin asphalt surfacing road sections: The first transversal section, presented in Figure 9.8*a*, corresponds to a former loading experiment on SC rutting which had been covered by a standard 6-cm BC course outside the rutting. Figure 9.9 describes the structure and presents a comparison of the two types of radar profiles (3 and 1.5 GHz).

The sizeable EM contrast pertains to high amplitudes of reflected echoes at the interface between BC and SC. Owing to a relatively large thickness (6 cm and above), both radar profiles can detect the BC course and determine the arrival time of echoes

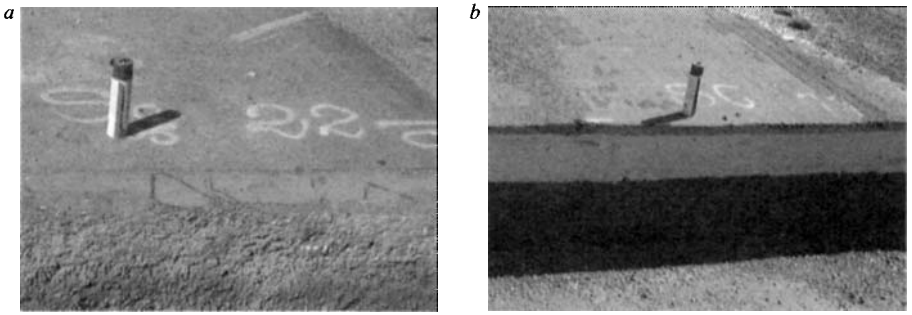

Figure 9.8 Trenches of two different sections of the circular pavement fatigue test track

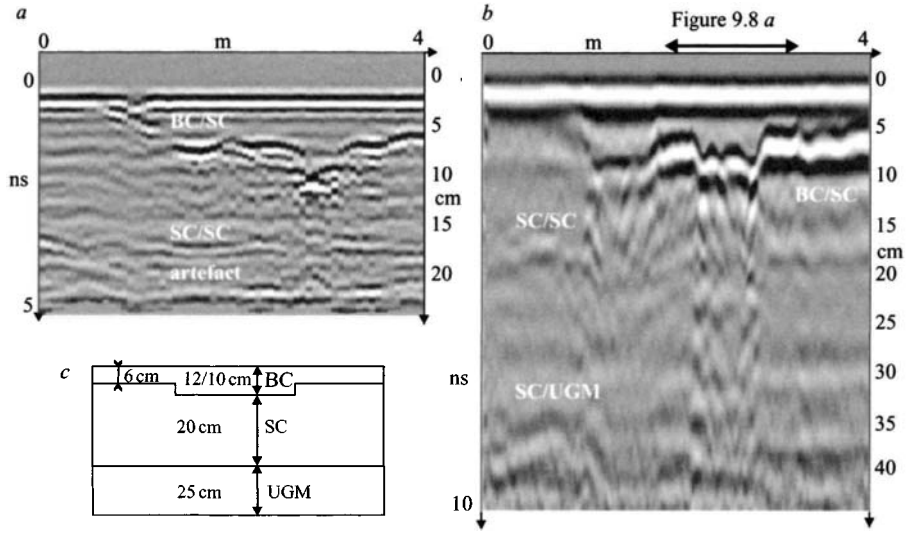

Figure 9.9 Radar testing parallel to trench 9.8a
a Step-frequency profile at 3 GHz; *b* GSSI profile at 1.5 GHz; *c* pavement structure

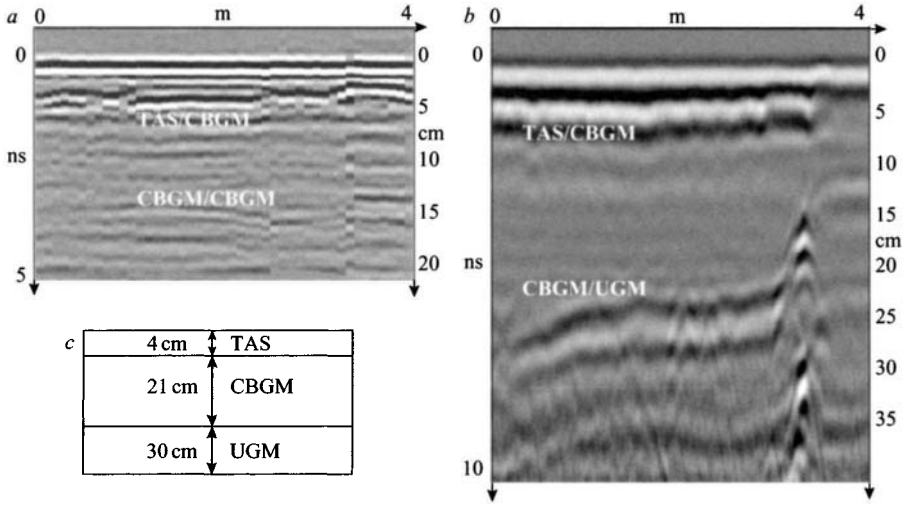

Figure 9.10 *Radar testing parallel to trench 9.8b*
a Step-frequency profile at 3 GHz; *b* GSSI profile at 1.5 GHz; *c* pavement structure

for thickness measurements, following a coring calibration. In both cases, it is easy to localise the excess thickness due to rutting.

A range of 10 ns, for the 1.5-GHz radar profile in Figure 9.9*b*, enables detection of the limits of bound and unbound granular materials. Moreover, due to a compaction gradient on thick layers, every interface between two successive elementary SC layers composing the base structure can also be identified.

The next transversal section, shown in Figure 9.8*b*, proposes a 4-cm TAS laid on a CBGM base. As for the previous structure, the EM contrast is sizeable as a result of the change in binder (asphalt and cement) at the TAS/CBGM interface. Owing to a thinner TAS course and a low central frequency, the 1.5-GHz profile (Figure 9.10*b*) is not able to isolate the TAS/CBGM interface without any processing, even though it is visible on the profile. Nevertheless, the technique does yield a good global view of the pavement structure.

With respect to the 3-GHz profile from Figure 9.10*a*, the pulse wavelength is short enough to distinguish the TAS/CBGM interface from the surface without any processing and to determine the arrival times accurately. A 4-cm layer is thus perfectly included within the testing domain of such a frequency range.

9.2.2.6 Very thin asphalt surfacing road section: Another portion of the LCPC circular pavement fatigue test track has been devoted to tyre and road wear. Two kinds of VTAS (0/10 and 0/6 grading analysis, respectively) were laid over a structure composed of a 7-cm BC wearing course and a 37-cm BBGM base. Figure 9.11 and Figure 9.12 provide a similar presentation to that in Figure 9.10.

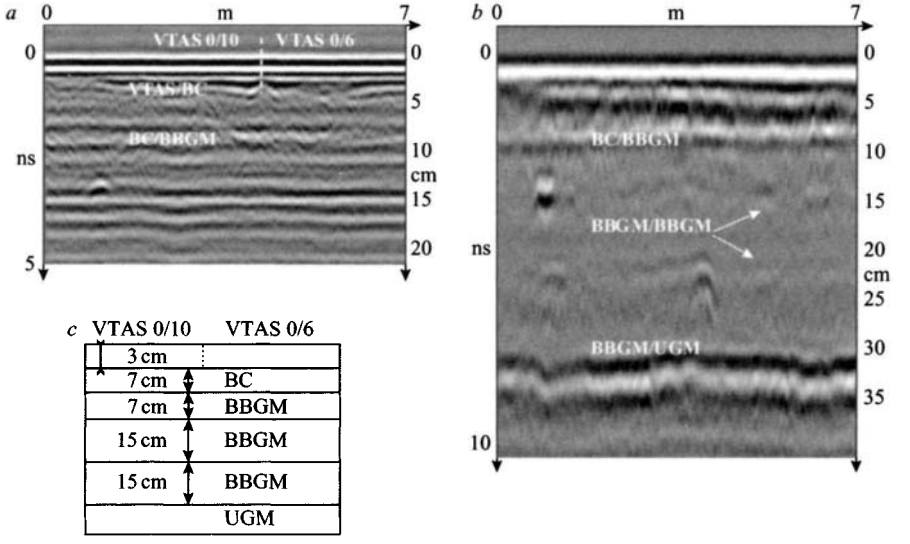

Figure 9.11 *Radar testing along the wheel axis on another pavement with VTAS*
a Step-frequency profile at 3 GHz; *b* GSSI profile at 1.5 GHz; *c* pavement structure

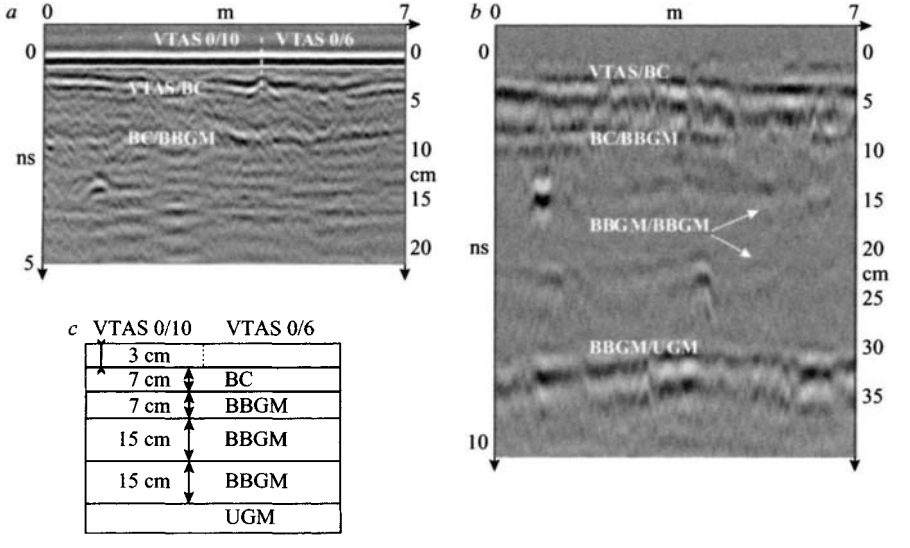

Figure 9.12 *Radar profiles from Figure 9.11 after processing*
a Processed step-frequency profile (3 GHz); *b* processed GSSI profile (1.5 GHz); *c* pavement structure

Two general remarks can be made regarding Figure 9.11. Owing to identical components (aggregate and binder characteristics) in the two VTAS, no GPR distinctions appear using the first approach. The BC thickness thus appears to be closer to 4 cm than the expected 7 cm.

Although the first two layers are detected by the 3-GHz profile in Figure 9.11*a*, the VTAS thickness cannot be determined without any signal processing. As for the 1.5-GHz profile (see Figure 9.11*b*), the general structure is revealed, including some punctual striping between elementary BBGM courses. Nevertheless, the frequency range is too low to correctly detect the VTAS layer.

At this stage of the interpretation, some signal processing becomes necessary in order both to increase the signal-to-noise ratio and to eliminate any constant noise (including the surface echo). One such processing is called background removal: any time domain signal is subtracted from a constant one (or the average of several), with the result being presented in Figure 9.12. Similar processing could be used, but is not necessary for short profiles of this type.

For the step-frequency data, processing has begun from the maximum of the surface echo in order to analyse the figure more thoroughly. Owing to the short pulse length, Figure 9.12*a* is able to present both the surface echo and the VTAS/BC interface. On the other hand, the size of the 1.5-GHz pulse wavelength leads to both echoes from the upper and lower VTAS interfaces merging so closely that only the complete signal should be processed.

In both cases, the improved signal-to-clutter ratio has increased to allow better interpretation. Every course of the road structure is detected from the 1.5-GHz central frequency. Moreover, the VTAS/BC interface can be determined for thickness measurements at the 3-GHz central frequency.

9.2.2.7 Summary: The design of a step-frequency radar technique for very thin pavement layers has been studied. A network analyser, operating over the 500- to 6000-MHz range, has been combined with ultra-wideband antennas of more than one decade (450 MHz–10 GHz). Laboratory experiments have been conducted on various LCPC road test sites and results compared with classical impulse GPR.

The step-frequency profiles derived from these test sites have demonstrated the ability to detect and measure the thickness of both VTAS (3-cm average thickness) and the second course in the base structure, with a 3-GHz central frequency. Although these experiments were done with laboratory devices, the evolution in electronics will enable an increase in the step-frequency performance, both in terms of high rate acquisition and spatial resolution, and for it to become an operational technique. The new generation of network analysers should provide this capability.

Owing to the lower central frequency, experiments with a 1.5-GHz impulse GPR confirm the inability to detect such thin layers. Nevertheless, this central frequency range has enabled investigation of the quasi-global road structure and production of a correct diagnostic evaluation of the structure.

These experiments confirm that the GPR technique is part of high-speed nondestructive testing to be widely used in road surveys. In any event, signal processing, like background removal, and calibration are necessary for attaining sufficient

accuracy, while keeping in mind that GPR data interpretation is a delicate task and requires a GPR specialist.

9.2.2.8 Acknowledgments: I would like to thank the LEAT for a continuous and profitable collaboration and the LCPC Road Department, which is in charge of the circular pavement fatigue test track.

9.2.3 High resolution GPR testing of conduits and pavements

Dr Bob Whiteley

9.2.3.1 Introduction: Society has a major investment in built infrastructure – in particular, roads and, underground, nonferrous pipes. Wear, damage and normal aging processes mean that these assets require regular assessment and maintenance. Throughout the world, condition assessment of these assets that guides decisions to repair or replace is mainly achieved by visual or CCTV inspection. It is increasingly recognised that visual inspection alone is inadequate to effectively manage this infrastructure, and other technologies such as ground penetrating radar (GPR) are needed. These technologies have the advantage of penetrating the construction, non-invasively and nondestructively, and of observing conditions within and beyond the visible surfaces of tunnel liners and pavements.

A high frequency ground-penetrating impulse radar system operating at 1400 MHz has been developed to assist condition assessment of tunnel liners and pavements and to improve on visual assessment or CCTV methods. Features of this system include a portable, rugged antenna and control unit that allows safe field operation remotely in difficult and wet environments. A copper cable link with transformer isolation connects this unit to a remote voice intercom and digital acquisition/display system. Both analogue radar data and 2-way, hands-free voice communications are achieved over distances exceeding 500 m without any reduction in radar data quality.

Laboratory and field physical modelling using concrete models containing voids and other features that simulate deteriorated liners and pavements shows that the system has a minimum spatial resolution of 19 mm and can easily detect voids 50 mm thick at a depth of 200 mm.

Case studies from Australia demonstrate that the system locates distress and deterioration in concrete and brick liners and voids in concrete pavements. The studies show that the radar system can distinguish the sub-base and varying construction features in asphalt pavements.

It is anticipated that this high frequency radar system will be increasingly applied to improve the management of wastewater and road transport infrastructure.

The theory of the GPR method and its application are treated elsewhere [21, 22]. Essentially GPR exploits the large electrical property differences, principally dielectric constant, that are present between engineered materials in good or design condition and those that have deteriorated or are not performing to specification.

These electrical contrasts arise because specified structural materials (e.g. concrete, asphalt etc.) exhibit a small range of electrical property variation, whereas natural materials (e.g. air, water, soil, rock) exhibit a large range of variation and very different electrical property magnitudes from the engineered materials.

To be effective for liner and pavement testing a GPR system must, at a minimum, have the following characteristics: an effective operational depth range from about 50 mm to 0.5 m in a wide range of materials; an ability to operate in a wide variety of environments (wet or dry, surface or underground); immediate display for quality control; and optimisation of field procedures and interpretation.

A high frequency GPR system has been designed and constructed that meets or exceeds these requirements. Physical laboratory and field models, built to simulate damaged concrete liners and voided pavements, demonstrate the responses of this system to good and deteriorated conditions. Field examples show the successful application of the system at a number of Australian sites.

9.2.3.2 1400 MHz radar system: CSIRO originally designed a high resolution impulse radar system for a range of applications [23] with a centre frequency in the range from 800 MHz to 3000 MHz. In 1998 this system was modified and ruggedised by Murray *et al.* [24] to achieve the necessary characteristics for liner and pavement testing, and antennas were re-designed with a centre frequency of 1400 MHz. The system is shown schematically in Figure 9.13, configured for underground operations. It has a nominal pulse resolution of 30 mm that is produced by a waterproof, bistatic antenna with the transmitter and receiver in one unit. The portable antenna has dimensions of 200 mm by 100 mm by 100 mm and is connected, via a short waterproof cable, to the control unit, which is mounted in a waterproof backpack carried by the operator. This enables safe operation in relatively difficult or hostile environments without direct visual contact. The control unit allows the operator to vary the radar acquisition time base from 4 to 25 ns, to set a variable gain in the range 0 to 40 dB and

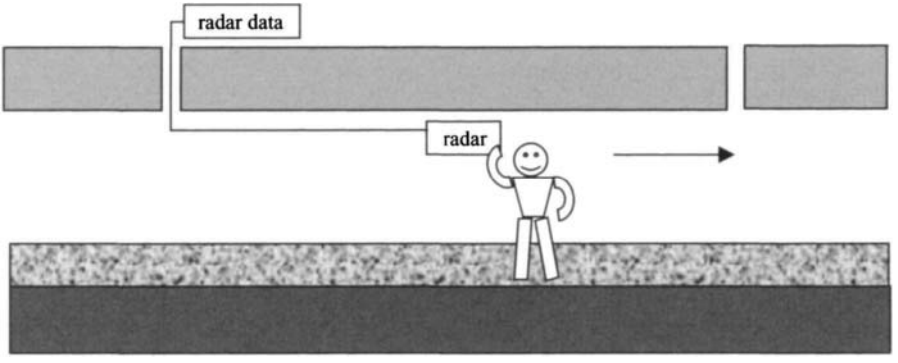

Figure 9.13 Schematic diagram of 1400 MHz radar system configured for underground use

to choose from a number of linear gain slope functions. This unit is powered by its own 12 V supply and can operate for up to 7 h without recharging. It is connected via a copper cable link with transformer isolation to a remote voice intercom and digital data acquisition system. The combined analogue data and voice intercom has proved safe and reliable in many hours of operation. The isolated cable system (Figure 9.13) is a twin pair cable, each with its own shield and a shield around the pair.

Screened audio-type transformers are used for both information channels and have a frequency response of 100 Hz to 5 kHz. Three winding pulse transformers transmit the frame synchronisation pulse, which has a width of 15 μs at a repetition frequency of 56 Hz. At the remote data collection site (Figure 9.13) 12-bit digital data is acquired on a portable PC using specially written GPR Viewer V202 software (A.F. Siggins and Associates). This software allows the GRP data to be displayed as it is acquired and saved as a bitmap or in SEGY format for further processing. The remote GPR operator calls location information over the intercom, and position marks are manually placed on the GPR record by single keystrokes at the computer. The radar data is displayed at 16 colour levels, and this display allows the computer operator to assess data quality and to request repeated or additional radar scans with different equipment settings if desired. This feature is particularly useful when anomalous features are observed on the radar images as more scans can be completed at the time without the necessity to re-occupy difficult sites.

9.2.3.3 Physical model simulations: The radar system was tested in the laboratory on a physical model constructed to simulate concrete tunnel liners with various levels of damage represented by sand, cemented sand, and cemented crushed rock with voids and metal reinforcing bars. The experimental set-up and results obtained are presented in more detail by Siggins and Whiteley [25]. For these models the system demonstrated a depth of investigation of at least 200 mm in concrete made lossy basaltic aggregate (a worst-case scenario), a spatial resolution of 19 mm, and detected metal-reinforcing rods and small voids (i.e. completely corroded reinforcing at 200 mm depth).

Figure 9.14 (from Siggins and Whiteley [25]) shows the radar image obtained with the system over one of the liner models. The crushed rock represents a heavily leached concrete zone. The cylindrical void represents a completely corroded reinforcing rod within the leached zone. The raw radar image shows both of these features clearly. Note that the direct pulse effectively obscures any information from the upper 50 mm of the model. The hyperbolic signature of the small void may be further processed using a diffraction stack algorithm [26] to sharpen the image of this feature. The processed image is also shown on Figure 9.14.

For pavement simulation, three 500 mm by 500 mm voids alternately in-filled with air, sand and water were placed below a 3 m by 3 m cast in-place concrete slab 150 mm thick (Figure 9.15). The slab was placed on natural clayey/sand soils and a quartz aggregate was used in the concrete mix. This simulation was 'blind' as the locations of the voids were not provided prior to the radar tests. The objective was to locate the voids below the pavement and determine the nature of the in-fill in each void.

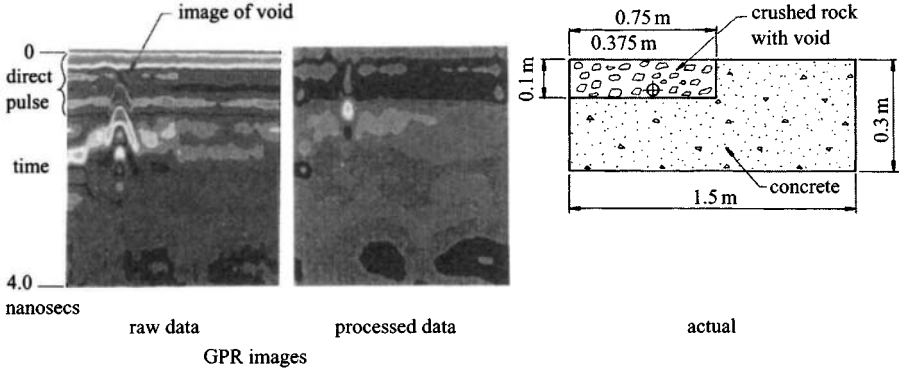

Figure 9.14 Raw and processed radar images over a 'damaged' liner model

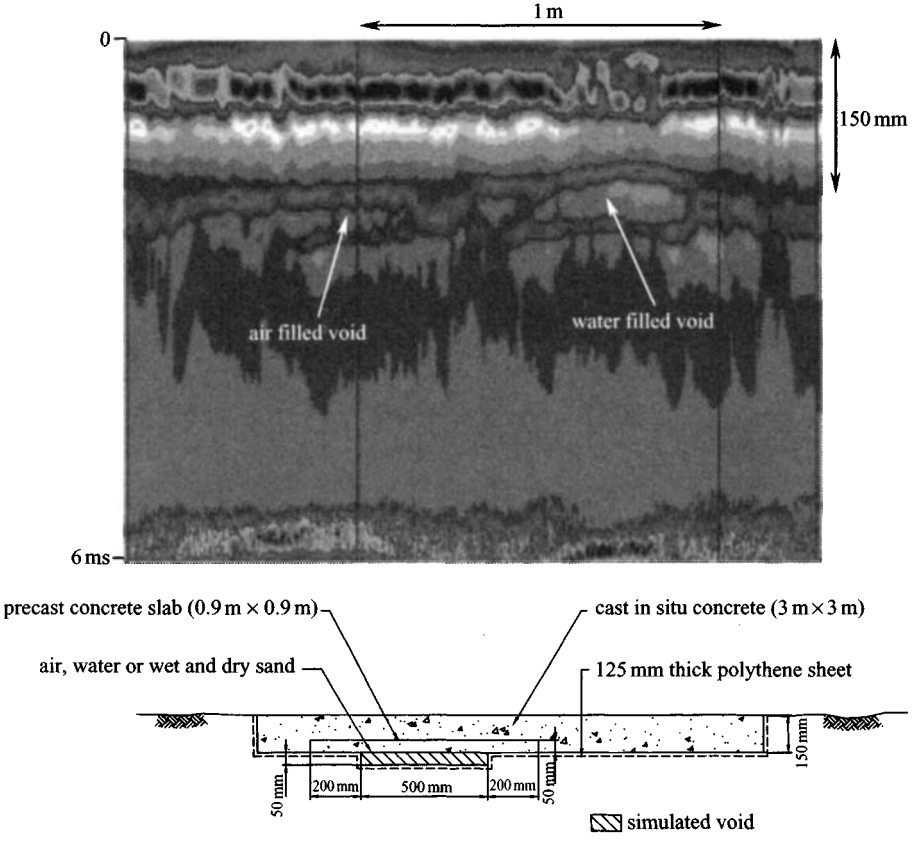

Figure 9.15 Radar image over 'blind' voids beneath model pavement

Figure 9.15 shows one of the GPR scans that crossed two buried features. These were interpreted to represent voids with air and water infill, respectively. This interpretation subsequently proved to be correct and demonstrated the ability of the 1400 MHz radar system to define narrow voids below typical pavements.

9.2.3.4 Case studies of tunnel liners: There are many types of tunnel liners in current usage, and the assessment of these provides considerable challenges [27].

9.2.3.5 Concrete liner: Prior to the construction of the Northside Storage Tunnel in year 2000 [28] the sewerage and wastewater requirements of about 1 million people on the northern side of Sydney were served by the NSOOS (Northern Suburbs Ocean Outfall Sewer). This is a cast-in-place concrete conduit with a flat or arched roof about 2.3 m by 2.3 m that was built over 70 years ago and extended since that time. According to design documents, the concrete liner is from 230 to 300 mm thick. A significant length of an older section of this conduit was hand-tunnelled in sandstone/shale rock, and it was known that construction problems were experienced where the tunnel intersected large joints and faults. Regular visual or CCTV inspection showed some areas of liner deterioration. A 5-km length of this tunnel was scanned with the GPR system in 'live' conditions. Access to the sewer was achieved via manholes that were about 500 m apart. Although it was not necessary to bypass-pump the fluids during the radar testing, even in low flow periods some sections had to be tested from a specially constructed raft to ensure that the radar antenna was in intimate contact with the liner. It was also necessary to rough-brush the liner surface along the radar scan profiles to remove excess sludge and other materials. In fact, this proved to be the major difficulty in acquiring high quality radar data.

The liner proved to be in relatively good condition overall considering its age except for a number of sections that the radar testing identified. Figure 9.16 shows a radar image of one 20 m length that shows significant liner distress. Where the liner

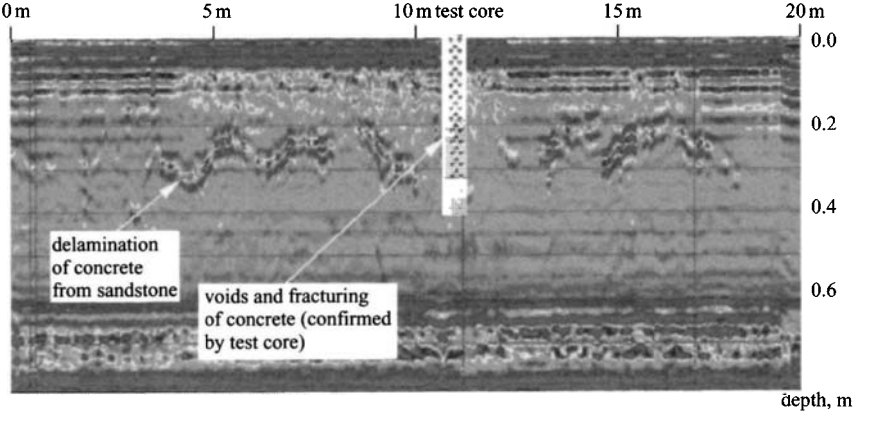

Figure 9.16 Radar image showing significant distress in concrete liner

was in fair or good condition and in relatively intimate contact with the rock (some minor voiding may be present), the GPR images show regular reflections as observed on the image from 0 m to 4 m. Where the liner surface is deteriorated, the shallow reflections become more irregular, e.g. from about 4 m to 12 m and from 16 m to 17 m. These areas were often noted on the CCTV inspection records but were sometimes missed because the sludge coating frequently thickened where the liner surface was degraded. The irregular radar reflection between about 0.2 and 0.3 m depth near the back of the liner represents the more serious problem of voids forming as a result of delamination of the liner from the sandstone rock which no longer supports it. A core of the material taken at 11 m showed that the liner was in poor condition with many pinhead voids, some as large as 5 to 10 mm in diameter in the interval 0.11 to 0.2 m. An open fracture was observed at the back of the concrete at 0.32 m with sandstone beyond this depth.

9.2.3.6 Brick liner: Some of the oldest and deepest buried infrastructure beneath major cities is the ovoid brick sewers and drains. Many are over 100 years old, well beyond their design life, but are still functioning. Unfortunately, they require substantial maintenance and are increasingly expensive to replace. High frequency GPR scanning of these conduits is a cost-effective method of assessing their condition. Figure 9.17 shows a cross-section of a typical double-brick drain in Melbourne,

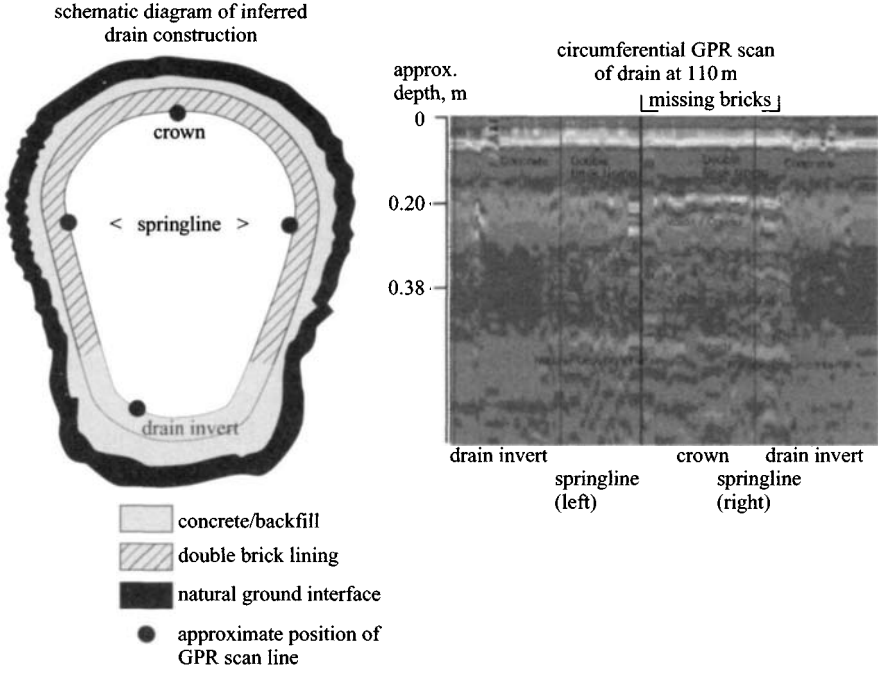

Figure 9.17 Circumferential radar scan of brick drain

Australia. In this case the double brick liner was cemented to the surrounding basalt rock in which the drain was constructed. The approximated dimensions are 1.5 m by 1 m.

The positions of four longitudinal 1400 MHz radar scans of this drain are also shown with an interpreted circumferential radar scan at 110 m along the drain. This image shows a common form of distress observed in the crown of these structures. Missing bricks at the crown provide further visual evidence of deterioration. Voids at the back of the brickwork near 0.2 m depth can be seen. The degraded concrete behind the brickwork produces a disturbed radar image. Further evidence from the radar image shows voids near the back of the concrete liner, indicating that it has delaminated from the rock. A drain in this condition was considered in danger of collapse, particularly if a surcharge event occurred after heavy rain. This condition was notified and the distressed liner was subsequently repaired.

9.2.3.7 Case studies of pavements: introduction: Road pavements are subjected to continuous wear and are exposed to the natural elements; consequently, major efforts are expended in condition assessment. A number of radar systems [29] have been developed for this purpose using both ground and air-coupled antennas that are deployed at relatively high speeds. While these systems allow considerable information to be gathered rapidly over a road network they generally lack the detail that can be achieved with the high frequency system described earlier deployed at slower speed (<10 km/h) with the antenna housed in a sacrificial casing and dragged along the actual pavement. The high frequency radar system may be used to examine new construction as well as the condition and style of older construction.

9.2.3.8 Concrete pavement: A new section of highway in Brisbane, Australia, was recently constructed with concrete pavement in two lifts each about 150 mm thick. Some construction problems were experienced and the owner requested that GPR testing and targeted coring be completed prior to commissioning. Figure 9.18 shows a GPR image of a 50 m length of this roadway. The section from about 230 to 255 m shows distress in the upper 150 mm of the pavement. The core obtained from this section has large irregular voids extending from the upper 50 mm (Figure 9.18). The voided section of pavement identified by radar testing was subsequently replaced.

9.2.3.9 Asphalt pavement: Most suburban roads in Australia's cities and towns are constructed with asphaltic concrete (asphalt) – a mixture of cement, aggregate and bitumen on a compacted gravel sub-base. Over the years many of these roads have been repaired, widened and resurfaced. Records of these improvements are frequently incomplete or nonexistent, and managers are hampered in their ability to plan works programs without slow and costly coring at many sites. As asphalt has a good electrical contrast with the various sub-base materials, radar can be applied to determine pavement thicknesses. Also, electrical contrasts between different types of asphalt pavements and those laid at different times allow the construction history to be determined with the minimum of direct testing.

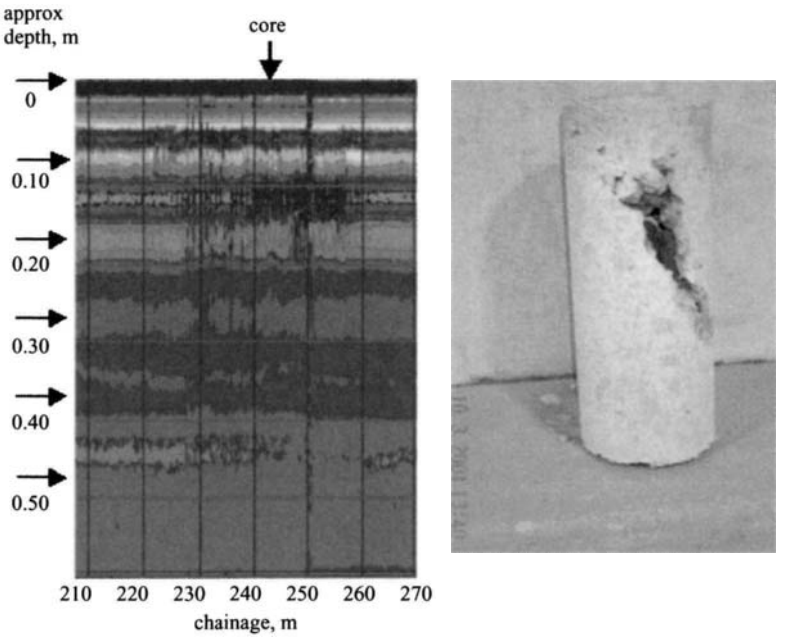

Figure 9.18 Radar image of concrete pavement and core showing voids

For this application the high frequency radar system is used along short sections of pavement around a selected area. This is normally achieved without road closure and with minimal disruption to traffic. As considerable variations are often observed within a given area, different radar signatures are also calibrated by coring. Figure 9.19 shows 20-m length samples of high frequency radar images from either side of an asphalt road in Melbourne, Australia. Below the western side of the road a total asphalt thickness of 0.19 m is present over a gravel base. On the western side of the road the total thickness exceeds this and is beyond the radar scan range that was set; however, a further 0.05-m layer of foamed asphalt has been added.

9.2.3.10 Summary: The specially designed and ruggedly constructed high frequency radar system operating at a central frequency of 1400 MHz has proved to be a useful and versatile tool for examination of the internal conditions of concrete and brick tunnel liners, readily identifying voids and distress. For pavements the radar system has demonstrated the ability to locate voids in concrete pavements and to discern the sub-base and differing construction in asphaltic pavements.

There are many improvements to the processing and analysis of the radar data gathered with this system that can be achieved for specific conditions and problems, including signal stacking, deconvolution and migration. It is anticipated that this and similar radar systems will be increasingly applied to improve the management of road and waste transport infrastructure.

Next Page

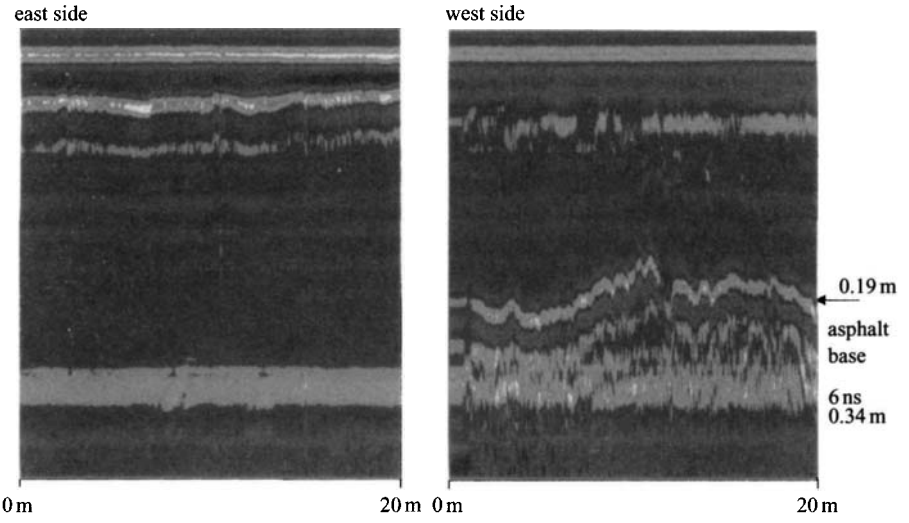

Figure 9.19 Radar images of sections of asphalt pavement

9.2.3.11 Acknowledgments: Sydney Water and Maunsell Engineering (Hong Kong) are gratefully acknowledged.

9.3 Concrete

Dr John Bungey
University of Liverpool, UK

Radar testing of structural concrete is part of a research programme at Liverpool University that has been undertaken since 1990 by a team led by Dr J. H. Bungey. The work has been supported by SERC in co-operation with several industrial organisations and with Professor Forde of Edinburgh University. Attention has been concentrated on assessing the capabilities of commercially available apparatus applied to practical problems in the laboratory and on site. This has involved specially cast concrete slab specimens as well as the use of an oil–water emulsion tank facility developed to simulate slabs with a range of concrete properties, and to permit rapid variations to parameters such as reinforcing bar, pre-stressing duct or void configurations. This facility avoids the need for casting and curing of large numbers of concrete specimens and has permitted an extensive library of characteristic responses to be established.

Measurements were carried out using centre frequencies between 500 MHz and 1 GHz by means of GSSI SIR 8 and SIR 10 equipment.

A coaxial transmission line system has been developed to assess the relative permittivity and electrical conductivity of both fluids and hardened concrete specimens over a wide frequency range, and results are shown in Figure 9.20. This has assisted the development of emulsions for the simulation tank and permits concrete specimens

Previous Page

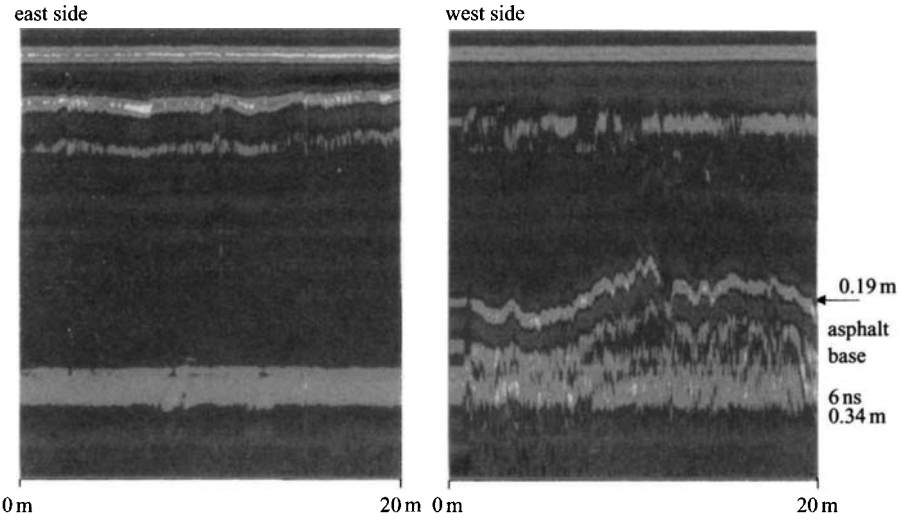

Figure 9.19 Radar images of sections of asphalt pavement

9.2.3.11 Acknowledgments: Sydney Water and Maunsell Engineering (Hong Kong) are gratefully acknowledged.

9.3 Concrete

Dr John Bungey
University of Liverpool, UK

Radar testing of structural concrete is part of a research programme at Liverpool University that has been undertaken since 1990 by a team led by Dr J. H. Bungey. The work has been supported by SERC in co-operation with several industrial organisations and with Professor Forde of Edinburgh University. Attention has been concentrated on assessing the capabilities of commercially available apparatus applied to practical problems in the laboratory and on site. This has involved specially cast concrete slab specimens as well as the use of an oil–water emulsion tank facility developed to simulate slabs with a range of concrete properties, and to permit rapid variations to parameters such as reinforcing bar, pre-stressing duct or void configurations. This facility avoids the need for casting and curing of large numbers of concrete specimens and has permitted an extensive library of characteristic responses to be established.

Measurements were carried out using centre frequencies between 500 MHz and 1 GHz by means of GSSI SIR 8 and SIR 10 equipment.

A coaxial transmission line system has been developed to assess the relative permittivity and electrical conductivity of both fluids and hardened concrete specimens over a wide frequency range, and results are shown in Figure 9.20. This has assisted the development of emulsions for the simulation tank and permits concrete specimens

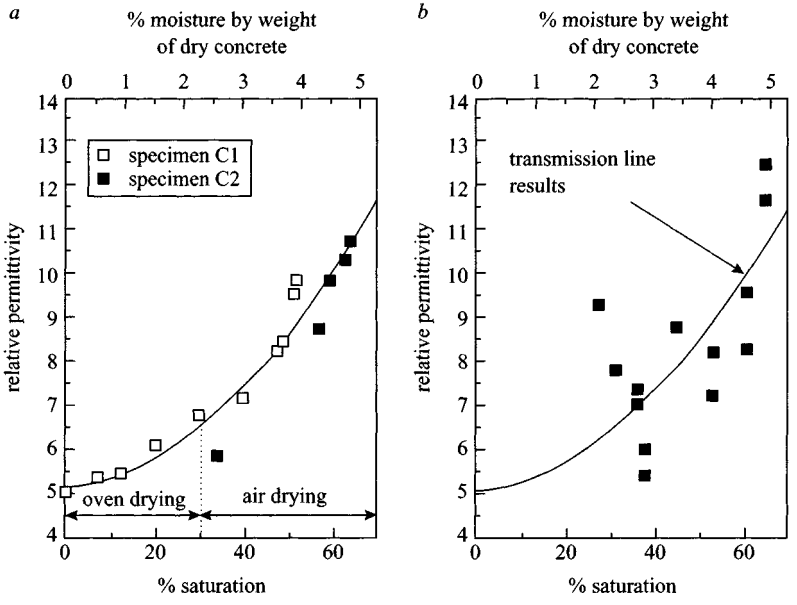

Figure 9.20 Measured variation in the relative permittivity of a concrete as a function of moisture content

to be removed for conditioning. It has been used to assess the effects of concrete moisture content, which is a key factor in the successful use and interpretation of radar surveys. Work is about to commence to establish fundamental properties for a wide range of concrete types using this facility.

Computer modelling, using specially developed 2- and 3-dimensional ray-tracing programs and a commercially available finite element package, has been actively progressed.

The results from the studies at Liverpool University have permitted realistic assessment of the capabilities and shortcomings of the technique at its current stage of development with commercially available apparatus and software. The effects of reinforcing steel in masking deeper features are of particular importance, and effective minimum limiting spacings of between 100 mm and 200 mm have been suggested for 1 GHz apparatus, depending upon bar diameter and depth. Similarly, it may be possible to identify individual reinforcing bars at spacings down to 100 mm centres depending on bar size and cover. Void and crack detection is influenced by shape, size and depth, and whether air- or water-filled. Cubic voids are easier to detect than spherical, and water-filled voids easier than air-filled. Whilst 50-mm air voids could generally be detected, smaller sizes down to 20 mm required very precise apparatus adjustment, highlighting the practical difficulties in locating a small void or similar feature whose presence is unknown. Buried honeycombing is particularly difficult to detect, and highlights the critical aspect of optimum transducer orientation to minimise reinforcement influences.

It is clear that further improvements in interpretation capability hinge on knowledge of the fundamental electrical properties of concretes, with especial reference to the influence of pore fluids. For example, the accuracy of current depth estimates to reflective features may range from about +45% to −15% due to such uncertainties with a commonly adopted relative permittivity for concrete of 6.5, although this can be improved by calibration drilling.

Signal processing can be most valuable when trying to detect or identify small or complex features, but is expensive, and it is questionable whether extensive use of such facilities is justified in straightforward applications. Simple equipment giving basic monochrome plots may similarly often be adequate.

Ray tracing programs have been very successful in simulating radar responses to complex configurations. Finite element modelling incorporating open boundary elements is also highly successful in demonstrating the propagation of radar waves in materials with varying properties and discontinuities, and simulated scan patterns can be generated which closely match those obtained in practice. Such results provide a valuable aid to understanding and interpretation. Further information can be obtained from the Concrete Society UK, whose website address is http://www.concrete.org.uk/index.htm.

They have published a guide to the radar examination of concrete structures and further information on the report on 'Guidance on radar testing of concrete structures' [22] is given in http://www.concrete.org.uk/publication_tech.htm. Further information is given in References [30–35].

9.4 Concrete structures

Dr Christiane Maierhofer

The radar method is meanwhile applied as a very effective technique for investigating the integrity of concrete structures thanks to technological advancements over the past decade [22, 36–40]. In this context it is particularly suited for the assessment of large structures like pre-stressed concrete bridges [36, 39, 41–43], nonballasted railway tracks [44], and highways and tunnels [45–47]. Owing to the age of these structures, enhanced inspection efforts are required today [47], but radar can also be used as a part of a quality assurance system reducing high maintenance costs.

Typical testing problems related to these applications are the detection of reinforcement and tendon ducts [36, 42], dowels and anchors [48, 49], voids and honeycombing [45, 47, 48, 50], the thickness measurements of structures which are only accessible from one side [51], the location of delaminations between layered structures [43, 44, 50], and the detection of airgaps and moisture at interfaces [52, 53].

Table 9.2 presents a survey of frequently encountered problems when investigating concrete structures together with suitable alternative or complementary testing techniques and their respective limitations.

The applied radar measurement techniques have to be optimised to these problems by selecting the appropriate antenna type, antenna frequency, antenna combination and configuration, polarisation of the radiated electric field and the traces along which the measurements have to be performed. For data analysis, mostly filtering techniques are used for enhancing the contrast of detected objects to the background.

Table 9.2 Fields of application of nondestructive testing methods for structural investigation of concrete structures

Inspection problem	Method	Limiting conditions (guide only)
Location of untensioned reinforcement	Cover meter, impulse radar	Spacing between rebars should not be less than 7 cm for measurements with impulse radar. Concrete cover should be less than 10 cm for measurements with cover meter.
Location of tendon ducts	Impulse radar, ultrasonic	For both methods, the concrete cover should be less than 40 cm. The spacing of the rebars above the tendon ducts should be not less than 7 cm for radar measurements.
Detection of voids inside the tendon duct (compaction faults)	Ultrasonic, still under development	—
Determination of thickness of concrete elements, which are only accessible from one side (e.g. concrete base plate)	Impulse radar, ultrasonic, impact-echo	Maximum thickness which can be measured: Radar: 0.5 m (500 MHz antenna). Ultrasonic: 2 m (max. grain size: 8 mm). Impact-echo: several m for stilts.
Determination of the thickness of different layers at layered structures (i.e. nonballasted track beds)	Impulse radar	The maximum depth resolution is 2 cm (2.5 GHz antenna).
Determination of compression strength of concrete	Ultrasonic transmission	In any case, the destructive determination of compressive strength of a few cores is needed for correlation with the sound velocity.
Location of voids in masonry and of compaction faults in concrete	Impulse radar, ultrasonic	The voids should be larger than 50 mm. The depth should be less than 0.5 m. Ideally, untensioned reinforcement should not be present (radar).
Detection of cracks in masonry and concrete	No method has proven particularly suitable up to now; ultrasonic is under development	—

9.4.1 Location of reinforcement and tendon ducts

In bridge construction, impulse radar has been applied very effectively in a number of cases to locate tendon ducts [36, 42].

With this method it is possible to prevent damage of tendon ducts caused by drilling to install noise protection walls or by taking cores. The location of tendon ducts is also important in combination with other nondestructive testing techniques such as the ultrasonic echo method used to locate compaction faults and magnetic field measurements to detect cracks of tendons [53, 54]. The measurement data presented in Figures 9.21 and 9.22 have been recorded on a pre-stressed concrete bridge with a length of about 150 m [43, 53]; see Figure 9.23. The supporting layer contained tendon ducts in the longitudinal and transverse directions. The ducts in the transverse direction had a diameter of 4 cm. The thickness of the supporting layer was 20 to 25 cm. Nondestructive investigations had to be performed for the location of concrete damage and defects in tendon ducts.

Figure 9.21 demonstrates three radar images recorded with different antennas in both polarisation configurations along a longitudinal trace of about 2.5 m in a

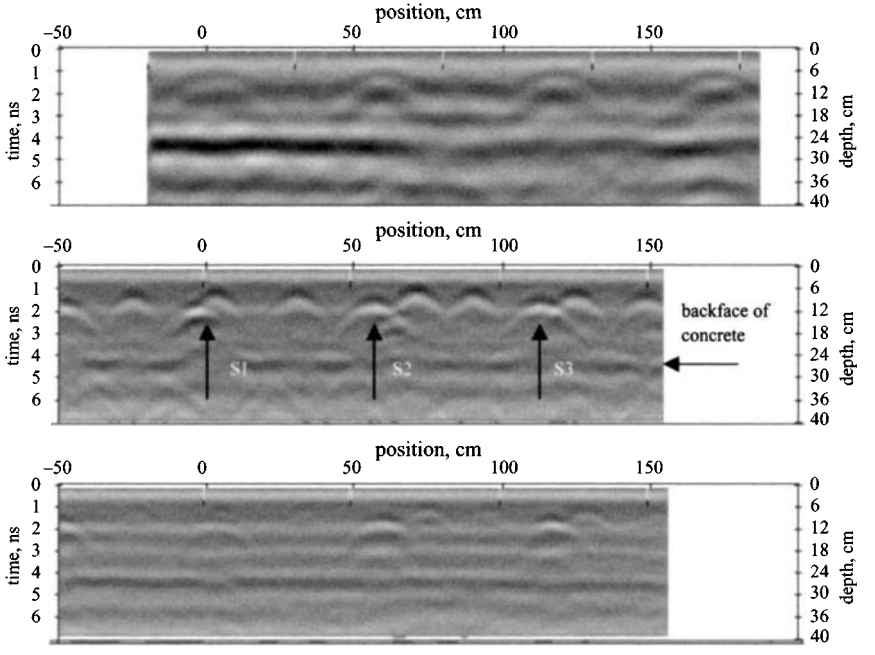

Figure 9.21 *Radar images along a 2.5 m long trace in longitudinal direction at area 1 (reference area)*
Top: 900 MHz antenna, polarisation parallel to antenna movement. Middle: 1.5 GHz antenna, polarisation perpendicular to antenna movement. The tendon ducts (S1 to S3) are marked with arrows. Bottom: 1.5 GHz antenna, polarisation parallel to antenna movement

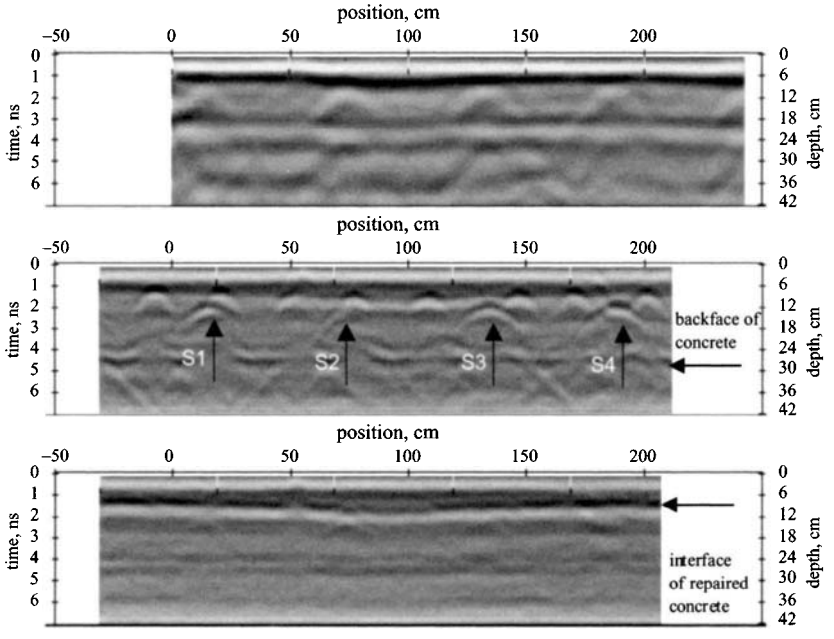

Figure 9.22 *Radar images along a 2.5 m long trace in longitudinal direction at area 2 (repaired area)*
Top: 900 MHz antenna, polarisation parallel to antenna movement. Middle: 1.5 GHz antenna, polarisation perpendicular to antenna movement. The tendon ducts (S1 to S4) are marked with arrows. Bottom: 1.5 GHz antenna, polarisation parallel to antenna movement

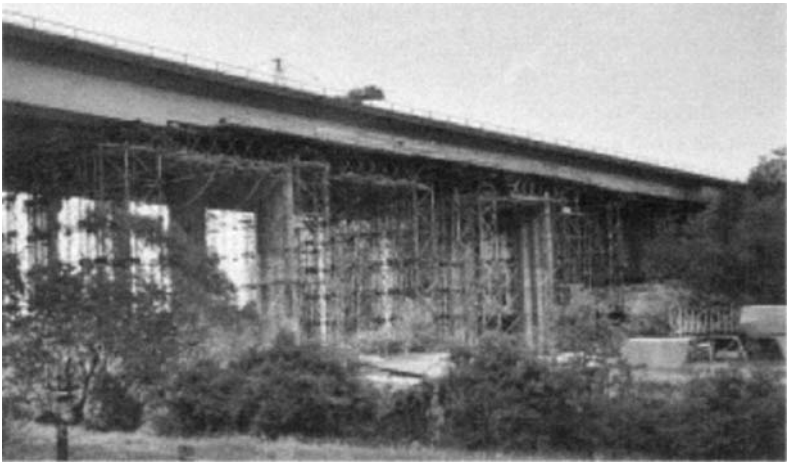

Figure 9.23 *Pre-stressed reinforced concrete bridge where tendon ducts should be located*

reference area (without visible deterioration). For the top diagram the 900 MHz antenna was used. The polarisation was perpendicular to the crossed reinforcement to suppress the reflection from the rebars. The radar image shows reflections at four transversal tendon ducts and at the bottom side of the supporting layer. The middle radar image was recorded with the 1.5 GHz antenna and the polarisation was parallel to the crossed rebars. Now the reflections from the rebars can be observed together with the reflection from the tendon ducts with much better resolution than at the top radar image recorded with lower frequency. Despite the depth, the reflections from the tendon ducts cannot be distinguished from the reflections from the rebars. Therefore, measurements with the 1.5 GHz antenna in the other polarisation configuration have also been performed. In the bottom radar image, the reflections from the tendon ducts are now stronger compared to the reflections from the rebars. The position of the tendon ducts is shown in the middle radar image by arrows. From these radar images, a concrete cover of the rebars of 5 to 6 cm and of the tendon ducts of 8 to 10 cm can be determined.

In Figure 9.22, three radar images belonging to a trace in a repaired area (repair section was visible) are presented. The traces have been taken by the same antenna combination and polarisation configuration as in Figure 9.21. The reflections from the tendon ducts as well as from the rebars are clearly visible. The concrete cover above the ducts is 10 cm, and the reflection from the bottom side appears at a depth of 25 cm. In the bottom radar image only a continuous reflection can be seen at a depth between 6 and 10 cm. This can be related to the reflection at the interface of the repaired area to the concrete deck containing detachments.

9.4.2 Location of dowels and anchors in concrete highways

In highway construction, concrete roads are designed with transversal and longitudinal false joints into which steel dowels or anchors are placed at right angles to each planned crack. The fitting of these dowels or anchors in fresh concrete is performed mechanically by pushing and shaking. If dowels or anchors are tilted relative to their planned positions, irregular cracks can occur which might result in concrete removal. Thus, for quality assurance the position of the dowels and anchors has to be controlled. After the fresh concrete has been hardened, this can be performed nondestructively by radar [49]. With this method it is possible to investigate the embedded depth (11 to 15 cm), an inclined position relative to the highway plane and an inclined position relative to the normal of the false joint.

To obtain the exact orientation of each dowel or anchor in three dimensions, a minimum of three parallel radar images has to be recorded. To minimise the errors related to slippage of the survey wheel, these three radar images should be taken simultaneously with three connected antennas and one survey wheel. Alternatively, a more precise positioning system should be used. The performance of radar measurements with the 1.5 GHz antenna and survey wheel is demonstrated in Figure 9.24, but this configuration might lead to larger positioning errors.

Figure 9.25 shows two radar images recorded with the 1.5 GHz antenna in two polarisation configurations along a trace parallel to and near a transversal joint. In both

Figure 9.24 *Radar measurements with the 1.5 GHz antenna and survey wheel along a false joint*

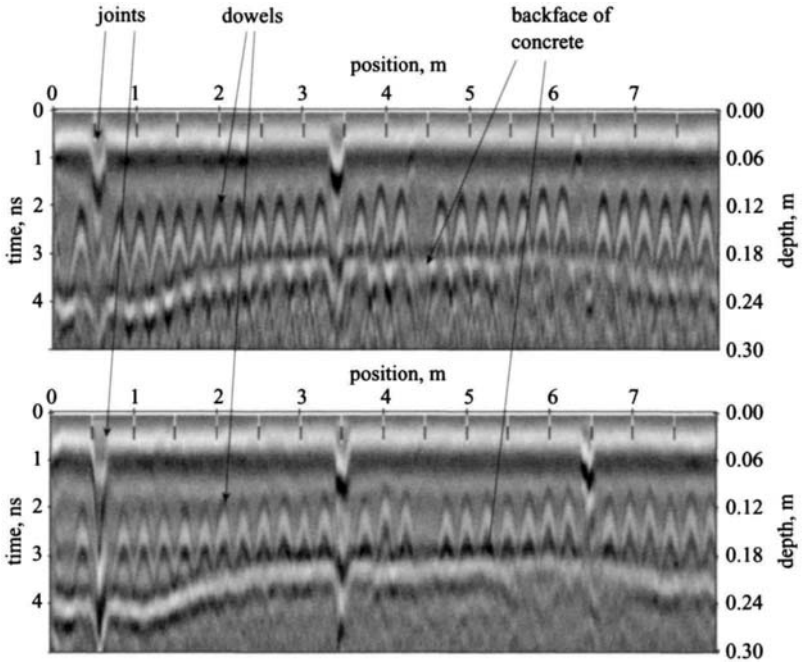

Figure 9.25 *Radar images along an 8 m long transversal trace close to a joint of a highway concrete deck*
The data have been recorded with the 1.5 GHz antenna. Top: polarisation parallel to the dowels; bottom: polarisation perpendicular to the dowels

polarisations, the horizontal position as well as the varying depth of each dowel can be determined from these data very easily and automatically by using special software routines. Also the reflection from the back-side of the concrete deck (interface concrete/underground) is visible, showing a concrete thickness between 17 and 23 cm. Some missing dowels can be detected in the otherwise regular structure.

9.5 Buildings

Dr R. de Vekey
Building Research Establishment, England

Radar will give reflections for many of the boundaries within built structures, and as a result can give information on (i) presence/position/size of nonvisible (hidden) features of buildings and (ii) on the quality of known features. For the scale of objects in built structures the bandwidth 0.3–1 GHz is the most appropriate.

The important boundaries in the built systems are:

(a) at the interface between solid material and a significant void
(b) at the interface between good concrete and poor concrete/mortar
(c) at the interface between concrete/masonry and insulation materials
(d) at the interface between large metal inclusions, e.g. reinforcement and other components
(e) at the interface between dry material and damp/wet material (since moisture alters the dielectric constant)
(f) where signals are re-radiated from metal objects which tune in some way to the wavelength used. Small objects such as ties, bolts etc. are likely to respond in this manner to the wavelength used for these investigations.

The main problems are:

1. If the material is wholly saturated or very wet the signal attenuation is such as to prevent the satisfactory use of the equipment.
2. New damp concrete or mortar has a very high attenuation and is virtually impossible to investigate.
3. Continuous metal, i.e. sheet or fine mesh reinforcement, will reflect all the incident ray, thus preventing any investigation of what lies behind it.
4. Some components of buildings are so complex that it is difficult to resolve the signals from the various reflecting objects.

9.5.1 Introduction

Most of the work carried out by the Building Research Establishment UK was carried out using a GSSI radar system on the following artefacts: walls and other structures made from mortared or dry-stacked bricks, blocks, dressed stone blocks, rubble and plain concrete.

9.5.2 Masonry

Although masonry is complicated by the array of bricks and joints, it is often relatively simple in structure, being composed of layers or sheets joined by bonding or by metal ties.

If a wavelength or antenna-orientation is chosen so that it is optional for the dimensions of the required target, then the following features can be detected in solid masonry: the position and layout of hidden voids such as chimneys; air ducts and other features; internal cracking; the thickness of walls; infilling of walls with rubble or poor concrete; the numbers of wythes (or rings in arches); the presence of buried metal such as cramps; reinforcement; fixings; straps; lintels; hidden pipe runs; chases and electric cabling; and, where localised, the position of damp areas. Work on detection of hidden objects is reported by Botros *et al.* [55] and Carr *et al.* [56]. Some work on masonry tunnels has been reported by Transbarger [57].

In addition, the following features can be detected in cavity walls: the thickness of the leaves, the cavity width, the layout and, to some extent, type of wall-ties, the presence of larger objects or blockages of the cavity. Only very limited research has been carried out and very little has been published. The technique has been covered in a review by de Vekey [58], and some examples of applications are given by Baston-Pitt [59].

9.5.3 Concrete system walls and floors

Typically, concrete walling and flooring elements consist of planes (flanges) of reinforced or pre-stressed concrete planks or prisms connected at intervals by webs and incorporating voids. Often site concreted joints and additional reinforcement are also present.

Walls may additionally have a finish such as wet plaster or dry lining of plasterboard over bats. The hollow sections may be filled with sand to increase the sound insulation. Floors typically have a finish on the soffit which may incorporate nominal reinforcement and a screed on the top surface which may incorporate heating tapes, reinforcement, pipes, conduit etc. They may also have additional reinforcement in the site-cast joints. Externally exposed components may also incorporate layers of insulation and surface weather protection.

Radar can give information on the dimensions, position, voids etc. in the various layers. A brief description of an investigation of some system flats using radar is given by de Vekey *et al.* [60–62].

9.5.4 Joints in concrete system buildings

These joints consist of a complicated junction between the top of a reinforced wall slab, an intersecting floor and the base of the next slab. They incorporate site-placed tying reinforcement, concrete and void-filling dry-pack mortar and insulation layers and a facing panel on the exterior. Although this represents the most difficult 3-dimensional structure to interpret, it has probably been the largest commercial application to date. On real structures it is very difficult to interpret the data from normal analogue radar

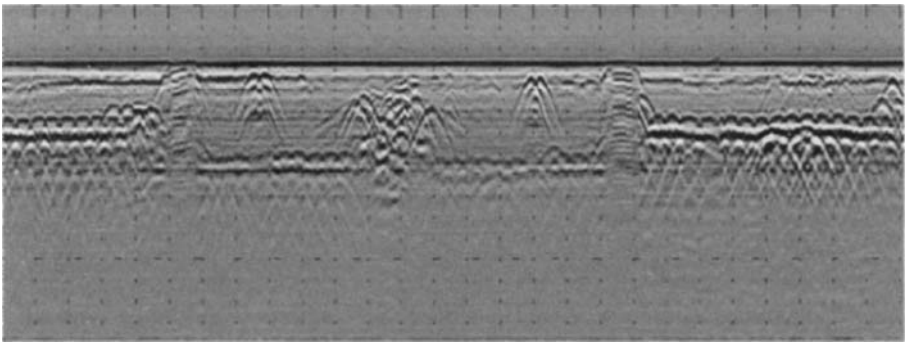

Figure 9.26 *Typical radar image of concrete floor showing rebars, joints, rods etc. (courtesy ERA Technology)*
1 ns duration impulse; horizontal markers every 10 cm; vertical scale 0.5 m

because of the complexity of the structure and the number of reflecting features. Analysis of the investigation of dry-pack quality on Ronan Point gave a disappointing correlation between radar data and visual exposure of the beds. De Vekey *et al.* [60] obtained some more statistically valid information by investigating model joints in a laboratory trial. With care the GPR image of the internal structure of buildings can reveal much about the internal structure, as Figure 9.26 shows.

Recent developments in in-situ characterisation of building materials are reported by Zhang *et al.* [63].

9.6 Tunnels

David J. Daniels

During the 19th century, when the railway system was the dominant means of mass transport, many tunnels and bridges were built as the rail network spread throughout Europe. These structures were generally made from brick and, owing to the high level of safety margin generally used by railway constructors, have survived well for over a century. The railway network in the UK still regularly passes through brick lined tunnels and over brick bridges. In the UK the outstanding pioneers of railway expansion were the Stephensons, both father and son, and Isambard Brunel, and their engineering and management skills still inspire admiration.

Some idea of the scale of the undertakings can be gained from the statistics of the work involved in building the railway line from London to Bristol in the early part of the 19th century. In 1836, Brunel started work on the longest tunnel then ever attempted, of some two miles (3.2 km), at Box. Six permanent and two temporary shafts of 8.5 m diameter were sunk from hilltop to railway level. The deepest shaft was nearly 93 m deep and, when the shafts were complete, work on the tunnel excavation

proper was started by the contractors. This excavation ran through mixed conditions: clay, blue marl, inferior oolite and oolite, and was eventually lined for 75% of its length with bricks. Gunpowder was used to blast away the rock, which formed 25% of the tunnel, but the remaining length was excavated by manpower and horsepower working in candlelight. Over the two and a half years taken to complete the tunnel excavation, a ton each of gunpowder and candles was used each week. Some 30 000 bricks were used to line the tunnel and over a quarter of a million cubic yards of soil was hauled out of the shafts in buckets by horsepower. The tunnel was completed in June 1841 although, even in those days, the final cost of tunnel construction was over twice the original estimates.

The safety record of such structures has been excellent, not only because of their intrinsic strength but also because of regular inspection procedures which have been carried out for many years. In the UK, the railway operators may wish to gather information on the integrity of the tunnel linings by inspecting both their internal condition and the depth of the masonry lining, and has therefore identified a need for an economical, rapid, nondestructive technique for tunnel-line inspection. Several examples of tunnel inspection using radar follow the first example of a bridge abutment.

A photograph of the abutment of the bridge is shown in Figure 9.27. The total area of the abutment wall examined was 3 by 6 m. A grid of 10 cm spacing was used in collecting data, and this produced an array of 30 by 60 time domain waveforms for processing.

Each x, z-plane of data was suitably processed, and it can be seen from the processed image in Figure 9.27 (lower) that there is a strong radar reflection in the centre of the scan (horizontal axis 6 m, vertical axis 1.5 m). This image (by virtue of its low-frequency energy content) was successfully interpreted to indicate an anomalous water saturated zone. Subsequent trial core samples confirmed the interpretation.

To generate radar images from known situations, a test rig with suitably simulated voids and anomalies 12.5 m long, approximately 1 m deep and 1.5 m high was built, as illustrated in Figure 9.28. The test rig comprised three continuous sections: the first section was designed to simulate various thicknesses of tunnel lining (varying from one brick to five bricks), the second to simulate vertical and horizontal delaminations, and the third to simulate various voids. The test rig was subsequently modified by extending the depth using a sand backwall. The void is in the centre of the radar image in Figure 9.28 (lower).

Radar measurements were taken on Gonerby Tunnel, which lies approximately 1250 m northwest of Grantham (UK) (Long. 0° 41′W and Lat. 52° 55.5′). The tunnel runs west-northwest, is approximately 520 m long and serves a dual track railway line. The tunnel was constructed in Victorian times and passes through lower lias clay with calcareous siltstones and thin sandstones and underneath middle lias, grey, sandy clay and micaceous clay 15–30 m thick.

The roof of the tunnel lining varies in height from the railway line by typically plus or minus 0.75 m and in addition there is a step reduction in height at a distance of some 80 m from the south entrance of the tunnel. Photographs of the tunnel and its lining are shown in Figures 9.29 and 9.30. The tunnel was surveyed at the crown of the roof

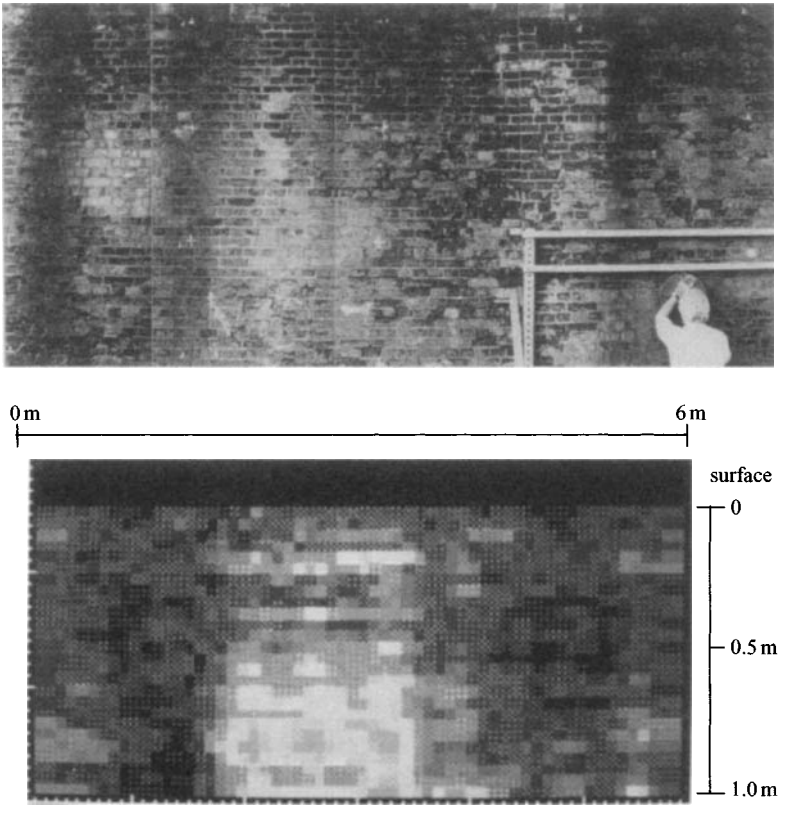

Figure 9.27 Radar survey of bridge abutment (courtesy British Rail)

and a continuous radar image was recorded. A radar image of a typical undisturbed region is shown in Figure 9.31 and the thickness of the lining was calculated to be 0.56 m. A radar image of a typical disturbed region is shown in Figure 9.32. From this a composite map of high-level radar reflections was produced.

Since the work reported in the first edition SPR/GPR has become established as a recognised method by the rail industry. GPR surveys have been adopted as a best practice element for all Network Rail track renewal projects in the UK, and provide a continuous view of the ballast thickness and condition. GPR is a powerful tool in preventing 'wet beds' and hard spots, which have an adverse effect on ride quality and lead to rapid deterioration of the track.

Section 7.5 of the Network Rail Code of Practice recommends the use of non-destructive techniques including GPR, thermography and other geophysical methods as part of tunnel examinations. Tunnel surveys often use GPR and ground conductivity to provide a more comprehensive condition assessment than visual or hammer tapping surveys.

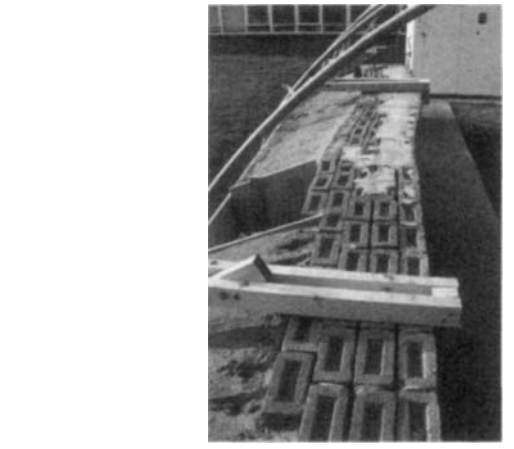

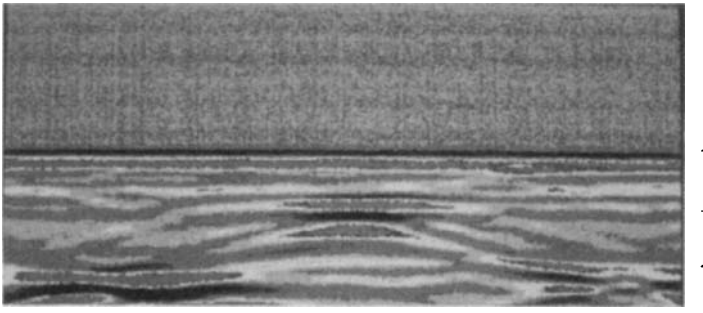

Figure 9.28 Radar survey of tunnel lining rig (courtesy British Rail)

Figure 9.29 Gonerby railway tunnel (courtesy British Rail)

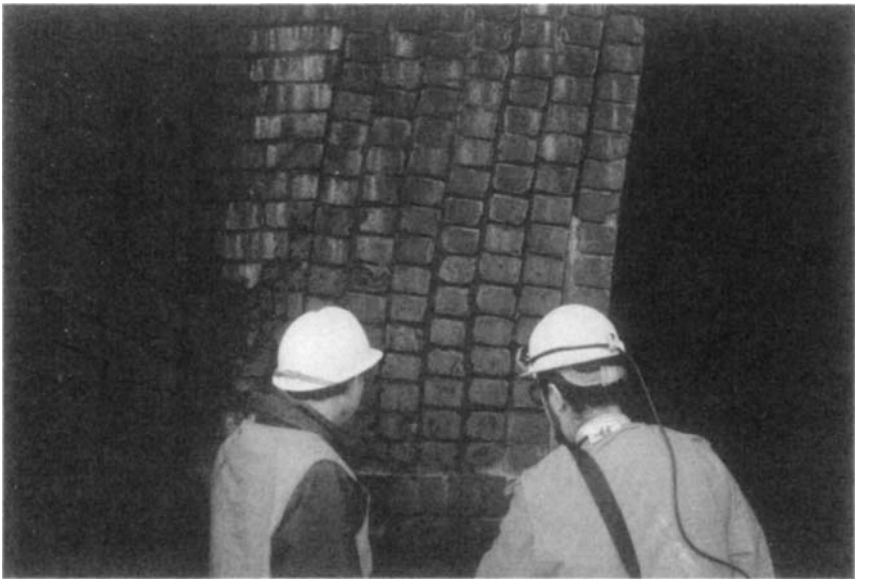

Figure 9.30 Gonerby railway tunnel lining (courtesy British Rail)

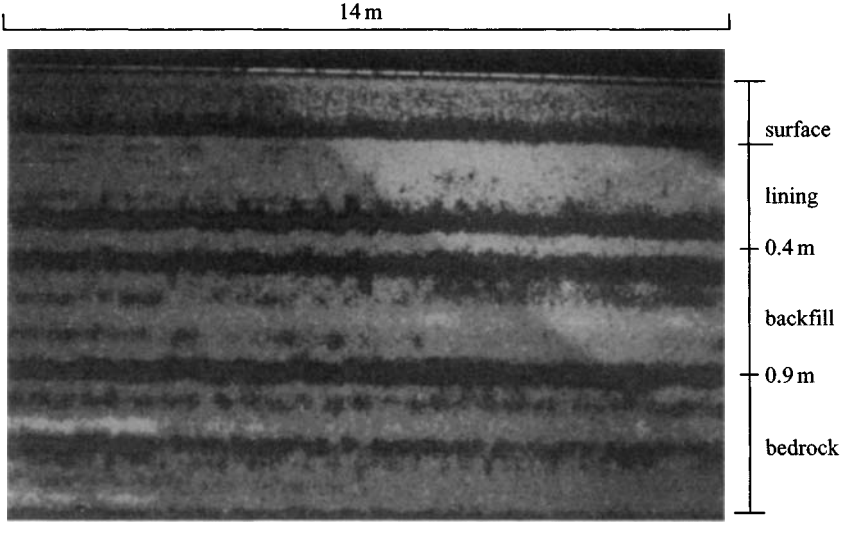

Figure 9.31 Radar image of clear section of tunnel lining (courtesy British Rail)

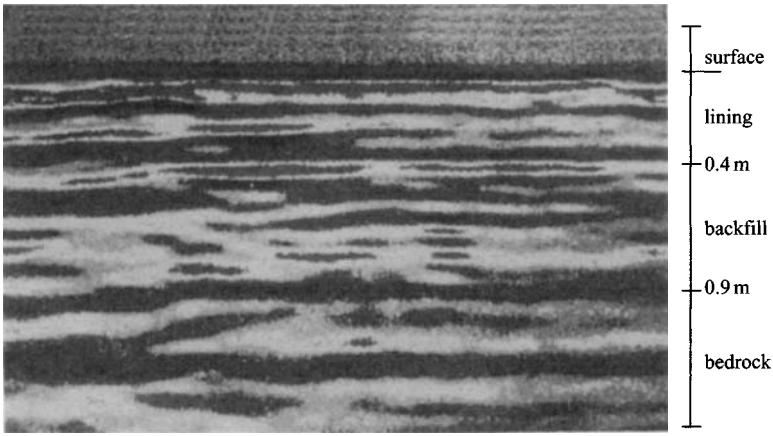

Figure 9.32 Radar image of disturbed section of tunnel lining (courtesy British Rail)

9.7 Summary

GPR is used extensively in nondestructive testing of civil engineering structures and has proved a valuable tool for assessing their quality and condition. This application is one of the most successful uses of GPR, and road inspection in particular is now almost a routine NDT method. Provided that the velocity of propagation within the material is known, then it is possible to obtain accurate information and reconstruction of the internal composition of the structure. Road structures can be assessed in terms of the wearing course and condition of the sub-base. The quality of placement of internal steel re-inforcing mats can also be determined nondestructively. GPR has established a major role in this area, and for quality assurance of the state of structures will continue to develop and mature.

9.8 References

[1] XIAOJIAN, Y., HAIZHONG, Y., and HUILIANG, W.: 'The applications of GPR to civil engineering in China'. Proc. IEEE Int. Conf. on Geoscience and remote sensing, 1997 (IGARSS '97). 'Remote sensing – a scientific vision for sustainable development', 3–8 August 1997, Vol. 1, pp. 232–234

[2] WU, R., LI, X., and LI, J.: 'Continuous pavement profiling with ground-penetrating radar'. *IEE Proc. Radar Sonar Navig.*, 2002, **149**, (4), pp. 183–193

[3] FERNANDO, E.: 'Highway speed pavement thickness surveys using radar'. Final Report prepared for the Federal Highway Administration, Texas Transportation Institute, 1992

[4] FERNANDO, E., and MASER, K. R.: 'Development of a procedure for the automated collection of flexible pavement layer thicknesses and materials: Phase IIB' – Final Report. Florida DOT State Project 99700-7550, 1996

[5] MASER, K.: 'Ground penetrating radar surveys to characterize pavement layer thickness variations at GPS sites'. Strategic Highway Research Program, SHRP–P-397, 1994

[6] MASER, K. R.: 'Evaluation of pavements and bridge decks at highway speed using ground penetrating radar'. Proc. ASCE Structures Congress XIV, Chicago, IL, 15–18 April 1996

[7] MESHER, D., DAWLEY, C., and PULLES, B.: 'Application of ground-penetrating radar technology for evaluating and monitoring asphalt thickness concrete pavement structures'. EBA Engineering Consultants Ltd., Edmonton, Alberta, Canada, 1997

[8] SCULLION, T., LAU, C. L., and CHEN, Y.: 'Implementation of the Texas ground penetrating radar system'. Research Report 1233-1. Texas Transportation Institute, 1992

[9] MESHER, D. E., DAWLEY, C. B., and PULLES, B. C.: 'A comprehensive radar hardware, interpretation software and survey methodology paradigm for bridges deck assessment'. Proc. 6th Int. Conf. on Ground penetration radar, Sendai, 1996, pp. 353–358

[10] ROBERTS, R. L., and PETROY, D.: 'Semi-automatic processing of GPR data collected over pavement'. Proc. 6th Int. Conf. on Ground penetration radar, Sendai, 1996, pp. 347–352

[11] BROSSEAUD, Y.: 'Very thin and ultra thin wearing courses using hot mixed bituminous materials. A review of use and performance'. TRB, 78th Annual Meeting, Washington, 1999, Session 270, Paper no. 990987

[12] AFNOR standard NFP 98-132, 2000: Asphalt – Wearing course and base courses: thin layer asphalt concrete-Definition-Classification-Characteristics-Manufacturing-Laying. French standard

[13] AFNOR standard NFP 98–137, 1992: Asphalt – Wearing course and base courses: very thin layer asphalt concrete-Definition-Classification-Characteristics-Manufacturing-Laying. French standard

[14] GIBSON, P. J.: 'The Vivaldi aerial'. Digest of 9th Eur. Micr. Conf., Brighton, 1979, pp. 120–124

[15] CARIOU, J., COLOMBEL, J. H., DELAMARRE, E., CHEVASSU, G., and LE MOAL, J. Y.: 'Measurement of road surface layer thickness using radar methods'. Proc. Int. Conf. COFREND on NDT, Nantes, 1997, pp. 709–714

[16] HAMRAN, S. E., GJESSING, D. T., HJELMSTAD, J., and AARHOLT, E.: 'Ground penetrating synthetic pulse radar: dynamic range and modes of operation'. *J. Appl. Geophys.*, 1995, **33**, pp. 7–14

[17] KONG, F. N., and BY, T. L.: 'Performance of a GPR system which uses step frequency signals'. *J. Appl. Geophys.*, 1995, **33**, pp. 15–26

[18] KONG, F. N., WESTERDAHL, H., and GELIUS, L.: 'A very wide bandwidth step frequency GPR for testing concrete re-bars'. Proc. 7th Int. Conf. on Ground-penetration radar, Lawrence, 1998

[19] GUILLANTON, E., DAUVIGNAC, J. Y., PICHOT, C., and CASHMAN, J.: 'A new design tapered slot antenna for ultrawide-band applications', *Microw. Opt. Technol. Lett.*, 1998, **19**, (4), pp. 286–289

[20] LANGLEY, J. D. S., HALL, P. S., and NEWHAM, P.: 'Balanced antipodal Vivaldi antenna for wide bandwidth phased arrays'. *IEEE Proc. Microw. Antennas Propag.*, 1996, **143**, (2), pp. 178–181

[21] REYNOLDS, J. M.: 'An introduction to applied and environmental geophysics'. (John Wiley & Sons, UK, 1997, Chap. 10), pp. 682–749

[22] The Concrete Society: 'Guidance on radar testing of concrete structures'. Concrete Society, Slough, Technical Report 48, 1997, 88 pp.

[23] MURRAY, W., LEWIS, C., YANG, Z., and POLLOCK, J. T. A.: 'Development of high resolution GPR hardware in the frequency range 300 MHz to 3.5 GHz'. Proc. 6th Int. Conf. on Ground penetrating radar, Sendai, Japan, 30 Sept.–3 Oct. 1996

[24] MURRAY, W., LEWIS, C., WILLIAMS, C., SIGGINS, A. F., SIGGINS, B,F., and WHITELEY, R. J.: 'Submersible radar for civil engineering applications'. Proc. 8th Int. Conf. on Ground penetrating radar, GPR2000, Gold Coast, Aust., 23–26 May 2000, pp. 55–59

[25] SIGGINS, A. F., and WHITELEY, R. J.: 'Laboratory simulation of high frequency GPR responses of damaged tunnel liners'. Proc. 8th Int. Conf. on Ground penetrating radar, GPR2000, Gold Coast, Aust., 23–26 May 2000, pp. 805–811

[26] SIGGINS, A. F.: 'Ground probing radar in geotechnical applications'. *Explor. Geophys.*, 1990, **21**, pp. 175–186

[27] HUTCHINSON, R. E., and WHITELEY, R. J.: 'The physical assessment of sub-surface assets'. Proc. Trenchless Asia, Singapore, 14–16 February 1995, Int. Soc. for Trenchless Technology, 4.4.1–4.4.5

[28] WHITELEY, R. J., and PARKER, C.: 'Application of geophysical and geotechnical technologies to major tunnels in Sydney, Australia, 2001'. Proc. Rapid excavation and tunneling Conf., SMME, San Diego, Ch. 24, pp. 285–298

[29] ROIMELA, P., SALMENKAITA, S., MAIJALA, P., and SAARENKETO, T.: 'Road analysis – a tool for cost effective rehabilitation measures for Finnish roads'. Proc. 8th Int. Conf. on Ground penetrating radar, GPR2000, Gold Coast, Australia, 23–26 May 2000, pp. 107–112

[30] BUNGEY, J. H., and MILLARD, S. G.: 'Radar inspection of structures'. *Proc. ICE (Struct. Build.)*, 1993, **99**, pp. 173–186

[31] BUNGEY, J. H., MILLARD, S. G., SHAW, M. R., and THOMAS, C.: 'Operational aspects of radar investigations'. *Br. J. Non-Destr. Test.*, 1991, **33**, (12), pp. 599–605

[32] BUNGEY, J. H., MILLARD, S. G., and SHAW, M. R.: 'A simulation tank to aid interpretation of radar results on concrete'. *Mag. Concr. Res.*, 1993, **65**, (164), pp. 187–195

[33] SHAW, M. R., MILLARD, S. G., HOULDEN, M. A., AUSTIN, B. A., and BUNGEY, J. H.: 'A large diameter transmission line for the measurement of the relative permittivity of construction materials'. *Br. J. Non-Destr. Test.*, 1993, **35**, (12), pp. 696–704

[34] BUNGEY, J. H., SHAW, M. R., and MILLARD, S. G.: 'The influence of reinforcing steel on radar surveys of concrete structures', in

FORDE, M. C. (Ed.): 'Structural faults and repair' (Eng. Technics Press, Edinburgh, 1993, Vol. 3), pp. 43–50

[35] MILLARD, S. G., BUNGEY, J. H., and SHAW, M. R.: 'The assessment of concrete quality using pulsed radar reflection and transmission techniques', in BUNGEY, J. H. (Ed.): 'N.D.T. in civil engineering' (Brit. Inst. N.D.T., 1993, Vol.1), pp. 161–185

[36] BUNGEY, J. H., MILLARD, S. G., and SHAW, M. R.: 'Radar assessment of post-tensioned concrete', in FORDE, M. C. (Ed.): Proc. 7th Int. Conf. on Structural faults and repair (Engineering Technics Press, Edinburgh, 1997, Vol. 1), pp. 331–339

[37] WIGGENHAUSER, H.: 'Research in non-destructive testing in civil engineering', in UOMOTO, T. (Ed.): Proceedings of Seiken Symposium No. 26, Non-Destructive Testing in Civil Engineering 2000, Tokyo, Japan, (Elsevier, 2000), pp. 23–39

[38] KONG, F.: 'Choice of antenna type and frequency range for testing concrete structures'. Proc. 8th Int. Conf. on Ground penetrating radar, The University of Queensland, Gold Coast, Australia, 2000, CDROM

[39] AZEVEDO, S. G., MAST, J. E., NELSON, S. D., ROSENBURY, E. T., JONES, H. E., McEWAN, T. E., MULLENHOFF, D. J., HUGENBERGER, R. E., STEVER, R. D., WARHUS, J. P., and WIETING, M. G.: 'HERMES: A high-speed radar imaging system for inspection of bridge decks'. *SPIE Proc.*, 1996, Vol. 2946, pp. 195–204

[40] GÖTTEL, R., MÖNICH, G., and MAIERHOFER, CH.: 'High frequency radar antennas for resolution enhancement of concrete structure images', in Lammasniemi, J. *et al.* (Eds.): Proceedings of the EOS/SPIE International Symposia on Industrial lasers and inspection & envirosense, Vol. 3827, Washington, USA: SPIE – The International Society for Optical Engineering, 1999, pp. 96–103

[41] KRAUSE, M., KRIEGER, J., and WIGGENHAUSER, H.: 'Erprobung und Bewertung zerstörungsfreier Prüfverfahren für Betonbrücken'. *Bautechnik*, 1999, **76**, (1), pp. 16–26

[42] FUNK, TH., MAIERHOFER, CH., LEIPOLD, S., and BORCHARDT, K.: 'Non-destructive location of tendon ducts in concrete for the installation of noise insulating walls using impulse radar', in FORDE, M. C. (Ed.): Proc. 7th Int. Conf. on Structural faults and repair, Vol. 2, Edinburgh, Engineering Technics Press, 1997, pp. 323–329

[43] MAIERHOFER, CH., KRAUSE, M., MIELENTZ, F., MILMANN, B., and MÜLLER, W.: 'Kombinierter Einsatz von Radar und Ultraschallarray-Verfahren zur Strukturuntersuchung von Brückenbauteilen'. Berichtsband 73 der DACH-Jahrestagung der Deutschen Gesellschaft für Zerstörungsfreie Prüfung (DGZfP), 2000, pp. 519–534

[44] COLLA, C., KRAUSE, M., MAIERHOFER, CH., HÖHBERGER, H., and SOMMER, H.: 'Combination of NDT techniques for site investigation of non-ballasted railway tracks.' *NDT & E Int.*, 2002, **35**, (2), pp. 95–105

[45] CLEMENA, G. M., SPRINKEL, M. M., and LONG, R. R.: 'Use of ground-penetrating radar for detecting voids under a jointed concrete pavement', in 'Transportation research record 1109', National Academy of Sciences, 1997, pp. 1–10

[46] MASER, K. R.: 'Condition assessment of transportation infrastructure using ground penetrating radar,' *J. Infrastruct. Syst., ASCE*, 1996, pp. 94–101

[47] STEINWAY, W. J., ECHARD, J. D., and LUKE, C. M.: 'Locating voids beneath pavement using pulsed electromagnetic waves'. NCHRP Report 237, National Academie of Sciences, 1981

[48] Bundesregierung: 'Zweiter Bericht über Schäden an Bauwerken der Bundesverkehrswege. Unterrichtung durch die Bundesregierung, Deutscher Bundestag 13. Wahlperiode, Drucksache 13/3970 vom 05.03.1996, Bonn

[49] MAIERHOFER, C.: 'Impulsradar zur Untersuchung der inneren Struktur von Beton', *Betonwerk + Fertigteil-Technik*, 2000, **11**, pp. 94–101

[50] RÖSCH, A., and SCHAAB, A.: 'An in-situ NDT-method to detect incorrectly positioned dowel bars in carriage way slabs of concrete highways', in SCHICKERT, G., and WIGGENHAUSER, H. (Eds.): Proc. Int. Symposium NDT-CE, 1995, Berlin: DGZfP, pp. 269–276

[51] MAIERHOFER, C., BRINK, A., RÖLLIG, M., and WIGGENHAUSER, H.: 'Detection of shallow voids in concrete structures with impulse thermography and radar', in FORDE, M. C. (Ed.): Proc. 10th Int. Conf. on Structural faults & repair, 2001, London, Engineering Technics Press, CD-ROM

[52] KRAUSE, M., MAIERHOFER, C., and WIGGENHAUSER, H.: 'Thickness measurement of concrete elements using radar and ultrasonic impulse echo techniques, in FORDE, M. C. (Ed.): Proc. 6th Int. Conf. on Structural faults & repairs, London, Engineering Technics Press, 1995, Vol. 2, pp. 17–24

[53] MAIERHOFER, CH., KRAUSE, M., and WIGGENHAUSER, H.: 'Non-destructive investigation of sluices using radar and ultrasonic impulse echo'. *NDT& E Int.*, 1998, **31**, (6), pp. 421–427

[54] KRAUSE, M., MIELENTZ, F., MILMAN, B., MÜLLER, W., SCHMITZ, V., and WIGGENHAUSER, H.: 'Ultrasonic imaging of concrete members using an array system'. *NDT& E Int.*, 2001, **34**, (9), pp. 403–408

[55] BOTROS, A. Z., OLVER, A. D., CUTHBERT, L. G., and FARMER, G. A.: 'Microwave detection of hidden objects in walls', *Electron. Lett.*, 1984, **20**, pp. 824–825

[56] CARR, A. G., CUTHBERT, L. G., and LIAU, T. F.: 'Signal processing techniques for short-range radars applied to the detection of hidden objects'. Proc. 7th Eur. Conf. on Electrotechnics: EURCON 86, Paris, 1986

[57] TRANSBARGER, O.: 'FM radar for inspecting brick and concrete tunnels', *Mater. Eval.*, 1985, **43**, (10), pp. 1254–1261

[58] DE VEKEY, R. C.: 'Non-destructive test methods for masonry structures'. 8th IBMAC Proc., 1988, Vol. 3, p. 1673

[59] BASTON-PITT, J. D.: 'The role of impulse radar in the investigation, restoration and change of use of old buildings'. Proc. 3rd Int. Mas. Conf., London, 1992

[60] DE VEKEY, R. C., BALLARD, G. S., and ADDERSON, B. W.: 'The effectiveness of radar for the investigation of complex LPS joints'. Proc.ISE/BRE Conf. on Life of structures, 1989, Vol. 1, p. 116
[61] DE VEKEY, R. C., MATTHEWS, R. S., and BALLARD, G. S.: 'An evaluation of impulse radar for floor and wall assessment in concrete system buildings'. Proc. CIB.92, 1992, Vol. 1, p. 190
[62] DE VEKEY, R. C., MATTHEWS, R. S., and BALLARD, G. S.: 'Using impulse radar for floor and wall assessments in concrete system buildings'. National Research Council of Canada, Construction Technology Update, 1993
[63] ZHANG, J., NAKHKASH, M., and HUANG, Y.: 'In-situ characterisation of building materials'. Eleventh Int. Conf. on Antennas and propagation, 2001, IEE Conf. Publ. No. 480, 2001, Vol. 1, pp. 269–274

9.9 Bibliography

ARNDT, D., BORCHARDT, K., CROY, P., GEYER, E., HENSCHEN, J., MAIERHOFER, C., NIEDACK-NAD, M., RUDOLPH, M., SCHAURICH, D., WEISE, F., and WIGGENHAUSER, H.: Anwendung und Kombination zerstörungsfreier Prüfverfahren zur Bestimmung der Mauerwerksfeuchte im Deutschen Dom. Forschungsbericht 200 der BAM, (Wirtschaftsverlag NW Verlag für neue Wissenschaft, Berlin, 1994), 75 pp.

GIROT, D., BENOIST, J. M., and GODARD, J. F.: 'Utilisation d'un radar impulsionnel pour l'étude des structures de chaussées', *Bull. Lab. Pts Ch.*, 1985, **139**, pp. 71–76

KRAUSE, M., and WIGGENHAUSER, H.: 'Ultrasonic testing in civil engineering', in Proc. NDT in progress, Trest, CZ, Czech Society for NDT, Eigenverlag, Prag, 2001, pp. 17–28

MAIERHOFER, C., and WÖSTMANN, J.: 'Investigation of dielectric properties of brick materials as a function of moisture and salt content using a microwave impulse technique at very high frequencies'. *NDT& E Int.*, 1998, **31**, (4), pp. 259–263

National Cooperative Highway Research Program Synthesis 255: 'Ground-penetrating radar for evaluating subsurface conditions for transportation facilities'. Transportation Research Board, National Research Council, March 1998

SCHEEL, H., and HILLEMEIER, B.: 'Capacity of the remanent magnetism method to detect fractures of steel in tendons embedded in prestressed concrete'. *NDT& E Int.*, 1997, **30**, (4), pp. 211–216

Chapter 10

Forensic applications

10.1 Introduction

Forensic investigation using GPR has become a recognised method of forensic archaeology by means of some high profile case histories.

GPR techniques are one among a number of methods that can be used in forensic investigations and can greatly assist police investigations by pinpointing suspicious areas and thus saving unnecessary excavation.

In the UK, the Forensic Science Advisory Group provides impartial advice and technical support to the UK Police Forces. The Forensic Search Advisory Group represents a consortium of individuals with expertise in the location of buried or hidden remains. All members of the group have direct scene of crime experience and are committed to the use and development of technical and field skills for forensic purposes. The group and its aims have been recognised by the Association of Chief Police Officers (ACPO) Crime, Scientific Support Sub-Committee. The group is also advancing detection and recovery methodologies through an active programme of basic and applied research. It has been involved in international investigations and has contacts with similar groups in other countries.

The group also has an active publishable research programme part of which is based on controlled burial sites using animal carcasses. Four sites are currently in operation: two of these are dedicated to geophysical survey detection (one specifically for ground penetrating radar); one for aerial interpretation; and one for thermal change and the decay of associated materials. Other research is also being conducted at the universities of Bradford, Birmingham and Bournemouth on a range of associated topics. Search themes are also integral components of presentations delivered by members to police forces and associated personnel at various centres in the UK. Further information can be found on their website at http://www.brad.ac.uk/acad/archsci/external/fsag/fsagcode.html.

In the US, NecroSearch International is a nonprofit organisation that specialises in the search of clandestine gravesites and evidence. The goal of NecroSearch is to

develop a cost-effective systems approach, involving many different disciplines, that could result in a more efficient method of locating clandestine graves. NecroSearch pioneered a long-term field study, in which swine carcasses are buried and then subjected to ongoing scientific study. The research facility is located at the Highlands Ranch Law Enforcement Training Facility, Douglas County, Colorado, http://www.douglas.co.us/sheriff/Divisions/Investigations/NecroSearch.htm.

Forensic investigations should be multi-disciplinary and the following aspects should be considered when considering using GPR:

- availability of site plans of utilities
- availability of site information on burial sites of pet animals
- correct recording of scene and site evidence
- methods of removing surface vegetation and obstructing artefacts (note that GPR requires a reasonably flat surface to gather good data)
- time, manner and cause of death (state of decay of corpse)
- identification of state of remains to aid GPR interpretation
- recovery procedures of remains.

Because of the variability of the sites, the interpretation of GPR B-scan images is not easily carried out by those without significant experience of GPR forensic surveying. There have been situations where graduate students or general technicians have been employed to work on forensic surveys. Often these individuals have had little training and minimal experience and should never have been involved.

For good GPR survey results it is also vital that the ground is undisturbed by either the passage of heavy vehicles (which tend to compress the soil and give rise to unwanted reflections) or by digging. Once digging has been carried out, the soil structure is disturbed and effective GPR surveying becomes extremely difficult. The

Figure 10.1 Police investigations on Saddleworth Moor (copyright BBC News)

golden rule is that the site should be in a virgin state for best GPR results. For example, the situation shown in Figure 10.1 carried out in 1986 would make the use of GPR very difficult.

An excellent introduction to the principles of forensic investigation is provided by Hunter in 'Studies in crime' [1].

10.2 Principles of GPR forensic search

Dr Jon Dittmer

Police and law enforcement agencies frequently need to conduct searches which involve locating buried or concealed objects such as human remains, weapons caches, hides and drugs caches. Invariably, such operations are expensive, time-consuming and are manpower intensive.

The scale of the search will determine the potential costs that are incurred. For example, if the search is for a single human cadaver in a typical suburban garden, it will require the investigation of a variety of locations. A garden may contain flower-beds, lawns, structures built on a hard-standing, patios, paths etc. A search will require all these to be investigated. The police scenes of crime investigators have a number of methods which can be employed to help narrow down the sites to be excavated. Such tools include dogs, forensic archaeologists using other geophysical techniques and initial evidence. Such methods may be helpful for soft ground, but for hard ground, such as concrete, these methods are of little help. In most cases, a complete excavation is required which will inevitably be extremely costly. The site needs to be thoroughly excavated, and if nothing is found the garden has to be reinstated.

GPR provides the means to conduct rapid, nondestructive investigations, which can alleviate the need to carry out extensive and expensive excavations. In skilled hands, GPR can be employed to search for and locate the types of target sought by the forensic investigators. Unlike searching for utilities and services, where the radar signatures tend to be well defined and typically hyperbolic in form, radar signatures of forensic targets are varied and, due to the wide variety of targets and scenarios, never the same. However, with experience an operator will begin to be accustomed to general patterns within the radar images.

It must be emphasised that GPR cannot provide an image of the buried remains. After several high profile cases where GPR had been used, the media portrayed GPR as a 'magic wand' which showed wonderfully clear images of skeletal remains 'grinning' at the operator. This is nonsense. GPR is simply another tool, which requires careful and skilled use. However, it can be a very useful and cost-effective way of searching a site and reducing unnecessary excavation.

10.2.1 Method

The key to a successful forensic search is, as with all surveying techniques, a sound systematic procedure. The site to be examined is scanned in two directions because the GPR antennas have maximum performance in a given direction of search. This is done so that a full picture of the sub-surface can be formed in the operator's mind.

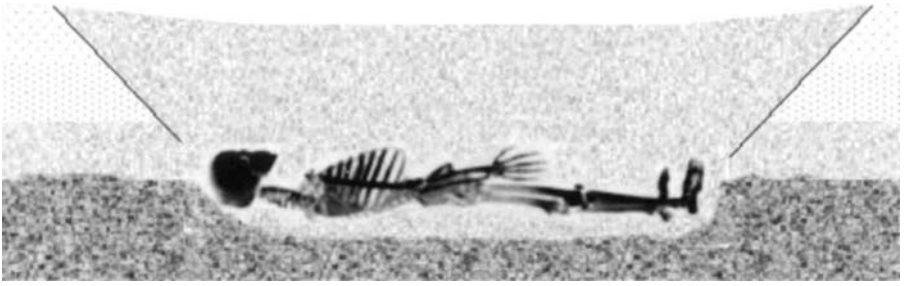

Figure 10.2 Generalised sketch of a grave

Even though the final aim of the survey is to locate items of forensic interest, the actual search must be a complete survey, locating pipes, cables and services. The basis of the survey is to locate anomalous features in the area. By a process of elimination, anything that cannot be readily explained must be regarded as suspicious. Therefore, the GPR investigator must know, as far as possible, the full layout of the property.

10.2.2 Graves

The principal targets of most forensic searches are human remains, or more specifically graves. A grave is simply a backfilled excavation in the ground, with buried human remains in some state. This means that there are two structures which can be used to identify the grave: the excavation and the remains. Figure 10.2 shows a sketch of a grave showing all the main features that may provide a measurable return. These features can be split into two groups, based on their origin: those that are due to the hole and those that are due to the human remains.

10.2.3 Remains

The remains are the objective of the investigation and therefore indications of a body are going to be the first thing the operator will look for. The state of the remains will determine the level of any return signal. The decay of the remains is influenced by a number of factors, including the length of time the body has been buried as well as the type of soil present.

Bodies buried in soils with a low bacterial content will tend to show lower levels of decay than those buried in soils rich in bacteria and oxygen. The wrapping around the body is also important as it can provide as large a radar target as the body. For example, if the remains are wrapped in carpet, the heavy carpet material will provide a sizeable target.

Bodies that have been dismembered will tend to decay more swiftly, but in addition the grave may appear smaller as the body parts can be stacked in a smaller hole. A concrete or other hard-standing solid cover over the grave will prevent a direct through flow of water, due to rain or other meteorological phenomena.

The way the body has been laid out will also affect the appearance of the corpse and size of the grave. Not all bodies are laid out full length and on their back. As mentioned above, a dismembered body may be stacked in a smaller hole. It is also not unusual for a body to be buried in a foetal position. This will again reduce the size of a grave.

10.2.4 Excavation

The excavation is also a source of potentially anomalous features which can be used to locate a grave.

If the ground at the suspected grave-site has a distinct structure, particularly horizontal layering, a cut may be visible. This effect may be visible as a distinct break in a clearly visible layer in the data, whereby the layer is absent for a short distance. In addition, this break may be accompanied by a region of disturbance, the fill of the grave. If the grave is under a concrete floor, the decay of the body and the subsequent settling of the grave may cause a void to form. This cavity will be obvious, as it will tend to cause the radar signal to resonate within the cavity, giving an enhanced return.

Figure 10.3 shows a radar section across a private garden. The regions of disturbance are typical of a response of a grave, either human or animal. One of the most frequently encountered graves in a forensic investigation is the pet grave, such as a cat or dog. An investigation will usually identify the probable presence of such a grave prior to the search. The detection and location of a grave will be desirable during the search, as it will give the investigator an idea of the likely state of preservation of a body in the prevailing environment, and will enable the search team to discount areas of the garden.

10.2.5 Test grave sites

To obtain a fuller understanding of how a grave can change over time, a number of police and associated scientific research groups have carried out programs of work on the graves of animals. Clearly, the use of genuine human remains is going to raise

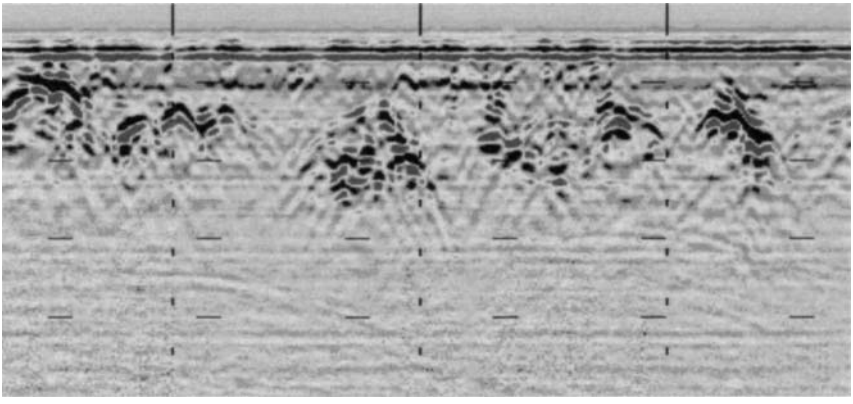

Figure 10.3 Radar sections showing regions of disturbance typical of grave sites

ethical questions. However, the more typical occupant of a controlled test grave site is an animal that has died of natural causes. Pigs are often employed as they are similar in size to a human adult and more importantly have flesh and fat that decay similarly.

One such test site in the UK consisted of eight graves. There were many possible parameters that could be altered. Some of these were: the integrity of the remains, i.e. the rate of decomposition; the wrapping material, such as plastic bags, carpet etc. around the animal; and the overburden, i.e. concrete/hard-standing cover.

There are many combinations, but eight were chosen which covered most situations to some degree. Four were covered with concrete and four left open to the elements. The graves contained a variety of animals, some wrapped and some dismembered. Over a period of 5 years, the grave-sites were periodically scanned with GPR and a regular monitoring of the GPR images was carried out.

Figure 10.4 shows a B-scan cross-section of the grave site after 5 years' burial and corresponds to the survey line shown dotted in Figure 10.5 which shows a plan view of the test site. Figure 10.5 shows a depth slice approximately 40 cm below the

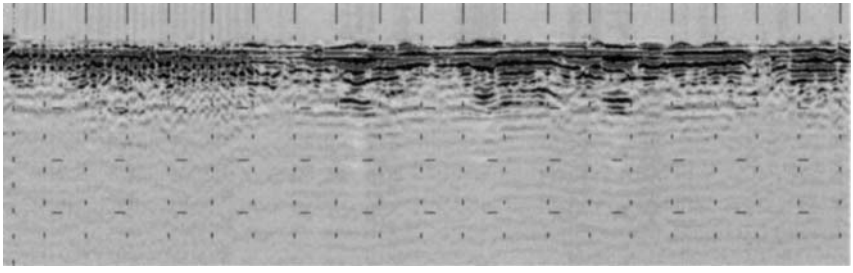

Figure 10.4 Radar B-scan image of test grave sites

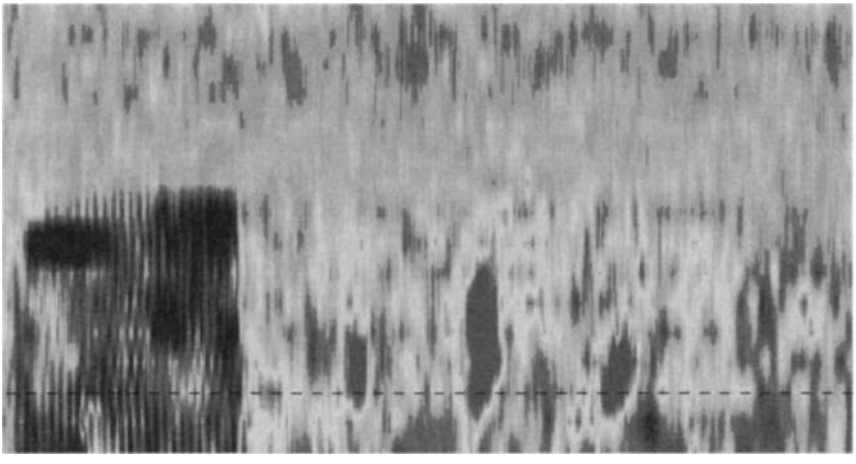

Figure 10.5 Plan (C-scan) view of test grave-site

surface. In the bottom central half of the plan, three distinct patches can be seen. These anomalies are due to voiding that has appeared beneath the concrete, which covers the four graves in the lower part of the Figure. In a real investigation, such anomalies would be regarded as suspicious. The forensic search team would be alerted to possible grave sites, which would be excavated. In addition to these anomalies, a patch of reinforcing can be seen towards the lower left half of the site. The presence of a reinforcing mesh might give cause for suspicion if it occurred in a location which did not require strengthening, or if it was isolated.

10.3 Case histories

The following Sections provide a short description of some recent case-histories where GPR has been successfully used to assist investigations. Given the evidential nature of the GPR search results, confidentiality limits full disclosure. The cases in Sections 10.3.1 and 10.3.2 were carried out by the ERA Technology survey team using SPR scan radar systems.

10.3.1 Frederick West

ERA Technology

GPR was brought to the attention of the general public in a dramatic fashion by the world's media in the case of Frederick and Rosemary West. The police investigation was carried out by Detective Superintendent John Bennett of Gloucester Constabulary, aided by pathologist Prof. Bernard Knight. Media attention was considerable, as with all cases involving the most depraved and sadistic human behaviour. Some of the headlines are shown in Figure 10.6.

In February of 1994, the Gloucester police started to dig the garden at 25 Cromwell Street. They were searching for and found the remains of his daughter Heather, who had disappeared several years earlier. However, pathology evidence showed indication of other bodies and a more extensive search was commissioned. The structure of the property was regarded as unsafe, so that normal excavation of the cellars and other rooms would have been hazardous. A GPR survey carried out by a team from ERA Technology located suspicious sites within 25 Cromwell Street and enabled the police to recover the remains without excessive excavation (see Figure 10.7).

The West's victims first found in the garden of Cromwell Street were Alison Chambers, 17, from Swansea, who was murdered in 1977, Shirley Robinson, 18, lodger and Fred's lover, who was murdered in 1977, and Heather West, 16, Fred and Rose's eldest daughter, who was murdered in 1977. In the building at Cromwell Street the following were found:

- Linda Gough, 21, a seamstress from Gloucester, who was murdered in 1973
- Lucy Partington, 21, a university student, from Gotherington, who was murdered in 1973
- Carol Cooper, 15, a schoolgirl from Worcester, who was murdered in 1974
- Juanita Mott, 19, from Newent, Glos, who was murdered in 1975

Figure 10.6 Media coverage of the West case

- Shirley Hubbard, 15, a schoolgirl from Worcester, who was murdered in 1975
- Therese Siegenthaler, 21, a Swiss hitchhiker, who was murdered in 1977.

Charmaine West, 8, who was murdered in 1972, was found beneath 25 Midland Road, Gloucester. The fields at Much Marcle contained the graves of Ann McFall, who was murdered in 1967, and Rena Costello (Fred's first wife), who was murdered in 1970.

Frederick and Rosemary West were arrested and sent for trial. On New Year's Day 1995, just as the media interest was waning, Frederick West hanged himself in Birmingham's Winson Green prison, where he was awaiting his trial on 12 murder charges.

In October 1995, Rosemary West was tried at Winchester Crown Court for 10 murders. She was found guilty on all 10 counts by unanimous decision and jailed for life. The Home Secretary has since told her that she will never be released. The case against Rosemary West was closed and, in October 1996, Gloucester City Council demolished 25 Cromwell Street.

Various speculative theories were proposed by individuals as to the existence of further murder victims. Media interest continued in view of the notoriety of the

Figure 10.7 *Radar investigation by ERA radar team of the garden of 25 Cromwell Street (copyright Gloucestershire Echo)*

case, and some tabloid papers suggested that further police investigation should be carried out.

10.3.2 Marc Dutroux

ERA Technology

GPR was called in by the Belgian Police to help search for the victims of Marc Dutroux.

Marc Dutroux was convicted in 1989 for the rape and abuse of five young girls and sentenced to 13 years in prison. He served three years before being released for good behaviour in 1992. On 15 August 1996, Belgian police raided Dutroux's house, where they discovered a soundproof concrete dungeon in the basement. This was cunningly concealed behind a false concrete wall mounted on steel runners, and an earlier inspection by police had failed to discover the dungeon. Inside were two young girls, Sabine Dardenne, 14, and Laetitia Delhez, 12. Both girls had been sexually assaulted and filmed pornographically by Dutroux.

It was clear that many unexplained disappearances of young girls and women in the region of the properties owned by Dutroux and his associates might be solved by extensive searching with GPR (Figure 10.8). The ERA Technology radar search team, working in heavy rain and gale-force winds, during late August 1996, found several suspicious areas in a shed in a garden at Jumet (see Figure 10.9). These were

Figure 10.8 *Radar investigation by ERA radar team of the field at Much Marcle (copyright Gloucestershire Echo)*

Figure 10.9 *Site at Jumet under investigation (Photo DR)*

Figure 10.10 The grave markers of the seven 1918 Spanish flu victims in the Longyearbyen Cemetery (courtesy Sensors and Software)

subsequently identified as the graves of Eefje Lambrecks, 19, and An Marchal, 17, who had been missing since August 1995.

The police investigation was not seen by the Belgian public as effective or efficient, and in mid-October, 1996, following the dismissal of Jean-Marc Connerotte, the investigative judge in the case, one of the largest peacetime marches in Belgium's history since World War II took place. Allegations of an extensive perversion of justice and impeding of the investigation by corrupt officials led to a march through the centre of Brussels by more than 300 000 people dressed in white, a symbol of innocence. They demanded reforms within the political and judicial system.

Six years after his arrest, Marc Dutroux first heard the charges read out to him. A public announcement was expected. Investigating judge Jacques Langlois would be likely to focus the indictment on Dutroux' responsibility for the kidnapping, sexual abuse and imprisonment of six girls and the subsequent death of four of them.

10.3.3 Victims of the 1918 Spanish flu epidemic

Les Davis

In 1918 Spanish flu swept the world. Over a period of 18 months between 20 and 40 million people died.

In 1997, an international group of scientists travelled to the graveyard of Longyearbyen, a remote mining town on the Norwegian island of Spitzbergen, 1300 km from the North pole, to investigate the grave sites of seven Norwegian miners who were buried there after succumbing to the Spanish flu (see Figure 10.10). The graves are now 80 years old and the team used ground penetrating radar to locate the burial site and retrieve the bodies of the seven miners from the permafrost. Davis *et al.* [2] reported the site investigation in detail.

The objective of the investigation was to recover tissue from the corpses, which should have remained frozen in the permafrost. The reconnaissance survey was conducted in Svalbard, Norway, by Mr Les Davis of Sensors & Software (SSI) and Mr Alan Heginbottom of the Geological Survey of Canada, along with a team of leading scientists from Canada, the United Kingdom, Norway and the USA. The subsurface graves were located using a pulseEKKO 1000 ground penetrating radar (GPR) system, which uses radio waves to nonintrusively map changes from underground features.

The GPR findings indicated the probable grave locations of seven young men who died from the 1918 Spanish flu virus in the acute stage of the epidemic. The GPR data also suggest that the bodies may have remained frozen for the past 80 years, because there were indications of reflections from within the permafrost layer. This information helped the scientists evaluate whether it is feasible to safely recover traces of the Spanish flu virus from the bodies. The GPR results also enabled the virologists to progress to the second phase of the project, namely exhumation of the bodies. Exhumation would be conducted with strict attention to safety, conservation of heritage aspects, and with respect for the deceased.

Pinpointing the graves minimises the area to be excavated, which can ultimately save time and money. The chances of the recovered material being infectious are small due to the permafrost ground temperature and the depth of the graves. Over the past 80 years, the annual range of ground temperature ranged between approximately $-4°C$ and $-10°C$, a very poor environment for survival of viable virus. Despite the extremely low risk, the second phase of the project was conducted with every safety precaution.

On 21 August 1999 excavation was started. With suitable biological protection equipment, the team started excavation of the site indicated by GPR. The first three coffins were discovered within a metre of the ground surface and finally all seven coffins were discovered to have been above the permafrost and thus subject to higher temperatures, which would not have preserved the tissues. The coffins were opened to salvage whatever scraps of tissue and bone they could find, in a last ditch effort to get genetic traces of the virus.

(For more information on the 1918 Spanish flu project, please contact Dr Kirsty Duncan, Project Leader, by fax: 416-247-2126, or for technical information about the GPR surveys contact Les Davis by email: terad@sympatico.ca)

10.3.4 Investigation of potential mass grave locations for the Tulsa Race Riot

A significant investigation was carried out by Dr Robert Brooks (State Archaeologist) and Dr Alan H. Witten (University of Oklahoma), and this sub-Section is a précis of their paper, which is found on the website at *The Investigation of Potential Mass Grave Locations for the Tulsa Race Riot*. This section is an abstract from their publications [3–6].

On the nights of 31 May and 1 June 1921, the City of Tulsa witnessed a racial conflict between whites and the minority black population living in the Greenwood section.

There were an undetermined number of deaths, both black and white, with estimates ranging from the official count of 36 to approximately 300.

In the spring of 1998, it was recommended to the Tulsa Race Riot Commission that a search for mass grave sites be attempted through use of geophysical investigations. Based on the cost-effectiveness of examining large areas and the noninvasive nature of the methods, geophysical examination of Newblock Park, Oaklawn Cemetery, and Booker T. Washington Cemetery appeared to be the most reasonable approach to study of this issue. The Commission at their February 1999 meeting approved the use of geophysics to examine for potential mass grave sites.

The search for mass graves at the three locations was carried out with a Sensors and Software pulse EKKO 1000 ground penetrating radar unit (GPR). Ground penetrating radar was selected for this initial examination because of its successful use in detecting both prehistoric and historic graves in a variety of settings. As noted in the Maki and Jones report [6] the GPR unit may locate anomalies through reflections from disturbed soil associated with the grave shaft such as bones, coffins, grave goods, and breakdown in normal soil conditions. Antennas with two different frequencies, 450 MHz and 225 MHz, were used. The higher frequency antenna was used to obtain better resolution, although this frequency also experienced a loss in the depth of ground-penetration. The antenna utilised was determined by local soil conditions at each locality. Each of the three potential mass grave locations was also sketched and a grid imposed over the area to be examined.

10.3.4.1 Summary: Between July 1998 and November 1999, geophysical investigations were conducted at three locations thought to potentially represent sites of mass graves for victims of the Tulsa Race Riot. Examination of select areas at Newblock Park and Booker T. Washington Cemetery through use of ground penetrating radar failed to reveal any features suggestive of a mass grave.

Initial study of Oaklawn Cemetery with ground penetrating radar revealed a number of individual internments but no evidence of a mass grave. With an eyewitness account permitting a narrowing of the search window, a second examination was conducted at Oaklawn Cemetery. Through use of electromagnetic induction and ground penetrating radar, a 5-m (15-ft) square anomaly with vertical walls was identified within the area pointed out by the eyewitness as where a trench was dug for burying riot victims.

While this evidence is compelling, it cannot be viewed as factual until the feature has been physically examined by excavation to determine if this represents a grave site, and, more importantly, if a grave, whether it contains multiple individuals. The situation at Oaklawn Cemetery has been further complicated by cemetery records indicating that an adult white male had been buried there shortly before the riot and two white children were buried within the boundaries of this feature following the riot. This information seems contradictory to the presence of a mass grave at this location.

10.4 Summary

GPR has been used very successfully to assist forensic investigations. Its prime benefit is to pinpoint suspicious areas within a generally specified zone. This saves considerable wasted excavation. The survey should be carried out by an operator experienced in forensic applications of GPR and one who can use information from site drawings and other search techniques to eliminate spurious results. GPR cannot generate images of the resolution of X-ray images, but it is invaluable as an aid to improving the efficiency and cost effectiveness of forensic investigations.

For good GPR survey results it is essential that the ground is undisturbed by either the passage of heavy vehicles (which tend to compress the soil and give rise to unwanted reflections) or by digging. Once digging has been carried out, the soil structure is disturbed and effective GPR surveying becomes extremely difficult. The golden rule is that the site should be in a virgin state for best GPR results. This means that the police or investigating authorities should call in GPR surveying at the outset of the investigation.

10.5 References

[1] HUNTER, J., ROBERTS, C., and MARTIN, A.: 'Studies in crime'. Batsford, 1996, ISBN 0713479019

[2] DAVIS, J. L., HEGINBOTTOM, J., ANNAN, P., DANIELS, R., BERDAL, P., BERGAN, T., DUNCAN, K., LEWIN, P., OXFORD, J., ROBERTS, N., SKEHEL, J., and SMITH, C.: 'Ground penetrating radar surveys to locate 1918 Spanish Flu victims in Permafrost', *ASTM J. Forens. Sci.*, Jan. 2000, **45**, (1), pp. 68–76

[3] ELLSWORTH, S.: 'Death in a promised land: the Tulsa Race Riot of 1921' (Louisiana State University Press, Baton Rouge, 1982)

[4] WYNN, J. C.: 'Archaeological prospection: an introduction to the special issue: Geophysics in archaeology', *Geophysics*, 1986, **51**, (3), pp. 533–539

[5] HEIMMER, D. H.: 'Near-surface, high resolution geophysical methods for cultural resource management and archaeological investigations' (National Park Service, US Government Printing Services, Denver, 1992)

[6] MAKI, D., and JONES, G.: 'Search for graves from the Tulsa Race Riot using ground penetrating radar'. Archaeo-Physics, Report of Investigations Number 5, 1998

Chapter 11

Geophysical applications

11.1 Introduction

This Chapter describes some of the geophysical applications of ground penetrating radar (GPR). There is now a wealth of information on the probing of rocks, soils, snow and ice, and the contributors to the second edition have concentrated on two specific applications, namely frozen materials and borehole radar. The reader should not infer that probing of rocks and soils has not been a major activity over the last decade, and papers by Peters *et al.* [1], Pettinelli *et al.* [2], and Sato and Lu [3] are typical examples of the variety of studies and applications of GPR to geophysical applications. The author felt that there was sufficient information in the various conference proceedings, referred to in the introductory chapters, on conventional GPR probing of rocks and soils, and it would be useful to emphasise the more specialised applications of GPR in terms of geophysical probing. Thus, the material of the first edition has been retained, but the contributions to the second edition have emphasised those particular aspects of GPR. For those readers wishing to research the broad range of GPR studies related to stratigraphic analyses, the following organisations have regular conferences and publications. The Geological Society of America (GSA) at http://www.geosociety.org/ and the Society of Exploration Geophysics (SEG) at http://www.seg.org/ will be valuable sources of information.

As an example, a conference of the GSA in November 2003 at Seattle, USA (Advances in stratigraphic analyses using ground penetrating radar) considered the following topics:

1. hydrocarbon reservoir characterisation, whether on actual reservoir rocks or analogues
2. environmental site characterisation, where the development of facies models is used to make predictions on contaminant transport and/or fate
3. hydrogeophysics, including fracture characterisation of aquifers
4. geological hazard analysis, including volcanogenic, seismic or landslide related

5. analyses of stratigraphic facies development, including aeolian, fluvial, glaciological, coastal (both lacustrine and marine).

Further information on the GSA conferences can be obtained from Harry M. Jol, University of Wisconsin-Eau Claire, e-mail: jolhm@uwec.edu.

11.2 Applications relating to frozen materials

An early use of radar to probe into glaciers was by Steenson [4]. Steenson concluded that radar techniques were a viable method of measuring ice thickness. Cook [5] proposed an airborne system, and many surveys have been subsequently carried out from helicopter and fixed wing aircraft.

Waite and Schmidt [6] found that pulsed radar altimeters gave erroneously low readings over ice and snow in the Antarctic, and suggested that some accidents may have been caused by incorrect readings. In 1963 at the Scott Polar Institute, Cambridge, UK, Evans [7] used radar techniques to measure ice thickness and glacier depth of up to 3 km in the Antarctic (see Figure 11.1).

There followed much work by researchers from the USSR, USA and UK in the Antarctic investigating the ice and snow cover. A popular review of Antarctic ice work is by Radok [8] and also by Kovacs and Morey [9] in a series of reports for the US Army.

Biggs [10] reported on the profiling of the Great Lakes using a 2.8 GHz short pulse radar which was initially mounted on an aircraft and subsequently towed above the ice surface.

Hall [11] described the use of a short pulse radar of centre frequency 480 MHz, mounted on a helicopter, to perform an aerial survey of the route of the Alaskan pipeline. The radar profiled the permafrost to depths of 3 m. Permafrost was also investigated by Unterberger [12], who used an airborne radar of conventional design.

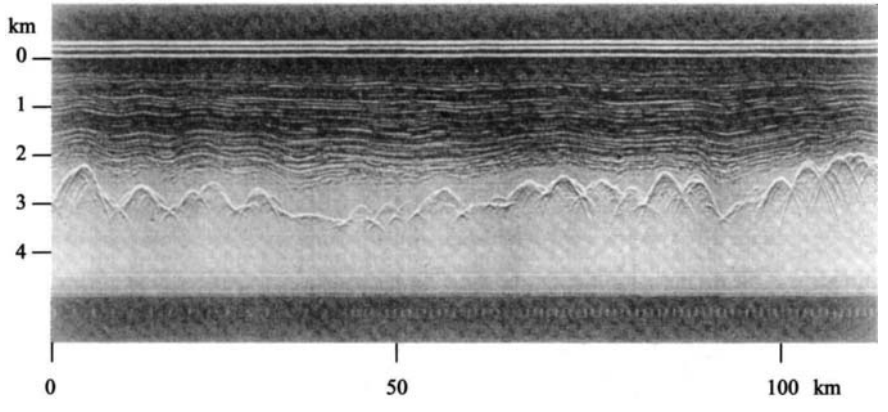

Figure 11.1 Radar profile of Antarctic ice (courtesy Scott Polar Institute)

This operated at a centre frequency of 250 MHz with a pulse length of 2 s, radiated by a ten element Yagi antenna array. Working in Alaska at Umiat he probed up to 600 m in permafrost test wells. Rodeick [13] showed the clear detection of a 'thaw bulb' in permafrost using a 120 MHz antenna and an impulse radar.

Work in the USSR involved radar probing of ice in the Siberian sea and glaciers on the island of Bendetta. Using an airborne radar operating at 38 MHz, and with phaseshift keying modulation, Lukashenko *et al.* [14] (USSR) probed through ice formations. From a height of 1500 m the radar detected reflections at ice depths of up to 120 m.

Finkelstein [15] (USSR) reviewed a number of applications of airborne radar to investigate sea ice and freshwater ice. By means of a system operating in the frequency region 20–130 MHz, measurement of sea ice thickness up to 2.5 m was achieved. Annan and Davis [16] also describe measurement of ice thickness and freshwater bathymetry. Recent investigations of seawater ice have been made by Cambridge Consultants Ltd (UK), and aspects of this work are reported in Oswald [17].

Work by Bishop *et al.* [18] resulted in probing the Vatnajökull icecap in Iceland to a depth of 600 m using 2 MHz radiation transmitted from 60 m resistively loaded wire antennas. Dong *et al.* [19] reported probing of the Hispar glacier.

Stratigraphy of snow has been the subject of a number of studies, including those by Ellerbruch and Boyne [20] and by Fujino *et al.* [21]. These involved FMCW systems [21] using the frequency range 2–12 GHz. Such frequencies, high by most sub-surface radar standards, are possible in snow probing because of the low loss of frozen water, and because its density is low (mean relative permittivity in the region of 1.5).

An Anglo–Swedish team investigated glaciers using a pulsed radar with a central frequency of approximately 60 MHz. This work was carried out in the Swedish Arctic at Storglaciaren. Successful probing of the glacier at depths of up to 40 m were achieved. Deeper penetration was obtained with a radar working at 5 MHz. Multifrequency (8–10 GHz) holographic investigation of snow has recently been reported by Sakamoto and Aoki [22] with a view to location of objects buried by snow avalanches. Similar investigations have been carried out by Daniels as a means for detecting skiers engulfed in avalanches. A picture of one of the volunteers and the radar reflection is shown in Figure 11.2.

11.3 Snow and ice research with ground penetrating radar

Steven A. Arcone

11.3.1 Introduction

This Section describes recent progress at the US Army Cold Regions Research and Engineering Laboratory. Radar studies of snow and ice, and of the systems used, appear to have expanded exponentially since the early 1990s. Almost every issue of the *Journal of Glaciology* and the *Annals of Glaciology* contains several studies that either exploited radar to achieve their objectives or developed radar to further research.

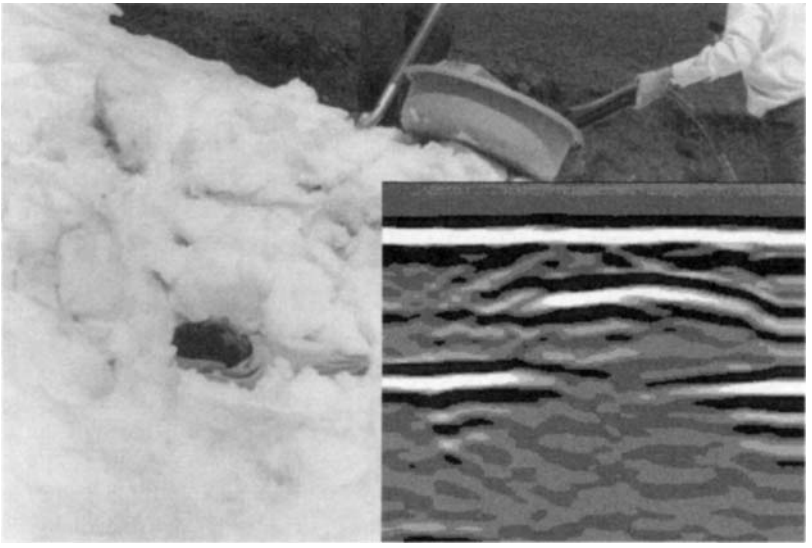

Figure 11.2 *Trials on detecting skiers trapped in an avalanche (courtesy ERA Technology)*
Radar image inset

Both ground-based and airborne studies have spanned depth ranges from a few cm of river ice sheets [23] to multi-km soundings in Greenland and Antarctica [24–26]. The objectives have included not only the determination of sheet thickness, but also of internal layering [26], delineation of hydraulic pathways [27], crevasse detection [28], delineation of possible cavities and water bodies [29], and precise delineation of bed topography and reflectivity [30]. The systems used include the classical, airborne radio echo sounder (RES) [24], standard short-pulse transient radar [31], CHIRP modifications to the RES system [32], frequency modulated continuous wave FMCW radars [23, 27, 33] and synthetic pulse radars [34]. Although the purpose of these efforts was to investigate glaciologic or climatologic processes, a secondary objective of system development pervades because each research group usually designed, modified or found a novel way to use radar to achieve their objectives.

At the US Army Cold Regions Research and Engineering Laboratory (USA CRREL), a division of the US Army Engineering Research and Development Command (ERDC), we have been developing and applying GPR to snow and ice problems in Alaska and Antarctica since the 1970s. We have generally used pulses with frequency spectra centred above about 50 MHz, and this limit, for short-pulse transient GPR, has generally defined the lower limit of 'high resolution'. Although such frequencies can well penetrate the 2–4 km thickness of Antarctic ice, the need to digitise these signals for accurate reproduction currently prohibits their use over the time ranges needed to sound such depths. Consequently, they are used for the top few hundred metres or less. As a general rule, the higher the frequency the less the penetration

recorded, but not necessarily the actual signal penetration that occurred. In pursuit of ever-improved vertical and horizontal resolution, USA CRREL developed the first continuously profiling FMCW system in the early 1990s, first investigated the possibility of beam forming for bed topography mapping in the late 1990s, and, since 1999, have obtained firn and ice profiles with 400-MHz commercial, short-pulse GPR at time ranges and depths which exceed by a factor of ten those previously published. This work is reviewed in this Section.

11.3.2 Transient short-pulse and FMCW radar

By far the most common types of radars used for high-resolution studies are transient short-pulse and frequency-modulated continuous-wave systems. Transient short-pulse radar, long referred to as impulse radar, is currently commercially available from at least four manufacturers. In these systems pulse brevity is all important. A short current pulse is fed to a short dipole, which is resistively loaded and closely spaced with the receiver dipole (Figure 11.3). The loading ensures that the current pulse will be totally attenuated by the time it reaches the end of the antennas. The short lengths produce very wide radiation directivity patterns.

Nevertheless, the dielectric properties of the ground cause the beam to narrow somewhat in both principal radiation planes [35]. The peak power output is usually less than a few watts for antennas that radiate pulses with spectra centred at about 400 MHz and higher, and less than about 30 cm apart, but may be several hundred watts for separations greater than 1 m. This latter case is typically of frequencies below 100 MHz.

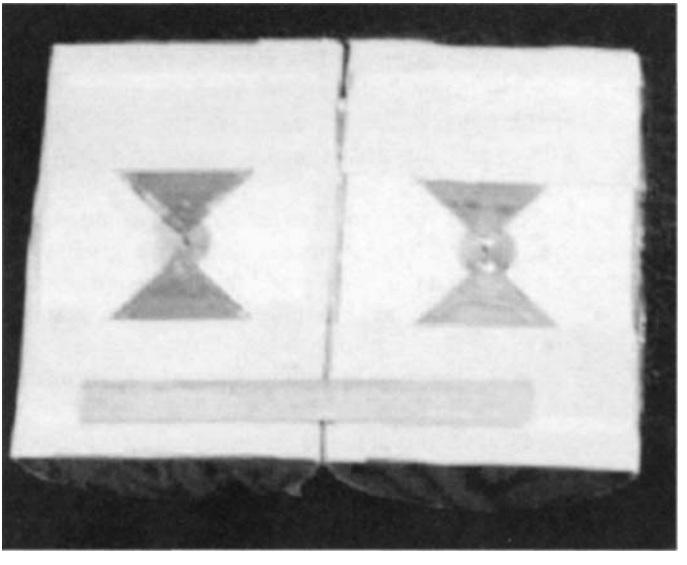

Figure 11.3 A pair of shielded, 500-MHz short dipoles used in GPR. The ruler is 30.5 cm (12 inches) long.

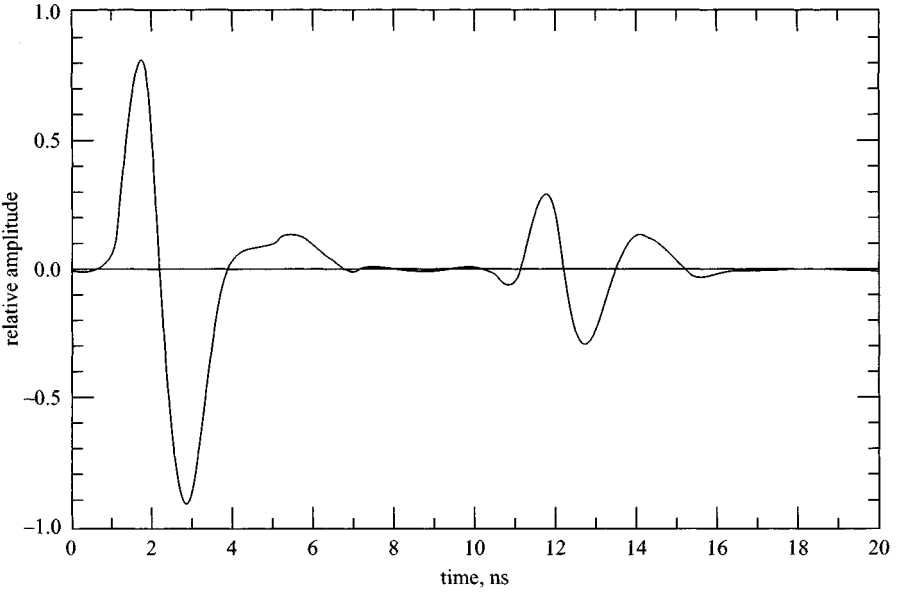

Figure 11.4 Pulse waveform radiated from a GSSI Model 5103 '400-MHz' antenna unit. The initial signal is the direct coupling.

A typical radiated short-pulse shape, or wavelet, is shown in Figure 11.4, along with the directly coupled signal between transmitter and receiver antennas. Theoretically, a doublet (one cycle) is the shortest pulse that can be transmitted. Practically, it seems that the $1\frac{1}{2}$ cycle pulse of Figure 11.4 is the shortest that can be achieved. A certain degree of 'ground-loading' also occurs when the antennas are in contact with the ground; the fields induced in the near-surface react on the propagating current pulse to slow it down and alter its frequency characteristics. This, of course, results in decreased resolution. Fortunately, snow and ice generally have little effect on the wavelet, and so it appears very similar to the shape transmitted in air when the antennas are raised above ground. The major advantages of transient systems are the ability to view the waveform and thus to interpret frequency and phase changes for target information, and a flexibility to determine any time range within acceptable digitisation parameters.

FMCW radars (Figure 11.5) operate differently. The signal fed from the transmitter to the transmitter antenna is continuous but of increasing frequency, and repeats every few to tens of milliseconds. Over this duration frequency may change as little as from 1.0 to 1.2 GHz or as much as from 1.0 to 13.0 GHz. The wider bandwidths give increased resolution. While the signal is radiating from the transmitter antenna, it is simultaneously fed directly by cable to the receiver circuit. The reflections from distant targets then combine with this directly fed reference signal through a mixer. The degree to which the two signals are out of frequency synchronisation depends on the target distance. The mixed signal is then lowpass filtered to obtain the difference

Figure 11.5 18 dB gain horn antennas for a 1–2 GHz FMCW antenna system

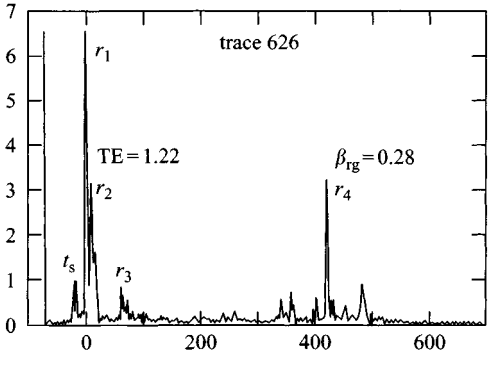

Figure 11.6 FMCW airborne radar data from an ice sheet

between target and reference signals, and then converted to a frequency spectrum with a fast Fourier transform.

The resulting spectrum is discrete (Figure 11.6), with different frequency spikes representing 'pulse' returns from various targets. Events are: a time sidelobe (artefact of processing), t_s; reflection from snow surface, r_1, reflection from snow bottom, r_2; multiple reflection between surface and helicopter, r_3; and probable conduit, r_4. The major advantages of this system are the very little power per frequency radiated, the simplicity of construction, and the direct digitisation of the mixed signal. The major disadvantages are the slow trace acquisition rate and, so far, a practical difficulty in gaining any performance on the ground below about 500 MHz with low gain antennas. To date most systems have been used above the ground with directive horn antennas

operating at about 500 MHz and higher, whereas transient radars have been used from 2 to 1500 MHz.

11.3.3 Firn layering and isochrones

For geological applications radar is primarily a reflection profiling device rather than a detector of anomalies. Radar horizons in polar ice [24, 26] and firn [36] reveal depositional processes which are assumed to represent isochronal events. As such they are used for core site selection, to calculate historical accumulation rates, and to understand the dynamics of stratigraphic genesis. The coarse vertical resolution (about 15 m) of the waveforms of the more commonly used, classical airborne 35–60-MHz RES system does not lend itself to interpreting yearly or even decadal accumulation processes, especially near the surface. This resolution limitation has led to the use of higher frequency, FMCW or chirped radar profiles to determine recent historical accumulation rates [34, 37] in firn. The use of such radar can thus overcome the spatial limitations of snow pit studies and possibly resolve annual or multi-year depositions, which are on the order of tens of cm/year in water equivalent, throughout much of Antarctica. In topographically complex areas, local accumulation rates are affected by the interaction of topography and wind [38, 39], which might significantly thin, thicken, fade or pinch annual stratigraphy and thus also affect local chemical deposition rates.

ITASE [40] is primarily a climatologic research study covering the last few hundred years (Figure 11.7). The traverses radiated from Byrd Surface Camp (BSC). The dashed portions of traverse except for those near the South Pole show where a particular set of horizons were continuously tracked from 30 to 90 m depth. The dashed segment near the South Pole also allows continuous tracking of horizons.

From 1999 to 2002 a 400-MHz radar was used to profile firn in different parts of West Antarctica (Figures 11.7 and 11.8) in order to find sites suitable for coring, and to extrapolate the dated horizons between core sites [40, 41]. The 400-MHz pulse length appears to offer optimum vertical resolution while still being able to penetrate the entire firn regime. Horizons at 1500 ns at 8192 16-bit samples/trace were finally detected through constant experimentation and recording through the 1999 and 2000 seasons. This time range is about ten times greater than previously reported for this frequency range with a transient type GPR. Generally, reflections fill the record to a time delay of about 1000 ns, or about 92-m depth. In interior West Antarctica, ice, defined as firn of about 0.83 kg/m^3 density (at which point the firn is no longer permeable), is encountered by about 60–70 m depth. In early December 2001, section was profiled in which reflections were discernible throughout the entire record [40].

More important than penetration, however, is continuity, examples of which are shown in Figures 11.9 and 11.10. This profile is 181 km long and stretches west from Byrd Surface Camp. The 348 X horizontal compression reveals strong stratigraphic changes caused by differences in accumulation rates between hills and valleys. The profile was the first attempt to cover the firn regime in Antarctica. It was recorded at only 600 ns (about 56 m depth), and it shows the most dramatic stratigraphic changes seen throughout the entire programme. The apparent folding is not of tectonic origin

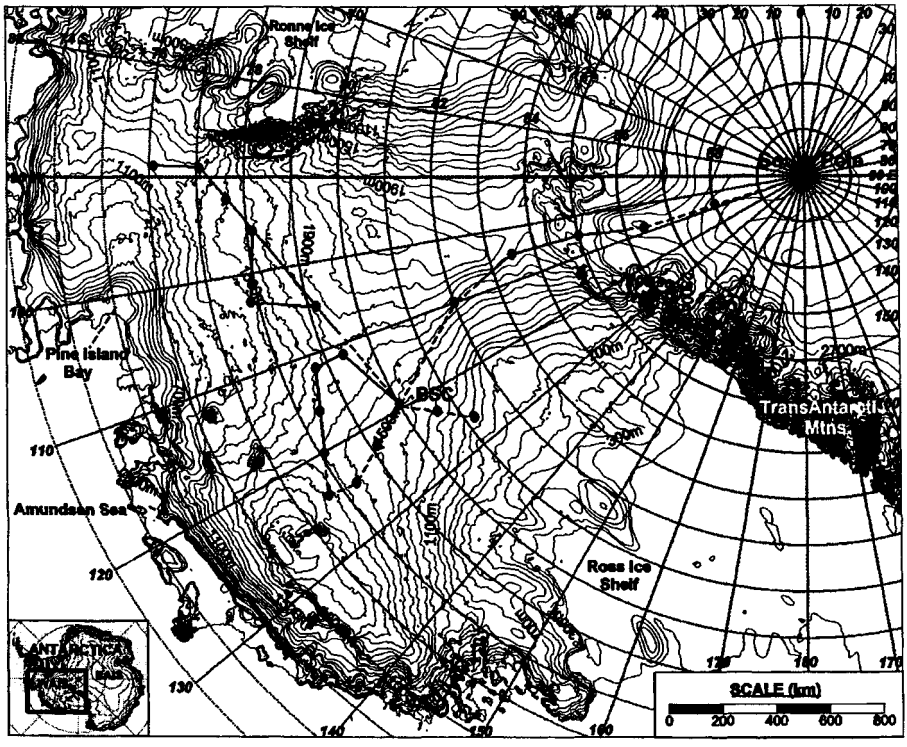

Figure 11.7 *Traverses of the International Trans-Antarctic Scientific Expedition (ITASE) in West Antarctica superimposed on a topographic map*

(the ice is actually in extension here), but is primarily caused by a combination of accumulation differences between leeward slopes (less deposition) and windward slopes (more deposition) and ice velocities (from left to right) of nearly 50 m/year. Both the full profile and the detail show the degree to which a single horizon can change its depth relative to the surface. The full profile contains horizons that change as much as 36 m just within the firn regime, while the detail shows a horizon at 11 m depth (at 76 km) that drops to 27 m at 80 km. By following the structure of vertical sequences, one can track a particular horizon or set of horizons throughout the entire record. In Figure 11.9 at least two of the deeper horizons have been tracked as far south from Byrd Surface camp as 334 km, as far west as another 181 km and about 200 km north (see the dashed lines in Figure 11.7).

The cause of these horizons is debatable. It is well accepted that in firn at high frequencies, only density can cause radar reflections [31, 42]. The known conductivity values of firn [43], and probable level of conductivity anomalies based on electrical current measurements [44], suggest that conductivity contrasts could only provide about a −90 dB reflectivity value at 400 MHz. Add to this geometric spreading losses,

Figure 11.8 *The caravans of the ITASE*
The arrow indicates a small sled that towed the 400-MHz GPR antenna. The radar was operated from within the van on the left, which is behind a fuel sled. The caravan on the right hauled the kitchen, core boxes and work tents

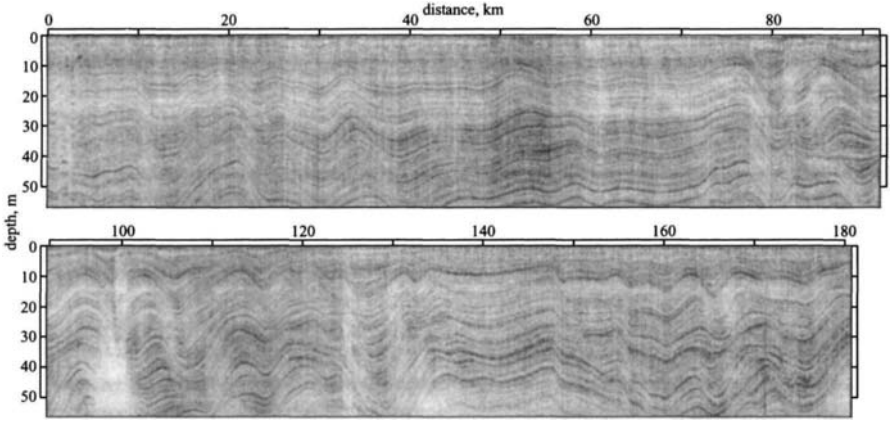

Figure 11.9 *A 600-ns profile running east to west starting from Byrd Surface Camp*

and the 16-bit 96 dB dynamic range of the radar system is then greatly exceeded. The question then is: what kind of density contrast could persist over huge areas? Currently we believe that it is thin ice layers, usually situated above hoar layers, evidence for which over wide areas is discussed by Shuman *et al.* [45, 46]. If true, these radar

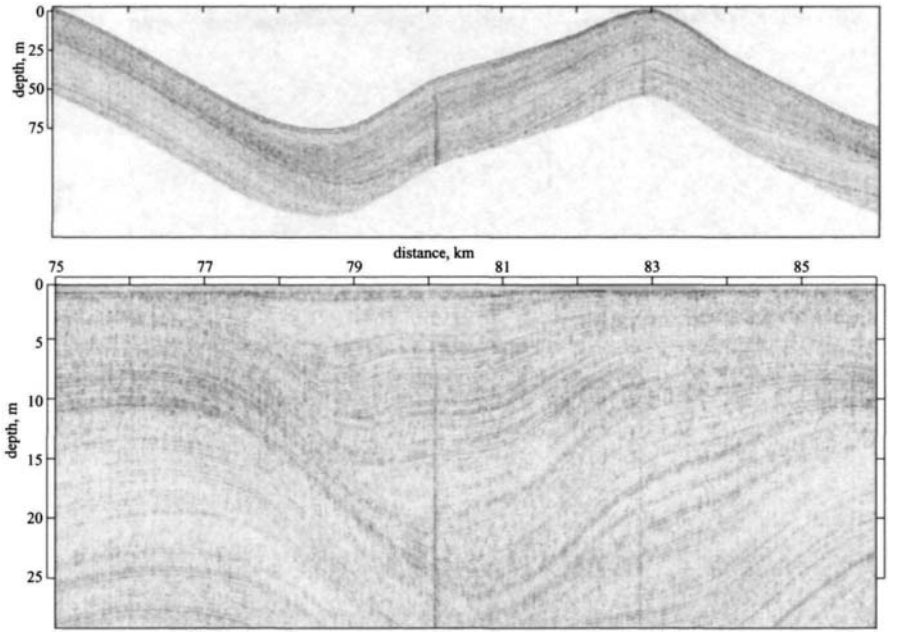

Figure 11.10 Detail from Figure 11.9

records document a history of thermal events. These layers are far more numerous per metre than are annual layers, so that they probably represent a superposition of closely spaced isochronal events but not individual annual events.

Further possible evidence that they are associated with hoar events is shown in a profile (Figure 11.11) from near Siple Dome in West Antarctica, which compares radar horizons with layers of hoar, but much more sophisticated correlations are needed. In the Figure, note that the hoar layers documented in a snow pit along the profile (data courtesy of Gary Koh, USA CRREL). Currently, we think that all such very shallow layers in polar firn profiled at 400 MHz and higher are continuous layers of relatively low density hoar or relatively high density ice.

Firn in polar regions is well below 0°C, dry, and provides the best penetration of radar signals for any geology. The transformation of polar firn to ice takes 40–100 m, which might represent hundreds of years given accumulation rates of only 30–50 cm of snow per year. In contrast, on temperate glaciers, by early summer the deeper firn can be near saturation. This greatly limits penetration but speeds up the ice formation process in winter. Firn depths can range from a few to tens of metres, but rarely more. The heavy accumulation rates of meters per year in areas such as southern Alaska can provide many reflecting surfaces through one year, and the total depth of firn may represent only tens of years accumulation.

Figure 11.12 shows a 135-MHz airborne profile recorded over the Bagley Ice Field in southern Alaska, along with a high altitude photograph obtained on 7 September,

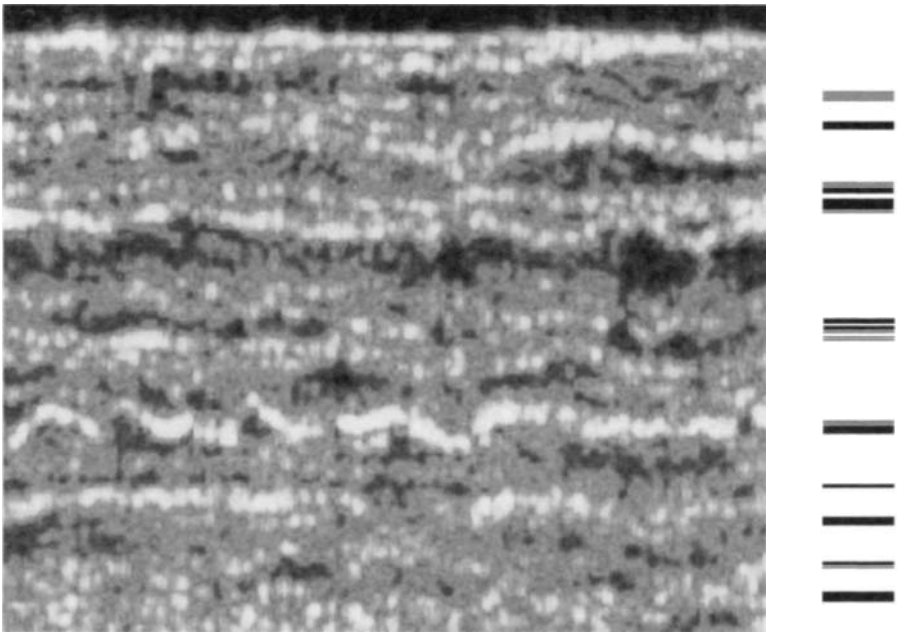

Figure 11.11 *A 2–6 GHz FMCW profile of the upper few metres of snow near Siple Dome in West Antarctica*
Horizontal scale 100.0 m; vertical scale 2.0 m

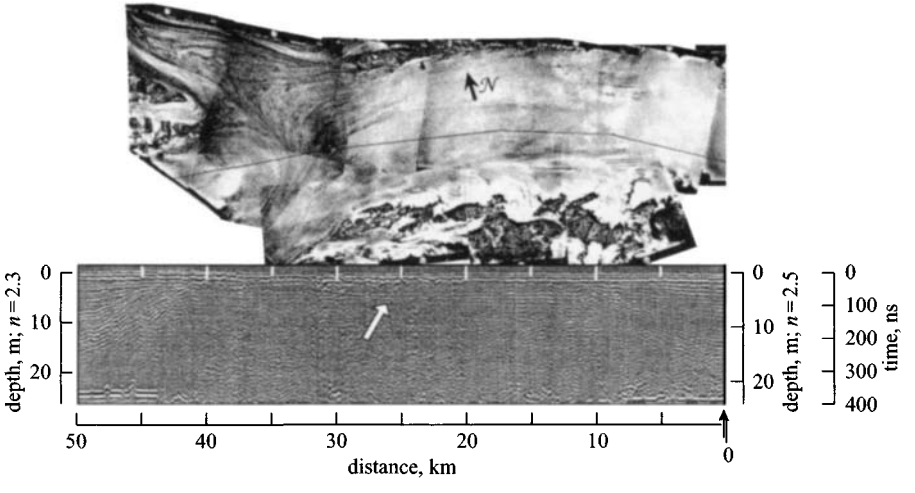

Figure 11.12 *A 135-MHz airborne profile, 23 June 1994, across the saddle of the Bagley Ice Field, located in the Chugach Mountains of south central Alaska*

1994 (thin line is flight line). The Bagley feeds the Bering Glacier, and the two together form the largest single glacier system in North America. The profile is 50 km long and shows the onset of firn formation both to the east and to the west. In the middle is where the Bering Glacier begins. There are only a few distinct layers before the layering fades beyond recognition, at a maximum depth on each side of about 20–25 m. The ice depth here may be as great as 800 m. However, the maximum penetration we were able to achieve was only about 60 m [47].

The horizontal compression of the profile eliminated numerous diffractions from buried crevasses, and revealed the layered firn stratigraphy within the accumulation zones. The large arrow indicates a multiple reflection between the antenna and the surface. Arcone [47] shows how diffractions were used to calculate radiowave velocity, from which water contents were derived. The velocities were used to calibrate the depth scales on the east and west sides, and the quantity n is the average refractive index of the firn.

11.3.4 Crevasse detection

Transient GPR is now commonly used in Antarctica for advance crevasse detection. The complex structure of crevasses provides a myriad of diffractions which allow advance detection at distances of as much as 20 m. This distance is sufficient for very slow moving vehicles. In addition, deeply buried crevasses are often overlain by sagging snow bridges, whose dipping layers can be detected in advance, also. Crevasses usually exist within the highly stratified firn, so that the termination of the layers against the crevasse walls provides ample diffractions. In addition, crevasses can contain exfoliated ribbons of ice that cross the cavities, ice lenses in the snow bridges and delaminated and sagging bridge layers, all of which provide strong diffractions. As for the crevasse itself, the void presents a discontinuity in the firn stratigraphy and so is often well imaged in a reflection profile. The process is analogous to seismic detection of unstratified salt domes existing within an otherwise highly stratified sedimentary sequence of rocks.

Figure 11.13 shows a profile of one of several crevasses that exist within a shear zone near McMurdo Station, Antarctica. The profile was recorded with a 400-MHz antenna positioned about 5 m in front of a snowmobile. The slope of the hyperbolic diffraction asymptotes gives a radiowave speed of about 0.21 m/ns, which is the correct value for firn of about 0.5 kg/m^3 density. The approximate width of the crevasse is correct, considering the oblique crossing of the profile relative to the strike of the crevasse.

11.3.5 Hydraulic pathways

Glacial discharge provides water for some European communities, and the drainage system is related to surging characteristics of glaciers. The drainage begins with surface melt, which first drains through crevasses and moulins (a large hole that formed when water continued to cut through the lip of a crevasse as the crevasse closed up with glacier movement). Some glaciers have fields of potholes, the origin

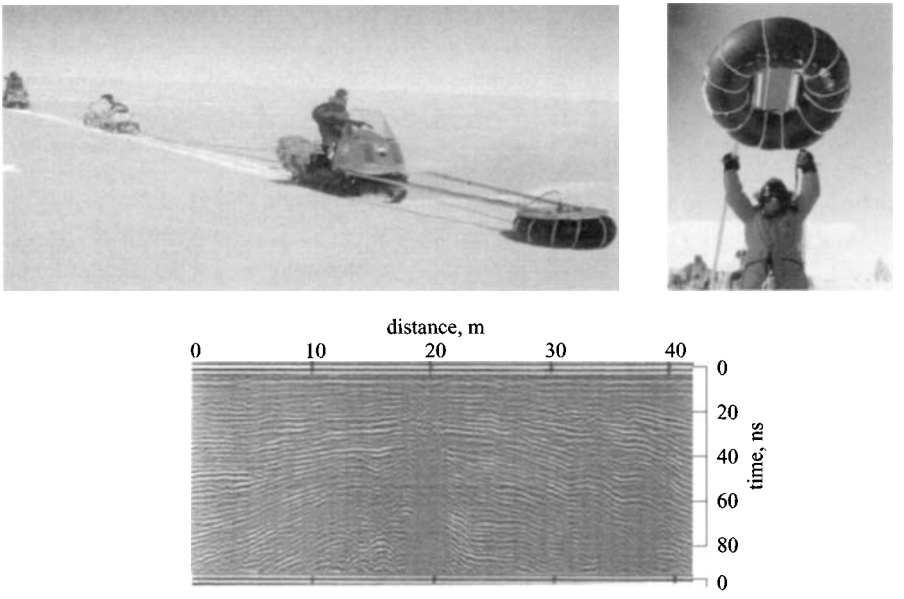

Figure 11.13 *A crevasse profile (bottom) from a shear zone located on the Ross Ice Shelf in Antarctica*
The disruption in the firn stratification forms the void at 20 m distance. The raised tyre tube on the right contains the antenna unit used to obtain the profile. Arcone and Delaney [28] discuss crevasse detection

of which is not well understood. Such a system exists in the high accumulation areas of the Black Rapids Glacier in central Alaska (Figure 11.14).

In 1996 a 1.2–1.7 GHz FMCW radar (Figure 11.5) was tested on this glacier to delineate any possible drainage structures. The snow surface was windblown smooth and the snow cover was marginal because we were in the ablation zone. Some of our results are shown in Figure 11.15. The radar horizons are actually sequences of hyperbolic diffractions and not a continuous horizon. The narrow beamwidth of the antenna may have allowed us to image only parts of this feature. Based on these intermittent returns and our proximity to the pothole field, we speculate that these horizons are sinuous drainage channels [27]. The dip of the horizons is less than about 16 degrees. Sub-surface drainage channels nearly parallel with the surface do exist, because in the summer water is commonly observed to rush in and out of these potholes.

11.3.6 Bed topography

The lack of a directional sub-surface beam pattern for GPR requires either wave migration to resolve bed topography or a synthetic aperture procedure to artificially produce a narrow beam. Both procedures require many measurements at precisely defined positions to obtain three-dimensional data coverage.

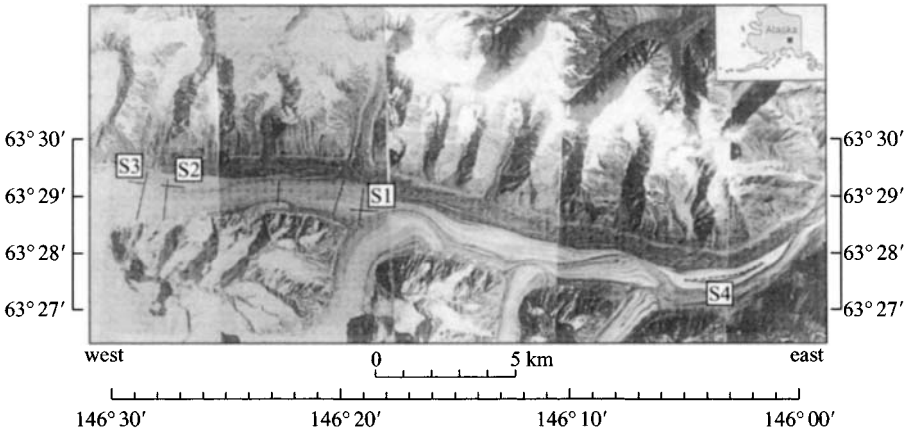

Figure 11.14 *Aerial photograph of the Black Rapids Glacier in central Alaska*
The glacier flows from west to east. The marked lines are radar traverses obtained in 1996 [27]. The Black Rapids is a temperate glacier which surged in 1937

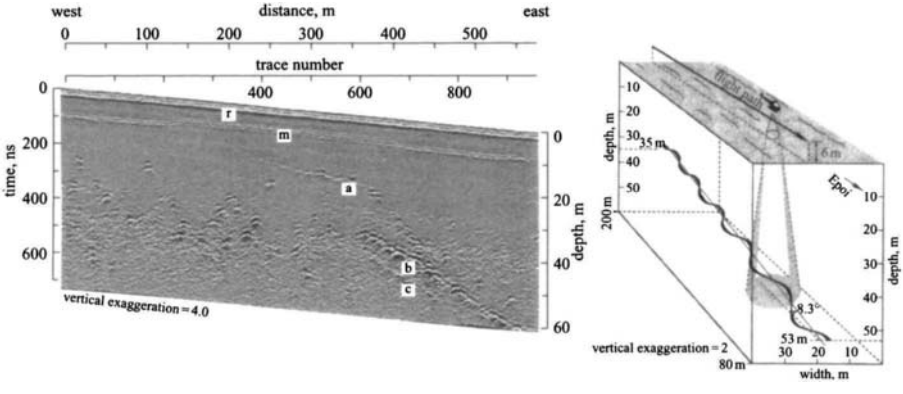

Figure 11.15 *Radar horizons (left) beneath transect S3 (Figure 11.14)*
These are constructed of diffractions, and interpretation of one of the events as a sinuous drainage channel (right). The labelled events on the left are surface reflection, *r*, surface multiple, *m*, possible conduits, *a* and *b*, and possible conduit reflection multiply reflected between the surface and the helicopter, *c*. The intersections of the radar beam with parts of a meandering conduit possibly cause the diffractions

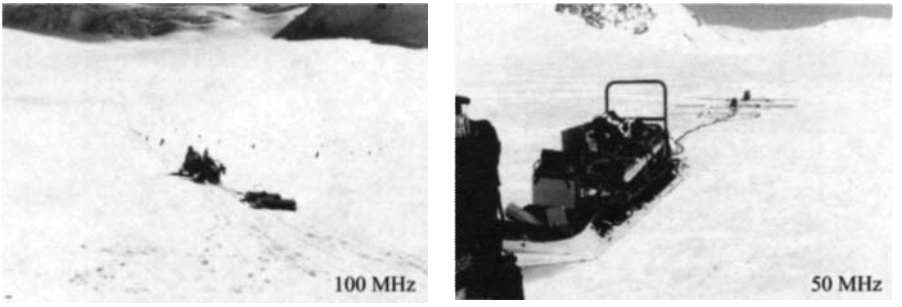

Figure 11.16 *Radar profiling high up on the Gulkana Glacier in 1997*
The transects, flagged in the figure on the left, were positioned with GPS, and the snowmobile stayed within about ±1 m along the lines

We tried a synthetic aperture scheme for data we recorded in 1997 on the small Gulkana Glacier, located in central Alaska. We located a 100 m × 300 m grid near one of the margins to ensure complexly dipping bottom topography, and recorded 50 parallel profiles with a 50-MHz short-pulse GPR (Figure 11.16).

Background clutter was removed from the data, data were deconvolved, and surface elevation corrections were applied. The surface recordings were separated into several sub-arrays and we synthesised a narrow 'flashlight' beam which could point in any direction, both beneath the sub-array and outside it. It was determined that the beam was correctly pointing in the normal direction to the bottom surface gradient when the returning signal was focused; i.e. the return signal appeared as close as possible to the waveform shown in Figure 11.3. In this way the bottom surface was synthesised, point-by point (Figure 11.17). The results showed large differences from conventional two-dimensional migration, as well as a complexly dipping bed that could never have been resolved with standard, two-dimensional schemes.

Figure 11.17 was generated using data recorded in overlapping sub-arrays (small rectangle at surface). Rays from different directions and ranges were added until a focused wavelet (coloured portion in upper left (as shown on the CD enclosed)) was formed. Moran *et al.* [30] show how this was done.

11.3.7 Lake ice

This final example is also the simplest. Lake ice covers are generally smooth, composed of columnar ice, and the water below is highly reflective. In the Arctic, lakes can freeze to 1.5 m deep and so the ice is often grounded. In 1993 several lakes were profiled near Prudhoe Bay, Alaska, with FMCW 5- and 10-GHz radars to delineate the grounded from the wet portions. The antennas were mounted from a Hagglunds all-terrain vehicle (Figure 11.18). The profiles (Figure 11.19) not only revealed the thickness of the ice but also that of the snow cover. In addition, by contrasting the reflection strengths between the water and grounded bottoms the dielectric constant of the grounded bottom was estimated.

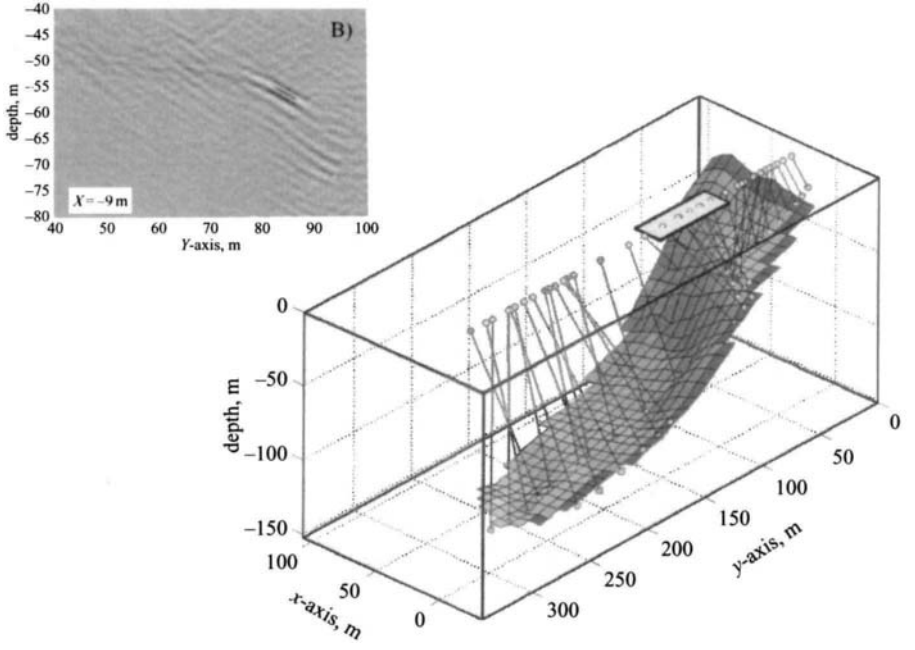

Figure 11.17 The constructed bottom topography based on the results of beam forming

Note that in Figure 11.19 the Arctic lake is partially frozen to the bottom [33]. Three traces from the X-band profile are shown. The floating character of the ice is interpreted from the strong reflections, and a multiple reflection is apparent in these segments of the profile. The penetration of these short wavelengths shows that space-borne radars are capable of sensing snow and ice to several, if not tens, of metres.

11.3.8 Future directions

Future developments are driven by scientific and logistical questions. Two important scientific questions regard the state (frozen or unfrozen) and disposition of the bed of polar ice sheets, and the continuity of highly resolved internal layers. These data will help to answer questions regarding past climatic variability and the future of ice sheets with regard to global warming. A high-resolution, bottom-mapping radar is needed to obtain the same kind of data shown in Figure 11.17, but at depths of up to 4 km and over immensely larger areas. Such radar systems are being developed but the logistics of maintaining precise positional control over hundreds of kilometres remains difficult.

Logistical requirements in polar areas primarily require crevasse detection but over large regions where research parties might plan to situate. RADARSAT (5-GHz) imagery, produced and provided by the Canadian Space Agency, has already shown

Figure 11.18 *C-band (4–6 GHz) FMCW antennas mounted from a tracked vehicle travelling just south of Prudhoe Bay, Alaska*

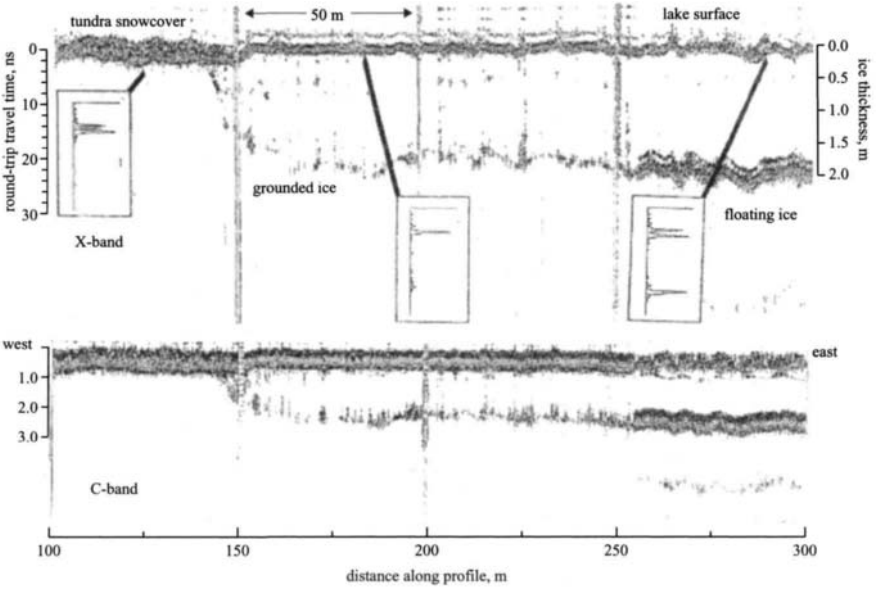

Figure 11.19 *FMCW C- and X-band (8–12 GHz) profiles of the ice thickness on an Arctic lake*

its ability to detect not only crevassed areas, such as shear margins, but possibly even crevasses themselves, such as the one shown in Figure 11.13. As resolution improves, we will be able to determine whether the 5-GHz signals respond to the crevasse itself or to the snow bridge, and over what area.

11.4 GPR sounding of polythermal glaciers

Prof. Svein-Erik Hamran

11.4.1 Introduction

Radar sounding of glaciers was one of the first application areas of ground penetrating radars [24]. Glacier ice is a very radar friendly material, where the permittivity, approximately 3.2, is almost constant as a function of ice temperature and radar frequency. Water is often encountered in snow and ice, and has a permittivity of 88. This makes a large contrast to ice, and water is therefore easily detected with radar. The electrical conductivity is very small in ice, making the absorption loss as the wave propagates through the ice very small. Thus, the glacier ice is almost transparent for radar waves in the frequency range 1–1000 MHz. This makes it possible to sound the glacier with wavelengths from some hundred metres to a few centimetres. The wavelength can then be chosen depending on the physical scale to be studied.

A glacier is built up by physical structures covering a large span of length scales. The large-scale structure is the depth or bottom topography of the glacier. The internal structure of the glacier may be layers or inclusions like free water. The exact physical size of the free water inclusions may not be known, but may range from metre to millimetre length scales. The snow depth ranges from centimetres to a few metres, and the snow pack may have firn layer and ice lenses with dimensions from cm to mm. To map all the different scales that exist on a glacier, a GPR-system able to cover the frequency range from 1 to 1000 MHz should be used.

In the following, a description of the glacier where the data are taken, and the radar system used to collect the data, is given. Then experimental radar data are used to illustrate the effect of using different radar wavelengths to study the bottom topography, internal structure and snow cover of a polythermal glacier.

11.4.2 Polythermal glacier

The radar data used in this Chapter were collected at Finsterwalderbreen, Svalbard, Norway. Svalbard is an island north of Norway almost up to 80 degrees north. The glacier (see Figure 11.20) is land-terminated, 11 km long, with an area of 35 square km. The glacier is classified as polythermal, as most of the glaciers on Svalbard are [48]. A cold glacier is frozen and has a temperature lower than zero degrees. A temperate glacier is at the pressure-melting point and has free water inside. A polythermal glacier has regions where part of the glacier can be temperate and other parts can be cold (see Figure 11.21 for a vertical cross-section of a polythermal glacier). The temperature of the accumulation area is very often at the pressure-melting point

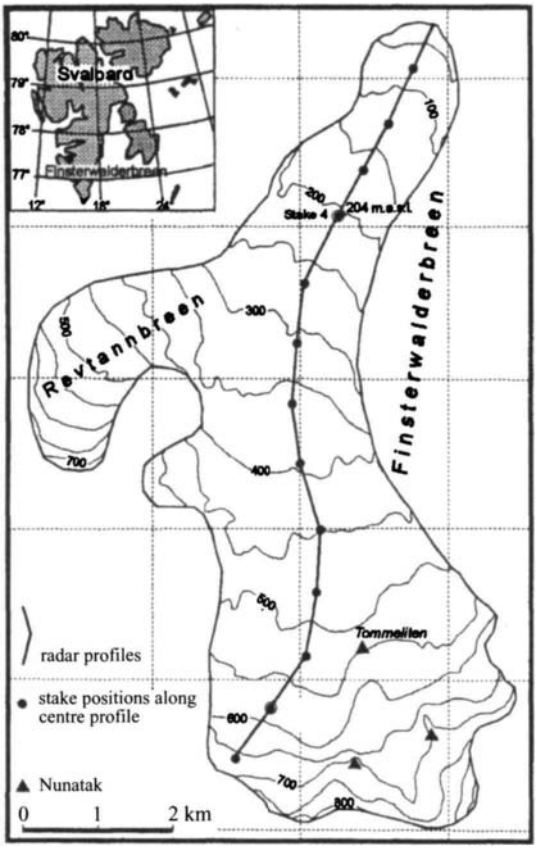

Figure 11.20 Map of Finsterwalderbreen showing positions of radar profiles

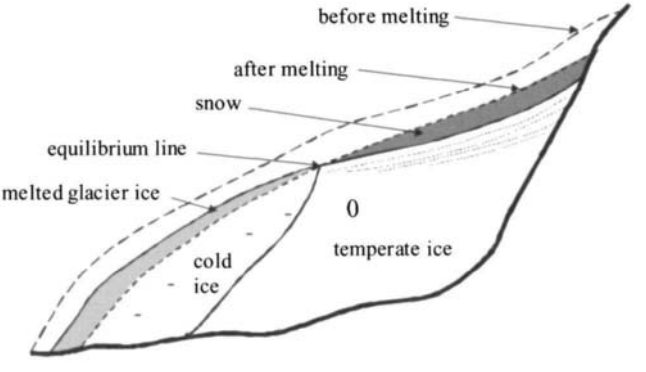

Figure 11.21 Vertical cross-section of a polythermal glacier

down to the bed, except for a thin surface layer, which reaches a few metres during winter. Ice at pressure melting point at high altitude is due to percolation and refreezing of melt water. The release of latent heat in summer eliminates the conductive heat loss during winter. The ablation area at lower altitude on the glacier usually has a cold surface layer of 30–100 m, and is underlain by warm temperate ice. Close to the margins and at the front, the glacier is usually frozen to the bed. The thermal structure is important for ice flow velocities, hydrology and surging behaviour of glaciers.

11.4.3 Radar system

The ground penetrating radar system used to collect these data was a time-gated step-frequency radar [49]. The system has been used in several data collection campaigns on glaciers [48, 50–53].

The step-frequency waveform is time-gated to remove the direct signal between the transmitter antenna and the receiver antenna [49]. The radar system covers the frequency range 1 MHz to 3 GHz. The frequency range transmitted depends on what antennas are used. In this study three frequency bands were used: 30–80-MHz end-fed broadbanded dipoles, 320–370-MHz Yagi antennas and 600–1000-MHz log-periodic antennas. The radar was mounted on a sledge and pulled by a snow-scooter (see Figure 11.22). The transmitter and receiver antennas were positioned at each side of the sled mounted on a fibreglass tube. Power was supplied from a generator on the sled. A wheel behind the sledge with an optical trigger device controlled the horizontal distance between each measurement. The radar data were stored directly on hard disk on a portable computer during data collections. Typical mapping speed was 10–20 km/h.

Figure 11.22 The photograph shows the radar set-up with UHF Yagi antennas and odometer wheel at the back

The radar transmits 201 frequencies for each collected range profile. The frequency domain data are zero padded and multiplied by a Hanning window function, before an inverse Fourier transform is taken to generate the reflection profile in the time domain. The data presented here are intensity modulated plots of the magnitude of the reflection profiles on a logarithmic scale. The depth scale is obtained using a relative permittivity value of 3.18 for the ice. In the snow pack a value of 2.1 was used.

11.4.4 Bottom topography

When radars designed for cold ice measurements were used on temperate glaciers the bottom could very often not be detected [54, 55]. The cold ice radars were operating in the VHF- and UHF-bands. The reason for not detecting the bottom echo was not that the absorption of the radar wave as the wave propagates through the water inclusions was too large. Very often the problem was scattering from the free water inclusions inside the ice. The radar is probing with a spherical wave, so scattering from water inclusions may come in the same range cell as the bottom echo. The scattering from the free water may be stronger than the bottom reflection, effectively covering it up.

The solution was to reduce the frequency so that the radar wavelength was much longer than the size of the water inclusions. Then the scattering from the free water was reduced and the bottom echo could be detected. If a frequency of 5–20 MHz is used, the scattering from the water inclusions on a polythermal glacier on Svalbard is not seen [48]. Figure 11.23*a* shows a radar profile, at 30–80 MHz, along the centreline of Finsterwalderbreen. The glacier depth is starting at 30 m and increases down to 250 m. In the beginning of the profile only the bottom echo is seen. At around 2 km distance some internal scattering from the glacier in seen. This is scattering from the free water inside the glacier. From 4 to 5 km the bottom echo is difficult to see due to scattering. The horizontal layers in the upper 20 m of the data are ringing noise due to a fault in one of the antennas.

11.4.5 Internal structure

Already at 30–80 MHz, as seen in Figure 11.23*a*, scattering from the free water in the temperate zone is visible. Increasing the frequency up to 320–370 MHz gives even more scattering, as shown in Figure 11.23*b*. The two radar profiles are taken along the same tracks. The temperate layer is starting at distance 700 m and is seen all along the profile. The bottom echo can be seen as a diffuse reflector down to 170 m. Internal scattering horizons have been detected on several glaciers on Svalbard [56–58].

Detailed studies combining radar measurements and temperature measurements in boreholes have shown that the depth of the first radar scattering corresponds to the pressure-melting point isotherm [52]. Based on a combination of bottom topography and UHF-sounding, the overall thermal structure of the glacier can be mapped by radar sounding.

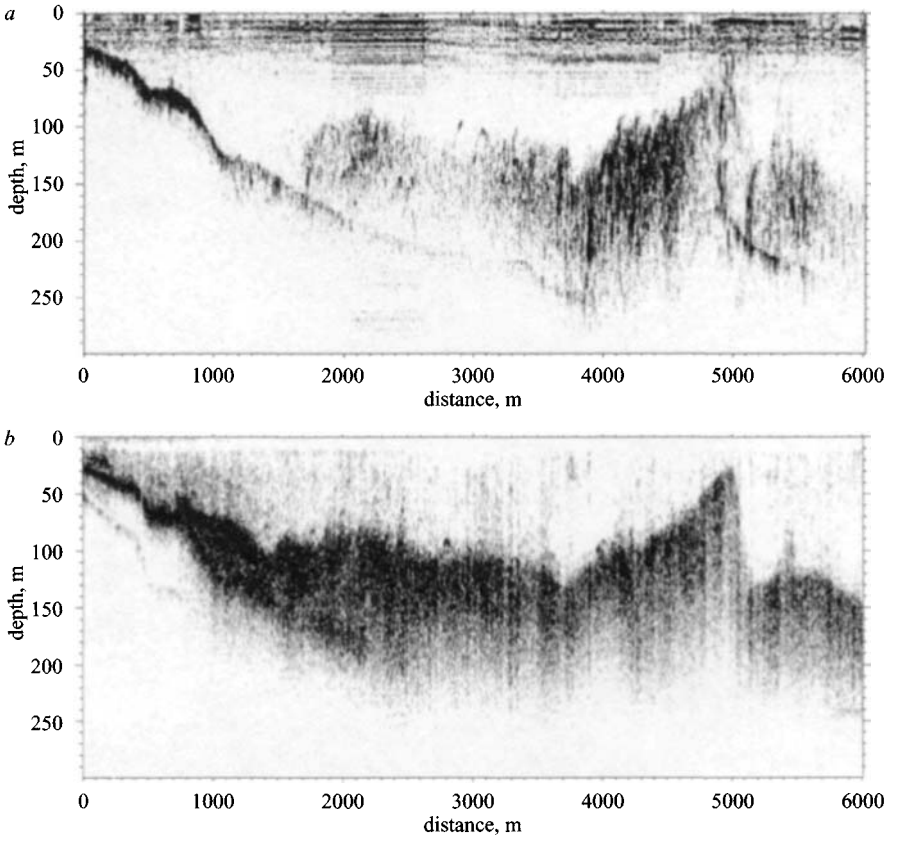

Figure 11.23 *Radar profiles along the centreline on Finsterwalderbreen at frequencies (a) 30–80 MHz and (b) 320–370 MHz (from Hamran* et al. *[59])*

11.4.6 Snow cover

The snow thickness is mapped using frequencies at 600–1000 MHz, Figure 11.24*a*. The first 2.4 km show a reflection stemming from the snow/ice interface. From 2.4 km and beyond, strong scattering at increasing depth is clearly seen. From 3.3 km at depths of 5–20 m even stronger scattering is present, which is believed to come from ice layers. This is also indicated in the UHF (320–370 MHz) profile in Figure 11.24*b*. The temperate layer seen as strong scattering in the beginning of the profile is coming up to the surface at around 3 km.

11.4.7 Summary

A GPR system covering the frequency range from 5 to 1000 MHz can map all the major physical regions in a polythermal glacier. Low frequencies (5–20 MHz) can map the bottom topography, UHF frequencies (320–370 MHz) can detect the pressure

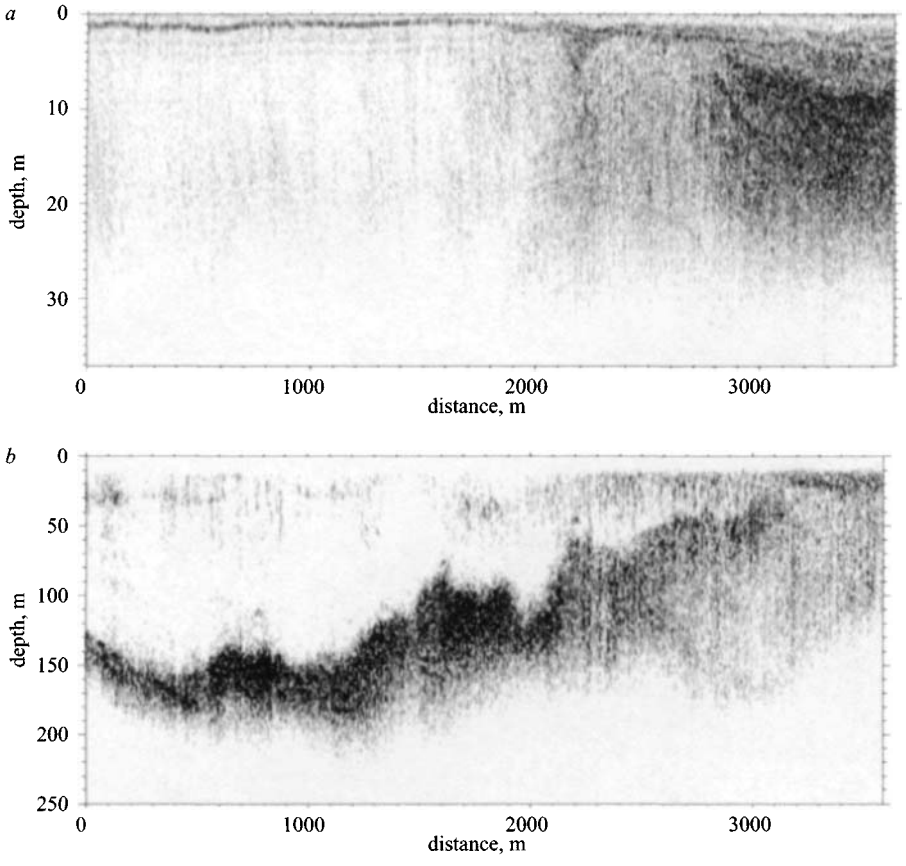

Figure 11.24 *(a) Radar profile at 600–1000 MHz showing the snow thickness in the accumulation zone on Finsterwalderbreen; (b) radar profile at 320–370 MHz along the same profile as (a) (from Hamran et al. [59])*

melting point isotherm, and frequencies at 600–1000 MHz can map the snow cover. Together, the radar measurements give a picture of the cold ice zone, the temperate ice zone and the snow layer.

11.5 The Prestige oil spill

Dr Henrique Lorenzo

The Prestige oil tanker was carrying more than 77 000 tons of oil cargo when, on 13 November 2002 it was damaged in a fierce storm, 45 km off the coast of Spain. Almost immediately, 5000 tons of oil leaked into the ocean and washed ashore along the Galician coastline (see Figure 11.25).

Figure 11.25 Carnota beach on the Galicia coast

During the next 6 days the Spanish authorities and salvage ships tried to tow the Prestige further out to sea. However, the first 2 days the Prestige was towed NW, but then it went to the south, parallel to the coast of Galicia. During this time, about 20 000 tons of oil from the Prestige leaked and arrived on the Galician coast. The Prestige had suffered extensive damage, so it soon took on water, broke in half and sank on 19 November. The remaining cargo, over 50 000 tons of oil, remained trapped in the cargo hold and went down to the ocean floor with the rest of the ship. The ship is today on the bottom of the ocean, at 4000 m depth, and still leaking oil to the sea through cracks in its two parts. It is not clear how the wreck will be dealt with or when action will be taken.

About 900 km of the coast in Galicia, north of Spain, Portugal and France are affected by the oil spill and more than 200 beaches just in Galicia are contaminated (see Figure 11.26).

The major issue in identifying the level of contamination rests with the action of the tides, wind and weather. The tidal process is that the first tide brings fuel over the sand but, if it is not removed, the next tide puts clean sand over the fuel and the beaches appear to be clean. Layers of fuel contamination appear at different depths in the sand, from some cm to 1–2 m. The lateral extent of the contamination can vary, from less than 1 cm to more than 1 m. The fuel can be in compact layers, but also in small pieces called 'coockies'.

The use of GPR is difficult due to the presence of salt water from the sea, where the attenuation of the salt laden wet sand is excessive (see Figure 11.27). Tides on the coast of Galicia are strong in the winter, with differences of 3–4 m between low and high tide, and also with high sea storms. We are using GPR in some inland areas,

Figure 11.26 Cies Islands beach during clean-up operations

Figure 11.27 Surveying the beaches of Galicia after the oil spill with GPR

which are also under the influence of these storms and high winter tides. Most of these places normally remain out of the influence of the tides during spring and summer time. Sand may be dry or wetted from the rain; this is also a problem because of salt particles present in the sand.

The issues in using GPR are due to:

- the effect of salt water
- oil layers at different depths and with different lateral extents
- multiple layers
- changes in the electromagnetic properties of fuel versus time: it emulsifies with the sea water; it also emulsifies with the fresh water if it is exposed to the rain; it dries in contact with sand (also depending on water content in sand pores); it is an organic mixture which evolves with the attack of micro-organisms
- changes in the electromagnetic parameters of sand depending on weather conditions and tidal influence (it affects the impedance contrast between sand and fuel).

Remedial work is also complicated because accurate location of contamination is needed and this is difficult because markers are simply washed away by the tides.

Ten tests at different beaches have been conducted to investigate the following:

- dry sand versus liquid emulsified fuel: this showed good contrast at 50 cm depth, 10 cm wide layer
- dry sand versus very dehydrated fuel: this showed poor contrast at 50 cm depth, 20 cm width and 25 cm depth
- fresh water versus wet sand versus liquid emulsified fuel: this showed very good contrast
- salty water/wet sand versus fuel: this showed high attenuation in the first cm, but some surprising good results depending on salt content and influence of rain (fresh water) and the water table.

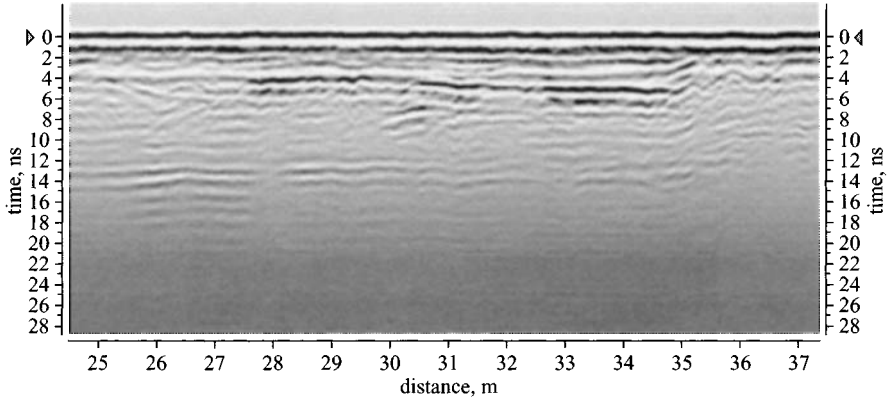

Figure 11.28 Radar image from layers of oil in sand

Radar systems operating at 500, 800 and 1000 MHz have been used, depending on the estimated depth of the layers and their widths (see Figure 11.28). A cart with wide wheels has been adapted to survey the beaches. A survey wheel has been used to acquire data and a differential GPS to obtain UTM co-ordinates of the positions of the profiles and the layers detected.

11.6 Peatland investigations

Dr Paul Hanninen
Geological Survey of Finland.

The Geological Survey of Finland have carried out many surveys of peatland. Peat thickness results obtained by means of ground radar in peatland investigations are substantially more comprehensive than those yielded by drilling. The radar profile provides data on the thickness of peat layer and the nature of the underlying mineral soil (Figure 11.29) as well as information on the internal structure of the peat (Figure 11.30). Accurate depth maps for the bog concerned can be provided by combining radar cross-sections. Although it is impossible to identify layers of gyttja, e.g. lake mud, which are rich in organic material, they can be distinguished from peat fairly easily when they are rich in mineral material.

Ground penetrating radar can be utilised best for the examination of open, unditched peatland areas, but is more difficult to use in bogs, which support forest or contain a dense network of ditches. The results can be used for the planning of ditching (outlet ditches, environmental ditches, field ditches), road networks and precipitation basins in peat mining areas, and for evaluating the quantities of garden peat and fuel peat obtainable from peat mining areas.

80–500 MHz antennas can be used in peatland investigations, the low frequency ones lending themselves best to the measurement of peat layer thickness and the high frequency ones to the obtaining of data on the surface layer and on moisture differences between peats. The use of high frequency antennas is hampered by their sensitivity to interference, as a result of which there must be no other medium between

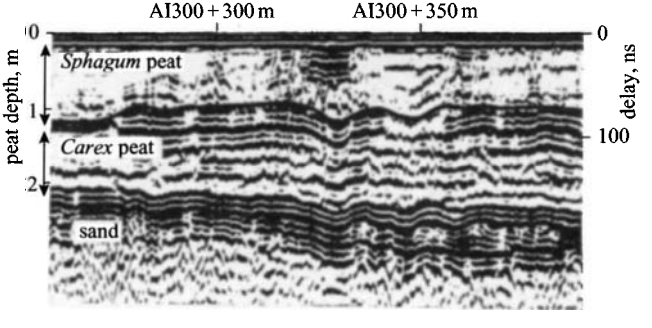

Figure 11.29 Radar cross-section of a peat bed (courtesy Geological Survey of Finland)

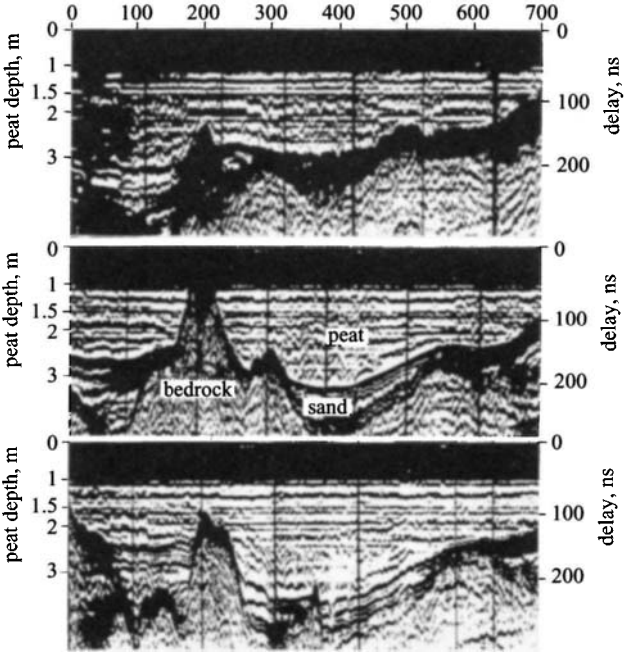

Figure 11.30 *Radar cross-section of a peat bed and bedrock (courtesy Geological Survey of Finland)*

the antenna and the object measured. This means in practice that the antenna cannot be pulled on a plastic or glass fibre sledge, for example, but must be moved along the bog surface at walking pace.

11.7 Soil contamination

Dr Jan K. van Deen
Grondmechanica Delft, Holland

Spill of polluting substances heavier than water is one of the serious problems of environmental engineering. From the source of pollution the substance migrates more or less vertically through permeable layers until it meets an impervious (e.g. clay) layer. From there on it spreads horizontally, collects in shallow depressions of the clay layer, follows the slope of the clay boundary and may even leak through missing parts (holes) of the clay layer. It is generally difficult to discern the pollutant itself directly in the radar reflection; however, delineating accurately the upper surface of the clay layer is as effective, since it guides the sampling strategy to the depressions where large amounts of pollutant may be expected and to the holes with their possible risk of leakage to deeper layers. Figure 11.31 shows a contour map of the top of the clay layer in a situation where the primary surface (clay) had been artificially covered by a 3–5-m-thick sand layer as a foundation layer and working area for industrial activities.

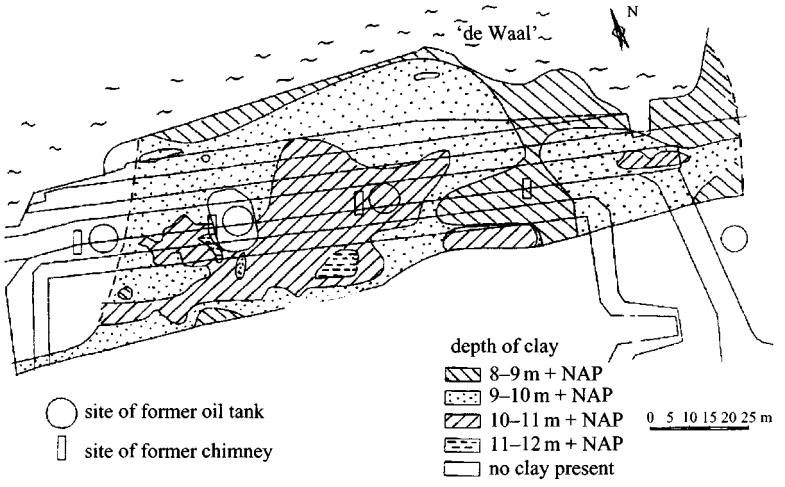

Figure 11.31 Contour map of reclaimed site (courtesy Delft Geotechnics)

The Figure shows clearly the (former) topography as well as a large missing part in the clay at the west side of the terrain.

11.8 Geological structures

Dr van Overmeeren
TNO Institute of Applied Geoscience, Holland

The accuracy of present surface based geophysical methods to study shallow sub-surface geology, i.e. down to 40 m below the surface, is not always adequate. A higher definition is required, for example, for dealing with soil and groundwater pollution, for measuring the groundwater level, for the construction of deep foundations and tunnels, etc. A ground penetrating radar (GPR) system is being developed at TNO Institute of Applied Geoscience. This combines a greater exploration depth with a more complete integration of acquisition, processing and interpretation of data, while remaining highly cost-effective. The ground penetrating radar system will contribute to the more efficient management, exploitation and protection of the sub-surface environment.

High resolution, seismic reflection methods fail to provide sub-surface images of the shallow zones (<40 m), which become increasingly more important in hydro-geological and, often related, environmental investigations. GPR at low frequencies (<200 MHz) is a geophysical technique that is similar and complementary to seismic reflection methods; based on wave propagation, highly detailed continuous sub-surface images (sections), showing reflecting interfaces between contrasting layers, are obtained by both methods. The deeper zones, where seismic reflection reigns, are out of reach for GPR. In the shallow zones, however, GPR is indispensable for obtaining images of high resolution.

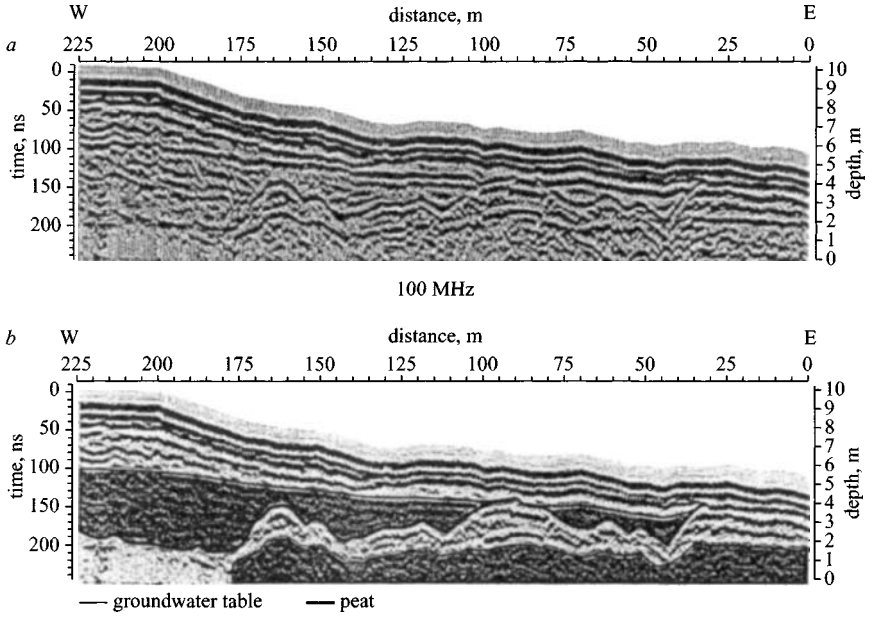

Figure 11.32 Radar cross-section of sand dunes (courtesy TNO)

For several decades, GPR has been used for engineering surveys, at depths of several metres below the surface. Only recently, however, with the advent of digital instrumentation and low frequency antennas, exploration depths have been extended (in favourable terrain) to several tens of metres, opening the door for GPR to the groundwater domain – hence the name 'ground penetrating radar'.

The use of GPR for groundwater can be applied to sandy sedimentary environments of high electrical resistivity.

In the Netherlands, its use is confined, limited to the elevated areas of the east where sandy deposits in push moraines and terraces prevail, and groundwater is found at depths ranging from 10 to over 40 m. In the lowlands of the western part of the country, clayey deposits and brackish and saline groundwater at small depths having low electrical resistivities mostly impede the use of GPR because of attenuation of the radar waves. The coastal sand dunes here constitute radar-friendly exceptions, and typical radar cross-sections are shown in Figure 11.32.

11.9 Soil erosion

Dr Jan K. van Deen
Delft Geotechnics

Part of the coastline of the Netherlands consists of dikes, which are at many places provided with a revetment of rip-rap, asphalt or concrete blocks to protect the clay surface layer of the dike against wave attack and erosion. Behind the concrete blocks,

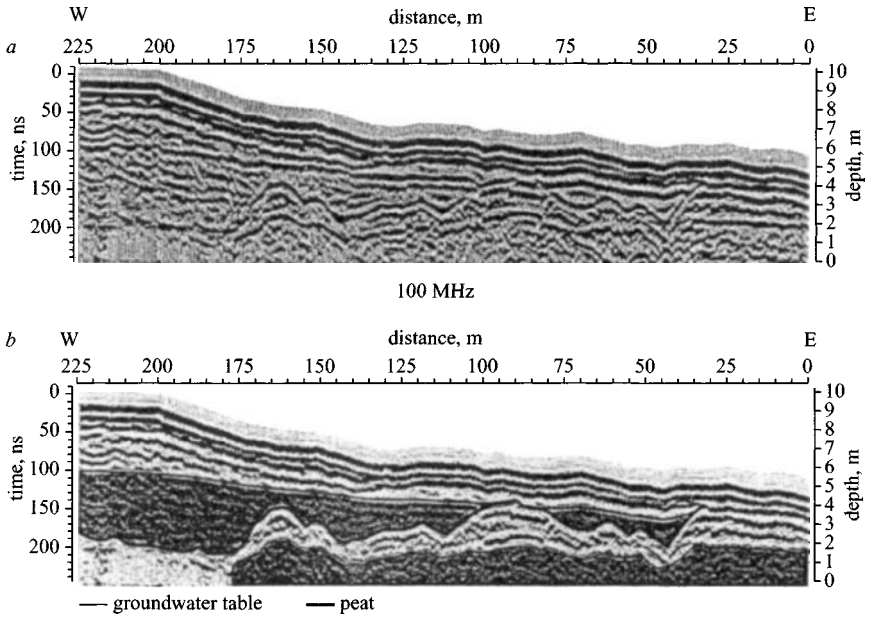

Figure 11.32 Radar cross-section of sand dunes (courtesy TNO)

For several decades, GPR has been used for engineering surveys, at depths of several metres below the surface. Only recently, however, with the advent of digital instrumentation and low frequency antennas, exploration depths have been extended (in favourable terrain) to several tens of metres, opening the door for GPR to the groundwater domain – hence the name 'ground penetrating radar'.

The use of GPR for groundwater can be applied to sandy sedimentary environments of high electrical resistivity.

In the Netherlands, its use is confined, limited to the elevated areas of the east where sandy deposits in push moraines and terraces prevail, and groundwater is found at depths ranging from 10 to over 40 m. In the lowlands of the western part of the country, clayey deposits and brackish and saline groundwater at small depths having low electrical resistivities mostly impede the use of GPR because of attenuation of the radar waves. The coastal sand dunes here constitute radar-friendly exceptions, and typical radar cross-sections are shown in Figure 11.32.

11.9 Soil erosion

Dr Jan K. van Deen
Delft Geotechnics

Part of the coastline of the Netherlands consists of dikes, which are at many places provided with a revetment of rip-rap, asphalt or concrete blocks to protect the clay surface layer of the dike against wave attack and erosion. Behind the concrete blocks,

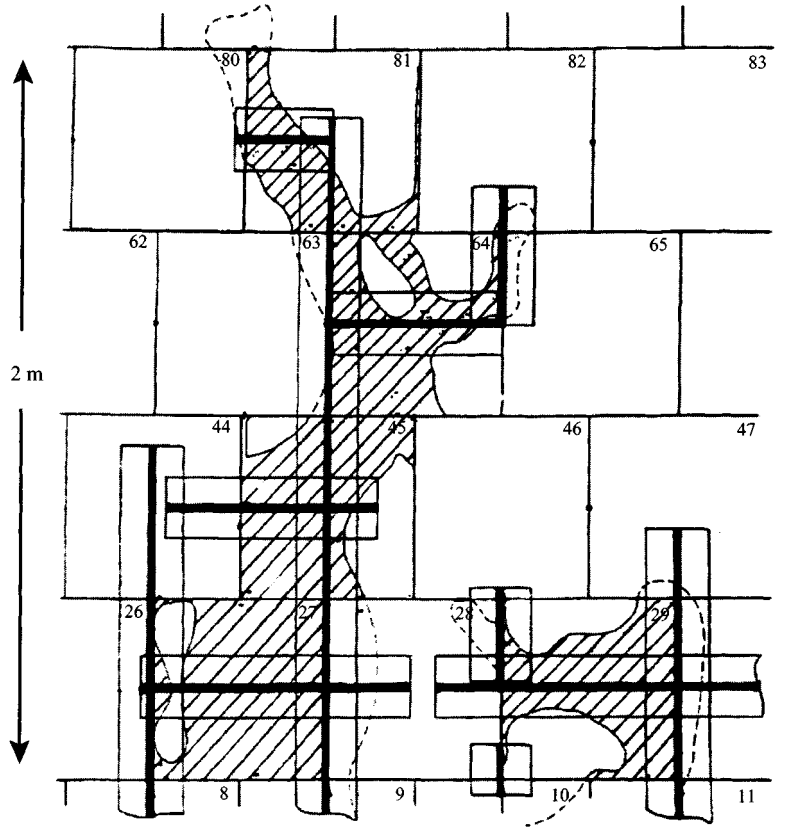

Figure 11.33 Radar map of erosion channels (courtesy Delft Geotechnics)

however, erosion channels develop through erosion of the clay due to water entering through the seams at high tide and flowing behind the blocks (Figure 11.33). Due to the clamping of the blocks, these erosion channels are generally not visible from the outside but may nevertheless develop into extended and dangerous proportions. Under large wave attacks, the revetment may instantaneously collapse, leaving the soil unprotected to the waves.

To determine the presence and extent of erosion channels, measurements were performed along traverses in a square grid of 50 × 50 cm. After the data had been analysed and interpreted in terms of erosion channels, part of the 20-cm-thick blocks were removed and an accurate record taken of the features showing up. Figure 11.33 shows a map of the erosion channels as recorded below the blocks removed, in conjunction with the data records of the particular radar sections. Quantitative comparison of 'radar' and 'real' holes demonstrated a success percentage of 85 of the scan line length. Most of the remaining 15% was located directly beside the channels. The

measurements are nowadays repeated on a yearly basis in order to follow the evolution of the erosion patterns and to check the effectiveness of remedial measures like grouting.

11.10 Coal and salt

Ground penetrating radar has been usefully used in the exploration of rocks and minerals. The earliest work was carried out by Cook [60], Unterberger [61] and Unterberger [62], and coal, rock salt, oil shales and gypsums as well as limestones and granites have been investigated. Cook [60] carried out numerous experiments and developed a predictive method for determining the depth of probing as a function of material loss in $\mathrm{dB\,m^{-1}\,GHz^{-1}}$. Cook's paper provides details of the dielectric properties of 38 different types of rock, and a selection is reproduced in Table 11.1 of the loss measured at 100 MHz and the maximum range for a radar with a 100 dB dynamic range. More recent work is reported by Ralston *et al.* [63].

Unterberger [61, 62] carried out a number of investigations into the use of radar to probe salt structures. Using a 230 MHz pulse radar he investigated the Pine Prairie

Table 11.1 Cook's tables

Material	Country	Loss in $\mathrm{dB\,m^{-1}}$	Detection range
Granite (dry)	Switzerland	2.7	57
Granite (wet)	Switzerland	4.35	40
Limestone	New Mexico	6.9	28.3
Limestone	Texas	7.03	27.74
Limestone	Italy	7.35	27.13
Coal	Pittsburg	8.86	21.95
Coal	Virginia	12	20.11
Concrete	Various	12.8	18.89
Coal	Colorado	14.2	17.37
Oil shale (rich)	Colorado	15.0	16.13
Tar sand (rich)	Alberta	15.5	15.54
Gypsum	England	15.8	15.24
Quartzite	New Mexico	17.6	14.63
Schist	Washington DC	18.5	14.02
Concrete (wet)	Texas	19.6	13.72
Limestone (wet)	Arizona	21.7	13.41
Limestone (wet)	Italy	22	13.1
Limestone (wet)	New Mexico	22.4	12.8
Sandstone	New Mexico	23.5	11.88
Gypsum	England	25	10.97
Coal	Ohio	28.3	10.06
Schist	Washington DC	29.5	9.75

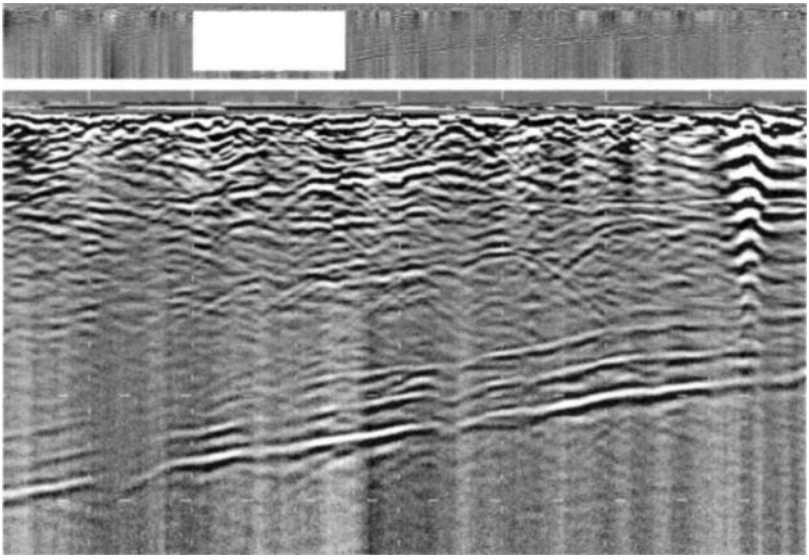

Figure 11.34 Radar image of bedding plane of UK salt mine (courtesy ERA Technology)

salt dome in Louisiana. An interpretative cross-section and a contour map of the near flank of the dome was confirmed by surface gravity data. The lower flank position was confirmed by slant drilling, which intercepted the salt sediment interface at 2700 m. A similar radar was used in the Cote Blanche salt dome, and a one-way penetration of 900 m was achieved. An included pillar discontinuity within the salt seam was discovered. In the UK measurements of the thickness of a salt seam were obtained and are shown in Figure 11.34. Note the effect of a shoring bolt on the right-hand side. The data were taken using a 250 MHz antenna and the scale is 10 m horizontal and 10 m vertical. The upper part of the graph shows the complete scan over a horizontal distance of 50 m.

An interesting technique for measuring the thickness of rock and coal by means of a noncontacting sensor has been developed by Chufo [64]. The technique used a sector network analyser and IEEE 488 bus controller and a servo controlled L-band antenna positioner.

The antenna was moved so as to vary the distance between the material and the antenna over a distance of 40 cm in increments of 1.27 cm. At each antenna position the reflection coefficient of the material was measured over a frequency range of 0.6 to 1.4 GHz in 2 MHz intervals.

The principle of the technique uses a spatial domain concept to modulate the received signal so as to remove reflections that are not along the axis of the antenna motion.

The measurement system is calibrated by measuring a reflecting metal surface. The theory of the calibration method is based on a revised version of the Linear

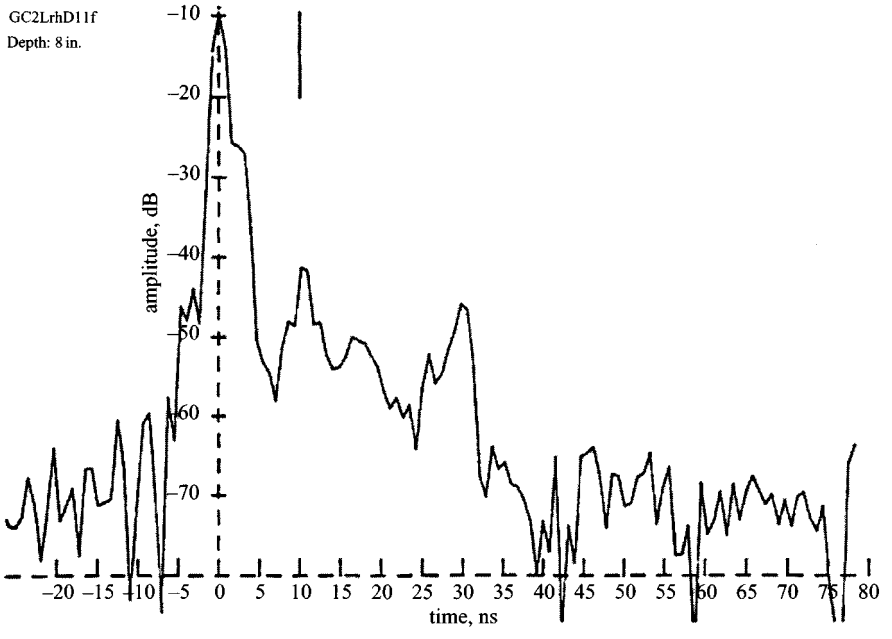

Figure 11.35 Radar measurement of coal thickness (courtesy US Bureau of Mines)

Reduction method, and the technique has been used to measure the reflections from the coal/shale or coal/rock interface in order to determine the coal thickness remaining between the cutter head of a mining madure and the mine roof rock above the coal.

The technique can also be used to measure the dielectric constant of each layer of a multi-layer medium such as a coal seam.

Chufo showed that the technique could be used to measure a variety of materials such as salt, granite and coal with accuracies in the order of better than 5%. A typical measurement is shown in Figure 11.35.

A number of ultrawideband impulse radars have been investigated for coal seam measurements, in the USA, South Africa and the UK. Daniels [65], on behalf of the then National Coal Board (UK), showed that measurement of coal seam thickness of up to 0.2 m was feasible and inclusion of layers of iron pyrites could be detected at thicknesses up to 0.3 m.

11.11 Rocks

Dr Sylvie Tillard
CEA, France

As part of a project on the qualification studies carried out on nuclear waste storage in deep geological formations, part of the R&D work of the Waste Storage and Disposal Department of the Atomic Energy Commission (CEA) in France is focused

on the optimisation of geophysical techniques. The objective is to locate geological discontinuities liable to allow the migration of radionuclides from the storage chambers to the biosphere. The acquisition of the parameters needed for the modelling of the hydro-mechanical behaviour of geological rock formations is the aim of the programme.

The core of the CEA research is the evaluation of continuous and nondestructive investigation methods either from boreholes or in galleries in the vicinity of storage chambers. The principle of 3D visualisation of the massif geology using 2D soundings over the largest possible range of investigation distances was chosen. The objective of an optimised probing range that is compatible with the dimensions of the geological discontinuities is dictated by a concern to minimise prospecting costs and also to avoid any excessive disturbance or weakening of the natural environment. A borehole, even refilled, is liable to constitute a preferential pollution pathway during storage lifetime.

In the case of storage in a crystalline formation, efforts in geophysical research must be focused on locating and characterising hydraulically effective fractures. The radar technique appeared to be a promising technique. Granite is a mechanically dense and electrically resistant material, with a low propagation attenuation coefficient for electromagnetic waves. The latter are particularly sensitive to the presence of water. The work undertaken at the AEA has consisted in studying the suitability of radar tools. On account of, on the one hand, the similarity of the acquisition, restitution and interpretation principles of radar data with those of seismic data, and on the other hand, the importance of signal processing in seismic analyses, the ultimate objective is to work on the transposition or the adaptation of the programmes developed by seismologists to radar records.

This task implies, first of all, fully mastering the operating conditions of a ground penetrating radar (GPR) and defining the physical processes that determine the propagation of a high frequency electromagnetic wave in a geological environment. Because of the cost of drilling or of a borehole measurement campaign, it was deemed more economical to conduct preliminary studies with an adaptable surface equipment (EKKO IV Pulse, manufactured by Sensors & Software).

One of the problems treated was the determination of wave propagation velocity versus depth. This subject has seldom been dealt with in the literature. However, a knowledge of the variations of this parameter as a function of the propagation distance is essential for working with seismic migration software and defining geological sections graduated in distance rather than in two-way travel time. Moreover, the accuracy with which this value can be known allows an assessment to be made of the uncertainties affecting radar location of geological discontinuities or anomalies. In many cases, radar operators content themselves with extrapolating the direct underground velocity to the whole formation. The applicability of this value for the whole structure is debatable, especially in the case of superficial alteration of the terrain. Depending on the configuration of the environment of interest, AEA focused its attention on the portion of terrain affected by direct propagation. AEA were able to establish that a road surface of about 25 cm over dry sand or a concrete surface of the same thickness covering the ground of a gallery dug in granite did not have a quantifiable effect. This was taking into account the uncertainty that affects any velocity calculation; the

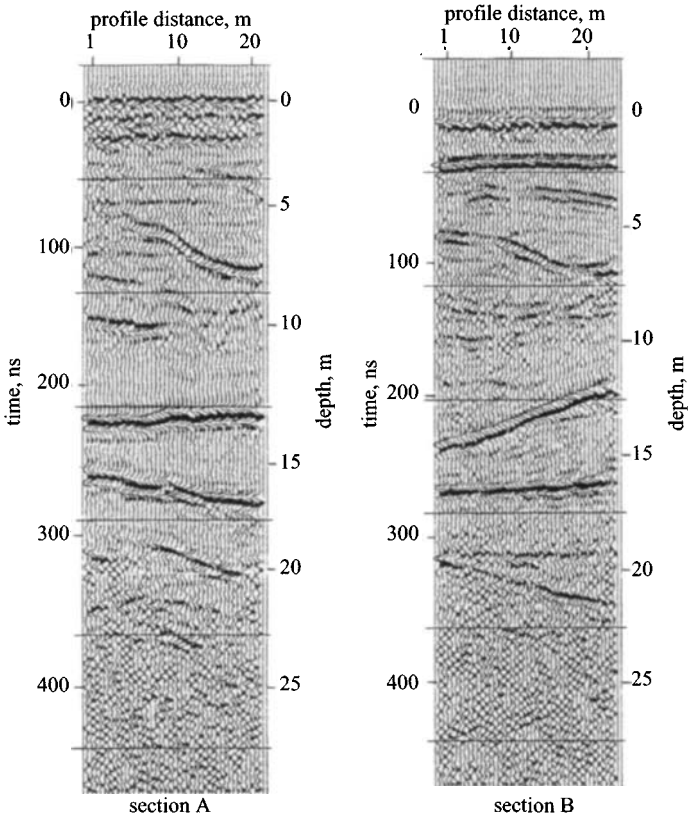

Figure 11.36 Radar measurement of granite (courtesy CEA France)

velocity obtained with the transmitter/receiver in contact with the geological material was similar to the value found in the presence of an interface.

The approximation mentioned above may not be sufficient, in particular in the case of a deep investigation. A study was conducted in order to evaluate the relevance of velocity analyses as they are programmed in seismic studies based on 'Normal Move Out' corrections (determination of root mean square (RMS) velocities and interval velocities). The site chosen for this study was a granite quarry made of a succession of sub-horizontal banks (stratiform rock). The radar experimentation aimed to provide 3D visualisation of the limits of these banks, similar to millimetre fissures (see Figure 11.36).

The interpretation of the RMS data relative to the 'wide angle' or 'common mid-point' (CMP) sections, recorded in different directions for apparent different dips and using three transmission frequencies (50, 100 and 200 MHz), made it possible firstly to verify that no velocity dispersion occurred with a frequency and secondly to show the influence of slight dips ($<15°$) that we had considered disregarding at

the beginning of the study. As a result, only the data recorded according to the CMP configuration are now utilised.

Despite the care taken in determining the RMS velocities and in reading the arrival times of each reflection on a great number of high-quality records, the instability of the interval velocities calculated using Dix's formula led us to reject this technique for future work. It seemed more satisfactory to limit ourselves to defining the propagation law from the RMS profile, reduced by a few percent, as is the practice in seismic analyses. AEA showed the relevance of a velocity analysis made in this manner by comparing the depth scale obtained by data processing with the reflector depths read on cores from an available borehole in the quarry and with the depths calculated with recourse to the direct wave velocity or bibliographical values. However, these analysis methods borrowed from seismic research have limits inherent in, among other things, the hypotheses set for simplifying the equations describing wave propagation. For sites with high reflectivity such as our test quarry (fissure density = 1.3 fissure per metre), it seemed difficult to determine a velocity law with an uncertainty of less than 10%.

The purpose of velocity calculation is not solely locating deep discontinuities. AEA also showed that when direct propagation velocities are determined with low uncertainties, these values can be utilised to differentiate rocks of the same nature but of different composition in the same site (a numerical example: the differentiation of an oolithic limestone from a comblanchien limestone by means of wave propagation evaluated at 77 ± 4 m/s for the first compared to 85 ± 4 m/s for the second). In this case, the inversion of the velocities in dielectric permittivities allows a qualitative interpretation of the radar signal to be made in petrophysical parameters (porosity, clay content, ...).

Large velocity variations in the case of propagation in an anisotropic environment have been observed during radar prospection in schists. In the case of propagation parallel to the direction of the schistosity, a velocity twice as high as that calculated when the propagation is perpendicular to the same schistosity was found (100 ± 5 m/s and 50 ± 10 m/s). The uncertainty affecting these velocities was higher for perpendicular propagation because of the greater attenuation of the waves that occurs for an electric field directed parallel to the schist layers. These results were confirmed by dielectric measurements carried out in the laboratory on rock samples cut in different directions in relation to the schistosity. These schists are an extreme case of anisotropy but the tests that were made prove that particular attention should be given to velocity measurement in a complex site.

Besides the effects of anisotropy on wave propagation, the 'volumic scattering' effect due to the heterogeneity of the massif was determined. To do so, data were collected according to different geometrical configurations of the antennas (antennas parallel or perpendicular to the measurement line, transmitter parallel or perpendicular to the receiver...). The terrain measurements were completed by data processing using a program perfected for seismic studies concerning shear wave birefringence. The complexity of prospection on a site where volumic scattering occurs was shown by comparing the radar response recorded with the antennas set perpendicular to

each other with the one recorded with the antennas arranged colinearly: with no volumic scattering, no reflection is collected with perpendicular antennas, whereas when volumic scattering occurs the heterogeneities reflected the waves differently according to their position in relation to the antenna planes E and H.

The above-mentioned tests give a general idea of the studies scheduled to determine the investigation possibilities offered by radar techniques in geophysics: the diversity of the studies that must be undertaken in order to draw as much information as possible from a radar measurement campaign is large. The lessons drawn from our preliminary tests made on several very different sites with surface equipment should be of use for research on the technique implemented in boreholes or in galleries in configurations representative of those encountered in waste storage site qualification work. Further effort has to be invested in signal processing so as to achieve dynamic hydraulic characterisation of a granitic formation.

11.12 Borehole radar

Dr Declan Vogt [*]

11.12.1 Borehole radar for long-distance GPR imaging in-mine

GPR works effectively within mining excavations in resistive rock, but is limited in range by two factors:

- It is difficult to lower the frequency of GPR to achieve additional range, because low frequency antennas become very large and unmanageable in the limited space underground within a mine.
- At very long ranges, there is significant clutter from air reflectors. The problem occurs because loss in rock is exponential, whereas in air it is only geometric. Most of the energy from a GPR is coupled into the rock, so air reflectors are not a problem close to the radar. However, at long ranges, even the small percentage of energy from the transmitter that is coupled into the air can become a large percentage of the received signal. Air reflectors are always a potential problem for GPR at longer ranges, but the problem is worse underground because the tunnels act as guides for VHF radio waves. Any obstacle within the tunnel, even more than 100 m away from the antenna, can produce reflectors that overwhelm the desired reflector from within the rock.

For long range probing underground, both these problems can be overcome by putting the GPR antennas within a borehole, producing a borehole radar. Long low frequency antennas are no less manageable than short high frequency antennas once within a borehole, and there is very little air around the antenna to sustain reverberation. In addition, because borehole radar requires a borehole, that borehole can be drilled to provide access to the target over substantial ranges. Conventional GPR requires access from within a tunnel, which limits its applicability within mines.

11.12.2 Borehole radar design

For the mining problem, the key parameter is range, so systems typically use low frequencies; 20 and 60 MHz are common bandwidths. Borehole radar is also used for geotechnical investigations in short boreholes. Here the emphasis is on resolution; so, higher frequencies are used, with bandwidths as high as 1 GHz.

The key design issues are:

- mechanical design
- where to do data acquisition? In the probe, or outside the hole?
- how to convey data from the probe to the data acquisition system?

In shallow boreholes, less than 30 m deep, it is feasible to suspend a suitable antenna on a cable, and operate the borehole radar in the same way as a conventional GPR, with pulse generation and digitisation occurring in the control unit outside the borehole. This is the model followed by the PulseEkko range of borehole antennas. However, as the borehole gets deeper, the losses in the cables to and from the antennas become too large to be ignored. In addition, the cable provides a good guide for radar waves, contaminating the recorded data with reflections from waves transported along the cable. Borehole radars used in deep boreholes are usually suspended on optical fibre cables to avoid problems with reflections along the cable.

Mechanical design is critical: it can be assumed that boreholes will contain water, so the borehole antenna must be watertight. If the system is designed to operate in deep boreholes, it must tolerate the substantial water pressures present at great depths – 10 MPa for each 1000 m.

Antennas are usually simple resistively loaded dipoles. Resistive loading reduces the ringing that would otherwise occur. Sato's group in Japan have developed slot antennas that create radar waves with transverse electric polarisation, rather than the transverse magnetic polarisation of the conventional dipole. Transmitting in one polarisation and receiving in the alternative polarisation offers additional discrimination compared to operation with a single polarisation.

If optical fibres are used for communication with the probes. The signal can be digitised down the borehole and transmitted in digital form to the surface, or the analogue signal can be transmitted to the surface. The advantage of digital transmission is the ease with which it can be transferred from the electrical to the optical domain and vice versa, and hence the ease with which it can be transferred through systems like rotary joints. The advantage of analogue transmission is a very simple receiver down the borehole. Since there is a risk of probe loss, a simple, cheap receiver is advantageous. On the other hand, probe loss is always a disaster. If expensive probes are used, perhaps they will be treated with more care, reducing the risk of probe loss.

The pre-eminent deep hole borehole radar is the RAMAC from Malå GeoScience. It uses a conventional stroboscopic sampler in the receiver probe communicating digitally with the surface over an optical fibre. The receiver is triggered directly by the transmitter, which may be in the same hole or an adjacent hole. The ability to work with the transmitter in one hole and the receiver in a separate hole allows

borehole radar to produce tomographic images as well as conventional reflection images. RAMAC can be configured with a number of antennas: 20, 60, 100 and 250 MHz antennas are available. It has also recently been re-engineered to work in boreholes down to 2500 m deep if required.

Another commercially available deep hole borehole radar is the Aardwolf, from the CSIR. The Aardwolf receiver is also triggered directly by the transmitter and digitises in the borehole. The principal difference between RAMAC and Aardwolf is the digitisation philosophy. RAMAC uses conventional stroboscopic sampling with 16 bits of dynamic range but acquiring only 1 sample per transmitted trace. Aardwolf captures the trace instantaneously, but with only 8 bits of dynamic range. The dynamic range is then improved through stacking. Instantaneous sampling is simple, but does not easily lend itself to the application of time varying gain. The Aardwolf is designed for narrow boreholes and is only 36 mm in diameter.

The DMT in Germany markets a deep hole borehole radar that has been certified for use in explosive atmospheres. It is a substantial instrument: 80 mm in diameter, and up to 20 m long, depending on the antennas that are chosen. The DMT digitiser follows a middle path between stroboscopic sampling and instantaneous sampling: it samples at 8 MHz, or every 125 ns, with 16-bit resolution. Higher sample rates are achieved by sampling over several waveforms. For example, 1 ns sampling can be achieved by sampling 125 traces. The DMT radar does not use optical fibre but a standard seven-core borehole logging cable. The receiver is carefully decoupled from the cable. The radar has a system bandwidth of 120 MHz.

Both the RAMAC and the DMT radars have directional capability. In each case, directionality is added by acquiring data from two loop antennas measuring H-field data. All data are received and digitised so that a pattern sensitive to a particular direction can be synthesised during interpretation. The DMT tool also acquires a single E-field channel to remove ambiguity from the H-field antennas. The RAMAC tool can use either a directional module or a conventional E-field antenna.

The University of Sydney is promoting a borehole radar with a simple analogue to optical converter in the receiver. The signal from the receiver and a trigger pulse from the transmitter are both taken out of the borehole through analogue optical fibre links. Initially the system digitised the signals using a standard digital sampling oscilloscope, but it has now migrated to using high speed ADC cards mounted in a dedicated PC. The philosophy is to keep complexity within the hole to a minimum, and hardware outside the hole to commercially available equipment.

The group at Tohoku University have produced a number of innovative ideas, including the use of different polarisations. They have also worked with a novel sensor: they use a $LiNbO_3$ crystal to directly modulate an applied optical pulse with the electric field present at the terminals of the receive antenna. The down hole receiver is thus completely passive and does not even contain batteries. It is then simple to build up antenna arrays that can be used to synthesise directionality in both azimuth and elevation. The recording system is a network analyser outside the borehole. The transmitter is driven by a signal from the network analyser, converted to an optical signal for transmission down the borehole. More detail follows in Section 11.13.

11.12.3 Example borehole radar data

The majority of gold in South Africa occurs in thin, gently dipping sedimentary packages with very large horizontal extent, around the rim of the Witwatersrand Basin. The Basin itself is about 300 km from east to west. The last gold reef to be deposited was capped by the outpouring of the Ventersdorp lavas, about 2700 million years ago, and is known as the Ventersdorp Contact Reef, or VCR. The strong physical property contrast between the Ventersdorp Lavas and the underlying rocks (mostly quartzites and shales) makes the VCR an excellent geophysical reflector, both for seismic reflection and for GPR and borehole radar.

Mining is usually undertaken by developing horizontally haulages on strike on discrete levels, 60 m–100 m apart vertically. Cross-cuts are then developed horizontally in the dip direction to the reef plane (Figure 11.37). The imaging problem for borehole radar is to determine continuity of the reef horizon between levels, in advance of mining. The vertical distance between crosscuts makes GPR not viable. Dislocations of the reef of greater than 1 m must be mapped accurately. Smaller dislocations can be mined through, but larger dislocations require redevelopment. The 1 m resolution defines the radar bandwidth: the host rocks typically have relative permittivities of less than 9, so the velocity of propagation is about 100 m/μs. A wavelength of 2 m is required to achieve a resolution of 1 m, so the bandwidth required is at least 50 MHz.

To test the principle of borehole radar, a number of trials were conducted at a surface VCR test site. The geometry of the test site is illustrated in Figure 11.38. A reflection survey was conducted in the diagonal hole, BH1, at two frequencies, 20 and 60 MHz, using a Malå RAMAC radar. The reflection results are illustrated in Figures 11.39 and 11.40. The improved resolution and poorer range at the higher bandwidth are both obvious. The lower frequency has the additional feature that it is less sensitive to smaller reflectors than to the most prominent reflectors. In this case, the most prominent reflector is the VCR, so the low frequency data enhance the

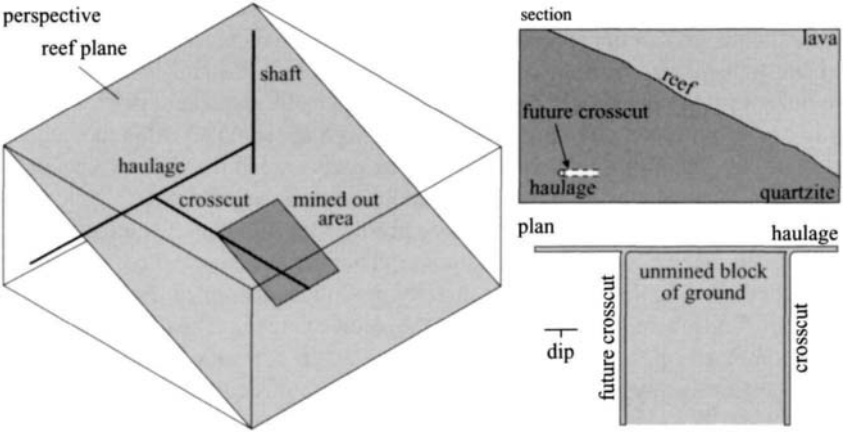

Figure 11.37 Cross-section through a typical Witwatersrand mining operation

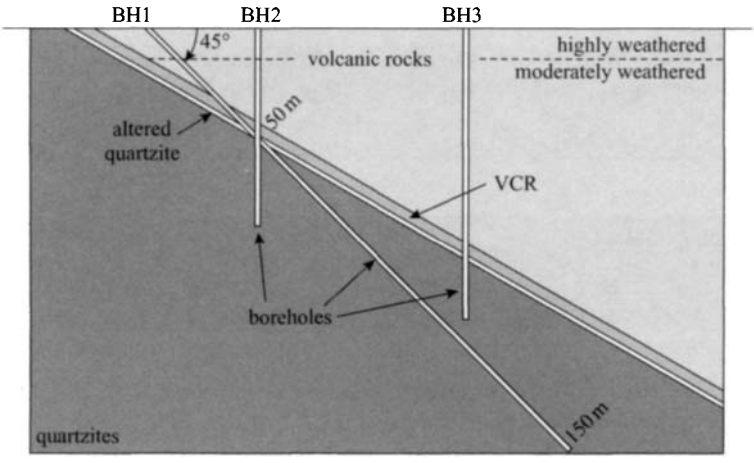

Figure 11.38 VCR test site cross-section

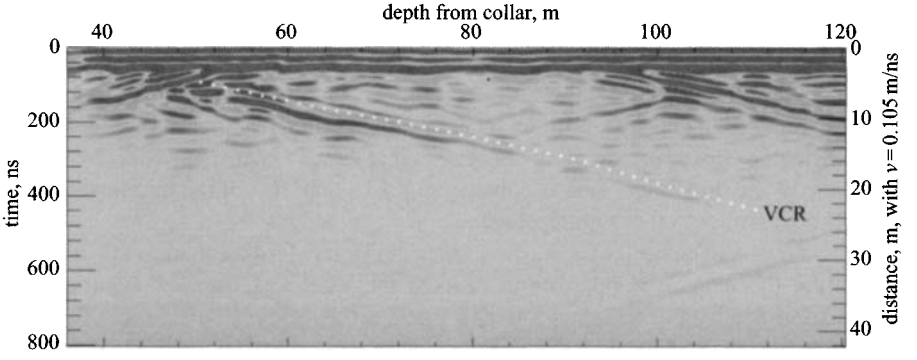

Figure 11.39 20-MHz results from surface VCR test site, BH1

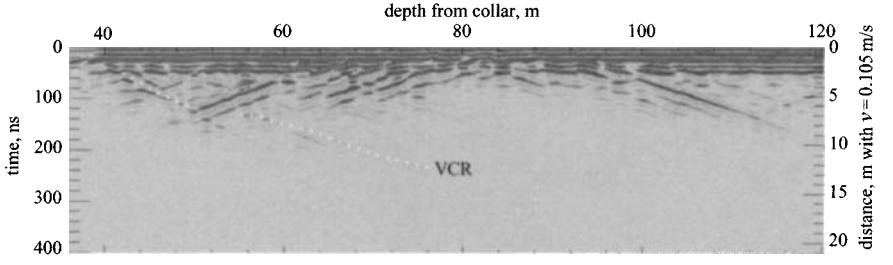

Figure 11.40 60-MHz results from surface VCR test site, BH1

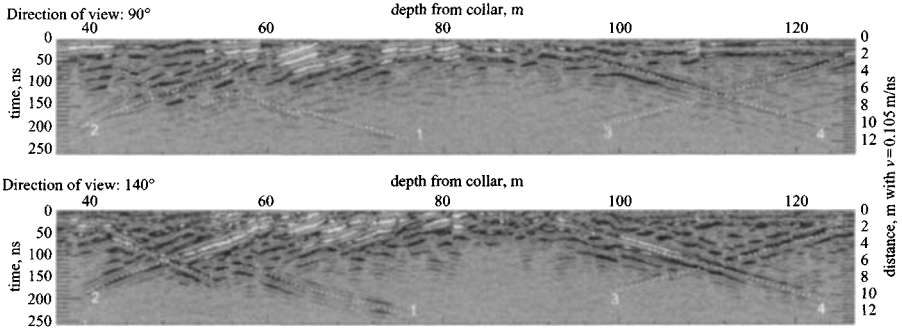

Figure 11.41 *Two views in different directions synthesised from the directional antenna data collected at the VCR test site, BH1*

interpretation process. In other environments, it may ignore the desired reflector, and higher frequency data may be required.

The directional ambiguity was investigated by using the RAMAC 60-MHz directional antenna. Two results are illustrated in Figure 11.41. The radar images illustrated show that one family of reflectors is dominant in the 80° data, and another family is dominant in the 180° data. The dominant reflectors in the 180°data 1, 2 and 4 are roughly horizontal, and represent the VCR and sedimentary sequences below it. The other reflector, 3, is approximately vertical, and represents a vertical fault. Note that the range of the directional data is considerably less than that of the omnidirectional 60-MHz data presented in Figure 11.40.

Another way of dealing with the directional ambiguity is to use a priori information to analyse the data. It is possible to process the VCR test site data ignoring the information from the directional antenna that there is a family of vertical features represented in the radar image. The process is illustrated in Figure 11.42. When the borehole radar crosses a flat reflector (a), the radar image shows the reflector as moving toward the borehole, then away from it, in a characteristic inverted V (b). It is possible to separate out the reflectors moving toward the borehole from those moving away, (c and d) then rotate moving away reflectors into their correct orientation (e). This process is only valuable if all the reflectors are assumed to lie in a single plane. The borehole can also be orientated correctly to aid interpretation (f), producing the radar image shown in Figure 11.43. A fault is now interpreted on Figure 11.43, based on a dislocation in the VCR reflector. The fault was confirmed by the presence of a fault in the core from the borehole.

Cross-hole results from the surface test site are illustrated in Figure 11.44. Cross-hole tomographic data were collected between boreholes 2 and 3, as illustrated in Figure 11.38. A velocity tomogram is presented as Figure 11.44*a*. Cross-hole tomographic data are inherently of poorer resolution than reflection data, because they integrate rock properties over a volume, but it is possible that the resolution of tomograms can be improved by incorporating reflection data. In Figure 11.44*b*, a single cross-hole radar image is presented. The first arrival is clearly visible, but slightly

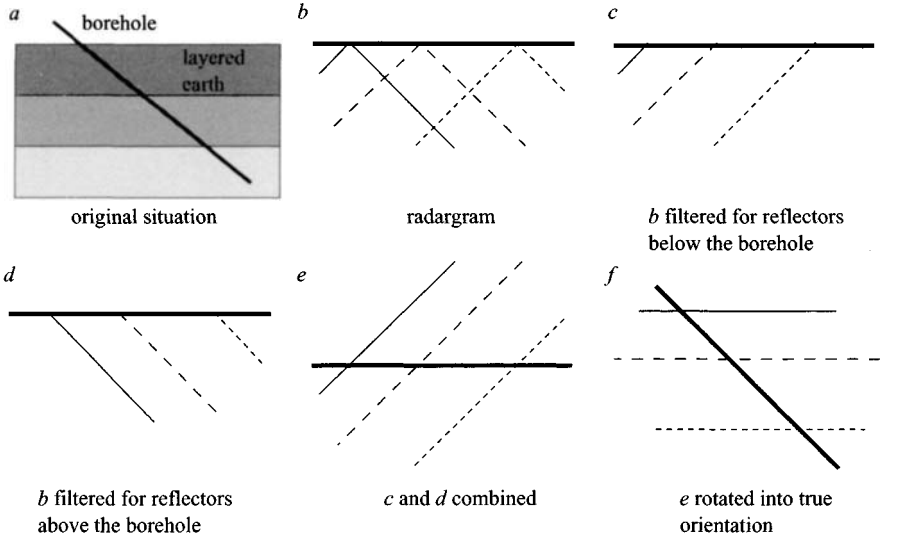

Figure 11.42 Processing sequence for corrected borehole radar data

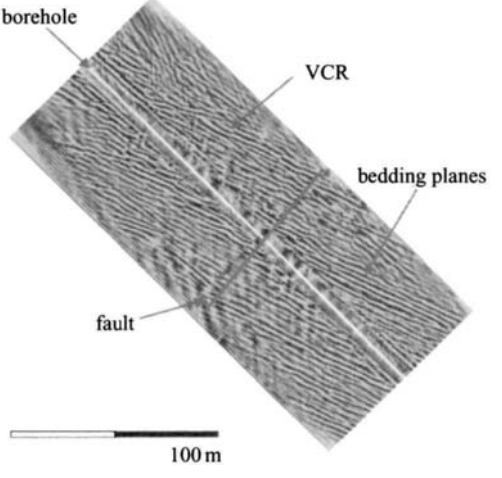

Figure 11.43 Data from the VCR surface test site processed as illustrated in the previous Figure

later in time there is a second arrival that corresponds to a cross-hole reflection of the VCR surface.

After the success of borehole radar at the surface site, it has been implemented underground, again on the VCR. On the VCR, gold grade is associated with topography: slopes typically contain less gold than horizontal terraces. If the topography is determined before mining, it is possible to preferentially mine high grade areas

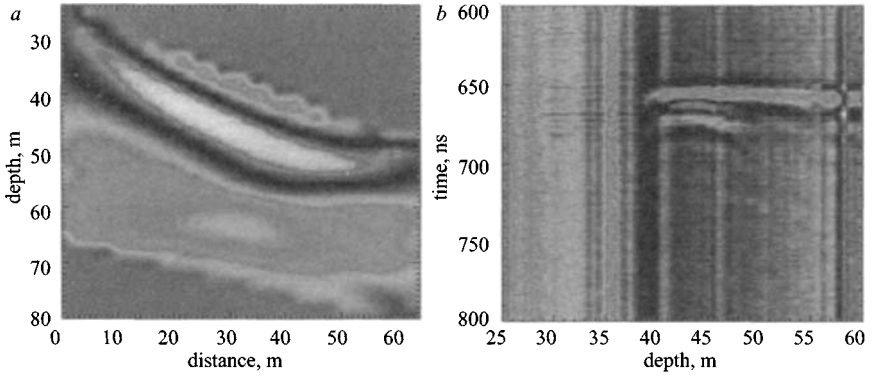

Figure 11.44 Cross-hole results: tomography and reflection

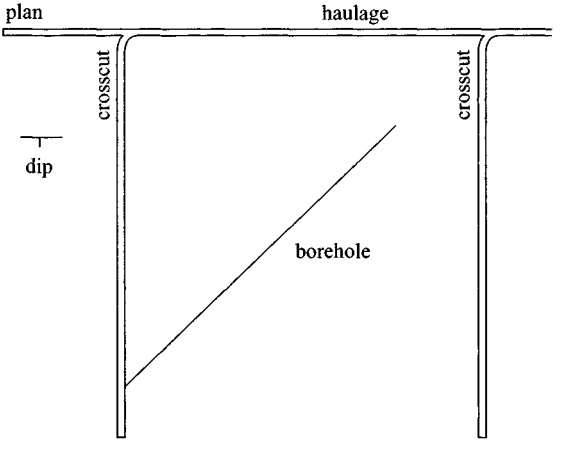

Figure 11.45 In-mine application of borehole radar

and support pillar locations can be targeted for low grade areas. The geometry is illustrated in Figure 11.45: A 200 m borehole was drilled oblique to strike within the lava above the reef, and was designed to remain 20 m away from the reef horizon. An Aardwolf system was applied in the small diameter borehole, and produced the radargram illustrated corrected for borehole dip in Figure 11.46a. Four small faults, each of less than 1 m displacement were defined, three of which corresponded to faults mapped in the borehole. The topography of the area is also clear: steep slopes and relatively horizontal areas are defined. The pink triangles in Figure 11.46*a* (see CD attached for colour image) and the surface perpendicular to the borehole in Figure 11.46*b*, is the estimate of the reef elevation determined from 3D surface seismics. The radar result confirms the seismics and adds considerable resolution.

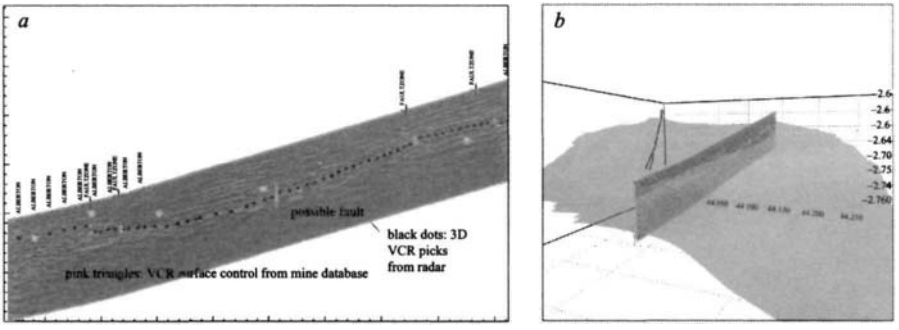

Figure 11.46 Result of in-mine investigation

11.13 Polarimetric borehole radar for characterisation of sub-surface fractures

Prof. Motoyuki Sato

11.13.1 Sub-surface fracture characterisation

Sub-surface fractures and groundwater migration through fractures are important issues in many civil engineering applications. For example, rock stability is closely related to sub-surface fractures, and investigation of fractures is required for any kinds of constructions. Nuclear disposal in geology is under discussion in many countries, and the ground water condition in the deposit site has to be studied precisely.

Borehole radar is one form of ground penetrating radar (GPR) which is used in drilled boreholes for measurement of deep sub-surface structures. The targets of borehole radar include sub-surface fracture, natural fault, geology and tunnel. It is known that water content determines the dielectric constant in most sub-surface material. Therefore, borehole radar has often been successfully used for monitoring and detecting water flow through sub-surface fractures.

Since the aperture shape and the inner structure of sub-surface fractures determine water permeability, detailed structure of sub-surface fracture will be used for estimation of water permeability of the fracture. However, most conventional borehole radar systems have been operated in the frequency range lower than 100 MHz in order to achieve a deeper penetration depth from a borehole. Therefore, the radar resolution was poor and cannot estimate the structure of sub-surface fracture, whose aperture is normally less than 1 mm.

An idea of the radar polarimetry can be used to solve this problem [66–68]. Radar polarimetry is a new radar technology, which can improve radar information [69, 70]. Most conventional borehole radar systems use dipole antennas for a transmitter and a receiver, and measure only co-polarised reflection waves. On the contrary, if we measure reflection of a set of polarisation states, we can obtain more information

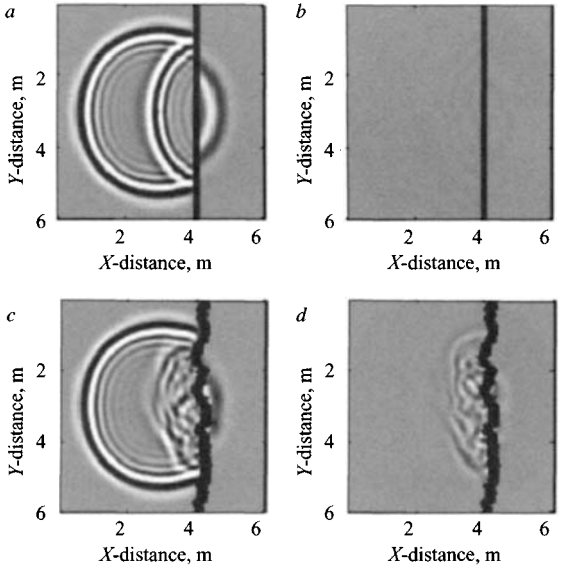

Figure 11.47 *Electromagnetic scattering from sub-surface fractures having flat and rough surfaces, simulated by FDTD: (a) flat surface, co-polarisation; (b) flat surface, cross-polarisation; (c) rough surface, co-polarisation; (d) rough surface, cross-polarisation*

about the structure of the sub-surface fracture. Although the radar polarimetry cannot give direct information about the sub-surface fracture, it can be used for classification of fractures.

Figure 11.47 shows electromagnetic scattering from sub-surface fractures having flat and rough surfaces, simulated by FDTD [71–73]. In these Figures, a transmitting antenna, which is a small dipole antenna polarised to the z-direction is located at the centre of the Figure. The incident field radiated from the antenna is spherically spreading and reflected by a thin layer at $x = 4$(m). The layers in Figure 11.47*a*,*b* have flat surfaces and those in Figure 11.47*c*,*d* have rough surfaces, which models geological sub-surface fractures.

The dielectric constant of the homogeneous space and the layer have different values, which models the sub-surface fracture condition. The fields shown in Figure 11.47*a* and *c* are the electric field of a z-component, which is the co-polarisation component to the incident field, while Figure 11.47*b*,*d* show the y-component of the electric field, that is the cross-polarised wave from the incident field. We can observe that the incident field appears only in the co-polarisation field, because the incident field does not change its polarisation while propagating in a homogeneous medium.

In Figure 11.47*a*, the scattered and the transmitted waves through the layer are clearly seen, while these waves do not appear in Figure 11.47*b*. This indicates that, when the layer is flat, a cross-polarisation wave is not generated. On the contrary,

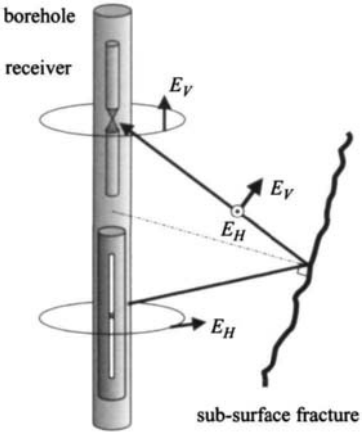

Figure 11.48 Sub-surface fracture measurement by polarimetric borehole radar

we can see scattered waves even in the cross-polarised component, when the layer has a rough surface, which is shown in Figure 11.47*d*. From this simulation, we can understand that a natural geological structure having a rough surface generates a cross-polarised field component to the incident field [72, 74].

11.13.2 Radar polarimetry

In the borehole radar measurement, the surface condition of radar targets is closely related to the polarisation state of the scattered wave. This polarisation state can be described by using a scattering matrix **S**, which is defined as [69]

$$\begin{pmatrix} E_H^s \\ E_V^s \end{pmatrix} = \mathbf{S} \begin{pmatrix} E_H^i \\ E_V^i \end{pmatrix} = \begin{pmatrix} S_{HH} & S_{HV} \\ S_{VH} & S_{VV} \end{pmatrix} \begin{pmatrix} E_H^i \\ E_V^i \end{pmatrix}$$

where the subscripts V and H denote the vertical and horizontal polarisations, respectively, and the superscripts i and s denote the incident and scattered field, respectively. Figure 11.48 shows the antennas set in a down hole radar sonde and a sub-surface fracture in polarimetric borehole radar measurement.

A schematic diagram of a radar system, which we used for data acquisition, is shown in Figure 11.49. This is a stepped-frequency radar system based on a vector network analyser. Owing to high attenuation, we cannot use a long coaxial cable for connecting the network analyser to the transmitting and receiving antennas. This system is using an analogue optical link to send the radio-frequency signal through optical fibres. The radar data are acquired in the frequency domain and transformed to the time domain by FFT. The elements of a scattering matrix can be measured with the combinations of dipole and slot antennas [67, 68]. The received radar signals in the time domain can be expressed as follows.

$$\begin{pmatrix} E_{HH}(t) & E_{HV}(t) \\ E_{VH}(t) & E_{VV}(t) \end{pmatrix} = \begin{pmatrix} S_{HH}E_H^i(t) & S_{HV}E_V^i(t) \\ S_{VH}E_H^i(t) & S_{VV}E_V^i(t) \end{pmatrix}$$

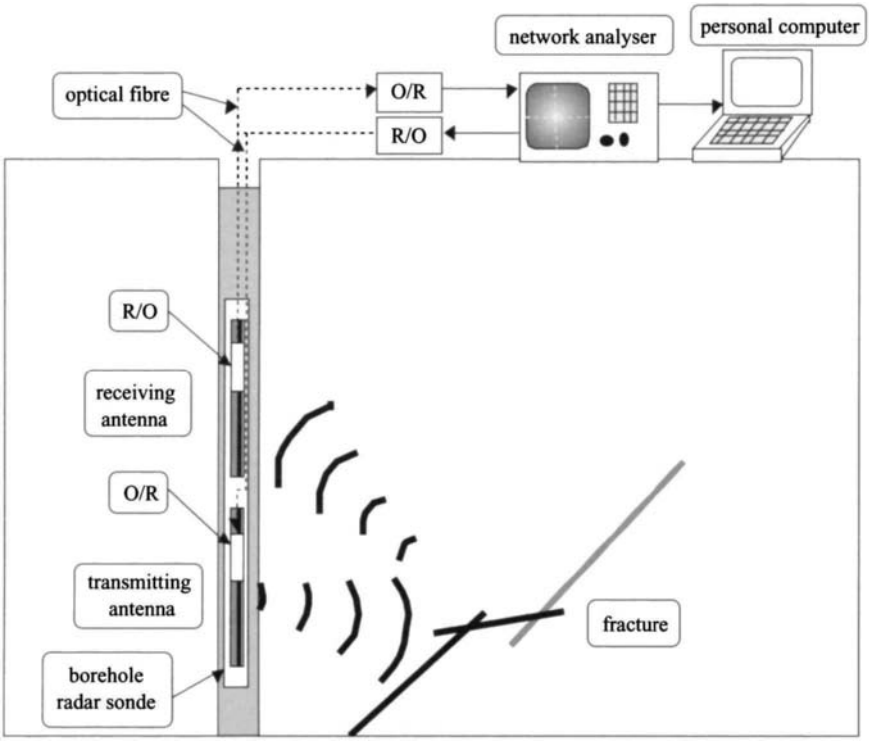

Figure 11.49 *Polarimetric borehole radar system – a stepped frequency radar system based on a vector network analyser*
The surface controlling unit and down hole systems are connected by analogue optical link

11.13.3 Field experiment

The field experiment was carried out in the Mirror Lake site, NH, USA. U.S. geological survey has carried out many borehole tests, including borehole radar in this test site, to understand the hydraulic conditions in fractured granite rock [12]. Figure 11.50 shows the radar sonde and Figure 11.51 the schematic structure of the fracture orientations. The data was acquired by a directional type borehole radar by the U.S. geological survey [12]. The directional borehole radar can determine the dip and strike of each fracture. Figure 11.51 shows a simple extension of a fracture orientation measured near the borehole. We can observe that the fractures are crossing the borehole FSE1 at around 25 and 45m. Many fractures are crossing the borehole in the section of 40–45m.

In the actual polarimetric borehole radar measurement, the vertical and horizontal incident waves $E^i_H(t)$ and $E^i_V(t)$ are radiated from two different antennas. In our radar system, they are dipole and slot antennas. To represent the characteristics of scattering

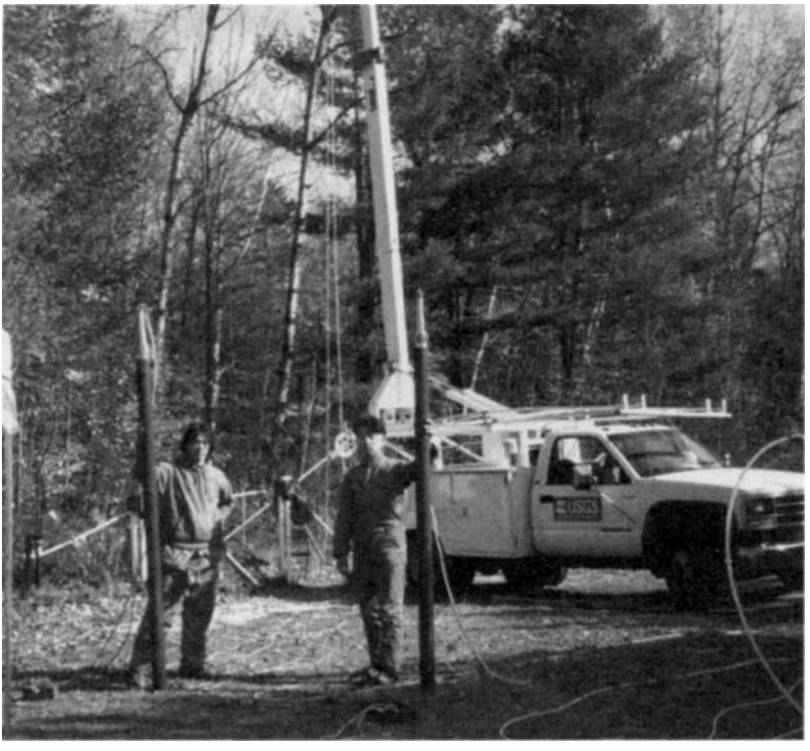

Figure 11.50 Borehole radar sonde

of sub-surface fractures, we introduce a matrix which is given by energy contained in the scattering matrix, and define the energy scattering matrix $\boldsymbol{P}$ as

$$\boldsymbol{P} = \begin{pmatrix} P_{HH} & P_{HV} \\ P_{VH} & P_{VV} \end{pmatrix} = \begin{pmatrix} \int_0^T E_{HH}^2(t)\,\mathrm{d}t & \int_0^T E_{HV}^2(t)\,\mathrm{d}t \\ \int_0^T E_{VH}^2(t)\,\mathrm{d}t & \int_0^T E_{VV}^2(t)\,\mathrm{d}t \end{pmatrix}$$

The integration is taken over a time window containing reflection from one radar target.

Profiles were measured in a borehole FSE-1 by polarimetric borehole radar [68, 72]. In the radar profiles in Figure 11.52, V-shaped reflections from sub-surface fractures are clearly observed. The depth of each fracture is already determined and we can correlate the radar profile to the physical properties of each fracture. From these observations, we found that most of these reflections are caused by water-filled fractures. In this experiment, the strata of schist, migmatite and pegmatite could not be detected, although they can be detected by acoustic techniques. We can detect fractures and anomalies in a borehole by geophysical exploration techniques. Figure 11.53 shows the energy scattering matrix of several different sub-surface fractures. It is clear that sub-surface fractures in this borehole can be classified into two clusters

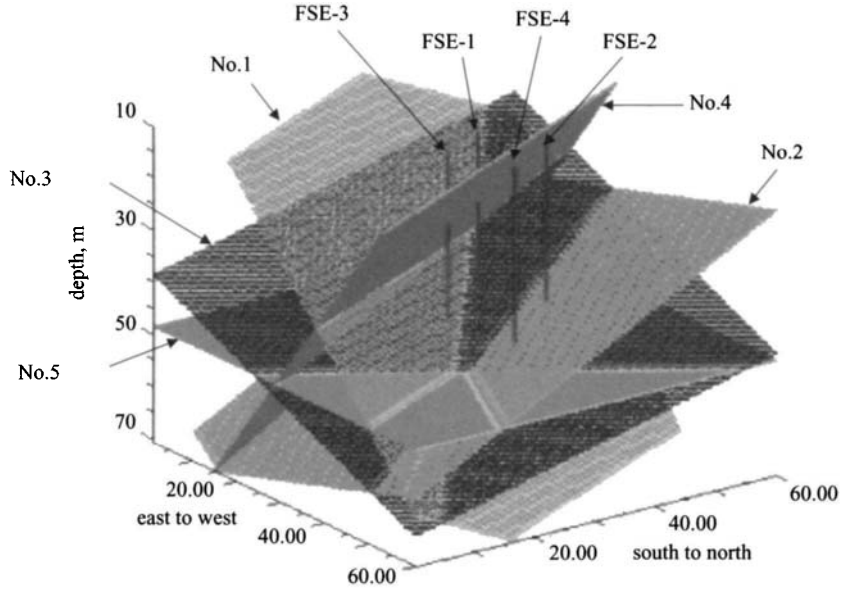

Figure 11.51 *Fracture orientation at Mirror lake test site*
Orientation information was obtained by a directional borehole radar by US Geological Survey

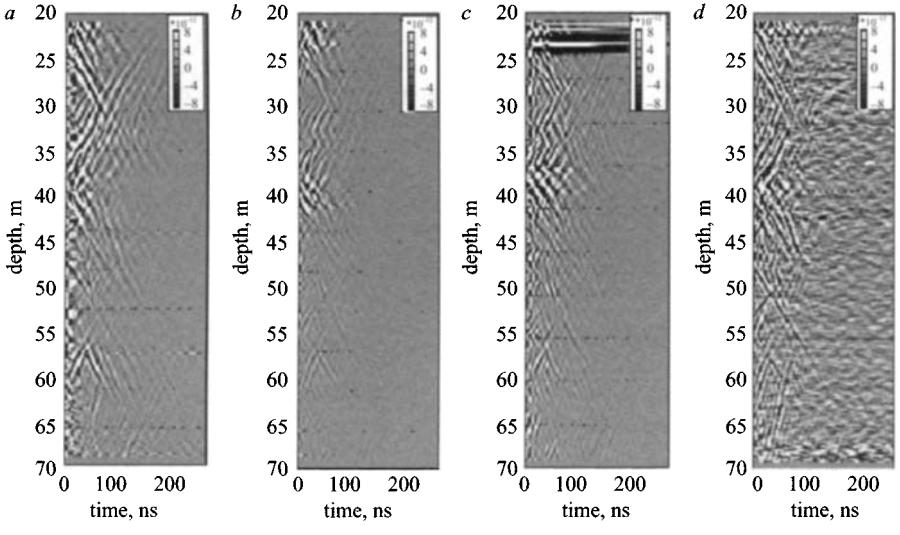

Figure 11.52 *Polarimetric borehole radar profiles: (a) V-V; (b) V-H; (c) H-V; and (d) H-H*

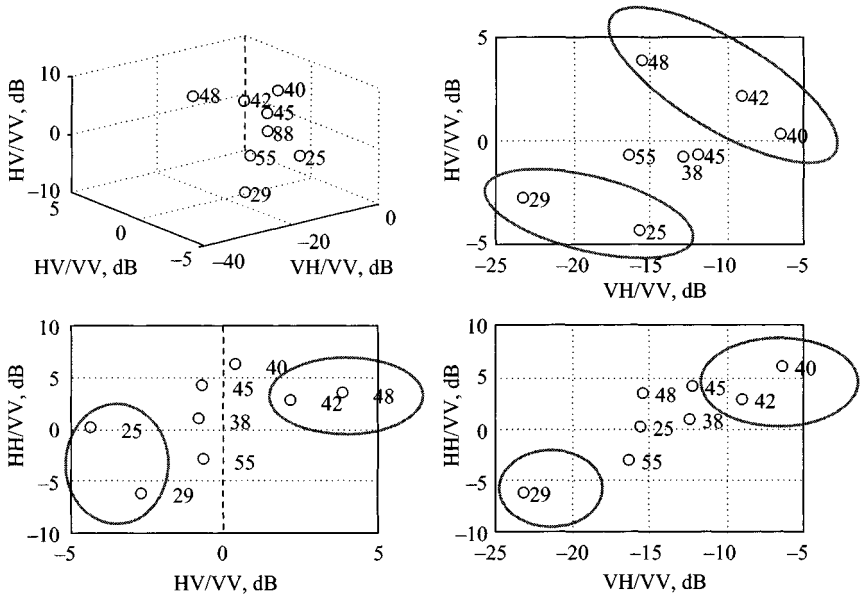

Figure 11.53 *Classification of sub-surface fractures by measured energy scattering matrix of sub-surface fractures*
The numbers denote the borehole intersection depth of each fracture. Two clusters are observed

having different energy scattering matrix characteristics. The surfaces of the sub-surface fractures at depths of 40, 42 and 48 m are estimated to be rough, because these sub-surface fractures have strong cross-polarised components. From the hydraulic test information of this site, we could find that the water permeability of these sub-surface fractures is high [77]. We think fractures having rough surfaces are not healed, and the water permeability can be high.

11.14 VHF band slimline borehole radar experiences in the South African mining industry

Ian M. Mason (ARCO) and J. H. Cloete (University of Stellenbosch)

11.14.1 Introduction

Conventional exploration tools lack the resolution to reveal the <20 m features that endanger miners. Synthetic aperture and interferometric borehole radar is emerging as a tactical tool with which to ensure the safe development of stopes. We have built a series of ultra-slim digital borehole radars in order to map sub-metre scale objects on target horizons from AXT (47 mm) and EXT (37 mm) boreholes driven into highly

stressed areas ahead of ultra-deep gold mine workings. Hard rock mine boreholes are narrow (<47 mm). However, modern components are small enough to allow us to build borehole radars to the same specifications as surface ground penetrating radars. Ours is the only radar currently capable of entering AXT and EXT boreholes.

The purpose of this Section is to introduce the geophysical community to some of the development work being carried out by our research groups, present some results and outline future potential for the instrument.

11.14.2 BHR specifications

The system currently being utilised (see Figure 11.54) is configured as follows:

Diameters: 32.5 mm, 25 mm
Lengths: 1.7 m (Tx), 1.5 m (Rx)
PRF: 2–64 kHz, 1–4 kHz
Tx power: 20 kW (1 kV into 50 Ω)
Bandwidth: 10–125 MHz.

11.14.3 Digital data acquisition

Borehole radar profiling is conceptually similar to marine echo sounding. A pulsed signal generated by a borehole transmitter is reflected and acquired by a receiver in the same hole. Owing to the harsh conditions in ultra-deep mines a robust acquisition system is essential. We have built a rotating computer into the spool of a winch drum (Figure 11.55). This reduces optical losses, raises cable life, and provides shock resistance. The computer houses an optical RF demodulator, a 250 MS/s 8-bit

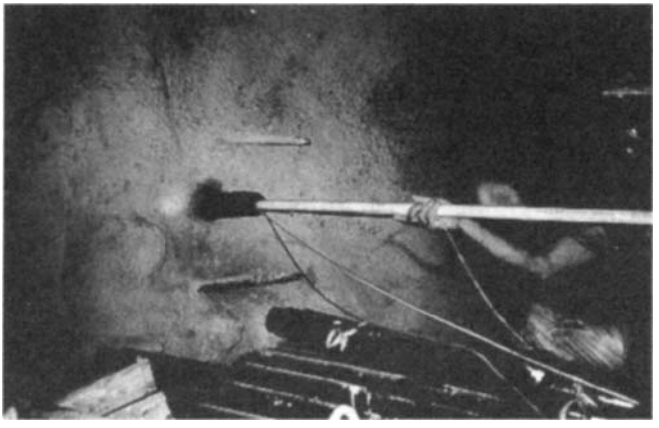

Figure 11.54 Deployment of the borehole radar in a cover-hole at East Driefontein (Goldfields)

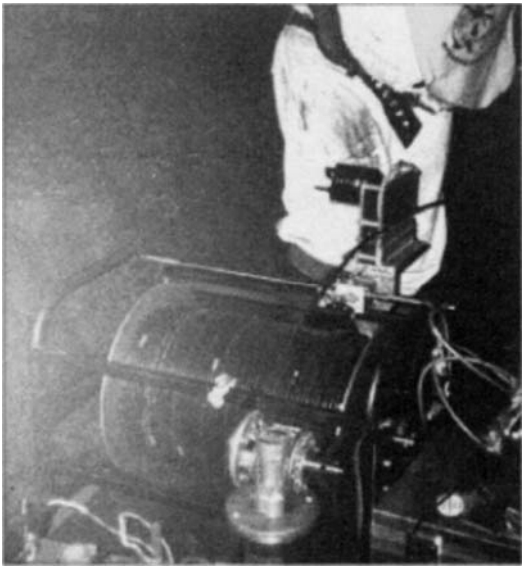

Figure 11.55 Robust digital data acquisition computer located inside winch, on site at Mponeng (Anglogold)

real-time analogue to digital converter, a stacking unit that enhances the dynamic range to an equivalent of 11–12 bits, a 486 motherboard and flash memory. The winch drum is capable of carrying more than 375 m of optical fibre. Traces can be viewed as they are acquired.

11.14.4 Typical problem

The Ventersdorp Contact Reef (VCR) currently produces around 6% of the world's gold [87]. But South African reserves above the current cutoff mining depth are falling rapidly. Only one-sixth of the 66 000 tons above 3.5-km depth remain. Stress and fault free paths have to be found well in advance of deep excavation if mines are to go safely down to 5 km. Mining hazards rise with depth. The VCR is a rolling, dipping sheet, cut by braided palaeo-stream channels, then covered by 100+ m of lava before being buried. The topography causes a facies related variation in ore grade and stress concentrations that can be uncontrollable if terrace edges are encountered by stopes (see Figure 11.56).

The Section below proves that a borehole radar can map ahead of and thereby protect the advance of ultra-deep tunnels and stopes. The Venterspost lavas overlying the VCR are translucent at VHF. The object of primary interest, the VCR, is the dominant radar reflector. The VCR can be seen in reflection at 100-m ranges. Small <1 m objects on the VCR draw into focus when range drops below 50 m.

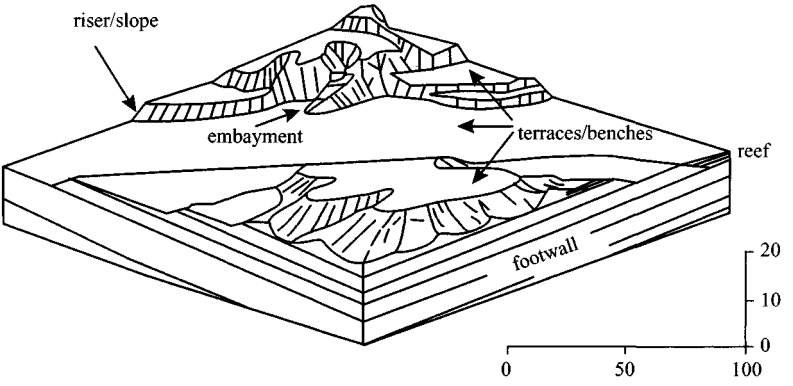

Figure 11.56 Topography of VCR (McWha, 1988 [76])

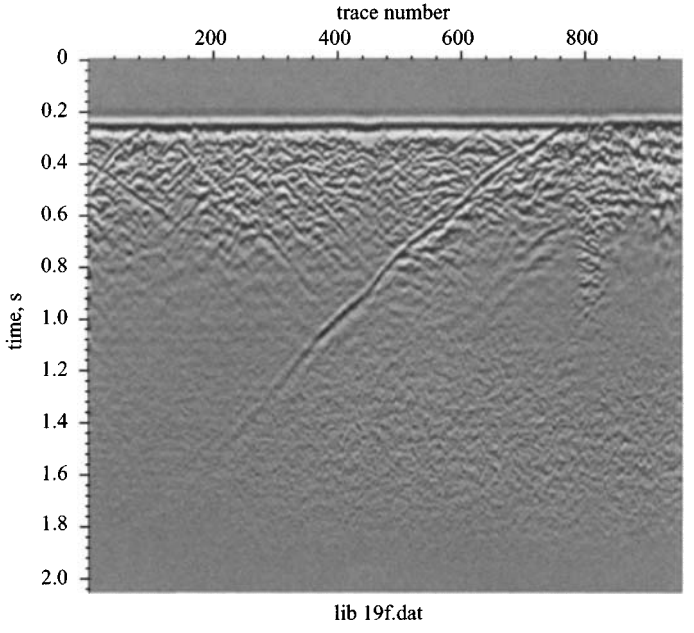

Figure 11.57 ARCOLAB radar profile of a part of the VCR from an inclined borehole

11.14.5 Signal and image processing

An important strategy around the design of the radar has been a signal and image processing system which can be deployed in the field by mine geologists. This means that prelimary images can be produced by the geologist himself within an hour or two of data acquistion (Figure 11.57). This processing is carried out using the Seiswin package, which has evolved from its seismic roots over the past 30 years [78].

At present we are studying methods for extending the borehole data processing to three dimensions [80, 81]. Both inteferometric synthetic aperture radar and convolutional techniques are being investigated.

11.14.6 Electromagnetic modelling

Pulsed radar systems traditionally utilise heavily damped antennas to radiate signals and received real time data which is directly interpretable. The design of these antennas is difficult, especially if bandwidth and efficiency need to be optimised. Indeed, knowledge of the propagation through complex rock structures (forward modelling) is important for image interpretation and the development of software to execute the inverse problem. A number of students are tackling these problems at Masters and PhD level, using sophisticated computational electromagnetic codes [79].

At present the radar operates in bistatic mode (a length of fibre acts as a spacer). A new development is to operate without the spacer, still in bistatic mode, but simplifying the deployment of the antenna, which is now just one unit.

The dielectric properties of the host rock are critical to the successful deployment of the radar. We have carried out extensive studies of rock properties (permittivity measurements of cores) and are attempting to produce a simple test jig which can remove the need for extensive sample preparation.

11.14.7 Summary

We have presented the concept of a slim-line, pulsed, borehole radar which can be deployed in the narrow boreholes found in hard rock mining. Together with this radar and the signal and image processing capabilities of the package *Seiswin*, the potential exists for operational planning staff of mines to utilise the radar in situ for decision making.

The system must, however, be seen as experimental, since the research programmes running in parallel will improve both the hardware and software, thereby simplifying operation and improving performance. We hope that continuous interaction with operational problems over the next few years will lead to a system which will make an impact on mine safety and operational cost.

11.15 Summary

This Chapter has considered some of the geophysical applications of GPR . This is one of the main founding applications for GPR and this Chapter, in conjunction with Chapter 4 on the properties of materials, should provide a suitable reference source for the reader. There is now a wealth of information on GPR techniques for the probing of rocks, soils, snow and ice. Given the considerable amount of work that has been carried out on conventional GPR probing of rocks and soils, the contributors to the second edition have concentrated on two specific applications, namely frozen materials and borehole radar. Most geophysical probing is carried out at the lower end of the frequency range for GPR, and this in turn brings different hardware configurations into existence.

11.16 References

[1] PETERS, L. P., Jr., DANIELS, J. J., and YOUNG, J. D.: 'Ground penetrating radar as a subsurface environmental sensing tool', *Proc. IEEE*, 1994, **82**, (12), pp. 1802–1822

[2] PETTINELLI, E., BEAUBIEN, S. E., MARZANO, F. S., and PIERDICCA, N.: 'Comparison of GPR field results from a stratified limestone terrain with model simulations'. Proc. Int. Geoscience and Remote Sensing Symposium, 1995 (IGARSS '95), 'Quantitative remote sensing for science and applications', 10–14 July 1995, Vol. 3, pp. 1705–1707

[3] SATO, M., and LU, Q.: 'Ground water migration monitoring by GPR'. Proc. IEEE Int. Geoscience and Remote Sensing Symposium, 2002 (IGARSS '02), 2002, Vol. 1, pp. 345–347

[4] STEENSON, B. O.: 'Radar methods for the exploration of glaciers'. PhD thesis, California Institute of Technology, Pasadena, CA, 1951

[5] COOK, J. C.: 'Proposed monocycle-pulse very-high-frequency radar for airborne ice and snow measurement', *AIEE Commun. Electron.*, 1960, **51**, pp. 588–594

[6] WAITE, A. H., and SCHMIDT, S. J.: 'Gross errors in height indications from pulsed radar altimeters operating over thick ice and snow', *Proc. IRE*, 1962, **50**, pp. 1515–1520

[7] EVANS, S.: 'Dielectric properties of ice and snow – a review', *J. Glaciology*, 1965, **5**, pp. 773–792

[8] RADOK, U.: 'The Antarctic ice', *Sci. Am.*, 1985, **253**, pp. 82–89

[9] KOVACS, A., and MOREY, R. M.: 'Estimating sea ice thickness using time-of-flight data from impulse radar soundings'. CRREL Report 89-22, US Army Cold Regions Research and Engineering Laboratory, December 1989

[10] BIGGS, A. W.: 'Sea ice thickness measurements with short pulse radar systems'. URSI Commission F, 1977, La Baule, France, pp. 159–163

[11] HALL, D. K.: 'A review of the utility of remote sensing in Alaskan permafrost studies', *IEEE Trans.*, 1982, **GE-20**, pp. 390–394

[12] UNTERBERGER, R. R.: 'Subsurface dips by radar probing of permafrost'. Proc. 3rd Int. Conf. on Permafrost, 1978, pp. 573–579

[13] Rodeick, C. A: 'Pipeline route selection by ground-penetrating radar'. Pipeline Industry, September 1983, pp. 39–44

[14] LUKASHENKO, Y. I., MASLOV, A. I., TERLETZKIY, N. A., and TSIURUPA, L. A.: 'Subsurface sounding in the UHF band of lenses of ground water and continental glaciers', *Telecommun. Radar. Eng.*, 1979, **34**, (4), pp. 94–95 (English translation)

[15] FINKELSTEIN, M. I.: 'Subsurface radar', *Telecomm. Radio Eng.*, Pt.2 (USA), 1977, **32**, pp. 18–26 (English translation)

[16] ANNAN, A. P., and DAVIS, J. L.: 'Impulse radar applied to ice thickness measurement and freshwater bathymetry', *Geol. Soc. Canada*, 1977, **1B**, p. 77

[17] OSWALD, G. K. A.: 'Geophysical radar design' *IEE Proc. F, Commun. Radar Signal Process.*, 1988, **135**, pp. 371–379

[18] BISHOP, J. F., CUMMING, A. D. G., FERRARI, R. L., and MILLER, K. J.: 'Results on impulse radar ice-depth sounding on the Vatnajokull ice-cap, Iceland'. Proc. Conf. on Int. Karakoram Proj., 1980, Vol.1, pp. 126–134 (see also pp. 111–125)

[19] DONG, Z.-B., FERRARI, R. L., FRANCIS, M. R., MUSIL, G. J., OSWALD, G. K. A., and ZHANG, X.-S.: 'Impulse radar sounding on the Hispar glacier'. Proc. Conf. on Int. Karakoram Proj., 1980, Vol. 1, pp. 100–110

[20] ELLERBRUCH, D. A., and BOYNE, H. S.: 'Snow stratigraphy and water equivalence measured with an active microwave system', *J. Glaciol.*, 1980, **26**, (94), pp. 225–233

[21] FUJINO, K., WAKAHAMA, G., SUZUKI, M., and MATSUMOTO, T.: 'Snow stratigraphy measured with an active microwave sensor'. Proc. IEE Int. Symp. Ant. & Prop., 1985, pp. 671–674

[22] SAKAMOTO, Y., and AOKI, Y.: 'An under snow radar using microwave holography'. Proc. Int. Symp. Ant. and Prop., Japan, 1985, pp. 659–661

[23] YANKIELUN, N. E., ARCONE, S. A., and CRANE, R. K.: 'Thickness profiling of freshwater ice using a millimeter-wave FM-CW radar', *IEEE Trans. Geosci. Rem. Sens.*, 1992, **80**, (5), pp. 1094–1100

[24] BOGORODSKY, V. V., BENTLEY, C. R., and GUDMANDSEN, P. E.: 'Radioglaciology' (D. Reidel, Dordrecht, Holland, 1985)

[25] JACOBEL, R. W., and HODGE, S. M.: 'Radar internal layers from the Greenland summit', *Geophys. Res. Lett.*, 1995, **22**, (5), pp. 587–590

[26] FAHENSTOCK, M., ABDALATI, W., LUO, S., and GOGINENI, S.: 'Internal layer tracking and age-depth-accumulation relationships for the northern Greenland ice sheet', *J. Geophys. Res.*, 2001, **106**, (D24), pp. 33 789–33 797

[27] ARCONE, S. A., and YANKIELUN, N. E.: '1.4-GHz radar penetration and evidence of drainage structures in temperate ice: Black Rapids Glacier, Alaska, U.S.A.', *J. Glaciol.*, 2000, **46**, (154), pp. 477–490

[28] ARCONE, S. A., and DELANEY, A. J.: 'GPR images of hidden crevasses in Antarctica'. Proc. Eighth Int. Conf. on Ground-penetrating radar, 23–26 May 2000, Gold Coast, Australia

[29] ARCONE, S. A., LAWSON, D. E., and DELANEY, A. J.: 'Short-pulse radar wavelet recovery and interpretation of dielectric contrasts within englacial and basal ice of the Matanuska Glacier, Alaska, U.S.A.', *J. Glaciol.*, 1995, **41**, (137), pp. 68–86

[30] MORAN, M. L., GREENFIELD, R. J., ARCONE, S. A., and DELANEY, A. J.: 'Delineation of a complexly dipping temperate glacier bed using short-pulse radar arrays'. *J. Glaciol.*, 2000, **46**, (153), pp. 274–286

[31] ARCONE, S. A.: 'High resolution of glacial ice stratigraphy: A ground-penetrating radar study of Pegasus Runway, McMurdo Station, Antarctica', *Geophysics*, 1996, **61**, (6), pp. 1653–1663

[32] GOGINENI, S., CHUAH, T., ALLEN, C., JEZEK, K., and MOORE, R. K.: 'An improved coherent radar depth sounder', *J. Glaciol.*, 1998, **44**, (148), pp. 659–669

[33] ARCONE, S. A., YANKIELUN, N. E., and CHACHO, E. F. Jr.: 'Reflection profiling of arctic lake ice using microwave FM-CW radar', *IEEE Trans. Geosci. Rem. Sens.*, 1997, **35**, (2), pp. 436–443

[34] RICHARDSON, C., AARHOLT, E., HAMRAN, S.-E., HOLMLUND, P., and ISAKSSON, E.: 'Spatial distribution of snow in western Dronning Maud Land, East Antarctica, mapped by a ground-based snow radar', *J. Geophys. Res.*, 1997, **102** (B9), pp. 20 343–20 353

[35] ARCONE, S. A.: 'Numerical studies of the radiation patterns of resistively loaded dipoles', *J. Appl. Geophys.*, 1995, **33**, pp. 39–52

[36] VAUGHN, D. G., CORR, H. F. J., DOAKE, C. S. M., and WADDINGTON, E. D.: 'Distortion of isochronous layers in ice revealed by ground-penetrating radar', *Nature*, 1999, **398**, 25 March, pp. 323–326

[37] KANAGARATNAM, P., GOGINENI, S. P., GUNDESTRUP, N., and LARSEN, L.: 'High-resolution radar mapping of internal layers at NGRIP', *J. Geophys. Res.*, 2001, **106**, (D24), 33 799–33 811

[38] GOW, A. J., and ROWLAND, R.: 'On the relationship of snow accumulation to surface topography at "Byrd Station," Antarctica', *J. Glaciol.*, 1965, **5**, (42), pp. 843–847

[39] MOSLEY-THOMPSON, E., THOMPSON, L. G., PASKIEVITCH, J. F., POURCHET, M., GOW, A. J., DAVIS, M. E., and KLEINMAN, J.: 'Recent increase in South Pole snow accumulation', *Ann. Glaciol.*, 1995, **21**, pp. 131–138

[40] ARCONE, S. A.: 'Stratigraphic profiling of Antarctic firn with 400-MHz GPR at 1500 ns. Proc. Ninth Int. Conf. on Ground-penetrating radar, 29 April–2 May 2002, Santa Barbara, CA

[41] ARCONE, S. A., MAYEWSKI, P. A., and HAMILTON, G.: 'Stratigraphic profiling of the West Antarctic firn regime with 400-MHz GPR'. Proc. 71st Annual Mtg. Society of Exploration Geophysicists, San Antonio, TX, 10–14 Sept. 2001

[42] FUJITA, S., MAENO, H., URATSUKA, S., FIRIKAWA, T., MAE, S., FUJI, Y., and WATANABE, O.: 'Nature of radio echo layering in the Antarctic ice sheet detected by a two-frequency experiment', *J. Geophys. Res.*, 1999, **104**, (B6), pp. 13 013–13 024

[43] SHABTAIE, S., and BENTLEY, C. R.: 'Electrical resistivity sounding of the East Antarctic Ice Sheet', *J. Geophys. Res.*, 1995, **100**, (B2), pp. 1933–1954

[44] MOORE, J. C.: 'Dielectric variability of a 130 m Antarctic ice core: implications for radar sounding', *Ann. Glaciol.*, 1988, **11**, pp. 95–99

[45] SHUMAN, C. A., ALLEY, R. B., and ANANDAKRISHNAN, S.: 'Characterization of a hoar-development episode using SSM/I brightness temperatures in the vicinity of the GISP2 site, Greenland', *Ann. Glaciol.*, 1993, **17**, pp. 183–188

[46] SHUMAN, C. A., ALLEY, R. B., FAHNESTOCK, M. A., FAWCETT, P. J., BINDSCHADLER, R. A., WHITE, J. W. C., GROOTES, P. M., ANANDAKRISHNAN, S., and STEARNS, C. R.: 'Detection and monitoring of stratigraphic markers and temperature trends at the Greenland Ice Sheet Project 2 using passive-microwave remote-sensing data', *J. Geophys. Res.*, 1997, **102**, (C12), pp. 26 877–26 886

[47] ARCONE, S. A.: 'Airborne-radar stratigraphy and electrical structure of temperate firn: Bagley Ice Field, Alaska', *J. Glaciol.*, 2002, **48**, (161), pp. 317–334

[48] BJØRNSSON, H., ERLINGSSON, B., GJESSING, Y., HAGEN, J. O., HAMRAN, S.-E., and LIESTØL, O.: 'Temperature regime of sub-polar glaciers mapped by multi frequency radio echo sounder', *J. Glaciol.*, 1996, **42**, (4), pp. 23–32

[49] HAMRAN, S.-E., GJESSING, D. T., HJELMSTAD, J., and AARHOLT, E.: 'Ground penetration synthetic pulse radar; dynamic range and modes of operation', *J. Appl. Geophys.*, 1995, **33**, pp. 7–14

[50] ODEGARD, R. S., HAMRAN, S.-E., BØ, P. H., ERTZELMULLER, B., VATNE, G., and SOLLID, J. L.: 'Thermal regime of valley glacier, Erikbreen, Northern Spitsbergen', *Polar Res.*, 1992, **11**, (2), pp. 69–76

[51] HAMRAN, S.-E., AARHOLT, E., HAGEN, J. O., and MO, P.: 'Estimation of relative water content in a sub-polar glacier using surface-penetration radar', *J. Glaciol.*, 1996, **42**, (142), pp. 533–537

[52] ODEGARD, R. S., HAGEN, J. O., and HAMRAN, S.-E.: 'Comparison of radio-echo sounding (30–1000 {MHz}) and high-resolution borehole-temperature measurements at Finsterwalderbreen, southern Spitsbergen, Svalbard', *Ann. Glaciol.*, 1997, **24**, pp. 262–267

[53] HAMRAN, S.-E., ERLINGSSON, B., GJESSING, Y., and MO, P.: 'Estimate of the sub glacier dielectric constant of an ice shelf using a ground-penetrating step-frequency radar', *IEEE Trans. Geosci. Rem. Sens.*, 1998, **36**, (2), pp. 518–525

[54] SMITH, B. M. E., and EVANS, S.: 'Radio echo sounding: absorption and scattering by water inclusion and ice lenses', *J. Glaciol.*, 1972, **11**, (61), pp. 133–146

[55] GOODMAN, R. H.: 'Radio echo sounding on temperate glaciers', *J. Glaciol.*, 1975, **14**, (70), pp. 57–69

[56] BAMBER, J. L.: 'Internal reflecting horizons in the Spitsbergen glaciers', *Ann. Glaciol.*, 1987, **9**, pp. 5–10

[57] KOTLYAKOV, V. M., and MACHERET, Y. Y.: 'Radio-echo-sounding of sub-polar glaciers in Svalbard: some problems and results of Soviet studies', *Ann. Glaciol.*, 1987, **9**, pp. 151–158

[58] BAMBER, J. L.: 'Ice/bed interface and englacial properties of Svalbard ice masses deduced from airborne radio-echo data', *J. Glaciol.*, 1989, **35**, (119), pp. 30–37

[59] HAMRAN, S.-E., HAGEN, J. O., and ODEGARD, R. S.: 'Glacier radar sounding using multiple frequency bands'. GPR 2000 8th Int. Conf. on Ground-penetrating radar, SPIE Vol. 4084, 2000, pp. 218–221

[60] COOK, J. C.: 'Radar transparencies of mine and tunnel rocks', *Geophys.*, 1975, **40**, pp. 865–885

[61] UNTERBERGER, R. R.: 'Radar and sonar probing of salt'. 5th Int. Symp. on Salt, 1978, Hamburg (Northern Ohio Geological Society), pp. 423–437

[62] UNTERBERGER, R. R.: 'Radar and sonar probing of rocks', *Trans. Soc. Min. Eng. AIME*, 1985, **276**, pp. 1864–1874

[63] RALSTON, J. C., HAINSWORTH, D. W., and McPHEE, R. J.: 'Application of ground penetrating radar for coal thickness measurement'. Proc. TENCON '97, IEEE Region 10 Annual Conf. on Speech and image technologies for computing and telecommunications, 2–4 December 1997, Vol. 2, pp. 835–838

[64] CHUFO, R. L.: 'Noncontacting coal and rock thickness measurements with a vector network analyser'. Proc. RF Expo East Conf., Tampa, FL, USA, 22–24 September 1992, pp. 41–50

[65] DANIELS, D. J.: 'Short-pulse radar for stratified lossy dielectric layer measurement', *IEE Proceedings F. Communications, Radar and Signal Processing*, 1980, **127**, pp. 371–379

[66] SATO, M., OKUBO, T., and NIITSUMA, H.: 'Cross polarization borehole radar measurements with a slot antenna', *Journal of Applied Geophysics*, 1995, **33**, (1-3), pp. 53–61

[67] MIWA, T., SATO, M., and NIITSUMA, H.: 'Subsurface fracture measurement with polarimetric borehole radar', *IEEE Trans. Geosci. Remote Sensing*, 1999, **37**, (2), pp. 828–837

[68] SATO, M., and MIWA, T.: 'Polarimetric borehole radar system for fracture Measurement,' *Subsurface Sensing Technologies and Applications*, 2000, **1**, (1), pp. 161–174

[69] MOTT, H.: 'Antennas for Radar and Communications' (John Wiley & Sons, New York, 1992)

[70] YAMAGUCHI, Y., NISHIKAWA, T., SENGOKU, M., and BOERNER, W. M.: 'Two dimensional and full polarimetric imaging by a synthetic aperture FM-CW radar', *IEEE Trans. Geosci. Remote Sensing*, 1995, **33**, pp. 421–427

[71] KUNZ, K., and LUEBBERS, R.: 'The Finite Difference Time Domain for Electromagnetics' (CRC Press, Boca Raton, 1993)

[72] SATO, M., and TAKESHITA, M.: 'Estimation of Subsurface Fracture Roughness by Polarimetric Borehole Radar', *IEICE Trans. Electronics*, 2000, **E83-C**, (12), pp. 1881–1888

[73] YEE, K. S.: 'Numerical Solution of Initial Boundary Value Problem Involving Maxwell's Equation in Isotropic Media', *IEEE Trans. Antennas Propagt.*, 1966, **AP-14**, (3), pp. 302–307

[74] PHU, P., ISHINARU, A., and KUGA, Y.: 'Copolarized and cross-polarized enhanced backscattering from Two-dimensional very rough surface at Millimeter Wave Frequencies', *Radio Science*, 1994, **29**, (5), pp. 1275–1291

[75] OH, Y., SARABANDI, K., and ULABY, F.: 'An Empirical Model and an inversion technique for radar scattering from bare soil surfaces', *IEEE Trans. Geosci. Remote Sensing*, 1982, **30**, (2), pp. 370–381

[76] ULABY, F., BATLIVALA, P., and DOBSON, M.: 'Microwave backscatter dependence on surface roughness, soil moisture, and soil texture: Part I-bare soil', *IEEE Trans. Geosci. and Remote Sensing*, 1978, **GE-16**, (4), pp. 286–295
[77] LANE, J. W. Jr., HAENI, F. P., and PLACZEK, G.: 'Use of borehole-radar methods to detect a saline tracer in fractured crystalline bedrock at Mirror Lake, Grafton County, New Hampshire, USA', Proceedings of 6th International Conf. on *Ground penetrating Radar*, Sendai, Japan, 1996, pp. 185–190
[78] http://www.es.usyd.edu.au/Research_centres/res_centres.html
[79] http://www.emss.co.za/
[80] INGGS, M. R., MUKHOPADHYAY, K. P., and WILKINSON, A. J.: 'Borehole interferometric SAR: a preliminary simulation study'. *Proc. IEEE Geoscience Remote Sensing Symp., IGARSS'01*, Sydney, Australia, July 2001
[81] MASON, I. M., LIU, Q., OSMAN, N., and ZHOU, L. M.: 'Broadband synthetic aperture borehole radar interferometry'. GPR2000, Brisbane, May 2000
[82] MASON, I. M., HARGREAVES, J. E., CLAASSEN, D. M., GREENHALGH, S. A.: 'Evolution of a slimline borehole radar'. GPR2000, Brisbane, May 2000
[83] TURNER, G., MASON, I. M., HARGREAVES, J. E., and WELLINGTON, A.: 'Borehole radar surveying for orebody delineation'. Australian IMM Conference, April 2000
[84] TRICKETT, J. C., MASON, I., HARGREAVES, J., STEVENSON, F., and MEYERING, M.: 'The application of borehole radar to South Africa's ultra-deep gold mining environment'. GPR2000, Brisbane, May 2000
[85] MASON, I. M., ZHOU, B., HARGREAVES, J. E., and CLAASSEN, D. M.: 'Borehole radar study of contaminated karsts beneath an old nitrocellulose factory'. Proc. Int. Symp. Engineering & environmental geophysics, Chengdu, 1997, pp. 181–188
[86] CLAASSEN, D. M., BANSAL, R., MASON, I. M., and HARGREAVES, J. E.: 'Resistively loaded insulated antennas for narrow borehole radar'. Proc. IEEE Int. Symp. Geoscience & Remote Sensing, Firenze, 1995
[87] ROBERTS, M. K., and SCHWEITZER, J. K.: 'Geotechnical areas associated with the Ventersdorp Contact Reef, Witwatersrand Basin, South Africa', *Journal of the South African Institute of Mining and Metallurgy*, 1999
[88] McWHA, M.: 'The geomorphology of the Ventersdorp Contact Reef at Western Deep Levels South Gold Mine', Ext. Abstr., VCR Symp., 1988

11.17 Bibliography

ALBERT, M. R., KOH, G., and PERRON, F.: 'Preferential melt pathway in a natural snow pack', *Hydrol. Process.*, 1999, **13**, pp. 2991–3000
ARCONE, S. A., LAWSON, D. E., MORAN, M. L., and DELANEY, A. J.: '12–100 MHz depth and stratigraphic profiles of temperate glaciers'. Proc. Eighth Int. Conf. on Ground-penetrating radar, 23–26 May 2000, Gold Coast, Australia

CLARKE, T. S., and BENTLEY, C. R.: 'High-resolution radar on Ice Stream B2, Antarctica: measurements of electromagnetic wave speed in firn and strain history from buried crevasses', *Ann. Glaciol.*, 1994, **20**, pp. 153–159

CUMMING, W. A.: 'The dielectric properties of ice and snow at 3.2 centimeters', *J. Appl. Phys.*, 1952, **23**, (7), pp. 768–773

HAMRAN, S.-E., GUNERIUSSEN, T., HAGEN, J. O., and ODEGARD, R.: Proc. IEEE Int. Conf., Geoscience and Remote Sensing (IGARSS '97), 'Remote sensing – a scientific vision for sustainable development', 1997, 3–8 August 1997, Vol. 2, pp. 634–636

HEMPEL, L., THYSSEN, F., GUNDESTRUP, N., CLAUSEN, H. B., and MILLER, H.: 'A comparison of radio-echo sounding data and electrical conductivity of the GRIP ice core', *J. Glaciol.*, 2000, **46**, (154), pp. 369–374

HOLMGREN, J., STURM, M., YANKIELUN, N. E., and KOH, G.: 'Extensive measurements of snow depth using FMCW radar'. *Cold Reg. Sci. Technol.*, 1998, **27**, (1), pp. 17–30

KOH, G., YANKIELUN, N. E., and BAPTISTA, A. I.: 'Snow cover characterization using multiband FMCW radars', *Hydrol. Process.*, 1996, **10**, pp. 1609–1617

KOH, G., and JORDAN, R.: 'Sub-surface melting in a seasonal snow cover', *J. Glaciol.*, 1995, **41**, pp. 474–482

KOH, G.: 'Effect of wind on FMCW radar backscatter from a wet snow cover', *IEEE Trans. Geosci. Rem. Sens.*, 1992, **30**, (3), pp. 619–621

LAWSON, D. E., STRASSER, J. C., EVENSON, E. B., ALLEY, R. B., LARSON, G. J., and ARCONE, S. A.: 'Glaciohydraulic supercooling: a freeze-on mechanism to create stratified, debris-rich basal ice: I. Field evidence', *J. Glaciol.*, 1998, **44**, (148), pp. 547–562

LEGRAND, M., and MAYEWSKI, P. A.: 'Glaciochemistry of polar ice cores: A review', *Rev. Geophys.*, 1997, **35**, pp. 219–245

LI, S., and STURM, M.: 'Patterns of wind-drifted snow on the Alaskan Arctic slope detected with ERS-1 interferometric SAR', *J. Glaciol.*, in press

MORAN, M. L., GREENFIELD, R. J., ARCONE, S. A., and DELANEY, A. J.: 'Multidimensional GPR array processing using Kirchhoff migration', *J. Appl. Geophys.*, 2000, **43**, pp. 281–295

MORAN, M. L., GREENFIELD, R. J., and ARCONE, S. A.: 'Modeling GPR radiation and reflection characteristics for a complex temperate glacier bed', *Geophys.*, 2003, **68**, (2), pp. 559–565

RETZLAFF, R., and BENTLEY, C. R.: 'Timing of stagnation of Ice Stream C, West Antarctica, from short-pulse radar studies of buried surface crevasses', *J. Glaciol.*, 1993, **39**, (133), pp. 553–561

STURM, M., HOLMGREN, J., and PEROVICH, D. K.: 'Winter snow cover on the sea ice of the Arctic Ocean at the surface heat budget of the Arctic Ocean (SHEBA): Temporal evolution and spatial variability', *J. Geophys. Res.*, 2002, **48**, (163), pp. 495–504

Chapter 12

Mine detection

12.1 Introduction

Ground penetrating radar is one of a number of technologies that has been extensively researched as a means of improving mine detection efficiency. It is useful to provide a background to both the civil and military programmes which involve the technology of GPR. The military programmes are largely based on the requirement to maintain the pace of military operations and have different requirements in terms of speed and detection performance to civil or humanitarian programmes. This Chapter will concentrate mainly on humanitarian applications, although where appropriate reference to national military programmes will be made. Further reading on the mine issue can be found in the following references: 'A guide to mine action' (GICHD, 2003), 'Mine action equipment study of global needs' (GICHD, 2002) and 'International mine action standards' (GICHD CD ROM). A detailed analysis is given in 'Hidden killers' [1], for example.

At the International Workshop of Technical Experts on Ordnance Recovery and Disposal in the Framework of International Demining Operations held in Stockholm, Sweden, 8–10 June 1994, arranged by the Swedish FOA, in co-operation with the United Nations Under-Secretary General for Humanitarian Affairs, the United Nations High Commissioner for Refugees summarised the situation as follows.

Landmines are a humanitarian challenge because they indiscriminately kill and maim civilians. Landmines are weapons that cannot distinguish between a soldier and a civilian, and they remain active for decades. As a result, most of the victims of mines are innocent men, women and children. Landmines are a humanitarian challenge to UNHCR because they are used in so many conflicts, in such large numbers and so indiscriminately that during war they are a cause of displacement, and after hostilities they endanger the lives of returnees and humanitarian aid workers, delay return and impede reintegration and reconstruction. Landmines are also being used in current conflicts to block humanitarian access. Since that workshop the history

of international actions towards a mine-free world has been driven by many factors, which are described below.

The overall political and legal framework is covered by the Ottawa Treaty, which was signed in December 1997. All signatories who have ratified the Treaty have committed to report to the Secretary-General of the UN on their progress in destroying their stockpiled mines by 1 March 2003 (Article 4) and destroying all mines in the territories under their jurisdiction by 1 March 2009 (Article 5). The provisions of the Ottawa Treaty, which has become international law, provide an impetus to the development and procurement of more efficient mine detection and disposal techniques. Further details of the landmine situation can be found in the 'Landmine monitor report' [2] and 'Hidden killers' [1].

Mines can be either buried or surface laid. They are emplaced by a variety of techniques, including being scattered on the surface by vehicles or helicopters. Thus mines may be found in regular patterns, or in irregular distributions. Where environmental conditions result in soil erosion and movement caused by rain over several seasons the mines may be lifted and moved to new locations and can be covered or exposed. Mines are encountered in desert regions (i.e. Somalia, Kuwait), mountains (i.e. Afghanistan, El Salvador), jungles (i.e. Cambodia, Vietnam) as well as urban areas (i.e. Beirut, Former Yugoslavia). The variety of mines that can be encountered is considerable and details can be found on the US Department of Defense CD Minefacts ©, which contains details of over 675 landmines, as well as the US Department of Defense, Naval Explosive Ordnance, CD Ordata ©, which is a guide to UXO identification or many of the websites of Mine Action Centres and nongovernmental organisations (NGOs).

The variety of environmental conditions in which mines can be found is enormous. Minefields are not only neat ordered rows of mines in flat deserts but can also be found among the debris of burnt-out buildings and post-conflict urban and rural environments. An example of a cleared minefield situation is shown in Figure 12.1. Clearly, mine detection equipment has to be designed to work in a wide range of physical environments, and the statement of operational requirements issued by end-users will reflect this need. Detection equipment must be able to be operated in climatic conditions, which range from arid desert, hillside scree to overgrown jungle. Ambient operating temperatures can range from below −20°C to 60°C. Rain, dust, humidity and solar insolation must all be considered in the design and operation of equipment. The transport conditions of equipment can be arduous, and these, as well as man–machine interface issues, are vitally important to the design of detectors.

In general, most pressure sensitive mines are not designed to operate when buried deeply. The overburden ground material acts as a mechanical bridge and inhibits triggering of the detonator mechanism and also reduces the force of the explosion. This fact is often taken into account in the specification of performance for a mine detector. For example, a hand-held mine detector should be able to detect AT mines at depths up to 300 mm and AP mines at depths up to 100 mm with spacing between the detector head and ground surface of 100 mm. Vehicle based close-in mine detectors generally require a greater ground clearance. However, mines can be encountered at

Figure 12.1 Cleared minefield in the Republic of Serbska (courtesy ERA Technology)

depth well beyond the range of most detection systems. Mine detection systems can be employed in several different roles: for close-in hand-held detection, for vehicle mounted stand-off detection or as a remote sensor mounted on low flying fixed or rotary wing aircraft. These are mostly synthetic aperture radars (SAR).

The need for improved products to achieve greater efficiency and lower costs per metre cleared has been identified. However, it is not clear whether the international political and legal framework has really resulted in an impetus to facilitate more efficient demining techniques.

The new technology product(s) being offered must offer good detection performance, significant improvements in false alarm rate over current technology, must be simple and easy to use, in all countries, and not significantly more expensive on a sensor to sensor basis than current metal detectors. New sensors should detect minimum metal/nonmetallic mines and ideally the explosive contained therein.

The way forward, based on the feedback from an end-user survey as well as consideration of a wide range of technical issues, suggests that the ideal detector will comprise a minimum metal mine detector in combination with an explosive detector. Technically this is possible, but reliable explosive detection technology may not meet cost, weight or low power requirements. However, it is technically feasible to develop a combined metal detector and minimum metal detector that meets simplicity of operation, cost, weight, low power requirements and achieves the goal of significant reduction of false alarms.

Considerable efforts are being made on a world-wide basis to develop a solution to the problem of mine detection both for military and humanitarian applications. National Military Organisations, Universities, Industrial Research and Technology Organisations as well as private companies are conducting these programmes. Among the leading contacts for the dissemination of information in the United States are the US Department of Defence, DARPA, Minawara, James Madison University, etc. (see References [3, 4], for example). Information can also be obtained from the United Nations, particularly concerning field operations and statements of operational requirements. In Europe the European Commission Joint Research Centre (JRC) has implemented a network of excellence (ARIS) which acts as a focal point for interchange between active research members (see Reference [5]). This group also has links to the Nordic NRDF. Many European research and development programmes for humanitarian demining are co-ordinated and supported by both the European Commission and by various European industrial partners via Esprit and other projects. Information on European Commission support for research and development (R&D) on demining can be found on a CD produced by the JRC. The proceedings of the JRC De-mining Technologies Conference held in Sept/Oct 1998 provides useful references to the R&D activities of the majority of the international participants. EUREL, via the IEE in the UK, has organised several conferences each held in Edinburgh in 1996 and 1998 on the subject of research and development [6, 7] (see also Reference [8]). Information on research publications can be found from organisations such as SPIE, IEEE and IEE, and are included in their proceedings, transactions and conference publications. Recent publications on the design, technology and signal and image processing of GPR mine data are given in References [9–56]. The author has also presented developments in GPR technology for mine detection in Daniels [57–78]. More recent conferences such as Scot-Eudem Brussels [79] contain current papers on GPR technology and applications.

Unfortunately, and in spite of considerable research funding, a plethora of publications and periodic bursts of marketing enthusiasm, at the time of writing very little technology has been placed in the hands of the humanitarian deminer. The reasons for this are simple.

There is no conventional commercial market for humanitarian demining products. The real budget holders are the donor governments, and the multiplicity of donors, decision-makers and end-users, who all have different agendas, has resulted in a lack of a clear specification for equipment required. As a result, and over nearly a decade, the scientific and technical communities in many nations have all carried out programmes which might be considered to be largely duplicative. In many cases, the lack of thorough literature searches by the academic researchers has compounded the problem. Lessons learned in the 1970s and earlier have been subsequently relearned at considerable additional time and expense.

The European Commission has funded 50% of the cost of various humanitarian research programmes. The total cost of the EU research programmes has exceeded 55M€ and, while this has provided regular technical conferences and many technical papers, hardly any of the programmes have resulted in production

or even pre-production equipment. This may have been because of a fundamental lack of appreciation of the process of equipment development by the administrators. The sanguine assumption has been that an influx of pump-priming research funding into multi-partner, academically biased, consortia will result in field-usable products.

Such programmes are often unable do this because a large proportion of the academic organisations involved do not have the capability to design, produce and deliver field-usable equipment to acceptable standards. Whether these standards are environmental, EMC, performance, reliability, etc. is less important than the realisation that the vast majority of the research humanitarian R&D programmes are unlikely to ever deliver production technology to the deminer.

The consequence of this is that, despite the high profile of demining research, those carrying out demining still have not received any significant technology improvement over the current generation of metal detectors. This is a critical issue and needs to be addressed by the national policy-makers and fund-holders. The side-effect of the failure to deliver new technology to the deminer in the minefield is a loss of credibility in the research and development fraternity by the deminers. It has always been 'jam tomorrow'.

This does not mean that there is no hope that deminers will receive better tools, and it is quite possible that these will be based on radar technology. However, the mechanism does not exist at present to design, develop, manufacture, supply and carry out in-service upgrades for products for a niche market whose timescales do not fit normal commercial product development parameters. It is also considered that the market size and take-up rates do not lead to economical large-scale production runs. New detectors will only be developed and produced if there is direct and full funding for the costs of development and production, as the unique nature of the market does not meet any normal criteria for commercial investment decisions. This issue was discussed by Newnham and Daniels [80].

The challenge that faces those committed to improving the efficiency of humanitarian demining operations, by means of the provision of new and more effective detection technology, concerns bridging the gap between research concept and product. As long as technology remains at the stage of the research prototype, the deminer is denied the benefit of more effective detection.

The starting point in terms of the humanitarian end-user is defined by the UN Statement of Requirement:

> 'The area should be cleared of mines and UXOs to a standard and depth, which is agreed to be appropriate to the residual/planned use of the land and which is achievable in terms of the resources and time available. The contractor must achieve at least 99.6% of the agreed standard of clearance. The target for all UN sponsored clearance programmes is the removal of all mines and UXO to a depth of 200 mm' [81].

The scope of the problem can be illustrated by the experience in Afghanistan, one of the countries most seriously affected by mines. According to the Mine Clearance Planning Agency, over a 15 year period an estimated 20 000 civilians have been killed

and 400 000 wounded by landmines. The current rate is 4000 killed and another 4000 wounded annually. The UN has been making a dedicated effort to clear the 9 million mines. Since 1989, 34 km^2 of land have been cleared of 63 000 mines. The annual cost runs to US$ 15 million to clear 13 km^2. Treatment and rehabilitation averages $5000 per victim.

Afghanistan is not unique. There are an estimated 60–100 million mines in place in 62 countries. Some of the most affected are countries that are or have been of concern to UNHCR, such as Angola, with 9–14 million mines, Cambodia with 8–10 million and Mozambique with over 1 million. The casualties are correspondingly high. The estimated number of people who have had limbs amputated by mines in Cambodia is 30 000, in Mozambique it is 8000, while in Angola the figure for just lower limbs is 15 000. Worldwide, landmines are taking 800 lives each month, according to the International Committee of the Red Cross.

The large majority of civilian casualties are caused by anti-personnel mines, which come in a wide variety of types. Many are designed only to maim. The blast-type anti-personnel mine will cause a traumatic amputation to a foot or leg, often injuring the other leg and genitals as well. Fragmentation mines are far more deadly. Some models shoot hundreds of metal fragments in an arc that reaches out 50 m. Other types spring into the air when triggered and then explode at waist level. Anti-personnel mines can be buried in the ground or placed on the surface and can be set off by pressure, trip wire, remote control or sensors. They can be laid by hand, dropped from airplanes or spread by artillery. Many are made of plastic, which means they cannot be located by metal detectors during clean-up operations.

Anti-vehicle mines are less numerous but more powerful. A mine that can disable a tank will destroy a civilian vehicle and kill its occupants. These mines usually cannot be detonated by a person's body weight alone, although when they are fitted with an anti-handling device they become anti-personnel weapons. Anti-vehicle mines are a particular threat to humanitarian aid workers, who must travel on roads before they have been systematically cleared.

The situation for the military requirement is much more straightforward. Most military programmes have clear requirements and well organised procedures for the procurement of equipment.

This Chapter will review the various National Programmes with specific reference to radar techniques and will provide a description of a cross-section of various programmes, both military and humanitarian. It will then consider some issues related to test methodologies, basic detection principles and will then describe several projects that appear to be high on a technology readiness level.

12.2 Humanitarian and military national programmes

In this Section a very brief overview of the various national humanitarian and military programmes that relate to GPR technology is provided.

12.2.1 Australia

Dr Alan Rye
Head, Countermine Technologies, Weapons Systems Division DSTO Edinburgh Australia

The Australian national programme comprises hand-held and vehicle mounted developments. The HILDA Dual Sensor Hand-Held Mine Detection System is based on the pairing of a Minelab F1A4 metal detector with a developmental GPR designed and fabricated by the Australian Commonwealth Scientific and Industrial Research Organisation (CSIRO). Integration and software development has been managed by DSTO. The system was originally developed in 1996, and has shown promising performance. A recent software and hardware upgrade has been carried out. This GPR is an impulse GPR of unique design, using CSIRO's proprietary technology, which is adapted to produce a uniquely low-noise and low-cost GPR. The GPR is designed with interchangeable antennas with centre frequencies of 800 MHz, 1.2 and 1.6 GHz. Bandwidth is approximately 80% of centre frequency. The GPR has been used in conventional, differential and bistatic modes. The system transfers its sensor data to a separately carried laptop PC, where basic processing is carried out with visual output to an LCD VGA display or to a commercial HUD. No further fusion is implemented. The system has not been evolved beyond its developmental status. Plans exist to upgrade the metal detection element to the current Minelab F3 model, and to improve data acquisition, detection and display performance, as well as implementing limited data fusion. Funding to initiate this program has been programmed by the Australian Army as part of its Land 144 acquisition plans.

The vehicle based programme entitled RRAMNS was funded June 2000 and has been vigorously pursued since. It is intended as a demonstration unit to allow the development of underlying technologies prior to adoption by the Australian Defence Force. The RRAMNS CTD system includes the Minelab STMR (single transmit, multiple receive) metal detector, the GeoCenters Model 403 GPR array and three commercial cameras. It is designed to detect over a 3 m track width. The GPR is an impulse GPR design, covering the frequency range of 0.7–1.3 GHz. The system implements GeoCenters' 'energy focusing' approach with programmable time-gated selection of transmit/receive groups. The IR cameras are Inframetrics units, spanning the usual 3–5 μm and 8–12 μm regions. A conventional commercial video camera covers the visible region. A precise position and timing system using GPS, a road wheel and a digital compass maintains local registration of detection data to an accuracy of a few centimetres, through a combination of differential GPS and derived dead reckoning. Electronic integration and data fusion software is furnished by Tenix Defence Systems, implementing approaches and algorithms evolved by DSTO and Tenix.

The system is fitted to a purpose designed trolley, which is pushed ahead of a medium-sized 4WD truck. The trolley is substantially nonmetallic ahead of its wheels, maximising the performance of the metal detector. The RRAMNS system had its first major trials in May 2003, and will be the test-bed for developing system concepts for the Australian Army's Land 133 Project.

The RRAMNS CTD project is regarded as one of the most successful CTD projects in the Australian Defence Department, and will undergo evolutionary development, mostly in software areas, during the next few years, as its technology is transferred into production for the Australian Defence Force.

12.2.2 Belgium

Prof. Marc Acheroy
Royal Military Academy

In 1996, a Belgian project on humanitarian demining (HUDEM) was initiated by the Belgian Ministry of Defence and is supported by the Belgian Ministry of Defence and the Belgian State Secretariat for Development Aid. It is carried out in collaboration with laboratories of other Belgian universities and co-ordinated by the Royal Military Academy (RMA). The research project aims at contributing in solving the anti-personnel landmine problem by funding research grants devoted to basic research on mine detection. In the scope of the HUDEM project the work on GPR is mainly done by the Royal Military Academy, the 'Université Catholique de Louvain' (UCL) and the 'Vrije Universiteit Brussel' (VUB).

In the SIC laboratory of the RMA a study was carried out on the use of an ultra-wideband GPR for the detection of anti-personnel landmines [82]. Three main contributions have been made in association with this study. First a dielectric-filled TEM horn was developed and tested. It was found that the dielectric-filled TEM horn is a good candidate for an ultra-wideband GPR as it is capable of radiating and receiving very fast transient pulses, without too much ringing. A second main contribution was made in the domain of system modelling. In this study the whole system, i.e. GPR system, ground and target, is described in the time domain by considering it as a cascade of linear responses, resulting in a *time domain GPR range equation*. Finally, a novel migration method is proposed that integrates the time domain model of the GPR in the migration scheme. A synthetic 3D point spread function of the GPR, i.e. a synthetic C-scan of a small point scatterer, is calculated by forward modelling. The 3D point spread function, containing system characteristics like the waveform of the excitation source, the combined antenna footprint and the impulse response of the antennas, is then used to deconvolve the recorded data. Results of this migration method on real data obtained by an ultra-wideband GPR system show that the migration method is able to reconstruct the top contour of small targets like AP mines, in some cases even with the correct dimensions. The method is also capable of migrating oblique targets into their true position. The migration scheme is not computationally intensive and can easily be implemented in real time.

In the EMIC laboratory of the UCL, promising advances have been made on the forward and inverse modelling of the radar signal for identifying the soil dielectric properties [83, 84]. The method relies on a specifically designed GPR consisting in an ultrawide band (UWB) stepped frequency continuous wave (SFCW) radar combined with a monostatic TEM horn antenna to be used off-ground. Additionally to its high mobility, this radar configuration allows for an accurate and efficient modelling of

the radar–antenna–sub-surface system, which is based on linear system components in series and parallel describing the antenna, and on the exact solution of the three-dimensional Maxwell equations for wave propagation in a horizontally multilayered medium representing the shallow sub-surface. The model was validated in laboratory conditions on a tank filled with a two-layered sand subject to different water content levels. The model agreed very well with the measurements and the soil dielectric properties were accurately determined from the GPR signal inversion. Henceforth the antenna model constitutes a field-usable tool to improve sub-surface sensing using monostatic GPR. Yet research on the soil dielectric characterisation and mine identification still pertain to concept demonstrators that have to be progressively improved and validated in conditions closer to the reality.

In the ETRO-IRIS Department of the VUB, two research topics were pursued during the HUDEM project, namely GPR data processing and object classification and imaging. For object characterisation/classification a five step scheme was implemented. Starting from GPR data acquired over an area, the first processing block corresponds to a *pre-processing* phase consisting in estimating and removing the clutter, followed by a *detection* phase allowing the detection of the scatter due to the presence of an object. From the detected samples, temporal and frequential *features* are estimated to characterise the object, which in turn are used to *classify* the detected object. The classification is based on the parametric and/or nonparametric models estimated in a learning phase and includes combination of several classifiers (one for each feature space) and relaxation stages. The developed scheme was tested on laboratory and realistic field data [85, 86]. Research in imaging yielded the implementation and comparison of two algorithms: a synthetic aperture radar (SAR)-like focusing algorithm and a migration algorithm. Both algorithms take into account surface refraction and ground attenuation; moreover, the needed parameters such as antenna height and sub-surface permittivity were estimated out of the data. The algorithms resulted in three-dimensional views of the sub-surface objects of acceptable resolutions and shape.

12.2.3 Canada

The Canadian programme is carried out by DRDC in Suffield and in addition to many other technologies includes information on GPR Mine Detectors and Wide Area Detection/Remote Detection at the following URL: http://www.dres.dnd.ca.

The main thrust of the Canadian military programme consists of a vehicle based system with GPR manufactured by ELTA of Israel as well as metal detection and infra-red systems. The ILDP system built by General Dynamics consists of a remotely controlled vehicle carrying three scanning sensors which operate while the system is in motion, a metal detector array (MMD) based on electromagnetic induction (EMI), an infra-red imager (IR), ground penetrating radar (GPR), and a confirmatory sensor which requires the system to be stationary and near a target of interest, consisting of a thermal neutron analysis (TNA) detector. Each of the sensors provides information concerning the presence (or absence) of physical properties which accompany the presence of landmines. For example, IR provides a measure of thermal

anomalies, EMI reports anomalies in electrical conductivity, GPR detects anomalies in dielectric and other electromagnetic properties, and the TNA provides a measure of nitrogen content. The system utilises detection-level data fusion and requires each of the sensors to provide a position estimate and a measure of the confidence that the respective property, detectable by that sensor, is present in a local patch of ground about the reported position. A vehicle control station (VCS) is housed in a Command and Control trailer that follows the detection vehicle. The VCS serves as the operator interface as well as the data processing and display capabilities. The concept of deployment assumes that a suitable protection vehicle precedes the detector vehicle to remove small anti-personnel and tripwire-activated landmines and that the detector and vehicle will not activate typical anti-tank landmines.

The advanced development model (ADM) was completed in October 1997, and testing and improvements are ongoing. Despite being an ADM, tests at the Defence Research Establishment Suffield (DRES), Alberta, Canada, involving hundreds of operating hours and hundreds of kilometres travelled, have shown its robustness.

In US government tests in summer 1998 at Aberdeen Proving Grounds, Maryland, and Socorro, New Mexico, the ILDP system placed first or second out of five competitors on every test even without fully utilising the TNA detector (the ILDP system was the only competitor with a confirmatory sensor). The exceptional performance of the ILDP system in extreme conditions has validated the utility of a tele-operated landmine detector system employing multiple sensor types and data fusion.

Based on the success of the ILDP system, the Canadian Forces have initiated a follow-on project to build and procure four systems, using the detection technologies and operating principles developed during the Improved Landmine Detection Project. The first of these systems, which are planned to be deployed in Canadian Forces' theatres of operation, was scheduled for delivery in April 2001.

12.2.4 European Commission programmes

The aim of the ESPRIT R&D area on humanitarian demining is to research, develop and validate equipment and practices to improve the speed, efficiency and safety of humanitarian demining operations worldwide.

12.2.4.1 Single-sensor systems:

26293 MINEREC proposed to couple high-performance computing and algorithms with a ground penetrating radar sensor array to improve the detection and false-alarm rates in recognition of buried anti-personnel mines.

29902 DEMINE: the aim was to develop an advanced low-cost ground penetrating radar. Validation was planned through tests at the JRC in Ispra and in the field by mid-2000.

12.2.4.2 Multi-sensor systems:

26331 DREAM proposed to develop and demonstrate data fusion algorithms and human–machine interface concepts for the elaboration of a multi-sensor system

to detect, localise and classify anti-personnel landmines. The resulting methods, algorithms and architecture will be used in follow-up projects INFIELD and LOTUS.

29944 INFIELD is to develop and test a hand-held system with an integrated metal detector, ground penetration radar and radiometric sensing. The system will be validated at the JRC in Ispra, and field tests will be conducted in Bosnia and an SADC country. Short-term deployment (1999–2000) was targeted.

29870 HOPE is to develop a portable system integrating a gradiometer metal detector, an advanced ground penetrating radar and a microwave radiometer. Validation would be performed at the JRC in Ispra and field tests in Angola, Iraq and Bosnia. The prototype was expected to be completed and tested by the end of year 2000.

29895 PICE aims at developing a man-portable system integrating a metal detector and ground penetrating radar. Addition of a gas sensor is to be explored later. Laboratory tests will be made at the JRC in Ispra and at the FOA Research Centre in Sweden. The system was expected to be deployed in 2003.

12.2.4.3 Vehicle-based multi-sensor systems:

26337 GEODE proposes to develop and demonstrate computer architectures and data fusion algorithms for the elaboration of a multi-sensor system to detect, localise and classify anti-personnel landmines. The results would feed into follow-up project LOTUS.

29812 LOTUS proposes to further develop sensors based on metal detection, infrared and ground penetrating radar, the necessary multi-sensor fusion and the integration on a tele-controlled vehicle platform. The work would perform integration of the multi-sensor platform on the vehicle for a proof of concept operational demonstration.

12.2.5 France

Research is very active, and the substantial budgets allocated make it possible for the DGA to fund activities in the three basic technical areas of mine clearance: detection, decoy (where the idea is to trigger the mine remotely by simulating the presence of a target) and neutralisation (aimed at destroying the mine avoiding detonation in order to prevent any collateral damage).

The 'Salamander' project (duration: 3 years), carried out by Thomson CSF Detexis, is aimed at designing a vehicle-mounted, multi-sensor demonstrator detection system, by combining the best detection technologies currently available (electromagnetic, ground penetrating radar, radiometry and opto-electronics). The system will include high-performance algorithms for merging information stemming from various detectors. The project is supplemented by longer term studies aimed at selecting and developing other promising technologies: detection using neutron flows, acoustic or seismic waves, quadrupole magnetic resonance, olfactory sensing, etc. Through the assessment of new portable detectors currently showing up on the market, we are also preparing to acquire the best available equipment whenever the staff of command expresses the need.

To assess and develop these new technologies, a benchmark minefield is to be built at the Technical Institution of the city of Bourges (ETBS), which belongs to the DGA. This minefield will offer better security and reproducibility conditions for assessment tests of countermining techniques on both fake and real landmines.

12.2.6 Germany

Germany has several research and development programmes, and the one involving the close-in detection and neutralisation of mines systems is termed MMSR. MMSR is required as a vehicle mounted multi-sensor system to detect single mines, both ATM and APM. Sensor technology to be used in the present system is UV, NIR, MIR, EMI (metal detector) and GPR (ground penetrating radar). The current system, consisting of a nonmetallic rack with integrated sensors, is used for proving the efficiency of single sensors and data fusion mounted on a vehicle for initial measurement trials. The technology of the confirmation sensor for explosives which is required additionally has not yet been decided, as possible technology NQR is considered. Two test ranges for conducting trials are available: one in the area of the main industrial contractor MaK System Gesellschaft, Unterlüß, and the other at the test site of Technical Centre 52, Oberjettenberg. Neither of these test sites includes live mines but only surrogate mines and false targets.

12.2.7 Netherlands
Prof. Alex Yarovoy

Information on the Dutch National programmes regarding *3D signal processing for GPR* and *Advanced Re-locatable Multi-Sensor System for Buried Landmine Detection*, can be found at the following URL: http://www.tno.nl/instit/fel/os/prg/the_mine_detection.html.

Since 1996 a number of research and development programs in the area of demining have been carried out in the Netherlands. The major part of these programs (such as HOM2000, 'Advanced relocatable multi-sensor system for buried landmine detection', 'Improved GPR technology', VIRLAD) are national programs sponsored by the Netherlands Ministry of Defence and Dutch National Technology Foundation (STW). In addition, Dutch organisations participate in international projects, programs and initiatives. The main goal of these programs is the development of technology and methods for landmine detection.

The main Dutch research organisations in the area of landmine detection technology are TNO-FEL (National Defence Laboratory) and TU Delft (Delft University of Technology). The main direction of the national research in the area of landmine detection technology is in advanced sensor development. The most dominant research topic is the development of GPR sensor technology for landmine detection. TU Delft is playing a leading role in this area, not only within the Netherlands, but also internationally. In the past few years more than 80 man-years of research was done on this topic. The overall aim of the research is to investigate the feasibility of using GPR

with integration of multiple microwave-sensor technologies to enhance the landmine detection rate and to decrease the false alarm rate.

The TU Delft research activities resulted in development of two types of dedicated landmine detection GPRs: a video impulse radar and stepped-frequency radar. The principal novelty of the system is its multi-waveform (for the video impulse radar) or multi-frequency (for the stepped frequency radar) operation. The radars are equipped with advanced processing tools, which include polarimetric algorithms for sub-surface imaging, advanced detection algorithms, feature extraction and classification algorithms. The performance of the radars has been tested (as a single sensor and as a part of a multi-sensor system as well) at the test site for landmine detection systems located at the TNO-FEL. Environmental influence (soil type and moisture, temperature, etc.) on the detectability and the false alarm rate has been investigated carefully.

12.2.8 Russia

Information on the Russian humanitarian programme is given at the following URL: http://www.rslab.ru/english: Remote control mine detection system with holographic GPR and metal detector, Passive-active mm radiometer for detection of mines installed on the ground surface, and Airborne minefield detection for humanitarian operations.

12.2.9 Sweden

For several years, research and development in the area of ammunition and mine clearance has been carried out by the Swedish Defence Research Agency (FOI). This activity started as a response to the articulated military need for more efficient reconnaissance and clearance techniques. Gradually the need for R&D has been further accentuated, caused by the increase of Swedish engagement in different international programmes. For further information please see the following web sites: http://www.foi.se/english/ and http://www.swedec.mil.se.

A man-carried multi-sensor system was the goal for the EU-project called P.I.C.E. (Pinpoint, Identification, Clearance and Ensurance), in which FOI was involved. It was planned as a two-year project ending 31 December 2000. The FOI's task was, among others, to develop classification algorithms and to support the co-ordinating industry (the Swedish defence company SAAB) in issues concerning GPR techniques. However, some difficulties, especially concerning the development of the integrated sensor head, called for an extended project time schedule of one year. Owing to circumstances not fully known to FOI, the EC decided not to accept such an extension, and the project was terminated before the goal was obtained in December 2001. Owing to lack of financing, FOI have had to postpone the multi-sensor MD/GPR and concentrate on GPR as a single detector. Up to now FOI has demonstrated real time in field detection and classification of anti-tank mines. The signal processing algorithm discriminates between stones and metal fragments, and detects forward mines and mine-like objects.

During 2002 the project focused on adding a positioning sensor to the antenna head in order to be able to use two-dimensional scanning information used for three-dimensional classification processing. Preparation was also being made for participation in international test and evaluation of GPR-systems at the EC Joint Research Centre (JRC) in Ispra, Italy, in spring 2003. This T&E activity is a project within ITEP (the International Test and Evaluation Program for Humanitarian Demining), and the lead partner is the JRC. Evaluation of the HUMUS-DSS experimental radar has also taken place in Croatia during 2003. Further information can be obtained from the Mine Radar Group Swedish Defence Research Agency.

12.2.10 United Kingdom

In the UK there are two main programmes. The humanitarian programme is composed of MINETECT sponsored by the Department of International Development and the PHMD developed by QinetiQ under UK Treasury Funding. In addition, the Mineseeker programme was developed by a consortium of Virgin and QinetiQ, and was trialled in Kosovo, as detailed in Section 12.7.2.

The military programme is based around both vehicle and hand-held systems, and competitive feasibility assessments for a vehicle based system called MINDER were carried out by separate consortia led by Ultra Electronics and Thales in 2002. The programme moved onto two further stages, Mounted Countermine Capability (MCMC) and Dismounted Countermine Capability (DCMC), which are planned for in-service use during the next decade. Further information can be obtained from the UK MoD Defence Procurement Agency and DSTL Fort Halstead.

12.2.11 US Army military programme

12.2.11.1 Ground Standoff Mine Detection System (GSTAMIDS): The vehicle based Ground Standoff Mine Detection System (GSTAMIDS) is being developed in three phases, termed blocks.

In GSTAMIDS block 0, the primary mission is mine detection and marking in support of route clearance operations. It consists of a remotely controlled mine detection vehicle (MDV), which employs ground penetrating radar, an infra-red camera and metal detectors to detect and mark metallic and nonmetallic anti-tank mines. A blast-protected control vehicle remotely operates the MDV.

GSTAMIDS block 1 provides enhanced detection capability and faster clearance through emerging mine confirmation and neutralisation technologies. The MDV may have an on-board neutraliser, or a different platform may be used to neutralise the marked mines. The program will use a commercially available chassis for the MDV to cut costs and increase performance. Features of this evolutionary block include integration of advanced capabilities, a confirmation sensor, automatic mine detection, faster detection speeds and mine clearing capability. Standard communications channels linked to the manoeuvre commander will report minefield information.

GSTAMIDS block 2 will be modular so that it can be attached to a variety of military vehicles. The primary improvement will be the capability of forward-looking detection and avoidance.

12.2.11.2 Hand-held Standoff Mine Detection System (HSTAMIDS): The HSTAMIDS is a hand-held device with sensors to detect all metallic and nonmetallic anti-tank and anti-personnel mines. If a mine is detected, an audio cue alerts the operator. Built-in warning and test equipment also alerts the operator of potential system malfunctions and assists unit maintenance personnel in locating the problem. Current mine detectors detect only mines with metal content and generally have difficulty picking up mines with low metal content. They also have trouble distinguishing nails, shrapnel and other clutter that often leads to false alarms. Operating in magnetic soils can present problems as well.

The HSTAMIDS is a vast improvement over today's metallic hand-held mine detectors in that it employs an advanced state-of-the-art metal detector in addition to ground penetrating radar (GPR). This is coupled with an advanced microprocessor array and software to provide a high probability of detection (in excess of 95%) for both large and small metallic and nonmetallic anti-tank and anti-personnel mines. The result is a greatly improved system that will protect the soldier and enhance his ability to detect landmines. HSTAMIDS weighs approximately 8 pounds (3.6 kg), uses standard batteries and can be operated by a single soldier.

In addition, the US humanitarian programme has three elements: *USHDRD – US Humanitarian Demining Research & Development Technology Program*, *Minefield Identification System* and *Camcopter-Landmine Survey and Detection System*. For further information please see the following URL: http://www.humanitarian-demining.org.

12.3 Performance and test assessment

The key issue with any sensor for mine detection including GPR is the probability of detection and false alarm rate. The key to this issue is the statistical confidence with which the claims of a particular hardware design, algorithm or software, sensor or combination of sensors performs. For this reason it is appropriate to explore some of the issues related to this topic.

Elementary statistical sampling theory can be used to show that the confidence that can be placed in a test of a limited sample set is fundamentally related to the size of the sample set. If 10 mines are tested and even if all are detected (a probability of detection of 100%), the statistical confidence in the claim is limited by the number in the set. At the 95% limit, the upper and lower confidence bounds can be derived from the binomial distribution to show that, with a sample set of 10, the bounds as shown in Figure 12.2 exist. The x-axis shows the proportion of the sample set detected, and the y-axis shows the probability of detection.

In contrast, the limits for a sample set of 100 are much closer and are shown in Figure 12.3. These values are based on the small sample interval for calculating confidence intervals, and a Mathcad™ programme is provided to calculate limits based on the binomial distribution.

A fully detailed consideration of the issues is given by Simonson [87], who considers the difference between the small sample approach based on the binomial

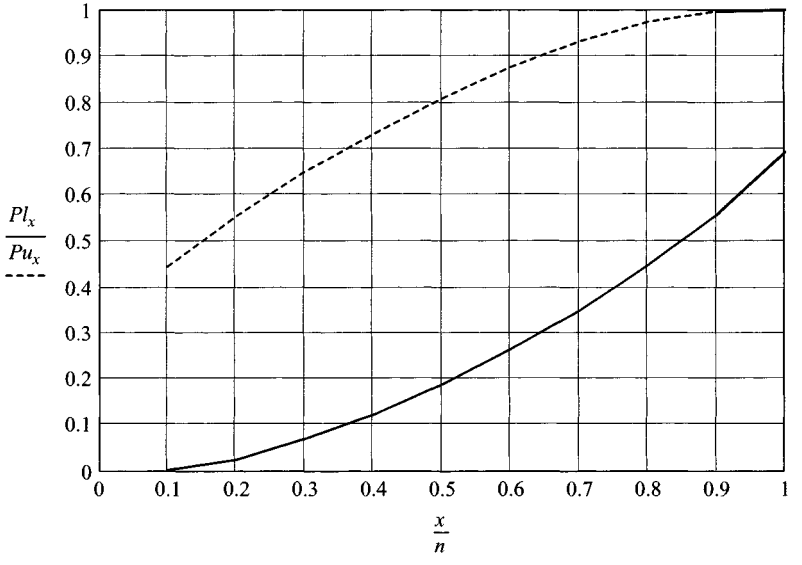

Figure 12.2 Upper and lower confidence bounds for a sample set of 10 (binomial distribution)

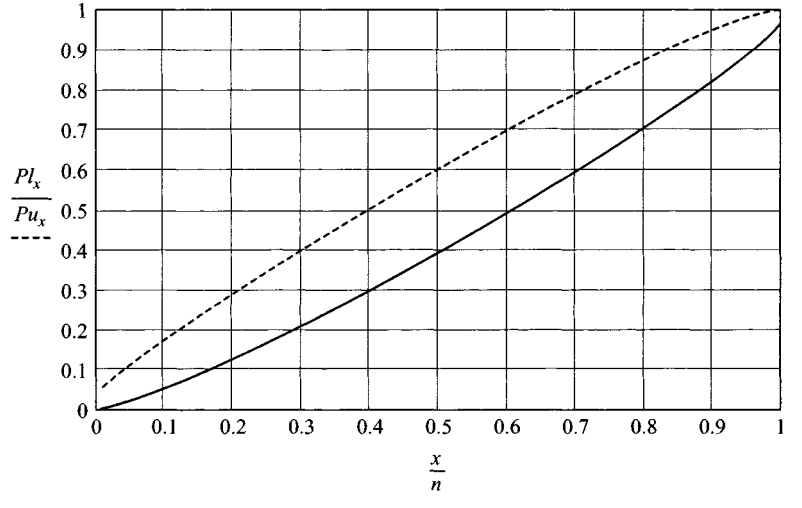

Figure 12.3 Upper and lower confidence bounds for a sample set of 100 (binomial distribution)

distribution and a large sample approach using the normal distribution. Note that the large sample distribution suggests a closer interval between the bounds.

Voles [88] also considers these issues and shows that, based on a Poisson distribution, even if no mines were missed in a test of 100, then at the 95% confidence limit the highest value of probability of detection that can be claimed is 97%. Voles also showed that to achieve the 99.6% probability of detection at a confidence level of 95% would require a test of 750 mines and none should be missed. The issue of false alarms was considered, and for a maximum probability of 1% per m^2 no more than 4 false alarms over an area of 900 m^2 should be generated by the detector.

An alternative way of considering the performance of a GPR system is to consider the receiver operating characteristic (ROC) curve. The ROC is a method of plotting the probability of detection against the probability of false alarm. It is extremely useful in measuring the performance of systems, and an example based on a hand-held GPR system tested as part of an International Test and Evaluation Programme (ITEP) is shown in Figure 12.4. Essentially the ROC curve shows the probability of false alarm (PFA) for a given probability of detection (PD). In the example the PD = 1 and the PFA = 0.15. Note that the size of the sample set should also be known in order to establish the confidence bounds. In the case given, the lower confidence bound is 87% at the 95% confidence limit.

The tests should, of course, be conducted on identical mines in identical soil conditions at identical depths at identical mine angles, otherwise the comparability of results will not be valid.

The testing of GPR systems should ensure that there is an adequate statistical distribution of:

- AP and AT mines
- GPR clutter
- ground topography

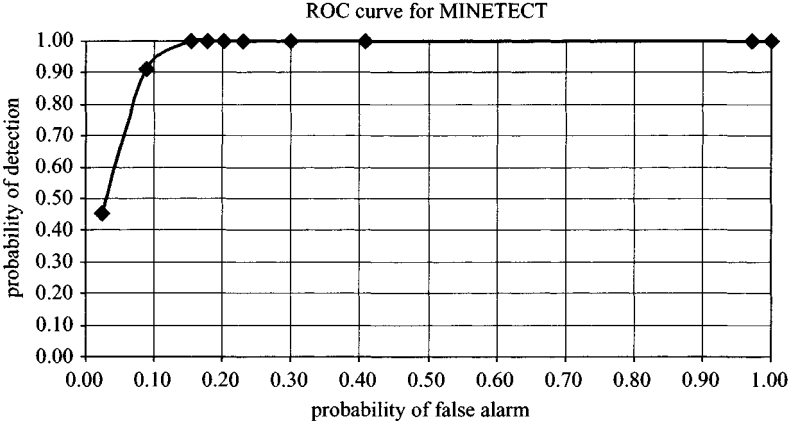

Figure 12.4 ROC curve for GPR mine detector

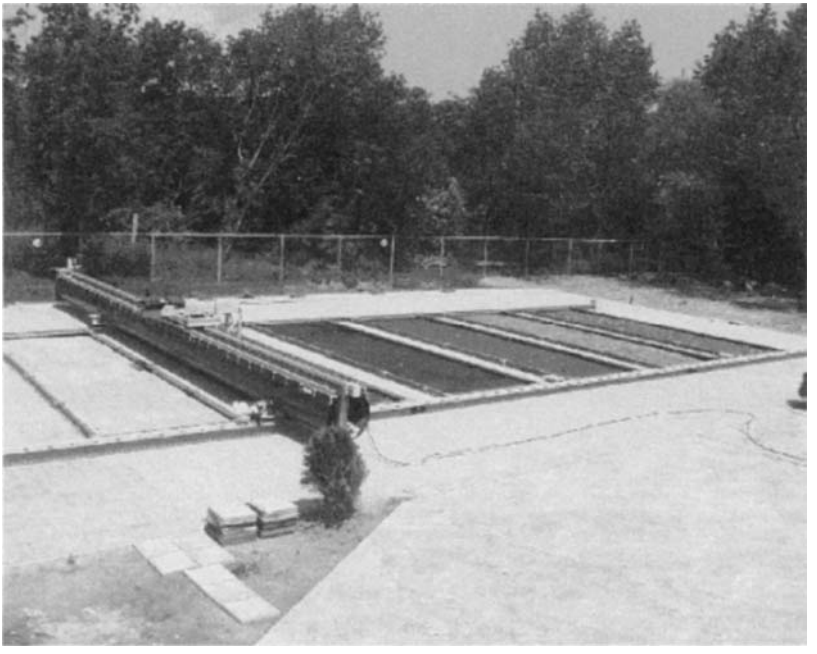

Figure 12.5 Overview of the six test lanes (each 10 m long and 3 m wide) and the measurement platform at TNO Holland

Figure 12.6 Cleared minefield in Southern Lebanon (courtesy ERA Technology)

Figure 12.7 Mine test lanes in Sarejevo (courtesy ERA Technology)

- soil conditions (water content, etc.)
- operator variance
- product batches.

In testing mines the following points should be considered in emplacing the mine:

- type of mine, surrogate, inert, etc.
- size of mine
- internal structure of mine (are surrogates valid?)
- explosive content of mine (test with explosive content?)
- depth of mine
- attitude of mine, horizontal, angled, etc.
- proximity to other targets, i.e. AT mines.

The type of clutter is just as important in that GPR will respond to:

- stones
- animal burrows
- cracks in the soil surface
- pooled water in sub-surface hollows
- tree roots
- changes in vertical or lateral soil structure
- changes in surface topography.

There are significant differences between most of the test sites used for mine testing and real field conditions, as the photographs in Figures 12.5 to 12.7 show.

Comparison of real minefield sites with test sites shows that the level of surface clutter is far higher in real life than on the test site, and test results from current mine test sites could easily lead to an over-optimistic assessment of GPR performance.

12.4 Mine detection with GPR

There are some key issues that the developer of GPR mine detection technology should identify before any project is started. These relate to the specification for the equipment performance, the selling price for the system and the operator requirements for operation, training and in-service support. Too many mine detector development projects have failed because the basic disciplines of project assessment and management have been neglected.

No major GPR mine detection project should be started without a clear User Requirements Document (URD) and from this follows a System Requirements Document (SRD). As far as the user is concerned the parameters that matter are listed in Table 12.1 which, for illustration, has been geared around a hand-held detector.

There have been a vast number of research and development programmes, and the literature available on the subject of GPR for mine detection is considerable. The papers range from modelling studies to field trials. A literature survey is included in the list of references, and those papers by Carin, Miller, Gader, Rappaport, Peters, Young, Chen, O'Neill and Yarovoy [89–107] are recommended as being valuable

Table 12.1 GPR mine detector system parameters

Parameter	Typical issues
Environmental performance	Max. and min. temperatures Dust protection Water protection Shock and vibration
Ergonomics	Use by female and male deminers. Controls, balance etc.
Weight	Use by female and male deminers. Less than 5 kg?
Battery life	12, 24, 48 h, 1 month, 2 months, D cells?
Serviceability and maintainability	Can it be repaired in the field? Can it be repaired in Third World workshop?
Upgradeability	Can new software and hardware upgrades be field implemented?
Operating bounds	Does the detector warn operator when soil is too lossy?
Variance in unit performance	How does the detection performance vary from unit to unit?
Interference	Do power lines and mobile phones interfere?
Compatibility	Do units interfere with one another and at what distance?
Compliance	Do units meet ETSI, FCC, EU and national radio and EMC standards?
Product liability	What does the manufacturer accept?

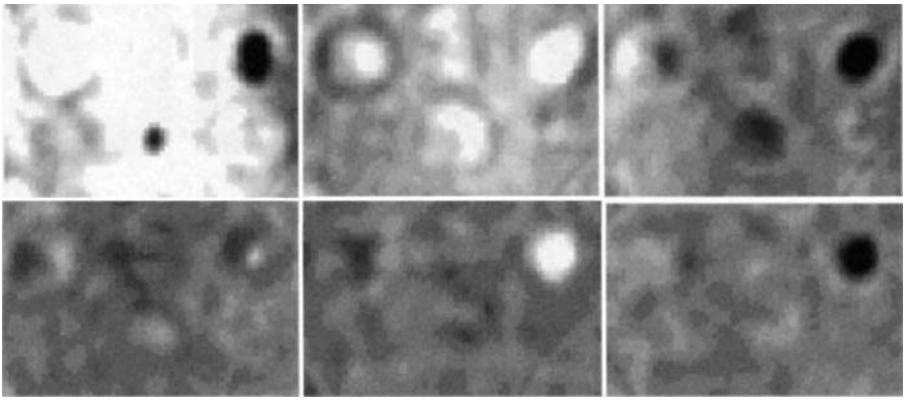

Figure 12.8 Short sequence of GPR C-scan data from buried mines (courtesy ERA Technology)

source material for researchers and developers. The PhD theses by Brunzell [108], Scheers [82], Martel [109] and Brooks [110] are also highly relevant to the mine detection problem.

It is not always easy to obtain quantifiable and comparable results from many of the research projects although the JRC at ISPRA has a database of GPR mine signatures which readers may find useful. Some data are included in the CD and a preview of these data is given in Figure 12.8. The data are processed GPR data from the EU DREAM project (courtesy ERA Technology). The image covers an area 1 m by 0.6 m and represents C-scans at intervals of 200 ps. There are six mine targets distributed evenly over the area. The CD contains the processed data in two stages and also Paintshop Pro Animation™ sequences of the GPR image.

A key feature of GPR noncontacting ground antennas is their illuminating footprint. A simple geometric model of an isotropic radiator is useful to illustrate the issue. If the ground to antenna spacing is increased in 10 cm steps from 10 cm to 50 cm the diameter of the illuminating footprint on the ground will also increase. This is shown in Figure 12.9. As the resultant radar image is effectively the convolution of the antenna footprint with the target radar spatial cross-section, the target image becomes blurred. This effect increases with antenna to ground spacing and eventually results in targets with small radar cross-section (AP mines) becoming vanishingly small. A simulation of a sequence of radar images as a function of incremental footprint diameter (each frame shows a doubled footprint diameter) is shown in Figure 12.10. The area of each frame is 1 m by 1 m and various targets of different size and reflection coefficient are shown. An 8-bit greyscale is used.

It can be seen that the effect of the loss of spatial resolution is significant and the smaller targets become rapidly lost in the image. In addition to this effect, the fundamental probability of detection of the GPR as a system should be considered. In the absence of any clutter whatsoever in the ground and assuming a complete removal of the front surface reflection, it is possible to calculate the probability of

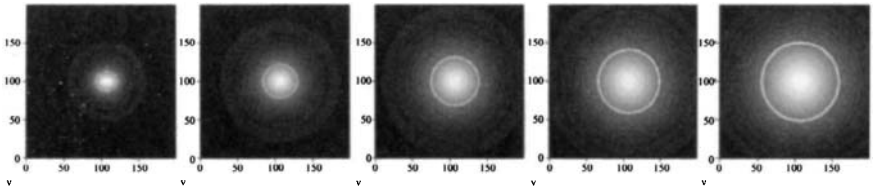

Figure 12.9 *Calculated isotropic radiator ground footprints over a 2 m by 2 m area for increasing ground to antenna spacing from 10–50 cm in 10 cm increments*
The 3 dB level is shown highlighted. An 8-bit greyscale dynamic range is used

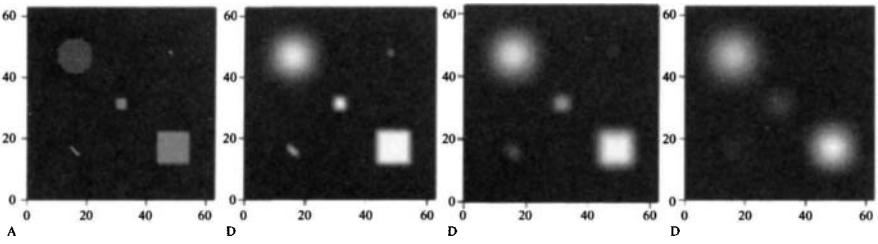

Figure 12.10 *Calculated target images over a 1 m by 1 m area for increasing doubling footprint diameter for various targets*
An 8-bit greyscale dynamic range is used

detection as a function of target range and target size. This is shown in Figure 12.11. The family of curves represents the probability of detection (PD) versus range for dielectric cylinders of diameters 5 cm to 50 cm working from left to right. It has been assumed that the signal to noise ratio (SNR) of the radar receiver is 14.6 dB and the mine signal is 6 dB greater than the SNR. A frequency of 1 GHz was used with a target $\varepsilon_r = 2.2$, soil $\varepsilon_r = 6$ and ground attenuation of 30 dBm^{-1}. The antenna to ground spacing is 10 cm. The PD for the smallest diameter target falls below 0.9 at a depth of 10.25 cm below the surface of the ground.

The same model can be used to calculate the PD at frequencies of 0.5 GHz (Figure 12.12), and 2 GHz (Figure 12.13), and the effect on the PD is significant. At 2 GHz the PD degrades significantly.

In addition to the increased attenuation losses at frequencies above 1 GHz, the situation regarding clutter should also be considered. Figure 12.14 shows a comparison between images taken at 1 GHz and 2 GHz. The 2 GHz image contains much more information than the 1 GHz image and on first sight would appear to be a better choice of frequency to use. However, the increased information also entails an increase in clutter, and a careful assessment of the impact of this on the overall system performance should be carried out.

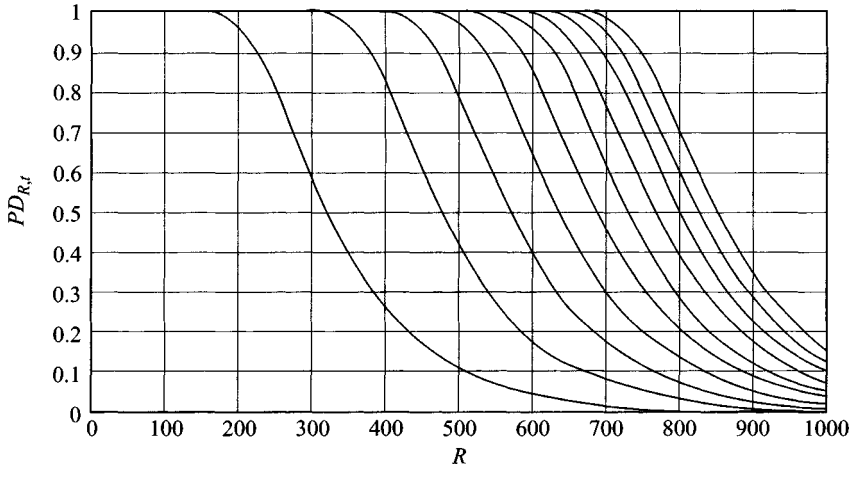

Figure 12.11 *Probability of detection versus range for cylinder diameters 5 cm to 50 cm*
Clutter ratio −6 dB; frequency 1 GHz; target $\varepsilon_r = 2.2$; soil $\varepsilon_r = 6$; attenuation 30 dB m^{-1}; spacing 10 cm

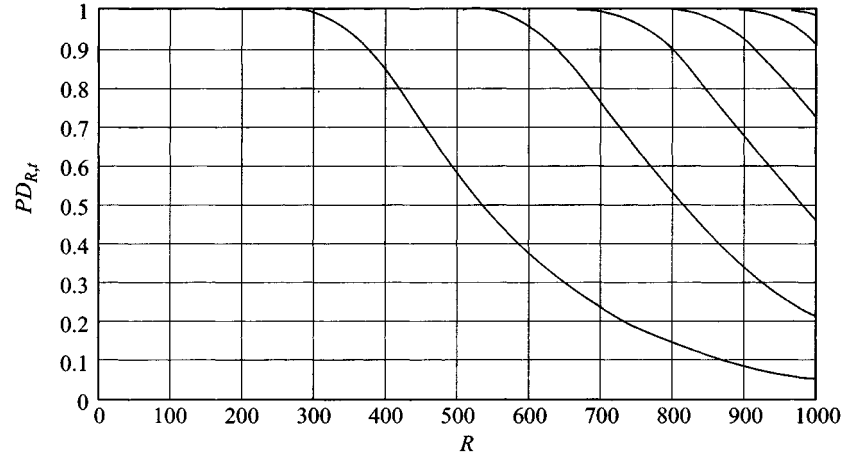

Figure 12.12 *Probability of detection versus range for cylinder diameters 5 cm to 50 cm*
Clutter ratio −6 dB; frequency 0.5 GHz; target $\varepsilon_r = 2.2$; soil $\varepsilon_r = 6$; attenuation 30 dB m^{-1}; spacing 10 cm

Next Page

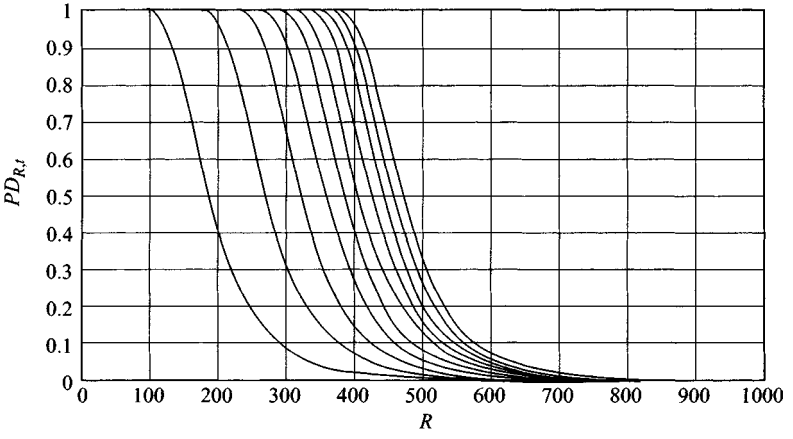

Figure 12.13 *Probability of detection versus range for cylinder diameters 5 cm to 50 cm*
Clutter ratio −6 dB; frequency 2 GHz; target $\varepsilon_r = 2.2$; soil $\varepsilon_r = 6$; attenuation 30 dB m^{-1}; spacing 10 cm

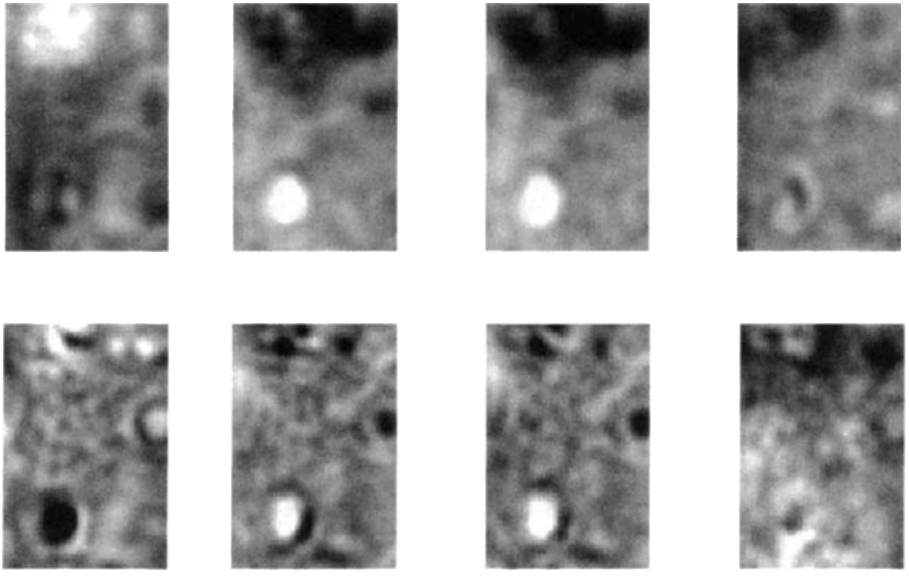

Figure 12.14 *Comparison of radar images at 1 GHz (upper) and 2 GHz (lower) over the same area and depth range of 1 m by 0.6 m with two mines present (courtesy ERA Technology)*

12.5 Hand-held mine detection

A possible specification for hand-held mine detectors for humanitarian use might be as follows:

- weight (all up) <3 kg
- battery life (D cells) >12 h
- upright or prone single operator Yes
- head width (x-axis) <200 mm
- mine/no mine indication Yes
- depth range for all targets/all soils 300 mm
- PD >99.95%
- FAR <0.01 m^{-2}
- all soils advise
- mine classification Yes
- demining environmental conditions (temp, shock, vibration, etc.) all world

It is more than likely that a GPR system will be combined with a metal detector. There will be certain requirements on a metal detector and these should also be considered during system design. The most advanced systems in terms of technology readiness level (TRL) are the US Army HSTAMIDS hand-held detector under development by Cyterra (US) and the MINETECT humanitarian detector under development by ERA Technology (UK). The HSTAMIDS is in limited production and is at the highest TRL, while the MINETECT system is working through a field trials programme. The HSTAMIDS system combines a metal detector system manufactured by Minelab of Australia with a three antenna stepped frequency GPR system developed under US Army funding by Cyterra. The MINETECT system combines a metal detector system manufactured by Vallon of Germany with a two antenna impulse radar GPR system developed for the Department of International Development (UK) by ERA Technology. This system is described later in this Chapter. Many other national programmes have attempted the development of a hand-held mine detector, but the TRL of these developments is probably lower than the HSTAMIDS and MINETECT.

There are differences between the requirements for military and humanitarian detectors, and these should be clearly identified during development programmes. The level of field support required (in military parlance, Integrated Logistics Support (ILS)) is radically different for military and humanitarian detectors. It might be considered that humanitarian detectors have greater requirements for field survivability because of the lower ILS regimes.

It is useful for those proposing projects on hand-held demining to consider the millions of dollars that have been spent on the US HSTAMIDS programme which has resulted in a useful output. While there is a superficial attraction in involvement with mine detection programmes, the resources required to bring a credible solution to fruition are considerable and should be in place at the start of the programme. Failure to do so will simply add yet another project report to the growing pile.

12.6 Vehicle mounted

There is much interest in high speed array radar systems for mine detection and work is being carried out on various national (US, UK, Germany, France) as well as international CEU programmes. Arrays are typically between 1 and 4 m in width and can operate at speeds up to 10 kmh^{-1}. While not exhaustive, this Section gives some idea of the different approaches that are being taken to vehicle mounted mine detection using GPR. There are several options that can be considered in terms of design. The radar can look down into the ground or it can look ahead in forward-look mode. The latter is obviously preferable operationally as it removes the need for the vehicle to have overpass capability.

There is potentially a restriction on system performance for forward-look radars. If it is supposed that at or greater than the Brewster angle there is no reflected signal, then a radar looking forward will no longer be able to detect buried targets in the ground when the angle of the boresight of the radar exceeds the critical Brewster angle. If this is true, then for a given height, the performance of the radar will be set by the relative dielectric constant of the ground and the radar forward velocity. The braking distance in metres of a vehicle on a concrete road is given by

$$D = 0.306(0.023v^2 + 0.68v) \tag{12.1}$$

where v = speed in kmh^{-1}.

It can be shown that the effective range of the vehicle is defined by both speed and the relative dielectric constant of the ground and is shown in Figure 12.15, which relates to a radar mounted 3 m above the surface of the ground. Note that for low values

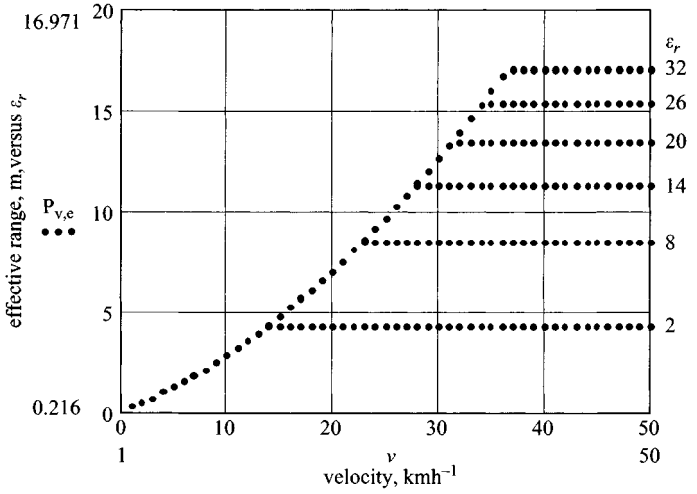

Figure 12.15 Effective range of 3 m high forward-look radar system as a function of forward velocity and ground relative dielectric constant

of relative dielectric constant ($\varepsilon_r = 2$ = desert conditions) the vehicle speed would be limited to 15 kmh^{-1}, whereas in wet conditions ($\varepsilon_r = 20$ = winter conditions) the vehicle speed would be limited to 33 kmh^{-1}. Effectively, for a given ground condition the vehicle speed is limited by the effective forward range. This may be of little consequence for a vehicle for humanitarian use but could pose a severe limitation for military applications.

There is fundamentally no such restriction on a downward-looking radar. Most radar systems designed for mine detection use an integral array design and exploit the increased capability offered by combining multiple looks and SAR processing. With all array systems, it is important that the surface clutter is properly removed. Close coupling of the antenna to the ground surface is one method. An alternative relies on coherent subtraction but this often means that the ground topography must be relatively smooth. Where removal of the surface clutter is not easy then antennas operating off-normal incidence can be used. However, this in turn brings other problems and antenna near-field effects must be accounted. The effect of grazing angle can be a limitation as it limits the potential for full 3D imaging because of the refractive index of the ground compressing the beam within the soil.

Alternative approaches have been adopted by companies in the US (Planning Systems, GeoCenters, BASystems (ex GDE), Mirage, ARL, Jaycor, SRI, Coleman), UK (ERA Technology, Thales and PipeHawk), France (Thales, Satimo), Germany (Rheinmetall) and Israel (Elta), who have developed array systems as an integral design rather than combining existing single channel radars. Work in the United States under the MURI programmes has enabled universities to contribute to the development of radar technology and processing techniques. Research programmes on radar using 2D arrays and synthetic focusing are reported by Benjamin *et al.* [103]. The principle of this approach applies synthetic focusing to an oblong horizontal stand-off array, where all the voxels in a vertical slice underneath the centre-line of the array are synthesised electronically.

Where arrays are well spaced away from the zone of interest, then the SAR processing approach is viable, insofar that the vehicle is moving forward and traditional SAR techniques are sideways-look. Forward-look radar systems require cross-scanning and hence an array of antennas in order to create a SAR data stream. The downward-look radar approach has limitations in terms of the cross-range resolution because of the limited number of antenna elements that can be used in an array. (See Figure 12.16.)

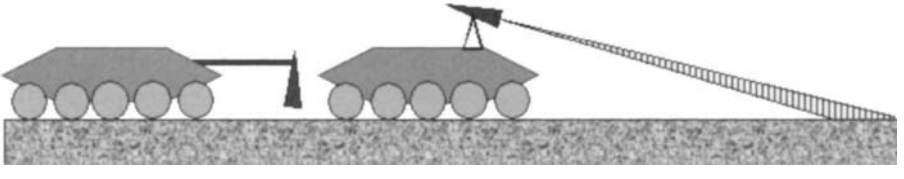

Figure 12.16 Downward-look and forward-look vehicle mounted radar systems

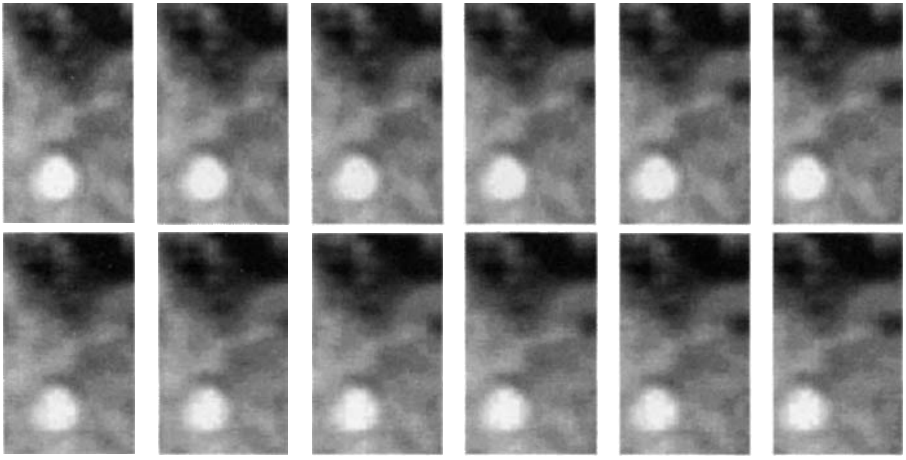

Figure 12.17 *Effect of reduction of number of elements in an array*
Upper sequence 1 cm resolution; lower sequence 4 cm x and 6 cm y

The effect of spatial under-sampling on the radar image degrades the image quality. This was investigated by scanning a radar at high resolution (1 cm in both x- and y-directions) and then reducing the data by thinning to 4 cm in the x-dimension and 6 cm in the y-dimension and then interpolating (linearly) between thinned data samples. The results of this process are shown in Figure 12.17; gradual degradation in image quality can be observed. For AP mines once the array resolution becomes greater than 15 cm the image quality significantly decreases.

Where the array elements are close to the ground, then multiple-look processing suffers from path attenuation and diffraction from clutter generating objects. Hence it is found that the close-in downward look needs to be processed in a different way from downward look where the antenna array is raised above the surface of the ground, where cross-range spatial resolution is compromised. Further details of the tests carried out on five vehicle based systems in 1998 in the United States are given by Rotondo *et al.* [112]. These systems were multi-sensor based and were tested against predominantly AT mines. Of all the sensors the GPR performed best, although as expected buried minimum metal mines were the most difficult to detect. Several examples of recent developments and the different design approaches are described below.

An example of a recent development is the vehicle developed for the UK MoD MINDER Competitive Assessment Phase (CAP) programme by a consortium comprising Ultra Electronics, General Dynamics and ERA Technology and shown in Figure 12.18. This was a remotely operated vehicle with multiple sensors and the 4-m-wide GPR array can be seen at the front of the vehicle.

The following material is quoted from a paper by Daniels *et al.* [76] from the IEE International Conference, Radar 2002. The key issues for the design of multi-element GPR systems lie in the channel-to-channel performance and tracking over

Figure 12.18 Photograph of UK Minder vehicle (courtesy ERA Technology)

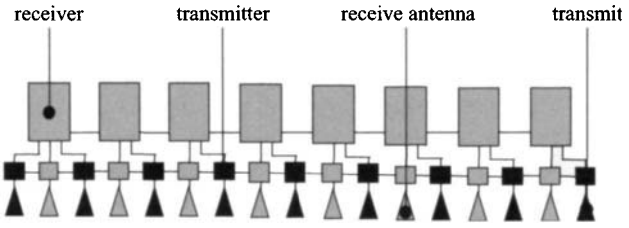

Figure 12.19 Block diagram of 16-channel radar system

the desired operational environmental range. A 32-channel GPR system, for example, must maintain calibration of both start time and time linearity for all channels to within demanding limits. In addition, the relative gain and, if used, time varying gain profile, must also match to within close tolerances. Where the antenna array is spaced off the ground there may also be the need to compensate for variations in surface topography. A further aspect to be considered is the antenna element spacing. This needs to be adequate to provide proper resolution of the wanted target and it can be shown that the probability of detection with respect to small targets is closely related to the density of the elements of the antenna array.

An example section showing 16 elements of a 4-m-wide swathe radar system with a total of 32 antenna elements is shown in Figure 12.19. The architecture of the system is based around 16 receivers (8 only shown) each of which sequentially samples the

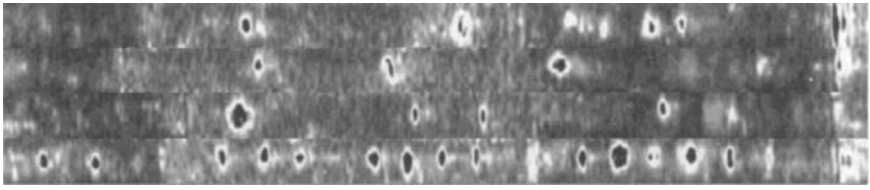

Figure 12.20 Example of AT mine images taken over a 4-m by 20-m test site with the ERA wide swathe GPR

signal incident on receive antenna elements. The transmitters are synchronised by adjacent receivers and a central master clock. The overall system was developed initially as part of an ERA private venture development programme and subsequently for the UK MoD MINDER CAP programme. The system is designed to be modular in that it can be either increased in width or alternatively in density and up to 64 channels can be configured. The transmitter–receiver modules can be used either singly or up to $N/2$, where N is the number of antenna elements. This offers the possibility of employing the transmitter-receiver module as a core building block for a hand-held GPR system and potentially simplifies maintainability. An example of the image output of the prototype PV 1-m array radar system is shown in Figure 12.20. The system was successfully trialled at DRES in Canada and subsequently in the UK.

An alternative approach has been taken by GeoCenters in the United States. The GeoCenters' Energy Focusing Ground Penetration Radar (EFGPR) incorporates both bistatic impulse radar and synthetic aperture (SAR) principles by using a two-dimensional array of precisely timed transmitters and receivers to actively image the area under the array. This provides the advantages of multiple transmitters to illuminate the scanned area with broadband energy, multiple receivers to detect back-scattered energy, and provides additional clutter rejection through time-domain synchronisation of multiple impulse radars. By independently controlling the firing and gating of each transmitter and receiver, the system focuses radar energy to a point, then moves that point to scan the area under the array. The data collected form a sub-surface time domain image of the back-scattered energy without requiring processing-intensive translation from the frequency domain. This image is analysed in real time using multiple, independent target recognition algorithms in parallel. Outputs from the target recognition are fused in real-time to declare mine targets and their location. The way in which GeoCenters' EFGPR uses its controlling electronics to trigger multiple transmitters and receivers to focus is unique and patented. The EFGPR operates by firing groups of four independent transmitters and sampling groups of four independent receivers for each voxel location. For any given voxel, the timing of the impulse from each of the four antennas is precisely controlled so that transmitted energy is coincident in time and thus is focused at the desired voxel location. Likewise, the sampling of each receive antenna is independently timed to be coincident with the transit time of the scattered energy return, focusing the receivers on the desired voxel. On-board software models the time-of-flight through the air/ground media, calculates the timing settings required to achieve this precise alignment, and

uploads these 'focus tables' to the controlling electronics. This method of focusing multiple transmitters and receivers both enhances the signal return from a given location and reduces the signal level from other areas not being focused upon (incoherence in scattered returns from other voxels causes them to be 'out of focus'). Changing the relative timing between the four antennas allows the focus to be scanned left to right, generating voxel data in the crosstrack dimension. As the scanning process is entirely controlled by uploaded focus tables, the number and spacing of sampled voxels is completely programmable. Typically, the crosstrack spacing between voxels is 2″ (50 mm), and the depth increment is approximately 1/4″ (6 mm). GeoCenters' EFGPR is designed to raster-scan the ground, focusing the combined energy from multiple transmitters on each voxel and only sampling the receivers when the scattered return from that voxel is expected. This obviates the need to collect and analyse massive volumes of data to isolate the scattered return from an object. Successive raster scans are averaged over a constant interval of down-track motion (typically over every 2 inches of forward travel), resulting in high-precision high signal-to-noise spatially normalised radar images. This continuous down-track scanning generates a complete three-dimensional sub-surface radar image of the traversed area. As the output of the EFGPR system is already image data, no additional processing steps are required to produce a three-dimensional volume of image data. The resulting image data can be analysed using standard image processing techniques for enhancement and target detection. GeoCenters' Automated Target Recognition (ATR) algorithms function on these three-dimensional data as the data are collected, and provide a confidence mapped plan view output as well as target reports in real time (see Figure 12.22).

The down-track energy (depth plot) in Figure 12.21 provides the best graphical representation of the raw EFGPR signal that results from buried and surface laid landmines. As can be seen in the upper right side of Figure 12.21, a mine signature consists of a number of 'hyperbolic' radar returns. This is the signature that the down-track feature extraction algorithm is looking for. To enhance the contrast of this signature, the program creates a down-track gradient data representation. In addition, a feature is extracted from the cross-track energy distribution. A gradient representation of these data is also created.

A very different approach is being taken by Planning Systems Inc. in the US. This system uses a forward-look radar with multiple receivers and transmitters to form an SAR image of the buried mines. This system was described by Bradley *et al.* [105] and is a forward-looking synthetic aperture stepped-frequency ground penetrating radar (see Figure 12.23).

The electronics bandwidth covers the range 400–4000 MHz and all parameters are user selectable. It uses compact, lightweight, Archimedean spiral antennas which have an effective bandwidth over 750–4000 MHz. The radar has 30 receiver channels over a 2.16-m aperture or 46 receiver channels over a 3.36-m aperture. The system has three transmitter modes: 3-element vertical , 7-element vertical, dual 3-element vertical. The TX/RX array is tiltable over a 0–33 degree range. It achieves real-time multi-look beam-forming at 5 km h^{-1} for a resolution of 10 cm.

Significantly better images of buried mines can be produced by combining looks from multiple closely spaced along-track positions. The processing algorithms are

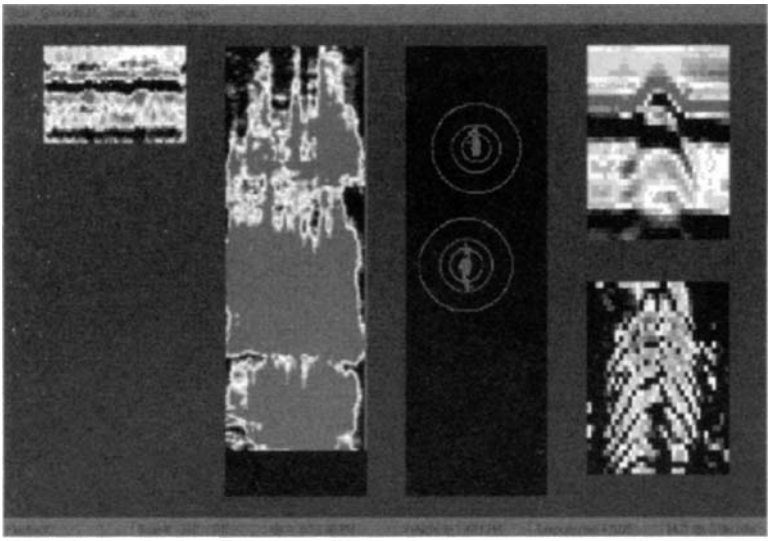

Figure 12.21 GeoCenters' radar image display

Figure 12.22 Three-metre-wide model 403 EFGPR arrays in initial testing at Australia's Defense Science and Technology Organisation (DSTO) (courtesy GeoCenters)

Figure 12.23 Planning Systems' Stand-off GPR array (courtesy Planning Systems)

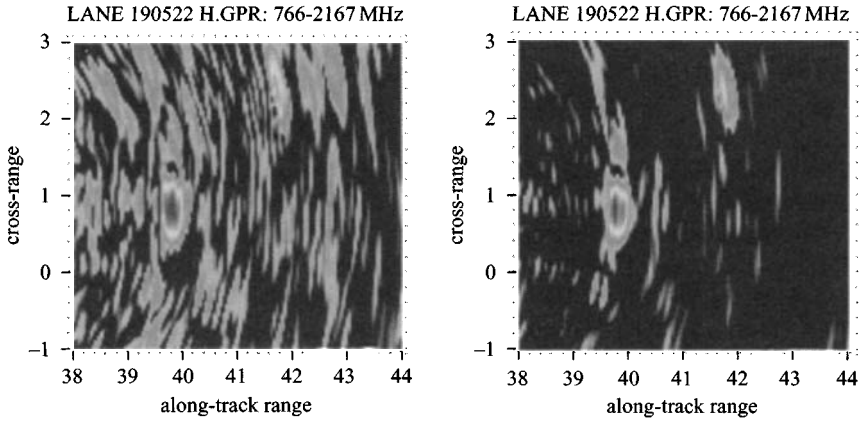

Figure 12.24 Single-look (lhs) and multi-look (rhs) processing for a buried mine (20 dB dynamic range) (courtesy Planning Systems)

very simple and robust and results are achieved with uniform shading and no corrections for roll, pitch and yaw which have been implemented in real time. Increased performance may be obtained through the use of optimum array apodisation, improved spatial filters and other processing techniques.

Forward-looking mine detection was demonstrated from a continuously moving platform. Planning Systems Inc. believe that multi-look processing significantly improves forward-looking mine detection and are working on a next generation system which offers increased detection range, speed of advance and sensitivity by means of a combination of electronics, mechanical and processing modifications. An example of the difference between single-look and multi-look for flush buried TM62M mines with a radar tilt angle of 22 degrees is shown in Figure 12.24.

12.7 Airborne

12.7.1 Introduction

Several attempts have been made to detect minefields from airborne platforms. SRI International have shown that mines can be detected from a fixed wing platform, and more details on this are given in Chapter 14 on remote sensing. Work by the Schiebel company on the Camcopter has shown that Unmanned Airborne Vehicles (UAV) may be feasible to carry lightweight SAR radars. An interesting development is the Mineseeker Project which is reported in detail in the following Section.

12.7.2 The Mineseeker airship project

Mineseeker Foundation
Dr G. N. Crisp, Dr P. K. Bishop, QinetiQ plc

12.7.2.1 Introduction: The Mineseeker Foundation is a not-for-profit joint venture between Lightship Europe Ltd (LEL) and QinetiQ which brings to bear two unique technologies to assist humanitarian demining through technical survey whilst also promoting the cause of humanitarian mine action on the world stage. The Mineseeker System uses a radar-equipped airship to safely and cost-effectively locate and delineate dangerous areas at a rate of $100\,m^2\,s^{-1}$. The sensor technology used is the QinetiQ ultra-wideband synthetic aperture radar (UWB SAR) – a unique technology, capable of airborne detection of plastic landmines, developed over many years for UK defence programmes and now made available for use in humanitarian demining.

A prototype Mineseeker System has been tested and evaluated in the UK and in Kosovo, producing outstanding results (see Figure 12.25). The System is ready to proceed to an 18 month period of further development to deliver an operational system ready for further rigorous testing and evaluation and deployment to mine affected countries, subject only to the project receiving the required funding.

12.7.2.2 Airship platform: There are currently no operational airborne land mine survey systems. Conventional fixed and rotary wing aircraft are not suited to carrying UWB SAR due to its size (the radar antennas will be installed within the airship envelope, which provides both space and protection) and the requirement for a low vibration, near metal-free environment.

Figure 12.25 The Mineseeker airship on trial in Kosovo

An airship provides a mobile, stable platform that has long endurance, low noise and vibration, no propeller downwash (whilst retaining the capability to remain near stationary for long periods of time when required), exceptionally low risk of critical failure, a large payload capacity and a good operator environment to overfly safely and locate mined areas. In environments where helicopters may be perceived as a threat, an airship can provide a nonthreatening solution for which high public awareness of the humanitarian role is easily achievable. The airships used by Mineseeker are uniquely inexpensive, easily deployable and sustainable in remote regions, making them an ideal platform for this role. The presence of an airship in a post-conflict environment offers further possibilities including identifying safe routes for food-aid movement, refugee movement monitoring and land use monitoring.

12.7.2.3 Ultra wideband radar: Over the last decade QinetiQ (previously the UK MoD's Defence Evaluation and Research Agency, DERA) has developed an advanced UWB SAR capability. Impulse radar techniques are employed to provide what is believed to be a high bandwidth, highest resolution imagery, capable of penetrating foliage and detecting buried objects, such as landmines.

The desire to use a high bandwidth (to achieve high range resolution) together with a low mean operating frequency leads directly to the concept of UWB radar. When combined with synthetic aperture techniques (UWB SAR), a very high range *and* azimuth resolution is achievable. For a given mean frequency, the resolution achievable by UWB radar is significantly greater than that of narrowband radar. High resolution whilst operating at low mean frequencies is unique to UWB systems and is crucial to achieving foliage and ground-penetration. The radar range resolution

is determined by the transmitted pulse duration – high range accuracy implies very short pulse duration. This resolution, coupled with exceptionally high digitisation rates, allows detection of even plastic anti-personnel landmines. The fact that the radar cross-section (RCS) of dielectric targets (i.e. plastic mines) increases rapidly with frequency and that low frequency energy is needed for good ground and foliage penetration make it unlikely that narrowband systems could be used for reliable detection of landmines.

UWB radar uses waveforms whose frequency spectrum extends from low MHz up to several GHz as determined by the required resolution. A simple implementation of this concept is achieved by using impulse waveforms which may be readily generated with durations down to 100 ps at amplitudes of many kilovolts. Such pulses give a theoretical range resolution of approximately 1.5 cm (range resolution is comparable to pulse width), with a frequency spectrum extending from a few hundred MHz to several GHz.

An initial feasibility study suggested that a resolution of 50 mm in range and 0.5 m in azimuth would be required to adequately detect mines. To achieve this range resolution the system would need an instantaneous bandwidth of approximately 3 GHz, extending from 200 MHz to over 3 GHz.

12.7.2.4 Mine signatures: Metal mines totally reflect radar waves so that the signal detected by the radar depends primarily on the target geometry and the properties of any surrounding soil. For plastic mines the situation is different and a substantial proportion of the incident radar energy can be transmitted into the mine. Some energy is reflected directly back to the radar by the outer surface of the mine and some of the transmitted energy is reflected later in time. For surface laid mines this can result in a complex signature of relatively long duration. The detailed structure of such signatures may be used to identify the nature of the target. Figure 12.26 shows UWB radar data for a metal mine-like target. The metal mine-like target is clearly discernible in the centre of this image. As the airship travels forward, each pulse emitted by the radar results in a single range profile being recorded, and this represents the energy scattered from the scene. The closer the scatterer is to the radar, the earlier in time the energy it scatters arrives at the receiver. In this case the dominant scatterer is the outer surface of the metal mine and causes a specular reflection.

Figure 12.27 shows data for a set of four surface laid plastic mine-like targets and shows distinct differences between the metal mine in the last figure and the plastic mines shown here. The plastic mine-like targets are again clearly discernible and the characteristic signatures of plastic mines are visible. It is seen that energy is received by the radar over an elongated period of time for each target detected. The first return (top-most) is due to the specular reflection from the front of the plastic mine case, and the largest return, later in time, is due to the reflection of energy coupled into the mine body and reflected at the rear surface.

The Mineseeker Airship trials in Kosovo allowed testing of the prototype radar system and data gathering to aid further development towards a capability to positively identify mined areas and submunitions on the ground and therefore reduce the area being searched by the mine and battle area clearance organisations.

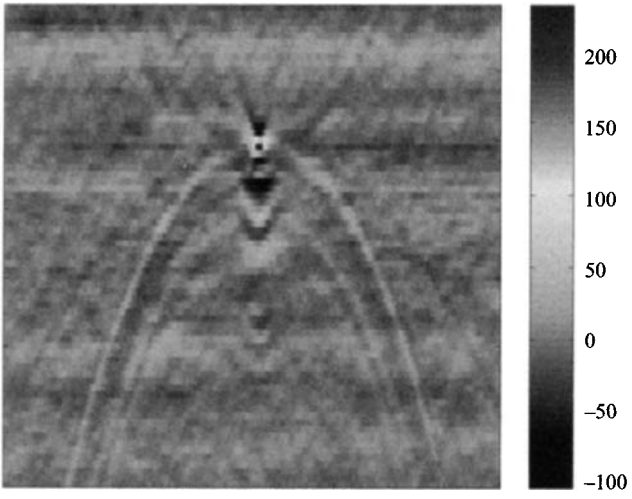

Figure 12.26 UWB SAR image (metal mine-like target)

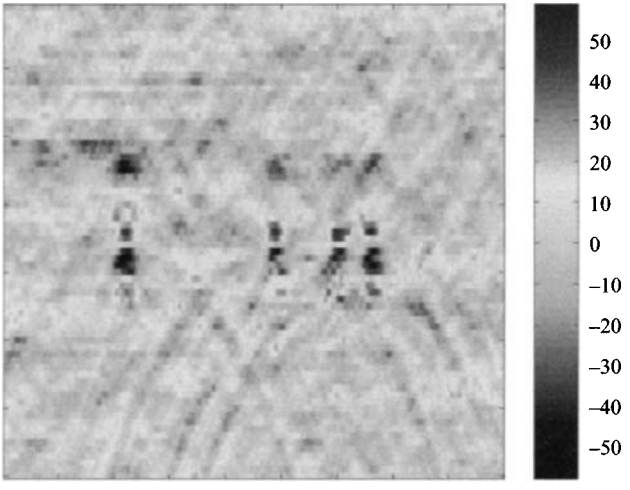

Figure 12.27 UWB SAR image (plastic mine-like targets)

The radar was tested against surface laid, foliage obscured and buried mines and UXO. Additionally, and most importantly, the UWB SAR was tested against the United Nations Mine Action Coordination Centre explosive detection dog accreditation site, a fully ground truthed live mine site. Both the sites were of strategic importance during the conflict in Kosovo, with the result that both sites are realistically uneven, cratered and littered with the debris of conflict.

12.7.2.5 Example results: Each of the results shown are raw data that have been subject to SAR processing (focusing) only. No further data processing techniques, detection or discrimination algorithms have been applied.

The data were collected from 60–70 ft (18–21 m) altitude with the radar antennas pointed at 45 degrees to the ground. All plots have azimuth and range sample points spaced by approximately 15 mm. In all cases the azimuth direction (direction of airship travel) is along the front of the plot and the range direction (distance from the radar to the target) is along the side of the plot. Amplitudes of the scattered signal are relative values. Both VV and HH polarisations were collected; the polarisation displayed is indicated in the Figure caption (Figures 12.28–12.31).

12.7.2.6 Summary: UWB SAR technology could produce immediate and quantifiable reduction of the social and economic impact of landmines, through airborne delineation of mine and UXO contaminated areas. This should reduce the risk of

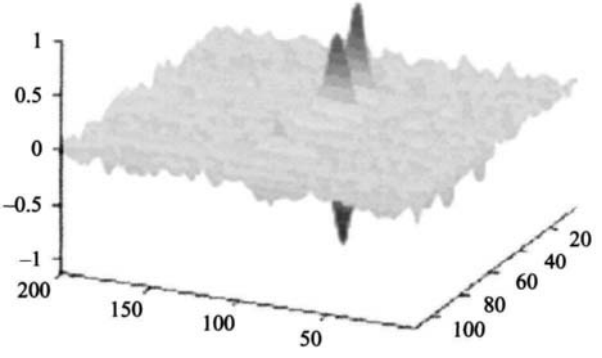

Figure 12.28 Surface laid calibration sphere, HH polarisation

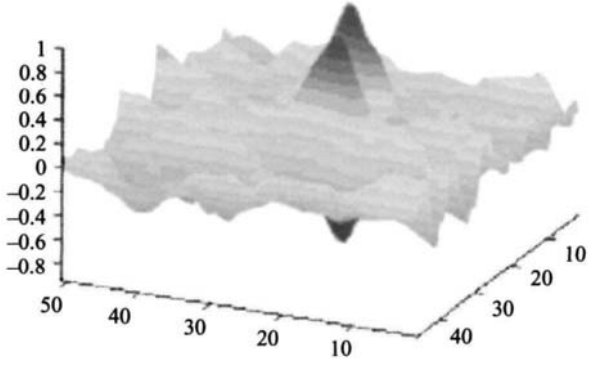

Figure 12.29 Surface laid RBL755 (cluster bomb sub-munition – inert), VV polarisation

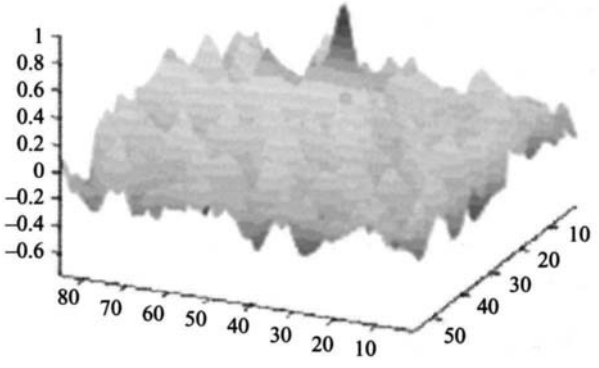

Figure 12.30 *Buried RBL755 (cluster bomb sub-munition – inert), HH polarisation*

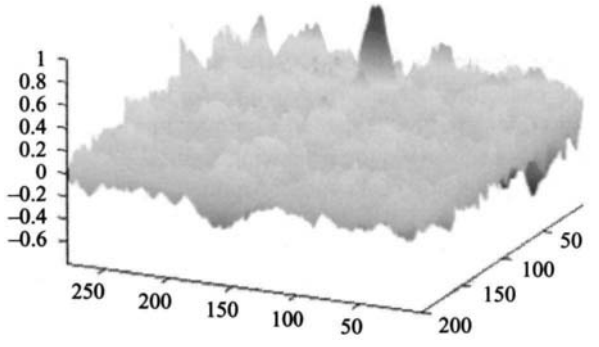

Figure 12.31 *Buried PMR2a – live, VV polarisation*

unintentional entry into hazardous areas, contribute to the efficient allocation of scarce clearance resources and immediately release land for productive use in order to encourage economic growth and stability.

A 20% improvement in the effectiveness of level 2 (technical) surveys could save US$200-250K for each square kilometre of contaminated land in addition to a potential cereal crop yield of US$47 000 per square kilometre per year as reported by the GICHD.

Mineseeker harnesses radar and airship technologies to release a mined area survey capability that is fast, accurate and efficient. UK testing and the deployment in Kosovo of a prototype system has demonstrated that an airship platform has a significant degree of capability in a mine action role and has investigated the current level of performance of the prototype radar. It was possible to survey ground at 100 square metres per second during radar trials.

Previous Page

12.8 Case studies

12.8.1 Introduction

The following Section provides case studies on a variety of approaches to mine detection.

12.8.2 Detection of buried landmines with GPR
Dr Martin Fritzsche

12.8.2.1 Introduction: This contribution discusses the application of ground penetrating radar sensors to the detection and classification of buried landmines. A novel detection and classification scheme is described, which combines image processing of horizontal plane views for object localisation with signal processing and pattern recognition techniques for object classification. Based on the modelling of transient scattering from spheres it is shown how internal object structure determines scattering characteristics. Various types of time–frequency transforms can thus be used to extract salient signal features and to associate each radar signal to one possible category, i.e. as being caused by a mine, by any type of nonhazardous object or simply by the soil background. The investigated techniques are applied to a large data set obtained in field trials and show quite promising results.

The first part of this Section deals with the modelling of transient scattering from spheres, buried in realistic soils. The intention is to illustrate how the characteristics of scattered signals are affected by the internal object structure as well as by soil parameters. In the second part, a novel detection algorithm is presented, which is based on the application of image processing techniques to horizontal plane views, obtained with a projection approach. Detections, thus obtained, serve as regions of interest in the subsequent feature extraction and classification steps, which are performed for each signal, to discriminate between mines, nonmine objects and background. For feature extraction, major emphasis is put on the use of wavelet transforms, as a special form of time–frequency transform. For a detailed discussion of the approach presented here the reader is referred to Reference [114].

The main effort of this work is concentrated on the development of concepts and algorithms for the categorisation of radar signals, based on object-typical scattering. Up to now, a coherent approach, which combines both the detection and the classification step, has hardly been investigated. Whereas the detection step can answer the question *where* an object is located, only the classification step can give hints as to *what* kind of object has been encountered.

12.8.2.2 Modelling of transient scattering from spheres buried in lossy soil: Various measurements, conducted in a US military training site (*Jefferson Proving Ground*, Indiana) provided the basis for the simulations discussed in Reference [115]. Soil samples were taken from different depths (100, 500 and 1000 mm). Every sample was tested three times: first with the natural water content, second dried and third

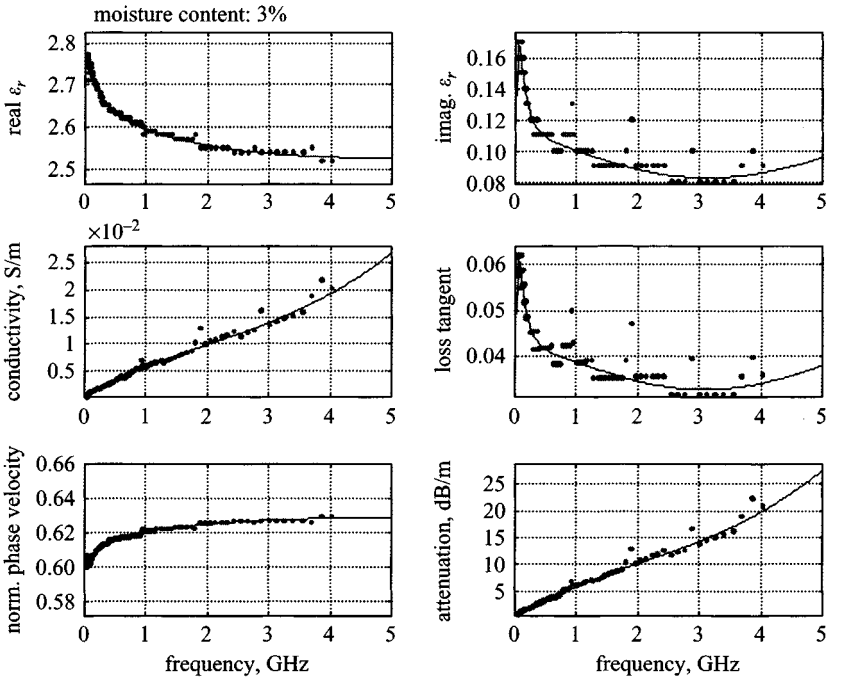

Figure 12.32 *Dielectric soil properties for a small soil moisture content (3%)* Dotted values were derived directly from the measured complex permittivity. The solid line was obtained via interpolation

with a water content near saturation, given below as percentage of volume. The complex permittivity was recorded in the frequency range from 45 MHz to 5 GHz. For a typical soil sample and different volumetric moisture content, Figures 12.32 and 12.33 show curves for the real and imaginary parts of soil permittivity, loss tangent, normalised phase velocity and attenuation.

Measured values, respectively values derived directly from measured values, are represented as dots. Solid lines were obtained via interpolation. Outliers at 0.85 GHz, 1.7 GHz and higher frequencies were caused by resonances in the probe mount. These curves illustrate a noticeable change of dielectric parameters with increasing soil moisture. The real part of the relative permittivity increases from 2.6 for 3% soil moisture to 4.6 for 12%. Propagation velocities are decreased accordingly. At the same time for frequencies around 2 GHz attenuation increases from 10 dB/m for dry soil (3% moisture) to 25 dB/m for moderately humid soil (12% moisture). At the saturation level (49% moisture, not shown here) attenuation will have already reached 100 dB/m. Together, these examples point out the dependency of GPR on the soil moisture content and thus show the limitations of applicability.

Owing to the complexity of object geometry and not sufficiently known soil conditions, a realistic simulation of electromagnetic waves scattering from mines is hardly

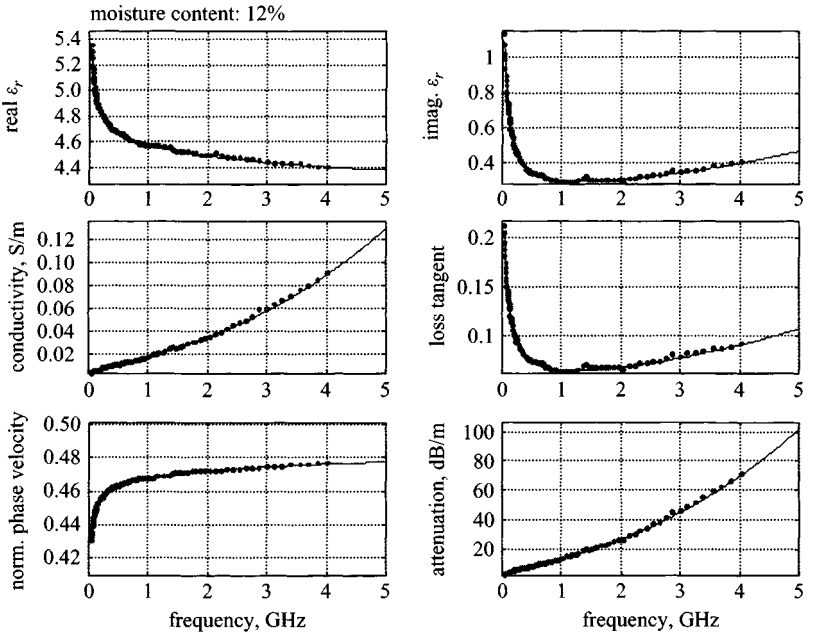

Figure 12.33 *Dielectric soil properties for a medium soil moisture content (12%)* Dotted values were derived directly from the measured complex permittivity. The solid line was obtained via interpolation

feasible. Therefore, the intention of this paragraph is to highlight the dependency of characteristic object signatures from:

- material parameters (contrast of dielectric properties, attenuation, dispersion)
- geometrical object structure (solid sphere, dielectric shell)
- frequency spectrum of the incident pulse.

The simulated data served as a starting point for the development of time–frequency methods for feature extraction, described below.

The scattering of electromagnetic waves from spheres is discussed in great detail in the literature; see, for example, Reference [116]. As incident signal pulse, a Ricker–Wavelet was used, defined by

$$g(t) = (1 - 2\pi^2 f_M^2 t^2) e^{-\pi^2 f_M^2 t^2} \tag{12.2}$$

with the centre frequency f_M of the pulse given by

$$G(f) = \frac{2}{\sqrt{\pi}} \frac{f^2}{f_M^3} e^{-f^2/f_M^2} \tag{12.3}$$

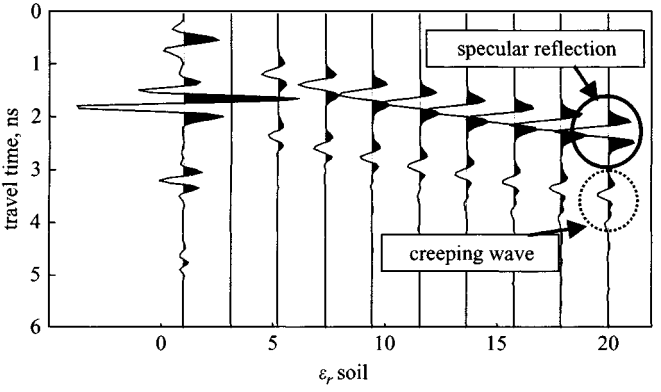

Figure 12.34 *Scattering from a dielectric solid sphere ($\varepsilon_r = 3$, $r = 50\,mm$) as a function of soil permittivity*
The signal on the left relates to scattering in air

With bandwidth defined as the distance of the 3-dB points, one obtains for $f_M =$ 1 GHz, resp. 2 GHz, a bandwidth of 1.15 GHz, resp. 2.3 GHz.

Figure 12.34 shows scattering results for a solid sphere with permittivity $\varepsilon_r = 3$ and a radius of $r = 50$ mm as a function of the permittivity of the surrounding soil. Here, soil parameters are assumed as real-valued. Two-way travel time increases from top to bottom. The first signal relates to scattering in air. The different responses are caused by the specular reflection, followed by creeping waves that travel around the circumference of the sphere.

As a simulation model for the scattering responses illustrated in Figure 12.35, a spherical shell, buried in soils of different moisture contents, was chosen. The sphere consists of an inner core of explosives, surrounded by a concentric air layer. Calculations were carried out with increasing centre frequency of the signal pulse, defined in (12.2). Signals were calculated as a function of airgap thickness, 1 mm and 10 mm (Figure 12.35*a*, *b*). The motivation for the airgap is the assumption that air-filled pockets inside mines significantly contribute to characteristic reverberations, observed for several types of buried landmines. For display reasons all sub-plots shown are scaled independently to their maximum signal amplitude. Several conclusions can be drawn from the simulation results in Figure 12.35.

For the case of 3% soil moisture and an airgap of 1 mm (top plot in Figure 12.35*a*) the polarity of the specular reflection is reversed in polarity, compared to the scattering response for 12% moisture. The reason is a reversal in permittivity contrast between the surrounding soil and the explosive inner core ($\varepsilon_{r,\,Expl.} \approx 3.1$). Owing to low soil attenuation, no loss in signal amplitude can be observed.

For 12% moisture and high frequencies the airgap acts as a differentiation filter, due to the interference of the specular reflection from the outer and inner core, with opposite polarities. Creeping waves, travelling around the inner core, can also be observed.

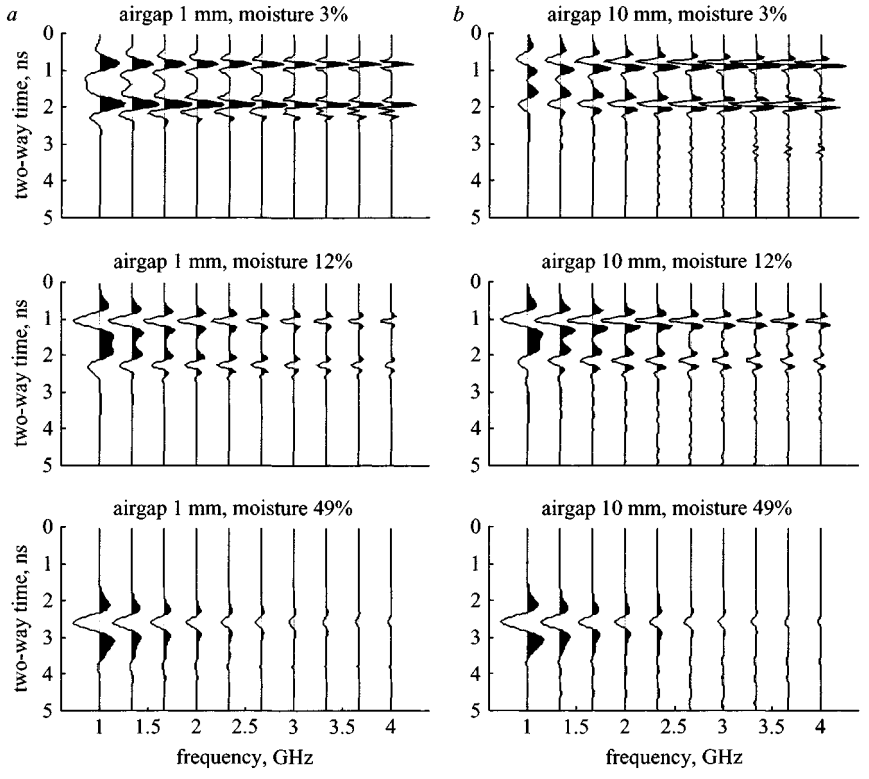

Figure 12.35 *Scattering from a buried sphere ($r = 50$ mm), consisting of a core made of explosive surrounded by an airgap of different thicknesses, as a function of frequency and soil moisture*

Attenuation effects are already visible for 12% moisture. Creeping waves have already decayed considerably, compared to the dry soil case. Only in the 2-GHz case can creeping waves be observed separated from specular reflections.

Soils with high moisture content act as a lowpass filter. Signals are strongly attenuated and the influence of the airgap has vanished completely.

In conclusion, these simulations show that for strong soil attenuation scattering signals do not exhibit any dependency of the inner sphere structure, due to the loss of high signal frequencies, but for weak attenuation a significant influence can clearly be observed.

For different spherical shells, all with the same outer diameter, but with different interior structures, a large number of scattering signals were generated, for more than 60 different soil samples. All spheres were assumed buried in a random burial depth between 50 and 200 mm (as the majority of APMs are located in this depth). The techniques for signal feature extraction were then applied to find the salient features to discriminate the sphere objects. With the algorithms detailed below, a correct object

classification rate of more than 97% was achieved, for soils with up to 25% moisture content [114].

Characteristic scattering signals thus offer potential for object discrimination. Based on features extracted from time–frequency transforms, this concept will be applied to field data, recorded with real mines (see Sections 12.8.2.6–12.8.2.9).

12.8.2.3 New algorithms for object detection: In several approaches that have been published so far, the detection problem is formulated as a binary hypothesis test for individual A-scans; see, for example, References [117, 118]:

H_0: measured signal consists of soil volume scattering plus noise;
H_1: measured signal consists of object scattering plus noise.

Both authors use some kind of suppression technique to cancel the surface reflection, which generally and unfortunately represents the fraction of the signal with the largest amplitude and which may mask objects buried at shallow depth. Results obtained with alternative but similar techniques are presented in References [119, 120], for example.

A principal disadvantage of these techniques lies in the isolated consideration of single scans. So-called A-scans (in the terminology of Daniels [121]), acquired at adjacent sampling points, are highly correlated, i.e. they cannot be regarded as independent. Given a surface sampling grid of sufficient density, every buried object can be *seen* from more than one sampling location. Therefore one can conclude that the robustness and the performance of a detection system can be improved when neighbourhood relationships are taken into account. Further, the processing of three-dimensional data sets opens up new possibilities to utilising the potential object's shape as a discriminating factor.

In the following, a new approach is presented, which makes use of an orthogonal transform to project a 3D data set onto a limited number of horizontal planes. Consequently, these planes are searched for objects of circular shapes.

If data acquisition is performed along parallel profiles, or with an array of several antennas, a 3D data cube is generated. This cube may be visualised as a sequence of horizontal planes, where every plane represents the distribution of scattering amplitudes for a constant time. For interpretation purposes, these horizontal views are more readily accessible to the human eye than vertical GPR cross-sections, with their characteristic signal pattern. Buried objects may then be discriminated due to their shape, where in vertical cross-sections only a fraction of a scattering hyperbola may be visible.

Figure 12.36 shows a sequence of adjacent horizontal planes. The first plane (at 2 ns) is located directly underneath the surface. Assuming a permittivity of $\varepsilon_r = 5$, these planes are separated by a vertical distance of 27 mm. The horizontal dimensions are 1×1.5 m, with an equidistant sampling interval in the x- and y-directions of 20 mm. In this example, six mines were buried, five of which had a significant metal content and one plastic mine (burial position in the top left corner). Below 6 ns the images are dominated by soil clutter. The signal amplitudes of consecutive planes are highly correlated, and thus a 3D data cube contains a certain degree of redundant information.

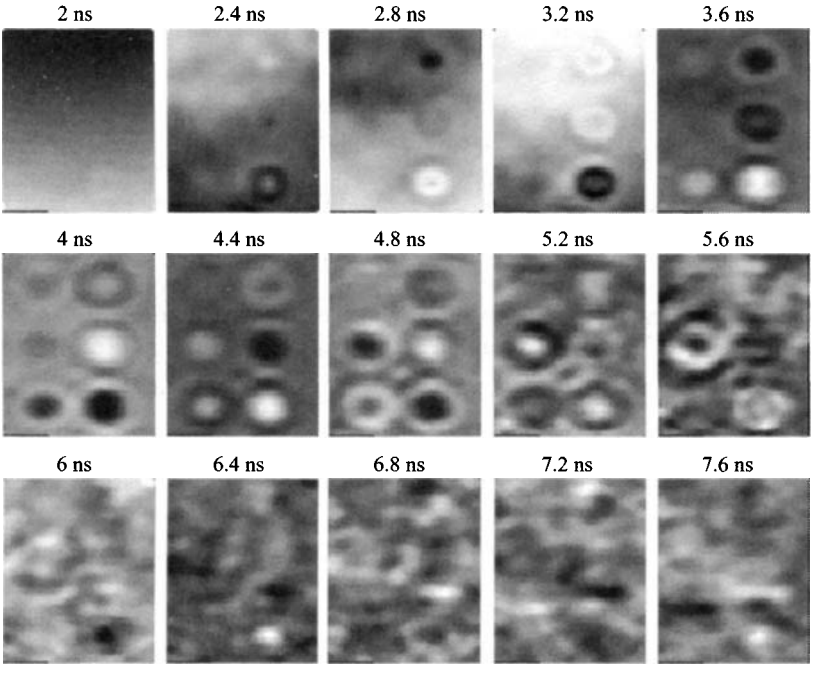

Figure 12.36 *Horizontal plane views of the underground, obtained as surfaces of constant two-way travel time*
The scanned area is 1 × 1.5 m

12.8.2.4 A projection algorithm: When viewing a sequence of horizontal planes as a movie, a visual impression is derived which proves to be very helpful for the detection of objects. Whereas those parts of the signal that are caused by soil clutter will fluctuate more or less over time, signal parts that are due to actually present objects will appear at a fixed location. Scattering caused by them will be observable within a certain time window. To model this perception of the human eye, a transform was sought that allows the suppression of redundant information and which achieves a projection of a full data cube onto a limited number of horizontal planes. A well suited candidate is the so-called *Karhunen–Loève transform*, which is also known as *principal component analysis* (PCA).

For a data cube with N_x, resp. N_y, samples in the horizontal directions and N samples in time (vertical direction), the following matrix can be defined:

$$X = X_{t,l} \text{ with } X_{t,l} = x_{m,n}(t),\ l = m + (n-1)\,N_x, m \in [1; N_x],\ n \in [1; N_y] \tag{12.4}$$

With (12.4) the data cube is rearranged into a two-dimensional matrix, where every row contains all samples of a single horizontal plane. Thus, the number of rows is given by N, and the number of columns is determined by $L = N_x N_y$.

The N sampling values per A-scan span an N-dimensional space, which now is to be projected onto an M-dimensional sub-space in a favourable manner. This is exactly what PCA does: the transform can be viewed as a translation, followed by a rotation. PCA is determined from the first two statistical moments – the expectation value $\boldsymbol{\mu}$ and the covariance $\boldsymbol{K}$ [122]:

$$\begin{aligned} \boldsymbol{\mu} &= E\{\boldsymbol{X}\} \\ \boldsymbol{K} &= E\left\{(\boldsymbol{X}-\boldsymbol{\mu})(\boldsymbol{X}-\boldsymbol{\mu})^{\mathrm{T}}\right\} \end{aligned} \tag{12.5}$$

The solution of the eigenproblem with the covariance $\boldsymbol{K}$ provides pairs of eigenvalues λ_m and eigenvectors $\boldsymbol{b}_m$, sorted in decreasing order. The transform and its inverse are then given by:

$$\begin{aligned} \boldsymbol{W} &= \boldsymbol{B}^{\boldsymbol{T}}\,(\boldsymbol{X}-\boldsymbol{\mu}) \\ \hat{\boldsymbol{X}} &= \boldsymbol{B}\boldsymbol{W}+\boldsymbol{\mu} \end{aligned} \tag{12.6}$$

$\boldsymbol{B}$ is a rectangular matrix of size $N \times M$, containing the eigenvectors as columns, which in this application may also be denoted as *eigensignals*. $\boldsymbol{W}$ contains the transformed and dimensionally reduced signals as columns. The reconstructed signals $\hat{\boldsymbol{X}}$ are only given for the sake of completeness; they are not required for the subsequent processing. PCA provides a basis in which the transformed signals are decorrelated. Thus every original signal can be represented as a weighted superposition of the eigenvectors.

The subtraction of the expectation value in (12.6) implies the simplest form of a background subtraction. The vertical dimension in matrix $\boldsymbol{W}$ does not relate to time any longer, but corresponds with the sorted eigenvalues. Reversal of the sorting process in (12.4) results in the transformed representation of the data cube, with dimensions reduced from N to M. Instead of using the time domain data $\boldsymbol{X}$ one may also apply an FFT before calculating the principal components, which in general will lead to a reduction of the computational effort, as signal spectra can be limited to a certain frequency bandwidth.

Figure 12.37 displays an example of the first 25 horizontal planes. With increasing eigenvalues the frequency content of these *eigenspectra* is shifted towards higher spatial frequencies. Low eigenvalues give a rather coarse view, more and more fine structure is visible for higher eigenvalues: λ_{23} shows the wave patterns emanating from the corners of the image. These patterns are caused by reflections from the experimental set-up.

Objects of circular shape show up quite clearly in the derived projection planes. Thus, shape-based detection algorithms are an obvious choice for object detection, with the major advantage stemming from the fact that single A-scans are not looked at in isolation, but in conjunction with those in a close neighbourhood. The details of the processing sequence are given in Reference [114]; therefore only the major steps are given here. From the transform planes depicted in Figure 12.37 only the first four are used.

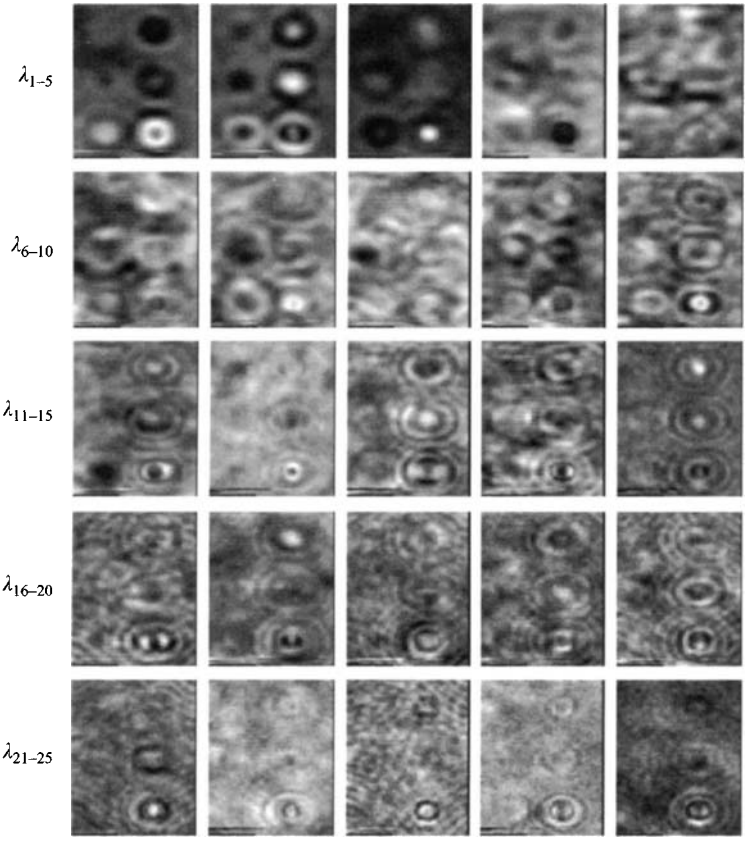

Figure 12.37 *Horizontal cross-sections through the sub-soil, obtained with principal component analysis*
The spatial frequency content increases with increasing eigenvalues

A major problem still arises when a strong scatterer, e.g. a metal mine, is located next to a weak scatterer, e.g. a plastic mine. In this case, the weak scatterer may not be visible owing to an insufficient contrast, but with a rather simple technique a workaround can be found. For this purpose, not the projections $\boldsymbol{W}$ but their *Hilbert transform* $\mathrm{H}\{\boldsymbol{W}\}$ are used [123]. This leads to four complex-valued images, where the real parts are given by the original projections $\boldsymbol{W}$ and the imaginary parts by a $\pi/2$ phase-shifted version. Figure 12.38 demonstrates the result of the phase-shift operation. The bottom row of sub-images show the imaginary parts. Whereas some objects do not show up in the real part (see encircled object in the third image from the left), it can be observed quite clearly in the imaginary part.

12.8.2.5 Detection of circles: The next major step consists in applying a *Hough transform* [124] to the eight image planes, obtained for every data set, such as in

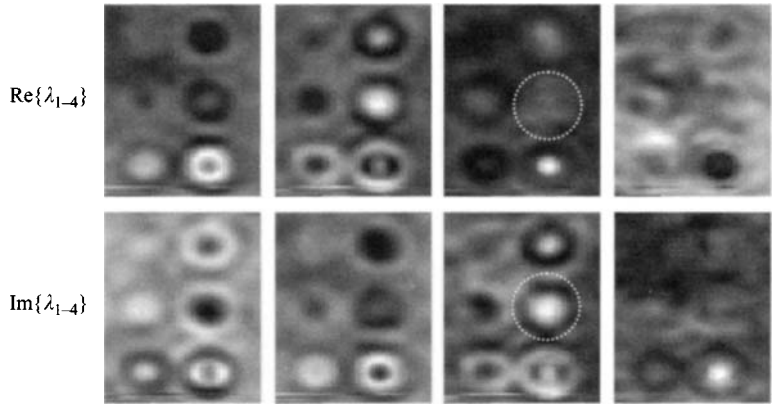

Figure 12.38 *Result of a Hilbert transform, applied to the horizontal projections, obtained with principal component analysis*
Owing to the phase-shift, the encircled object is clearly visible in the imaginary part

Figure 12.38. This type of transform is most commonly used to extract linear features from images, like roads in remote sensing images. This transform can readily be extended to circles, defined by a radius parameter r and a centre position (x, y). Every pixel on the circumference of a circle in the data plane will sum into a single point in the transform space. Consequently circles will appear as bright spots in Hough-space, whereas noncircular shapes will be smeared. The transform is performed for a discretised range of radius values (in pixels), and thus every 2D image pixel is mapped to a 3D Hough-space. The resolution of the third dimension is determined by the sampling of the circle radius, depending on the object size. The application of a threshold will turn the transform planes into binary images, with the position of potential circles indicated in every radius plane.

The processing described so far can be applied in parallel to each of the eight projection planes. What is needed next is a means to combine the information derived from all planes. In theory, only actually present objects will consistently appear in the same location, and therefore an enormous reduction of false alarms can be achieved with a logical combination of these binarised images. A simple realisation was implemented such that at least four pixels are required to be above the threshold.

Detection results obtained with the algorithm described above, when applied to field data, are presented in Sections 12.8.2.10 and 12.8.2.12. Once these circular shaped regions are extracted, they can serve as regions of interest for the classification step, i.e. dedicated signal processing for A-scan feature extraction and classification can be restricted to small sub-sets of data, which means a significant reduction of the computational effort. The approach described here is very robust and requires only a very limited number of parameters to be optimised, such as the number of transform planes and the threshold to binarise the Hough-transformed images.

12.8.2.6 Time-frequency transforms for object classification: At every measurement location a GPR produces signals that contain a certain amount of information about the illuminated sub-soil. For some applications the use of integral signal attributes, such as signal energy, may be enough to answer the question *where* an object is located. To find an answer to the question *what* kind of object we are confronted with, we need to consider the signal structure.

For this purpose time–frequency transforms are the logical choice. *Short-time Fourier transforms* and the *Wigner–Ville transform* are the best known representatives of linear, respectively quadratic transforms. In recent years wavelet- or wavelet-packet-transforms have also become very popular. Their major advantage is that the wavelet basis functions are localised in both the time and the frequency domains. A rather novel approach is the extension of wavelets to so-called *multi-wavelets*. The underlying mathematics has been described in great detail elsewhere and goes beyond the scope of this Chapter. The interested reader is therefore referred to References [125, 126] for wavelets in general, to Reference [127] for multi-wavelets and to Reference [128] for wavelet-packets.

12.8.2.7 Statistical pattern recognition techniques: The extraction of meaningful features is of central importance for every statistical pattern recognition system. Common to many classification tasks is that some sensor produces large amounts of data per time unit. This leads to the requirements to separate important from unimportant or redundant information, a strategy which is also called *reduction of dimension*. The classification procedure, consisting of four major steps, is shown in Figure 12.39.

Formally speaking, the aim of statistical pattern recognition is to provide a mapping from the feature space, where every measured signal is represented by a number of features, to a decision space, i.e. every measurement is associated with one of a certain set of possible classes – in our case mine, nonmine object or soil background. The searched connection between measured data and the classification results is described with examples. Available data are divided into two parts: a learning set, to optimise the mapping and a testing set to check the effect with some statistical measures. The latter serves to simulate the application of the classifier in the 'real world'.

12.8.2.8 Time–frequency transforms: The decomposition of a signal into a number of N constituents is at the core of the linear methods:

$$x(t) = \sum_{k=0}^{N-1} a_k \Phi_k(t) \tag{12.7}$$

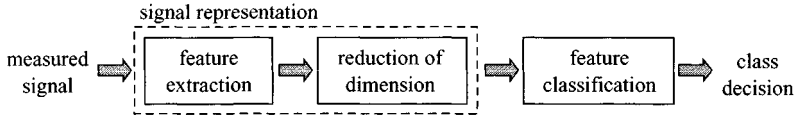

Figure 12.39 Classification model

where $x(t)$ is a measured signal and $\Phi_k(t)$ is a basis function with coefficient a_k. Desired properties of the basis functions are orthogonality, good localisation in the time and frequency domains, as well as the possibility for efficient implementation of the algorithm. As wavelet transforms turned out to produce the most favourable results in terms of recognition rate, some more details are given on the relevant processing scheme. For a more complete comparison of several transform techniques and the results obtained therewith, the reader is referred to Reference [114]. The *discrete wavelet transform* (DWT) can be understood as a form of multi-resolution analysis; the mathematical concept can be described by two-scale difference equations, with filter coefficients $h(k)$ and $g(k)$. The first filter can be understood as a lowpass or scaling filter, whereas the second filter acts as a highpass or wavelet filter. These filter coefficients have to fulfil certain criteria to provide an orthogonal basis system. The overall signature of the signal (i.e. the lowpass signature) will be contained in the outputs of the scaling filter, and the detailed information will be derived from the wavelet filter. Cascaded application of the filters leads to the well known decomposition trees.

The kind of filters that are selected is important, as this has a major impact on the number of coefficients required to represent the signal with a tolerable reconstruction error. Although signal reconstruction is not our primary goal here, one can state that for signal classification the same considerations hold as for signal compression: the fewer coefficients the better, because then a maximum degree of information is represented by a minimum number of coefficients. Ideally the wavelet shape should somehow resemble the investigated signal. For this work a biorthogonal spline wavelet [125] was chosen.

Figure 12.40 gives an example of a wavelet-packet-transformed chirp signal. The original signal is displayed as *level* 0; every transform step comprises the application of the low- and highpass filters, followed by a sub-sampling with a factor of 2. The result one would obtain with the standard wavelet transform is highlighted in grey.

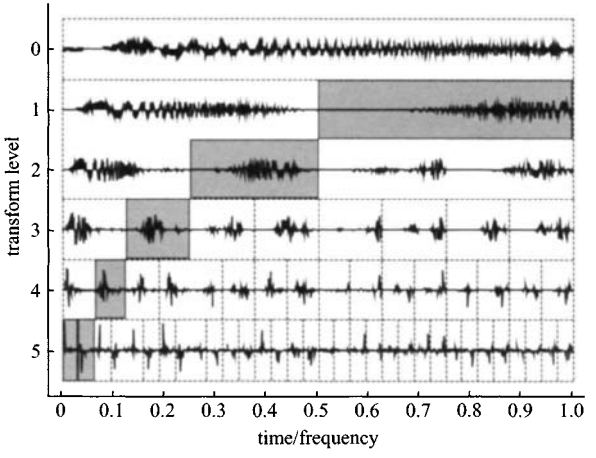

Figure 12.40 Exemplary application of the wavelet packet transform (DWPT)

In contrast to the standard wavelet transform (highlighted in grey) a complete decomposition tree is calculated.

To derive features from the coefficients, two possibilities exist: one can either use the coefficients in selected sub-bands themselves or calculate statistical moments, e.g. mean, standard deviation or measures such as energy or entropy for the coefficients in a single sub-band. However, with this approach one important deficiency of the classical DWT or DWPT has to be taken into account. Due to the sub-sampling, which is performed in every transform step, the resulting coefficients are not invariant under translations of the input signal. What does this mean? If we apply a circular shift to the original signal by one or more samples, different coefficients and thus different features will arise. This is, of course, not acceptable, as then two identical objects buried in different depth would produce different features, i.e. they may not be interpreted as belonging to the same kind of class. In Reference [114] a simple extension to the classical transforms is presented, which will allow us to derive coefficients and thus features that are invariant under translations of the input signal. The extension is equally applicable to wavelet-packet, wavelet- and *multi-wavelet transforms* (MWT) and increases computational cost by a factor of only 2. MWTs are the latest member in the zoo of wavelet transforms; their mathematical details are given in Reference [127]. The extension 'multi' relates to the fact that more than one filter pair is used.

A thorough comparison of the classification results obtained with the above-mentioned time–frequency transforms is given in Reference [114]. In the following sub-Section the transform that produced the best results is stated.

12.8.2.9 Detection and classification results: The data on which this investigation is based were recorded in a multi-sensor trial campaign, with several mines, mine-like objects and various clutter objects buried under different soil conditions and depth. The mine types used were both metallic (Maus-1) and with minimum metal content (VSMK2, AUPS, VAR40), with diameters around 70–90 mm (see Figure 12.41).

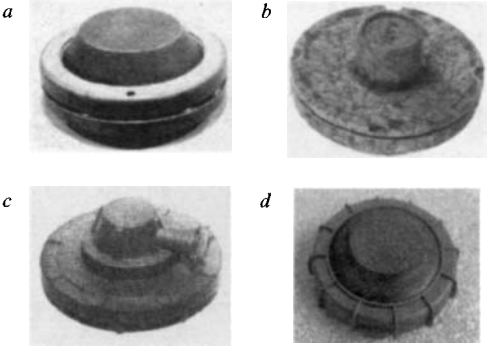

Figure 12.41 *Anti-personnel mines used in the field trials: (a) Maus/1, (b) AUPS, (c) VAR/40, (d) Valsella-VSMK2*
Types (*b*) to (*d*) are minimum metal mines

Further to mines, the measured metallic objects were: cartridges, safety pins (from mines), pieces of aluminium and squashed coke cans. As metal-free objects we used stones of different sizes, pieces of wood and holes pressed into the terrain surface. In total, 254 different object measurements were made.

The soil types investigated were the existing terrain on the trial site (the Joint Research Centre of the European Commission in Ispra, Italy), a grass field, dry and sandy ground, an earthy soil covered with a thick layer of leaves and a more agricultural terrain (rough surface, earthy). Burial depth varied between 0 and 150 mm, and the inclination angle of the mines, with respect to the horizontal, varied between 0 and 30°. Variations of object burial conditions are a prerequisite for a statistical recognition approach and thus should comprise as many variations as possible, because objects' scattering properties may exhibit dependencies on their orientation with respect to the incident radiation.

The objects under test did not include anti-tank mines. In general these are larger in size and, although some species with low metal content exist, they are easier to detect. Therefore the procedures detailed above will be equally applicable. The sensor used was the Superscan© system, a pulsed ultra-wideband ground penetrating radar by ERA Technology, with 1 GHz centre frequency. The sensor was attached to a scanning frame, to enable repeatability of the measurements and to minimise position errors. Per measurement, an area of $1 \times 1.5\,\mathrm{m}^2$ was sampled on a 20×20 mm grid. At every location a signal of 12.8 ns length was recorded, which in dry sandy soil ($\varepsilon_r \approx 4$) relates to a depth range of almost 1 m. For more details concerning the trial campaign or to download the measured data, the reader is referred to Reference [129].

To be able to estimate the influence of the antenna height above ground, measurements were performed at 100-mm, respectively 150-mm, ground distance. Results published in Reference [130] showed that no influence on detection results could be observed, and therefore no distinction between these two cases is made in the following.

12.8.2.10 Detection results: The detection method, detailed in Section 12.8.2.3, was applied to all 42 3D datasets. Using principal component analysis every dataset was reduced to 4 horizontal projections, i.e. after performing the Hilbert transform the procedure for circle detection had to be applied to 8 planes, as described in Section 12.8.2.5. An object is counted as correctly detected when the centre of a hypothetical object lies within a circular halo with radius r_H around the actual position. The value for r_H was taken as 4 sampling intervals, relating to 160-mm diameter. This value resulted as the average radius of all detected (potential) objects. The size of this halo is a characteristic of the sensor and relates to the antenna footprint. If there is more than one object in this region they cannot be resolved. As this may have direct consequences on false alarm rates, this effect was taken into consideration when the layout of the experiments was planned.

If we denote A the area of the scanned trial ground and N_{Obj} the number of objects buried in this area, the maximum number of false alarms is given by

$$N_{FA} = \left(A - N_{Obj}\pi r_H^2\right) \Big/ \left(\pi r_H^2\right) \tag{12.8}$$

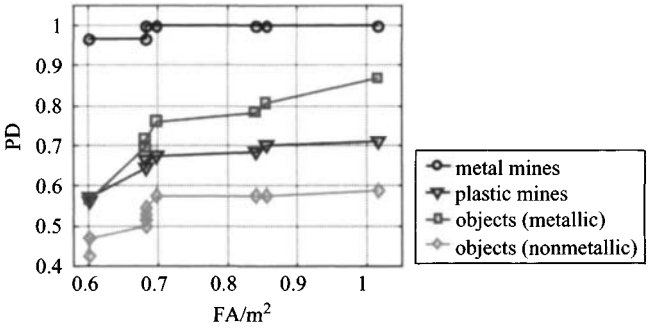

Figure 12.42 *Detection probability (PD) as a function of the number of false alarms (FA) per m^2*
Different symbols denote different object categories

In the following the number of false alarms per area is given instead of false alarm probabilities. In practice, this allows a better comparison of different sensors, due to the independence of this measure from sensor footprints or characteristic object sizes. Figure 12.42 shows object detection probabilities (PD) as a function of false alarms (FA) per square metre. This type of graph is also denoted as a ROC-curve (receiver operating characteristics). The curve was obtained through variation of the binarisation threshold, applied to the Hough-transformed horizontal planes. The results in Figure 12.42 represent overall ROC-curves, without distinction of soil type. Soil specific results are given in Reference [114].

Given one false alarm per m^2 all metallic mines are detected, which is not too surprising, as these mines cause prominent scattering responses that can be detected based on the signal energy only. Around 71% of minimum metal mines are detected. In contrast to an 87% detection rate of metallic objects (nonmine type), only 59% of nonmetallic natural targets or clutter objects are detected.

12.8.2.11 Combination of object detection and signal classification: The detection step generates only a binary decision: either a hypothetical object is present or not, i.e. no statement can be made regarding the potential danger associated with it. The only possibility to extract further information is to look directly at the radar signals. This is exactly why detection *and* feature extraction/classification have to be combined. In the methodology presented in this Chapter, the detection step serves as pre-processing for the classification step (see Figure 12.43). Only A-scan signals located within the contour of a potential object are subject to further processing. This enables an enormous reduction in processing power requirements, as only a fraction of the measured signals have to be dealt with.

12.8.2.12 Classification results: To be able to evaluate classification performance independently of detection performance, the entity of all available objects was looked at first. In the second step the classification algorithm was applied only to those alarms

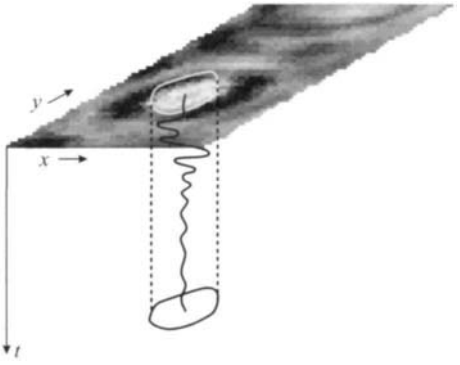

Figure 12.43 *The detection step serves as pre-processing to feature extraction and classification*
Only A-scans located within the white contour line of a potential object have to be subject to further processing

Table 12.2 *Recognition error rates in percent, obtained with shift-invariant multi-wavelet transforms (SIMWT) and FFT transforms*

Method/soil category		All soils	Field	Sandy soil	Meadow	Field (agricult.)
1	SIMWT	48.5	34.4	39.2	8.1	37.3
2	FFT Spectra	53.8	53.3	38.9	42.4	55.0

that were output by the detection method. As classification technique a quadratic polynomial classifier was used. The major advantage of this technique is that its adaptation does not require iterative and thus time-consuming calculations, like the case for neural networks [122], for example. For adaptation and testing all available object data are randomly split into two sets – one used for the learning and the other for the testing phase. The testing data thus serves to investigate the classifier's generalisation capability. To increase robustness, false alarms, i.e. A-scans that were not associated with an actually existing object, are added to both datasets. Every A-scan is represented by a feature vector with 14 elements, generated from the coefficients of one of the various transforms. The classifier then associates every A-scan with one of the three possible classes (mine, nonmine object or background class). The decision on the entity of signals belonging to one object – as represented by the contour line in Figure 12.43 – is then made as a majority vote.

Table 12.2 lists the recognition rate obtained with two different transform techniques for all available objects, i.e. also for those that were not detected by the detection step. Results are given for the entity of all soils and also separated according to soil type. Row 1 represents the classification errors obtained for shift-invariant

Table 12.3 Confusion matrix obtained with the classification of detected objects only

Truth\actual	Mines	Objects	Background
Mines (metal and plastic)	88 (84%)	7 (7%)	10 (9%)
Other objects	15 (21%)	44 (60%)	14 (19 %)
Background	9 (20%)	13 (30%)	22 (50%)

Vertical position indicates the true object category, whereas the horizontal direction denotes classifier decision. False negatives are highlighted in dark grey, false positives in light grey. Numbers in brackets indicate relative fractions.

multi-wavelet transforms, which was shown to be the best-suited transform technique. For comparison, the recognition error rate obtained with features generated from Fourier spectra (reduced in dimension with PCA) are given in row 2. The wavelet technique clearly outperforms standard Fourier spectral techniques. The results also show a strong dependency of classification error on soil type. This is caused by a substantial variation of clutter background, due to different soil and surface characteristics.

To combine the classification with the detection processing the SIMWT method is selected. Related results are listed in Table 12.3, in the form of a confusion matrix. The column direction indicates true object class, and the horizontal axis denotes the decision output by the classifier. Ideally the matrix should have a diagonal form; off-diagonal elements are false decisions. To come to a risk assessment of a decision, costs would need to be assigned. Correct decisions do not cause any cost. Obviously, the cost associated with false negatives (object present, but *not* detected) are a lot higher than those of false positives. Whilst the latter only means to prod the ground in vain, which does of course raise the clearance costs, the first may lead to loss of sensor equipment or worse.

Almost 84% of detected mines are classified correctly. If we combine the results from the detection and classification steps of the 71% detected plastic mines, 59% are associated correctly.

12.8.2.13 Summary and conclusions: Currently employed techniques for mine clearance almost exclusively rely on mechanical prodding, mine dogs and metal detectors. For the detection of minimum metal mines the latter are of only limited use. Consequently, sensors such as ground penetrating radars, with their ability to detect dielectric discontinuities in the ground, seem to be an appropriate choice. In this context, the development of new sensors and algorithms, which allow a significant increase in detection probabilities and at the same time a considerable decrease of false alarms, are of high priority.

In this Section a new approach has been described, which for the first time shows how the detection of potentially hazardous buried objects can be combined with an interpretation of individual signal characteristics. The assumption that objects of different categories can be separated due to object specific signatures was proven

on the basis of simulated data and consequently applied to field data. The presented detection method shows how data that were recorded along parallel profiles or with an antenna array and thus forming a 3D-data cube can be projected onto a small number of horizontal cross-sections. In this way redundant information can be reduced and detection probabilities increased.

Central to the new approach is the use of the time–frequency transform to derive salient features for every radar signal. These features form a so-called feature vector, representing the input of a statistical classifier. This classifier maps the feature into a decision space, i.e. every signal is categorised as mine, as nonmine (nonhazardous) object or simply as soil background or clutter.

For this application shift-invariant multi-wavelets were proven to produce the best results. When combining the results of the detection and classification step, 59.5% of the mines are attributed to the correct object category. Related to the entity of detected mines, 84% are classified correctly. It needs to be emphasised that these results were not obtained on the basis of a couple of sandbox measurements, with drastically simplified soil conditions, but with field data, recorded for various soils, with variations in soil and surface properties. The soil clutter and the influence of the reflection at the air/soil interface were shown to be the most important factors that limit GPR system performance.

Even though a reliable use of GPR sensors for mine detection, to achieve the 99.6% detection rate, as specified by the UN, is not feasible yet, this contribution does open up new possibilities for substantial improvements in the work towards this goal.

12.8.3 MINETECT

David J. Daniels

12.8.3.1 Introduction: A prototype detector (MINETECT) has been developed by ERA Technology for the UK Department for International Development (DFID); see Figure 12.44. The detector has been designed specifically for humanitarian demining and uses affordable metal detection and ground-probing radar technologies. The detectors are man-portable and similar in form, fit and function to a standard metal detector, and use a backpack to house the electronics.

The prototypes have been developed to reduce the false alarm rate normally experienced when searching, with a metal detector only, for minimum metal anti-personnel mines. The improvement in performance is achieved by using the GPR as a complementary sensor, as it will only respond to targets with an appreciable radar cross-section.

The MINETECT system comprises a metal detector and a ground penetrating radar. The original metal detector was a Guartel MD8, but was changed to a Vallon VHMD 2.1 to cope with conductive soils. The ground penetrating radar is a pulsed ultra-wideband system with a pulse repetition of 1 MHz and pulse duration of 1 ns. The audio output from the radar system has two degrees of freedom: frequency and

Figure 12.44 MINETECT under test in Sarejevo

volume. The depth of the buried object varies the frequency of the audio output, whilst the size of the object varies the volume of the audio output. The ground penetrating radar employs novel operator audio interface techniques embodied in European patent number 99306164.7. Shallow targets sound high in frequency, whilst deep targets sound low in frequency. The relationship between target depth and MMI output frequency is illustrated in Figure 12.45. It can be seen that the typical hyperbolic target response in a B-scan is heard as a variation in the audio frequency output. If the ground surface reflection could be heard, it would be audible as a continuous tone. This ground surface reflection is removed through the algorithms applied to the radar data.

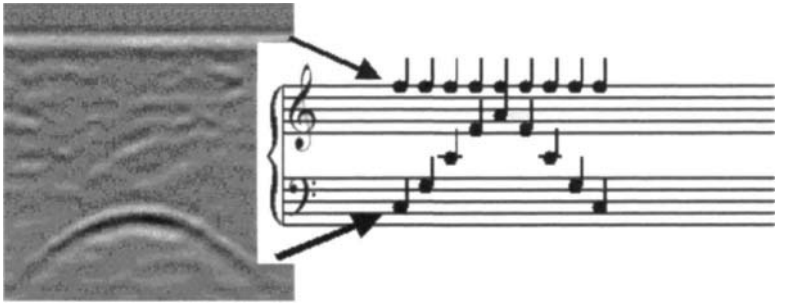

Figure 12.45 Principle of MINETECT operator interface

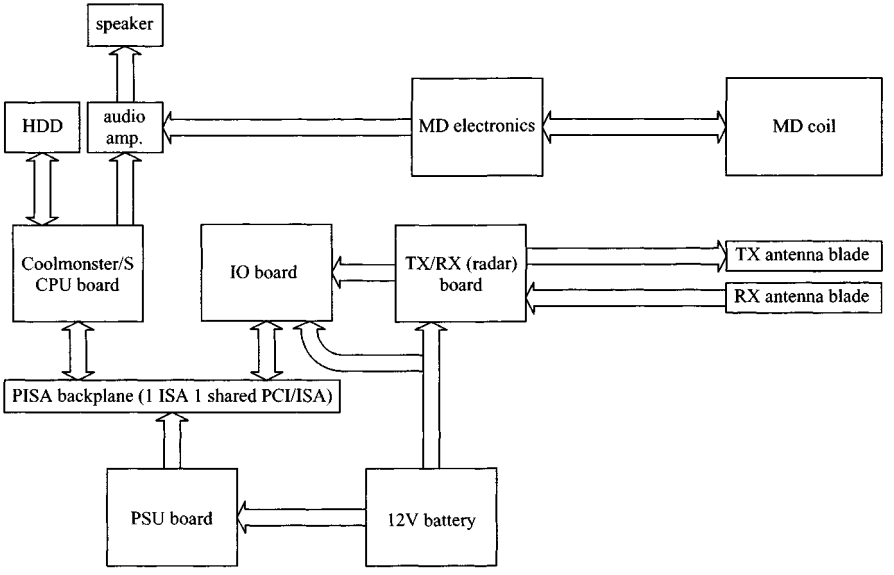

Figure 12.46 Block diagram of MINETECT system

The specific aim of the program of trials carried out during the MINETECT programme was to determine the probability of detection (PD) and the false alarm rate per metre squared (FAR per m^2) of the prototype detectors. The project was aimed at reducing the incidence of false alarms compared with the false alarm rate of a standard metal detector alone. This reduction in false alarm rate reduces the number of excavations that would have to take place as part of a demining operation and hence improves the productivity of a demining team. This will increase the amount of land that can be cleared in a given time, with a given number of demining operatives.

The block diagram of the system is shown in Figure 12.46.

The software that implements the MINETECT system runs on the single board computer. The software is written in C++ and utilises proprietary algorithms owned by ERA Technology Ltd. The program is responsible for processing the radar data. It relies upon a set of known signal processing algorithms and a novel MMI (man–machine interface), which converts radar signals into sound signals. The software currently runs on a popular Windows based operating system, and remote administration is achieved using the LAN (local area network) connection supported by this operating system.

MINETECT can be used as a combined detector in one of two ways. The user can operate the detector in either sequential mode or combined mode. Sequential mode has been used throughout the testing phase as it allows analysis of PD and FAR for the MD and GPR as separate sensors if required.

The MINETECT system was trialled in different ways. Each of the trials had different objectives, as described below.

12.8.3.2 Initial tests at ERA: The initials tests at ERA were aimed at determining initial values for PD and FAR for the combined detector. The trial was also aimed at assessing the performance that an inexperienced user could achieve in a first trial. A number of operators with different skills were assessed on a number of different types of soil, and an example of the variance between operators is given in Table 12.4 for one soil type only. The range of performances can be seen from this trial.

The GPR antenna of the MINETECT system is shown in Figure 12.47 and an AV clip of the system in action is provided on the CD.

12.8.3.3 Quantified trials: The quantified trials were conducted at a US Army test facility. The trial was aimed at evaluating the incidence of false alarms when compared with the false alarm rate of a metal detector alone. The trial site is a performance benchmarking facility, which allows comparison with the detection characteristics of other demining tools. The trial facility is comprised of 223 calibration test cells

Table 12.4 Operator performance matrix

Operator ID	Surface	Mine	Found	Missed	FAR, m^2	PD
1	Sand	12	10	2	0.2	0.833
2	Sand	12	12	0	0	1
3	Sand	12	12	0	0	1
4	Sand	12	11	1	0.04	0.917
5	Sand	12	11	1	0	0.917
6	Sand	12	10	2	0	0.833
7	Sand	12	11	1	0.08	0.917
8	Sand	12	12	0	0.04	1
9	Sand	12	12	0	0.12	1

Figure 12.47 Photograph of MINTECT GPR antenna mounted on a Guartel MD

each 1m in area and 1008 calibration test cells each 1 m in area. Only the contents of the calibration test area were released to the trials team after they had been surveyed. The blind grid results are assessed by the host organisation. ROCs (receiver operating curves) were produced for both the calibration and blind sites. The calibration site consisted of lanes A–L with a total number of 223 test cells; there were 44 mines within these squares with a depth of cover up to 10 cm. The blind site comprised lanes A–L with a total number of 1008 test cells. The calibration site contained the following: 32 blank cells, 35 nonmetallic clutter cells,112 metallic clutter cells, 3 AT metal mines, 10 AT minimum metal mines, 3 AP metal mines and 28 AP minimum metal mines. Some of the metallic clutter cells were of such a size that the GPR would have classified them as valid targets, so only small metallic clutter was included in the derivation of the ROC curve, shown in Figure 12.48.

Further details of the trial results can be found in papers by Daniels and Curtis [131]. The initial results from the detailed analysis of the calibration are:

- 100% of all the mines were detected
- 65% of all test cells were correctly classified
- 77% of all possible clutter was correctly classified
- a 2 : 1 reduction in clutter was achieved.

When considering mines, blanks and level one metallic clutter, as plotted in the ROC curve in Figure 12.48, it was shown that 100% of mines were found. This level of

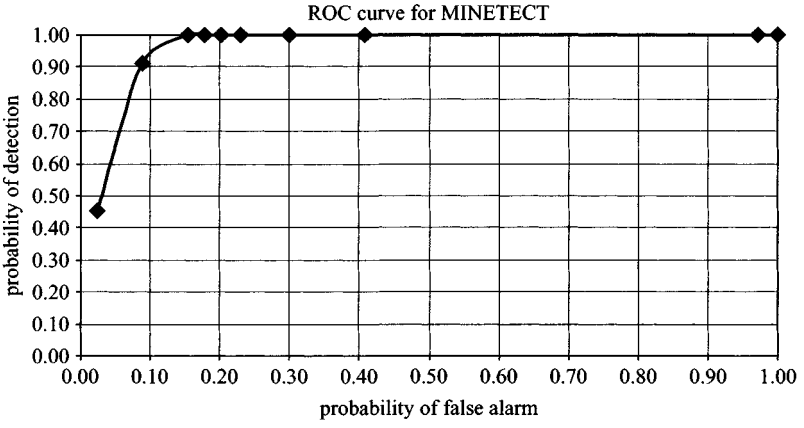

Figure 12.48 ROC curve for mines, blanks, nonmetallic clutter and level one clutter

performance was achieved with a FAR of only 0.07 per m^2, assuming a cell area of 1 m^2. When assessing the detection performance against all clutter, the system achieved 100% detection, with a FAR of 0.125 per m^2, assuming a cell area of 1 m^2.

The combined blind lane ROC curve for units 1 and 2, including blanks and clutter, showed a breakpoint of 92% detection with a FAR of 0.41. This compares with the ROC curve for unit 2 for the calibration lane, which showed a breakpoint of 100% detection with a FAR of 0.3. It became evident that the metal detector function was missing some minimum metal mines because of the conducting soils at the site. This was noted as an aspect needing change for future stages of the programme.

12.8.3.4 Trials in Bosnia: The in-country trials were conducted at Norwegian Peoples Aid's (NPA) facility in Sarajevo, Bosnia and Herzegovina. The trial was aimed at determining an accurate figure for the probability of detection in evaluation sites close to minefields. The trial also introduced the concept of a live audio GPR system to the demining end-user. Three test sites were used. The first test site consisted of a gravel layer approximately 150 mm thick with a layer of clay type soil underneath the gravel. The test site was divided into 200 cells of size 1 m by 0.5 m. The second test site was formed of minimal grass vegetation on native Balkan topsoil. The test site consisted of some 200 cells of size 1 m by 0.5 m. The third site was constructed on native grass and topsoil in an area with many naturally occurring false alarms. The site consisted of a 3 m by 1 m lane with tapes marking the boundaries. Three mines were buried in the test lane with a number of naturally occurring false alarms. NATO SFOR (stabilisation force in Bosnia and Herzegovina) representatives from the British Army, the French Army and Australian Army were present (Figure 12.49).

On the gravel site, the MINETECT operator detected 100% of the 33 mines, which were predominantly PMA2 and PMA3 AP mines. On the soil sites the GPR achieved a 94% detection rate and the MD a 91% detection rate. The GPR operator missed two mines in the soil test facility; the first target missed was a PMA3 at a

Figure 12.49 MINETECT under assessment by SFOR in Bosnia

depth of 100 mm, while the second target was a PMA2 at a depth of 100 mm. The MD operator missed both these targets, plus a PMA2 at a depth of 50 mm with a 15° angle. On the third test site with many metallic false alarms, the MD detected 14 targets, 12 of which were false alarms. The MD missed the PMA2 without a fuse. The GPR detected four targets, one of which was a false alarm, the other three being mines. This demonstration showed that with the GPR there were 10 fewer false alarms, and proved that the GPR was capable of detecting completely nonmetallic mines.

12.8.3.5 Trials in Lebanon: Trials of MINETECT were carried out over the period November/December 2002 in southern Lebanon. The main base for the trials was Tyre, and tests were carried out in Tyre as well as at Baraachit, Tibnine and Naquora. Site visits were also made to Al Tira, Bayt Lief and Shamaa. Figure 12.50 shows a typical mine training area, and the large stones and variable ground topography are typical of the area (see Figure 12.51).

A series of trials were carried out on mines to determine the performance of the GPR in the highly conducting Lebanese soils at several sites. Two sets of information were gathered on detection range performance (Table 12.5) and FAR (Table 12.6).

12.8.3.6 Target classification: Following the trials in the Lebanon it became evident that further reduction in FAR could be achieved by classification of the A-scan data. The next logical step for the development is to build in a signature library for known mine types, whereby the signature of mines and stones can be separated. The operating

Figure 12.50 Cleared mine lane in southern Lebanon

Figure 12.51 Example of terrain and rocks in cleared mine lanes

Table 12.5 Detection range performance against specific mines for the GPR only

Mine type	Training site	Baraachit	Naquora
Israeli AP No. 4 (fuse)	200 mm	Not available	150 mm
Israeli AP No. 4 (no fuse)	100 mm	Not available	50 mm (not tested deeper because of ground conditions)
French AP Model 1951	130 mm	50 mm	100 mm
French AT Model 1947	200 mm	Not available	Not available
PMA-3	Not available	Not available	100 mm
BLU	150 mm	Not available	100 mm
VS50	150 mm	50 mm	Not available
T46	300 mm	Not available	Not available

Table 12.6 FAR against specific sites for the MD and GPR

Site location	MD FAR	GPR FAR	Reduction in FAR
Baraachit 1	$2\,m^{-2}$	$0.375\,m^{-2}$	5.3 : 1
Baraachit 2	$1.75\,m^{-2}$	$0.5\,m^{-2}$	3.5 : 1
Training 1 (BLU)	$0.875\,m^{-2}$	$0.125\,m^{-2}$	7 : 1
Training 1 (BLU)	$0.94\,m^{-2}$	$0.125\,m^{-2}$	7 : 1
Training 2	$1.15\,m^{-2}$	$0.7\,m^{-2}$	1.6 : 1

procedure would be to record the signature of known mines and then compare this with each new detection. This would be done by holding the GPR head directly over the peak position of the new detection for one or two seconds and the GPR electronics would search the library for the best match. An audio announcement would provide the operator with the results.

To assess the potential of improved target recognition, an initial experiment was carried out at ERA Technology using a PMA-3 and VS50 mine. These were buried in one of the test zones at ERA Technology and their signatures were recorded. These signatures were then compared with a large stone (>100 mm diameter) and a simulated animal tunnel (thin wall buried pipe of 40 mm diameter). All the targets were buried at 75 mm in ballast soil.

Results: Photographs and GPR data from each of the targets are shown in Figures 12.52–12.54.

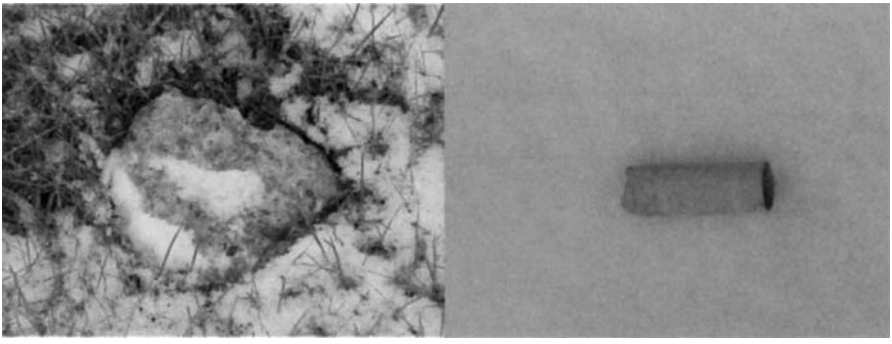

Figure 12.52 Photograph of stone and simulated animal burrow

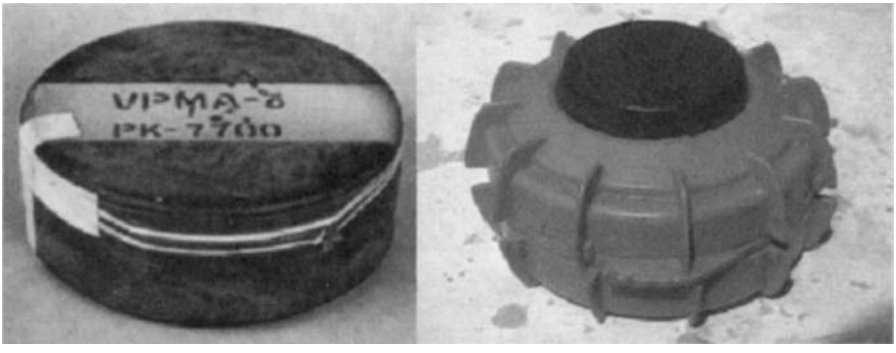

Figure 12.53 Photographs of PMA-3 and VS-50 AP blast mines

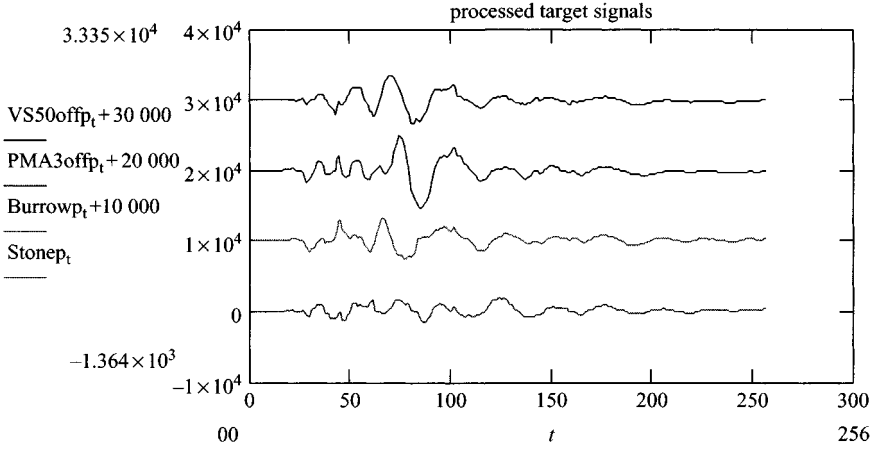

Figure 12.54 Time domain radar data from the VS50, PMA3, burrow and stone

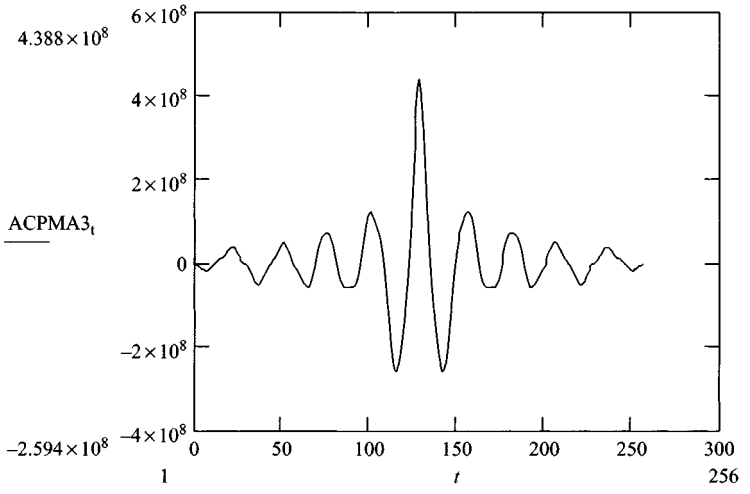

Figure 12.55 Crosscorrelation function of PMA-3 signature

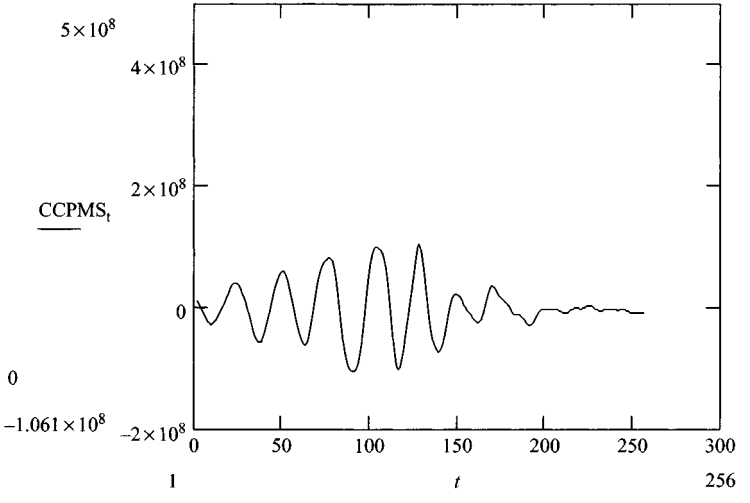

Figure 12.56 Crosscorrelation of PMA-3 and stone time domain signatures

One approach to classifying targets is to consider their correlation function. This technique compares the time domain signal to a time-reversed version of the matching signal. In the case of comparing the PMA-3 to itself the graph in Figure 12.55 shows the result which is actually the auto-correlation of the PMA-3 radar time domain signatures. In contrast the crosscorrelation of the PMA-3 with the stone is shown in Figure 12.56. It can immediately be seen that the shapes of the correlation functions

are different, their amplitudes are different, and hence correlation can be used as a means of discriminating between types of target.

The following Section assesses some parameters of the time domain functions and their correlation functions. The Corr function is the Pearson r correlation coefficient of the elements in A and B.

The Kurt is the kurtosis of a set of values and indicates how flat or peaked the distribution is when compared to the normal distribution. Kurt(M) > 0 indicates a relatively peaked distribution. Kurt(M) < 0 indicates a relatively flat distribution.

The Cvar function is the covariance of A and B, and the skewness of a set of values measures the asymmetry about the mean. Skew(M) $= 0$ indicates that a distribution is symmetric about its mean. Skew(M) > 0 indicates that most of the distribution is located near the origin and the 'tail' extends towards postive values. Skew(M) < 0 indicates that the tail extends towards more negative values.

Using the parameters of the auto- and crosscorrelation functions and the modulus of the latter, a set of parameters can be compiled that classify the mine targets, the stone and the burrow.

Table 12.7 records the parameters of the correlation functions of the mines , stone and burrow data.

If all the parameters are normalised to the highest value and summed to provide a maximum value of 10, the following rank order is obtained (no weighting has been applied to any parameter):

PMA-PMA	10,	VS50-VS50	9
PMA-VS50	6,	PMA-VS50	6
PMA-burrow	3,	VS50-burrow	5
PMA-stone	2,	VS50-stone	3

The normalised (to the highest ranking value) parameters of the modulus of the CCFs are given in Table 12.8. Note that the modulus provides a wider separation of target and clutter classes.

Table 12.7 Crosscorrelation parameters of the four targets

Data	Correlation	Kurtosis	Variance ($\times 10^{15}$)	Skew
PMA3-PMA3	1	5.742	9.21	0.837
PMA3-VS50	0.674	4.696	4.52	0.284
PMA3-burrow	0.141	1.367	3.07	0.578
PMA3-stone	0.518	0.436	1.8	0.074
VS50-VS50	1	7.763	2.6	0.969
PMA3-VS50	0.674	4.696	4.52	0.284
VS50-burrow	0.432	2.159	1.6	0.757
VS50-stone	0.396	1.411	0.95	0.344

Table 12.8 Modulus of crosscorrelation parameters of the four targets

Data	Correlation	Kurtosis	Ratio	Skew
PMA3-PMA3	10	8	9	9
PMA3-VS50	9	6	7	8
PMA3-burrow	4	3	6	5
PMA3-stone	5	0	4	4
VS50-VS50	10	10	10	10
PMA3-VS50	9	6	7	8
VS50-burrow	5	4	6	6
VS50-stone	4	1	5	5

If all the parameters are normalised to 10 the following rank order is obtained (no weighting has been applied to any parameter):

PMA-PMA	9,	VS50-VS50	10
PMA-VS50	8,	PMA-VS50	8
PMA-burrow	5,	VS50-burrow	5
PMA-stone	3,	VS50-stone	4

Correlation methods appear to be a promising means of target classification using the MINETECT GPR data. However, the small data set of four targets is inadequate, so a larger data set must be gathered to assess the robustness of the technique. Trials were planned for September 2003 under the auspices of ITEP to gather a much larger data set of over 1000 samples.

12.8.4 TU Delft research activities in the area of advanced GPR technology

Prof. Alex Yarovoy, Prof. Piet van Genderen, Prof. Peter van den Berg and Prof. Leo Ligthart

12.8.4.1 Introduction: Ground penetrating radar (GPR) is a widely used tool for sub-surface utilities surveys, road and runway checks, avalanche victim search, landmine detection, etc. The first GPR systems were designed just to penetrate through the air–ground interface and detect the level of ground water or depth of ice, whereas current generation GPR systems are designed to both detect and identify small centimetre scale targets.

These are the main design differences between previous generation GPR systems and systems currently under development. The early systems detected the field scattered from a buried target (i.e. distinguish this field from all other electromagnetic fields), whereas the latter measure the scattered field accurately (i.e. determine the magnitude of the field as a function of time).

Table 12.8 Modulus of crosscorrelation parameters of the four targets

Data	Correlation	Kurtosis	Ratio	Skew
PMA3-PMA3	10	8	9	9
PMA3-VS50	9	6	7	8
PMA3-burrow	4	3	6	5
PMA3-stone	5	0	4	4
VS50-VS50	10	10	10	10
PMA3-VS50	9	6	7	8
VS50-burrow	5	4	6	6
VS50-stone	4	1	5	5

If all the parameters are normalised to 10 the following rank order is obtained (no weighting has been applied to any parameter):

PMA-PMA	9,	VS50-VS50	10
PMA-VS50	8,	PMA-VS50	8
PMA-burrow	5,	VS50-burrow	5
PMA-stone	3,	VS50-stone	4

Correlation methods appear to be a promising means of target classification using the MINETECT GPR data. However, the small data set of four targets is inadequate, so a larger data set must be gathered to assess the robustness of the technique. Trials were planned for September 2003 under the auspices of ITEP to gather a much larger data set of over 1000 samples.

12.8.4 TU Delft research activities in the area of advanced GPR technology

Prof. Alex Yarovoy, Prof. Piet van Genderen, Prof. Peter van den Berg and Prof. Leo Ligthart

12.8.4.1 Introduction: Ground penetrating radar (GPR) is a widely used tool for sub-surface utilities surveys, road and runway checks, avalanche victim search, landmine detection, etc. The first GPR systems were designed just to penetrate through the air–ground interface and detect the level of ground water or depth of ice, whereas current generation GPR systems are designed to both detect and identify small centimetre scale targets.

These are the main design differences between previous generation GPR systems and systems currently under development. The early systems detected the field scattered from a buried target (i.e. distinguish this field from all other electromagnetic fields), whereas the latter measure the scattered field accurately (i.e. determine the magnitude of the field as a function of time).

The demand for accurate measurement of the electromagnetic field scattered from the sub-surface requires a new approach to GPR development. GPR hardware should be designed and developed according to increased system stability, measurement accuracy and data processing. Different inverse scattering methods will be applied in GPR software to determine localisation, size, shape and even spatial distribution of dielectric permittivity within the buried target from the measured values of the scattered field.

Using its long experience of near-field antenna measurements and its expertise in time domain measurements, the International Research Centre for Telecommunications-transmission and Radar (IRCTR), together with the Laboratory for Electromagnetic Research (both Faculty Information Technology and Systems) and the Centre for Applied Geophysics (Faculty (ES)), all of Delft University of Technology, are carrying out a full scale research programme on the development of a new generation of GPR systems. This programme includes the development of concepts for video impulse GPR and a stepped frequency continuous wave radar (SFCW radar), the development of improved GPR-antennas (including adaptive antennas), the development of a multi-sensor platform for precision high resolution sub-surface imaging, and the development of new methods of sub-surface imaging based on interferometry and polarimetry. The overall aim of the research programme is to investigate new improved GPR technology, which will allow the creation of new GPR systems with challenging specifications.

Since 1996 a number of research and development programmes in the area of GPR have been carried out at the Delft University of Technology, the Netherlands. The major part of these programmes (such as 'Advanced relocatable multi-sensor system for buried landmine detection', 'Improved GPR technology', VIRLAD) are national programmes sponsored by Dutch National Technology Foundation (STW) and the Netherlands Ministry of Defence. Up to now, the main goal of the programmes carried out is the development of advanced technology for GPR.

12.8.4.2 Radar design: In the framework of the project two radars have been developed – a stepped-frequency continuous wave (SFCW) radar system [132] and a multi-waveform full-polarimetric video impulse radar system (VIR) [133].

12.8.4.3 Stepped frequency continuous wave radar (SFCW): The IRCTR improved SFCW radar has been designed to cover an extreme ultra-wide frequency band from 400 to 4835 MHz. To decrease data acquisition time a new solution has been implemented: the radar will radiate and receive eight frequencies simultaneously. This is achieved by developing an 8-channel transmitter and receiver system. Owing to this solution an excellent data acquisition time is achieved.

The main specifications of the SFCW radar are as follows:

- synthesised bandwidth: 4445 MHz (400–4845 MHz)
- power at transmit antenna terminals for each frequency: 10 dB m
- spiral antennas in bistatic configuration
- noise figure: 4.2 dB

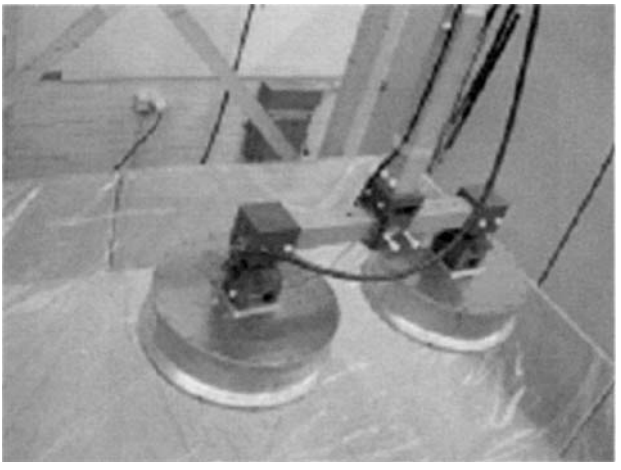

Figure 12.57 SFCW radar antennas

- dynamic range: up to 82 dB
- data acquisition time for one set of 128 frequencies: 1.7 ms.

The SFCW source is based on a direct digital synthesiser (DDS). The output from the DDS is split 8 ways and up-mixed to impart bandspread. The final bandwidth extends from 400 to 4845 MHz across 8 channels. These outputs are then combined in a Wilkinson combiner after amplification. This output is then passed to the antenna. On reception, the signals are split into the constituent channels based on bandpass filtering. They are down-mixed to a suitable intermediate frequency. These IF signals are given to quadrature detectors. The final I and Q outputs from the detectors are then fed to the ADC, housed on a data acquisition board hosted in a PC. Since these signals are slowly varying DC (depending upon the velocity of the antennas on the scanner system), a low speed ADC will suffice. The signals are sampled to provide one I and Q value per channel for all the 8 channels.

The radar operates on two antennas (Figure 12.57), one for transmission and one for reception. This will have no impact on the performance of the combiner/resolver as these are buffered by amplifiers, the former by the RF amplifier and the latter by a wideband LNA. This ensures 60 dB of isolation between the antennas from the point of view of reduction of AM noise.

Measurements were made with several metallic as well as nonmetallic objects having different shapes and dimensions as well as different separations, and SAR processing was applied (Figure 12.58). The objects are numbered as follows: 1, 20-cm metallic disc; 2, 3×3-cm metallic object; 3, 5-cm-diameter plastic mine; 4, tinfoil covered tennis ball; 5, 12×13 metallic span; 6, 23×4.5-cm metallic strip; 7, 3×3-cm metallic object; and 8, 13-cm-diameter plastic mine. The distance between the objects numbered 1 and 2 is 6 cm while the distance between 6 and 7 is 4 cm. It can be seen that objects 1 and 2 are clearly resolved, which means that the cross-range resolution

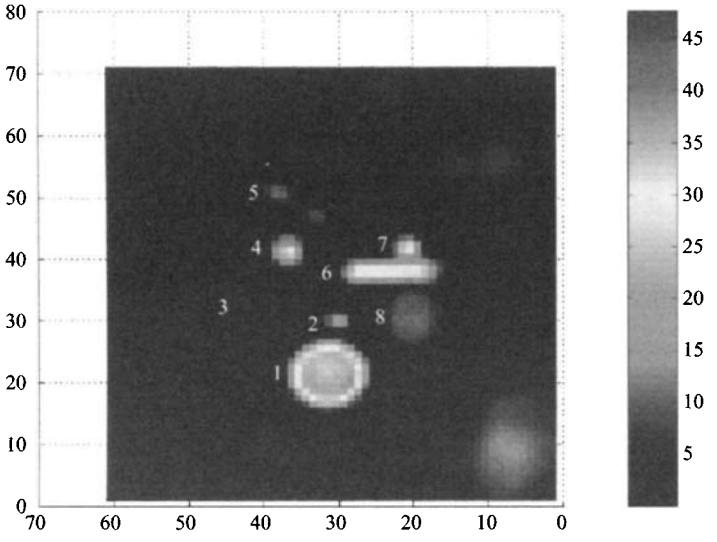

Figure 12.58 C-scan at the level of the ground surface with several objects laid on the scene, after average clutter subtraction and SAR processing

is better than 6 cm. In fact, even objects 6 and 7 located at 4 cm apart are visible, but as they are conjoined so we can estimate that the cross-range resolution is somewhere between 4 and 5 cm.

12.8.4.4 Video impulse radar (VIR): A new antenna system design (which was first tested at the predecessor of the current system, a so-called VIRLAD system [134]), an internal calibration channel and the ability to perform quasi-simultaneous measurements with two transmit polarisations and in two different frequency bands are main novel aspects of the radar. In comparison with commercially available video impulse GPR systems the front-end has considerably larger bandwidth, the ability to measure the polarimetric structure of the scattered field and a very high precision of scattered field measurements.

The main specifications of the video impulse radar (Figure 12.59) are as follows:

- multi-waveform operation
- instantaneous bandwidth at 10 dB level: 1550 MHz (from 420 to 1970 MHz) and 2170 MHz (from 780 to 2950 MHz)
- full polarimetric antenna array in bistatic configuration
- dynamic range: 66 dB without averaging and 79 dB with averaging
- jitter: less than 0.3 ps RMS
- time drift: less than 1.5 ps/h.

The radar enables high-resolution images (Figure 12.60) of sub-surface (up to 16 different images, which correspond to two different bandwidths, two orthogonal

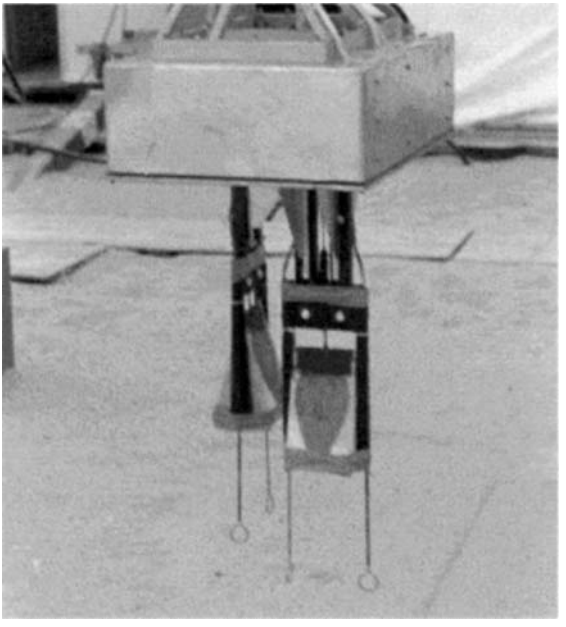

Figure 12.59 Video impulse radar

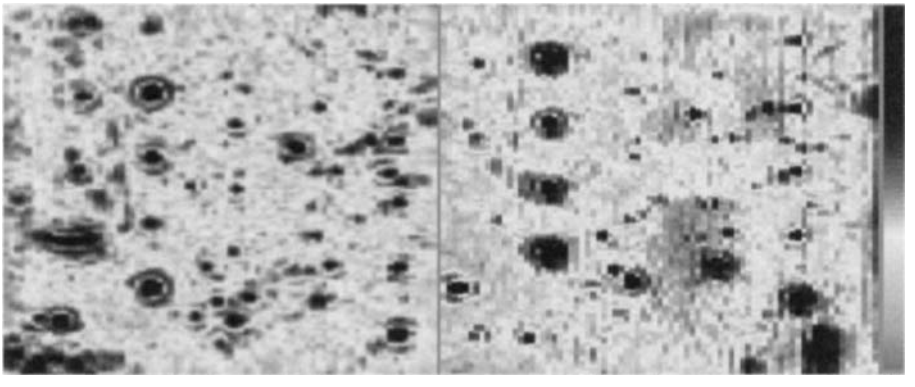

Figure 12.60 Energy projections of SAR images obtained using two orthogonal transmit polarisations
Vertical scale = 453 sample points, horizontal scale = 80 sample points, amplitude scale = 36 dB

transmit polarisations and four receive antennas with different orientation and configurations) to be obtained.

The overall performance of the radar including advanced processing methods is characterised by the ROC curve shown in Figure 12.61.

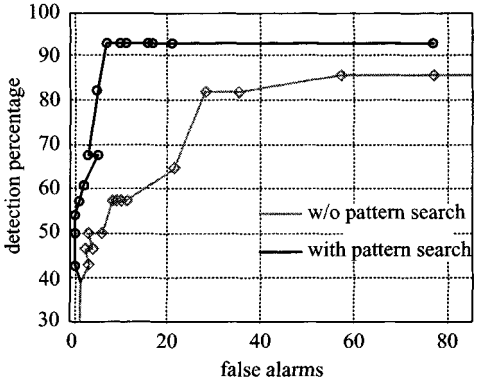

Figure 12.61 *ROC curve for small low (or none) metal content antipersonnel mines with the radar*
The results are based on a single sub-surface image (no image fusion has been applied)

12.8.4.5 Antenna design: The performance of any GPR system heavily depends on its antennas. To improve performance of the radars a number of new antennas have been specially designed: the dielectric embedded dipole antenna [135], the dielectric wedge antenna [136], the capacitively loaded antenna [137], the shielded spiral antenna [138] and the adaptive p-i-n diode antenna [139] (Figure 12.62). The dielectric wedge antenna is an impulse-radiating antenna, which means that in the whole frequency range it has linear phase characteristic, very low dispersion and linear polarisation. The antenna is designed to radiate short pulses with monocycle waveform and operates in the frequency band from 0.5 to 4.2 GHz. Artificial dielectrics are widely used in this antenna in order to decrease antenna ringing and decrease antenna sensitivity to external interference.

Whilst for conventional antennas their characterisation in free space is sufficient, for GPR antennas it is not the case. The ground situated in the near field of these antennas influences their performance. Thus facilities, which allow measurements of the near field of these antennas directly in the ground, are necessary for comprehensive characterisation of GPR antennas. Such facilities have been created in IRCTR [140]. It was decided to use dry sand as a 'standard ground'. A wooden box with dimension $2.5 \times 2.5 \times 1.5$ m is filled with 'homogeneous' sand. The dielectric permittivity of the sand is assumed to be equal to 2.7. The test-range is separated from the surroundings by wooden walls, covered with a waterproof plastic coating. A home-made sensor is used in order to measure the electromagnetic field just below the air–ground interface in the centre of the box. To position an antenna under test in a proper place a 3D scanner has been mounted above the test range.

The test site is used for waveform measurements of the field radiated into the ground, the dependence of this radiated field on the antenna under test (AUT) elevation (so-called elevation profile) and the antenna radiation footprint in the

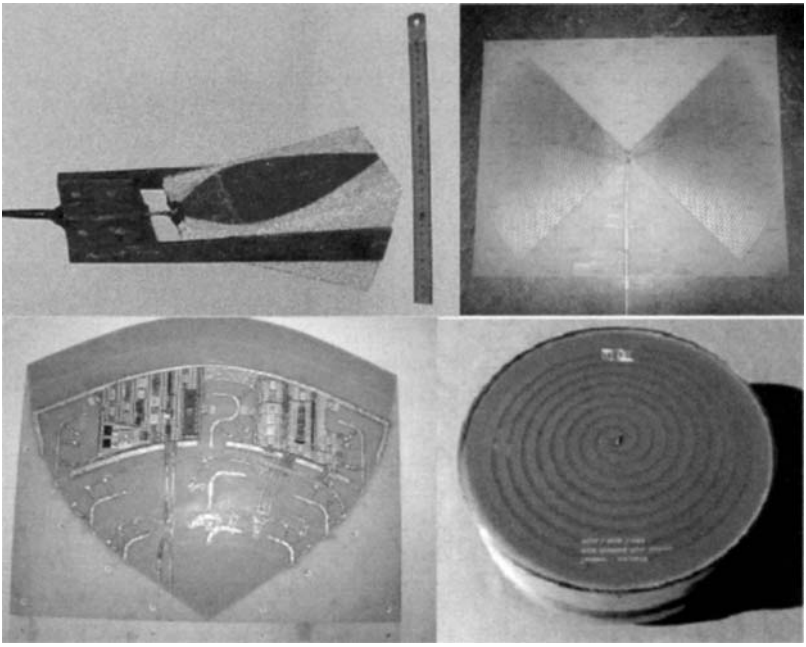

Figure 12.62 *Prototype antennas: dielectric embedded dipole antenna (top left), dielectric wedge antenna (top right), capacitively loaded antenna, the shielded spiral antenna (bottom right) and adaptive p-i-n diode antenna (bottom left)*

ground. The elevation profile is obtained by the measurement of the radiated field in the ground for different elevations of the antenna and provides important information about the antenna-to-ground coupling and the influence of the ground on the antenna performance. The antenna coupling in the presence of the ground is also measured in the GPR test range. The time domain reflectometry of GPR antennas is done also in this test site.

12.8.4.6 Signal processing, imaging and inversion: Our approach to optimise GPR for the problem of landmine detection is somewhat different from that followed in most other research groups around the world and stems from our unique experience in inverse scattering methods gained in the past decade. Instead of blindly applying classification methods to the electromagnetic field measured by GPR, creating and storing databases of 'target signatures', 'training' the system on sample targets, etc. we resort to the very physical and mathematical basis of the landmine detection problem.

Indeed, irrespective of the type of detection algorithm applied, the characteristic quantity is the electromagnetic field governed by the system of Maxwell's equations. This system of equations provides the most precise known description of the relation

between the material (constitutive) parameters of the target and the measured electromagnetic field. Within this theoretical mainframe every natural or man-made object is adequately described by a function of its electromagnetic parameters, defined over an area of space and an interval of time. Reconstruction of the unknown constitutive parameters from the known field is called *inversion*, and is at the heart of our detection strategy.

(1) Signal processing: The main aspect in our research on signal processing was to enhance the quality of the measured data. The first step in this direction is compensation of all time drifts in the hardware. The second step is synthesis of maximally short pulses from the raw data. Such synthesis is based on our exact knowledge of hardware properties like the system bandwidth, the transfer function, the antenna footprint, etc. The third step is suppression of the ground clutter by using data from mono-static and bi-static channels and using the vectorial nature of the electromagnetic field. Typically, GPR systems measure only one component of the scattered electromagnetic field. Simultaneous measurement of the 2×2 polarisation matrix and use of polarisation-sensitive processing is a logical development in considering the full vector nature of the scattered electromagnetic waves. This provides a possibility to enhance certain types of objects immersed in a set of distributed objects of different types (important for enhancement of landmines buried in soil).

(2) Forward modelling: An accurate and efficient forward modelling method was developed and extensively used to get a thorough understanding of GPR. We have applied the recently developed reduced-order modelling technique [141] to model a realistic three-dimensional configuration: a plastic landmine buried 0.25 m below the air–soil interface. We have generated synthetic data for a bi-static source–receiver set-up with several central frequencies of the wavelet. The data obtained in this way served as input for the imaging and effective inversion algorithms.

(3) Imaging: Existing imaging algorithms have been implemented and tested both with synthetic and experimental data [142]. At the moment we are concentrating on improving the quality of obtained images taking into account the vectorial nature of the electromagnetic field and antenna footprints. It is well known that the elementary imaging techniques (such as time-domain backpropagation or frequency-domain migration) produce distorted images when applied to the near-field zone of GPR. The pictures are usually blurred and shifted with respect to the true profile of the scatterer. Newly developed imaging methods perform much better than conventional algorithms, resulting in a considerably lower level of the sidelobes in the image.

The most important aspect of synthetic aperture radar is that it is a coherent imaging system, retaining both amplitude and phase information in the radar echoes during data acquisition and subsequent processing. The interferometry can exploit this coherence to obtain differential range and range change of SAR images. In this manner very high resolution topographic maps of the surface and 3D images of the sub-surface can be produced. However, the known interferometric algorithms have been developed for far-field measurements and they are not directly applicable for GPR systems, which are typical near-field systems. That is why a principally new approach for near-field UWB interferometry was investigated.

Another innovative idea in the project is to exploit the vector nature of the sounding electromagnetic field in GPR. We have found that it is possible to enhance the images using the polarimetric signatures on a pixel-by-pixel basis. When all polarisation matrix elements have been determined on a pixel-by-pixel basis, the images can be generated of various potentially useful parameters such as the total power P, the Stokes parameters S, and the characteristic elements of the polarisation sphere, which include null polarisations, the polarisation fork angle, etc.

(4) Effective inversion: The new method of Effective Inversion has been developed within this project [143]. It consists of an effective scattering model and a simple optimisation routine for real-time estimation of the average permittivity of the buried object. Originally, the method used a single circular effective scatterer; however, lately it has been extended onto multiple scatterers and arbitrary boundaries. Both the new conforming version of the method and the previous realisation with a circular model have been tested with synthetic and experimental data. Latest tests have indicated that our method works especially well with plastic and wooden low-contrast landmines.

(5) Full-scale inversion: While the previous stages of our research are virtually complete, this part is just starting. It will include both imaging and effective inversion. As a particular result, obtained within the present project, we can mention the time-domain version of the contrast source inversion (CSI) method. The method attempts to solve the full-scale inverse scattering problem for the GPR configuration with multi-source multi-receiver data acquisition. The method has been tested with synthetic time-domain data in two dimensions and has shown promising results.

(6) Feature extraction and object classification: The main objective of this research is the extraction of target information such as size, shape and material properties from VIR data. The extracted information can be used for target identification, which is crucial for the reduction of the false alarm rate in demining operations. In contrast to imaging and inversion, the processing techniques described here operate on a single A-scan or a set of A-scans forming a scattering matrix acquired over the target in question. Consequently, the processing techniques can be applied to both platform mounted and hand-held GPR systems.

In general, the GPR response of a surface-laid or buried target depends on target orientation. Hence, in order to make target identification possible, it is necessary to measure the full scattering matrix and transform the target response into the so-called target frame. In the target frame, the response of the target becomes orientation invariant. From measurements with the VIR system over various targets, we found that its antenna configuration is well suited for quasi-simultaneous measurement of scattering matrices, which satisfy reciprocity. Because of this property, the transformation into the target frame can be achieved by simple matrix diagonalisation in the frequency domain. The resulting scattering matrices are diagonal and their diagonal elements are indeed orientation invariants as verified by repetitive measurements for different target orientations.

Once the target response has been transformed into the target frame, it is possible to extract target information. To better understand the information content of the target response in the target frame, a physical model for the axial far-field impulse response

of a dielectric mine-like target embedded in a lossless or lossy soil has been derived using the Born scattering approximation. According to this model, the target differentiates the waveform of the incident field. Furthermore, the length of the impulse response is a measure of the target height, whereas its magnitude is proportional to the target cross-section and the permittivity contrast between the target and the soil. Losses in the soil lead to weak additional backscatter due to the conductivity contrast and damping of the backscatter contribution from the bottom of the target. Responses predicted by the physical model were compared against responses obtained from finite-difference time-domain (FDTD) simulations, and good agreement was found.

A new deconvolution algorithm [144] has been developed which estimates the impulse response of a target based on its scattering response in the target frame and knowledge of the incident field. The novelty of the deconvolution algorithm lies in the fact that it uses the physical impulse response model described in the previous paragraph as a priori information. As a result, the estimated impulse responses can be characterised by a few parameters making them suitable for input into classification schemes. Initial tests with FDTD data demonstrate that differences in target size are reflected proportionally in these parameters, making it possible to distinguish between different targets. Furthermore, since the estimated impulse responses adhere to the physical model, it is possible to determine the permittivity of a buried dielectric target (e.g. a plastic mine) from its impulse response and that of a calibration target (e.g. a metal plate). Further verification of these results based on measured VIR data is the subject of current research.

Over the years the TU Delft research team has gained remarkable expertise and knowledge in the area of GPR. The unique aspect of this expertise is that it covers the whole GPR chain, from electromagnetic properties of the ground through to object classification.

This knowledge and expertise resulted in the development of two novel GPR sensors for landmine detection, which not only successfully detect centimeter scale objects in the ground, but are also able to classify them as 'mines' or 'friendly objects'. Outdoor testing of these radars at the Test Facility For Landmine Detection Systems, located at TNO-FEL, has proven the effectiveness and efficiency of these new approaches.

12.8.5 Lotus project
Dr Richard Chignell

The Lotus project was directed by PipeHawk plc, with part funding from the European Commission. It was of a development nature and was aimed at showing how technology, particularly GPR, could produce an effective vehicle based solution to the mine detection problem. The sensor suite involved the Minerec GPR array from PipeHawk plc, a metal detector array from Foerster's in Germany and an infra-red camera from TNO-FEL in the Netherlands, who also carried out the data fusion. DEMIRA, a German NGO who carry out de-mining in Bosnia, provided the field test facilities in that country close to their live de-mining operations.

The small size of mines demands that for antennas close to the ground a series of closely spaced scans are performed. In the Minerec array the antenna elements were

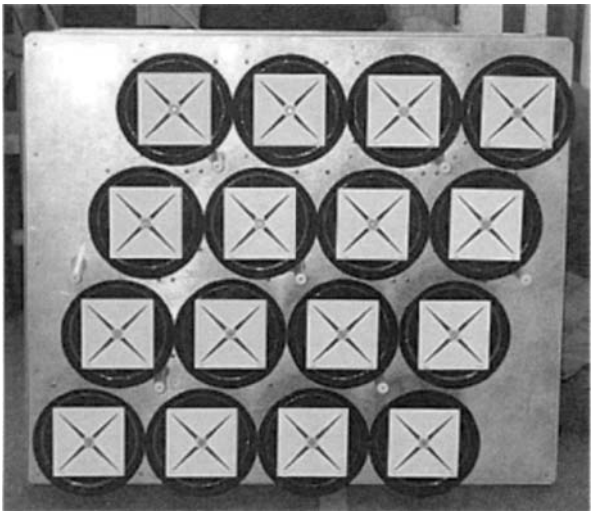

Figure 12.63 GPR antenna array for Lotus *vehicle based radar system*

Figure 12.64 The Lotus *system under test*

spaced to give a separation between scans of 50 mm. The individual antenna elements are physically much longer than this spacing, leading to the staggered array geometry shown in Figure 12.63. This array was built as a sub-array of a vehicle based system in which four such arrays would search a swathe 3-m wide, simply by the vehicle driving forward. The array elements are based upon resistively loaded dipoles, and the equivalent frequency range of the radar system spans much of the upper UHF and lower microwave bands.

In the Lotus project the Minerec array was used at a nominal height at 100 mm off the ground. For the real-time demonstration of mine detection in Bosnia the sensors were simply mounted on a telescopic framework ahead of a vehicle to search a swathe 0.75-m wide. Operationally this is clearly not an effective deployment method, but it was appropriate for a demonstration on test lanes. The metal detector was deployed at the front of the frame as far from the vehicle as possible. The infra-red camera looked down through the metal free zone behind the metal detector and was followed by the Minerec radar array. The complete vehicle is shown in Figure 12.64.

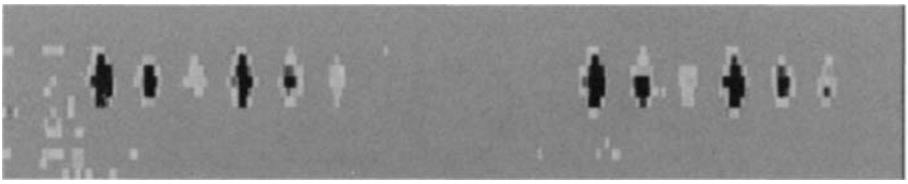

Figure 12.65 The C-scan output produced by the MINEREC radar in a mine test lane

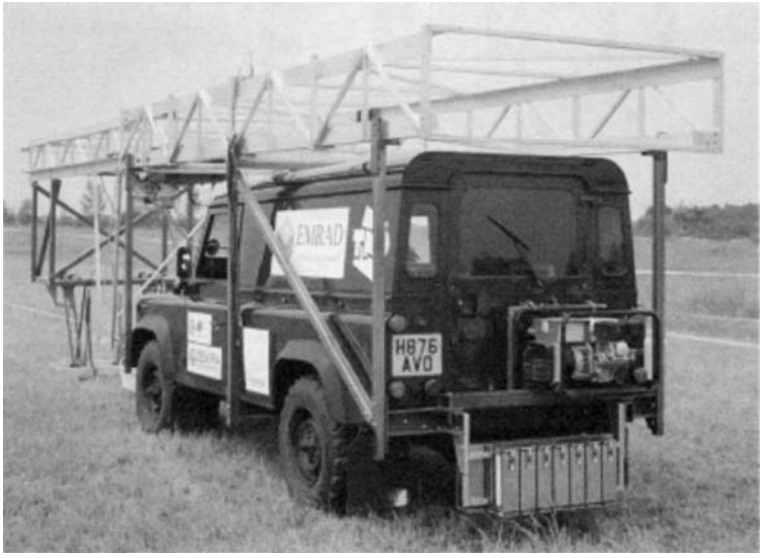

Figure 12.66 Rear of LOTUS vehicle showing paint marking system

All the data were analysed in real time. Figure 12.65 shows the 'C'-scan, map-type output from the radar. Following processing, all the sensors produced comparable outputs which were then combined in a fusion computer to generate the real-time output on the presence or absence of a mine-like target. This output from the sensor suite was then employed to drive a series of paint jets on the rear of the vehicle (see Figure 12.66).

If a mine was present a small patch of biodegradable paint indicated the position. In the Bosnia demonstration all the mines were detected and the false alarm rate was negligibly small. The number of mines measured was large for a short trial but small compared to the testing required prior to operational use. The trial served to demonstrate the role of GPR in the solution of this problem. It is projected that operational systems of the type indicated by the LOTUS demonstrator could, in appropriate terrain, search at least one square kilometre per week. Working continuously, four such fully developed systems could search more land in a year than was cleared by the eight major donors in 2000.

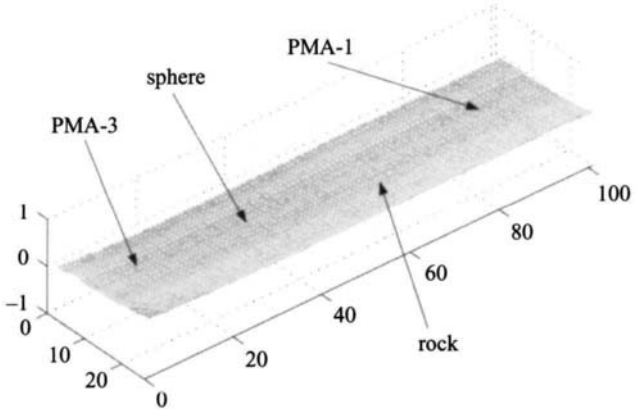

Figure 12.67 C-scan of clutter at surface

12.8.6 Data processing for clutter characterisation and removal

Prof. Hichem Sahli, Luc van Kempen and John W. Brooks
Vrije Universiteit Brussel

12.8.6.1 Introduction: A large part of the work presented in this Section was performed in the framework of the DEMINE project. The authors wish to thank the TUI, one of the DEMINE partners, who provided the data used in many parts of this report. The other data used were acquired with a set-up that is the result of the collaboration with the DeTeC group of the EPFL.

12.8.6.2 Clutter environment:

(1) Introduction: Detection of buried targets with a GPR is rather simple. Almost anything under the surface of the ground presents a return signal which may be confused with a valid and possibly lethal target. In this respect, the characterisation of the radar returns in the context of the environment is essential. It is not sufficient to say that 'something' is buried; rather, in application to humanitarian demining, it is essential that a lethal target be detected with a probability of detection close to 100% in any soil type or condition.

This Section develops a basic understanding of the technical issues involved with processing GPR data. The data files used were taken from a number of sources, including the laboratories of the École Polytechnique Fédérale de Lausanne (EPFL), Vrije Universiteit Brussel (VUB) and the Technische Universität Ilmenau (TUI).

(2) Statement of the problem: The detection of nonmetallic (NM) and minimum-metal (MM) anti-personnel landmines (APs) with ground penetrating radar (GPR) is made very difficult because of the extreme clutter environment within the first 50 mm

of the soil surface. On the other hand, most APs are placed within that region to ensure reliable detonation when trodden upon.

Three distinct types of radar (GPR) return are defined:

1. Data which contain information about a mine target.
2. Data which contain information about a nonmine target but which may be confused as a mine.
3. Clutter returns caused by inhomogeneous soil and small metallic fragments which may not be confused with a valid mine target, and antenna effects (see Section 12.8.6.3.)

(3) Near-surface clutter: The clutter environment within the first few cm of the soil surface exhibits strong radar reflections with highly nonstationary statistics. This is illustrated in Figures 12.67 to 12.72, which show the return at varying depths following an adaptive clutter removal technique. The mines and other targets are placed in accordance with the test protocol developed for TUI, further explained in Section 12.8.6.11; the mine types used are PMA-1 and PMA-3. The velocity of wave propagation in the sand was estimated to be approximately 7.0×10^9 cm/s. The depths denoted in the Figures are rough estimates only, as it is difficult to determine exactly when the radar wave enters the soil. The mines, rock and sphere were all placed such that the top of each target was located at a depth of 5.0 cm. The maximum response for the sphere, however, appears later due to the currents moving on the surface of the sphere. It is quite clear that the clutter environment close to the surface is highly variable and exhibits a varying texture, even after a significant amount of background has been removed.

(4) Target discrimination: Figure 12.73 shows the environment encountered in dry sand, when multiple target types are involved. It can be seen that target intensity alone is not an acceptable discriminator; it is also clear from Figure 12.74 that simple

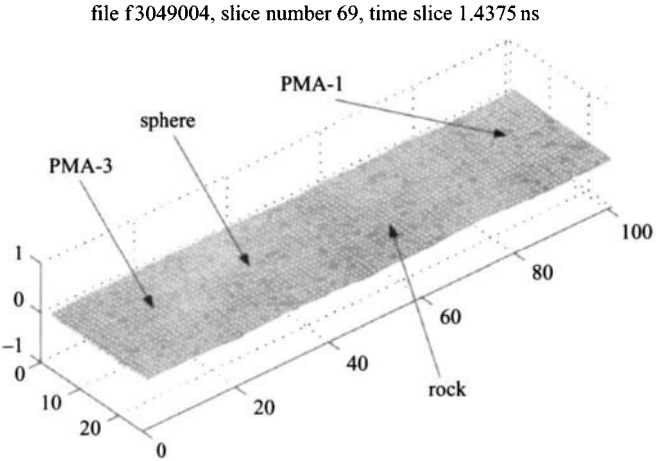

Figure 12.68 Clutter at 1.0 cm depth

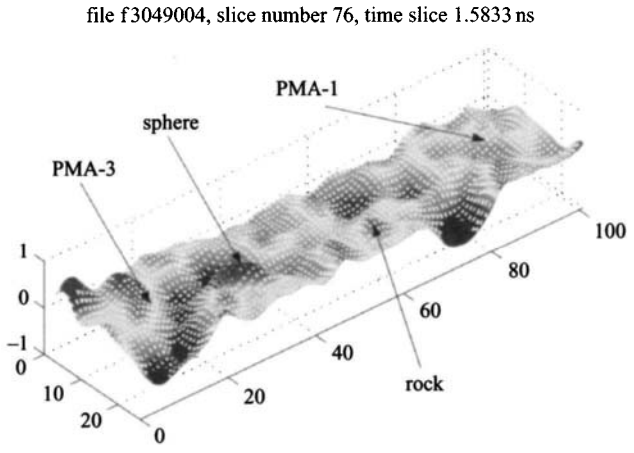

Figure 12.69 Clutter at 2.0 cm depth

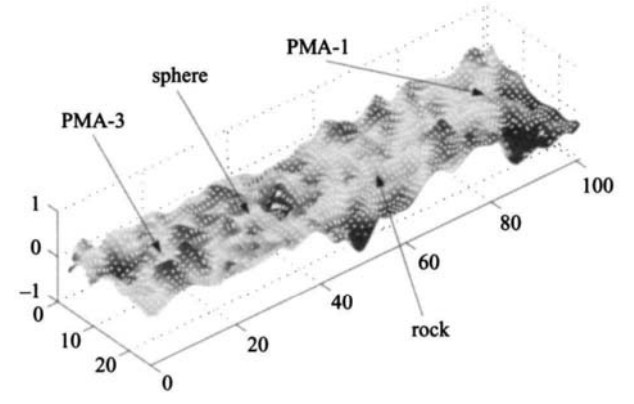

Figure 12.70 Clutter at 3.0 cm depth

examination of peak intensity of a target return is not a reliable indicator of target depth. All lower targets were placed at a uniform depth 100 mm below the top target. Figure 12.75 shows a surface representation of an intensity image of a B-scan, showing the effect of a surface depression at the edge of the scan. The surface return bifurcates at the surface discontinuity, making accurate determination of the surface location very difficult. Note, also, the presence of the PMA-3 mine return which is in the middle of a large clutter/antenna response curve. If the average background of this B-scan is removed as shown in Figure 12.76, the residual effects of the surface depression are quite clear.

(5) Signal-to-noise ratio (SNR) and signal-to-clutter ratio (SCR): Although expressions for the SCR of buried targets are available [137, 138], they do not lend

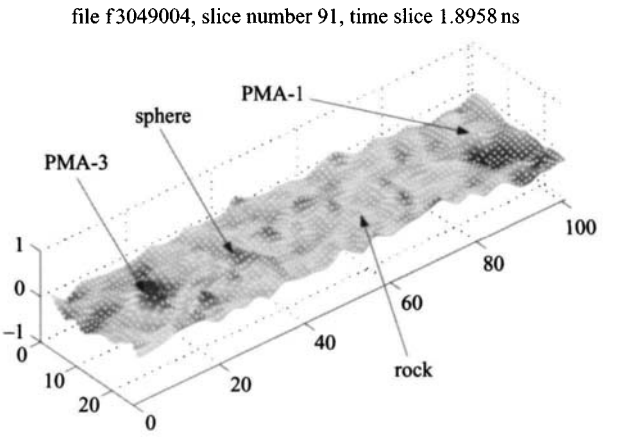

Figure 12.71 Clutter at 4.0 cm depth

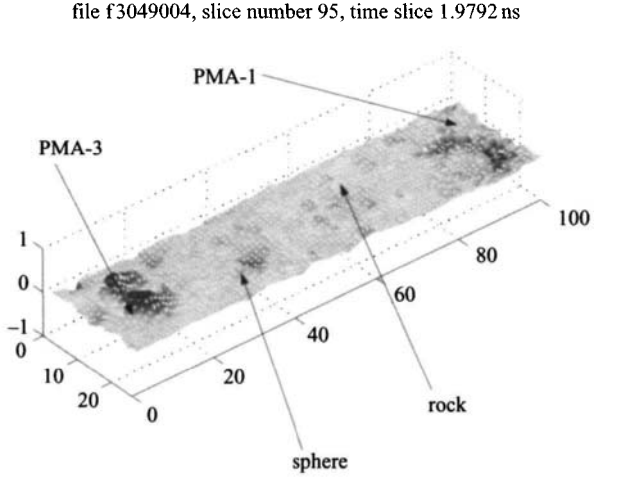

Figure 12.72 Clutter at 5.0 cm depth

themselves well to the mine detection problem. This is because, for each time slice of the C-scan, the particular unit volume scatterer used for the comparison between target energy and clutter energy varies greatly over the target location. In the raw, unprocessed data, the target return is quite small compared to the background clutter, as shown in Figure 12.77. Difficulties arise because, in general, the actual 'noise' (in the sense of zero-mean white Gaussian noise (WGN)) in the radar data is quite small because some form of integration is used in all data considered here. The dominant interference in each of the scan representations is correlated clutter, i.e. interference

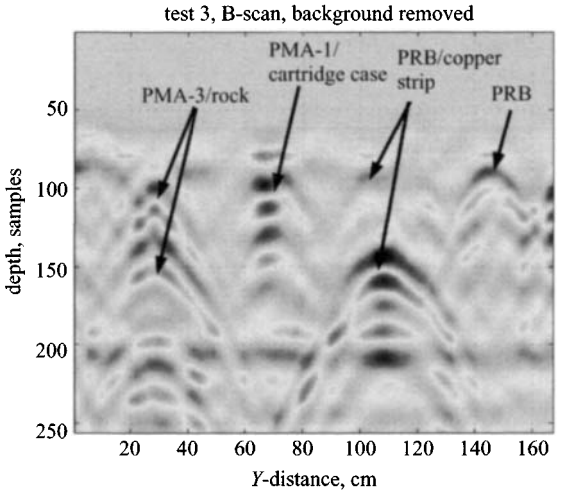

Figure 12.73 *B-scan of various targets and target separation in dry sand*

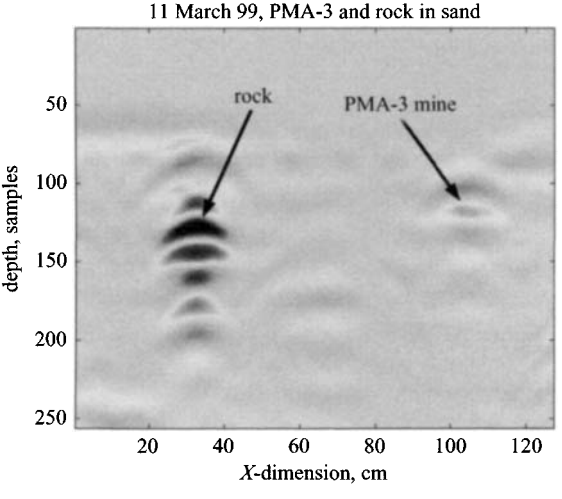

Figure 12.74 *Comparison between rock and mine targets*

which has a large correlation coefficient for lags greater than zero. A spectral decomposition of the mine return (Figure 12.77) fails to reveal much about any 'signal component', because the residual clutter has essentially identical spectral characteristics as the signal itself. Therefore, we shall evaluate clutter reduction methods in the context of improvements in feature extraction or classification performance in Section 12.8.6.12.

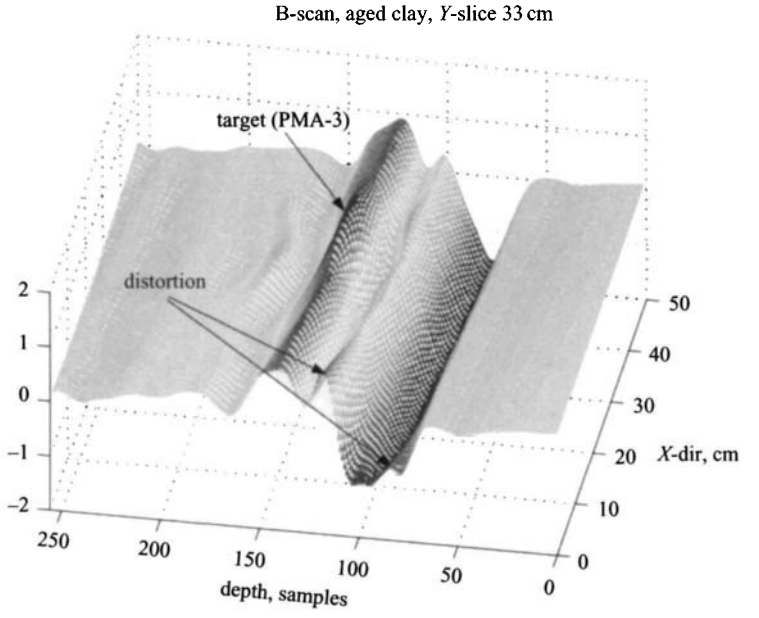

Figure 12.75 Surface plot showing B-scan distortion caused by soil depression

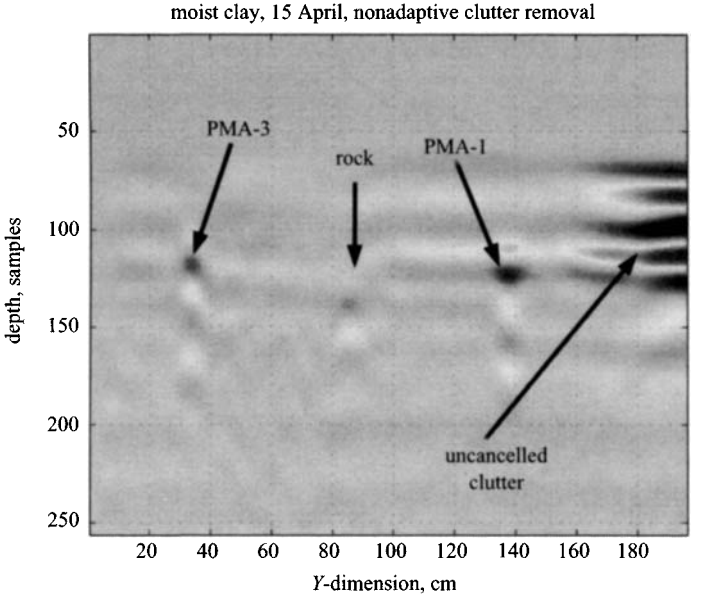

Figure 12.76 Residual surface clutter caused by soil depression

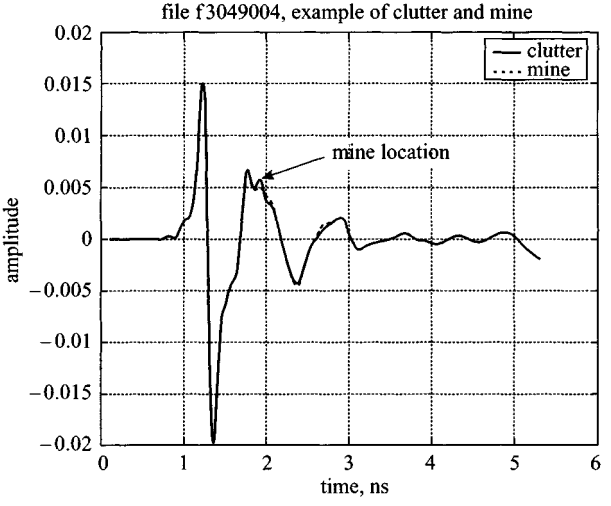

Figure 12.77 Clutter limited nature of the GPR target

12.8.6.3 Clutter characterisation: GPR clutter includes many components: crosstalk from transmitter to receiver antenna; initial ground reflection; and background resulting from scatterers within the soil. In this Section, we consider all of these components to be undesired signals which require estimation and subsequent removal in order to enhance the target signal. As mentioned previously, the target signal can be either a mine or nonmine; it is the objective of the post-processing to make the decision between the two.

To estimate this clutter, there are several possible approaches. One approach is to scan an area of ground which is known to be clear of any targets and store an average A-scan for subsequent processing. This is a form of *sensor calibration.* Such processing may involve determination of system function ('transfer function') coefficients or pole–zero locations in the complex z- or s-domains.

Another possible approach is to attempt to determine the autoregressive moving average (ARMA) parameters of the clutter; these parameters may then be compared to similar parameters of samples of clutter-plus-target, and subsequent target discrimination. One final approach exploits the observation that the clutter is highly variable with depth. In this approach, the target information is considered to be contained within the residue of the clutter process, and a smoothing/prediction approach is used.

In practice, the ARMA parameters of the clutter and clutter-plus-target are so close that meaningful target separation was found not to be possible, so the approaches considered in this Section are based on sensor calibration with a reference clutter signal and subsequent adaptive processing, and the prediction/smoothing approach. The methods used are based in part on parametric modelling by *system identification* approaches, both nonparametric and parametric. The nonparametric method results

in a direct *deconvolution* of the target from the reference clutter signal; the parametric methods result in estimates of the system functions for the clutter and target components.

12.8.6.4 System identification methods, introduction: System identification methods [147] offer considerable promise in GPR signal processing. One goal of system identification is to attempt to determine a target impulse response which will (hopefully) be invariant with aspect angle and soil conditions. In general, this will not be possible [148–152]. Aspect-invariant impulse responses, characterised by the natural resonant poles of the system, are valid only when the target is perfectly conducting and in free space. However, target impulse responses may be used to infer shape information about the target, and possibly to construct features for further target classification; that is the context of this Section.

Target parameter estimation can have several meanings. On the one hand, it can imply physical parameters such as length, height, material, etc. On the other hand, it can mean the calculation of system function parameters, such as filter coefficients, which represent something unique about the target. Both approaches can be combined; for example, clutter system function coefficients may be estimated as shown in Section 12.8.6.6(2), and the results can be used to determine physical parameters as in Section 12.8.6.12(1). As mentioned previously, aspect- and depth-invariant system parameters are generally not unique with targets made of dielectric materials; however, class separability between mine and nonmine targets may still be possible using estimated target parameters.

System identification methods fall into two categories, *nonparametric* and *parametric*; the differences between the two will become apparent in the following Sections.

Briefly, the goal of nonparametric methods is to characterise a linear, time-invariant (LTI) system by its frequency response, whereas parametric methods attempt to 'fill in the blanks' of transfer function or state-space models so that the relationships between the input and the output of the system can be defined by the transfer function or state-space model.

In any modelling effort, we can only hope to achieve a rough approximation of the 'real world' environment. This is due mainly to the fact that we model a natural, continuous process by approximating the process as samples of measured data. This sampling process can only approximate the natural process, because, unlike the natural process, we are constrained to a finite dimensional view of the process. Thus, whereas natural processes are best described by sets of partial differential equations, we approximate the process with sets of finite-order difference equations. In the following Sections, we assume that the target, clutter and noise processes are discrete samples of a continuous-time input–output process, and thus we shall work in the z-domain versus the s-domain.

12.8.6.5 Parametric system identification: Parametric system identification attempts to determine the parameters (e.g. transfer function coefficients) of a linear time-invariant (LTI) system or signal [147, 153].

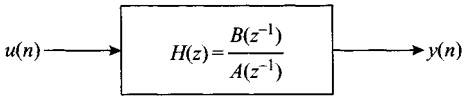

Figure 12.78 Discrete LTI block diagram

(1) Basic principles: Consider a discrete LTI system described by the difference equation

$$\begin{aligned} &y(n) + a_1 y(n-1) + a_2 y(n-2) + \cdots + a_{n_a} y(n-n_a) \\ &\quad = b_0 u(n) + b_1 u(n-1) + \cdots + b_{n_b} u(n-n_b) \end{aligned} \tag{12.9}$$

where $y(n)$ is the output sequence, $u(n)$ is the input sequence, and n_a, n_b are the *orders* of the output and input processes, respectively. For causality, $n_a \leq n_b$. The system described by (12.9) may be written in transfer function format as

$$H(z) = \frac{B(z^{-1})}{A(z^{-1})} \tag{12.10}$$

where:

$$\begin{aligned} A(z^{-1}) &= 1 + a_1 z^{-2} + a_2 z^{-2} + \cdots + a_{n_a} z^{-n_a} \\ B(z^{-1}) &= b_0 + b_1 z^{-2} + b_2 z^{-2} + \cdots + b_{n_b} z^{-n_b} \end{aligned} \tag{12.11}$$

This system may be illustrated as in Figure 12.78.

The more general case includes additional measurement noise $e(n)$, which is assumed to be i.i.d. with mean zero. In this case, the input–output relation is written

$$y(n) = H(z)u(n) + e(n) \tag{12.12}$$

which is the *output-error model* in system identification language [139]. We define the *parameter vector* $\boldsymbol{\theta}$ as

$$\boldsymbol{\theta} = [a_1, a_2, \ldots, a_{n_a}, b_0, b_1, \ldots, b_{n_b}]^{\mathrm{T}} \tag{12.13}$$

and the elements of this vector are the parameters to be estimated.

It is shown in [145] that the solution of (12.13) is given by

$$\hat{\boldsymbol{\theta}} = (\boldsymbol{\Psi}^{\mathrm{T}}\boldsymbol{\Psi})^{-1}\boldsymbol{\Psi}^{\mathrm{T}}\boldsymbol{y} \tag{12.14}$$

where $\boldsymbol{\Psi}$ is the matrix

$$\boldsymbol{\Psi} = \begin{bmatrix} \psi^{\mathrm{T}}(n+1) \\ \psi^{\mathrm{T}}(n+2) \\ \vdots \\ \psi^{\mathrm{T}}(n+N) \end{bmatrix} = \begin{bmatrix} -y(n_a) & \cdots & -y(1) & u(n_b+1) & \cdots & u(1) \\ -y(n_a+1) & \cdots & -y(2) & u(n_b+2) & \cdots & u(2) \\ \vdots & \ddots & \vdots & \vdots & \ddots & \vdots \\ -y(n_a+N-1) & \cdots & -y(N) & u(n_b+N) & \cdots & u(N) \end{bmatrix} \tag{12.15}$$

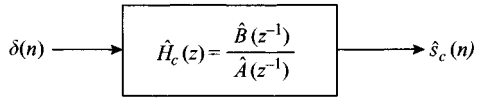

Figure 12.79 Representation of clutter parametric model

where N is the length of a sliding data window; $N \gg n_a + n_b$. Equation (12.14) is nothing more (and nothing less) than the *min-norm solution* to a linear system described by

$$\mathbf{y} = \boldsymbol{\Psi}\boldsymbol{\theta} + \mathbf{e} \tag{12.16}$$

so (12.16) may be compactly written as

$$\hat{\boldsymbol{\theta}} = \boldsymbol{\Psi}^{\diamond}\mathbf{y} \tag{12.17}$$

where $\boldsymbol{\Psi}^{\diamond}$ is the *Moore–Penrose pseudo-inverse* [146] of $\boldsymbol{\Psi}$.

(2) The Steiglitz–McBride algorithm: The Steiglitz–McBride algorithm [147, 155] is an iterative algorithm which solves (12.12) subject to a white measurement noise process. The algorithm has been found to be very effective in determining the clutter model shown in Figure 12.79. The algorithm is as follows.

Given the output-error model

$$y(n) = \frac{B(z^{-1})}{A(z^{-1})}u(n) + e(n) \tag{12.18}$$

solve first the least-squares problem

$$A(z^{-1})y(n) = B(z^{-1})u(n) + e(n) \tag{12.19}$$

by the method described in Section 12.8.6.2 (3). This results in the preliminary estimates $\hat{A}(z^{-1})$ and $\hat{B}(z^{-1})$.

Filter the data through the pre-filter

$$y_F(n) = \frac{1}{\hat{A}(z^{-1})}y(n), \quad u_F(n) = \frac{1}{\hat{B}(z^{-1})}u(n) \tag{12.20}$$

Solve the equation

$$A(z^{-1})y_F(n) = B(z^{-1})u_F(n) + e(n) \tag{12.21}$$

by the method described in Section 12.8.6.2 (1). Repeat steps 2 and 3 until $\hat{A}(z^{-1})$ and $\hat{B}(z^{-1})$ have converged.

12.8.6.6 GPR signal model: Estimating the target parameters is the goal of system identification applied to GPR signal processing. If specific parameters of the target can be isolated in some domain, then it may be possible to classify the target further into 'mine' and 'nonmine' categories. In this Section, the parameters are the system function parameters mentioned previously. The roots of the transfer function polynomials may be plotted in either the z-domain or the s-domain (see, for example,

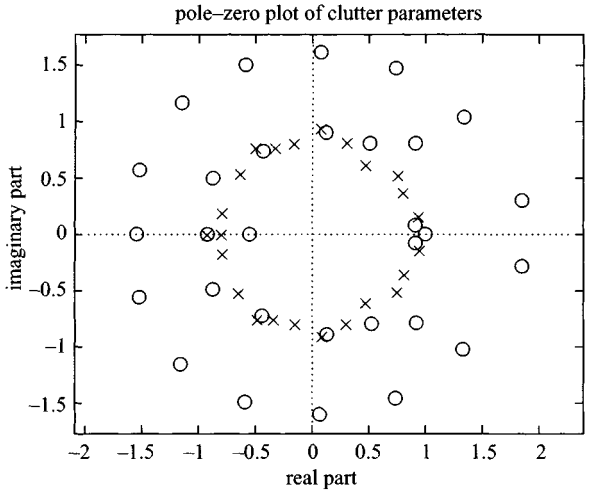

Figure 12.80 Pole–zero map of estimated clutter parameters

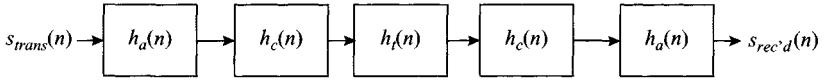

Figure 12.81 Overview of system impulse response

Figure 12.80, which illustrates the poles and zeros of the estimated clutter model of Figure 12.79) and an appropriate distance function can be applied to separate the target sets. Figure 12.81 shows the basic structure of the input–output relationship between the transmitted signal and the received signal. From this diagram,

$$s_{rec'd}(n) = s_{trans}(n) \otimes h_a(n) \otimes h_c(n) \otimes h_t(n) \otimes h_c(n) \otimes h_a(n) \qquad (12.22)$$

where $h_a(n)$, $h_c(n)$ and $h_t(n)$ are the impulse responses of the antenna, clutter and target, respectively. The antenna and clutter impulse responses are shown twice to reinforce the fact that the radar wave passes through both components twice. Strictly speaking, in a bistatic array environment, the antenna impulse responses should be denoted $h_{a_{rec}}(n)$ and $h_{a_{trans}}(n)$ to denote the receiver and transmitter antenna responses, which will, in general, be different.

In the context of this Section, *clutter* includes all environmental effects including scatterers from the soil, crosstalk and surface interface. In addition, the antenna effects are included in the clutter signal, because there is no possibility of measuring the actual antenna effects in the field, under varying conditions.

In addition, *noise* specifically refers to the random measurement noise which is added to the composite signal. The correlation properties of the noise may be deduced from the estimation of ARMA parameters if required.

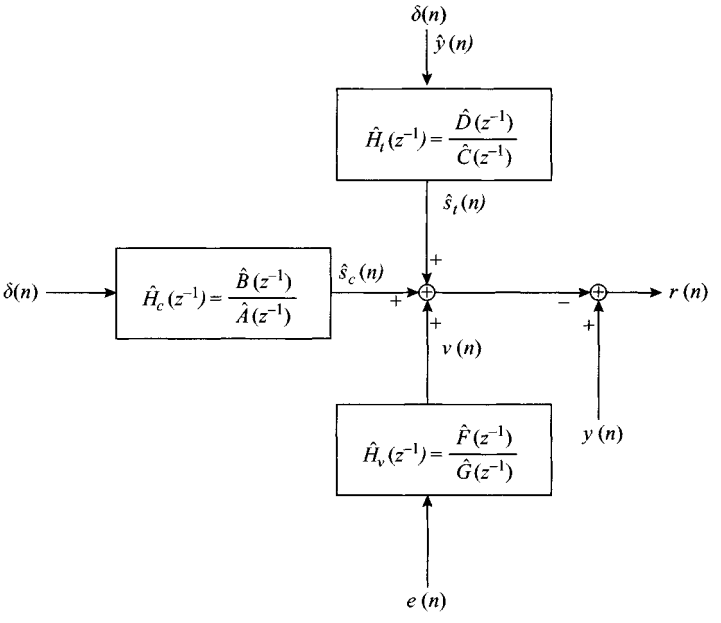

Figure 12.82 General block diagram representation of system identification

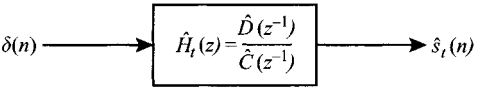

Figure 12.83 Representation of target parametric model

The representation of (12.22) can be formalised by the structure shown in Figure 12.82. Estimated parameters (for example, ARMA coefficients) may be used for feature extraction; an example of clutter features which result from parameter estimation using the Steiglitz–McBride algorithm (see Sections 12.8.6.5(2) and 12.8.6.7) is shown in Figure 12.80.

(1) Target model: The target model is shown in Figure 12.83. The impulse response of the target is $h_t(n)$, and we denote the input–output relationship as shown, with a Dirac δ function as the input, and the output sequence by $\hat{s}_t(n)$. As stated previously, the goal will be to estimate the parameters of the transfer function, $\hat{D}(n)$ and $\hat{C}(n)$, given by the composite parameter vector

$$\hat{\boldsymbol{\theta}}_t = [c_1, c_2, \ldots, c_{n_c}, d_0, d_1, \ldots, d_{n_d}]^{\mathrm{T}} \tag{12.23}$$

where n_c, n_d represent the order of the respective polynomials in z^{-1}.

The parameters of the target may be estimated only after the clutter/antenna parameters are determined.

(2) Clutter model: In a similar way, the clutter model may be represented by

$$\hat{\boldsymbol{\theta}}_c = [a_1, a_2, \ldots, a_{n_a}, b_0, b_1, \ldots, b_{n_b}]^{\mathrm{T}} \tag{12.24}$$

The input to the clutter block diagram is indicated by the δ-function in the absence of any knowledge of the true input waveform. In this way, the clutter model includes all of the effects noted in Section 12.8.6.3. In general, the shape of the transmitted pulse will not be known. Indeed, as with the data collected at TUI, there is no 'pulse' per se, but only a synthesised pulse by virtue of the stepped frequency modulation. The modelling methods described in this Section, however, lend themselves equally well to the case where the input (transmitted) pulse is known; simply replace the δ-function with the known pulse.

(3) Noise model: When modelling dynamical or signal systems, it is usually necessary to include a noise model which will account for any random disturbances caused by the measurement equipment, etc. Such disturbances may be nonstationary, and may also be non-Gaussian and display some specific spectral characteristics other than a flat ('white') spectrum. The inclusion of a (possibly time-varying) noise model is therefore indicated.

Such a noise process model can be described by

$$\hat{\boldsymbol{\theta}}_v = [g_1, g_2, \ldots, g_{n_g}, f_0, f_1, \ldots, f_{n_f}]^{\mathrm{T}} \tag{12.25}$$

and the model is shown in Figure 12.84.

The input to the noise model is a vector of independent, identically distributed (i.i.d.) samples with a Gaussian amplitude distribution of zero mean and constant spectral intensity. The input is applied to a filter which will provide appropriate spectral and amplitude shaping to represent the measured noise from A-scan to A-scan; it may not be necessary to apply this filter if the noise from A-scan to A-scan is sufficiently de-correlated. This is explained further in Section 12.8.6.7.

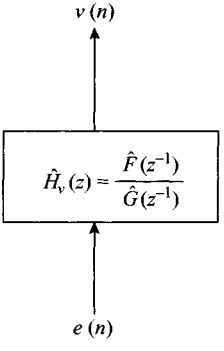

Figure 12.84 Representation of added noise parametric model

12.8.6.7 Implementation of model-based formulation: For a general description of the parametric system identification algorithms described in this Section, reference is made to Figure 12.82 and the additional Figures immediately following. The clutter model may be estimated by applying the *Steiglitz–McBride algorithm* described in Section 12.8.6.5(2). The clutter model is derived from a reference clutter sample, as is the case in all the techniques described herein except for some types of recursive (adaptive) methods, which will be described in Section 12.8.6.8. This should not, in most cases, be a drawback to the general method; representative clutter samples may be collected at various times during the mine scanning process.

Because the data collected at TUI consisted of frequency-domain samples (from a stepped-frequency radar), the derived time-domain signal represents a composite of a transmitted 'pulse' convolved with the clutter. Thus, we denote the input signal as a Dirac δ-function as shown in Figure 12.79. The noise model shown in Figure 12.84 can be estimated by determining the ARMA parameters of the residue found by subtracting successive A-scans and then using those coefficients to create correlated noise samples $v(n)$ which are of appropriate amplitude to match the power of the original residue. It has been determined experimentally that, with the data samples of interest here, the noise transfer function may be omitted; in other words, the scan-to-scan noise is closely approximated by the input $e(n)$. In this case, the noise modelling is accomplished by the MATLAB code fragment for a series of length-64 A-scans. In this case, the noise samples were found to be represented by WGN:

```
diff_clut=slice(:,n)-slice(:,n-1);
in=(1/sqrt(64))*sqrt(max(xcorr(diff_clut)))*randn(64,1);
```

If an examination of the correlation properties of the differenced A-scans determined that the residue had significant correlations at lags much greater than zero, it would be necessary to determine the noise model ARMA parameters as, for example, described in Reference [156]. That reference uses higher-order statistics (cumulants) to determine ARMA parameters assuming the data are correlated and possibly non-Gaussian. Other ARMA estimation methods may be used, such as those in Reference [147] if the process is found to be linear and Gaussian. In practice, it was found that WGN was a close approximation to the true process; in no case was an ARMA model greater than ARMA(4,4) determined to be of use.

As an example of the efficacy of the model-based approach, Figures 12.85 and 12.86 show the 'before' and 'after' B-scans of a cylindrical copper plate buried 30 cm in sand. The uncancelled clutter in Figure 12.86 may be due to undulations in the sand surface. As mentioned previously, this method is nonadaptive in this example, but the basic model may be refined to include adaptivity, in which case such surface clutter may be reduced.

Once the clutter estimate and noise processes are determined, the target may be easily extracted by simply subtracting the sum of those estimates from the measured signal. If desired, the target filter coefficients may be easily determined by the Steiglitz–McBride algorithm applied to the new target estimate signal as for the clutter signal described above.

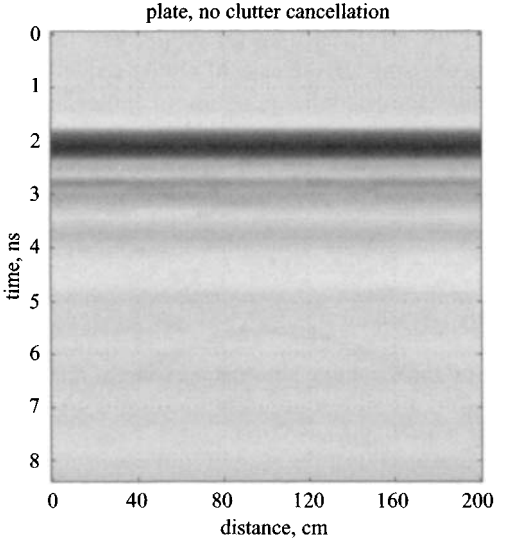

Figure 12.85 B-scan of copper plate buried 30 cm in sand

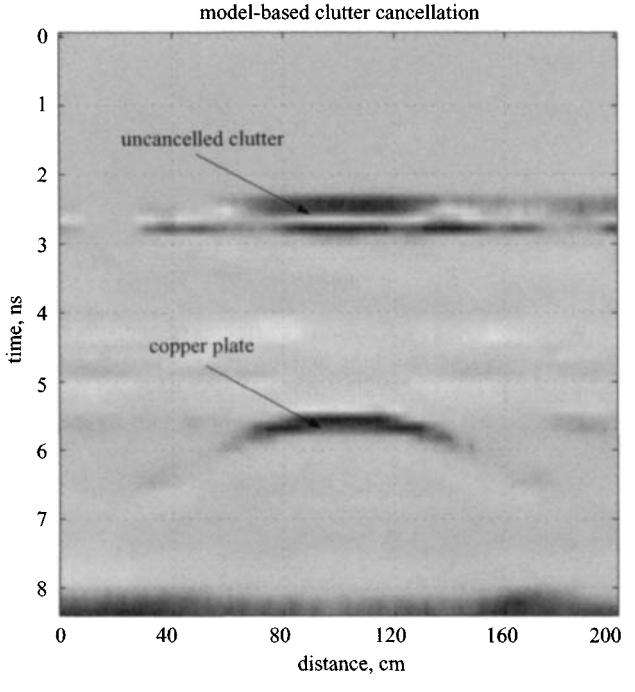

Figure 12.86 Result of model-based clutter removal

12.8.6.8 Recursive (time-varying) methods: Recursive algorithms, also known as *adaptive algorithms* [139, 149], are used for *on-line processing* of data as opposed to *batch or off-line processing*. In the case of clutter reduction, two approaches are addressed in this Section: the case where a sample of clutter is available for estimation, and the case where there is no a priori clutter information. In either case, the ultimate goal is to determine the parameter vector $\hat{\boldsymbol{\theta}}_t$ given by (12.23).

(1) Recursive least squares (RLS) methods: This method can be found in Reference [147], Chapter 11.

Consider the scalar–vector form of (12.16),

$$\mathbf{y}(n) = \boldsymbol{\Psi}^{\mathrm{T}}(n)\boldsymbol{\theta}(n) + e(n) \tag{12.26}$$

The general expression for recursive parameter estimation is

$$\hat{\boldsymbol{\theta}}(n) = \hat{\boldsymbol{\theta}}(n-1) + \mathbf{k}(n)(\mathbf{y}(n) - \hat{\mathbf{y}}(n)) \tag{12.27}$$

where $\mathbf{k}(n)$ is the *adaptation gain vector*. Given an initial parameter vector

$$\boldsymbol{\theta}_0(n) = \boldsymbol{\theta}_0(n-1) + \mathbf{w}(n) \tag{12.28}$$

where $\mathbf{w}(n)$ is assumed to be i.i.d., the general algorithm for recursive parameter estimation is therefore:

$$\begin{aligned}
\hat{\boldsymbol{\theta}}(n) &= \hat{\boldsymbol{\theta}}(n-1) + \mathbf{k}(n)[\mathbf{y}(n) - \hat{\mathbf{y}}(n)] \\
\hat{\mathbf{y}}(n) &= \boldsymbol{\Psi}^{\mathrm{T}}(n)\hat{\boldsymbol{\theta}}(n-1) \\
\mathbf{k}(n) &= \mathbf{Q}(n)\boldsymbol{\Psi}(n) \\
\mathbf{Q}(n) &= \frac{\mathbf{P}(n-1)}{R_2 + \boldsymbol{\Psi}^{\mathrm{T}}(n)\mathbf{P}(n-1)\boldsymbol{\Psi}(n)} \\
\mathbf{P}(n) &= \mathbf{P}(n-1) - \frac{\mathbf{P}(n-1)\boldsymbol{\Psi}(n)\boldsymbol{\Psi}^{\mathrm{T}}(n)\mathbf{P}^{\mathrm{T}}(n-1)}{R_2 + \boldsymbol{\Psi}^{\mathrm{T}}(n)\mathbf{P}(n-1)\boldsymbol{\Psi}(n)} + R_1
\end{aligned} \tag{12.29}$$

where $R_1 = \mathrm{E}[\mathbf{w}(n)\mathbf{w}^{\mathrm{T}}(n)]$ and R_2 is the variance of the innovations in (12.26), $R_2 = \mathrm{E}[e^2(n)]$. This is the *Kalman filter* version of adaptive parameter identification. The covariance matrix $\mathbf{P}$ is typically initialised as a diagonal matrix of dimension $N \times N$, where $N = n_a + n_b$ as in (12.9), for example.

Often, a modification to the above equations is made to include a *forgetting factor* $\{\lambda : 0 < \lambda \leq 1\}$, in which case the two latter equations of (12.29) become, respectively,

$$\begin{aligned}
\mathbf{Q}(n) &= \frac{\mathbf{P}(n-1)}{\lambda + \boldsymbol{\Psi}^{\mathrm{T}}(n)\mathbf{P}(n-1)\boldsymbol{\Psi}(n)} \\
\mathbf{P}(n) &= \left[\mathbf{P}(n-1) - \frac{\mathbf{P}(n-1)\boldsymbol{\Psi}(n)\boldsymbol{\Psi}^{\mathrm{T}}(n)\mathbf{P}^{\mathrm{T}}(n-1)}{\lambda + \boldsymbol{\Psi}^{\mathrm{T}}(n)\mathbf{P}(n-1)\boldsymbol{\Psi}(n)}\right] \Big/ \lambda
\end{aligned} \tag{12.30}$$

Typical values for λ range from 0.95 to 0.99.

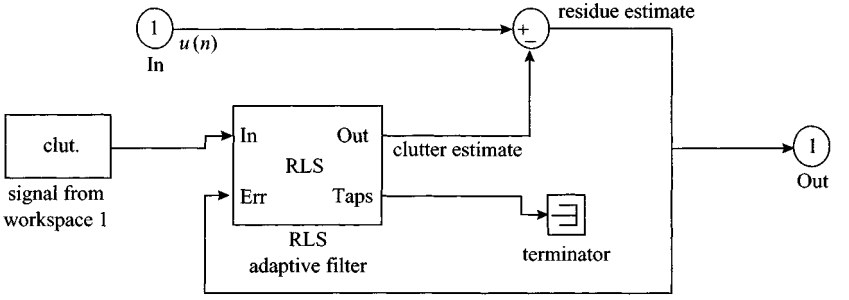

Figure 12.87 Simulink RLS model

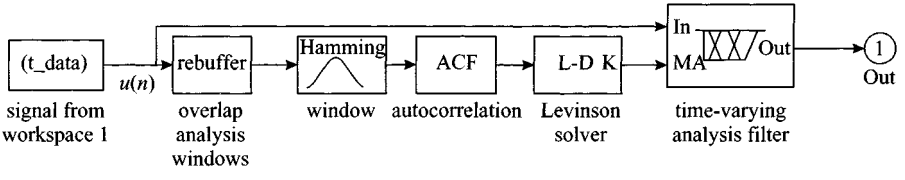

Figure 12.88 Simulink LPC model

The RLS algorithm may be implemented in Simulink and compiled to C-code. The Simulink block diagram is shown in Figure 12.87. As with many adaptive methods, a sample of clutter (here, clutter from the MATLAB workspace) is required for the RLS method to work. The clutter samples may be derived from an estimation process as described in Section 12.8.6.6, or samples of clutter may be measured in the field. In either case, the variability of the clutter with location must be considered. The 'In' port represents single A-scans of data. The 'Out' port represents the residual signal, or the signal with clutter removed.

(2) Linear predictive coding (LPC): LPC is a method of estimating the prediction-error coefficients for a linear regression model. Basically, the coefficients are determined by applying the *Levinson–Durbin algorithm* [147, 157] to the autocorrelation matrix of the input data in small blocks. The coefficients are then used to filter the input data, and the residual is found by subtracting the original data from the filtered estimate. This is explained by the following MATLAB code fragment. The variable t_data is the input A-scan. The data window in the following case is set to 5; this is a design parameter and can be changed to produce the best results. The function lpc is in the MATLAB Signal Processing Toolbox,

```
a=lpc(t_data,5);
f_est=filter([0 -a(2:end)],1,t_data);
est=t_data-f_est;
```

The LPC algorithm can be implemented in Simulink and then compiled into C-code. The Simulink block is shown in Figure 12.88. As can be seen, the LPC algorithm

applies the Levinson–Durbin algorithm to the windowed autocorrelation estimate of the data. The algorithm is described in References [157, 158], and will not be further detailed here. A unique feature of the LPC method is that no clutter sample is required; thus, it should prove useful when the surface of the soil is varying in height. The 'signal from workspace' is a Simulink signal source, and is represented by the variable t_data mentioned above. Each A-scan is input into the LPC block. The 'rebuffer' block converts the scalar input into a vector of a specified block length (for example, 5, as in the code fragment above), and the autocorrelation matrix of that vector is formed in the 'ACF' block. Finally, the Levinson–Durbin block calculates the filter coefficients, and the filtered output f_est is represented by the 'Out' port in the diagram.

(3) Discussion: The recursive parametric methods show great promise for clutter reduction. Additional work is needed to compensate for variations in the ground surface; a possible solution is adaptively shifting the A-scans in time to compensate for the surface variations. It is essential that raw, unprocessed data be used for all of these techniques; any interpolation or filtering of the data prior to application of these methods will lead to unsatisfactory results.

12.8.6.9 Target deconvolution by nonparametric system identification:

(1) Introduction: From (12.22), it is possible to extract the target from the composite clutter-plus-target signal by deconvolution. This is usually accomplished in the frequency domain, and two methods are described in this Section [147, 158].

The term *nonparametric* implies the absence of a transfer function defined explicitly in terms of the shift operator z^{-1}. In the case of nonparametric system identification, the time-domain correlation function or the frequency-domain power spectra are calculated. It is then possible, in some cases, to derive parameters from the frequency-domain information. In the following, we define the basic identities which are used in nonparametric system identification.

(2) Mathematical foundation: We list here a number of mathematical relationships which will be required in the remainder of this Section; the derivations may be found in Reference [158].

Consider a discrete signal $y(n)$, which may be considered to be the output of a linear, time invariant (LTI) system,

$$y(n) = x(n) \otimes h(n) + v(n) \tag{12.31}$$

where $h(t)$ is the impulse response of the system and $v(n)$ is an independent, identically distributed (i.i.d.) sequence with an auto-covariance function

$$R_v(k) = \mathrm{E}[(v(k) - m_v)(v(n-k) - m_v)^*] \tag{12.32}$$

In (12.31) the symbol $\otimes$ denotes convolution, defined as, for example,

$$x(n) \otimes h(n) = \sum_{k=-\infty}^{\infty} h(k)x(n-k) \tag{12.33}$$

In the discrete domain, the two-sided z-transform of a discrete sequence $\{x(n), n = -\infty, \ldots, -1, 0, +1, \ldots, +\infty\}$ is defined as

$$X(z) = \sum_{n=-\infty}^{\infty} x(n)z^{-n} \tag{12.34}$$

so (12.31) may be written as

$$Y(z) = X(z)H(z) \tag{12.35}$$

where $H(z)$ is referred to as the *system function*. The system function evaluated on the unit circle $|z| = 1$ is the *frequency response* of the system, $H(e^{j\omega})$.

Given a stochastic process $x(n)$, the *autocorrelation function* of the process is defined as

$$\Phi_{xx} = \mathrm{E}[x(n)x^*(m)] \tag{12.36}$$

where $\mathrm{E}[\cdot]$ is the expectation operator. For two stochastic processes $x(n)$ and $y(n)$, the *crosscorrelation function* is defined as

$$\Phi_{xy} = \mathrm{E}[x(n)y^*(m)] \tag{12.37}$$

The z-transform of the autocorrelation function is given by

$$\boldsymbol{\Phi}_{\boldsymbol{xx}}(z) = \sum_{k=-\infty}^{\infty} \Phi_{xx}(k)z^{-k} \tag{12.38}$$

and the following relationships apply:

$$\begin{aligned} \boldsymbol{\Phi}_{xx}(z) &= \boldsymbol{\Phi}^*_{xx}(1/z^*) \\ \boldsymbol{\Phi}_{xy}(z) &= \boldsymbol{\Phi}^*_{yx}(1/z^*) \end{aligned} \tag{12.39}$$

When evaluated on the unit circle, (12.38) results in the *power spectrum* of the process,

$$\boldsymbol{\Phi}_{xx}(e^{j\omega}) = \sum_{k=-\infty}^{\infty} \Phi_{xx}(k)e^{j\omega k} \tag{12.40}$$

and the next set of relationships relate the input–output crosspower spectrum $\boldsymbol{\Phi}_{xy}(e^{j\omega})$ and the output power spectrum $\boldsymbol{\Phi}_{yy}(e^{j\omega})$:

$$\begin{aligned} \boldsymbol{\Phi}_{xy}(e^{j\omega}) &= H^*(e^{j\omega})\boldsymbol{\Phi}_{\boldsymbol{xx}}(e^{j\omega}) \\ \boldsymbol{\Phi}_{yx}(e^{j\omega}) &= H(e^{j\omega})\boldsymbol{\Phi}_{\boldsymbol{xx}}(e^{j\omega}) \\ \boldsymbol{\Phi}_{yy}(e^{j\omega}) &= |H(e^{j\omega})|^2\boldsymbol{\Phi}_{\boldsymbol{xx}}(e^{j\omega}) \end{aligned} \tag{12.41}$$

Equations (12.41) form the basis for nonparametric system identification. In principle, the second equation of (12.41) can be used to find the estimated system function by forming the ratio of the estimated cross-spectrum (derived from the computed

crosscorrelation function) and the auto-spectrum (derived from the autocorrelation function) as

$$\hat{H}(e^{j\omega}) = \frac{\hat{\Phi}_{yx}(e^{j\omega})}{\hat{\Phi}_{xx}(e^{j\omega})} \tag{12.42}$$

Once the complex system function estimate has been computed, the system impulse response may be obtained by taking the inverse discrete Fourier transform (DFT) of (12.42).

In Reference [147], the disturbance spectrum estimate $\hat{\Phi}_{vv}(e^{j\omega})$ (see equation 12.31) is also derived as

$$\hat{\Phi}_{vv}(e^{j\omega}) = \hat{\Phi}_{yy}(e^{j\omega}) - \frac{|\hat{\Phi}_{yx}(e^{j\omega})|^2}{\hat{\Phi}_{xx}(e^{j\omega})} \tag{12.43}$$

Finally, the target transfer function may be determined directly by computing the ratio of the DFT of the measured signal with the DFT of the input signal as

$$\hat{H}_t(e^{j\omega}) = \frac{\hat{Y}(e^{j\omega})}{\hat{X}(e^{j\omega})} \tag{12.44}$$

12.8.6.10 Comments: The nonrecursive (nonadaptive) method described in Section 12.8.6.7 relies on a reference clutter sample (as do most methods described in this Section) and suffers from an inherent inability to cancel clutter caused by fluctuations in the soil surface. On the other hand, the basic block diagram may be implemented recursively to mitigate this limitation, given that clutter samples may be updated for each A-scan.

The LPC method presented in Section 12.8.6.8(2) removes the requirement for a reference clutter sample, exploiting instead the predictive (smoothing) nature of the LPC algorithm. As noted previously, the target information lies within the fine details of the signal envelope (which is mostly clutter).

The nonparametric methods described here proved to be of little use in determining target parameters due to the very low SCR exhibited in each unprocessed A-scan; the power spectra of clutter and signal-plus-clutter were simply too close in magnitude to be of any use.

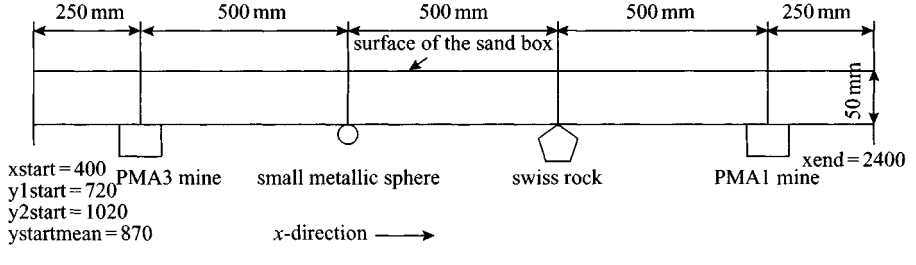

Figure 12.89 Measurement set-up at TUI Lab

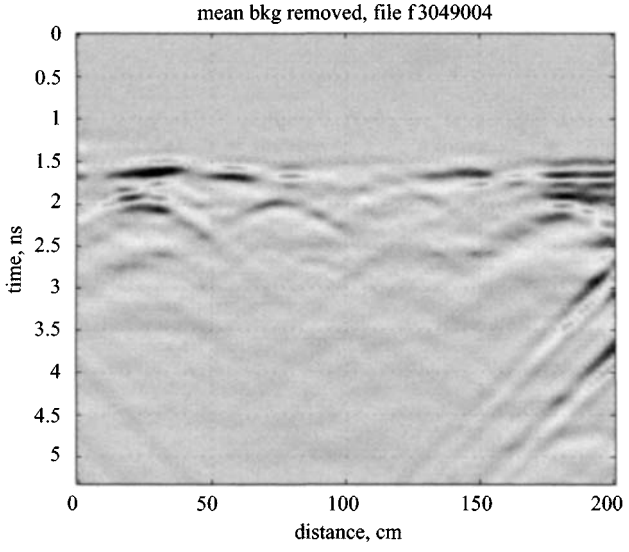

Figure 12.90 B-scan, mean background removal

12.8.6.11 Results: The various approaches described in the preceding Section were applied to data which were collected at the TUI for the EC-funded project: DEMINE (EP29902). The antenna used was a flat plate Vivaldi.

The test set-up at TUI is shown in Figure 12.89. Each target was buried such that the top of each target was 50 mm below the surface of the sand.

(1) Mean background removal: Figures 12.90 and 12.91 demonstrate the results of mean background removal. The slanted lines at the right of Figure 12.90 are reflections from the side of the sandbox. Some surface residual remains and the sphere and rock (nonmine targets) are still quite visible.

(2) Model estimated background removal: Figure 12.92 shows the result of the clutter and noise estimation described in Section 12.8.6.6. In this Figure, the far right side has been removed to eliminate the reflections from the wall of the sandbox. One can see that the correlated clutter represented normally by waves below the targets is suppressed. In this way, the dominant returns are only the tops of the targets. The reduction in correlated clutter is achieved by decorrelating the clutter by the addition of coloured ARMA noise. The noise model was estimated by differencing consecutive A-scans and evaluating the autocorrelation properties in order to establish the ARMA model order. Then, WGN was applied to the noise process transfer function shown in Figure 12.84. The clutter process was estimated by applying the Dirac delta function to the clutter transfer function of Figure 12.79 and experimentally determining the appropriate order by using a clutter A-scan sample. In this Figure, the clutter parameters are fixed, but the noise parameters are updated from A-scan to A-scan.

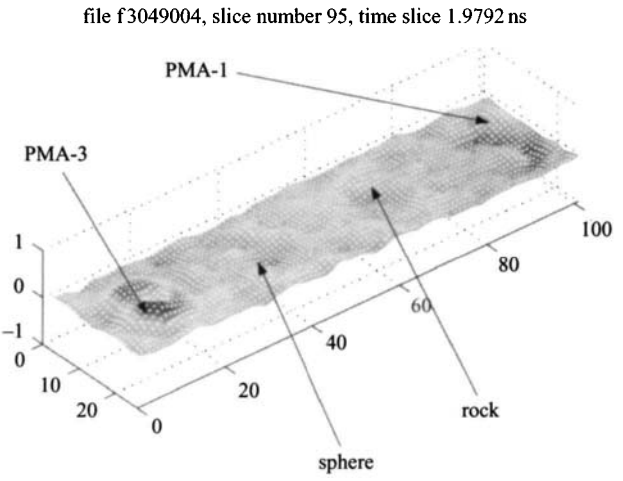

Figure 12.91 C-scan, mean background removal

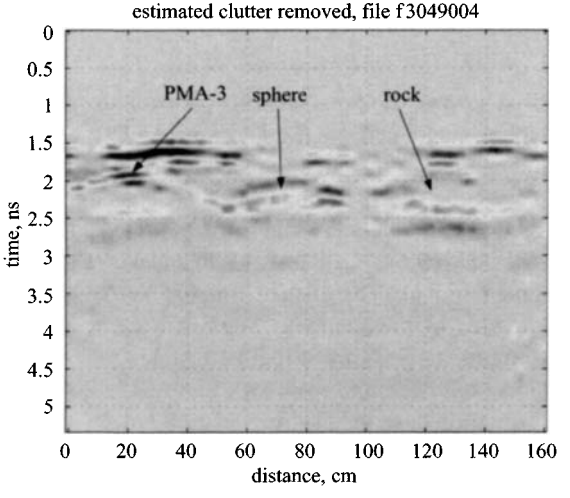

Figure 12.92 Parametric model background removal

Figure 12.93 is a C-scan of the 3D volume which clearly shows the mines. The poles and zeros from Figure 12.80 may be used also in the target model case as features for target classification.

(3) RLS background removal: Figures 12.94 and 12.95 show the results of the RLS adaptive approach. In this case, the clutter parameters are again considered fixed, but the signal minus clutter residue is adaptively estimated in time (depth) as well as

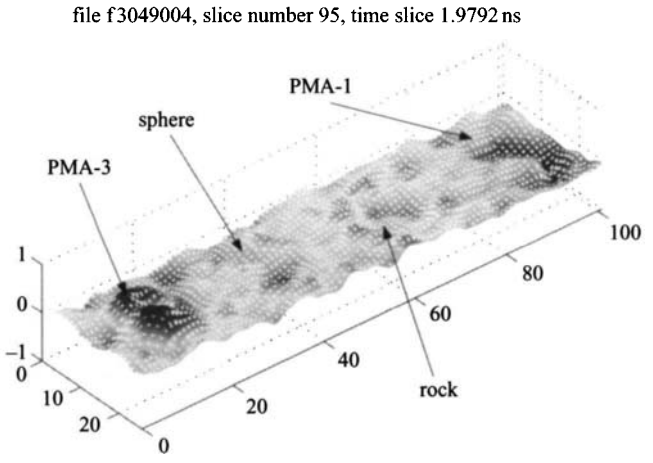

Figure 12.93 C-scan of parametric background removal

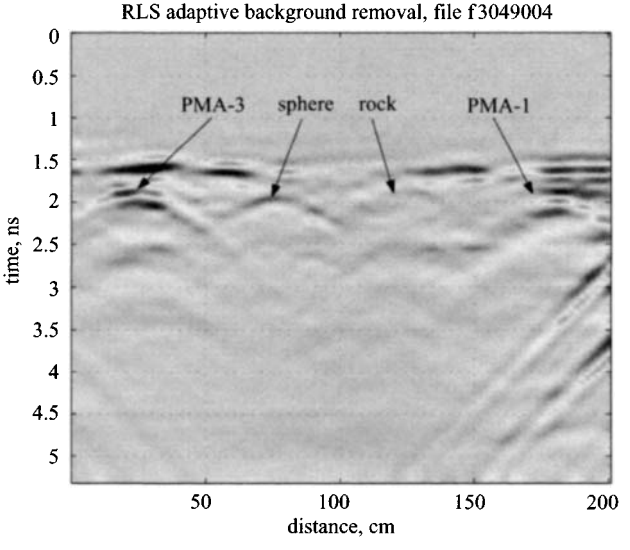

Figure 12.94 RLS background removal

from A-scan to A-scan. In this Figure, the sphere and rock returns are reduced, but the level of correlated clutter is more than in the previous approach.

(4) LPC background removal: The LPC approach in Figures 12.96 and 12.97 is based on Section 12.8.6.8(2). The Figures show the results of extracting the filtered residual from each A-scan as described by the MATLAB code fragment in that Section.

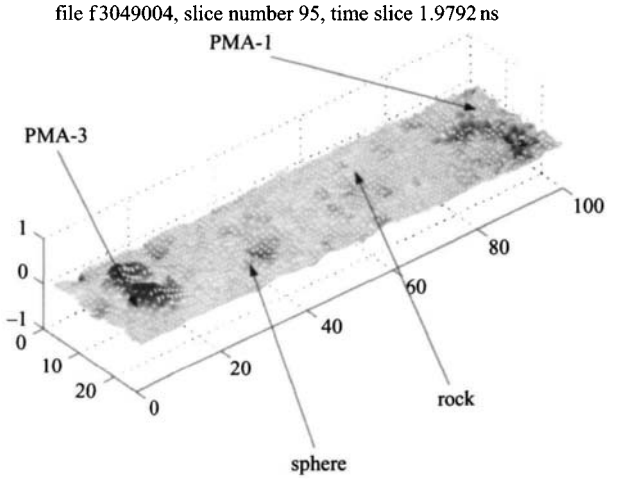

Figure 12.95 C-scan, RLS background removal

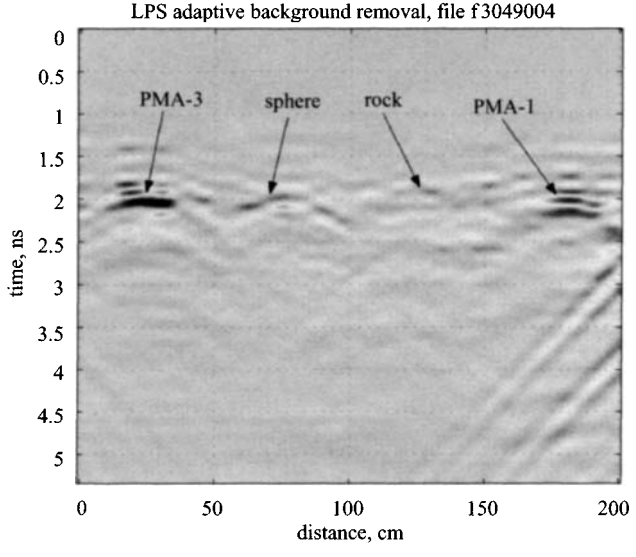

Figure 12.96 LPC background removal

12.8.6.12 Performance measures of clutter reduction methods: As stated in Section 12.8.6.2(5) we do not consider SNR or SCR to be valid measures of performance (MOP) in GPR evaluation. Rather, we evaluate GPR MOP in the context of improvement in, for example, target classification. In the following Sections, physical

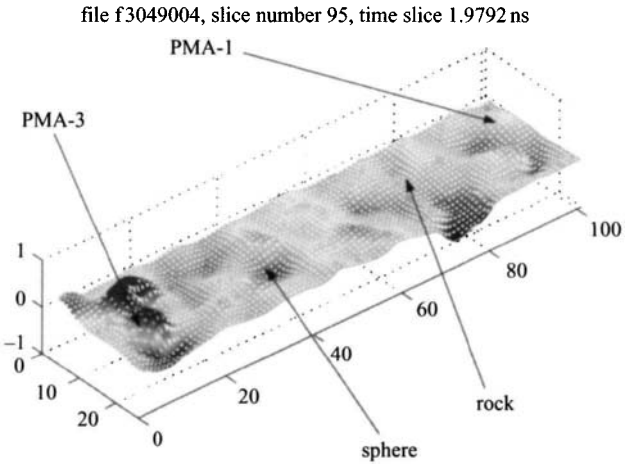

Figure 12.97 C-scan, LPC background removal

target parameters and target discrimination performance are evaluated following adaptive background removal by the RLS method.

(1) Physical parameter estimation: An important parameter in the processing of GPR data is the knowledge of the velocity of propagation in the medium. The velocity estimation is based on the detected hyperbolas in the B-scan image. In the following we compare the estimated hyperbola parameters and velocities for both GPR raw data (after simple average subtraction) and pre-processed data after clutter removal. The detection of hyperbolic forms in a B-scan image is done using a generalised Hough-transform on the detected edge pixels. Edge detection was made using multi-scale Gabor filters. The following equation for the general hyperbolic parameters was considered:

$$t^2 = \alpha + \beta(x - \gamma)^2 \tag{12.45}$$

where t and x represent the vertical and horizontal co-ordinates and γ the eccentricity. Figures 12.98 and 12.99 show the detected hyperbolas for the raw data and the pre-processed data.

We see that in both cases a number of hyperbolas are detected at each of the object positions. There are, however, also some other hyperbolas which are present and do not correspond to real objects. Noisy hyperbolas are detected using a correlation between the detected hyperbolas on a C-scan. For each target we can then calculate the local velocity of propagation,

$$v = \frac{2\Delta x}{\sqrt{\beta}\Delta t} \tag{12.46}$$

and the depth,

$$z = v\sqrt{\alpha} \tag{12.47}$$

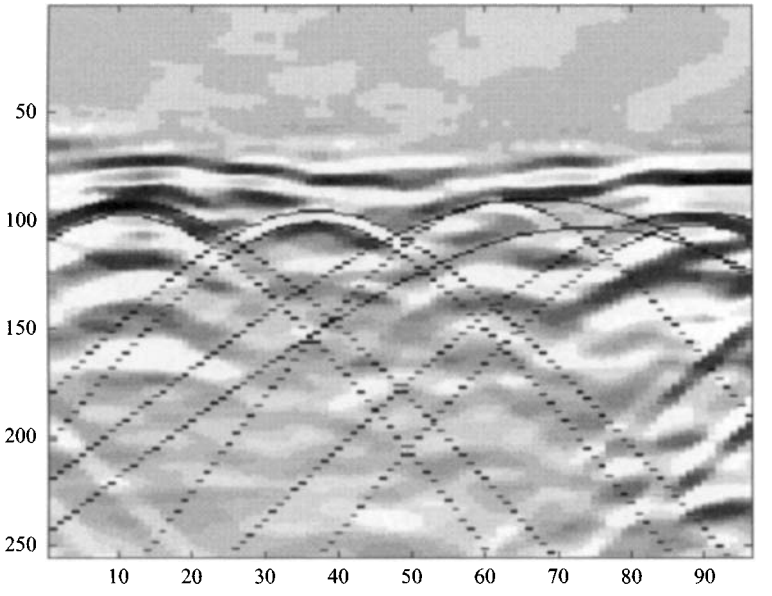

Figure 12.98 Detected hyperbolas in raw data, slice 16

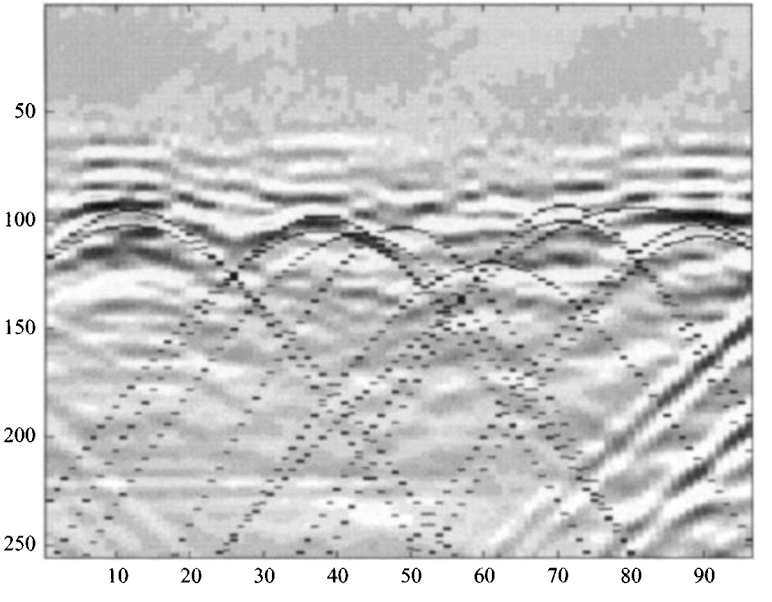

Figure 12.99 Detected hyperbolas in pre-processed data, slice 16

Table 12.9 Feature comparison between raw and pre-processed data

	Raw data			Pre-processed data		
	Depth, mm	Velocity	Eccentricity	Depth, mm	Velocity	Eccentricity
PMA-3	47	5.7×10^7 m/s	20.5	56	6.9×10^7 m/s	19.8
Sphere	65	6.4×10^7 m/s	21.0	61	7.1×10^7 m/s	19.9
Rock	49	6.7×10^7 m/s	20.8	64	6.5×10^7 m/s	19.1
PMA-1	81	7.0×10^7 m/s	23.1	56	7.2×10^7 m/s	19.8

where Δx is the horizontal distance between two sample points (the horizontal scanning step), Δt is the difference in time between two sample points (the inverse of the sampling frequency). In Table 12.9 we compare velocity, depth and eccentricity for both raw data and pre-processed data.

It can be seen that, with the pre-processed data, the estimated depth is approximately 50 mm, which is the correct value, and the velocity estimates for the mines are approximately identical. Finally, the eccentricity is almost identical for all the objects.

(2) Target class discrimination: This Section presents a short summary of target discrimination based on raw and pre-processed data, using time, frequency and wavelet-domain features [159]. To compare the results for both types of data, we will estimate how well the selected features are clustered within each of the classes separately, and how effective those features are in separating the classes.

The selection of the best features out of the larger feature vectors, composed of all the data samples in the time, frequency and wavelet domains, is based on the estimation of Wilks' lambda [160]. This entity is defined as follows:

$$\lambda = \frac{\det\left[\sum_{j=1}^{N}\sum_{i=1}^{n_j}(X_{ij} - \bar{X}_j)(X_{ij} - \bar{X}_j)^{\mathrm{T}}\right]}{\det\left[\sum_{j=1}^{N}\sum_{i=1}^{n_j}(X_{ij} - \bar{X})(X_{ij} - \bar{X})^{\mathrm{T}}\right]} \tag{12.48}$$

where:
X_{ij} feature i in class j
n_j number of features in class j
$\bar{X}$ overall feature mean
$\bar{X}_j$ feature mean for class j
N number of classes.

In this formula the denominator represents the determinant of the *within class scatter matrix*. This value will express how well the selected features are clustered

within each of the classes separately. A small value of the denominator will represent a well clustered feature set.

The numerator represents the determinant of the *total scatter matrix*. This value will express how much the combined feature set is extended over the feature space. A large value can be interpreted as the fact that the distance between the class means will be large.

The combination of the two requirements leads to the selection of those features that have the smallest values of Wilks' lambda.

The actual comparison between the raw and pre-processed data will be made based upon two items: the *clustering* within a class and the *separability* between classes.

For the clustering within a class, the assumption is made that the values of the selected features conform to a Gaussian distribution. The *covariance matrix* Co_j of these selected features for class j can be expressed as

$$Co_j = \sum_{i=1}^{n} (X_{ij} - \bar{X}_j)(X_{ij} - \bar{X}_j)^{\mathrm{T}} \tag{12.49}$$

The feature cloud will have an elongated shape in the feature space, in the case that the features are not well clustered (Figure 12.100a), and a spherical shape in the case they are well clustered (Figure 12.100b).

In Figure 12.100, λ_1 and λ_2 are the first and second eigenvalues of the covariance matrix. The ratio λ_1/λ_2 will thus express how well the classes are clustered (a smaller value will represent a better clustering).

The logical way to express the separability between classes is to use the quotient of the distance between the class mean and total mean, and the largest eigenvalue (expressing the spread). This value will have to be maximised.

Table 12.10 shows the comparison results, based on the defined values, for time, frequency and wavelet features separately, or when using all (combined) features. The clustering within the class is for the three objects (mine, sphere and rock), is, in most of the cases, better for the pre-processed data than for the raw data. Finally, the classes are better separated using the pre-processed data.

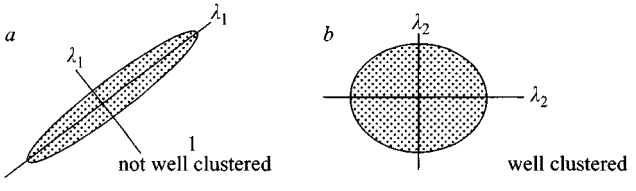

Figure 12.100 The shape of the feature cloud for a not well clustered (a) and a well clustered (b) class

Table 12.10 Comparison results based on feature selection

	Raw data				Pre-processed data			
	Clustering (λ_1/λ_2)			Separability	Clustering (λ_1/λ_2)			Separability
	Mine	Sphere	Rock		Mine	Sphere	Rock	
Time	1.45	3.96	3.06	5.76	1.06	4.29	1.23	8.14
Freq.	3.33	3.19	2.83	4.47	1.99	2.74	2.67	3.31
Wavel.	3.21	2.65	1.38	2.77	2.92	2.68	2.49	4.23
All	16.42	21.52	4.46	1.19	2.17	1.67	2.67	6.85

12.9 Summary

GPR is beginning to be fielded as a sensor for mine detection where its ability against the minimum metal mine often surpasses the ubiquitous metal detector. The US HSTAMIDS hand-held detector is now being evaluated in Afghanistan. Throughout the world, airborne, vehicle mounted and hand-held systems have been extensively researched, developed and trialled. The process has taken over two decades from the early systems devised for Vietnam and the Falkland Islands and has often been fragmented and intermittent.

In most soils, GPR can detect mines at greater depths than the metal detector, but in clay or salt-laden soils it does not perform as well. However, in some mineralised soils where the metal detector struggles, GPR has a performance advantage.

This suggests that it is important that the processing built into a GPR sensor can recognise difficult soil conditions and alert the operator to a potential performance degradation. Furthermore, GPR has to overcome many potential sources of false alarm due to clutter, which include large stones, animal burrows, cracks in the soil surface, pooled water in surface and sub-surface hollows, tree roots, changes in surface topography and changes in vertical or lateral soil structure.

As GPR is now reaching a level of technology readiness, it is vital that it is tested in a way that exposes all aspects of performance. Many test procedures developed for metal detector technology are inappropriate for GPR, which must take into account not just the mass of metal in the mine but the type of mine, surrogate, inert etc., the size of mine, the internal structure of mine, the explosive content of mine, the depth of mine, the attitude of mine to the horizontal and the proximity to other targets such as AT mines.

The testing of GPR systems should ensure that there is an adequate statistical distribution of AP and AT mines, GPR clutter, ground topography, soil conditions (water content etc.), operator variance and product batch quality control.

The performance bounds of GPR systems can be evaluated, but as yet there is not the wealth of understanding of the effects of clutter that is common in conventional

Table 12.10 Comparison results based on feature selection

	Raw data				Pre-processed data			
	Clustering (λ_1/λ_2)			Separability	Clustering (λ_1/λ_2)			Separability
	Mine	Sphere	Rock		Mine	Sphere	Rock	
Time	1.45	3.96	3.06	5.76	1.06	4.29	1.23	8.14
Freq.	3.33	3.19	2.83	4.47	1.99	2.74	2.67	3.31
Wavel.	3.21	2.65	1.38	2.77	2.92	2.68	2.49	4.23
All	16.42	21.52	4.46	1.19	2.17	1.67	2.67	6.85

12.9 Summary

GPR is beginning to be fielded as a sensor for mine detection where its ability against the minimum metal mine often surpasses the ubiquitous metal detector. The US HSTAMIDS hand-held detector is now being evaluated in Afghanistan. Throughout the world, airborne, vehicle mounted and hand-held systems have been extensively researched, developed and trialled. The process has taken over two decades from the early systems devised for Vietnam and the Falkland Islands and has often been fragmented and intermittent.

In most soils, GPR can detect mines at greater depths than the metal detector, but in clay or salt-laden soils it does not perform as well. However, in some mineralised soils where the metal detector struggles, GPR has a performance advantage.

This suggests that it is important that the processing built into a GPR sensor can recognise difficult soil conditions and alert the operator to a potential performance degradation. Furthermore, GPR has to overcome many potential sources of false alarm due to clutter, which include large stones, animal burrows, cracks in the soil surface, pooled water in surface and sub-surface hollows, tree roots, changes in surface topography and changes in vertical or lateral soil structure.

As GPR is now reaching a level of technology readiness, it is vital that it is tested in a way that exposes all aspects of performance. Many test procedures developed for metal detector technology are inappropriate for GPR, which must take into account not just the mass of metal in the mine but the type of mine, surrogate, inert etc., the size of mine, the internal structure of mine, the explosive content of mine, the depth of mine, the attitude of mine to the horizontal and the proximity to other targets such as AT mines.

The testing of GPR systems should ensure that there is an adequate statistical distribution of AP and AT mines, GPR clutter, ground topography, soil conditions (water content etc.), operator variance and product batch quality control.

The performance bounds of GPR systems can be evaluated, but as yet there is not the wealth of understanding of the effects of clutter that is common in conventional

radar engineering. This is an important area which needs to be understood better if predictions of the statistical performance of GPR are to be better quantified.

The most successful developments have been where GPR is used in conjunction with other sensors (primarily the metal detector).

The market for humanitarian mine detectors is fragmented and very cost sensitive and will be difficult to develop, but it is to be hoped that parallel developments and procurements for military applications will result in products being used to meet the humanitarian need.

There are good reasons for being hopeful that the next few years will see GPR in action for mine clearance.

12.10 References

[1] 'Hidden killers, 1998. The global landmine crisis'. Report 10575, US Department of State, Bureau of Political-Military Affairs by the Office of Humanitarian Demining Programs (www.state.gov/www/global/arms/rpt_9809_demine_ch3a.html)

[2] 'Landmine monitor report', 1999. ICBL, ISBN 1-56432-231-9

[3] 'Humanitarian demining operations equipment planning guide'. US Dept of Defense, August 1997

[4] Proc. Conf. on Sustainable humanitarian demining : trends techniques and technologies, Zagreb, Croatia, 30 Sept.– 2 Oct. 1997. Humanitarian Demining Information Center, James Madison University

[5] Proc. European Commission JRC Conf. on De-mining technologies, Ispra, Italy, Sept/Oct 1998

[6] Proc. EUREL Int. Conf. on Detection of abandoned landmines, Edinburgh, UK, 7–9 October 1996. IEE Conf. Publ. 431

[7] Proc. EUREL 2nd Int. Conf. on Detection of abandoned landmines, Edinburgh, UK, 12th–14th October 1998. IEE Conf. Publ. 458

[8] 'Humanitarian demining within South East Europe – an analysis of capability shortfalls and user needs'. Geneva International Centre for Humanitarian Demining, May 2000

[9] LEE, K.-H., CHEN, C.-C., and LEE, R.: 'A numerical study of the effects of realistic GPR antennas on the scattering characteristics from unexploded ordnances'. Proc. IEEE Int. Geoscience and Remote Sensing Symposium, 2002 (IGARSS '02), Vol. 3, pp. 1572–1574

[10] GILMORE, C., COLLINS, D., JEFFREY, I., PETERS, S., and LO VETRI, J.: 'Design, implementation and testing of a prototype 1.1–2.1 GHz SFCW GPR for use in landmine detection'. Proc. IEEE Canadian Conf. on Electrical and computer engineering, 2002 (CCECE 2002), Vol. 1, pp. 291–296

[11] EARP, S. L., HUGHES, E. S., ELKINS, T. J., and VICKERS, R.: 'Ultra-wideband ground-penetrating radar for the detection of buried metallic mines'. Proc. 1996 IEEE National Radar Conf., 13–16 May 1996, pp. 7–12

[12] CARIN, L., GENG, N., McCLURE, M., SICHINA, J., and NGUYEN, L.: 'Ultra-wideband synthetic aperture radar for mine field detection'. Proc. of IEEE Conference on Ultra-wideband short-pulse electromagnetics 4, 1998, pp. 433–441

[13] LANGMAN, A., and INGGS, M. R.: 'A 1–2 GHz SFCW radar for landmine detection'. Proc. 1998 South African Symposium on Communications and Signal Processing, 1998 (COMSIG '98), 7–8 Sep. 1998, pp. 453–454

[14] STEINWAY, W. J., DUVOISIN, H. A., III, TOMASSI, M. S., THOMAS, J. E., BETTS, G., MORRIS, C., KAHN, B., STERN, P., KRYWICK, S., JOHNSON, K., DENNIS, K., SIMONEAUX, W., and BLOOD, B.: 'Multi-sensor system for mine detection'. Proc. IEEE Int. Geoscience and Remote Sensing Symposium, 1998 (IGARSS '98), 6–10 July 1998, Vol. 1, pp. 228–230

[15] STRIFORS, H. C., GUSTAFSSON, A., ABRAHAMSON, S., and GAUNAURD, G. C.: 'Fuzzy-cluster representation of time-frequency signatures as a means for automatic classification of buried mine-like targets'. Proc. IEEE-SP Int. Time-Frequency and Time-Scale Analysis Symposium, 1998, 6–9 Oct. 1998, pp. 597–600

[16] CAREVIC, D., CHANT, I., and CAELLI, T.: 'Feature extraction and classification of minelike targets from GPR data using Gaussian mixture models'. Proc. Information, Decision and Control Conf., Adelaide, Australia, 1999, IDC 99

[17] PERRIN, S., BIBAUT, A., DUFLOS, E., and VANHEEGHE, P.: 'Use of wavelets for ground-penetrating radar signal analysis and multisensor fusion in the frame of land mine detection'. Proc. IEEE Int. Conf. on Systems, man, and cybernetics, 2000, Vol. 4, pp. 2940–2945

[18] BUDKO, N. V., REMIS, R. F., and VAN DEN BERG, P. M.: 'Advances in GPR data processing for antipersonnel landmine detection'. Proc. IEEE Int. Geoscience and Remote Sensing Symposium, 2000 (IGARSS 2000), Vol. 1, pp. 19–22

[19] BARKAT, B., ZOUBIR, A. M., and BROWN, C. L.: 'Application of time-frequency techniques for the detection of anti-personnel landmines'. Proc. Tenth IEEE Workshop on Statistical signal and array processing, 2000, pp. 594–597

[20] ZHAN, H., RAPPAPORT, C., EL-SHENAWEE, M., and MILER, E.: 'Mine detection under rough ground surfaces using 2-D FDTD modeling and hypothesis testing'. IEEE Int. Antennas and Propagation Society Symposium, 2001, Vol. 3, pp. 756

[21] BENJAMIN, R., CRADDOCK, I. J., HILTON, G. S., LITOBARSKI, S., McCUTCHEON, E., NILAVALAN, R., and CRISP, G. N.: 'Microwave detection of buried mines using non-contact, synthetic near-field focusing', *IEE Proc., Radar Sonar Navig.*, 2001, **148**, (4), pp. 233–240

[22] EARP, S. L., HUGHES, E. S., ELKINS, T. J., and VICKERS, R.: 'Ultra-wideband ground-penetrating radar for the detection of buried metallic mines', *IEEE Aerosp. Electron. Syst. Mag.*, 1996, **11**, (9), pp. 30–39

[23] MONTOYA, T. P., and SMITH, G. S.: 'Land mine detection using a ground-penetrating radar based on resistively loaded Vee dipoles', *IEEE Trans. Antennas Propag.*, 1999, **47**, (12), pp. 1795–1806

[24] STILES, J. M., APTE, A. V., and BEH, B.: 'A group-theoretic analysis of symmetric target scattering with application to landmine detection', *IEEE Trans. Geosci. Rem. Sens.*, 2002, **40**, (8), pp. 1802–1814

[25] GARREAU, P., COTTARD, G., BERTHAUD, P., BEAUMONT, E., and BOLOMEY, J. C.: 'Potentials of microwave tomographic imaging for on line detection of land mines'. EUREL Int. Conf. on The detection of abandoned land mines: a humanitarian imperative seeking a technical solution. IEE Conf. Publ. 431, 7–9 Oct. 1996, pp. 164–166

[26] BROOKS, J. W., and MAIER, M. W.: 'Application of system identification and neural networks to classification of land mines'. EUREL Int. Conf. on The detection of abandoned land mines: a humanitarian imperative seeking a technical solution, IEE Conf. Publ. 431, 7–9 Oct. 1996, pp. 46–50

[27] BROOKS, J. W., MAIER, M. W., and VECHINSKI, S. R.: 'Applying system identification and neural networks to the efficient discrimination of unexploded ordnance'. Proc. IEEE Aerospace Conf., 1997. 1–8 Feb. 1997, Vol. 2, pp. 449–467

[28] O'NEILL, K.: 'Exploration of innovative radar sensing schemes for subsurface object detection'. Proc. IEEE Int. Conf. on Geoscience and remote sensing, 1997 (IGARSS '97), 'Remote sensing – a scientific vision for sustainable development', 1997, 3–8 Aug. 1997, Vol. 3, pp. 1135–1137

[29] LO VETRI, J., PRIMAK, S., VAN LEERSUM, B. J. A. M., and ZWAMBORN, A. P. M.: 'Feasibility study into the identification of landmines using UWB radar: an analysis using synthesized data'. Proc. Fourth Int. Conf. on Ultra-wideband short-pulse electromagnetics, Tel Aviv, Israel, 1998, pp. 425–432

[30] YAROVOY, A. G., SAI, B., HERMANS, G., VAN GENDEREN, P., LIGTHART, L. P., SCHUKIN, A. D., and KAPLOUN, I. V.: 'Ground penetrating impulse radar for detection of small and shallow-buried objects'. Geoscience and Remote Sensing Symposium, 1999 (IGARSS '99)

[31] SAI, B., and LIGTHART, L. P.: 'Detection and imaging of small buried 3D non-metallic objects with multistatic phase-based GPR signatures'. Proc. IEEE Int. Geoscience and Remote Sensing Symposium, 2002 (IGARSS '02), Vol. 4, pp. 1988–1990

[32] HALMAN, J. I., SHUBERT, K. A., and RUCK, G. T.: 'SAR processing of ground-penetrating radar data for buried UXO detection: results from a surface-based system', *IEEE Trans. Antennas Propag.*, 1998, **46**, (7), pp. 1023–1027

[33] CHEN, C.-C., NAG, S., BURNSIDE, W. D., HALMAN, J. I., SHUBERT, K. A., and PETERS, L., Jr.: 'A standoff, focused-beam land mine radar', *IEEE Trans. Geosci. Remote Sens.*, 2000, **38**, (1), pp. 507–514

[34] CHANT, I. J., and RYE, A. R.: 'Overview of current radar land mine detection research at the Defence Science and Technology Organisation, Salisbury,

South Australia'. EUREL Int. Conf. on The detection of abandoned land mines: a humanitarian imperative seeking a technical solution. IEE Conf. Publ. 431, 7–9 Oct. 1996, pp. 138–142

[35] AMAZEEN, C. A., and LOCKE, M. C.: EUREL Int. Conf. on The detection of abandoned land mines: a humanitarian imperative seeking a technical solution. IEE Conf. Publ. 431, 7–9 Oct. 1996, pp. 172–176

[36] CHEN, C. C., HIGGINS, M. B., and O'NEILL, K.: 'Advanced classification of buried UXO using a broadband, fully polarimetric ground penetrating radar'. IEEE Int. Geoscience and Remote Sensing Symposium, 2002 (IGARSS '02), Vol. 3, pp. 1569–1571

[37] FISCHER, C., and WIESBECK, W.: 'Multistatic GPR for antipersonnel mine detection'. IEEE Int. Geoscience and Remote Sensing Symposium, 2001 (IGARSS '01), Vol. 6, pp. 2721–2723

[38] FRIGUI, H., GADER, P., and KELLER, J.: 'Fuzzy clustering for land mine detection'. Conf. of the North American Fuzzy Information Processing Society – NAFIPS, 20–21 Aug. 1998, pp. 261–265

[39] DEMING, R. W.: 'Automatic buried mine detection using the maximum likelihood adaptive neural system (MLANS)'. Intelligent Control (ISIC), 1998. Held jointly with IEEE Proc. IEEE Int. Symposium on Computational intelligence in robotics and automation (CIRA), Intelligent systems and semiotics (ISAS), 14–17 Sep. 1998, pp. 428–433

[40] XU, X., MILLER, E. L., SOWER, G., and BROACH, T.: 'Detection of buried mines from GPR array measurement: a statistical approach'. Proc. IEEE Int. Geoscience and Remote Sensing Symposium, 2000, IGARSS 2000, Vol. 4, pp. 1637–1639

[41] VAN KEMPEN, L., and SAHLI, H.: 'Signal processing techniques for clutter parameters estimation and clutter removal in GPR data for landmine detection'. Proc. 11th IEEE Signal Processing Workshop on Statistical signal processing, 2001, pp. 158–161

[42] SCHEERS, B., PIETTE, M., and VANDER VORST, A.: 'The detection of AP mines using UWB GPR'. 2nd Int. Conf. on the Detection of abandoned land mines, 1998. IEE Conf. Publ. 458, 12–14 Oct. 1998, pp. 50–54

[43] FISCHER, C., and WIESBECK, W.: 'Laboratory verification for a forward-looking multi-receiver mine-detection GPR'. Proc. IEEE Int. Geoscience and Remote Sensing Symposium, 2000. IGARSS 2000. Vol. 4, pp. 1643–1645

[44] VAN DER MERWE, A., and GUPTA, I. J.: 'A novel signal processing technique for clutter reduction in GPR measurements of small, shallow land mines', *IEEE Trans. Geosci. Remote Sens.*, 2000, **38**, (6), pp. 2627–2637

[45] JAGERBRO, P., BRUSMARK, B., CHRISTIANSEN, A.-L., and LAUBERTS, A.: 'Combination of GPR and metal detector for mine detection'. 2nd Int. Conf. on the Detection of abandoned land mines, 1998. IEE Conf. Publ. 458, 12–14 Oct. 1998, pp. 177–181

[46] USCHKERAT, U.: 'Comparing UWB GPR measurements and simulation of simple shaped buried targets'. 2nd Int. Conf. on Detection of Abandoned Land Mines, 1998. IEE Conf. Publ. 458, 12–14 Oct. 1998, pp. 41–44

[47] MILLOT, P., and BERGES, A.: 'Ground based SAR imaging tool for the design of buried mine detectors'. EUREL Int. Conf. on The detection of abandoned land mines: a humanitarian imperative seeking a technical solution. IEE Conf. Publ. 431, 7–9 Oct. 1996, pp. 157–159

[48] LOHLEIN, O., and FRITZSCHE, M.: 'Classification of GPR data for mine detection based on hidden Markov models'. 2nd Int. Conf. on Detection of abandoned land mines, 1998. IEE Conf. Publ. 458, 12–14 Oct. 1998, pp. 96–100

[49] BOURGEOIS, J. M., and SMITH, G. S.: 'A complete electromagnetic simulation of a ground penetrating radar for mine detection: theory and experiment'. IEEE Antennas and Propagation Society International Symposium Digest, 1997, 13–18 July, 1997, Vol. 2, pp. 986–989

[50] GADER, P., KELLER, J. M., FRIGUI, H., LIU, H., and WANG, D.: 'Landmine detection using fuzzy sets with GPR images'. Proc. IEEE Int. Conf. on Fuzzy systems, 1998. IEEE World Congress on Computational Intelligence., 4–9 May 1998, Vol. 1, pp. 232–236

[51] GAO, P., TANTUM, S., COLLINS, L., WEAVER, D., MOULTON, J., MAKOWSKY, L., and REIDY, D.: 'Statistical signal processing techniques for the detection of low-metal landmines using EMI and GPR sensors' (Topic area: E.1). Proc. IEEE Int. Geoscience and Remote Sensing Symposium, 1999 (IGARSS '99), Vol. 5, pp. 2465–2467

[52] CIRILLO, L. A., BROWN, C. L., and ZOUBIR, A. M.: 'Polynomial phase signal based detection of buried landmines using ground penetrating radar'. Proc. 11th IEEE Signal Processing Workshop on Statistical signal processing, 2001, pp. 166–169

[53] KARLSEN, B., LARSEN, J., SORENSEN, H. B. D., and JAKOBSEN, K. B.: 'Comparison of PCA and ICA based clutter reduction in GPR systems for anti-personal landmine detection'. Proc. 11th IEEE Signal Processing Workshop on Statistical signal processing, 2001, pp. 146–149

[54] GADER, P. D., MYSTKOWSKI, M., and YUNXIN ZHAO.: 'Landmine detection with ground penetrating radar using hidden Markov models', *IEEE Trans. Geosci. Rem. Sens.*, 2001, **39**, (6), pp. 1231–1244

[55] O'NEILL, K.: 'Discrimination of UXO in soil using broadband polarimetric GPR backscatter', *IEEE Trans. Geosci. Remote Sens.*, 2001, **39**, (2), pp. 356–367

[56] STURGESS, K., HAPP, L., KURTZ, J., and COLLINS, M.: 'Results of a remote sensing experiment using a low frequency ultra-wideband SAR to investigate the phenomenology of landmines'. Proc. Int. Geoscience and Remote Sensing Symposium, 1996 (IGARSS '96), 'Remote sensing for a sustainable future', 27–31 May 1996, Vol. 4, pp. 2027–2029

[57] DANIELS, D. J., and DITTMER, J. K.: 'Design challenges for ultra-wideband radar for AP mine detection'. Ecole Polytechnique Fédérale de Lausanne, Switzerland, July 1995

[58] DANIELS, D. J.: 'High resolution radar detection of buried anti-personnel mines for humanitarian clearing operations'. ISMCR '96, Brussels, Belgium, 9–11 May 1996

[59] DANIELS, D. J., and MALLINSON, P.: 'Impulse radar mine detection', 'The detection of abandoned land mines: a humanitarian imperative seeking a technical solution'. EUREL Int. Conf., ICC Edinburgh, 7–9 October 1996
[60] DANIELS, D. J.: 'Radar techniques for mine detection'. SUSDEM '97, Zagreb, 29 Sep–1 Oct 1997
[61] DANIELS, D. J.: 'Applications of impulse radar technology'. Radar '97 Conference, Edinburgh, 14–16 Oct 1997
[62] DANIELS, D. J.: 'Multi-sensor radar techniques for mine detection'. IEEE CESA '98, Tunisia, 1–4 April 1998
[63] DANIELS, D. J.: 'Ground probing radar techniques for mine detection'. GPR '98, Kansas, USA, 26–30 May 1998, 05–14
[64] DANIELS, D. J.: 'Detection of ground probing radar target images in clutter'. EUREL/IEE Meeting on Radar and sonar signal processing, Peebles, Scotland, UK, 5–8 July 1998
[65] DANIELS, D. J.: 'Advances in the ultra-wideband imaging of buried mines'. IEEE PIERS '98, Nantes, France, 13–17 July 1998
[66] DANIELS, D. J.: 'A low cost, hand-held, microwave radiometer for surface laid mines'. EUREL/IEE Int. Conf. on The detection of abandoned landmines. Edinburgh, Scotland, UK, 12–14 October 1998
[67] DANIELS, D. J.: 'Surface penetrating radar image quality'. EUREL/IEE Int. Conf. on The detection of abandoned landmines, Edinburgh, Scotland, UK, 12–14 October 1998
[68] DANIELS, D. J.: 'Advances in radar techniques for mine detection'. CLAWAR '98 – Special Session on Mine clearance and mine detection vehicles, Brussels, Belgium, 26–28 November 1998
[69] DANIELS, D. J.: 'RF detection of mines'. URSI, Toronto, Canada, 13–21 Aug 1999
[70] DANIELS, D. J.: 'An overview of RF sensors for mine detection. Part 1: Radiometry; Part 2: Quadrupole resonance; Part 3: Radar'. MINE 99, Florence, 1–4 October 1999
[71] DANIELS, D. J., MARTEL, C., and PHILLIPAKIS, M.: 'Progress in GPR for mine detection'. GPR 2000, Gold Coast, Australia, 23–26 May 2000
[72] DANIELS, D. J., MARTEL, C., and PHILLIPAKIS, M.: 'Progress in ultra-wideband short range radar detection of buried mines'. EUROEM, Edinburgh, 31May-2 June 2000
[73] DANIELS, D. J.: 'Advances in ground penetrating radar technology for mine detection'. Int. Meeting on Advances in NQR detection of land mines and explosives (NQR-DLME), 8–11 June 2000, Stefan Institute, Ljubljana, Slovenia
[74] DANIELS, D. J., and MARTEL, C.: 'Radar technology for mine detection'. European Microwave Conf., London, 24–28 Sept. 2001
[75] DANIELS, D. J.: 'RF techniques for mine detection'. NATO RTO SET Symposium, Prague, 22–23 April 2002
[76] DANIELS, D. J., BROOKS, D., DITTMER, J., MITCHELL, O., and HUNT, N.: 'Wide swathe multi-channel GPR systems for mine detection'. Int. IEE Radar Conf. 2002, Edinburgh, October 2002

[77] DANIELS, D. J., and CURTIS, P.: MINETECT, SPIE 17th Annual Aerosense Symposium, 2003, Orlando, Florida, USA, 21–25 April 2003
[78] DANIELS, D. J., and CURTIS, P.: MINETECT, 2nd Int. Workshop on Advanced ground penetrating radar, Delft University of Technology, 14–16 May 2003
[79] DANIELS, D. J., and CURTIS, P.: MINETECT, EUDEM2-SCOT 2003, Brussels, 15–18 September 2003
[80] NEWNHAM, P., and DANIELS, D. J.: 'The market for advanced humanitarian mine detectors'. SPIE, Orlando, Florida, 16–21 April 2001
[81] UNITED NATIONS: International Mine Action Standards, 1997 (standard section 5, paragraph 10)
[82] SCHEERS, B.: 'Ultra-wideband ground penetrating radar, with application to the detection of anti personnel landmines'. Doctoral thesis, Université Catholique de Louvain and Royal Military Academy, Belgium, March 2001
[83] LAMBOT, S., SLOB, E. C., VAN DEN BOSCH, I., STOCKBROECKX, B., SCHEERS, B., and VANCLOOSTER, M.: 'Estimating soil dielectric properties from monostatic GPR signal inversion in the frequency domain', *Water Resour. Res.*, Accepted for publication, 2003
[84] LAMBOT, S., SLOB, E. C., VAN DEN BOSCH, I., STOCKBROECKX, B., and VANCLOOSTER, M.: 'Accurate modeling of GPR signal for an accurate characterization of the subsurface dielectric properties', *Water Resour. Res.*, Submitted, 2003
[85] VAN KEMPEN, L., SAHLI, H., NYSSEN, E., and CORNELIS, J.: 'Signal processing and pattern recognition methods for radar AP mine detection and identification'. MD'98, IEE 2nd Int. Conf. on the Detection of abandoned landmines, 12–14 October 1998, Edinburgh, UK, pp. 81–85
[86] VAN KEMPEN, L., SAHLI, H., BROOKS, J., and CORNELIS, J.: 'New results on clutter reduction and parameter estimation for landmine detection using GPR'. GPR2000, 8th Int. Conf. on Ground penetrating radar, 23–26 May, 2000, Gold Coast, Australia
[87] SIMONSON, K.: 'Statistical considerations in designing tests of mine detection systems, 1'. Sandia Report SAND98 – 1769/1, August 1998
[88] VOLES, R.: 'Confidence in trials of landmine detection systems', *Math. Today*, April 2000
[89] CARIN, L., GENG, N., McCLURE, M., SICHINA, J., and NGUYEN, L.: 'Ultra-wideband synthetic aperture radar for mine field detection', *Ultra-Wideband Short-Pulse Electromagnetics 4*, (IEEE Cat. No. 98EX112), 1998, pp. 433–441
[90] CARIN, L., SICHINA, J., and HARVEY, J. F.: 'Microwave underground propagation and detection', *IEEE Transactions on Microwave Theory and Techniques*, 2002, **50**, (3), pp. 945–952
[91] CARIN, L., GENG, N., McCLURE, M., SICHINA, J., and LAM NGUYEN: 'Ultra-wide-band synthetic-aperture radar for mine-field detection', *IEEE Antennas and Propagation Magazine*, 1999, **41**, (1), pp. 18–33

[92] CARIN, L., KAPOOR, R., and BAUM, C. E.: 'Polarimetric SAR imaging of buried landmines', *IEEE Transactions on Geoscience and Remote Sensing*, 1998, **36**, (6), pp. 1985–1988

[93] MILLER, E. L., and WILLSKY, A. S.: 'A multiscale, decision-theoretic algorithm for anomaly detection in images based upon scattered radiation'. Proceedings of ICIP-94, the IEEE International Conference on *Image Processing*, Austin, Texas, USA, 1994, **1**, pp. 845–849

[94] GADER, P. D., MYSTKOWSKI, M., and ZHAO, Y.: 'Landmine detection with ground penetrating radar using hidden Markov models', *IEEE Transactions on Geoscience and Remote Sensing*, 2001, **39**, (6), pp. 1231–1244

[95] GADER, P., KELLER, J. M., FRIGUI, H., HONGWU LIU, and DAYOU WANG: 'Landmine detection using fuzzy sets with GPR images'. Proceedings of the IEEE International Conference on *Fuzzy Systems*, Alaska, USA, 1998, **1**, pp. 232–236

[96] RAPPAPORT, C., and EL-SHENAWEE, M.: 'Modeling GPR signal degradation from random rough ground surface'. Proceedings of IGARSS 2000, the IEEE *International Geoscience and Remote Sensing Symposium*, Honolulu, Hawaii, 2000, **7**, pp. 3108–3110

[97] RAPPAPORT, C. M., and WEEDON, W. H.: 'Efficient modeling of electromagnetic characteristics of soil for FDTD ground penetrating radar simulation', *Antennas and Propagation Society International Symposium*, AP-S. Digest, 1996, **1**, pp. 620–623

[98] PETERS, L. P., Jr., DANIELS, J. J., and YOUNG, J. D.: 'Ground penetrating radar as a subsurface environmental sensing tool', Proceedings of the IEEE, 1994, **82**, (12), pp. 1802–1822

[99] YOUNG, J.: 'Radar imaging from ramp response signatures', *IEEE Transactions on Antennas and Propagation*, 1976, **24**, (3), pp. 276–282

[100] CHEN, C. C., PETERS, L., Jr., and BURNSIDE, W. D.: 'Ground penetration radar target classification via complex natural resonances', *Antennas and Propagation Society International Symposium*, AP-S. Digest, 1995, **3**, pp. 1586–1589

[101] CHEN, C. C., NAG, S., BURNSIDE, W. D., HALMAN, J. I., SHUBERT, K. A., and PETERS, L., Jr.: 'A standoff, focused-beam land mine radar', *IEEE Transactions on Geoscience and Remote Sensing*, 2000, **38**, (1), pp. 507–514

[102] CHEN, C. C., HIGGINS, M. B., and O'NEILL, K.: 'Advanced classification of buried UXO using a broadband, fully polarimetric ground penetrating radar'. Proceedings of IGARSS 2002, the IEEE *International Geoscience and Remote Sensing Symposium*, Ontario, Canada, 2002, **3**, pp. 1569–1571

[103] O'NEILL, K.: 'Discrimination of UXO in soil using broadband polarimetric GPR backscatter', *IEEE Transactions on Geoscience and Remote Sensing*, 2001, **39**, (2), pp. 356–367

[104] O'NEILL, K.: 'Broadband bistatic coherent and incoherent detection of buried objects beneath randomly rough surfaces', *IEEE Transactions on Geoscience and Remote Sensing*, 2000, **38**, (2), pp. 891–898

[105] O'NEILL, K.: 'Exploration of innovative radar sensing schemes for subsurface object detection'. Proceedings of IGARSS '97, the IEEE *International Geoscience and Remote Sensing Symposium*, Singapore, 1997, **3**, pp. 1135–1137

[106] YAROVOY, A. G., SAI, B., HERMANS, G., VAN GENDEREN, P., LIGTHART, L. P., SCHUKIN, A. D., and KAPLOUN, I. V.: 'Ground penetrating impulse radar for detection of small and shallow-buried objects', Geoscience and Remote Sensing Symposium (IGARSS '99)

[107] VAN KEMPEN, L., SAHLI, H., NYSSEN, E., and CORNELIS, J.: 'Signal processing and pattern recognition methods for radar AP mine detection and identification'. Proceedings of the IEE's Second International Conference on *Detection of abandoned land mines*, Edinburgh, Scotland, 1998, pp. 81–85

[108] BRUNZELL: 'Signal processing techniques for the detection of buried landmines using GPR'. PhD thesis, Department of Signals and Systems, Chalmers University of Technology, Goteborg, 1998

[109] MARTEL: 'Modelling and design of antennas for GPR systems'. PhD Thesis, School of Electronics, Department of Electrical Engineering, University of Surrey, October 2001

[110] BROOKS, J. W.: 'The detection of buried non-metallic anti-personnel land mines'. PhD dissertation, University of Alabama, Huntsville, USA, August 2000

[111] BENJAMIN, R., HILTON, G., NILAVALAN, R., LITOBARSKI, S., and McCUTCHEON, E.: 'Synthetically-focused surface-penetrating radar for operation from a moving vehicle'. Bristol University. 2nd Int. Conf. on the Detection of abandoned land mines, 1998. IEE Conf. Publ. 458, Oct. 1998, Edinburgh, UK, pp. 60–63

[112] ROTONDO, F., ALTSHULER, T., ROSEN, E., DION-SCHWARZ, C., and AYERS, E.: Report on the Advanced technology demonstration of the vehicular mounted mine detection systems at Aberdeen, Maryland, and Socorro, New Mexico. IDA Document D-2203, 1999

[113] BRADLEY, M., DUNCAN, M., SITTON, D., McCUMMINS, R., and WITTEN, J. R. T.: 'Mine detection with a multi-look forward-looking ground penetrating radar'. Proceedings of SPIE Aerospace conference on *Detection and remediation technologies for mines and minelike rargets*, Orlando, Florida, 2003

[114] FRITZSCHE, M.: 'The application of pattern recognition techniques to landmine detection with ground penetrating radars'. Dissertation, High Frequency Laboratory, University of Karlsruhe, 2001 (in German)

[115] CURTIS, J. O.: 'Site characterisation investigations in support of UXO technology demonstrations, Jefferson Proving Ground Indiana'. Technical Report GL-98-20, Sept. 1998

[116] KERKER, M.: 'The scattering of light and other electromagnetic radiation' (Academic Press, New York, 1969)

[117] BRUNZELL, H.: 'Detection of shallowly buried objects using impulse radar', *IEEE Trans. Geosci. Remote Sens.*, 1999, **37**, (2), pp. 875–886

[118] CAREVIC, D.: 'Clutter reduction and detection of minelike objects in ground penetrating radar data using wavelets'. SPIE Conf. Proc. on Detection and remediation technologies for mines and minelike targets, Vol. 3710, Orlando, FL, April 1999

[119] ISKANDER, D. R., ZOUBIR, A. M., and CHANT, I.: 'Time-varying spectrum based detection of landmines using ground penetrating radar. Proc. Int. GPR-Conf. 2000, Perth, Australia

[120] YU, S. H. *et al.*: 'Automatic mine detection based on multiple features'. SPIE Conf. on Detection and remediation technologies for mines and minelike targets, Vol. 4038, Orlando, FL, April 2000

[121] DANIELS, D. J.: 'Surface penetrating radar'. IEE Radar, Sonar, Navigation and Avionics Series 6, 1996

[122] SCHÜRMANN, J.: 'Pattern classification – a unified view of statistical and neural approaches' (Wiley-Interscience, New York, 1996)

[123] TITCHMARSH, E. C.: 'Conjugate trigonometrical integrals'. Proc. London Mathematical Society (Series 2), Vol. 24, 1926, pp. 109–130

[124] HOUGH, P. V. C.: 'Method and means for recognizing complex patterns'. United States Patent Office, Patent 3,069,654, 18 December 1962

[125] DAUBECHIES, I.: 'Ten lectures on wavelets'. (SIAM, 1992)

[126] STRANG, G., and NGUYEN, T.: 'Wavelets and filter banks' (Wellesley-Cambridge Press, Wellesley, 1996)

[127] STRELA, V., HELLER, P. N., STRANG, G., TOPIWALA, H., and HEIL, C.: 'The application of multiwavelet filter banks to image processing', *IEEE Trans. Image Process.*, 1999, **8**, pp. 548–563

[128] COIFMANN, R. R., and WICKERSHAUSER, M. V.: 'Entropy-based algorithms for best basis selection', *IEEE Trans. Inf. Theory*, 1992, **38**, pp. 713–718

[129] 'MACADAM trials execution report'. TME/DM/1998/3728/PH/IG. Report prepared by Thomson Detexis. To be found at http://apl-database.jrc.it.

[130] FRITZSCHE, M., and LÖHLEIN, O.: 'Sensor fusion for the detection of landmines', *J. Subsurf. Sens. Technol. Appl.*, 2000, **1**, (2), pp. 247–267

[131] DANIELS, D. J., and CURTIS, P.: MINETECT, SPIE 17th Annual AeroSense Symposium, Orlando, Florida, USA, 21–25 April 2003

[132] VAN GENDEREN, P., HAKKAART, P., VAN HEIJENOORT, J., and HERMANS, G. P.: 'A multi frequency radar for detecting landmines: design aspects and electrical performance'. Proc. 31st Eur. Microwave Conf., 2001, Vol. 2, pp. 249–252

[133] YAROVOY, A. G., SCHUKIN, A. D., KAPLOUN, I. V., and LIGTHART, L. P.: 'Polarimetric video impulse radar for landmine detection', *Subsurf. Sens. Technol. Appl.*, 2002, **3**, pp.271–293

[134] YAROVOY, A. G., VAN GENDEREN, P., and LIGTHART, L. P.: 'Ultra-wideband ground penetrating impulse radar', in P. D. SMITH and S. R. CLOUDE, (Eds).: 'Ultra-wideband, short-pulse electromagnetics 5', (Kluwer Academic) pp. 183–189

[135] DE JONGH, R. V., YAROVOY, A. G., LIGTHART, L. P., KAPLOUN, I. V., and SCHUKIN, A. D.: 'Design and analysis of new GPR antenna concepts'. Proc. 7th Int. Conf. on Ground penetrating radar, 27–30 May 1998, University of Kansas, Lawrence, Kansas, USA, Vol. 1, pp. 81–86

[136] YAROVOY, A. G., SCHUKIN, A. D., KAPLOUN, I. V., and LIGTHART, L. P.: 'The dielectric wedge antenna', *IEEE Trans. Antennas Propag.*, 2002, **50**, (10), pp. 1460–1472

[137] LESTARI, A. A., YAROVOY, A. G., and LIGTHART, L. P.: 'Improvement of bow-tie antennas for pulse radiation'. IEEE Antennas & Propagation Society Int. Symposium, 2002 Digest, San Antonio, Texas, 16–21 June 2002, Vol. 4, pp. 566–569

[138] NICOLAESCU, I., VAN GENDEREN, P., and ZIJDERVELD, J.: 'Archimedean spiral antenna used for stepped frequency radar-footprint measurements'. Proc. AMTA2002, Cleveland, Ohio, USA, 2002, pp. 555–560

[139] YAROVOY, A. G., SCHUKIN, A. D., KAPLOUN, I. V., and LIGTHART, L. P.: 'Adaptive bow-tie antenna with variable current distribution'. IEEE Antennas & Propagation Society International Symposium, 2002 Digest, San Antonio, Texas, 16–21 June 2002, Vol. 2, pp. 516–519

[140] YAROVOY, A. G., AUBRY, P. J., and LIGTHART, L. P.: 'GPR antenna measurements in time domain'. Conf. Proc. on CD-ROM, EUREL Millennium Conference on Antennas & Propagation, Davos, Switzerland, 9–14 April 2000, pp. 1–4

[141] REMIS, R. F., BUDKO, N. V., and VAN DEN BERG, P. M.: 'Numerical modeling of ground penetrating radar. Part 1: Reduced-order forward modeling'. Proc. Int. Conf. on Electromagnetics in advanced applications (ICEAA 99), Torino, Italy, 1999, pp. 75–78

[142] GROENENBOOM, J., and YAROVOY, A. G.: 'Data processing and imaging in GPR system dedicated for landmine detection', *Subsurf. Sens. Technol. Appl.*, 2002, **3**, (4), pp.387–402

[143] BUDKO, N. V., REMIS, R. F., and VAN DEN BERG, P. M.: 'Numerical modeling of ground penetrating radar. Part 2: Imaging and effective inversion'. Proc. Int. Conf. on Electromagnetics in advanced applications (ICEAA 99), Torino, Italy, 1999, pp. 79–82

[144] VAN DER LIJN, F., ROTH, F., and VERHAEGEN, M.: 'Estimating the impulse response of buried objects from ground penetrating radar signals'. Proc. Detection and remediation technologies for mines and minelike targets VIII, 21–25 April, 2003, Orlando, FL, USA, to be published

[145] ULABY, F. T., MOORE, R. K., and FUNG, A. K.: 'Microwave remote sensing, Vol. II' (Artech House, 1982)

[146] ALLEN, C. T., SHI, K., and PLUMB, R. G.: 'The use of ground-penetrating radar with a cooperative target', *IEEE Trans. Geosci. Remote Sens.*, 1998, **36** pp. 1821–1825

[147] LJUNG, L.: 'System identification: theory for the user' (Prentice-Hall, Englewood Cliffs, NJ, 1987)

[148] VITEBSKIY, S., and CARIN, L.: 'Resonances of perfectly conducting wires and bodies of revolution buried in a lossy dispersive half-space', *IEEE Trans. Antennas Propag.*, 1996, **44**, pp. 1576–1583
[149] VITEBSKIY, S., CARIN, L., RESSLER, M. A., and LE, F. H.: 'Ultra-wideband, short-pulse ground-penetrating radar: Simulation and measurement', *IEEE Trans. Geosci. Remote Sens.*, 1997, **35**, pp. 762–772
[150] BAUM, C. E.: 'On the singularity expansion method for solution of electromagnetic interaction problems'. MP Note Series, EMP Interaction Note 88, Air Force Weapons Lab., Kirtland AFB, Albuquerque, NM, USA, December 1971
[151] BAUM, C., ROTHWELL, E., and NYQUIST, D. P.: 'The singularity expansion method and its application to target identification', *Proc. IEEE*, 1991, **79**, pp. 1481–1491
[152] VECHINSKI, S. R., and SHUMPERT, T. H.: 'Natural resonances of conducting bodies of revolution', *IEEE Trans. Antennas Propag.*, 1990, **38**, pp. 1133–1136
[153] HSIA, T. C.: 'System identification' (Lexington Books, Lexington, MA, 1976)
[154] GOLUB, G. H., and LOAN, C. F. V.: 'Matrix computations' (Johns Hopkins University Press, Baltimore, 1996, 3rd edn)
[155] STEIGLITZ, K., and McBRIDE, L. E.: 'A technique for the identification of linear systems', *IEEE Trans. Autom. Control*, 1965, **AC-10**, pp. 461–464
[156] SWAMI, A., and MENDEL, J. M.: 'Identifiability of the AR parameters of an ARMA process using cumulants', *IEEE Trans. Autom. Control*, 1992, **37**, pp. 268–273
[157] HAYKIN, S.: 'Adaptive filter theory' (Prentice-Hall, Englewood Cliffs, NJ, 1996, 3rd edn)
[158] FARHANG-BOROUJENY, B.: 'Adaptive filters: theory and applications' (John Wiley & Sons, Inc., New York, 1998)
[159] VAN KEMPEN, L., SAHLI, H., NYSSEN, E., and CORNELIS, J.: 'Signal processing and pattern recognition methods for radar AP mine detection and identification'. MD'98: IEE EUREL 2nd Int. Conf. on the Detection of abandoned landmines, Edinburgh, UK, October 1998, pp. 81–85
[160] VAN KEMPEN, L., NYSSEN, E., SAHLI, H., and CORNELIS, J.: 'Pattern recognition experiments for ultra-sonic and radar AP-mine detection'. Proc. SusDem conference on Sustainable humanitarian demining: trends, techniques & technologies, Croatia, 1997, pp. 297–304

12.11 Bibliography

ALLEN, C. T., SHI, K., and PLUMB, R. G.: 'The use of ground-penetrating radar with a cooperative target', *IEEE Trans. Geosci. Remote Sens.*, 1998, **36**, pp. 1821–1825
ASTANIN, L. Y., GREPPENER, V. V. *et al.*: 'Ultrawideband ground probing radar signal processing methods'. Proc. Image and multidimensional digital signal processing '98, Alpbach, Austria, July 1998, pp. 259–261

BAUM, C. E.: 'On the singularity expansion method for solution of electromagnetic interaction problems'. MP Note Series, EMP Interaction Note 88, Air Force Weapons Lab., Kirtland AFB, Albuquerque, NM, USA, December 1971

BAUM, C., ROTHWELL, E., and NYQUIST, D. P.: 'The singularity expansion method and its application to target identification', *Proc. IEEE*, 1991, **79**, pp. 1481–1491

BOURGEOIS, J. M., SMITH, G. S.: 'A complete electromagnetic simulation of the separated-aperture sensor for detecting buried land mines', *IEEE Trans. Antennas Propag.*, 1998, **46**, (10), pp. 1419–1426

BUDKO, N. V., REMIS, R. F., and VAN DEN BERG, P. M.: 'Numerical modeling of ground penetrating radar. Part 2: Imaging and effective inversion'. Proc. Int. Conf. on Electromagnetics in advanced applications (ICEAA 99), Torino, Italy, 1999, pp. 79–82

CARIN, L., FELSEN, L., (Eds.): 'Ultra-wideband short pulse electromagnetics'. Proc. 2nd Int. Conf., Brooklyn, USA, April 1994, pp. 125–131

CHANT, I. J., and RYE, A.R.: 'Overview of current radar land mine detection research at the Defence Science and Technology Organisation, Salisbury, South Australia'. EUREL Int. Conf. on the Detection of abandoned land mines: a humanitarian imperative seeking a technical solution. Conf. Publ. 431, 7–9 Oct. 1996, pp. 138–142

DANIELS, D. J.: 'Surface penetrating radar image quality'. EUREL/IEE Int. Conf. on Detection of abandoned landmines, Edinburgh, Scotland, UK, 12–14 October 1998

DANIELS, D. J.: 'Multi-sensor radar techniques for mine detection'. IEEE CESA '98, Tunisia, 1–4 April 1998

DANIELS, D. J.: 'Detection of ground probing radar target images in clutter'. EUREL/IEE Meeting on Radar and sonar signal processing, Peebles, Scotland, UK, 5–8 July 1998

DANIELS, D. J.: 'Ground probing radar techniques for mine detection'. GPR '98, Kansas, USA, 26–30 May 1998, 05-14

DANIELS, D. J.: 'High resolution radar detection of buried anti-personnel mines for humanitarian clearing operations'. ISMCR '96, Brussels, Belgium, 9–11 May 1996

DANIELS, D. J.: 'Radar techniques for mine detection'. SUSDEM '97, Zagreb, 29 Sep.–1 Oct. 1997

DANIELS, D. J.: 'Resolution of ultrawideband signals', *IEE Proc., Radar Sonar Navig.*, 1999, **146**, (4), pp. 189–194

DANIELS, D. J.: 'Ultra-wideband detection of buried objects'. IEEE IGARSS Proc., Singapore, 3–8 August 1997, pp. 1278–1281

DE JONGH, R. V., YAROVOY, A. G., LIGTHART, L. P., KAPLOUN, I. V., and SCHUKIN, A. D.: 'Design and analysis of new GPR antenna concepts'. Proc. 7th Int. Conf. on Ground penetrating radar, 27–30 May 1998, University of Kansas, Lawrence, Kansas, USA, Vol. 1, pp. 81–86

DUVOISIN, H. A., STEINWAY, W. J. *et al.*: 'Multi-sensor system for mine detection'. Proc. Conf. on Infrared technology and applications, San Diego, USA, July 1998, pp. 705–715

EARP, S. L., HUGHES, E. S.: 'Ultra wideband ground penetrating radar for the detection of buried metallic mines', *IEEE Aerosp. Electron. Sys. Mag.*, 1996, **11**, (9), pp. 30–34

EARP, S. L., HUGHES, E. S. *et al.*: 'Ultra-wideband ground penetrating radar for the detection of buried metallic mines'. Proc. IEEE National Radar Conf., Ann Arbor, USA, May 1996, pp. 7–12

FARHANG-BOROUJENY, B.: 'Adaptive filters: theory and applications' (John Wiley & Sons, Inc., New York 1998)

GOLUB, G. H., and LOAN, C. F. V.: 'Matrix computations' (Johns Hopkins University Press, Baltimore, 3rd ed., 1996)

GROENENBOOM, J., and YAROVOY, A. G.: 'Data processing and imaging in GPR system dedicated for landmine detection', *Subsurf. Sens. Technol. Appl.*, 2002, **3**, (4), pp.387–402

HAYKIN, S.: 'Adaptive filter theory' (Prentice-Hall, Englewood Cliffs, NJ, 3rd ed., 1996)

HSIA, T. C.: 'System identification' (Lexington Books, Lexington, MA, 1976)

LESTARI, A. A., YAROVOY, A. G., and LIGTHART, L. P.: 'Improvement of bow-tie antennas for pulse radiation'. IEEE Antennas & Propagation Society International Symposium, 2002 Digest, San Antonio, Texas, 16–21 June 2002, Vol. 4, pp. 566–569

LJUNG, L.: 'System identification: theory for the user' (Prentice-Hall, Englewood Cliffs, NJ, 1987)

MONTOYS, T. P., and SMITH, G. S.: 'VEE dipoles with resistive loading for short pulse ground penetrating radar', *Microw. Opt. Technol. Lett.*, 1996, **13**, (3), pp. 132–137

NICOLAESCU, I., VAN GENDEREN, P., and ZIJDERVELD, J.: 'Archimedean spiral antenna used for stepped frequency radar-footprint measurements'. Proc. AMTA2002, Cleveland, Ohio, USA, 2002, pp. 555–560

NOON, D., STICKLEY, G. F.: 'Antenna ring-down, range sidelobes and quality factor of time and frequency domain GPR systems'. Proc. 7th Int. Conf. on Ground penetrating radar, Kansas USA, 27–30 May 1998

REMIS, R. F., BUDKO, N. V., and VAN DEN BERG, P. M.: 'Numerical modeling of ground penetrating radar. Part 1: Reduced-order forward modeling'. Proc. Int. Conf. on Electromagnetics in advanced applications (ICEAA 99), Torino, Italy, 1999, pp. 75–78

SCHEERS, B.: 'Ground penetrating radar for anti-personnel mine detection', *Rev. HF*, 1998, Part 3, pp. 25–33

SIMONSON, K. M.: 'Statistical considerations in designing tests of mine detection systems'. SANDIA report SAND98-1769/1

STEIGLITZ, K., and McBRIDE, L. E.: 'A technique for the identification of linear systems,' *IEEE Trans. Autom. Control*, 1965, **AC-10**, pp. 461–464

STEINWAY, W. J., DUVOISIN, H. A., TOMASSI, M. S. *et al.*: 'Multi-sensor system for mine detection'. Proc. IGAAS '98, Seattle, USA, 1998, Vol.1, pp. 228–233

SWAMI, A., and MENDEL, J. M.: 'Identifiability of the AR parameters of an ARMA process using cumulants,' *IEEE Trans. Autom. Control*, 1992, **37**, pp. 268–273

ULABY, F. T., MOORE, R. K., and FUNG, A. K.: 'Microwave remote sensing, Vol. II' (Artech House, 1982)

VAN DER LIJN, F., ROTH, F., and VERHAEGEN, M.: 'Estimating the impulse response of buried objects from ground penetrating radar signals'. Proc. Detection and remediation technologies for mines and minelike targets VIII, 21–25 April 2003, Orlando, FL, USA, to be published

VAN GENDEREN, P., HAKKAART, P., VAN HEIJENOORT, J., and HERMANS, G. P.: 'A multi frequency radar for detecting landmines: design aspects and electrical performance'. Proc. 31st Eur. Microwave Conf., 2001, Vol. 2, pp. 249–252

VAN KEMPEN, L., NYSSEN, E., SAHLI, H., and CORNELIS, J.: 'Pattern recognition experiments for ultrasonic and radar AP-mine detection'. Sustainable humanitarian demining: trends, techniques & technologies, 1999, pp. 297–304

VAN KEMPEN, L., SAHLI, H., NYSSEN, E., and CORNELIS, J.: 'Signal processing and pattern recognition methods for radar AP mine detection and identification'. MD'98: IEE EUREL Second Int. Conf. on the Detection of abandoned landmines, Edinburgh, UK, October 1998, pp. 81–85

VECHINSKI, S. R., and SHUMPERT, T. H.: 'Natural resonances of conducting bodies of revolution', *IEEE Trans. Antennas Propag.*, 1990, **38**, pp. 1133–1136

VITEBSKIY, S., and CARIN, L.: 'Resonances of perfectly conducting wires and bodies of revolution buried in a lossy dispersive half-space', *IEEE Trans. Antennas Propag.*, 1996, **44**, pp. 1576–1583

VITEBSKIY, S., CARIN, L. *et al.*: 'Ultra-wideband, short-pulse ground-penetrating radar: simulation and measurement', *IEEE Trans. Geosci. Remote Sens.*, 1997, **35**, (3), pp. 762–72

VITEBSKIY, S., CARIN, L., RESSLER, M. A., and LE, F. H.: 'Ultra-wideband, short-pulse ground-penetrating radar: simulation and measurement', *IEEE Trans. Geosci. Remote Sens.*, 1997, **35**, pp. 762–772

YAROVOY, A. G., SCHUKIN, A. D., KAPLOUN, I. V., and LIGTHART, L. P.: 'Polarimetric video impulse radar for landmine detection', *Subsurf. Sens. Technol. Appl.*, 2002, **3**, pp.271–293

YAROVOY, A. G., VAN GENDEREN, P., and LIGTHART, L. P.: 'Ultra-wideband ground penetraing impulse radar', in P. D. Smith and S. R. Cloude (Eds): 'Ultra-wideband, short-pulse electromagnetics 5', (Kluwer Academic) pp. 183–189

YAROVOY, A. G., AUBRY, P. J., and LIGTHART, L. P.: 'GPR antenna measurements in time domain'. Conf. Proc. on CD-ROM, Millennium Conf. on Antennas & Propagation, Davos, Switzerland, 9–14 April 2000, pp. 1–4

YAROVOY, A. G., SCHUKIN, A. D., KAPLOUN, I. V., and LIGTHART, L. P.: 'Adaptive bow-tie antenna with variable current distribution'. IEEE Antennas & Propagation Society International Symposium, 2002 Digest, San Antonio, Texas, 16–21 June, 2002, Vol. 2, pp. 516–519

YAROVOY, A. G., SCHUKIN, A. D., KAPLOUN, I. V., and LIGTHART, L. P.: 'The dielectric wedge antenna', *IEEE Trans. Antennas Propag.*, 2002, **50**, (10), pp. 1460–1472

Chapter 13

Utilities

13.1 Introduction

Many attempts have been made to develop cost-effective GPR for utility detection. The goal of most of the commissioning organisations is to map all the buried utilities and structures to enable rapid installation of new plant with the minimum disruption and damage to existing plant. All of the utilities – gas, water, sewage, electricity, telephone, cable, etc. – need to co-exist and avoid collateral damage. The effects and costs of damage, the costs of restitution, insurance and local legislation all provide powerful incentives to improve underground mapping and enable trenchless installation. Organisations such as GRI and EPRI in the United States, the utility companies in Japan, UK, Germany, France, etc., have all invested heavily in development.

While there has been gradual market penetration of GPR technology, several factors have limited its acceptance. The first and most important is that the soil attenuation in particular soils, in any country, limits the potential areas of use. In regions where there is heavy clay then GPR does not work. This means realistically that only 60–70% of the total land area may be suitable for GPR surveying. In the UK, London is built on significantly large regions of heavy clay and GPR often struggles to detect buried targets. The second factor concerns the density of utility plant in major urban areas. Where there is the usual interwoven 'spaghetti' of pipes, cables, etc. it is difficult to clearly image the situation. This is just where such clarity is needed. The third factor is the cost per square metre of providing accurate and well registered, three-dimensional maps. The cost of the final product (the map) is still high.

Although significant funding has been made into GPR development for utility operation there is still no easy way of overcoming basic physics. A brief view around the websites of those organisations developing and manufacturing GPR survey equipment for utilities would lead the reader to believe that GPR has solved the end-user problems. Their marketing departments have invented new acronyms, claimed performances that really are not achievable on a consistent basis and are still generally

Table 13.1 Performance table

Soil type (measured in mid-winter)	Maximum depth for 25 mm plastic pipe	Maximum depth for 25 mm metal pipe	Maximum depth for 300 mm plastic pipe	Maximum depth for 300 mm plastic pipe
Sandy soil				
Loamy soil				
Sand/shingle				
Heavy clay				

overstating the potential for GPR. The reality is that all the claims should be backed up by quantified evidence in terms of what percentage of plant was detected in what percentage of the land area. From a practical view, one might suspect that this was in the region of 60% of all plant in 60% of a country's land area (the 60/60 performance). The end-user should request the suppliers of equipment or services to complete a table similar to Table 13.1 with a confidence level of 95% (established by ground truth).

The suppliers of equipment or services should also be able to define the accuracy of location both vertically and laterally as well as the resolution between pipes/cables.

There are several organisations that specialise in the information relating to advanced surveying techniques (which include GPR). One of these is The International Society For Trenchless Technology (ISTT), which was established in 1986 with the following objectives:

- to advance the science and practice of Trenchless Technology for the public benefit, and
- to promote education, training, study and research in that science and practice.

The ISTT website is found at http://www.istt.com/.

The reader may also find a wealth of information at the Civil Engineering Coolsites at http://zerlina.emeraldinsight.com/vl=4543569/cl=26/nw=1/rpsv/abstracts/icea/coolsites/ge_reviews.htm.

This Chapter contains most of the material of the first edition, but with the addition of information on the currently active specialists in GPR for utilities. The standard GPR systems have not been included as most of the material is readily available on company websites. General information on GPR techniques is given by Daniels [1–7] and approaches using neural networks are described by Costamagna *et al.* [8], Ciochetto *et al.* [9] and Gamba *et al.* [10, 11].

13.2 Technology

13.2.1 Pipes and cables

Howard F. Scott
British Gas Research and Technology, UK

The very first system specifically developed for pipe detection was the Terrascan system designed by Microwaves Associates and Ohio State University in the 1970s. The system showed some promise and the then British Gas (now Transco) started a development programme to build a plastic pipe locator with a target 90/90 performance.

The Engineering Research Station of British Gas pursued the development of its prototype to the stage where six pre-production units were manufactured.

The best performance from a surface-penetrating radar system, particularly one for the detection at high resolution of shallow objects, is obtained when the whole of the system is designed around a specific target type or geometry.

The detection of utilities' plant imposes a particular set of constraints on the design of an effective surface-penetrating radar system. The majority of buried plant is within 1.5 to 2 m of the ground surface, but it may have a wide variation in its size, may be metallic or nonmetallic, may be in close proximity to other plant and may be buried in a wide range of soil types involving large differences in electromagnetic absorption. As a result, obtaining adequate penetration of the emitted radiation coupled with good resolution of neighbouring plant is not straightforward, and some compromise has to be accepted in the design. The particular feature of utilities' plant which may be used to advantage in the design of a radar detection system is that almost all the objects sought are long and thin, which results in a particular action on the polarisation of a reflected wave. This feature has been used in the design of the British Gas pipe locating radar, to be described in more detail below.

Ground penetrating radar equipment, being an emitter of radio signals, is subject to licensing and control in the country of use. An additional requirement, therefore, is that any equipment used must comply with the legal requirements locally in force, which in the UK are set by the Department of Trade and Industry. It is also essential that the radiation levels are below the relevant safety thresholds.

A pipe location system should have the ability to detect and map all classes of buried pipes and cables. Although not essential, the further attribute of being able to detect other sub-surface features such as voids and ground obstructions (concrete, etc.) would be an advantage.

The ability to detect all buried plant down to a depth of 1.5 m is desirable. If this could be achieved, then approximately 90% of all buried plant could be located under all conditions. In practice, there is an approximate relationship between pipe diameter and burial depth; for example, 25 mm PE gas service pipes are not often laid deeper than 500 mm cover, while plant laid at more than 1 m cover is predominantly of diameter 125 mm or greater. Consequently, the penetration characteristics of a practical pipe and cable locator must be consistent with the observed depth distribution of diameters.

All plant location equipment is limited in its ability to resolve closely spaced objects. For example, the horizontal resolution of conventional inductive locators is usually expressed as a function of burial depth: they can resolve adjacent plant when their spacing, in the horizontal plane, is approximately the same as their depth. A desirable resolution is the ability to distinguish multiple buried plant as separate targets when they are spaced more than 150 mm apart, in either depth or plan.

In the British Gas radar system equipment, the antennas are planar logarithmic spirals, interleaved so as to be electrically orthogonal. The impulse is approximately 1 ns in duration and the antenna output is in the frequency range 200 to 1000 MHz. The use of a planar spiral antenna has three principal advantages. First, very broadband transmission is possible so that there is no need to select different antennas for different circumstances. Second, the emitted radiation is circularly polarised so that a pipe will be detected at whatever horizontal angle it may lie relative to the antenna. Third, a planar design means that it may be positioned close to the ground surface while still maintaining mobility for rapid surveying.

A rotating antenna system has been found to give a significant reduction in levels of ground clutter and noise, when the received signals are suitably processed. Data are collected during each half or full rotation of the antenna as the trolley on which it is mounted is moved forward over the ground. Each set of data, after processing, is stored along with an indication of the position along the surveyed line to which it corresponds. The position is provided by a shaft encoder attached to one of the trolley wheels.

The radar system consists of two main parts. There is a mobile trolley (Figure 13.1) and a base station, which resides in the support vehicle shown in Figure 13.2. The two

Figure 13.1 Radar head (courtesy British Gas)

Figure 13.2 Radar base unit (courtesy British Gas)

are connected by an umbilical cable to provide power and to transfer data. Primary power is supplied by a portable petrol generator of approximately 1 kW capacity. The trolley contains the impulse generator, which is connected through a rotating microwave joint to the transmitting antenna. Together with the receiving antenna, this is contained in a cylindrical drum rotated by a drive motor. The received signal is transferred to an amplifier and sampling receiver, which delivers data, digitised to 16 bits, to a real-time digital signal processor unit. Processed data are taken by the umbilical link to the base station for storage. The link also provides power to the antenna drive motor and to a voltage converter unit which supplies the electronic modules. Mechanically, the trolley chassis plate is mounted on a plastic suspension frame with leaf spring and wishbone damping supported by four plastic and rubber wheels. To one of these wheels is attached a shaft encoder linked to the processor unit by optical fibres. There is a GRP cover, in the top of which is fitted a back-lit LCD to provide essential information to the operator.

The base station is a custom-built computer unit using a versatile modular system of construction. It contains a hard disk for data storage, a 68020 microprocessor with a floating point co-processor, a framestore to drive the VDU and a tape streamer for archiving. Information may be input via a keyboard, but operation is otherwise controlled by a mouse or by a touch screen. The base station also contains ac to dc power converters for the whole system.

The radar emissions are in the frequency range 200 to 1000 MHz, at a mean power of 10 mW. The transmitter has been type-approved by the UK Department of Trade and Industry, and it is operated under a telemetry licence.

Maximum benefit is obtained from a survey of buried plant when the output is available in the form of a map. To that end, the area to be surveyed is scanned by moving the equipment over a grid with a rectangular boundary, with each stored data item being logged with the co-ordinates of the point where it was collected. By means of trigger signals from the encoder attached to one of the trolley wheels, data are collected every 0.1 m of linear travel as the trolley is propelled along a straight line, usually defined by a stretched cord near the ground surface.

The present umbilical cable allows lines up to 100 m in length to be surveyed. The spacing between adjacent lines of the grid is determined according to the circumstances of the work to be performed and is affected by any prior knowledge of the plant contained in the area under investigation. An extreme case is when the lines are set at 0.1-m spacing to give a square grid. It is often convenient to sub-divide large areas into a number of smaller ones for survey purposes.

Speed of survey is normally set at one linear metre per second, or an area rate (not allowing for turn-around time) of 6 m^2 per minute at the maximum data density; an increase in data quality can be achieved with a reduction to 0.5 ms^{-1}. The data can be stored in the base station at the same rate as they are collected and are available for viewing in a pseudo-colour representation once the survey of a grid has been completed.

At the beginning of a survey the operator enters at the base station a range of parameters, such as grid size and location, as well as notes relating to ground conditions and weather. During the data collection stage the base station performs the data storage with no operator intervention, but at the end of the survey the results are available for examination on a VDU in a range of formats, and some image processing techniques may be applied if necessary to aid interpretation. Data may be archived onto magnetic tape for attention at a later time if required. The data on tape, or a derivative of it, would be suitable as an input to the British Gas digital records system once the interface software has been developed.

It is usual to have two operators working a site, with the equipment transported in, and operated from, an estate car. Beside the operation of the radar equipment it is necessary to perform some basic land surveying to establish the grid position in relation to the site as a whole and to record this on a map or plan. A simple CAD package is used to generate such plans.

13.2.1.1 Presentation of results: After performing a grid survey, the data stored in the computer is in the form of a three-dimensional block. To examine this block, for indications of linear targets, it is possible to section it in either vertical or horizontal planes. The data contained within one plane are, normally, represented in pseudo-colour, that is, different colour, or shade of colour, and assigned to a data point depending upon the numerical value.

An example of a field trial result is shown in Figure 13.3. This is a horizontal section of a survey of part of a test site. At a depth corresponding to this section, there are visible five items of plant. Other items are apparent at other depths. All items of plant detected in the survey were later confirmed as those known to be present in the test area. The soil was light clay, covered with loam.

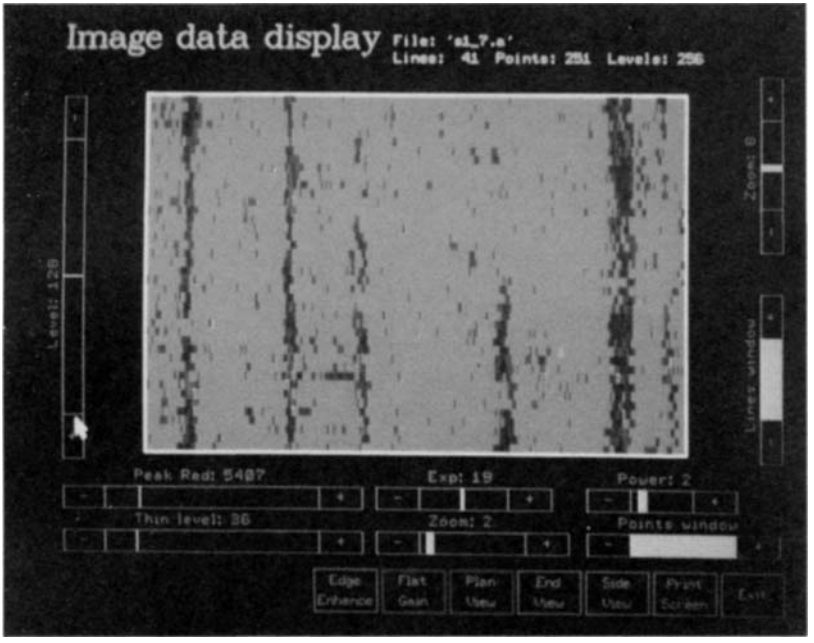

Figure 13.3 Radar image of buried pipes (courtesy British Gas)

13.2.2 PipeHawk

Dr Richard Chignell

PipeHawk plc is a UK based company that focuses its commercial operations upon the use of its PipeHawk radar systems for the detection and mapping of underground utilities.

The PipeHawk product was initially developed by the EMRAD Company, which was founded by Dr Richard Chignell. EMRAD was awarded development funding from NYGAS, a consortium of New York Gas companies. The objective of the consortium was to improve the efficiency of their operations.

The first system developed by EMRAD was the PipeHawk I system, which incorporated a GPR system using crossed dipole antennas and an on-board data processing capability into rugged and purpose built housing for utility use. The production company for PipeHawk I considered that market penetration for the first generation system was slow, due to the purchase price of £38 000, and set about developing a second generation system to sell at £25 000. Following extensive development and significant re-engineering, the PipeHawk II (Figure 13.4) is now available and is specifically designed for utility applications. Following reorganisation of the company, EMRAD is now the Technology Division of PipeHawk plc (Chairman, Gordon Watt).

From its inception, the design of the PipeHawk system was targeted upon the nonspecialist radar operator, typically the foreman in a utility company or a backhoe operator. This required a distinct approach to GPR system design. Little reliance may

Figure 13.4 PipeHawk II utility detection GPR system (courtesy PipeHawk plc)

be placed upon the skill of the operator, and the system must be highly tolerant of variations in ground conditions. This leads to much sophistication, most of which is hidden.

For example, it is not considered to be acceptable that the operator should be required to change antennas. Casual operators may not have the experience to select a narrowband antenna and are also intolerant of the need to transport several antennas. The bandwidth of the PipeHawk antenna is specified to extend from 150 MHz to 1 GHz, which with a suitable pulse generator allows the highest frequency allowed by the lowpass filter characteristics of the ground to be used for target detection.

Two main antenna options are provided with PipeHawk: co-polar and cross-polar models. The polarisation properties of pipe like targets implies that the co-polar model achieve the deeper ground-penetration in more difficult soils while the cross-polar model provides greater resolution at shallower depths. The cross-polar antenna typically allows shallow extensive telecommunications networks to be resolved. Often operators prefer the co-polar option because if they can map the sewer at great depth they have confidence that all the other services generally at shallower depths have been found.

The PipeHawk antenna is used in contact with the ground and the sacrificial wear membrane protects the outer skin. The membrane has a life of a few weeks, for harsh environments such as the ballast of railbeds, to many months in paved streets. The antenna is mounted on a robust plastic cart with large-diameter wheels. An optical

shaft encoder is employed to automatically trigger the radar at regular measurement intervals, and also allows the radar to be repositioned over the target after detection. The unit is totally self-contained with no trailing cables. This allows the radar to be used in busy street environments, frequently without any need for the management of pedestrian traffic.

The PipeHawk User Interface consists of a large LCD colour display with seven soft keys, with one intuitive menu structure. Essentially two software options may be provided reflecting the different needs for detailed pipe mapping and mark out requirements. The latter may be most appropriate in a less dense pipe environment.

In the mark out mode the operator may make long scans. The data are displayed in a B-scan format. Signal pre-processing enhances the visibility of the hyperbolae generated from pipes, and the operator notes their position as detections. The operator may then reverse the radar to the pipe positions and mark their positions with environmentally friendly paint. By marking out a series of scans in this way the line of a pipe on the ground may be defined. Generally in mark out mode neither the position of the scans nor the radar data is retained; reliance is made upon the operator's marks.

Much more extensive software is provided for the mapping mode. The method of operation is also different. The operator should establish a convenient base line for the area to be scanned. This is often a kerb line. A series of ideally seven (minimum three) parallel scans are then made over the area of interest. The separation of the scans is typically 0.5 m, so that seven scans cover a width of 3 m. The analysis of the scans also takes place in 3 m lengths so that the output data may be treated as 3 m square 'tiles' over the area of interest.

Normally the operator will collect all the data as rapidly as possible. They are stored on a large hard disc. The data may either be analysed in the street or returned to an office for processing. The full sequence of processing and map generation is normally completed on site in a support vehicle, to ensure all the data of the required integrity have been captured. Additional processing takes place in the office for quality assurance purposes.

The map processing takes a set of scans and individually processes them. The sequence of algorithms applied includes an adaptive migration process which, having calibrated the scan for dielectric constant, carries out a migration to focus the hyperbolae to a point-like target (a fuzzy bright spot). It also generates a depth scale.

This process is automatically carried out for every scan and the scans are then automatically combined to give C-scans. A widowing function allows, for example, a shallower telecommunications or lighting cable to be seen in a different depth slice than a sewer.

The system operates from a 24 V 9.5 Ah lead acid battery, which is mounted near the balance point between the wheels. Normally two batteries ensure a full day's operation. Facilities are provided to download data from the machine by peer to peer PC transfer.

Further details of the PipeHawk II system may be found on the website at http://www.PipeHawk.com/home.htm.

13.3 Array based utility mapping

Witten Technologies

Cart Imaging System Computer assisted radar tomography, Witten Technologies Inc., 295 Huntington Ave, Boston, MA, USA. 02115 617 236 0019, www.Wittentech.com; Info@Wittentech.com

Four organisations have grouped together to develop an array based GPR survey system. These are *Malå Geoscience*, *EPRI*, *GTI* and *Schlumberger*. The system is quoted directly as being Gp*i*R,

> 'which stands for **G**round-**P**enetrating **i**maging **R**adar. GP*i*R is a standard term for GPR surveys (or systems) that combine efficient radar surveying with precise positioning control and advanced signal processing that allows the creation of high-resolution radar images of the subsurface on a large scale. By "large-scale" and "high-resolution", we mean surveys covering thousands of square meters with a resolution of centimetres. Such images take on the quality of satellite radar images. In fact, in many ways, GP*i*R has more in common with (a scaled-down version of) satellite radar or 3D seismic imaging than with standard GPR profiling.'

Further details can be found on the Wittentech website at http://www.wittentech.com/technical_GPiR.html.

A hidden toll of the collapse of the World Trade Center on 11 September 2001 was extensive damage to the underground utility network that supports lower Manhattan. Sponsored by a grant from the Swedish government, a project using radar tomography to map below streets near ground zero has been under way since December 2001 to help with reconstruction of the network (Figure 13.5). In less than two months, a continuous 3D radar image down to a depth of about 6 feet was created beneath 320 000 square feet of lower Manhattan with the *CART Imaging System**, a new type of ground-penetrating *imaging* radar that uses an array of antennas to dramatically increase the density and efficiency of underground coverage. Figure 13.6*a* shows horizontal slices through the radar image at depths of 24 and 42 in (610 and 1067 mm) below street level near the southwest corner of the Trade Center quadrangle (see Figure 13.5). Numerous underground features, including gas, electrical, sewer and water services, are clearly visible in these two high-resolution image slices, which cover roughly 10 000 square feet with a pixel size of about 3 in. (Slices are created at 1-in depth increments in the full image.) The images are being used to help locate underground facilities not clearly shown on maps, to provide 'ground truth' to design engineers planning new installations, and to reduce the number of test pits needed to validate designs. The project is being done in collaboration with City of New York Department of Design and Construction, ConEdison and the Urban Utility Center of Polytechnic University. NASA Jet Propulsion Laboratory (CalTech) is helping with analysis of the underground images.

* Mark of Witten Technologies, Inc. Radar components by Malå Geoscience AB.

Figure 13.5 Underground radar tomography at ground zero

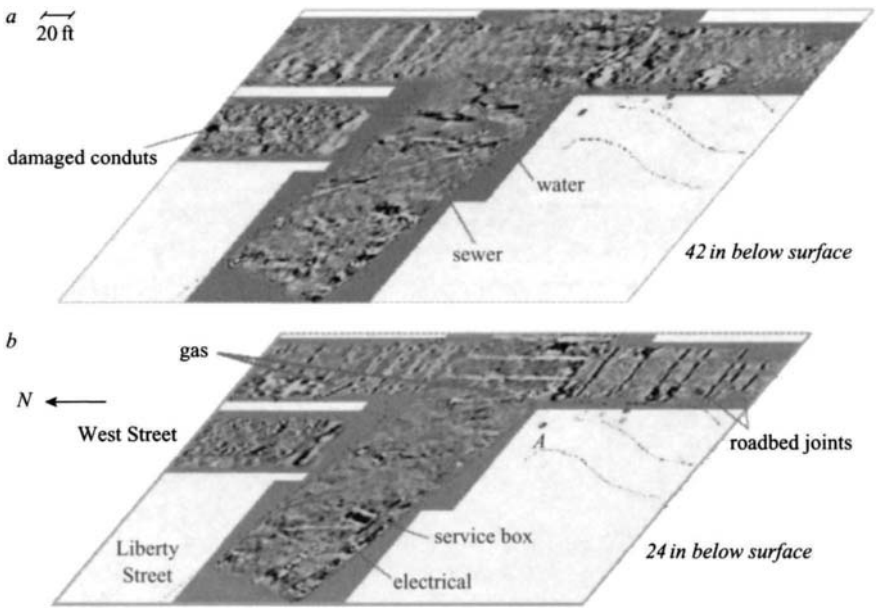

Figure 13.6 Radar images of West Street and Liberty Street New York taken after September 11

13.4 Case histories

13.4.1 Drainage of a football pitch
Dr Jon Dittmer

A football club had been having problems with old drainage inspection chambers opening up during games – a situation which clearly had the potential to lead to severe injury to a player. A radar survey was carried out to determine whether any more inspection chambers or voids were present (Figure 13.7). No plans of the drainage existed so, in order to locate any likely targets, a full survey of the field was required. It became apparent that the easiest way to locate the chambers was to map the drains, the thinking being that the inspection chambers would occur at the junctions.

The economics of the survey meant that the whole area needed to be surveyed in a single day, and results produced in real time. This was achieved by surveying the field systematically, by traversing up and down the pitch on lines approximately 0.5 m apart. When a service or target was encountered, a flag was placed in the ground. All the data were recorded for further processing if that was required. After some 600 flags had been placed, obvious drain lines were marked with boundary tape, and most of the flags recovered for further use. During the day over 10 km of data were collected.

The archived data were re-examined at a later date. On this occasion, it was reviewed employing software that enables the data to be viewed in plan view rather than the traditional cross-sectional view. In this form, several features could be seen which could not possibly be appreciated in cross-section.

Figure 13.7 Survey in progress

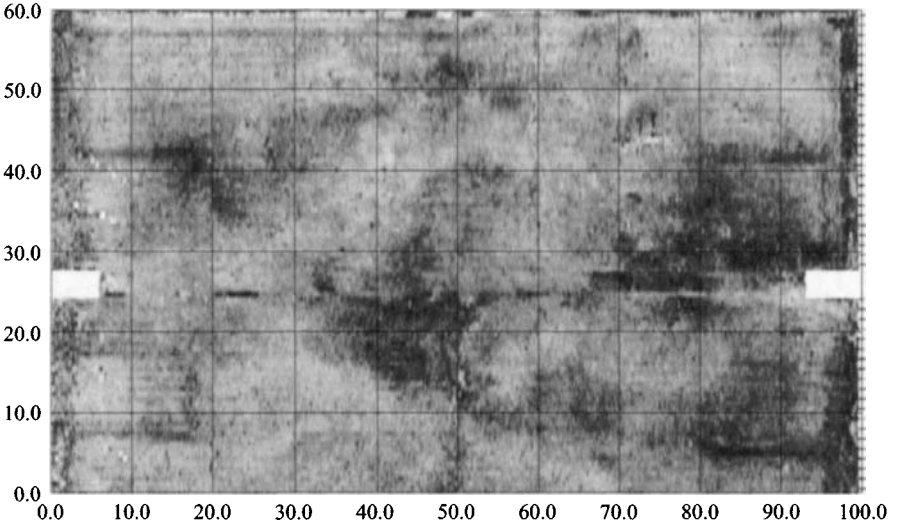

Figure 13.8 Plan view of the very surface of the football pitch

The top few centimetres of the ground exhibit profound differences in moisture, primarily caused by varying levels of compaction. Figure 13.8 shows a plan view within the top 15 cm of the soil. Several things can be made out: the edge of the playing area, the edges of the penalty area or 18 yard box, and in the centre the area where players congregate.

Slicing deeper into the ground, the drainage pattern appears. The herring-bone pattern is due to the ash filled trenches forming one phase of the drainage pattern. This can be seen in Figure 13.9. Compare the pattern seen in Figure 13.9 with the photograph taken on the day of the survey, Figure 13.10.

13.4.2 Services on a proposed building site
Dr Jon Dittmer

Often, the owners of a large campus wish to redevelop or build on a new site within the campus. However, it is not unusual for services and utilities to have been installed beneath the areas to be developed. Surveys are carried out as a matter of routine to locate and map these services, so that they can be avoided or rerouted.

One such survey was conducted on a campus in southwest England. The owners of the site wished to build a new office block on a previously un-built-on grassed area. The flatness of the site and lack of buildings meant that a very detailed survey could be performed. Measurements were taken at profile lines spaced 0.5 m apart. The soil was chalky and extremely good for radar. Figure 13.11 shows the quality of the GPR data collected.

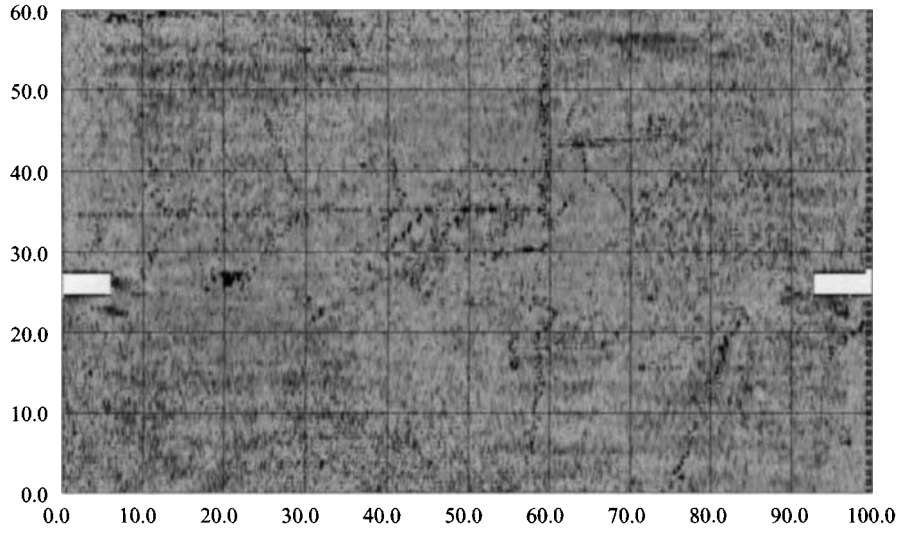

Figure 13.9 Plan view layer showing drainage pattern

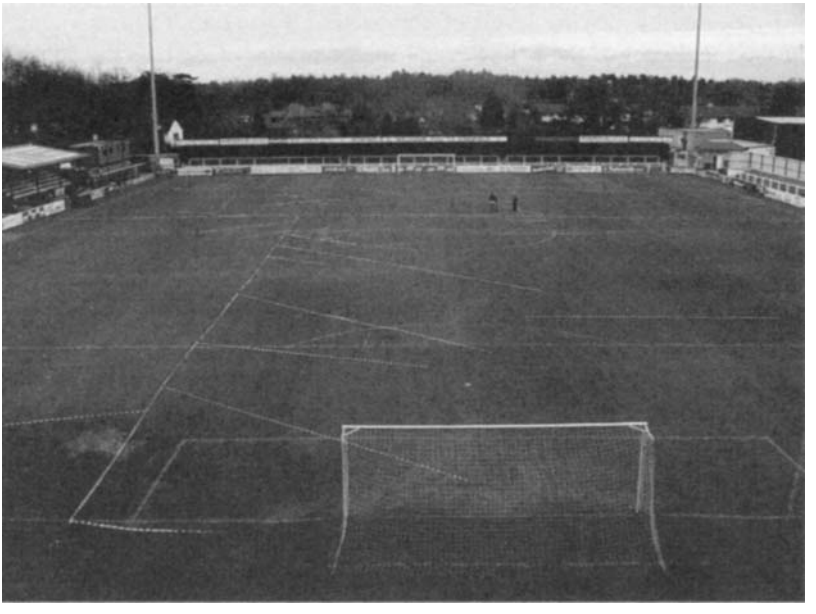

Figure 13.10 Photograph showing the marked-out drainage pattern

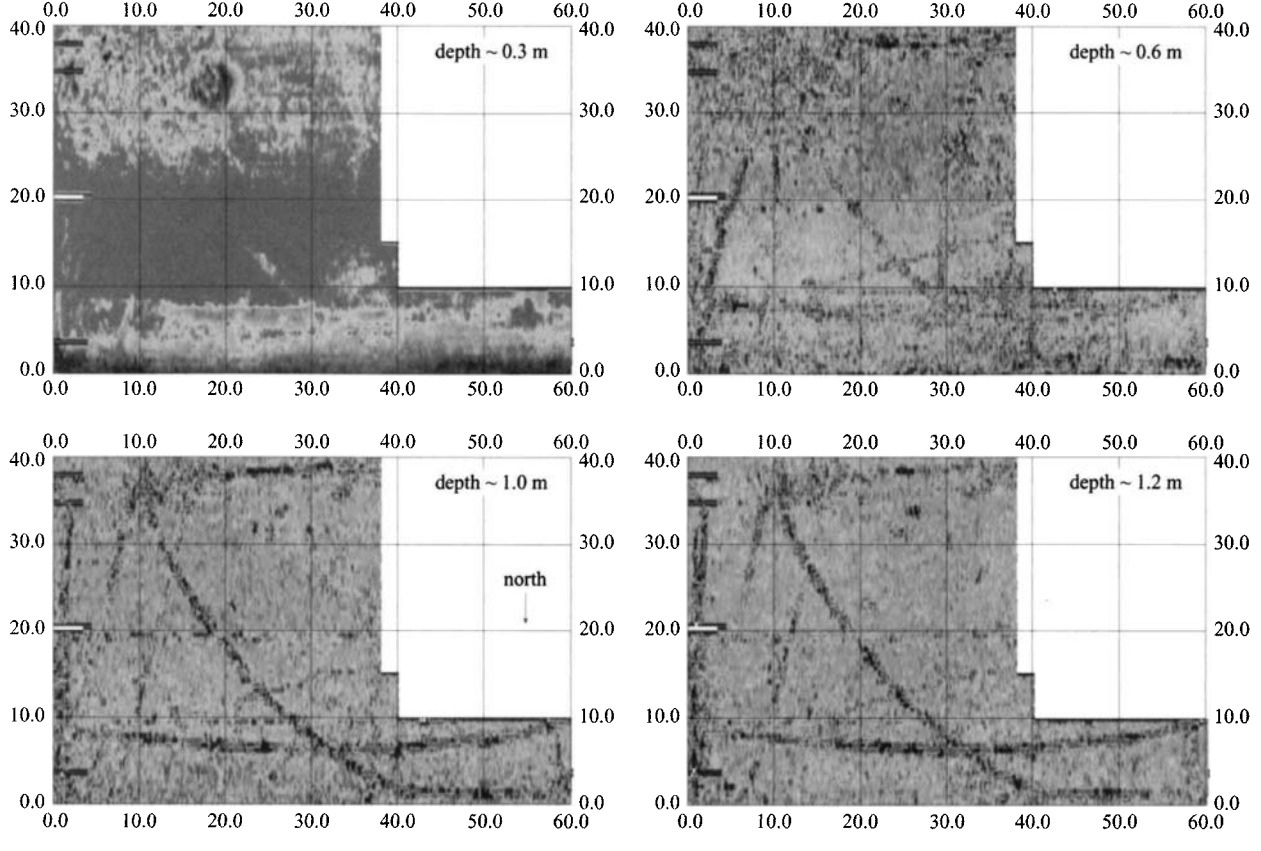

Figure 13.11 Building site survey

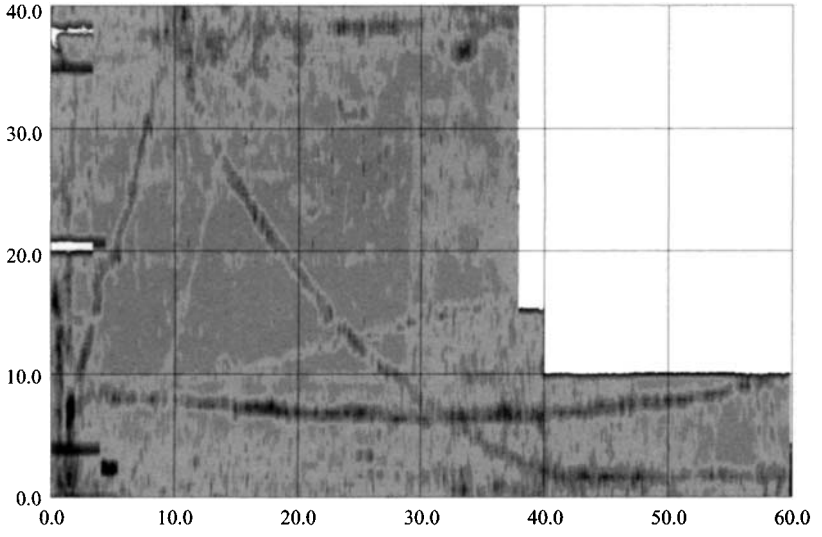

Figure 13.12 Integrated C-scan of site

Figure 13.12 shows a radar plan view of the site. In this case, the plot shows the average energy in all of the individual A-scans. This is therefore not a time/depth slice but a total view of the data. As can be seen, the resolution is reduced. In practice, when interpreting such data, each time slice is viewed. Figure 13.13 shows a montage of several time slices for this site.

The quality of these data is such that the utilities can be clearly seen and traced directly to a drawing.

13.4.3 GPR surveying in central London

Dr Jon Dittmer

An example of the complexity of GPR data interpretation is taken from a B-scan acquired in London. The photograph (Figure 13.14) shows work near St Paul's Cathedral, and the data in Figures 13.15 and 13.16 are from the district of St Pancras. There are many hyperbolic features in the image, and it would be wrong to conclude that they are all utility services. The only way to determine the identity of the hyperbolic features is to produce a C-scan of the area and then plot the extent of possible candidate utility services.

13.5 Surveying a car park

Dr Jon Dittmer

During a survey of a car park, it was noticed that the parking space demarcation lines were clearly visible in a plan view. In addition, there were some other markings

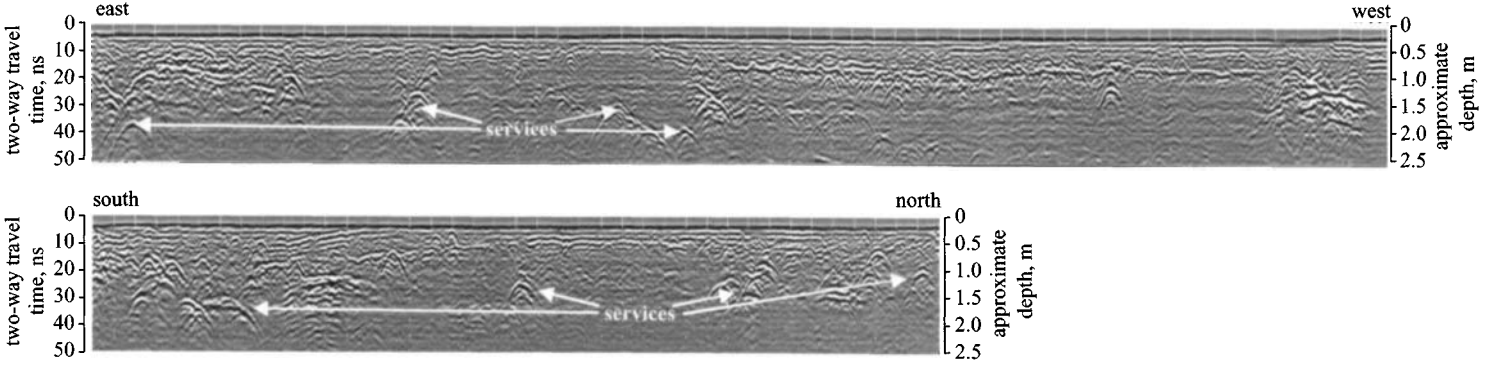

Figure 13.13 Radar sections

Figure 13.14 Surveying central London

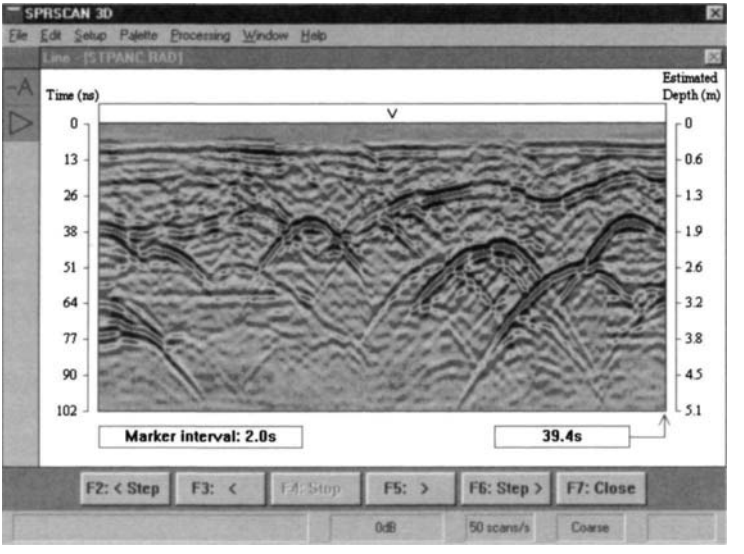

Figure 13.15 Radar survey in central London (St Pancras)

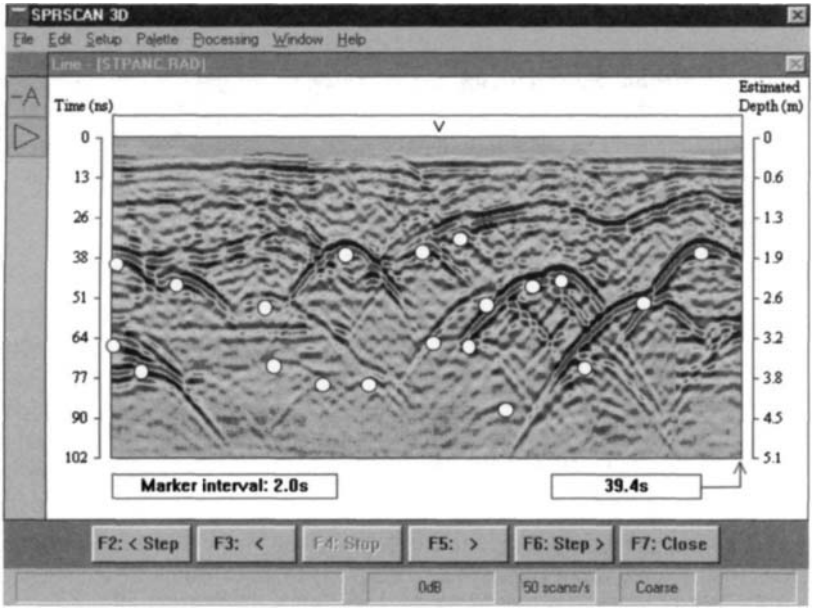

Figure 13.16 Radar survey in London (St Pancras) with hyperbolic peaks marked

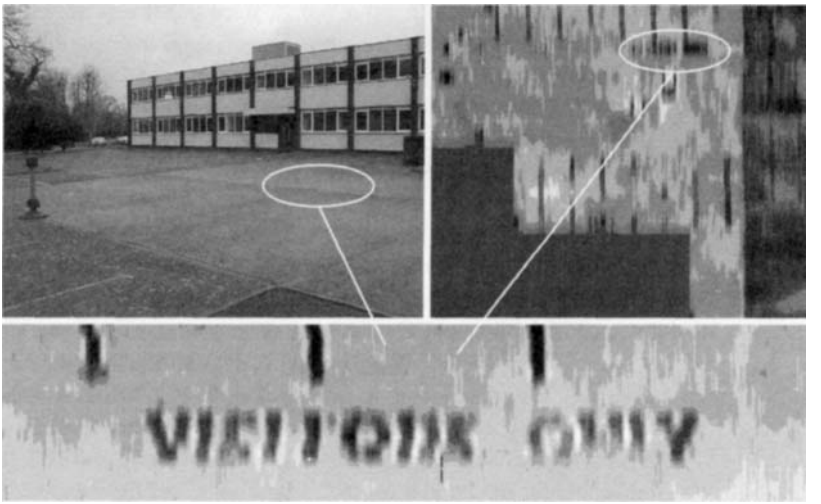

Figure 13.17 Radar survey of car park

present in the data which did not agree with what was visible on the ground. Careful comparison between the data and the visible markings revealed that the two did not match, and the writing painted on the asphalt surface also did not correlate with the data. Elsewhere in the car park, where the surface was composed of reinforced concrete, the markings were actually thin metallic tape, coloured yellow. These markings gave a clear radar response. It transpired that the radar was detecting old markings beneath the asphalt.

The survey team was intrigued, and wanted to know what the other markings were and, if they were a written sign, could they be read. Using a higher frequency antenna, and with a very fine survey grid, the team surveyed the area local to the markings. The results are displayed in Figure 13.17.

13.6 Internal inspection of pipes

David J. Daniels

Much of Britain's 475 000 km network of sewers and water mains is continuously assessed for structural integrity. Many of the sewers in major cities are over 150 years old, dating back to the start of the industrial revolution. The replaceable assets of the water system were worth, at the beginning of the 1980s, over £50 billion (80% of which is accounted for by the underground sewers and water mains). Sewer collapses can cause dangerous subsidence of road surfaces and sometimes nearby buildings. One of the problems faced by the water authorities is a lack of detailed knowledge of what there is underground. Teams trying to stabilise collapsed sewers often find uncharted ones underneath. However, the extensive use of television cameras and a radar to detect voids underground is helping to make the unpleasant task of surveying much easier. The proper condition of sewers and pipelines is vital to ensure that dirty water is transported without pipeline leaks causing contamination and possible health hazards. It is generally difficult to establish the condition of the material surrounding the pipe wall. Radar systems can be used from inside the pipe to assess the state of the surrounding ground. The pipe should, of course, be constructed from nonmetallic material.

ERA Technology has been involved in the development of a purpose-designed radar system to work from inside the sewer to produce a radar image of the material adjacent to the sewer wall. The radar antenna consists of four quadrants which enable four sectors of the sewer to be surveyed. The antenna has a diameter of 180 mm and is designed for use in sewer pipes of an internal diameter of 200 mm. Several trials have been carried out with the antenna, and results show that small voids of 50-mm diameter can just be detected. A photograph of the radar antenna is shown in Figure 13.18 and a typical test result in Figure 13.19. Within the test rig and effectively on top of the 200-mm-diameter pipe under test are a number of artificial voids. Their reflections can also be seen in the radar image. The radar reflection from the 150-mm-diameter pipe, which crosses the pipe under test, can be seen on the right-hand side and then the reflections from the 200-mm and 100-mm voids can be seen adjacent to the pipe under test. Also to be seen is the reflection from the interface between the

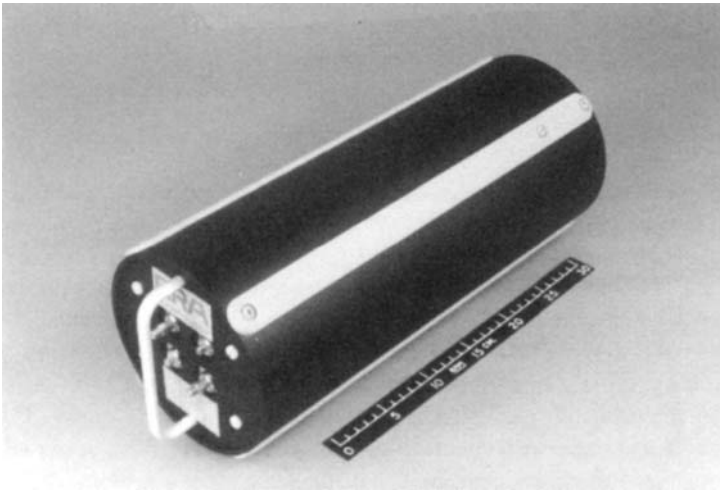

Figure 13.18 Pipe inspection antenna system (courtesy ERA Technology)

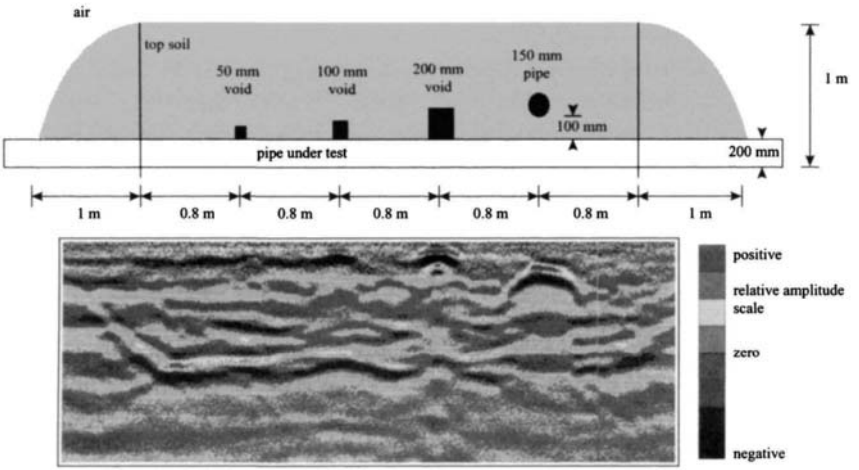

Figure 13.19 Radar image from one channel of a pipe inspection radar (courtesy ERA Technology)

top soil and the air which appears inverted in the radar image. Further details of the project can be found in Daniels and Schmidt [12].

The very first system specifically developed for pipe detection was the Terrascan system designed by Microwaves Associates and Ohio State University in the 1970s. The system showed some promise and the, then British Gas (now Transco), started

a development programme to build a plastic pipe locator with a target 90/90 performance. This is reported in Gunton and Scott [13].

13.7 Summary

The detection of buried utilities has been a standard application of GPR for several decades. However, the performance of GPR is limited by the physics of propagation and in many countries there are significantly large regions where the attenuation of the ground limits the application. Unlike the simpler low radio frequency pipe detection technology, GPR is more expensive and requires, at least for single channel systems, a systematic search pattern. This makes the cost per unit area more expensive. One way of looking at the predicted performance could be on a statistical basis with an estimate of the probability of detection per percentage of the country. This might suggest that in a country with significant regions of clay then 60% of buried utilities could be expected to be detected in 60% of the country in question. The economic case for both investment and survey can then be more accurately considered. As many GPR systems use only a single polarisation, then survey in orthogonal directions is necessary to ensure that all utilities are detected. Multi-element systems are being successfully used in those places where access is possible. However, in the city streets of many European countries the pedestrian walkways, parked cars and street furniture severely limit access.

The use of GPR is one method among a number that can be used for utility detection, and the prospective user should take much of the marketing of GPR with a pinch of salt. The type of ground should be established before survey operations, with the aim of estimating the achievable performance from the outset.

13.8 References

[1] DANIELS, D. J.: 'Ground probing radar', *IGE J.*, March 1984, pp. 111–116
[2] DANIELS, D. J.: 'Gascopact', *IGE J.*, April 1984, pp. 712, 719
[3] DANIELS, D. J.: 'Location of underground services by ground probing radar', NODIG 85 Int. Conf., April 1985, pp. 5.1.1, 6
[4] DANIELS, D. J., and HO, A. T. S.: 'High resolution radar imaging of sub-surface anomalies'. DIG 87 Int. Conf., April 1987, pp. 1, 2.1, 10
[5] DANIELS, D. J.: 'Detection of pipes using circular polarisation'. Tunnelling Systems Symposium, Brussels, Belgium, June 1988
[6] DANIELS, D. J., GUNTON, D. J., and SCOTT, H. F.: 'Introduction to sub-surface radar', *IEE Proc. F, Commun. Radar Signal Process.*, Special Issue, 1988, **135**, (4), pp. 278–321
[7] DANIELS, D. J.: 'Advances in impulse radar system technology for the detection of buried pipes'. Invited Paper, GRI Workshop on Plastic Pipe Location, Chicago, Illinois, 1/2 May 1990

[8] COSTAMAGNA, E., GAMBA, P., and LOSSANI, E.: 'A neural approach to the interpretation of ground penetrating radar'. IGARSS'98, 1998, Vol. 1, pp. 412–414

[9] CIOCHETTO, G., DELBO, S., GAMBA, P., and ROCCATO, D.: 'Fuzzy shell clustering and pipe detection in ground penetrating radar data'. IGARSS'99, 1999, Vol. 5, pp. 2575–2577

[10] GAMBA, P., and LOSSANI, S.: 'Neural detection of pipe signatures in ground penetrating radar images', *IEEE Trans. Geosci. Remote Sens.*, 2000, **38**, (2) pp. 790–797

[11] GAMBA, P., and LOSSANI, S.: 'Neural detection of pipe signatures in ground penetrating radar images', *IEEE Trans. Geosci. Remote Sens.*, 2000, **38**, pp. 790–797

[12] DANIELS, D. J., and SCHMIDT, D.: 'The use of ground probing radar technology for the non-destructive testing of pipes and their surroundings'. Int. Symposium on NDT in civil engineering, 26–28 September 1995, Berlin, Germany

[13] GUNTON, D. J., and SCOTT, H. F.: 'Radar detection of buried pipes and cables'. Communication 1345, The Institution of Gas Engineers, Presented at 53rd Autumn Meeting, London, 24 November 1987

Chapter 14

Remote sensing

14.1 Introduction

This Chapter describes some of the work that has been carried out on radar systems for remote sensing below the surface of the earth and the planets. Radar systems can be mounted on aircraft or on satellites. The types of radar used are radically different from typical GPR systems, and the aim of this Chapter is to provide an insight into the remarkable results and sophistication of radar systems. Most of the work is based on synthetic aperture radar (SAR) processing and there is a wealth of material available on this topic.

Sub-surface imaging by radar from satellites is possible where the topographic cover is radar smooth and the material penetrated is fine grained, no more than a few metres thick and very dry. Where the thickness of the cover is less than the skin depth, the return signal can be significantly increased because of refraction of the electromagnetic wave, and reduction of backscatter due to oblique incidence. Kadaba [1] has reported data on the penetration of 0.1–1.5 GHz radiation into the earth's surface for remote-sensing applications. Elachi *et al.* [2] (Jet Propulsion Laboratory, USA) demonstrated that the satellite radar SIR-A (shuttle-imaging radar) could detect dry river beds beneath the Sahara Desert. This ability is due to the hyper-arid conditions existing in desert regions where the skin depth of the sand can be 5 m or more. Blom *et al.* [3] (USA) describe the detection of igneous dykes beneath the Mojave Desert. The Seasat satellite L-band radar provided the basic data to generate the image. The dykes are buried under 1–2 m of alluvial cover. Recently, a range of other reports has appeared of SIR-B results of features covered by desert sand. The Apollo 17 Lunar Sounder experiment was described in detail by Brown [4] before the launch. Both amplitude and phase characteristics of the echo were to be measured so as to extract maximum information from the measurements. Surface-clutter-reduction techniques were to be used. Porcello *et al.* [5] detailed the results of the mission, and showed that the Apollo 17 experiment could provide profile information on sub-surface geological structures. This is possible on the moon

because of the very low attenuation of electromagnetic radiation found in lunar rocks. Using a synthetic-aperture radar operating at 5, 15 and 150 MHz they photographed the radar data in conventional SAR form and returned them to earth for processing. The 150 MHz VHF system was used for imaging the Mare Crisium. The same area was investigated by Maxwell and Phillips [6] (USA), who detected interfaces at depths of 1400 m and 1000 m in the central region. These results were achieved using a 5 MHz radar.

14.2 Airborne SAR systems for earth sensing

The first application of airborne ground penetrating radar was by the development of ice profiling radars by the Scott Polar Research Institute of Cambridge (UK), the Technical University of Denmark, and Cambridge Consultants (UK), as well as other workers in the Arctic and Antarctic. Their main objective was in the profiling of ice layers at depths of greater than 1000 m.

The realisation that improved resolution and image quality could be gained by the use of ultrawideband (UWB) radars provided an impetus to the development of such systems. Radar systems operating from airborne platforms were developed in the 1970s and were assessed experimentally. SRI International operated a commercial service over a period of 7 years in Borneo. Areas of central Kalimantan were mapped through tropical forest using a UWB radar profiler operating from 200 to 400 MHz. Interestingly, the radar penetrated the forest cover and the soil below.

In 1989, SRI International constructed a VHF SAR for the purpose of looking through foliage and imaging man-made objects such as roads and buildings. Other organisations also developed airborne VHF SAR radars using a variety of modulation techniques such as stepped FM, FMCW and impulse. FOA in Sweden developed the Carabas radar, and SRI (US) and ERIM (US) developed foliage-penetrating radars. The Norwegian University of Science and Technology (NTNU) is developing a totally flexible radar, complex waveforms derived from an arbitrary function generator. In the UK the airship based REMIDS system was a precursor for the UWB SAR impulse system developed for the MINESEEKER foundation.

Impulse radar systems have limitations due to field breakdown in the antenna and feed components. Very short duration impulses become progressively more difficult to handle and an operational altitude of 2000 m with a 2 km swath width is the highest performance that has been achieved with impulse technology at the time of writing. In general, over that height it has been found better to use higher average powers which make system design easier and technology more amenable.

As with most GPR systems, the depth of burial, size of target and soil conditions radically affect the probability of detection. It has been shown that it is feasible to detect AT mines in dry soil conditions using radar systems that operate over the frequency range 0.2–1 GHz. An example of a radar SAR image (courtesy of Dr R. Vickers and SRI) is shown in Figure 14.1. This was taken from an altitude of 400 m above the Yuma desert. The radar operated at a depression angle of 45 degrees and achieved a nominal resolution of 80 cm. It was capable of detecting metal AT mines of 300-mm diameter buried at a depth of 150–300 mm in a soil of conductivity 8–10 mS m^{-1}. Further details can be obtained from SRI USA.

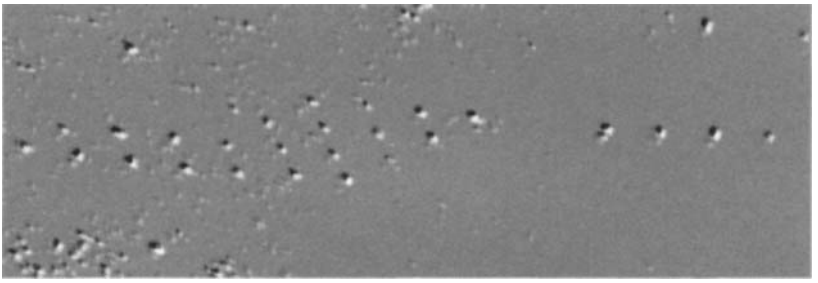

Figure 14.1 UWB SAR image of buried AT mines in the Yuma Desert, aircraft at 400 m altitude (courtesy SRI International USA, Dr R. Vickers)

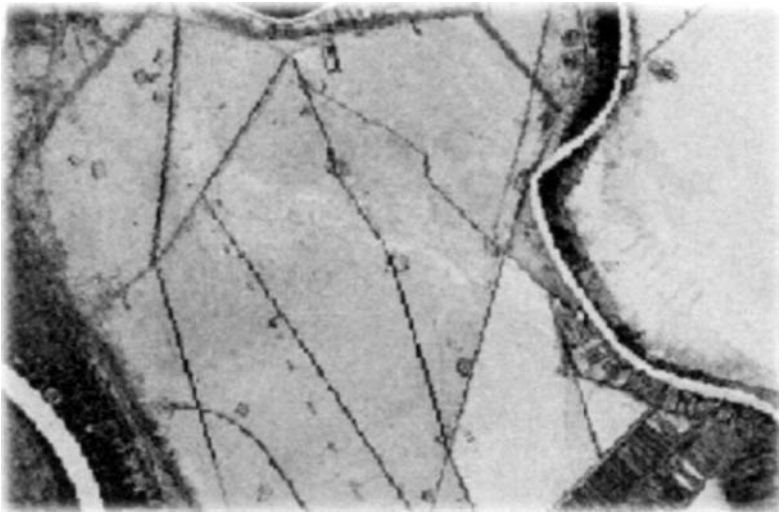

Figure 14.2 Example of airborne SAR image of buried pipelines in desert conditions

Pipelines, which are buried deeper but which are long, extended targets, can be imaged with much lower frequencies. The CARABAS radar has reported detection of underground pipelines many kilometres in length with its sub-100 MHz radar. Foliage penetration has been proven extensively in the 200–400 MHz band, with better than 1 m resolution, but with a much higher clutter level than the CARABAS radar, for example, operating at lower frequencies and a 3–4 m resolution. A typical example of SAR images of buried pipes in desert conditions is shown in Figure 14.2. The light regions are waterways while the dark linear features are pipes.

14.3 Satellite based systems for earth sensing

Dr Gerald Schaber
United States Department of Interior, USA

The first NASA Shuttle Imaging Radar (SIR-A and SIR-B) images acquired over Egypt and Sudan demonstrated the capability of space-borne 240-mm-wavelength

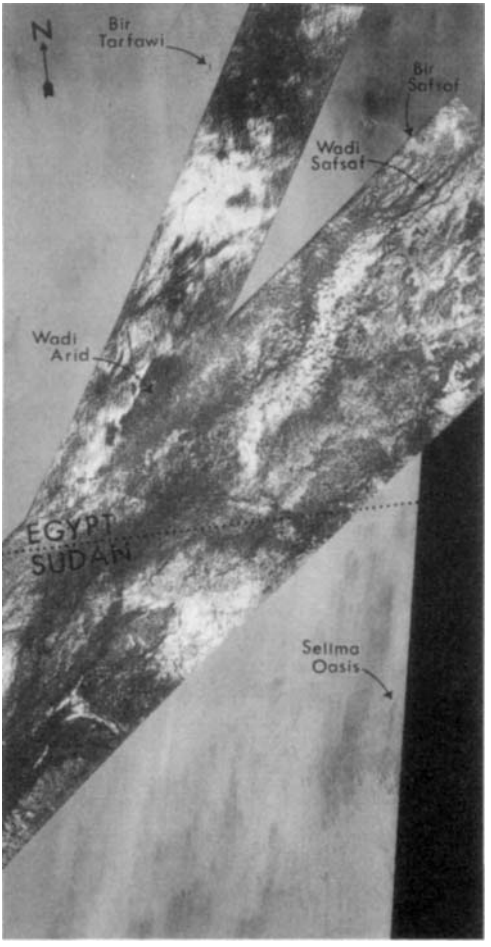

Figure 14.3 SIR image of desert landscape (courtesy US Dept of Interior)

(L-band), synthetic-aperture radar (SAR) signals to return geological information from depths of 1–2 m within the loose sand cover and the semi-consolidated alluvium typical of this desert surface [7, 8]; see Figure 14.3. Images produced by the return of SIR signals from beneath the surficial sediment reveal patterns of previously unknown, fully aggraded, stream valleys and erosional surfaces that are at present mantled by a thin sand cover [9, 10]. The importance of this discovery lies in: (i) its application to new interpretations of the Cenozoic geology of the northeastern Sahara; and (ii) recognition of the possible use of these fluvial pathways during the late Quaternary by Stone Age people. These questions have been explored by geologists from the US Geological Survey in collaboration with geologists, geomorphologists and archaeologists from the USA and Egypt [11–19]. The desert in south-western Egypt and north-eastern Sudan, about the size of the US state of Arizona, is uninhabited

and was poorly known until about 20 years ago. It was considered unusual because it lacks surface drainage features; instead it has an almost ubiquitous and complex Quaternary eolian veneer. The scattered, extensively wind eroded, decametre-scale outcrops do not display clear fluvial patterns either on the ground or on conventional visible or near infra-red wavelength images such as Landsat and SPOT.

The radar sensor's portrayal of the buried river valleys and their surrounding relict fluvial topography came about because the surface sand in this part of the Sahara is underlain by both a regional duricrust of secondary calcium carbonate (caliche or calcrete) deposited in the sediments of alluvial valleys during periods wetter than the present [7] and by bedrock terraces that mark the shores of the old alluvial valleys [13]. The deflated, hard caliche substrate now remains as a regional carapace that mimics and preserves the patterns of successive geomorphic surfaces and associated stream courses that episodically occupied the buried valleys between early Tertiary and middle Holocene times [13]. The probing Shuttle Imaging Radar sensor revealed these features through the thin, sand-sheet cover. Sub-surface imaging of natural terrains using long-wavelength SAR from space-borne (and air-borne) platforms has been demonstrated only where the topographic surface is radar smooth (dark on the radar image) and where the shallow sub-surface contains a dielectric interface or disseminated dielectric inhomogeneities that are 'radar-rough' (bright on the radar image). For successful radar imaging of the shallow sub-surface, the penetrated material must be fine grained, no more than a few metres thick and extremely dry. The single most important factor in the SIR portrayal of sub-surface geology in the north-eastern Sahara is a change in loss tangent ($\tan \delta$, which reflects a change in the imaginary part of the permittivity) due to scattering in dry and clay-free alluvial materials underlying a thin and equally dry sand sheet [7]. Similar radar penetration from space altitudes has been demonstrated in the Badan-Jaran Desert of China [11, 20], in Saudi Arabia [21] and in the Mojave Desert of California [3, 22]. Long-wavelength SAR sub-surface mapping using multi-frequency airborne SAR sensors had been demonstrated in the deserts of California [23, 24], and later in the deserts of south-western and north-central Arizona [25]. Schaber *et al.* [7] found from field studies in southern Egypt (including the study of 150 hand-dug pits and 82 backhoe trenches) that the maximum 'radar-imaging depth' (RID) for 24 cm-wavelength (L-band) SIR signals to a buried dielectric interface in the sandy alluvium typical of the hyper-arid Western Desert of Egypt could be expressed as

$$\text{RID} = 0.25(1/a)$$

where $1/a$ is the electrical skin depth or attenuation length. The field attenuation coefficient (a) for low-loss media ($1 \gg \tan \delta$) is $a = 1/2 \tan \delta$, and k is the wavenumber [26].

Schaber *et al.* [7] further found that dense, dry caliche nodules disseminated in the upper part of the sandy alluvium in the Western Desert of Egypt result in strong volume scattering. Such scattering enables discrimination on the SAR images between the radar-bright regions between small fluvial channels and the channels that are radar-dark due to mirror-like reflection from the flat, gravel-rich surfaces below a very thin sand mantle.

Using SIR-A results in the Sahara reported by McCauley *et al.* [9], Elachi *et al.* [2] showed, theoretically, that the presence of a thin low-loss (dry) sand layer as thick as two-thirds of the attenuation length (or skin depth) will in effect enhance the radar's capability to image the sub-surface interface with HH polarisation. A similar sand layer as thick as one-quarter of the attenuation length will enhance the radar's capability to image the sub-surface interface with VV polarisation. For an attenuation length of 6 m, Elachi *et al.* [2] found that this favourable effect will occur for sand layers up to 4-m thick for HH and up to 1.5-m thick for VV. They also showed that, even though the absolute backscatter cross-section decreases as a function of incidence angle (θ), the presence of a dry sand layer and the resulting refraction effect can enhance the capability to image the sub-surface, particularly at large incidence angles (about 50° or greater).

The radar images obtained from the Eastern Sahara during SIR-A and SIR-B, though few, indicate that this remote sensor can be applied to regional exploration for shallow ground water associated with sand-buried paleovalley systems [13, 14]. Radar can also be used to map the distribution of certain types of duricrusts, such as calcrete, ferricrete and gypcrete, which are diagnostic of various paleoclimatic conditions. The radar data can be used synergistically with information from other types of remote sensing (such as spectral data from Landsat or SPOT multispectral images) to provide simultaneous information on both the surface and sub-surface of desert regions [27].

As part of NASA's third Shuttle Imaging Radar Mission (SIR-C/X-SAR) (two launches in 1994), acquisition of additional SAR image data over the Sahara, the Arabian Peninsula and other major deserts, was planned; this will help reconstruct the scope and trends of major paleodrainage systems. Another objective will be to evaluate further the optimal sensor and geologic parameters conducive to sub-surface mapping and delineation of duricrusts in desert terrains, which are expected to provide evidence for regional changes in paleoclimate. The SIR-C/X-SAR platform includes an X-band (3-cm-wavelength) SAR (VV polarisation) developed by the German Space Agency and the Italian Space Agency and fully polarimetric (HH-HV, VV-VH) C- (6 cm) and L-band (23 cm) SARs developed by NASA's Jet Propulsion Laboratory (Pasadena, California), and the description of all of the radar images is provided courtesy of NASA/JPL/Caltech and their website. Figure 14.4 shows an optical image and an equivalent L-band radar image of the Saf-Saf Oasis in Egypt. These images show two views of a region of south-central Egypt, each taken by a different type of space-borne sensor. On the left is an optical image from the Landsat Thematic Mapper, and on the right is a radar image from the space-borne Imaging Radar-C/X-band Synthetic Aperture Radar (SIR-C/X-SAR). This comparison shows that the visible and infra-red wavelengths of Landsat are only sensitive to the materials on the surface, while the radar wavelengths of SIR-C/X-SAR can penetrate the thin sand cover in this arid region to reveal details hidden below the surface. Field studies in this area indicate that the L-band radar can penetrate as much as 2 m (6.5 ft) of very dry sand to image buried rock structures. Ancient drainage channels, shown at the bottom of this image, are filled with sand more than 2 m (6.5 ft) thick and therefore appear dark because the radar waves cannot penetrate them. Only the most recently active channels are

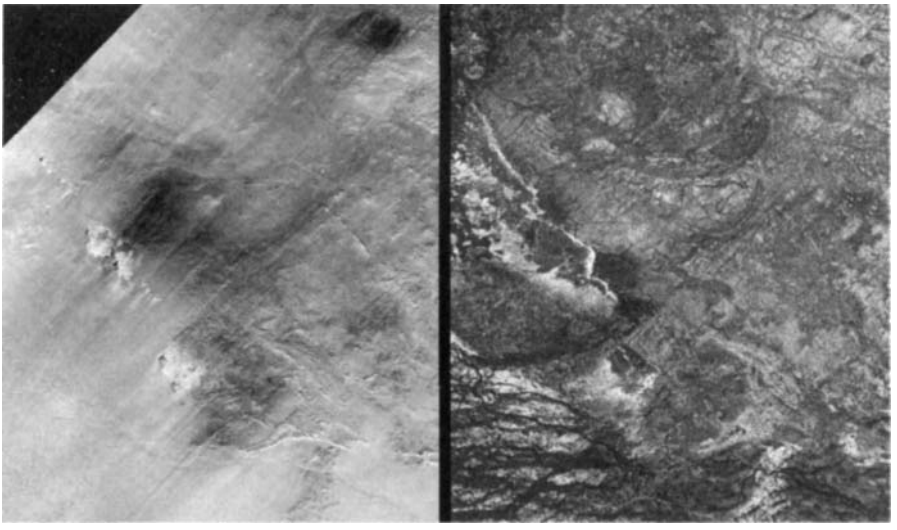

Figure 14.4 *SIR-C optical and L-band SAR image of Saf-Saf Oasis Egypt (courtesy NASA/JPL/Caltech)*

visible in the Landsat scene. Some geological structures at the surface are visible in both images. However, many buried features, such as rock fractures and the blue circular granite bodies in the upper centre of the image on the right, are visible only to the radar. The following description requires that the colour images on the CD are viewed. The Saf-Saf Oasis is located near the bright yellow feature in the lower left centre of the Landsat image. Scientists are using the penetrating capabilities of radar imaging in desert areas to study structural geology, mineral exploration, ancient climates, water resources and archaeology. Each image is 30.8 km by 25.6 km (19.1 miles by 15.9 miles) and is centred at 22.7 degrees north latitude, 29.3 degrees east longitude. North is toward the upper right. In the Landsat image, the colours are assigned as follows: red is band 7 (mid-infrared); green is band 4 (near infra-red); and blue is band 1 (visible blue light). The colours assigned to the radar frequencies and polarisations are as follows: red is L-band, horizontally transmitted and received; green is C-band, horizontally transmitted and received; and blue is X-band, vertically transmitted and received. The radar image was acquired by the space borne imaging radar-C/X-band synthetic aperture radar (SIR-C/X-SAR) on 16 April 1994, on board the space shuttle Endeavour. SIR-C/X-SAR, a joint mission of the German, Italian and United States space agencies, is part of NASA's Earth Science Enterprise. The Landsat Program is managed jointly by NASA, the National Oceanic and Atmospheric Administration and the United States Geological Survey. The hidden and dried up rivers can be clearly seen in the lower part of the image produced by the L-band SAR radar.

The ability of a sophisticated radar instrument to image large regions of the world from space, using different frequencies that can penetrate dry sand cover, produced

the discovery in this image: a previously unknown branch of an ancient river, buried under thousands of years of windblown sand in a region of the Sahara Desert in North Africa. This area is near the Kufra Oasis in southeast Libya, centred at 23.3 degrees north latitude, 22.9 degrees east longitude, and is shown in Figure 14.5. The

Figure 14.5 SIR-C L- and C-band SAR image of Wadi Kufra Libya (courtesy NASA/JPL/Caltech)

image was acquired by the space-borne imaging radar-C/X-band synthetic aperture (SIR-C/X-SAR) imaging radar when it flew aboard the space shuttle Endeavour on its 60th orbit on 4 October 1994. This SIR-C image reveals a system of old, now inactive, stream valleys, called 'paleodrainage systems', which, during periods of wetter climate, carried running water northward across the Sahara. The region is now hyper-arid, receiving only a few millimetres of rainfall per year, and the valleys are now dry 'wadis', or channels, mostly buried by wind-blown sand. Prior to the SIR-C mission, the west branch of this paleodrainage system, known as the Wadi Kufra (the dark channel along the left side of the image), was recognised and much of its course outlined. The broader east branch of Wadi Kufra, running from the upper centre to the right edge of the image, was, however, unknown until the SIR-C imaging radar instrument was able to delineate its dimensions: at least 5 km wide and nearly 100 km long (3 miles by 62 miles). The two branches of Wadi Kufra converge at the Kufra Oasis, the cluster of circular fields at the top of the image. The farms at Kufra depend on irrigation water from the Nubian Aquifer System. The paleodrainage pattern unveiled by SIR-C suggests that the location of productive wells at the confluence of the old river valleys is no accident. Quite likely, the water supply for the Kufra Oasis has been recharged by episodic runoff and by groundwater that moved northward in the alluvial fill of the old stream channels. Rainfall was more abundant in this region during parts of the late Quaternary when Stone Age (Paleolithic and later Neolithic) people left their implements along the riverbanks. The SIR-C image, which clearly shows river channels cut into the surrounding bedrock, provides a 'road map' for geoarchaeologists to locate artefacts and to better interpret the history of early people and climatic conditions in this region. The area shown is approximately 120 km by 78 km (74 miles by 48 miles). North is toward the upper left. The colours in this image were obtained using the following radar channels: red represents the L-band (horizontally transmitted and received); green represents the average of the C- and L-band (horizontally transmitted and received); blue represents the C-band (horizontally transmitted and received). Please view the colour images on the CD supplied.

14.4 Planetary exploration

14.4.1 Mars 96 mission

Prof. Tor Hagfors
Max Planck Institut fur Aeronomie, Germany

The Max Planck Institut fur Aeronomie (Prof. Hagfors and Dr Nielsen) contributed to the Russian Mars 96 mission which was due to start in the late autumn of 1996. This was intended to make extensive measurements of particles, composition and fields in the atmosphere of Mars and to make maps of the surface of Mars from a satellite in orbit round the planet. The instrumentation includes a long-wavelength radar designed as a topside ionosonde to explore the upper ionosphere of the planet, a region which has previously only been investigated in occultation experiments and in brief periods during the descent of Mars probes. This topside sounder is a

swept-frequency radar which operates between 170 kHz and 5 MHz. During night time on Mars the maximum ionospheric plasma frequency falls well below 1 MHz, and a wide frequency window opens in which the observed echoes are from the Martian surface rather than from the ionospheric plasma.

The use of this window to explore the surface offers exciting new possibilities for the study of Mars. Except for the polar caps, the surface has the appearance of a dry desert. The observation of ancient riverbeds and areas which must have been flooded, however, suggests that the surface of Mars cannot always have been so. Indeed, water must have flowed in abundance at some time in the past to create the fluvial features. This water cannot all have escaped from the surface, and current opinion holds that much of the water has been captured and is held under the surface in the form of ice, and that the depth of this ice is a function of Martian latitude. There is also observational evidence, based on the shape of some of the surface features of Mars, that ice must exist under the surface. Estimates of the depth of this ice or icy layers range from a few tens to a few hundreds of metres. This layered structure of the surface must lead to quite characteristic variation of the reflection coefficient with frequency. The simplest model of such a frequency variation is provided by a dielectric medium of thickness L and relative permittivity ε_1 resting on top of a semi-infinite region with relative permittivity ε_2. In this case the power reflection coefficient of the surface at normal incidence takes the form

$$R^2 = \frac{R_1^2 + R_2^2 e^{-2\tau} + 2R_1R_2e^{-\tau}\cos\theta}{1 + R_1^2R_2^2e^{-2\tau} + 2R_1R_2e^{-\tau}\cos\theta} \tag{14.1}$$

where

$$\theta = \frac{4\pi f}{c}\left(\sqrt{\varepsilon_1'}\right)L \tag{14.2}$$

$$R^2 = \frac{2\pi f}{c}\left(\sqrt{\varepsilon_1'}\right)L\tan\Delta_1 = \frac{\theta}{2}\tan\Delta_1 \tag{14.3}$$

where θ is the phase path through the upper layer and back and where Δ_1 is the ratio of the imaginary and real parts of the relative permittivity. The reflection coefficients are defined as for semi-infinite half-space as:

$$R_1 = \frac{\left(\sqrt{\varepsilon_1'}\right) - 1}{\left(\sqrt{\varepsilon_1'}\right) + 1} \tag{14.4}$$

$$R_2 = \frac{\sqrt{\varepsilon_2'/\varepsilon_1'} - 1}{\sqrt{\varepsilon_2'/\varepsilon_1'} + 1} \tag{14.5}$$

In the absence of absorption in the upper dielectric, the reflection coefficient will oscillate with frequency between the two values with the thickness determining the

Table 14.1 Mars 96LWR experiment parameters

Parameter	Value	Units
Frequency range	0.17–4.93	MHz
Transmitter bandwidth in frequency band 1: 0.18–2.1 MHz	2660	Hz
Transmitter bandwidth in frequency band 2: 1.9–5.0 MHz	665	Hz
Number of discrete frequencies	56	
Range of linear frequency modulation	15	kHz
Pulse repetition frequency	300–900	Hz
Time of measurements at each frequency	270 or 1080	s
Dipole antenna length	2×20	m
Peak voltage at antenna input	1.2	kV
Power	100	W
Total mass	35	kg

period of the oscillation in the frequency domain:

$$\frac{\text{Max}}{\text{Min}} = \frac{(R_1 \pm R_2)^2}{(1 \pm R_1 R_2)^2} \tag{14.6}$$

It is, of course, unlikely that the real situation will be as simple as this model. There may be a gradual transition in the relative permittivity with depth, the thickness of the layer may change in a random fashion with position on the surface and there may be substantial attenuation in the surface layer. The purely oscillating behaviour of the reflectivity will then probably be replaced by a gradual and nonoscillating behaviour of the reflection coefficient. Even so, the form of the transition will identify the thickness of the layer and the dielectric properties of the surface material, and may serve to confirm the presence of a buried ice layer on Mars.

The properties of the orbit and the radar system carried in the Mars 96 satellite are listed in Table 14.1. The radar system will feed into a dipole antenna consisting of two 20 m retractable booms. The radar equipment is integrated into the spacecraft which is shown in Figure 14.6. The spacecraft was scheduled to be launched in Autumn 1996 and to be injected into orbit the next year.

14.4.2 Mars 96 project

Florence Nicollin
University of Rennes, France

This work was supported by CNES (MARS 96 balloon project and Radar Research and Technology Program).

14.4.2.1 Introduction: One of the instruments of the Mars 96 balloon mission is a ground penetrating radar system, which is planned to be integrated inside the guide rope (ballast of the balloon made of a series of 18 metallic cylinders), with the

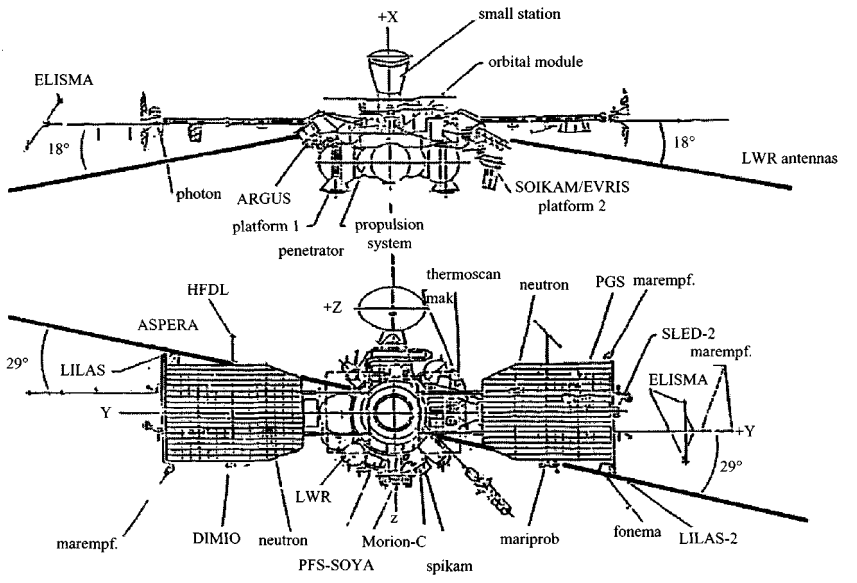

Figure 14.6 Mars 94 Orbiter (courtesy Max Planck Institut fur Aeronomie)

scientific goals of measuring the thickness of the Martian permafrost and sub-surface layers and of determining their electromagnetic characteristics [28]. The sub-surface depth-penetration capability of this radar must be of the order of 1 km with a resolution of about 10 m. The CNRS (Service d' Aeronomie and CEPHAG at Verrieres le Pouisson and Grenoble) and the Riga Aviation University (Latvia) have built an impulse-radar system including a variable-gain receiver and repetitive-trace coherent integration. Preliminary experiments were carried out on glaciers and on sand dunes to test the equipment and to obtain representative experimental GPR profiles. Then, numerical simulations were made to estimate the performance of the prototype system from specific Martian sub-surface models.

14.4.2.2 Technical solutions: Most of the design of the Mars 96 balloon mission GPR is constrained by the mechanical shape of the guide rope, the allocated mass, the working and storage temperatures, and the limited power available. In these limits, and according to the deep penetration objective, the CNRS and the University of Riga have built an impulse-excitation radar working in the 10 MHz frequency range [29]. The guide rope modules house the radar electronics and the power supply (Figure 14.7). A 12-m-long flexible dipole consisting of the guide rope as one arm and a thick metallic cable as the other arm forms the antenna. The simple transmitting system consists of short pulse excitation of the dipole resistively loaded in its centre. The antenna, which can be modelled as a leaky open-ended line [30], radiates a transient HF field for about 100 ns. Experimental tests show a centre frequency of

Figure 14.7 Mars 96 project antenna (courtesy University of Rennes)

approximately 12 MHz and a usable bandwidth of 6 MHz, corresponding to a depth resolution of about 12 m in permafrost. At the end of the transmitted pulse, the antenna is connected to the protected receiver which recovers its nominal linear regime after about 250 ns from the beginning of the pulse, corresponding to a blind depth of 20 m in permafrost. The direct 'flash' digital conversion of the complete received signal is made, so that every shot produces a full trace. Thus, it is possible to perform in real time the coherent integration of 256 successive traces to give a 24 dB improvement in signal-to-noise ratio. In the receiver, a time varying gain corrects the geometrical spreading loss, rising from 15 to 60 dB in 3 μs. Practical limitations in the data flow back to Earth drastically limit the amount of data. At the beginning of each night of the ten-day Mars 96 mission, four 4O-traces profiles will be performed, separated by some 5 km. The profile length will be of the order of 400 m with a spacing of about 10 m between sounding points.

14.4.2.3 Experimental results: Numerous profiles have been collected on the Pyla dune (south of the Arcachon basin in France), on the Mont-de-Lans glacier (French Alps) and in Antarctica [31, 32]. The data are processed to remove coherent system ringing and by inverse filtering to improve the resolution and enhance the reflected echoes. On profiles recorded on the Pyla dune (a long dune up to 117-m thick consisting of homogeneous sand overlaying the water table), the echo from the bottom of the dune is clearly visible. Profiles recorded on cold parts (ice below 0°C) of the Mont-de-Lans glacier clearly show the echo from the ice–bedrock interface at a depth in the range 50–100 m.

Figure 14.8 shows the radar image. This echo consists of a mixture of reflected (specular reflection) and backscattered (diffuse reflection) waves from an interface which may be considered as a rough surface with respect to the wavelength. Similar results are obtained from profiles recorded in Antarctica, showing the ice-bedrock interface at depth down to 900 m over distances of some 30 km. Profiles record temperate parts (ice at 0°C) of the Mont-de-Lans glacier exhibiting widely scattered energy decreasing with depth. This has been explained because the scattering effect in

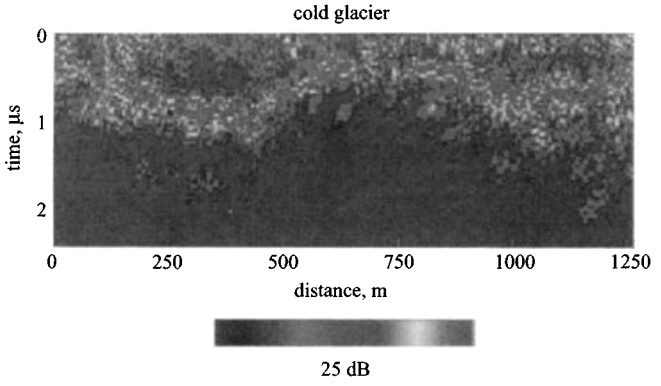

Figure 14.8 Mars 96 Project – radar image of Mont-de-Lans glacier (courtesy University of Rennes)

the temperate glacier can be modelled as a layer of ice containing inclusions of liquid. Numerical simulations, using a first-order multiple-scattering approximation and the Rayleigh-scattering model, show that, when the reflection at the basal interface is lost in the scattered power, the received power decreases as a function of depth in the same way as the energy decreases in the experimental data. With these results, it is possible to estimate the depth of the ice–bedrock interface given electromagnetic characteristics of the temperate glacier.

14.4.2.4 Martian modelling: Geological models of the Martian sub-surface show a thick regolith (blanket of debris resulting from impact processes), which could be interbedded volcanic flows or sedimentary deposits, and which contains a significant quantity of water as ground ice making a permafrost [33, 34]. From two models of the planned sites of the Mars 96 mission, several electromagnetic models were built in order to perform numerical simulations. The regolith is represented by a homogeneous porous medium containing a uniform distribution of spherical blocks of basalt. The porous medium is basaltic sands, mixed with Mars atmosphere in the upper dry layer, with ice in the permafrost and with liquid water below the permafrost. Values of the physical parameters are derived from the Viking observations. With a first-order multiple-scattering approximation, we calculated the received power, consisting of scattered power in the inhomogeneous medium and power reflected at the different interfaces. These simulations show that, even if the block size is very much smaller than the wavelength (50 times smaller), it is not possible to neglect scattering effects of inclusions in these absorbing media. Nevertheless, if the medium has a tenuous content of heterogeneities (poor blocky regolith) or if it consists of sedimentary deposits, the ground penetrating radar has the capability to detect the bottom of the permafrost at depths.

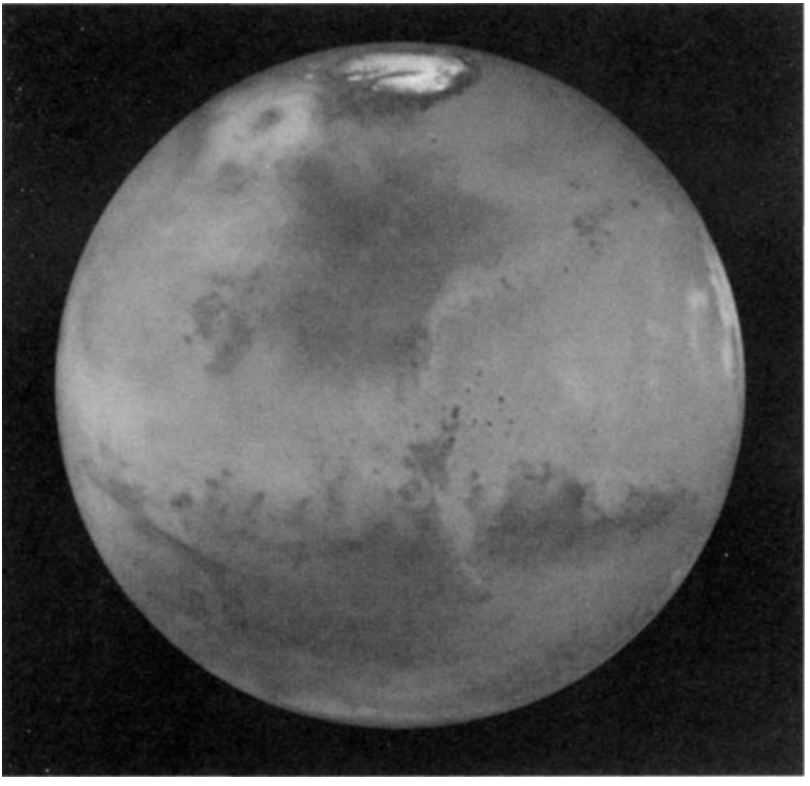

Figure 14.9 Mars (courtesy NASA/JPL/Caltech)

14.5 Radar for measuring interplanetary bodies

Prof. Giovanni Picardi

14.5.1 Introduction

The primary scientific objectives that can be accomplished with a radar devoted to the study of any celestial body, such as Mars shown in Figure 14.9, are the surface characterisation, the sub-surface geological probing, and the mapping of the distribution of water, both liquid and solid, in the upper portions of the crust. Detection of such reservoirs of water will address key issues in the hydrological, geological, climatic, and possible biological evolution.

The sub-surface geological probing is another scientific objective that can be accomplished with a radar devoted to the study of frozen surfaces. Sub-surface geological probing consists of characterising and mapping geological units and structures in the third dimension. Detection of sub-surface geological boundaries allows: determination of the thickness and properties of sedimentary units such as outflow

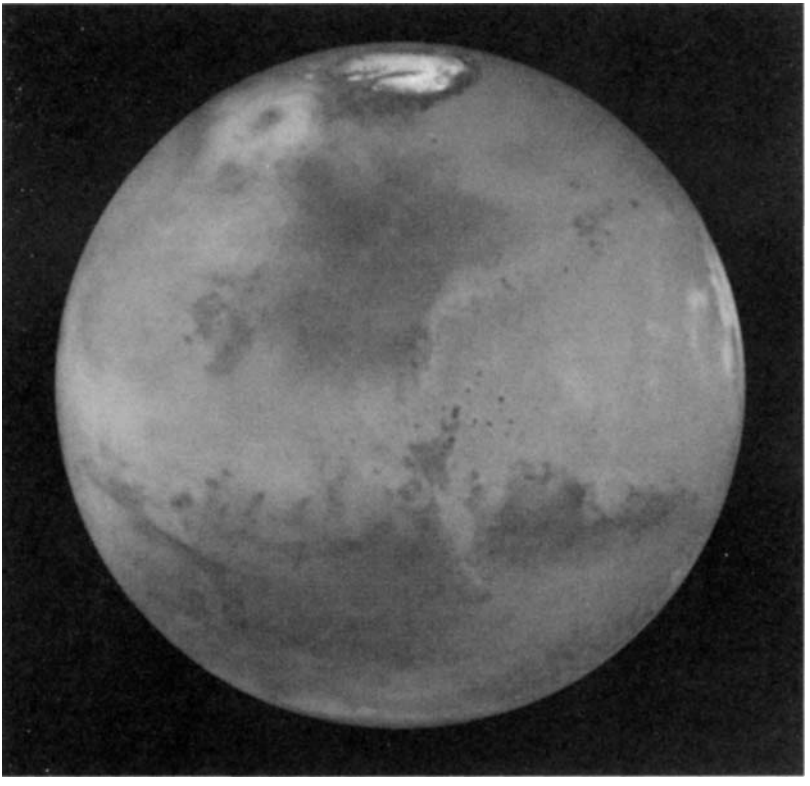

Figure 14.9 Mars (courtesy NASA/JPL/Caltech)

14.5 Radar for measuring interplanetary bodies

Prof. Giovanni Picardi

14.5.1 Introduction

The primary scientific objectives that can be accomplished with a radar devoted to the study of any celestial body, such as Mars shown in Figure 14.9, are the surface characterisation, the sub-surface geological probing, and the mapping of the distribution of water, both liquid and solid, in the upper portions of the crust. Detection of such reservoirs of water will address key issues in the hydrological, geological, climatic, and possible biological evolution.

The sub-surface geological probing is another scientific objective that can be accomplished with a radar devoted to the study of frozen surfaces. Sub-surface geological probing consists of characterising and mapping geological units and structures in the third dimension. Detection of sub-surface geological boundaries allows: determination of the thickness and properties of sedimentary units such as outflow

channel deposits and possible lacustrine materials; mapping of the thickness of polar layered deposits and measurements of their physical properties that are likely to record climate variations; an inventory of mobile materials such as dust and sand deposits; study of volcanic stratigraphy to understand eruptive processes and crustal evolution; and mapping of sub-surface geological structures (e.g. folds and faults) to understand tectonics.

To design the radar sounder, preliminary models of the electrical properties of the layers and interfaces are required. The modelling should result in estimates of thickness of layers, depth to interfaces, dielectric properties of the materials and an interpretation of the properties of the materials including composition. Detection of a crustal interface between layers of differing material requires that a set of conditions be met. The most critical conditions are that the interface represents a contrast in the real dielectric constant, the attenuation of the signal is small during its round-trip from the instrument and through the crust, and the competing signals, primarily from the surface 'clutter', do not mask the sub-surface echo when the sub-surface sounding is the objective.

Two main crustal models can be considered: crust heterogeneous in composition, with interbedded layers, sedimentary rocks, with porosity, holes and fractures saturated with ice; and surface covered with an icy shell.

The first one, for example, is the model that is used to represent the Martian Crust. The latter is applicable to Europa (Titan satellite). Concerning the surface, it is necessary to characterise the geometric structure in terms of a large-scale morphology, on which a small-scale geometric structure, due to rocks, is superimposed. Recently the structure of the planet's surface was described by means of fractals. The design approach of the Mars Advanced Radar for Subsurface and Ionosphere Sounding (MARSIS), which is supported by Italy Space Agency (ASI) and by NASA, and planned for the Mars Express Mission, will be described in relation to the available Mars models. MARSIS is devoted to the study of the Martian upper portions of the crust, for surface characterisation, sub-surface geological probing and mapping of the distribution of water, both liquid and solid. The MARSIS instrument is pioneering planetary radar sounding and is influencing the design and development of the SHARAD (a new mission on Mars, planned for 2005) and of Europa Orbiter Radar Sounder EORS.

The MARSIS instrument is a low-frequency nadir-looking pulse limited radar sounder and altimeter with ground-penetration capabilities, which uses synthetic aperture techniques and a secondary receiving antenna to isolate sub-surface reflections. MARSIS can be effectively operated at any altitude lower than 800 km. In standard operative mode the instrument will be able to transmit any of the following bands: 1.3–2.3 MHz (centred at 1.8 MHz), 2.5–3.5 MHz (centred at 3 MHz), 3.5–4.5 MHz (centred at 4 MHz) and 4.5–5.5 MHz (centred at 5 MHz).

A 1 MHz bandwidth allows a vertical resolution of 150 m in vacuum, which corresponds to 50–100 m in the sub-surface, depending on the EM wave propagation speed in the crust. The typical spatial resolution of the MARSIS will be 5 km × 10 km in the along track and crosstrack directions, respectively. In standard operative mode,

up to four echo profiles (each consisting of 205, 16-bit, range bins collected at one of the frequency bands and one of the two antennas) will be produced at intervals of ~1 s, resulting in a spatial sampling rate of ~5 km. The acquired profiles will be stored for down-link at a rate <10.4 kbit/s. The possibility of down-linking raw data for a small region of particular interest is also offered. Ground processing will extract from the down-linked profiles significant information on the surface topography and composition, as well as on the location and possibly the dielectric properties of sub-surface discontinuities.

14.5.2 Scientific objectives

The set of scientific objectives for the MARSIS investigation was defined in the context of the objectives of the Mars Express mission and in the more general frame of the current open issues in the study of Mars. This set was the main reference in driving the instrument requirements and in deciding design tradeoffs. The MARSIS primary objective is to map the distribution of water, both liquid and solid, in the upper portions of the crust of Mars.

Three secondary objectives are defined for the MARSIS experiment: sub-surface geological probing, surface characterisation and ionosphere sounding. The additional secondary objective is to acquire information about the surface of Mars. The specific goals of this part of the experiment are to characterise the roughness of the surface at scales of tens of metres to kilometres, to measure the radar reflection coefficient of the upper surface layer, and to generate a topographic map of the surface at approximately 10 km' lateral resolution. These data sets can be used to address a wide range of scientific questions, including: the large-scale surface roughness of various geologic units; implications for the processes of emplacement and modification; determination of the bulk density (providing constraints on the composition) of upper crust materials; and a global topographic data set to complement those derived by other techniques.

A final secondary objective is to use the MARSIS as an ionosphere sounder to characterise the interactions of the solar wind with the ionosphere and upper atmosphere of Mars. Radar studies of the ionosphere will allow global measurements of the ionosphere electron density and investigation of the influence of the Sun and the solar wind on the electron density.

14.5.3 Reference models

14.5.3.1 Crust structure and composition: Although a multitude of different chemical compositions is present at the surface of Mars, as listed in Table 14.2*a*, according to the suggestions of planetary scientists, it is necessary to select a few representative materials as most relevant for electromagnetic studies. Table 14.2*b* lists the values of dielectric constant of the materials, which can be considered as end members of the range in which the first layer of the Martian surface materials may vary. The dielectric properties of the water and ice filling the pores are listed in Table 14.2*c*.

Table 14.2 Summary of the sub-surface material dielectric properties

Category	ε'	ε''	$\tan\delta$
(a)			
Carbonate	6.5–8	0.04	0.006
Dense basalt ($d_p < 1$ km)	5	0.02	0.004
Dense basalt ($d_p > 1$ km)	9	0.27	0.03
Eolian sediment	2.4	0.08	0.03
Fluvial sediment	1.5–8.5	0.08	0.03
Durated sediment	2.1–2.8	0.08	0.03
Crater ejecta	8	0.11	0.014
Layered basalt	7.1	0.1	0.014
Vesicular basalt	7.1	0.1	0.014
Volcanic ash	5.6–6.5	0.085–0.25	0.013–0.04
(b)			
I (Andesite)	5		0.004
II	9		0.03
III (Basalt)	7.1		0.014
(c) Dielectric characteristics of pore-filling materials			
Gas	1	0	0
Solid H_2O (ice)	3.15	0.000663	0.0002
Liquid H_2O (water)	88	0.0088	0.0001

Moreover, a 50% surface porosity of the regolith is consistent with estimates of the bulk porosity of Martian soil as analysed by the Viking Landers, and a lower bound for the surface porosity can be taken at 20%, a value derived from measured porosity of lunar breccias. A model of the decline of porosity with depth due to the lithostatic pressure can be obtained by adapting a similar model devised for the Moon, based on seismic data which are not available for Mars:

$$\phi(z) = \phi(0)e^{-\frac{z}{K}} \tag{14.7}$$

where $\phi(z)$ is the porosity at depth z, and K is a decay constant that, for Mars, can be computed by scaling the measured lunar decay constant for the ratio between the lunar and Martian surface gravitational acceleration, under the assumption of comparable crust densities. The resulting value for Mars is $K = 2.8$ km.

The reference models, representing the two detection situations against which performance of the instrument shall be evaluated, are the following.

Ice/water interface detection: According to the model, the porosity of the Martian megaregolith is maximum at the surface and its decay with the increasing depth is given by the exponential law in (14.7). The pores are filled with ice from the surface down to a depth below which liquid water is stable and becomes the pore-filling material. The change of the pore-filling material causes a discontinuity of the overall dielectric constant, which can be detected by the radar sounder. The ice–water interface is supposed to be located at a depth between 0 m and 5000 m below the surface.

Dry/ice interface detection: This model is based on the same assumptions as the previous model w.r.t. the properties of the Martian megaregolith. However, here the pore-filling material is considered to be gas or some other vacuum-equivalent material up to a depth, below which ice fills the pores. Hence the interface to detect is between dry regolith and ice-filled regolith. Such an interface is expected to be located between 0 m and 1000 m below the surface.

14.5.3.2 Surface geometry: Images of Mars' surface from Viking Landers and Mars Pathfinder depict a gently undulating surface strewn with rocks having sizes ranging from a few centimetres to metres. Although these images cover only a minute portion of the planet surface, Mars' thermal and radar properties have prompted extensive modelling of a rock population scattered over the entire planet surface. We will thus characterise Mars' surface geometric structure in terms of a large-scale morphology on which a small-scale geometric structure, due to rocks, is superimposed. It is assumed that the surface can be described as a random distribution of heights, characterised by a variance σ_h, a correlation length L and a local surface RMS slope m. By making the assumption that the correlation function is Gaussian, the RMS slope is given by $ms = \sqrt{2}\sigma_h / L$, so that the distribution is completely determined once the values of two of these parameters are known. The terms 'large-scale' and 'small-scale' refer to different approximations in the modelling of the radar backscattering coefficient, as will be discussed in the following. The divide between 'large-scale' and 'small-scale' is essentially the radar wavelength: a plausible range for the parameters describing the surface geometry is listed in Table 14.3.

Table 14.3 Summary of the value range for the geometric parameters of the surface

Large-scale model		Small-scale model	
RMS slope (m_s)	Correlation length (L)	RMS slope (m_{s2})	RMS height (σ_{h2})
0.01–0.1 rad (0.57°–5.7°)	200–5000 m	0.1–0.6 rad (5.7°–34.3°)	0.1–1 m

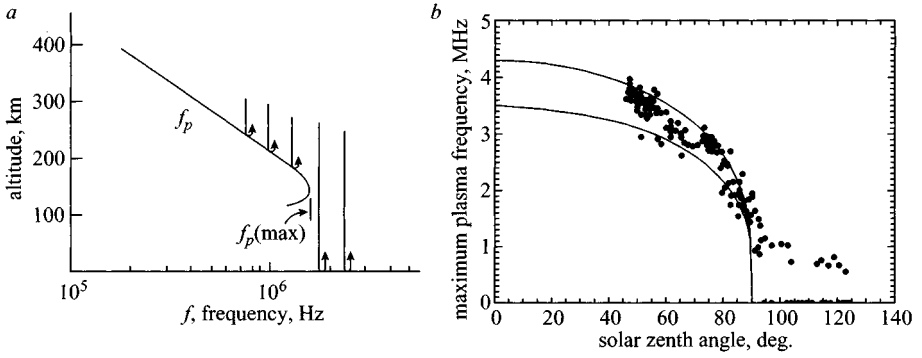

Figure 14.10 *(a) Typical plasma frequency vertical profile; (b) plasma frequency behaviour with solar zenith angle*

Following recent attempts to describe the structure of the planet's surface by means of fractals, and several papers on the analysis of MOLA (Mars Orbital Laser Altimeter) data, from the Mars Global Surveyor, a fractals model will be taken into account.

14.5.3.3 Ionosphere: It is well known that the electromagnetic radiation cannot propagate at frequencies below the electron plasma frequency (f_p), which is proportional to the square root of the electron number density. Figure 14.10*a* shows the vertical profile of f_p and the behaviour against solar zenith angle.

Normally, the electron plasma frequency has a single, well defined maximum, f_p(max), at an altitude of about 125 to 150 km. Radio signals from a sounder passing over at an altitude of several hundred km are reflected by the ionosphere at all frequencies below f_p(max). Sub-surface soundings are possible only at frequencies greater than f_p(max). Since sub-surface soundings require frequencies as low as possible, the global distribution of the ionospheric electron density (hence plasma frequency) becomes an important factor in selecting the operating frequency of the sounder and the optimal orbital strategy for data collection. The lowest frequency that can penetrate the Martian ionosphere varies from about 4 MHz on the dayside of Mars to somewhat below 1 MHz on the nightside of Mars. Clearly, the best region for carrying out sub-surface soundings is on the nightside, at solar zenith angles greater than 90°. Unfortunately, very little is known about the ionosphere on the nightside of Mars. A typical nightside maximum plasma frequency appears to be about 800 kHz.

Even when the sounding frequency is higher than the plasma frequency, the propagation through the ionosphere will produce a phase shift which must be compensated in some way when using long time dispersed pulse compression waveforms, such as chirps.

14.5.3.4 Orbit requirements: From previous considerations, the MARSIS' main objective is the mapping of the global distribution of the water on Mars. The following is required:

- detection of the water/ice and dry/water interfaces in the regolith
- direct measurement of the thickness of the polar deposits
- determination of the dielectric properties of detected interface.

To accomplish this requirement, MARSIS desires night-side opportunity at all latitudes: the ionospheric plasma frequency drops significantly from the day to the night side of the planet, allowing the use of lower frequencies, which have greater sub-surface penetration depths. Although the instrument can acquire useful data in its dayside mode, it is recommended that an orbit with substantial nightside periapsis passes be considered. Low latitudes are highest priority for deep night periapsis. Moreover the high inclination orbit is preferred (inclination $>85°$), to allow coverage in the scientifically interesting polar regions, and for the general goal of increased (global) coverage.

Ionospheric sounding observations will be integrated with the sub-surface sounding in order to give global coverage of the ionospheric electron density (day sounding mode).

The baseline orbit has the following characteristics:

- distance at periapsis: 250 km
- distance at apoapsis: 10 142 km
- inclination: 86.35°
- orbital period: 6.75 h.

In Figure 14.11, the tangential and radial components of the spacecraft orbital velocity are shown, as a function of altitude above the Martian equatorial radius.

MARSIS was designed in order to operate at any altitude lower than 800 km; performance improves with lower altitudes of operation. A highly eccentric orbit, such as the baseline orbit, places the spacecraft within 800 km for a period of about 26 min. This would allow mapping of about 100 deg. of arc on the surface of Mars each orbit.

14.5.4 Surface and sub-surface scattering models

To assess the interface detection performance of the Radar Sounder it is required to evaluate the strength of the returned echoes from the surface and sub-surface layers, as operative conditions change. These can be expressed in term of cross-sections as follows:

$$S_S = \Gamma_S f_S(\sigma_h, L_s, \lambda) \tag{14.8}$$

$$S_{SS} = \gamma(z')\Gamma_{SS} f_{SS}(\sigma_{h2}, L_{ss}, \lambda) \tag{14.9}$$

where Γ_S and Γ_{SS} are the Fresnel reflectivity terms, which deal with the surface and sub-surface dielectric properties, respectively. f_s and f_{ss} are the geometrical

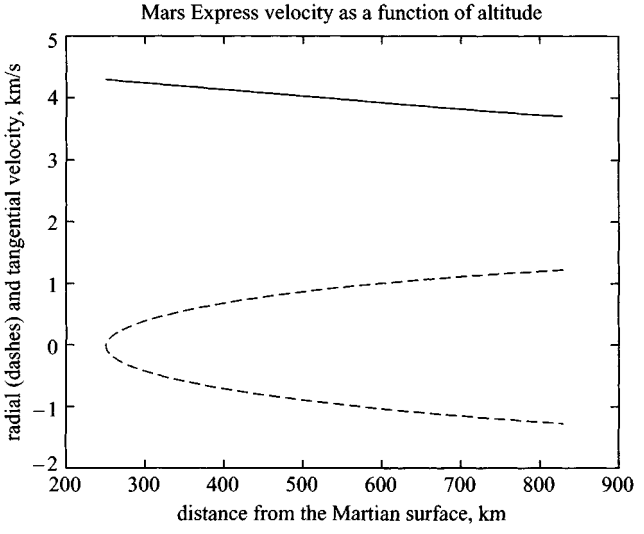

Figure 14.11 Radial and tangential spacecraft velocity

scattering terms, which deal with the geometrical structure of the surface and sub-surface, respectively, and $\gamma(z')$ is the first layer two-way attenuation (z' is the depth of the layer).

In the following Sections we will evaluate both the Fresnel terms and the geometric scattering terms developing simplified models against the reference scenarios defined in the previous Sections.

14.5.4.1 Fresnel coefficients and sub-surface attenuation: It should be noted that, since porosity depends on the depth, so will the effective dielectric constants of the mixture. To evaluate the mixture dielectric constants, the Maxwell–Garnett model [35] can be used:

$$\varepsilon_m(z) = \varepsilon_h \frac{1 + 2\phi(z)y}{1 - \phi(z)y} \tag{14.10}$$

where

$$y = \frac{\varepsilon_i - \varepsilon_h}{\varepsilon_i + 2\varepsilon_h} \tag{14.11}$$

and $\phi(z)$ is the porosity at depth z.

Using (14.10), the effective dielectric constant of the mixtures which have been selected to represent the Martian porous regolith (see also Table 14.2) can be evaluated, as a function of the depth, and of the surface porosity. Therefore the well known surface Fresnel reflectivity for nadir incidence (from free-space propagation) can be

Table 14.4 Fresnel reflectivity for ice water and dry ice models

	$\Gamma_{s\|dB}$			
	I/W		*D/I*	
	50%	20%	50%	20%
I	−9.5	−9	−12	−9.5
II	−7.5	−6.5	−9	−7
III	−8.5	−7.5	−10	−8

evaluated:

$$\Gamma_S = \left|\frac{1-\sqrt{\varepsilon_{r1}(0)}}{1+\sqrt{\varepsilon_{r1}(0)}}\right|^2 = R_{01}^2 \tag{14.12}$$

$\varepsilon_{r1}(0)$ being the real dielectric constant of the crust evaluated at the surface ($z = 0$).

The selected models make the surface reflectivity ranging between −6 dB and −10 dB for the ice/water situation and −7 dB and −12 dB for the dry/ice situation (Table 14.4).

The Fresnel reflectivity for a sub-surface layer located at a depth z' can be expressed as follows:

$$\Gamma_{SS,z'} = R_{12,z'}^2(1-R_{01}^2)^2 10^{-0.1\int_0^{z'}\alpha(z)\,dz} = R_{12,z'}^2(1-R_{01}^2)^2 10^{-0.1\gamma(z')} \tag{14.13}$$

$R_{12,z'}^2$ being the reflection coefficient of such an interface:

$$R_{12,z'}^2 = \left|\frac{\sqrt{\varepsilon_{r1}(z')}-\sqrt{\varepsilon_{r2}(z')}}{\sqrt{\varepsilon_{r1}(z')}+\sqrt{\varepsilon_{r2}(z')}}\right|^2 \tag{14.14}$$

By the defined crust materials, we have obtained for the two situations (Table 14.5):

$$\begin{aligned} &\text{Ice water:} && R_{12,z'}^2 \cong (-10 \div -18) - 3\,\text{dB/km} \\ &\text{Dry ice:} && R_{12,z'}^2 \cong (-20 \div -28) - 3\,\text{dB/km} \end{aligned} \tag{14.15}$$

where the first term is related to the first layer porosity and the last one is due to the decrease of the porosity with the depth. Notice that the $R_{12,z'}^2$ is near crust material independent. Concerning the two-way attenuation:

$$\alpha_{dB/m}(z) = 1.8 \times 10^{-7} f_0 \sqrt{\varepsilon(z)} \tan\delta(z) \tag{14.16}$$

we have obtained, as a good approximation, the functions detailed in Table 14.6.

Table 14.5 Reflection coefficient of interfaces for ice water and dry ice models

z', m	$R^2_{12,z'}\|_{dB}$			
	I/W		*D/I*	
	50%	20%	50%	20%
0	−10	−17	−22	−25
1000	−12	−20	−26	−32
2000	−15	−23	−28	−36
3000	−18	−26	−31	−38
4000	−21	−28	−33	−42
5000	−24	−31	−35	−46

Table 14.6 Ice water and dry ice model values (z depth in km)

	$\alpha(z)\|$ dB/km MHz			
	I/W		*D/I*	
	50%	20%	50%	20%
I	$(0.8 + 0.1z)$	$(1.3 + 0.05z)$	$(0.9 + 0.1z)$	$(1.3 + 0.05z)$
III	$(3.7 + 0.54z)$	$(6 + 0.25z)$	$(4.3 + 0.54z)$	$(6.3 + 0.25z)$
II	$(8.5 + 1.1z)$	$(13.3 + 0.5z)$	$(9.5 + 1.1z)$	$(13.7 + 0.5z)$

By supposing that the surface and the sub-surface interfaces have the same roughness, we can write

$$S_S|_{dB} = \Gamma_s|_{dB} + f_s|_{dB}$$

$$S_{SS}|_{dB} = R^2_{12}\Big|_{dB} + \gamma|_{dB} + f_{ss}|_{dB} \Leftrightarrow f_{ss}|_{dB} = f_s|_{dB}$$

$$\frac{S_{SS}}{S_S}\Big|_{dB} \cong R^2_{12}\Big|_{dB} + \gamma|_{dB} - \Gamma_s|_{dB} = \alpha_{SS}|_{dB} \tag{14.17}$$

so that we can obtain the depth related to a proper dynamic range, usually defined by the noise power to surface return echo:

$$\frac{S_{SSMIN}}{S_S}\Big|_{dB} = \frac{P_N}{S_S}\Big|_{dB} \Rightarrow \text{depth} \tag{14.18}$$

Moreover, by Table 14.7 we obtain the attenuation detailed in Table 14.8 and in Figure 14.12, so that the depths available for S/N 40 and 50 dB, to be evaluated from surface data (MOLA) are shown in Table 14.9.

Table 14.7 Reflection values for ice water and dry ice model values

	$R_{12\|dB} - \Gamma_{s\|dB} + 3$ dB/km			
	I/W		*D/I*	
	50%	20%	50%	20%
I	0	−8	−9.5	−15.5
II	−2	−10.5	−12.5	−18
III	−1	−10	−11.5	−17

Table 14.8 Attenuation values for ice water and dry ice model values

	$\alpha_{SS\|dB}$		
	I	II	III
I/W 50%	$-(3+0.8f_0)z - 0.05f_0z^2$	$-2-(3+9f_0)z - 0.55f_0z^2$	$-1-(3+4f_0)z - 0.27f_0z^2$
I/W 20%	$-8-(3+1.3f_0)z - 0.025f_0z^2$	$-10.5-(3+13.5f_0)z - 0.25f_0z^2$	$-10-(3+6f_0)z - 0.125f_0z^2$
D/I 50%	$-9.5-(3+0.8f_0)z - 0.05f_0z^2$	$-12.5-(3+9f_0)z - 0.55f_0z^2$	$-11.5-(3+4f_0)z - 0.27f_0z^2$
D/I 20%	$-15.5-(3+1.3f_0)z - 0.025f_0z^2$	$-18-(3+13.5f_0)z - 0.25f_0z^2$	$-17-(3+6f_0)z - 0.125f_0z^2$

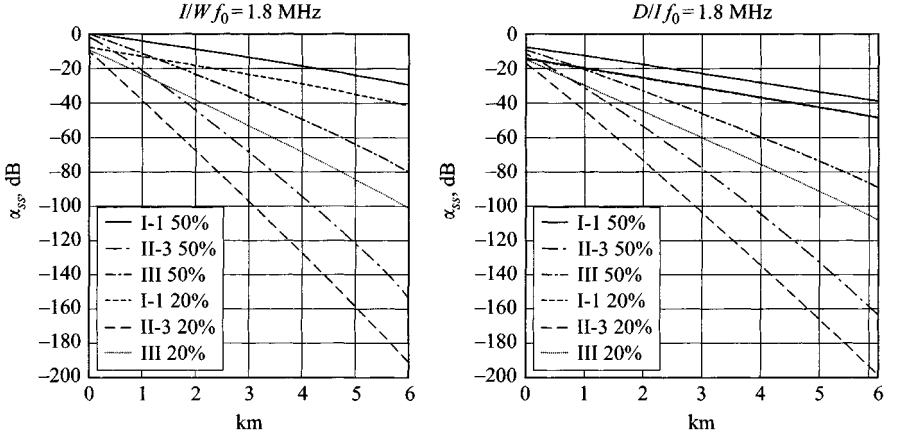

Figure 14.12 Attenuation versus range for ice water and dry ice

Table 14.9 Parameter values for various model situations

	ε'	$\tan\delta$	I/W Depth, km (40 dB)	I/W Depth, km (50 dB)	D/I Depth, km (40 dB)	D/I Depth, km (50 dB)
I	5	0.004	>5	>5	4.4 –>5	>5
II	9	0.03	1.1 – 1.8	1.5 – 2.2	0.8 – 1.3	1.1 – 1.8
III	7.1	0.014	2.1 – 3.3	2.8 – 4	1.6 – 2.5	2.3 – 3.3

14.5.4.2 Surface backscattering models: Taking into account Table 14.3, we can form the hypothesis that the Martian surface back scattering can be described considering two main terms: (i) large scale scattering contribution, resulting from gentle geometrical undulations of the surface on a scale of many hundreds to thousands of metres; (ii) small scale scattering contribution, explaining the fast, slight variations of the surface height over a horizontal scale of some tenths of metres.

From the statistical point of view, the surface height was modelled as a Gaussian random process, σ_h being the total surface RMS height. At a second order level we can write the characteristic function:

$$\langle e^{j\frac{2\cos\theta}{c}(\omega_1 z_1-\omega_2 z_2)}\rangle = e^{-2\sigma_{h1}^2\frac{\cos^2\theta}{c^2}(\omega_1^2+\omega_2^2-2\rho(x_1,x_2,y_1,y_2)\omega_1\omega_2)} \tag{14.19}$$

where $\rho(x_1, x_2, y_1, y_2)$ is the two-dimensional correlation coefficient of the surface; moreover, if we suppose (as usual) an isotropic correlation coefficient and we turn to the polar co-ordinates axis, we can use the simplified notation $\rho(|\vec{r}_2 - \vec{r}_1|)$.

Simple approximate methods can be applied for surfaces which present a unique roughness scale, with either a big correlation length (gently undulating surface) or a very small RMS height (slightly rough surface) compared to the incident wavelength. Specifically, the Kirchhoff method can be applied for gently undulating surfaces, which respect the tangent plane conditions, and the small perturbation method can be applied to slightly rough surfaces. The classical studies on the validity conditions of these two models [35] have been recently updated [36], and regions of validity currently defined are reported in Figure 14.13. It is evident from these Figures that the Kirchhoff approximation can be used to evaluate the large scale backscattering contribution, whereas the small perturbation method can be used for the small scale contribution.

14.5.4.3 Large scale (Kirchhoff) contribution: Under Kirchhoff approximation hypotheses the scattered electric field E_S from an irregular surface S, due to a spherical incident wave e^{jkR_1}/R_1, is given by [37]

$$E_S = -\frac{j}{2\lambda}\int_S R(P)\frac{\hat{n}(2\hat{R}_1)}{R_1^2}e^{-jk2R_1}\,\mathrm{dS} \tag{14.20}$$

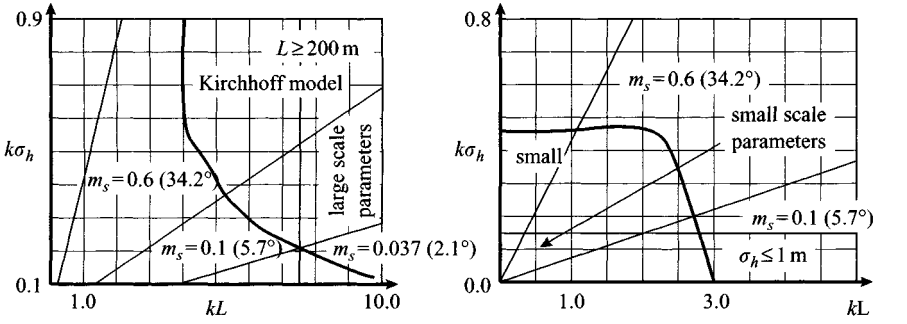

Figure 14.13 *Kirchhoff and small perturbation approximation validity conditions $K = 2\pi/\lambda$, σ_h = rms surface height, L = correlation length, m_s = rms surface slope*

where P is the generic point on the surface, λ is the wavelength, $R(P)$ is the Fresnel reflection coefficient of the point P on the surface S, R_1 is the distance from radar to the point P, $\hat{R}_1$ is the unit vector corresponding to the path from the radar to the point P, $\hat{n}$ is the unit vector normal to the surface in the point P, and finally $k = 2\pi/\lambda$ is the wavenumber. If, on the contrary, the radar transmits a pulse $f(t)$, the scattered electric field becomes

$$E_S(t) = \frac{1}{2\pi}\int_{-\infty}^{\infty} F(\omega) E_S e^{j\omega t}\, \mathrm{d}\omega \tag{14.21}$$

where $F(\omega)$ is the Fourier transform of the transmitted pulsed waveform. Therefore (14.20) becomes

$$E_S(t) = \frac{1}{2\pi}\int_{-\infty}^{\infty} F(\omega)\left(-\frac{j}{2\lambda}\right)\int_S R(P)\frac{\hat{n}(2\hat{R}_1)}{R_1^2} e^{-jk2R_1}\, \mathrm{dS} e^{j\omega t}\, \mathrm{d}\omega \tag{14.22}$$

and exchanging the integration variables we have

$$E_S(t) = -\frac{1}{4\pi c}\int_S R(P)\frac{\hat{n}(2\hat{R}_1)}{R_1^2}\int_{-\infty}^{\infty} j\omega F(\omega) e^{j\omega\left(t-\frac{2R_1}{c}\right)}\mathrm{d}\omega\mathrm{dS} \tag{14.23}$$

If we make the further hypothesis that surface tilts are small enough to allow that we confuse the local normal to the surface with the vertical axis, we have $\hat{n}\cdot\hat{R}_1 \approx \hat{z}\cdot\hat{R}_1 = \cos\theta$, where θ is the incidence angle with respect to the vertical. Moreover the distance from the radar to the generic point P(x, y, z) can be approximated, under the far-field approximation, as

$$R_1 \approx H - z\cos\theta + \frac{x^2 + y^2}{2H} \tag{14.24}$$

where H is the distance from the radar to the mean surface. With all these assumptions, (14.23) becomes

$$E_S(\tau) = -\frac{2}{4\pi c}\frac{\cos\theta}{H^2}R(\theta)\int_S \mathrm{d}S \int_{-\infty}^{\infty} e^{j\omega(\tau-\frac{x^2+y^2}{Hc}+\frac{2z\cos\theta}{c})} j\omega F(\omega)\,\mathrm{d}\omega \quad (14.25)$$

where $\tau = t - 2H/c$ and the angle of incidence θ has been supposed to undergo no significant variation within the pulse limited integration area, and has therefore been taken out of the surface integral.

The average scattered power at time τ can be evaluated taking the average of the product of the scattered electric field with its complex conjugate:

$$\begin{aligned}&\langle E_S(\tau)E_S^*(\tau)\rangle \\ &= \frac{4\Gamma_S(\theta)}{(4\pi cH^2)^2}\cos^2\theta \int \mathrm{d}\omega_1 \int \mathrm{d}\omega_2\omega_1\omega_2 F(\omega_1)F^*(\omega_2)e^{j(\omega_1-\omega_2)\tau} \\ &\quad\cdot \int_{S_1}\mathrm{d}S_1\int_{S_2}\mathrm{d}S_2 e^{-\frac{j}{cH}[\omega_1(x_1^2+y_1^2)-\omega_2(x_2^2+y_2^2)]}\langle e^{j\frac{2\cos\theta}{c}(\omega_1 z_1-\omega_2 z_2)}\rangle\end{aligned} \quad (14.26)$$

where $\Gamma_S(\theta) = |R(\theta)|^2$ is the Fresnel reflection coefficient and the statistic averaging operation (two-dimensional characteristic function) is given by (14.19); therefore the previous equation can be rewritten as

$$\begin{aligned}&\langle E_S(\tau)E_S^*(\tau)\rangle \\ &= \frac{4\Gamma_S(\theta)}{(4\pi cH^2)^2}\cos^2\theta \int_{-\infty}^{\infty} \mathrm{d}\omega_1 \int_{-\infty}^{\infty} \mathrm{d}\omega_2\omega_1\omega_2 F(\omega_1)F^*(\omega_2)e^{j(\omega_1-\omega_2)\tau} \\ &\quad\cdot \int_{S_1}\mathrm{d}S_1\int_{S_2}\mathrm{d}S_2 e^{-j\frac{1}{cH}(\omega_1 r_1^2-\omega_2 r_2^2)}e^{-2\frac{\sigma_h^2}{c^2}\cos^2\theta(\omega_1^2+\omega_2^2-2\omega_1\omega_2\rho(|\vec{r}_2-\vec{r}_1|))}\end{aligned} \quad (14.27)$$

Assuming a Gaussian correlation coefficient (Gaussian roughness spectrum),

$$\rho(|\vec{r}_2-\vec{r}_1|) = e^{-\frac{|\vec{r}_2-\vec{r}_1|^2}{L^2}} \quad (14.28)$$

we can write with good approximation (validate for $|\vec{r}_2-\vec{r}_1| = 0$ and $|\vec{r}_2-\vec{r}_1| = \infty$),

$$e^{4\frac{\sigma_h^2}{c^2}\omega_1\omega_2\cos^2\theta\rho(|\vec{r}_2-\vec{r}_1|)} \approx \left[e^{\frac{4\sigma_h^2}{c^2}\omega_1\omega_2\cos^2\theta}-1\right] e^{-\frac{4\sigma_h^2\omega_1\omega_2\cos^2\theta|\vec{r}_2-\vec{r}_1|^2}{c^2L^2\left(1-\exp\left\{-\frac{4\sigma_h^2}{c^2}\omega_1\omega_2\cos^2\theta\right\}\right)}} + 1 \quad (14.29)$$

and (14.27) becomes

$$\langle E_S(\tau)E_S^*(\tau)\rangle = I_1 + I_2 \quad (14.30)$$

where I_1 (coherent contribution) is given by

$$I_1 = \frac{4\Gamma_S(\theta)}{(4\pi cH^2)^2}\cos^2\theta \int_{-\infty}^{\infty} d\omega_1 \int_{-\infty}^{\infty} d\omega_2 \omega_1\omega_2 F(\omega_1)F^*(\omega_2)e^{j(\omega_1-\omega_2)\tau}$$
$$\cdot \int_{S_1} dS_1 \int_{S_2} dS_2 e^{-j\frac{1}{cH}(\omega_1 r_1^2-\omega_2 r_2^2)} e^{-2\frac{\sigma_h^2}{c^2}\cos^2\theta(\omega_1^2+\omega_2^2)} \tag{14.31}$$

Moreover

$$\int_{S_1} dS_1 \int_{S_2} dS_2 e^{-j\frac{1}{cH}(\omega_1 r_1^2-\omega_2 r_2^2)}$$
$$= \frac{2\pi^2 cH}{j(\omega_1-\omega_2)} \int_0^{\infty} r' e^{j\frac{\omega_1\omega_2}{cH(\omega_1-\omega_2)}r'^2} dr' = \frac{\pi^2 c^2 H^2}{\omega_1\omega_2} \tag{14.32}$$

Therefore

$$I_1 = \frac{\Gamma_S(\theta)}{4H^2}\cos^2\theta \left| \int_{-\infty}^{+\infty} F(\omega_1)e^{j\omega_1\tau} e^{-\frac{2\sigma_h^2}{c^2}\cos^2\theta\omega_1^2} d\omega_1 \right|^2 \tag{14.33}$$

and I_2 (noncoherent contribution) is given by

$$I_2 = \frac{4\Gamma_S(\theta)}{(4\pi cH^2)^2}\cos^2\theta \int_{-\infty}^{+\infty} d\omega_1 \int_{-\infty}^{+\infty} d\omega_2 \omega_1\omega_2 F(\omega_1)F(\omega_2)e^{j(\omega_1-\omega_2)\tau}$$
$$\cdot \left[e^{-\frac{2\sigma_h^2}{c^2}(\omega_1-\omega_2)^2} - e^{-\frac{2\sigma_h^2}{c^2}(\omega_1^2+\omega_2^2)} \right] \cdot \int_{S_1} dS_1 \int_{S_2} dS_2 e^{-j\frac{1}{cH}(\omega_1 r_1^2-\omega_2 r_2^2)}$$
$$\cdot \exp\left[-\frac{4\sigma_h^2\omega_1\omega_2\cos^2\theta\,|\vec{r}_2-\vec{r}_1|^2}{c^2L^2\left(1-\exp\left\{-\frac{4\sigma_h^2}{c^2}\omega_1\omega_2\cos^2\theta\right\}\right)} \right] \tag{14.34}$$

We can write

$$I_2 = \frac{\Gamma_S(\theta)}{2cH^3}\cos^2\theta \int_{-\infty}^{+\infty} d\omega_1 \int_{-\infty}^{+\infty} d\omega_2 \omega_1\omega_2 F(\omega_1)F(\omega_2)e^{j(\omega_1-\omega_2)\tau}$$
$$\cdot \left[e^{-\frac{2\sigma_h^2}{c^2}(\omega_1-\omega_2)^2} - e^{-\frac{2\sigma_h^2}{c^2}(\omega_1^2+\omega_2^2)} \right] \int_0^{\infty} d\tau_d e^{-j(\omega_1-\omega_2)\tau_d}$$
$$\cdot \int_0^{\infty} dr' r' J_0\left(2r'\sqrt{\frac{\omega_1\omega_2\tau_d}{cH}}\right)$$
$$\cdot \exp\left[-\frac{4\sigma_h^2\omega_1\omega_2\cos^2\theta r'^2}{c^2L^2\left(1-\exp\left\{-\frac{4\sigma_h^2}{c^2}\omega_1\omega_2\cos^2\theta\right\}\right)} \right] \tag{14.35}$$

so that

$$I_2 = \frac{\Gamma_S(\theta) c L^2}{4H^3\sigma_h^2} \int_{-\infty}^{+\infty} d\omega_1 \int_{-\infty}^{+\infty} d\omega_2 F(\omega_1) F(\omega_2)$$
$$\cdot \left[e^{-\frac{2\sigma_h^2}{c^2}(\omega_1-\omega_2)^2} - e^{-\frac{2\sigma_h^2}{c^2}(\omega_1^2+\omega_2^2)} \right] \left(1 - \exp\left\{ -\frac{4\sigma_h^2}{c^2}\omega_1\omega_2 \cos^2\theta \right\} \right)$$
$$\cdot \int_0^{\infty} d\tau_d e^{j(\omega_1-\omega_2)(\tau-\tau_d)}$$
$$\cdot \exp\left[-\frac{c^2 L^2 \left(1 - \exp\left\{ -\frac{4\sigma_h^2}{c^2}\omega_1\omega_2 \cos^2\theta \right\} \right) \tau_d}{\sigma_h^2 c H \cos^2\theta} \right] \tag{14.36}$$

By considering a Gaussian shape for the compressed pulse,

$$f(t) = e^{-\frac{t^2}{4\sigma_P^2}} \cos\omega_0 t \tag{14.37}$$

we have a Gaussian pulse spectrum

$$F(\omega) = \frac{1}{2}\{S[j(\omega-\omega_0)] + S[j(\omega+\omega_0)]\} \quad \longrightarrow \quad S(j\omega) = \frac{\sigma_P}{\sqrt{\pi}} e^{-\sigma_P^2\omega^2} \tag{14.38}$$

where ω_0 is the carrier frequency and σ_P is related to the system bandwidth B_W by the relation $\sigma_P \approx 0.37/B_W$.

Applying (14.38) to (14.33) we obtain the coherent (specular) scattering component,

$$I_1 = \frac{\Gamma_S(\theta)}{4H^2} \cos^2\theta P_c(\tau) \longrightarrow P_c(\tau) = \frac{1}{1+F} e^{-\frac{(2k\sigma_{h1}\cos\theta)^2}{1+F}} e^{-\frac{\tau^2}{2\sigma_P^2(1+F)}} \tag{14.39}$$

where

$$F = \frac{1}{2}\frac{\sigma_{h1}^2 \cos^2\theta}{\left(\frac{c\sigma_P}{2}\right)^2} \quad \text{normalised projected roughness}$$

$$\sigma_{eq} = \sqrt{\sigma_P^2 + \left(\frac{2\sigma_{h1}\cos\theta}{c}\right)^2} = \sigma_P\sqrt{1+2F} \quad \text{equivalent pulse width}$$

$$\beta = \frac{c\sigma_P}{2H}\frac{\sqrt{1+2F}}{m_s^2\cos\theta}\left(1 - e^{-(2k\sigma_{h1}\cos\theta)^2}\right) \quad \text{surface parameter}$$

These hypotheses lead to the following results:

$$\langle E_S(\tau) E_S^*(\tau) \rangle = \Gamma(\theta)\frac{1}{4H^2}\cos^2\theta(P_c + P_{nc1} - P_{nc2}) \tag{14.40}$$

where $P_c(\tau)$ is

$$P_c(\tau) = \frac{1}{1+F} e^{-\frac{(2k\sigma_{h1}\cos\theta)^2}{1+F}} e^{-\frac{\tau^2}{2\sigma_P^2(1+F)}} \tag{14.41}$$

while $P_{nc}(\tau) = P_{nc1}(\tau) - P_{nc2}(\tau)$ is the noncoherent (diffuse) scattering component.

$$P_{nc1}(\tau) = \frac{\beta}{\sqrt{1+2F}} \sqrt{\frac{\pi}{2}} e^{\frac{\beta^2}{2}} e^{-\beta\frac{\tau}{\sigma_P\sqrt{1+2F}}} \operatorname{Erfc}\left[\frac{1}{\sqrt{2}}\left(\beta - \frac{\tau}{\sigma_P\sqrt{1+2F}}\right)\right] \tag{14.42}$$

$$P_{nc2}(\tau) = \frac{\beta}{\sqrt{1+F}\sqrt{1+2F}} \sqrt{\frac{\pi}{2}} e^{-\frac{(2k\sigma_{h1}\cos\theta)^2}{1+F}} e^{\frac{\beta^2(1+F)}{2(1+2F)}} e^{-\beta\frac{\tau}{\sigma_P\sqrt{1+2F}}} \cdot \operatorname{Erfc}\left[\frac{1}{\sqrt{2}}\left(\beta\sqrt{\frac{1+F}{1+2F}} - \frac{\tau}{\sigma_P\sqrt{1+F}}\right)\right] \tag{14.43}$$

where

$$F = \frac{1}{2}\frac{\sigma_{h1}^2\cos^2\theta}{\left(\frac{c\sigma_P}{2}\right)^2} \quad \text{normalised projected roughness}$$

$$\sigma_{eq} = \sqrt{\sigma_P^2 + \left(\frac{2\sigma_{h1}\cos\theta}{c}\right)^2} = \sigma_P\sqrt{1+2F} \quad \text{equivalent pulse width}$$

$$\beta = \frac{c\sigma_P}{2H}\frac{\sqrt{1+2F}}{m_s^2\cos\theta}\left(1 - e^{-(2k\sigma_{h1}\cos\theta)^2}\right) \quad \text{surface parameter}$$

The cross-section of the large scale surface model is given by

$$\sigma_1(\tau) = \frac{\langle E_S(\tau)E_S^*(\tau)\rangle}{\langle E_I(\tau)E_I^*(\tau)\rangle} 4\pi H^2 \tag{14.44}$$

and therefore we have:

$$\sigma_1(\tau) = \pi H^2 \Gamma_S(\theta)\cos^2\theta(P_c + P_{nc1} - P_{nc2}) \tag{14.45}$$

The maximum power is received if full coherent reflection occurs, i.e. when the surface is perfectly flat ($\sigma_{h1} = 0$). In such a condition it is easy to verify that $P_{nc1} = P_{nc2}$ and the noncoherent term P_{nc} decreases to zero, while the coherent term P_c approaches the shape of the transmitted pulse, which is maximum for $\tau = 0$, so that

$$\sigma_{1,MAX}(0) = \Gamma_S(0)\pi H^2 \tag{14.46}$$

which is a value consistent with the backscattering of the perfectly flat surfaces. As the surface becomes rougher ($\sigma_{h1} \gg \lambda$) the coherent component decreases towards

zero and the noncoherent scattering becomes:

$$\sigma_{1MAX,NC} = \Gamma_S(0)\pi H^2 \frac{\beta}{\sqrt{1+2F}} \sqrt{\frac{\pi}{2}} 2e^{-\frac{\beta^2}{2}} \approx \Gamma_S(0)\pi H \frac{c\sigma_P}{2} \sqrt{2\pi} \frac{1}{m_s^2}$$
$$= \Gamma_S(0)\pi H \frac{c(0.37)}{2B_w} \sqrt{2\pi} \frac{1}{m_s^2} = \Gamma_S(0)\pi H \frac{c}{2B_w} \frac{1}{m_s^2} \tag{14.47}$$

according to the geometrical optics model. Also, $\sqrt{2Hc/(2B_w)}$ is the radius of the pulse-limited region of the well known radar altimeter, which is expected to be around 15/30 km.

The analytical model used here is based on the assumption that a sufficiently large number of independent scatters can be averaged within the area illuminated by the propagating pulse. Therefore taking into account the radius of the pulsed limited region, correlation lengths have been considered up to a few km. On the other hand, when the correlation length of the surface exceeds the pulse limited area dimension, performing the ensemble average on the scattering area is invalid, because it appears that the radar was observing a locally flat tilted plane, rather than a gently undulating surface: as a consequence the scattered power is expected to be almost entirely due to the coherent component, corrected with a random periodical term which modulates the intensity of the reflected wave. This case cannot be analysed using the developed model and must be studied by means of numerical simulations.

As regards the frequency dependence of the Kirchhoff backscattered power, it is evident that, as long as the geometrical optics model hypotheses hold, there is no significant variation of the backscattered power with the wavelength. On the contrary, for each value of the RMS slope, a frequency dependence is expected when the correlation length decreases, because the RMS height decreases correspondingly, making inappropriate the applicability of the geometrical optics model.

14.5.4.4 Small scale contribution: According to the region of validity reported in Figure 14.13, the small scale scattering term can be computed by means of the small perturbation method [35], which allows us to express the backscattering coefficient as follows:

$$\sigma^0_{pp}(\theta) = 8k^4\sigma^2_{h2}|\alpha_{pp}(\theta)|^2 \cos^4\theta W_2(K_B) \tag{14.48}$$

where $k = 2\pi/\lambda$ is the wave number, θ is the incidence angle, $\alpha_{pp}(\theta)$ is the Fresnel reflection coefficient for the *pp* polarisation, $W_2(K_B)$ is the surface roughness small scale spectrum:

$$W_2(K_B) = \int_0^\infty \rho_2(\xi) J_0(K_B\xi)\xi \, d\xi \tag{14.49}$$

ρ_2 is the correlation coefficient, and K_B is the Bragg frequency, given by

$$K_B = 2k \sin\theta$$

The Fresnel coefficient is given for both like-polarisations by the following relations:

$$|\alpha_{hh}(\theta)|^2 = |R_h(\theta)|^2 = \Gamma_{hh}(\theta) = \left| \frac{\cos\theta - \sqrt{\varepsilon_r - \sin^2\theta}}{\cos\theta + \sqrt{\varepsilon_r - \sin^2\theta}} \right|^2 \tag{14.50}$$

$$|\alpha_{vv}(\theta)|^2 = \left| (\varepsilon_r - 1) \frac{\sin^2\theta - \varepsilon_r(1 + \sin^2\theta)}{(\varepsilon_r \cos\theta + \sqrt{\varepsilon_r - \sin^2\theta})^2} \right|^2 \tag{14.51}$$

Hence the small scale scattered cross-section can be retrieved by the following integral:

$$\sigma_2(\tau) = 8k^4\sigma_{h2}^2 \int_0^{2\pi} \int_0^{\infty} |\alpha(\theta)|^2 \cos^4(\theta) W_2(2k\sin\theta) f\left(\tau - \frac{\rho^2}{cH}\right) \rho \, d\rho \, d\phi \tag{14.52}$$

where ρ, ϕ are the polar co-ordinates for the antenna illuminated surface, θ is the incidence angle with respect to the nadir, $f(t)$ is the transmitted pulse waveform after compression, and the following relations apply:

$$\theta = \tan^{-1}\frac{\rho}{H}$$

$$\rho \cong \sqrt{Hct} \Rightarrow t \cong \frac{\rho^2}{cH} \tag{14.53}$$

The Fresnel coefficient $\alpha(\theta)$ changes very smoothly with the incidence angle for both polarisations, so that we can neglect its variation within the area illuminated by the pulse. Moreover we will assume for the sake of simplicity a rectangular shape (time length T) for the transmitted pulse after compression (i.e. the effect of the waveform sidelobes will be neglected), and two kinds of roughness spectra:

1. Gaussian law small scale roughness spectrum

$$W_G(K) = \frac{L^2}{2} e^{-\left(\frac{KL}{2}\right)^2} \tag{14.54}$$

related to a Gaussian correlation coefficient,

$$\rho_G(\xi) = e^{-\frac{\xi^2}{L^2}} \tag{14.55}$$

L being the correlation length of the surface. The backscattering cross-section can be found to be

$$\sigma_{2,G}(\tau) = Q_0(\tau)\left(1 - e^{-k^2L_2^2\frac{cT}{H}}\right) e^{-kL_2^2\frac{c\tau}{H}} \tag{14.56}$$

where

$$Q_0(\tau) = 4\pi H^2 k^4 \sigma_{h2}^2 \left|\alpha\left(\sqrt{\frac{c\tau}{H}}\right)\right|^2 \cos^4\left(\sqrt{\frac{c\tau}{H}}\right)$$

2. Exponential law small scale roughness spectrum
The roughness spectrum

$$W_E(K) = L^2[1 + (KL)^2]^{-\frac{3}{2}} \tag{14.57}$$

corresponding to an exponential correlation coefficient

$$\rho_E(\xi) = e^{-\frac{|\xi|}{L}} \tag{14.58}$$

entails

$$\sigma_{2,E}(\tau) = Q_0(\tau)\left[\left(1 + 2kL_2\sqrt{\frac{c\tau}{H}}\right)e^{-2kL_2\sqrt{\frac{c\tau}{H}}} - \left(1 + 2kL_2\sqrt{\frac{c(\tau+T)}{H}}\right)e^{-2kL_2\sqrt{\frac{c(\tau+T)}{H}}}\right]$$

We can now summarise the surface backscattered power, summing up the large scale and small scale contributions. Assuming as a reference case a Gaussian correlation for the large scale component and an exponential correlation for the small scale one, we have for the global cross-section

$$\sigma_T(\tau) = \sigma_1(\tau) + \sigma_2(\tau)$$

Figures 14.14 and 14.15 show the surface cross-section (thick lines) given by (14.34), assuming the worst case small scale contribution and the large range of parameters for the large scale term. The plots are normalised so that the zero-dB axis

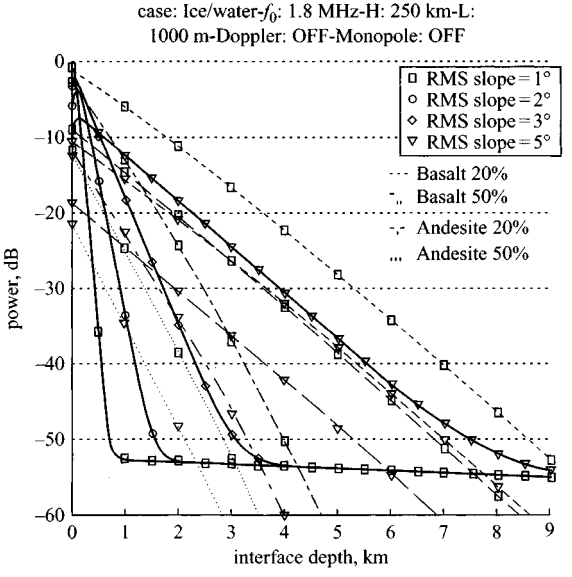

Figure 14.14 Ice/water (band I), H = 250 km

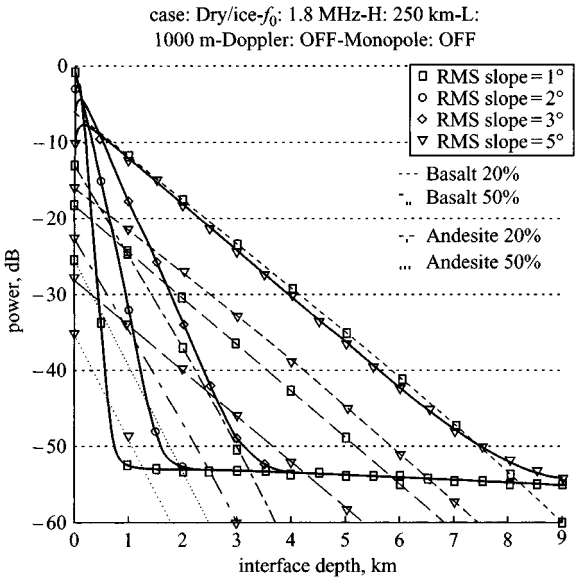

Figure 14.15 Dry/ice (band I), $H = 250$ km

indicates the maximum possible cross-section, which is given again by (14.46). As seen in the Figure, the scattering cross-section is maximum at nadir and rapidly falls down as the 'equivalent depth' increases, up to a level at which it becomes practically a constant. This behaviour is easily understood considering the superimposition of the two scale contributions: in fact the large scale Kirchhoff component determines the cross-section fall-off rate (due to the small value of m_{s1}), while the small perturbation component is responsible for the flat behaviour of the same cross-section when the Kirchhoff contribution vanishes. In the same Figures the return echoes from sub-surface discontinuities are shown, taking into account the first layer material composition of Table 14.2.

14.5.5 Sub-surface interface detection performance

14.5.5.1 Dynamic range and detection performance: Detection of a sub-surface interface will be possible only if the following conditions are satisfied:

- the level of the sub-surface reflection is higher than the noise level
- the surface/sub-surface dynamic is included in the system dynamic range
- the sub-surface reflection is higher than the corresponding surface clutter reflection.

The first point entails a proper design of the receiver and transmitter sections. In MARSIS the noise level is about 60 dB below the fully coherent surface return echoes. Moreover, the availability of an overall 60 dB dynamic range requires a proper control

of the sidelobes (due to the range compression, assuming the transmitted signal is a chirp) and nonlinearities.

The limits to the penetration depth imposed by the surface clutter level can be found using the above considerations to find, at each frequency, the depth at which the sub-surface power is equal to the surface clutter power. Analysing the behaviour of Figures 14.14 and 14.15, the maximum penetration depth can be assumed as the depth at which the sub-surface curves intersect the surface clutter curves. Looking at the previous Figures and remembering that a maximum dynamic of 60 dB has been allowed, it appears that the surface clutter contribution will be the limiting factor for the penetration depth under rough surface condition.

14.5.5.2 Detection in presence of surface clutter: In the presence of rough surfaces the dynamic range is strongly reduced by the surface clutter, as shown in the previous Section. Three techniques can be used to increase the detection performance against surface clutter:

- Doppler filtering of the along-track off-nadir surface clutter echoes
- dual antenna cancellation of the crosstrack off-nadir echoes
- dual frequency cancellation of the crosstrack off-nadir echoes.

14.5.5.3 Doppler filtering of surface clutter: The first technique ('Doppler filter' or well known 'synthetic aperture radar' (SAR) approach) takes advantage of the forward motion of the spacecraft to distinguish along-track displaced echoes in the Doppler frequency domain.

The Doppler spectrum is Nyquist sampled providing a proper PRF, and then a lowpass filter is applied in each range cell to cut off the high frequency contributions, which correspond to off-nadir received echoes.

Notice that the Nadir scattering area (in the noncoherent scattering case, where the surface clutter reduction is a relevant problem), given by (14.47)

$$S_C = \pi 2H\Delta \longleftrightarrow \Delta = \frac{c}{2B_w} \tag{14.59}$$

where Δ is the range resolution, considering the output of the only central Doppler filter and assuming that the along-track spatial resolution is K, is reduced to

$$S_{CR} = 2K\sqrt{2H\Delta} \tag{14.60}$$

The off-nadir surface scattering area, corresponding to the sub-surface scattering from the z depth, is also reduced by the Doppler filtering from the value given by (14.60) to

$$C_{CR} = 2K\sqrt{2H\Delta}\left(\sqrt{\frac{z}{\Delta}} - \sqrt{\frac{z}{\Delta} - 1}\right)$$

$$C_C = \pi 2H\Delta \tag{14.61}$$

In consequence, the ratio between sub-surface received power and surface clutter power is improved by a factor

$$IF = \sqrt{\frac{z}{\Delta}}\left(1 - \sqrt{1 - \frac{\Delta}{z}}\right) \tag{14.62}$$

so that an $IF \approx 12$ dB can be obtained by this technique at high depths.

14.5.5.4 Dual antenna clutter reduction: The radar sounding geometry is depicted in Figure 14.16. The main problem to be faced in this operative mode is given by the fact that, operating with only the dipole antenna, the unwanted off-nadir surface echoes from the zones called A and B in the Figure (crosstrack direction) arrive at the radar superimposed with the wanted nadir echo from the sub-surface discontinuity.

Operating with only the dipole antenna, the unwanted off-nadir surface echoes from the zones in the crosstrack direction arrive at the radar superimposed with the wanted nadir echo from the sub-surface discontinuity.

Moreover, by considering the selected orbit ($250 < H$ (km) < 800) and the maximum expected depth of C, the off-nadir angle θ is given by

$$\theta = \cos^{-1}\left[\frac{1}{1 + \sqrt{\varepsilon}d/H}\right] \tag{14.63}$$

where ε is the real part of the dielectric constant of the sub-surface medium, H is the orbit height and d is the penetration depth.

This corresponds to zones A and B and is included in the range from 10 to 16 deg. (Figure 14.16), so it must be expected that the echoes coming from A and B are very strong with respect to the echo coming from C. Moreover, a secondary monopole antenna, oriented along the nadir axis, will receive mostly the off-nadir surface returns,

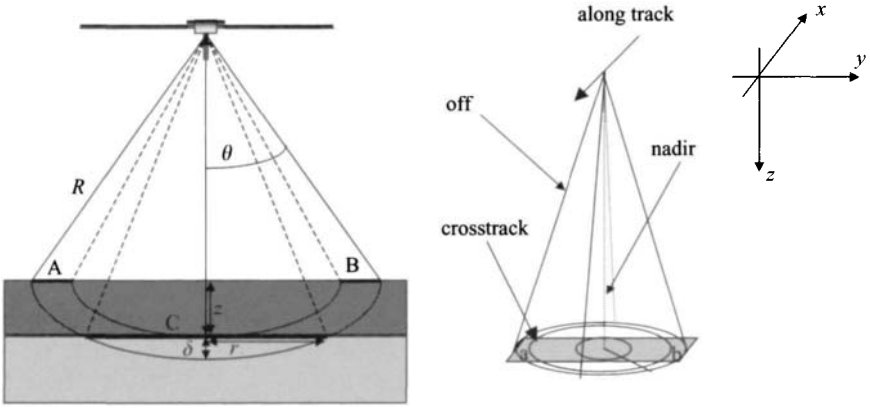

Figure 14.16 Radar sounding geometry

so that could be subtracted by the primary antenna composite signal, further reducing the surface clutter level (~15–20 dB).

14.5.6 Summary

Notice that, on the dayside of Mars, the ionosphere Figure 14.10 does not allow the use of frequencies < ~3 MHz for sounding. Hence, on day side operations only the 4 MHz and 5 MHz frequencies will be able to penetrate the ionosphere and will be used for sub-surface sounding. The best penetration capabilities will be obtained during night side observation, when also the longest wavelengths can be operated.

The multi-frequency observation will allow the estimation of the material attenuation in the crust and will give significant indications on the dielectric properties of the detected interfaces.

To maximise the sounding depth against rough surfaces, three different methods to separate sub-surface reflections from synchronous echoes coming from off-nadir surface reflections (surface clutter) can be used:

(i) Doppler beam sharpening: the Doppler azimuth processing significantly reduces the surface echoes coming from along-track off-nadir reflections. The improvement on the overall surface clutter attenuation has been shown to be ~10–12 dB at high depths.
(ii) Moreover, a secondary monopole antenna, oriented along the nadir axis, will receive mostly the off-nadir surface returns, which could thus be subtracted by the primary antenna composite signal, further reducing the surface crosstrack clutter level (~15–20 dB).
(iii) Echo profiles collected at two different frequencies can be processed to separate the sub-surface reflections, which are strongly dependent on the frequency, from the surface reflections, which are mostly frequency independent. The achieved improvement can reach 10–15 dB.

The first surface reflection echoes in sounder operations will be processed to give estimations of the average height, roughness and reflection coefficient of the surface layer, according to the classical altimetric approach (surface altimetry).

By measuring the time delay of the echo, it will be possible to estimate the average distance of the radar from a reference flat surface level, while the duration of the waveform leading edge will be proportional to the large scale surface roughness averaged over the pulse limited spatial resolution cell. Finally, the peak value of the average echo waveform will be used to estimate the backscattering coefficient and, in conjunction with the roughness value, to estimate the Fresnel reflection coefficient of the surface.

14.6 Summary

While most GPR systems are used in close proximity to the ground, remote sensing using airborne systems has been able to map ice formations and glaciers, and penetrate

through forest canopy on the earth. The use of SAR radar techniques to penetrate the vegetation and dry soil of the earth has provided some outstanding examples of the capability of GPR techniques for remote sensing. Airborne GPR, processed using synthetic aperture techniques, has been used to detect buried metallic mines from a height of several hundred metres in SAR (synthetic aperture radar) mode. In addition, the SIR-C satellite SAR radar has imaged buried artefacts in desert conditions, and the JPL website http://southport.jpl.nasa.gov/sir-c/ is an important source of radar imagery. As can be seen by the contributions in this Chapter, the science of planetary exploration is developing and models of our neighbouring planets are developing apace, particularly for Mars. GPR has established a role not only in the exploration of our own planet but for space exploration.

14.7 References

[1] KADABA, P. K.: 'Penetration of 0.1 GHz to 1.5 GHz electromagnetic waves into the earth surface for remote sensing applications'. Proc. IEEE SE Region 3 Conf., 1976, pp. 48–50

[2] ELACHI, C., ROTH, L. E., and SCHABER, G. G.: 'Spaceborne radar subsurface imaging in hyperarid regions', *IEEE Trans.*, 1984, **GE-22**, (4), pp. 383–388

[3] BLOM, R. G., CRIPPEN, R. E., and ELACHI, C.: 'Detection of subsurface features in SEASAT radar images of Means Valley, Mojave Desert, California', *Geology*, 1984, **12**, pp. 346–349

[4] BROWN, W. E.: 'Lunar subsurface exploration with coherent radar'. Proc. Conf. on Lunar geophysics, Lunar Science Institute, Houston, TX, USA, 1971, pp. 113–127

[5] PORCELLO, L. J., JORDAN, R. L., ZELENKA, J. S., ADAMS, G. F., PHILLIPS, R. J., BROWN, W. E., WARD, S. H., and JACKSON, P. L.: 'The Apollo lunar sounder radar system', *Proc. IEEE*, 1974, **62**, pp. 769–783

[6] MAXWELL, T. A., and PHILLIPS, R. J.: 'Stratigraphic correlation of the radar-detected subsurface interface in Mare Cranium', *Geophys. Res. Lett.*, 1978, **5**, pp. 811–814

[7] SCHABER, G. G., McCAULEY, J. F., BREED, C. S., and OLHOEFT, G. R.: 'Shuttle imaging radar: physical controls on signal penetration and subsurface scattering in the Eastern Sahara', *IEEE Trans.*, 1986, **GE-24**, (4), pp. 603–623

[8] SCHABER, G. G., OLHOEFT, G. R., McCAULEY, J. F., BREED, C. S., and DAVIS, P. A.: 'The 'radar rivers' of the eastern Sahara: signal penetration and surface scattering observed by the Shuttle Imaging Radar', in LUCIUS, J. E., OLHOEFT, J. R., and DUKE, S. K. (Eds.): Abstracts of the Technical Meeting of the 3rd Int. Conf. on Ground penetrating radar, Lakewood, CO, USA, 1990. US Geological Survey Open-File report 90-414, 61

[9] McCAULEY, J. F., SCHABER, G. G., BREED, C. S., GROLIER, M. J., HAYNES, C. V., ISSAWI, B., ELACHI, C., and BLOM, R.: 'Subsurface valleys and geoarcheology of the Eastern Sahara revealed by Shuttle Imaging Radar', *Science*, 1982, **218**, pp. 1004–1020

[10] BREED, C. S., SCHABER, G. G., McCAULEY, J. F., GROLIER, M. J., HAYNES, C. V., ELACHI, C., BLOM, R., ISSAWI, B., and McHUGH, W. P.: 'Subsurface geology of the Western Desert in Egypt and Sudan revealed by Shuttle Imaging Radar (SIR-A)'. Proc. 1st Spaceborne Imaging Radar Symposium, Jet Propulsion Laboratory, Pasadena, CA, USA, 1983, pp. 10–12

[11] BREED, C. S., McCAULEY, J. F., SCHABER, G. G., WALKER, A. S., and BERLIN, G. L.: 'Dunes on SIR-A images' in CIMINO, J. B., and ELACHI, C. (Eds.): 'Shuttle imaging radar-A (SIR-A) experiment'. NASA Jet Propulsion Laboratory, USA, 1982, 82-77, 4-52-4-87

[12] BREED, C. S., McCAULEY, J. F., and DAVIS, P. A.: 'Sand sheets of the Eastern Sahara and ripple blankets on Mars', in FROSTICK, L., and REID, I. (Eds.): 'Desert sediments – ancient and modern'. London Geological Society special publication 35, 1987, pp. 337–359

[13] McCAULEY, J. F., BREED, C. S., and SCHABER, G. G.: 'Megageomorphology of the radar rivers of the Eastern Sahara'. Proc. 2nd Spaceborne Imaging Radar Symposium, 1986, NASA Jet Propulsion Laboratory publication 86-26, 25-35

[14] McCAULEY, J. F., BREED, C. S., SCHABER, G. G., McHUGH, W. P., HAYNES, C. V., ISSAWI, B., GROLIER, M. J., and EL-KILANI, A.: 'Pale drainages of the Eastern Sahara: the radar rivers revisited', *IEEE Trans.*, 1986, **GE-24**, (4), pp. 624–648

[15] McHUGH, W. P., BREED, C. S., SCHABER, G. G., McCAULEY, J. F., and SZABO, B. J.: 'Acheulian sites along the 'radar rivers' southern Egyptian Sahara', *J. Field Archeol.*, 1988, **15**, pp. 361–379

[16] McHUGH, W. P., McCAULEY, J. F., BREED, C, S., and SCHABER, G. G.: 'Paleorivers and geoarchaeology in the southern Egyptian Sahara', *Geoarcheology*, 1988, **3**, (1), pp. 1–40

[17] McHUGH, W. P., SCHABER, G. G., BREED, C. S., and McCAULEY, J. F.: 'Neolithic adaptation and the Holocene functioning of tertiary paleodrainages in southern Egypt and northern Sudan', *Antiquity*, 1989, **63**, pp. 320–336, Applications 259

[18] SZABO, B. J., McHUGH, W. P., SCHAHER, G. G., and HAYNES, C. V.: 'Uranium-series dated authigenic carbonates and Acheulian sites in Southern Egypt', *Science*, 1989, **243**, pp. 1053–1056

[19] ISSAWI, B., and McCAULEY, J. F.: 'The Cenozoic rivers of Egypt: the Nile problem in the followers of Horus – studies in memory of Michael A. Hoffman' (Oxbow Press, Oxford 1992), pp. 1–18

[20] GUO, H., SCHABER, G. G., and BREED, C. S.: 'Shuttle imaging radar response from sand and subsurface rocks of Alashan Plateau on north-central China'. Proc. 7th Int. Symposium on Remote sensing for resources development and environmental management, Enschede, Netherlands, Balkema, Boston, USA, 1986, pp. 137–143

[21] BERLIN, G. L., TARABZOUNI, M. A., AL-NASER, A., SHEIKHA, K. M., and LARSON, R. W.: 'SIR-B subsurface imaging of a sand-buried landscape: At Labbah Plateau, Saudi Arabia', *IEEE Trans.*, 1986, **GE-24**, pp. 595–602

[22] FARR, T. G., ELACHI, C., and CHOWDHURY, K.: 'Microwave penetration and attenuation in desert soil: a field experiment with the Shuttle Imaging Radar', *IEEE Trans.*, 1986, **GE-24**, pp. 590–594

[23] ELLERMEIER, R. D., SIMONETT, D. S., and DELLWIG, L. F.: 'The use of multi-parameter radar imagery for the discrimination of terrain characteristics'. IEEE Int. Convention Record, 1967, Pt.2, pp. 127–135

[24] DELLWIG, L. F.: 'An evaluation of multifrequency radar imagery of the Pisgah Crater area, California', *Mod. Geol.*, 1969, **1**, pp. 889–892

[25] SCHABER, G. G., and BREED, C. S.: 'Subsurface mapping with imaging radar in deserts of Africa and Arizona', in THORWEIHE, U., and SCHANDELMEIR, H. (Eds.): 'Geoscientific research in Northeast Africa'. Proc. Int. Conf. on Geoscientific research in Northeast Africa, 1993, A. A. Balkema, Rotterdam, pp. 761–765

[26] ULABY, F. W., MOORE, R. K., and FUNG, A. K.: 'Microwave remote sensing – active and passive in radar remote sensing and surface scattering and emission theory' (Addison-Wesley, 1982, Vol. 2), pp. 816–921

[27] DAVIS, P. A., BREED, C. S., McCAULEY, J. F., and SCHABER, G. G.: 'Surficial geology of the Safsaf region, south-central Egypt derived from remote sensing and field data', *Remote Sens. Environ.*, 1993, **46**, pp. 183–203

[28] LAPLACE, H., MORELIERE, M., and GROSE, C.: 'The Mars 96 balloon guiderope: an autonomous system in extreme environmental conditions'. Proc. Int. Symposium on Missions, technologies and design of planetary mobile vehicles, CNES, CEPADUES, 1992, pp. 417–421

[29] BARBIN, Y., NICOLLIN, F., KOFMAN, W., ZOLOTAREV, V., and GLOTOV, V.: 'Mars 96 GPR program', *J. Appl. Geophys.*, 1995, **13**, pp. 27–37

[30] FINKELSTEIN, M., KUTEV, V., and ZOLOTAREV, V.: 'Applications of subsurface radar in geology' (Nedra, Moscow, 1986), p. 128

[31] NICOLLIN, F., BARBIN, Y., KOFMAN, W., MATHIEU, D., HAMRAN, S. E., BAUER, P., ACHACHE, J., and BLAMONT, J.: 'An HF bi-phase shift keying radar; application to ice sounding in Western Alps and Spitzbergen glaciers', *IEEE Trans.*, 1992, **GE-30**, pp. 1025–1033

[32] NICOLLIN, F., and KOFMAN, W.: 'Ground penetrating radar sounding of a temperate glacier; modelling of a multilayered medium', *Geophys. Prospect.*, 1994, **42**, pp. 715–734

[33] FANALE, F. P.: 'Martian volatiles: their degassing history and geochemical fate', *Icarus*, 1976, **28**, pp. 179–202

[34] CARR, M. H.: 'Formation of Martian flood features by release of water from confined aquifers', *J. Geophys. Res.*, 1979, **84**, pp. 2995–3007

[35] ULABY, F. T., MOORE, R. K., and FUNG, A. K.: 'Microwave remote sensing: active and passive', Vol. II–III (Addison Wesley Publishing Co., London, 1986)

[36] FUNG, A. K., LI, Z., and CHEN, K. S.: 'Backscattering from a randomly rough dielectric surface', *IEEE Trans.*, 1992, **GE-30**, (2), pp. 356–369

[37] FUNG, A. K., and EOM, H. J.: 'Coherent scattering of a spherical wave from an irregular surface', *IEEC Trans. Ant. Prop.*, 1983, **AP-31**, pp. 68–72

[38] PICARDI, G., BICCATI, D., SEU, R., MARINANGELI, L., JOHNSON, W.T.K., JORDAN, R.L., PLAUT, J., SAFAENILI, A., GURNETT, D.A., ORI, G.G., OROSEI, R., CALABRESE, D., and ZAMPOLINI, E.: 'Performance and surface scattering models for the Mass Advanced Radar for Subsurface and Ionosphere Sounding (MARSIS)', *Planetary and Space Science*, 2004, **52**, pp. 149–156

14.8 Bibliography

BARBIN, Y., KOFMAN, W., ELKIN, M., FINKELSTEIN, M., GLOTOV, V., and ZOLOTAREV, V.: 'Mars 96 subsurface radar'. Proceedings of ESA Int. symposium on Radars and lidars in Earth and planetary sciences, 1991, ESA SP-328, pp. 51–58

BERRY, M. V.: 'The statistical properties of echoes diffracted from rough surfaces'. Willy Physics Lab., Univ. of Bristol, UK, 17 Feb 1973, Vol. 273A1237, pp. 611–654

BICCARI, D., PICARDI, G., SEU, R., and MELACCI, P. T.: 'Mars surface models and subsurface detection performance in MARSIS'. Proc. IEEE Int. Symposium on Geoscience and remote sensing (IGARSS 2001), Sydney, Australia, 9–13 July 2001.

BIGGS, A. W.: 'Sea ice thickness measurements with short pulse radar systems'. URSI Commission F, La Baule, France, 1977, pp. 159–163

BISHOP, J. F., CUMMING, A. D. G., FERRARI, R. L., and MILLER, K. J.: 'Results on impulse radar ice-depth sounding on the Vatnajokull ice-cap, Iceland'. Proceedings of Conf. on the International Karakorum Project, 1980, Vol. I, pp. 126–134 (see also pp. 111–125)

CIAFFONE, A., PICARDI, G., and SEU, R.: 'Application of the PARIS concept to the GPS signals'. STS, Rome, Italy, Technical Report #TR-1-3/1/95, ESA contract 142286-27/06/94

DONG, Z.-B., FERRARI, R. L., FRANCIS, M. R., MUSIL, G. J., OSWALD, G. K. A., and ZHANG, X.-S.: 'Impulse radar sounding on the Hispar glacier'. Proc. Conf. on the International Karakorum Project, 1980, Vol. 1, pp. 100–110

FINKELSTEIN, M. I.: 'Subsurface radar', *Telecomm. Radio Eng.*, 1977, Part 2, **32**, pp. 18–26 (English translation)

GRADSHTEYN, R.: 'Tables of integrals, series and products' (Academic Press, 1965)

GRANDJEAN, G., PAILLOU, P., DUBOIS-FERNANDEZ, P., AUGUST-BERNEX, T., BAGHDADI, N. N., and ACHACHE, J.: 'Subsurface structures detection by combining L-band polarimetric SAR and GPR data: example of the Pyla Dune (France)', *IEEE Trans. Geosci. Remote Sens.*, 2001, **39**, (6), pp. 1245–1258

GREGORWICH, W.: 'An airborne ground penetrating radar system'. Proc. IEEE Aerospace Applications Conf., 1996. 3–10 Feb. 1996, Vol. 1, pp. 157–161

HALL, D. K.: 'A review of the utility of remote sensing in Alaskan permafrost studies', *IEEE Trans.*, 1982, **GE-20**, pp. 390–394

LUKASHENKO, Y. I., MASLOV, A. I., TERLETZKI, N. A., and TSIURUPA, L. A.: 'Subsurface sounding in the uhf band of lenses of ground water and continental glaciers', *Telecomm. Radar Eng.*, 1979, **34**, (4), pp. 94–95 (English translation)

PAILLOU, P., AUGUST-BERNEX, T., GRANDJEAN, G., DREUILLET, P., and ACHACHE, J.: 'Sub-surface imaging by combining airborne SAR and GPR: application to water detection in arid zones'. Proc. IEEE Int. Geoscience and Remote Sensing Symposium, 2001 (IGARSS '01), Vol. 3, pp. 1384–1386

PICARDI, G., SORGE, S., SEU, R., FEDELE, G., FEDERICO, C., and OROSEI, R.: 'Mars advanced radar for subsurface and ionosphere sounding (MARSIS): models and system analysis'. Infocom Technical Report N.007/005/99, 1999

VICKERS, R. S.: 'Design and applications of airborne radars in the VHF/UHF band', *IEEE Aerosp. Electron. Syst. Mag.*, 2002, **17**, (6), pp. 26–29

WAITE, A. H., and SCHMIDT, S. J.: 'Gross errors in height indications from pulsed radar altimeters operating over thick ice and snow', *Proc. Inst. Radio Eng.*, 1962, **50**, pp. 1515–1520

Chapter 15
Equipment

15.1 Introduction

There is an ever increasing range of commercially available equipment for surface-penetrating radar applications. There are now a number of manufacturers and suppliers of equipment, and a list is provided in Section 15.2. This Chapter provides a brief introduction to selecting equipment.

Prospective users of equipment must satisfy themselves that their selection meets their perceived needs in terms of application, material environment, speed of operation, etc. Section 15.2 does not imply any recommendation or endorsement of any of the products or their manufacturers. It is to be hoped that incremental developments in the overall performance of radar systems will result in a more sophisticated and user friendly generation of equipment. The end-user requires value for money, lightweight, compact, rugged equipment and easy to interpret radar images. The designers and manufacturers should be encouraged to meet these needs.

All equipment should meet National and International regulations and no equipment (of whatever age) should be operated in contravention of these requirements. Operators of surface-penetrating radars are required to comply with their country's licensing and EMC requirements and any safety regulations, for example intrinsic safety in hazardous environments.

As a general rule it is unlikely that one size of antenna will cover a full range of applications and it will be necessary to use large antennas to achieve greater range and small antennas to provide increased resolution. In general, manufacturers of surface-penetrating radar offer a range of antennas which can be used with a single control unit. There are considerable variations in system characteristics, and the prospective user should evaluate the manufacturers' stated specifications.

The power per spectral line radiated by the antenna is of prime importance in judging the performance potential of a particular system. One way of evaluating this is to consider the RF pulse repetition frequency (prf) and the effective bandwidth of the RF pulse (applied to the antenna terminals). In the case of a radar with a 50 kHz prf

and an effective RF pulse bandwidth of 50 kHz to 1 GHz, the power to the antenna is spread over 20 000 spectral lines each separated by 50 kHz. Thus a transmitter applying a 100 V peak voltage pulse to a 50-input impedance antenna will apply 200 W peak power, and the peak power per spectral line applied to the antenna will be 10 mW.

A radar with a 1 MHz prf and a 22 V peak voltage pulse applied to the same antenna will provide the same peak power per spectral line but the peak field strength across the antenna terminals will be reduced by a factor of nearly 5, thus enabling the latter to offer more inherent compliance with intrinsic safety requirements.

The overall performance of a radar system can be considered using the following example. Given a comparable radiated power per spectral line the performance of a radar is primarily defined by the performance of the receiver. Here it is the receiver signal to noise ratio and the clutter performance which are of prime importance.

The noise of the receiver can be derived from

$$N_o = K(T_a + T_r + L_r T_e)B_n \tag{15.1}$$

where K = Boltzmann's constant
T_a = antenna noise temperature
T_r = noise temperature of the RF connection between the antenna and receiver
L_r = loss of the RF components (cables etc.)
T_e = receiver noise temperature
B = receiver bandwidth

or

$$N_o = K(T_a + T_r + L_r T_o(F_n - 1))B_n \tag{15.2}$$

where T_o = reference temperature of 290 K and F_n = noise figure of the receiver.

Most impulse radar systems use a sequential sampling diode receiver whose noise figure is generally poor compared with conventional radar systems. Certainly, values for the noise figure of between 10 dB to 30 dB are not unusual.

If a system with the following values is assumed (F = 30 dB, L_r = 6 dB losses, temperature = 290 K and a 1 GHz bandwidth), then

$$N_o = 1.38 \times 10^{-23}(290 + 1051 + 4.625 \times 290(10^3 - 1)) \times 10^{-9}$$
$$= 1.85 \times 10^{-8}\ \text{W} \tag{15.3}$$

Hence the receiver rms noise voltage assuming a 50 Ω input impedance for the receiver

$$E_o = 1\ \text{mV rms}$$

and for a 5 : 1 signal to noise ratio the signal is given by

$$E_s = 5\ \text{mV rms or } 7\ \text{mV}_{pk}$$

As, in general, most RF sampling diodes are not capable of accepting input voltages greater than 1 V_{pk} in their linear region of operation, the receiver has an effective

dynamic range given by

$$D_R = \frac{\hat{E}_{\max}}{\hat{E}_s} \tag{15.4}$$

and in this example

$$D_R = 20 \log \left(\frac{1}{7 \times 10^{-3}} \right) = 43 \text{ dB} \tag{15.5}$$

This value can be increased either by reducing the RF system bandwidth or by applying time varying gain prior to the RF sampling head and thus reducing the peak signal level at close ranges. Typically a compression of up to 30 dB is practical, thus immediately improving the receiver dynamic range to 68 dB. Note that applying time varying gain after the RF sampling process does not increase the receiver dynamic range. Alternatively, averaging the RF sampled signal effectively improves the signal to noise ratio in proportion to 20 log N, where N is the number of samples. Averaging prior to digitisation can only improve the signal to noise ratio to a level defined by the dynamic range of the analogue/digital converter which, for a 16-bit module, would be 96 dB. Further averaging of the sampled data would have to take place in software and will slow down the rate of system data acquisition in direct proportion to the number of averages.

For example, a 60 dB improvement in signal to noise ratio from a 16-bit analogue to digital converter would require 106 averages to be performed. A radar with a data transfer rate of 50 scans/s would be slowed to a rate of approximately 4 scans/day, which is clearly impractical.

Other issues that the user should consider are the radiated pulse fidelity and the rate of decay in time of the latter. Evidently the radiated pulse should be localised in time and not be spread over many nanoseconds due to either multiple reflections within the antenna or antenna feed system. Practically a rate of decay in excess of 20 dB per pulse length is necessary for uncluttered radar images.

Additionally the user should confirm that the receiver does not exhibit nonlinear RF sampling characteristics, and a practical test is, in a clear outdoor area, to use a flat metal plate target of 1 m^2 and observe the received signal while increasing the range between the target and antenna. The reflected signal should be localised in time and no spurious echoes should be observed at other times.

It is possible to draw up a 'shopping list' of rule of thumb user requirements against which to select suitable equipment. These are given below but the user is advised to assess performance on a calibrated test rig or site wherever possible.

Table 15.1 provides an indication of suitable pulse durations, centre frequency and achievable depth resolution for a range of target depths given certain assumptions. Any variations on these will change the appropriate selection.

The following example should enable the user to compare how closely a particular piece of equipment meets a particular requirement (Table 15.2). For convenience all powers are referred to as 1 mW and are expressed in dBm (dB with respect to 1 mW). The procedure is to work through the list checking that the parameters specified are

Table 15.1 Equipment parameters

Target depth, m[a]	Pulse duration, ns[b]	Centre frequency, MHz[c]	Depth resolution, m[d]
<0.25	0.5	2000	0.025
<0.5	1	1000	0.05
<1	2	500	0.1
<2	4	250	0.2
<4	8	125	0.4
<8	16	62.5	0.8
<16	32	31.25	1.6

[a] Depth in a medium loss (<20 dB m^{-1} attenuation) material
[b] Pulse duration to the half power width of the main peak
[c] Assumes a transmitted pulse in the general form of a Rayleigh wavelet
[d] Assumes a material of relative permittivity = 9

met by the system under consideration. The exercise allows variations to be identified and the user to determine whether such variations can be accepted.

The example chosen is a 1.0-ns-duration radar with a target depth range of <0.5 m.

The example given should enable the potential user to identify, at least on paper, the salient features of the system to be assessed, but practically a field test on a calibrated site is usually the best method of deciding whether a particular piece of equipment will meet the requirements of the applications.

15.1.1 Survey methods

An operator of a surface-penetrating radar equipment must have a fundamental understanding of the principles of the technique as well as expertise in the evaluation of the radar data. Unless this is the case it is more than likely that the equipment will not be used to its maximum capability and both the operator and the client will be disappointed in the outcome. The effect of the material and its structure can significantly change the set-up of the equipment and its mode of operation, and the correct selection is needed for the site under investigation.

Ideally an informed and accurate site description should be obtained prior to survey or, failing this, an on-site assessment should be carried out. Whenever possible local geological maps should be used, together with, if available, site or structural plans. By these means it is possible to determine in advance the type of equipment, its pulse length or operating frequency range, recording and signal processing requirements. Where required the equipment should be capable of on-site data presentation. There is a significant difference in the equipment needed for general search activities and, for example, a road survey where multiple sets of equipment are often employed.

Accurate records of the site are essential to subsequent data analysis and interpretation. The site characteristics recorded should consist of the following whenever the information is available.

Table 15.2 Check list for system requirements

ID	System requirement	Specified value	Enter value for system under consideration
A	Pulse duration, s	1.10^{-9}	?
B	Peak pulse power, V	50 V	?
C	Pulse interval, s	1.10^{-6}	?
D	Peak pulse power, W	50 W	?
E	Mean pulse power in watts (D times A/C)	50 mW	$= D \times A/C$
F	Mean pulse power, dBm	17 dB m	?
G	Receiver bandwidth (−3 dB bandwidth)	1 GHz	?
H	Thermal noise power (KTB)	−84 dB m	?
I	Receiver noise power referred to the input (usually a measured value)	−78 dB m	?
J	Receiver min detectable signal power (usually 14 dB greater than I)	−64 dB m	?
K	Averaging improvement = 20 log N, where N = number of averages prior to digitisation	= 10 dB	= 20 log N
L	Receiver minimum detectable signal power	= −74 dB m	?
M	Time varying gain variation prior to RF sampling	= 30 dB	?
N	Receiver max input signal with no time varying gain (TVG). Measured value	= +13 dB m	?
O	Receiver max input signal with TVG = $M + N$	= +43 dB m	= $M + N$
P1	Equivalent receiver dynamic range = $O - L$	= 117 dB	= $O - L$
P2	Actual receiver dynamic range = $N - L$	= 87 dB	= $N - L$
Q	Antenna Tx/Rx isolation	−40 dB	>?
R	Peak receiver signal ($D - Q$)	+6.9 dB m	= $D - Q$
S	Check is $R \ll 0$	Yes	?
T	Pulse ringdown per pulse length	>−20 dB	?
U	Spurious reflections (to be less than the dynamic range)	>−100 dB	?
V	Analogue to digital converter dynamic range (to be greater than P2) (16-bit)	96 dB	?
W	Data transfer rate in samples/s to meet P2 requirement (assumes an equivalent pulse interval of 1.10–5 s)	0.4 Msamples/s	?
W1	Effective sample acquisition time (pulse interval × number of averages)	1.10–5 s	?
W2	Data transfer rate in samples/s to meet P2, V and W1 (V/W1)	1.6 Msamples/s	?
X	Data transfer rate in scans/s to meet P2 requirement	100 scans/s	?

Table 15.2 Continued

ID	System requirement	Specified value	Enter value for system under consideration
Y	Software: Processing File Format SEG, etc. Archiving	TBD	?
Z	Power consumption at 12 V 110 V 240 V	TBD	?
AA	Total system components Total system weight Shock/vibration/temperature	TBD	?
BB	Maintainability Upgradeability Flexibility Speed of deployment and use	TBD	?
CC	Type of target: planar–delamination, geological linear–pipe, cable void cylindrical spherical	TBD	?
DD	Parallel dipole shielded Parallel dipole unshielded Crossed dipole shielded Crossed dipole unshielded TEM horn shielded TEM horn unshielded Array size/elements	TBD	?
EE	Licensing and CE mark	Compliant	?

15.1.2 Site characteristics

Access by vehicle/foot
Grid reference
Ordnance survey map reference
Local plans
Aerial photographs
Ground photographs
Construction plans
Historical records

Interior/exterior characteristics
Weather conditions
Time, date

15.1.3 Surface characteristics

Man-made or natural
Site use
Surface flatness
Vegetation
Boundaries
Tracks/paths
Disturbance/anomalies
Surface water/frost/ice/snow

15.1.4 Material characteristics

Man-made, e.g. concrete/bitumen/slabs/brick/wood
Natural, e.g. grass/soil (clay, clay loam, sandy silt loam etc.)/rock
Sub-surface geology
Bedrock geology

15.1.5 Target characteristics

Description of target
Size of target
Target composition
Depth of target
Date of construction

Various methods can be used to record the site dimensions, ranging from simple tape measurements and careful marking out, to electronic distance measurers of the total station type. The latter can be used to log data onto a separate computer. However, there is still a need to crossreference data gathered by the radar and integrate these with an accurate plan of the site. One approach is to use a measurement system which automatically triggers the radar at predetermined spatial intervals. Alternatively, positions can be defined by a differential GPS co-ordinate system. These must be correctly set up to achieve the accuracy needed for GPR data recording.

There are two main types of survey: the linear (B-scan) or a survey area (C-scan). The linear survey is in general suitable for road structures where a planar structure is under investigation. Where features such as pipes or cables are sought a B-scan is often insufficient to establish the line of a pipe, as a single point reflector such as a large stone can cause the same radar image as a scan over a pipe. A C-scan is therefore useful as a means of producing a plan view of the area of interest. The general assessment of the area to be surveyed should take into account the dimensions of the target and the grid size should be adequate to resolve its area dimensions. It may be

necessary to estimate a maximum spacing which can be reduced over a particular area of interest in order properly to resolve that feature. The requirements for detection are less stringent than for imaging. For detection a survey grid spacing may only need to be sufficient to cover the area of the target, whereas target imaging must meet general sampling requirements and in addition each line must be correctly registered with respect to its neighbour.

Another consideration is the plane of polarisation of the electromagnetic energy. For targets with one large area dimension such as a pipe, the radar cross-scattering section will be larger when the polarisation vector is in line with the pipe. This means that any area that is surveyed with, say, parallel dipoles must be surveyed in orthogonal directions to ensure that no targets are missed. The same principle also relates to crossed-dipole antennas.

The speed of survey must also take into account sampling considerations. A survey wheel is generally used to control either the speed of operation of the radar or to place distance markers on the data record. The speed of survey is usually governed by the effective data-acquisition rate of the radar. It is appropriate to consider the spatial sampling interval in terms of either the interval between each A-scan or the number of A-scans per metre. If the effective data-acquisition rate of the radar system s given by t_a and the spatial sampling interval is given by d, the maximum speed of survey is given by

$$V_a = \frac{d}{t_a} \tag{15.6}$$

At a very small spatial sampling interval, the amount of data that can be generated is large, and consideration must be given to the storage medium and whether this has adequate capacity for the proposed survey. Unprocessed B-scan data are often collected in a 16-bit word format. For example, each A-scan of 256 samples generates 0.5 kbyte of data. At a spatial sampling interval of 1 cm each metre of ground traversed would create 50 kbyte of data. A total length of 1 km would need a 50 Mbyte file length. For multiple-head radar systems using, say, four radar heads, the data-storage requirements multiply accordingly unless data-compression techniques are used. A general guide to the spatial interval required is that the spatial sampling interval should be 20% of the linear x, y dimensions of the target. In general, it is advisable that the radar data be monitored as the survey is carried out.

It is also important that the radar survey can be referenced to a local marking point and that the accuracy of the radar survey is known. The traditional method of achieving this is with a survey wheel which either places markers on the B-scan or controls the rate of data acquisition. Unfortunately, such wheels can accumulate errors over a large distance and an additional means of logging known positional information is desirable. As with most survey methods, some flexibility in investigation procedure is important in order to carry out more detailed or supplementary investigations. Both the client and the survey operator should allow for variations to the planned work. It is also useful to obtain on-site 'ground truth' by means of excavation or endoscopic inspection to validate any calibration information previously made.

15.2 List of companies offering GPR technology

The following is a list of companies associated with the development manufacture and supply of GPR equipment. The prospective purchasers of goods or services should satisfy themselves that the materials or services are fit for purpose. No endorsement is implied by the inclusion of these companies. Given the easy availability of information, via the Internet, the reader should be easily able to find information via a search engine and make a suitable selection of goods or services.

AB Geotechnics Ltd
Aperio
CelsiusTech Electronics
Centre Research Institute of Radio & Electronic Systems (TsNIIRES)
Coleman Research Corporation
Dolphin Geophysical Services
ERA Technology Ltd
GBG
GDE Systems
GeoModel Inc.
GeoRadar Inc.
Geosphere Inc.
Geophysics Australia/GroundSearch
GSSI
Hager-Richter Geoscience, Inc.
IDS S.p.A.
Interpex Ltd
Lamont
MALA Geoscience
Northeast Geophysical Services
Omnitron
Patriot Scientific
Phoenix International, Inc.
Radar Data Service
Radar Systems, Inc.
Road Radar Ltd
Roadscanners Oy
Rock Creek Geophysics, Inc.
Sandmeier Scientific Software
Sensors & Software
Terraplus USA Inc.
Utsi Electronics

Chapter 16

Regulation, radiological aspects and EMC

16.1 Regulation

For over three decades GPR systems have been used with virtually no evidence to suggest that they cause interference to other users of the radio spectrum. There are good reasons for this situation.

Compared with the number of mobile phones, GPS users and other occupants of the same bandwidth, the number of GPR systems is very small, hence the potential for interference is low. GPR systems are not operated for extended duration and their mean radiated power is very low. GPR systems are often operated in areas where there is a low density of population. GPR systems are designed to radiate energy into the ground, where it is quickly absorbed. For all these reasons it is not surprising that properly documented and recorded incidents of interference are minuscule in number.

GPR systems operate from 10 MHz up to 5 GHz with a decade bandwidth within that range. This characteristic puts GPR into the most extreme class of ultra-wideband radars. Like most other ultra-wideband technologies, GPR devices fall outside any formal regulatory framework, and concerns have been raised about their potential interference with licensed radio frequency receivers.

In many countries, waivers to existing rules have been given to GPR systems that are equipped with a shut-off switch that automatically stops the radiation when the GPR system is lifted from the ground surface, or is not operated horizontally. This additional requirement acknowledges that emissions into the air from GPR under normal operating conditions are unintentional.

16.1.1 Europe

Within the European Union (EU) there are two main considerations governing the use of ultrawideband radar (UWB) or ground penetrating radar (GPR). These are the use of the equipment as a deliberate radio frequency radiator and as an equipment that must satisfy the EMC requirements of the EU.

The use of an ultrawideband radar or ground penetrating radar as an intentional radiator over a wide frequency spectrum suggests that it can be considered to fall within the category of short range devices (SRDs) such as movement detectors and metal detectors. This comes within the scope of the R&TTE Directive, which covers SRDs.

Currently, Draft European Standard ETSI EN 302 066-1 V1.0.0 is proposed. However, until this is approved each member country has dealt with UWB/GPR on an individual basis subject to approval by the national radio licensing authority. Information on ETSI standards can be found at http://www.etsi.org. Planned legislation and an ETSI specification at some time in the future means that this equipment will eventually need to conform to the R&TTE Directive. In the short term until a new product specification is introduced and formally published in the Official Journal of the European Communities then the EMC Directive should be applied.

The draft ETSI document ETSI EN 302 066-1 V1.0.0 (2003–02) applies to short range devices (SRDs) for specifically ground- and wall-probing radars with transmitters and receivers using ultra-wideband (UWB) spread spectrum technology. Specifically:

(a) ground penetrating radars (GPR) operating in the frequency range 30 MHz to 12.4 GHz radiating directly downwards into the ground. Any horizontal radiation is caused by leakage and is considered as spurious emission
(b) wall-penetrating radars operating in the range from 3.1 to 10.6 GHz with averaged and peak power densities up to −51.3 dBm/1 MHz and −34 dBm/3 MHz, respectively.

In the UK, GPR technology has been used under temporary use licenses under approval by the UK Radiocommunications Agency, which is currently working on legislation to permit the use of GPR. In Germany and Belgium, the appropriate licensing authorities have permitted the use of GPR systems under strict controls. In practical terms, this involves the use of a 'dead man's handle' to require positive operation of the transmitter as well as a proximity sensor to ensure proper coupling with the ground.

All equipment, including ultra-wideband radar or ground penetrating radar, must be CE marked to demonstrate that it satisfies the relevant directives of the European Union. The CE mark may only be applied when the requirements of all other relevant EU Directives, such as safety, have also been demonstrated. Europe has defined electromagnetic environments and agreed European Norm (EN) specifications with test levels defined. These specifications have product, product family and generic requirements with the application in that order of precedence. For commercial EMC, there are emissions and immunity requirements. The emission requirements have been defined through the CISPR international committees and the immunity through the IEC committees.

There are two European Directives under which the UWB/GPR EMC requirements could be defined.

The EMC Directive (89/336/EEC) has been applicable to all electrical and electronic equipment since January 1996. In the R&TTE Directive (1999/5/EC), which

came into force in April 2000, the requirements are specifically related to radio equipment and telecommunications terminal equipment. It references both EMC and safety (low voltage directive). With respect to radio devices, the emphasis is on those devices having a specific transmission function; receiver only type equipment remains within the requirements of the EMC Directive.

For both the EMC and R&TTE Directives, EMC specific requirements are defined by the harmonised generic or product specifications with crossreference to common basic test procedures for the different types of test defined. The product specifications generally define operating and functional performance requirements more specifically than generic specifications.

For European Union requirements, the specification considered relevant to the application for emissions is the residential, commercial and light industrial generic emissions specification EN 50081-1. The radiated emission level is defined as 30 dB μV/m (30–230 MHz) and 37 dB μV/m (230–1000 MHz) at a 10-m measurement distance. Tests are recommended to be extended up to 10 GHz to provide information on the emission spectrum where this is appropriate.

Immunity requirements should be based on the criticality of the equipment and the severity of the operational environment. For this type of equipment, a performance malfunction could have a fatal outcome for either the operator or civilian personnel. As a result, the industrial generic EMC specification EN 61000-6-2 is recommended with modifications as the minimum requirement.

The applicable tests recommended are:

- radiated immunity at 10 V/m plus modulation (80–1000 MHz) with an over test to 20 V/m for confidence, with the test to be extended to cover the 1.75 GHz mobile cell phone band
- electrostatic discharge tests but with the limits increased to cover the application of this equipment in very dry conditions (±15 kV air and ±8 kV contact discharges).

16.1.2 United States

An excellent paper on the situation was produced by Olhoeft [1] (see website http://www.g-p-r.com/), who summarised the situation in the United States, which is as follows. The Federal Communications Commission (FCC) and National Telecommunications and Information Administration (NTIA) jointly regulate radio spectrum use in the United States. Within the FCC, the Office of Engineering and Technology (OET) provides advice on technical and policy issues pertaining to spectrum allocation and use. OET also maintains the FCC's 'Table of Frequency Allocations'. The International Telecommunication Union (ITU), headquartered in Geneva, Switzerland, is the international organisation within which governments co-ordinate global telecom networks and services. The United States is a member of the ITU. Further assessments of the issues concerning UWB radar systems and other users is given by Anderson *et al.* [2, 3], Brunson *et al.* [4], Hoffman *et al.* [5] and Kissick [6], and reports by Johns Hopkins University [7], NTIA [8] and RTCA [9].

Until the FCC produced the First Report and Order (R&O 02-48) on 14 February 2002, the use of GPR was only officially permitted for those who had received waivers

from the FCC or NTIA. Legal waivers to manufacture GPR were issued to US Radar Inc. (using technology developed by ERA Technology UK), Time Domain Inc. and Zircon Corp. in June 1999, and expired with the R&O.

Waivers to build or use ground penetrating radar were issued to the US Geological Survey, US Army and US DOE by NTIA (or predecessors) from about 1976.

In May 2002, the FCC published a Notice of Proposed Rule Making (NPRM) on ultra-wideband transmission systems for public comment before the new rules were ratified. The new regulations took effect on 15 July 2002, with last minute modifications made on 12 July 2003.

Anyone owning GPR equipment in the US had to register with the FCC by the 15 October 2002. New equipment owners must also register. Approval for manufacturers follows the procedure described below. Each GPR/antenna must be tested by an independent laboratory for compliance with the regulations. The manufacturer will then submit a detailed description of the GPR/antenna to the FCC. The FCC will in turn certify the system and issue an ID number for that particular model antenna/system. The ID number is applied to every new antenna shipped. After 15 July 2002, new users must register with the FCC by submitting the same form, but with the antenna ID listed for each antenna.

Part of the proposed limitations on GPR relate to the levels of radiated signal, and a graph of the EIRP limit in dBm is shown in Figure 16.1.

Current information can be found on the following websites and points of contact:

golhoeft@mines.edu
http://www.ntia.doc.gov
http://www.itu.int
http://www.fcc.gov.

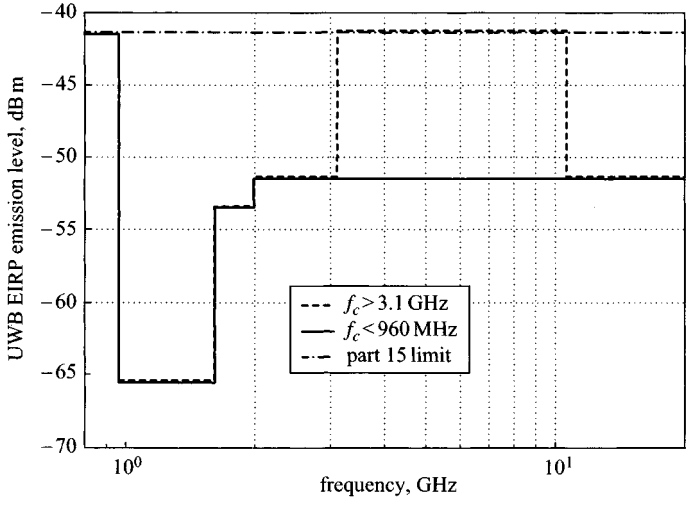

Figure 16.1 FCC proposed emission limits

16.1.3 Summary

The user of existing equipment should ensure compliance with existing national regulations and the new user should ensure that equipment is compliant with new legislation. The changing nature of much of the ITU, European (ETSI) and US standards is such that up to date information should be obtained. Many other countries will have specific requirements and proper advice should be sought.

16.2 Radiological aspects

In the UK, the National Radiological Board (NRPB) has responsibility for providing advice on appropriate restrictions on the exposure of people to electromagnetic fields and radiation. These include static, power frequency (50 Hz) and other extremely low frequency (ELF) electric and magnetic fields, and radiofrequency (RF) fields and radiation. Guidance limiting exposure to time varying electric and magnetic fields is issued at regular intervals. There has been a long history of research into radiological aspects, and the NRPB [10, 11] reported on health issues.

NRB recommendations are based on an assessment of the possible effects on human health derived from biological information [12–14], from dosimetric data [15, 16], and from studies of exposed human populations [11, 17]. They apply equally to workers and to members of the public but not to people who are exposed to electromagnetic fields and radiation for medical diagnostic or therapeutic purposes; guidance for the protection of patients and volunteers during clinical magnetic resonance diagnostic procedures has been issued separately (ANSI [18]). These recommendations are intended to provide a framework for a system of restrictions on human exposure to these fields and radiations [19].

A large number of studies of human populations exposed to electromagnetic fields and radiation have been carried out. They have examined general health, birth outcome and cancer incidence. These epidemiological studies have been reviewed in Reference [11]. In addition, an Advisory Group set up by the Board has examined in detail the evidence for an association between the incidence of childhood and adult cancers and exposure to electromagnetic fields.

The NRB advise that electromagnetic radiation of frequencies greater than 100 kHz and less than 300 GHz both induce current and thermal effects are relevant, but above 100 MHz, only thermal effects are considered. The specific absorption rate (SAR) is measured in units of watts per kilogram ($W\,kg^{-1}$), and given in Table 16.1.

Further information is available from the FCC at the following website: rfsafety@fcc.gov; see also Reference [20].

The IEEE have published a number of papers dealing with the issue of biological effects, and further details can be gathered from the following organisations:

- ANSI [18]
- IEEE [21]
- National Council on Radiation Protection and Measurements [22]

Table 16.1 Permitted absorption levels

Frequency range	Quantity	Basic restriction
100 kHz to 10 MHz	Current density in the head and trunk	$F/100\,mA\,m^{-2}$
100 kHz to 10 GHz	SAR averaged over the body and over any 15-min period	$0.4\,W\,kg^{-1}$
100 kHz to 10 GHz	SAR averaged over any 10 g in the head and foetus and over any 6-min period	$10\,W\,kg^{-1}$
100 kHz to 10 GHz	SAR averaged over any 100 g in the neck and trunk and over any 6-min period	$10\,W\,kg^{-1}$
100 kHz to 10 GHz	SAR averaged over any 100 g in the limbs and over any 6-min period	$20\,W\,kg^{-1}$

- American Conference of Governmental Industrial Hygienists [17]
- National Radiological Protection Board [11]
- International Radiation Protection Association [23].

The available evidence indicates that moderate absorption rates (approximately 1 W/kg) can be tolerated by human beings. Some standards also provide data on maximum allowable partial body exposures and criteria for avoiding RF shocks and burns.

It should be noted that SAR criteria do not apply to exposures at low frequencies (<100 kHz), for which nerve stimulation (shock) occurs, or at frequencies >6 GHz, for which surface heating prevails.

It is most unlikely that GPR radiation levels will approach the permitted levels as the radiated power levels of typical GPR systems are to the rear of an antenna in the region of $nW\,m^{-2}$.

16.3 EMC

Some examples of GPR waveforms and measured spectra as well as typical sources of interference to GPR systems are described in this Section. A typical time domain GPR system transmits a pulse of the form shown in Figure 16.2.

The calculated frequency domain representation of such a pulse repeated at a rate of 1 μs takes the form shown in Figure 16.3 and on an expanded scale in Figure 16.4.

The measured spectrum from a GPR radar with an impulse of 2 ns' duration and amplitude 2.5 V repeated at 1 μs intervals is shown in Figures 16.5 and 16.6.

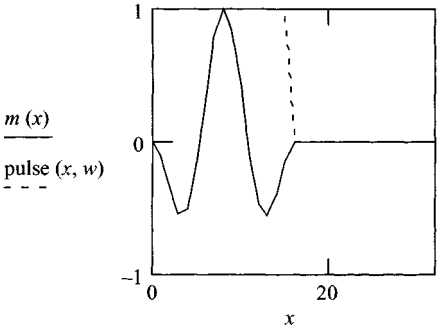

Figure 16.2 Typical radiated GPR pulse waveform

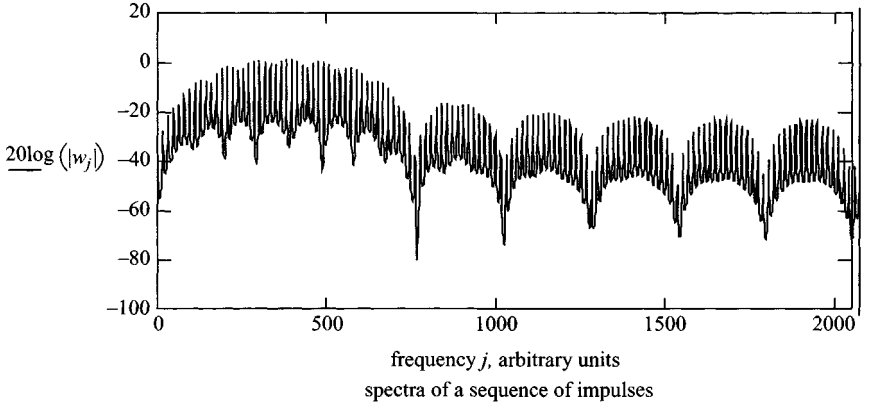

Figure 16.3 Frequency domain representation of repetitive pulse waveform in Figure 16.2

A simple example shows the level of radiated power from a typical GPR system with certain assumptions in terms of antenna efficiency:

Peak voltage applied to the antenna = 10 V for 2 ns duration every 1 μs
Antenna efficiency = 10%
Peak power radiated by the antenna (50Ω) = $0.1(10^2/50)$
Total mean power radiated by antenna, P_{mean} = peak power times the duty factor
$= 0.2 \times 2 \times 10^{-9}/1 \times 10^{-6}$
$= 0.4\,\text{mW}$

This is the power radiated omni-directionally from the antenna. However, the antenna is normally closely coupled into the ground and the sidelobes and backlobes of the antenna are significantly lower than the front lobes. Typically, the backlobe should be less than −40 dB compared with the front lobe on a well designed antenna.

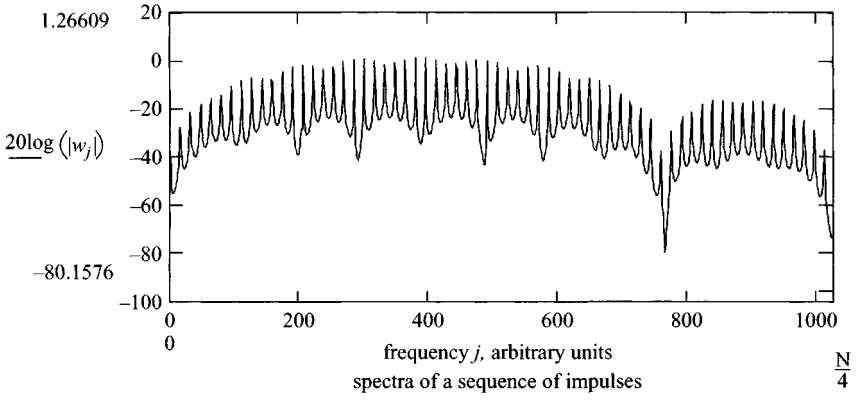

Figure 16.4 Frequency domain representation of repetitive pulse waveform in Figure 16.2 (expanded scale)

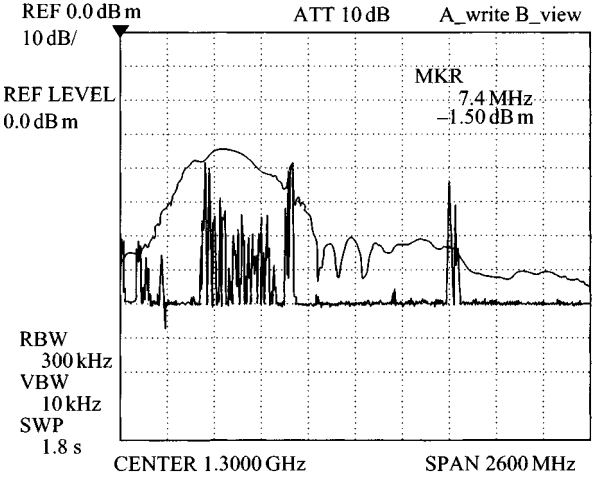

Figure 16.5 Measured spectrum up to 2.6 GHz of 2 ns' duration impulse with measuring antenna facing transmit antenna at a distance of 1 m

The mean power radiated into free space from the rear of the antenna, when on the ground, is

$$P_{rear} = P_{mean} \times 0.01 = 4\,\mu W$$

If we assume that this power is radiated uniformly over a hemisphere in a co-sinusoidal pattern then the power radiated per unit solid angle is given by

$$P_{hemi} = P_{rear} \times 1.6/2\pi = 1\,\mu\text{W per steradian}$$

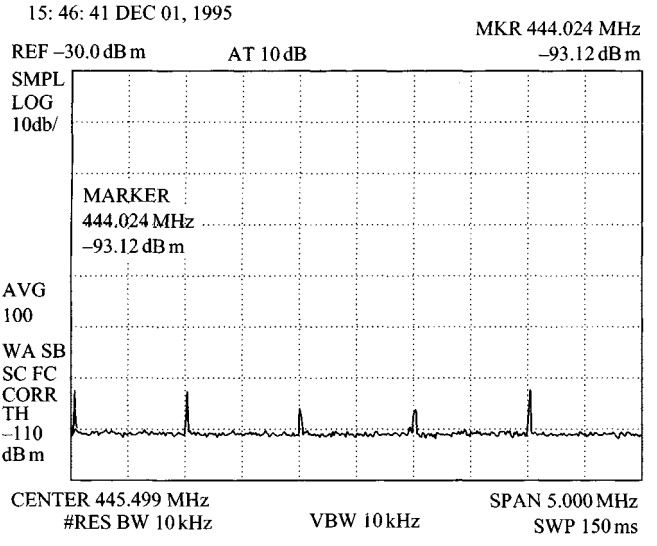

Figure 16.6 Measured spectrum over 10 MHz about 445 MHz of 2 ns' duration impulse with measuring antenna facing transmit antenna at a distance of 1 m

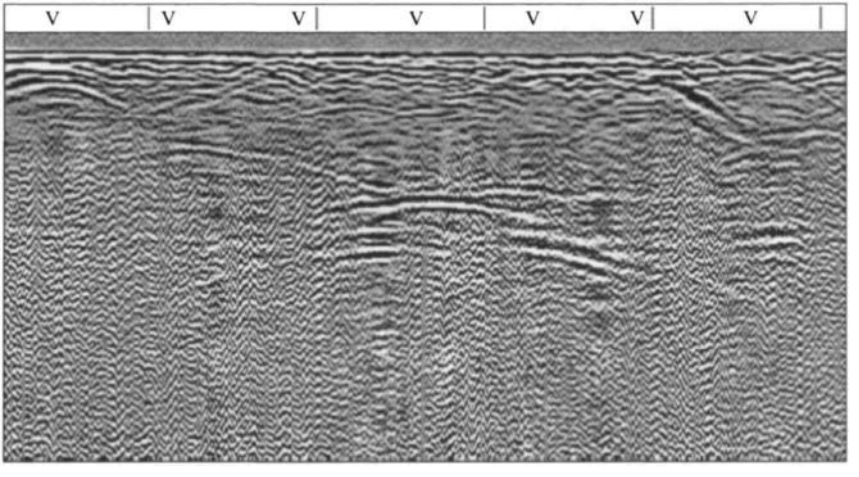

Figure 16.7 Effect of interference by a mobile phone on GPR image

It can thus be seen that the potential for interference by GPR with other users is small given that this is the mean power over the band of interest.

Another more serious issue is the potential for interference by other users, and an example of interference by a mobile phone in close proximity is shown in Figure 16.7.

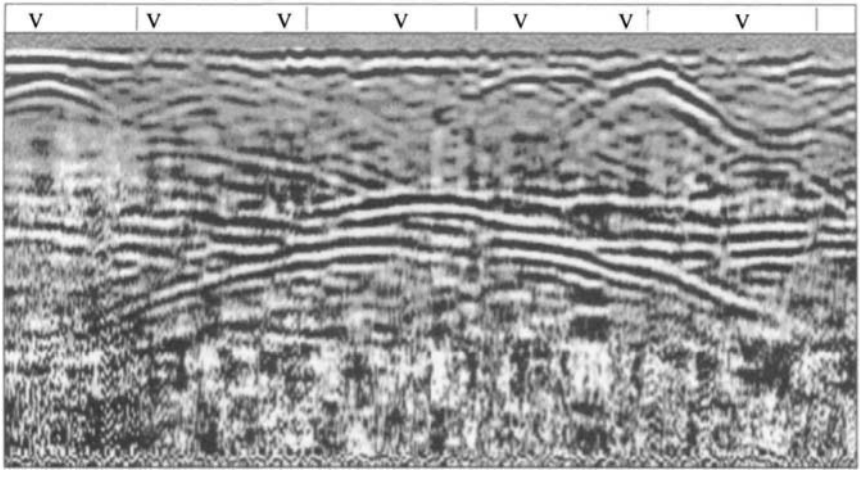

Figure 16.8 Lowpass filtered version of Figure 16.7

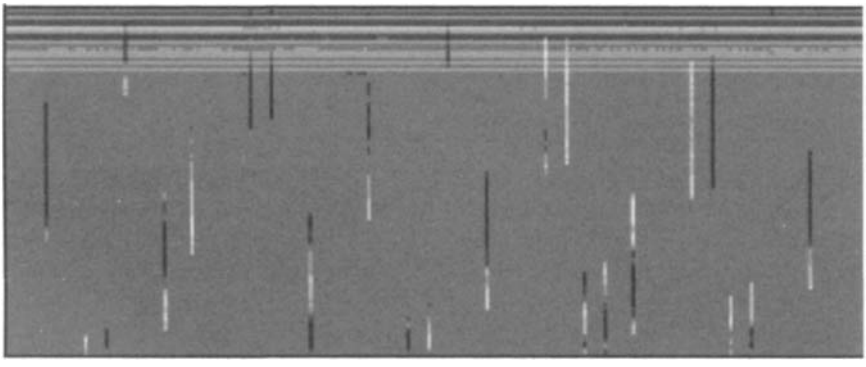

Figure 16.9 Interference by a 1 GHz radar system on a GPR

The interference can be filtered out by suitable lowpass filters, and this is shown in Figure 16.8.

GPR is also vulnerable to interference by conventional radar systems, and an example is shown in Figure 16.9.

16.4 Summary

The relatively low numbers of GPR in use throughout the world suggests that GPR is not a major source of electromagnetic radiation. As most GPR systems radiate into the ground the likelihood of interference is very low. For these reasons the licensing authorities appear to have been persuaded that GPR poses little threat. However, both

the FCC and ETSI will be supervising the use of GPR more strictly in the future, and manufacturers, developers and users should ensure that they comply with all of the statutory requirements.

The vast majority of GPR systems radiate at levels well below the internationally agreed limits for radiological hazard.

Care should be taken by users of GPR that mobile phones and other sources of possible interference do not contaminate the data being gathered, but fairly simple filtering can be used to post-process the data and remove the effects of interference.

16.5 References

[1] OLHOEFT, G. R.: 'Maximizing the information return from ground-penetrating radar', *J. Appl. Geophys.*, 2000, **43**, (2–4), pp. 175–187 (see appendix on cell phone interference)

[2] ANDERSON, D. S., DROCELLA, E. F., JONES, S. K., and SETTLE, M. A.: 'Assessment of compatibility between ultrawideband (UWB) systems and global positioning system (GPS) receivers'. NTIA Special Publication 01-45 (http://www.ntia.doc.gov), 2001

[3] ANDERSON, D. S., DROCELLA, E. F., JONES, S. K., and SETTLE, M. A.: 'Assessment of compatibility between ultrawideband (UWB) systems and global positioning system (GPS) receivers (report addendum)'. NTIA Special Publication 01-47 (http://www.ntia.doc.gov), 2001

[4] BRUNSON, L. K., CAMACHO, J. P., DOOLAN, W. M., HINKLE, R. L., HURT, G. F., MURRAY, M. J., NAJMY, F. A., ROOSA JR., P. C., and SOLE, R. L.: 'Assessment of compatibility between ultrawideband devices and selected federal systems'. NTIA Spec. Pub. 01-43 (http://www.ntia.doc.gov), 2001

[5] HOFFMAN, J. R., COTTON, M. G., ACHATZ, R. J., STATZ, R. N., and DALKE, R. A.: 'Measurements to determine potential interference to GPS receivers from ultrawideband transmission systems'. NTIA Report 01-384 (http://www.ntia.doc.gov), 2001

[6] KISSICK, W. A. (Ed.): 'The temporal and spectral characteristics of ultrawideband signals'. NTIA Report 01-383 (http://www.ntia.doc.gov), 2001

[7] Johns Hopkins University Applied Physics Laboratory, 2001, Final Report, UWB-GPS compatibility analysis project: (available in FCC comments)

[8] NTIA, 2001, NTIA Manual of Regulations & Procedures for Federal Radio Frequency Management (January 2000 Edition with January/May/September 2001 Revisions), US Gov. Printing Office S/N 903-008-00000-8, Washington, DC, and at http://www.ntia.doc.gov

[9] RTCA Special Committee 159: Second interim report to the Department of Transportation, 'Ultra-wideband technology frequency interference effects to global positioning system receivers and interference encounterscenario development'. RTCA Paper Mo. 086–01/PMC-139, 2001, 77 p. +corrigendum (available in FCC comments)

[10] NRPB: 'Electromagnetic fields and the risk of cancer'. Report of an Advisory Group on Non-ionising Radiation, 1992, Doc. NRPB, 3, No. 1

[11] NRPB: 'Restrictions on human exposure to static and time varying electromagnetic fields and radiation: Scientific basis and recommendations for the implementation of the Board's Statement'. Doc. NRPB, 1993, Vol. 4, No. 5, 7. National Radiological Protection Board, Chilton, Didcot, Oxon, UK

[12] FLODERUS, B., PERSSON, T., STENLUND, C., WENNBERG, A., OST, Ä., and KNAVE, B.: 'Occupational exposure to electromagnetic fields in relation to leukaemia and brain tumours: A case-control study in Sweden', *Cancer Causes and Control*, 1993, **4**, pp. 465–476

[13] GUENÉL, P., RASKMARK, P., ANDERSEN, J. B., and LYNGE, E.: 'Incidence of cancer in persons with occupational exposure to electromagnetic fields in Denmark', *Br. J. Ind. Med.*, 1993, **50**, p. 758

[14] TYNES, T., ANDERSEN, A., and LANGMARK, F.: 'Incidence of cancer in Norwegian workers potentially exposed to electromagnetic fields', *Am. J. Epidemiol.*, 1992, **136**, p. 81

[15] FEYCHTING., M., and AHLBOM., A.: 'Magnetic fields and cancer in people residing near Swedish high voltage power lines.' Stockholm, IMM-rapport 6/92, 1992

[16] OLSEN, J. H., NIELSEN, A., and SCHULGEN, G.: 'Residence near high-voltage facilities and risk of cancer in children', *Br. Med. J.*, 1993, **367**, p. 891

[17] ACGIH: 'Annual Report of the Committees on Threshold limit values and biological exposure indices'. American Conference of Governmental Industrial Hygienists, Cincinnati, OH, 1993

[18] ANSI: 'American National Standard Safety levels with respect to human exposure to radio frequency electromagnetic fields, 300 kHz to 100 GHz'. ANSI C95.1-1982, American National Standards Institute, New York, NY

[19] ELDER, J. A., and CAHILL, D. F. (Eds.): 'Biological effects of radiofrequency radiation'. EPA Report No. EPA-600/8-83-026F. US Environmental Protection Agency, Research Triangle Park, NC 27711, 1984

[20] Federal Communication Commission: Notice of Proposed Rule Making, ET Docket 93-62, 58 Federal Register 19,393, 1993

[21] ANSI/IEEE C95.1: 'IEEE Standard for Safety levels with respect to human exposure to radio frequency electromagnetic fields, 3 kHz to 300 GHz'. ANSI/IEEE C95.1-1992 (Revision of ANSI C95.1-1982), Institute of Electrical and Electronics Engineers, Inc., Piscataway, NJ

[22] NCRP: 'Biological effects and exposure criteria for radiofrequency electromagnetic fields'. Report 86, National Council on Radiation Protection and Measurements, Bethesda, MD, 1986

[23] IRPA: 'Electromagnetic fields (300 Hz to 300 GHz), environmental health criteria, 137'. International Radiation Protection Association, World Health Organization, Geneva, Switzerland, 1993

Chapter 17

Bibliography

ANIL, J.: 'Fundamentals of digital image processing' (Prentice Hall, 1989). ISBN 0-13-336165-9

ASTANIN, L. Y., and KOSTYLEV, A. A.: 'Ultra-wideband radar measurements systems'. IEE Radar Sonar Navigation and Avionics Series (IEE, London, 1997)

BARTON, D. K.: 'Radar system analysis' (Artech House Inc, 1986). ISBN 0890060436, 608pp.

BARTON, D. K.: 'Modern radar system analysis' (Artech House, 1988). ISBN 089006170X, 583pp.

BAUM, C. (Ed.): 'The detection and identification of visually obscured targets' (Taylor and Francis, 1998). ISBN 1-56032-533-X

CARIN, L.: 'Synthetic aperture radar for mine detection and identification' (Final progress report 1 Mar 1998–31 Aug 1999). Dept. Electrical Engineering, Duke University, USA, August 1999, 11pp. NTIS ADA370415/XAB

CLOUDE, S.: 'An introduction to electromagnetic wave propagation and antennas' (UCL Press, 1995). ISBN 1-85728-240-X HB (241 PB)

COOK, C. E., and BERNFELD, M.: 'Radar signals, an introduction to theory and application' (Artech House, 1993), 531pp. ISBN 0-89006-733-3.

DANIELS, D. J.: 'Surface penetrating radar' (IEE, 1996), Radar Sonar Navigation and Avionics Series, Vol. 6. ISBN 0 85296 862 0

DUBEY, A. C., CINDRICH, I. *et al.*: Proc. International Society for Optical Engineering Conf. on Detection technologies for mines and minelike targets, Orlando, FL, USA, April 1995. Proc. SPIE, Vol. 2496, USA, 1995. ISBN 0891418528, 1036pp.

DUBEY, A. C., HARVEY, J. F., BROACH, J. T., and DUGAN, R. E. (Eds): 'Detection and remediation technologies for mines and minelike targets V'. Presented at Aerosense 2000, 24–28 April 2000, Orlando, Florida. SPIE, USA ISBN: 0-8194-3664-X, 1564pp.

GALATI, G. (Ed.): 'Advanced radar techniques and systems'. IEE Radar Sonar Navigation and Avionics Series (IEE, London, 1993)

GRIFFITHS, D. H., and KING, R. F.: 'Applied geophysics for geologists and engineers. The elements of geophysical prospecting' (Pergamon Press, 1981, 2nd edn), 230pp.

HARRIS, J. W., and STOCKER, H.: 'Handbook of mathematics and computational science' (Springer-Verlag, 1998). ISBN 0-387-94746-9

HEIMMER, D. H.: 'Near-surface, high resolution geophysical methods for cultural resource management and archaeological investigations'. Geo-Recovery Systems, September 1992, 143pp.

HUNTER, J., ROBERTS, C., and MARTIN, A.: 'Studies in crime' (Batsford, 1996). ISBN 0713479019

KADAR, I.: 'Signal processing, sensor fusion, and target recognition IX' Presented at Aerosense 2000, 24–28 April 2000, Orlando, Florida. SPIE, USA ISBN: 0-8194-3678-X, Vol. 4052, 396pp.

KANASEWICH, E. R.: 'Time sequence analysis in geophysics' (University of Alberta Press, Edmonton, Alberta, Canada, 1975, 3rd edn)

KELLER, G. V., and FRISCHKNECHT, F. C.: 'Electrical methods in geophysical prospecting' (Pergamon Press, Oxford, 1966)

KLEIN, L. A.: 'Sensor and data fusion concepts' (SPIE Press, 1999, 2nd edn). ISBN 0-8194-3231-8

LAHAIE, I. J. (Ed.): 'Ultrawideband radar'. SPIE Vol. 1631, USA, 1992. ISBN 0819407771, 317pp.

NATHANSON, F. E.: 'Radar design principles'. 1996, ISBN 07-046047-7

NGUYEN, C.: 'Subsurface sensing technologies and applications II'. Presented at SPIE's 45th Annual Meeting, 30 July–4 August 2000, San Diego, CA. SPIE, USA ISBN: 0-8194-3774-3, Vol. 4129, 684pp.

ROBINSON, E. A., and TREITEL, S.: 'Geophysical signal analysis' (Prentice Hall Inc, Englewood Cliffs, NJ, 1980), 466pp.

RUCK, G. T.: 'Radar cross section handbook' (Plenum Press, 1970). LCC 68-26774 ISBN 306 30343-4

SHAFER, G. A.: 'Mathematical theory of evidence' (Princeton University Press, USA, 1976). ISBN: 0-691-08175-1, 297pp.

SKOLNIK, M. (Ed.): 'Radar handbook' (McGraw-Hill, 1990, 2nd edn). ISBN 0-07057913-X

TAYLOR, J. D. (Ed.): 'Introduction to ultra-wideband radar systems' (CRC Press, 1995). ISBN 0849344409, 670pp.

VON HIPPEL, A. R.: 'Dielectric materials and applications' (Chapman & Hall, London, 1954). ISBN: 0-89006-805-4, 438pp.

VON HIPPEL, A. R.: 'Dielectrics and waves' (Artech House, 1994). ISBN 0890068038, 284pp.

WAIT, J. R.: 'Electromagnetic probing in geophysics' (Golem Press, Boulder, CO, 1971)

WAIT, J.: 'Introduction to antennas and propagation' (Peter Peregrinus, 1986). ISBN 0-86341-054-5

WEHNER, D. R.: 'High resolution radar'. 1987, ISBN 0-089006-194-7

Glossary of terms

Abbreviation	Description
ABC	absorbing boundary conditions
ACF	auto-correlation function
A-D	analogue to digital
AM	amplitude modulation
AP	anti-personnel
AR	autoregressive
ARMA	autoregressive moving average
AT	anti-tank
B	bandwidth
CCF	crosscorrelation function
CD	compact disc
CMP	common midpoint
CP	circular polarisation
CRP	common reflection point
CW	continuous wave
D-A	digital to analogue
DGPS	differential global positioning system
DMO	depth migration offset
DSP	digital signal processor
E	electric field vector
EC	European Commission
ECCM	electronic counter counter measures
ECM	electronic counter measures
EMC	electromagnetic compatibility
ETSI	European Telecommunication Standards Institute
EU	European Union
FCC	Federal Communication Commission
FDFD	finite difference frequency domain

FDTD	finite-difference time domain
FET	field effect transistor
FFT	fast Fourier transform
FLOPS	floating point operations per second
FM	frequency modulation
FMCW	frequency modulated continuous wave
FT	Fourier transform
GaAs	gallium arsenide
GPR	ground penetrating radar
GPS	global positioning system
H	magnetic field vector
HM	holographic modulation
HP	horizontal polarisation
IEE	Institution of Electrical Engineers
IEEE	Institute of Electrical and Electronic Engineers
IF	intermediate frequency
IFFT	inverse fast Fourier transform
IFT	inverse Fourier transform
INS	inertial navigation system
IR	impulse response
IRA	impulse radiating antenna
IRF	impulse response function
ITU	International Telecommunications Union
JPL	Jet Propulsion Laboratory
LASS	light activated semiconductor switch
LHCP	left-hand circular polarisation
LNA	low noise amplifier
MA	moving average
MAC	mine action centre
MOM	method of moments
MTI	moving target indicator
MUSIC	multiple signal classification
NGO	nongovernmental organisation
NM	noise modulation
NMO	normal moveout
NRPB	National Radiological Board
NTIA	National Telecommunications and Information Administration
PC	personal computer
PCSS	photoconductive semiconductor switch
PIN	P – intrinsic – N
PM	phase modulation
PML	perfectly matched layer
PRBS	pseudo-random binary sequence
PRC	pseudo-random coded

PSD	power spectral density
PVC	polylvinyl chloride
R	range
RAM	radar absorbing material
RF	radio frequency
RHCP	right-hand circular polarisation
ROC	receiver operating characteristic
SAR	synthetic aperture radar
SFCW	step frequency continuous wave
SI	synthesised impulse
SIR	satellite imaging radar
SNR	signal to noise ratio
SPIE	Society of Photonic Instrumentation Engineers
SPM	synthesised pulse modulation
SPR	surface penetrating radar
SRD	system requirements document
TDR	time domain reflectometry
TEM	transverse electromagnetic
TNT	trinitrotoluene
TVG	time varying gain
URD	user requirements doc.
UWB	ultra-wideband
UXO	unexploded ordnance
VCO	voltage controlled oscillator
VIR	video impulse radar
VP	vertical polarisation
VSWR	voltage standing wave ratio

List of symbols

Symbol	Description	Units
c	velocity of light in free space	ms^{-1}
d	depth	m
E	instantaneous electric field component of EM wave	Vm^{-1}
E_0	original electric field component ($e = 0, t = 0$) of EM wave	Vm^{-1}
$E(z,t)$	electric field at z, t of propagating EM wave	Vm^{-1}
f	frequency	Hz
H	instantaneous electric field component of EM wave	Am^{-1}
j	$\sqrt{-1}$	
k	phase constant	
x	Cartesian co-ordinate value	
y	Cartesian co-ordinate value	
z	Cartesian co-ordinate value	
A_r	aperture of receive antenna	m^2
B	bandwidth	Hz
G_r	gain of receive antenna	
G_t	gain of transmit antenna	
P_r	received power	W
P_t	transmitted power	W
q	charge	C
R or r	range of target from transmitter	m
$f(t)$	function of time	
$f(\omega)$	function of frequency	
F	Fourier transform	
F^{-1}	inverse Fourier transform	
N	number of averages	
n	sample number	
α	attenuation constant in nepers	m^{-1}
α'	attenuation constant	dB m^{-1}
β	phase constant	m^{-1}

$\tan\delta$	material loss tangent	
ε	absolute permittivity of medium	Fm^{-1}
ε_0	absolute permittivity of free space	Fm^{-1}
ε_r	relative permittivity of medium	
ε'	real part of permittivity of medium	Fm^{-1}
ε''	imaginary part of permittivity of medium	Fm^{-1}
ε_s	low frequency static permittivity of medium	Fm^{-1}
ε_∞	high frequency infinite permittivity of medium	Fm^{-1}
ε_m	permittivity of medium	Fm^{-1}
ε_w	permittivity of water	Fm^{-1}
η	intrinsic impedance of medium	Ω
λ	wavelength	m
τ	relaxation time of water	s
ω	angular frequency	Hz
μ	permeability of medium	Hm^{-1}
μ_0	absolute permeability of free space	Hm^{-1}
μ_r	relative permeability of medium	
π	pi	
σ_{DC}	DC or ohmic conductivity of medium	Sm^{-1}
σ'	real part of ohmic conductivity of medium	Sm^{-1}
σ''	imaginary part of ohmic conductivity of medium	Sm^{-1}
v	velocity of propagation of EM waves in air	ms^{-1}
v_r	velocity of propagation of EM waves in material	ms^{-1}
δ	loss factor in material	

Index

This page has been reformatted by Knovel to provide easier navigation.

This page has been reformatted by Knovel to provide easier navigation.

This page has been reformatted by Knovel to provide easier navigation.

This page has been reformatted by Knovel to provide easier navigation.

This page has been reformatted by Knovel to provide easier navigation.

This page has been reformatted by Knovel to provide easier navigation.

This page has been reformatted by Knovel to provide easier navigation.

This page has been reformatted by Knovel to provide easier navigation.

This page has been reformatted by Knovel to provide easier navigation.

This page has been reformatted by Knovel to provide easier navigation.

This page has been reformatted by Knovel to provide easier navigation.

This page has been reformatted by Knovel to provide easier navigation.